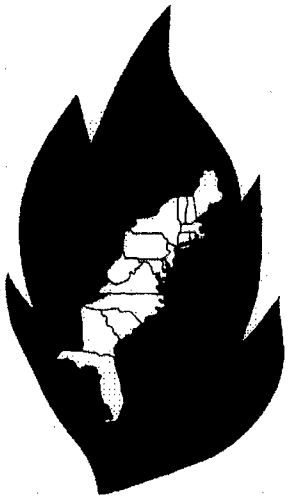
ARO 40373.1-EG-CF

Chemical and Physical Processes of Combustion

The Fall Technical Meeting of the Eastern States Section of the Combustion Institute





DISTRIBUTION STATEMENT A
Approved for Public Release
Distribution Unlimited

North Carolina State University
Raleigh NC
October 10-13, 1999

DTIC QUALITY INSPECTED 4

20001122 129

REPORT DOCUMENTATION PAGE

Form Approved
OMB NO. 0704-0188

Public Reporting burden for this collection of information is estimated to average 1 hour per response, including the time for reviewing instructions, searching existing data sources, gathering and maintaining the data needed, and completing and reviewing the collection of information. Send comment regarding this burden estimates or any other aspect of this collection of information, including suggestions for reducing this burden, to Washington Headquarters Services, Directorate for information Operations and Reports, 1215 Jefferson Davis Highway, Suite 1204, Arlington, VA 22202-4302, and to the Office of Management and Budget, Paperwork Reduction Project (0704-0188,) Washington, DC 20503.

1. AGENCY USE ONLY (Leave Blank)	2. REPORT DATE October 2000	3. REPORT TYPE AND DATES COVERED Final Report

4. TITLE AND SUBTITLE
Chemical and Physical Processes of Combustion

5. FUNDING NUMBERS
DAAD19-99-1-0354

6. AUTHOR(S)
William L. Roberts, principal investigator

7. PERFORMING ORGANIZATION NAME(S) AND ADDRESS(ES)
North Carolina State University
Raleigh, NC 27695-7514

8. PERFORMING ORGANIZATION REPORT NUMBER

9. SPONSORING / MONITORING AGENCY NAME(S) AND ADDRESS(ES)
U. S. Army Research Office
P.O. Box 12211
Research Triangle Park, NC 27709-2211

10. SPONSORING / MONITORING AGENCY REPORT NUMBER
ARO 40373.1-EG-CF

11. SUPPLEMENTARY NOTES
The views, opinions and/or findings contained in this report are those of the author(s) and should not be construed as an official Department of the Army position, policy or decision, unless so designated by other documentation.

12 a. DISTRIBUTION / AVAILABILITY STATEMENT	12 b. DISTRIBUTION CODE
Approved for public release; distribution unlimited.	

13. ABSTRACT (Maximum 200 words)

Experts assembled in the field of combustion science in order to provide a forum for exchange of research results, foster interactions among research groups, and to speed technology transfer.

The Eastern States Section of the Combustion Institute held its Fall Technical Meeting in Raleigh, NC in October 1999. It brought together researchers from government, industry and academia. Combustion science is central to the Army's development of advanced gun, rocket and vehicle propulsion systems.

14. SUBJECT TERMS

15. NUMBER OF PAGES

16. PRICE CODE

17. SECURITY CLASSIFICATION OR REPORT	18. SECURITY CLASSIFICATION ON THIS PAGE	19. SECURITY CLASSIFICATION OF ABSTRACT	20. LIMITATION OF ABSTRACT
UNCLASSIFIED	UNCLASSIFIED	UNCLASSIFIED	UL

NSN 7540-01-280-5500

Standard Form 298 (Rev.2-89)
Prescribed by ANSI Std. 239-18
298-102

DTIC QUALITY INSPECTED 4

PROGRAM CHANGES AND ANNOUNCEMENTS

(Relative to Yellow Program Mailed by Combustion Institute)

Presentations:

1. Paper #28, "A Modeling Study of Benzene Formation in Aliphatic Flames" by C. J. Pope and J. A. Miller, scheduled for Monday, October 11 at 4:40 pm in Session A-2 has been withdrawn.

2. Paper #93, "Sub- and Super-Critical Pyrolysis of Endothermic Fuels" by I. Glassman, J. F. Stewart, and S. P. Zeppieri, scheduled for Wednesday, October 13 at 11:30 am in Session A-5 has been moved to Monday, October 11 at 4:40 pm in Session A-2.

3. Paper #36, "Flame Inhibition by Ferrocene, Carbon Dioxide, and Trifluoromethane Blends: Synergistic and Antagonistic Effects" by G. T. Linteris and M. D. Rumminger, scheduled for Monday, October 11 at 2:30 pm in Session C-2 has been withdrawn.

4. Paper #64, "Fast Chemical Reaction Effect Upon Diffusivity" by W. T. Ashurst, N. N. Najm, and P. H. Paul scheduled for Tuesday, October 12 at 2:30 in Session A-4 has been withdrawn.

5. Paper #108, "Further Studies of NOX-Sensitized Oxidations at Low Temperature" by M. Jazbec, J. H. Bromly, F. J. Barnes, and B. S. Haynes has been added to the program and will be presented on Wednesday, October 13 at 11:30 am in Session A-5.

Banquet

The Meeting Banquet will be held on Tuesday Evening at the Velvet Cloak Inn with a "no-host" reception starting at 6:00 pm and dinner being served at 7:00 pm.

Lab Tour

A Tour of the Applied Energy Research Laboratory at North Carolina State University will be arranged starting at 1:30 pm on Wednesday, October 13. Transportation will be provided from the meeting hotels. A sign up sheet will be available during the meeting.

Chemical and Physical Processes of Combustion

The Fall Technical Meeting of the Eastern States Section of the Combustion Institute



North Carolina State University
Raleigh NC
October 10-13, 1999

Welcome

Welcome to the 1999 Fall Technical Meeting of the Eastern States Section of the Combustion Institute! We hope that you find the meeting productive and enjoyable. Our section's format consciously encourages presentation and discussion of new results, especially by promoting the participation of student presenters.

In addition to the technical program, we have also arranged for the traditional welcoming reception on Sunday night; a barbeque lunch (North Carolina BBQ!) and reception on Monday; and the traditional banquet. These events should help us maintain the collegial atmosphere that we value so much at our Fall Technical Meetings.

We are grateful for local sponsorship of this meeting by North Carolina State University and for all the contributions of time, facilities, and other resources toward the success of this meeting.

The 28th International Symposium on Combustion will be held on July 30-August 4, 2000, in Edinburgh, Scotland (http://www.efm.leeds.ac.uk/edin2000/). As in 1998, we will not have a 2000 Fall Technical Meeting. Instead, in the spring of 2001 we will participate at Berkeley in a 2nd Joint Meeting of the US sections of the Combustion Institute. This event is following up on the great success of the first joint meeting, hosted earlier this year at The George Washington University by our section. Our next Fall Technical Meeting then will be in the fall of 2001. You can keep up-to-date by checking periodically on our section's Web page, http://www.ecs.umass.edu/ESSCI/.

Bill Pitts, Program Chair
Phil Westmoreland, Papers Chair
Bill Roberts, Local Arrangements Chair
Houston Miller, Arrangements Chair
October 1999

Executive Committee of the Section, 1997-1999

Chair:	Frederick C. Gouldin, *Cornell University*
Vice-Chair / Chair-Elect:	Meredith B. "Med" Colket III, *United Technologies Research Center*
Secretary:	W. Terry Rawlins, *Physical Sciences, Inc.*
Treasurer:	Clarke E. Hermance, *University of Vermont*
Program Chair:	William M. Pitts, *National Institute of Standards and Technology, BFRL*
Papers Chair:	Phillip R. Westmoreland, *Univ. Massachusetts Amherst*
Arrangements Chair:	J. Houston Miller, *The George Washington University*
Ex officio members:	Baki Cetegen, *University of Connecticut*
	Anthony M. Dean, *Exxon Research & Engineering*
	Michael A. Delichatsios, *Renewable Resources Associates*
	Richard G. Gann, *National Institute of Standards and Technology BFRL*
	K. Kailasanath, *Naval Research Laboratory*
	Lisa D. Pfefferle, *Yale University*
	William L. Roberts, *North Carolina State University*
	Mitchell D. Smooke, *Yale University*
	Stephen R. Turns, *The Pennsylvania State University*
	M. J. "Judy" Wornat, *Princeton University*

General Program

Sunday, October 10, 1999		
5:00- 8:00 PM	Registration and Reception, Velvet Cloak Inn	

Monday, October 11, 1999		
8:15 AM	Welcoming Remarks	
8:30 AM	I. Invited Speaker: "Combustion 2000 - Burning Coal in the 21st Century," Daniel J. Seery, United Technologies Research Center; Chair: M. B. Colket, United Technologies Research Center	p. 1
9:30 AM	Sessions A-1, B-1, C-1	
12:10 PM	Barbeque lunch (catered)	
1:30 PM	II. Invited Speaker: "Computations of Turbulent Combustion with Detailed Chemistry," Stephen B. Pope; Chair: P. R. Westmoreland, University of Massachusetts	p. 9
2:30 PM	Sessions A-2, B-2, C-2	

Tuesday, October 12, 1999		
8:30 AM	III. Invited Speaker: "Ether Additives for Reduced Diesel PM: Chemistry and Vehicle Emissions," M. Matti Maricq, Ford Motor Company; Chair: W. M. Pitts, NIST	p. 12
9:30 AM	Sessions A-3, B-3, C-3	
1:30 PM	IV. Invited Speaker: "Chemical Fire Suppressants: How Can We Replace Halon?" James W. Fleming, Naval Research Laboratory; Chair: P. R. Westmoreland, University of Massachusetts	p. 16
2:30 PM	Sessions A-4, B-4, C-4	
5:30 PM	Business meeting	
6:00 PM	Social and banquet, Velvet Cloak Inn	

Wednesday, October 13, 1999		
8:30 AM	V. Invited Speaker: "Flow Dynamics of Buoyant Plumes and Diffusion Flames," Baki M. Cetegen, University of Connecticut; Chair: J. H. Miller, George Washington University	p. 24
9:30 AM	Sessions A-5, B-5, C-5	

Monday morning, October 11, 1999 **Page**

8:15 AM **Welcoming Remarks**

8:30 AM **I. Invited Speaker: "Combustion 2000 - Burning Coal in the 21st Century," Daniel J. Seery, United Technologies Research Center;** 1

Chair: M. B. Colket, United Technologies Research Center

Session A-1 **Theoretical Thermodynamic and Kinetics Studies** Chair: H. Wang, University of Delaware			
9:30	1.	"An Evaluation of Acetylene + O_2 Oxidation System: HCCH+$O_2(^3\Sigma)$, HCCH + $O_2(^1\Delta)$ and Vinylidene + $O_2(^3\Sigma)$ via Isomerization of HCCH," **C. Sheng and J. W. Bozzelli, New Jersey Institute of Technology**	33
9:50	2.	"Reaction Pathways and Kinetic Analysis on Methyl *tert*-Butyl Ether Pyrolysis and Oxidation Reactions," **C-J. Chen and J. W. Bozzelli, New Jersey Institute of Technology**	37
10:10		Break	
10:30	3.	"*Ab initio* Calculations and Thermochemical Analysis on Cl Atom Abstractions of Chlorine from Chlorocarbons and the Reverse Alkyl Abstractions: $Cl_2 + R\cdot <=> Cl\cdot + RCl$," **J. W. Bozzelli and J. Lee, New Jersey Institute of Technology; J. P. Sawerysyn, University of Lille, France**	41
10:50	4.	"Thermochemical Properties of Methyl and Chloro-Methyl Oxychlorides and Reaction of Methyl Radical with ClO," **D. Jung, C.-J. Chen, and J. W. Bozzelli, New Jersey Institute of Technology**	45
11:10	5.	"Modeling Study on Thermal Oxidation of 1,3-Hexachlorobutadiene at 773-1373K," **J. W. Bozzelli and L. Zhu, New Jersey Institute of Technology; J-P. Sawerysyn, University of Lille, France**	49
11:30	6.	"Theoretical Study on the Unimolecular Decomposition of c-C_5H_6 and c-C_5H_5: *Ab Initio* MO/Statistical Theory Study," **L. V. Moskaleva, L. K. Madden, and M. C. Lin, Emory University**	53
11:50	7.	"Theoretical Study of H-for-X Substitution in the H + C_6H_5X (X = D and CH_3) Reactions," **I. V. Tokmakov and M. C. Lin, Emory University**	57
12:10		Adjourn, Lunch	

Monday morning, October 11, 1999 **Page**

8:15 AM **Welcoming Remarks**

8:30 AM **I. Invited Speaker: "Combustion 2000 - Burning Coal in the 21st Century," Daniel J. Seery, United Technologies Research Center;** 1

Chair: M. B. Colket, United Technologies Research Center

Session B-1 **Experimental Diagnostics** Chair: S. G. Buckley, University of Maryland			
9:30	8.	"Combining Two Tomographic Inversion Methods to Reconstruct a Complex Concentration Field," **M. Y. Feng and F. C. Gouldin, Cornell University**	61
9:50	9.	"Application of Optical Flow Velocimetry in Turbulent Flows," **J. Fielding and M. B. Long, Yale University**	65
10:10		Break	
10:30	10.	"A Novel Method for Non-Intrusive Temperature Measurements in High Pressure Combustors," **M. S. Brown, Metrolaser Inc.; Y. Li and W. L. Roberts, North Carolina State University**	69
10:50	11.	"Measurement of Species and Temperature Using Difference Raman Scattering," **A. M. Schaffer, R. K. Mohammed, M. B. Long, and M. D. Smooke, Yale University**	73
11:10	12.	"Ultrafast Imaging of a Gas Turbine Spark Igniter," **J. R. Gord, Air Force Research Laboratory; G. J. Fiechtner and K. D. Grinstead, Jr., Innovative Scientific Solutions, Inc.; M. J. Cochran and J. R. Frus, Unison Industries**	77
11:30	13.	"Temperature Measurements in Ar-H_2 DC-Arc Plasmas Utilized in Thermal Spray Processing," **S. Y. Semenov and B. M. Cetegen, University of Connecticut**	81
11:50	14.	"Obtaining and Interpreting Near-Infrared Wavelength Modulation Absorption Signals from Hot Fire Gases: Practical Issues," **L. G. Blevins and B. W. Peterson, NIST**	85
12:10		Adjourn, Lunch	

Monday morning, October 11, 1999 **Page**

8:15 AM **Welcoming Remarks**

8:30 AM **I. Invited Speaker: "Combustion 2000 - Burning Coal in the 21st Century," Daniel J. Seery, United Technologies Research Center;** 1

Chair: M. B. Colket, United Technologies Research Center

Session C-1 **Fire and Water Mist** Chair: C. R. Kaplan, Naval Research Laboratory			
9:30	15.	"Mine Fire Detection in the Presence of Diesel Emissions," **J. C. Edwards, R. A. Franks, G. F. Friel, C. P. Lazzara, and J. J. Opferman, National Institute for Occupational Safety and Health**	89
9:50	16.	"Window Breakage of Multi-Pane Glazing Due to Radiant Exposure," **M. S. Klassen, J. A. Sutula, M. M. Holton, and R. J. Roby, Combustion Science & Engineering, Inc.; T. Izbicki, Schirmer Engineering Corporation**	93
10:10		Break	
10:30	17.	"Simulating Fire Whirls - Inviscid Swirl and Buoyancy," **F. Battaglia, R. G. Rehm, and H. R. Baum, NIST**	97
10:50	18.	"Progress Towards a Computational Tool for the Study of Fire Suppression in a Complex Geometry," **K. Prasad, Science Application International Corporation, VA; G. Patnaik and K. Kailasanath, Naval Research Laboratory**	101
11:10	19.	"Inhibition of Premixed Methane-Air Flames by Water Mist," **S. P. Fuss, D. J. Dye, B. A. Williams, and J. W. Fleming, Naval Research Laboratory**	105
11:30	20.	"Water Mist Suppression of Non-Premixed Counterflow Flames," **E. J. P. Zegers, B. A. Williams, R. S. Sheinson, and J. W. Fleming, Naval Research Laboratory**	109
11:50	21.	"Extinction of Counterflow Diffusion Flames with Fine-Water Droplets," **A. K. Lazzarini, A. M. Lentati, and H. K. Chelliah, University of Virginia**	113
12:10		Adjourn, Lunch	

Monday afternoon, October 11, 1999 **Page**

1:30 PM **II. Invited Speaker: "Computations of Turbulent Combustion with Detailed Chemistry," Stephen B. Pope;** 9

Chair: P. R. Westmoreland, University of Massachusetts

Session A-2 **Detailed Chemical Kinetic Modeling** Chair: F.C. Gouldin, Cornell University			
2:30	22.	"A Computational Study of Dry CO/O_2 Opposed-Jet Diffusion Flame and Its Flammability Limits," **F. C. Frate, Case Western Reserve University; H. Bedir, Bogazici University, Turkey; J. S. T'ien, Case Western Reserve University**	117
2:50	23.	"Destruction of Flame Generated NO Near a Platinum Surface," **N. Khadiya and N. G. Glumac, Rutgers University**	121
3:10		Break	
3:30	24.	"Improving Kinetic Models for Ethylene Flat Flames," **T. Carrière and P. R. Westmoreland, University of Massachusetts**	125
3:50	25.	"A Comprehensive Mechanism of C_2H_x and C_3H_x Fuel Combustion," **H. Wang, A. Laskin, and Z. M. Djurisic, University of Delaware; C. K. Law, S. G. Davis, and D. Zhu, Princeton University**	129
4:10	26.	"On the Structure of n-Heptane/Air Partially Premixed Flames Computed by Using a Detailed Reaction Mechanism," **H. S. Xue and S. K. Aggarwal, University of Illinois at Chicago**	133
4:30	27.	"Detailed Kinetic Modeling of Benzene and Toluene Combustion," **H. Wang and Z. M. Djurisic, University of Delaware**	137
4:50	28.	"A Modeling Study of Benzene Formation in Aliphatic Flames," **C. J. Pope and J. A. Miller, Sandia National Laboratories**	141
5:10	28a.	"Sub- and Super-Critical Pyrolysis of Endothermic Fuels," **I. Glassman, J. F. Stewart, and S. P. Zeppieri, Princeton University**	145
5:30		Adjourn	

Monday afternoon, October 11, 1999			Page
1:30 PM		**II. Invited Speaker: "Computations of Turbulent Combustion with Detailed Chemistry," Stephen B. Pope;** Chair: P. R. Westmoreland, University of Massachusetts	9
Session B-2 **Practical Combustion Systems** Chair: M. R. Hajaligol, Philip Morris, USA			
2:30	29.	"Unmixed Combustion: An Alternative to Fire," **R. K. Lyon, P. J. Garthier, and J. A. Cole, Energy and Environmental Research Corporation**	149
2:50	30.	"Adsorption of Mercury on Coal Flyash," **S. D. Serre and G. D. Silcox, University of Utah**	153
3:10		Break	
3:30	31.	"Interactions Between Lead Vapor and Sorbents at High Temperatures," **S. B. Davis and J. O. L. Wendt, University of Arizona; W. P. Linak, U. S. Environmental Protection Agency**	157
3:50	32.	"On the Performance Estimates of Pulse Detonation Engines," **K. Kailasanath and G. Patnaik, Naval Research Laboratory**	160
4:10	33.	"Synthesis of Unagglomerated, Non-Oxide Nanophase Powders in a Turbulent Jet Flame," **L. J. Rosen, Z. Sun, and R. L. Axelbaum, Washington University in St. Louis**	164
4:30	34.	"Testing and Modeling of a Plasma Torch Reactor for Destruction of Navy Shipboard Solid Waste," **S. H. Peterson, D. A. Counts, R. V. Richard, and E. L. Keating, Geo-Centers, Inc.; B. D. Sartwell, Naval Research Laboratory; T. Marino, J. W. Cofield, and E. E. Nolting, Naval Surface Warfare Center**	168
4:50	35.	"Light-Scattering Measurements of Morphologically Evolving Flame-Synthesized Oxide Aggregates," **U. O. Koylu, Florida International University; Y. Xing and D. E. Rosner, Yale University**	172
5:10		Adjourn	

Monday afternoon, October 11, 1999			Page
1:30 PM		**II. Invited Speaker: "Computations of Turbulent Combustion with Detailed Chemistry," Stephen B. Pope;** Chair: P. R. Westmoreland, University of Massachusetts	9
Session C-2 **Inhibition and Extinguishment** Chair: R. G. Gann, NIST			
2:30	36.	"Flame Inhibition by Ferrocene, Carbon Dioxide, and Trifluoromethane Blends: Synergistic and Antagonistic Effects," **G. T. Linteris, NIST; M. D. Rumminger, Sandia National Laboratory**	176
2:50	37.	"Equivalency of the Rankings of Inhibitor Effectiveness for Combustion of Hydrocarbon Fuels," **V. Babushok, W. Tsang, and W. Grosshandler, NIST**	180
3:10		Break	
3:30	38.	"An Investigation of Extinguishment by Thermal Agents Using Detailed Chemical Kinetic Modeling of Opposed Flow Diffusion Flames," **W. M. Pitts and L G. Blevins, NIST**	184
3:50	39.	"Effect of Dilution on Extinction Limits of Surface Interacting Diffusion Flames with Detailed Chemistry and Transport," **M. Gummalla and D. G. Vlachos, University of Massachusetts, Amherst; M. A. Delichatsios, Renewable Resources Associates**	188
4:10	40.	"Unsteady Extinction Behavior of Counterflow Diffusion Flames: Experiments and Modeling," **V. S. Santoro, A. Liñán, and A. Gomez, Yale University**	192
4:30	41.	"Vortex Injection of Noble Gases in an Opposed-Jet Burner," **G. J. Fiechtner, Innovative Scientific Solutions, Inc.; J. R. Gord, Air Force Research Laboratory; C. D. Carter, K. D. Grinstead, Jr., and V. R. Katta, Innovative Scientific Solutions, Inc.; P.-H. Renard and J. C. Rolon, Laboratoire d'Énergétique Moléculaire et Macroscopique, France**	196
4:50	42.	"Flow Field Considerations for Counterflow Burners," **M. P. Davis, J. W. Fleming, B. A. Williams, and H. D. Ladouceur, Naval Research Laboratory**	200
5:10		Adjourn	

Tuesday morning, October 12, 1999			**Page**
8:30 AM		**III. Invited Speaker: "Ether Additives for Reduced Diesel PM: Chemistry and Vehicle Emissions," M. Matti Maricq, Ford Motor Company;** Chair: W. M. Pitts, NIST	12
Session A-3 **Ignition** Chair: L. D. Pfefferle, Yale University			
9:30	43.	"Experimental Observation of the Formation and Development of a Laser Ignition Kernel," **T. X. Phuoc and F. White, Federal Energy Technology Center**	205
9:50	44.	"Preliminary Test of Flame Kernel-Vortex Interaction," **Y. Xiong and W. L. Roberts, North Carolina State University**	209
11:10		Break	
10:30	45.	"Non-Premixed Ignition of n-Heptane and iso-Octane in a Laminar Counterflow," **J. D. Blouch and C. K. Law, Princeton University**	213
10:50	46.	"Development of an Analytical Criterion for the Ignition of Premixed Alkane/Air Mixtures Near Platinum Surfaces," **P. Aghalayam and D. G. Vlachos, University of Massachusetts Amherst**	217
11:10	47.	"Investigation of the Effect of Additives on the Composite Ignition Delay of JP-7 and JP-8," **D. C. Kirk, J. L. Graham, and S. S. Sidhu, University of Dayton Research Institute; L. Q. Maurice, Air Force Research Laboratory**	221
11:30	48.	"Measurement of Ignition Delay Time of PMMA Spheres in Reduced Gravity," **J. Conley, M. Hillen, B. Dericks, S. Shaw, W. Abraham, and J. C. Chen, Rowan College**	225
11:50	49.	"Controlling the Self-Ignition Behavior of Silane," **W. Tsang and V. Babushok, NIST**	229
12:10		Adjourn, Lunch	

Tuesday morning, October 12, 1999			**Page**
8:30 AM		**III. Invited Speaker: "Ether Additives for Reduced Diesel PM: Chemistry and Vehicle Emissions," M. Matti Maricq, Ford Motor Company;** Chair: W. M. Pitts, NIST	12
Session B-3 **Diffusion Flames** Chair: K. M. Lyons, North Carolina State University			
9:30	50.	"NO_2 Emission from Burke-Schumann Flames," **J. E. Navedo and R.-H. Chen, University of Central Florida**	233
9:50	51.	"NO Emission Indices From Time-Varying and Steady Methane-Air Jet Diffusion Flames," **E. M. Wilson and J. H. Miller, George Washington University**	237
10:10		Break	
10:30	52.	"A Flamelet-Based Approach for Direct Numerical Simulation of Laminar Methane-Air Jet Diffusion Flame Structure," **A. Trouvé, George Washington University; D. D. Myre, U. S. Naval Academy; C. Mavriplis and J. H. Miller, George Washington University**	241
10:50	53.	"Spectral Element Direct Numerical Simulations of Laminar Diffusion Flames," **A. Tanborn, University of Maryland Baltimore County; C. Mavriplis, and J. H. Miller, George Washington University**	245
11:10	54.	"Experimental Computational Study of Coflow Laminar Diffusion Flames in a Microgravity Environment," **K. T. Walsh, J. Fielding, M. B. Long, and M. D. Smooke, Yale University**	249
11:30	55.	"Simultaneous PIV and OH-PLIF Measurements in an Unsteady Counterflow Propane-Air Diffusion Flame," **E. J. Welle and W. L. Roberts, North Carolina State University; C. D. Carter, Innovative Scientific Solutions, Inc.; J. M. Donbar, Wright-Patterson Air Force Base**	253
11:50	56.	"Computational and Experimental Study of Ammonium Perchlorate Diffusion Flames," **M. D. Smooke, Yale University; R. A. Yetter, Princeton University; T. P. Parr and D. M. Hanson-Parr, Naval Air Warfare Center**	257
12:10		Adjourn, Lunch	

Tuesday morning, October 12, 1999			**Page**
8:30 AM		**III. Invited Speaker: "Ether Additives for Reduced Diesel PM: Chemistry and Vehicle Emissions," M. Matti Maricq, Ford Motor Company;** Chair: W. M. Pitts, NIST	12

Session C-3 **Solid Fuels and Processes** Chair: R. S. Miller, Clemson University			
9:30	57.	"Thermo-Chemical Conversion of the Intermediates of Biomass Pyrolysis," **T. Fisher, M. R. Hajaligol, B. Waymack, and D. Kellogg, Philip Morris USA**	261
9:50	58.	"Pyrolysis and Oxidation of Polyethylene in a Steady State Flow Reactor," **B.-K. Park and J. W. Bozzelli, New Jersey Institute of Technology**	265
10:10		Break	
10:30	59.	"Competitive Chlorination of Benzene and Phenol over Model Fly Ash Surfaces," **P. Edwards, R. Striebich, and S. Sidhu, University of Dayton Research Institute**	269
10:50	60.	"Chlorination of Raw Meal Organics in Cement Kiln Preheat Zone," **N. Kasti, S. Sidhu, and R. Striebich, University of Dayton Research Institute**	273
11:10	61.	"Characterization of Chars from Poly-Phenolic Compounds," **R. Sharma, M. R. Hajaligol, P. Martoglio, J. Wooten, and V. Baliga, Philip Morris USA**	277
11:30	62.	"Pyrolysis Kinetics of Cellulosic Materials," **B. Waymack, M. R. Hajaligol, T. Fisher, Philip Morris USA**	281
11:50	63.	"Evaluation and Comparison of Heat of Combustion Value and Fuel Test Data for a Synthetic Refuse-Derived Fuel," **S. S. Thipse and C. Sheng, New Jersey Institute of Technology**	285
12:10		Adjourn, Lunch	

Tuesday afternoon, October 12, 1999 **Page**

1:30 PM **IV. Invited Speaker: "Chemical Fire Suppressants: How Can We Replace Halon?" James W. Fleming, Naval Research Laboratory;** 16

Chair: P. R. Westmoreland, University of Massachusetts

Session A-4 **Reaction Rates** Chair: E. R. Ritter, Villanova			
2:30	64.	"Fast Chemical Reaction Effect Upon Diffusivity," **W. T. Ashurst, H. N. Najm, and P. H. Paul, Sandia National Laboratories**	289
2:50	65.	"Reaction of Unimolecular Dissociation of Formyl Radical, HCO -> H+CO, Studied Over 1 - 100 Bar Buffer Gas Pressure Range," **L. N. Krasnoperov and E. N. Chesnokov, NJIT**	293
3:10		Break	
3:30	66.	"Kinetic and Mechanistic Studies of the Reaction of Hydroxyl Radicals with Trichloroethylene," **L. B. Tichenor, A. El-Sinawi, T. Yamada, and P. H. Taylor, University of Dayton Research Institute; J. Ping, X. Hu, and P. Marshall, University of North Texas**	296
3:50	67.	"Kinetics of Radical-Radical Reactions: $C_2H_5 + C_2H_5$, $C_2H_5 + CH_3$, and $C_3H_5 + CH_3$," **V. D. Knyazev, E. Shafir, and I. R. Slagle, Catholic University of America**	300
4:10	68.	"The Reaction of C_6H_5 with CO: Kinetic Measurement and Theoretical Correlation with the Reverse Process," **G.-J. Nam, W. Xia, J. Park, and M. C. Lin, Emory University**	304
4:30	69.	"Experimental and Theoretical Studies of the $C_6H_5 + C_6H_6$ Reaction," **J. Park, S. Burova, A. S. Rodgers, and M. C. Lin, Emory University**	308
4:50	70.	"Kinetic Study on Vinyl Radical Addition to Chloroethene," **T. Yamada, M. Steiger, and P. H. Taylor, University of Dayton Research Institute; J. W. Bozzelli, NJIT**	312
5:10	71.	"Unimolecular Reactions of *o*-C_6H_4: the Significant Effect of Isomerization on the Decomposition Process," **L. V. Moskaleva, L. K. Madden, and M. C. Lin, Emory University**	316
5:30		Business meeting	
6:00		Banquet	

Tuesday afternoon, October 12, 1999 **Page**

1:30 PM **IV. Invited Speaker: "Chemical Fire Suppressants: How Can We Replace Halon?" James W. Fleming, Naval Research Laboratory;** 16

Chair: P. R. Westmoreland, University of Massachusetts

Session B-4 **Soot** Chair: J. H. Miller, George Washington University:			
2:30	72.	"Application of Laser Induced Incandescence to the Detection of Soot Yields in Combustion Test Facilities," **W. T. Rawlins, B. L. Upschulte, P. A. Mulhall, K. R. McManus, J. H. Frank, E. T. Wetjen, and M. G. Allen, Physical Sciences, Inc.; C. Wey, Dynacs, Inc.; M. J. Rabinowitz, NASA Glenn Research Ctr**	320
2:50	73.	"A Simple Two-Angle Laser-Scattering Technique for Characterization of Soot in Flames," **U. O. Koylu, Florida International University**	324
3:10		Break	
3:30	74.	"The Shock Tube as a Device for Examining Particulate Emissions from the Combustion of Alternative Diesel Fuels," **J. L. Graham, D. C. Kirk, R. C. Striebich, and S. S. Sidhu, University of Dayton Research Institute**	328
3:50	75.	"Experimental Study of Nonfuel Hydrocarbons and Soot in Coflowing Partially Premixed Ethylene/Air Flames," **C. S. McEnally and L. D. Pfefferle, Yale University**	332
4:10	76.	"Sooting Characteristics of Normal and Inverse Diffusion Flames," **C. R. Kaplan and K. Kailasanath, Naval Research Laboratory**	336
4:30	77.	"Growth of Soot Particulates in Laminar, Premixed Flames," **M. Liscinsky, M. Colket, B. True, R. Hall, and A. Bhargava, United Technologies Research Center**	340
4:50	78.	"Towards Quantitative Modeling of Soot Formation in Coflow Diffusion Flames," **M. D. Smooke, Yale University; M. B. Colket and R. J. Hall, United Technologies Research Center**	344
5:10	79.	"Calculations of Soot Aggregate Growth and Oxidation Using a Sectional Size Representation," **R. J. Hall and M. B. Colket, United Technologies Research Center**	348
5:30		Business meeting	
6:00		Banquet	

Tuesday afternoon, October 12, 1999 **Page**

1:30 PM **IV. Invited Speaker: "Chemical Fire Suppressants: How Can We Replace Halon?" James W. Fleming, Naval Research Laboratory;** 16
Chair: P. R. Westmoreland, University of Massachusetts

Session C-4 **Partially Premixed and Premixed Flames** Chair: L. G. Blevins, NIST			
2:30	80.	"Preferential-Diffusion Effects on Premixed Hydrogen-Fueled Flames: Measurements and Predictions," **O. C. Kwon and G. M. Faeth, University of Michigan**	351
2:50	81.	"Temperatures of Positively and Negatively Stretched Flames," **K. Yamamoto, Toyohashi University of Technology, Japan; S. Ishizuka, Hiroshima University, Japan**	355
3:10		Break	
3:30	82.	"Burning Velocity Measurements in Micro-Gravity Conditions," **M. Ulinski, Z. Li, M. Elia, C. Fletcher, and M. Metghalchi, Northeastern University**	359
3:50	83.	"On the Establishment of Stationary Flame Balls," **L. He, S. D. Tse, and C. K. Law, Princeton University**	363
4:10	84.	"On the Branched-Chain Mechanism of Hydrogen-Chlorine Reactions: Laminar Flame Speed Experiments and Kinetic Modeling of $H_2/Cl_2/N_2$ Mixtures," **J. C. Leylegian and C. K. Law, Princeton University; H. Wang, University of Delaware**	367
4:30	85.	"Impact of Hydrogen-Doping on Lean-Premixed Methane Flame Stability," **Y. Cong and G. S. Jackson, Univ. of Maryland**	371
4:50	86.	"Modified Form of the Equation of Motion and Its Solution for Laminar Flow Over Flat Plate and Through Circular Pipes and The Modified Helmholtz Vorticity Equation," **S. H. Sohrab, Northwestern University**	375
5:10	87.	"Numerical Simulation of Acoustic-Flame Interactions in a One-Dimensional Tube," **A. A. Thaker and H. K. Chelliah, University of Virginia**	379
5:30		Business meeting	
6:00		Banquet	

Wednesday morning, October 13, 1999 **Page**

8:30 AM **V. Invited Speaker: "Flow Dynamics of Buoyant Plumes and Diffusion Flames," Baki M. Cetegen, University of Connecticut;** 24

Chair: J. H. Miller, George Washington University

Session A-5 **Flow Reactor Studies** Chair: J. W. Bozzelli, New Jersey Institute of Technology			
9:30	88.	"Computational and Experimental Study of Coflowing Partially Premixed Methane/Air Flames," **B. A. V. Bennett, M. D. Smooke, C. S. McEnally, and L. D. Pfefferle, Yale University**	383
9:50	89.	"Effects of Reaction Kinetics and Heat Transfer on Combustion Oscillation of Methane in Perfectly Stirred Reactor," **M. T. McGarry and H. Wang, University of Delaware**	387
10:10		Break	
10:30	90.	"Thermal Decomposition of Dichlorofluoromethane: An Experimental and Modeling Study," **M. A. Smith and E. R. Ritter, Villanova University**	391
10:50	91.	"The Oxidation of Iso-Octane in the Intermediate Temperature Regime Under Both Lean and Diluted Stoichiometric Conditions," **J.-S. Chen and T. A. Litzinger, The Pennsylvania State University; H. J. Curran, Lawrence Livermore National Laboratory**	395
11:10	92.	"De Novo Synthesis Mechanism of Polychlorinated Dibenzofurans from Polycyclic Aromatic Hydrocarbons and Characteristic Isomers of Polychlorinated Napthalenes," **F. Iino, University of Tokyo, Japan; T. Imagawa and M. Takeuchi, National Institute for Resources and Environment, Japan; M. Sadakata, University of Tokyo, Japan; R. Weber, Ishikawajima-Harima Heavy Industries Co., Ltd., Japan**	399
11:30	93.	"Further Studies of NO_x-Sensitised Oxidations at Low Temperature," **Melita Jazbec and Brian S. Haynes, University of Sydney**	403
11:50		Adjourn	

Wednesday morning, October 13, 1999			Page
8:30 AM		**V. Invited Speaker: "Flow Dynamics of Buoyant Plumes and Diffusion Flames," Baki M. Cetegen, University of Connecticut;** Chair: J. H. Miller, George Washington University	24

Session B-5 **Turbulent Combustion** Chair: F. Battaglia, Iowa State University			
9:30	94.	"LIF-LII Images of a Turbulent Gas-Jet Diffusion Flame," **R. L. Vander Wal, National Center for Microgravity Research**	407
9:50	95.	"Flamelet Orientations and the Burning Rate Integral of SI Engine Flames," **D. A. Knaus and F. C. Gouldin, Cornell University; P. C. Hinze and P. C. Miles, Sandia National Laboratory**	411
10:10		Break	
10:30	96.	"Large-Eddy Simulation of a Turbulent Piloted Methane/Air Diffusion Flame (Sandia Flame D)," **H. Pitsch and H. Steiner, Stanford University**	415
10:50	97.	"A Modified Coherent Flame Model to Describe Turbulent Flame Propagation in Mixtures With Variable Composition," **J. Hélie, Institut Français du Pétrole, France; A. Trouvé, George Washington University**	419
11:10	98.	"Direct Numerical Simulation of Forced Compressible Turbulence at Supercritical Pressure: Nitrogen-Hydrocarbon Mixtures," **R. S. Miller, Clemson University**	423
11:30	99.	"The New Regimes of 'Intensely Wrinkled' and 'Shredded' Nonpremixed Flames - Images of the Reaction Zone," **A. Ratner and J. F. Driscoll, University of Michigan; J. M. Donbar, Wright-Patterson AFB; C. D. Carter, Innovative Scientific Solutions, Inc; J. A. Mullin and W. J. A. Dahm, University of Michigan**	427
11:50	100.	"The IRST Model for Turbulent Premixed Non-Adiabatic Methane Flames. Verification of Temperature Prediction," **J. B. W. Kok and J. J. J. Louis, University of Twente, Netherlands**	431
12:10		Adjourn	

Wednesday morning, October 13, 1999 **Page**

8:30 AM **V. Invited Speaker: "Flow Dynamics of Buoyant Plumes and Diffusion Flames," Baki M. Cetegen, University of Connecticut;** 24

Chair: J. H. Miller, George Washington University

Session C-5 **Two-Phase Combustion** Chair: J. C. Chen, Rowan College			
9:30	101.	"Initial Observations on the Burning of an Ethanol Droplet in Microgravity," **A. Kazakov, B. Urban, J. Conley, and F. L. Dryer, Princeton University**	435
9:50	102.	"Benchmark Database for Input and Validation of Multiphase Combustion Models," **J. F. Widmann, S. R. Charagundla, and C. Presser, NIST**	439
10:10		Break	
10:30	103.	"Effect of Vorticity Generation on the Droplet Dispersion of a High-Pressure Outward Opening Injector," **C. Cairoli, A. A. Thaker, and H. K. Chelliah, University of Virginia; W. Ren, Siemens Automotive**	443
10:50	104.	"Laser Induced Fluorescence Imaging of the Hafnium Monoxide Radical in the Reaction Zone Surrounding Burning Hafnium Metal Droplets," **L. F. Ernst, R. A. Yetter, and F. L. Dryer, Princeton University**	447
11:10	105.	"Combustion of Boron by $O_2/NF_3/N_2$ Oxidizers," **D. G. Keil, E. L. Dreizin, and V. K. Hoffman, Titan Corporation; H. F. Calcote, ChemIon, Inc.**	451
11:30	106.	"Numerical Study of the Impact of Collisions on Particle Dispersion in a Shear Layer," **M. C. Soteriou and J. H. Mosley, University of Connecticut**	455
11:50	107.	"Effects of Pressure, Molecular Weight and Oxygen Potential on Hydrocarbon Droplet Gasification and Combustion Characteristics under Supercritical Pressure Environments," **Y. D. Yeboah, J. X. Nie, and K. B. Bota, Clark Atlanta University**	459
12:10		Adjourn	

INVITED PAPERS

COMBUSTION 2000 – BURNING COAL

IN THE 21st CENTURY

Daniel J. Seery
United Technologies Research Center
411 Silver Lane
East Hartford, CT 06108

The Department of Energy (DOE) has recognized the need to make significant improvements to the overall thermal efficiency of coal-burning plants, while decreasing their environmental impact. Of all the proposed options for future plants, the highest efficiencies are achieved by using Brayton cycles (gas turbines) rather than exclusive reliance on Rankine cycles (steam turbines). The DOE then initiated the research effort for a High Performance Power Generating System (HIPPS), which utilizes gas turbines but excludes all coal combustion products from the working fluid, thus avoiding the expense of hot gas cleanup and/or the corrosion of turbine blades by coal ash. The specific goals for the HIPPS program are shown in Table 1.

Table 1

DOE Goals for HIPPS

Green Field 300 MWe Commercial Plant Performance and Environmental Goals

1. Power plant net thermal efficiency (higher heating value) of 47%.
2. Minimum 65% coal energy input; path to 95% coal process.
3. Cost of electricity at least 10% less than comparable NSPS power plant.

4. Environmental performance requirements:

	New Source Performance	HIPPS **Phase II**
• Sulfur Oxides (lb/MMBtu)	0.40*	0.06
• Nitrogen Oxides (lb/MMBtu)	0.50	0.06
• Particulate (lb/MMBtu)	0.03	0.003
• Solid Wastes	Benign	Benign

* Based on 90% reduction of the total sulfur in the fuel with the design coal (5.98 pounds of SO_2 per MMBtu; or 2.57 kg of SO_2 per million kJ) and a 65/35 ratio of coal and natural gas.

In the HIPPS design the gas turbine working fluid (air) is heated indirectly, thus the highest air temperature that can be reached by coal combustion is limited by heat exchanger materials and will fall short of the ideal turbine inlet temperature for highest efficiency. To achieve the desired turbine inlet temperature (approximately 2500°F) the program allows for up to 35% use of a premium fuel (e.g., natural gas or no. 2 heating oil) in a topping cycle. The design is still required to have a growth path to all coal as improvements in materials allow for a high temperature, corrosion/resistant heat exchanger. For the near term (<5 years) it is unlikely that there will be structural ceramics available that can withstand molten coal ash at temperature >2700°F for long times (10,000 hours). Therefore the present design must be based on materials available now and accept temporary limitations on the maximum air temperature from coal combustion.

UTRC is heading up a team of seven research organizations to develop concepts and evaluate designs for a 300 MW_e indirect fired combined cycle plant. The optimized design employs both radiative and convective air heaters to transfer the energy from coal combustion to the gas turbine working fluid. Figure 1 is a simplified diagram of the HIPPS concept.

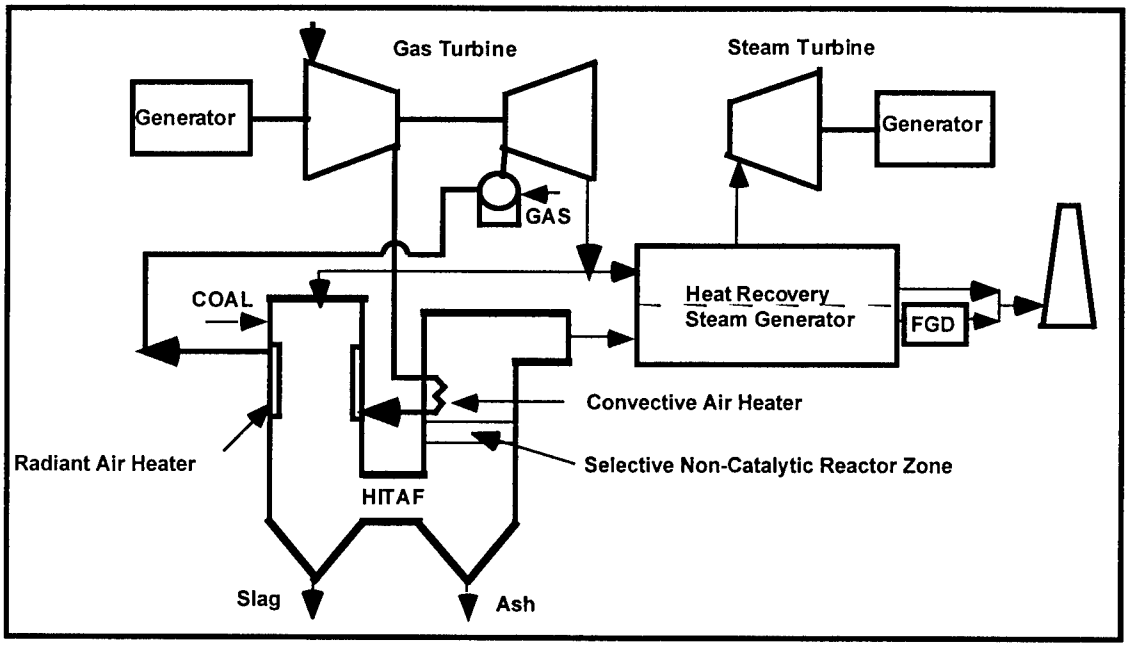


Figure 1

Simplified HIPPS Process Diagram

Approach

The UTRC team has developed a design based on a thermodynamic optimization study of a combined cycle 300 MW plant, using an advanced aeroderivative gas turbine and a commercially available steam turbine. The working fluid is heated, using both radiative and convective air

heaters. The convective air heater is constructed of ferritic alloy and a radiative air heater that is constructed from Ni-based superalloy protected by ceramic refractory tiles.

The three major elements of the system are the High Temperature Air Furnace (HITAF), the gas turbine, and the steam turbine. The HITAF supplies 55% of the temperature rise required by the gas turbines, bringing the compressor discharge air to 1700°F. The air then goes to a duct burner, where natural gas combustion boosts the temperature to that required by the turbine. The turbine exhaust stream, along with that from the HITAF, furnishes waste heat to a heat recovery steam generator (HRSG) and steam turbine. The overall efficiency of this system exceeds 47%(HHV), significantly better than typical PC plants.

HITAF Air Heater

Since the high temperature products of coal combustion will provide the heat source for the proposed HITAF concept, the air heaters must be capable of operation under unusually severe conditions. While conventional coal-fired steam power plants experience similar operating conditions, the air temperature required from the HITAF is of the order of 1700°F or more compared to only about 1000°F for steam, and air is a poor heat transport fluid compared to steam. The process of transferring heat from coal combustion products at about 2800-3000°F to high pressure air will require special structural design of the air heaters in order to avoid excessive mechanical and thermal stresses. Moreover, the mineral content of most coals at typical combustion temperatures produces ash particles in the combustion gas stream, resulting in potential for heat transfer performance degradation, as well as corrosion and erosion of air heater surfaces. Although erosion of air heater surfaces by impinging ash particles is not expected to be a problem because gas and particle velocities will not be excessive, special provisions will be made to minimize heat transfer degradation and to prevent corrosion.

In order to produce the high air temperature required for acceptable gas turbine efficiency, the coal combustion temperature will have to be sufficiently high to produce molten slag which can potentially foul and corrode heat transfer surfaces. Since the entire air heater cannot be maintained hot enough to produce continuous slag flow from all heat transfer surfaces, the transition from wet slag to dry ash will be controlled by separation into two different types of air heaters which will be designed to deal exclusively with slag or ash. The radiant air heater (RAH) will operate at the higher temperature levels required, while the convective air heater (CAH) will function at the lower temperature regime. The air heaters will be arranged for counter flow of the gas turbine air and the coal combustion gas so as to achieve the highest possible temperature differential. A slag screen will be located between the two air heaters to establish the wet-dry interface (wet slag to dry ash) and to remove most of the ash from the hot gas stream before it can enter the convective air heater. To prevent excessive sintering of ash deposits on heater surfaces and to provide a suitable temperature zone for selective non-catalytic reduction of NO_X, the combustion gas temperature will be reduced to about 1800°F by introducing flue gas recirculation immediately upstream of the convective air heater. This arrangement of the air heaters and the slag screen are shown schematically in Figure. 2 along with expected operating

temperature levels. The rationale for this arrangement of the air heaters, their respective operating conditions, and unique design features are discussed below in relationship to operating temperature levels and slag and ash environments.

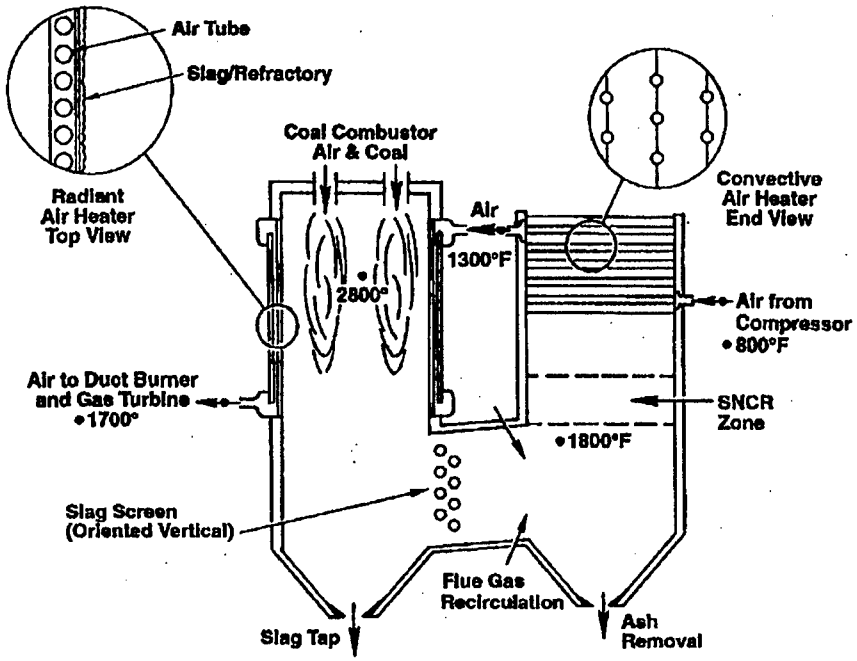


Figure. 2.
UTRC Arrangement of HITAF Components

Radiant Air Heater Design Concepts

Conceptual design for the radiant air heater is shown in Figure. 3. The radiant air heater will consist of an array of tubes contained in a panel that can be uniformly heated by radiation. The panel is protected by refractory tiles, which line the inside walls of the coal combustion furnace. The gas turbine air will be distributed to the many small passages within these panels by an arrangement of headers, manifolds, and ducts, which will be staged to avoid excessive thermal stresses. Ceramic refractory tiles will insulate the firesides of the hollow panels to prevent slag-induced corrosion. Although the radiant air heater is adaptable for either parallel or counter flow of the hot and cold gas streams, parallel flow will enhance draining of liquid slag from the radiant heater surface by producing the highest surface temperature at the lowest point of the heater. The high temperature coal combustion products at 2800°F or higher will heat the panels by radiant transfer and, as the gas turbine air flows through the alloy tubes, the air will be heated by forced convection from about 1300°F to 1700°F or higher, depending on heater material and availability of supplemental heating by direct combustion of natural gas or oil. If the air temperature out of the radiant heater is limited to <2000°F, nickel-based metal alloys which have been developed for the aircraft gas turbine industry can be used.

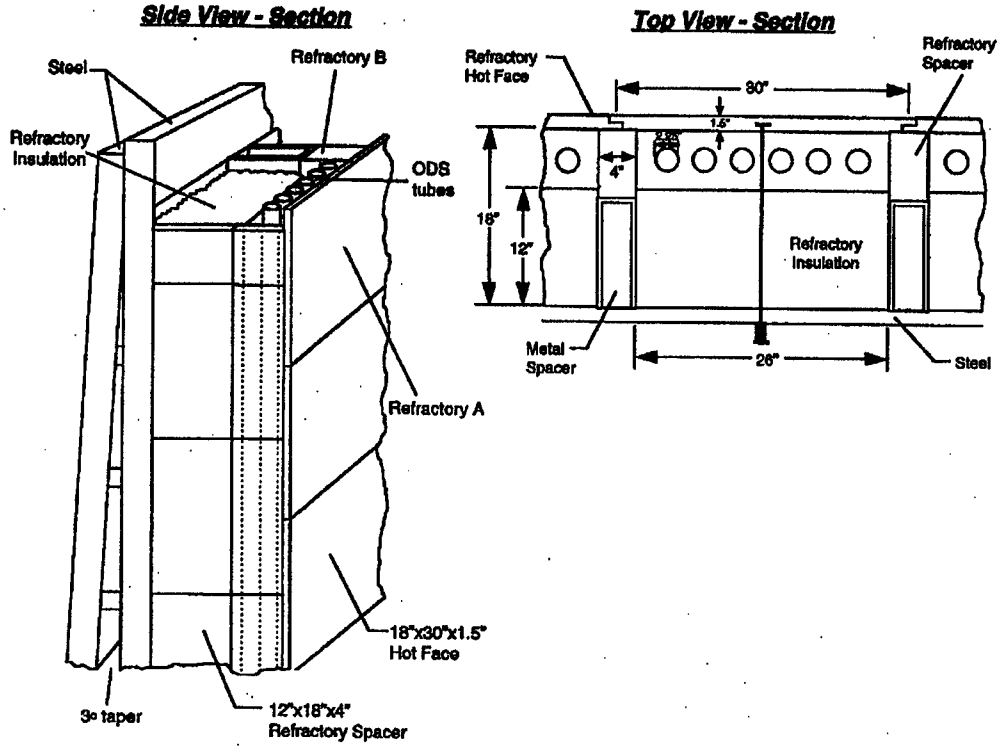


Figure. 3.
Hot Sections of Radiant Air Heater

Air Heater Materials

Materials are the key enabling technology for successful operation and commercialization of the HIPPS system. The use of high temperature heat exchangers in a coal combustion environment, coupled with the cost constraints, makes proper materials selection a considerable challenge. Nonetheless, utilization of state of the art materials and joining methods, as well as advanced oxidation and corrosion resistant coatings, can yield reasonable compromises.

The RAH must tolerate running coal slag on it's inner surface, while providing protection and reasonable heat transfer to the working fluid (air) contained near the outer walls of the coal combustor.

The use of a metallic based RAH, particularly under moderated temperatures and environments afforded by the 65% coal combustion case offers several advantages: 1) ease of fabrication, (i.e. conventional processes can be used to shape and weld components); 2) existence of a significant supplier base; and 3) high strength under moderate (65% coal) system conditions. These alloys offer superior performance compared to the steels, currently utilized in similar applications such as water wall slagging coal combustors. However, it is clear that, for the radiant air heater section, a system of refractory ceramic linings (with or without supplemental thin coatings on the base alloy) will be required to protect the alloy from the slagging coal ash environment.

The metal based approach to the RAH clearly offers a high probability of success for fabricating and operating a prototype HIPPS system. All of the various material elements (metals, coatings, and ceramics) that make up this approach to the RAH wall will require careful testing to determine survivability in coal combustion environments. In addition to selecting and testing of metals, coatings, and refractory ceramic liners, consideration must be given to both on-line and off-line repair of the materials during use. Techniques for bonding, joining and attaching both the dissimilar materials of construction and individual wall subsections will require development and validation.

Testing in the Pilot-Scale Slagging Furnace

The pilot-scale slagging furnace design is designed to be as fuel-flexible as possible, with furnace exit temperatures of at least 2700°F in order to maintain desired slag flow. It has a nominal firing rate of 2.5 million Btu/hr and a range of 2.0 to 3.0 million Btu/hr using a single burner. The design is based on a bituminous coal (Illinois No. 6, 11,100 Btu/lb) and a nominal furnace residence time of 3.5 seconds. Resulting flue gas flow rates range from roughly 425 to 640 scfm, with a nominal value of 530 scfm based on 20% excess air. Firing a subbituminous coal or lignite increases the flue gas volume, decreasing residence time to roughly 3 seconds. However, the high volatility of the low rank fuels results in a high combustion efficiency (>99%). The furnace is oriented vertically (downfired) and base the burner design on a swirl burner currently used on two EERC pilot-scale pulverized coal (pc)-fired units that are fired at 600,000 Btu/hr. Slagging furnace dimensions will be 48-in. inside diameter (ID) by roughly 16 ft in length. Combustion air preheat capabilities range from 300° to 900°F.

The primary burner is both natural gas- and coal-capable, with coal particle size assumed to be a standard utility grind, 70% -200 mesh. Burner development and testing are not objectives within this activity. However, some burner turndown is desirable and has been factored into the burner design. Flame stability is be assessed by observation of the flame and its relation to the burner quarl as a function of secondary air swirl and operating conditions at full load and under turndown conditions. The basic burner design, an International Flame Research Foundation (IFRF)-type adjustable secondary air swirl generator. An IFRF-type adjustable secondary air swirl generator uses primary and secondary air at approximately 15% and 85% of the total air, respectively, to adjust swirl between 0 and a maximum of 1.9.

Secondary air swirl is used to stabilize the flame. In the absence of swirl, loss of flame may result, increasing the risk of dust explosion. As swirl is applied to the combustion air, coal particles are entrained in the internal recirculation zone, increasing the heating rate of the particles, leading to increased release of volatiles and char combustion. The flame becomes more compact and intense as swirl is increased to an optimum level, which is characterized in existing EERC pilot-scale test facilities as the point at which the flame makes contact with the burner quarl. Increasing swirl beyond this level can pull the flame into the burner region, unnecessarily exposing metal burner components to the intense heat of the flame and possible combustion in the coal pipe.

Increasing swirl to provide flame stability and increased carbon conversion can also affect the formation of NOx. The high flame temperatures and increased coal-air mixing associated with increased swirl create an ideal situation under which NOx may form. In full-scale burners with adjustable vanes, swirl is often increased to reach the optimum condition and then decreased slightly to reduce the production of NOx. Although NOx emissions are of interest, their control is not a key objective for the pilot-scale slagging furnace. Therefore, burner operational settings are based on achieving desired furnace exit temperatures and slag conditions in the furnace.

Flame stability under turndown conditions is characterized by firing the test fuel at reduced load (typically 66% to 85% of the full load rate), maintaining the same primary air flow and adjusting the secondary air flow to meet excess air requirements. The existing burner design can be scaled up by simply increasing the combustion air volumetric flow rates. Observation ports are located in the furnace to permit visual observation of the primary burner flame, auxiliary burner flame, RAH panels, slag screen, and slag tap.

An auxiliary gas burner (500,000 Btu/hr is located in the area of the furnace exit in order to ensure desired slag flow from the furnace and the slag screen. This auxiliary burner compensates for heat losses through the furnace walls, site ports, and RAH test panels. The use of the auxiliary gas burner is beneficial during start-up to reduce heatup time and to prevent the freezing of slag on the slag screen when initially switching to coal firing. The auxiliary gas burner is fired at stoichiometric conditions to avoid high excess air levels in the system. Also, the auxiliary gas burner is fired at relatively low rates (<200,000 Btu/hr) once the furnace reaches thermal equilibrium. The overall pilot-slag furnace is illustrated in Figure. 4.

Results and Conclusions

A primary result of the model testing is that the RAH and CAH function as designed. That is, the RAH transfers heat at a rate that meets the design requirements, it accommodates the differential thermal expansion of the alloy and ceramic components, and it withstands the slagging ash corrosion. The testing of the CAH was similarly successful in that it matches the heat transfer effectiveness of the design, stands up to ash corrosion and offers the potential for expansion of the temperature range.

Both the RAH and the CAH were instrumented to help evaluate their performance. In the RAH the backface of the refractory bricks, and the length and circumference of the alloy tubes have high temperature thermocouples judiciously placed to evaluate the radiative heat transfer and the temperature gradients in the RAH. These measurements are complemented by infrared detectors viewing the refractories.

The results of some of these measurements indicate that for these air flow rates and furnaces conditions this scaled version of our RAH can raise the air temperature high enough and fast enough for our baseline designs. In practical terms it means the RAH design is successful in that it can:

- Raise the temperature 400°F
- Transfer heat at the design point 98,000 BTU/hr

- Survive the high temperature corrosive atmosphere for significant lifetimes

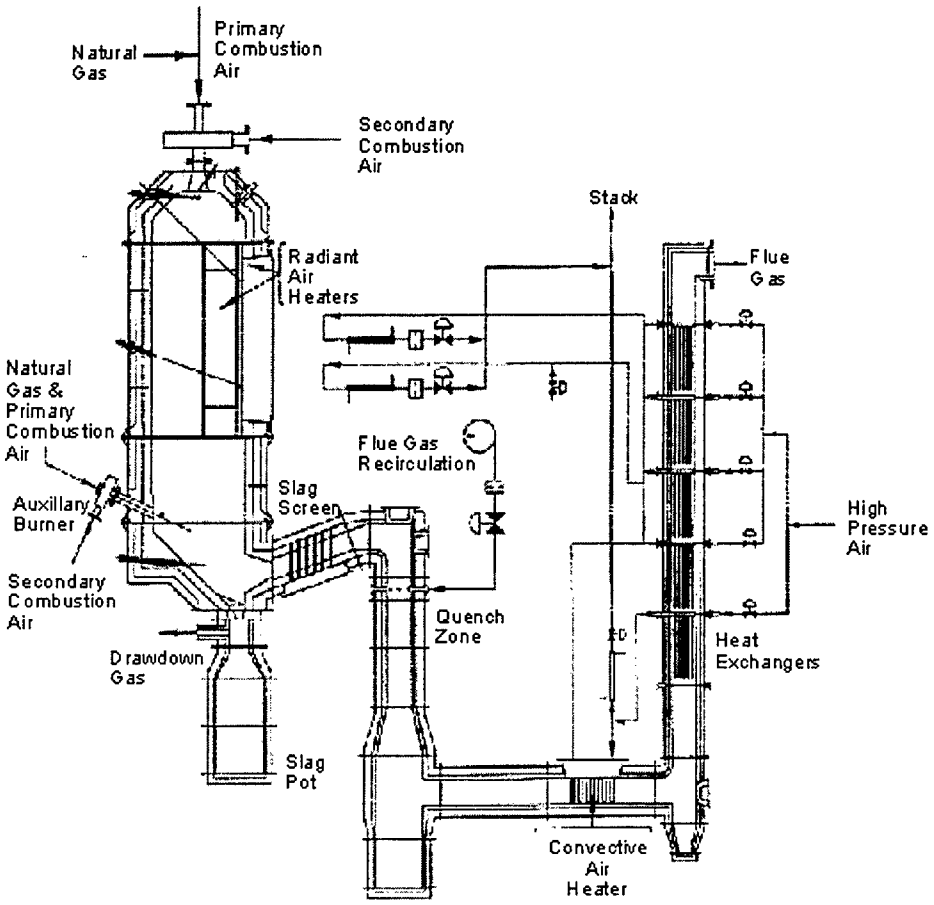


Figure. 4
Combustion 2000 Furnace and Support Systems

In turn, the performance of the RAH supports the design studies and cycle analysis which, at their optimum, result in thermal efficiencies of >55% (HHV) while still adhering to cost goals and the operating ranges of present day materials.

Acknowledgements

In addition to UTRC, the team includes Bechtel Corporation, ABB Combustion Engineering, Kraft Work Systems, PSI Technology, University of North Dakota EERC, University of Utah/ Reaction Engineering and Fluor Daniel.
This work was carried out under DOE contract DE-AC22-95PC95144 which is monitored by the Federal Energy Technology Center , Pittsburgh , Pennsylvania .The Contracting Officer's Representative is Arun Bose .

Computation of Turbulent Combustion with Detailed Chemistry

Stephen B. Pope
Cornell University
Mechanical and Aerospace Engineering
Ithaca, NY 14853
pope@mae.cornell.edu

Recent advances at Cornell on modelling turbulent combustion are reviewed. These include the ISAT algorithm (*in situ* adaptive tabulation) for the efficient implementation of combustion chemistry, and PDF calculations of nonpremixed piloted jet flames with local extinction.

PDF Methods

In PDF methods (Pope 1985), a modelled transport equation is solved for the joint probability density function of certain fluid properties, including the thermochemical composition. A principal advantage of this approach is that the turbulent fluctuations of species and temperature are fully represented. As a consequence, arbitrarily complicated and nonlinear chemical reactions can be treated exactly, without the closure problem experienced by moment closures.

Recent work is based on the joint PDF of velocity, composition and turbulence frequency. The turbulence modelling aspects of this approach are described by Van Slooten, Jayesh and Pope (1998). A mixing model is required, to model the effects of molecular diffusion. The EMST model developed by Subramaniam and Pope (1998) is used (which is based on Euclidean minimum spanning trees). Compared to other models, this has the important advantage of modelling mixing locally in composition space.

Efficient Implementation of Combustion Chemistry

As stated above, a valid claim of PDF methods is that arbitrarily complex chemical kinetics can be treated without turbulence-modelling approxima-

tions of the reaction-rate terms. In practice, the claim is hollow unless the chemistry can be implemented in a computationally tractable way. A significant recent advance is the development of the ISAT algorithm (*in situ* adaptive tabulation, Pope 1997), which accelerates—by up to a factor of 1,000—the computational treatment of combustion chemistry, and hence makes practical PDF calculations with realistic combustion chemistry.

As an illustration of ISAT's capabilities, Saxena & Pope (1998) performed PDF calculations of a piloted jet nonpremixed flame, using a 16-species 41-reaction skeletal mechanism for methane. The use of the ISAT algorithm reduced the overall CPU time by a factor of 40, and reduced the fraction of this time consumed by chemistry calculations from 98% to 60%.

Nonpremixed Piloted Jet Flames

Pioneered by Masri, Dibble and Bilger (1986), nonpremixed piloted jet flames have proved to be an extremely good test case for turbulent combustion models. The recent measurements of Barlow and Frank (1998) investigate in detail the behavior of the flame for conditions including substantial local extinction.

We report PDF calculation of these flames (performed by J. Xu) which show quantitative agreement for local extinction and the subsequent downstream reignition. These calculations are based on the 16-species augmented reduced mechanism (ARM) for methane developed by Sung, Law and Chen (1998). The ARM includes C_2 species, and this is found to remedy the discrepancies observed in earlier calculations (Saxena and Pope 1998) based on the skeletal C_1 mechanism.

References

Barlow, R. S. and J. H. Frank (1998). Effects of turbulence on species mass fraction in methane/air jet flames. In *Twenty-Seventh Symp. (Int'l) on Combust.*, Pittsburgh, pp. 1087–1095. Combustion Institute.

Masri, A. R., R. W. Dibble, and R. W. Bilger (1986). Turbulent nonpremixed flames of methane near extinction: mean structure from raman measurements. *Combust. Flame 71*, 245–266.

Pope, S. B. (1985). PDF methods for turbulent reactive flows. *Prog. Energy Combust. Sci. 11*, 119–192.

Pope, S. B. (1997). Computationally efficient implementation of combustion chemistry using *in situ* adaptive tabulation. *Combust. Theory Modelling 1*, 41–63.

Saxena, V. and S. B. Pope (1998). PDF calculations of major and minor species in a turbulent piloted jet flame. In *Twenty-Seventh Symp. (Int'l) on Combust.*, Pittsburgh, pp. 1081–1086. Combustion Institute.

Subramaniam, S. and S. B. Pope (1998). A mixing model for turbulent reactive flows based on Euclidean minimum spanning trees. *Combust. Flame 115*, 487–514.

Sung, C. J., C. K. Law, and J.-Y. Chen (1998). An augmented reduced mechanism for methane oxidation with comprehensive global parametric validation. In *Seventh Symp. (Int'l) on Combust.*, Pittsburgh, pp. 295–304. Combustion Institute.

Van Slooten, P. R., Jayesh, and S. B. Pope (1998). Advances in PDF modeling for inhomogeneous turbulent flows. *Phys. Fluids 10*, 246–265.

Ether Additives for Reduced Diesel PM: Chemistry and Vehicle Emissions

M. Matti Maricq
Research Laboratory, Ford Motor Company
P.O. Box 2053, MD 3083, Dearborn, MI 48121
email: mmaricq@ford.com

Introduction

There is currently considerable interest in improving the fuel economy of motor vehicles. One means to achieve this would be by increased use of diesel engines. However, controlling NO_x and particulate matter to future emissions standards poses a difficult challenge. The three way catalyst used to reduce NO_x from gasoline engines does not perform well under the lean conditions of diesel combustion. Particulate matter emissions from diesel vehicles tend to outweigh those from spark ignition engines, but altering combustion conditions to reduce the PM levels generally raises the NO_x emissions. Recent studies indicate that dimethyl ether (DME) is both an excellent diesel fuel, having a high cetane number, and one that produces low PM emissions [1,2,3,4]. While DME is a gas, and therefore requires modification of the fuel system for use in motor vehicles, the related ether, dimethoxy methane (DMM), is a low boiling liquid that has also been observed to reduce particulate mass emissions, even when used as a mixture in conventional diesel fuel [5].

We are investigating DME and its analogs in two ways: one aim is to understand why this class of compounds provides good diesel fuels, and the other is to examine in detail the ways in which they affect vehicle tailpipe emissions, both gaseous and particulate. Some ethers, such as methyl *tert*-butyl ether (MTBE) is used as a gasoline fuel additive to enhance octane, whereas other ethers, such as DME, are good compression ignition fuels. What is different about the oxidation chemistry of these ethers that leads to the contrasting engine performance? The answer to this question requires a better understanding of the oxidation mechanism and the chemical kinetics that are involved in the combustion of these ethers. From the other perspective, given that reductions in smoke number have been observed in engine dynamometer studies, what can we learn about the sizes and numbers of the particles, and how do these vary with engine operating conditions?

Gas phase kinetics

The oxidation of DME begins either by its thermal dissociation or by hydrogen abstraction. In the latter case, the resulting hydrocarbon radical reacts with O_2 to form the corresponding peroxy radical;

$$CH_3OCH_2 + O_2 \rightarrow CH_3OCH_2O_2^* \quad (1)$$

Near ambient temperature and pressure, the stabilized peroxy radical is normally the dominant product. However, the observation of OH radicals and formaldehyde has led us to the postulate a Lindemann mechanism, whereby

$$CH_3OCH_2O_2^* + M \rightarrow CH_3OCH_2O_2 \quad (2)$$

$$CH_3OCH_2O_2^* \rightarrow 2\,CH_2O + OH \quad (3)$$

The pressure dependence of the formaldehyde formation, illustrated in Figure 1, corroborates this mechanism.[6] At pressures above about 100 Torr, third body collisions are sufficiently frequent to stabilize better than about 90% of the initially formed peroxy radicals. As the total pressure falls, the energized peroxy radical has sufficient time to rearrange and dissociate, presumably through a CH_2OCH_2OOH intermediate. Preliminary evidence shows an analogous rearrangement and dissociation to occur in the oxidation of DMM.

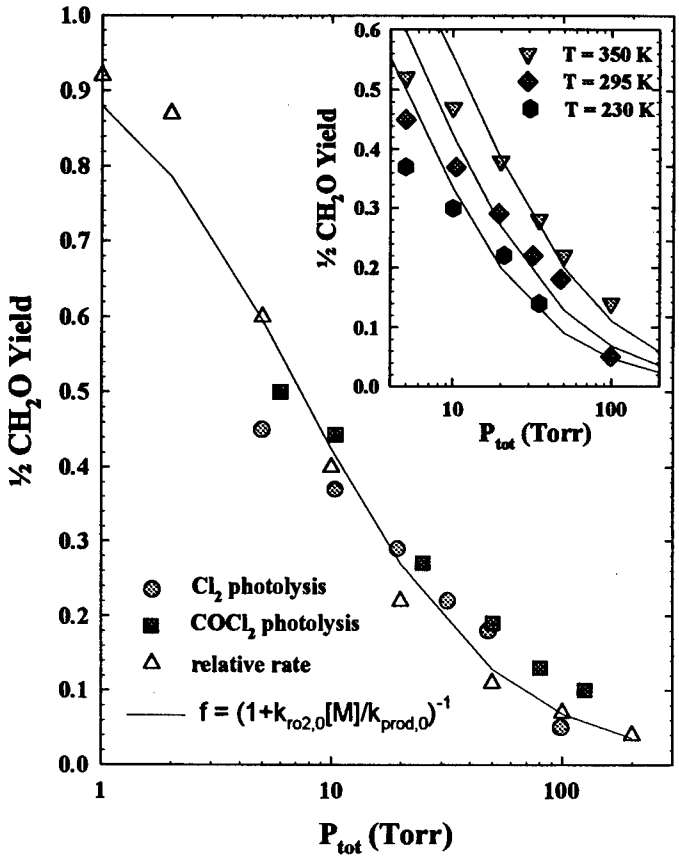


Figure 1. Formaldehyde yield from the $CH_3OCH_2 + O_2$ reaction. The temperature dependence is shown in the insert. The lines represent fits to the Lindemann mechanism.

That formaldehyde formation is observed at pressures below 100 Torr is not particularly relevant to combustion chemistry. In the analogous reaction between ethyl radicals and O_2, Kaiser [7] found the ethylene + HO_2 yield to be quite small for temperatures below ~ 450 K. However, above this temperature the yield increased dramatically. The hypothesis for this behavior is that above about 450 K the peroxy formation reaction becomes reversible; thus, repeated formation and dissociation of the RO_2 radical allows the energized peroxy intermediate to be revisited numerous times, thereby greatly increasing the probability of its rearrangement to the ethylene + HO_2 products. Whether or not the analogous mechanism operates in the DME case is under current investigation. If it does, the formation of OH radicals and formaldehyde could become important under conditions relevant to combustion chemistry.

Vehicle PM emissions

The second part of our program to investigate the use of ethers as clean compression ignition fuels concerns the effect that they have on vehicle tailpipe emissions. Because DME is a gas under ambient temperature and pressure, the work to date has been on dimethoxy methane so as to avoid the necessity of altering the test vehicle's fuel injection system. The tests have compared PM and NO_x emissions for a base diesel fuel to those from a DMM/diesel fuel mixture (17% - 30% by volume). They have been performed using both an engine dynamometer and with a vehicle run on a chassis dynamometer. The emissions have been compared for both steady state operation at fixed speed and load and over the FTP transient drive cycle.

FTP emissions tests were performed on a 1995 European passenger vehicle with a 1.8 L IDI turbocharged diesel engine and equipped with an oxidation catalyst.[8] Particulate matter was collected on filter media by sampling from a dilution tunnel a portion of the diluted exhaust gas. The PM mass dropped by (36±8)% from 83 mg/mi for the three-bag FTP average using the base fuel to 53 for a 16.6% DMM/base fuel mixture. Under steady state conditions ranging from 40 to 60 mph and from 4 to 20 hp, the PM mass emissions decreased by between 25%-50% when using a 30% DMM/base fuel blend. These results are consistent with the reduction in exhaust gas opacity observed in tests on a Caterpillar diesel engine.[5] In contrast to the PM reduction, the NO_x emissions remained unaffected by the addition of DMM to the diesel fuel.

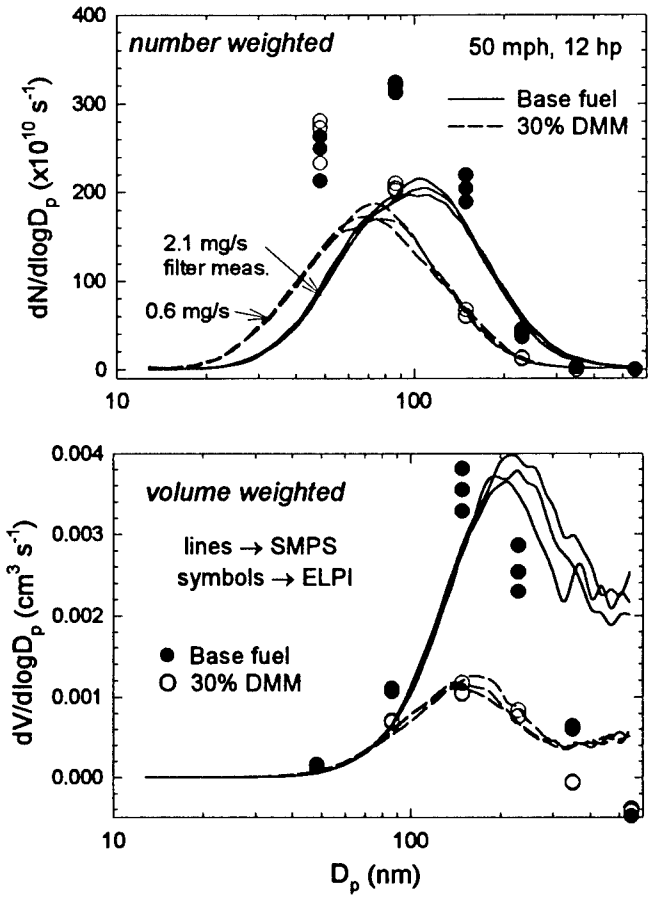


Figure 2. Particle size distributions for the base diesel fuel versus the DMM/base fuel blend. Top panel shows the number weighted distributions; bottom panel shows the volume weighted distributions.

To obtain a more complete picture of the effect on DMM on the PM emissions, particle size distributions were also recorded. These are illustrated in Figure 2 for steady state operation of the vehicle at 50 mph and a 12 hp load. The lines represent the particle size determined using a scanning mobility particle sizer, whereas the symbols denote the particle size measured with an electrical low pressure impactor. The volume weighted (mass weighted if scaled by an approximate particle density of 1 gm/cm^3) distributions in the lower panel show the same reduction in particulate mass when using the DMM/diesel fuel blend as measured gravimetrically using the particle filters.

The top panel tells a different story. It plots the number weighted particle size distributions for the DMM/base versus base fuel. The number of particles emitted from the tailpipe declines only slightly (~15%) when using the 30% DMM/diesel blend; but the average particle size decreases from about 100 nm to 70 nm. The reduction in particle mass emissions does not come from fewer particles being emitted; rather, it is due to the particles being smaller. Why the DMM additive leads to smaller particles is a question that is still under investigation. Whether or not DMM improves the PM emissions cannot be answered at present, because the biological mechanism of the adverse health effects of PM is not sufficiently well understood. If the mechanism depends on the mass of particles a person is exposed to, then the DMM additive may prove beneficial; if particle number concentration proves to be the key exposure parameter, then the DMM additive would presumably have no beneficial value.

Acknowledgment

The author would like to thank Dick Chase, Bill Kaiser, Diane Podsiadlik, and Joe Szente for their involvement in and contributions to the ether diesel fuel studies.

References

[1] Fleisch, T.; McCarthy, C.; Basu, A.; Udovich, C.; Charbonneau, P.; Slodowske, W.; Mikkelsen, S.-E.; McCandless, J. "A new clean diesel technology: demonstration of ULEV emissions on a Navistar diesel engine fueled with dimethyl ether," SAE Tech. Pap. Series, Paper No. 950061 (1995).

[2] Sorenson, S. C.; Mikkelsen, S.-E. "Performance and emissions of a 0.273 L direct injection diesel engine fueled with neat dimethyl ether," SAE Tech. Pap. Series, Paper No. 950064 (1995).

[3] Kapus, P. E.; Cartellieri, W. P. "ULEV potential od a DI/TCI diesel passenger car engine operated on dimethyl ether," SAE Tech. Pap. Series, Paper No. 952754 (1995).

[4] Kajitani, S.; Chen, Z. L.; Konno, M.; Rhee, K. T. "Engine performence and exhaust characteristics of a direct-injection diesel engine operated with DME," SAE Tech. Pap. Series, Paper No. 972973 (1997).

[5] Dodge, L.; Naegeli, D. "Combustion characterization of methylal in reciprocating engines," NREL Report #TP-425-6345, Golden, CO, June 1994.

[6] Maricq, M. M.; Szente, J. J.; Hybl, J. D. "Kinetic studies of the oxidation of dimethyl ether and its chain reaction with Cl_2", *J. Physical Chemistry*, **1997**, *101*, 5155.

[7] Kaiser, E. W. *J. Physical Chemistry*, **1995**, *99*, 707.

[8] Maricq, M. M.; Chase, R. E.; Podsiadlik, D. H.; Siegl, W. O.; Kaiser, E. W. SAE Tech. Pap. Series, Paper No. 982572 (1998).

Chemical Fire Suppressants: How Can We Replace Halon?

James W. Fleming
Navy Technology Center for Safety and Survivability, Code 6185
Naval Research Laboratory, Washington, DC 20375-5342
fleming@code6185.nrl.navy.mil
phone: 202-767-2065; fax: 202-767-1716

INTRODUCTION

Halons, halogenated hydrocarbons containing bromine, appeared on the scene for fire suppression in the late 1940's following a U.S. Army study to identify effective agents. Halon 1301, bromotrifluoromethane, with its low boiling point is extremely effective in total flooding applications, which rely on the agent completely filling the space to be protected. Halons that exhibit good fire suppression properties but have boiling points closer to room temperature (Halon 1211, bromochlorodifluoromethane, and Halon 2402, dibromotetrafluoroethane) are more suitable for streaming agents which can be directed toward the fire threat as a liquid stream, typically from hand-held units. Interestingly, Halon 1301 was not the most effective total flooding compound on the list. However, Halon 1301 provides a near optimum combination of good fire suppression effectiveness, low toxicity, suitably low boiling point, and a reasonably low density and molecular weight. The combined effectiveness and desirable properties quickly accelerated the use of halons to a wide range of fire suppression applications, including movable platforms such as ships and planes. Dependence on halons increased as more and more fire suppression systems were engineered around these compounds.

In 1974, Rowland and Molina called the world community's attention to the fact that chlorofluorocarbons (CFCs), although very unreactive at ground level, have the potential to catalytically destroy stratospheric ozone once the chlorine is released through uv photolysis. Subsequent research including work done at NRL in 1976 showed that bromine containing halons are more deleterious to ozone than CFCs. When released in the stratosphere, bromine catalytically destroys O_3 : $Br + O_3 \rightarrow BrO + O_2$; $BrO + O_3 \rightarrow BrO_2 + O_2 \rightarrow Br$. CF_3Br is very stable to attack by OH and uv wavelengths present at ground level, the primary removal mechanisms of compounds in the troposphere. Thus, Halon 1301 has an undesirably long atmospheric lifetime that allows transport of the problematic bromine into the stratosphere.

The search for environmentally acceptable fire suppression halon replacements requires identifying compounds that have: good suppression efficiencies compared to Halon 1301, very low potential for destroying the stratospheric ozone, minimal impact on global warming, low human toxicity, and desirable boiling points. Significant efforts are underway to find halons replacements to protect both new construction as well as retrofitting current systems [1]. Different applications require different criteria. Suppression system weight and space constraints on retrofitting current systems make replacement particularly challenging. The search for acceptable replacements must be more than a random walk through an extremely large number of possibilities. Replacement choices demand compromises and systematic methodologies for

identifying suitable replacements based on fire suppression mechanistic understanding. An understanding of the suppression mechanism can effectively guide the search in promising directions. Modeling predictions are valuable for providing insight. Models must be validated against experimental data for a range of conditions and for a number of compounds. This paper covers current and past activities related to our efforts in halon replacement in a variety of flame environments. Some of the projects presented are part of the current Department of Defense's Next-Generation Fire Suppression Technology Program which seeks retrofit halon replacements for military applications [2].

PHYSICAL SUPPRESSION

Flame suppression agents can be generally categorized into chemical agents, such as those containing bromine or iodine, and physical agents such as nitrogen. However, an agent can only be a purely physical agent if it suffers no degradation in the flame, either via chemical attack or thermal decomposition. Molecular nitrogen and other physical agents are effective at flame suppression through heat extraction and dilution of oxygen. The amount of N_2 required for adequate protection is very costly in terms of total system volume and weight, including storage containers and dispersal hardware. Both volume and weight are critical parameters in movable platforms such as vehicles, ships, and planes. Although CO_2 can be used in some applications, the concentration required for flame suppression exceeds the human toxicity levels. In occupied spaces, the potential of accidental release is a very serious threat to human safety.

In terms of sensible enthalpy per unit mass, liquid water is the best physical agent. A key issue is how to take advantage of the latent heat of vaporization (> 40% of the sensible enthalpy) in an actual fire suppression application, including dissemination and distribution of the optimum droplet size. If the drops are too small they will not make it to the fire; droplets which are too large will not completely evaporate. Water spray typically discharged from overhead water sprinklers is characterized by very large (> 500 μ diameter) water drops. Although water spray can control a fire, smaller droplets (< 200 μ diameter) characteristic of water mist, are much more effective at heat abstraction due to their higher evaporation. The increased evaporation rate of water mist also leads to higher oxygen dilution in the air stream.

Lentati and Chelliah [3] predicted that ~ 25 μ water droplets should be near the optimum size to extract the greatest amount of heat yet large enough to just survive traveling through a low strain rate counterflow diffusion methane/air flame when seeded from the air side. Studies at NRL on water mist suppressed propane/air flames are consistent with these predictions and are reported at this meeting [4]. In these studies, water droplets are monitored throughout the flowfield using phase Doppler anemometry to determine the optimum droplet size as well as the quantity of mist required to extinguish the counterflow diffusion flames. Recent results also presented at this meeting on the flame speed inhibition by very fine water mist, nominal 0.3 μ diameter droplets, show that the theoretical heat extraction potential of water can be achieved [5]. The combination of the heat extraction by fine water mist and a chemical suppression component by an additive has the potential to impact a significant chemical suppression component to the overall flame extinction mechanism. Our laboratory is currently assessing the effectiveness of water additives for suppressing both counterflow diffusion flames and premixed

Bunsen flames.

CHEMICAL SUPPRESSION

All agents have a physical component to suppression. In addition, they can have a chemical component that significantly increases effectiveness. Halon 1301 is effective at fire suppression because the bromine can chemically combine H radicals and remove them from the flame: H + Br → HBr, HBr + H → H_2 +Br. Catalytic removal is possible because the H, OH, and O radicals controlling the flame chemistry are at superequilibrium concentrations in the flame front. Designing bromine containing molecules that do not make it to the stratosphere (e.g. tropodegradable compounds) is one area of current study. Inclusion of chemical structures that promote oxidation or photolysis leads to compounds with higher boiling points, toxicity concerns, and less suitability as "drop-in" Halon 1301 replacements. Iodine containing compounds are also tropodegradable and have good chemical suppression efficiency but also suffer from the problem of toxicity and low volatility concerns. Although these compounds are less likely to be used as total flooding agents, many of them have potential for use in other applications.

In the mid 1970's Sheinson and others at NRL began studies on the extinction of small liquid pool fires in a cup burner [6]. Extinction concentration data provided suppression effectiveness ranking for a large number of compounds (exclusively gases). Real scale tests show that the cup burner extinction concentration (plus a small margin) is usually adequate to extinguish most fires due to the very stable cup burner flame. Cup burner data have been used to derive recommended agent concentrations for suppression systems. However, realistic scale results are still needed to evaluate non-scaling effects such as agent mixing, by-product formation, and fire extinguishment times.

From the large number of compounds measured in the NRL Cup Burner, Sheinson derived a suppression predictive capability based on physical and chemical properties [7]. These studies also provide a great deal of understanding concerning the interplay of chemical and physical properties of various compounds [8]. They reported the enhanced suppression effect of combining chemically acting and physically acting agents [9] which has been further explored by Saso et al. [10]. The source for this enhancement results from the impact of the agent on the temperature field and the flame radical concentrations.

An outgrowth of the NRL Cup Burner studies on hydrofluorocarbon compounds (HFCs) was the recognition that there was an increased chemical contribution to suppression if the fluorines are arranged on the hydrocarbon in CF_3-groups [7]. The increased effectiveness observed was significantly greater than that predicted based on the heat capacity of the CF_3-group. This observation led to the commercialization of CF_3CHFCF_3 (HFC-227ea, heptafluoropropane noted here as HFP). In addition, of the HFCs that have multiple isomeric forms, those that have been commercialized as fire suppression agents have the fluorines and hydrogens arranged to maximize the number of CF_3-groups. NRL suppression testing and full scale evaluation of HFP resulted in the implementation of HFP by the U.S. Navy as one of the replacements for Halon 1301 in the next class of ships to be constructed [11].

NRL extinction strain rate studies in counterflow diffusion flames showed that the

distribution of fluorine atoms on the HFC that maximizes the number of CF_3-groups leads to better suppression across a range of strain rates [12]. Extinction strain rate curves for hydrofluorocarbon agents cluster into groupings corresponding to the number of CF_3-groups on the molecules. The similarity of the thermochemical properties of these compounds suggests that the higher extinction effectiveness associated with the CF_3-groups might be due to differences in chemical kinetics.

Our laboratory has investigated the chemical kinetic pathways relevant to inhibition by HFCs in low pressure flat flames [13]. Flame structure information using laser induced fluorescence was compared to flame modeling calculations; a kinetic sub-model was used for HFP that was developed by Hynes et al [14]. Reaction pathway analysis points to a combination of events rather than one specific source to explain the CF_3-group enhanced effectiveness. For HFP there is a strong suppression dependence on agent decomposition, whether thermal or via flame radical attack. Regardless of the initiation step, the thermodynamically favored by-product for HFP or any partially fluorinated hydrocarbon will be HF. The human health hazard HF presents is cause for concern when using fluorine containing agents in occupied spaces or ones that must be entered after application of the agent.

A method to reduce the amount of HF has been patented by NRL [15] and combines the use of water spray with the fluorinated agent. Large reductions in HF can be achieved, resulting from the significantly lower temperature and oxygen dilution due to the water spray, which greatly weakens the flame and thus reduces the HFP decomposition.

ULTRA-HIGH EFFICIENCY AGENTS

Compounds containing elements other than the halogens have shown potential for chemical fire suppression many times greater than bromine. Babushok points out the very high flame speed reduction potential for a number of compounds, including iron and alkali metals [16]. Recent studies at NIST show that iron pentacarbonyl, $Fe(CO)_5$, is some 70 times more effective than Halon 1301 in reducing the flame speed of a methane/air flame by 25% [17]. The mechanism responsible is postulated to be a catalytic removal of both H and O atoms. Unfortunately, above ~ 200 ppm of added Fe (in the form of $Fe(CO)_5$) there is a leveling off of effectiveness with increased Fe addition. This diminished effectiveness comes at much lower concentrations than the expected slowdown for catalytic agents [18] due to the flame H, O, and OH radical concentrations approaching their equilibrium values. Early onset of decreased effectiveness has been attributed to the condensation of gas phase iron atoms at the higher concentrations [19]. It is likely that other iron compounds will be impacted by the thermodynamic limit of the gas phase Fe or FeO concentration.

The effectiveness of sodium and potassium bicarbonate powders was measured in counterflow diffusion flames [20]; Hamins reported results for sodium bicarbonate in a cup burner [21]. Potassium bicarbonate powders are at least twice as effective as sodium bicarbonate for similar particle sizes and flame strain rate; small particles of both compounds are more effective than Halon 1301. Determining the mechanism for particle suppression requires particle size and surface area information. Although these studies confirmed the enhanced effectiveness as particle size decreases, quantifying the effectiveness as a function of particle size is difficult

for powder samples. Although a nominal particle size can be determined by sieving, obtaining an *in situ* particle size or surface area is not possible. Optical techniques assume a spherical particle (phase Doppler Anemometry measures the local radius of curvature) or provide a generalized shape (diffraction-based or imaging methods). The assumption that an off-line size determination is the size delivered to the flame is questionable, especially for very small particles where several factors including humidity and static charges can affect the particle size distribution. Despite this limitation, results on sodium and potassium bicarbonate flame extinction effectiveness based on sieving size show that effectiveness is controlled by particle size [22]. These studies suggest that there is a limiting small size below which there is no increase in effectiveness based on mass of the alkali metal compounds. It should be possible to quantify the chemical effects of various powders if sufficiently small particle samples are studied.

Studies are underway in our lab to assess the mechanistic reasons for the higher effectiveness observed for potassium over sodium and the generally observed increase in effectiveness as one goes down the row of alkali metals (Li < Na < K < Rb). Preliminary flame speed calculations have been carried out for sodium inhibited flames [23]. Only the sodium chemistry currently has a sufficient number of reported reaction rate coefficients. In general alkali metal atoms and metal hydroxide molecules can combine H and OH flame radicals according to

$$M + OH \rightarrow MOH \quad (1)$$

$$MOH + H \rightarrow M + H_2O \quad (2)$$

where M represents an alkali metal atom. Calculations assuming similar chemistry and kinetics for lithium suggest that thermochemistry alone does not account for the higher effectiveness of potassium relative to sodium. However, thermodynamics does limit the amount of Li relative to LiOH which in turn greatly diminishes the effectiveness of the Li + OH + M $\rightarrow$ LiOH / LiOH + H $\rightarrow$ Li + H_2O catalytic cycle.

Flame speed versus added sodium plots show the typical limiting behavior at high agent concentration characteristic of very efficient catalytic agents. Calculations predict that methane/air flames inhibited with an "ideal" agent, one which causes the H + OH recombination rate to equal the collision rate with no added thermal mass, can reduce the flame speed from ~ 39 cm/s to ~ 8 cm/s. This is not enough to extinguish the flame in the absence of any other heat losses. For agent addition beyond the chemical saturation point, even an ultra-high efficient chemical agent begins to act more like a physical agent, essentially only adding thermal mass. The resulting heat loss is more effectively accomplished using an efficient physical agent such as water mist.

CONCLUSIONS

Finding a true, drop-in replacement for Halon 1301 with identical properties yet environmentally acceptable is not likely. However, there are environmentally acceptable compounds that hold real promise as potential retrofitable replacements. Exactly what chemical form is best and how to get it to or in the flame are key issues. As we decide on halon

replacement options, there will also be the need for more critical assessment of the areas requiring protection and other means of minimizing fire damage. It is apparent that future choices of which agent to use will be based as much on the fire protection requirements and the area to be protected as on the agent itself. Choices will obviously result in tradeoffs and engineering compromises.

Combining a highly efficient chemically acting agent with a physically acting agent holds the greatest promise for future systems. This might be done in a single designer molecule or perhaps in a dual system. Combining the superior chemical suppression capability of additives such as iron or potassium at low concentrations with the large heat extraction capabilities of fine water mist is a combination worthy of further study. Such systems will present storage and delivery issues and engineering challenges to meet both reliability requirements and weight and volume restrictions. The need for environmentally acceptable replacements for halons will continue to drive the creativity and ingenuity of both chemists and engineers to meet these challenges.

ACKNOWLEDGMENTS

I would like to thank the members of the Combustion Dynamics Section at NRL whose work is presented here: Ron Sheinson, Brad Williams, and Alex Maranghides. Others contributing to the NRL halon replacement efforts have included: Paul Papas (NRC Postdoc, counterflow flame extinction studies), Drew L'Esperance (NRC Postdoc, fluorinated agents in low pressure flames), Eric Zegers (NRC Postdoc, water mists and fluorinated agents in counterflow flames), Paul Fuss (ASEE Postdoc, flame speed inhibition by water mist), Mark Reed (WPI MS Fire Protection Engineering, work on dry powders), Mike Davis (BS M.E. Notre Dame, modeling calculations and velocity field measurements), Mike Kozma (MS E.E, Lehigh U., instrumentation assistance) and Professor Betta Fisher (Cornell U., NRL Summer ASEE Faculty, counterflow flame studies).

We acknowledge the financial support of the U.S. Naval Sea Systems Command and the Department of Defense's Next Generation Fire Suppression Technology Program, funded by the DoD Strategic Environmental Research and Development Program (SERDP).

REFERENCES

1. Halon Replacements – Technology and Science, ACS Symposium Series 611, A.W. Miziolek and W. Tsang, eds., American Chemical Society, Washington, DC (1995). The U.S. Navy's program is reviewed by R.S. Sheinson in Ch. 16, "The U.S. Navy Halon Total Flooding Replacement Program: Laboratory Through Full-Scale".
2. Information can be found at the NGP web site: www.dtic.mil/ngp/.
3. "Dynamics of Water Droplets in a Counterflow Field and their Effect on Flame Extinction", "A.M. Lentati and H.K. Chelliah, *Combust. Flame* **115**: 158-179 (1998).
4. "Water Mist Suppression of Non-Premixed Counterflow Flames", E.J.P. Zegers, B.A. Williams, R.S. Sheinson, and J.W. Fleming, Eastern States Section: The Combustion Institute, 1999 Fall Technical Meeting, Raleigh, NC, 11-13 October 1999.

5. "Inhibition of Premixed Methane-Air Flames by Water Mist", S. P. Fuss, D. J. Dye, B. A. Williams, J. W. Fleming, Eastern States Section: The Combustion Institute, 1999 Fall Technical Meeting, Raleigh, NC, 11-13 October 1999.
6. "Quantification of Physical Fire Suppression of Heptane Pool Fires", R.S. Sheinson, J.E. Hahn, K. Geary, and F.W. Williams, Eastern Section of The Combustion Institute, Chemical and Physical Process in Combustion, Proceedings of the 1977 Fall Technical Meeting, East Hartford, CT, IV/30-35 (1977).
7. "Quantification of Fire Suppressant Action on Liquid Pool Fires", R.S. Sheinson, G.I. Gellene, F.W. Williams, and J.E. Hahn, Eastern Section of The Combustion Institute, Chemical and Physical Process in Combustion, Proceedings of the 1978 Fall Technical Meeting, Miami Beach, FL, 18/1-4 (1978); "The Physical and Chemical Action of Fire Suppressants", *Fire Safety Journal*, **Vol. 15**, 437-450 (1989).
8. "Fire Suppression Agent Effectiveness Prediction and Implications for Fire Extinguishment Tests", R.S. Sheinson and S.P. Baldwin, Proceedings of the Eastern States Section: The Combustion Institute, Princeton, NJ, pp. 483-486, 1993.
9. "The Cup Burner as a Suppression Mechanism Research Tool: Results, Interpretations, and Implications", R.S. Sheinson and A. Maranghides, Proceedings of the 1997 Halon Options Technical Working Conference, pp. 19–30 (1997).
10. "Binary CF_3Br- and CHF_3-Inerst Flame Suppressants: Effect of Temperature on the Flame Inhibition Effectiveness of CF_3 and CHF_3", Y. Saso, Y. Ogawa, N. Saito, and H. Wang, *Combust. Flame* **118**: 489-499 (1999).
11. "A Holistic Approach to Halon Replacement System Design: A Case Study", A. Maranghides, R.S. Sheinson, T. Friderichs, B.H. Black, M Peatross, and W.D. Smith, Proceedings of the International Conference on Ozone Protection Technologies, Washington, DC, pp. 578-582, (1996).
12. "Effect of Fluorinated Ethanes and Propanes and Sulfur Hexafluoride on the Extinction Strain Rate of Methane/Air and Propane/Air counterflow Diffusion Flames", B.A. Williams, E.M. Fisher, E.J.-P Zegers, J.W. Fleming, R.S. Sheinson, 27th International Symposium on Combustion, Abstracts of Work-in-Progress Posters, W1A10, p. 10 (1998).
13. "Intermediate Species Profiles in Low Pressure Premixed Flames Inhibited by Fluoromethanes", D. L'Esperance, B. A. Williams, and J.W. Fleming, *Combust. Flame* **117**: 709-731 (1999); "Intermediate Species Profiles in Low Pressure Methane/Oxygen Flames Inhibited by 2-H Heptafluoropropane: Comparison of Experimental Data with Kinetic Modeling", B.A. Williams, D. L'Esperance, and J.W. Fleming, *Combust. Flame,* in press.
14. "Inhibition of Premixed Hydrogen-Air Flames by 2-H Heptafluoropropane", R.G. Hynes, J.C. Mackie, and A.R. Masri, *Combust. Flame* **113**: 554-565 (1998); "Shock-tube Study of the Pyrolysis of the Halon Replacement Molecule CF_3CHFCF_3", R.G. Hynes, J.C. Mackie, and A.R. Masri, *J. Phys. Chem. A*, **103**: 54-61 (1999); "Sample Probe Measurements on a Hydrogen/Ethane/Air/2-H Heptafluoropropane Flame", R.G. Hynes, J.C. Mackie, and A.R. Masri, *Energ. Fuel.* **13**: 485-492 (1999).

15. "Water Spray Cooling System – A Gaseous Suppression System Enhancer", A. Maranghides, R.S. Sheinson, B.A. Williams, and B.H. Black, Proceedings of the Eight International Interflam Conference, Edinburgh, Scotland, pp. 627-637 (1999).
16. "Relative Flame Inhibition Effectiveness of Metallic Compounds", V. Babushok and W. Tsang, Proceedings of the 1997 Fall Technical Meeting: The Eastern States Section of the Combustion Institute, Hartford, CT, pp. 79-82 (1997).
17. "Numerical Study of the Inhibition of Premixed and Diffusion Flames by Iron Pentacarbonyl", M.D. Rumminger, D. Reinelt, V. Babushok, and G.T. Linteris, *Combust. Flame* **116**: 207-219 (1999).
18. "Chemical Limits to Flame Inhibition," V. Babushok, W. Tsang, G.T. Linteris, and D. Reinelt, *Combust. Flame* **115**: 551-560 (1998).
19. "Role of Particles in Flame Inhibition by Iron Pentacarbonyl", M.D. Rumminger and G.T. Linteris, Proceedings of the 1999 Halon Options Technical Working Conference, Albuquerque, NM, in press.
20. "Behavior of Bicarbonate Powders in Counterflow Diffusion Flames", M.D. Reed, B.A. Williams, R.S. Sheinson, and J.W. Fleming, Proceedings of the Eastern States Section: The Combustion Institute, pp. 83-86, 1997; "Extinction Studies of Propane/Air Counterflow Diffusion Flames: The Effectiveness of Aerosols", J. W. Fleming, M.D. Reed, E.J.P. Zegers, B.A. Williams, and R.S. Sheinson, Proceedings of the 1998 Halon Options Technical Working Conference, pp. 403-414, 1998.
21. "Flame Extinction by Sodium Bicarbonate Powder in a Cup Burner", A. Hamins, Proceedings of the Twenty-Seventh (International) on Combustion/The Combustion Institute, Pittsburgh, PA, 2857-2864 (1998).
22. Flame Extinction Properties of Dry Chemicals; Extinction Concentrations for Small Diffusion Pan Fires", C.T. Ewing, F.R. Faith, J.T. Hughes, and H.W. Carhart, *Fire Technology* **25**, 134 (1989).
23. "Suppression Mechanisms of Alkali Metal Compounds", B.A. Williams and J.W. Fleming, Proceedings of the 1999 Halon Options Technical Working Conference, Albuquerque, NM, in press.

UNSTEADY FLOW DYNAMICS OF BUOYANT PLUMES AND DIFFUSION FLAMES

B. M. Cetegen
Mechanical Engineering Department
University of Connecticut, Storrs, CT 06269-3139
[cetegen@engr.uconn.edu]

Introduction:

Buoyant plumes and flames have been of interest in science and engineering for many years. Many technologically and environmentally important flows are influenced by buoyancy at many different length scales [1]. These scales span distances from a few centimeters for buoyant plumes and diffusion flames in a laboratory setting to many kilometers in geophysical events such as volcanic eruptions and alike. Buoyant plumes and diffusion flames exhibit unsteady flow dynamics under certain regimes [2-5]. The unsteady vortical flow field in these flows influence entrainment, mixing and combustion characteristics. Since buoyancy is generated or modified within the flow field itself, the buoyancy generated motions are intimately coupled with the underlying density field upon which the gravity acts. In non-reacting buoyant plumes, for example, buoyancy at the plume source is modified continuously due to mixing with the ambient fluid which determines the strength of the buoyant convection. This buoyancy induced flow is, in turn, responsible for mixing characteristics. In buoyant diffusion flames, entrainment of ambient air is dominated by buoyancy and part of this entrained air is utilized for combustion and heat release which is the main source of buoyancy in this case. In this paper, a review of our work on buoyant plume dynamics is presented. First part of this presentation concerns buoyant non-reacting plumes of helium and helium-air mixtures. Both planar plumes originating from long aspect ratio rectangular nozzles as well as axisymmetric plumes originating from round nozzles are considered. The experiments included determination of stability maps for transition from steady laminar plumes to pulsating unsteady plume regime. Pulsation frequency and its scaling on the relevant flow parameters were also established. The second part concerns the characterization of buoyant diffusion flame dynamics and formulation of a phenomenological entrainment model based on the observed unsteady flow features.

Experimental Set-up:

The typical experimental set-up is schematically shown in Fig. 1 below. It consists of a plume nozzle assembly placed under a hood. Plumes are shielded from the ambient disturbances by means of screen curtains. The experimental diagnostics include: (1) imaging of non-reacting plume effluent seeded with mineral oil smoke by planar laser Mie scattering, (2) direct visualization of buoyant diffusion flames from natural soot radiation; and (3) detection of small dynamic pressure fluctuations along the plume centerline to determine the oscillation frequencies. For this purpose, two differential pressure transducers of capacitance type were connected to probes situated at different heights above the nozzle exit. The pressure transducer signals were first amplified and subsequently analyzed using a spectrum analyzer. The video images of these plumes and flames are obtained using a high speed video camera (Kodak Ektapro 1000) and a video camcorder (SONY TR71). The first imager was used to analyze the quantitative features of the vortex formation and convection events.

Different nozzle assemblies were used in the plume experiments. Circular nozzles of various diameters (3.6, 5.2, 7.3, 10.2, 15.2 and 20.3 cm) were employed. In some of our experiments, acoustic forcing of plume effluent was studied using a loudspeaker placed at the bottom of the

nozzle assembly. Planar plumes were studied using large aspect ratio rectangular nozzles of different widths (2.0 to 7.0 cm in increments of 1.0 cm) and a breath of 20 cm.

Buoyant diffusion flame experiments were conducted using circular burners of different diameters (0.05, 0.10, 0.15, 0.3 and 0.5 m) under a 2.4 x 2.4 m cross section, 1.8 m deep large hood. Commercial grade propane was used as the fuel.

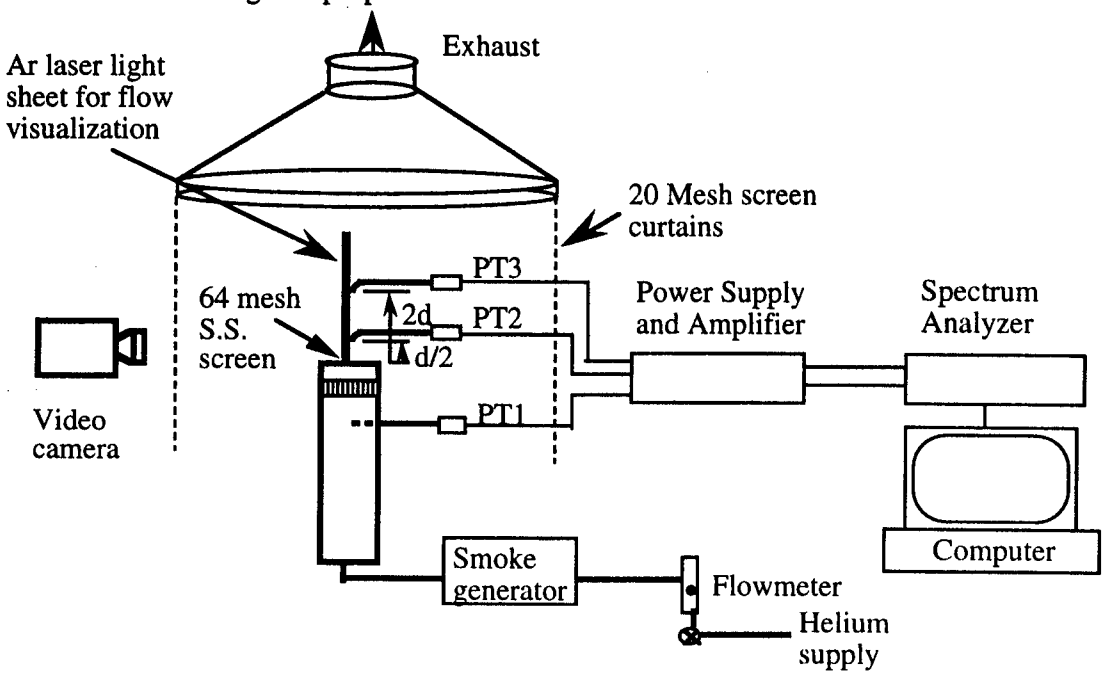


Fig. 1. Typical set-up for buoyant non-reacting plume experiments

Results and Discussion

Experiments on non-reacting buoyant plumes

A series of experiments were conducted with axisymmetric and planar buoyant plumes of helium and helium-air mixtures with the objective of defining the stable and unstable flow regimes and the scaling of oscillation frequencies. Figure 2 shows non-oscillating and oscillating plume images for planar and axisymmetric plumes.

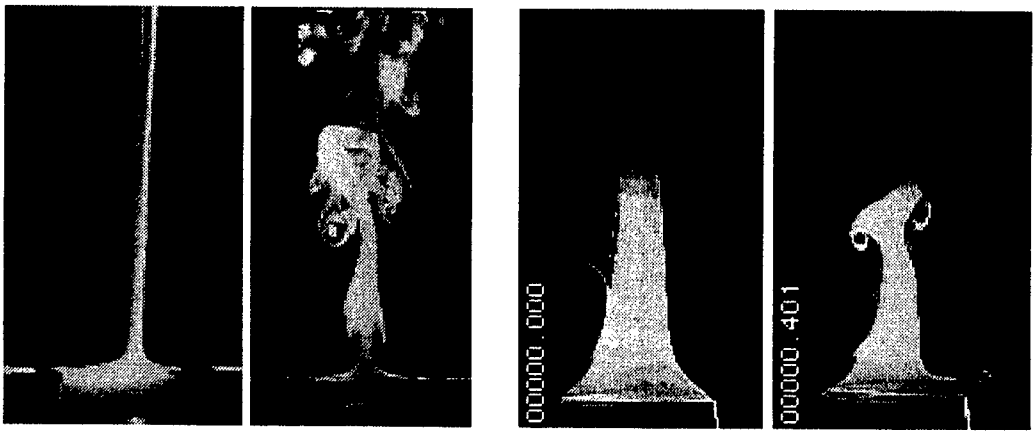


Fig. 2: Non oscillating and oscillating buoyant plumes of helium. Left pair for planar plumes and right pair for axisymmetric plumes

Plume boundaries undergo a sharp contraction as a result of rapid buoyant acceleration of light plume fluid in the surrounding air medium. As the velocity of the plume fluid at the nozzle exit is increased, plume begins to exhibit oscillations which eventually lead to a periodic oscillatory state. In this case, the transition from the non-oscillatory to the oscillatory state is of interest.

Figures 3 and 4 show the stability diagrams for planar and axisymmetric plumes [6,7]. For experiments spanning a range of nozzle widths and diameters and plume fluid densities (ρ_p/ρ_∞.= 0.14 to 1.0), it was found that the transition can be best represented in terms of a Reynolds number, $Re = V_p w/\nu_p$ or $V_p d/\nu_p$ versus ρ_p/ρ_∞ . Plumes to the left of the transition boundary were found to be oscillatory within a downstream distance of two nozzle diameters (or width) from the nozzle exit. As the density ratio increases, i.e. plume fluid density becomes closer to that of the ambient, oscillatory behavior is observed at higher nozzle exit velocities. In fact, unstable axisymmetric plumes are not found beyond a density ratio, ρ_p/ρ_∞. of about 0.6. This observation is consistent with those of Kyle and Sreenivasan [8]. Planar plumes, on the other hand, appear to be less stable than axisymmetric plumes based on the stability limits. For planar plumes, the nozzle exit configuration has an influence on plume stability with plumes originating from nozzles with a flat plate flush with the nozzle exit being less stable than those originating from free standing nozzles. This can be explained based on the differences in the flow field near the nozzle [7].

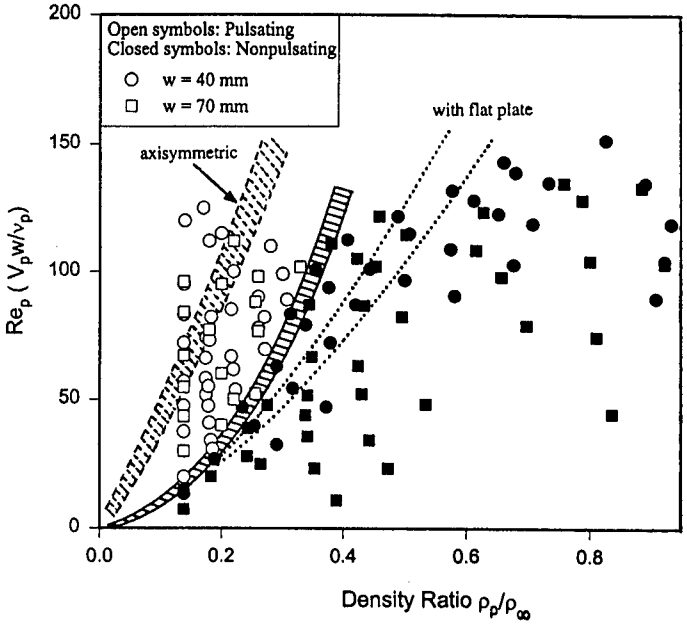


Fig. 3. Stability diagram for planar buoyant plumes of helium and helium-air mixtures

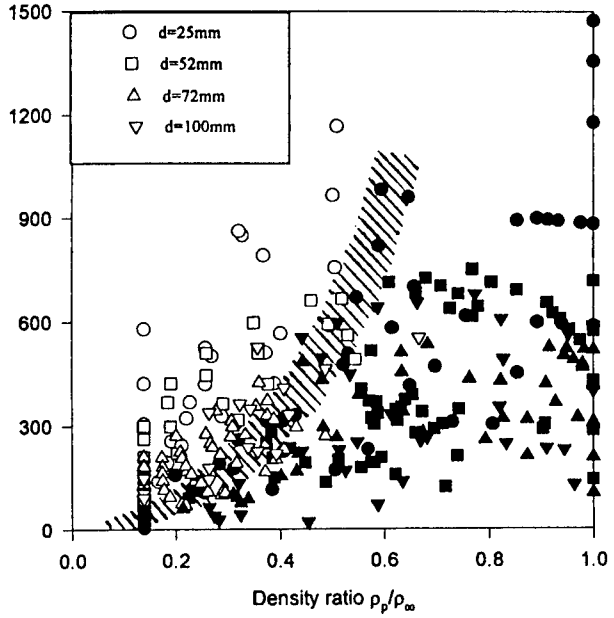


Fig. 4. Stability diagram for axisymmetric buoyant of helium and helium-air mixtures

In the oscillatory regime, the plume pulsation frequencies were determined from frequency spectra of the small dynamic pressure oscillations along plume centerline. Plume pulsation frequencies were correlated in the form of Strouhal number, $St = fw/V_p$ or fd/V_p versus Richardson number as shown in Figs. 5 and 6. It is found that the frequency data are well correlated for both planar and axisymmetric geometries. Planar plume pulsation frequency is independent of the nozzle configuration and it is slightly different than the correlation for the axisymmetric case. The correlation for axisymmetric plumes exhibits a transition between Ri = 200 and 500. It is found that for Ri > 500, plumes become turbulent and hence the change in scaling [5].

Instability mechanism and numerical simulations

Along with experiments, a complete understanding of the instability mechanism requires numerical simulations of the flow field and the underlying flow dynamics. Simulations allow

numerical experiments that can not be easily performed or that are limited to a certain range of parameters in the experiments. The numerical model in our studies is a two dimensional Lagrangian transport element method, TEM [9]. Such a model accurately captures the unsteady vortex dynamics of the flow, an essential element in understanding of this type of flow. The results from TEM

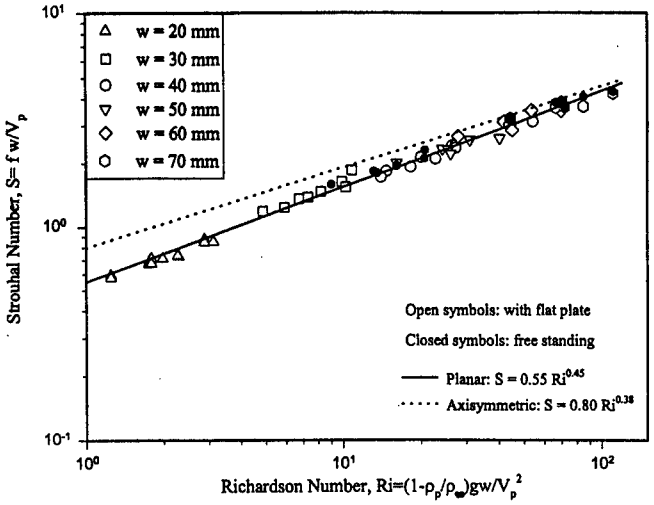


Fig. 5. Pulsation frequency correlation for planar buoyant plumes

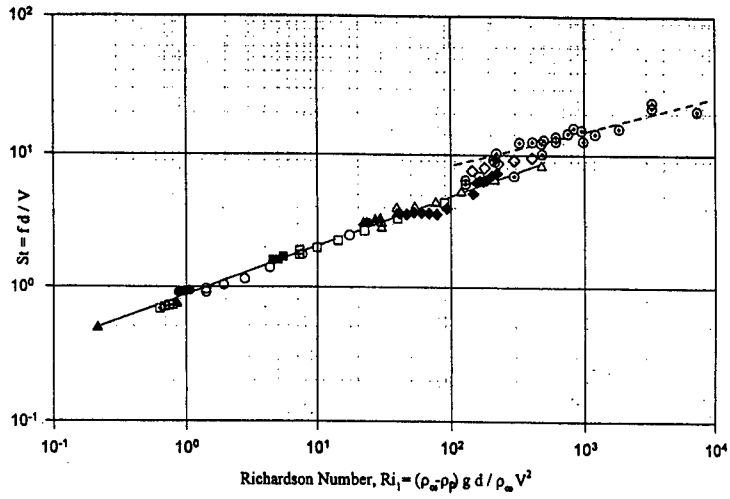


Fig. 6. Pulsation frequency correlation for axisymmetric buoyant plumes

were compared with the experiments of planar plumes. Figure 7 shows the comparison of pulsation frequency indicating the excellent ability of the computational model to capture the correct scaling and values of the pulsation frequency. Beyond this, model was tested to check its ability to predict transition from non-oscillatory to oscillatory behavior. It was found that the numerical simulations indeed bracket the transition boundaries shown in Fig. 3. Thus, numerical model could be used with confidence to study the instability mechanism in these flows.

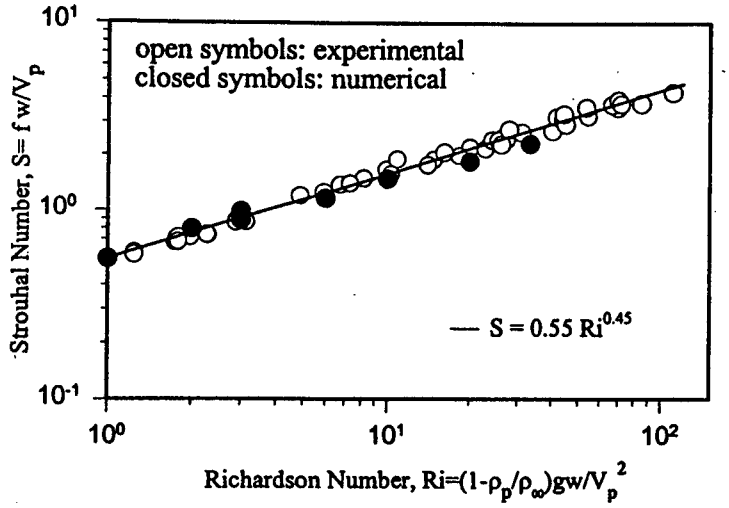


Fig. 7: Comparison of pulsation frequencies predicted from the TEM with the experiments

The instability leading to a periodic state was earlier [4,5] explained based on the experimental results. It was suggested that the rapid acceleration of the plume fluid results in the formation of a

vortical structure (a vortex pair or a toroidal ring) that convects downstream. As the plume flow is continuously supplied upstream of the vortex, interaction of the upstream buoyant flow with the vortex occurs. Through this interaction, a periodic state is established. In numerical simulations, similar phenomenon is observed. The vorticity is continuously deposited into the flow due to buoyancy as shown in Fig. 8. Total circulation in the flow increases with increasing downstream distance in the absence of any vortical structure in the plume flow. However, when a large scale vortical structure is present nearby, it provides the stretching of the vorticity layer upstream keeping the interface as a contracting front. As it convects downstream, its influence diminishes and the vorticity layer becomes thicker due to the accumulation of vorticity. This accumulation of vorticity results in bulging out of the plume boundaries as observed in Fig. 8. This becomes the inception of a new vortical structure and the process repeats itself. This mechanism is consistent with experimental findings and the dependence of pulsation frequency on flow parameters. The pulsation frequency dependence can be obtained from a simple kinematic model [5] which relies on convection and induction of vortical structures.

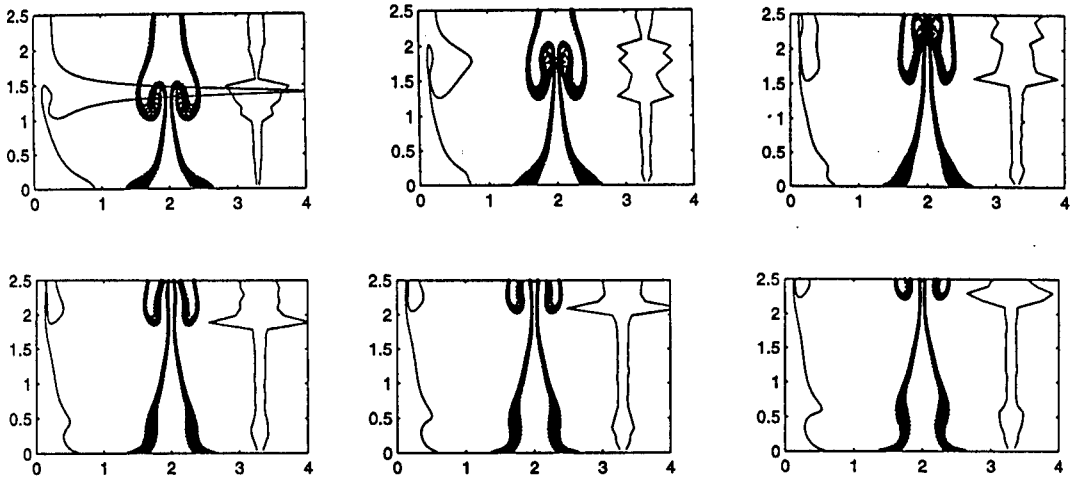


Fig. 8: Numerical TEM simulations of planar helium plumes. Each image displays the vortex elements in the flow field (middle), total circulation (right) and residence time (left)

Experiments on buoyant diffusion flames

Characteristics of buoyant diffusion flames, while being similar to non-reacting plumes qualitatively, exhibit some differences due to the variation of buoyancy along the flame length as compared to non-combusting plumes. In a diffusion flame, local buoyancy is sustained by heat release along the flame length. In non-combusting plumes, the local buoyancy is reduced due to mixing and dilution. It is well-established that buoyant diffusion flames oscillate with a frequency that scales as scales as $f = 1.5\ d^{-1/2}$ where f is the frequency in Hertz and d is the source diameter in meters [4,10]. Through a variety of experiments with buoyant diffusion flames [4], it has been shown that the instability mechanism described above is responsible for buoyant flame oscillations as well [4].

Recently, we have found a duality on the unsteady behavior of buoyant diffusion flames originating from small diameter nozzles [11]. These diffusion flames can exhibit a commonly observed "varicose" mode and a "sinuous" mode as depicted in Figs. 9 and 10. The two modes have different oscillation frequencies with varicose mode exhibiting the $d^{-1/2}$ dependence. It was also observed that a flame could switch back and forth between the two different modes [11]. Figure 11 shows the frequency of the two modes. The varicose frequency scaling clearly shows the $d^{-1/2}$ dependence while the "sinuous" mode has a weaker diameter dependence of $d^{-0.1}$. Figure 12 shows the probability of the "varicose" mode as a function of Richarson number. For large diameter nozzles, "varicose" mode is commonly observed as in pool fires.

The effects of altering the global buoyancy in diffusion flames were also explored in our studies [11]. This involved burning of propane diffusion flames in synthesized atmospheres of helium-oxygen mixtures. It was found that the flame oscillations can be completely suppressed when flames were burned in high helium containing mixtures. It was also determined that the flame oscillation frequency in "varicose" mode can be reduced by this change in buoyancy as shown in Fig. 13. In fact, it can be shown that the studied altered buoyancy conditions correspond to partial gravity conditions.

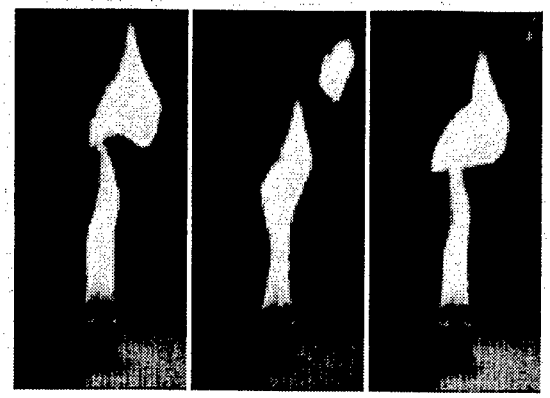


Fig. 9. Varicose oscillation mode of 0.8 kW propane flame on 2.54 cm dia. burner

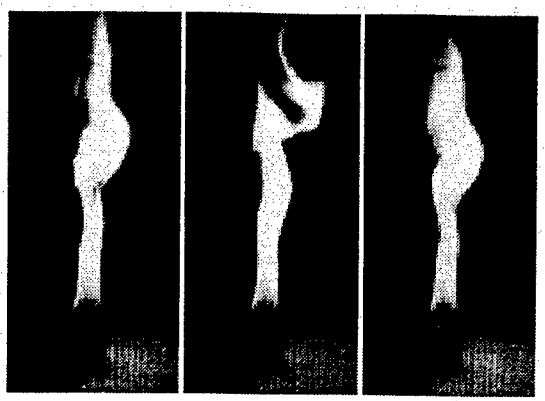


Fig. 10. Sinuous oscillation mode of 0.8 kW propane flame on 2.54 cm dia. burner

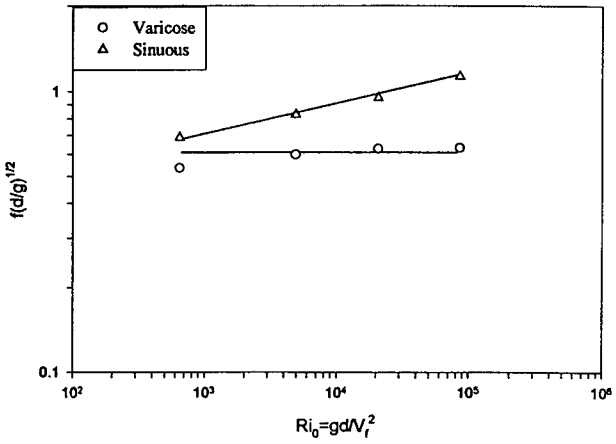


Fig. 11. Oscillation frequency for the "varicose" and "sinuous" modes

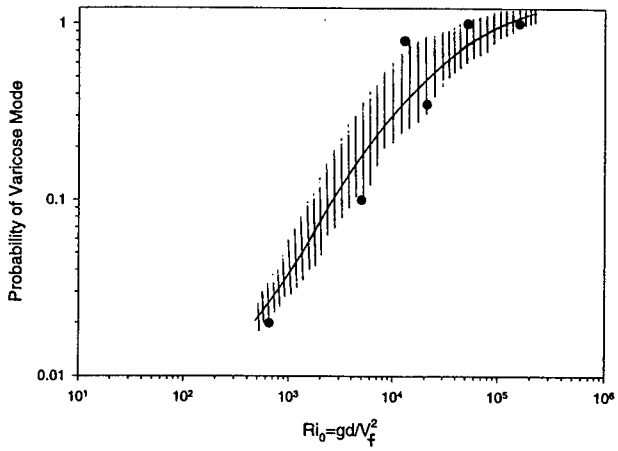


Fig. 12. Probability of the varicose mode as function of Richardson number

Phenomenological model of entrainment in pool fires

Periodically shed large scale toroidal vortices strongly affect the entrainment process in the flaming regions of a fire. Figure 14 shows a buoyant propane diffusion flame originating from a 10 cm dia. nozzle around which the ambient air is made visible by smoke trails. The distortion of the smoke trails around the large scale vortices, clearly indicate that the ambient air is engulfed by the toroidal vortical structures

The model assumes that the periodic engulfment by large scale toroidal vortices is responsible for entrainment into the fire plume. These toroidal vortices (or vortex rings) provide a

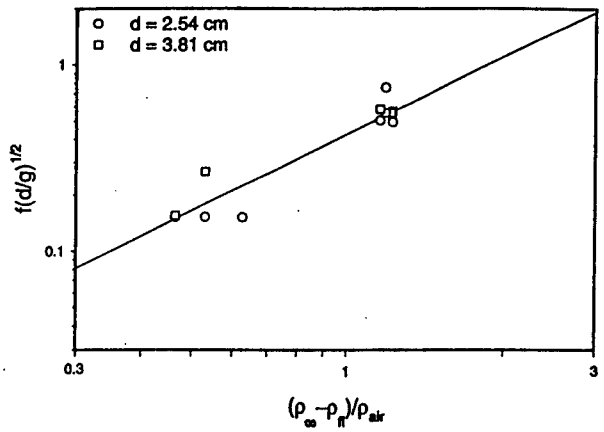


Fig. 13: Effect of global buoyancy on pulsation frequency of buoyant flames

means of periodically pumping of ambient air into a fire plume. The strength of vorticity (or vortex circulation) determines the strength of the pumping action during each vortex convection event. The volume of entrained fluid per vortex convection cycle, Q_{ent} can be determined analytically from a convecting vortex ring model [12]. This engulfed volume of air per vortex convection cycle is then multiplied by the vortex shedding frequency and the ambient air density, ρ_o to obtain the mass entrainment rate of air into the flame as:

$$\dot{m}_{ent} = \rho_o \, Q_{ent} \, f$$

The presence of multiple toroidal vortices is also accounted for in this expression by superposition of each vortex contribution to the entrainment. This is admissible considering that the entrained volume is computed based on vortex velocity in the potential flow region. The vortex circulation can be readily related to its self-induced convection using a thin core vortex ring expression [13]. Combining these results, the entrainment rate can be written as [12],

$$\dot{m}_{ent} = \frac{3\,\pi\,\rho_o\,[1 + \ln(a)]}{2} \; \frac{z\,d^{3/2}}{\left[\log\left(\frac{4}{1-a}\,\frac{d}{z}\right)\right]}$$

The result of the normalization of entrainment rates with respect to this correlation is shown in Fig. 15. It is seen that the data for all three different diameter burners [14] now lie at a constant level of 1.5 ± 0.5, suggesting that the model properly accounts for the variations with respect to z and d. The reasonable values of the vortex core constant "a" chosen between 0.7 and 0.9 were found to be quite insensitive with respect to the quality of the correlation. The entrainment data of Gore and coworkers [15] presented in a Froude number correlation suggests a dependence on height and burner diameter as $m \; \alpha \; z^{0.78} \, d^{1.72}$ in the visible flame region. Thus, the model presented here is in reasonable agreement with their experimental results as well.

Acknowledgments:
Author would like to acknowledge the work of his students, T. Ahmed, K. Kasper, Y.Dong. Many discussions on this topic with my colleagues, Prof. Marios Soteriou, late Prof. Ed Zukoski, Drs. John deRis, George Markstein and Michael Delicatsios were invaluable. Most of the work was sponsored by NSF Grant, No. CTS-8909176 and several internal grants from UConn. Research Foundation

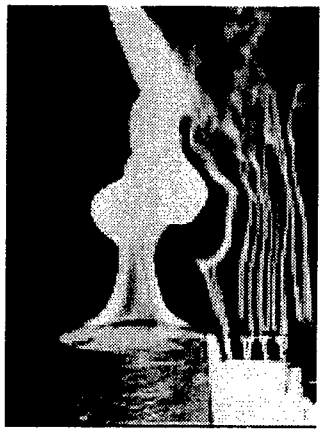


Fig. 14: Image of entrained flow into a 2.6 kW propane flame

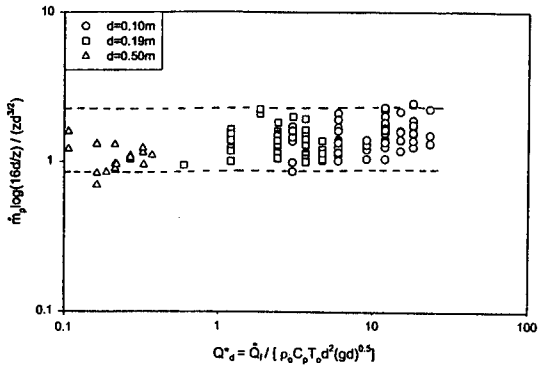


Fig. 15: Scaling of plume mass flux data with respect to the model correlation as a function of dimensionless heat release parameter. Experimental data in the visible flame region is from ref. [14].

References:

1. Turner, J. S., Buoyancy Effects in Fluids, Cambridge University Press, London,1973.
2. Gebhart, B., Instability, transition and turbulence in buoyancy-induced flows, *Annu. Rev. Fluid Mech.*, Vol. 5, p. 213, 1973
3. A. Hamins, A. ,Yang J. C. and Kashiwagi, T., An experimental investigation of the pulsation frequency of flames, *Proc. of the 24th Symp. (Int'l) on Combust.*, p. 1695, 1992
4. Cetegen, B. M. and Ahmed, T., "Experiments on the periodic instability of buoyant plumes and pool fires", *Combustion & Flame,* Vol.93, pp.157-184, 1993
5. Cetegen, B. M. and Kasper, K. D. , Experiments on the Oscillatory Behavior of Buoyant Plumes of Helium and Helium-Air Mixtures, *Physics of Fluids*, **8**(11),p. 2974, 1996

6.Cetegen, B. M., Dong, Y., and Soteriou, M. C., "Experiments on stability and oscillatory behavior of planar buoyant plumes", *Physics of Fluids*, Vol. 10, No. 7, p. 1658, 1998

7. Cetegen, B. M., "Behavior of naturally oscillating and periodically forced axisymmetric buoyant plumes of helium and helium-air mixtures", *Physics of Fluids*, Vol. 9. No. 12 , p. 3742, 1997
8. Kyle, D. M. and Sreenivasan, K. R., The stability and breakdown of a round variable density jet, *J. Fluid Mech.*, Vol. 249, p. 619, 1993
9. Soteriou, M. C. and Ghoniem, A. F., Numerical simulation of unsteady combustion using the transport element method, *ESAIM Proceedings*, Vol. 1, p. 429, 1996
10. P. J. Pagni, Pool fire vortex shedding frequencies, in *Some Unanswered Questions in Fluid Mechanics*, L. M. Trefethen and R. L.Panton eds. Appl. Mech. Rev.,Vol.43, No.8, p.166, 1990
11. Cetegen, B. M. and Dong, Y., "Experiments on instability modes of buoyant diffusion flames and effects of ambient atmosphere on instabilities", submitted to *Experiments in Fluids*, March 1999
12. Cetegen, B. M., "A phenomenological model for near-field fire plume entrainment", *Fire Safety Journal*, Vol. 31, p. 299, 1998
13. Saffman, P. G., Vortex dynamics, Cambridge University Press, London, 1992
14. Cetegen, B. M. , Zukoski, E. E. and Kubota, T, Entrainment in the near and far field of fire plumes, *Combust. Sci. & Tech.*, Vol. 39, p. 305,1984
15. Zhou, X. C. and Gore, J. P., Air Entrainment Flow Field Induced by a Pool Fire, *Combust. and Flame*, Vol. 100, p. 52, 1995

MONDAY SESSIONS
OCTOBER 11TH

An Evaluation of Acetylene + O_2 Oxidation System: HCCH+ $O_2(^3\Sigma)$, HCCH + $O_2(^1\Delta)$ and Vinylidene + $O_2(^3\Sigma)$ via Isomerization of HCCH

Chad Sheng and Joseph W. Bozzelli
Department of Chemical Engineering, Chemistry and Environmental Science
New Jersey Institute of Technology, Newark, NJ 07102

Acetylene is an important intermediate in hydrocarbon combustion systems. Most detailed models on combustion of hydrocarbon species include reactions for both formation and oxidation of acetylene. Several researchers, in efforts to model the combustion of hydrocarbon, have indicated that they cannot account for induction times and flame speeds, in their models, without a direct HC≡CH + O_2 reaction.[1-5] These studies offer a number of different exothermic product sets for the reaction: HCO + HCO, HC•=C=O + H, H2C=C=O + O, or 2CO + 2H. Recent evaluations[5] generally agree that any radical in the product set which results in propagation reactions will allow detailed models to match experimental data.

Miller *et al*[2] postulated three possible reaction products,

$C_2H_2 + O_2 \Leftrightarrow HCCO + OH$ $\quad \Delta H_f^{(0)}{}_0$ = -5 kcal/mol
$C_2H_2 + O_2 \Leftrightarrow CH_2O + O$ $\quad \Delta H_f^{(0)}{}_0$ = -6 kcal/mol
$C_2H_2 + O_2 \Leftrightarrow HCO + HCO$ $\quad \Delta H_f^{(0)}{}_0$ = -36 kcal/mol

any of which can be used in their model to fit the observed experimental data satisfactorily. Miller *et al* chose the first product set, ketenyl plus hydroxyl radicals, for inclusion in their mechanism. This is the same product set that Marinov *et al* chose; however, the pre-exponential A-factor, of Miller *et al* is 5 times higher than that chosen by Marinov *et al* at the same E_a, 30.1 kcal/mol.[6]

Four plausible reaction systems are investigated and compared: HCCH+ $O_2(^3\Sigma)$ to form an adduct with further reaction of this triplet adduct; conversion of triplet adduct to singlet by collision and then reaction of singlet adduct to products; HCCH + $O_2(^1\Delta)$ (direct formation of a singlet adduct); and HCCH ⇔ CH_2=C: and then CH_2=C: + $O_2(^3\Sigma)$. *ab initio* and density functional calculations are employed to estimate thermodynamic properties of reactants, transition states and products in the HCCH+ $O_2(^3\Sigma)$ and the conversion of triplet adduct to singlet adduct system. The HCCH + $O_2(^1\Delta)$ system was proposed by Benson as a plausible pathway.[7] Isomerization of acetylene to vinylidene and then addition of $^3O_2$ to the vinylidene and reaction of an insertion adduct to products was proposed by Laskin and Wang.[8,9] ChemKin modeling is performed for all four systems.

HCCH + $O_2(^3\Sigma)$ reaction is initiated by addition of molecular oxygen to a carbon atom, forming a triplet peroxy-ethylene biradical. A triplet glyoxal biradical is formed from this adduct, through a 3-member carbon-oxygen-oxygen (dioxirane) ring intermediate. Dissociation of the triplet glyoxal biradical can form a glyoxal radical plus hydrogen atom or 2 formyl radicals. Ketenyl plus hydroxyl radicals are a less favored product, formed by the reaction of the initial peroxy-ethylene biradical, through a cyclic intramolecular hydrogen transfer (carbon-oxygen-oxygen-hydrogen) transition state. The major products are either two formyl radicals or glyoxal radical plus hydrogen atom. (Figure 1)

A CHEMKIN integrator computer code is utilized to calculate the concentration profile of reactants, stabilized adducts and products[10] versus time. Concentration profiles are calculated at pressures of 0.013, 0.1 and 1 atm and temperatures of 1000, 1600 and 2000K are presented for initial concentration conditions of 5% HCCH, 15% $^3O_2$ and 80% N_2. Figure 2 shows concentration profiles determined by CHEMKIN for BHandH/6-31g(d) density functional calculated data for 5% HCCH, 15% O_2 and 80% N_2 at 1 atm for temperatures of 1000, 1600 and 2000K. Product formation at 1600K and 1 atm is about 10.2% and at 2000K 80.4% conversion is observed after 35 milliseconds. Based on *ab initio* and density functional calculation, the estimated overall forward rate constant for HCCH + O_2 → H + •C=OCHO is determined to be 3.75×10^{11} $T^{1.165}$ exp(-51.09 kcal/RT) and for HCCH + O_2 → HCO + HCO the overall forward rate constant is estimated to be 6.22×10^7 $T^{1.341}$ exp(-51.19 kcal/RT) from B3LYP/6-31g(d,p) at 1 atm for $300 \leq T \leq 2500$K. These forward rate constants are determined from QRRK analysis of the overall triplet reaction system, based on all three wells.

Benson[7] presented a system where triplet oxygen converts to the singlet state; then singlet oxygen adds to acetylene forming a singlet biradical. This singlet biradical undergoes ring closure, forming a cyclic 4-member dioxitane radical. 1, 2 ethanedial is then formed, via cleaving the weak O-O peroxide bond and forming two carbonyl bonds. Two formyl radicals are

produced via dissociation of chemically activated glyoxal. Benson estimated the thermochemical kinetic parameters for this system, based on group additivity[11], bond additivity and empirical thermochemical analysis. Benson infers that at combustion temperatures $^3O_2 \Leftrightarrow {}^1O_2$ will be in equilibrium.

A small mechanism file was generated, based upon rate constants and activation barriers provided by Benson[7], for pathways in the singlet oxygen addition to acetylene system. The singlet oxygen addition pathway can be reasonably expressed with control by three reaction steps and assuming all reactions, after formation of dioxitene (cyclic C=C-O-O), which are exothermic by over 50 kcal/mol, rapidly go to products. The three controlling reaction steps, along with rate constant expressions are listed as:

Reaction	Rate Constant (cc/mol-sec)
$^3O_2 + M \Leftrightarrow {}^1O_2 + M$	$k = 10^{13} \exp(-23.0/RT)$
$^1O_2 + HCCH \Leftrightarrow {}^1\bullet C{=}COO\bullet$	$k = 6.95 \times 10^7 T^{1.8} \exp(-7.6/RT)$
$^1\bullet C{=}COO\bullet \Leftrightarrow$ (cyclic C=C-O-O)	$k = 2 \times 10^{12} \exp(-6.0/RT)$
(cyclic C=C-O-O) $\Leftrightarrow$ O=CH-CH=O$^{\neq} \Leftrightarrow$ HCO + HCO (fast)	
E_a in kcal/mol; M = buffer gas	

Benson estimated the net forward reaction for the triplet to singlet oxygen conversion and addition of oxygen to acetylene to be $2 \times 10^{12} \times (T/300)^{1.8} \exp(-30.6/RT)$. The pre-exponential A-factor for the subsequent isomerization reactions were not provided by Benson. We estimate the A-factor for this isomerization to be constant at 2×10^{12} from calculations of Mebel *et al*[12] on vinyl peroxide cyclization. Product yields determined from ChemKin results for acetylene oxidation, through the singlet channel as proposed by Benson, is higher by an order of magnitude than for the reaction on the triplet surface as determined by BHandH/6-31g(d,p) at temperatures of 1600 and 2000K at 1 atm. (See Figure 3)

We have performed B3LYP/6-31g(d,p) calculations on the singlet peroxy-ethylene biradical and the singlet TS1 to further validate the path proposed by Benson. Comparison of heat of formation for the singlet peroxy-ethylene biradical, between Benson's estimation technique and DFT calculations show reasonable agreement. Benson reports a ΔH_{rxn} for the net reaction of $^3O_2 + HCCH \rightarrow {}^1\bullet OOCH{=}C\bullet H$ about 24 kcal/mol, where 23 kcal/mol is required for the $^3O_2 \Leftrightarrow {}^1O_2$ conversion. B3LYP/6-31g(d,p) calculates a ΔH_{rxn} for $^3O_2 + HCCH \rightarrow {}^3\bullet OOCH{=}C\bullet H$ as 26.42 kcal/mol, and BHandH/6-31g(d) determined a value of 24.86 kcal/mol. This would suggest the difference between the heat of formation for singlet and triplet peroxy-ethylene biradical is less than 3 kcal/mol difference, as is also suggested by Benson.

B3LYP/6-31g(d,p) calculations for the transition state of **singlet oxygen** addition to acetylene yield estimate on $H_f(298K) = 102.22$ with a $S^2 = 0$. The B3LYP/6-31g(d,p) enthalpy of formation for the **triplet peroxy biradical** transition state is almost 20 kcal/mol lower than the singlet transition state, making HCCH + $^3O_2$ the more favorable reaction path. One needs to evaluate the transition state energy for HCCH + $^1O_2$ more thoroughly. A significant problem with Benson's scheme exists, if this calculation is correct and no other lower energy transition states are found for adduct formation by HCCH + $^1O_2$. The difference between the triplet peroxy ethylene biradical adduct and the singlet peroxy ethylene biradical adduct is about 1 kcal/mol, as calculated from B3LYP/6-31g(d,p) and in agreement with Benson.

Laskin and Wang[8,9] have recently proposed an alternative pathway to explain a direct acetylene plus O_2 process. They invoke acetylene isomerization to singlet vinylidene (CH_2=C:), and infer that reaction kinetics of $^1CH_2$=C: + $^3O_2$ will be similar to that of $^1CH_2 + {}^3O_2$. Laskin and Wang determine thermodynamic properties of vinylidene using the G2 composite method based on B3LYP/6-31g(d) geometry. The activation barrier for isomerization of acetylene to vinylidene was reported as 43 kcal/mol. The vinylidene can insert into $^3O_2$ forming a triplet $CH_2{=}C(O\bullet)O\bullet$ adduct, which can dissociate to $^3CH_2 + CO_2$. Other spin conserved and non-conserved reactions are also suggested. The vinylidene + $^3O_2$ reaction to products is highly exothermic and is assumed to proceed rapidly; the HCCH $\Leftrightarrow$ CH_2=C: reaction is indicated as rate controlling. The initial work of Laskin and Wang does not, however, consider fall-off (pressure dependence) for formation of the active vinylidene species ($^1CH_2$=C:).

Comparison of rate constants between our B3LYP/6-31g(d,p) determined $^3O_2$ + HCCH system and that of Laskin and Wang's[8,9] vinylidene pathway, based on their G2//B3LYP/6-31g(d) analysis are shown in Figure 4a and 4b. The assumption used in determining Laskin and Wang's rate constants is that the isomerization of acetylene is the rate limiting reaction. That is once vinylidene is formed it immediately reacts with molecular oxygen to products, which we choose as

methylene ($^3CH_2$) and carbon dioxide using spin conservation. The enthalpy of formation for vinylidene is 97 kcal/mol determined from the E_a provided by Laskin and Wang and literature value of acetylene.

We further evaluate the kinetics on the vinylidene path using Laskin and Wang's[8,9] low pressure limit second order rate coefficient. A high pressure limit rate constant is calculated for the isomerization from literature data and canonical transition state theory. We then estimated fall-off using a QRRK with modified strong collision analysis on the bimolecular reaction: HCCH ⇔ H_2C=C:. The QRRK results show acetylene isomerization to vinylidene starts to fall off (deviate from the low pressure limit) above 8 atm for T = 1000 K.

The rate constant for HCCH + $^3O_2$, as calculated from B3LYP/6-31g(d,p), is faster than acetylene isomerization to vinylidene over the pressure range from 10^{-3} to 3 atm. Further reaction on the triplet surface are, however, rate controlling. Figure 4b compares rate constants to the formation of products, i.e. formyl radicals from HCCH + $^3O_2$ on the triplet surface (this study) and $^3CH_2$ + CO_2 from $^1CH_2$=C: + $^3O_2$, over the pressure range of 10^{-3} to 3 atm. Analysis on the formation of products shows that the vinylidene pathway is more favorable than the $^3O_2$ addition and reaction on the triplet surface at 1000K and pressures above 0.1 atm. This suggests that for low temperature (ca 1000K) and high-pressure systems, acetylene isomerization is a viable pathway.

An additional reaction process is considered, addition of triplet oxygen to acetylene, forming ^{3}HC•=CHOO•. This triplet biradical adduct converts to the singlet biradical, i.e. ^{3}HC•=CHOO• + M ⇔ ^{1}HC•=CHOO• + M, with an estimate k_{forw} = 10^{13} exp(-1.02/RT) cc/mol-s. We feel the assumption of pre-exponential A-factor = 10^{13} cc/mol-s for ^{3}HC•=CHOO• + M ⇔ ^{1}HC•=CHOO• + M, about 1 in 40 collisions is conservative. The singlet biradical adduct then proceeds to 2 HCO as in Benson's scheme. Overall rate constants, via conversion of the triplet biradical adduct to singlet biradical adduct, at 1 atm as determined by QRRK analysis is $k_f = 2.21 \times 10^7\ T^{1.46}$ exp(-33.1/RT) cc/mol-s.

Comparison of CHEMKIN mechanism results for product formation between Benson's HCCH + $^1O_2$ and the HCCH + $^3O_2$ ⇔ ^{3}Adduct ⇔ ^{1}Adduct reaction paths are performed and are similar. (Refer to Figure 5) The products compared are glyoxal for Benson's HCCH + $^1O_2$ system and formyl radicals for the ^{3}Adduct ⇔ ^{1}Adduct conversion. The concentration of glyoxal after 34.9 ms is 0.053 mole fraction and for formyl radical products it is about 0.10 mole fraction for the same residence time. The doubling of mole fraction concentration for the formyl radical concentration is due to the formation of 2 moles of formyl radical for every mole of glyoxal.

Miller *et al*[2], Marinov *et al*[6] and Benson's[7] rate constants are shown in Figure 6. Marinov *et al* and Miller *et al*'s rate constants are for HCCH + O_2 ⇔ HCCO + OH, while Benson's is for HCCH + O_2 ↔ •OOCH=C•H, formation of first adduct only. The overall rate constants for the system described in the previous paragraph is also shown in Figure 6. Our rate constants for the triplet formation, then conversion to singlet system, result in values that are less than 1 order of magnitude lower than that recommended by Marinov *et al*; but 2.5 orders of magnitude lower than recommended, by Miller *et al*, as needed to model the data.

REFERENCE:

(1) Tan, Y.; Dagaut, P.; Cathonnet, M.; Boether, J. C. *Comb. Sci. and Tech.* **1995**, *102*.

(2) Miller, J. A.; Mitchell, R. E.; Smooke, M. D.; Kee, R. J. "Toward a Comprehensive Chemical Kinetic Mechanism for the Oxidation of Acetylene: Comparison of Model Predictions With Results From Flame and Shock Tube Experiments"; Nineteenth Symposium (International) on Combustion, 1982.

(3) Gardiner Jr., W. C.; Walker, B. F. *J. Chem. Phys.* **1968**, *48*, 5279.

(4) Jachimowski, C. J. *Combust. Flame* **1977**, *29*, 55.

(5) Hidaka, Y.; Hattori, K.; Okuno, T.; Inami, K.; Abe, T.; Koike, T. *Combust. Flame* **1966**, *107*, 401.

(6) Marinov, N. M.; Pitz, W. J.; Westbrook, C. K.; Vincitore, A. M.; Castaldi, M. J.; Senkan, S. M.; Melius, C. F. *Combustion and Flame* **1998**, *114*, 192-213.

(7) Benson, S. W. *International Journal of Chemical Kinetics* **1996**, *28*, 665-672.

(8) Laskin, A.; Wang, H. "On Initiation Reactions of Acetylene Oxidation in Shock Tubes. A Kinetic Modeling and Quantum Mechanical Study."; First Joint Meeting of the U.S. Sections of the Combustion Institute: Western States, Central States, Eastern States, 1999, Washington, DC.

(9) Laskin, A.; Wang, H. *Chemical Physics Letters* **1999**, *303*, 43-49.

(10) Kee, R. J.; Miller, J. A.; Jefferson, T. H. CHEMKIN: Fortran Chemical Kinetics Code Package, 1980.

(11) Benson, S. W. *Thermochemical Kinetics*, 2nd ed.; Wiley-Interscience: New York, 1976.

(12) Mebel, A. M.; Diau, E. W. G.; Lin, M. C.; Morokuma, K. *J. Am. Chem. Soc.* **1996**, *118*, 9759-9771.

Figure 1. Potential Energy Diagram for HCCH + O2(Triplet).

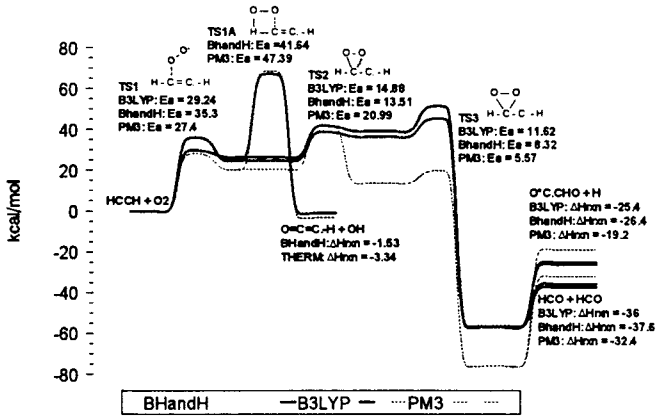


Figure 2. Concentration profiles for HCCH + $^3O_2$ -> Products.
Initial concentration: HCCH=5%; $^3O_2$=15%; N_2=80%
Solid Lines=1600K; Dash Lines=2000K

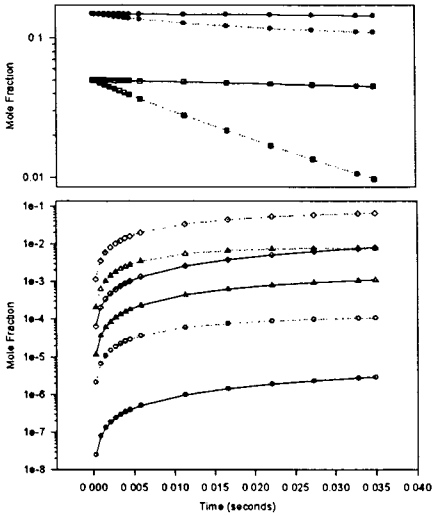


Figure 3. Concentration profiles for HCCH + $^1O_2$ -> Products.
Initial concentration: HCCH=5%; $^3O_2$=15%; N_2=80%
Solid Lines=1600K; Dash Lines=2000K

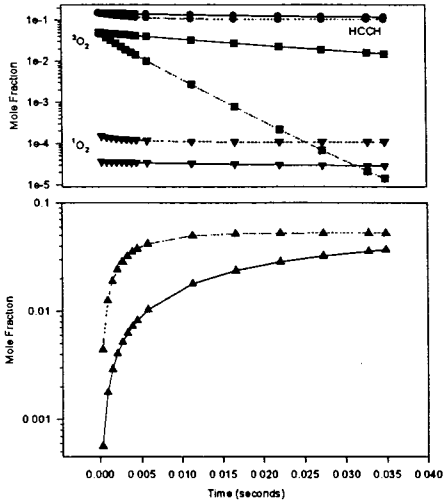


Figure 4. Comparison of rate constants between HCCH + $^3O_2$ and via isomerization to vinylidene. (a) forward rate constant (b) rate constant to products.
Solid Lines = Addition; Dash Lines = Isomerization.

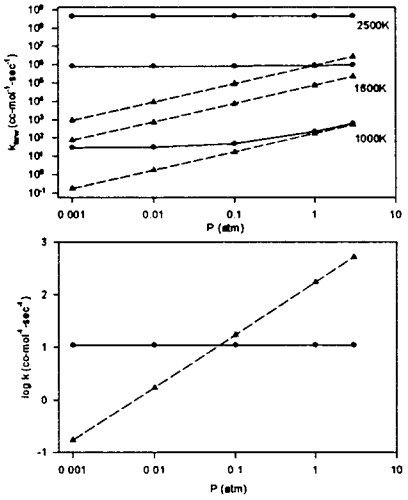


Figure 5. Concentration profile for triplet biradical adduct conversion to singlet biradical adduct.
Solid Lines = 1600K; Dash Lines = 2000K

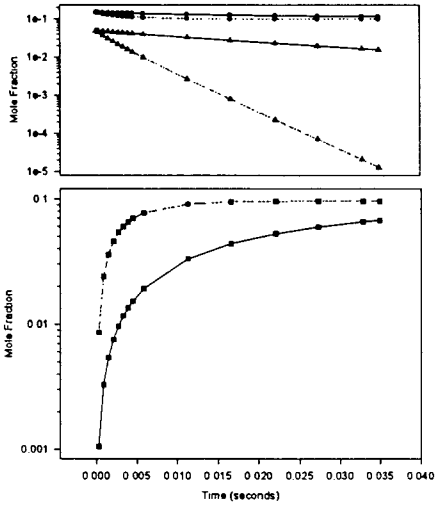
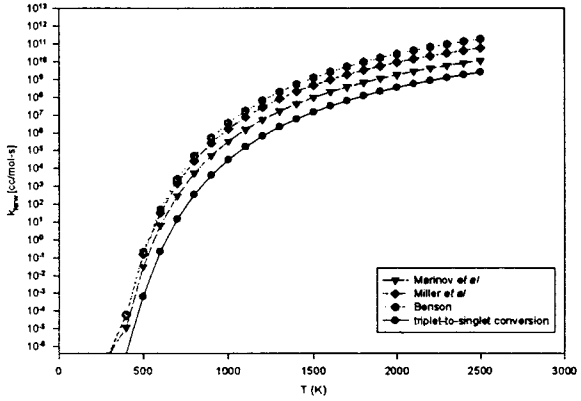


Figure 6. Comparison of forward rate constants from literature.



Reaction Pathways and Kinetic Analysis on Methyl *tert*-Butyl Ether Pyrolysis and Oxidation Reactions

Chiung-Ju Chen and Joseph W. Bozzelli

Department of Chemical Engineering, Chemistry and Environmental Science,
New Jersey Institute of Technology, Newark, NJ 07102

Introduction

Thermochemical kinetic parameters of reactants, intermediates, transition states and products are developed for each elementary reaction pathway in MTBE unimolecular decomposition and oxidation reaction systems. Chemical activation kinetic analysis on radical plus O_2 reactions is presented using quantum Rice-Ramsperger-Kassel (QRRK) theory for k(E) and modified strong collision analysis for fall-off. Thermodynamic properties ($H_f°_{298}$, $S°_{298}$, and Cp(T) $300 \leq T/K \leq 1500K$) of reactants, intermediate radicals, transition states, and final products are calculated at B3LYP/6-31g(d), B3LYP/6-311+g(3df,2p) //B3LYP/6-31g(d) and CBS-q// B3LYP/6-31g(d) levels. Results of the computational thermodynamic calculations are used for kinetics analysis in this study. CBS-q calculations are chosen because Jungkamp et al.[1,2], Petersson et al.[3] and our group[4] have shown that they result in reasonable accurate thermodynamic enthalpy data for these oxygenated molecular systems. Density function B3LYP is chosen to provide accurate geometries. CBS-q and G3(MP2) are probably the best methods for the large systems and CBS-q//B3LYP is ca. 2/3 the computation time to G2(MP2).

Method

Heat of Formation

Heat of formation ($\Delta H_f°_{298}$) for reactants, intermediate radicals, transition states and products are calculated using isodesmic reactions and various levels of calculations: B3LYP/6-31g(d), B3LYP/6-311+g(3df,2p)//B3LYP/6-31g(d) and CBS-q//B3LYP/6-31g(d). The initial geometry of each compound or transition states is pre-optimized using UHF/PM3 in MOPAC[5] program, followed by optimization and vibrational frequency calculation at B3LYP/6-31G(d) level of theory using GAUSSIAN 94 programs[6]. The TS geometries are identified by the existence of only one imaginary frequency in the normal mode coordinate analysis, evaluation of the TS geometry, and TST reaction coordinate vibration information. Zero-point vibrational energies (ZPVE), vibrational frequencies and thermal contributions to enthalpy from harmonic frequencies are scaled with factors as recommended by Scott et al[7]. Single point energy calculations are carried out at the B3LYP/6-311+g(3df,2p)//B3LYP/6-31g(d). The CBS-q//B3LYP/6-31g(d) calculation modified from complete basis set (CBS-q) method of Petersson and coworkers[7,9,10] are used in determining enthalpies.

Eight group balance isodesmic reactions are used to calculate stable molecules C3COC, C2C(CQ)OC, C2CCQ, C*C(C)CQ, C*(C)COC, C3COCQ, and HOCOOH.

		ΔH_{rxn} (kcal/mole) (CBS-q//B3Lyp/6-31g(d))
For C3COC	C3COC + COH → C3COH + COC	-2.63
For C2C(CQ)OC	C2C(CQ)OC + CC → C3COC + CCOOH	-2.08
For C(OH)2	COCOC + 2 COH → C(OH)2 + 2 COC	-1.89
For C3COCQ	C3COCQ + CCOH + COH → C2C(CQ)OC + C(OH)2 + CC	-0.20
For C2CCQ	C2CCQ + COH → C2CCOH + COC	-0.03
For C*C(C)CQ	C*C(C)CQ + C*CC + COH → C2C*C + C*CCOH + COOH	2.45
For C*C(C)OC	C*C(C)OC + C=COH + CCOH → C=C(C)OH + C=COCC+COH	1.70
For C2CYCCOCO	C2CYCCOCO + COH → CYCCOCO + C3COH	1.97
For HOCOOH	HOCOOH + CC → CCOH + COOH	-1.09

Enthalpies of formation of radicals, C3·COC, C3COC·, C2C(CQ·)OC, C2C(CQ)OC·, C2·C(CQ)OC ,C2C·CQ, C3COCQ·, C3·COCQ, and ·OCOOH are calculated from following isodesmic reactions and bond enthalpies of $DH°_{298}$ (CH_3CH_2-H), $DH°_{298}$ (CH_3OCH_2-H), and $DH°_{298}$ (CH_3OO-H).

		ΔH_{rxn} (kcal/mole) (CBS-q//B3Lyp/6-31g(d))
For C3·COC	C3COC + CC· → C3·COC + CC	2.16
For C3COC·	C3COC + COC· → C3COC· + COC	-1.16
For C2C(CQ·)OC	C2C(CQ)OC + COO· → C2C(CQ·)OC + COOH	-2.65
For C2C(CQ)OC·	C2C(CQ)OC + COC· → C2C(CQ)OC· + COC	-0.95
For C2·C(CQ)OC	C2C(CQ)OC + CC· → C2·C(CQ)OC + CC	0.48
For C2C·CQ	C2CCQ + CC· → C2C·CQ + CC	1.57
For C3COCQ·	C3COCQ + COO· → C3COCQ· + COOH	0.68
For C3·COCQ	C3COCQ + CC· → C3·COCQ + CC	0.81
For ·OCOOH	COCOOH + CO· → ·OCOOH + COH	0.78

Enthalpies of formation of TSs are estimated from average value of $\Delta H_{298,reactants}$ plus the reaction enthalpy ($\Delta H^{\neq}_{TS1-reactants}$) and $\Delta H_{298,products}$ plus reaction enthalpy ($\Delta H^{\neq}_{TS-products}$) at B3LYP/6-31g(d), B3LYP/6-311+g(3df,2p)//B3LYP/6-31g(d) and CBS-q//B3LYP/6-31g(d) levels.

Entropy and Heat Capacity

Contributions of translation, rotation, and vibration to entropies and heat capacities are calculated from scaled vibrational frequencies and moments of inertia of the optimized structures. The method of Pitzer and Gwinn[11] is used to calculate hindered internal rotational contribution to S and Cp(T). The number of optical isomers and spin degeneracy of unpaired electrons is also incorporated.

High-Pressure Limit A Factors (A_∞) and Rate Constants (k_∞) Determination

For the reactions where thermodynamic properties of TS are calculated by *ab initio* density functional, k_∞s are fit by three parameters A_∞, n, and E_a over temperature range from 298 to 2000K: $k_\infty = A_\infty(T)^n \exp(-E_a/RT)$
Entropy differences between reactant and TS are used to determine the Arrhenius pre-exponential factor, A, via conventional transition state theory (TST) for unimolecular and bimolecular reactions: $A = (k_bT/h_p)\exp(\Delta S^{\neq}/R)$ and $A = (ek_bT/H_p)\exp(\Delta S^{\neq}/R)$, respectively. Where h_p is Plank's constant, k_b is the Boltzmann constant.

Kinetics Analysis

Multi-frequency Quantum Rice-Rampsperger-Kassel (QRRK) analysis with modified strong collision analysis for fall-off calculation is used to estimate rate constants to products and stabilized adducts as a function of temperature and pressure. Those calculations utilize the potential energy surface and thermodynamic properties are determined in this study.

Results

Table 1 lists the thermodynamic properties for reactants, intermediates, TSs and products calculated from CBS-q//B3LYP/6-21g(d). Figure 1 shows the potential energy diagram for MTBE unimolecular elimination. Figures 2a and 2b show the reaction pathways of two MTBE radicals' unimolecular decomposition and oxidation reactions. The MTBE parent forms radicals (loss of H atom) through abstraction by a reactive radical, such as OH, HO_2, H, CH_3 etc. MTBE radicals once formed then undergo β-scission or react with molecular oxygen, which is abundant under atmosphere and troposphere conditions, to form the energized adducts MTBE-OO*. The energized adducts can be stabilized, dissociate to products or reactants. Table 2 lists reaction enthalpies obtained from B3LYP/6-31g(d), B3LYP/6-311+g(3df,2p)//B3LYP/6-31g(d) and CBS-q//B3LYP/6-31g(d) calculations. Table 3 lists high pressure limit rate constants (k_∞) for QRRK (Based on CBS-q//b3lyp/6-31g(d) calculation). Figure 3 illustrates the predicted effect of temperature for both reactants to products and reactants to intermediates at pressure 1.08atm.

References

1. Jungkamp, T. P. W.; Smith, J. N.; Seinfeld, J. H. *J. Phys. Chem.* **1997**, 101, 4392.
2. Jungkamp, T. P. W.; Seinfeld, J. H. *J. Chem. Phys.* **1997**, 107, 1513.
3. Ochterski, J. W.; Petersson, G. A. *J. Chem. Phys.* **1996**, 104, 2598.
4. Takahiro Yamada; Lay, T. H.; Bozzelli, J. W. *27th Symposium (Intern'l) on Combustion, The Combustion Inst.*, **1998**.

5. Stewart, J. J. P.,*MOPAC 6.0*, Frank J. Seiler Research Lab., US Air Force Academy: Colorado, **1990**.
6. Frisch, M.j.; Truck, G. W.; Head-Gordon, M.; Gill, P. M. W.; Wong, M. W.; Foresman, J. B.; Johnson, B. G.; Schelgel, H. B.; Robb, M. A.; Peplogle, E. S.; Gromperts, R.; Andres, J. L., Raghavachari, K.; Binkley, J, S., Gonzalez, C.; Martin, R. L.; Fox, D. J.; Defrees, D. J.; Baker, J.; Stewart, J. J. P.; Pople, J. A.; Eds., *Gaussian 94 Computer Program, Revision C 2*, Gaussian Inc.: Pittsburgh, **1995**.
7. Nyden, M. R. Petersson, G. A. *J. Chem. Phys*. **1991**, 75, 1843.
8. Scott, A. P., Radom, L. *J. Phys. Chem.***1996**, 100, 16502.
9. Petersson, G. A. *J. Chem. Phys*. **1994**, 94, 6081.
10. Montgomery, J. A.; Petersson, G. A. *J. Phys. Chem.* **1994**, 101, 5900.
11. Pitzer, K. S.; Gwinn, W. D. *J. chem. Phys*. **1942**, 10, 428.

Table 1. Ideal Gas Phase Thermodynamic Properties Using CBS-q//b3lyp/6-31g(d)

Species	$Hf°_{298}$ [a]	$S°_{298}$ [b]	Cp(300)	Cp(400)	Cp(500)	Cp(600)	Cp(800)	Cp(1000	Cp(1500)
C3COC	-68.02	85.62	32.2	40.3	47.7	53.97	63.75	70.95	82.25
C3COC•	-24.59	89.17	32.82	40.53	47.31	52.93	61.53	67.86	77.86
C3•COC	-16.36	93.12	33.38	40.57	47.00	52.45	60.99	67.38	77.58
C3COCQ	-94.67	103.1	40.18	49.98	58.43	65.29	75.39	82.43	93.14
C3COCQ•	-59.79	102.1	38.48	47.46	55.2	61.52	71.00	77.83	88.38
C3•COCQ	-44.36	109.8	41.12	50.1	57.65	63.73	72.63	78.88	88.49
C2C(CQ)OC	-85.81	106.9	40.12	49.32	57.47	64.23	74.39	81.62	92.66
C2C(CQ•)O	-54.26	105.5	38.01	46.49	54.00	60.27	69.92	76.96	87.88
C2C(CQ)OC	-42.17	110.0	40.76	49.57	57.1	63.21	72.22	78.56	88.31
C2•C(CQ)O	-35.83	111.4	40.99	49.4	56.66	62.63	71.63	78.06	88.03
TS1	-37.55	89.06	35.49	45.45	54.08	61.17	71.72	79.11	90.21
TS2	-30.78	95.76	35.93	45.25	53.41	60.2	70.5	77.86	89.00
TS3	-24.35	110.7	39.57	48.14	55.66	61.83	71.04	77.51	87.39
TS4	-14.23	108.7	38.68	47.2	54.6	60.71	69.93	76.53	86.73
TS5	-16.52	110.3	38.36	46.76	54.23	60.46	69.85	76.54	86.8
TS6	-38.92	88.45	35.49	45.68	54.4	61.49	71.96	79.28	90.28
TS8	-26.85	107.5	37.95	47.13	55.01	61.4	70.77	77.31	87.27
TS9	1.49	91.89	30.46	37.73	44.43	50.17	59.17	65.85	76.38
TS10	-6.74	89.54	31.58	39.00	45.74	51.47	60.32	66.82	76.99
TS11	-29.41	94.39	37.04	46.44	54.44	60.95	70.7	77.69	88.58
TS13	13.49	92.65	32.46	39.54	45.8	51.08	59.47	65.85	76.16
TS12	-6.84	85.29	32.17	40.22	47.68	54.07	64.05	71.36	82.65
C*C(C)OC	-36.03	81.44	23.46	28.62	33.52	37.82	44.79	50.08	58.49
C*C(C)CQ	-24.53	90.51	28.25	34.76	40.48	45.18	52.22	57.19	64.77
O•COOH	-23.05	74.21	16.93	20.21	22.98	25.16	28.11	29.96	32.47
C2C•COOH	-6.26	97.77	28.62	34.90	40.86	46.01	53.98	59.71	68.42

Table 2. Reaction Enthalpies

	CBS-q	b3lyp /6-31g*	b3lyp /6311+g(3df,2p)
C3COC -> TS12	61.36	57.16	55.39
C2C*C + CH3OH -> TS12	44.78	41.13	46.27
C3•COC -> TS9	18.02	23.31	22.23
C2C*C + CH3O• -> TS9	1.15	3.44	5.49
C3•COC -> TS13	30.06	28.57	26.50
C*C(C)OC + CH3 -> TS13	14.51	14.98	17.09
C3COC• -> TS10	17.44	14.32	13.67
C3C• + CH2O -> TS10	7.98	7.84	9.64
C2C(CQ•)OC -> TS1	17.86	18.54	16.63
C2C(CQ)OC• -> TS1	3.47	-0.13	3.51
C2C(CQ•)OC -> TS2	24.57	26.83	23.87
C2•C(CQ)OC -> TS2	3.96	2.51	4.69
C2C(CQ)OC• -> TS3	16.43	12.54	11.88
C2C•COOH -> TS3	9.82	8.83	10.93
C2•C(CQ)OC -> TS4	21.17	18.62	17.66
C*C(C)OC + C•H2OOH -> TS4	7.63	9.34	13.91
C2•C(CQ)OC -> TS5	19.54	16.38	15.09
C*C(C)COOH + CH3O• -> TS5	3.82	4.19	6.81
C3COCQ• -> TS6	21.96	22.93	20.79
C3•COCQ -> TS6	4.35	0.84	3.64
C3•COCQ -> TS8	15.78	11.90	10.62
C2C*C + O•COOH -> TS8	-1.55	0.49	3.08
C3•COCQ -> TS11	14.09	12.17	11.31
C2CYCCOCO + OH -> TS11	53.67	47.31	49.32

Unit: kcal mole^{-1}

Table 3. Input Parameters and High - Pressure Limit Rate Constants (k_∞) for QRRK (Based on CBS-q//b3lyp/6-31g(d) calculation)

Reaction	A	n	Ea
C3OC → C2C*C + CH3OH	7.48×10^{9}	1.11775	61.06
C3OC· → C3C· + CH2O	1.68×10^{12}	0.3648	18.19
C3·OC → C2C*C + CH3O	6.33×10^{12}	0.02285	18.29
C3·OC → C*C(C)OC+CH3	1.90×10^{12}	0.30135	30.31
C3COC· + O2 → C3COCQ·	3.60×10^{12}	0.	0.0
C3COCQ· → C3COC· + O2	9.39×10^{14}	0.	32.63
C3COCQ· → C3COCO·+O	3.57×10^{14}	0.	56.20
C3COCQ· → C3·COCQ	2.00×10^{6}	1.26772	20.34
C3·COCQ → C3COCQ·.	5.49×10^{6}	0.49069	5.18
C3·COCQ → C2C*C+O·COOH	4.01×10^{12}	0.00293	17.95
C3·COCQ → C2YCCOCO+OH	3.66×10^{9}	0.02724	15.23
C3·COC + O2 → C2C(CQ·)OC	3.60×10^{12}	0.	0.0
C2C(CQ·)OC → C3·COC + O2	1.57×10^{15}	0.	35.65
C2C(CQ·)OC → C2C(CO·)OC +O	3.26×10^{14}	0.	58.33
C2C(CQ·)OC → C2C(CQ)OC·	3.56×10^{4}	1.65439	15.95
C2C(CQ·)OC → C2·C(CQ)OC	3.84×10^{7}	1.1448	23.14
C2C(CQ)OC·→ C2C(CQ·)OC	3.93×10^{6}	0.58188	4.32
C2C(CQ)OC·→ C2C·COOH+CH2O	1.62×10^{12}	0.39674	18.15
C2·C(CQ)OC → C2C(CQ·)OC	4.12×10^{8}	0.30401	5.00
C2·C(CQ)OC → C*C(C)OC+C.H2OOH	1.67×10^{12}	0.12863	22.04
C2·C(CQ)OC → C*C(C)CQ +CH3O	5.62×10^{12}	0.06063	19.75

Figure 1. Potential Energy Diagram for MTBE unimolecular elimination to isobutene and methanol

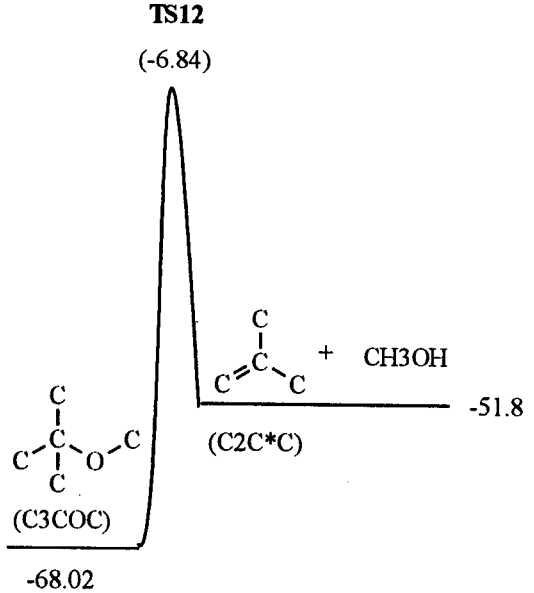


Figure 2a. Potential Energy Diagram for C3COC• + O2 -> Products

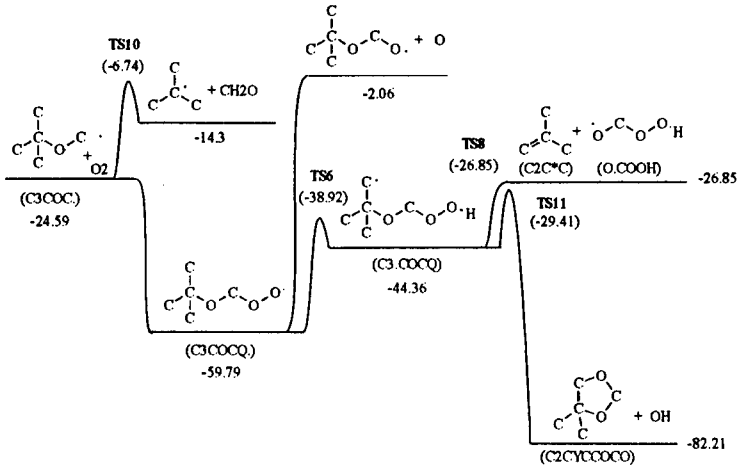


Figure 2b. Potential Energy Diagram for C3•COC + O2 -> Products

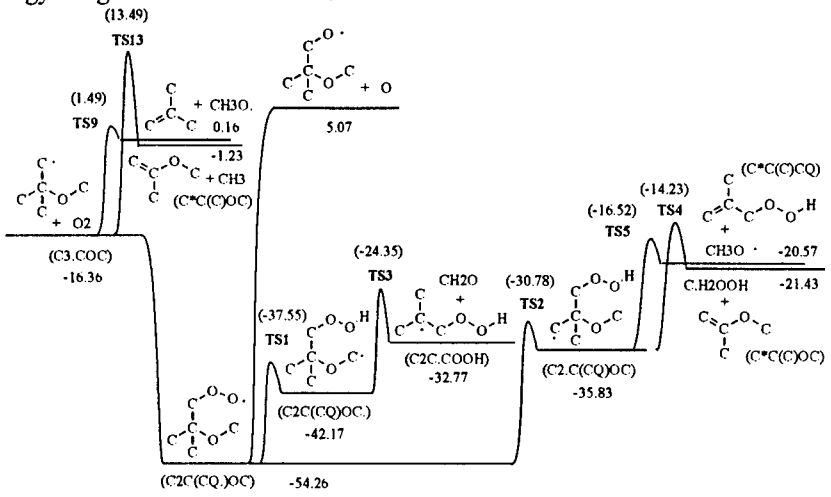
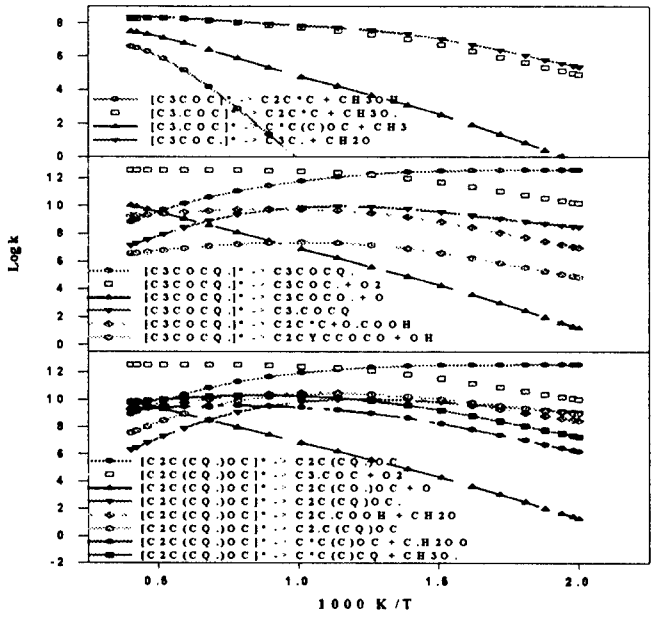


Figure 3. Calculated rate constants for chemically activated reactions of MTBE unimolecular decomposition and oxidation systems, pressure at 1.08atm



ab initio Calculations and Thermochemical Analysis on Cl Atom Abstractions of Chlorine from Chlorocarbons and the Reverse Alkyl Abstractions: $Cl_2 + R. \leftrightarrow Cl. + RCl$

Joseph W. Bozzelli* and Jongwoo Lee
Department of Chemical Engineering, Chemistry, and Environmental Science,
New Jersey Institute of Technology, Newark, NJ 07102, *bozzelli@tesla.njit.edu
and
J. P. Sawerysyn, Combustion and Kinetics, University of Lille, Villa d'Ascq, France

Abstract

Thermodynamic Parameters, $\Delta H^\circ_{f(298)}$, $S^\circ_{(298)}$ and Cp(T) are evaluated for C_1 and C_2 chlorocarbon molecules and radicals. These thermodynamic properties are used in evaluation and comparison of $Cl_2 + R. \Rightarrow Cl. + RCl$ (defined forward direction) reaction rate constants from the kinetics literature. Data from some 20 reactions in the literature show linearity on a plot of Ea_{fwd} vs. $\Delta H_{rxn,fwd}$, yielding a slope of (0.38 ± 0.04) and intercept of (10.12 ± 0.81) kcal/mole. A correlation of average Arrhenius pre-exponential factor for $Cl. + RCl \Rightarrow Cl_2 + R.$ (reverse rxn) of (4.44 ± 1.58) x 10^{13} cm^3/mol-sec on a per chlorine basis is obtained with $Ea_{Rev} = (0.64 \pm 0.04) * \Delta H_{rxn,Rev} + (9.72 \pm 0.83)$, where Ea_{Rev} is 0.0 if $\Delta H_{rxn,Rev}$ is more than 15.2 kcal/mole exothermic. Kinetic evaluations are also performed for classes of reactions. $Ea_{fwd} = (0.39 \pm 0.11) * \Delta H_{rxn,fwd} + (10.49 \pm 2.21)$ kcal/mole and average A_{fwd} = (5.89 ± 2.48) x 10^{12} cm^3/mole-sec for hydrocarbons: $Ea_{fwd} = (0.40 \pm 0.07) * \Delta H_{rxn,fwd} + (10.32 \pm 1.31)$ kcal/mole and average A_{fwd} = (6.89 ± 2.15) x 10^{11} cm^3/mole-sec for C_1 chlorocarbons: $Ea_{fwd} = (0.33 \pm 0.08) * \Delta H_{rxn,fwd} + (9.46 \pm 1.35)$ kcal/mole and average A_{fwd} = (4.64 ± 2.10) x 10^{11} cm^3/mole-sec for C_2 chlorocarbons: Thermodynamic properties ($\Delta H^\circ_{f(298)}$, $S^\circ_{(298)}$ and Cp(T) from 300 to 1500 K) for reactants, adducts, transition states, and products in reactions of CH_3 and C_2H_5 with Cl_2 are calculated using CBSQ//MP2/6-311G(d,p). Molecular structures and vibration frequencies are determined at the MP2/6-311G(d,p), with single point calculations for energy at QCISD(T)/6-311+G(d,p), MP4(SDQ)/CbsB4 and MP2/CBSB3 levels of calculation. Vibration frequencies are scaled by 0.9748 for zero point energies. Contributions of rotational frequencies for $S^\circ_{(298)}$ and Cp(T)'s are calculated based on rotational barrier heights and moments of inertia using the method of Pitzer and Gwinn[1].

Introduction

High chlorinated solvents such as CH_2Cl_2, $CHCl_3$, CCl_4, C_2Cl_4, C_2HCl_3, $C_2H_3Cl_3$'s and fluoro chloro-carbon solvents or chemicals are in widespread use in the chemical, pharmaceutical and cleaning industries. The monomers are also present in a number of valuable and versatile polymers. The combustion, incineration or high temperature pyrolysis of these chlorocarbons includes reactions at or near surfaces and in liquids or polymers where oxygen is not present or is low in concentration. Chlorine atom abstraction of chlorine from the chlorocarbon is often the important chain propagation process in these systems; yet there is limited or almost no direct experimental kinetic information on these chlorine atom abstraction reactions. This is a due to the Cl abstraction of Cl from R-Cl being endothermic, as the Cl-Cl bond is 57.8 kcal/mole, while a typical R-Cl bond energy ranges from 71 kcal/mole in CCl_4 to 95 or 98 in vinyl chloride and chlorobenzene, respectively. Most chlorocarbons also have a hydrogen which is readily abstracted by Cl atoms, where the rate constants have high Arrhenius pre-exponential factors (> 10^{13}) and little or no energies of activation. (ca 1.0 kcal/mole if thermo neutral or exothermic). Pyrolysis of trichloroethylene, for example, shows extensive molecular weight growth products such as hexachloro-benzene, pentachloro-butadiene, etc which likely result from radical processes.[2] We estimate kinetic data for these $Cl. + RCl \Rightarrow Cl_2 + R.$ reactions in this study by assembling and evaluating thermodynamic property data : $\Delta H^\circ_{f(298)}$, $S^\circ_{(298)}$, and Cp(T) on chlorocarbon and several fluoro chlorocarbon molecules and radicals. We use the thermochemical properties with available literature data on the abstractions of Cl from Cl_2 by alkyl radicals and microscopic reversibility to evaluate trends in the forward and reverse rate constants.

Thermodynamic properties ($\Delta H^\circ_{f(298)}$, $S^\circ_{(298)}$ and Cp(T) from 300 to 1500 K) for reactants, adducts, transition states, and products in reactions of CH_3 and C_2H_5 with Cl_2, are determined using CBSQ//MP2/6-311G(d,p) *ab initio* calculations and kinetic predictions compared with evaluated data.

Thermodynamic Properties

Evaluated thermodynamic parameters: $\Delta H^{\circ}_{f(298)}$, $S^{\circ}_{(298)}$, and Cp(300) to Cp(1500) for species in the reaction schemes are listed in Table 2 along with literature references. Enthalpies of chlorocarbon (C_1 and C_2) radicals are from literature data and some from calculations in this study using isodesmic reactions: for example $C.H_2CH_2Cl$ is from a calculated ΔHrxn for ($CH_3CH_3 + C.H_2CH_2Cl$ ==> $CH_3CH_2Cl + C.H_2CH_3$) and the known $\Delta H^{\circ}_{f(298)}$ for ethane, chloroethane and ethyl radical. Entropies and Cp(T) values of C_2H_3, C_2H_5 are from use of Hydrogen Bond Increment(HBI) method. [3] The HBI group technique is based on known thermodynamic properties of the parent molecule and calculated changes that occur upon formation of a radical via loss of a H atom.

Thermodynamic Analysis for the Reactions

Arrhenius pre exponential factors on a per chlorine basis, energies of activation and enthalpies of reaction, A_{Rev}, $A_{Rev}/Cl\#$, Ea_{Rev} and $\Delta H^{\circ}_{rxn,fwd}$ are calculated using literature reference data on the forward reactions A_{fwd} and Ea_{fwd} , the evaluated thermodynamic properties of reactants and products, and microscopic reversibility. The forward reaction direction is defined as $Cl_2 + R.$ => Cl. + RCl. Allyl radical C_3H_5 and propargyl radical C_3H_3 have resonant structures each having two radical sites with near equal population at temperature of the experimental data, 500-700K. (Ref. 10 in Table 1) We assess these radical reactions with Cl_2 as occurring via both radical sites, and estimate similar rates for each site. The experimental rate constant for the forward direction is multiplied by 0.5 to obtain the forward rate constant on a per radical site basis.

***ab initio* Calculations on CH_3 and C_2H_5 Plus Cl_2 Reaction Systems**

Thermodynamic properties ($\Delta H^{\circ}_{f(298)}$, $S^{\circ}_{(298)}$ and Cp(T) from 300 to 1500 K) for reactants, adduct intermediates, transition states, and products in reactions of CH_3 and C_2H_5 with Cl_2 are calculated using the established CBSQ//MP2/6-311G(d,p) composite method of Petersson's research group[4-5]. The CBSQ calculation sequence is performed on the MP2/6-311G(d,p) geometry and followed by single point calculations at the theory level of QCISD(T)/6-311+G(d,p), MP4(SDQ)/CbsB4 and MP2/CBSB3 CBSExtrap=(Nmin=10,Pop).

Summary

Thermodynamic Parameters, $\Delta H^{\circ}_{f(298)}$, $S^{\circ}_{(298)}$ and Cp(T) are evaluated for reactants and products in $Cl_2 + R.$ <=> Cl. + RCl reactions. The forward rate constants are evaluated from the literature. The reverse rate constants are calculated from our evaluated thermodynamic properties of reactants and products and microscopic reversibility. The trends of Ea_{fwd} vs $\Delta H_{rxn,fwd}$ and Arrhenius pre-exponential factor for overall, hydrocarbons, C_1 chlorocarbons, and C_2 chlorocarbons are evaluated.

We recommend a rate expression of average $A_{fwd} = (2.35 \pm 3.07) \times 10^{12}$ cm^3/mole-sec and $Ea_{fwd} = (0.38 \pm 0.04) * \Delta H_{rxn,fwd} + (10.12 \pm 0.81)$ kcal/mole for overall, average $A_{fwd} = (5.89 \pm 2.48) \times 10^{12}$ cm^3/mole-sec and $Ea_{fwd} = (0.39 \pm 0.11) * \Delta H_{rxn,fwd} + (10.49 \pm 2.21)$ kcal/mole for hydrocarbons, average A_{fwd} of $(6.89 \pm 2.15) \times 10^{11}$ cm^3/mole-sec and $Ea_{fwd} = (0.40 \pm 0.07) * \Delta H_{rxn,fwd} + (10.32 \pm 1.31)$ kcal/mole for C_1 chlorocarbons, and average A_{fwd} of $(4.64 \pm 2.10) \times 10^{11}$ cm^3/mole-sec and $Ea_{fwd} = (0.33 \pm 0.08) * \Delta H_{rxn,fwd} + (9.46 \pm 1.35)$ kcal/mole for C_2 chlorocarbons.

We have performed *ab initio* calculation on $CH_3 + Cl_2$ <=> $CH_3Cl + Cl$ and $C_2H_5 + Cl_2$ <=> $C_2H_5Cl + Cl$ reaction. The canonical transition state calculations agree well with experimental data for these two, low Ea_{fwd}, reaction systems. The carbon atom which undergoes bonding to the Cl has a negative charge of –0.34 and –0.25 in CH_3 and C_2H_5, respectively, which becomes more negative, -0.35 and –0.31 in $TSCH_3XCl_2$ and $TSC_2H_5XCl_2$, respectively, then the charge increases, becomes less negative, –0.26 and –0.21 in CH_3Cl and C_2H_5Cl, respectively.

Reference

1. Pitzer, K. S.; Gwinn, W. D. Energy Levels and Thermodynamic Functions for Molecules with Internal Rotation. I. Rigid Frame with Attached Tops. *J. Chem. Phys.* **1942**, 10, 428
2. Earl, B. L.; Titus, R. L. Novel Products in the CO2-laser Induced Reaction of Trichloroethylene *Collect. Czech. Chem. Commun.* **1995**, 60, 104
3. Lay, T. H.; Bozzelli, J. W.; Dean, A. M.; Ritter, E. R. Hydrogen Atom Bond Increments for Calculation of Thermodynamic Properties of Hydrocarbon Radical Species *J. Phys. Chem.* **1995**, 99(39), 14514-14527
4. Petersson, G. A.; Nyden, M. R. Interference Effects in Pair Correlation Energies: Helium *L*-limit Energies *J. Chem. Phys.* **1981**, 75, 3423
5. Petersson, G. A.; Al-Laham, M.A. A Complete Basis Set Model Chemistry.II. Open-shell Systems and the Total Energies of the First-row Atoms *J. Chem. Phys.* **1994**, 94, 6081

Table 1. Cl_2 + Radicals ——> Products + Cl

REACTIONS	A_{fwd}*	Ea_{fwd}*	A_{Rev}**	A_{Rev}/Cl#	Ea_{Rev}**	$\Delta H°_{rxn,fwd}$**	P(torr)	T (K)	Reference*
<HYDROCARBONS>									
1. $Cl_2 + CH_3$ ——> $CH_2Cl + Cl$	3.02E+12	0.53	2.99E+13	2.99E+13	26.10	-25.50	1.9-2.8	296-712	9
2. $Cl_2 + C_2H_5$ ——> $C_2H_5Cl + Cl$	7.59E+12	-0.30	8.51E+13	8.51E+13	26.66	-27.18	1.7-2.2	295-498	9
3. $Cl_2 + i\text{-}C_3H_7$*** ——> $i\text{-}C_3H_7Cl + Cl$	1.51E+13	-0.48	1.03E+15	1.03E+15	25.82	-26.80	1.4-1.9	295-498	9
4. $Cl_2 + t\text{-}C_4H_9$*** ——> $t\text{-}C_4H_9Cl + Cl$	2.40E+13	-0.01	4.04E+15	4.04E+15	26.37	-27.11	1.4-1.8	295-498	9
5. $Cl_2 + C_2H_3$ ——> $CH_2CHCl + Cl$	5.25E+12	-0.48	4.49E+13	4.49E+13	37.10	-37.72	1.4-1.7	298-435	10
6. $Cl_2 + C_3H_5$ ——> $C_3H_5Cl + Cl$	4.67E+12	4.30	1.58E+13	1.58E+13	16.52	-12.29	2.0-3.6	487-693	10
7. $Cl_2 + C_3H_3$ ——> $C_3H_3Cl + Cl$	8.30E+12	6.70	7.00E+13	7.00E+13	20.01	-13.49	2.6-4.1	525-693	10
(Avg.)	9.70E+12			7.59E+14	(not recommended)				
If $i\text{-}C_3H_7$, $t\text{-}C_4H_9$, C_2H_3 are excluded, (Avg.)	(5.89 +/- 2.48)E+12			(5.02 +/- 3.27)E+13					
<C_1 CHLOROCARBONS>									
8. $Cl_2 + CH_2Cl$ ——> $CH_2Cl_2 + Cl$	9.10E+11	0.98	4.83E+13	2.42E+13	22.87	-21.90	1.7-4.3	295-719	11
9. $Cl_2 + CHCl_2$ ——> $CHCl_3 + Cl$	5.18E+11	2.46	1.30E+14	4.34E+13	21.09	-18.78	1.8-4.6	357-719	11
10. $Cl_2 + CCl_3$ ——> $CCl_4 + Cl$	4.08E+11	5.26	6.00E+13	1.50E+13	17.91	-13.02	3.1	690-700	12
11. $Cl_2 + CF_3$ ——> $CF_3Cl + Cl$	2.69E+12	3.60	1.83E+14	1.83E+14	30.55	-27.27	2.3-2.6	487-693	12
12. $Cl_2 + CF_2Cl$ ——> $CF_2Cl_2 + Cl$	7.76E+11	1.91	6.89E+13	3.44E+13	24.13	-22.56	1.8-2.9	376-626	12
13. $Cl_2 + CFCl_2$ ——> $CFCl_3 + Cl$	8.32E+11	3.35	4.74E+13	1.58E+13	20.12	-17.18	1.5-2.6	435-693	12
(Avg.)	1.02E+12			5.26E+13	(not recommended)				
If CF_3 is excluded, (Avg.)	(6.89 +/- 2.15)E+11			(2.66 +/- 1.22)E+13					
<C_2 CHLOROCARBONS>									
14. $Cl_2 + C_2Cl_3$ ——> $C_2Cl_6 + Cl$	2.00E+11	5.50	2.17E+14	3.61E+13	19.04	-13.94	50	298-423	13
15. $Cl_2 + CHCl_2CHCl$ ——> $(CHCl_2)_2 + Cl$	6.31E+11	2.70	4.92E+14	1.23E+14	21.39	-18.61	50	298-423	13
16. $Cl_2 + CH_2ClCCl_3$ ——> $CH_2ClCCl_3 + Cl$	6.92E+11	4.10	4.29E+14	1.07E+14	18.49	-14.44	50-300	298-321	14
17. $Cl_2 + CH_2ClCHCl$ ——> $CH_2ClCHCl_2 + Cl$	2.00E+12	2.00	1.05E+15	3.49E+14	22.47	-20.53	80-280	298-328	15-(1)
18. $Cl_2 + CHCl_2CH_2$ ——> $CH_2ClCHCl_2 + Cl$	6.31E+11	0.90	5.37E+13	1.79E+13	27.09	-26.19	50	298-423	13
19. $Cl_2 + CCl_3CHCl$ ——> $CHCl_2CCl_3 + Cl$	3.16E+11	5.10	7.96E+13	1.59E+13	21.61	-17.16	50	298-423	13
20. $Cl_2 + CHCl_2CCl_2$ ——> $CHCl_2CCl_3 + Cl$	3.16E+11	5.10	1.96E+14	3.91E+13	16.88	-12.43	50	298-423	13
(Avg.)	6.84E+11			9.83E+13	(not recommended)				
If $CH_2ClCHCl$ is excluded, (Avg.)	(4.64 +/- 2.10)E+11			(5.65 +/- 4.65)E+13					
TOTALS (TOTAL Avg.)	3.80E+12			3.03E+14	(not recommended)				
If $i\text{-}C_3H_7$, $t\text{-}C_4H_9$, C_2H_3, CF_3, $CH_2ClCHCl$ are excluded, (Avg.)	(2.35 +/- 3.07)E+12			(4.44 +/- 1.58)E+13					

UNITS :: A_{fwd} and A_{Rev} : cm^3/(mole-sec)
Ea and $\Delta H°_{rxn,fwd}$: kcal/mole
A_{fwd} = (2.35 +/- 3.07)*10^{12} cm^3/(mole-sec)
A_{Rev}(avg)/cl = (4.44 +/- 1.58)*10^{13} cm^3/(mole-sec)
($i\text{-}C_3H_7$, $t\text{-}C_4H_9$, C_2H_3, CF_3, $CH_2ClCHCl$ are excluded in calc.of A_{fwd} and A_{Rev}(avg)/cl)

* : references for A_{fwd} and Ea_{fwd}
** : calculated from Thermodynamic Properties of reactants and products
- microscopic reversibility -
*** : $i\text{-}C_3H_7$, $t\text{-}C_4H_9$ Symmetries = 162 & 18 respectively

Table 2. Evaluated Thermodynamic Property Data

SPECIES	Hf(298)	S(298)	Cp300	Cp400	Cp500	Cp600	Cp800	Cp1000	Cp1500	REF(a)
CH3	34.82	46.38	9.26	10.05	10.82	11.54	12.89	14.09	16.29	JANAF(16)
TSCH3XCl2	32.10	74.11	15.86	17.27	18.43	19.42	21.06	22.41	24.82	CBSQ(in this study)
CH3Cl	-19.60	56.00	9.77	11.51	13.19	14.66	17.05	18.87	21.76	TRC(17)
C2H5	29.30	57.42	11.89	14.57	16.95	19.09	22.76	25.66		LAY/BOZ95(3)
TSC2H5XCl2	24.20	84.10	19.94	22.96	25.60	27.84	31.46	34.25	38.82	CBSQ(in this study)
C2H5Cl	-26.80	66.01	15.03	18.57	21.61	24.22	28.37	31.44	36.16	JANAF(16)
i-C3H7	21.02	70.39	16.58	20.27	24.03	27.49	33.13	37.52	44.37	LAY/BOZ95(3)
i-C3H7Cl	-34.70	73.41	20.85	25.88	30.48	34.34	40.33	44.92		WONG/BOZ(26)
t-C4H9	11.90	75.67	22.33	27.04	31.82	36.27	43.62	49.34	58.53	LAY/BOZ95(3)
t-C4H9Cl	-44.13	76.42	26.66	33.67	39.89	45.02	52.53	57.84		WONG/BOZ(26)
C2H3	71.64	53.79	10.10	11.93	13.57	14.97	17.22	18.95		LAY/BOZ95(3)
CH2CHCl	5.00	63.08	12.89	15.56	17.80	19.61	22.35	24.35		LI/BOZ98(22)
C3H5	40.75	62.05	14.87	18.66	21.88	24.63	28.95	32.10	36.78	LAY/BOZ95(3)
C3H5Cl	-0.46	73.31	18.14	22.12	25.51	28.40	32.94	36.28	41.45	SWS(20)
C3H3	81.58	59.57	13.76	16.10	18.10	19.80	22.48	24.43	27.31	LAY/BOZ95(3)
C3H3Cl	39.17	68.78	17.26	20.10	22.45	24.39	27.33	29.42	32.62	TRC(17)
CH2Cl	27.99	58.61	10.08	11.45	12.53	13.38	14.66	15.64	17.30	TAY/DEL91(18)
CH2Cl2	-22.83	64.57	12.20	14.24	15.93	17.30	19.32	20.76	22.91	JANAF(16)
CHCl2	23.50	68.10	12.90	14.16	15.09	15.79	16.76	17.44	18.46	KAFAFI89(freq.)(19)
CHCl3	-24.20	70.66	15.76	17.83	19.34	20.44	21.91	22.86		SWS(20)
CCl3	19.00	70.92	15.25	16.66	17.56	18.16	18.83	19.18	19.56	JANAF(16)
CCl4	-22.94	74.02	19.98	21.92	23.09	23.82	24.64	25.05	25.47	JANAF(16)
CF3	-113.01	63.42	11.93	13.68	15.05	16.09	17.46	18.22	19.07	JANAF(16)
CF3Cl	-169.20	68.17	16.04	18.53	20.32	21.59	23.16	24.02	24.98	JANAF(16)
CF2Cl	-66.02	67.72	13.17	14.73	15.93	16.83	17.98	18.59	19.25	RAYEZ94(21)
CF2Cl2	-117.50	71.91	17.36	19.68	21.28	22.37	23.68	24.39	25.16	JANAF(16)
CFCl2	-21.60	69.17	14.02	15.42	16.49	17.28	18.26	18.77	19.34	RAYEZ94(21)
CFCl3	-67.70	74.07	18.71	20.84	22.22	23.13	24.19	24.74	25.33	TRC(17)
C2Cl5	9.06	95.68	28.56	31.13	32.72	33.75	34.93	35.54	36.20	TRC(17)
C2Cl6	-33.80	94.77	32.67	36.11	38.29	39.69	41.29	42.11		SWS(20)
CHCl2CHCl	11.53	84.51	21.49	24.59	26.84	28.49	30.64	32.05	34.08	TRC(17)
C2H2Cl4	-36.00	84.86	23.74	27.67	30.65	32.89	35.99	38.01	40.66	TRC(17)
CH2ClCCl2	7.65	84.56	21.39	24.09	26.15	27.70	29.95	31.50	33.77	TRC(17)
CH2ClCCl3	-35.71	85.07	24.67	28.36	31.16	33.28	36.24	38.17	40.70	TRC(17)
CH2ClCHCl	14.65	78.56	18.33	21.15	23.40	25.19	27.82	29.73	32.70	TRC(17)
CH2ClCHCl2	-34.80	79.71	20.40	24.47	27.74	30.29	33.85	36.15	39.29	TRC(17)
CHCl2CH2	20.31	74.64	18.95	21.99	24.28	26.05	28.54	30.31	33.01	TRC(17)
CCl3CHCl	11.28	88.26	25.57	28.51	30.38	31.62	33.13	34.03	35.25	TRC(17)
CHCl2CCl3	-34.80	91.18	28.30	31.96	34.52	36.34	38.64	40.17	41.99	TRC(17)
CHCl2CCl2	6.55	90.65	23.88	26.74	28.78	30.23	32.15	33.32	34.89	TRC(17)

UNITS : Hf(kcal/mol), S(cal/K*mol), Cp(cal/K*mol) (a) : reference for Cp(T) and S only

$Cl_2 + R. \longrightarrow RCl + Cl$

	R.	$\Delta H^\circ_{rxn,fwd}$	Ea_{fwd}	Reference
1	CH_3	-25.50	0.53	JANAF(16)
2	C_2H_5	-27.18	-0.30	CIO/LIU97(23)
3	i-C_3H_7	-26.80	-0.48	LAY/BOZ95(3)
4	t-C_4H_9	-27.11	-0.01	LAY/BOZ95(3)
5	C_2H_3	-37.32	-0.48	LAY/BOZ95(3)
6	C_3H_5	-12.29	4.30	LAY/BOZ95(3)
7	C_3H_3	-13.49	6.70	LAY/BOZ95(3)
8	CH_2Cl	-21.90	0.98	Seet98(24)
9	$CHCl_2$	-18.78	2.46	ROUX/PAD87(25)
10	CCl_3	-13.02	5.26	JANAF(16)
11	CF_3	-27.27	3.60	JANAF(16)
12	CF_2Cl	-22.56	1.91	RAYEZ94(21)
13	$CFCl_2$	-17.18	3.35	RAYEZ94(21)
14	C_2Cl_5	-13.94	5.50	CIO/LIU97(23)
15	$CHCl_2CHCl$	-18.61	2.70	CIO/LIU97(23)
16	CH_2ClCCl_2	-14.44	4.10	CIO/LIU97(23)
17	$CH_2ClCHCl$	-20.53	2.00	CIO/LIU97(23)
18	$CHCl_2CH_2$	-26.19	0.90	CIO/LIU97(23)
19	CCl_3CHCl	-17.16	5.10	CIO/LIU97(23)
20	$CHCl_2CCl_2$	-12.43	5.10	CIO/LIU97(23)

FIGURE 1.

Ea_{fwd}(R.+ Cl_2 --> RCl + Cl.) = (0.38 +/- 0.04) $\Delta H^\circ_{rxn,fwd}$ + (10.12 +/- 0.81)

Ea_{Rev}(RCl + Cl. --> R. + Cl_2) = (0.64 +/- 0.04) $\Delta H^\circ_{rxn,Rev}$ + (9.72 +/- 0.83)

if $\Delta H^\circ_{rxn,Rev}$ <= -15.19 Ea_{Rev} = 0.0

(* : i-C_3H_7, t-C_4H_9, C_2H_3, CF_3, $CH_2ClCHCl$ are excluded.)

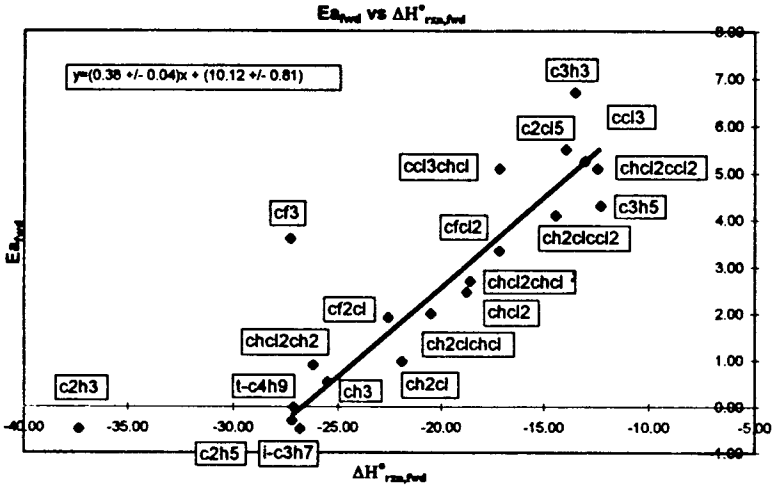
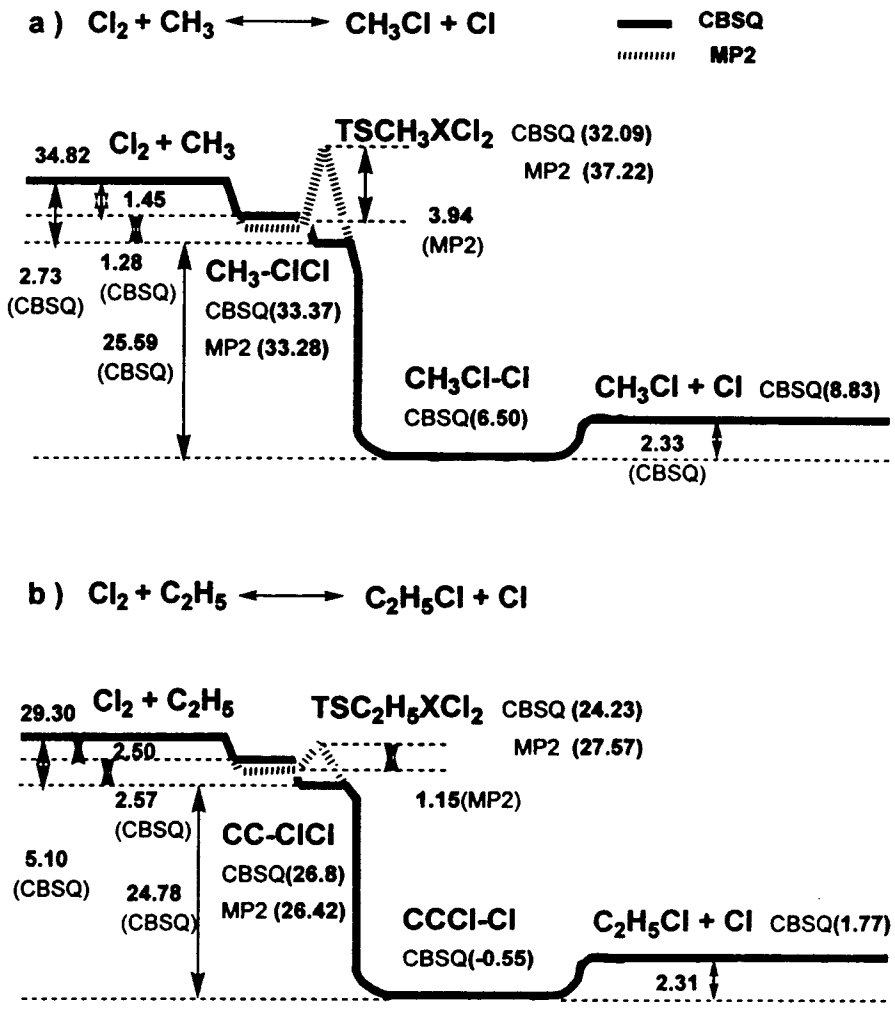


FIGURE 6 Reaction path diagrams in CH_3 with Cl_2 and C_2H_5 with Cl_2



Thermochemical Properties of Methyl and Chloro-methyl Oxychlorides and Reaction of Methyl radical with ClO

Dawoon Jung, Chiung-ju Chen and Joseph W Bozzelli
Department of Chemistry, Chemical Engineering and Environmental Science,
New Jersey Institute of Technology, Newark, NJ 07102

Abstract

Methyl and chloro– methyl oxychlorides are the simplest alkyl hydrocarbon oxychlorides with chlorine and oxygen. They are important fundamental species and the thermochemical property data are needed by both the atmospheric photochemistry and combustion communities. These oxygenated chlorocarbon molecules are formed in oxidation processes of combustion and atmospheric photochemistry of chlorocarbons. Enthalpy, $\Delta H^{\circ}_{f(298)}$, entropy, $S^{\circ}_{(298)}$ and heat capacities $C_p(T)$ from 300 to 1500K are determined for four oxychlorides density functional, B3LYP/6-31g(d,p) B3LYP/6-311+g(3df,2p), ab initio QCISD(T)/6-31g(d,p) and CBSQ calculation methods. Molecular structures and vibration frequencies are determined at the B3LYP/6-31g(d,p) density functional calculation level, with single point calculations for energy at the B3LYP/6-311+g(3df,2p), QCISD(T)/6-31g(d,p) and CBSQ levels of calculation. Vibration frequencies are scaled by for zero point energies and for thermal corrections. Enthalpies of formation are determined at each calculation level using the ΔH°_{rxn} and known enthalpies of other reactants in each of 7 different reactions. Contributions to entropy and heat capacity from internal rotation of the oxy-chloride group are estimated by the program, rotator[1]. Evaluation of data from the reactions, several of which are isodesmic, results in recommended $\Delta Hf_{(298)}$ values for CH_3OCl of –12.41, CH_2ClOCl of –22.70, $CHCl_2OCl$ of –26.71 and CCl_3OCl of –28.43 kcal/mol. The CBSQ calculation data are selected for enthalpies. Reactions of Methyl radical with ClO are analyzed using a quantum version of Rice-Ramsperger-Kassel theory (QRRK) for k(*E*) and a modified strong collision approach for falloff.

Introduction

Chlorocarbons are widely used chemicals as solvents in synthesis and in cleaning agents, as synthesis starting materials and in polymer, pesticide and other product manufacture. Chlorocarbons and other halocarbon compounds are present in the atmospheric from evaporation of these solvents and other anthropogenic activities. They often exhibit relatively long tropospheric lifetimes due to their slow decay or low reaction rates with OH radical.[2,3] Partially chlorinated alkanes undergo initial destruction reactions via loss of an alkyl hydrogen in the troposphere, (abstraction reaction) with OH.[3] Reaction of chlorinated or partially chlorinated alkenes and aromatics involve addition of OH radical, with formation of a hydroxyl adduct, which then further reacts with oxygen and or NO.[4]

Reactions of chloroalkanes in combustion include initial radical formation by abstraction of the alkyl H atoms, by chlorine atom elimination or HCl molecular elimination, which forms singlet carbenes, olefins or carbonyls. Chloroalkenes and aromatics can undergo addition of OH radical with either formation of a stable adduct or reaction (dissociation) of the adduct before stabilization. Fully chlorinated alkanes undergo loss of chlorine atom to form a radical or molecular elimination reaction to form unsaturated (alkene or carbonyl) products. The desired fate of Cl atoms is formation of HCl, but oxygen rich (fuel lean) and high temperature environments of combustion often shift the limited hydrogen available to stronger O-H or H-OH bonds. This results in significant steady state levels of atomic and molecular chlorine as well as chlorine oxide in the combustion environment. These species all react rapidly with alkyl radicals, with ClO radicals

undergoing association to form chemical activated oxychlorides that can be stabilized or further react to new products. ClO also serves to convert CO to CO_2.

The reactions of the radicals formed by initiation reactions with varied chlorocarbons or with chlorine atoms involve further reaction with oxygen and or nitric oxide. All of these atmospheric and combustion processes involve formation and reaction of oxygenated chlorocarbon species. Thermodynamic property data on the species formed are needed for evaluation of both reaction paths and kinetic processes, as well as stability of intermediate adducts and the oxy-chlorocarbon species formed as products. These properties are also needed in kinetic modeling and in equilibrium codes. There is very little or no data on thermodynamic properties of these oxygenated chlorocarbons in the literature, with one exception of acid carbonyl (acid chloride) species. This research is an attempt to estimate fundamental thermodynamic property data on these species using ab initio and density functional calculations and to calculate kinetic data in the reactions of methyl radical with ClO.

Enthalpy, $\Delta H^{\circ}_{f(298)}$, entropy, $S^{\circ}_{(298)}$ and heat capacities $C_p(T)$, ($300 < T/K < 1500$) are determined for the oxychlorides, CH_3OCl, CH_2ClOCl, $CHCl_2OCl$ and CCl_3OCl using density functional B3LYP/6-31g(d,p), B3LYP/6-311+g(3df,2p) and ab initio QCISD(T)/6-31g(d,p) and CBSQ calculation methods. Vibration frequencies are scaled by for zero point energies and for thermal corrections. Enthalpies of formation are determined at each calculation level using the ΔH°_{rxn} and known enthalpies of other reactants in each of 7 different reactions. Contributions to entropy and heat capacity from internal rotation of the oxy-chloride group are estimated by the program of rotator.[1] Reactions of Methyl radical with ClO are analyzed using a quantum version of Rice-Ramsperger-Kassel theory (QRRK) for k(*E*) and a modified strong collision approach for falloff and the evaluated thermochemical and transition state data of this study.

Result

Frequencies of oxychlorides from B3LYP/6-31g(d,p) density functional calculations are listed in Table 1. Enthalpies of formation for each calculation level and the 7 reactions are listed in Table 2. Evaluated accurate $\Delta Hf_{(298)}$ values for oxychlorides, CH_3OCl, CH_2ClOCl, $CHCl_2OCl$ and CCl_3OCl are −12.41, −22.70, −26.51and −28.43 as listed in Table 3. The potential energy diagram for $ClO + CH_3 = CH_3OCl$ = products is illustrated in Figure 1. The major forward product channel is formation of ClO + methyl radicals is methoxy radical + Cl atom. Rate constants for $CH_3 + ClO \rightarrow$ products versus temperature at 1atm pressure are shown in Figure 2.

Reference

1. Lay T.H. ; Kranosperov L. N.; Venanzi C. A.; Bozzelli J. W. *J. Phys. Chem.* **1996**, *100*, 8240.
2. Carol S.A.; Müller R.; Moortgat G. K.; Crowley J. N. *J. Phys. Chem.* **1996**, *100*, 17191.
3. Crowley J. N.; Campuzano-Jost P.; Mootgat G. K. *J. Phys. Chem.* **1996**, *100*, 3601.
4. Helleis F.; Crowley J. N.; Mootgat G. K. *J. Phys. Chem.* **1993**, 97, 11464.
5. Farman, J. G.; Gardiner, B.G.; Shanklin, J. D. *Nature* **1985**, *315*, 207.
6. Solomon, S. *Nature*. **1990**, *347*, 347.

TABLE 1: Vibrational Frequencies[a] (ν cm^{-1})

species	ν1[b]	ν2	ν3	ν4	ν5	ν6	ν7	ν8	ν9	ν10	ν11	ν12
CH_3OCl	259	364	660	1019	1175	1198	1463	1471	1523	3026	3104	3125
CH_2ClOCl	124	321	448	651	692	987	1063	1265	1347	1467	3091	3171
$CHCl_2OCl$	102	213	259	354	423	687	713	803	1051	1254	1329	3148
CCl_3OCl	115	166	247	249	316	390	392	534	689	766	840	1037

[a] Nonscaled. Frequencies are calculated at the B3LYP/6-31G(D,P) level of theory. [b] Torsional Frequencies. These frequencies are not included in the calculation of thermodynamic properties.

TABLE 2: Reaction Enthalpies (in kcal/mol) at 298.15 K[a]

reaction	therory levels			
	b3lyp6-31[b]	b3lyp6-311[c]	qcisd(t)[d]	CBSQ[e]
1 $CH_3OCl + CH_4 \rightarrow CH_3OH + CH_3Cl$	-32.16	-33.94	-32.25	-38.24
$CH_2ClOCl + CH_4 \rightarrow CH_3OH + CH_2Cl_2$	-26.46	-29.13	-27.18	-30.82
$CHCl_2OCl + CH_4 \rightarrow CH_3OH + CHCl_3$	-24.62	-27.63	-24.96	-29.72
$CCl_3OCl + CH_4 \rightarrow CH_3OH + CCl_4$	-21.64	-25.33	-21.93	-28.30
2 $CH_3OCl + CH_3CH_3 \rightarrow CH_3OH + CH_3CH_2Cl$	-36.15	-38.06	-36.67	-43.23
$CH_2ClOCl + CH_3CH_3 \rightarrow CH_3OH + CH_3CHCl$	-32.33	-35.07	-34.32	-39.29
$CHCl_2OCl + CH_3CH_3 \rightarrow CH_3OH + CH_3CCl_3$	-30.59	-33.49	-33.22	-40.00
$CCl_3OCl + CH_3CH_3 \rightarrow CH_3OH + CH_2ClCCl_3$	-32.31	-35.12	-34.24	-40.37
3 $CH_3OCl + H_2O \rightarrow CH_3OH + HOCl$	4.39	5.66	5.63	3.71
$CH_2ClOCl + 2H_2O \rightarrow CH_3OH + 2HOCl$	45.87	50.17	48.68	54.44
$CHCl_2OCl + 3H_2O \rightarrow CH_3OH + 3HOCl$	80.88	89.22	87.24	98.79
$CCl_3OCl + 4H_2O \rightarrow CH_3OH + 4HOCl$	112.75	125.12	123.24	141.66
4 $CH3OCl + H_2 \rightarrow CH_3OH + HCl$	-51.17	-54.51	-51.56	-56.96
$CH2ClOCl + 2H_2 \rightarrow CH_3OH + 2HCl$	-65.25	-70.18	-65.69	-66.91
$CHCl2OCl + 3H_2 \rightarrow CH_3OH + 3HCl$	-85.79	-91.31	-84.32	-83.24
$CCl3OCl + 4H_2 \rightarrow CH_3OH + 4HCl$	-109.49	-115.58	-105.50	-101.04
5 $CH_3OCl + H_2 \rightarrow CH_4 + HOCl$	-18.51	-20.90	-18.79	-22.32
$CH_2ClOCl + H_2 \rightarrow CH_3Cl + HOCl$	-13.59	-15.99	-13.62	-13.54
$CHCl_2OCl + H_2 \rightarrow CH_2Cl_2 + HOCl$	-14.35	-16.64	-13.04	-12.50
$CCl_3OCl + H_2 \rightarrow CCl_3H + HOCl$	-15.66	-18.28	-13.37	-12.87
6 $CH_3OCl + HOOH \rightarrow CH_3OOH + HOCl$	-1.85	-1.73	-1.44	-4.34
7 $CH_3OCl + CH_3OH \rightarrow CH_3OOH + CH_3Cl$	8.75	12.74	10.32	9.43

[a] Reaction enthalpies include thermal correction and zero-point energy correction . [b] B3LYP/6-31G(D,P), [c]B3LYP/6-311+G(3DF,2P), [d]QCISD(T)/6-31G(D,P). [e]CBSQ calculation method.

TABLE 3: Ideal Gas Phase Thermodynamic Properties[a]

Species and Symmetric no.		$\Delta H_f^0{}_{298}$[b]	$S^0{}_{298}$[c]	C_{p300}[c]	C_{p400}	C_{p500}	C_{p600}	C_{p800}	C_{p1000}	C_{p1500}
CH_3OCl	TVR[d]		60.92	11.46	13.54	15.52	17.25	20.02	22.09	25.31
(3)[g]	internal rotor[e]		4.85	2.17	1.85	1.65	1.51	1.34	1.24	1.12
	total	-12.41	65.77	13.63	15.39	17.17	18.76	21.36	23.33	26.43
	Melius[f]	-14.00	65.40	13.44		17.72		21.89	23.82	26.85
CH_2ClOCl	TVR		68.98	13.85	16.37	18.44	20.08	22.47	24.11	26.54
(1)	internal rotor		6.32	3.24	2.48	1.93	1.56	1.11	0.85	0.51
	total	-22.70	75.30	17.09	18.85	20.37	21.64	23.58	24.96	27.05
$CHCl_2OCl$	TVR		75.63	17.50	20.04	21.92	23.30	25.14	26.29	27.86
(1)	internal rotor		5.69	2.15	1.91	1.67	1.49	1.27	1.14	0.95
	total	-26.51	81.32	19.65	21.95	23.59	24.79	26.41	27.43	28.81
CCl_3OCl	TVR		79.11	21.70	24.23	25.82	26.85	28.02	28.62	29.26
(3)	internal rotor		4.71	3.11	2.97	2.70	2.43	1.95	1.58	1.04
	total	-28.43	83.82	24.81	27.20	28.52	29.28	29.97	30.20	30.30

[a] Thermodynamoc properties are referred to a standard state of an ideal gas of pure enantiomer at 1atm. One torsional frequency is excluded in the calculation of entropies and heat capacities. Instead, the contributions from hindered rotations about the C-O bond are calculated. [b] $\Delta H_f^0{}_{298}$ is the average value of CBSQ in kcal /mol. [c] Units in cal/mol K. [d] The sum of contributions from translations, external rotations, and vibrations. [e] Contributions from internal rotation about C-O bond. [f] Melius unpublished BAC/MP4 data. [g] Symmetry number is taken into account (-R ln (number of symmetry)).

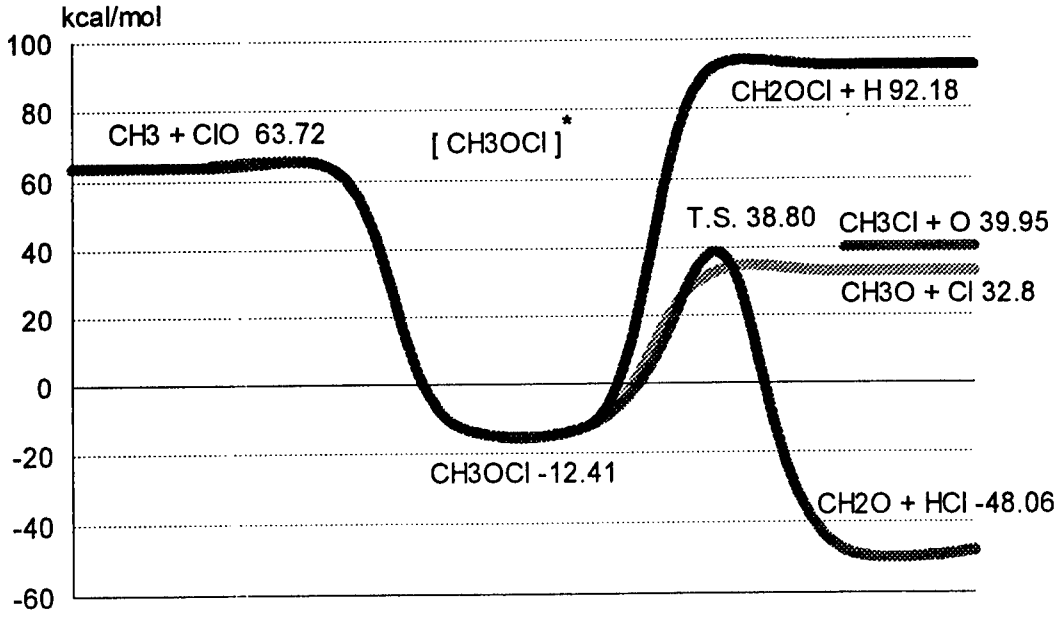


Figure 1. Potential energy diagram for CH_3 + ClO , Enthalpy (kcal/mol).

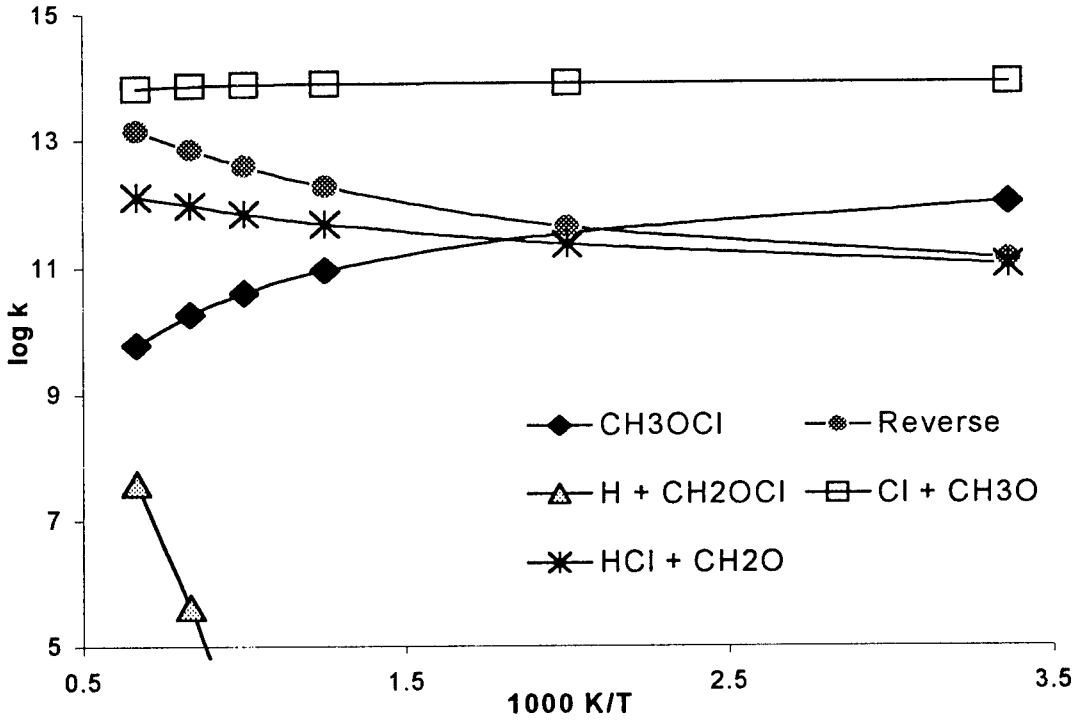


Figure 2. Rate constants at different temperatures and 1atm for chemically activated reactions: CH_3 + ClO → products

Modeling Study on Thermal Oxidation of 1,3-Hexachlorobutadiene at 773-1373K

Joseph W. Bozzelli and Li Zhu
Department of Chemical Engineering, Chemistry and Environmental Science, New Jersey Institute of Technology, Newark, New Jersey 07102, USA

J-P. Sawerysyn
Laboratoire de Cinitique et Chimie de la Combustion URA-CNRS 876 Universiti des Sciences et Technologies de Lille, 59655, Villeneuve d'Ascq-France

Abstract
We present a thermochemical analysis and modeling study on a reported experiment [1] of the thermal degradation and oxidation of 1000ppmv 1,3-hexachlorobutadiene (Cl_2C=CCl-CCl=CCl_2) at 1 atm air and 773-1373K at 2 seconds residence time. About 30 species from C1 to C8 formed by pyrolysis/oxidation are identified in the experiment. A mechanism consisting of ~240 reactions and ~80 species is developed then the results are compared with the experimental profiles on reactant (1,3-C_4Cl_6) and major products (Cl_2, CO, CO_2, $COCl_2$, C_2Cl_4, CCl_4) as a function of temperature. Relatively good agreement is obtained between computed and experimental species profiles. Thermochemical data of each species are estimated from studies on our previous thermochemical properties of chlorocarbons and oxychlorocarbons. Model includes reaction path analysis and evaluation of the kinetic parameters of abstraction, dissociation/combination, addition/elimination. QRRK/modified strong collision analysis is used for estimation of dissociation and chemical activation kinetic parameters versus temperature.

Modeling
1. Thermodynamic property estimation
Thermodynamic parameters, $\Delta H_f°_{298}$, $S°_{298}$, Cp°(T) ($300 \le T/K \le 1500$), for all species in this system are obtained from evaluation of literature and calculations performed in this NJIT thermochemical kinetics research group. Thermodynamic properties for the oxychlorocarbon species have been calculated by *ab initio* and density functional methods and isodesmic reactions. [2-5] We have also derived groups for Group Additivity estimation of these molecules for their thermodynamic properties using the "THERM" computer code. [2-9]

Potential energy diagram for degradation of 1,3-C_4Cl_6 is shown in Figure 1.

Table 1: Input parameters of 1,3-C_4Cl_6 dissociation for QRRK calculation[a,b,c]

Reaction		A	n	Ea
C=C-C=C → C=C-C.=C + Cl	(1)	5.58E+15	0	72.13
C=C-C=C → C=C-C=C. + Cl	(2)	1.51E+16	0	81.23
C=C-C=C → 2 C_2Cl_3	(3)	1.02E+17	0	106.09

k_1: from k_{-1} and <microscopic reversibility>. A_{-1} = 2×3E13 (estimated from trend plot of Cl association to alkyl radicals). Ea_{-1} = 0. k_2: from k_{-2} and <mr>. A_{-2} = 2×2.25E13 (see A_{-1}), Ea_{-2} = 0. k_3: from k_{-3} and <mr>. A_{-3} = 1E12 (see A_{-1}), Ea_{-3} = 0. a: A in s^{-1}; Ea in kcal/mol. b: Lennard-Jones parameters: σ = 6.5Å; ε/k = 650K. c: Reduced frequency sets: 158.3 cm^{-1} (11.018), 401.5 cm^{-1} (4.895), 1035.1 cm^{-1} (7.587).

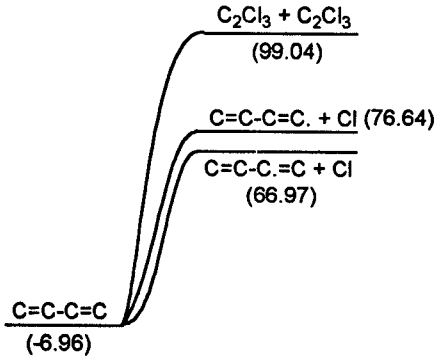


Figure 1: in kcal/mol

2. Input data requirements for the QRRK calculations (Table 1)

High pressure limit pre-exponential factors (Arrhenius A factors) for QRRK calculations are obtained from the literature, and from trend analysis of rate constants in homologous series of reactions as listed below.

A modified QRRK analysis we use in this work is described by Chang et al. [10] It is shown to yield reasonable results and provides a framework by which the effects of temperature and pressure can be evaluated in complex reaction systems. Fall-off is incorporated using modified strong collision approach (beta collision) of Gilbert et al. [11]

2.1. Kinetic parameters of abstraction reactions [12]

Chlorine atom is the species present in highest concentration and the abstraction of Cl by Cl atoms is a major chain propagation sequence in this reaction system. Review of the abstraction rate constant on a number of RCl + Cl ↔ R. + Cl_2 type of reactions with the use of thermodynamic properties of relative species and microscopic reversibility <mr> yields an Evans-Polanyi relation that Ea_{fwd} (in kcal/mol) = $0.64 \times \Delta H_f°_{rxn}$ + 9.7; Literature combined with <mr> yield the pre-exponential Arrhenius A factor (per Cl atom) of 4.44E13 $cm^3mol^{-1}s^{-1}$.

2.2. Kinetic parameters of addition reactions of Cl atom to vinyl chlorides [13]

Through the analysis of literature rate constants for Cl atom addition to chlorinated and olefinic bonds, Pre-exponential terms for Cl atom addition to the above bonds are evaluated as:

A = 2.25E13 for Cl + Cd/Cl_2 groups.

A = 3.0E13 for Cl + Cd/C/Cl/ groups.

Ea for this type of addition reaction is determined to be 0.0.

2.3. Kinetic parameters of combination Reactions of chloromethyl radicals [13]

Combination reactions of varied chloromethyl radicals are treated with Ea of 0 kcal/mol and with pre-exponential A factors decreasing with increasing degree of chlorine substitution.

Model results and relative sensitivities

Chemkin is used for mechanism interpretation, calculation of reverse reaction rates from thermodynamic parameters, and integration to reaction time at constant pressure and temperature.

Thermal degradation of 1,3-hexachlorobutadiene is initiated by the breaking of C-Cl bonds which are weaker than the C-C bonds, to generate primary and secondary pentachlorobutadienyl radicals via two unimolecular reactions: (A in s^{-1}, Ea in cal/mol, enthalpies of reactions in kcal/mol)

	A	n	Ea	$\Delta H_f°_{rxn}$
C=C-C=C ↔ C=C-C.=C + Cl	1.29E+51	-10.60	89200	73.93
C=C-C=C ↔ C=C-C=C. + Cl	8.15E+67	-15.60	105000	83.60

Formation of secondary C_4Cl_5 radicals is energetically favored over primary C_4Cl_5 radicals. Unimolecular reaction of 1,3-C_4Cl_6 to secondary C_4Cl_5 + Cl is the most sensitive reaction for overall conversion in early to mid stages of reaction. These initial chlorinated vinylic radicals, secondary and primary C_4Cl_5, then combine with O_2 at the radical site and result in rapid formation of chlorinated phosgene and aldehydic species through chemical activation reactions that involve several intermolecular isomerization prior to dissociation:

	A	n	Ea
C=C-C(OO.)=C ↔ CCl_2O +C=CC.=O	8.98E+26	-5.26	25400
C=C-C=COO. ↔ CClO + C=C-C=O	1.79E+48	-11.14	37700

Phosgene is the major chlorinated intermediate produced by the overall oxidation of 1,3-hexachlorobutadiene. Its formation occurs primarily via chemical activation reactions of pentachlorobutadienyl, trichlorovinyl and trichloromethyl radicals with O_2: $CCl_3 + O_2 \Leftrightarrow CCl_3OO^* \xrightarrow{(slow)} ClO + COCl_2$.

C_2Cl_4 and CCl_4 are the main organics produced in this overall thermal degradation of 1,3-hexachlorobutadiene. C_2Cl_4 is generated by Cl addition to the vinylic carbon, then cleavage of the stronger C-C single bonds and by C_2Cl_3 abstraction of Cl from Cl_2. These reactions are slightly endothermic and occur primarily on 1,3-C_4Cl_6, C=C-C=C=O, and C=C-C=O. C_2Cl_4 is also formed by decomposition of C_2Cl_6 and C_2Cl_5 that are formed by $CCl_3 + CCl_3$ combination and by $C_2Cl_3 + Cl_2 \rightarrow C_2Cl_4 + Cl.$; CCl_4 is formed by the reactions involving CCl_3 radical as a precursor species such as Cl, Cl_2, or ClO.

The loss of CCl_3 by reactions with O_2 and dissociation of the CCl_3OO peroxy adduct are critical to the CCl_4 profile versus temperature. The only reaction rate adjusted in mechanism development, at this initial stage, is the barrier of CCl_3OO isomerization. It is shifted +3 kcal/mol from the initial estimate of $\Delta H_f°_{rxn}$ + ring strain + Ea(abstraction) for $CCl_3OO \leftrightarrow C.Cl_2OOCl$ isomerization, where the chloroperoxide rapidly decomposes to lower energy products ($ClO + COCl_2$) with 2 kcal/mol barrier. The barrier effects the chemical activation reaction of $CCl_3 + O_2$ and dissociation of CCl_3OO.

Carbon monoxide production is primarily through thermal decomposition of species containing carbonyl groups, such as C=CC=C=O, C=CC=O and COCl. In absence of source of hydrogen (to form OH), oxidation of CO to CO_2 is essential due to the reactions with O_2, O and ClO:

$CO + O_2 \rightarrow CO_2 + O;$

$CO + O + M \rightarrow CO_2 + M;$

$CO + ClO \rightarrow CO_2 + Cl.$

These oxidation processes are quite slow in comparison with the oxidation of CO by OH radical as usually occurs in the oxidation of hydrocarbons.

Taking account into the high concentration of Cl atoms released in the thermal degradation of 1,3-hexachlorobutadiene, molecular chlorine as a final product is generated via recombination of Cl atoms. It is also formed by reaction of Cl with ClO which is some 6 kcal/mole endothermic, but because O atom is reactive; the loss of O to form carbonyls shifts this reaction toward Cl_2.

Some C6 to C8 species are detected by GC/MS, and we include them in the mechanism. A C_2Cl_3 radical addition to a vinyl acetylene (C=CC≡C) forms a secondary C_6Cl_7 linear adduct that can easily undergo unimolecularly isomerization to a primary C_6Cl_7 radical then cyclization to form a highly reactive cyclic-C_6Cl_7-2,4-diene radical. This radical is most likely stabilized by lose a Cl atom and/or under go further reaction to form C8. We show in this example how molecular weight growth occurs and formation of chlorobenzenes from small, low molecular weight chlorocarbons.

Comparisons between computed and experimental profiles are shown in Figures 2 and 3.

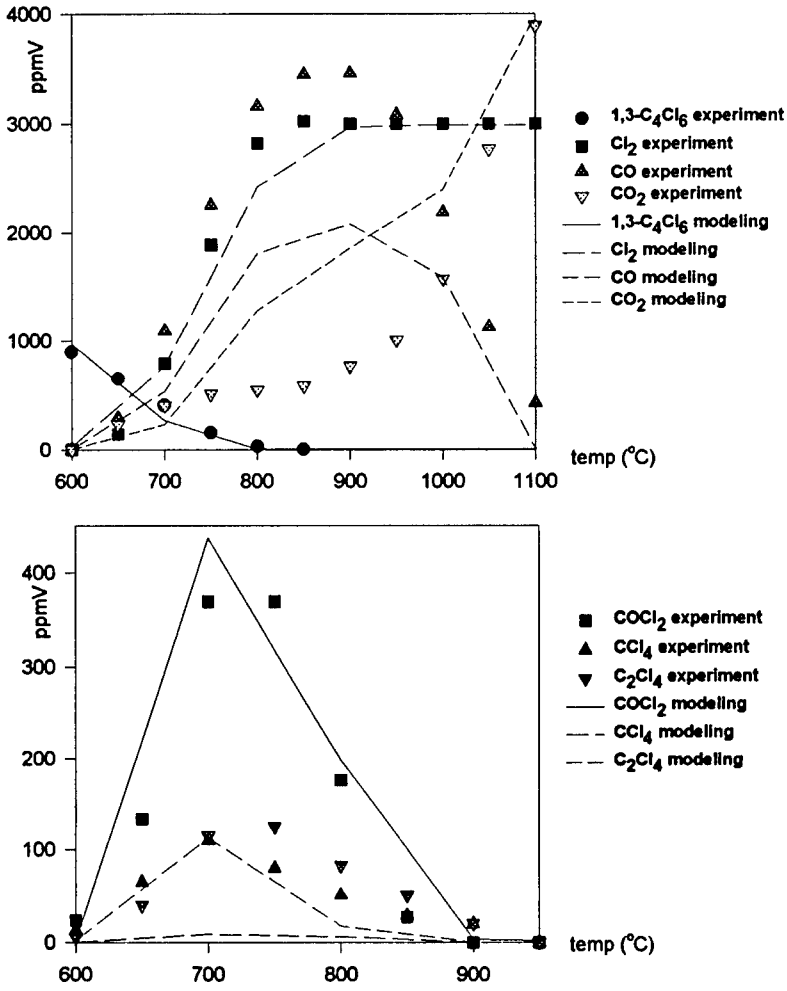
Acknowledgement

The authors are grateful for the financial support from the USEPA Northeast Research Center and the USEPA-CalTech-MIT-NJIT Research Center on Airborne Organics.

References

1. Baillet, C.; Fadli, A.; Sawerysyn, J-P. "Experimental study on the thermal oxidation of 1,3-hexachlorobutadiene at 500-1100°C." *Chemosphere*. **1996**, *32*,1261.
2. Chen, Chiung-ju; Wong, D.; Bozzelli, J. W. *J. Phys. Chem.* **1998**, *102*, 4551.
3. Zhu, L.; Bozzelli, J. W.; Lay, T. H. *Ind. Eng. Chem. Res.* **1998**, *37*, 3497.
4. Sun, H.; Chen, C.; Bozzelli, J. W. "Thermodynamic Properties, $\Delta H_f°_{298}$, $S°_{298}$, Cp°(T), of Chloromethyl Oxychlorides: CH_3OCl, CH_2ClOCl, $CHCl_2OCl$, and CCl_3OCl: Density Functional and *ab initio* Calculations." *Submmitted to J. Phys. Chem. Aug. 1999.*
5. Jung, D.; Chen, C.; Bozzelli, J. W. "Thermochemical Properties of Methyl and Chloro-methyl Oxychlorides and Reaction of Methyl radical with ClO." *32nd Mid-Atlantic Regional Meeting of the ACS*, Florham-Madison Campus of Fairleigh Dickinson University in Madison, NJ, May, 1999.

6. Benson, S. W. *Thermochemical Kinetics*; John Wiley: New York, 1976.
7. Ritter, E. R. *J. Chem. Info. Comp. Sci.* **1991**, *31*, 400.
8. Lay, T. H.; Bozzelli, J. W. *J. Phys. Chem.* **1997**, *101*, 9505.
9. Ritter, E. R.; Bozzelli, J. W. *Int. J. Chem. Kinetics* **1991**, *23*, 767.
10. (a) Chang, A. Y.; Bozzelli, J. W.; Dean, A. M. *In process of submittal to J. Phys. Chem.*; (b) Bozzelli, J. W.; Chang, A. Y.; Dean, A. M. *First Joint Meeting of the US Sections of the Combustion Institute: Western, Central and Eastern States.* The George Washington University, Washington DC, 1999, pp 140.
11. Gilbert, R. G.; Luther, K.; Troe, J. *Ber. Bunsenges. Phys. Chem.* **1983**, *87*, 169.
12. Bozzelli, J. W.; Lee, J., *First Joint Meeting of the US Sections of the Combustion Institute: Western, Central and Eastern States.* The George Washington University, Washington DC, **1999**, pp 300.
13. Bozzelli, J. W.; Zhu L. "Trends in Rate Constants of Association Reactions of Chloromethyl Radicals and Addition Reactions of Cl Atom to Vinyl Chlorides." *In process.*



Figures 2 & 3

Theoretical Study on the Unimolecular Decomposition of c-C_5H_6 and c-C_5H_5: *Ab Initio* MO/Statistical Theory Study

L. V. Moskaleva*, L. K. Madden and M. C. Lin**
Department of Chemistry, Emory University, Atlanta, GA 30322
e-mail: *lmoskal@emory.edu, **chemmcl@emory.edu

Introduction

The relevance of the cyclopentadienyl (c-C_5H_5) radical to the formation of polycyclic aromatic hydrocarbons and soot in hydrocarbon combustion has gained increasing attention lately, thanks to the results of recent theoretical calculations.[1,2]

In hydrocarbon combustion, c-C_5H_5 can be directly produced from the decomposition of C_6H_5O (phenoxy radical)[3-6] and from the reaction of C_2H_2 with C_3H_3 (propargyl radical), which are known to coexist near sooting conditions.

The mechanism for the decomposition of the phenoxy radical producing CO + c-C_5H_5 has been studied theoretically in detail,[7,8] whereas that for the decomposition of c-C_5H_5 or its reverse process, $C_3H_3 + C_2H_2$, is not well-understood.

Experimentally, the mechanism as well as the kinetics of the unimolecular decomposition of c-C_5H_5 have been studied recently by two research groups with shock tubes[9,10] as a secondary process in the cyclopentadiene decomposition:

$$c\text{-}C_5H_6 \rightarrow C_5H_5 + H \qquad (1)$$

The kinetics for the formation of $C_2H_2 + C_3H_3$:

$$c\text{-}C_5H_5 \rightarrow C_2H_2 + C_3H_3 \qquad (2)$$

has been analyzed by assuming the involvement of different C_5H_5 intermediates.

This study aimed to calculate theoretical rate constants for reactions (1) and (2), to elucidate the mechanism for reaction (2) and to provide the combustion community a realistic estimate for its rate constant and those of potential isomerization reactions which are believed to exist under varying T, P-conditions.

The unimolecular decomposition of c-C_5H_6 and its reverse bimolecular reaction

The recombination of c-C_5H_5 and H atom is a barrierless process for which no distinct transition state can be found. We used canonical variational transition state theory, cVTST,[11,12] to calculate the rate constant for the c-C_5H_6 decomposition.

The dissociation/recombination profile was first generated at the UB3LYP (Unrestricted Becke's Three Parameter Hybrid Method[13] with the LYP Correlation Functional of Lee, Yang, and Parr[14]) level of theory with the 6-311G(d,p) basis set and then refined at the CASPT2 level[15] in order to take care of a multireference nature of the system along the reaction coordinate. The CASPT2 method is known to underestimate dissociation barriers when a number of unpaired electrons in products is higher than in the reactant. This was the case with the c-C_5H_6 dissociation for which CASPT2 rendered 74.8 kcal/mol to be compared with the experimental value of 84 kcal/mol. The latter value is consistent with the 65 kcal/mol for the c-C_5H_5 heat of formation which we theoretically confirmed[16] with high level *ab initio* calculations.

We have fitted the CASPT2 profile with the Lippencot potential, $V(r) = D_e(1 - e^{-\alpha(r-r_0)^2/2r_0})$ and used fit parameters, α and r_0, in combination with a more reasonable G2M(rcc,MP2)[17] dissociation energy ($D_e + \Delta ZPE$ = 83.2 kcal/mol) to generate a new profile upon which the cVTST calculations were based.

The cVTST predicted rate constant for the c-C_5H_6 dissociation (Fig. 1) agrees quite well with experiment, particularly with what we consider the best experimental data, by Frank et al.[10]

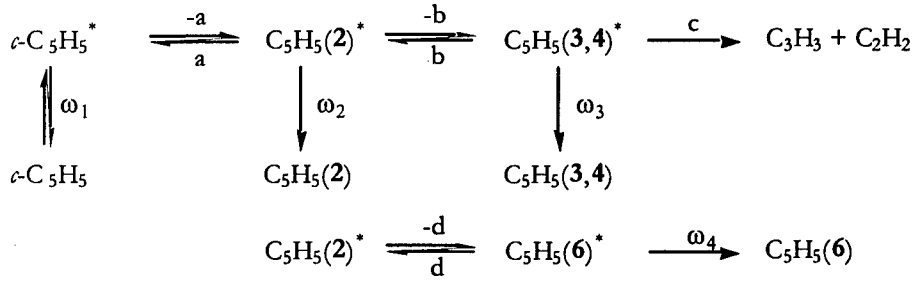
$C_5H_5 \rightarrow C_3H_3 + C_2H_2$ and reverse bimolecular process

The geometry optimizations were performed at the density functional level using the B3LYP/6-31G(d,p) method. Vibrational frequencies, calculated at this level, were used for characterization of stationary points, zero-point energy (ZPE) and RRKM computations.

The reaction paths of the c-$C_5H_5 \rightarrow C_2H_2 + C_3H_3$ reaction were produced by complete optimization of structural parameters for the reactants, products, transition states and intermediates. The energetics along the reaction paths were established by single point energy computations with the higher level *ab initio* methods including the restricted open shell coupled cluster, ROHF-CCSD(T), the second-order multiconfigurational perturbation theory based on a CASSCF reference function, CASPT2, and the G2M(rcc,MP2). ROHF-CCSD(T) energies were adapted for further RRKM rate constant calculations.

All MO computations were performed with GAUSSIAN 94[18] and MOLPRO 96[19] programs.

The potential energy diagram for the C_5H_5 isomerization and dissociation is presented in Fig. 2. The multichannel RRKM calculations for the reaction (2) were based on the following detailed mechanism:



In the simplified scheme above, C_5H_5(**3,4**) stands for all acyclic isomers, except **6** which is denoted as C_5H_5(**6**). We treated the two pathways originating from **2** towards **3a** and **4** as degenerate and ignored the geometric isomers of 1,3,4-pentatrieneyl, see Fig. 2. We also assumed the formation of **6** directly from **2** via **TS8**.

The comparison with the experimental results of Kiefer et al.[9] for the overall reaction (2) for the 150 torr pressure and 1700-3000 K temperature range gave a satisfactory agreement taking into account large experimental scatter. In their modeling, Kiefer et al. assumed that reaction (2) proceeds in a single step, which is a rather severe approximation. Indeed, the experimental C_2H_2 concentration profile exhibits an initial induction period of about 0.1 ms that indicates a multistep process.

Frank et al.[10] assumed the decyclization transition state (**TS2**, **TS6**, **TS8** in the present work) to be the rate determining contrary to our conclusions. For kinetic modeling they used high-pressure limit rate constants, which must be a poor approximation also, since the RRKM calculations reveal significant pressure dependence for the overall process as well as for elementary steps.

Burcat and Dvinyaninov[20] in their modeling of the cyclopentadiene decomposition derived the rate constant for the reaction c-$C_5H_5 \rightarrow C_5H_5$(**6**) (based on the concentration profiles of the decomposition products). Comparison with our results indicates a significant deviation.

We could see that, contrary to our expectations, the reaction rate is controlled by the first transition state **TS1**, rather than **TS5** and **TS7**. We can point to the pronounced pressure effect on the total disappearance rate coefficient as well as those for branching fractions especially at high temperatures.

Acknowledgment

The authors gratefully acknowledge the support received from the Department of Energy, Office of Basic Energy Sciences, Division of Chemical Sciences through Contract DE-FGO2-97ER14784. Also, we are thankful to the Cherry L. Emerson Center for Scientific Computation for the use of various programs and computing facilities.

References

1. C. Melius, M. E. Colvin, N. M. Marinov, W. J. Pitz, and S. M. Senkan, *26th Symp. (Int.) Combust. Proc.,* 1996, p.685.
2. L. V. Moskaleva, A. M. Mebel, and M. C. Lin, *26th Symp. (Int.) Combust. Proc.,* 1996, p.521.
3. I. Glassman, *Combustion,* 2d ed.; Academic Press, New York, 1985.
4. A. J.Colussi, F. Zabel, and S. W. Benson, *Int. J. Chem. Kinet.,* **9**, 161 (1977).
5. C.-Y. Lin, and M. C. Lin, *J. Phys. Chem.,* **90**, 425 (1986).
6. P. Frank, J. Herzler, Th. Just, and C. Wahl, Proc. *25th Symp. (Int.) Combust. Proc,.* 1994, p.833.
7. E. W. Diau, M. C. Lin, and C. F. Melius, *J. Chem. Phys.*, **101**, 3923 (1994).
8. S. Olivella, A. Sole, and A. Garcia-Raso, *J. Phys. Chem.*, **99**, 10549 (1995).
9. R. D. Kern, J. Yao Zhang, B. S. Jursic, R. S. Tranter, M. A. Greybill, and J. H. Kiefer, *27th Symp. (Int.) Combust. Proc.,* 1998.R. D. Kern, J. Yao Zhang, B. S. Jursic, R. S. Tranter, M. A. Greybill, and J. H. Kiefer, *27th Symp. (Int.) Combust. Proc.,* 1998.
10. K. Roy, C. Horn, P. Frank, V. G. Slutsky, and T. Just, *27th Symp. (Int.) Combust. Proc.,* 1998.
11. Garret, B. C.; Truhlar, D. C. *J. Chem. Phys.*, **70**, 1593 (1979).
12. Isaacson, A. D.; Truhlar, D. G.; *J. Chem. Phys.*, **76**, 1380 (1982).
13. A. D. Becke, *J. Chem. Phys.*, **98**, 5648 (1993).
14. C. Lee, W. Yang and R. G. Parr, *Phys. Rev. B*, **37**, 785 (1988).
15. K. Andersson, P. A. Malmqvist, B. O. Roos, A. J. Sadlej, and K. Wolinski, *J. Phys. Chem.*, **94**, 5483 (1990).
16. Moskaleva, L. V.; Lin, M. C.; *J. Comput. Chem.* Submitted.
17. A. M. Mebel, K. Morokuma, and M. C. Lin, *J. Chem. Phys.*, **103**, 7414 (1995).
18. M. J. Frisch, G. W. Trucks, H. B. Schlegel, P. M . W. Gill,. B. G. Johnson, M. A. Robb, J. R. Cheeseman, T. Keith, G. A. Petersson, J. A. Montgomery, K. Raghavachari, M. A. Al-Laham, V. G. Zakrzewski, J. V. Ortiz, J. B. Foresman, J. Cioslowski, B. B. Stefanov, A. Nanayakkara, M. Challacombe, C. Y. Peng, P. Y. Ayala, W. Chen, M. W. Wong, J. L. Andres, E. S. Replogle, R. Gomperts, R. L. Martin, D. J. Fox, J. S. Binkley, D. J. Defrees, J. Baker, J. P. Stewart, M. Head-Gordon, C. Gonzalez, and J. A. Pople, *GAUSSIAN 94, REVISION A.*1; Gaussian, Inc., Pittsburgh PA, 1995.
19. MOLPRO is a package of *ab initio* programs written by H.-J. Werner and P. J. Knowles, with contributions from J. Almlöf, R. D. Amos, A. Berning, D. L. Cooper, M. J. O. Deegan, A. J. Dobbyn, F. Eckert, S. T. Elbert, C. Hampel, R. Lindh, A. W. Lloyd, W. Meyer, A. Nicklass, K. Peterson, R. Pitzer, A. J. Stone, P. R. Taylor, M. E. Mura, P. Pulay, M. Schütz, H. Stoll and T. Thorsteinsson.
20. A . Burcat and M. Dvinyaninov, *Int. J. Chem. Kinet.,* **29**, 505 (1997).

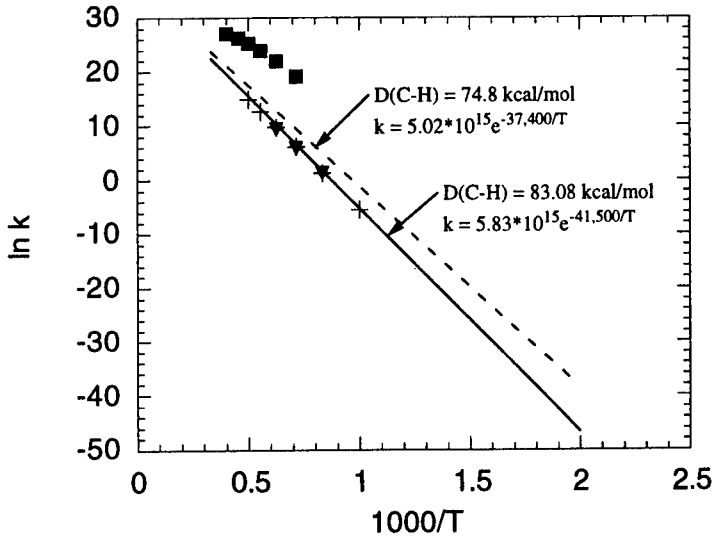


Figure 1. Arrhenius plot of the rate data for the $C_5H_6 \rightarrow C_5H_5 + H$ reaction. Dashed line: cVTST with CASPT2 energies; solid line: cVTST with energies fitted to G2M barrier; Squares: Ref. 9; triangles: Ref. 10; crosses: Ref. 20.

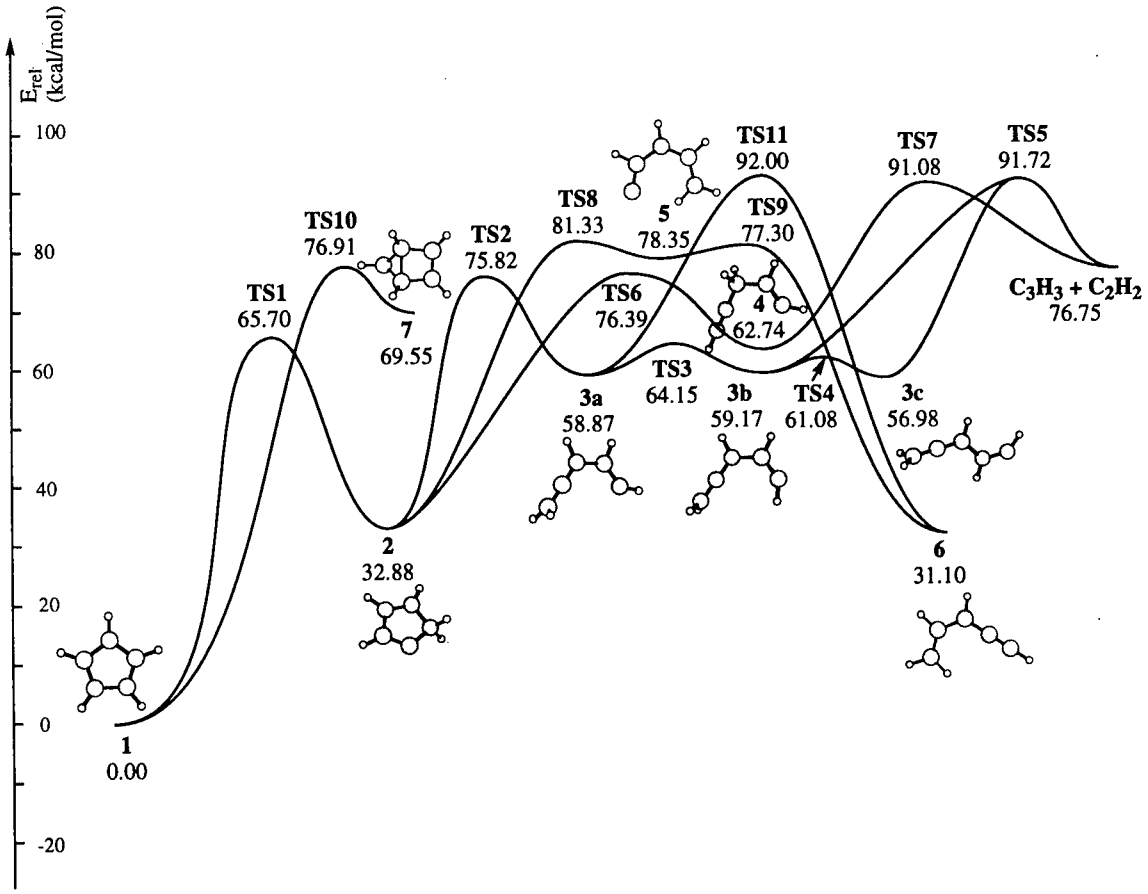


Figure 2. Potential energy diagram for the c-C_5H_5 radical isomerization/decomposition reaction. ZPE corrected energies are given as calculated at the ROHF-CCSD(T)/6-31G(d,p) level.

THEORETICAL STUDY OF H-FOR-X SUBSTITUTION IN THE H + C_6H_5X (X = D and CH_3) REACTIONS

I. V. Tokmakov and M. C. Lin***

Department of Chemistry

Emory University, Atlanta, GA 30322

*E-mail: *itokmak@emory.edu, **chemmcl@emory.edu*

Introduction

Over the past years, many investigations of fuel combustion processes had focused on the formation and growth of polyaromatic hydrocarbons (PAH). Typically, the initial step in the pyrolysis of aromatic molecules involves the C-H bond cleavage and H atoms can be formed in appreciable concentrations in the incipient stages of the pyrolysis. Then secondary reactions with H atoms, such as H-for-X substitution, become very important. Therefore, reliable rate constants for these processes are essential for modeling the product yields and establishing the mechanism of the pyrolysis.

Detailed studies of the desubstitution reactions in the aromatic substrates could provide valuable results for environmental chemists as well. Treatment with H_2 or other sources of the H atom can be applied to highly chlorinated industrial waste.[1] Haloaromatic derivatives are very resistant to Ar-X homolysis but they can be removed via reactions with H atoms, which promote cracking down to benzene. The potential extension of this technique to other substituted aromatic derivatives (e.g. PAH), which are known as dangerous pollutants, is also highly desirable.

In this work, we focused on the hydrodealkylation of the simplest alkyl aromatic hydrocarbon – toluene. The H atom can attack different sites in toluene:

$$C_6H_5CH_3 + H \rightleftharpoons (ipso\text{-}, o\text{-}, m\text{-}, p\text{-})\ C_6H_6CH_3^* \xrightarrow{[M]} (ipso\text{-}, o\text{-}, m\text{-}, p\text{-})\ C_6H_6CH_3 \quad (1a\text{-}1d)$$

$$\longrightarrow C_6H_5CH_2 + H_2 \quad (2)$$

$$\longrightarrow (o\text{-}, m\text{-}, p\text{-})\ C_6H_4CH_3 + H_2 \quad (3a\text{-}3c)$$

$$\rightleftharpoons ipso\text{-}C_6H_6CH_3^* \longrightarrow C_6H_6 + CH_3 \quad (4)$$

Here reaction 4 represents the hydrodemethylation of toluene as an addition/elimination sequence. Neither of the abstraction channels (2, 3a-3c) lead to desubstitution of toluene in their subsequent reactions. However, these processes are important for modeling the $H + C_6H_5CH_3$ system especially at high temperatures when they become prevailing over the addition channel (1). The mechanism of desubstitution could also be complicated by H-migration from the site of addition to the neighboring positions:

$$ipso\text{-}C_6H_6CH_3 \rightleftharpoons o\text{-}C_6H_6CH_3 \rightleftharpoons m\text{-}C_6H_6CH_3 \rightleftharpoons p\text{-}C_6H_6CH_3 \quad (5)$$

A direct experimental evidence for H-migration around the ring in the cyclohexadienyl radicals is difficult to obtain. Trying to explain the measured rates of isotope exchange in the $H(D) + C_6H_6/C_6D_6$ systems, different groups[2,3] reached opposite conclusions about the possibility of scrambling H and D atoms in the $C_6H_xD_{7-x}$ intermediates. In order to investigate the importance of this process, we have studied the $H + C_6H_5D$ model system, which is less

computationally demanding than $H + C_6H_5CH_3$ and provides qualitatively accurate estimates of the rates of reactions 1, 3, 5 from the homologous processes (6-8):

$$C_6H_5D + H \rightarrow (ipso\text{-}, o\text{-}, m\text{-}, p\text{-})\ C_6H_6D \quad (6)$$

$$C_6H_5D + H \rightarrow C_6H_4D + H_2 \quad (7)$$

$$ipso\text{-}C_6H_6D \rightleftharpoons o\text{-}C_6H_6D \rightleftharpoons m\text{-}C_6H_6D \rightleftharpoons p\text{-}C_6H_6D \quad (8)$$

Some theoretical estimates were already available from the study of the H + C_6H_6 reaction carried out in this laboratory by Mebel et al.[4] That study, however, did not address the possibility of H-migration in the C_6H_7 intermediates. Another reason to revisit the reaction of H atoms with benzene was an opportunity to evaluate the performance of *ab initio* methods by comparing our theoretical predictions with the experimental rate constants measured for different isotopic variations of this system.

Computational Methods

The equilibrium geometries of the reactants, transition states and products were found by the hybrid density functional B3LYP/6-311++G(d,p) method.[5,6] Vibrational frequencies calculated at the same level of theory were employed for zero-point energy (ZPE) correction, characterization of stationary points and RRKM calculations of the rate constants. All the energies herein include ZPE corrections. For a more accurate evaluation of the energetic parameters, higher level single point calculations were carried out on the optimized geometries.

For the H + C_6H_5D = C_6H_6 + D reaction, we have tested the performance of several modified GAUSSIAN-2 (G2M) computational schemes[7] which calculate a series of CCSD(T), MP4(SDTQ) and MP2 energies with various basis sets to approximate the CCSD(T)/6-311+G(3df,2p)//B3LYP/6-311++G(d,p) energy with an additional "higher level correction" (HLC) based on the number of paired and unpaired valence electrons.

For the reaction of hydrogen with toluene, we have consistently studied favorable reaction channels (eq. 1, 2 and 4) at the G2M(cc,MP2) level.

For all molecular orbital calculations the GAUSSIAN 94 program package[8] was used.

Results and Discussion

The potential energy profiles for the H-for-X processes in the reactions of H atoms with C_6H_5D and $C_6H_5CH_3$ are shown in Figs. 1 and 2.

Because of the scattering in the reported heats of H-addition to C_6H_6, we used isodesmic reactions to compute accurate enthalpies of formation of the C_6H_7 and *ipso*-C_7H_9 radicals and heats of reactions 1a and 6. Our recommended $\Delta_fH°_0(C_6H_7)$ is ≈54.5 kcal/mol, $\Delta_fH°_0(C_7H_9)$≈49.3 kcal/mol. The examination of the theoretical energetic parameters revealed that the calculated heats of reactions and barriers contained errors due to various theoretical deficiencies. Generally, the G2M and B3LYP predictions were the most useful as they deviated from the actual values by relatively small amounts in opposite directions. Reasonable adjustments of the G2M(cc,MP2) energetic parameters allowed us to calculate the rate constants that were consistent with the most reliable experimental data on the H + $C_6H_5CH_3$ and H(D) + C_6H_6/C_6D_6 reactions.

We found from the B3LYP/6-311++G(3df,2p) and G2M(cc,MP2) estimates that the activation energy for H- or D-migration to the neighboring carbon atom in the cyclohexadienyl radical is ~45–47 kcal/mol. This is much higher than the barrier for H- (or D-) elimination. Our calculated RRKM rate constants confirm that the role of the H-migration channel is negligible for a wide range of temperatures and pressures.

The dominant reaction channel changes upon varying temperature and pressure. At low temperatures the major process is H-addition to the aromatic ring, and the corresponding rate constants are essentially at the high pressure limit (HPL). For the reaction of H atoms with benzene, the rate constant is at the HPL for pressures as low as 10 torr at T<500K. This rate constant is shown in Fig. 3. The G2M(cc,MP2) barrier for H-addition to C_6H_6 had to be lowered by 3.5 kcal/mol to reproduce the experimental rate constants.[2,9] A similar adjustment was applied to the theoretical barrier of H-addition to toluene. In the reaction of H atoms with toluene, addition takes place preferably at the *ortho*-position. The formation of the *ipso*-adduct is least favorable. The newly formed *ipso*-$C_6H_6CH_3$* radical may, however, quickly decompose via TS4 to the new products (reaction 4). This desubstitution channel becomes more important at higher temperatures and low pressures. The other competing process is H-abstraction from the methyl group. This channel consumes a significant portion of the reactants at T>500K.

The H-for-X process in the reactions of H with C_6H_5D and $C_6H_5CH_3$ is most competitive in the middle T range and low pressures. For example, Fig. 4 shows the portion of the reactants consumed by this channel in the reaction of H atoms with toluene. The maximum is reached at 1100-1200K (760 Torr), and it shifts to lower temperatures as the pressure decreases.

The H-abstraction from the ring becomes important only at very high temperatures (T>1500K). In this region the H-abstraction channels dominate and the total rates of the H + C_6H_5X reactions are essentially independent of pressure.

References

1. (a) Manion, J. A.; Mulder, P.; Louw, R. *Envir. Sci. Technol.* **1985**, *19*, 280; (b) Louw, R.; Senden, M. M. G.; Mulder, P.; Tels, M. *Recycling Int.* **1984**, 999; (c) U.S. Pat. 4,851,600; Eur. Pat. 0175406.

2. Nicovich, J. M.; Ravishankara, A. R. *J. Phys. Chem.* **1984**, *88*, 2534.

3. Manion, J. A.; Louw, R. *J. Phys. Chem.* **1990**, *94*, 4127.

4. Mebel, A. M.; Lin, M. C.; Yu, T.; Morokuma, K. *J. Phys. Chem. A* **1997**, *101*, 3189.

5. (a) Becke, A. D. *J. Chem. Phys.* **1993**, *98*, 5648; (b) Becke, A. D. *J. Chem. Phys.* **1992**, *96*, 2155; (c) Becke, A. D. *J. Chem. Phys.* **1992**, *97*, 9173.

6. Lee, C.; Yang, W.; and Parr, R. G. *Phys. Rev. B* **1988**, *37*, 785.

7. Mebel, A. M.; Morokuma, K.; Lin, M. C. *J. Chem. Phys.*, **1995**, *103*, 7414.

8. Frisch, M. J.; Trucks, G. W.; Schlegel, H. B.; Gill, P. M. W.; Johnson, B. G.; Robb, M. A.; Cheeseman, J. R.; Keith, T.; Petersson, G. A.; Montgomery, J. A.; Raghavachari, K.; Al-Laham, M. A.; Zakrzewski, V. G.; Ortiz, J. V.; Foresman, J. B.; Cioslowski, J.; Stefanov, B. B.; Nanayakkara, A.; Challacombe, M.; Peng, C. Y.; Ayala, P. Y.; Chen, W.; Wong, M. W.; Andres, J. L.; Replogle, E. S.; Gomperts, R.; Martin, R. L.; Fox, D. J.; Binkley, J. S.; Defrees, D. J.; Baker, J.; Stewart, J. P.; Head-Gordon, M.; Gonzalez, C.; Pople, J. A. GAUSSIAN 94, Revision D.3; Gaussian, Inc.; Pittsburgh: Pennsylvania, **1995**.

9. (a) Sauer, M. C.. Jr.; Mani, I. *J. Phys. Chem.* **1970**, *74*, 59; (b) Sauer, M. C., Jr.; Ward, B. *J. Phys. Chem.* **1967**, *71*, 3971; (c) Knutti, R.; Buhler, R. E. *Chem. Phys.* **1975**, *7*, 229; (d) Yang, K. *J. Am. Chem. Soc.* **1962**, *84*, 3795.

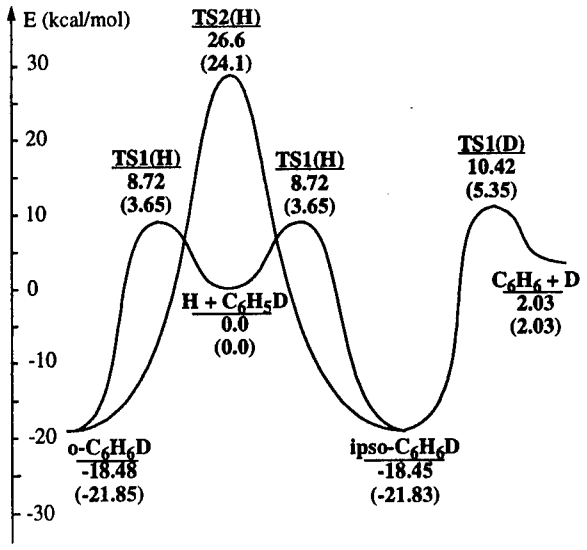


Fig. 1. A schematic potential energy diagram for the $C_6H_5D + H = C_6H_6 + D$ reaction. Energies are calculated at the G2M(cc,MP2) and B3LYP/6-311++G(3df, 2p) (in parentheses) levels.

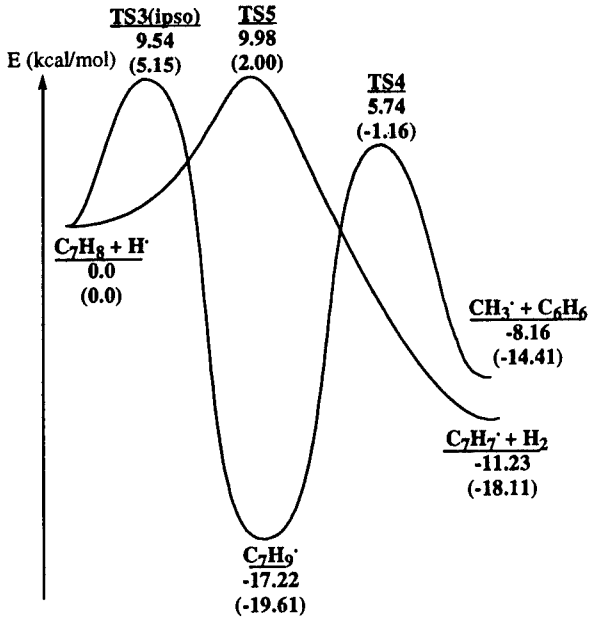


Fig. 2. A schematic potential energy diagram for the $C_7H_8 + H$ reaction. Energies are calculated at the G2M(cc,MP2) and B3LYP/6-311++G(3df, 2p) (in parentheses) levels.

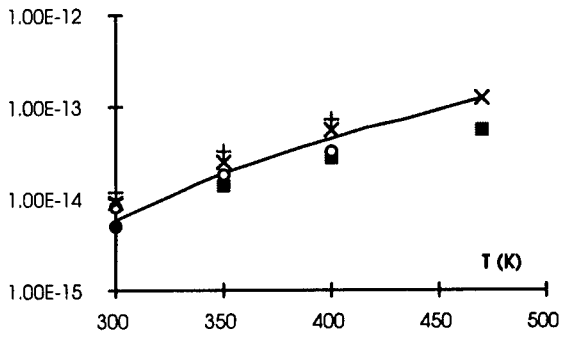


Fig. 3. Low T rate constant of H-addition to benzene per 1 site: calculated from the adjusted G2M(cc,MP2) barrier (solid line); from ref. 2 (x), ref. 9a (+), ref. 9b (open circles), ref. 9c (filled circle), ref. 9d (filled squares).

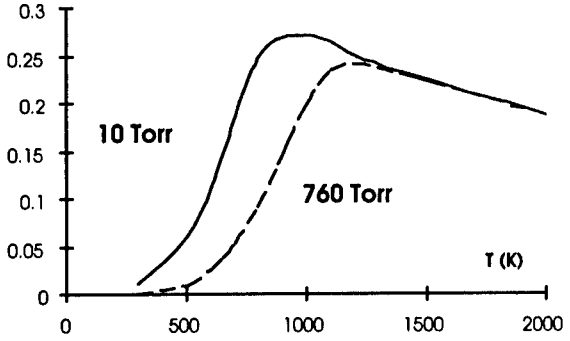


Fig. 4. Estimated ratio $k_4/k(H+C_6H_5CH_3)$, where $k(H+C_6H_5CH_3)=k_1+k_2+k_3+k_4$, at different temperatures and pressures. Rate constants are calculated from the adjusted G2M(cc,MP2) energetic parameters.

Acknowledgment

The authors gratefully acknowledge the support received from the Department of Energy, Office of Basic Energy Sciences, Division of Chemical Sciences through Contract DE-FGO2-97ER14784. Also, we are thankful to the Cherry L. Emerson Center for Scientific Computation for the use of various programs and computing facilities.

Combining Two Tomographic Inversion Methods to Reconstruct a Complex Concentration Field

Michael Y. Feng (mf29@cornell.edu) and Frederick C. Gouldin (fcg2@cornell.edu)
Sibley School of Mechanical and Aerospace Engineering
Cornell University Ithaca, NY 14853

Introduction

Laser absorption tomography has been proposed for in-situ measurement of complex concentration distributions in gaseous flows because it is non-intrusive and quicker than point-by-point probe sampling measurements. We propose using two tomographic inversion methods in tandem: the Adaptive Finite Domain Direct Inversion (FDDI) Method [1, 2] and the Tomographic Reconstruction via a Karhunen-Loève Basis (TRKB) Method [3].

The TRKB method needs *a priori* data obtained by another technique but then requires fewer absorption measurements than Adaptive FDDI and other contemporary inversion methods. Fewer absorption measurements means less optical access required and less time to obtain the necessary quantity of data for a tomographic reconstruction. TRKB's chief weakness is its requirement for *a priori* data. So, TRKB is most useful for monitoring a set of familiar distributions with very few absorption measurements provided the *a priori* data are available.

Previously, probe sampling measurements were used for generating the *a priori* data, a set of expected distributions, for TRKB. However, probe sampling is not always possible such as for an unsteady distribution and/or is too time-consuming. We propose using the alternative tomography system, Adaptive FDDI, to generate the *a priori* data for TRKB. In the work reported here we evaluate the utility of finding the required *a priori* information via tomography.

Background

We solve for the two-dimensional concentration distribution, $n(x,y)$, from a set of line integrals of n at different locations. The Lambert-Beer law (Eq. 1) relates the line integral of the species concentration to laser absorption along the integration path. This laser absorption measurement is termed a line-of-sight projection, p, and is characterized by an offset, s, and a view angle, θ. See Figure 1.

$$p(s,\theta) \equiv -\ln\left(\frac{I_\nu^t}{I_\nu^0}\right) = \sigma_\nu \int_{-\infty}^{+\infty} n(x,y)\,dt \qquad (1)$$

where: $\nu \equiv$ frequency of light, $I^t_\nu \equiv$ transmitted light intensity at ν, $I^0_\nu \equiv$ initial light intensity at ν, $t \equiv$ coordinate along line-of-sight, and $\sigma_\nu \equiv$ absorption cross section of absorbing gas at ν. Note temperature is constant.

Both inversion methods solve for $n(x,y)$ with a series expansion solution. The Adaptive FDDI method uses local basis functions, i.e. functions that are localized to a subset of the domain. On the other hand, the TRKB method uses global basis functions, i.e. functions that span the entire domain. Both methods project the basis functions along the same lines as the projection measurements to form an overdetermined, least squares problem where the rms difference between line integrals of the weighted basis functions and the projection measurements is minimized by the choice of weighting coefficients. This least squares problem is solved by the singular value decomposition [4]. The overdeterminedness reduces the effect of noise in the projection measurements, so increasing the number of projection measurements or decreasing the number of basis functions is crucial to minimizing random error.

The Adaptive FDDI method utilizes consistent basis functions derived from the Kaiser window [1] and assigned to a triangular grid point in the domain. In the first solution for n, we use 97 basis functions, i.e. K=97. Using this preliminary solution for n, 50 grid points are added in areas with high concentration gradient. Then a new least squares problem is solved for 147 weighting coefficients as opposed to the original 97.

The TRKB method uses the Karhunen-Loève (KL) procedure [5, 6] to create the basis functions from the *a priori* data, a set of distributions called the training set. The KL basis functions are the eigenvectors of a real, symmetric matrix formed from two-point correlations of the training set. The corresponding eigenvalues represent the training set average of the square of the inner product of the eigenfunction and a training set distribution. In terms of function space, the largest eigenvalue eigenfunction is the most parallel to all of the training set distributions on average. Then the second largest eigenvalue eigenfunction is as parallel to all of the training set distributions on average with the restriction that it be orthogonal to the first eigenfunction and so on for the other eigenfunctions. The maximization of the inner products implies large eigenvalue basis functions are critical in representing training set distributions for tomographic reconstruction. Conversely, small eigenvalue basis functions do not contribute much to reconstruction accuracy.

Like the basis functions for Adaptive FDDI, the KL basis functions are used in a series solution for $n(x,y)$. However, in the present case there are only nine basis functions in comparison to the 147 used in Adaptive FDDI, so the least squares problem is easier to compute. In addition, fewer projection measurements are needed to keep the least squares formulation overdetermined, so the experimental complexity decreases. If we truncate the small eigenvalue basis functions from the series solution, i.e. use fewer basis functions, even fewer computational steps and lines-of-sight are required.

Experimental Apparatus

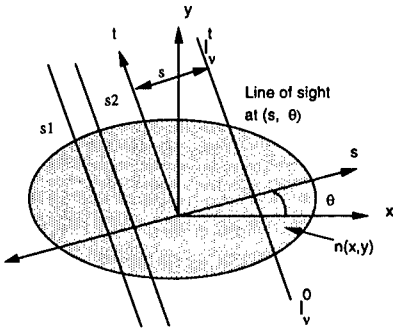


Figure 1. The coordinate system.

The experimental apparatus is divided into three parts: the flow facility, the probe sampling system, and the line-of-sight measurement system. It allows probe sampling measurements at many different points and line-of-sight projection measurements along many different lines. See Figure 2 for a schematic of the experimental apparatus. Three steady, methane-argon jets surrounded by a co-flow of air create a steady, non-axisymmetric distribution of methane. A single HeNe laser, split into three beams, lasing at 3.39μm which overlaps the P7 absorption line in the ν_3 band of methane is used for the probe sampling measurements and line-of-sight measurements. A tapered quartz probe draws the sample out of the flow into an absorption cell where the methane concentration is measured by absorption of the HeNe laser beam. The other two beams are for the line-of-sight projection measurement and a reference signal to account for power fluctuations in the laser. To improve the signal-to-noise ratio, phase-sensitive detection of the absorption cell signal, the line-of-sight measurement signal, and the reference signal is employed.

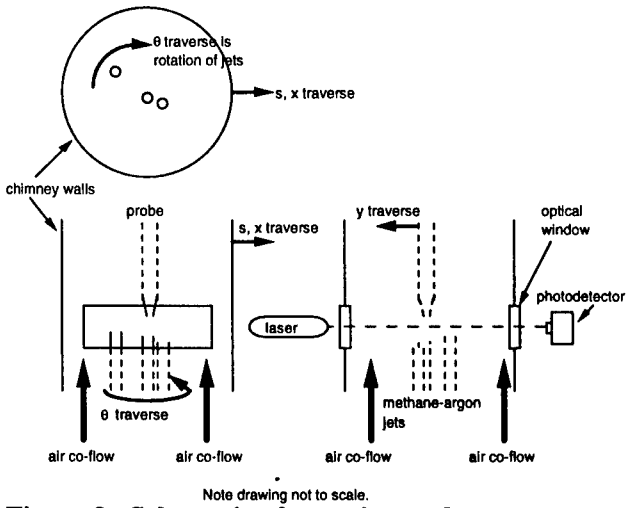


Figure 2. Schematic of experimental apparatus.

Nine different distributions were measured with a probe and with laser absorption line-of-sight measurements. Probe measurements occurred on rectangular grid points spaced at 2.5 mm intervals. Only points over and near jets were sampled; points further away were assumed to contain no methane. Lines-of-sight occurred from s = – 32.5 mm to +32.5 mm in 2.5 mm intervals along 12 view angles in 15° intervals. Therefore, there were 324 lines-of-sight per distribution.

Results and Conclusions

From a visual examination, Adaptive FDDI reconstructions capture the large-scale features of their corresponding probe sampled distribution, e.g. Figure 3. The locations of peaks in the reconstruction coincide with those in the probe sampled distribution, and the heights of the reconstructed methane concentration peaks are within 10% of those in the probe sampled distribution. However, smaller features present in the probe sampled distributions are smoothed out in the Adaptive FDDI reconstructions.

Another test of the Adaptive FDDI method is to compare the KL basis functions generated from Adaptive FDDI reconstructions and probe sampled distributions. First, we compare the set of eigenvalues associated with the KL basis functions (termed an eigenvalue spectrum). Then we visually inspect the KL basis functions themselves for a more qualitative evaluation.

A plot of the eigenvalue spectra for the two KL basis function sets is shown in Figure 4. The eigenvalues and their corresponding eigenfunctions are ordered from largest eigenvalue to smallest eigenvalue. Both spectra decrease to one percent of the first eigenvalue by the fourth eigenvalue. In addition, the first four eigenvalues have similar values between the two spectra. Therefore, both KL basis function sets can be truncated to the first three KL basis functions to reconstruct a training set distribution well, and these two subsets of KL basis functions have similar eigenvalue spectra.

The first three KL basis functions (Figures 5, 6, and 7) all contain peaks similar in width and location to the peaks seen in the training set distributions. An immediate resemblance can be noticed between the distributions in Figure 3 and Figure 5, the first KL basis function. This is because the first KL basis function has the maximum magnitude of inner product with all of the training set distributions on average.

The first three KL basis functions can be multiplied by a scalar and reordered to show the two basis function subsets are very similar in shape. If Adaptive FDDI eigenfunction #1 is multiplied by a negative scalar then it looks very similar to probe sampled eigenfunction #1. This operation is valid because the weighting coefficient in the series expansion can be negative or positive. Because eigenvalues #2 and 3 are very similar, reordering the two corresponding eigenfunctions is justified. A comparison of probe sampled eigenfunction #2 and Adaptive FDDI eigenfunction #3 shows both have a positive left peak and a negative right peak. The middle peak is either slightly negative or zero. Likewise, probe sampled eigenfunction #3 and Adaptive FDDI eigenfunction #2 are similar. The left peak is negative; the middle peak is negative; and the right peak is positive.

The probe sampled training set and the Adaptive FDDI training set both result in KL basis function sets that can be truncated to the first three KL basis functions to reconstruct distributions with one, two, or three peaks at the location of the jets. Quantitative and qualitative comparisons indicate the two KL basis function subsets are very similar. Therefore, Adaptive FDDI should be able to acquire the *a priori* information required by TRKB.

Further research will focus on refining the Adaptive FDDI reconstruction by reducing errors in the projection data and adjusting parameters in the Adaptive FDDI algorithm. We will vary the shape and quantity of the FDDI basis functions and explore the effects of finite spatial resolution of the probe and laser beam measurements. These changes should lead to more accurate reconstructions and improved probe measurements.

Acknowledgements

We wish to thank Dr. Jisoo HA of Hyundai Heavy Industries. We also acknowledge the support of the U.S. Army under ARO grant # DAAL03-92-G-0113 and the U.S. Office of Naval Research under ONR grant #N00014-99-1-0447.

References

[1] M. Ravichandran and F.C. Gouldin. *Applied Optics*, 27:4084, 1988.

[2] J. Ha, M. Feng, and F.C. Gouldin. Laser tomographic reconstruction in a complex concentration flow field. *In 37th Aerospace Sciences Meeting and Exhibit of the AIAA*, number AIAA-99-0444, 1999.

[3] E.D. Torniainen and F.C. Gouldin. Tomographic reconstruction of 2-d distributions using a karhunen-loève basis. *Applied Optics*, 1999. In submission.

[4] G. H. Golub and C. F. Van Loan. Matrix Computations. Johns Hopkins University Press, 1985.

[5] L. Sirovich and R. Everson. *Int. J. of Supercomputer Applications*, 6:50, 1992.

[6] G. Berkooz, P. Holmes, and J.L. Lumley. The proper orthogonal decomposition in the analysis of turbulent flows. *Annual Review of Fluid Mechanics, 25:539, 1993.*

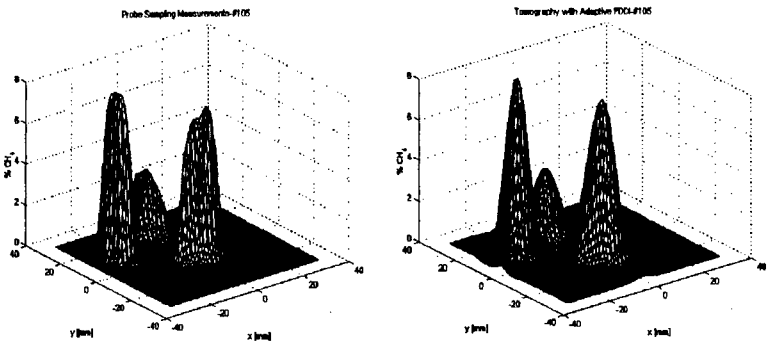


Figure 3. Left: typical probe sampled distribution. Right: corresponding Adaptive FDDI reconstruction.

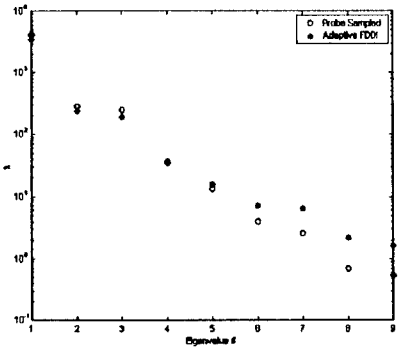


Figure 4. Comparison of eigenvalue spectra.

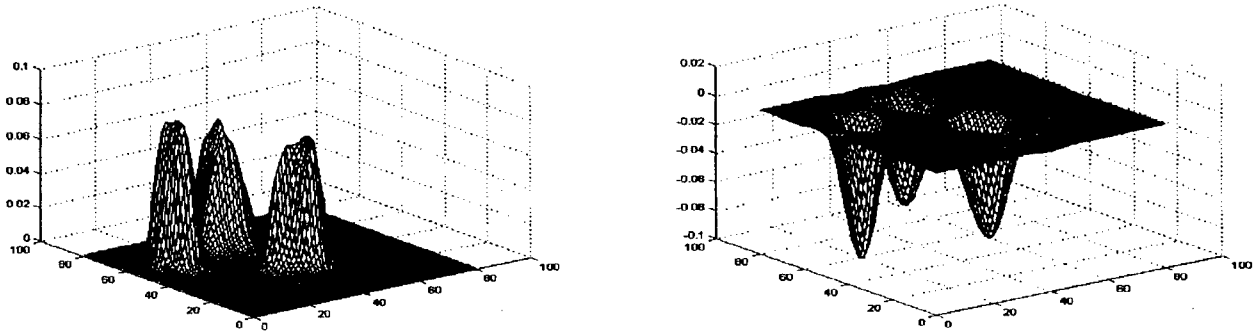


Figure 5. Eigenfunction #1. Left: probe sampled. Right: Adaptive FDDI.

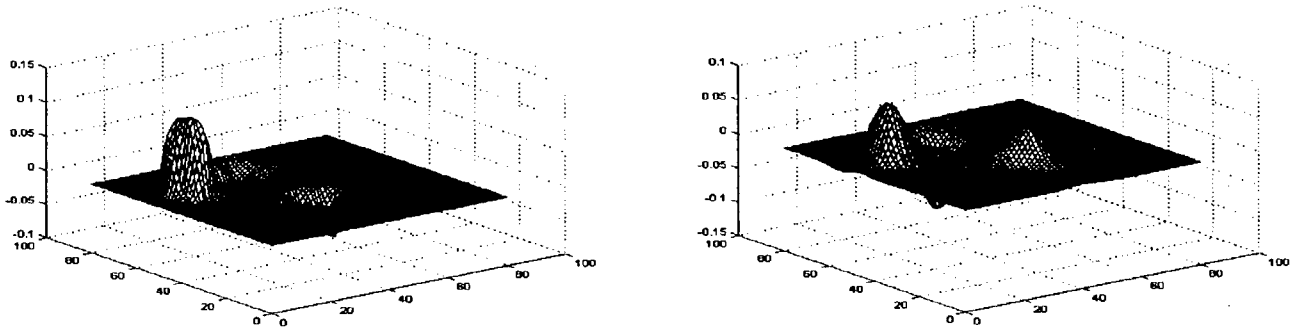


Figure 6. Eigenfunction#2. Left: probe sampled. Right: Adaptive FDDI.

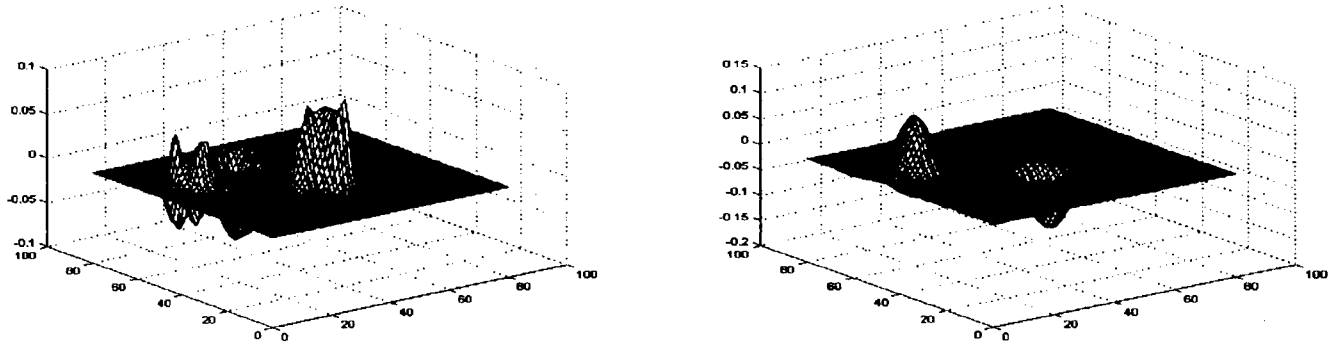


Figure 7. Eigenfunction#3. Left: probe sampled. Right: Adaptive FDDI.

Application of Optical Flow Velocimetry in Turbulent Flows

J. Fielding and M.B. Long
Yale University
Department of Mechanical Engineering and Center for Laser Diagnostics
New Haven, Connecticut, USA 06520-8284
marshall.long@yale.edu

An experimental method is described for the validation of optical flow velocimetry algorithms in turbulent flows. These techniques present an alternative to conventional seeded velocimetry which complicates some simultaneous two-dimensional laser-based measurements. Our approach involves scalar imaging from a molecular tracer using fluorescence and results are presented from a turbulent isothermal air jet.

Introduction

Measuring the two-dimensional projection of the velocity field in reacting and non-reacting flows is typically achieved by imaging Lorenz-Mie scattering from particles, either with particle image velocimetry (PIV) or particle tracking velocimetry (PTV). It has been demonstrated that PIV can be combined with scalar measurements by using laser-induced fluorescence [1], however, particle-based techniques complicate simultaneous laser-based measurements of certain scalar quantities due to spectral interference. In particular, simultaneous imaging of Rayleigh scattering is impossible, making temperature and mixture fraction measurements difficult. A number of "non-particle" velocimetry approaches have been applied in turbulent flows, though few have found broad applicability under reacting conditions. For instance, the Scalar Imaging Velocimetry approach of Dahm et al. [2] produces a velocity field by inverting the scalar transport equation. The Image Correlation Velocimetry (ICV) technique of Tokumaru and Dimotakis [3] provides a basis for measuring the displacement fields of gas-phase fluid motions. Extension of this approach to reacting flows appears feasible [4,5] provided appropriate scalars are selected for imaging and validation experiments are carried out. Recent work on dynamic programming algorithms has been reported to achieve results which in some cases are superior to conventional PIV [6].

These velocimetry techniques obviate the need for seeding by obtaining velocity vectors from the displacement fields of molecular flow tracers, thus preserving the nonintrusiveness of the measurement. Extracting velocity from a pair or sequence of images is a concept derived from the field of optical flow. Optical flow is the apparent motion of the brightness or intensity pattern in an image pair or sequence [7]. If the intensity **I** at a point (x, y) and time t is constant between frames

$$\mathbf{I}(x+\Delta x, y+\Delta y, t+\Delta t) = \mathbf{I}(x, y, t)$$

then the velocity is simply the displacement of that point over the interframe time. In general, further assumptions are required to solve the problem, employing constraints based on the smoothness of the velocity field or derived from the equations of fluid motion.

Optical flow algorithms are generally broken down into categories based on differential techniques, region-based matching, and frequency methods; a review of these approaches can be found in Ref. 8. Region-based methods appear to hold the most promise for fluid dynamic applications, and while algorithms are sometimes calibrated using synthetic images, there are no established comparisons between velocities obtained from optical flow and PIV. Here, we report novel experiments involving split-frame measurements of Mie scattering from seed particles and dual-frame laser-induced fluorescence of acetone as a tracer in a turbulent isothermal air jet. This arrangement allows for determination of velocity from cross-correlation PIV and by applying a region-based matching optical flow algorithm.

Experiment

The experimental setup is shown in Figure 1. The fourth harmonic (266 nm) of a double-pulsed Nd:YAG laser (Continuum, Powerlite 8000) is used to illuminate the seed particles for PIV and excite acetone fluorescence for the scalar measurements. The beam is formed into a sheet approximately 5 mm high with a beam energy of ~2 mJ per pulse and a pulse separation of 57 μs. Submicron sugar particles are introduced into the air flow using an aerosol seeder (TSI Model 9306), which provides a constant seeding density. A portion of the overall air flow is sent through a heated bubbler unit filled with acetone. The bubbler consists of a porous tube submerged in 500 mL of acetone at 20° C, and the output stream passes through a one-liter container to help maintain constant acetone concentration over the course of an experiment. The nozzle used in these experiments consists of a straight tube with a 4.57 mm inner diameter. The turbulent jet issues into an unconfined low velocity coflow of air (~1 m/s).The results presented here correspond to a Re=2000 jet with an exit velocity of 6.8 m/s.

Lorenz-Mie scattering from the particles is collected using an f/11 quartz camera objective (Nikon Nikkor UV) coupled to a liquid-cooled UV-sensitive (QE=10%) CCD camera (Photometrics CH350). A UV–enhanced aluminum front-surface mirror is mounted to a DC motor rotating at approximately 50 Hz to spatially separate the two pulses from the laser on the CCD (2000 × 2000 pixels) allowing for cross-correlation velocimetry to be performed. Timing of the experiment is controlled by reflecting a HeNe laser from the mirror onto a photodiode to synchronize the cycle.

Acetone fluorescence occurs broadband between 350 and 550 nm, and the signal is sufficiently strong for unintensified imaging. Fluorescence from the two laser pulses is imaged using an interline progressive-scan transfer CCD camera (PCO/Cooke Corp. SensiCam) coupled with a large format f/1.4 camera objective. This equipment allows the acquisition of two images (temporally separated by at least 1 μs) which makes it well-suited for either PIV or time-resolved scalar imaging. A clear glass filter (Schott WG305) is used to block any residual Mie-scattering.

Discussion

Figure 2 shows a scalar image pair from the turbulent jet, with velocity vectors derived from two different techniques. In frame (a), vectors have been determined by cross-correlation of the corresponding particle images within 64 × 64 pixel interrogation windows. The vectors in frame (b) are obtained by applying a region-based matching algorithm [8,9] to the fluorescence image pair. A number of optical flow methodologies exist, and here we have employed the approach of Anandan [9] because it does not suffer from the difficulties associated with numerical differentiation or the requirement of small displacements as is the case with differential techniques [3,8]. Briefly, the implementation depends on minimization of the sum-of-squared differences (a distance measure) within a window of size $n \times n$. A coarse-to-fine strategy is employed where displacements are determined first at the coarsest level (using smoothed and sub-sampled images), with subsequent refinement at each finer level. User inputs include window size, number of hierarchical refinement levels, and number of constraint iterations within each level.

This approach and others can at best provide an approximation to the instantaneous two-dimensional fluid velocity given a planar scalar measurement. The approximation is valid when the velocity in the third, unmeasured direction is small, or the scalar gradient in that dimension is small [3]. However, this requirement is no more restrictive than with two-dimensional PIV. Other conditions exist for using optical flow algorithms for velocimetry applications. Large spatial regions lacking sufficient variation in intensity can cause problems because some optical flow algorithms will produce small or zero velocities in these regions. Generally, this condition of inhomogeneity should not pose a problem in sufficiently turbulent flows and can be overcome to some extent by adjusting the smoothness constraint.

Consistency between frames presents an additional requirement. Large interframe times can be problematic for fast flows if the pixel displacements are too large. Also, excessive artificial intensity variation introduced from post-processing will introduce spurious optical flow velocities.

As can be seen from Fig. 2(b), qualitative agreement between the velocity vectors from region-based matching and PIV in Fig.2(a) is quite good for the conditions considered here. One limitation of this algorithm is that it does not include the equations of fluid motion as constraints to the problem. For the present flow conditions, this does not appear to be a significant liability. Further analysis of the validation data will be performed to assess the quantitative accuracy of these techniques in terms of magnitude and angular deviations. The experimental data obtained from this work will provide a valuable test bed for developing and evaluating optical flow algorithms for velocimetry.

Acknowledgments

The authors would like to thank Dr. Gabriel Fielding for his assistance in implementing the optical flow algorithm used in this work.

References

[1] J.H. Frank, K.M. Lyons, and M.B. Long, "Simultaneous Scalar/Velocity Field Measurements in Turbulent Gas-Phase Flows," *Combust. Flame*, **107**:1-12 (1996).

[2] Dahm, W.J.A., Su, L.K., Southerland, K.B., "A Scalar Imaging Velocimetry Technique for Fully Resolved Four-Dimensional Vector Velocity Field Measurements in Turbulent Flows," *Phys. Fluids A*, **4**:2191-2206 (1992).

[3] Tokumaru, P.T., Dimotakis, P.E., "Image Correlation Velocimetry," *Exp. In Fluids*, **19**:1-15 (1995).

[4] Komiyama, M., Miyafuji, A., Takagi, T., "Flamelet Behavior in a Turbulent Diffusion Flame Measured by Rayeligh Scattering Image Velocimetry," *Twenty-Sixth Symposium (International) on Combustion*, The Combustion Institute, Pittsburgh, PA, pp. 339-346 (1996).

[5] Grunefeld, G., Graber, A., Diekmann, A., Kruger, S., Andresen, P., "Measurement System for Simultaneous Species Densities, Temperature, and Velocity Double-pulse Measurements in Turbulent Hydrogen Flames," *Combust. Sci. and Tech.*, **135**:135-152 (1998).

[6] Levy, Y., Golovanevsky, B., Kowalewski, T.A., "Fluid Image Velocimetry for Unseeded Flow," *9th International Symposium on Applications of Laser Techniques to Fluid Mechanics*, Lisbon, Portugal, July 13-16 (1998).

[7] Horn, B.K.P. and Schunk, B.G., *MIT Artificial Intelligence Laboratory* , Memo No. 572 (1980).

[8] Barron, J.L., Fleet, D.J., and Beauchemin, S.S., "Performance of Optical Flow Techniques," *Int. J. Comp. Vision*, **12**:43-77 (1994).

[9] Anandan, P., "A Computational Framework and Algorithm for the Measurement of Visual Motion," *Int. J. Comp. Vision*, **2**:283-310 (1989).

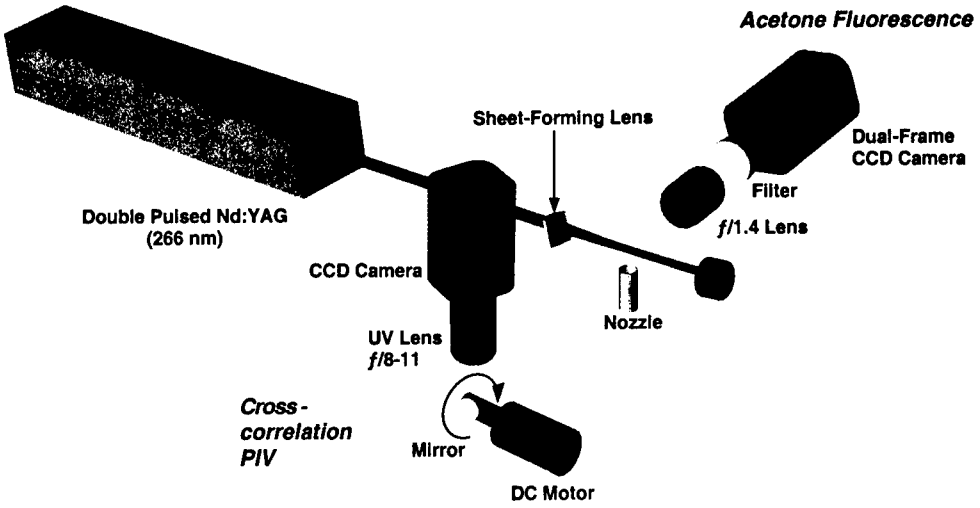


Figure 1. Schematic of the simultaneous cross-correlation PIV and dual-frame acetone fluorescence setup.

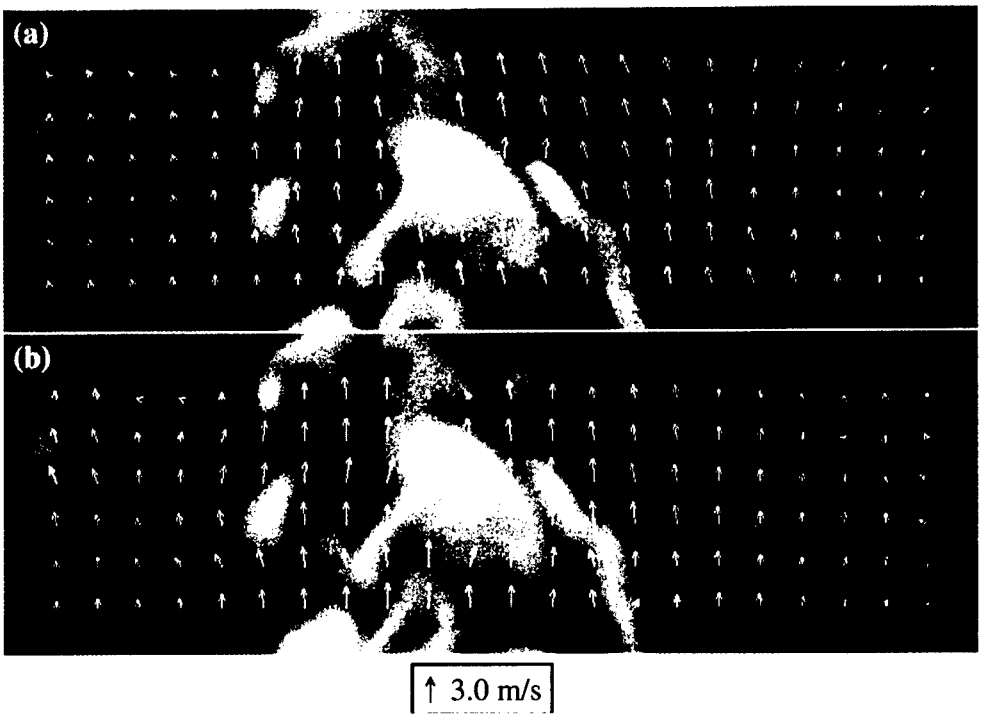


Figure 2. Acetone fluorescence image pair with velocity vectors. (a) t_0; vectors obtained from cross-correlation PIV. (b) $t_0 + 57\ \mu s$; vectors obtained from region-based matching optical flow algorithm of Ref. [9].

A Novel Method for Non-intrusive Temperature Measurements in High Pressure Combustors

Michael S. Brown,[1] Yuanyuan Li[2] and William L. Roberts[2]

[1]Metrolaser Inc.
18010 Skypark Circle, Suite 100
Irvine, CA 92614
[2]Department of Mechanical and Aerospace Engineering
North Carolina State University
Raleigh, NC 27695-7910

Abstract

A frequency-based laser diagnostic technique, transient grating spectroscopy (TGS), is explored for the measurement of temperature in high pressure combustors. This technique relies on the scattering of a cw laser beam off of a dynamic grating generated by a pair of crossed, pulsed pump beams. The temporal modulation frequency of the signal beam is a function of the local sound speed from which a temperature can be extracted. This technique is coherent and frequency based, the signal strength increases with pressure, and the presence of soot makes a positive contribution, thus it is ideally suited for high-pressure, multiphase and limited optical access environments.

Introduction

The temperature field of fossil fuel combustors is a key diagnostic parameter. The local temperature is established by the local chemistry, fluid dynamics and heat transfer of the combustion gases. The accurate measurement of temperature is imperative for the purpose of testing combustor design and verification of predictive computational models of combustors. Major challenges to optical diagnostics of practical combustors include high pressure, the presence of particulates, a high background luminosity, optical thickness and limited optical access. Recently, the application of laser-induced gratings has shown the ability to overcome some of these difficulties in real combustors.[1] This abstract reports on advances we've been made in the TGS technique for high pressure flames.

The TGS technique involves the first-order Bragg scattering of a probe laser off of a dynamic grating generated by two crossed pump laser beams. When two laser beams with linear, parallel polarization are spatially and temporally overlapped, an intensity grating is formed in the medium through various mechanisms.[2] For the work presented here, only two mechanisms are of importance: 1) electrosrtiction and 2) thermalization. The grating spacing, Λ, is given by:

$$\Lambda = \frac{\lambda}{2\sin\left(\frac{\theta}{2}\right)} \quad . \tag{1}$$

where λ is the wavelength of the grating-inducing pump beams and θ is the full angle between the pump beams. The local hydrodynamic response of intensity gratings forms: a) a non-propagating but diffusing entropy or thermal wave and b) two counterpropagating sound waves which form a standing wave. The probe laser beam is scattered off of both of these type of waves. If the Bragg condition is satisfied, the

reflected probe beam will generate a coherent signal beam. The temporal behavior of this signal beam is observed to have a gradual decay due to diffusion with an oscillation superimposed upon it, as seen in Figure 1. The oscillation frequency due to electrostrictive gratings is twice as that due to thermal gratings.[3] Both gratings can be generated in flame environments (Figure 2). Temperature can be extracted from a TGS measurement through the use of the ideal gas expression for the sound speed and the definition of the TGS frequency,

$$C_s = \sqrt{RT\frac{\gamma}{M}} \quad \text{and} \tag{2}$$

$$f_B = \mathrm{m}\frac{C_s}{\Lambda} \quad \text{, respectively.} \tag{3}$$

where R is the gas constants, T is the temperature, γ is the heat capacity ratio, M is the molecular mass of the gas mixture, and m=1 and 2 for thermal or electrostrictive grating signals respectively. By inverting Equation 2 and making use of the definition in Equation 3, the experimentally determined temperature by TGS technique can be expressed as:

$$T = f_B^2 \frac{\Lambda^2}{m^2}\left(\frac{M}{\gamma}\right)\frac{1}{R} \quad . \tag{4}$$

Experiments

The optical setup for our TGS experiments is shown schematically in Figure 3. The frequency-doubled output of a Nd:YAG laser is split into two pump beams of equal energy (~50 mJ, 5~7 ns pulse length) and passed through a 500 mm focusing lens. The 514 nm probe beam from an Argon ion laser is directed toward the same lens, parallel to the pump beams. During the alignment of the detector, ~ 4% of the probe beam is split off and directed at the lens so as to trace out the path of the actual TGS signal beam. The signal beam is directed by a mirror through spatial and spectral filters and then onto a photomultiplier tube.

The flowing vessel of the High Pressure Burner (HPB) is 12.7 cm in diameter, encased in a water jacket. The internal pressure is regulated with a needle valve on the exhaust port of the vessel. The flame is generated in a water-cooled, sintered bronze porous plug burner, 6 cm in diameter. To provide optical access, three 25.4 mm thick BK-7 windows are mounted at 90° to each other in the horizontal plane, with the porous plug surface in the lower field of view. Fuel and air are metered with high pressure mass flowmeters and mixed before entering the HPB. In most test runs, only ethylene and air were used, and the equivalence ratio was varied between stoichiometric and two.

Once the initial alignment is established, the electrostrictive response from static air is used to optimize the TGS signal and calibrate the actual grating spacing. After signal optimization, the burner is lit and stabilized near stoichiometric conditions at one atmosphere. The exhaust valve is partially closed on the HPB and the gas flow rates are increased iterativelly to reach the desired high-pressure and sooty flame conditions. At this point, the TGS signals are acquired by a digital oscilloscope. A B-type thermocouple (Pt/Rh) is used to measure the temperature as well. The intersection of the three incident laser beams and the thermocouple bead are maintained at the same height above the burner surface and a couple of millimeters apart horizontally.

Results and Summary

TGS experiments were made at various pressures, stoichiometries, and axial locations above the porous plug burner. To perform the TGS thermometry, the acquired signals are analyzed by curve fitting to determine the oscillation frequency, f_B.[4] In Figure 2, we show a single-shot TGS signal acquired in an ethylene/air flame at 6 atm at nearly stoichiometric C_2H_4 /air ratio. The signals were acquired 7 mm above the burner surface in the burnt gas region. One can see both electrostrictive and thermal grating signals. In this case, the calculated temperature is 1352 °K while the uncorrected thermocouple reading is 1290 °K. As the flame becomes richer, the TGS signals are usually dominated by thermalization. This is because that soot particles work as blackbody absorbers. Thus it is more efficient for laser energy heating the gas producing a thermal gratings. Therefore local index modulation is mainly through thermalization other than electrostriction in sooty flames. However, high soot volume fraction may cause a change in the local M/γ value, and therefore the calculated temperature. This can be compensated for by including deposition of C_2 and C_3 into the bath gas.

Fluctuations of the density and density gradients in the HPB produce beam steering. For some single shots, beam steering compromised the phase matching needed to generated a true TGS signal. Other shots are compromised by laser-induced breakdown. Therefore, we collected a large number of single shots, and by examining the histogram record, derive the desired thermometric information. In Figure 4 we show the histogram for 3000 shots recorded above the flat ethylene/air flame. The peak of the distribution has a value of about 300 shots indicating that 10% of all shots are true TGS signals in this harsh combustion environment.

The frequency-based TGS measurements have been performed in pressurized sooty flames. This technique is non-resonant and thus dose not require a tunable source or spectral resolution of the signal. The strength of signal increases with pressure and soot particles act as blackbody absorbers make TGS an ideal means to study the temperature inside the practical combustors.

Acknowledgement

This is work is supported by Air Force contract No. F33615-96-C-2656.

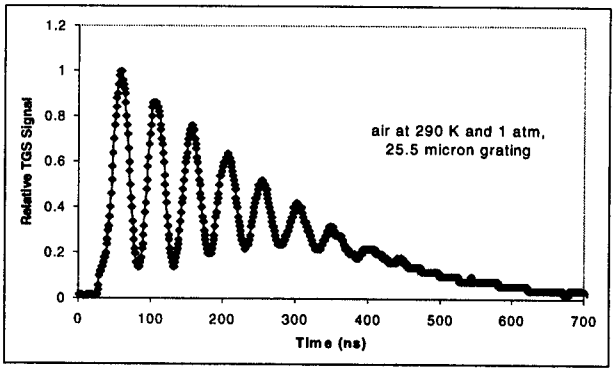


Figure1. Nonresonant TGS signal in air due to Electrostriction. (64 shots average)

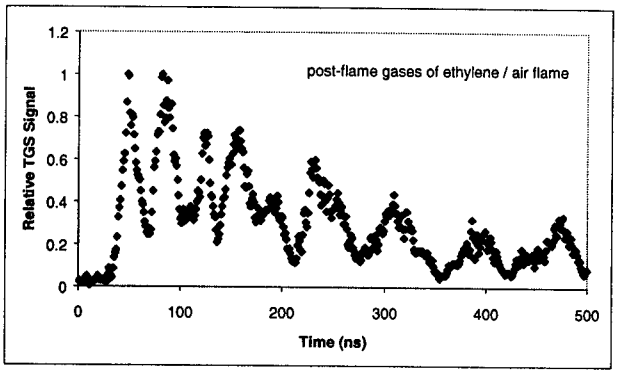


Figure 2. Raw TGS signal (single shot) acquired in C_2H_4 /air flame. Both electrostrictive and thermal gratings are shown.

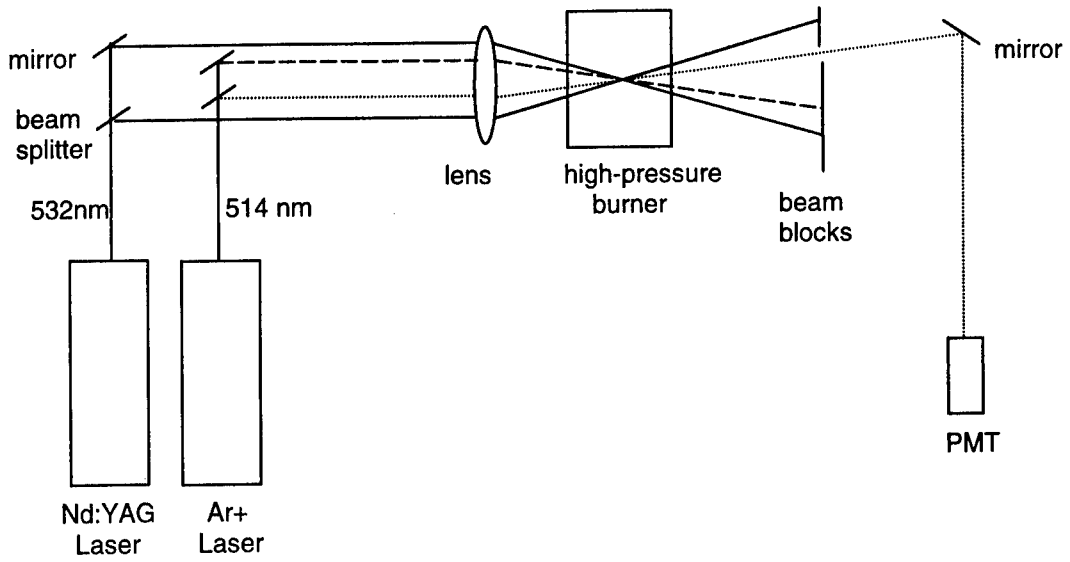


Figure 3. Schematic of the TGS optical setup. During alignment, 4% of the probe beam was picked off and used to trace the path of the signal beam.

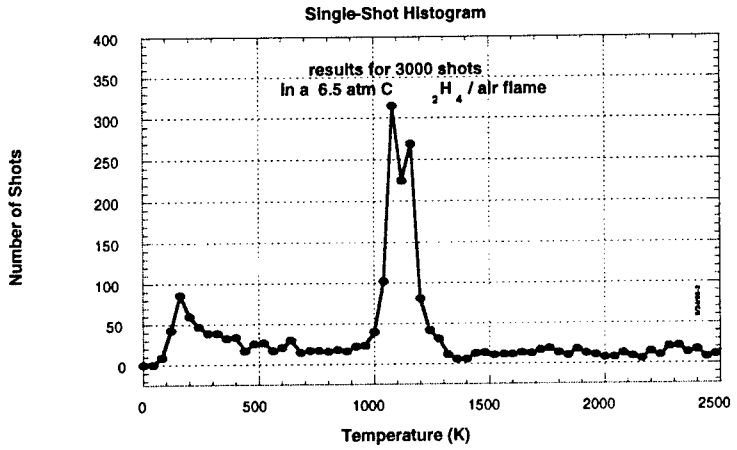


Figure 4. Histogram of single-shot signals acquired in a nearly stoichiometric ethylene/air flame.

References

1. B. Hemmerling, W. Hubschmid and A. Stampanoni-Panariello, "Temperature and mixture fraction measurements in gases by laser induced electrostrictive gratings", *Twenty-seventh Symposium (International) on Combustion,* The Combustion Institute, pp. 69-75, 1998.
2. H.J. Eichler, P.Gunter and D.W. Pohl, *Laser-Induced Dynamic Gratings*, Springer-Verlag, Berlin, 1986.
3. E.B. Cummings, I.A. Leyva, and H.G. Hornung, "Laser-induced thermal acoustics (LITA) signals from finite beams", *Applied Optics,* Vol. 34, No. 18, pp. 3290-3302, 1995
4. M.S. Brown and W.L. Roberts, "Single-point thermometry in high-pressure, sooting, premixed combustion environment", *Journal of Propulsion and Power*, Vol. 15, No.1, pp. 119-127. 1999.

Measurement of Species and Temperature Using Difference Raman Scattering

Schaffer, A.M., Mohammed, R.K., Long, M.B., Smooke, M.D.
Yale University Mechanical Engineering and Center for Laser Diagnostics
P.O. Box 208284 New Haven, CT 06520-8284 Phone:203-432-4227 Email:andrewm@pantheon.yale.edu

Introduction

For hydrocarbon diffusion flames, an abundance of hydrocarbon fragments and soot precursors are generated. C_2 and PAH produce broadband fluorescence in the visible when excited by a laser wavelength of 532 nm.[1] This makes vibrational Stokes-shifted Raman signals from species that exist slightly to the rich side of the flame front hard to discriminate against this interference.

In the present experiment, we measure two-dimensional profiles of temperature and mole fractions of N_2, CO_2, CH_4, H_2, O_2, CO, and H_2O in a time varying, axisymmetric, coflow, laminar methane diffusion flame. Similar time-varying diffusion flames have been studied.[2] The merits of studying this type of flame are the repeatable cyclic variations in flame structure that may help models of more complex turbulent combustion, and the ability to computationally model this flame. We obtain temperature and species concentrations with vibrational Stokes-shifted Raman scattering and Rayleigh scattering.. With Difference Raman Scattering, we are able to eliminate the C_2 fluorescence interference down to shot noise levels of the fluorescence signal. The experimental profiles are then compared to the computational profiles[3]. The effectiveness of the Difference Raman Scattering technique to discriminate the vibrational Raman signals from the interferences is discussed.

Difference Raman Scattering is the collection of vibrational Q-branch Raman scattered light intensities under two orthogonal linear polarizations: I_{zz} parallel and I_{yz} perpendicular to the laser polarization, using a linear polarized laser source. The Difference Raman signal is $I_{drs}= I_{yz}- I_{zz}= I_{yz}(1-\rho)$ where ρ is the depolarization of the scattering (averaged over all rotational levels). For Q-branch transitions ρ is typically 0.02-0.05[4], and therefore vibrational Q-branch Raman scattering (and Rayleigh scattering) is highly polarized along the polarization axis of the laser (assuming a linearly polarized laser). For laser-induced fluorescence, there is an initial preferred polarization of the dipole radiation. In the case of a molecule, if there are "fast" rotations of the molecule which occur in a time smaller than the decay time of fluorescence, the fluorescence is randomly polarized if the signal is averaged over its decay time.

Experimental Technique

The burner is axisymmetric with an open fuel tube of diameter 4 mm, with an annular air coflow region of diameter 5 cm. The fuel is 65% methane with nitrogen dilution. The flow in the fuel jet is acoustically forced with a loudspeaker driven by a 20 Hz sinewave, with a 50% velocity modulation. Particle image velocimetry in cold flow is used to verify the 50% modulation in velocity and the parabolic flow profile over all phases of the forcing.

Shown in Figure 1 is the experimental setup. The second harmonic of a flashlamp pumped, Q-switched Nd:YAG laser (10 Hz rep rate, 532 nm) is focused into a line over the center of the burner, with a beam waist of 300 μm. The laser is double pulsed to prevent breakdown of air (pulse separation of 95 μs), with an average energy of 300 mJ per double pulse. The scattered light is collected with a f/1.8 lens and focused onto the horizontal entrance slit (300 μm width) of an imaging spectrograph (f/4, 0.27 m f.l.). A modified liquid crystal shutter passes the desired polarization, enabling us to measure I_{zz} and I_{yz} independently. The dispersed light is focused onto a gated, image intensified, cooled CCD camera (1 μs gate time). Spatial resolution is approximately 200 μm (horizontal) x 300 μm (depth), and spectral resolution is approximately 3 nm.

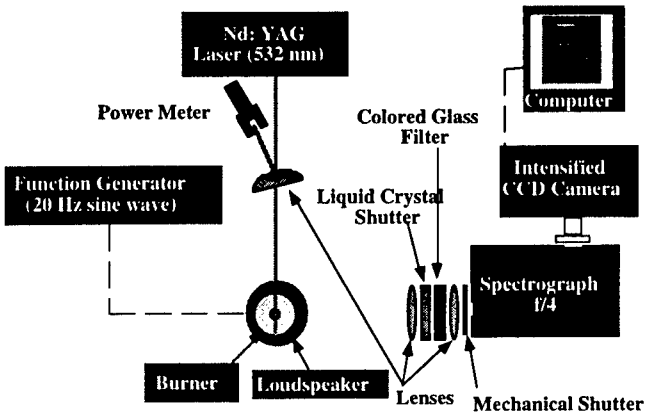


Figure 1. Experimental Setup.

Figure 2a shows a sample image for I_{zz}, I_{yz}, and I_{zz}-I_{yz}. Measurements are performed at heights above the burner surface of 2.5 mm to 52.5 mm, in steps of 0.5 mm closer to the surface and 1 mm farther downstream.

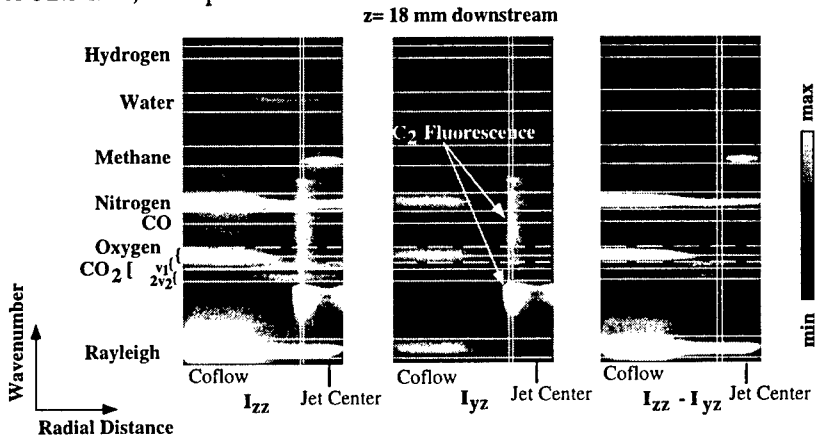


Figure 2a. Sample raw data images of I_{zz} and I_{yz} taken 18 mm downstream. Also shown is $I_{zz} - I_{yz}$. The horizontal white lines mark the spectral window for each species. The intensity scale saturates the stronger Raman lines in order to view the weaker lines.

Each measurement is an average over 1200 laser pulses, acquired for each polarization. The signals are integrated over a spectral window large enough to account for spectral broadening due to temperature increases, but small enough to minimize crosstalk with other species. These line measurements are then tiled together to form images. Data is acquired for the steady state flame, and for five equally spaced phases of the forced flame over one period.

Images are corrected for throughput and spectral efficiency using room temperature air and methane calibrations, and corrected for crosstalk and laser energy variation. Crosstalk between species is determined from room temperature air and methane calibrations, and from regions of difference Raman images where concentrations of species are well known. . A second order correction involving the scaling of a C_2 fluorescence image is used to correct for PAH Raman interferences to the O_2, CO_2, and CO signals[5]. Cold flow calibrations of pure fuels and air, along with the known values of (1-ρ) for each species, are used to obtain room temperature relative difference Raman cross sections for N_2, CO_2, CH_4, H_2. Cross sections for H_2O and CO are obtained from the post-flame region of a rich premixed flat flame. The temperature dependence of cross sections for all diatomics are modeled using Ramses code, taking into account the experimental spectral resolution and the spectral window for each species. The temperature dependence used for the cross sections of CH_4, H_2O is a simple Boltzmann term, and the CO_2 cross section is obtained from Miles (1996)[6]. An iterative technique is used to

determine species mole fractions and temperature, usually converging in three iterations.

We determine the spatial and spectral region of highest interference from the C_2 fluorescence in the flame, and investigate the time dependence of the polarization of this signal. The gate time of the image intensifier is shortened. I_{zz} and I_{yz} for the C_2 fluorescence are recorded at varying gate delays from the incident laser pulse.

Results and Discussion

We determine the C_2 fluorescence to be randomly polarized over the lifetime of the fluorescence. The Difference Raman technique reduces the interferences on Raman data to shot noise of the fluorescence.

Figure 2b shows a line plot of integrated signal intensity versus wavelength from the region of highest C_2 interference in the images of Figure 2a (region is marked with two vertical lines). From the plot of I_{zz} the interferences are quite apparent, especially the largest interference region which is marked. There also seems to be a broadband interference, most likely laser induced incandescence of the soot. From the plot of I_{zz}-I_{yz} the largest C_2 interference region is reduced to noise which has peak intensity smaller than most of the Raman signals shown. The broadband interference is also eliminated.

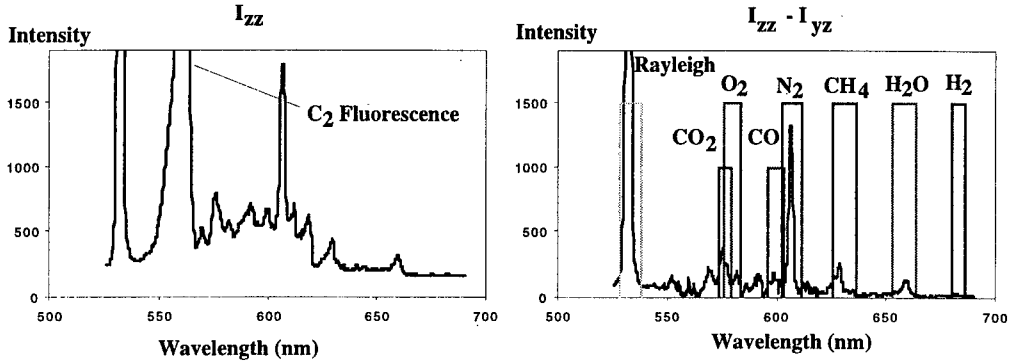


Figure 2b. Line plots of I_{zz} and I_{zz}-I_{yz} vs. wavelength, taken from the integrated region of of highest C_2 interference in the images of Figure 2a. The spectral window for each species is marked by the rectangles in the plot of I_{zz}-I_{yz}.

Figures 4 and 5 compare experimental (exp) and computational (comp) profiles of species concentrations and temperature for the case of no forcing (Figure 4) and over five phases of the forcing (Figure 5). Experimental results for the steady case show good agreement with computations. For the case of the forcing, the peak values of the experimental and computed profiles agree. However, it appears that the experimental velocity modulation is large than the modulation of the computations. The velocity flow boundary conditions must be checked again and compared with the modulation and flow boundary conditions of the computations.

To determine the effectiveness of the Difference Raman technique , one must compare the noise level of the C_2 signal with the Difference Raman signals. The weakest Raman signal, which also has significant interference from C_2 fluorescence, is CO. To obtain noise levels of the C_2 interference on CO, we look at the I_{yz} and I_{drs} images for CO. Since the peak intensity of I_{drs} is 90 counts and $\rho_{CO} = 0.038$[7], then I_{yz} should have negligible CO signal. Thus, all of I_{yz} is from fluorescence interference. It should be noted that I_{drs} has twice as much noise as I_{yz}. We find that I_{drs} is greater than twice the fluorescence noise of I_{yz} in all regions containing CO, and therefore the CO Difference Raman signal is effectively discriminated from the fluorescence noise.

The Difference Raman Scattering technique in the future will be applied to combustion systems where there are large interferences from soot.

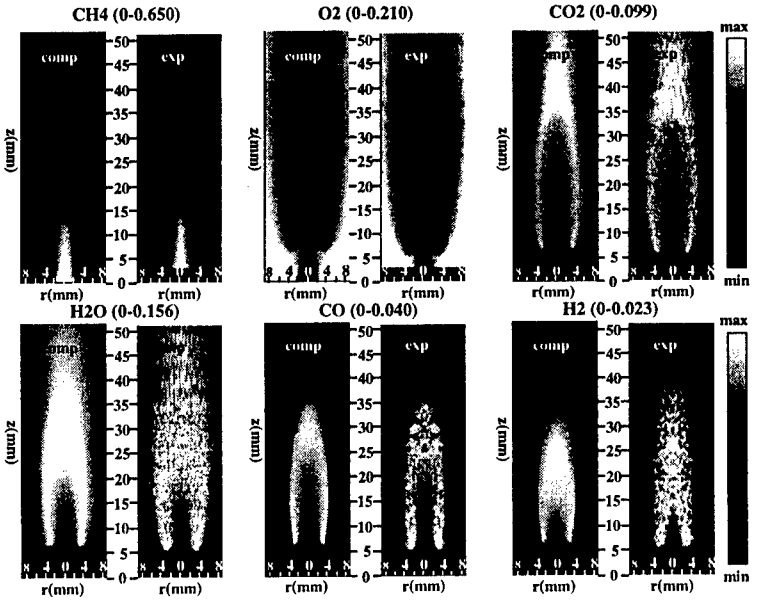


Figure 4. Mole Fractions of experimental and computational profiles. The range is in parentheses next to the species name.

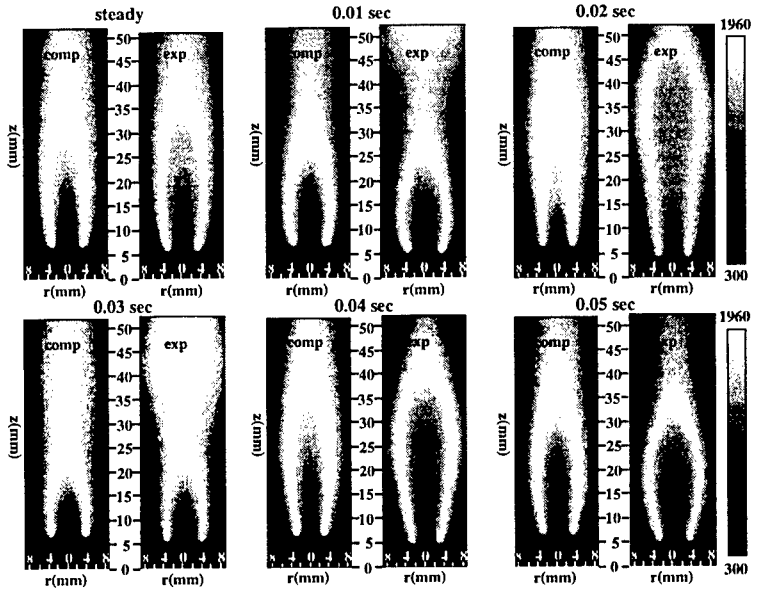


Figure 5. Temperature profiles (in degrees Kelvin) for the steady case and over five phases

---

[1] Beretta,F., Cincotti,V., D'Alessio,A., Menna,P., *Combust. Flame*, **61**:211-218 (1985).

[2] Smyth,K.C., Harrington,J.E., Johnson,E.L., and Pitts,W.M., *Combust. Flame*, **95**:229-239(1993).

[3] Mohammed,R.K., Tanoff,M.A., Smooke,M.D.,Schaffer,A.M., Long,M.B., *Twenty-seventh Symposium (International) on Combustion*, The Combustion Institute (1998).

[4] Penney, C.M., Goldman, L.M., and Lapp, M., *Nature Phys. Sci.* **235**:110 (1972).

[5] Maddams, W.F., Royaud, I.A.M., *Spectrochim. Acta, Part A* **46A**:309-314 (1990).

[6] Miles, P., Carbon Dioxide Spectral Synthesis code, Sandia National Labs (1996).

[7] Rowell, R.L., Aval, G.M.,Barrett, J.J *J. Chem. Phys.* **54:**1960 (1971)

Ultrafast Imaging of a Gas Turbine Spark Igniter

James R. Gord,*[a] Gregory J. Fiechtner,[b] Keith D. Grinstead, Jr.,[b]
Michael J. Cochran,[c] and John R. Frus[c]

[a]Air Force Research Laboratory, Propulsion Directorate, WPAFB, OH 45433-7103
[b]Innovative Scientific Solutions, Inc., 2766 Indian Ripple Road, Dayton, OH 45440-3638
[c]Unison Industries, 7575 Baymeadows Way, Jacksonville, FL 32256

1. Introduction

Experimental and computational techniques for the visualization of fluid flows have emerged as essential tools for increasing our understanding of the physics and chemistry of these flows. Indeed, many—if not most—of the breakthroughs in fluid mechanics and dynamics can be attributed to the understanding achieved through imaging of the various multidimensional structures in fluid flow. Flow visualization has played a powerful role in the process of validating computational models through comparisons of experiment and theory. For example, the development and validation of the UNsteady Ignition and COmbustion with Reactions (UNICORN) code at Wright-Patterson Air Force Base have been achieved through continuous improvement and refinement based on comparisons with experimental flow-visualization data.[1]

Spark-ignition systems play a critical role in the performance of essentially all gas turbine engines. Demanding applications such as cold start and high-altitude relight require continued enhancement of ignition systems. To characterize advanced ignition systems, we have developed a number of laser-based diagnostic techniques designed to exploit an ultrafast-framing charge-coupled-device (CCD) camera and high-repetition-rate laser sources including modelocked Ti:sapphire oscillators. Spontaneous-emission and laser-schlieren measurements have been accomplished with this instrumentation and the results applied to the study of a novel Unison Industries spark igniter that shows great promise for improved cold-start and high-altitude-relight capability as compared to that of igniters currently in use throughout military and commercial fleets.

The behavior of a spark igniter represents an ideal case study for the demonstration of ultrafast real-time imaging. Our experiments have been designed to exploit laser schlieren for visualizing refractive-index gradients in the flowfield produced during firing of the spark igniter. These simple schlieren experiments are straightforward to implement and require only a high-repetition-rate laser source for generation of the signal. The spatial variation in spark location from event to event limits the applicability of techniques that utilize a two-dimensional light sheet for illumination. Schlieren yields a line-of-sight image that captures the spark despite variations in position and morphology.

Early developments in real-time imaging based on flashlamp-pumped sources and modelocked lasers coupled with analog recording devices have been reviewed by Sklizkov.[2] Hanson and coworkers[3-6] accomplished instantaneous three-dimensional visualization of combusting flowfields by sweeping a single high-energy laser sheet through the flow using a scanning mirror and capturing a sequence of planar slices using a fast-framing camera system. More recently, Ben-Yakar and Hanson[7] developed an ultra-high-speed schlieren system to study cavity flameholders for ignition and flame stabilization in scramjets. Long and coworkers[8-10] explored high-speed digital imaging of turbulent flows, recording time-evolving digital images of gas concentrations and instantaneous three-dimensional fuel-concentration profiles through Mie scattering and biacetyl-fluorescence techniques. Lempert, Wu, and Miles[11,12] recently applied a megahertz-rate, pulse-burst laser system and a Princeton Scientific Instruments (PSI) ultrafast-framing camera to study supersonic shock-wave/boundary-layer interactions through images obtained via filtered Rayleigh scattering. Finally, at the Lund Institute of Technology, Kaminski and coworkers[13] have utilized high-speed visualization to study the effects of turbulence on spark-kernel evolution through PLIF measurements.

2. Experimental Apparatus

Spark events produced by a Unison Industries Vision spark-ignition system were visualized using an ultrafast real-time imaging system. The Vision system, which is utilized in both military and commercial aviation, is designed to produce a tailored ignition spark at the tip of the igniter plug through delivery of a pulse (nominal en-

*Correspondence: E-Mail: james.gord@pr.wpafb.af.mil; Telephone: 937 255 7431; Fax: 937 656 4570

ergy 4-12 J) from the Vision-system igniter box. The plug tip is composed of a ring electrode encompassing a center electrode. Upon delivery of the igniter-box pulse, an arc occurs across the center-electrode/ring-electrode gap. Because the location and physical characteristics (morphology, etc.) of this arc can vary from shot to shot, an ultrafast real-time imaging system is required to capture the detailed time-dynamics of the process. If the spark event were highly reproducible from shot to shot, phase-locked imaging could be applied rather than the real-time approach described below.

Laser-schlieren techniques were employed to visualize propagation of the shock produced during firing of the Unison Industries Vision-system spark igniter. The characteristics of the spark event demand high temporal resolution and ultrafast real-time imaging for capture of the physics of interest. To accomplish the required temporal resolution, two different high-repetition-rate laser sources were considered. The first is the Spectra-Physics "Merlin" intracavity-frequency-doubled Nd:YLF laser, and the second is the Spectra-Physics "Tsunami" modelocked Ti:sapphire laser.

The Merlin laser is a Q-switched Nd:YLF laser that operates at kilohertz repetition rates. The device installed at Wright-Patterson Air Force Base is configured for 50-kHz operation and produces a 13-W pulsetrain (260 μJ/pulse) at 527 nm through intracavity doubling of the Nd:YLF fundamental in lithium triborate (LBO). The multi-mode output beam provides a uniform spatial beam profile ideal for flow-visualization applications. While the Merlin's high spectral brightness and mode characteristics proved to be excellent for studies of the spark igniter, its repetition rate proved to be insufficient for resolving the shock phenomena of interest. This situation motivated a series of studies that employed the pulse-selected Tsunami as an excitation source.

The Tsunami modelocked Ti:sapphire laser employed in these studies is configured to produce an 82-MHz pulsetrain, spectrally tunable over the wavelength range 800-900 nm. Experiments were accomplished at 850 nm for all cases described here. When pumped by the 5-W, 532-nm output of a Spectra-Physics Millennia V intracavity-doubled (LBO) Nd:YVO_4 laser, the Tsunami provides ~1 W output power (12 nJ/pulse). The 82-MHz repetition rate is excessive for imaging the spark igniter while using the 1-MHz ultrafast framing camera described below; therefore, the repetition rate of the modelocked Ti:sapphire laser is reduced using a Spectra-Physics Model 3980 pulse selector. This device employs a TeO_2 acousto-optic modulator to select subsets of pulses from the full 82-MHz output pulsetrain. Losses in the pulse selector reduce the laser energy to 8 nJ/pulse.

Laser-schlieren images of the Unison Industries spark igniter were captured using a PSI ultrafast framing camera. This device features a CCD image sensor that can be exposed at rates up to 1 MHz and provides an on-chip storage array for 32 images. The array associated with the camera employed in these experiments is 180x90 pixels.

3. Data-Acquisition Strategies and Results

A number of configurations for experimental visualization of the spark igniter via ultrafast real-time imaging were explored. Preliminary experiments were designed to capture the spontaneous emission produced during firing of the spark igniter. Synchronization and timing of the various experimental events were achieved easily during these experiments. The camera was configured with an appropriate lens and placed to view the tip of the spark-igniter plug. In addition, a photodiode was arranged to collect light from the spark-ignition event. The camera was configured in the pre-trigger mode in which data frames are acquired continuously and processed through the on-chip storage array in a first-in-first-out (FIFO) arrangement. The spark igniter was fired via user-entered commands to a personal computer that was driving the Unison exciter box and the spark plug itself. The signal produced at the photodiode was employed to trigger the camera, terminating data acquisition in the pre-trigger mode and capturing the spark-igniter-image data in the on-chip storage array.

Laser-based schlieren studies of the spark igniter required a more sophisticated experimental arrangement, with greater attention to the details of synchronization and timing. Three unique strategies for schlieren-data acquisition were explored. In the first approach, the Merlin Q-switched Nd:YLF laser provided light for the schlieren measurements, and the 50-kHz laser served as the master oscillator for the experiment. The ultrafast framing camera was configured in the "multi" external trigger mode, with triggers being supplied by the spark-igniter event and the laser. Under these conditions, 32 frames of camera data were acquired in synchrony with the laser during the 640-μs period spanning the spark event. This approach provided tremendous optical energies and saturating signals at the camera; therefore, neutral-density filters were inserted into the optical path to attenuate the laser beam. Unfortunately, the 50-kHz repetition rate of the laser proved insufficient to resolve the progress of the spark-initiated shock wave adequately.

This situation prompted experiments conducted via the second approach in which the pulse-selected Tsunami Ti:sapphire laser was utilized for production of the schlieren signal. As in the previous experiments, the laser served as the master oscillator, and the camera was slaved to the laser and the spark event via the "multi" external trigger mode. This arrangement permitted the acquisition of image data at framing rates up to 800 kHz, improving the temporal resolution over that achieved in the Merlin experiments by a factor of sixteen.

The third and final approach, however, produced the optimum visualization and enabled spark imaging at the full 1-MHz data-acquisition bandwidth of the camera. For these experiments, the camera served as the master oscillator, and the pulse selector—and, therefore, the laser—were slaved to the camera. A block diagram of the experimental apparatus is depicted in Figure 1. The Millennia/Tsunami/pulse selector provide the laser pulse for schlieren measurements. The output pulsetrain is expanded to a nominal diameter of ~32 mm through two 4x telescopes. The collimated, expanded laser beam traverses a sample region in which the spark-igniter plug is suspended. A lens collects the transmitted light, which is focused to a point where a knife edge is inserted. Light traveling past the knife edge is imaged through a neutral-density filter (ND=1) and an interference filter (center frequency=850nm, bandwidth=10 nm) onto the ultrafast framing camera using a Nikon lens.

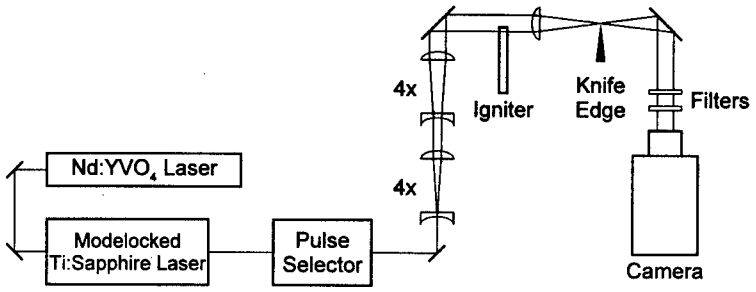


Figure 1. Experimental apparatus for ultrafast real-time laser-schlieren imaging of a Unison Industries spark igniter.

Details of the synchronization and timing are presented schematically in Figure 2. The ultrafast framing camera is configured in the post-trigger mode and, therefore, acquires images continuously until a spark event occurs. The spark event is initiated by the experimenter through entry of commands at the personal computer. These commands trigger the Unison exciter box, firing the spark plug and producing a trigger via the remote module that drives a digital delay generator (DDG). This DDG triggers the camera. Once the camera is triggered, it acquires and stores the 32 images that comprise the final data set. Trigger delays are carefully adjusted to ensure that the frames are acquired during the spark event. Once triggered, the camera is responsible for driving the pulse selector and synchronizing the laser with the image-acquisition process. The camera is configured to record images at its full 1-MHz acquisition rate. During each frame, the camera generates a vertical-strobe pulse that drives the pulse selector. This strobe pulse is shaped and further processed with a pulse generator and then mixed with the ~41-MHz signal from the Ti:sapphire modelocker. This process ensures that a single laser pulse is selected from the 82-MHz pulsetrain during the exposure time associated with each of the 32 camera frames. The vertical-strobe-driven pulse generator can be adjusted to select an envelope of pulses from the 82-MHz train during each framing event. For example, experiments were accomplished with 10 and 100 laser pulses per frame; however, the data presented in this paper were achieved with a single pulse for each frame. Those data, depicting the propagation of the spark-initiated shock, are presented in Figure 3.

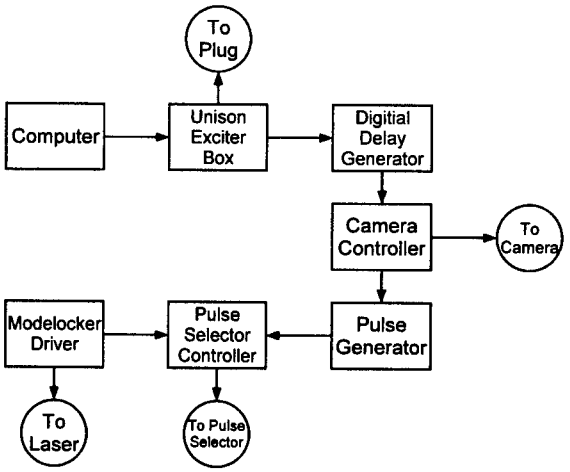


Figure 2. Diagram of electronic timing connections for ultrafast real-time laser-schlieren measurements.

4. Conclusions

Ultrafast real-time imaging of the shock structure produced by a Unison Industries spark igniter has been accomplished. Spontaneous-emission and laser-schlieren techniques have been demonstrated in conjunction with a number of high-repetition-rate laser sources (50-kHz, Q-switched Nd:YLF laser; pulse-selected, 82-MHz modelocked Ti:sapphire laser) and an ultrafast-framing CCD camera (framing rates up to 1 MHz). Future activity will be focused on applying the ultrafast methodology to measurements of other key spark parameters through the use of various advanced laser-based diagnostics including PLIF and planar Rayleigh scattering.

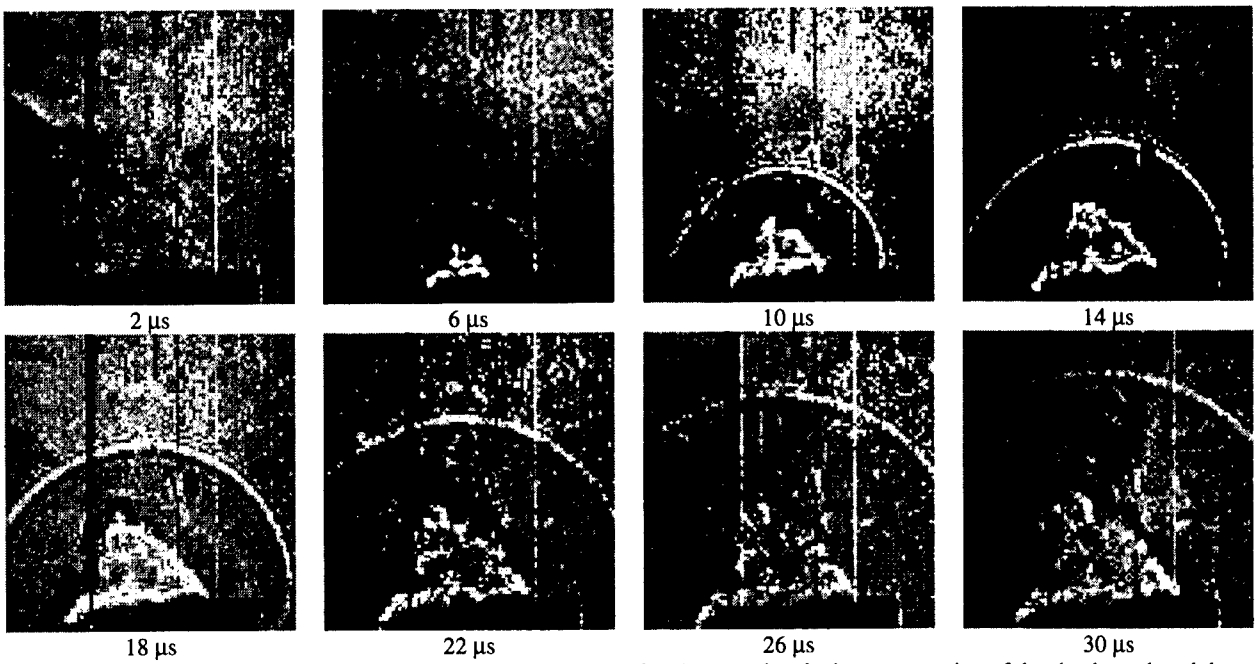


Figure 3. A selection of laser-schlieren images acquired at 1-MHz framing rate that depicts propagation of the shock produced during firing of the Unison Industries spark igniter.

Acknowledgments

The authors gratefully acknowledge the expert editorial assistance of Ms. M. M. Whitaker. This work is supported by research funding from the Air Force Office of Scientific Research (Dr. Julian Tishkoff, Program Manager) and U.S. Air Force Contract F33615-95-C-2507.

References

1. W. M. Roquemore and V. R. Katta, "Role of Visualization in the Development of UNICORN," presented at the International Conference on Optical Technology and Image Processing in Fluid, Thermal, and Combustion Flow, 6-10 December 1998, Yokohama, Japan, and published in the Proceedings.
2. G. V. Sklizkov, "Lasers in High-Speed Photography," in *Laser Handbook*, F. T. Arecchi and E. O. Schulz-Dubois, eds., Vol. 2, pp. 1545-1577, North-Holland, Amsterdam, 1972.
3. J. M. Seitzman, B. J. Patrie, P. H. Paul, and R. K. Hanson, "Instantaneous 3-D and Temporal Evolution Measurements by Rapid Acquisition of Planar Images," AIAA 91-0178 presented at the 29th AIAA Aerospace Sciences Meeting, Reno, Nevada, 1991.
4. B. J. Patrie, J. M. Seitzman, and R. K. Hanson, "Planar Imaging at High Framing Rates: System Characterization and Measurements," AIAA 92-0584 presented at the 30th AIAA Aerospace Sciences Meeting, Reno, Nevada, 1992.
5. B. J. Patrie, J. M. Seitzman, and R. K. Hanson, "Planar Imaging for 3-D Flow Visualization," 22nd International Congress on High Speed Photography and Photonics, SPIE Vol. 1801, 1992.
6. B. J. Patrie, J. M. Seitzman, and R. K. Hanson, "Planar Imaging at High Framing Rates: System Characterization and Measurements, II," AIAA 93-0364 presented at the 31st AIAA Aerospace Sciences Meeting, Reno, Nevada, 1993.
7. A. Ben-Yakar and R. K. Hanson, "Cavity Flameholders for Ignition and Flame Stabilization in Scramjets: Review and Experimental Study," AIAA 98-3122 presented at the 34th AIAA/ASME/SAE/ASEE Joint Propulsion Conference, Cleveland, Ohio, 1998.
8. M. Winter, J. K. Lam, and M. B. Long, "Techniques for High-Speed Digital Imaging of Gas Concentrations in Turbulent Flows," *Exp. Fluids* 5, pp. 177-183, 1987.
9. M. B. Long and B. Yip, "Measurement of Three-Dimensional Concentrations in Turbulent Jets and Flames," *Twenty-Second Symposium (International) on Combustion*, pp. 701-709, The Combustion Institute, Pittsburgh, 1988.
10. B. Yip, R. L. Schmitt, and M. B. Long, "Instantaneous Three Dimensional Concentration Measurments in Turbulent Jets and Flames," *Opt. Lett.* 13, pp. 96-98, 1987.
11. W. R. Lempert, P.-F. Wu, B. Zhang, R. B. Miles, J. L. Lowrance, V. Mastrocola, and W. F. Kosonocky, "Pulse-Burst Laser System for High-Speed Flow Diagnostics," AIAA 96-0179 presented at the 34th AIAA Aerospace Sciences Meeting, Reno, 1996.
12. W. R. Lempert, P.-F. Wu, and R. B. Miles, "Filtered Rayleigh Scattering Measurements Using a MHz Rate Pulse-Burst Laser System," AIAA 97-0500 presented at the 35th AIAA Aerospace Sciences Meeting, Reno, 1997.
13. C. F. Kaminski, A. Franke, J. Hult, M. Alden, and R. B. Williams, "Applications of a Multiple-Pulse YAG Laser/Framing Camera System for Ultrafast Visualization of Combustion Processes," Work-in-Progress poster presented at the 27th Symposium (International) on Combustion, Boulder, 1998.

TEMPERATURE MEASUREMENTS IN Ar-H_2 DC-ARC PLASMAS UTILIZED IN THERMAL SPRAY PROCESSING

Sergey Y. Semenov and Baki M. Cetegen
Mechanical Engineering Department
University of Connecticut, Storrs, CT 06269-3139
[serg@engr.uconn.edu, cetegen@engr.uconn.edu]

Introduction

Continuous DC arc plasmas have wide ranging applications in science and technology. One such application is thermal spraying of ceramic and metallic coatings on surfaces. These coatings are designed to provide barrier to wear, corrosion and high thermal loadings on components. Thermal barrier coatings, in particular, protect metallic components such as gas turbine blades from very high gas stream temperatures. Deposition of thin ceramic coatings is typically achieved by DC-arc plasma processing. Particles of a ceramic material such as yttria stabilized zirconia are injected through a plasma jet in which heat-up and acceleration of particle stream occurs. These particles form a coating upon impingement onto a substrate surface.

A detailed and complete knowledge of plasma temperature field and its dependence on the plasma power and gas flow rates is necessary for accurately determining particle heat-up in plasma thermal spray processes. In particular, the effects of transverse particle injection jets on the plasma thermal field need to be assessed for many applications which utilize transverse powder injection. Due to the very high temperatures in DC-arc plasma jets used in thermal spray processes, a spectroscopic technique was chosen to measure plasma temperatures based on the population of Ar-I species distributed in different electronic states based on Boltzmann statistics. While such techniques had been used in the past [1,2], the implemented technique enables determination of plasma temperatures along a thin slice across the plasma width (or diameter) at one instant, thus allowing to capture the temperature profiles along the full radial extent of the plasma jet. In axisymmetric plasmas, Abel's inversion can be effectively used to remove the effects of line-of-sight integration.

Experimental set-up

A continuous DC-arc plasma jet was formed using a commercial Metco Model 9MC plasma gun with a water cooled nozzle with an exit diameter 8.0 mm. The experimental set-up used for our measurements is schematically shown in Fig. 1. Plasma radiation was imaged using a single lens onto the entrance slit of a 0.5 m McPherson spectrometer. The height of the spectrometer entrance slit covered the diameter of the imaged plasma, thus each location along the slit corresponds to a physical location along the plasma diameter. The spectrometer disperses radiation across the slit width to its spectral content by using a 2400 grooves/mm diffraction grating with dispersion resolution of 0.83 nm/mm. The spectrally dispersed radiation is then imaged at the output of the spectrometer using a high spatial resolution (1317 x 1035 pixel) scientific CCD camera, Photometrics CE200 with 12-bit read-out. The spectral region spanned in these experiments cover 404 $nm < \lambda < 435$ nm, containing typically 10 emission lines belonging to Ar-I species. The spectral resolution on the CCD camera images was 0.00289 nm/pixel. The image processing of the digital images from the CCD camera allows determination of the temperature at each radial location using the Boltzmann plot technique [3]. Spectral sensitivity of the CCD chip was essentially constant in the wavelength region of interest.

Result and Discussion

Figure 2 shows a sample emission spectrum for a 14.4 kW Ar-H_2 plasma. Up to 10 Ar-I lines can be detected [4] for a typical exposure time of a millisecond. At each location, a number of spectra were obtained at different exposure times to determine the variability of the plasma

radiation and consequently the temperature distributions. In the axisymmetric plasmas, the recorded line-of-sight integrated emission needs to be inverted to obtain the local emission intensities using Abel's inversion. Local excitation temperatures were determined from the Abel inverted intensities. Figure 3 shows the three sample Boltzmann plots for three different locations in a plasma corresponding to three different temperatures. It is found that the emission line intensities follow the Boltzmann distribution well, indicating that the population of the different electronic excitation levels obey the Boltzmann distribution. In these figures, the excitation temperature is determined from the slope of the Boltzmann plot. If Boltzmann plots were created for the line-of-sight integrated emission intensities, they exhibit significant scatter indicating the importance of using local emission intensities in these calculations. Our subsequent temperature measurements were based on the emission intensities for two different lines with significantly different excitation energies at λ_1=420.067 nm and λ_2=418.188 nm as indicated in Figure 3.

The data reduction technique involved several steps: (1) smoothing of the recorded intensity profiles, (2) discrete Abel's inversion of each line intensity and respective background intensities, (3) subtraction background profile from both line intensity profiles and (4) finally calculating the radial temperature profiles from deconvoluted intensity profiles. Digitized images for each emission line and background were averaged in the spectral direction by binning 5 pixels for the emission lines and 10 pixels for the background. The discrete Abel's inversion was performed on the radially smooth data sets. Background subtraction was done after Abel's inversion. The local plasma excitation temperatures were calculated using Boltzmann distribution:

$$T = \frac{E_2 - E_1}{k \ln\left(\frac{A_2 g_2 \lambda_1 (I_1 - I_{1b})}{A_1 g_1 \lambda_2 (I_2 - I_{2b})}\right)}$$

where, E_i is the excitation energy levels, A_i is transition probability, g_i is statistic weight, λ_i is the wavelength, k is Boltzmann constant and I_i is the absolute intensity. Indices "1" and "2" correspond to the two selected Ar-I lines. I_b refers to the background intensity. Absolute intensities were measured in the experiment and line parameters were taken from [4]. The measurement error is less than 15% for temperatures above 3000 K. Experimental uncertainty is less than 10%.

Figure 4 and 5 show the measured excitation temperatures in the studied plasmas. Figure 4 shows the axial variation of the peak centerline plasma temperature at three different plasma power levels. Immediately downstream of the nozzle exit, peak temperatures in the range of 12,500 to 14,000 K are measured. With increasing downstream distance, plasma temperatures decay due to turbulent mixing with the ambient air. Figure 5 shows the distribution of radial temperature profiles for 14.4 kW plasma at different axial locations. It is found that the profiles exhibit a hot core region with decay of temperature towards the edges of the plasma. The radial profiles show variations that are closer to linear decay than gaussian distributions typically found in a turbulent jet.

Another aspect of plasma thermal environment is the effect of a cold transverse jet impinging onto the plasma as it occurs in thermal spray processing. The modifications of the temperature field by this jet are of interest in determining the particle stream heat-up. Figures 6 shows the effects of the transverse cold jet injection on the plasma temperatures. For these experiments, only line-of-sight integrated intensities were used to determine the temperatures because of the asymmetry created by the injection jet. At Z=1 mm, the plasma temperature distributions are very similar as expected. The cold jet injection occurs at an axial location of Z=5 mm. It is found that the overall temperature levels are not altered by this injection jet, but the whole temperature distribution is shifted in the direction of transverse jet. The amount of this

shift is found to be proportional to the relative momentum ratio of the injection jet and the main plasma jet.

Acknowledgments

The research reported herein was sponsored by the Office of Naval Research under grant No. N00014-97-0843 under the direction of Dr. Lawrence Kabakoff.

References:

1. A. Vardelle, J. M. Barronnet, M. Vardelle, and P. Fauchais, "Measurements of the Plasma and Condensed Particle Parameters in a DC Plasma Jet", IEEE Trans. Plasma Sci., Vol. PS-8, N 4, pp. 417-424, 1980.

2. M. Vardelle, A. Vardelle, P. Fauchais, and M. I. Boulos, "Particle Dynamics and Heat Transfer Under Plasma Conditions", AIChE. J, Vol. 34, No.4, pp. 567-573, 1988

3. N. K. Joshi, S. N. Sahasrabudhe, K. P. Sreekumar and N. Venkatramani, "Variation of Axial Temperature in Thermal Plasma Jets", Measurement Science & Technology, Vol.8, pp.1146-50, 1997

4. W. L. Wiese, J. W. Brault, K. Danzmann, V. Helbig, M. Kock, "Unified set of atomic transition probabilities for neutral argon", General Physics, Physical Review A, vol. 39, No. 5, pp.2461-2471, 1989

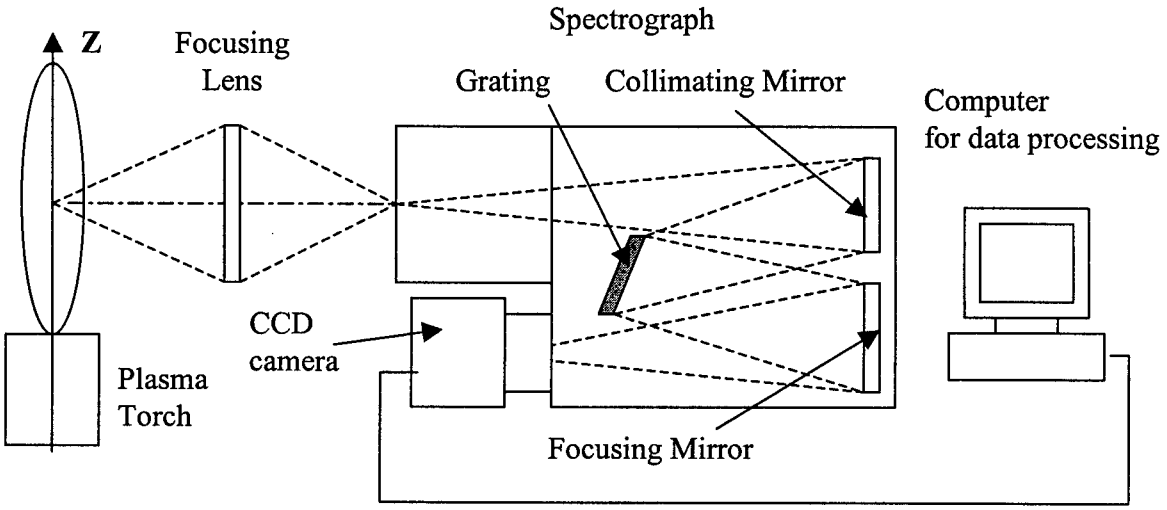


Figure 1. Experimental set-up for plasma temperature measurements

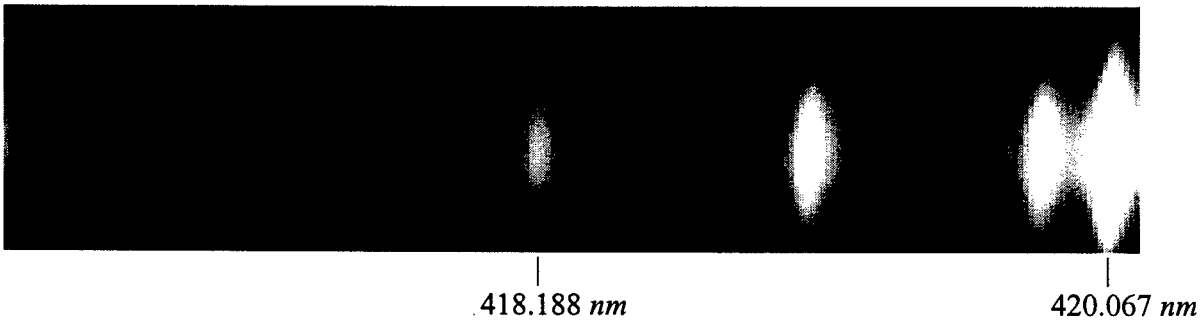


Figure 2. Argon Spectrum

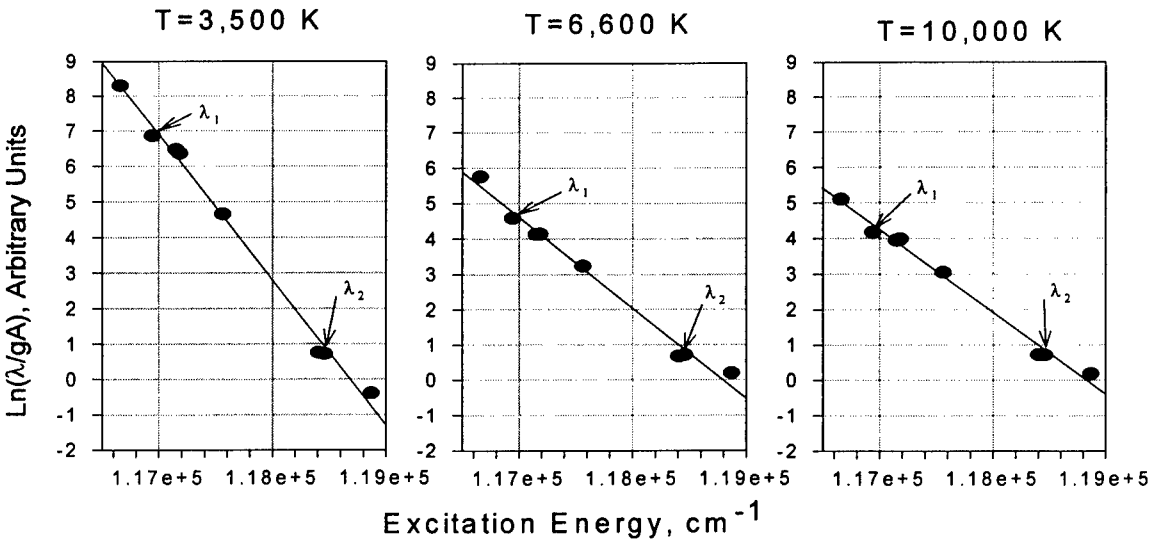


Figure 3. Boltzmann plots for determining excitation temperatures at three locations

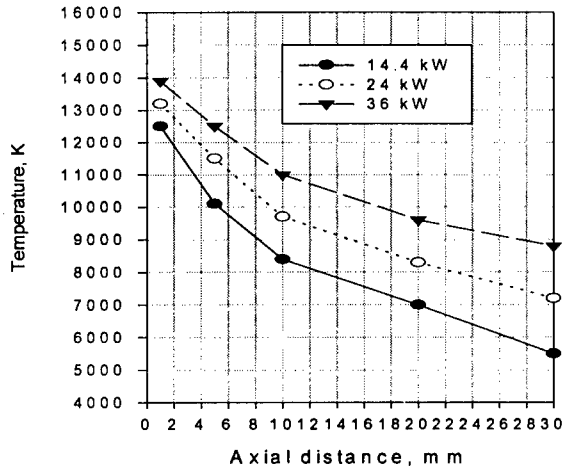


Figure 4. Axial distribution of plasma temperature at three different plasma input power levels

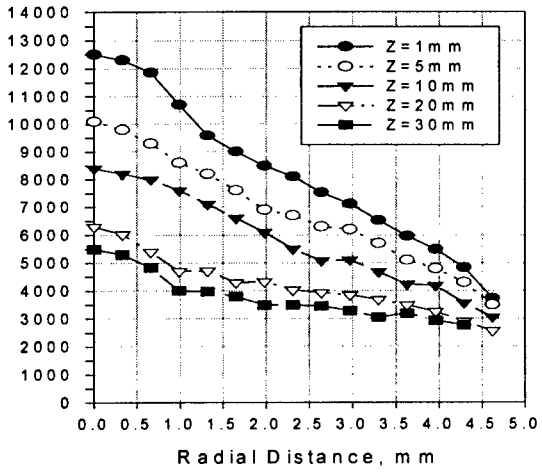


Figure 5. Radial distribution of plasma temperature at different axial locations for a plasma input power of 14.4 kW

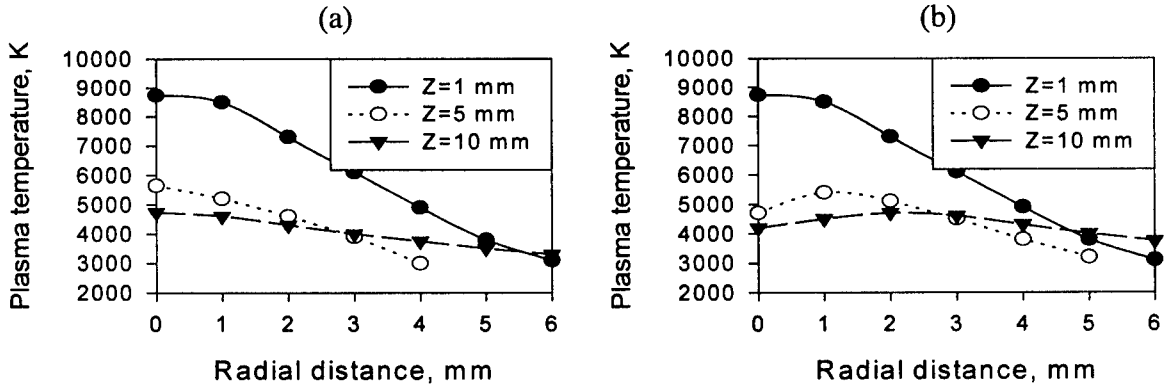


Figure 6. Radial temperature profiles: a) without carrier gas injection, b) with carrier gas injection

Obtaining and Interpreting Near-Infrared Wavelength Modulation Absorption Signals from Hot Fire Gases: Practical Issues

Linda G. Blevins and Bradley W. Peterson

National Institute of Standards and Technology (NIST), Building and Fire Research Laboratory
100 Bureau Drive, Stop 8653, Gaithersburg, MD 20899-8653 USA
linda.blevins@nist.gov, bradley.peterson@nist.gov

Introduction and Background

Near-infrared tunable diode laser absorption spectroscopy (TDLAS) shows promise for measuring concentrations of several gaseous species important in fires, including CH_4, O_2, C_2H_2, C_2H_4, CO, CO_2, and H_2O [1]. Researchers at NIST are presently studying the possible application of near-infrared TDLAS for rapid measurement of CO concentration in and around fires. Near-infrared diodes are compact, spectrally narrow, and rapidly tunable, and the potential exists to deliver diode light into and out of real-scale fires using rugged and readily-available silica fiber optics. The goal of the NIST project is to develop a diode laser sensor capable of measuring CO concentration at temperatures between 300 K and 1200 K in fire gases partially obscured by soot. This abstract describes some practical signal interpretation issues found to be important during sensor development.

Previous studies on the use of near-infrared diodes for CO measurement have focused on determining CO amounts in room-temperature absorption cells with controlled gas composition [2-5]. Some recent studies of CO in combustion gases employed rapid probe sampling with a multi-pass cell/diode laser arrangement [6], and an in situ measurement of CO concentration in the hot exhaust of a premixed methane/air flame was recently reported [7]. Near-infrared TDLAS has been used in fire research to quantify hydrogen fluoride concentration in post-flame gases following fire suppression [8].

Experiments and Modeling[1]

The amount of light absorbed by a molecule is quantified using the Lambert-Beer law, $\tau_{\tilde{\nu}} = \exp\left[-S(T)g(\tilde{\nu}-\tilde{\nu}_0)NL\right] = \exp\left[-\alpha(\tilde{\nu})\right]$, where $\tilde{\nu}_0$ is the transition center wave number (cm^{-1}), $\tau_{\tilde{\nu}}$ is the fractional transmittance at $\tilde{\nu}$, T is the gas temperature (K), S(T) is the T-dependent line strength (cm^{-1}/molecule·cm^{-2}), $g(\tilde{\nu}-\tilde{\nu}_0)$ is the line shape function normalized to unit area (cm), N is the absorber number density (molecule/cm^3), L is the path length (cm), and $\alpha(\tilde{\nu})$ is the absorbance. A Voigt profile, accounting for collisional (Lorentzian) and thermal (Doppler) broadening, is sufficient for computing $g(\tilde{\nu}-\tilde{\nu}_0)$ in most combustion work [1]. Wavelength modulation spectroscopy (WMS, [9]) is the sensitive detection scheme examined here. WMS signals resemble derivatives of the transmittance profile, and are modeled using Equations 1 through 6 of Ref. [10] for the present work.

The CO second overtone R(23) transition centered at 6410.9 cm^{-1} (near 1.56 μm) is targeted for this study. The T-dependent line strength for this transition taken from the HITEMP database [11] is $S = 8.78 \times 10^{-25}$ cm^{-1}/molecule·cm^{-2} at T = 300 K and $S = 9.14 \times 10^{-24}$ cm^{-1}/molecule·cm^{-2} at T = 1200 K. The air-broadened and self-broadened half-widths at half maximum (HWHM) at 296 K are 0.045 cm^{-1}/atm and 0.051 cm^{-1}/atm, respectively, with a T-dependence coefficient of 0.69. Assuming a minimum detectable absorbance of $\alpha(\tilde{\nu}_0) = 1 \times 10^{-5}$, the Lambert-Beer law predicts that a concentration of 0.7 % by volume of CO can be detected in a 10 cm path at 300 K, while 0.1 % can be detected at 1200 K. Concentrations of CO as high as 5 % by volume exist in the exhaust of underventilated enclosure fires [12]. Hence, the R(23) line should be sensitive enough to detect CO concentrations of interest in fire research.

The present diode laser is a fiber-coupled InGaAsP distributed-feedback laser packaged by Alcatel. The laser beam is delivered to the measurement location by a 10 m long, 9 μm diameter single-mode fiber and is collimated to

[1] To describe experimental procedures, it is occasionally necessary to identify commercial products by manufacturer's name or label. In no instance does such identification imply endorsement by the National Institute of Standards and Technology, nor does it imply that the particular products or equipment are necessarily the best available for that purpose.

a diameter of 0.5 mm using a gradient-index lens. The collimated beam is aimed across the optical path and focused by a convex mirror onto an InGaAs photodiode. For this study, either a room-T absorption cell or a flame are placed in the optical path. A laser diode controller is used to vary the laser wave number by changing either the laser temperature (coarse tuning) or the injection current (fine tuning). The laser is operated with a temperature of 51.4 °C and a nominal current of 50 mA. The steady-state DC laser tuning rate for 51.4 °C is 0.0245 cm^{-1}/mA.

Software developed by Southwest Sciences, Inc. for data acquisition and control was used on a personal computer to perform the present experiments [13]. A 39 Hz voltage ramp ranging from -0.4 V to +0.4 V was generated electronically and applied to the laser injection current via the diode controller. Combining these voltages with the controller transfer function (20 mA/V), the current ramp ranged between -8 mA and +8 mA. The ramp was generated in 256 bins at a rate of 100 μs per bin. A hyperbolic-tangent waveform with duration of 50 % of the sweep time was applied between sweeps to minimize electronic ringing. A modulating sine wave with a frequency of either 49 kHz (for 2f) or 24 kHz (for 4f) was superimposed on the slow ramp. The sine wave amplitude was either 0.4 V (8 mA) or 0.5 V (10 mA) for the experiments described here. The ramp and sine amplitudes cannot be converted directly from current to wave number using the DC laser tuning rate because of laser response-time effects. A digital lock-in amplifier (300 μs time constant) demodulated the transmitted signal at either twice or four times the modulation frequency. This high frequency detection scheme reduces laser excess noise (proportional to 1/f), allowing sensitive detection [9]. The lock-in output signal was normalized by the detector DC signal before processing, and 250 sweeps were averaged for each spectrum.

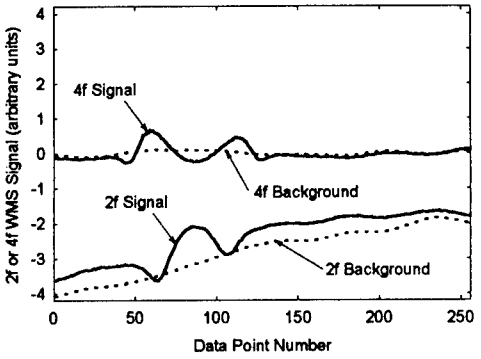


Fig. 1. 2f and 4f signals and backgrounds for CO in a 13-cm cell with P = 19.5 torr and T = 300 K.

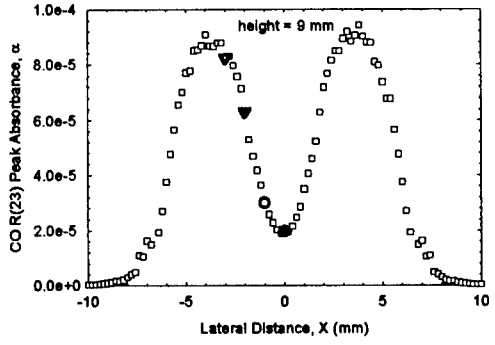


Fig. 2. Lateral profile of CO R(23) peak absorbance in the NIST Wolfhard-Parker burner at a height of 9 mm from the burner. Calculated from previous CO concentration and T measurements.

Sloping baselines caused by laser amplitude modulation were subtracted from the signals. Figure 1 shows 2f and 4f signals collected in a 13-cm absorption cell filled with low-pressure, pure CO, along with background signals collected in the absence of the cell. The 2f background has a strong non-zero slope caused by amplitude modulation, but the 4f background is relatively flat. Additionally, the 4f signal is slightly weaker than the 2f signal. The baseline slope limits the 2f measurement sensitivity by consuming the lock-in amplifier dynamic range. These trends agree with previous work concerning the behavior of diode-laser amplitude modulation at higher harmonics [9]. Because of the 2f backgrounds, more sensitive measurements can be made with 4f WMS in spite of the lower signal levels. Hence, 4f is used for the present study.

A Wolfhard-Parker (WHP) slot burner is used to achieve known CO mole fraction (χ_{CO}) and T combinations along a uniform, 4.1 cm path. The WHP flame has been studied extensively by Smyth and coworkers, and a comprehensive database is available [14]. T and χ_{CO} were measured previously with radiation-corrected thermocouples and mid-infrared TDLAS, respectively [15]. The burner operating condition used here is identical to that used previously. Figure 2 shows an expected lateral profile of peak CO absorbance calculated using the Lambert-Beer law. Table I provides information about the four data points from the profile used for sensor development.

Table I. Four WHP Data Points with T < 1200 K

Symbol	X (mm)	χ_{CO}	T (K)	$\alpha(\tilde{\nu}_0)$
closed circle	0	0.0075	550	2.0×10^{-5}
open circle	- 1	0.0094	660	3.0×10^{-5}
closed triangle	- 2	0.018	880	6.3×10^{-5}
open triangle	- 3	0.026	1170	8.2×10^{-5}

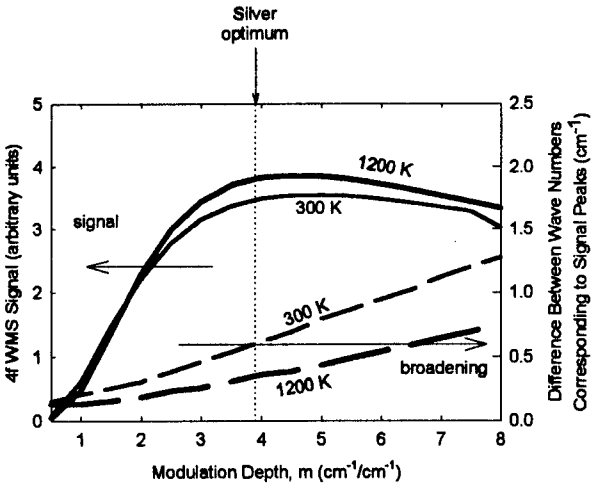


Fig. 3. Calculated effect of m on CO R(23) 4f signal and broadening for two temperatures.

Results: Modulation Depth Effects

WMS is characterized by the modulation depth, m, defined as the ratio of the modulating sine wave amplitude (cm^{-1}) to the HWHM of the spectral line (cm^{-1}). Reid and Labrie showed that 2f WMS signals are maximized when m = 2.2 [16]. Silver extended their analysis to higher harmonics and showed that m = 3.9 is optimum for 4f WMS [9]. Figure 3 shows results of an analysis like the one performed by Silver to reveal the optimum. While Silver's calculations were for general Doppler- and Lorentz-broadened lines, the present analysis is specific to the R(23) CO line and is based on Voigt profiles. The 4f WMS signal (defined as the peak-to-central-valley signal difference) and the wave number spacing between signal peaks are depicted as a function of m for T = 300 K and T = 1200 K. For low values of m, the signal increases with m, reaching a maximum near m = 3.9 and staying constant or decreasing thereafter. Values of m > 3.9 result in excess broadening of the 4f spectrum; this broadening is undesirable because broad signals are more likely to overlap with interfering signals from other species or exceed the laser scan width.

While the idea of selecting one optimum modulation depth and keeping it constant is appealing, it may not be practical for fire research applications because T varies with time and spectral linewidths vary with T. Figure 4 shows the HWHM of the atmospheric-pressure Voigt profile for the R(23) line as a function of T. The HWHM steadily decreases as T increases. It would be impractical to maintain a constant value of m for all values of T, since the modulating sine wave amplitude would need to be adjusted before every scan. In practice, a single sine wave amplitude is initially selected (perhaps using a room-T absorption cell) and used throughout data collection. Figure 4 shows predictions of the way that m would vary with T if (1) the modulation amplitude were initially optimized (m = 3.9) with a 300 K cell, or (2) the modulation amplitude were initially set to achieve m = 2.0 with a 300 K cell. For cases (1) and (2), m increases to 7 and 3.5, respectively, when T reaches 1200 K. Case (1) demonstrates that selecting the optimum modulation setting for room T will lead to over-broadened lines at higher temperatures. While not shown in this paper, experimental flame signals collected with the system optimized for a 300 K line were very broad. Case (2) is more desirable for practical measurements in fire gases.

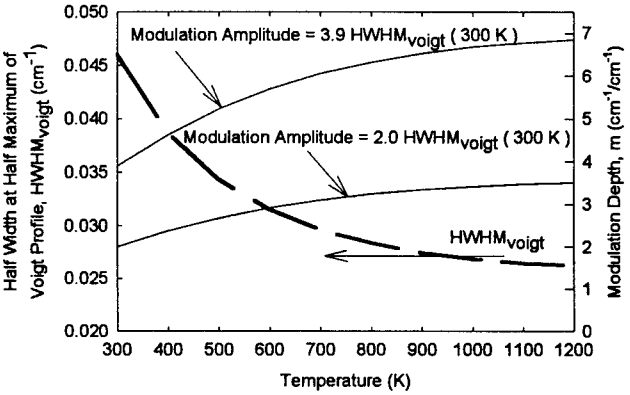


Fig. 4. Effect of T on CO R(23) HWHM and on m for different optimization methods.

Calibration is presently being explored as a method to quantify the measured signals. Calibration curves (graphs of 4f signal versus calculated peak absorbance) have been generated with known atmospheric-pressure mixtures of CO in air at T = 300 K and are shown on the left side of Fig. 5 for two modulation amplitudes. The calibrations are not expected to apply for T > 300 K because of lineshape variations. To check this hypothesis, WHP flame data are shown on the figure. (Refer to Fig. 2 for matching symbols). The high-T flame signals for the lower modulation amplitude (0.4 V or 8 mA) lie above the 300 K calibration curve. For the larger modulation amplitude (0.5 V or 10 mA), the flame signals lie closer to the 300 K calibration curve. The data trends can be understood by examining the right side of Fig. 5, which shows calibration curves generated by spectral modeling for cases (1) and (2) discussed earlier. The magnitudes of the curves are scaled so that the case (1) prediction matches the larger-modulation-amplitude experimental curve at its uppermost point. For case (1), the calibration curves for

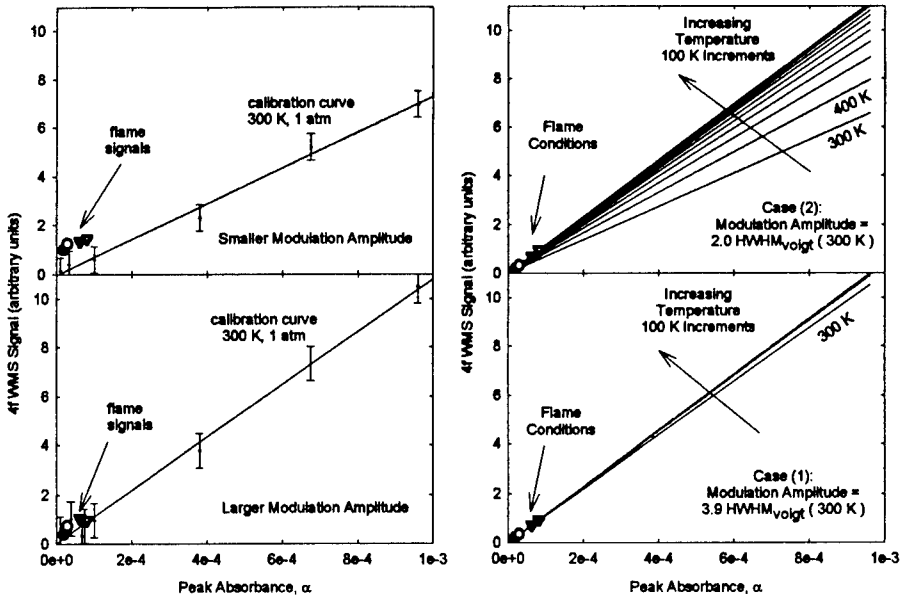


Fig. 5. Measured and calculated calibration curves and flame signals.

T > 300 K overlap, and the predicted flame signals fall on top of them, in agreement with the larger-modulation-amplitude experimental data behavior shown on the left half of the figure. For case (2), the calibration curves exhibit stronger T-dependence, in agreement with the experimental data shown on the left half of the figure. From these comparisons, it can be deduced that the larger-modulation-amplitude flame signals are over-modulated, while the smaller-modulation-amplitude flame signals are not. While the T-independence of the over-modulated calibration curves is desirable, the broadening caused by over-modulation is not.

Conclusions

For the present NIST laser system, 4f WMS is used rather than 2f WMS because 2f WMS sensitivity is limited by a strongly sloping background. Since m increases with T for the CO R(23) line, it should be set to a less-than-optimum value at room temperature to avoid over-broadening at higher temperatures.

Acknowledgments

Partial support was provided by the NIST Advanced Technology Program. Dr. David Bomse assembled the hardware and software used in the experiments and provided guidance. Mr. Marco Fernandez and Mr. Erik Johnsson are graciously acknowledged for their help. Thanks are extended to Dr. William Pitts for his leadership.

References

[1] Allen, M.G., *Meas. Sci. Technol.* 9:545 (1998).
[2] Sonnenfroh, D.M. and Allen, M.G., *Appl. Opt.* 36:3298 (1997).
[3] Gabrysch, M., Corsi, C., Pavone, F.S., and Inguscio, M., *Appl. Phys.B* 65:75 (1997).
[4] Schiff, H.I., Mackay, G.I., and Nadler, S.D., *Infrared Physics & Technology* 37:39 (1996).
[5] Cassidy, D.T. and Bonnell, L.J., *Appl. Opt.* 27:2688 (1988).
[6] Furlong, E.R., Mihalcea, R.M., Webber, M.E., Baer, D.S., and Hanson, R.K., *AIAA J.* 37:732 (1999).
[7] Upschulte, B.L., Sonnenfroh, D.M., and Allen, M.G., *Appl. Opt.* 38:1506 (1999).
[8] McNesby, K., Skaggs, R., Miziolek, A., Clay, M., Hoke, S., and Miser, C., *Appl. Phys. B* 67:443 (1998).
[9] Silver, J.A., *Appl. Opt.* 31:707 (1992).
[10] Philippe, L.C. and Hanson, R.K., *Appl. Opt.* 32:6090 (1993).
[11] Rothman, L.S., Camy-Peyret, C., Flaud, J.-M., Gamache, R.R., Goldman, A., Goorvitch, D., Hawkins, R.L., Schroeder, J., Selby, J.E.A., and Wattson, R.B., *JQSRT* (To Be Submitted).
[12] Pitts, W.M., *Progress in Energy and Combustion Science* 21:197 (1995).
[13] Bomse, D. S., *Tunable Diode Laser System Manual*, Southwest Sciences, Inc., Santa Fe, NM, 1998.
[14] Smyth, K.C., *http://www.bfrl.nist.gov/865/flamedata* (1999).
[15] Miller, J.H., Elreedy, S., Ahvazi, B., Woldu, F., and Hassanzadeh, P., *Appl. Opt.* 32:6082 (1993).
[16] Reid, J. and Labrie, D., *Applied Physics B* 26:203 (1981).

Mine Fire Detection In The Presence of Diesel Emissions

J.C. Edwards, R.A. Franks, G.F. Friel, C.P. Lazzara, and J.J. Opferman
National Institute for Occupational Safety and Health
Pittsburgh Research Laboratory
P.O. Box 18070, Cochrans Mill Road
Pittsburgh, PA 15236
(jce9@cdc.gov, rdf3@cdc.gov, gcf1@cdc.gov, cgl9@cdc.gov, jdo2@cdc.gov)

INTRODUCTION

A series of four coal combustion experiments (*1*)[1] was conducted at the National Institute for Occupational Safety and Health, Pittsburgh Research Laboratory in the Safety Research Coal Mine to evaluate the response of optical and ionization smoke and CO sensors to a small 0.61 m square smoldering coal fire which transitions to flaming combustion in the presence of diesel emissions. With the increased utilization of diesel engines in underground coal mines, it is important to be able to discriminate fire products-of-combustion (POC) from diesel emissions. One proposed method to accomplish this is the deployment and interpretation of multiple sensors.

EXPERIMENTAL PROCEDURES

A schematic of the airways of 2 m height and 4 m width in which the experiments were conducted is shown in figure 1. Electrical strip heaters were used to heat a mixture of pulverized and 6 cm diameter coal slowly through smoldering to a flaming combustion transition with a CO production rate of approximately 0.001 ppm/s in ventilation air of 5 cu m/s. The fire sensors were positioned near the airway roof 148 m downwind from the fire. Diesel engines were operating for three of the four experiments 79 m upwind of the sensors. A spatially averaged path measurement of the POC was made with an optical smoke sensor (SA) which consisted of an infrared transmitter and receiver separated by an optical path of 9.65 m. Point measurements of the POC were made with a chemical cell, CO sensor, and an ionization smoke sensor (SB). Smoke optical density was determined from the measured optical obscuration of light in the 0.4 – 0.7 micron range over a 1 m path.

RESULTS

The optical fire sensor SA and the ionization sensor SB were quite dissimilar in their response to the initiation of diesel emissions. For experiment No. 4, figure 2 shows the response of smoke sensor SA and the CO sensor to diesel emissions from two diesel operated pieces of mining equipment, and figure 3 shows the response of smoke sensor SB and the CO sensor to the same diesel emissions. Time zero refers to the initial heating of the coal. For the three experiments with diesel emissions present, the optical sensor SA responds rapidly to the diesel emissions when the diesel engines were started with maximum signal changes between 4.7 and 19.2 pct, but returns to an asymptote within 1.5 pct of the ambient signal in the steady state diesel emissions. The ionization sensor SB responds with a signal change to an asymptote offset between 10.8 and 26.7 pct from the ambient pre-diesel signal. The characteristic response of the sensors to diesel emissions is due to the greater responsiveness of optical sensors to smoke particle size, and of ionization sensors to smoke particle concentration.

---

[1]Italic numbers in parentheses refer to items in the list of references at the end of this report.

The response of smoke sensors SA and SB to the coal fire POC in the presence of diesel emissions for experiment No. 4 is shown in figures 4-5. The sensors respond continuously to a change in the POC associated with the increase in the measured CO concentration. Smoke sensors SA and SB respond similarly to the fire, as opposed to their characteristically different response to the diesel emissions in figures 2 and 3. The rate of increase in diesel emissions associated with starting the engine was much greater than the POC rate of increase associated with the coal combustion. In experiment No. 4, the average rate of increase in CO associated with the diesel engine's startup was 0.0716 ppm/s, and the average rate of rise in CO associated with the coal combustion was 0.00141 ppm/s. For the slowly developing coal fires in these experiments, sensor SA's signal had a small rate of increase, or remained constant, or continued to decrease for experiment Nos. 2, 3, and 4, respectively when the 5 ppm CO alert level was reached. However, a significant reduction in SA's signal, between 25.4 and 38.0 pct for experiment Nos. 2-4, had occurred in the case of coal combustion at the 5 ppm alert value as compared to the diesel engine's startup. Based upon previous considerations (*2*) for the definition of the alarm value for a smoke sensor with a continuous analog output signal as a 10 standard deviation change in the signal from its ambient value, the alarm times of the fire sensors were compared for the coal combustion processes. In the presence of steady diesel emissions, the ambient value is the time average in the diesel emissions background. The optical path smoke sensor alarmed earlier than the point type diffusion mode ionization smoke sensor, which alarmed prior to a CO alert value of 5 ppm above ambient for each of the coal combustion experiments. For the three coal combustion experiments with background diesel emissions, the average optical density at alarm time was 0.0025 m^{-1} for the optical sensor, 0.012 m^{-1} for the ionization point sensor, and 0.024 m^{-1} for the CO sensor.

A commercially available multiple sensor consisting of a NO and a CO chemical cell with an algorithm to use the history of the CO and NO produced by an operating diesel engine to discriminate from the CO produced by a fire was unable to distinguish a smoldering coal fire with a rate of increase of CO of 0.0014 ppm/s in a volumetric flow of 4.63 cu m/s. The sensor had been shown to be applicable to higher intensity fires.

CONCLUSIONS

The results of the experiments demonstrated that multiple sensors, which include an optical path smoke sensor and a CO sensor, can be used to detect a slowly developing coal fire in the presence of diesel emissions. This result is limited to the experimental conditions considered. An optical path smoke sensor and an ionization point smoke sensor alarmed earlier than the 5 ppm CO alert level for smoldering coal combustion in the presence of diesel emissions. Current research focuses upon a decision making process, such as a neural network, which can be applied to fire sensor response to a wide variety of fire and diesel emission conditions.

ACKNOWLEDGMENTS

The authors acknowledge the miners who maintain the Safety Research Coal Mine at the Pittsburgh Research Laboratory for their assistance in preparation of the experiments.

REFERENCES

1. Edwards, J.C., R.A. Franks, G.F. Friel, C.P. Lazzara, and J.J.Opferman. "Mine Fire Detection in the Presence of Diesel Emissions." Proceedings of the 8th U.S. Mine Ventilation Symposium, Univ. of Missouri-Rolla, Rolla, MO, June 11-17, 1999, Univ. of Missouri-Rolla Press, pp. 295-301.

2. Edwards, J.C. "Overview of Mine Fire Detection." Second International Conference on Fire Research and Engineering, August 3-8, 1997, NIST, Gaithersburg, MD, Society of Fire Protection Engineers, pp. 489-499.

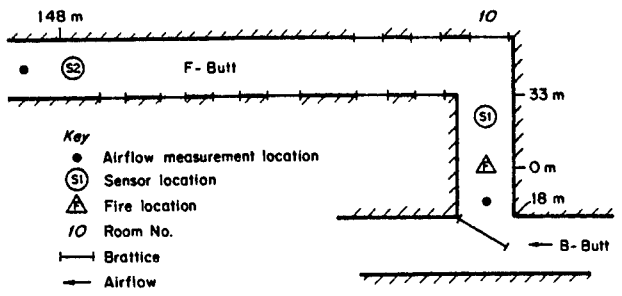


Figure 1.--Plan view of mine section.

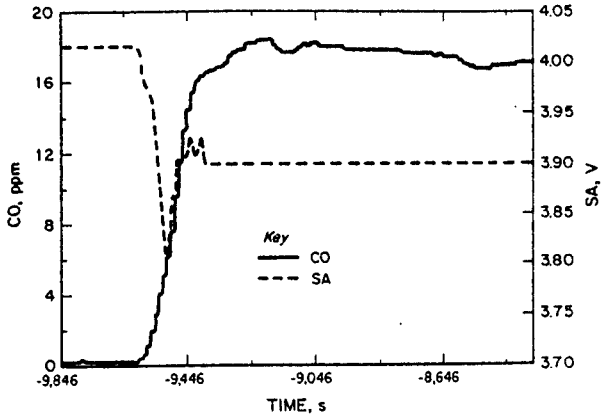


Figure 2.--CO and sensor SA response to diesel emissions.

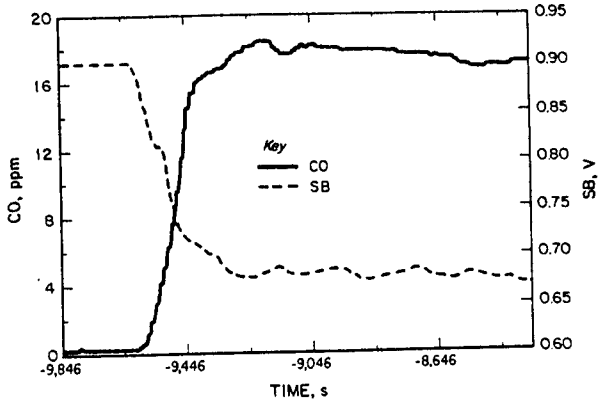


Figure 3.--CO and sensor SB Response to diesel emissions.

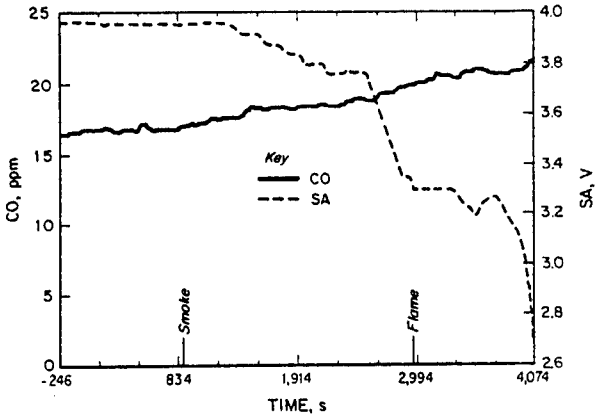


Figure 4.--CO and sensor SA response to coal fire.

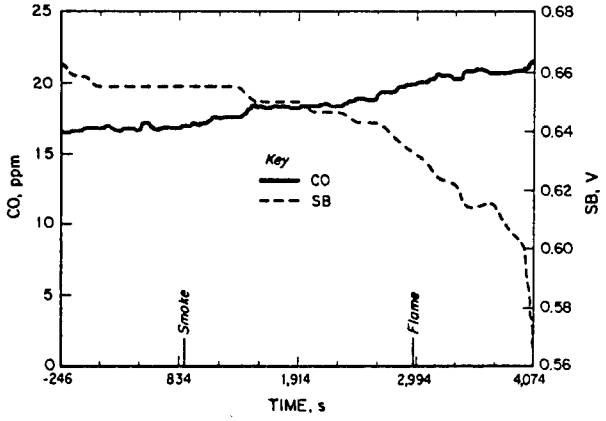


Figure 5.--CO and sensor SB response to coal fire

Window Breakage of Multi-Pane Glazing due to Radiant Exposure

Michael S. Klassen, Jason A. Sutula, Maclain M. Holton and Richard J. Roby
Combustion Science & Engineering, Inc., 9160 Rumsey Road Suite B1, Columbia, MD 21045
email: mklassen@csefire.com

and

Thomas Izbicki
Schirmer Engineering Corporation, 1701 North Collins Boulevard Suite 235, Richardson, Texas 75080-3553

Introduction

Currently, there is very little experimental data available in the scientific literature on window breakage in fires. Emmons raised this important issue in 1986 [1] by referring to a senior thesis at Harvard University by Barth and Sung in 1977 [2] as the first scientific study on this topic. Subsequently, Skelly, Roby and Beyler [3], Silcock and Shields [4], and Mowrer [5] reported experimental studies of window breakage in fires. Of these, only Mowrer's work involved windows exposed to radiant heat transfer from a simulated external fire. However, Mowrer only investigated fluxes from 2 kW/m^2 to 16 kW/m^2 and single pane glass. Thus, there is a dearth of experimental data upon which to base protection requirements for the situation of multi-pane or surface treated (i.e. coated, tinted, etc.) glass typical of many commercial applications (e.g. airport terminal installations) which may be exposed to large radiant fluxes from large fuel spill fires.

In some instances, the current standards that regulate fuel storage are quite restrictive in situations where large radiant exposures on glazings are possible from accidental fires. For example, NFPA 415-1997, Section 2-1.5 [6] requires protection in the form of a water deluge spray or automatic shutters for windows which may be within 100 feet of an aviation fuel spill. The primary concerns are the loss of the fire barrier formed by the window and transmission of sufficient radiant energy through the window to cause harm to people or materials inside the terminal. The Appendix for Section 2-1.5 asserts, without substantiation, that the need for protection arises "because the radiant heat release from a serious fuel spill fire can be expected to break glass windows up to 75 ft. (22.9 m) away and cause ignition of combustible materials within the building."[6] The purpose of this study is to obtain the data necessary to refute, substantiate or modify this requirement for window protection.

The major motivation for this study is the determination of the probability of injury or damage to people or property inside a building due to radiation from a large pool fire resulting from the ignition of a accidental fuel spill outside of the building. To fully understand this risk, it is necessary to understand the ignition criteria for various common materials found in airport terminals and also the susceptibility of human injury from exposure to radiation from fires.

Ignition of a material can vary depending on material thickness and the local conditions such as convective cooling. Research has shown that there are two primary mechanisms for solid fuel ignition; (1) heating and gasification of the solid and (2) onset of gas phase chemical reaction. These mechanisms are often competing with each other and this further complicates the development of an overall ignition "value" for a given material. Furthermore, chemical reaction may be initiated by an ignition source or may occur spontaneously (i.e. no pilot flame or spark is used). There is an abundance of literature (mostly for piloted ignition) which presents critical ignition heat fluxes (e.g. Quintiere and Harkleroad [7]), however, in general, minimum ignition fluxes will be above 10 kW/m^2.

Human tolerance to radiant heat is also very dependent on many factors (e.g. clothing, rate of heating). Data compiled from a number of different studies does indicate some scatter in the pain limits (which is probably due to the various radiant sources utilized), but the lower pain limits (around 2.5 kW/m^2) have been fairly well established [8].

In order to characterize the various glazing samples, measurements of radiant transmission, time to breakage, and surface temperature were made at various levels of incident flux. Both liquid-fuel pool fires and radiant panels were used as radiant sources. The minimum ignition flux and the lower pain limits will serve, in part, as criteria for rating the glazings and provide context for the measured transmittance, heat flux and temperature.

Sample Description

Several different types of glazing samples were tested. All samples tested during this study had dimensions of 12" x 12" or 2' x 4'. The types of glazing tested in this phase are described in Table 1.

Glazing ID	Number of Panes	Overall Thickness (in)	Description
A	2	0.5625	2 pieces of ¼" gray tinted tempered glass joined by 0.090" P.V.B. interlayer.
B	2	0.5625	2 pieces of ¼" gray tempered glass joined using a 0.060" polyvinyl butryal interlayer.
C	3	1.3125	¼" Solex green tinted tempered glass followed by 1/2" airspace followed by two pieces of 9/16" clear tempered glass laminated with Sentry Plus.
D	3	1.3125	¼" gray tinted tempered glass followed by 1/2" airspace followed by two pieces of 9/16" clear tempered glass laminated with Sentry Plus
E	2	0.5625	¼" green tinted tempered glass and ¼" clear tempered glass joined using a 0.090" P.V.B. interlayer
F	3	1.375	¼" Azurlite (Green) VE7-2M heat strengthened glass followed by a 1/2" airspace followed by two pieces of ¼" clear heat strengthened glass laminated with HRG-2
G	3	1.3125	¼" Azurlite (Green) VE7-2M heat strengthened glass followed by a 1/2" airspace followed by two pieces of ¼" clear heat strengthened glass joined by a high strength laminate.

Table 1. Glazing Descriptions.

Experiment Setup

Both liquid-fuel pool fires, burning jet fuel (Jet A), and a propane/air radiant panel served as sources of radiant energy for this study. A one-meter (diameter) burner was used for the pool fire tests. The overall setup was similar to that described in Klassen [9]. Fuel was maintained at a constant level in the pan to aid in obtaining a repeatable fire. Various levels of incident flux were obtained by changing the distance of the sample from the edge of the fire from 3 to 15 ft. Average levels of incident flux ranged from approximately 1 to 30 kW/m^2 when using the pool fire.

A radiant panel, burning premixed propane and air, was also used as a radiant source in this study. Incident flux ranges up to 50 kW/m^2 were applied to the glazing samples by varying the distance between the sample and the radiant panel. As expected, the radiant panel provided a much more uniform source than the pool fire.

Glazing samples were mounted in front of the radiant source in two different ways. In order to measure the transmittance of the glazing material (as a function of incident flux), the sample was mounted in a manner that minimized any shading of the front (or exposed) surface of the glazing. This was done in order to minimize the chance of the sample cracking due to thermal gradients. However, when determining the breakage characteristics of the glazing, the sample was held with a frame which cast a significant shadow over the exposed surface. The sample was isolated from the frame using standard foam weatherstripping.

Figure 1 depicts the arrangement of radiometers used to determine transmittance. Radiometers were placed in a plane just behind the glazing sample in a manner such that some where blocked by the sample, while others measured the unattenuated radiant flux from the source. A radiometer was also placed in the same plane as the front surface of the sample to measure the incident flux. Temperatures were also measured for both the exposed and unexposed surfaces of the sample. The thermocouples were attached to the sample with a high-temperature epoxy and high-temperature conductive paste. Radiant fluxes and temperatures were collected at 10 Hz using a data acquisition system and stored on a laboratory computer.

Results and Discussion

Figure 2 shows the trend of window breakage times (12" x 12" samples) as a function of incident flux. A number of overall trends are found from these tests. Regardless of the incident flux and the type of glazing, the temperature difference between the exposed and shaded region of the front pane was less than 200 °C at the time of window breakage. As expected, the time for the first pane to crack decreases with increasing incident flux level. In general, the front pane of the triple pane glazing tended to break quicker at a given incident flux level than the double pane glazings. However, the maximum transmittance for the triple pane glazings was still lower than double pane samples, even if the front pane of sample had cracked. Similar trends were seen for the larger sample size (2' x 4'), however the time to breakage were generally longer.

Figures 3 and 4 provide representative transmittance results as a function of incident flux level for both a 2-pane and a 3-pane glazing sample. Transmittance (and hence back-side heat flux) rose with increasing incident flux level for both 2 and 3-pane samples. In general, the triple pane glazings (Types C, D, F, and G) with an airspace performed better than the double pane laminates in the three data categories. This is not unexpected due to the additional optical surfaces in the triple pane glazings. The additional surfaces increased the amount of reflected and absorbed radiation, thus reducing the amount of radiation available to be transmitted through the glazing.

For incident heat flux levels of 30 kW/m^2 or lower, a number of general conclusions can be made. For the triple pane glazing samples, the transmittance was less than 10%, backside surface temperatures did not exceed 100 °C, and the backside heat flux did not exceed 4 kW/m^2. For double pane laminates, the transmittance was less than 25%, the back side temperature did not exceed 220°C, and the back side heat flux did not exceed 5 kW/m^2. At higher incident heat fluxes, the glazing samples degraded very quickly, generally buckling and losing integrity. At these high heat fluxes, the interior laminate vaporized and eventually ignited once the sample integrity was lost. Similar findings were found when using either the pool fire or the radiant panel as the source.

References

[1] Emmons, H.W., 1986, *Fire Safety Science – Proceedings of the Fire International Symposium*, eds. C. E. Grant and P. J. Pagni, Hemisphere, Washington, D. C., pp. 33-53.

[2] Barth, P.K, and H. Sung, 1977, "Glass Fracture under Intense Heating", Senior Project, Harvard University, Cambridge, MA.

[3] Skelly, M. J., R. J. Roby, and C. L. Beyler, 1991, *J. of Fire Prot. Engr*, 3(1), pp. 25-34.

[4] Silcock, G. W. and T. J. Shields, 1993, *Interflam '93*, pp. 747-756.

[5] Mowrer, F.W., 1998, National Institutes of Standards and Technology, NIST-GCR-98-751.

[6] NFPA 415, 1997, Standard on Airport Terminal Buildings, Fueling Ramp Drainage, and Loading Walkways, National Fire Protection Association, 1 Batterymarch Park, P.O. Box 9101, Qunicy, MA 02269-9101.

[7] Quintiere, J. G. and M. Harkleroad, 1985, New Concepts for Measuring Flame Spread Properties, *Fire Saftey:Science and Engineering ASTM STP 882*, (T. Z. Harmathy, Ed.), American Society for Testing and Materials, Philadelphia, pp. 239-267.

[8] Purser, David A., 1995, "Toxicity Assessment of Combustion Products", in SFPE Handbook of Fire Protection Engineering (Ed. P. DiNenno et. al.), National Fire Protection Association, 1 Batterymarch Park, P.O. Box 9101, Qunicy, MA 02269-9101.pp. 2-113 – 2-114.

[9] Klassen M., J. P. Gore, A. Hamins, T. Kashiwagi, 1992, *24th Symposium (International) on Combustion*, The Combustion Institute, Pittsburgh, 1713- 1719.

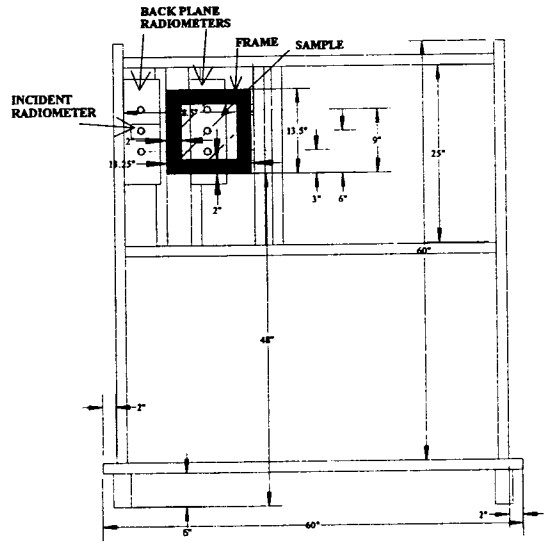


Figure 1. Schematic of radiometer and sample setup for radiant panel tests.

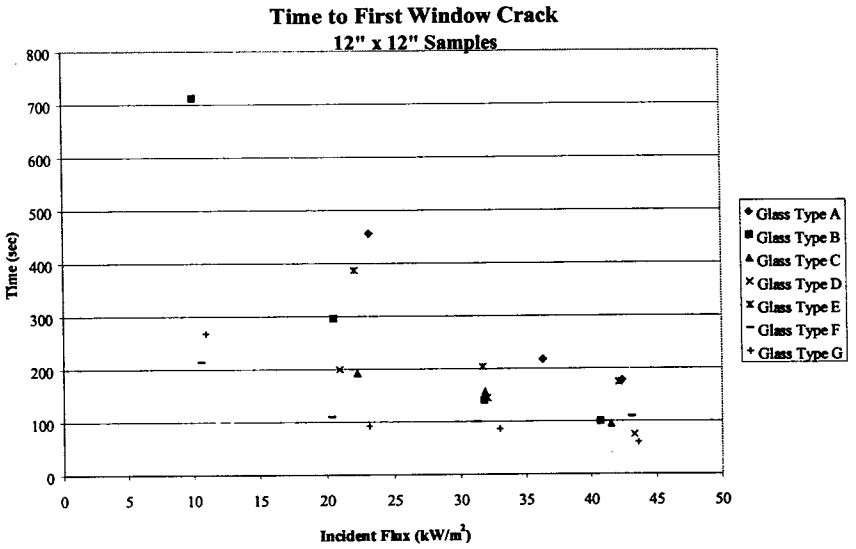


Figure 2. Breakage times of 12" x 12" samples versus incident flux.

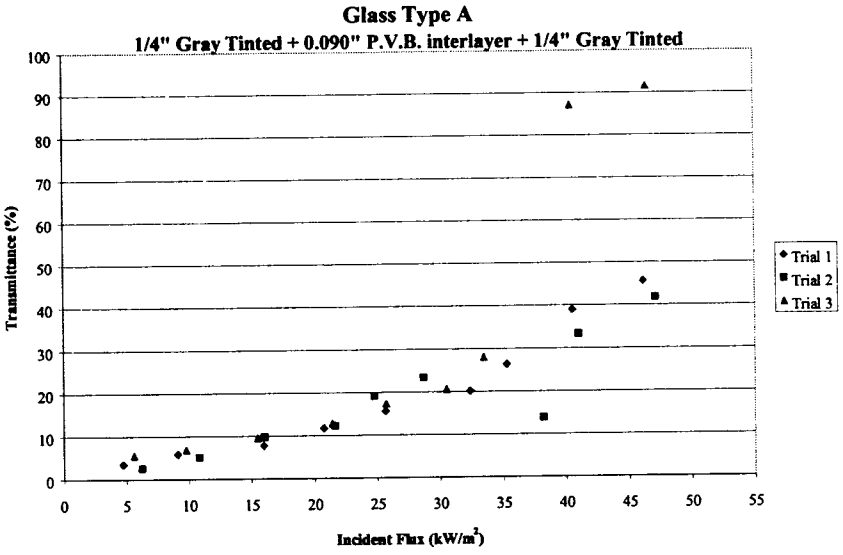


Figure 3. Representative results for 2' x 4' samples (2-pane sample).

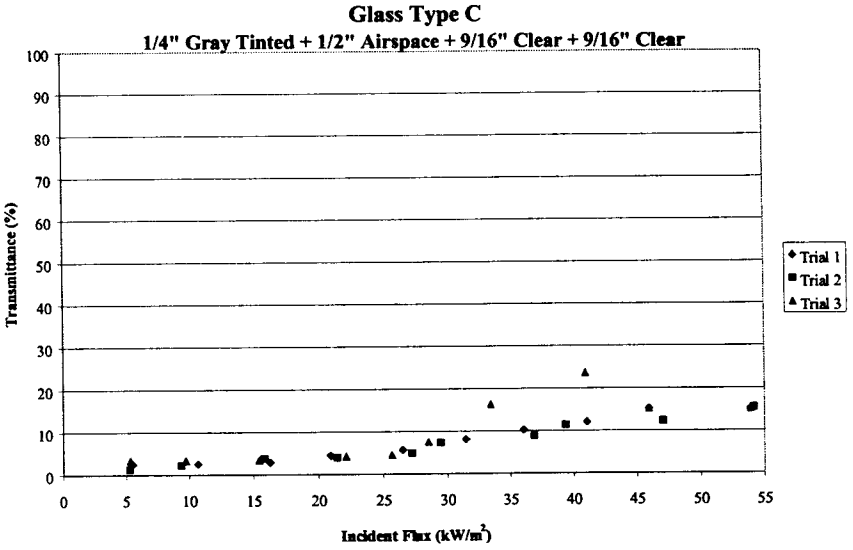


Figure 4: Representative results for 2' x 4' samples (3-pane sample).

Simulating Fire Whirls - Inviscid Swirl and Buoyancy

Francine Battaglia, Ronald G. Rehm and Howard R. Baum
National Institute of Standards and Technology
Building and Fire Research Laboratory
Gaithersburg, MD 20899
(francine@nist.gov, rehmro@nist.gov, hbaum@nist.gov)

I. Introduction

Fire whirls are a rare but potentially catastrophic form of fire. They require an organized source of angular momentum to produce the large swirl velocities observed as air is entrained into the fire plume. One of the earliest studies to systematically examine these phenomena experimentally was carried out by Emmons and Ying [1]. They produced a fire whirl by burning a pool of acetone within a rotating cylindrical screen. The most striking characteristic of the experiments is that a very tall slender column of burning gases can be produced above the pool when the cylindrical screen rotates to produce the organized angular momentum required. Such observations contrast with all other fire plume experiments without angular momentum where the plume above the pool fire grows radially as ambient fluid is entrained. These observations are even more startling because the height of the luminous region (the flame) can extend to 30 pool diameters or more.

The model proposed below is motivated by these observations: we wish to understand the mechanism by which such a long, slender cylindrical flame could arise. The most important physical phenomena involved in the fire whirl are the buoyancy generated by the gas-phase combustion and the swirl or angular rotation. While the experiments showed that the plume underwent some precession and while instabilities could arise under some conditions, often the long, slender plume stood erect for long periods of time. The behavior of the flame implies that mixing of ambient fluid is very inhibited, that dissipation is small and that the columnar flame is nearly time independent. Therefore, we assume a steady state model in which angular rotation and buoyancy are the key components, but dissipation is ignored. We leave the mathematical description of dissipation and of combustion using a mixture-fraction formulation for later analyses.

II. Methodology

The basic equations are the axisymmetric, steady state Euler equations for a perfect gas subjected to constant angular rotation. The fluid variables are density ρ, total velocity $\mathbf{u}$, the dynamic pressure p, and temperature T. The model has minimal complexity and is tractable. First, we formulate the problem under the Boussinesq approximation. Then we note that the more general non-Boussinesq problem can be reduced to that of the Boussinesq model by a simple transformation. For the Boussinesq model, the density is replaced by the ambient density ρ_0 in the inertial terms of the momentum equation. We define the head $\mathcal{H} \equiv (p - p_0)/\rho_0 + (1/2)|\mathbf{u}|^2 + gz$, a temperature function $(T - T_0)/T \equiv \Delta\theta\Theta$, and the circulation $\Gamma \equiv 2\pi r v$. The derivation of the governing equation

follows closely that presented by Batchelor [2, pp. 543-545]. We introduce a stream function ψ and find that the three quantities defined above are integrals of the equations of motion depending on ψ. Therefore, the temperature $\Theta = \Theta_0(\psi)$, the circulation $\Gamma = \Gamma_0(\psi)$, and the head $\mathcal{H} \equiv \mathcal{H}_0(\psi)$.

We find that the radial and axial components of the momentum equation can be reduced to a single equation for the stream function. We consider an upward vertical flow of gas with characteristic velocity U_0 and characteristic normalized temperature differential $\Delta\theta$ along the plane $z = 0$. Let r_0 be the characteristic radial dimension for this source of buoyant flow. Also, assume that the circulation increases with radius, approaching an asymptotic value of Γ_∞. Then, we can make the problem dimensionless using these characteristic values. Three dimensionless quantities arise: the Froude number, $\mathrm{Fr} = U_0/\sqrt{2gr_0\Delta\theta}$, the swirl number, $\mathrm{S} = \Gamma_\infty/(2\pi r_0 U_0)$, and the ratio of the "injection velocity" U_i to the scale velocity, $\epsilon = U_i/U_0$.

Then, the dimensionless equation for the stream function becomes

$$r\frac{\partial}{\partial r}\left(\frac{1}{r}\frac{\partial\psi}{\partial r}\right) + \frac{\partial^2\psi}{\partial z^2} = \frac{r^2}{2\pi^2}\left(\epsilon^2\frac{d\mathcal{H}_0}{d\psi} + \frac{z}{Fr}\frac{d\Theta_0}{d\psi}\right) - 4\,\mathrm{S}^2\Gamma_0\frac{d\Gamma_0}{d\psi}. \tag{1}$$

where, in this paper, we have chosen $\Theta_0(\psi) \equiv (1-\psi)^2, \Gamma_0(\psi) = 1 - \exp[-\psi/(1-\psi)]$, and $\mathcal{H}_0(\psi) \equiv (1-\psi)^2$. An asymptotic analysis, valid for large z, allows us to obtain an approximate solution which can be used to provide boundary conditions for this elliptic equation. Equation (1) has been solved numerically.

By the simple transformation, first introduced by Yih [3, p. 5], we can then generalize the Boussinesq model to account for large density and temperature variations. Define a density-scaled velocity $\mathbf{u}' \equiv \mathbf{u}\sqrt{(\rho/\rho_0)}$. If we use the same functional forms for H_0, Θ_0, and Γ_0 in the non-Boussinesq model as for the Boussinesq model, we must interpret Θ_0 somewhat differently: $T = T_0/[1 - \Delta\theta\Theta_0(\psi)]$ and $\rho/\rho_0 = 1 - \Delta\theta\Theta_0(\psi)$. Also, the real dimensionless velocities must now be obtained from the pseudo velocities $\mathbf{u}'$ as follows: $\mathbf{u} = \mathbf{u}'/\sqrt{1 - \Delta\theta\Theta_0(\psi)}$.

III. Discussion

Five swirl numbers, $S = 0.0, 0.5, 1.0, 1.5$ and 2.0, were investigated to provide a global picture of the interaction between buoyancy and circulation. The zero value of the swirl number represents the hydrodynamics of the plume in the absence of circulation. The maximum value of the swirl number was chosen to be 2.0. It was found that for swirl numbers greater than 2.0, the Boussinesq approximation was invalid as evidenced by the prediction of very large pressures which violate the construction of the model. As for the non-Boussinesq model, the ratio of ρ_0/ρ ranged from 1.0 to 4.0, providing a realistic range of temperature ratios that could occur in an experiment.

Temperature profiles at $z = 2.0$ are shown in Fig. 1 for the Boussinesq model ($\rho_0/\rho = 1.0$). The profiles show the shape of the plume when subjected to different values of circulation. The non-swirling flow is very broad near the base of the plume and the temperature profile extends to a radius of 3.0. Once circulation is imparted to the flow, the temperature profiles narrow in width. The non-Boussinesq or "thermally expandable" model ($\rho_0/\rho = 4.0$) shown in Fig. 2 emphasizes the large temperature and density gradients. Clearly, the peak temperatures along the centerline

increase by a factor of 2.0. Increasing the circulation has the same effect of constricting the radial spread of the plume.

The axial velocity also plays an important role in the plume development, and emphasizes the straining effects, as seen in Figs. 3–4. The plume in the absence of circulation for the Boussinesq model (Fig. 3) has a peak axial velocity that is the same order of magnitude as the characteristic buoyancy velocity U_0. The plume is very broad near the base and the axial velocity extends over several radii. Increased circulation dramatically increases the vertical velocity and constricts it radially. Figure 4 shows the effects of circulation for the non-Boussinesq flow. The axial velocities double in magnitude and produce a highly stretched plume. The axial velocity generates strain fields which contribute to the plume stretching.

The trends for the swirl (azimuthal) and radial velocities do not change as dramatically as the axial velocity between the Boussinesq and non-Boussinesq cases. However, the swirl velocity is still a contributor of the plume's development. The swirl velocity peak is offset from the plume nominal centerline, and the velocity decays further out radially. The maximum swirl velocity shifts closer to the centerline with increasing circulation, consistent with the other variables discussed. Furthermore, the azimuthal velocity also increases the straining effect observed in swirling plumes. As for the radial velocity, the values are negative and very small (on the order of 0.02). The negative values of radial velocity indicate that fluid is pulled toward the center of the plume to replace fluid displaced upward by the buoyant axial flow.

Figures 5 and 6 are plots of the dynamic pressure normalized by the dynamic reference pressure $0.5\rho_0 U_0^2$. In the swirling buoyant flow, both the axial and the azimuthal velocities become large and more confined to a "core" region near the axis when the swirl number is increased. Such large velocities imply that the dynamic pressure decreases and the normalized pressure becomes a relatively large negative number as seen in these figures. (For reference, the nondimensional static pressure is about 60,000 so that the total pressure, i.e., static and dynamic, remains positive.) Contrasting Figs. 5 and 6 shows that the the non-Boussinesq model undergoes far greater dynamic pressure deviations with increasing swirl than does the Boussinesq model.

References

[1] Emmons, H.W. and S.-J., Ying, The Fire Whirl, *Eleventh Symposium (International) on Combustion*, pp. 475–488 (1967).

[2] Batchelor, G.K., *The Theory of Homogeneous Turbulence*, Cambridge University Press, Inc., Cambridge, 1974.

[3] Yih, C.-S., *Dynamics of Nonhomogeneous Fluids*, The MacMillan Company, New York, 1965.

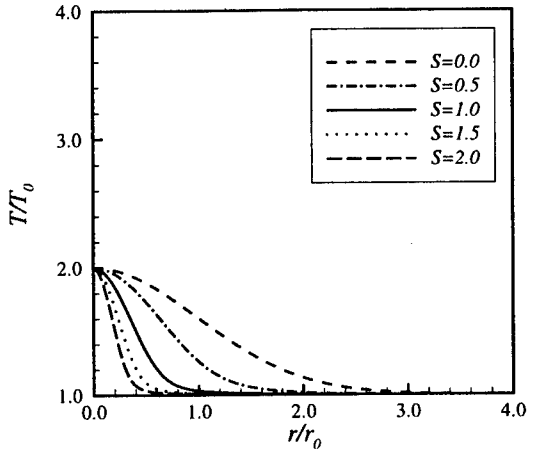


Figure 1: Profiles of temperature versus radius at $z = 2.0$ and $\rho_0/\rho = 1.0$.

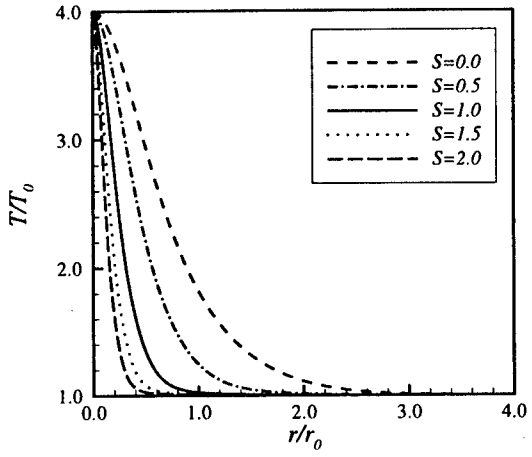


Figure 2: Profiles of temperature versus radius at $z = 2.0$ and $\rho_0/\rho = 4.0$.

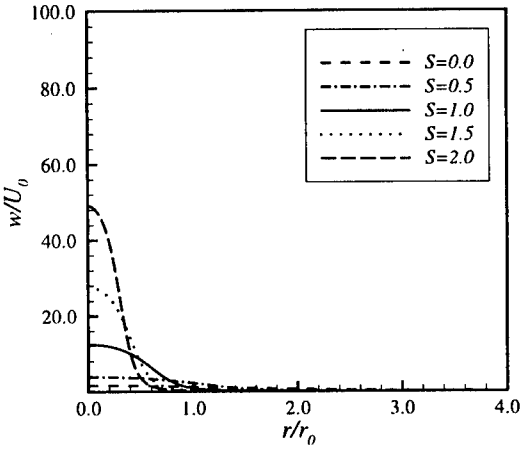


Figure 3: Axial velocity profiles versus radius at $z = 2.0$ and $\rho_0/\rho = 1.0$.

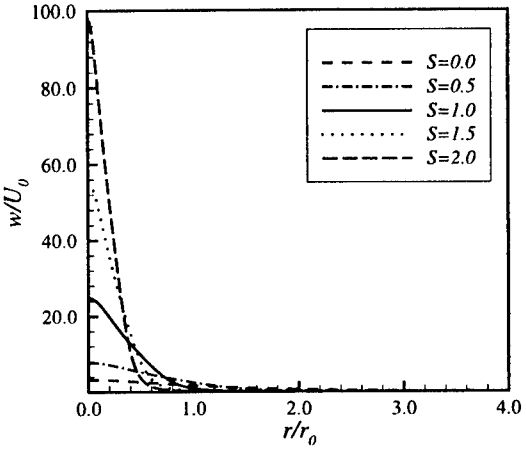


Figure 4: Axial velocity profiles versus radius at $z = 2.0$ and $\rho_0/\rho = 4.0$.

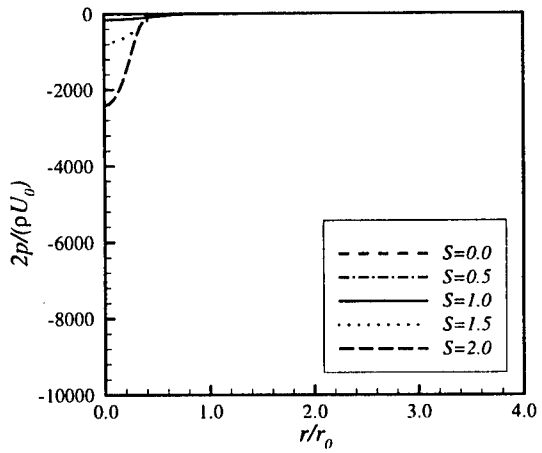


Figure 5: Profiles of the pressure coefficient versus radius at $z = 2.0$ and $\rho_0/\rho = 1.0$.

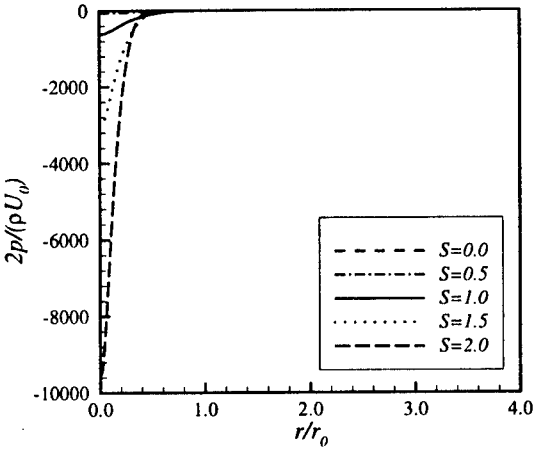


Figure 6: Profiles of the pressure coefficient versus radius at $z = 2.0$ and $\rho_0/\rho = 4.0$.

Progress towards a Computational Tool for the Study of Fire Suppression in a Complex Geometry

Kuldeep Prasad[1], Gopal Patnaik and K. Kailasanath
Laboratory for Computational Physics and Fluid Dynamics
Naval Research Laboratory, Washington DC.
prasad@lcp.nrl.navy.mil, patnaik@lcp.nrl.navy.mil, kailas@lcp.nrl.navy.mil

Shipboard fires present a variety of novel problems for firefighters due to the unique nature of the environment. In particular, the enclosed spaces permit heat and smoke to build to levels far in excess of those found in most structural fires. Further aggravating the situation is the high rate of heat transfer through the steel bulkheads and decks, which contributes to rapid fire spread. Firefighting in cluttered machinery spaces has its unique challenges. Presently, the impact of obstructions to the water mist nozzle spray pattern on fire suppression in highly cluttered machinery spaces is not well characterized. The role of water-mist system parameters such as flow rates, nozzle spacings and droplet diameter on overall fire suppression in large enclosures has not been systematically studied. Further, the effect of fire types, size and location on system performance is not well understood.

In the past, Prasad et. al [1], [2] have investigated the water-mist suppression of small scale liquid methanol pool fires. They developed a mathematical model for studying the suppression effects of water-mist on the evaporation and burning of a liquid methanol pool. A series of parametric studies was performed to determine the effect of droplet number density, injection velocity and diameter on entrainment and overall suppression of pool fires. These results were reported in terms of reduction in peak temperature, effect on burning rate and changes in overall heat release rate. The model used to simulate the fire was too complex to be used directly in large, complex geometries.

The objective of the current research is to develop an advanced computational tool that can be used to assess the damage (and effectiveness of control measures) to the interior compartment of a surface ship / submarine under different war fighting and peacetime scenarios. We will combine several recent developments in computational techniques to develop a tool that can be used to simulate the reactive flow inside the complex geometry of a ship compartment. The ultimate goal of this project is to evaluate the firefighting capabilities of the water mist system in a realistic machinery space environment. Fire models with varying degree of complexity will be incorporated to determine the appropriate level of detail required.

As a first step toward accomplishing this goal, we have performed computations to simulate a fire in a geometry that replicates the Shadwell 688 experiments. These tests serve as a demonstration of our capability to simulate fires and smoke spread in a large enclosure. Our results show the movement of hot gases through the various compartments on board the ex-USS Shadwell via the various doors and hatches. Velocity vectors and temperature profiles provide a detailed understanding of the complex flow field and vortical structures that are established within the ship compartment.

The Model

Several recent developments in computational techniques have been combined to develop a tool that can be used to simulate the reactive flow field inside the complex geometry of a ship compartment. The main obstacle in solving the reactive flow field inside a complex ship compartment is the difficulty of generating computational meshes. Another difficulty is the requirement that different physics be solved in different regions of the calculation. We have adopted a method of domain decomposition called "chimera" [3] which allows a system of relatively simple grids, each describing

[1]Science Application International Corporation, VA.

a component of the complex geometry, to be combined into a composite grid for complex geometries. Independent meshes communicate flow field information with adjacent meshes through a system of artificial boundaries also know as interpolation boundaries and hole creation boundaries,

Application of the chimera scheme requires two steps: 1) a description of how each mesh is to communicate flow field information to other meshes, and 2) execution of a flow solver that uses the communication information generated in step 1. Step 1 is performed by a code named PEGSUS [4] which determines the boundary points in a mesh which must be updated by interpolated flow variables from other meshes and calculates the required interpolation coefficients for these mesh points. In step 2, the composite mesh and the interpolation file are input into the flow solver. Conservation equations for mass, momentum and energy are employed to model the growth and spread of a fire through a three-dimensional geometry.

$$\frac{\partial \rho}{\partial t} + \frac{\partial(\rho u)}{\partial x} + \frac{\partial(\rho v)}{\partial y} = 0, \tag{1}$$

$$\frac{\partial(\rho u)}{\partial t} + \frac{\partial(\rho u^2 + P)}{\partial x} + \frac{\partial(\rho uv)}{\partial y} + \frac{\partial(\rho uw)}{\partial z} = 0, \tag{2}$$

$$\frac{\partial(\rho v)}{\partial t} + \frac{\partial(\rho vu)}{\partial x} + \frac{\partial(\rho v^2 + P)}{\partial y} + \frac{\partial(\rho vw)}{\partial z} = -\rho g, \tag{3}$$

$$\frac{\partial(\rho w)}{\partial t} + \frac{\partial(\rho wu)}{\partial x} + \frac{\partial(\rho wv)}{\partial y} + \frac{\partial(\rho w^2 + P)}{\partial z} = 0. \tag{4}$$

$$\frac{\partial(\rho E)}{\partial t} + \frac{\partial(\rho E + P)u}{\partial x} + \frac{\partial(\rho E + P)v}{\partial y} + \frac{\partial(\rho E + P)w}{\partial z} = \frac{\partial q_x}{\partial x} + \frac{\partial q_y}{\partial y} + \frac{\partial q_z}{\partial z} - \rho g v. \tag{5}$$

In these equations x, y and z denote the independent spatial coordinate and t denotes the temporal coordinate; ρ the mass density; u, v and w are the x, y and z components of the fluid bulk velocity; P, the pressure; E, the total energy per unit mass; g, the gravitational body force per unit mass. Chemical reactions between the fuel and oxidizer are simulated as a point exothermic energy release process. This representation of the flame was restricted to a single fine mesh surrounding the immediate vicinity of the fire.

The solution of three-dimensional reactive flow equations on a large number of grid points is a challenging computational task, beyond the capabilities of any existing single processor. The Chimera method requires that fairly small number of meshes with a large number of grid points be coupled together in a rather complex manner. This configuration is not easily adapted to a distributed memory parallel computer, but fits perfectly on a shared memory architecture as found in the SGI Origin 2000 or Cray C-90. At every timestep, equations 1-5 are solved using the BIC-FCT algorithm[5]. The BIC-FCT algorithm combines an explicit high-order, nonlinear FCT method [6] with an implicit correction process. Each equation is solved in parallel across the grid points. The meshes are processed sequentially in turn. At the end of the timestep, interpolation between meshes is performed. Shared memory turns the complex inter-mesh communication into a simple gather-scatter operation.

Results and Discussion

Numerical simulations have been completed to model a closed boat scenario in which all the external doors and hatches as well as the bilge hatches were closed. This situation corresponds to test 4-10 of the Submarine Ventilation Doctrine Test Plan [7]. A system of 17 independent, rectangular meshes (1.2 million grid points) were designed to model the 13 compartments and were coupled together using "PEGSUS" to obtain a composite mesh describing the 9 doors and 8 hatches that

connect the various compartments (meshes). The fire was located in the laundry room in 1.05 m square pan with a fuel mass loss rate of 0.025 kg/s and a heat release rate of 1 mW.

Figure 1 shows the instantaneous velocity vectors at $t = 2000\ s$ in the laundry room and passageway area only. Flow in the remaining compartments has not been shown. The velocity vectors are plotted on a horizontal plane located at a height of 0.5 m above the floor. These results clearly show the flow of hot gases from the laundry room to the various ship compartments through the doors and hatches. We observe the presence of large vortical structures in all the compartments that are continuously evolving through the flow field. The hot gases accelerate as they flow through the doors / hatches due to area reduction and slow down as they enter larger compartments. Figure 2 shows the temperature in the laundry room and the passageway as a function of time. The air temperature at a height of 2.4 m above the floor starts increasing after a lag of approximately 300 seconds. The perturbations in temperature are due to the presence of unsteady vortical structures that are observed in the laundry room.

More detailed simulations will be pursued to model the fire growth and spread in complex ship geometries. Ultimately, simulations of full scale tests of water-mist systems will be conducted in a cluttered machinery space of the ex-USS SHADWELL. These tests will demonstrate the potential ability of water mist to extinguish both shielded and unshielded fires in full scale, relatively cluttered, machinery space applications. Several changes will be made to the present algorithms to simulate machinery spaces. These include improvements to the fire model as well as adding details to the interior of the compartments using the VCE technique [8].

Acknowledgement

The work described in this paper was performed by the Laboratory for Computational Physics and Fluid Dynamics of the Materials Science and Component Technology Directorate, Naval Research Laboratory. The work was funded by the Office of Naval Research, Code 334, under the Damage Control Task of the FY-99 BA2 Surface Ship Hull, Mechanical and Electrical Technology Program (PE0602121N) and the NRL 6.1 Computational Physics Task Area.

Reference

1. Prasad, K., Li, C. and Kailasanath, K., "Numerical Modeling of Fire Suppression using Water Mist. 4 Suppression of Liquid Methanol Pool Fires," NRL/MR/6410-98-8303, 1998.

2. Prasad, K., Li, C. and Kailasanath, K., "Optimizing Water-Mist Injection Characteristics for Suppression of Co-Flow Diffusion Flames," 27^{th} Symposium (Int.) on Combustion, 1998.

3. Steger, J. L., Dougherty, F. C. and Benek, J. A., "A Chimera Grid Scheme," in *Advances in Grid Generation*, ASME FED-Vol. 5, 1983.

4. Suhs, N. E. and Tramel, R. W., " PEGSUS 4.0 Users Manual", AEDC - TR -91 - 8, 1991.

5. Patnaik, G., Guirguis, R. H., Boris, J. P. and Oran, E. S., "A Barely Implicit Correction for Flux-Corrected Transport", J. Comput. Phys., 71:1-20, 1987.

6. Boris, J. P. and Book, D. L., "Flux Corrected Transport I. SHASTA, A Fluid Transport Algorithm That Works,", Journal of Computational Physics, 11 (1) pp. 38-69 (1973).

7. Williams, F. W., Tatem, P. A., Cummings, W. M. and Scheffey, J. L., "Submarine Firefighting Program Test Plan," NRL Letter Report 6180/0134, 1995.

8. Landsberg, A. M. and Boris, J. P., "The Virtual Cell Embedding Gridding Method: A Simple Approach for Complex Geometries," AIAA Paper No. 97-1982, 1997.

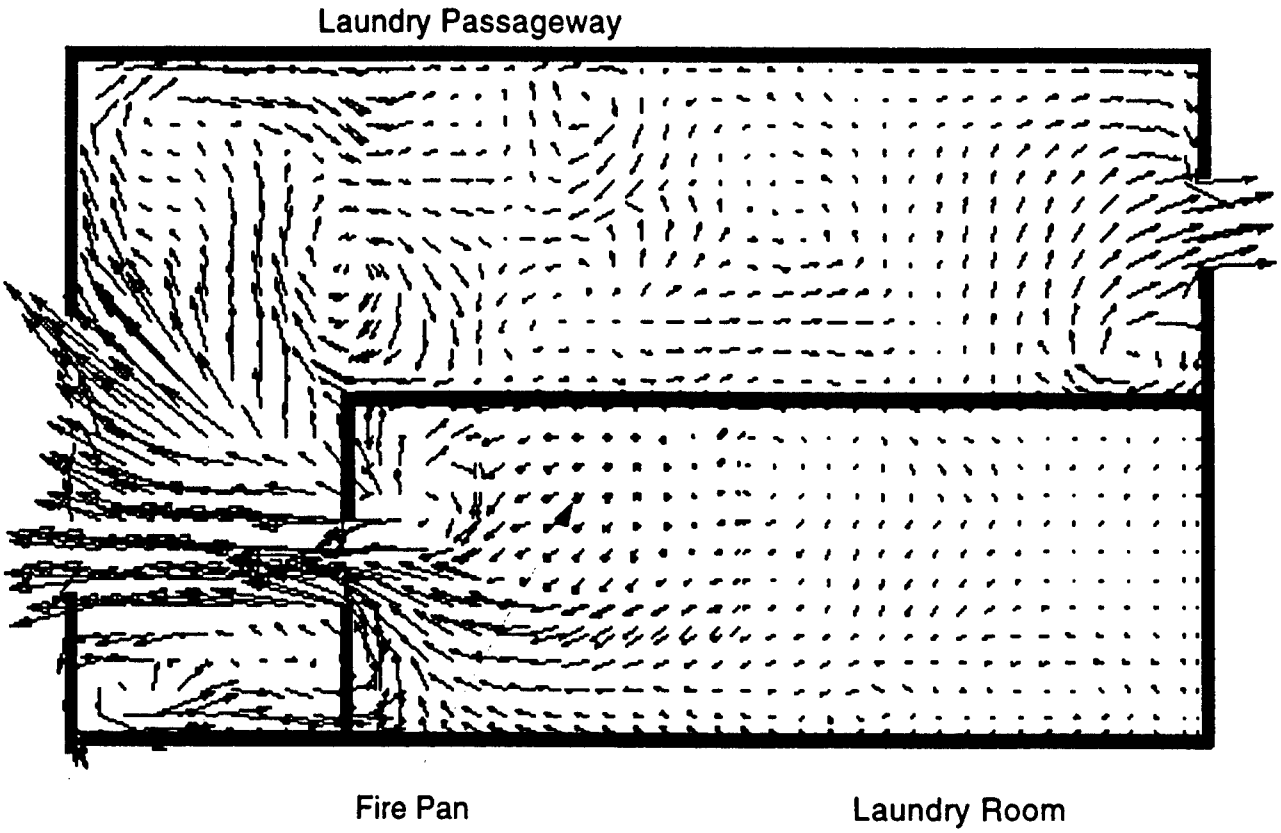


Figure 1: Instantaneous velocity vectors in the Laundry Room and passageway at time t=2000 s and a height of 0.5 m above the floor.

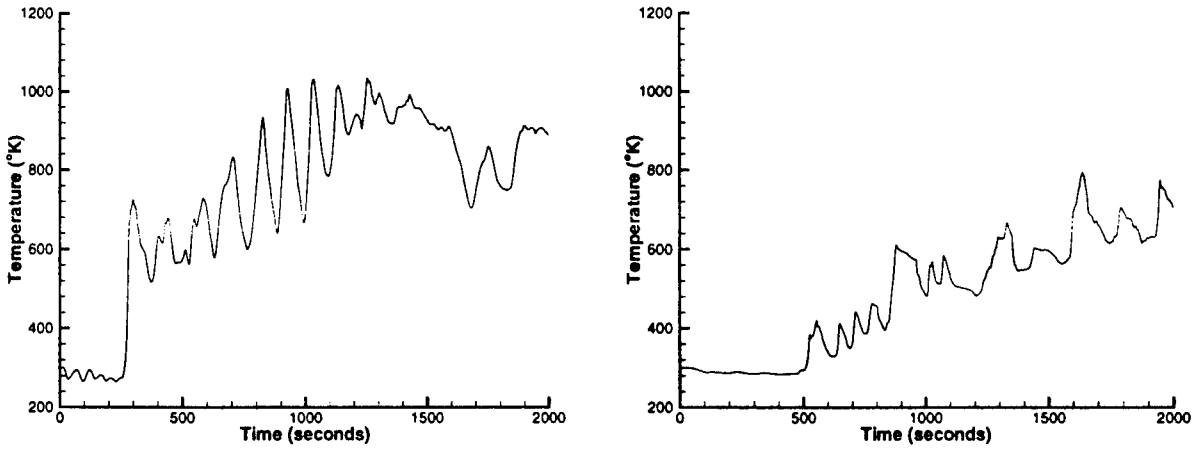


Figure 2: Temperature profiles as a function of time.

Inhibition of Premixed Methane-Air Flames by Water Mist

S. P. Fuss[1], D. J. Dye, B. A. Williams[2], J. W. Fleming
Combustion Dynamics Section, Code 6185, Chemistry Division
Naval Research Laboratory, Washington, D. C. 20375-5342 USA

[1] ASEE-NRL Postdoctoral Fellow
[2] Corresponding author: brad@code6185.nrl.navy.mil

Introduction

The ban on production of halons has prompted renewed interest in the use of water as a fire suppression agent. Since water is ubiquitous, non-toxic, environmentally benign, and has a high heat capacity per unit mass, it is in many respects an ideal fire suppression agent. Nevertheless, water is a liquid at ambient temperature rather than a gas like Halon 1301 and current fluorocarbon alternatives. Many engineering issues thus arise concerning droplet size distribution, delivery into the space to be protected, and complexity of the generation system. As a result, most fire suppression systems based on water use far more agent than should be required based on a comparison of its sensible enthalpy with that of nitrogen or carbon dioxide. In attempting to broaden the range of fire protection applications for which water can be used, it is desirable to determine to what degree the effect predicted based on water's thermal properties can actually be achieved under favorable conditions.

Furthermore, water may be useful as a delivery method for non-volatile chemical fire suppressants. A number of elements and compounds have been demonstrated to exhibit far better chemical fire suppression than bromine [1]. Most of these contain metallic elements, and have very low volatility. Water is a good solvent for many metallic compounds; thus it may be useful as a dispersing agent for many new suppressants. Since water's effect on flames is almost entirely thermal, it is unlikely to interfere with the chemical activity of a solute.

We have determined the effect of sub-micron water droplets on the flame speed of methane-air mixtures, as a first step toward investigation of enhancement by solutes. The laminar flame speed is an indicator of the effectiveness of inhibition. Inhibition and extinction are related but distinct concepts; extinction by water mists in non-premixed flames is addressed elsewhere in these proceedings [2]. Measurements were also performed using nitrogen and tetrafluoromethane (CF_4) as benchmark agents. These measurements were in good agreement with those from a previous study [3] and the nitrogen data was in good agreement with a numerical simulation.

Experimental Procedure

A Hencken burner apparatus was used to establish a premixed methane-air flame at atmospheric pressure. The nozzle diameter was 5.4 mm. Water mist was introduced into the flame by a stream of air flowing through a constant output atomizer (TSI Model 3076). Laboratory supply air was filtered and dried (Whatman 64-01) upstream of the atomizer, producing air with relative humidity less than 5%. Gas flow rates were set in the range 550 – 1750 ml/min using mass flow control devices (Sierra Model 860C). It was determined that the uninhibited flame speed was insensitive to the total flow rate over this range. Ultra High Purity methane (99.99% - Scott Specialty Gases) was used as the fuel gas.

Flame speeds were measured using the total area method as described by Andrews and Bradley [4]. The luminous flame surface was imaged with a digital camera in a 640 x 480 pixel array using a neutral density filter. Images were captured and averaged over a period of four seconds (10 samples) using custom designed applications in LabView 4.0 (National Instruments). A sixth-order polynomial was fit to each image and integrated to give the flame surface area.

The delivery of water mist into the flame was somewhat problematic. The constant output atomizer delivered a continuous stream of sub-micron sized droplets (0.35 μm @ 30 p.s.i.), however the high delivery pressures produced flow rates that were too high to stabilize a flame on the burner. Consequently, a portion of the air flow was bled to a dump stream with a calibrated rotameter to measure the flow rate. One

difficulty in controlling the water concentration is that, if metering valves are used, the water tends to collect in large droplets that do not get carried to the flame. Alternatively, controlling flow rates by varying the flow resistance introduces more surface area for droplets to collect on walls. Tube lengths between the droplet generator and the burner were minimized to eliminate droplet agglomeration on the walls. As a result, however, the range of concentrations for water was smaller than that for the gaseous agents.

Results

In order to establish the validity of the flame area measurement procedure, measurements were performed on flames inhibited by N_2 and CF_4; these results were compared with those from an earlier study [3]. Figure 1 shows these results, normalized by the uninhibited flame speed. Our measurements indicate slightly lower flame speeds for each agent than the measurements of Linteris and Truett. Modeled data are NRL calculations using PREMIX and GRI-Mech. Both sets of measurements indicate lower flame speeds for N_2 inhibited flames than are predicted by the model, however the agreement in general is fair. The precision of the measurements is high; the 95% confidence interval of the normalized N_2 inhibited flame speed is $\pm 2\%$.

The normalized flame speed is plotted in Figure 2 on a mass basis for the cases with water mist, N_2 and CF_4 as agents. The scatter in the water mist data reflects the difficulties inherent in the delivery and measurement of water mist to the flame. In spite of this, there is a clear trend towards a reduction in the flame speed with increasing agent concentration. Using least-squares fits to this data, it was determined that water mist is roughly three times more effective than both N_2 and CF_4 at reducing the flame speed on a mass basis. Table 1 (Column 3) lists the mass fraction of agent required to reduce the flame speed by 20% for each agent, based on our measurements. Previous studies [5,6] have shown that, in non-premixed flames, Halon 1301 (CF_3Br) is 2 - 2.5 times more effective at extinguishing flames than N_2 on a mass basis. If a similar relationship holds between CF_3Br and N_2 in premixed flames, the implication of this result, combined with the data in Figure 2, is that water mist can be at least as effective an inhibitor as CF_3Br on a mass basis.

Table 1 lists the calculated change in enthalpy required to raise the temperature of each agent from 300 K – 1600 K. The value for water mist includes the heat of vaporization at one atmosphere. Columns 3 and 4 list, respectively, the agent mass and mole fractions required to reduce the flame speed by 20% from the uninhibited case. Column 5 lists the product of column 2 and the ratio of agent mole fraction to oxygen mole fraction for the condition required to reduce the flame speed by 20%. Sheinson et al. [7] determined that the following quantity:

$$\Delta H = \sum_i \left(\frac{X_i}{X_{O_2}} \right) \int_{300}^{1600} c_{pi}^T \, dT \qquad (1)$$

is approximately constant for most gaseous thermal agents where the mole fractions (X) are specified as those at the condition required to extinguish a heptane pool fire. For smaller molecules such as N_2 the value is lower and the contribution of dilution and higher thermal conductivity of these molecules becomes more significant. In this expression the summation is over the agent and nitrogen present in the air. This is the expression that was used to calculate the values in column 5 of Table 1, with the exception that the calculation was performed only for the added agent. Additionally, the mole fraction used was not that for extinction but rather for the case where the uninhibited flame speed was reduced by 20%. Observation of the values in column 5 shows that the value for water is only slightly higher than those for N_2 and CF_4. This indicates that water mist can be delivered in such a way that its heat capacity is used nearly as effectively as if it were a gaseous agent.

Conclusions

Preliminary measurements performed in this study indicate that, when deployed effectively, water mist can be as effective as CF_3Br at inhibiting flames on a mass basis. This is consistent with the prediction

based on Ref. [7] that water is more efficient than Halon 1301 on diffusion flames. Water mist was shown to be approximately three times more effective by mass than other inert agents at reducing the flame speed of premixed methane-air flames (Fig. 2). Additionally, the results in Table 1 show that the thermal capacity of water mist is used effectively in comparison with gaseous thermal agents. Further measurements in this study will investigate the effectiveness of metal powders in liquid solution on reducing the flame speed. It is expected that this will enhance the effectiveness of the water mist as an inhibiting agent by adding chemical inhibition pathways to complement the physical mechanisms demonstrated here.

Table 1

Agent properties. Column 2 lists the change in enthalpy of each agent for a change in temperature from 300K – 1600K. Columns 3 and 4 list the mass and mole fractions, respectively, for the conditions required to reduce the flame speed by 20% from the uninhibited case. Column 5 is the product of column 2 with the ratio of agent mole fraction (X) to O_2 mole fraction for the condition where the flame speed is reduced by 20% from the uninhibited case.

Agent	$H_f^{1600K} - H_f^{300K}$ (kJ/mol)[a]	Mass Fraction	Mole Fraction	$(H_f^{1600K} - H_f^{300K})^* (X_{agent}/X_{O2})$ (kJ/mol)
N_2	42	5.4	5.4	12.6
CF_4	122	5.2	1.7	10.9
H_2O (l)	93	1.8	2.8	14.2

[a] Calculated from data in [8]

Acknowledgements

This work was primarily supported by the SERDP Next Generation Fire Suppression Program.

References

[1]. Babushok, V., and Tsang, W., "Relative Flame Inhibition Effectiveness of Metallic Compounds," Proceedings, 1997 Fall Technical Meeting, Eastern States Section of the Combustion Institute, Oct. 27-29, 1997, Hartford, CT, pp. 79-82.

[2]. Zegers, E. J. P., Williams, B. A., Fleming, J. W., and Sheinson, R. S., "Suppression of Non-Premixed Counterflow Flames by Water Mists," Proceedings, 1999 Fall Technical Meeting, Eastern States Section of the Combustion Institute, Oct. 11-13, 1999, Raleigh, NC.

[3]. Linteris, G. T., and Truett, L., 1996, "Inhibition of Premixed Methane-Air Flames by Fluoromethanes," *Combustion and Flame* 105, 15-27.

[4]. Andrews, G. E., and Bradley, D., 1972, "Determination of Burning Velocities: A Critical Review," *Combustion and Flame* 18, 133-153.

[5]. Hamins, A., Trees, D., Seshadri, K., and Chelliah, H. K., 1994, "Extinction of Nonpremixed Flames with Halogenated Fire Suppressants," *Combustion and Flame* 99, 221-230.

[6]. Zegers, E. J. P., Williams, B. A., Fisher, E. M., Fleming, J. W., and Sheinson, R. S., 1999, "Suppression of Non-Premixed Flames by Fluorinated Ethanes and Propanes," *Combustion and Flame*, currently in review.

[7]. Sheinson, R. S., Penner-Hahn, J. E., and Indritz, D., 1990, "The Physical and Chemical Action of Fire Suppressants," *Fire Safety Journal* 15, 437-450.

[8]. Chase Jr., M. W., Davies, C. A., Downey Jr., J. R., Frurip, D. J., McDonald, R. A., and Syverud, A. N., 1985, JANAF Thermochemical Tables, Third Ed.," *Journal of Physical and Chemical Reference Data* 14, Supplement 1.

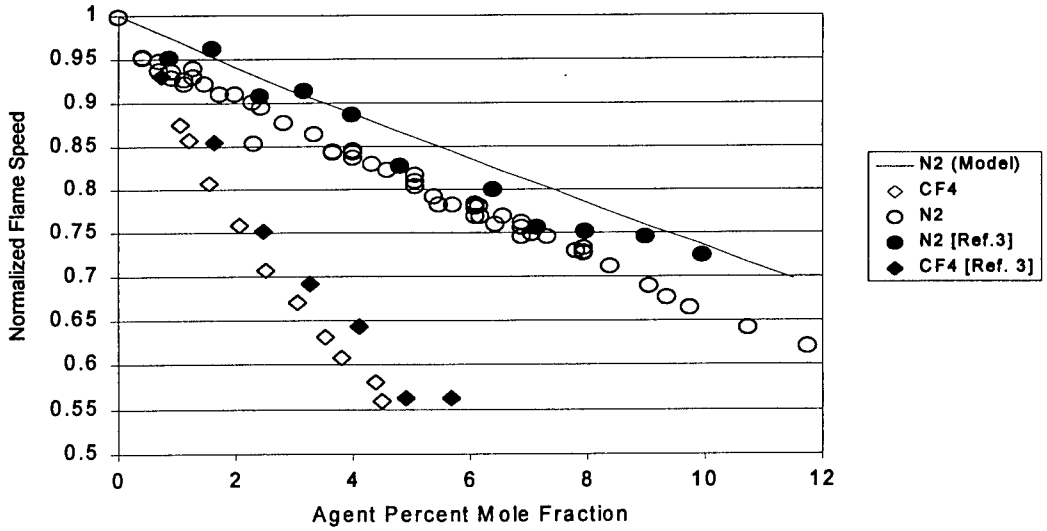


Figure 1: Premixed methane-air flame speed as a function of agent mole fraction, normalized by uninhibited flame speed. Open points are measurements from present study, filled points are from Ref. [3] and line represents model data for N_2.

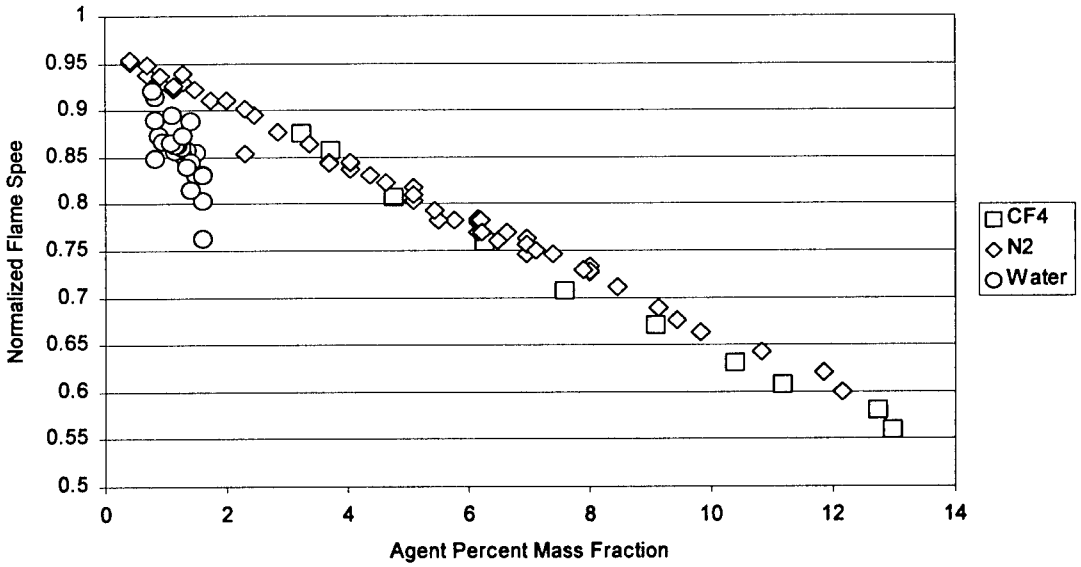


Figure 2: Premixed methane-air flame speed as a function of agent mass fraction, normalized by uninhibited flame speed. All points represent measurements from present study.

Water Mist Suppression of Non-Premixed Counterflow Flames

E.J.P. Zegers[1], B.A. Williams, R.S. Sheinson, and J.W. Fleming[2]
Combustion Dynamics Section, Code 6185, Chemistry Division
Naval Research Laboratory, Washington, DC 20375-5342 USA

[1] National Research Council Postdoctoral Fellow (1997-1999).
[2] Corresponding author: fleming@code6185.nrl.navy.mil .

Introduction

Water mists possess many attributes of the ideal fire suppressant. They are non-toxic, non-corrosive, and have zero ozone depletion and global warming potentials. Water mists also offer significant cooling capacity, due to the heat of vaporization associated with water in the liquid phase. Conventional sprinkler systems typically produce sprays of droplets with diameters on the order of 800 μm. Mists differ from sprays in that they are composed of droplets with diameters below 200 μm. The small droplet size leads to larger surface to volume ratios and longer suspension times, improving water vaporization in the fire. Less water is therefore required to extinguish the flames, and the liquid water residue is minimized. Small droplets also follow the combustion gases more closely, and have the capability of reaching obstructed areas. These attributes have prompted the U.S. Navy to adopt water mist systems as replacements for Halon 1301 systems, in machinery space total flooding applications aboard certain classes of ships.

Nevertheless, the nature of the interaction between water mists and flames has not been fully investigated. Mists extinguish flames mainly by increasing the heat capacity of the reactant streams. Water in the vapor phase also dilutes the reactants. The behavior of the droplets in the combustion flow field dictates where the droplets evaporate, the impact they have on the reaction zone, whether they evaporate completely or not, and thus the effectiveness of the mist. A better understanding of the relationship between mist droplet size, concentration, droplet evolution in the flow field, and flame extinction will guide water mist system optimization. Lentati and Chelliah (1998a, 1998b) investigate this relationship numerically, by modeling the behavior of water mists in methane/air counterflow flames. In the present study, the relationship is investigated through water mist experiments in non-premixed counterflow propane/air flames.

Experimental Setup

The counterflow burner used to conduct the water mist experiments has been described previously (Papas, 1996; Zegers, 1999). Fig. 1 shows a diagram of the burner setup. Propane flows from the top tube. The mist is supplied in the air stream from the bottom tube. The tubes are housed in a Plexiglas chamber, which is continuously purged with nitrogen. Both tubes have inner diameters of 10 mm, and are 10 mm apart. For gaseous reactants in this configuration, a relationship exists between the local strain rate imposed on the flame and the global strain rate, calculated from burner gap size and reactant velocities and densities (Fisher, 1997). This burner specific relationship is used in the present study to calculate local strain rates. The relationship provides the local strain rate that would be imposed on the flame if the mist were not present.

The mists are produced using a TSI Inc. model 3450 Vibrating Orifice Aerosol Generator (VOAG), based on the design of Berglund and Liu (1973). Water is forced through a pinhole that is piezoelectrically excited. At specific resonant frequencies, the water jet breaks up into a monodisperse droplet stream. This stream exits the generator through a hole in the dispersion cap. By forcing air to exit through this same hole, the droplet stream is dispersed into a cloud as it exits the droplet generator and enters the counterflow burner's bottom tube. The aerosol then mixes with a secondary air stream when additional air flow is needed, and the mixture proceeds up the tube to the reaction zone. Using a 5 μm diameter pinhole, monodisperse droplet streams with a size distribution peak at diameters of 14, 18, or 24 μm have been produced. With a 10 μm diameter pinhole, monodisperse streams of 25, 30, and 37 μm droplets have been obtained.

The evolution of the mists in the counterflow field is studied using Phase Doppler Particle Anemometry. Based on this technique, droplet diameters, axial velocities and number densities are measured at discreet points in the field. The PDA beams enter, and the light scattered by the particles exits the Plexiglas chamber through optical windows. The burner lies on a translation stage, such that the PDA probe volume can be positioned anywhere in the gap between the opposed tubes. In the present investigation, the axial position of the flame is determined by centering the PDA probe volume in the middle of the flame's visible emission zone.

Results

Droplet Behavior

Figures 2a and 2b show the size distribution evolution, in propane/air counterflow flames, of 30 and 18 μm mists respectively. The figures provide the number densities of the various size droplets in the flow as a function of axial position (x), along the burner's axis (r = 0 mm). The local strain rate (K) imposed on the flames corresponds to approximately 30% of the extinction strain rate for the uninhibited flame (K_{ext} = 608 s^{-1}). The air and droplets exit the lower tube at x = 0 mm; the propane exits the upper tube at x = 10 mm. The flames are located at x = 5 and 4.5 mm, in the 30 and 18 μm mist experiments respectively. In both cases, the diameter of the droplets changes very little before the flame is reached, with the 30 or 18 μm droplets dominating the size distribution. In the flame region, the droplets evaporate, and the peak in the size distribution shifts to smaller diameters. Very few droplets are detected 2 mm after the flame.

Figures 3a and 3b focus specifically on the number density profiles of the 30 and 18 μm droplets respectively. Number density is plotted versus axial position. In both experiments, the density first increases with axial position; then quickly drops in the flame region. Three effects combine to explain the shape of the number density profiles.

The main effect is related to the velocity profiles of the 30 and 18 μm droplets, provided in Figs. 3a and 3b respectively. At the lower tube exit, the droplets have roughly the same velocity as the gas stream. As the gas stream's axial velocity changes in the counterflow field, the equilibrium in velocity between the liquid and gas phases is lost, and the drag forces act to reestablish it. The droplet velocity profile therefore follows that of the gases: the velocity initially drops as the gases move towards the stagnation plane; it then increases when the hot gases expand in the reaction zone, before it drops down again, close to the stagnation plane. In regions where the droplets are decelerating, faster droplets catch up to slower ones, and the number density will tend to rise. In the flame region, the droplets accelerate, which tends to reduce their number density. Figures 3a and 3b show that the impact of axial velocity gradients on droplet number density is significant, with variations in number density well correlated with variations in velocity.

Furthermore, as the air exits the lower tube, the flow streamlines begin to diverge in the counterflow field, producing radial drag forces on the mist. Due to this effect, the droplets move away from the burner axis. The divergence of the air flow therefore acts to reduce the droplet number density along the centerline. The third effect is evaporation in the flame region, which causes the droplet size to decrease, and thus also contributes to the decrease in the number densities of the 30 and 18 μm droplets.

The suppression effectiveness of a mist depends more on the flux of droplets to the flame than the number density. Figures 4a and 4b show droplet flux profiles for the 30 and 18 μm mist experiments, respectively. The fluxes are normalized by the maximum value measured at x = 2 mm: 48.2 x 10^3 and 177.5 x 10^3 droplets/s/cm^2 for the 30 and 18 μm mist experiments, respectively. The droplet flux decreases as the flame is approached, under the effects of the diverging flow and evaporation. The scatter in the data is attributable in part to experimental uncertainties, in the PDA concentration measurements in particular. Slight variations in the position of the flame over the course of the experiment also contribute to the scatter.

Flame Extinction

The suppression effectiveness of the 30 μm mist was investigated at two different loadings in a non-premixed propane/air counterflow flame. Droplet fluxes were measured on the burner axis, at x = 2 mm and a strain rate within 10% of extinction. For water mist fluxes of 1.66 and 2.48 μl/s/cm^2, extinction strain rates of 354 and 267 s^{-1} are obtained, respectively. At these strain rates, the water extinction mass fractions are 2.4 and 4.5%, compared to Halon 1301 extinction mass fractions of 3.7 and 6.5% respectively (Zegers, 1999). These results are summarized in table 1.

Conclusions

Using piezoelectric generation of aerosol droplets, the behavior of 30 and 18 μm mists in non-premixed propane/air counterflow flames was investigated. For both size mists, the peak in the droplet size distribution does not change until the flame zone is reached. The peak then shifts to smaller diameters due to evaporation. Variations in number density with axial position are strongly correlated with variations in droplet axial velocity. 30 and 18 μm droplet fluxes drop between the air tube exit and the stagnation plane, due to the effects of the diverging flow and evaporation. For both 30 and 18 μm mists, very few droplets survive the flame, suggesting that, for these size droplets, in a counterflow flame at moderate strain rate, most of the suppression potential of the mist is being used.

On a mass basis, a 30 micron mist was found to be more effective than Halon 1301 at suppressing non-premixed propane/air counterflow flames, at strain rates of 44 and 58% of the uninhibited flame extinction strain rate. Experiments are currently being conducted to study 30 micron mist suppression at lower strain rates. Mist sizes other than 30 μm are also being investigated.

This research is sponsored by the US Department of Defense's Next Generation Fire Suppression Technology Program funded by the DoD Strategic Environmental Research and Development Program.

References

Berglund, R.N., and Liu, B.Y.H. (1973) *Env. Sci. & Tech.*, **7**, 147.

Fisher, E.M., Williams, B.A., and Fleming, J.W. (1997) *Chemical and Physical Processes in Combustion*, October 27-29, 1997, p. 191.

Lentati, A.M., and Chelliah, H.K. (1998a) *Comb. Flame*, **115**, 158.

Lentati, A.M., and Chelliah, H.K. (1998b) *Twenty-Seventh Symposium (International) on Combustion*, The Combustion Institute, Pittsburgh, p. 2839.

Papas, P., Fleming, J.W., and Sheinson, R.S. (1996) *Twenty-Sixth Symposium (International) on Combustion*, The Combustion Institute, Pittsburgh, p. 1405.

Zegers, E.J.P., Williams, B.A., Fisher, E.M., Fleming, J.W., and Sheinson, R.S. (1999) Suppression of non-premixed flames by fluorinated ethanes and propanes, submitted to *Comb. Flame*.

Table 1: 30 μm mist and Halon 1301 extinction mass fractions (%).

	Extinction Strain Rate	
Agent	**354 s^{-1}**	**267 s^{-1}**
30 μm mist	2.4	4.5
Halon 1301	3.7	6.5

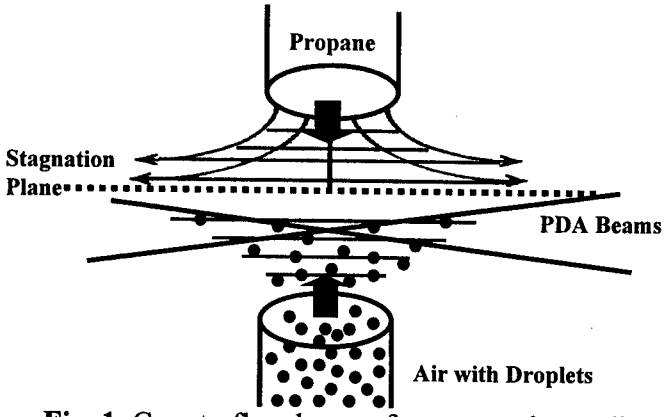


Fig. 1 Counterflow burner for water mist studies.

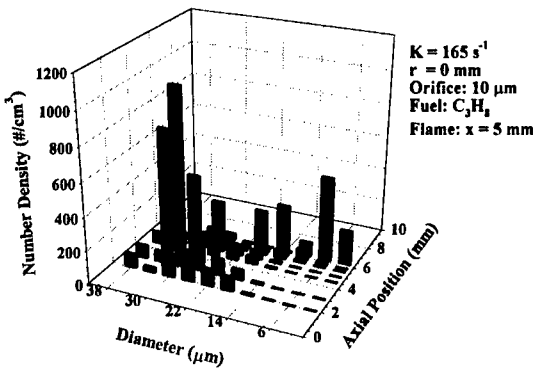


Fig. 2a Droplet size distribution evolution for 30 μm mist in propane/air counterflow flame.

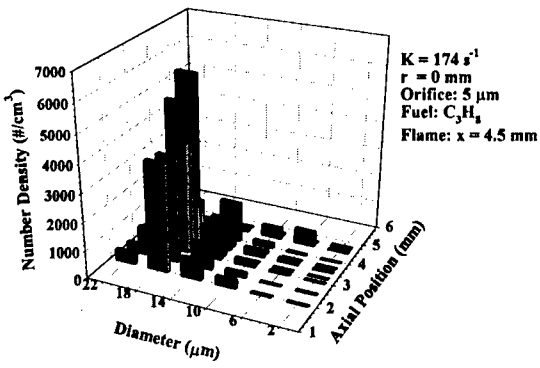


Fig. 2b Droplet size distribution evolution for 18 μm mist in propane/air counterflow flame.

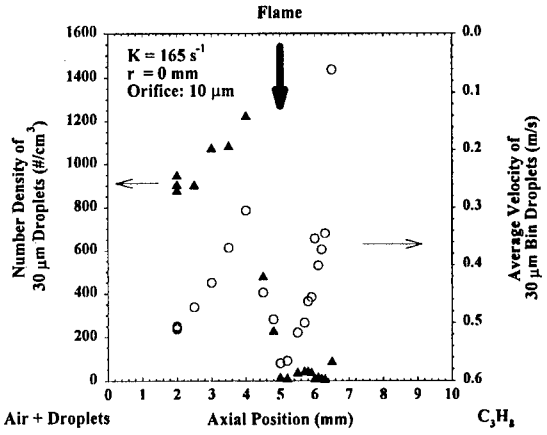


Fig. 3a Number density and velocity profiles for 30 μm droplets in propane/air/30 μm mist counterflow flame.

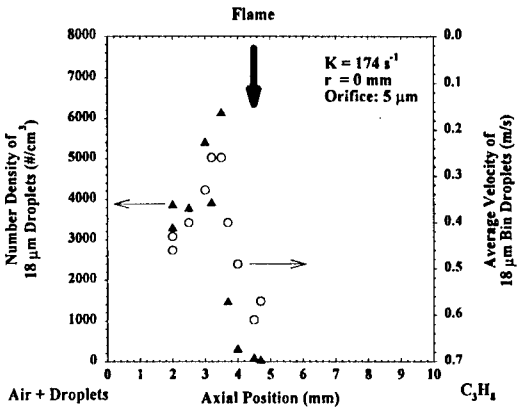


Fig. 3b Number density and velocity profiles for 18 μm droplets in propane/air/18 μm mist counterflow flame.

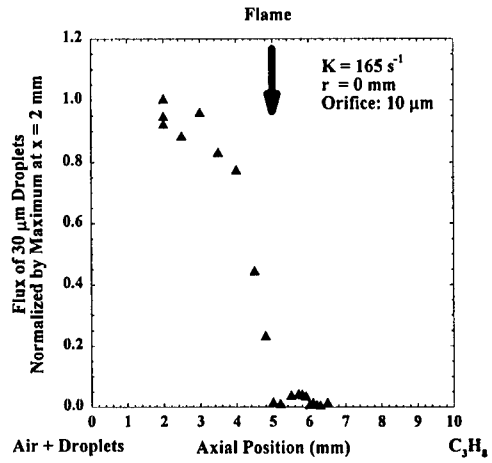


Fig. 4a 30 μm droplet flux profile for 30 μm mist in propane/air counterflow flame.

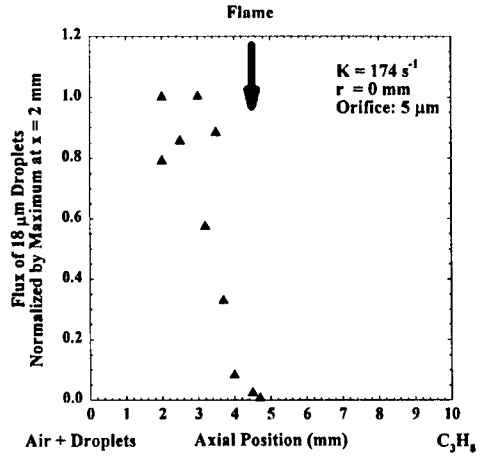


Fig. 4b 18 μm droplet flux profile for 18 μm mist in propane/air counterflow flame.

EXTINCTION OF COUNTERFLOW DIFFUSION FLAMES WITH FINE-WATER DROPLETS

A.K. Lazzarini, A.M. Lentati, and H.K. Chelliah
Department of Mechanical and Aerospace Engineering
University of Virginia
Charlottesville, VA 22903

Introduction

Interaction of fine-water droplets with laminar counterflow methane-air nonpremixed flames has been recently analyzed numerically in order to *quantify* the dominant mechanism of fire suppression [1,2]. These studies have shown that dilution of the air stream (or displacement of oxygen) with saturated water vapor reduces the extinction strain rate by about 12%. Further addition of water, in the form of fine droplets, causes thermal cooling of the flame front because of the large latent heat of vaporization. It has been shown that the droplet size has a nonmonotonic effect on the flame extinction strain rate. More importantly, addition of 3% of water by mass in the form of 20 μm droplets were shown to reduce the extinction strain rate by an additional 55%. The chemical and other physical effects associated with fine-water droplets were shown to have very small effect.

Another significant finding in these initial studies is that, on a mass basis, 20 μm water droplets are equally effective in suppressing counterflow flames as the chemical suppressant halon 1301 [2]. Since these numerical studies were not supported by any experimentation or analytical results, a major effort was undertaken to provide such validation data. This paper reports the details of this effort with very encouraging findings.

Experimental Method

In experiments, a steady, planar, nonpremixed flame established within the mixing layer of a counterflow of methane and air is employed. The fine-water droplets are introduced sufficiently upstream of the air stream so that the air is saturated and droplets are uniformly dispersed at the exit of the air nozzle. This experimental setup is very similar to that assumed in previous numerical calculations [1,2], while the key differences between experiments and numerics are discussed below.

The major challenges in experiments are generation of fine-water droplets in a steady manner, with a monodispersed drop size distribution. The latter can simplify the analysis of the droplet size effect on flame extinction. Achieving these two tasks simultaneously in an experimentally efficient manner proved to be rather difficult. Figure 1 shows a schematic of the experimental setup of the counterflow burner, where the fuel and air nozzles are made from Pyrex glass. As indicated in the figure, the droplet generator is located about 1 m above the exit of the air nozzle, and the Pyrex tubes proved to be very useful in observing the level of droplet/particle condensation on the inner walls. Two types of droplet generators were used, (a) piezoelectrically excited fluid jet atomization system acquired from Fluid Jet Associates [3] and (b) ultrasonic fluid surface breakup system acquired from Sono-tek. The first atomizer can generate truly monodisperse droplets, but this system with a very narrow

plate hole (10μm hole for about 20μm droplets) proved susceptible to clogging and erosion problems. By varying the plate hole diameter, this atomizer can be used to generate different monodisperse drop sizes. The second atomizer from Sono-tek was found to be rather simple to implement and is free of the operational problems of the Fluid Jet atomizer, but the droplets generated have a rather wide size distribution. The median droplet size of the ultrasonic atomizer can be varied by selecting a different nozzle tip length and resonance frequency. Two different water feed systems were developed for each type of atomizer because of the supply pressure requirements. The method of calibrating the mass flow rate is extremely important for data validation and considerable effort has been devoted to address this issue. The calibration method will be complemented with future PDPA experiments to be conducted at NIST.

Experimental Results and Comparison with Numerics

The ultrasonic atomizer described above with a median drop diameter of about 20 μm and a Sauter mean diameter (SMD) of about 30 μm is employed here to investigate interactions between water droplets and a nonpremixed laminar methane-air flame. In present experiments, the flame extinction is characterized by the extinction flow strain rate, evaluated based on Seshadri's global formula [4]. With increasing droplet number density (or mass fraction of water droplets in the air stream), it is expected that the flame extinction will occur more easily, hence a lower extinction strain rate. A plot of the measured water droplet mass fraction vs. extinction flow strain of a nonpremixed methane-air flame indicating such a trend is shown in Fig. 2 (symbols).

Also shown in Fig. 2 is the predicted variation of water droplet mass fraction as a function of extinction strain rate, for 20 μm monodisperse droplets. Irrespective of the assumption of monodisperse drop size distribution in simulations, the predicted trend is seen to be in close agreement with experiments. This discrepancy of drop sizes in simulations and experiments can be easily rectified by including the discrete sectional approach [5,6], once the drop size distribution is characterized using the PDPA at NIST. Another source of discrepancy is the unsteadiness of the droplet feed rate in experiments because of rather large step sizes of the stepper motor used in the syringe pump. This is being rectified using a motor with a much finer stepping (KDS model 101 with 0.088 μm per half-step). Once these differences are addressed and the numerical model is validated, considerable information on the interaction of condensed-phase agents with flames can be obtained.

In previous simulations with water droplet and flame interactions, the extinction condition was approached by maintaining a constant mass fraction in the condensed phase. However in experiments, maintaining a constant water droplet mass fraction is a tedious task. Instead, the amount of water introduced in condensed phase is held constant and the air and fuel flow rates are changed to bring the flame to extinction. For a given water droplet mass flow rate, depending on the initial strain rate of experiments with respect to the final extinction strain rate, when the nozzle exit velocities are increased it is possible to push the flame to a stronger burning state or higher temperature. This is a consequence of decreasing water *mass fraction* in the air stream because of the higher air flow with a constant water feed rate. This phenomenon has been predicted numerically and is shown in Fig. 3. As the extinction condition is approached, irrespective of whether the water droplet mass fraction or mass feed rate is held constant, the flame temperature is seen to decrease rapidly as shown in Fig. 3.

Acknowledgment: This work is supported by National Institute of Standards and Technology, Gaithersburg, MD.

References

[1] Lentati, A.M. and Chelliah, H.K., "The Dynamics of Water Droplets in a Counterflow Field and its Effect on Flame Extinction," *Combust. and Flame*, **115**:158-179 (1998).

[2] Lentati, A.M. and Chelliah, H.K., "Physical, Thermal and Chemical Effects of Fine-Water Droplets in Extinguishing Counterflow Diffusion Flames," *Twenty-Seventh (Int.) Symposium on Combustion*, The Combustion Institute, Pittsburgh (1998), pp. 2839-2846.

[3] Takahashi, F., Schmoll, W.J., and J.L. Dressler, J.L., "Characterization of a Velocity-Modulation Atomizer," *Rev. Sci. Instrum* **65**(11), pp. 3563-3569 (1994).

[4] Seshadri, K. and Williams, F.A., *Int. J. Heat Mass Transfer* **21**, 251 (1978).

[5] Greenberg, J.B., Silverman, I., and Tambour, Y., "On the Origin of Spray Sectional Conservation Equations," *Combust. and Flame* **93**:90-96 (1993).

[6] D'Angelo, Y., Silverman, I., Gao, L.P., Gomez, A., and Smooke, M.D., "Computational and Experimental Study of Counterflow Spray Diffusional Flames," Eastern-State Section, The Combustion Institute, Hilton Head, SC, Dec. 1996.

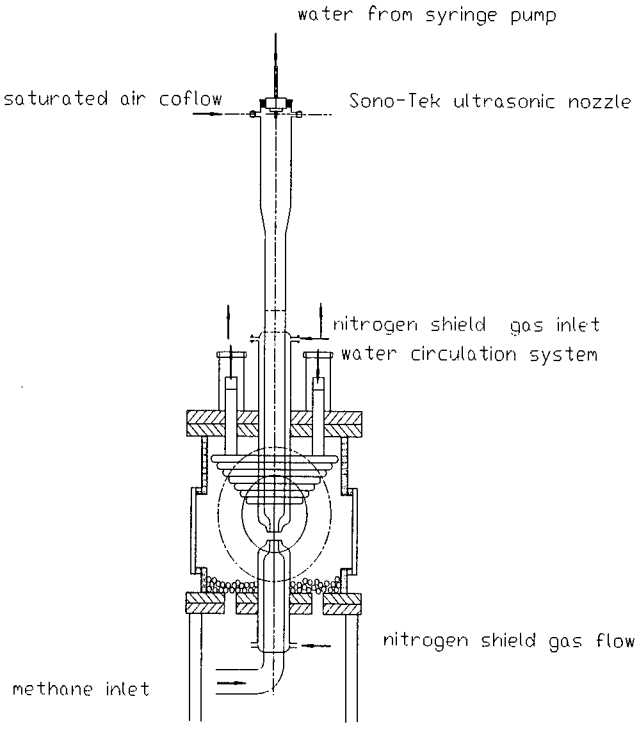


Figure 1: A schematic of the counterflow burner with the water droplet generation system.

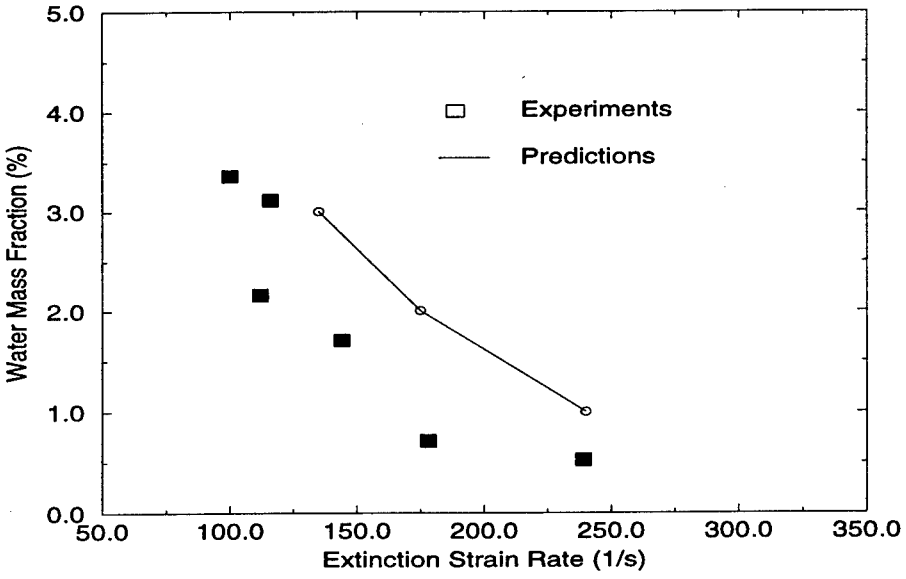


Figure 2: The water droplet mass fraction as a percentage in air vs. the flame extinction strain rate of a methane-air nonpremixed flame. Symbols are from experiments using ultrasonic atomizer and the solid line is from predictions assuming 20 μm monodisperse droplets.

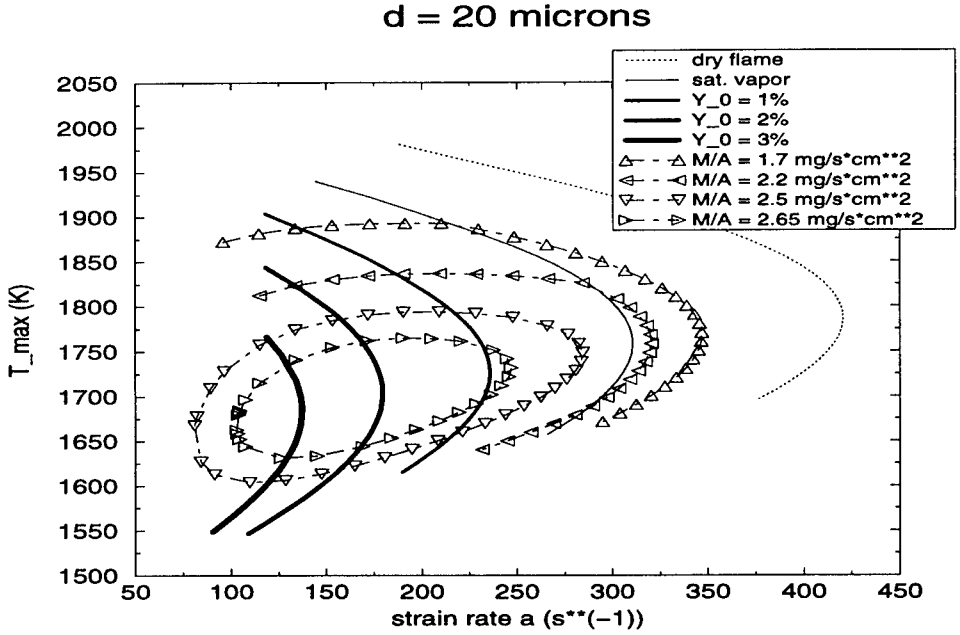


Figure 3: The variation of flame temperature as a function of flow strain rate, with water droplet mass fraction held constant (lines) and water droplet feed rate held constant (symbols).

A COMPUTATIONAL STUDY OF DRY CO/O_2 OPPOSED-JET DIFFUSION FLAME AND ITS FLAMMABILITY LIMITS

Franco C. Frate[1], Hasan Bedir[2], Chih-Jen Sung[1,3], and James S. T'ien[1,3]
[1]*Department of Mechanical and Aerospace Engineering, Case Western Reserve University, Cleveland, Ohio 44106*
[2]*Department of Mechanical Engineering, Bogazici University, Istanbul, Turkey*
[3]*National Center for Microgravity Research in Fluids and Combustion, Cleveland, Ohio 44135*
e-mail: fcf@po.cwru.edu

INTRODUCTION

Although under dry conditions (in the absence of the OH radical) the CO/O_2 diffusion flame is known to be difficult to study experimentally because of its sensitivity to hydrogen [1], the simplicity of its reaction mechanism makes it a good choice for a combustion system where both kinetics and radiation become important. In this work, a statistical narrow-band radiation model [2,3] is coupled to the OPPDIF program [4,5] to enable the study of the one-dimensional dry carbon monoxide-oxygen diffusion flame over the entire range of flammable stretch rates. Both the constant stretch rate and the two-point temperature-controlling continuation methods [6] are used to compare the extinction curves utilizing several differing reaction mechanisms found in the literature. Detailed kinetics, transport and thermal properties are used with the OPPDIF code to obtain the numerical solution for this pure gaseous diffusion flame with ambient boundary conditions of 1 atm and 300 K. This work also discusses the effect on flammability limits with and without the inclusion of a diluent/suppressant to both fuel and oxidizer streams.

METHODS

The OPPDIF program is modified with the constant stretch rate formulation and with the two-point temperature-controlling continuation method [6] and then used with the CHEMKIN II and TRANSPORT software packages [7,8] to obtain the numerical solutions for the dry CO/O_2 diffusion flame. OPPDIF is modified by changing the original program from a plug flow to a potential flow formulation. Therefore, the stretch rate, based on the radial velocity gradient on the fuel side, is the eigenvalue of the system. Radiation losses are known to become more important, percentage-wise, at low stretch rates as compared with the heat generation rate [9]. This leads to a quenching limit at low stretch rates, in addition to the blowoff limit (insufficient gas residence time) at high stretch rates. Only with the inclusion of a reasonably accurate radiation model can the flame structure and response be characterized quantitatively. A statistical narrow-band radiation model, which includes both Doppler and collision broadening, is used throughout this paper.

The first numerical study performed in this paper involves investigating the diffusion flame with and without the inclusion of radiation. For this purpose, the mechanism from reference [10] is chosen as a basis for the comparison. A comparison of an optically-thin radiation model and the narrow-band radiation model is also made. Though the path of the elementary reactions for dry CO/O_2 is known, several mechanisms in the literature use differing rate constants. Therefore, three of these schemes are chosen from the literature [1,10,11] and compared when radiation is considered in the purely gaseous diffusion flame. For the final numerical analysis presented, reference [10] is again chosen as the basis to study the effect that suppressant mole fraction has on the diffusion flame. A fundamental dilution limit is obtained for both the CO_2 and Ar suppressants, above which no flame can exist for any stretch rate.

RESULTS

The first set of results is obtained from considering reference [10] both with and without the inclusion of radiative losses. Figure 1 displays the effect radiation has on the extinction curve. First, comparing the adiabatic solution with the narrow-band radiation model, the high stretch turning point for the adiabatic case occurs at a fuel-side stretch rate value of $a \cong 46.6\ s^{-1}$, whereas when narrow-band radiation is included, $a \cong 38.7\ s^{-1}$. Notice that as the stretch rate decreases, the adiabatic solution will lead to a final maximum temperature that is approaching the adiabatic flame temperature ($\cong$ 2976 K). However, with narrow-band radiation included, there exists a second turning point (quench limit) at a low stretch rate ($a \cong 0.418\ s^{-1}$). The flame temperature at this low

stretch limit is around 1868 K, which is more than 1000 K below the value for the adiabatic flame. Another important result from this figure is that with an ambient temperature of 300 K the dry CO/O_2 system is flammable only within a narrow range of stretch rates ($a \cong 0.418\ s^{-1}$ to $a \cong 38.7\ s^{-1}$). Because of the low stretch rates, radiation is important over this entire range. This range of stretch rates is relatively small compared with those in most normal gravity combustion experiments. Figure 1 (see filled square symbols) shows that if one starts with a cold profile (uniform temperature at 300 K), the system will stay at this cold temperature when the entire range of stretch rates is investigated. Figure 1 also shows that including an optically-thin radiation model instead of the narrow-band model will underestimate the flammable range of stretch rates. The low stretch turning point for the optically-thin model ($a \cong 6.61\ s^{-1}$) is greater than the narrow-band model by an order of magnitude.

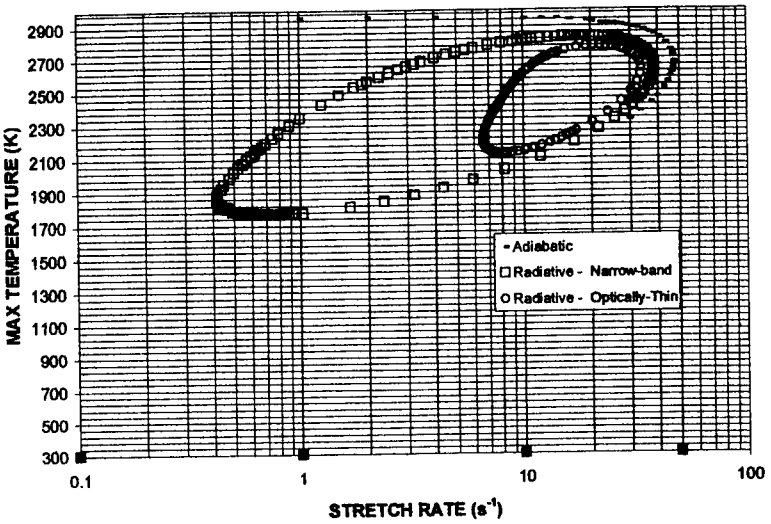


Figure 1 – Comparison of Extinction Curves with and without radiation (Kinetic scheme from [10])

Figure 2 shows a comparison of the detailed flame structure between two stable flames at a stretch rate of $1\ s^{-1}$, one flame without radiation and the other with the inclusion of the narrow-band radiation model. The flame profile is wider for the adiabatic flame as compared with the flame that includes radiative losses. The difference in maximum temperature is evident. The inclusion of radiation at this lower stretch rate has weakened the flame. Not including an accurate radiation model can lead to quantitative inaccuracies when studying the flame structure at low stretch rates.

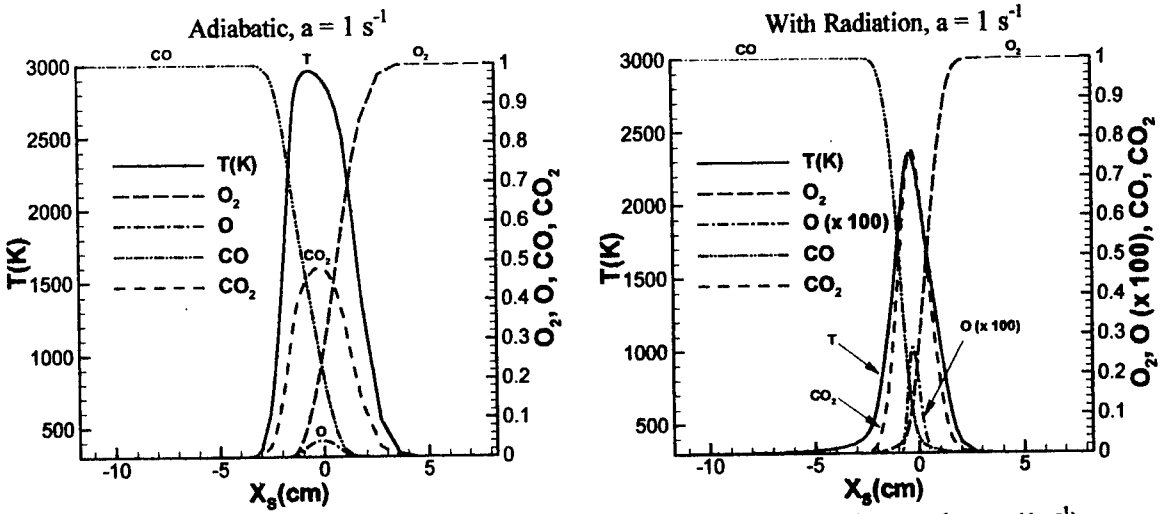


Figure 2 –Compares two stable flames with the same low fuel-side stretch rate ($1\ s^{-1}$)
To the left: without radiation. To the right: with radiation included. (Kinetic scheme from [10])

Figure 3 displays the results obtained from comparing the extinction isolas of three different reaction mechanisms when radiative losses are included. The three reaction mechanisms [1,10,11] differ near the high stretch "blowoff" turning point, but not as much at the low stretch turning point. The fuel-side stretch rate values at the two turning points for each is as follows:

Rightley and Williams [1],	$a_{HIGH} = 35.4\ s^{-1}$,	$a_{LOW} = 0.437\ s^{-1}$.
Allen et al. [10],	$a_{HIGH} = 38.7\ s^{-1}$,	$a_{LOW} = 0.418\ s^{-1}$.
Kim et al. [11],	$a_{HIGH} = 26.5\ s^{-1}$,	$a_{LOW} = 0.432\ s^{-1}$.

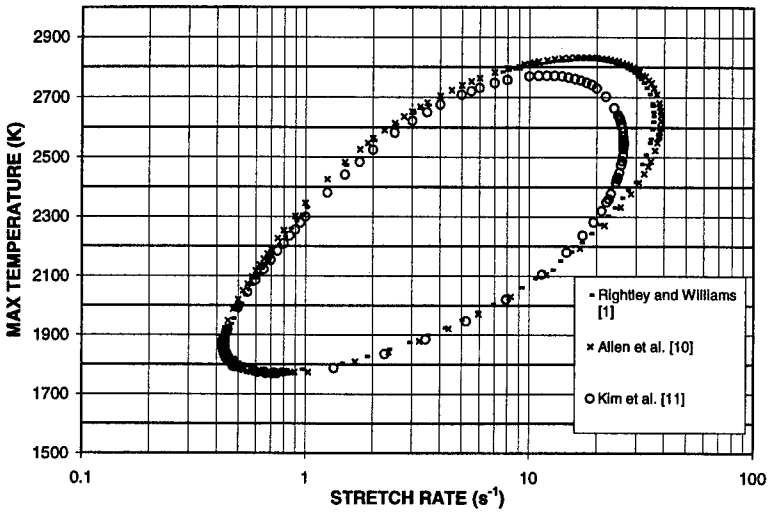


Figure 3 – Comparison of the Extinction Curves for three different reaction mechanisms [1,10,11], with the inclusion of a narrow-band radiation model.

Comparing the Rightley and Williams mechanism [1] with the Kim et al. mechanism [11], the two differ in pre-exponential factor and activation energy in the $CO+O+M=CO_2+M$ reaction. The Allen et al. mechanism, which includes pressure dependency and has different Arrhenius factors, was also tested (and used in Figures 1 and 2). As seen in Figure 3, this scheme [10] approximately matches the Rightley and Williams mechanism [11] in its extinction curve. At lower stretch rates, with the inclusion of radiative losses, all three predict a similar quenching turning point trend.

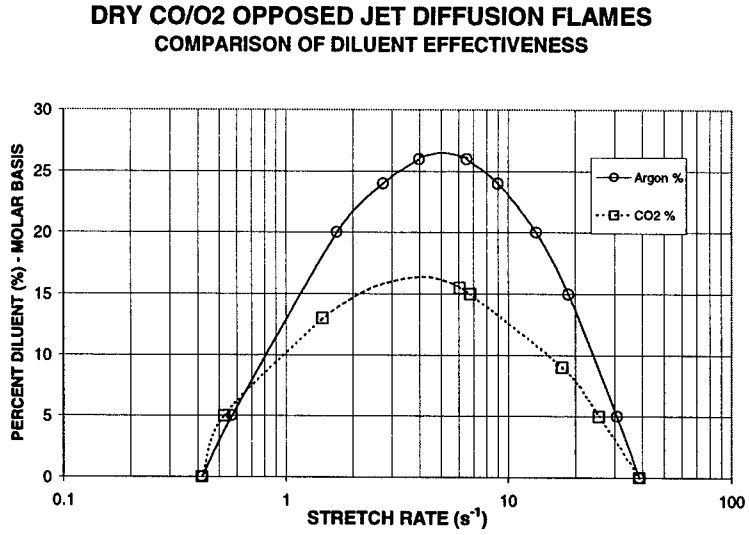


Figure 4 – Flammability Limits for the Dry CO/O_2 system – Comparing CO_2 and Ar Mole Fraction as a function of fuel-side stretch rate (Kinetic scheme from [10])

Figure 4 shows the results of the numerical study performed to map out the flammability limits when diluent/suppressant is added on a molar basis to both the fuel and oxidizer streams in equal amounts. Both the CO_2 and Ar curves show a trend toward a peak dilution percentage above which the system is not flammable for all stretch rates. This limit is referred to as the fundamental dilution limit. The fact that these limits are found at very low stretch rates (e.g. $X_{CO2} \cong 16$ % at $a \cong 4\ s^{-1}$ and $X_{Ar} \cong 26$ % at $a \cong 5\ s^{-1}$) has implications on fire safety. Figure 4 shows that CO_2 is more effective as a fire suppressant at higher stretch rates. On a molar basis, CO_2 has a higher heat capacity than Ar and is also radiatively active. The chemical kinetic effect of CO_2 has not been isolated in this work. This figure also shows the possibility (at low stretch rates) for the reversal in the trend of which diluent is more effective as a fire suppressant. Argon is more effective than CO_2 as a suppressant from the low stretch rates of $a \cong 0.4$ to $0.7\ s^{-1}$.

CONCLUSIONS

The dry CO/O_2 system has been shown to be flammable within a narrow range of low stretch rates. Radiation is shown to be very important in this flame, accounting for a maximum temperature difference of over 1000 K between the obtained quenching turning point and the maximum flame temperature for the adiabatic case at a stretch rate of $a \cong 0.418\ s^{-1}$. Only with a reasonably accurate radiation model included in the calculations can the true flame structure and response be obtained. Because of the simplicity of the dry CO/O_2 system, when coupled with an accurate radiation model, the system can be more confidently analyzed to help rate the effectiveness of various suppressants.

ACKNOWLEDGMENTS

This research has been supported by the NASA Microgravity Science and Applications Division. FCF would also like to acknowledge fellowship support by Timken Company. The authors would also like to thank Professor R. A. Yetter for providing our group with one of the reaction mechanisms [10] used in this work

REFERENCES

[1] Rightley, M. L., and Williams, F. A., *Combustion Science and Technology*, 125:181-200, (1997)
[2] Daguse, T., Croonenbroek, T., Rolon, J. C., Darabiha, N., and Soufiani, A., *Combustion and Flame*, 106: pages 271-287, (1996)
[3] Bedir, H., T'ien, J. S., Lee, H. S., Combustion Theory Modelling, 1: pages 395-404, (1997)
[4] Lutz, A. E., Kee, R. J., Grcar, J. F., Rupley, F. M., Technical Report SAND96-8243, Sandia Nat. Lab., (1996)
[5] Grcar, J. F., Kee, R. J., Smooke, M. D., and Miller, J. A., *Twenty-First Symposium (International) on Combustion, The Combustion Institute*, pages 1773-1782, (1986)
[6] Nishioka, M., Law, C. K., and Takeno, T., *Combustion and Flame*, 104: pages 328-342, (1996)
[7] Kee, R. J., Rupley, F. M., and Miller, J. A., Technical Report SAND89-8009B, Sandia National Lab., (1991)
[8] Kee, R. J., Dixon-Lewis, G., Warnatz, J., Coltrin, M. E., and Miller, J. A., Technical Report SAND86-8246, Sandia National Laboratories, (1991)
[9] T'ien, J. S., *Combustion and Flame*, 65: pages 31-34, (1986)
[10] Allen, M. T., Yetter, R. A., and Dryer, F. L, *Combustion and Flame,* 109: pages 449-470, (1997)
[11] Kim, T. J., Yetter, R. A., and Dryer, F. L., *Twenty-Fifth Symposium (International) on Combustion, The Combustion Institute*, pages 759-766, (1994)

Destruction of Flame Generated NO Near a Platinum Surface.

NAVIN KHADIYA and NICK G. GLUMAC*

Department of Mechanical and Aerospace Engineering, Rutgers University, Piscataway, NJ 08854, USA

**Corresponding Author. E-mail: glumac@jove.rutgers.edu.*

INTRODUCTION

The reduction of NO_x formed during combustion in various transportation and other industrial sources remains a predominant challenge. Measures such as modifications of fuel and/or combustion chamber have fallen short of achieving the required targets [1] and catalytic solutions remain necessary for some applications. A large body of work has been done in the fundamental aspects of catalytic combustion, and catalytically stabilized thermal combustion (e.g. [2, 3]). The new information on surface reactions obtained from those studies can be applied to study the post-flame catalysis such as has been presented in our earlier work [4]. A central issue in catalytic combustion and combustion near surfaces is the coupling of surface and gas phase chemistry [12].

In catalytic combustion studies, experimental and computational work has been done on the flat plate boundary layer [3], the stagnation flow geometry [2], and on chemical reactors with using a catalytically active wire/foil. The stagnation flow geometry is increasingly becoming the popular choice due to its one-dimensionality, which facilitates both measurements and modeling.

EXPERIMENTAL

The set-up consists of a vacuum combustion system with a flat flame in a downflow stagnation configuration over a constant temperature substrate fixed at 2.5 cm. For laser-induced fluorescence measurements, a frequency-doubled tunable dye laser system produces the UV beam which is focussed into the gap between burner and substrate. Fluorescence is collected at right angles to the beam through a monochromator to a photomultiplier. Specific system details can be found in [4].

Laser radiation at 225.9 nm was used to excite the $Q_1(16)$ (and satellite $Q_{21}(16)$) line in the (0, 0) band of the $A^2\Sigma \leftarrow X^2\Pi$ transition of NO. The $Q_1(16)$ line was chosen because it is sufficiently separated from adjacent main-branch transitions and because the population of the rotational level involved is fairly temperature insensitive in the encountered (400 to 1200 K) range. Laser powers of several μJ/pulse were used, and transitions were partially saturated. Fluorescence was collected over the (0, 2) band near 247.5 nm. Time resolved measurements of fluorescence were made at each point and were later integrated. The fluorescence signal as a function of time in the region 3 ns after the peak was fit to an exponential to obtain the de-excitation rate including collisional quenching. This scheme is then used to explicitly correct the integrated signal at each point for quenching as suggested in [5]. The fluorescence signal was averaged over 200 shots and corrected for power variation.

MODELING

The Sandia program SPIN [6] was used to model the flame, and detailed elementary gas-phase reactions and surface chemistry including surface coverage dependent reactions were specified. The detailed gas-phase chemistry used for both H/N/O system was obtained from the GRI 2.11 mechanism [7]. The H/O surface chemistry was obtained from Deutschmann *et al.* [8], while the N/O reactions were obtained from Fink *et al.* [9], except the NO sticking probability which was obtained from Yeo *et al.* [10]. For all cases, the energy equation was solved to generate a temperature profile, and mixture averaged approximation were used for the transport coefficients and diffusion fluxes. At the burner, a mass flux boundary condition was used but with vanishing radical concentrations. Physical considerations and experimental data from previous work [4] suggest radical concentrations approaching zero at the burner.

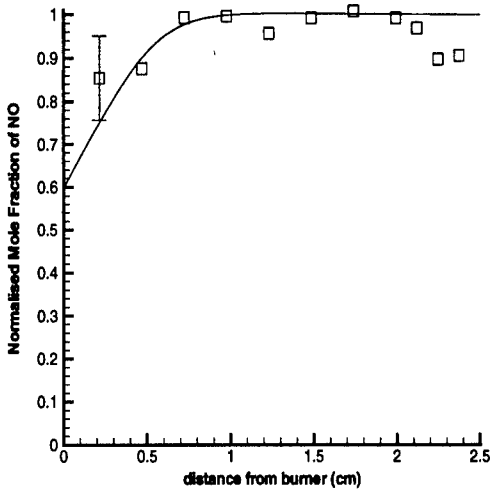


Figure 1: Experimentally determined X_{NO} profile versus the model. Substrate is fused silica. Substrate temperature: 735 K, Pressure 17.0 torr and H_2/O_2 Equivalence Ratio 1.0. X_{NH3} 0.01.

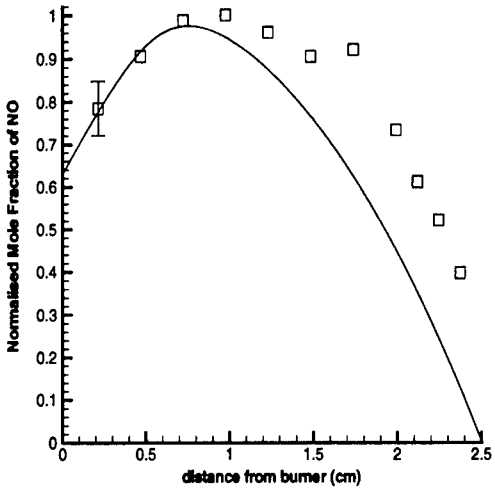


Figure 2: Experimentally determined X_{NO} profile versus the model. Substrate is platinum. Substrate temperature: 755 K, Pressure 17.0 torr and H_2/O_2 Equivalence Ratio 1.0. X_{NH3} 0.01.

RESULTS AND DISCUSSION

The measured profile of the NO mole fraction matches that which is predicted by the model, within the experimental uncertainties, when the substrate is made of fused silica, as shown in Figure 1. The surface chemistry is turned off in the model for this case. The NO mole fraction is seen to increase away from the burner and then to remain constant as is expected. Under similar conditions, when the substrate is replaced with platinum, however, the NO mole fraction registers a significant drop in the direction of the substrate as seen in Figure 2. The model which contains the NO adsorption, dissociation and N_2 desorption reactions at the surface also predicts a reduction, which is however, slightly larger than what is experimentally observed. This observed destruction is expected to be a result of both pure surface chemistry effects and the effect of the surface chemistry on the gas phase in the vicinity of the surface [12].

The experimental profile of NO mole fraction at a higher temperature (938 K) is shown in Figure 3, suggesting a smaller amount of destruction compared to the 755 K case. The model however

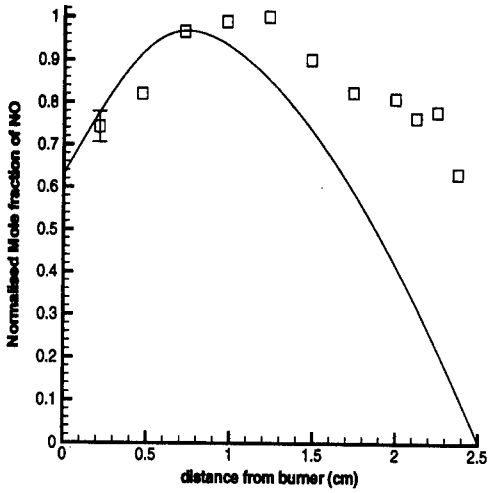


Figure 3: Experimentally determined X_{NO} profile versus the model. Substrate is platinum. Substrate temperature: 938 K, Pressure 17.0 torr and H_2/O_2 Equivalence Ratio 1.0. X_{NH3} 0.01.

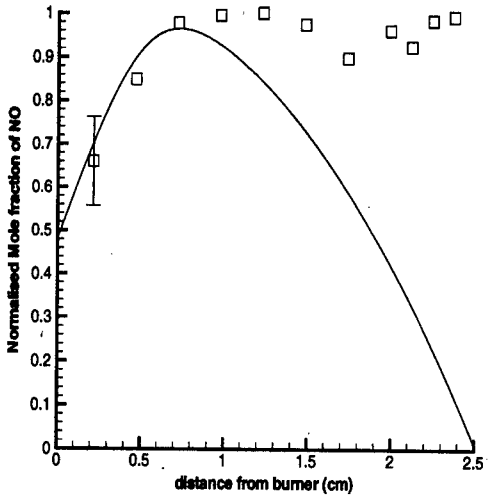


Figure 4: Experimentally determined X_{NO} profile versus the model. Substrate is platinum. Substrate temperature: 800 K, Pressure 17.0 torr and H_2/O_2 Equivalence Ratio 0.7. X_{NH3} 0.01.

predicts little or no change in the NO reduction between the two temperatures. Measurements at other substrate temperatures have demonstrated an inverse dependence of NO destruction on surface temperature. Lower surface NO mole fractions at cooler substrate temperatures were also found in numerical studies on inert surfaces by Aghalayam and Vlachos [11], and the effect observed here may be of a similar nature.

Studies were also done at different equivalence ratios and the NO profile obtained at an equivalence ratio of 0.7 is shown in Figure 4. The contrast between the experiment and the model prediction is striking. We observed a nearly constant NO mole fraction experimentally while the model predicts a near complete destruction. Fuel-lean conditions are known to result in a substantial decrease in the NO_x reduction activity of catalytic devices [1] which agrees with our experimental observation. The NO profiles under slightly rich conditions were found to be similar to that at stoichiometric conditions.

CONCLUSIONS

In the present work, we have measured the profiles of NO mole fraction in conditions where the effect of the surface can be clearly observed. The experimentally measured profiles can be used to validate existing surface chemistry models under moderate pressure conditions where the coupling of the surface and gas phase is significant [12] which is also the case in most real devices. The inability of existing models to predict the NO profiles under important conditions is observed, and requires detailed scrutiny.

This research was supported by the NSF under grant CTS-9634972.

REFERENCES

1. Fritz, A., Pitchon, V., J., *Appl. Catal. B* 13:1 (1997).
2. Ikeda, H., Sato, J., and Williams, F. A., *Surf. Sci.* 326:11 (1995).
3. Pfefferle, L. D., Griffin, T. A., Winter, M., Crosley, D. R., and Dyer, M. J., *Comb. Flame*, 76:325 (1989).
4. Khadiya, N., and Glumac, N. G., in *Proceedings of the Central States Section of the Combustion Institute*, June 1998, p. 146.
5. Cattolica, R. J., Cavalowsky, J. A., and Mataga, T. G., *Twenty Second Symposium(International)on Combustion*, The Combustion Institute, 1988, p. 1165.
6. Coltrin, M. E., Kee, R. J., Evans, G. H., Meeks, E., Rupley, F. M., and Grcar, J. F., Sandia National Laboratories Report SAND91-8003, 1991.
7. Bowman, C. T., Hanson, R. K., Davidson, D. F., Gardiner Jr., W. C., Lissianski, V., Smith, G. P., Golden, D. M., Frenklach, M., and Goldenberg, M. E., *http : //www.me.berkley.edu/gri_mech.*
8. Deutschmann, O., Schmidt, R., Behrendt, F., and Warnatz, J., *Twenty-sixth Symposium(International) on Combustion*, The Combustion Institute, 1996, p. 1747.
9. Fink, Th., Dath, J. -P., Basset, M. R., Imbihl, R., and Ertl, G., *Surf. Sci.*, 245:96 (1991).
10. Yeo, Y. Y., Vattuone, L., and King, D. A., *J. Chem. Phys.*, 104:3810 (1996).
11. Aghalayam, P., and Vlachos, D. G., *AIChE Journal*, (in press).
12. Gudmundson, F., Persson, J. L., Forsth, M., Behrendt, F., Kasemo, B., and Rosen, A., *J. Catal.*, 179:420 (1998).

For the Fall Technical Meeting, Eastern States Section: The Combustion Institute; Oct. 10-13, 1999, Raleigh NC

Improving Kinetic Models for Ethylene Flat Flames

Thierry Carrière and Phillip R. Westmoreland*
Chemical Engineering Department, University of Massachusetts, Amherst, MA 01003-3110
*Corresponding author, westm@ecs.umass.edu

ABSTRACT

A reaction set has been developed to model recent measurements made in a lean ethylene flame (Φ=0.75). It is able to predict MBMS data profiles from a variety of flames remarkably well, including both very lean and rich ethylene flames (Φ=0.21, 2.40, 3.06). However, relatively poor agreement was found for the lean, near-stoichiometric flame. Reaction path analysis on the flame suggests that the H-atom profile very possibly causes the general misprediction. Accordingly, H-atom combination on the burner surface is proposed as a possible resolution to the problem in modeling this flame and for improving predictions of other flames.

INTRODUCTION

Despite significant advances in the field of combustion modeling, some systems remain difficult to simulate. Successful modeling studies of flat flames have been reported for different fuels and a wide range of experimental conditions. It is now accepted that methane flames can be predicted accurately, using, for example, the reaction set proposed by Frenklach et al. (1995) known as GRIMech 1.2. Ethylene flames have also been modeled by various groups (Westbrook et al., 1982; Kiefer et al., 1983; Westbrook et al., 1988; Dagaut et al., 1990; Marinov and Malte, 1995; Hidaka et al., 1999). However, recently published data for a near-stoichiometric C_2H_4 flat flame (Bhargava and Westmoreland, 1998b) exhibit some features that are not well predicted using a "classical" kinetic reaction set.

Such mechanisms, including the one developed in our group, may do a good job under particular conditions but may also break down for other ones. As experimentalists, we recognize that data always have some degree of error. However, modeling may reveal errors and room for improvement in reaction sets and physical models.

The experimental data considered were mainly flat flames of C_2H_4: very lean (Φ=0.21) by Peeters and Mahnen (1973), lean (Φ=0.75) by Bhargava (1997, 1998b), rich (Φ=1.90) by Bhargava (1997, 1998a), and very rich (Φ=3.06) by Castaldi et al. (1996). A rich C_2H_2 flame (Φ=2.40) by Westmoreland (1986) was also used to assess the validity of the mechanism. All flames were at low pressures except that of Castaldi et al., whose 1-atm flame provides some testing of the pressure effects.

REACTION SET

The reaction set was developed using GRIMech 1.2 as a basis. GRIMech was carefully optimized for methane pyrolysis and combustion, and not unreasonably, it gave unsatisfactory predictions for ethylene flames. Here, the H_2/O_2 and C_1 subsets have not been modified, but have been taken to represent that chemistry well. However, extensive changes were made to the C_2 chemistry. The most significant changes were the addition of the results obtained by Bhargava (1997) for the reactions $C_2H_4+H \Leftrightarrow C_2H_3+H_2$ and $C_2H_4+OH \Leftrightarrow C_2H_3+H_2O$, *ab initio* calculations on the kinetics of C_2H_4+O by this group, and rates of reaction measured and fitted by Knyazev and Slagle (1996) for the reaction $C_2H_3+M \Leftrightarrow H+C_2H_2+M$. Other C_2 reactions were included from Tsang and Hampson (1986) and our calculations. The C_3 subset was built mainly around the work of Tsang and Hampson (1986), Wilk et al. (1989) and Dagaut et al. (1992). Finally, a C_4/C_6 subset was also added.

This set contains 80 species and 709 reactions. The calculations were performed using the PREMIX / CHEMKIN II codes (Kee et al., 1987, 1990, 1991) with full multicomponent molecular diffusion and with thermal diffusion of H and H_2.

RESULTS

Flame 1: Very lean C_2H_4 flame (Φ=0.21), P=40 torr, v=85 cm/s. This flame was predicted quite well. Predictions for the major species (C_2H_4, O_2, H_2, H_2O, CO, CO_2) can hardly be improved (Fig. 1). Radical

concentrations (H, O, OH) were also well predicted (Fig. 2). In particular, the O profile is very important since C_2H_4 reacts mainly with O at the lean conditions, following three distinct paths. The reactions of C_2H_4 with H and OH also contribute significantly to its decay. These results show that the mechanism does a good job on a fuel-lean, low-pressure, high-temperature flame, although it is much leaner and not as hot as our lean flame (Φ=0.75). Lean-flame-specific features are apparently not the cause of the poor predictions for the Φ=0.75 flame.

Flame 2: Rich C_2H_4 flame (Φ=1.90), P=20 torr, v=62.5 cm/s. Except for C_2H_4, predictions for all major species (O_2, H_2O, CO, CO_2) exhibited good agreement with the experimental measurements from this flame (Fig. 3). In particular, the ethylene decay was not predicted so well. Likewise in the H profile, things are happening a little too close from the burner (or a little too fast, Fig. 4). A difference from the lean condition is that the O atom is of secondary importance and HO_2 radicals play a much bigger role. The prediction of the latter shows a very early peak, but data are not available for this species, making any conclusion debatable. As expected in the absence of O atoms, the main reactions for C_2H_4 consumption are $C_2H_4+H\rightarrow C_2H_3+H_2$ (primary route) and $C_2H_4+OH\rightarrow C_2H_3+H_2O$. Here again, the coupling between the correctness of C_2H_4 and H profile predictions is clear.

Flame 3: Near-stoichiometric C_2H_4 flame (Φ=0.75), P=30 torr, v=30 cm/s. In this flame, the ethylene decay is quite poorly predicted (Fig. 5). At the same time, the level of H atom predicted near the burner is much too high, 15 times higher than the measured value. At the near-stoichiometric conditions of our flame, H atoms are produced in quite large amounts and can diffuse back towards the burner. On the other hand, we know that H atoms are involved in many reactions, many of them playing key roles in the model. The high level of H atoms is a reasonable explanation for the overpredicted levels of OH and O radicals (by a factor of about 2) due to the fast reactions occurring between them. That large pool of radicals in turn accelerates the rates of crucial reactions, such as $H+C_2H_4+M\rightarrow C_2H_5+M$, that excessively destroys C_2H_4 at the burner (Fig. 6) and initiates a chain of mispredictions.

It is not possible to point to one specific reaction or rate of reaction as a source of the error, as none of them appears to exhibit a strikingly incorrect value. The temperature profile used for the calculation can be questioned, as it is measured and lowered empirically by 100 K for probe perturbation. However, modeling indicated very low sensitivity of the species profiles to uncertainty in the temperature, leading to the conclusion that it is not responsible for the erroneous predictions.

On the other hand, a very plausible explanation for the overprediction of H near the burner would be neglect of possible H-atom losses by reaction on the burner. That type of catalytic boundary condition has not been often used in the past because the amount of H atom near the flat-flame burner is often so small. A surface reaction such as $H+H\rightarrow H_2$ then would not have a significant impact on the modeling and thus could be safely omitted. That can be seen in the two previous cases, where the H level near the burner is essentially zero. To our knowledge, this approach has only been implemented before by Miller et al. (1990, 1996) on rich acetylene flames to improve the agreement on the H-atom profile near the burner. As a test of this hypothesis, we applied an unrealistically high rate constant for the homogeneous gas-phase reaction $H+C_2H_3(+M)\Leftrightarrow C_2H_4(+M)$, forcing fast consumption of H at the burner. The improvement was remarkable, creating near-perfect predictions. We believe that this phenomenon should not be overlooked if one wishes to model flat flames, and we are testing modifications to the flame code that would include it properly as a surface reaction.

Comparison with other sets of data. As mentioned in the introduction, the model has been tested against somewhat independent data as well. The comparisons made here are only intended to provide further confirmation of the validity of our kinetics set. The rich-C_2H_2 flame (Φ=2.40) was also an MBMS study at low pressure (20 torr). The results of the simulation were acceptable for the main species, especially for the fuel decay.

Comparisons have been also made with the experimental data reported by Castaldi et al. (1996) and their predictions, presented in the same paper. That flame is not a low-pressure flame (P=1 atm) and would be a good test for our model developed initially for low-pressure systems. The agreement between our predictions and the data is noteworthy. All major species are in good agreement, and our model is also able to predict the C_2H_2 and CO_2 profiles well, the two principal mispredictions reported in that paper.

CONCLUSION

The ability of our reaction set to model major features of ethylene premixed laminar flames has been verified. The outstanding results obtained on the very lean flame, as well as favorable modeling of a rich and very rich flames under different pressures, indicates that the unsatisfactory modeling of the near-stoichiometric flame is likely not due to a major error in the reaction set. From a kinetic standpoint, key reactions are well represented. The observations reported here were not really concerned with the predictions of secondary species, and some of them may contribute to the problem we have encountered. We believe, though, that an improved model of the boundary condition for H atoms is necessary in this case.

ACKNOWLEDGMENT

Support by the United States Department of Energy (Basic Energy Sciences, Chemical Physics Division, Grant No. DE-FG02-91ER14192) is gratefully acknowledged.

REFERENCES

Bhargava, A., *Ph.D. dissertation*, Dept. of Chemical Engineering, University of Massachusetts, Amherst MA (1997).

Bhargava, A., and Westmoreland, P. R., *Combust. Flame*, 113, p. 333 (1998a).

Bhargava, A., and Westmoreland, P. R., *Combust. Flame*, 115, p. 456 (1998b).

Castaldi, M. J., Marinov, N. M., Melius, C. F., Huang, J., Senkan, S. M., Pitz, W. J., and Westbrook, C. K., *26th Symposium (International) on Combustion*, The Combustion Institute, Pittsburgh, p. 693 (1996).

Dagaut, P., Boettner, J. C ., and Cathonnet, M., *Int. J. Chem. Kinet.*, 22, p. 641 (1990).

Dagaut, P., Cathonnet, M., and Boettner, J. C., *Combust. Sci. Tech.*, 83, p. 167 (1992).

Frenklach, M., Wang, H., Yu, C. L., Goldenberg, M., Bowman, C. T., Hanson, R. K., Davidson, D. F., Chang, E. J., Smith, G. P., Golden, D. M., Gardiner, W. C., and Lissianski, V., GRI-Mech, An Optimized Detailed Chemical Reaction Mechanism for Methane Combustion, Report No. GRI-95/0058 (1995), http://www.me.berkeley.edu/gri_mech.

Hidaka, Y., Nishimori, T., Sato, K., Henmi, Y., Okuda, R., and Inami, K., *Combust. Flame*, 117, p. 755 (1999).

Kee, R. J., Grcar, J. F., Smooke, M. D., and Miller, J. A., A Fortran Program for Modeling Steady Laminar One-Dimensional Premixed Flames, SAND 85-8240, Sandia National Laboratories, Livermore, CA (1985). Modifications of PREMIX version 2.5 (1991).

Kee, R. J., Dixon-Lewis, G., Warnatz, J., Coltrin, M. E., and Miller, J. A., A Fortran Computer Package for the Evaluation of Gas-Phase, Multicomponent Transport Properties, SAND 87-8246, Sandia National Laboratories, Livermore, CA (1986). Modification of TRANLIB version 1.6 (1990).

Kee, R. J., Rupley, F. M., and Miller, J. A., The CHEMKIN Thermodynamic Data Base, SAND 87-8215, Sandia National Laboratories, Livermore, CA (1987).

Kiefer, J. H., Kapsalis, S. A., Al-Amani, M. Z., and Budach, K. A., *Combust. Flame*, 51, p. 79 (1983).

Knyazev, V.D., and Slagle, I. R., *J. Phys. Chem.*, 100, p. 16899 (1996).

Marinov, N. M., and Malte, P. C., *Int. J. Chem. Kinet.*, 27, p. 957 (1995).

Miller, J. A., Volponi, J. V., Durant, J. L., Goldsmith, J. E. M., Fisk, G. A., and Kee, R. J., *23rd Symposium (International) on Combustion*, The Combustion Institute, Pittsburgh, p. 187 (1990).

Miller, J. A., Volponi, and J. V., Pauwels, J.-F., *Combust. Flame*, 105, p. 451 (1996).

Peeters, J. and Mahnen, G., *14th Symposium (International) on Combustion*, The Combustion Institute, Pittsburgh, p. 133 (1973).

Tsang, W., and Hampson, R. F., *J. Phys. Chem. Ref. Data*, 15, p. 1087 (1986).

Wilk, W. J., Cernansky, N. P., Pitz, W. J., and Westbrook, C. K., *Combust. Flame*, 77, p. 145 (1989).

Westbrook, C. K., Thornton, M. M., Pitz, W. J., and Malte, P. C., *22nd Symposium (International) on Combustion*, The Combustion Institute, Pittsburgh, p. 863 (1988).

Westbrook, C. K., Dryer, F. L., and Schug, K. P., *19th Symposium (International) on Combustion*, The Combustion Institute, Pittsburgh, p. 153 (1982).

Westmoreland, P. R., *Ph.D. dissertation*, Dept. of Chemical Engineering, M.I.T., Cambridge, MA (1986).

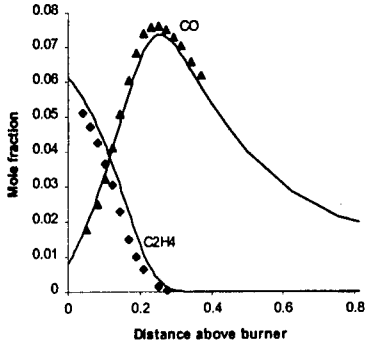


Figure 1. Mole fractions of CO and O_2 in the very lean flame of Peeters and Mahnen (1973)

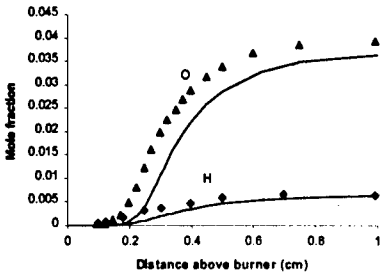


Figure 2. Mole fractions of O and H in the very lean flame of Peeters and Mahnen (1973).

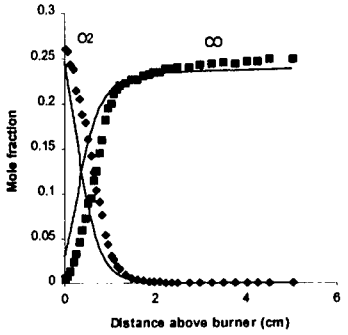


Figure 3. Mole fractions of O_2 and CO in the rich flame of Bhargava and Westmoreland (1998a).

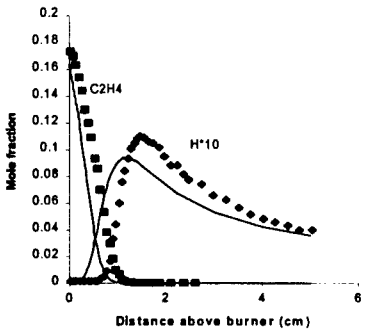


Figure 4. Mole fractions of C_2H_4 and H in the rich flame of Bhargava and Westmoreland (1998a).

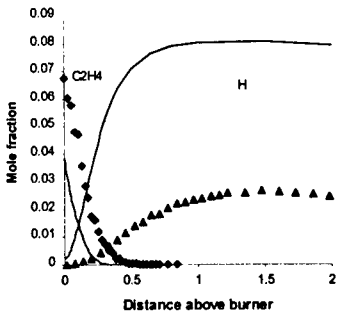


Figure 5. Mole fractions of C_2H_4 and H in the near-stoichiometric flame (Φ=0.75).

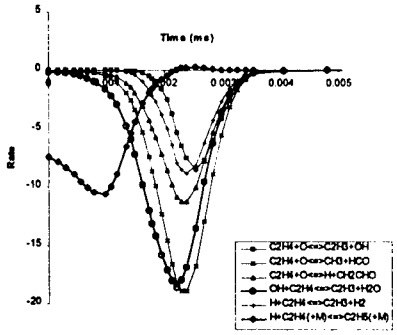


Figure 6. Rates of destruction of C_2H_4 in the near-stoichiometric flame (Φ=0.75).

A Comprehensive Kinetic Mechanism of C_2H_x and C_3H_x Fuel Combustion*

Hai Wang, Alexander Laskin and Zoran M. Djurisic
Department of Mechanical Engineering, University of Delaware, Newark, DE 19716
hwang@me.udel.edu
and
Chung K. Law, Scott G. Davis† and Delin Zhu
Department of Mechanical and Aerospace Engineering, Princeton University, Princeton, NJ 08544

In this paper we present a comprehensive chemical kinetic model of C_2 and C_3 fuel combustion. This work represents a part of a long-range experimental-computational effort directed toward the development of fundamental and predictive detailed chemical reaction mechanisms for combustion modeling.

The basic requirements for this model include: (a) fundamental input of thermochemistry and elementary reaction kinetics; and (b) predictive capability of the wide spectrum of combustion phenomena, from the response of homogeneous systems such as shock tube and auto-ignition delays, to the ignition, steady burning, and extinction of premixed and diffusion flames for which diffusive transport is present, and ultimately to the characteristics of pollutant formation. The reaction mechanism should also be applicable to a wide variety of hydrocarbon fuels and should incorporate pressure effects on the combustion responses.

There have been several comprehensive kinetic models reported in the literature for the combustion of acetylene and/or ethylene (e.g., refs 1-5). A variety of combustion properties have been successfully predicted by these models. However, recent progresses in fundamental reaction kinetics and noticeably in the reaction kinetics of the vinyl radical have brought with significant changes to the kinetic rates and pathways during the oxidation of acetylene and ethylene. In addition to the kinetics of the vinyl radical, comprehensive reviews of the kinetic data relevant to acetylene and ethylene combustion are also available and continuously being updated (e.g., refs 6-9). These factors, along with the critical importance of the acetylene and ethylene chemistry in high-hydrocarbon combustion, warrant a re-examination of the kinetic mechanisms of acetylene and ethylene combustion.

Recognizing the hierarchical nature of a chemical reaction mechanism and that the initial reactions during the combustion of higher hydrocarbon fuels lead primarily to C_2 and C_3 intermediates, a kinetic model of acetylene, ethylene, propyne, allene, propene, and propane combustion is naturally the starting point of our mechanism development effort. We note that many combustion mechanisms of aforementioned fuels have been reported, but few are capable of predicting a wide range of combustion phenomena. To achieve the goal of a predictive and fundamentally justifiable reaction model, experiments were conducted to acquire fundamental combustion data such as the laminar flame speeds and the extinction of stretched premixed and diffusion flames. These experimental data provide the necessary database for the validation and optimization of the comprehensive kinetic model. Concurrently, the kinetic model was developed on the basis of critical review of literature kinetic data and extensive *ab initio* quantum mechanical and Rice-Ramsperger-Kassel-Marcus (RRKM) calculations for determination and/or extrapolation of reaction-rate coefficients. The resulting model has been subject to validation test against a wide range of combustion data, over 60 sets in all, covering from ignition in shock tubes, to laminar flame propagation, and to detailed major and minor species profiles in burner-stabilized flames and in a flow reactor.

---

* For presentation at the 1999 Eastern States Section of the Combustion Institute Meeting, Raleigh, NC, October 1999.
† Presently at IRPHE - Laboratoire de Combustion, Service 252, Faculté de St. Jérôme, 13397 Marseille Cedex 20, France.

Reaction Mechanism

The detailed kinetic model compiled in the present study consists of 52 species and 367 elementary reactions. The small-species chemistry is largely based on the GRI-Mech.[9] We used Troe's fall-off formalism[10] to describe the pressure dependence of the rate coefficients for unimolecular dissociation and bimolecular combination reactions. The reaction kinetics of acetylene and ethylene is based on a series of works reported in the past.[11-14] The propyne, allene, propene, and propane sub-models were taken from refs. 15-17. A substantial amount of the kinetic data for propane and propene are based on the compilation and evaluation of Tsang.[18,19] The kinetic model retains a reasonable number of C_4-C_6 species to ensure proper simulation under the fuel-rich conditions and to make it possible for expansion to include large hydrocarbon chemistry. Numerical simulations were performed using the Sandia Chemkin-II codes.[20-22]

Simulation of Shock-Tube Experiments

The shock tube simulation was performed with a constant-density model for experiments conducted behind reflected shock waves and with the Sandia Shock code[23] for incident shock waves. When possible, the computational ignition was defined in the same fashion as that of the experiment. The kinetic model predicts very well the experimental shock-tube ignition delay data for acetylene, ethylene, propyne, allene, and propane. Selected results are presented in Figures 1-4. For acetylene, ethylene and propane, the data cover a wide range of pressure, concentration, and initial temperature variations. We note that the model prediction for acetylene ignition was made possible when vinylidene was considered as an intermediate in the initiation reaction. Our *ab initio* quantum mechanical calculations firmly point to the role of vinylidene in initiating the radical chain process.[14]

Simulation of Laminar Burning Velocity

The current model predicts reasonably well the laminar flame speed data of acetylene, ethylene, propyne, propene and propane at 1 atm and over a wide range of equivalence ratio, as seen in Figure 5. Burning velocities at reduced and elevated pressures were also included for model comparison. In general the quantitative dependence of the flame speed on pressure is well captured by the reaction model.

Simulation of Burner-Stabilized Flames and Flow Reactor Experiments

Several burner-stabilized flames were included in the model validation. The calculations were carried out for major and minor species concentration profiles. In general the model predicts very well the major species profiles as well as many minor radical species concentrations. Flow reactor experiments were performed for the pyrolysis and oxidation of propyne and propene at around 1200 K.[16,17] The oxidation experiments were carried out for equivalence ratios of 0.7, 1.0, and 1.4. In general the current kinetic model is capable of predicting the concentration profiles from both the pyrolysis and oxidation experiments, for the major as well as many minor species.

In summary, the present work has paved the ground for optimization of a comprehensive reaction model for small hydrocarbon fuels. It also provides a base model for the combustion of higher hydrocarbons from aliphatic to aromatic compounds.

The work was supported by the New World Vista Program of the Air Force Office of Scientific Research under the technical monitoring of Dr. Julian M. Tishkoff. A part of the computation was performed at the Facility for Computational Chemistry at the University of Delaware, which is funded by the NSF (CTS-9724404).

References

1. Warnatz, J. *Eighteenth Symposium (International) on Combustion*, The Combustion Institute, Pittsburgh, 1981, p. 369.
2. Miller, J. A., Mitchell, R. E., Smooke, M. D. and Kee, R. J. *Nineteenth Symposium (International) on Combustion*, The Combustion Institute, Pittsburgh, 1982, p. 181.
3. Westbrook, C. K. and Dryer, F. L. *Prog. Energy Combust. Sci.* **10**, 1 (1984).
4. Dagaut, P., Boettner, J.-C. and Cathonnet, M. *Int. J. Chem. Kinet.* **22**, 641 (1990).
5. Fournet, R., Bauge, J. C., Battin-Leclerc, F. *Int. J. Chem. Kinet.* **31**, 361 (1999).
6. Tsang, W. and Hampson, R. F. *J. Phys. Chem. Ref. Data* **15**, 1087 (1986).
7. Baulch, D. L., Cobos, C. J., Cox, R. A., Frank, P., Hayman, G., Just, Th., Kerr, J. A., Murrells, T., Pilling, M. J., Troe, J., Walker, R. W. and Warnatz, J. *J. Phys. Chem. Ref. Data* **21**, 411 (1992).
8. Baulch, D. L., Cobos, C. J., Cox, R. A., Frank, P., Hayman, G., Just, Th., Kerr, J. A., Murrells, T., Pilling, M. J., Troe, J., Walker, R. W. and Warnatz, J. *J. Phys. Chem. Ref. Data* **23**, 847 (1994).
9. Frenklach, M., Wang, H., Goldenberg, M., Smith, G. P., Golden, D. M., Bowman, C. T., Hanson, R. K., Gardiner, W. C. and Lissianski, V. *GRI-Mech–An Optimized Detailed Chemical Reaction Mechanism for Methane Combustion*, GRI Technical Report No. GRI-95/0058, 1995.
10. Gilbert, R. G., Luther, K., and Troe, J. *Ber. Bunsenges. Phys. Chem.* **87**, 169 (1983).
11. Wang, H., Hahn, T. O., Sung, C. J., and Law, C. K. *Combust. Flame* **105**, 291 (1996).
12. Sun, C. J., Sung, C. J., Wang, H. and Law, C. K. *Combust. Flame* **107**, 321 (1996).
13. Wang, H. and Frenklach, M. *Combust. Flame*, **110**, 173 (1997)
14. Laskin, A. and Wang, H. *Chem Phys. Lett.* **303**, 43 (1999).
15. Davis, S. G., Law, C. K., Wang, H. *Twenty-Seventh Symposium (International) on Combustion*, The Combustion Institute, Pittsburgh, 1999, pp. 305.
16. Davis, S. G., Law, C. K. and Wang, H. "Propyne Pyrolysis in a Flow Reactor: An Experimental, RRKM, and Detailed Kinetic Modeling Study," *J. Phys. Chem.*, in press.
17. Davis, S. G., Law, C. K. and Wang, H. "Propene Pyrolysis and Oxidation Kinetics in Flow Reactors and in Laminar Flames," *Combust. Flame*, in press.
18. Tsang, W. *J. Phys. Chem. Ref. Data,* **20**, 221 (1991).
19. Tsang, W. *J. Phys. Chem. Ref. Data,* **17**, 887 (1988).
20. Kee, R. J., Dixon-Lewis, G., Warnatz, J., Coltrin, M. E. and Miller, J. A. *A Fortran Computer Code Package for the Evaluation of Gas-Phase Multicomponent Transport Properties*, Sandia Report SAND86-8246.UC-32, Sandia, Albuquerque, New Mexico, 1986
21. Kee, R. J., Grcar, J. F., Smooke, M. D. and. Miller, J. A. *A Fortran Program for Modeling Steady Laminar One-Dimensional Flames*, Sandia Report SAND85-8240.UC-4, Sandia, Albuquerque, New Mexico, 1987.
22. Kee, R.J., Rupley, F.M. and Miller, J.A. *Chemkin II: A Fortran Chemical Kinetics Package for the Analysis of Gas-Phase Chemical Kinetics*, Sandia Report SAND 89-8009B, Sandia, Albuquerque, New Mexico, 1989.
23. Mitchell, R. E. and Kee, R. J. *A General Purpose Computer Code for Predicting Chemical Kinetic Behavior behind Incident and Reflected shocks*, Sandia Report SAND82-8205, Sandia, Albuquerque, New Mexico, 1982.
24. Homer, J. B. and Kistiakowsky, G. B. *J. Chem. Phys.* **47**, 5290 (1967).
25. Hidaka, Y., Eubank, C. S., Gardiner, W. C. Jr. and Hwang, S. M. *J. Phys. Chem.* **88**, 1006 (1984).
26. Burcat, A., Scheller, K., and Lifshitz, A. *Combust. Flame* **16**. 29-33 (1971).
27. Borisov, A. A. *Prog. Astro. Aero.* **114**, 124 (1988).
28. Curran, H., Simmie, J. M., Dagaut, P., Voisin, D., Cathonnet, M. *Twenty-Sixth Symposium (International) on Combustion*, The Combustion Institute, Pittsburgh, 1996, p. 613.
29. Egolfopoulos, F. N., Zhu, D. L. and Law, C. K. *Twenty-Third Symposium (International) on Combustion*, The Combustion Institute, Pittsburgh, 1990, p. 471.
30. Vagelopoulos, C. M., Egolfopoulos, F. N., and Law, C. K. *Twenty-Fifth Symposium (International) on Combustion*, The Combustion Institute, Pittsburgh, 1994, p. 1341.

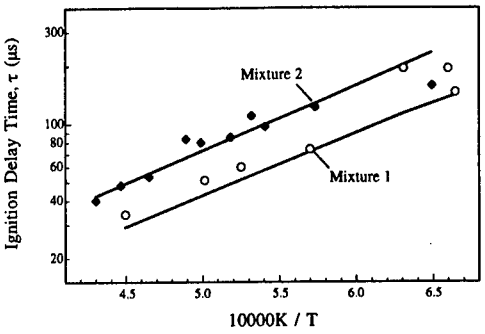


Figure 1. Ignition delay times (symbols: experimental;[24] lines: computed) for the oxidation of ethylene behind reflected shock waves. Mixtures 1: 0.5%C_2H_4-3%O_2 and 2: 0.5%C_2H_4-1%O_2.

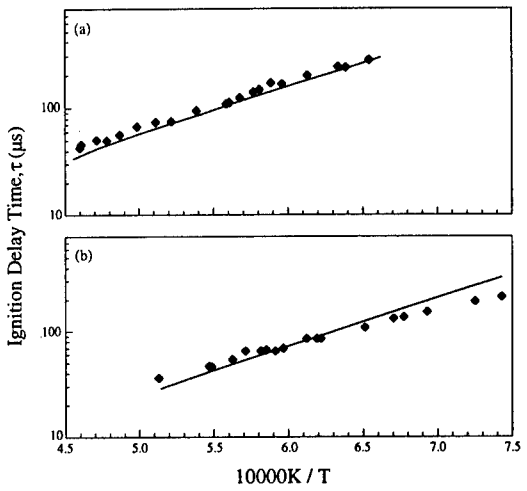


Figure 2. Ignition delay times (symbols: experimental;[25] lines: computed) for the oxidation of acetylene behind incident shock waves. (a) 0.5%C_2H_2-1.25%O_2-Ar and (b) 0.5%C_2H_2-5%O_2-Ar.

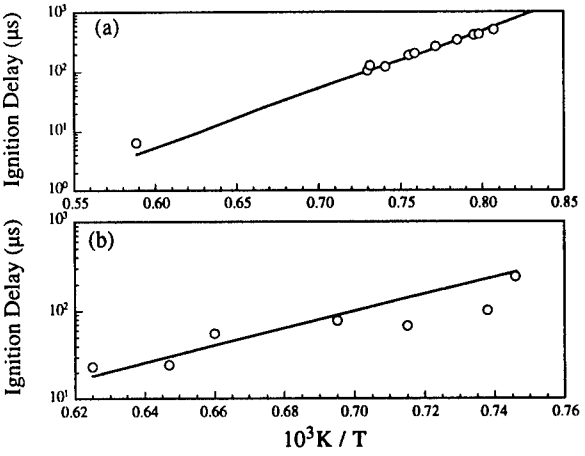


Figure 3. Ignition delay times (symbols: experimental; lines: computed) for the oxidation of propane behind reflected shock waves. (a) 3.22%C_3H_8-16.1%O_2-Ar,[26] (b) 3.3%C_3H_8-16.6%O_2-Ar.[27]

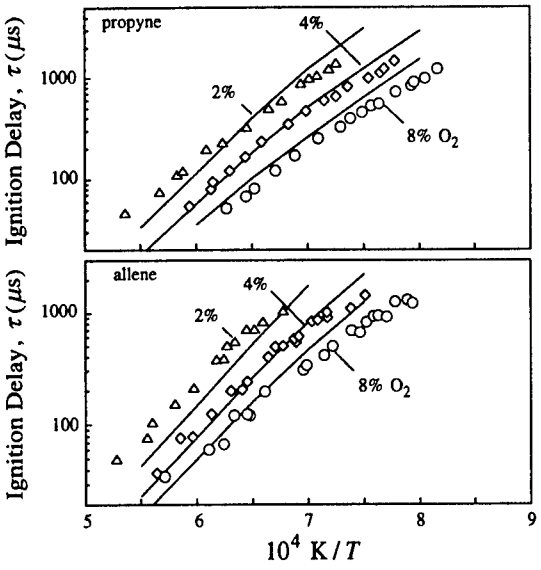


Figure 4. Ignition delay times (symbols: experimental;[28] lines: computed) for the oxidation of propyne and allene in *X*%oxygen-(99-*X*)%argon behind reflected shock waves.

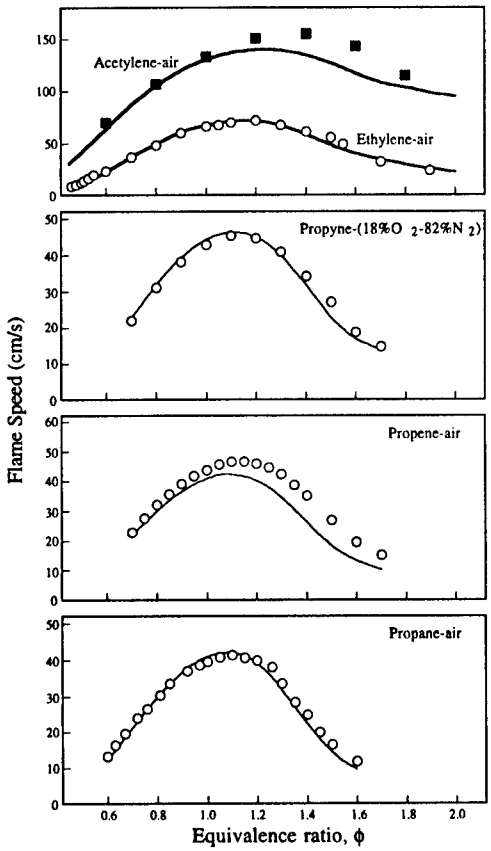


Figure 5. Experimental and computed laminar flame speeds of acetylene-,[29] ethylene-,[29] propyne-,[15] propene-,[17] and propane[30]-oxygen-nitrogen mixtures.

On the Structure of n-Heptane/Air Partially Premixed Flames Computed by Using a Detailed Reaction Mechanism

H. S. Xue and S. K. Aggarwal
Department of Mechanical Engineering
University of Illinois at Chicago
Chicago, IL 60607
Email: ska@uic.edu

ABSTRACT

The structure of a n-heptane/air counterflow partially premixed flame computed by using a detailed reaction mechanism is investigated. The flame contains two distinct reaction zones, a rich premixed reaction zone on the fuel side and a nonpremixed reaction zone on the air side. Results for an equivalence ratio $\phi = 2.0$ indicate that the fuel is completely consumed in the premixed zone with ethylene and acetylene being the major intermediate species. The reactions involving consumption of ethylene and acetylene are found to be the key rate-limiting reactions that characterize interactions between the two reaction zones. The larger molecules (C_6H_{12}, C_6H_{10}, C_5H_{10}, C_4H_8-1, C_3H_6) produced by the fuel consumption reactions reduce to C_3H_5, which is converted to C_4H_6, followed by the decomposition of C_4H_6 producing C_2 and C_1 species. As in methane/air partially premixed flames, C_2 chemistry represents an important part of the n-heptane oxidation in the premixed zone. CO and H_2 produced in the premixed reaction zone are transported to the nonpremixed reaction zone and converted to CO_2 and H_2O. In addition, a non-negligible amount of C_2H_2 is transported to the nonpremixed reaction zone and oxidized there.

INTRODUCTION

The partially premixed combustion has been a subject of considerable research in recent years. Using partial premixing, one can exploit the advantages of both nonpremixed and premixed flames regarding safety, lower pollutant emission levels, and flame stability. The partially premixed flames are also relevant to the understanding of turbulent nonpremixed combustion, which can contain regions of local extinction, followed by regions of partial premixing and re-ignition. Due to the availability of extensive experimental data and detailed chemistry models [1-4], the methane/air partially premixed flames have been investigated extensively during the past two decades. The n-heptane/air partially premixed flames, which are important in propulsion and energy-conversion applications, have not been studied so far.

Several detailed reaction mechanisms have been developed for n-heptane oxidation [5-8]. The mechanism employed in this study, which includes 41 species and 275 elementary reactions, is essentially the same as the Held's mechanism [6]. The decomposition and isomerization of n-heptyl isomers have been considered by Marchese et al. [5] and Bakali et al. [8]. However, the numerical results of Held et al. [6] indicated that predictions for various zero and one-dimensional, premixed combustion obtained without considering n-heptyl isomers compare well with the experimental results. Therefore, in order to reduce the computational efforts, the n-heptyl isomers are discarded in the present investigation, which focuses on the structure of partially premixed flames containing two reaction zones.

RESULTS AND DISCUSSION

The n-heptane reaction mechanism was first validated for predicting the laminar flame speeds for freely propagating mixture and the structure of a nonpremixed n-heptane flame. The freely propagating premixed flame speed (S_L) of n-heptane/air mixture was computed as a function of the equivalence ratio (ϕ) by using the Premix [9] and Chemkin packages [10]. The temperature of the unburned (pre-vaporized) fuel-air mixture was 298 K. The maximum premixed flame speed obtained was 39 cm/s corresponding to $\phi = 1.1$. The computed flammability limits were $0.5 \leq \phi \leq 1.7$. The computed results show reasonable agreement with the measurements [7].

For another validation, a n-heptane/air counterflow diffusion flame was simulated by using the Oppdif package [11]. The detailed description of the counterflow configuration can be found elsewhere [12]. The experimental data for a diffusion flame established over a n-heptane pool is reported by Chelliah et al. [13]. The boundary conditions employed in the computation are

$U = 2$ cm/s, $Y_{fuel} = 1.0$, $T = 373$ K at X=0 cm
$U = 21.1$ cm/s, $Y_{O2} = 0.185$, $T = 298$ K at X=1 cm

An important difference between the numerical model and the experiment is that there is no heat loss prescribed at X=0 cm in the computational model, while there is a non-negligible heat loss in the experiment due to fuel evaporation at the pool surface.

Figure 1 compares the computed and measured results in terms of the temperature profiles. The experimental profile is located closer to the left boundary compared to the computed profile, and the peak temperature in experiments (1635 K) is lower than that in computations (1705 K). In order to make a more effective comparison, the computed profile is shifted to the left by 0.05 cm such that its temperature gradient at X=0 matches with that from measurements. As indicated in Fig. 1, the shifted profile exhibits good agreement with measurements except for a small difference near the peak region, which can be attributed to the heat loss at the pool surface in the experiment.

The Computed Structure of a Partially Premixed n-Heptane/air Flame

A counterflow partially premixed n-heptane/air flame is computed by using the detailed reaction mechanism mentioned above. The fuel stream equivalence ratio (ϕ) is 2.0. The results are presented in Figs. 2-6.

Figures 2 and 3 show the temperature and major species mole fraction profiles for this partially premixed flame. The strain rate (a_s) is 15.8 s^{-1}. Similar to methane/air partially premixed flames, the flame contains two reaction zones, namely the rich premixed and the nonpremixed reaction zones. The fuel is completely consumed in the premixed reaction zone mainly by decomposition reaction R1 and atomic hydrogen abstraction reactions R2-R4

$C_7H_{16} \rightarrow CH_3 + 2C_2H_4 + C_2H_5$ (R1) $C_7H_{16} + H \rightarrow H_2 + C_4H_8\text{-}1 + C_2H_4 + CH_3$ (R2)

$C_7H_{16} + H \rightarrow H_2 + 3C_2H_4 + CH_3$ (R3) $C_7H_{16} + H \rightarrow H_2 + C_5H_{10} + C_2H_5$ (R4)

The atomic hydrogen abstraction reactions (R2-R4) actually represent the net effect of R5 and R6

$C_7H_{16} + H \rightarrow C_7H_{15} + H_2$ (R5) $C_7H_{15} \rightarrow$ smaller olefin + alkyl (R6)

R6 represents the β-scission process for n-heptyl isomers producing smaller olefins and alkyls. The n-heptyl decomposition and isomerization reactions are not considered in this study. These reactions occur at a very high rate, such that the n-heptyl isomers can be assumed to be in steady-state and discarded from the mechanism [5]. The major products of the fuel consumption are C_2-C_5 olefins, ethyl, methyl and hydrogen. The larger molecules (C_3-C_5) are then reduced to C_2 and C_1 species in the premixed reaction zone, which will be discussed later. Most of the CO is also produced in the premixed reaction zone by the oxidation of HCCO (50%), CH_2 (27%) and HCO (23%). The CO and H_2 species produced in the rich premixed reaction zone are transported to the nonpremixed zone, where they are oxidized to produce CO_2 and H_2O. Therefore, CO oxidation and H_2/O2 chemistry are dominant in the nonpremixed reaction zone, while the chemistry for fuel conversion to CO is important in the premixed reaction zone.

Figure 4 shows the mole fraction profiles for the major intermediate species larger than C_1. All the species in Fig. 4 are present only in the premixed region except for C_2H_2 which extends over to the nonpremixed zone. In the premixed zone, the mole fractions of C_2H_4 and C_2H_2 are significantly higher, by as much as 10 times, than those of other species. This implies that ethylene and acetylene are the most important intermediate species accumulated during the transient ignition process. At steady-state, they characterize the interaction between the two reaction zones. There are two sources for the production of ethylene in the premixed zone. The first one is directly from fuel decomposition and H-abstraction reactions (R1-R4), whereas the second one is from the C_2 chain. The C_2 chain is initiated by the recombination of methyl to ethane followed by the attack on ethane by H and OH producing ethyl. The ethyl radical is also produced in fuel consumption reactions (R1 and R4). The conversion of ethyl to ethylene occurs at a very fast rate making it a good assumption to consider ethyl at steady state. Ethylene is mainly consumed by conversion to vinyl (C_2H_3) which is intermediately converted to acetylene. A significant amount of acetylene is consumed in the rich premixed reaction zone producing HCCO (dominant), CH_2 and CO through reactions with O. There is also a non-negligible amount of acetylene consumption in the nonpremixed reaction zone occurring through the same reactions. The net reaction rates of ethylene and acetylene are shown in Fig. 5. In contrast to ethylene, which is nearly completely consumed in the premixed zone, the consumption of acetylene clearly shows a double flame characteristic. The conversion of HCCO produces CO and CH_2 in both reaction zones. In the premixed zone, CH_2 mainly reacts with O_2 producing CO, while the reaction with OH producing CH_3 also constitutes a non-negligible part. In the nonpremixed zone, CH_2 mainly reacts with OH producing CH_3. In the premixed zone, CH_3 recombines and forms ethane, reinforcing the C_2 chain. In addition, it also reacts with O producing CH_2O. In the nonpremixed zone, CH_3 is mainly converted to CH_2O.

The larger molecules, namely the C_6, C_5, C_4, species are produced and consumed only in the premixed reaction zone through reactions R7-R10.

$C_6H_{12} \rightarrow C_3H_5 + C_2H_4 + CH_3$ (R7) $C_6H_{10} \Leftrightarrow 2C_3H_5$ (R8)

$C_5H_{10} \Leftrightarrow C_3H_5 + C_2H_5$ (R9) $C_4H_8\text{-}1 \Leftrightarrow C_3H_5 + CH_3$ (R10)

Note that C_3H_5 is produced in each of the above reactions, indicating that C_3H_5 is an important intermediate for the flame. Figure 6 shows the reaction rate profiles for C_3H_5. The following two pairs of reactions, R11 and R12, and R13 and R14,

$C_3H_5 \Leftrightarrow C_3H_4 + H$ (R11) $C_3H_5 + H \Leftrightarrow C_3H_4 + H_2$ (R12)

$C_3H_6 \Leftrightarrow C_3H_5 + H$ (R13) $C_3H_6 + H \Leftrightarrow C_3H_5 + H_2$ (R14)

form two cycles with the net result that H atoms recombine and form H_2. The consumption of C_3H_5 actually occurs through reactions R15-R18.

$C_3H_5 + O \Leftrightarrow C_2H_3HCO + H$ (R15) $C_3H_5 + OH \Leftrightarrow C_3H_4 + H_2O$ (R16)

$2\,C_3H_5 \Leftrightarrow C_3H_4 + C_3H_6$ (R17) $C_3H_5 + C_2H_3 \Leftrightarrow C_3H_6 + C_2H_2$ (R18)

C_2H_3HCO mainly reacts with H and OH producing C_2H_3, HCO and H_2, while C_3H_4 conversion produces CH_2CO and C_3H_3. C_3H_3 then recombines with CH_3 going to C_4H_6, which is then consumed by the following two reactions:

$C_4H_6 + OH \rightarrow HCO + H + C_3H_5$ (R19) $C_4H_6 + H \Leftrightarrow C_2H_3 + C_2H_4$ (R20)

During the C_3H_5 consumption described above, R17, R18, and R19 also produce C_3H_6 and C_3H_5. Their subsequent consumption follows the same path as described by reactions R11 to R18. The production of C_2H_4 by R20 should be considered as a supplement to the two major C_2H_4 sources discussed previously.

CONCLUSIONS

The structure of a n-heptane/air counterflow partially premixed flame computed by using a detailed reaction mechanism is investigated. The flame contains a rich premixed reaction zone and a nonpremixed reaction zone. The fuel is completely consumed in the premixed reaction zone with CO and H_2 being the main products, which are transported to the nonpremixed reaction zone and oxidized to produce CO_2 and H_2O. The C_3-C_6 olefins reduce to C_3H_5 first, which are then converted to C_4H_6, followed by decomposition of C_4H_6 producing C_2 and C_1 species. In the premixed reaction zone, the mole fractions of C_2H_4 and C_2H_2 are significantly higher compared to other products of fuel consumption implying that these two are the major intermediate species accumulated up during the ignition. While ethylene is consumed in the premixed reaction zone, a non-negligible amount of acetylene is transported to the nonpremixed reaction zone. Consequently, in addition to CO and H_2, acetylene also participates in the interactions between the two reaction zones.

Reference

[1] Blevins, L. P., Gore, J. P., *Comb. Flame*, 116: 546-566 (1999).

[2] Shu, Z., Krass, B. J., Choi, C. W., Aggarwal,S. K., Katta, V. R., and Puri, I.K., *Twenty-Seventh Symposium (International) on Combustion*, The Combustion Institute, 1998, pp. 625-632.

[3] Shu, Z., Choi, C. W., Aggarwal, S. K., Katta, V. R., and Puri, I. K., *Combust. Flame*, 118: 91-107 (1999).

[4] Li, S. C. and Williams, F. A., *Combust. Flame*, 118: 399-414 (1999)

[5] Marchese, A. J., Dryer, F. L., and Nayagam, V., *Combust. Flame*, 116, 432-459 (1999).

[6] Held, T. J., Marchese, A. J., and Dryer, F. L. *Comb. Sci. Tech.* 123:107 (1997).

[7] Warnatz, J., *Twentieth Symposium (International) on Combustion*, The Combustion Institute, 1984, p. 845-856.

[8] Bakali, A. E., Delfau, J., and Vovelle, C., *Combust. Flame*, 118: 381-398 (1999).

[9] Kee, R. J., Grcar, J. F., Smooke, and M. D., Miller, J. A. *A Fortran program for modeling steady laminar one-dimensional premixed flames*. Sandia Report, SAND85-8240 (1993).

[10] Kee, R. J., Rupley, F. M., Miller, J. A. *Chemkin: A Fortran chemical kinetics package for the analysis of gas phase chemical kinetics*. Sandia Report 89-8009B (1993).

[11] Lutz, A. E. , Kee, R. J., Grcar, J. F. and Rupley, F. M. *OPPDIF: A Fortran program for computing opposed-flow diffusion flames*. Sandia Report 96-8243 (1997).

[12] Bollig, M, Pitsch, H. , Hewson, J. C., and Seshadri, K., *Twenty-sixth Symposium (International) on Combustion*, The Combustion Institute, 1996, p. 729-737.

[13] Chelliah, H. K., Bui-Pham, M., Seshadri, K., and Law. C. K., *Twenty-fourth Symposium (International) on Combustion*, The Combustion Institute, 1992, p. 851-857.

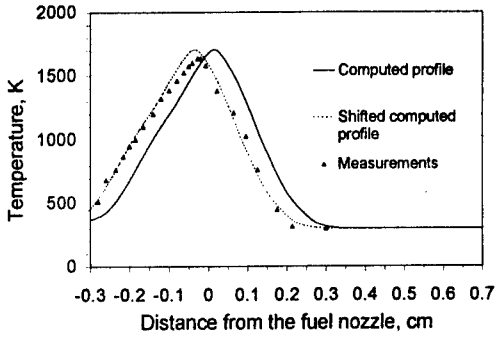


Fig. 1: computed temperature profiles before and after shift and the experimental measurements.

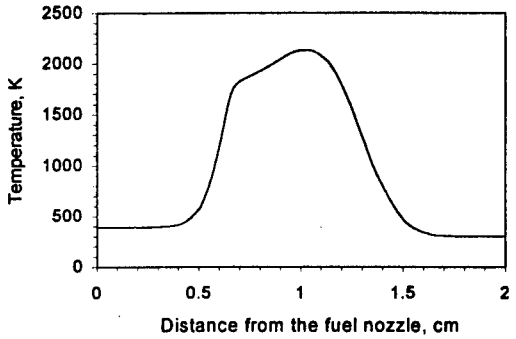


Fig. 2: computed temperature profile for the partially premixed flame.

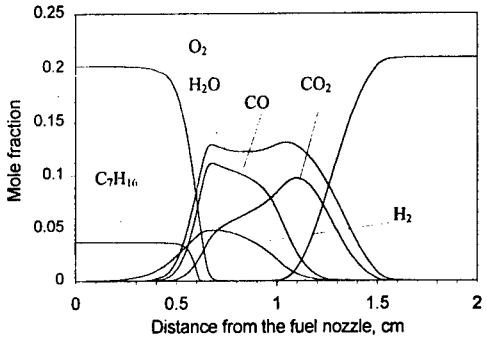


Fig. 3: mole fraction profiles for the major species

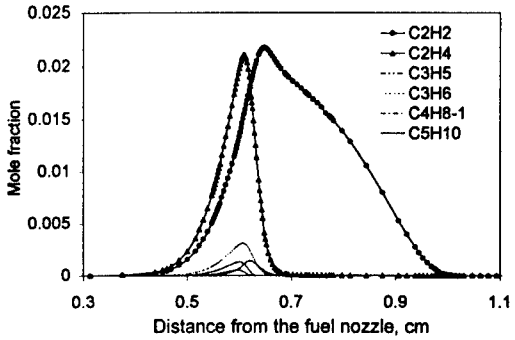


Fig. 4: mole fraction profiles for some important intermediate species.

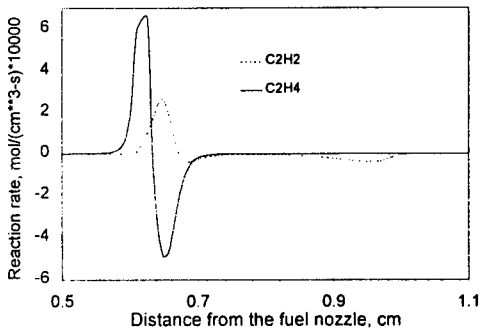


Fig. 5: reaction rate profiles ($\times 10^4$) for C_2H_4 and C_2H_2.

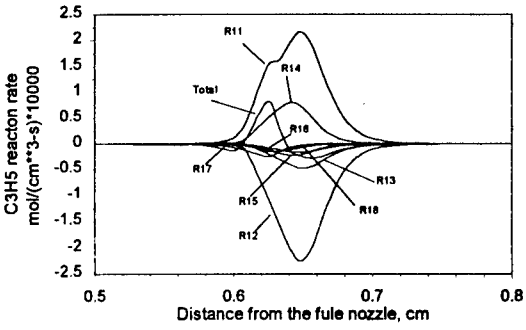


Fig. 6: C_3H_5 Reaction rate profiles ($\times 10^4$).

Detailed Kinetic Modeling of Benzene and Toluene Combustion*

Hai Wang and Zoran M. Djurisic

Department of Mechanical Engineering, University of Delaware, Newark, DE 19716
hwang@me.udel.edu

The kinetics of benzene and toluene oxidation are examined with the technique of detailed kinetic modeling. This work is motivated by both fundamental and practical considerations. In particular, while significant advance has been made in the understanding of the oxidation kinetics for aliphatic hydrocarbon combustion, comparatively fewer studies have been conducted on aromatics.[1,2] Such a disparity in emphasis is expected because of the significantly more complex nature of the aromatic kinetics. It is also obvious that since most practical fuel blends consist of large amounts of aromatics, satisfactory modeling and manipulation of the combustion processes would not be possible without a quantitative description of their oxidation kinetics. Such a concern is further substantiated by recognizing the role of aromatics kinetics in engine knock,[3] in soot production,[4-12] in the emission of polycyclic aromatic carcinogens,[13] in fullerene synthesis,[14] and in fuel-cell technology.[15,16]

Previously, Brezinsky and coworkers[2] proposed a detailed kinetic model of benzene and toluene oxidation. The model was developed on the basis of thermokinetic considerations and flow-reactor experiments. Several expanded kinetic models have been proposed and were tested against experimental data, including the species profiles in the burner-stabilized low-pressure benzene flame[17-19] of Bittner and Howard,[20] and the laminar flame speeds of benzene-air and toluene-air mixtures.[19,21,22] The proposed models predicted reasonably well each individual set of the experimental data. However, a comprehensive and physically justifiable model, which is capable of closely predicting *all* the available experimental data, is still lacking. Undoubtedly, such a situation manifests the significant uncertainties in the reaction kinetics of aromatic compounds.

The aim of this work is to examine the possibility of predicting the existing data of benzene and toluene combustion using a single unified kinetic model, and in doing so, to examine the remaining uncertainties in the reaction kinetics of benzene and toluene combustion. In this article, we report preliminary results obtained in this study. Specifically, a detailed kinetic model was compiled. The model is based on past kinetic modeling studies just described, recently published kinetic data, and our quantum mechanical and RRKM calculations for rate coefficient prediction and/or extrapolation. Numerical results are presented and compared to experimental data from previous flow reactor,[2] flames[20,21] shock-tube,[23] and stirred reactor[24] studies.

METHODOLOGIES

The current model of benzene and toluene combustion consists of 65 species and 340 elementary reactions. The reaction kinetics of C_1 and C_2 species are based on the GRI-Mech (version 1.2).[25] For larger species, the reaction pathways and rate coefficients are obtained from literature data (e.g., ref 26). Many rate parameters are analyzed using the RRKM methods in our previous studies,[27-29]

Calculations of the laminar flames are carried out using the Sandia Chemkin-II[30] and Premix[31] codes. The reverse rate coefficients are computed via equilibrium constants. While the thermochemical data of cyclopentadiene and cyclopentadiene derivatives are obtained through quantum chemical calculations,[29] others are taken from refs 27 and 32, and from the compilation of Burcat and McBride.[33]

RESULTS

Figure 1 presents the comparison of the experimental[2] and computed concentration profiles of selected species during benzene oxidation in a flow reactor at 1100 K and with the equivalence ratio equal to 0.67. It is seen that the present kinetic model predicts very well the concentrations of benzene, CO, acetylene, and cyclopentadiene. The model tends to underpredict the concentration of phenol. Figure 2 presents the comparison of species profiles during toluene oxidation at 1190 K and with the equivalence

* For presentation at the 1999 Eastern States Section of the Combustion Institute Meeting, Raleigh, NC, October 1999.

ratio equal to 1.33. Again, the major species profiles, including toluene, CO, benzene, phenol, benzaldehyde, methane, and acetylene are predicted well.

The experimental and computed major and minor species profiles are presented in Figure 3 for a burner-stabilized benzene-oxygen-argon flame at 20 torr.[20] It is seen that the model predicts very well the variation of the major species profile as a function of distance from the burner. The model also predicts well the shape and magnitude of such minor species as the H atom and the OH radical. However, for other important species like acetylene, phenol, and cyclopentadiene, the predicted mole fractions differ significantly from experimental data.

Figure 4 shows the comparison of the experimental[21] and computed laminar flame speeds of benzene- and toluene-air mixtures at atmospheric pressure. It is seen that the kinetic model predicts slightly larger flame speeds than the experimental data for benzene. However, the variation of the flame speed on the equivalence ratio is nicely predicted.

In Figure 5, we plot the experimental[23] and computed ignition delay time of a benzene-oxygen-argon mixture at a pressure of 2.5 atm. The present kinetic model appears to overpredict the data slightly, but the variation of the ignition delay on temperature is well reproduced.

DISCUSSION

We have shown that the preliminary kinetic model of benzene oxidation can account for the main features of benzene and toluene oxidation under a wide variety of combustion conditions. In general, a kinetic model based on the current understanding can account for the global combustion response for both benzene and toluene. At a more detailed level, however, significant uncertainties still remain. These uncertainties may include

(a) the reaction between benzene and the O-atom, whose branching ratios for the product channels (possibly C_6H_5OH, C_6H_5O+H, C_5H_6+CO, C_5H_5+HCO) are greatly uncertain;
(b) the production and destruction of phenoxy and phenol, as evidenced by predictions of phenol for the flow-reactor experiment (Figure 1), and for the burner-stabilized flame (Figure 3), and by the sensitivity coefficients of the reactions involving phenoxy and phenol (Figures 6 and 7);
(c) the nearly complete lack of experimental data for the reactions of benzoquinone;
(d) the reaction of cyclopentadienyl and cyclopentadiene.

Zhong and Bozzelli[34] recently performed a thermochemical and kinetic analysis of the chemically activated reactions between H, OH, HO_2, O, and O_2 with the cyclopentadienyl radical. This study presents an advance in the oxidation kinetics of the cyclopentadienyl radical, because previously there have been little theoretical/experimental information concerning these reactions. These reactions generally exhibit significant complexities as manifested by the multiplicity of product channels and the dependence of the branching ratios of various channels as a function of pressure and temperature. Clearly, additional experimental and theoretical work on the reaction kinetics of phenol, cyclopentadiene, and the radicals and molecules derived from phenol and cyclopentadiene is critically needed before a comprehensive, physically justifiable, and predictive model of benzene and toluene combustion can be achieved.

CONCLUSION

A detailed kinetic model of benzene and toluene oxidation is compiled. It is shown that the kinetic model predicts reasonably well the main feature of benzene and toluene oxidation in flow reactors, flames, and shock tubes. Significant uncertainties still remain at a more detailed level. These uncertainties may include the reaction kinetics of aromatic-ring oxidation reactions, and the subsequent breakage of the five-membered ring species.

Acknowledgment *The work is sponsored by the National Science Foundation CAREER Development program (CTS 9874768) under the technical monitoring of Dr. Farley Fisher. The computation was performed at the facility for computational chemistry at the University of Delaware, which is funded by the National Science Foundation (CTS-9724404).*

REFERENCES

(1) Brezinsky, K. *Prog. Energy Combust. Sci.* **1986**, *3*, 1.
(2) Emdee, J. L.; Brezinsky, K.; Glassman, I. *J. Phys. Chem.* **1992**, *96*, 2151.
(3) Sawyer, R. F. *Twenty-Fourth Symposium (International) on Combustion*; The Combustion Institute: Pittsburgh, 1992, pp. 1423-1432.
(4) Haynes, B. S.; Wagner, H. Gg. *Prog. Energy Combust. Sci.* **1980**, *7*, 229.
(5) Calcote, H. F. *Combust. Flame* **1981**, *42*, 215.
(6) Homann, K. H. *Twentieth Symposium (International) on Combustion*; The Combustion Institute: Pittsburgh, 1984, pp. 857-870.
(7) Bittner, J. D.; Howard, J. B. in *Soot in Combustion Systems and its Toxic Properties*; Lahaye, J.; Prado, G. Eds.; Plenum: New York, 1983.
(8) Bockhorn, H.; Fetting, F.; Wenz, H. W. *Ber Bunsenges. Phys. Chem.* **1983**, *87*, 1067.
(9) Frenklach, M.; Warnatz, J. *Combust. Sci. Technol.* **1987**, *5*, 265.
(10) Frenklach, M.; Wang, H. *Twenty-Third Symposium (International) on Combustion*; The Combustion Institute: Pittsburgh, 1991, pp. 1559-1566.
(11) Howard, J. B. *Twenty-Third Symposium (International) on Combustion*; The Combustion Institute: Pittsburgh, 1991, p. 1107.
(12) McKinnon, J. T.; Howard, J. B. *Twenty-Fourth Symposium (International) on Combustion*; The Combustion Institute: Pittsburgh, 1992, pp. 965-971.
(13) Longwell, J. P. *Nineteenth Symposium (International) on Combustion*, The Combustion Institute, Pittsburgh, 1982, pp. 1339-1350.
(14) Howard, J. B., *Twenty-Fourth Symposium (International) on Combustion*; The Combustion Institute: Pittsburgh, 1992, pp. 933-946.
(15) Otsuka, K.; Yamanaka, I.; Hosokawa, K. *Nature*, **1990**, 697.
(16) Otsuka, K.; Furuya, K. *Electrochim. Acta* **1992**, *37*, 1135.
(17) Lindstedt, R. P.; Skevis, G., *Combust Flame* **1994**, *99*, 551.
(18) Zhang, H.-Y.; McKinnon, J. T. *Combust. Sci. Technol.* **1995**, *107*, 261.
(19) Tan, Y. W.; Frank, P. *Twenty-Sixth Symposium (International) on Combustion*; The Combustion Institute: Pittsburgh, 1996, p. 677.
(20) Bittner, J. D.; Howard, J. B. *Eighteenth Symposium (International) on Combustion*; The Combustion Institute: Pittsburgh, 1980, p. 1105.
(21) Davis, S. G.; Wang, H.; Brezinsky, I.; Law, C. K. *Twenty-Sixth Symposium (International) on Combustion*; The Combustion Institute: Pittsburgh, 1996, p. 1025.
(22) Lindstedt, R. P.; Maurice, L. Q. *Combust. Sci. Technol.* **1996**, *120*, 119.
(23) Burcat, A.; Snyder, C.; Brabbs, T., NASA Technical Memorandum 87312, 1986.
(24) Chai, Y.; Pfefferle, L. D. *Fuel* **1998**, *77*, 313.
(25) Frenklach, M.; Wang, H.; Goldenberg, M.; Smith, G. P.; Golden, D. M.; Bowman, C. T.; Hanson, R. K.; Gardiner, W. C.; Lissianski, V. *GRI-Mech–An Optimized Detailed Chemical Reaction Mechanism for Methane Combustion*; GRI Technical Report No. GRI-95/0058, November 1, 1995.
(26) Baulch, D. L.; Cobos, C. J.; Cox, R. A.; Frank, P.; Hayman, G.; Just, TH.; Kerr, J. A.; Murrells, T.; Pilling, M. J.; Troe, J.; Walker, R. W.; Warnatz, J. *Combust. Flame*, **1994**, *98*, 59.
(27) Wang, H.; Frenklach, M., *J. Phys. Chem.* **1994**, *98*, 11465.
(28) Wang, H.; Frenklach, M., *Combust. Flame* **1997**, *110*, 173.
(29) Wang, H; Brezinsky, K. *J. Phys. Chem.* **1998**, *102*, 1530.
(30) Kee, R. J.; Rupley, F. M.; Miller, J. A., Sandia Report SAND 89-8009B; Sandia National Laboratories: Albuquerque, New Mexico, 1989.
(31) Kee, R. J.; Grcar, J. F.; Smooke, M. D.; Miller, J. A., Sandia Report SAND85-8240 UC4; Sandia National Laboratories: Albuquerque, New Mexico, 1985.
(32) Wang, H.; Frenklach, M., *J. Phys. Chem.* **1993**, *97*, 3867.
(33) Burcat, A.; McBride, B. *1997 Ideal Gas Thermodynamic Data for Combustion and Air-Pollution Use*; Technion Aerospace Engineering (TAE) Report # 804, 1997.
(34) Zhong, X.; Bozzelli, J. W. *J. Phys. Chem. A* **1998**, *102*, 3537.

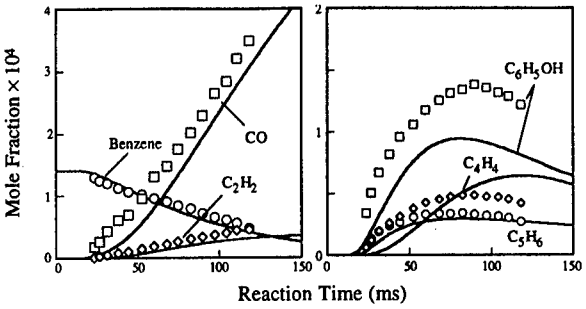


Figure 1. Experimental[2] and computed species profiles for benzene oxidation (0.14% C_6H_6-1.62% O_2-N_2, the equivalence ratio ϕ = 0.67) in a flow reactor at 1100 K and 1 atm pressure.

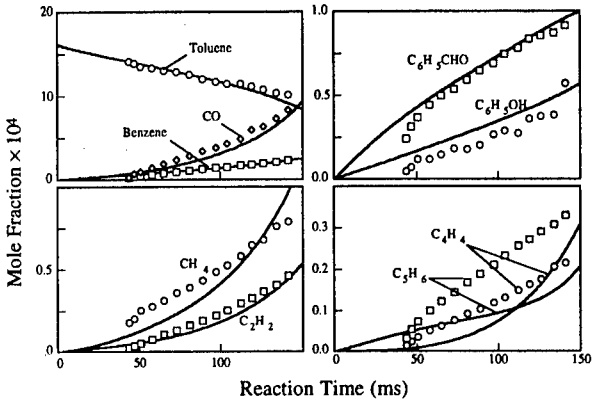


Figure 2. Experimental[2] and computed species profiles for toluene oxidation (0.162% C_7H_8-1.094% O_2-N_2, the equivalence ratio ϕ = 1.33) in a flow reactor at 1190 K and 1 atm pressure.

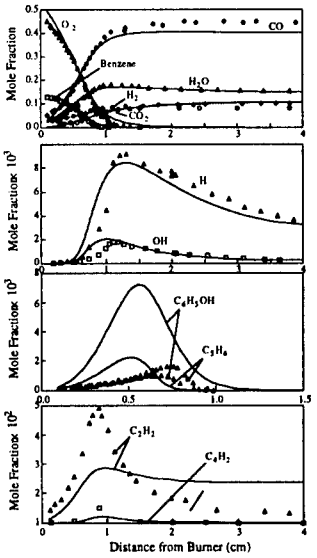


Figure 3. Experimental[20] and computed species profiles in a burner-stabilized laminar premixed flame, burning a 13.5% benzene-56.5 % O_2-Ar mixture at 20-torr pressure.

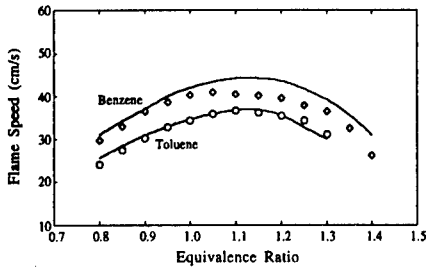


Figure 4. Experimental[21] and computed laminar flame speed of benzene- and toluene-air mixture at 1 atm pressure.

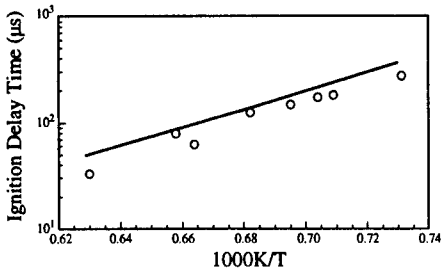


Figure 5. Experimental[23] and computed ignition delay time for a 1.69% benzene-12.675% O_2-Ar mixture at p_5 = ~2.5 atm.

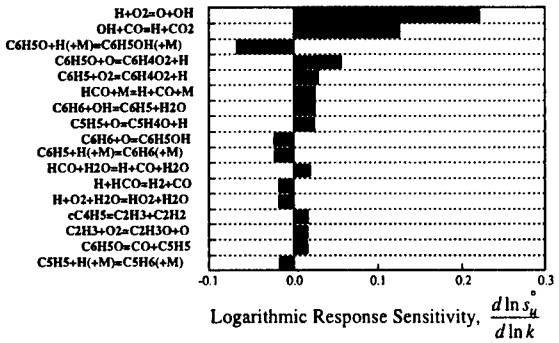


Figure 6. Ranked first-order sensitivity coefficients of flame speeds of the benzene-air mixture with ϕ = 1.

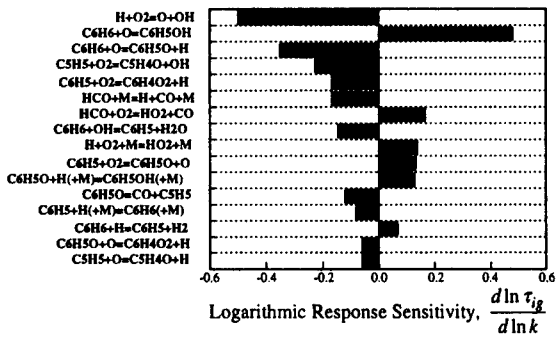


Figure 7. Ranked first-order sensitivity coefficients of ignition delay times at 1500 K, and with other conditions shown in Figure 5.

A MODELING STUDY OF BENZENE FORMATION IN ALIPHATIC FLAMES

Christopher J. Pope and James A. Miller
Combustion Research Facility
Sandia National Laboratories
Livermore, CA 94551-0969, USA

The predictive capabilities of three published chemical kinetics mechanisms are studied by comparing predictions of benzene (C_6H_6), phenyl radical (C_6H_5), and propargyl radical (H2CCCH) against data for three laminar premixed low-pressure flat flames of aliphatic fuels. Not only do the predictions differ greatly from each other, but reaction path and sensitivity analyses show that different reactions appear to be important for each mechanism. For all three mechanisms, reactions involving the propargyl radical are found to be significant contributors to ring formation for all three flames.

Approach

All flame calculations were performed using the CHEMKIN suite of modeling programs[1-5]. Full multicomponent diffusion, including thermal diffusion, was included in the calculations. The catalytic boundary condition for H-atom recombination at the burner surface was also included. Experimental temperature profiles were used as input, in lieu of solving the energy equation.

Concentration data from three aliphatic flames were used to test the mechanisms. The first flame (F1) is a 20-Torr $C_2H_2/O_2/45\%$ Ar flame[6], having an equivalence ratio (φ) of 2.5, a cold-gas velocity of 97 cm/s and a maximum temperature of 1866 K. The second flame (F2) is a φ=1.9 $C_2H_4/O_2/50\%$ Ar flame[7], with a pressure of 20 Torr, cold-gas velocity of 62.5 cm/s, and a maximum temperature of 2208 K. F3 is a $C_3H_6/O_2/25\%$ Ar flame[8], with φ=2.32, p=37.5 Torr, cold-gas velocity of 48.2 cm/s, and a maximum temperature of 2300 K. The three mechanisms used are those of Pauwels et al.[9](M1), Richter et al.[10](M2), and Marinov et al.[11](M3).

Each of the three mechanisms was used without any modification on all three of the flames, with the exception of M1, which did not contain reactions for C_3H_6 and C_3H_5 species, and therefore could not be used as is on F3. The focus of the present work is on the mechanisms of formation of the first aromatic ring. Therefore, the results discussed here will center on the C_6H_6, C_6H_5, and H2CCCH species.

Summary of Results

Table 1 shows the predicted and experimental peak mole fractions and locations (cm height above burner) for H2CCCH, C_6H_5, and C_6H_6 for all the calculations performed. Also shown are the ratios of the predicted peak mole fraction to the experimental peak mole fraction for all cases. In general, M2 most seriously underpredicts the formation of H2CCCH, C_6H_5, and C_6H_6. All three mechanisms underpredict C_6H_5 concentrations. M3 consistently overpredicts the C_6H_6 concentration, and except for F3, overpredicts the H2CCCH concentration.

Looking at the chemistry for H2CCCH in these mechanisms, a rate of production analysis shows $^1CH_2 + C_2H_2 = H2CCCH + H$ to be a major contributor to the production of propargyl for all three flames for M1 and M3. This reaction does not appear in M2, perhaps explaining the extent of

underprediction for propargyl and the different predicted shape of the profile. In M2, major propargyl formation pathways include HCCO + C_2H_2 = H2CCCH + CO (a reaction appearing in all three mechanisms) and CH_3 + C_2H = H2CCCH + H. In F3, formation via H-abstraction from the C_3H_4 species is also important. In M1 and M3, most of the consumption occurs via H-abstraction to form C_3H_2 for all flames. In M2, most of the propargyl reacts with CH_2 to form a C_4H_4 plus H atom.

A key formation pathway for C_6H_5 and C_6H_6 in all three flames is the combination of propargyl radicals in M1 and M3. In M1, the reaction is 2 H2CCCH = C6H5 + H, while in M3 2 propargyl radicals can also combine to directly form C_6H_6. The reverse reaction C_6H_6 = 2 H2CCCH appears as an important propargyl formation pathway in M3 for F3. Other important ring-formation pathways include: H2CCCH + AC3H5 (allyl) = fulvene + 2H (M3, F2 and F3); HCCHCCH + C_2H_2 = C6H5 (M1, F2); H2CCCCH + C_2H_2 = C6H5 (M3, all flames); and cyclization of linear C_6H_5 (M2, all flames). At the higher temperatures of F2 and F3, isomerization of fulvene to benzene is a major benzene formation route, whether by unimolecular isomerization or the reaction fulvene + H = benzene + H. Also, from H-abstraction and from C-H bond breaking in benzene (and the reverse reactions), there is a lot of interconversion between benzene and phenyl radical.

In addition to the above reactions, sensitivity analysis shows a dependence upon the rates of reactions forming and consuming $^1CH_2$, such as H + HCCO = $^1CH_2$ +CO (all mechanisms) and $^1CH_2$ + O_2 = CO + OH + H (all mechanisms, but M2 has a lower A factor), as well as upon the reaction O + OH = O_2 + H.

References

1) Kee, R. J., Rupley, F. M., and Miller, J. A., Sandia Technical Report SAND 89-8009, Sandia National Laboratories, Livermore, CA, December 1989.
2) Kee, R. J., Dixon-Lewis, G., Warnatz, J., Coltrin, M.E., and Miller, J. A., Sandia Technical Report SAND 86-8246, Sandia National Laboratories, Livermore, CA, December 1990.
3) Kee, R. J., Grcar, J. F., Smooke, M. D., and Miller, J. A., Sandia Technical Report SAND 85-8240, Sandia National Laboratories, Livermore, CA, December 1985.
4) Grcar, J. F., Kee, R. J., Smooke, M. D., and Miller, J. A., *Twenty-First Symposium (International) on Combustion*, The Combustion Institute, Pittsburgh, 1991, pp. 1773-1782.
5) Kee, R. J., Rupley, F. M., and Miller, J. A., Sandia Technical Report SAND 887-8215B, Sandia National Laboratories, Livermore, CA, December 1990.
6) Douté, C., Delfau, J.-L., Vovelle, C., *Combust. Sci. and Tech.*, 103:153-173 (1994).
7) Bhargava, A., and Westmoreland, P. R., *Combustion and Flame*, 113:333-347 (1998).
8) Atakan, B., Hartlieb, A. T., Brand, J., and Kohse-Höinghaus, *Twenty-Seventh Symposium (International) on Combustion*, The Combustion Institute, Pittsburgh, 1998, pp. 435-444.
9) Pauwels, J.-F., Volponi, J. V., and Miller, J. A., *Combust. Sci. and Tech.*, 110-111:249-276 (1995).
10) Richter, H., Grieco, W. J., and Howard, J. B., *Combustion and Flame*, accepted for publication.
11) Marinov, N. M., Pitz, W. J., Westbrook, C. K., Lutz, A. E., Vincitore, A. M., and Senkan, S. M., *Twenty-Seventh Symposium (International) on Combustion*, The Combustion Institute, Pittsburgh, 1998, pp. 605-613. Also references cited therein.

Table 1. Summary of experimental mole fraction predictions for H2CCCH, C_6H_5, and C_6H_6 for the three flames and three mechanisms.

C_2H_2/O_2 flame (F1)

H2CCCH	M1	M2	M3	data
peak mole fraction	5.35E-4	1.74E-4	1.89E-3	5.49E-4
predicted peak/exp. peak	0.97	0.32	3.44	----------
peak location (cm HAB)	0.74	0.88	0.72	0.55
C6H5				
peak mole fraction	2.07E-6	3.82E-8	1.39E-5	[no data]
peak location (cm HAB)	0.60	0.42	0.62	[no data]
C6H6				
peak mole fraction	2.32E-5	3.63E-6	6.75E-4	5.87E-5
predicted peak/exp. peak	0.40	0.07	11.50	----------
peak location (cm HAB)	0.55	0.47	0.62	0.55

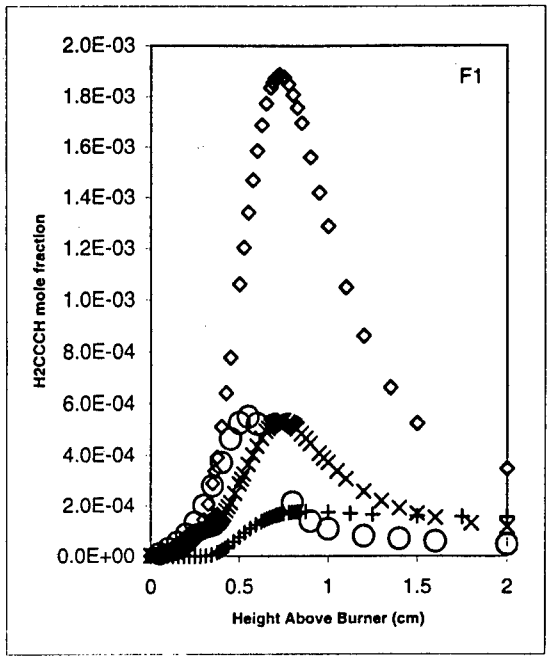
C_2H_4/O_2 flame (F2)

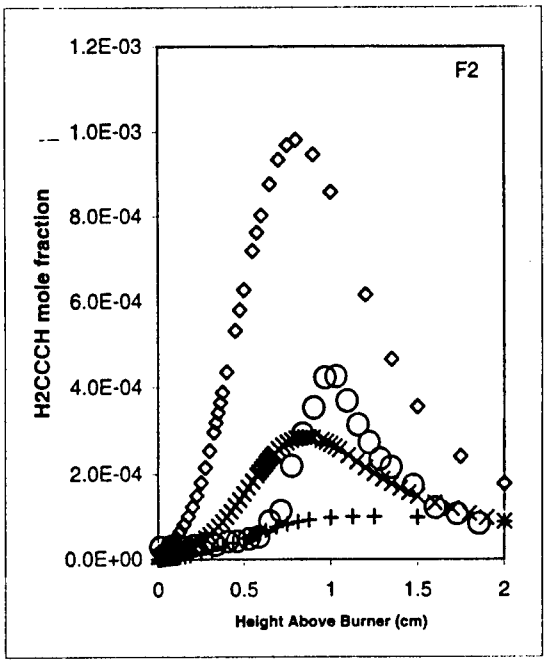
H2CCCH	M1	M2	M3	data
peak mole fraction	2.87E-4	1.02E-4	9.80E-4	4.26E-4
predicted peak/exp. peak	0.67	0.24	2.30	----------
peak location (cm HAB)	0.87	1.25	0.80	1.03
C6H5				
peak mole fraction	2.91E-7	9.50E-8	1.58E-6	1.70E-5
predicted peak/exp. peak	0.017	0.006	0.093	----------
peak location (cm HAB)	0.59	0.02	0.58	0.84
C6H6				
peak mole fraction	2.32E-6	9.37E-7	1.09E-4	3.33E-5
predicted peak/exp. peak	0.070	0.028	3.27	----------
peak location (cm HAB)	0.50	0.31	0.50	0.90

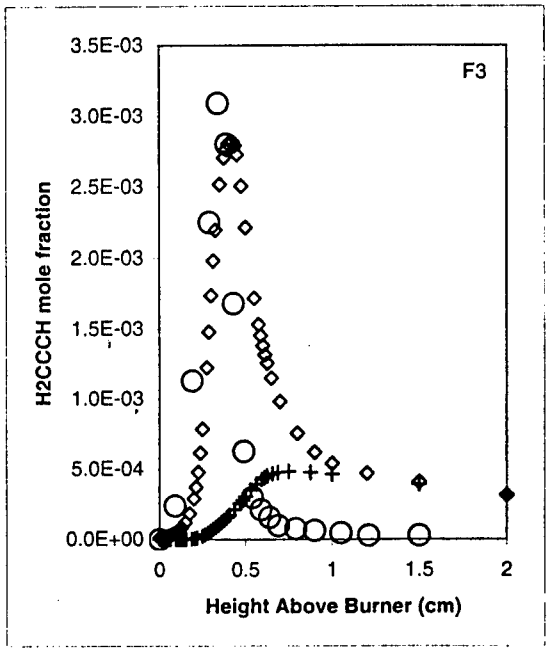
C_3H_6/O_2 flame (F3)

H2CCCH	M1	M2	M3	data
peak mole fraction	xxxx	4.86E-4	2.82E-3	3.09E-3
predicted peak/exp. peak	xxxx	0.16	0.91	----------
peak location (cm HAB)	xxxx	0.75	0.41	0.34
C6H5				
peak mole fraction	xxxx	1.20E-8	2.67E-5	7.43E-5
predicted peak/exp. peak	xxxx	0.0002	0.36	----------
peak location (cm HAB)	xxxx	0.19	0.38	0.29
C6H6				
peak mole fraction	xxxx	1.27E-6	2.83E-3	1.22E-3
predicted peak/exp. peak	xxxx	0.0010	2.31	----------
peak location (cm HAB)	xxxx	0.19	0.38	0.39

Figure 1. Predicted and experimental mole fraction profiles for H2CCCH, one graph for each flame (indicated in the upper right-hand corner). Legend: circles, data; x, M1; +, M2, diamonds, M3.







Acknowledgments

This work is sponsored by the Department of Energy, Office of Basic Energy Sciences, Division of Chemical Sciences. The authors also thank Henning Richter (M.I.T.) and Nick Marinov (LLNL) for providing electronic copies of their reaction sets and thermochemical properties, Burak Atakan (U. Bielefeld) and Phil Westmoreland (U. Mass. - Amherst) for machine-readable tables of their experimental data, and Fran Rupley (Sandia - Livermore) for assistance with the calculations.

Sub- and Super-Critical Pyrolysis of Endothermic Fuels

I. Glassman, J.F. Stewart, and S.P. Zeppieri
Department of Mechanical & Aerospace Engineering
Princeton University
Princeton, NJ 08544
Glassman@princeton.edu

I. Introduction

Projected next generation Air Force aircraft gas turbine engines will have compression ratios that will create pressure and temperature fields that will cause fuel lines to reach a supercritical state (1). Considering as well, that advanced aircraft may require special cooling abilities, a study of the sub- and supercritical pyrolysis of endothermic fuels methylcyclohexane (MCH), decalin and tetraline was undertaken. The driving force was to determine whether there were unique differences in rates and products between the two physical conditions and whether fuel fouling concerns could be prevalent under supercritical conditions. MCH is the alkyl derivative of toluene, decalin the alkyl derivative of naphthalene and tetralin is an alkyl-aromatic. Since they are napthenes, a component of residual and JP fuels, MCH and decalin are of further interest. Presented in this paper is a general comparison of the pyrolysis rates and product composition of these fuels under sub- and super-critical conditions.

II. Experimental Results

The subcritical experiments were performed at 1 atm in the Princeton Turbulent Flow Reactor (2,3) and the supercritical experiments in a recently developed unique reactor (4,5,6,7). Reported in Fig. 1 are the global kinetic rate data for the decomposition of the three endothermic fuels determined from a first order/pseudo first order analysis (6).

Fig. 2 summarizes the kinetic results and lists the rate constants and major products found. These results were obtained from detailed chemical analyses and for the supercritical case derived from numerous histograms. To be noted in Fig. 2, dimethylcyclopentane is not formed in the 1 atm studies with respect to MCH and methylhexahydroindane is not found in the 1 atm studies of decalin. If one examines the activation energies, one notes that all except the subcritical study are in the 270 kcal/mole range. Since it is likely that the original bond to be broken in all cases would be the same, one would expect similar values for the activation energy. Since the 10^{11} sec^{-1} A factor for decalin at 1 atm appears low, it is interesting to note this value would be 10^{13} sec^{-1} as for MCH if the activation energy of decalin were chosen in the 270 kcal/mole range. This suggestion is simply made to stress the very interesting point that the A factor for the supercritical results is about two orders of magnitude greater than the 1 atm results. This order of magnitude difference in the A factor may be significant in understanding of the supercritical process and has been under investigation (6).

As depicted in Fig. 2 the subcritical (gas phase) MCH pyrolysis results reveal that methylcyclopentane pyrolysis is β scission dominated, little, if any, PAH is found during the pyrolysis and the major products are ethene, 1,3 butadiene, methane and propane (1). Shown in Fig. 3, as well, is the general pyrolysis mechanism proposed and essentially validated. A detailed mechanism has been presented in the recent Ph.D. thesis of Stewart (6). This paper chooses not to present detailed mechanisms containing hundreds of reactions and their corresponding rate data, but instead to emphasize the key mechanistic steps which represent the best insight to the new fundamental concepts proposed. Characteristic of such an effort is the general pyrolysis mechanism of MCH reported in Fig. 3. Fundamental to subsequent discussion is the fate of the methylhexedienyl radical designated MHL in this figure.

III. Discussion

From the histograms obtained for MCH pyrolysis and summarized in Fig. 2, it is concluded that while β scission processes are still important under supercritical conditions, they are significantly slower. Further, dimethylpentane and methylcyclopentane are major products not found under subcritical conditions. Consistent with the similarity of the activation energy results presented in Fig. 2, the general steps to the formation of MHL remain the same as depicted in Fig. 3. Note, however, in Fig. 3, it is proposed that dimethylpentane develops from its corresponding MHL radical shown. The process by which the initial 6-member ring is converted to a 5-member ring is most apparently due to the phenomenon of caging, a phenomenon frequently discussed in the supercritical chemical process literature. Thus, it appeared quite evident that under supercritical conditions, MCH pyrolysis created MHL which then follows two possible routes to further change: β scission leading essentially to innocuous products, or a cyclization due to the phenomenon called caging and possibly leading to significant PAH formation. Obviously, the extent of either route depends on the physical parameters of the experiments.

To understand the phenomenon of caging, it is best to consider both routes simultaneously. To offer a simple phenomenological approach, consider that in the dissociative β scission process, the products of any β scission step must diffuse away in competition with a collision process that would cause a radical such as MHL to

form a new bond instead of breaking one and create a cyclohydrocarbon compound. One can visualize that this process would most likely occur under very high pressures. Thus it is quite apparent that in a practical system the amount of PAH and subsequent particulates that form is due to the competitive "rate processes," one controlled by the diffusion of dissociated species (β scission) and the other by a collision rate process that forms a new bond (caging).

A similar competition occurred in the case of decalin and the comparison of the results is correspondingly similar to the MCH results. As shown in Fig. 4, decalin during supercritical pyrolysis forms methylhexahydroindane via methylhexedienyl radicals and these precursors are available to form PAH and particulates. Also shown in Figs. 4 are two subcritical mechanisms, one proposed in this study (4) and the other by another investigator (8).

In order to estimate the effect of caging with respect to a chemical process, the general approach has been to apply transition state theory (9,10). What essentially has been considered in general transition state theory (10) is the rate of formation of a product through an intermediate (complex) in competition with the intermediate reforming the initial reactant. In essence, β scission is considered in competition with caging. However, the current effort with respect to pyrolysis has extended the concept in that the intermediate does not proceed back to the reactant, but has two possible routes to form different products, one a β scission route to innocuous products and the other a caging process leading to products which could cause fuel line fouling.

Now, following the classical chemical approach to evaluating the extent of a given route, the argument is presented that under supercritical conditions the extent of PAH formation would be determined by the ratio of the collisional rate of formation of the new cyclohydrocarbon due to caging to the diffusion rate of the β scission products "to get out of the cage". This ratio can be represented by the following expression [vd2 exp(-E/RT)/D] or [v exp(-E/RT)]/(D/d2). Where v is the collision frequency (sec^{-1}), d^2 the collision cross section, E the activation energy and D the mass diffusivity (cm^2/sec)(8). Essentially vd^2 is the pre-exponential kinetic A factor of the rate expression in the numerator. The preceding second representation above is formulated so that a ratio of characteristic times is presented. This time ratio will be recognized as a Damkohler number (9,10). Further, for the pyrolysis processes under consideration in this effort, the caging institutes a bond formation process and thus the activation energy is zero. Thus the relevant Damkohler number is $[v/(D/d^2)]$.

Typical small molecule diffusivities have been reported to be from 10^{-1} cm^2/sec for gases to 10^{-5} cm^2/sec in liquids (9). One would estimate that under the supercritical conditions of the experiments discussed here that the diffusivities of a supercritical fluid would be somewhere between the two values, say of the order 10^{-3} cm^2/sec . It is very tempting to speculate that the near two order of magnitude differences in A factor found between the sub and supercritical conditions reported in this research is due to two orders of magnitude difference between the diffusion under sub and supercritical conditions, but currently there is no real justification for this comparison. However, it is relevant to point out that, although supercritical fluids have in many instances greater similarity to liquids than gases, their diffusivities act more like gases in that they are inversely proportional to pressure. The diffusivities of liquids are independent of pressure. Certainly, these statements are true for the range of supercritical pressures in this study. Thus caging products should increase with pressure. Due to this concept, the ratio of intermediate methylhexahydroindane formation to the β scission route of decalin through methylhexahydroindane was measured as a function of pressure for a given temperature. The results are presented in Fig. 5. As will be noted in this figure, there is a substantial increase in methylhexahydroindane with pressure, nearly an order of magnitude increase with an increase from 1 to 85 atm in pressure. These results are of great significance, not only for their application to practical considerations in that a small amount of particulates could play havoc in an aircraft gas turbine fuel line, but also that they offer fundamental confirmation of the conceptual processes proposed and illustrate the important parameters which a design engineer must consider.

It is important to note, as well, that the necessary data to develop the concepts presented were best obtained with relatively low supercritical reactor residence times. To validate the projections put forth, experiments with MCH at 820 K and 82 atm were performed with reactor residence times that approached 120 secs. The results are reported in Fig. 6 and clearly show that the known precursors to particulates, such as soot, readily form.

Acknowledgments

This research was sponsored by the Air Force Office of Scientific Research, air Force Systems Command, USAF, under Grant number AFOSR Grant F49620-98-1-0134. The U.S. Government is authorized to reproduce and distribute reprints for Government purposes notwithstanding any copyright notation thereon.

References

1. Edwards, T., "USAF Supercritical Hydrocarbon Fuels Interests", AIAA Paper 93-0807 (1993).
2. Zeppieri, S., Brezinsky, K., and Glassman, I., "Pyrolysis Studies of Methylcyclohexane and Oxidation Studies of Methylcyclohexane/Toluene Blends," Combust. And Flame 108, 266 (1997)
3. Zeppieri, S., "Pyrolysis and Oxidation of Endothermic Fuels, Princeton University, Princeton University, Dept. of Mech. and Aero. Eng., Ph.D. Thesis, 1999.
4. Davis, G.D., "An Experimental Study of Supercritical Methylcyclohexane Pyrolysis," Princeton University, Dept. of Mech. And Aero. Eng., M.S.E. Thesis, 1994.
5. Stewart, J., Brezinsky, K., and Glassman, I., "Supercritical Pyrolysis of Decalin, Tetralin, and N-Decane at 700-800 K Product Distribution and Reaction Mechanism", Combust. Sci. and Tech. 136, 373 (1998).
6. Stewart, J., "Supercritical Pyrolysis of Endothermic Fuels", Princeton University, Dept. of Mech. and Aero. Eng., Ph.D. Thesis, 1999.
7. Stewart, J., Glassman, I., and Brezinsky, K., "Supercritical Methylcyclohexane Pyrolysis. A Flow Reactor Study," ACS Symposium on Structure of Fuels V, ACS 216th National Meeting, Boston, MA, Aug. 1998.
8. Ondruschka, B., Zimmermann, G., Remmler, M., Sedlackova, M., and Pola, I., "Thermal Reactions of Decalin", J. of Anal. And Appl. Pyrolysis, 18, 19 (1990).
9. Wu, B.C., Klein, M.T., and Sandler, S.I., "Solvent Effects on Reactions in Supercritical Fluids," Ind. Eng. Chem. Res., 30, 822 (1991).
10. Glassman, I., COMBUSTION, 3rd Ed., Chap. 3, Academic Press, LaJolla, CA, 1996.

Global Kinetic Rates

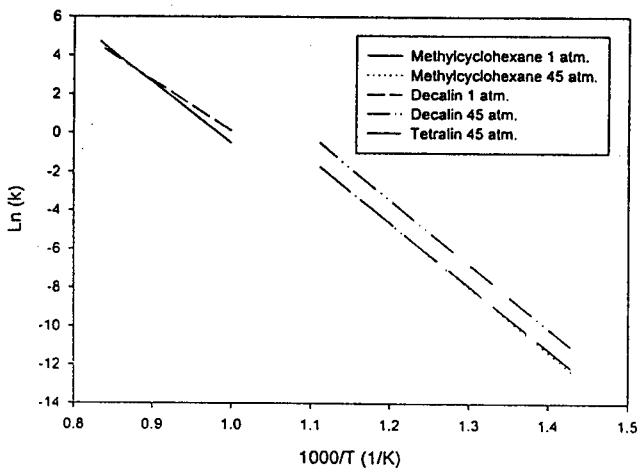


Figure 1

Integrated Research Summary

Fuel	Phase	A (1/sec)	Ea (kJ/mole)	Major Products
Methylcyclohexane	gas	2.55E+13	261	ethene, 1,3 butadiene, methane, propene
Methylcyclohexane	supercritical	2.51E+15	278	methane, ethane, propene, ethene, dimethylcyclopentane, propane, 1-methyl-1-cyclohexene, ethylcyclopentane
Decalin	gas	2.70E+11	218	methane, ethene, propene, 1,3 butadiene, benzene, toluene
Decalin	supercritical	6.31E+15	276	methane, propane, ethane, propene, ethene, butene, butane, methylhexahydroindane, indene
Tetralin	supercritical	1.26E+15	273	naphthalene, methylindane, ethane, methane, ethene, phenylbutane, propane, propene

Figure 2

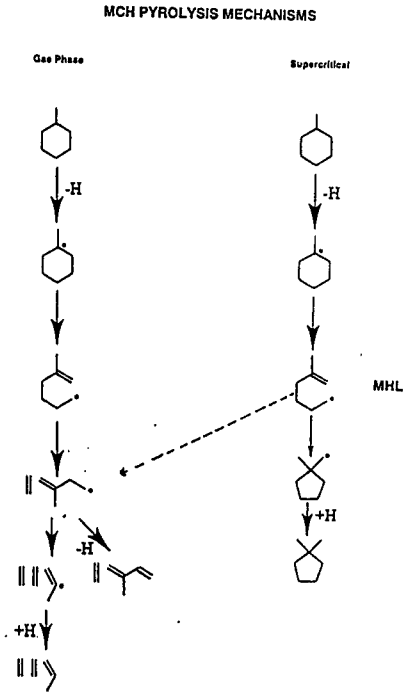
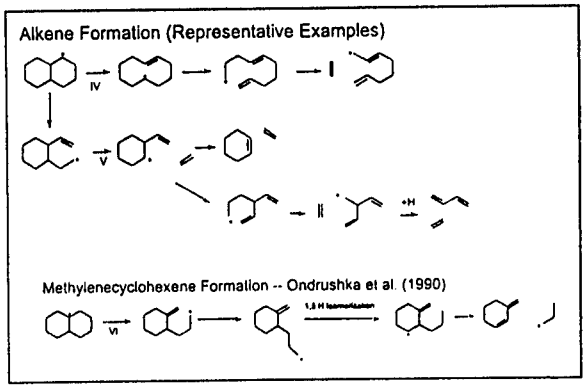


Figure 3

Decalin Pyrolysis Gas Phase



Supercritical Decalin Pyrolysis

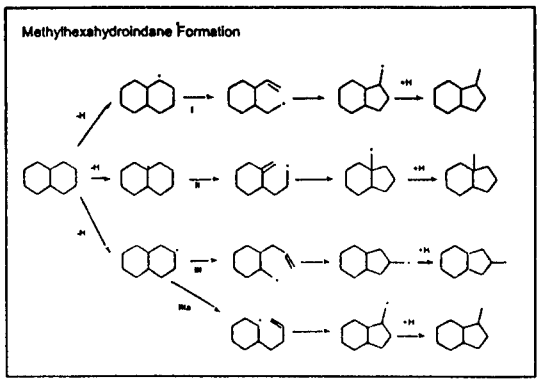


Figure 4

Effects of Supercriticality (Caging)

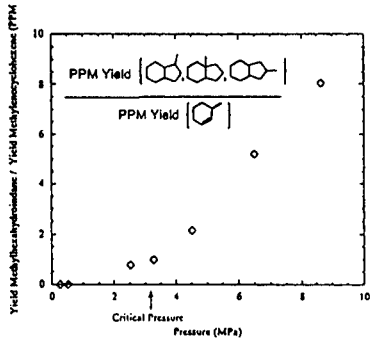


Figure 5

Polycyclic Aromatic Hydrocarbon Formation at 820K, 82 atm.: HPLC Analysis Identifies Species Larger Than 3-Rings

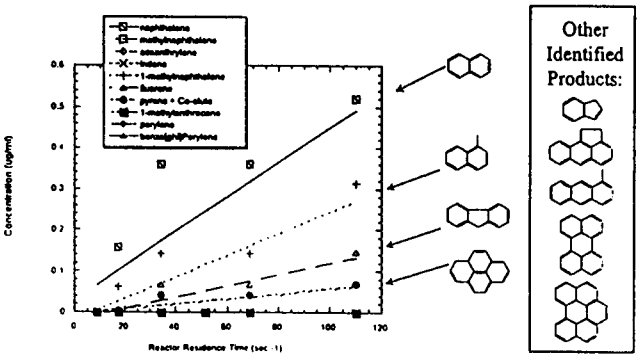


Figure 6

UNMIXED COMBUSTION: AN ALTERNATIVE TO FIRE

Richard. K. Lyon, Phillippe J. Garthier, and Jerald A. Cole

Energy and Environmental Research Corporation
18 Mason Drive
Irvine, CA, 92618
rlyon@eercorp.com

This paper describes a new form of combustion with properties which are greatly different from combustion via fire. In this new form of combustion, called unmixed combustion, fuel and air are alternately passed through a readily reduced metal oxide/readily oxidized metal or metal oxide, e.g. finely divided Cu/CuO supported on alumina or FeO/Fe_2O_3 supported on alumina. The full heat of combustion of the fuel is released, the fuel is converted to CO_2 and water, and the air is depleted of oxygen, all without any need for the fuel and air to mix. Thus unmixed combustion is an alternative to fire, another way of using fuel and air to generate heat.

In this paper we report experimental data on the properties/characteristics of unmixed combustion. These properties/characteristics are different from those of combustion by fire in a number of ways, some obvious, some subtle. A number of situations in which these different properties might prove practically useful are discussed.

One such possible application involves combustion systems in which it is difficult to provide complete mixing but in which complete combustion is required. In rotary kilns incinerators, for example, the supply of combustion air is a continuous flow but the organic materials being incinerated can enter as slugs, making the combustion briefly fuel rich and causing the discharge of a puff of unoxidized material. Laboratory data will be presented suggesting that a bed of an unmixed combustion catalyst (Cu/CuO on alumina) would be effective for suppressing puffs for a wide variety of organic materials.

A 2kW unmixed combustor was built using a Cu/CuO on alumina catalyst and shown to produce less than 0.03 ppm NOx when burning natural gas. In other experiments with a Ni/NiO on alumina catalyst followed by a Cu/CuO on alumina catalyst a high nitrogen fuel, pyridine, was burned with zero NOx production.

Experiments were done in which a bed of FeO/Fe_2O_3 catalyst in an electric furnace was alternately fluidized with nitrogen

and air. Burning thiophene produced two output gas streams, one consisting of oxygen depleted air and containing none of the fuel's carbon or sulfur , and the other consisting of nitrogen and all the SO_2 and CO_2 produced by the combustion. Experiments were also done in this setup with coal and using air and nitrogen + 5%SO_2 as the fluidizing gases. Samples of coal were injected while the bed was fluidized with the nitrogen + SO_2 mixture and it was observed that the carbon in the coal was rapidly and completely oxidized to CO_2. To determine whether or not sulfur was being retained in the bed the fluidizing gas was switched to nitrogen for a time sufficient to allow our SO_2 meter to return to baseline and then the fluidizing gas was switched to air. Since the switch to air did not produce any measurable SO_2 it was concluded that the sulfur was not being retained. The implications of these results to the combustion of coal in a manner that produces CO_2 and SO_2 that are directly ready for sequestration will be discussed.

Unmixed combustion differs from fire in that fire puts heat into the gas phase and, in many applications, that heat must subsequently be recovered by gas to solid heat transfer, a relatively slow process. In unmixed combustion, however, the heat is liberated directly within a solid and may be recovered by the relatively rapid process of conduction through the solid. Thus it is to be expected that unmixed combustion can provide greatly enhanced rates of heat recovery relative to fire. Experiments were done to confirm this expectation and a heat recovery rate of 22.2 watts/cm^2 was measured.

The ignition temperatures for several different unmixed combustion catalysts and various fuels were measured for catalysts which were initially in an oxidized state. For a Cu/CuO on alumina catalyst in an initially reduced state the ignition temperature was subambient. The implications of this result to the problem of rapid supplying of heat for cold starting will be discussed.

In another set of experiments unmixed combustion with excess fuel was shown to allow complete removal of oxygen from air. The implication of this result to the direct generation of dry inert gases will be discussed.

While combustion by fire is a nonselective process, catalytic combustion with noble metal catalysts can be quite selective. Thus, for example, a CO impurity in hydrogen can be removed by adding oxygen and passing the gas through a noble metal catalyst at a temperature sufficient for CO oxidation but insufficient for oxidation of the hydrogen. While there has been extensive research to develop this method for purifying

hydrogen for use in PEM fuel cells, there is the problem that this process is strongly exothermic but still requires very tight temperature control. In recent experiments we have found that Cu/CuO on alumina is also effective for selectively oxidizing traces of CO in hydrogen. The potential advantage of unmixed combustion over conventional catalytic combustion in this application is that in conventional catalytic combustion all of the heat of oxidation of the CO is released within the bed. Since, however, unmixed combustion with Cu/CuO is a two step process, only one third of the total heat release occurs during the oxidation of the CO by the CuO, the other two thirds occurring during the reoxidation of the Cu back to CuO.

In contrast to fire which generates heat in a very nonuniform manner, unmixed combustion can be used to generate heat uniformly throughout a volume, i.e. an unmixed combustion catalysts can be uniformly distributed throughout the volume and with each cycle of oxidation and reduction can generate an accurately defined amount of heat.

Experiments were done to examine the possible application of this approach to the production of hydrogen by steam reforming. While steam reforming is successfully used for hydrogen production in large petrochemical complexes, its use in smaller applications involves a number of problems. The process uses a catalyst, usually nickel based at elevated pressures and at temperatures in the 600°C to 800°C range, to carry out the endothermic conversion of steam and natural gas or other light hydrocarbon to an equilibrium mixture of H_2, H_2O, CO, and CO_2. Whatever sulfur the feed contained is contained in this mixture as H_2S. Supplying the heat this reaction consumes is awkward because the outer layers of the catalyst bed tend to insulate the inner layers. To provide an adequate rate of heat transfer, the catalyst is housed in long narrow lengths of superalloy tubing, a significant expense. The equilibrium mixture the reaction produces must be purified, a problem in small scale application. For military applications the hydrogen must be generated not from light hydrocarbons but from logistics fuel (i.e. diesel/jet fuel). The use of heavier hydrocarbons is, however, not practical because they form coke which accumulates and plugs the reactor.

In addition to improving the heat transfer situation the use of unmixed combustion may also allow improving the chemistry of steam reforming by adding CaO. In the presence of CaO the reaction $CaO + CO_2 = CaCO_3$ removes CO_2. Since CO is in equilibrium with CO_2 via the water gas shift reaction, it is also removed. In addition to driving the equilibrium toward the production of hydrogen of greater purity, the exothermicity of

the CaO + CO_2 = $CaCO_3$ reaction, ΔH -42.55 kcal/mole, more than balances the endothermicity of the steam reforming reaction, making the system overall slightly exothermic.

Of course, the CaO is eventually fully converted to $CaCO_3$. When this point is approached, the flow of steam and fuel through the bed is stopped and air is blown through it. Whatever coke may have accumulated is oxidized and nickel in the catalyst undergoes the highly exothermic Ni + $1/2O_2$ = NiO reaction, ΔH = -57.3 kcal/mole. If the ratio of nickel to calcium carbonate is 1 to 1.35, the oxidation of the nickel liberates the amount of heat consumed by the calcination of the $CaCO_3$ back to CaO.

Laboratory scale experiments were done with a packed bed reactor in a three zone electric furnace, i.e. with a reactor which was operated under isothermal conditions. At 700°C, 8 atm, a space velocity of 1700 hr^{-1} and a ratio of water to carbon inputs of 1.3, the production of 93% pure hydrogen (dry basis) was observed using commercial diesel fuel. For conditions calculated to correspond to 90+% conversion of the CaO to $CaCO_3$, purity remained high, 87.4% but fell to 63% for conditions calculated to correspond to exhaustion of the CaO. The hydrogen produced in this experiment showed no detectable H_2S (>1ppm). Production of 90+% pure hydrogen was also observed in experiments in which the commercial diesel fuel was doped with 2000 ppmw sulfur, but the hydrogen did contain 5ppm H_2S. It was also observed that the sulfur in the fuel was discharged from the bed as
SO_2 during air regeneration of the bed.

In the second series of experiments a prototype unmixed steam reformer was setup, a unit which operated autothermally and which was capable of producing enough hydrogen to power a 20kW fuel cell. Hydrogen was produced at the desired 20 kW rate for total operating times in excess of 1000 hours without problems. During this time it was observed that the system operated in a cyclic but highly stable manner with no tendency toward temperature runaway or developing hot spots. The hydrogen produced by the autothermal unit was of lower purity than produced by the isothermal laboratory unit. The thermodynamic reasons for this will be discussed.

Adsorption of Mercury on Coal Flyash

S.D. Serre[1*] (Serre.Shannon@EPA.Gov), G.D. Silcox[1] (Geoff@eng.utah.edu)

[1]University of Utah, Chemical and Fuels Engineering, 3290 MEB, Salt Lake City, UT 84112
[*] Currently at U.S. Environmental Protection Agency, Air Pollution Prevention and Control Division (MD-65), Research Triangle Park, NC 27711

Mercury has long been identified as a hazard to human health and the environment. Two sources of mercury in water and soil are municipal waste incinerators and coal-fired power plants. One method used to remove elemental mercury from flue gas involves the injection of large quantities of pulverized activated carbon (Gullett, 1993; Krishnan, 1994; Karatza, 1996). The purpose of this project was to determine whether the unburned carbon that remains in coal flyash could be used as an inexpensive and effective replacement for activated carbon. Bench-scale tests were conducted at conditions representative of those found in the flue gas trains of coal-fired power plants and municipal waste incinerators. Two types of data were obtained: equilibrium data suitable for obtaining adsorption isotherms and breakthrough data suitable for obtaining adsorption kinetics. Temperatures were varied from 121 to 177 °C and gas phase mercury concentrations ranged from 0.04 to 11 mg Hg/m^3. Four pulverized-coal flyashes, with carbon contents ranging from 2 to 36% by weight, were examined. The physical characteristics of these ashes are shown in Table 1.

Table 1
Physical Characteristics of Flyashes

Source of Ash (Power Plant)	Carbon Content (wt. %)	Initial Mercury Content (ppm)	Surface Area (m^2/g ash)
Nixon	2.0	0.33	6.81
Cherokee	8.7	0.25	34.1
Clark	32.7	1.1	65.1
Huntington	35.9	0.51	63.8

The adsorbed mercury as a function of flyash carbon content at a temperature of 121 °C is shown in Figure 1. The equilibrium results indicate that the flyashes used in this study can adsorb up to 800 ppmw of mercury. The amount of mercury adsorbed increased with increasing carbon content from a low of 30 ppm for the low carbon ash to 800 for the high carbon ash. The Clark and Huntington ashes have similar carbon contents but the Huntington adsorbed twice as much mercury. The difference is attributed to the lack of pore structure of the Clark ash.

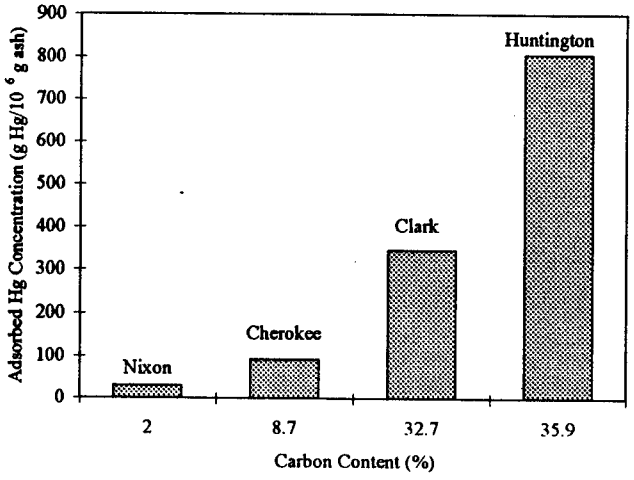


Figure 1 Adsorbed mercury as a function of flyash carbon content at a temperature of 121 °C and a gaseous mercury concentration of 4 mg Hg/m^3.

Temperature had a large impact on the adsorbed-phase mercury concentration as shown in Figure 2. As the temperature was increased from 121 to 177 °C the amount of mercury on the ash decreased. Figure 2 also shows that mercury capture was also found to decrease with decreasing gas phase mercury concentrations.

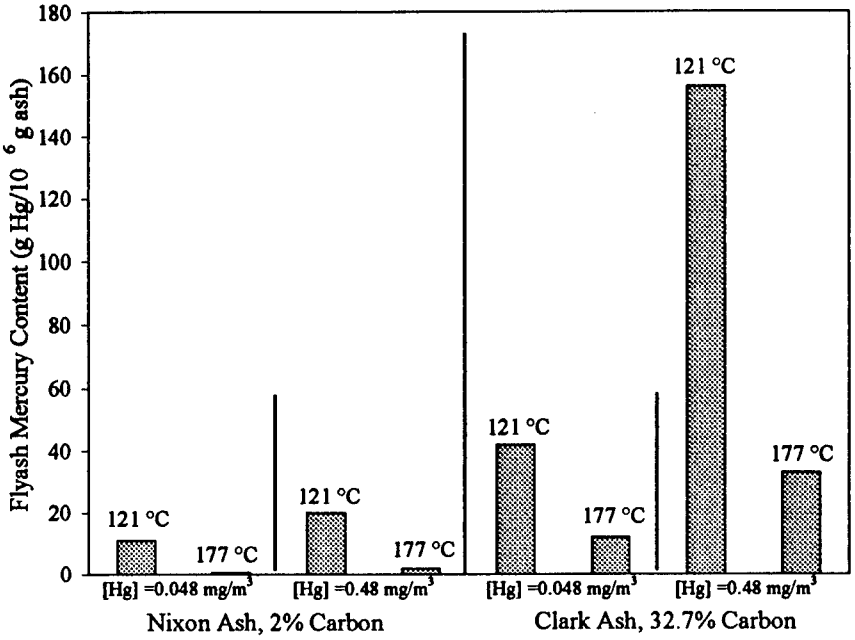


Figure 2 Ash loading results for the Nixon and Clark flyashes, showing the role of carbon content, temperature, and adsorbate concentration on adsorption.

The kinetics of mercury removal were described using Langmuir kinetics (Thomas, 1948) for the adsorption of a single solute from a fluid phase onto a solid adsorbent. The rate parameters were obtained from the experimental data that were collected. Two types of data were used to obtain parameters for the models: adsorption isotherms and breakthrough curves. From the adsorption isotherm values for the maximum loading (ω_{max}) and the equilibrium constant (K) were obtained. The breakthrough curves were then fit to obtain a value for the forward rate constant (k_1). A fit of a breakthrough curve is shown for the Nixon ash in Figure 3.

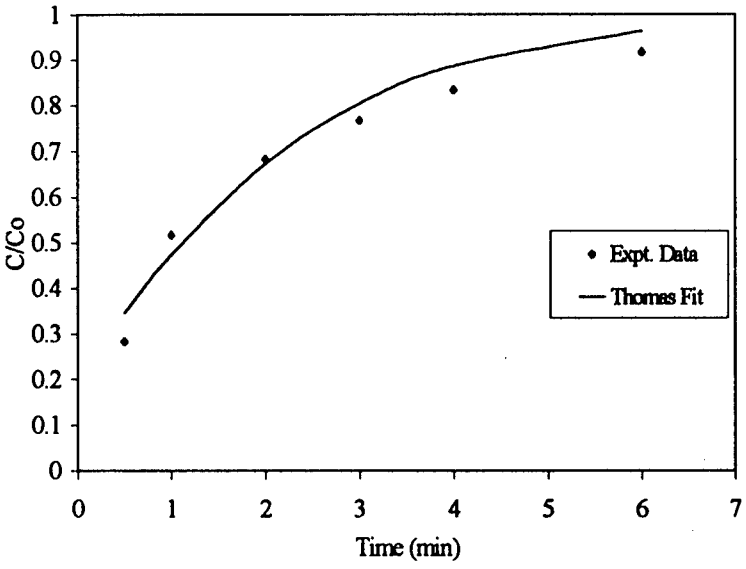


Figure 3 Comparison of the Thomas solution to experimental breakthrough data for the Nixon (2% C) ash at a temperature of 177 °C and a mercury concentration of 0.048 mg Hg/m^3.

The governing partial differential equation for the adsorption of mercury onto coal flyash in a packed bed is

$$D_{ax}\frac{\partial^2 C}{\partial Z^2} - V_i\frac{\partial C}{\partial Z} - \frac{\partial C}{\partial t} - \frac{1-\varepsilon}{\varepsilon}\frac{\partial \omega}{\partial t} = 0 \qquad (1)$$

An analytical solution for Equation 1 was developed by Thomas (1944, 1948). Equation 1 was coupled with an expression for the rate of adsorption. The rate of adsorption was taken to equal the difference between the rate of adsorption and the rate of desorption:

$$r_{ads} = \frac{\partial \omega}{\partial t} = k_1 C(\omega_{max} - \omega) - k_2\omega \qquad (2)$$

Two mathematical models were developed to simulate the removal of elemental mercury in flue gas ducts and in baghouses. Simulation results for capture in a flue gas duct indicate that a negligible amount of mercury can be adsorbed by a dilute suspension of flyash. Results for injection rates of 10, 50, and 100 mg ash/m^3 of gas are shown in Figure 4. Less than 5% of the vapor-phase mercury is removed when an injection rate of 100 g of ash per cubic meter of gas is used at a temperature of 121 °C and an initial vapor-phase mercury concentration of 1 mg Hg/m^3.

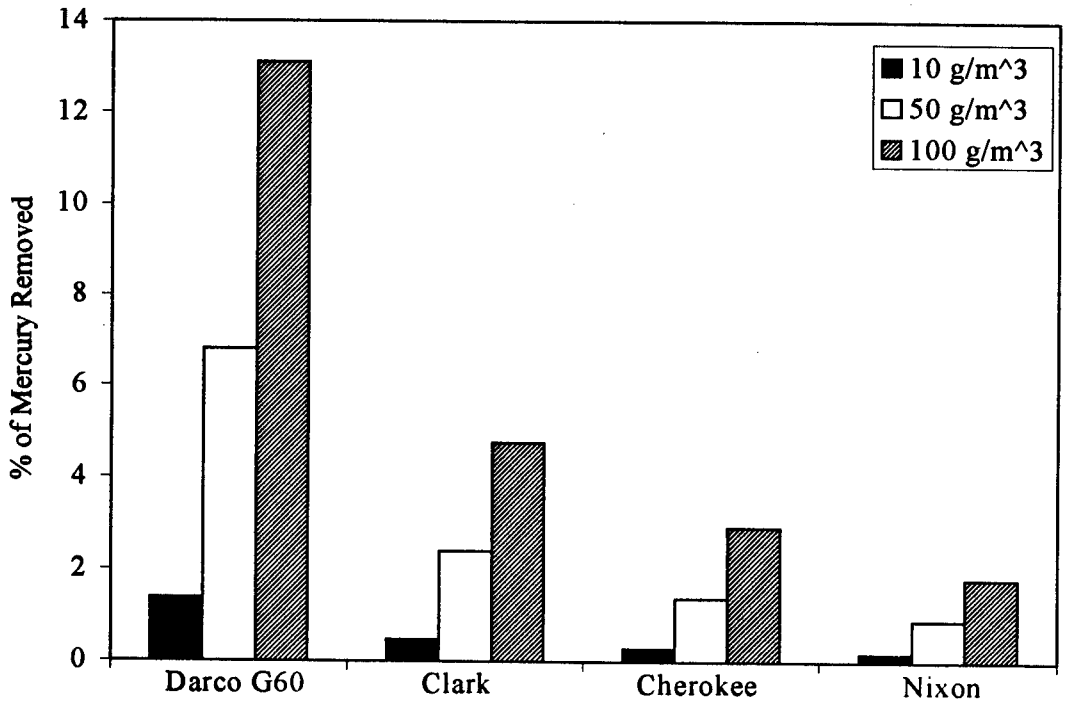


Figure 4 Dispersed phase simulation for the three flyashes and Darco G60 activated carbon at a temperature of 121 °C and a gaseous mercury concentration of 1 mg Hg/m^3. Injection rates of 10, 50, and 100 g/m^3 of gas were used. This figure shows the percent of mercury removed based on a given injection rate.

The best option for controlling mercury emissions using flyash is to inject the ash in pulses prior to a baghouse. Pulsed injection allows the carbon in the ash to adsorb mercury throughout the entire baghouse collection cycle. Figure 5 contains the model prediction for injecting a 32 wt.-percent-carbon flyash at a rate of 1200 g/m^3 of gas prior to the baghouse, for the first minute of a 60-min baghouse cycle. The simulation shows that pulsed injection at these conditions will result in the exit concentration staying 50% below an inlet concentration of 1 mg.

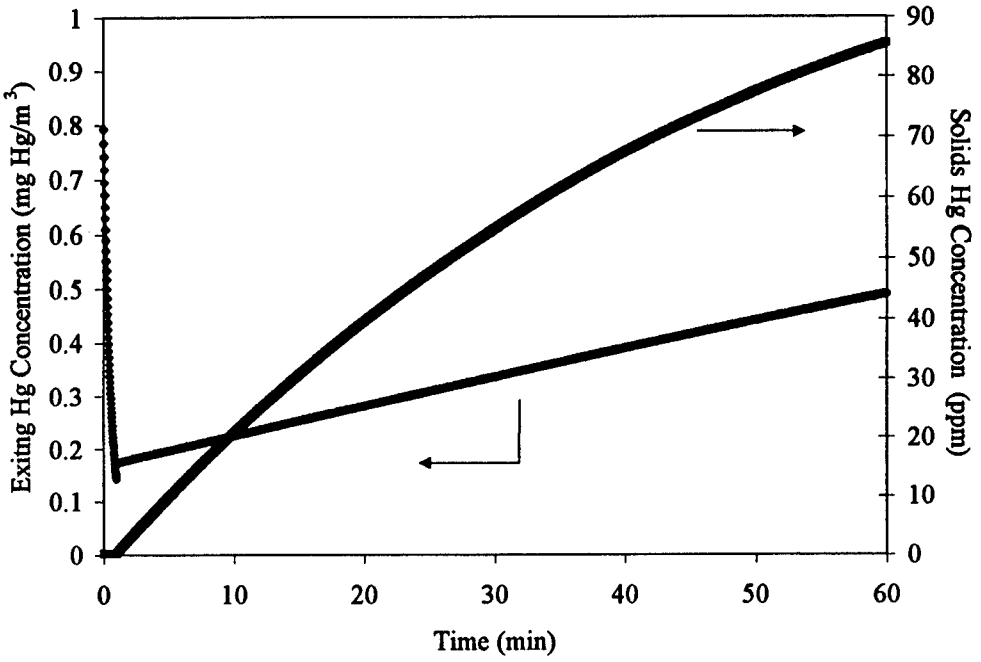


Figure 5 Simulation of baghouse capture showing the concentration of mercury exiting the system for the Clark (32.7% C) at 121 °C and a gaseous mercury concentration of 1 mg Hg/m^3. The prediction is for 60 min at an injection rate of 1200 g of sorbent per m^3 of gas for the first min, followed by no injection for the remaining 59 min.

References

Gullett, B.K., and W. Jozewicz, "Bench-Scale Sorption and Desorption of Mercury with Activated Carbon.", *1993 International Conference on Municipal Waste Combustion,* Williamsburg, VA, April, (1993).

Krishnan, S.V., B.K. Gullett, and W. Jozewicz, "Sorption of Elemental Mercury by Activated Carbons," *Environmental Science and Technology,* 28, (1994).

Karatza, D., A. Lancia, D. Musmarra, and F. Pepe, "Adsorption of Metallic Mercury on Activated Carbon," *Twenty-Sixth Symposium on Combustion,* Pittsburgh, PA, July 28-August 2, (1996).

Thomas, H.C., "Heterogeneous Ion Exchange in a Flowing System," *J. Amer. Chem. Soc.,* 66 (1664), 1664-1666, (1944).

Thomas, H.C., "Chromatography: A problem in kinetics," *Annals of the New York Academy of Science,* 49 (161), 161-182, (1948).

Interactions between Lead Vapor and Sorbents at High Temperatures

Sheldon B. Davis and Jost O.L. Wendt
Department of Chemical and Environmental Engineering
University of Arizona
Tucson, AZ 85712
email: Wendt@u.arizona.edu

and

William P. Linak
Air Pollution Prevention and Control Division, MD-65
National Risk Management Research Laboratory
U.S. Environmental Protection Agency
Research Triangle Park, NC 27711
email: Linak.Bill@epa.gov

INTRODUCTION

With the increasing concern about ultra-fine particle emissions from stationary combustion sources, the impetus to develop systems that prevent particle formation and emission has grown. One specific area of concern has been the presence of toxic heavy metals, e.g. lead, cadmium, and arsenic, in ultra-fine particles. This concern is warranted for many reasons. These metals are enriched in the submicron size range of combustion-generated particles. In this form, metals, which have well documented deleterious health effects (Vouk 1984), penetrate deep into the lungs where the body has the most difficulty coping with their presence. One approach to prevent particle formation is the use of sorbents to capture metal vapors.

The use of sorbents to capture lead vapor has been well demonstrated (Uberoi 1990, Scotto 1994; Linak, 1994). However, few studies have developed kinetic information (Agnitori 1998, Mwabe 1996). To design and construct practical systems, it will be necessary to have kinetic information concerning the reaction rates of metal capture. The objective of this work is to determine the global kinetic rates for the interactions that govern the capture of lead vapor by kaolinite and lime at high temperature. This ongoing collaborative work between the University of Arizona and the U.S. Environmental Protection Agency focuses on two sorbents, kaolinite and lime, for the capture of lead vapors at high temperatures.

EXPERIMENTAL

Figure 1 illustrates the two experimental combustors, an 18kW laboratory combustor and an 82kW refractory lined furnace, used in this research. The laboratory downflow combustor, which is located at the University of Arizona, is a 6m tall, 0.15m ID, downflow combustor. This combustor is designed to have residence times and temperatures similar to that of a full scale boiler or incinerator and can be modeled as a one-dimensional, plug flow, reactor. The U.S. EPA's 82kW refractory-lined furnace is a horizontal tunnel furnace that has an inner diameter of ~0.5m at the combustion zone which decreases to 0.3m ID after about 1m. Experiments that were performed for this research on the U.S. EPA furnace were conducted entirely within the 0.3m ID section. Figure 2 shows the time/temperature profiles of the two reactors.

Natural gas and air are introduced through a variable swirl natural gas burner. To obtain the desired metal vapor concentrations, an aqueous lead acetate solution was atomized and injected into the center of the flame.

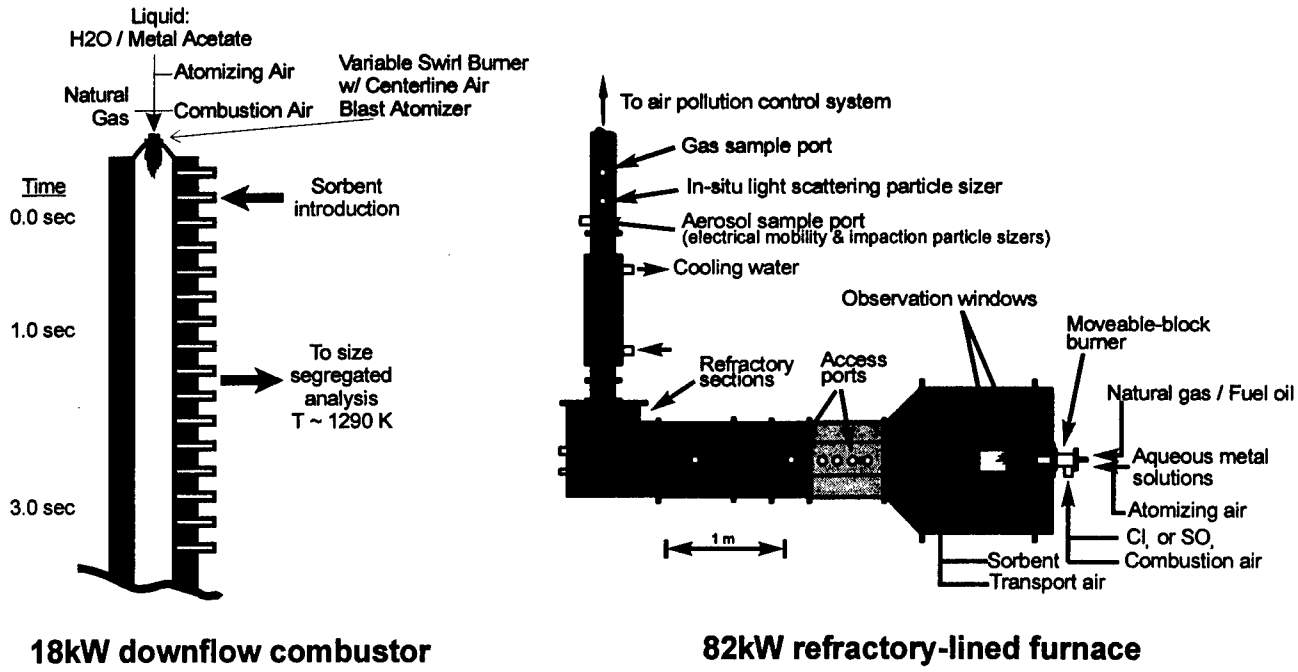


Figure 1: Experimental combustors

Powdered kaolinite and hydrated lime were pneumatically injected at various points along the combustor. Kaolinite which was obtained from Burgess Inc. has reported purity of 98%. Hydrated lime was provided by Global Stone-Tennessee Latrel, Inc. Primary work was performed with sorbents that had mean diameters of 0.8 (kaolinite) and 1.4μm (hydrated lime).

Isokinetic samples were extracted above the dew point of the metal vapor. Aerosols samples were withdrawn by a water-cooled, rapid nitrogen quench probe. The rapid nitrogen quench which occurs at the tip of the probe has two effects. As metal vapor enters the probe, the cooling rate is sufficient to force the metal to homogeneously nucleate in the presence of the pre-existing particle population. The second effect is to effectively reduce coagulation and other aerosol processes. The result is the ability to discriminate vapor and reacted material from within the furnace. From the probe, the samples were sent to a Berner low pressure impactor. Polycarbonate substrates, which were sprayed with Apiezon-L grease to prevent bounce off, were used as impaction surfaces. Each substrate was acid digested in 3HF:1HCL:1HNO3 and analyzed by atomic absorption. Additional samples were gathered for non-destructive analysis.

To determine the kinetics of metal vapor capture by powdered sorbents, a three factor-level experimental matrix was constructed to study lead/lime and lead/kaolinite interactions. Sorbent was injected at three different rates and at three different positions. The sampling location was held fixed for all experiments with the experimental matrix. The results of these tests are analyzed by response surface methodology and compared to a reaction model to determine the kinetic parameters.

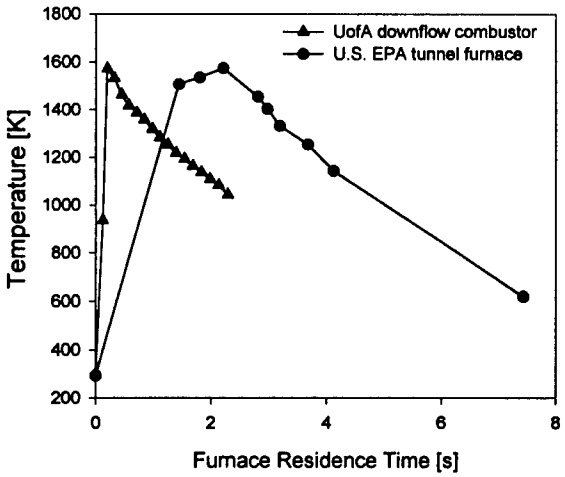


Figure 2: Experimental time/temperature profiles

RESULTS AND DISCUSSION

Preliminary results, gathered at the University of Arizona, for the interactions of lead vapor with kaolinite and lime are shown in figure 3. Figure 3 describes the percent of the total metal captured as a function of residence time/temperature. Each curve represents a constant ratio of the sorbent to metal as determined by the their respective injection rates. The sampling point was also held fixed and the sorbent injection position was varied which yielded three different injection temperature and residence conditions: (1) 1540K/1.0s, (2) 1440K/0.7s, and (3) 1370K/0.4s. Each point is, at least, an average of two individual tests. The greatest measured variation between any individual condition and the average of all similar conditions was 15%.

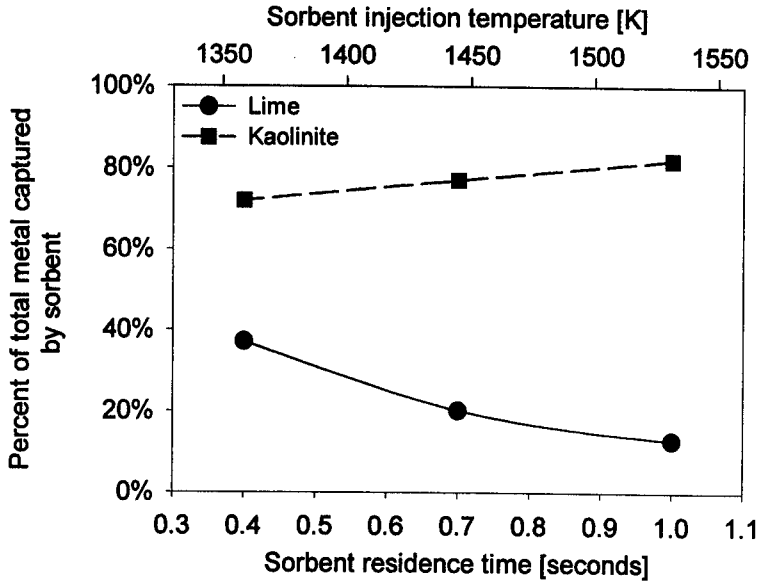


Figure 3: Preliminary results for reaction of lead vapor with kaolinite and lime

The upper curve in figure 3 shows the results for the interaction of lead and kaolinite. The molar ratio of sorbent to lead for each experiment was 2.5. Based on previous work where the product of the reaction between lead and kaolinite was determined to be $PbO{\cdot}Al_2O_3{\cdot}2SiO_2$ (Uberoi 1990), there is approximately twice as much sorbent as required for the complete capture of the lead present in the reactor.

The percent of the metal captured, ~80%, is similar each case. At the short residence time of 0.4s, the majority of the metal is captured and there are only nominal increases at longer residence times. Further, the reaction appears to be insensitive to the change in temperature

The results of the lead/lime interaction are represented by the lower curve in figure 3. For these experiments, the lead vapor to sorbent molar ratio was set to 44. As can be seen, the interaction between lead vapor and hydrated lime does not appear to proceed as rapidly as the lead/kaolinite interaction at these conditions. The maximum capture, 37%, occurred at the *shortest* residence time condition. The temperature behavior is dramatically different than the lead/kaolinite system. There appears to be a temperature inhibition when the lime is injected at higher temperature.

REFERENCES

Agnihotri, R., S. Chauk, et al. (1998). "Selenium Removal Using Ca-Based Sorbents - Reaction Kinetics." Environ. Sci. Technol. **32**(12): 1841-1846.

Linak, W. P., R. K.Srivastava and J. O. L. Wendt (1994). Sorbent Capture of Nickel, Lead, and Cadmium in a Laboratory Swirl Flame Incinerator. Twenty-Fifth Symposium (International) on Combustion. Pittsburgh, The Combustion Institute.

Scotto, M. V., M. Uberoi, et al. (1994). "Metal Capture by Sorbents in Combustion Processes." Fuel Processing Technology **39**: 357-372.

Uberoi, M. and F. Shadman (1990). "Sorbents for the Removal of Lead Compounds from Hot Flue Gases." AIChe Journal **36**(2): 307-309.

Vouk, V. B. and W. T. Piver (1983). "Metallic elements in fossil fuel combustion products: amounts and forms of emissions and evaluation of carcinogenicity and mutagenicity." Environ. Health Perspectives **47**: 201-225.

On the Performance Estimates of Pulse Detonation Engines

K. Kailasanath and G. Patnaik
Laboratory for Computational Physics and Fluid Dynamics
Naval Research Laboratory
Washington, DC 20375
kailas@lcp.nrl.navy.mil, patnaik@lcp.nrl.navy.mil

Introduction

Pulse detonation engines (PDEs) have received considerable attention during the past decade and significant progress has been made in their development [1,2]. Various applications, both civilian and military have been proposed. The advantages claimed for the proposed applications are based on estimates of the performance of a PDE. A review of the various theoretical and computational studies show that there is a wide variation in the predicted performance with estimates ranging from 3000 s to 8000 s for the specific impulse for a hydrogen-air PDE [3]. Very little experimental data on system performance has been reported. Therefore, there is significant uncertainity in the performance and hence the potential of PDEs.

The objective of this paper is to present the results of a systematic study of a PDE operating on a stoichiometric hydrogen-air mixture and use these results to provide an explanation for the wide variation in system performance reported in the literature. We first discuss the relative thermodynamic efficiencies of a detonation, constant pressure and a constant volume cycle.

Efficiency of the Detonation Cycle

A constant pressure engine cycle (characteristic of conventional propulsion systems) is compared to a constant volume and a detonation cycle in Fig. 1. For purposes of comparison, the only process that is different in the three cycles is the energy conversion or heat addition. The amount of heat added is also kept the same at 50 k.cal/mole for the three cycles. In all cases, the fuel-air mixture is initially compressed adiabatically from 1 to 3 atm. before heat addition. After heat addition, the products of combustion are expanded adiabatically to 1 atm. Finally the system is returned to its initial state. Since all process except for heat addition have been maintained the same, the relative thermodynamic efficiency of the three combustion processes can be obtained by comparing the areas enclosed by the curves. The thermodynamic efficiencies for the three cycles are: 27% for constant pressure, 47% for constant volume and 49% for detonation. From the figure and the above numbers we see that the thermodynamic efficiency of the detonation cycle is close to that of the constant volume cycle and significantly better than that of the constant pressure cycle. The process itself is different with a decrease in specific volume and a significantly higher pressure being attained during detonations. Therefore, from a thermodynamic point of view, detonations do provide an advantage over conventional constant pressure propulsion systems. A major challenge in the development of the PDE is attaining this higher potential efficiency in a practical device.

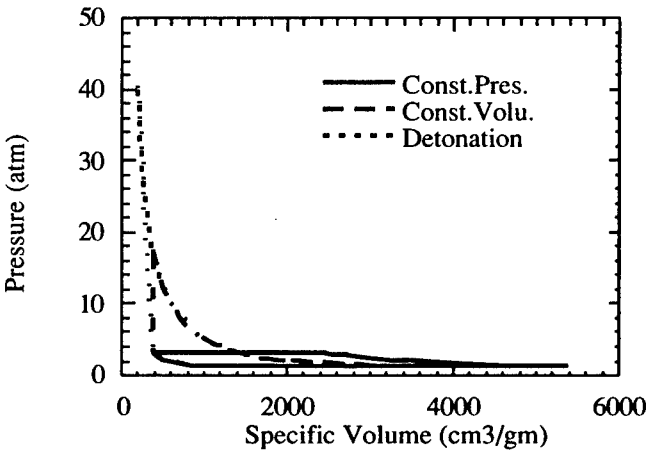


Fig. 1 Comparison of three cycles

The Numerical Model

Next, we briefly discuss the model and solution approach used in our basic study of the gas-phase reactive flow in a simple PDE. The compressible, time-dependent, reactive flow, conservation equations [4] are solved for density, momentum, total energy and the number densities of individual species. The terms in the conservation equations representing the different physical and chemical

processes are solved separately and coupled using timestep splitting techniques [4]. This procedure allows the individual processes to be integrated by appropriate and efficient techniques and also permits the easy substitution and elimination of different sub-models for the individual processes, as needed for specific applications.

The developed code can compute the three-dimensional, multi-species reactive flow in a simple geometry and allows for the inclusion of species diffusion, thermal conduction and radiative heat loss. It is based on the three-dimensional, flame code [5], except that the implicit convection is replaced with an explicit convection algorithm, as discussed below. For the short duration, single-cycle simulations discussed next, the diffusive and thermal processes will have a negligible effect and hence only the convective flow with detailed chemistry is considered. Furthermore to compare with previous results, the code is used to compute the one-dimensional flow, neglecting the variations in the other two directions.

For the high-speed reactive-flows that are typical of detonations, an explicit algorithm such as the Flux-Corrected Transport (FCT) [6] is very efficient and accurate for integrating the fluid convection. FCT is a conservative, monotonic algorithm with fourth-order phase accuracy. With various initial and boundary conditions, this algorithm has been used previously to solve a wide variety of problems involving detonations. A comprehensive model for hydrogen combustion with 8 species and 48 reactions is used. The reaction set is solved at each timestep with CHEMEQ, an integrator for stiff ordinary differential equations [7]. Because of the complexity of the reaction scheme and the large number of computational cells, the solution of the chemical rate equations can take a large fraction of the total computational time. Hence, the code has been developed directly for massively-parallel computers. The PARTI [8] and CHAOS [9] runtime support libraries were used to parallelize the structured and unstructured portions of the code respectively. New parallel algorithms to carry out dynamic load balancing have also been developed. The development of the parallel code allows us to compute efficiently well resolved systems for relatively long times.

The geometry of the system simulated is a simple detonation tube filled with a premixed, stoichiometric hydrogen-air mixture at 1 atm. pressure and 298 K. The 20 cm long tube is assumed to be closed at one end (Head end) and open at the other. The grid size used is 0.002 cm and the time step is variable.

Initial Conditions

One of methods for starting the simulations of a PDE is to assume a well-developed Chapman-Jouguet detonation as the initial condition. Another is to consider the pressure and temperature of a small region of the mixture to be at a higher value than the rest. Here, a high pressure (90 atm.) and high temperature (3000 K) region of 4 mm (2% of the entire system) filled with detonation products at the CJ plane conditions were used as initial conditions.

Boundary Conditions

Outflow boundary conditions at open boundaries are a challenging problem in numerical simulations. If the flow is fully supersonic, extrapolation of the conditions from the inside (zero-gradient conditions) works well since physically the flow outside the chosen computational domain should not affect the flow inside. Subsonic outflow is a major problem since physically, the flow inside the domain can respond to changes outside. There is no general solution to this problem since it depends on the specific experimental configuration and the physical conditions one is attempting to mimic. Therefore, several choices for the boundary condition have been tried and their effect on the flow field and performance evaluated.

For the cases discussed, the pressure is made to reach the ambient value in a fixed distance, the relaxation length, from the end of the detonation tube. The relaxation length can be varied from zero (which corresponds to fixing the pressure at the boundary to ambient pressure) to any non-zero value. A large value of the relaxation length implies a gradual relaxation of the pressure to the ambient.

Simulations of a Hydrogen-Air PDE

The impact of different boundary conditions is discussed next. The solutions are identical for all cases until the detonation reaches the open boundary.

Constant Pressure Case

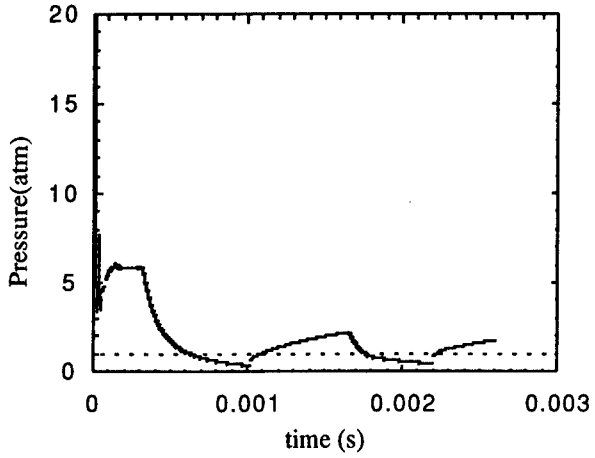


Fig. 2 Pressure at the closed end of the tube as a function of time

When the detonation reaches the open boundary, the pressure just inside the computational domain will suddenly rise to a high value. This creates a large pressure gradient at the exit since the boundary conditions require the flow to relax rapidly to the ambient value. The result is high flow velocities and over expansion that results in the pressure in the tube even at the closed end going below the ambient value (Fig. 2). The dotted line in the figure corresponds to the ambient pressure (1 atm.) If a valve were to open at the closed end, air or fresh fuel-air mixture would be aspirated into the tube. Here, the burnt products that flowed out earlier are brought back into the tube at the open boundary.

Slow Relaxation Case

In contrast to the above case, the flow field is significantly different if the pressure at the exit of the tube is allowed to gradually decrease to the ambient value. A variety of solutions is attained depending on the length chosen for the pressure relaxation. The head-end (closed end) pressure for the case when the relaxation length is 20 cm shows no discernable oscillations and the self-aspiration is essentially non-existent.

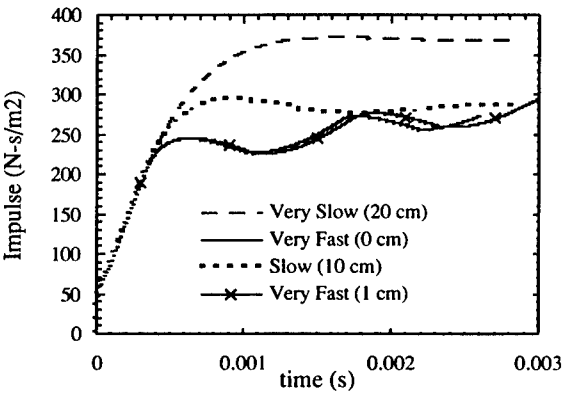


Fig. 3 Time history of Impulse for various cases.

Performance Estimates

For the simple device simulated, area integrated difference between the pressure at the head-end (closed end) of the tube and the ambient gives the thrust from the device. The time integral of the thrust gives the impulse. Since the simulations are one-dimensional, these performance parameters are given in the units of per unit area (m^2).

The impulse for various cases are compared in Fig.3. Because of the oscillations in the pressure when the flow relaxes rapidly, the thrust and hence impulse also oscillate. The highest impulse is attained for the slowest relaxation boundary condition tried (20 cm or 1 engine length).

Comparison with Previous Estimates

The specific impulse is a performance parameter that can be used to compare different systems less ambiguously since it does not directly depend on the system size. However, there are two factors that still need to be chosen. For some of the cases shown in Fig. 3, the impulse value chosen will depend on the time at which it is measured. In addition to the impulse, we also need to know the amount of reactants consumed to produce the measured impulse. For a multi-cycle simulation, average values per cycle can be used for these parameters. To get a bound for the specific impulse predicted using different boundary conditions, the lowest and highest values observed for the impulse is taken and the total amount of fuel initially in the tube is assumed to be consumed. With these values, the specific impulse is found be between 4850 s for the lowest value during the fast relaxation (constant pressure case) and 7930 s for the highest value during the very slow relaxation (20 cm) case.

It is interesting to compare these values with those predicted in past computational studies. The

lower bound is close to the value of 5151 s predicted by Sterling et al.,[10] who did indeed state that a constant pressure boundary condition was used. The two estimates are even closer if the first peak in the impulse curve is chosen for calculating the specific impulse. The upper bound is in the range of values quoted by Bussing et al. [11] of 7500-8000 s. The boundary conditions used for those estimates are not specified. Other values in the literature could be due to choice of boundary conditions with intermediate rates of relaxation as well as differences in other details in the models used. There is another set of predictions by Cambier and Tegner [12] of 3000 to 3975 s. In those predictions, the calculated impulse was corrected for the effect of the initiation process which was estimated to contribute between 17 to 27 %. If this is not considered, their values will also be in the range predicted here for uncorrected specific impulse. Additional studies are currently underway to estimate the influence of initial conditions. And these will be reported at the meeting.Thus the studies reported in this paper are useful in reconciling the various predictions made in previous computational studies.

Acknowledgments

This work has been sponsored by the Office of Naval Research through the Mechanics and Energy Conversion Division and the Naval Research Laboratory. Computer time was provided by the DoD HPCMO through the DoD Shared Resource Centers.

References

1. Eidelman, S., Grossmann, W., and Lottati, I., "Review of Propulsion Applications and Numerical Simulations of the Pulse Detonation Engine Concept," J. Prop. Power, Vol.7, No. 6, pp. 857-865, 1991.

2. Kailasanath, K., "Applications of Detonations to Propulsion: A Review," AIAA Paper 99-1067, 37th AIAA Aerospace Sciences Meeting and Exhibit, January 1999.

3. Kailasanath, K., Patnaik, G., and Li,C., "Computational Studies of Pulse Detonation Engines: A Status Report," AIAA 99-2634, 35th AIAA/ASME/SAE/ASEE Joint Propulsion Conference, June 1999.

4. Oran, E.S., and Boris, J.P., Numerical Simulation of Reactive Flow, Elsevier, New York, 1987.

5. Patnaik, G., Kailasanath, K., and Sinkovits, R.S., "A New Time-dependent Three-dimensional, Flame Model for Laminar Flames," *Twenty-sixth Symposium (International) on Combustion*, pp. 899-905, The Combustion Institute, Pittsburgh, PA. 1996.

6. Boris, J.P.,and Book, D.L., Journal of Com-putational Physics,11 (1), pp. 38-69, January 1973.

7. Young, T.R., and Boris, J.P., J. Phys. Chem. 81: 2424—2427, 1977.

8. Agrawal G, Sussman A and Saltz J, "Compiler and Runtime Support for Structured and Block Structured Applications," Supercomputing '93, (IEEE Computer Society Press) pp. 578-87, 1993.

9. Das R, Uysal M, Saltz J and Hwang Y., "Communication Optimizations for Irregular Sci-entific Computations on Distributed Memory Architectures," Department of Computer Science Report CS-TR-3163 University of Maryland: College Park, MD, 1993.

10. Sterling, J., Ghorbanian, K., Humphrey, J, Sobota, T. and Pratt, D., "Numerical Investiga-tions of Pulse Detonation Wave Engines," AIAA Paper 95-2479, July 1995.

11. Bussing, T.R.A., Bratkovich, T.E., and Hinkey, J.B., "Practical Implementation of Pulse Detonation Engines," AIAA 97-2748, July 1997.

12. Cambier, J.L., and Tegner, J.K., "Strategies for PDE Performance Optimization," AIAA Paper 97-2743, July 1997.

Synthesis of unagglomerated, non-oxide nanophase powders in a turbulent jet flame[§]

L.J. Rosen, Z. Sun and R.L. Axelbaum
Department of Mechanical Engineering, Washington University, St. Louis, MO USA

INTRODUCTION

Two critical challenges face the commercialization of any method used to synthesize nanopowders. First, the powders must be produced in a cost-effective manner that can minimize the extent of particle agglomeration. Second, the powders must be produced in such a way as to minimize impurities. For non-oxide nanophase powders the challenge of producing and maintaining high purity powders during handling is especially difficult. Many metals and non-oxide ceramics react with moisture or oxygen to form surface oxides, which can result in high levels of impurities due to the large specific surface areas of nanopowders. Methods of production must be developed that are capable of protecting the highly reactive powders from contamination during post-synthesis handling.

Where physically possible, flame processes for the synthesis of powder commodities have often replaced previous methods of synthesis (Ulrich, 1984). This is primarily due to the advantages that flame processes can offer over other competitive methods. Flame processes do not require multiple steps or the use of environmentally hazardous solvents or surfactants as do many wet-chemical routes. Furthermore, they are continuous processes as opposed to batch, and they are energy efficient. Finally, flame processes have demonstrated the ability to produce ultra-high purity materials, as evidenced by their use in the production of optical waveguides (Ulrich, 1984). However, due to the high temperatures and high particle number densities present in many commercial systems, powders produced are often highly agglomerated. Hard agglomerates can be distinguished from weak agglomerates by the necking (bridging) that occurs between the particles. While hard agglomerates are acceptable for many end uses of powders commercially produced in flames, they must be avoided in nanopowders that are to be consolidated into structural materials. The presence of hard agglomerates in the powder leads to the formation of pores in the consolidated body which act as crack formation sites and ultimately reduce the strength of the consolidate.

Recently, a sodium/halide flame synthesis process, conceptually similar to commercial flame processes, was extended to allow the production of unagglomerated, non-oxide nanopowders (DuFaux and Axelbaum, 1995; Axelbaum *et al.*, 1996, 1997). This technique employs an encapsulation step during the aerosol growth stage to control particle size, prevent the formation of hard agglomerates and protect the powders from oxidation/hydrolysis during post-synthesis handling. This process has been used to produce a variety of different metals and ceramics (e.g. Ti, W, Al, TiB_2, AlN, TiN) of various sizes (ca. 2-60 nm) using a laminar jet. An example of the sodium/halide chemistry for the synthesis of titanium metal (Calcote and Felder, 1993; Glassman *et al.*, 1993) is

$$TiCl_4 + 4Na + aAr \rightarrow Ti + 4NaCl + aAr. \quad (1)$$

For these flames the NaCl by-product acts as the encapsulate material. Sodium chloride is an excellent encapsulate material due to its moderate vapor pressure at typical flame temperatures as well as its high deliquescence relative humidity (DRH = 75%) at ambient temperatures. Thermodynamic yields for sodium/halide reactions typical of Eq. (1) are in excess of 99% with only modest dilution (Axelbaum *et al.*, 1996). The addition of inert also acts to control the encapsulation process as will be discussed later.

With the core particles (Ti in the above example) encapsulated in a salt matrix, the powder can be handled using standard techniques as long as the relative humidity is low. Further processing of the core particles can be accomplished by loading the encapsulated powders in the processing equipment, purifying the environment of any reactive gases and removing the salt encapsulate. Salt removal by vacuum sublimation has been successfully employed to remove the salt to less than 50 ppm. With further optimization of the salt removal process it is believed that this impurity level can be reduced even further. By processing the powders in such a way, the highly reactive, unagglomerated core particles can be prepared into high purity, fully dense parts.

[§] Submitted for presentation at the 1999 Fall Technical Meeting of the Eastern States Section of the Combustion Institute, October 11-13, North Carolina State University, Raleigh, NC.

ENCAPSULATION PROCESS

To gain insight into the mechanisms by which the core particles are encapsulated requires a model that is capable of treating both condensation and coagulation in a multi-component system. The model must be capable of retaining information on the final particle size (salt + core particles) as well as the size of the core particles under conditions of simultaneous coagulation and condensation/evaporation. Due to the limitations of the sectional method when applied to such a system, a Monte Carlo scheme was developed to simulate the system. This approach affords a statistical treatment of coagulation coupled with a deterministic treatment of condensation and evaporation. The details of the model are given elsewhere (Sun *et al.*, 1999) and thus only the results will be discussed below.

For the synthesis of metal and non-oxide ceramic materials typified by Eq. (1) the core (Ti) particles will have very low vapor pressures at typical flame temperatures (800-1600 K), while the encapsulate material will have a moderate vapor pressure depending on the flame temperature. For the chemistry of Eq. (1), Ti has a vapor pressure of 10^{-7} mm Hg at 1473 K and will thus undergo homogenous nucleation following its formation. Salt, on the other hand, has a vapor pressure of 84 mm Hg at 1473 K and will either be in the vapor or condensed phase depending on the temperature and pressure of the system and amount of inert present. Typical flame conditions are such that the salt is in the vapor phase immediately following its formation. Subsequent heat loss will result in condensation of salt on the core particles.

Condensation on nanoparticles is strongly influenced by the Kelvin effect. The Kelvin effect identifies a critical diameter, d*, below which condensation will not occur and above which condensation will occur. Thus, core particles larger than d* will receive salt while those smaller than d* will not. With conditions such that the salt is initially in the vapor phase and the aerosol is subject to heat loss, the evolving size distribution of the core particles will eventually interact with d*. Figure 1 shows this interaction for an aerosol subject to a heat loss of 2 W/cm^3. The time t=0 is defined as the time just prior to the onset of condensation. Figure 1 shows that the initial size distribution transitions into a bimodal size distribution as a result of rapid condensation. Because the system is modeled as a closed system, the salt vapor is eventually depleted. Due to the depletion of salt vapor, d* reaches a minimum and then begins to increase. This behavior results in only a portion of the core particles being encapsulated. Figure 2 shows the subsequent evolution of the aerosol in which the coarse mode grows by further condensation of salt and coagulation with the fine mode, while the fine mode grows only by coagulation with itself. Thus, the evolution of the core particle size distribution has transitioned from a coagulation controlled growth process to one that is a coagulation/scavenging type process.

For the core particles to be protected from oxidation/hydrolysis during post-synthesis handling, it is critical that the encapsulation efficiency approach 100%. High scavenging efficiency can be achieved when the number of scavengers is large and the nominal size of the fine mode is small enough to result in large diffusivities (Friedlander *et al.*, 1991, Jain *et al.*, 1997). Hence, processing conditions should be chosen so that (i) the initial formation of the coarse mode results in a large number of scavengers and (ii) the formation of the bimodal size distribution and subsequent scavenging process occurs before the fine mode has grown significantly.

Once the core particles have been scavenged, three possible structures can exist within the salt particle. First, if the core particles do not interact within the salt particle this solution is termed the *frozen* solution. Alternatively, if the core particles interact with each other, the final morphology of the core particles will depend on their rate of coalescence. For particles with high coalescence rates, the limit of this behavior is the *fully coalesced* solution. Particles with low coalescence rates will ultimately form small aggregates. Figure 3 shows the numerical results for the core particle size distribution for the two limiting cases (a) frozen solution and (b) fully coalesced solution. For the fully coalesced solution, the geometric standard deviation of the distribution is 1.09.

The encapsulation process can be summarized as follows. The core particles are formed by a chemical reaction similar to Eq. (1) with the encapsulate material remaining in the vapor phase. The size distribution of the core particles evolves similar to that of a coagulation-controlled aerosol. As a result of heat loss, heterogeneous condensation of the encapsulate material occurs on a fraction of the core particles in the tail of the distribution. This results in the formation of a bimodal size distribution with the coarse mode rapidly consuming the encapsulate material. The coarse mode then acts to scavenge the particles from the fine mode. Particles scavenged by the coarse mode will either remain separate, or, depending on their rate of coalescence, form small aggregates or fully coalesced single particles.

EXPERIMENTAL

While previous work was carried out with a non-premixed laminar jet flame (DuFaux and Axelbaum, 1995; Axelbaum *et al.*, 1996, 1997), this work was conducted with a non-premixed turbulent jet flame. Changing the system from a laminar facility to a turbulent facility allows significantly larger production rates to be attained thereby demonstrating the scalability of the process. Furthermore, turbulent flames yield more uniform product than laminar flames due to the enhanced mixing. Finally, use of a turbulent jet allows the synthesis of ceramic materials without premixing the metal and non-metal precursors. This has proved beneficial in the synthesis of AlN where the aluminum and nitrogen precursors cannot be premixed without undesirable reaction (Axelbaum *et al.*, 1997).

The reactants in Eq. (1) are delivered through a series of three concentric tubes. The metal chloride/inert mixture issues through a central tube with a jet diameter of 0.51 mm. An inert gas (or mixture of inert and another reactant gas in the case of ceramic synthesis) issues through the middle tube of I.D. 12 mm, and a mixture of sodium vapor and argon flow through the outer tube of I.D. 70 mm. The turbulent jet flame is enclosed by a graphite lined, stainless steel vessel to minimize metallic impurities. The reactor portion of the vessel has four independently controlled heater zones to allow control of the heat loss from the flame as well as the post-flame thermal gradient. The flame is operated in the momentum-dominated limit of the turbulent regime so that the orientation of the flame with respect to the direction of gravity has no influence on the flame geometry. The entire system is maintained at a temperature above the saturation temperature of sodium to prevent its condensation on the walls or the powder collected. Powder can be collected on a sintered stainless steel filter or thermophoretically sampled on a TEM grid injected into the gas stream.

Figure 4 shows TEM images of powders produced using the nano-encapsulation process in laminar sodium/halide flames. In each of these images, the dark particles are the core particles and the lighter material is the salt encapsulate. Figures 4a and 4b show titanium particles encapsulated in salt. The conditions during the synthesis of the particles shown in Fig. 4a favored high heat loss and thus the frozen solution is expected. As is evident from the image, the Ti particles are nominally 10 nm in size and appear to be unagglomerated. Titanium particles encapsulated in salt produced under conditions of moderate heat loss are shown in Fig. 4b. These particles are larger, presumably due to collision in the liquid phase and subsequent coalescence, and show evidence of faceted structure. Figure 4c shows AlN particles produced in a flame subject to moderate heat loss as well. These particles have formed small aggregates presumably due to collision in the liquid phase with incomplete coalescence. As the sintering rates for metals and ceramics are significantly different, this is to be expected. In all of the TEM images, the core particles appear to be nearly the same size indicating a narrow size distribution about the mean. These images demonstrate that unagglomerated, non-oxide powders with varying sizes can be produced using the nano-encapsulation technique.

ACKNOWLEDGEMENTS

This work was supported under NASA Grant NAG3-1910 and the Naval Air Warfare Center under contract #N68936-98-C-0106.

REFERENCES

Axelbaum, R.L., Huertas, J.I., Lottes, C.R., Hariprasad, S, Sastry, S.M.L. (1996). *Materials and Manufacturing Processes* 11(6):1043-1053.

Axelbaum, R.L, Lottes, C.R., Rosen, L.J. (1997). *Twenty-Sixth Symposium (International) on Combustion*, The Combustion Institute, pp. 1891-1897.

Calcote, H.F. and Felder, W. (1993). *Twenty-Fourth Symposium (International) on Combustion*, The Combustion Institute, pp. 1869-1876.

DuFaux, D.P. and Axelbaum, R.L. (1995). *Comb. Flame* 100:350-358.

Friedlander, S.K., Koch, W, Main, H.H. (1991). *J. Aerosol Sci.* 22(1):1-8.

Glassman, I, Davis, K.A., Brezinsky, K. (1993). *Twenty-Fourth Symposium (International) on Combustion*, The Combustion Institute, pp. 1-14.

Jain, S., Fotou, G.P., Kodas, T.T. (1997). *J. Colloid Interface Sci.* 185:26-38.

Ulrich, G.D. (1984). *Chem. Eng. News* 62:22.

Sun, Z., Huertas, J.I., Axelbaum, R.L. (1999). Paper presented at the *1999 Joint US Sections of the Combustion Institute Meeting*, Washington, D.C.

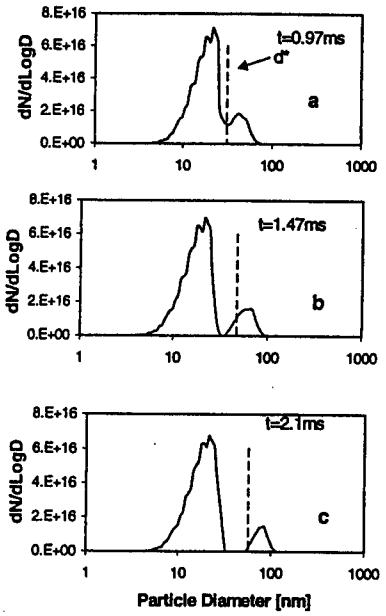


Fig. 1: The early stages of condensation of an aerosol undergoing rapid condensation of a second phase. Figure shows the development of a bimodal distribution

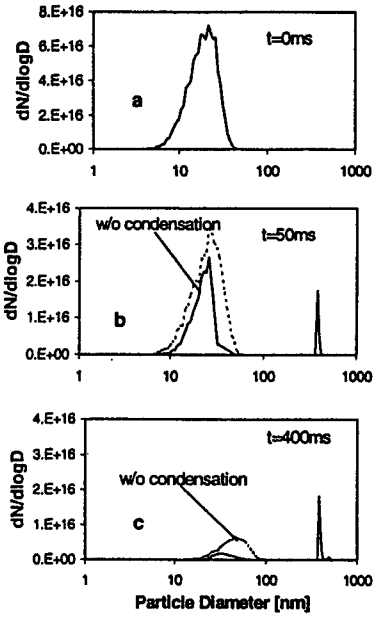
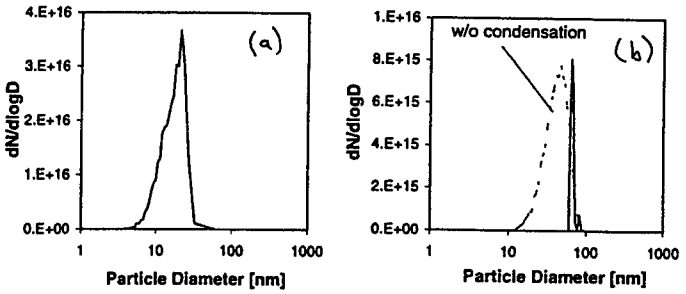


Fig. 2: Evolution of the aerosol in Fig. 1 showing the scavenging process. The dashed line shows the evolution of the distribution without condensation.

Fig. 3: Core particle distribution: (a) frozen solution where core particles do not interact and (b) fully coalesced solution where core particles collide and coalesce.



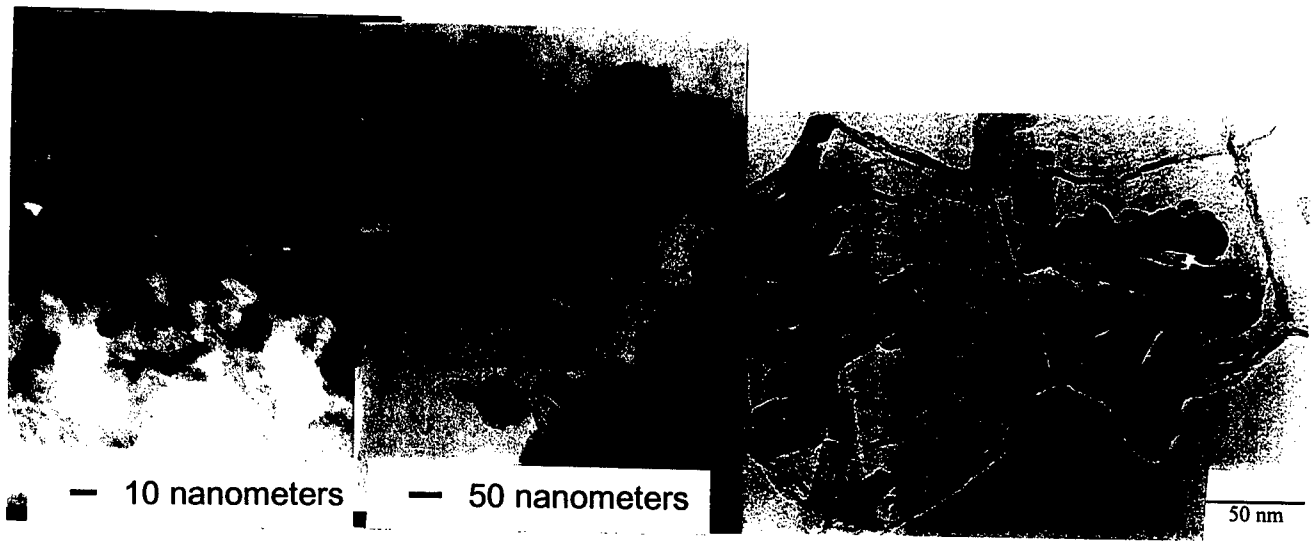


Fig. 4: NaCl encapsulated particles produced in sodium/halide flames: (a) titanium produced in a flame experiencing high heat loss (b) titanium produced in a flame experiencing moderate heat loss (c) aluminum nitride produced in a flame with moderate heat loss. The dark particles are the core particles and the lighter material is the NaCl encapsulation.

Testing and Modeling of a Plasma Torch Reactor for Destruction of Navy Shipboard Solid Waste

Steven H. Peterson, Ph.D. (peterson@ccf.nrl.navy.mil)
David A. Counts (dcounts@ccf.nrl.navy.mil)
Roy V. Richard, Ph.D. (rrichard@tech.geo-centers.com)
Eugene L. Keating, Ph.D. (ekeating@earthlink.com)
Geo-Centers, Inc., 4601 Presidents Drive, Lanham, MD 20706

Bruce D. Sartwell (sartwell@ccf.nrl.navy.mil)
U.S. Naval Research Laboratory, Code 6170, Washington, DC 20375

Thomas Marino (marinota@nswccd.navy.mil)
Jon W. Cofield (cofieldjw@nswccd.navy.mil)
Eugene E. Nolting, Ph.D. (noltingee@nswccd.navy.mil)
Naval Surface Warfare Center, Carderock Division
West Bethesda, MD 20817-5700

ABSTRACT

The U.S. Navy is currently engaged in development of a Plasma Arc Waste Destruction System (PAWDS) that employs a plasma fired eductor (PFE) to assure rapid thermal destruction of shipboard solid waste. Ship surveys have shown that Navy generated solid waste is quite similar to municipal solid waste in form but with a somewhat smaller per person generation rate. The Navy's Advanced Technology Demonstration (ATD) program is funding the development of a full-scale, land-based PAWDS to determine its utility for operation on a US Navy warship. Initial pre-prototype hardware tests of the design concept are currently underway at the Naval Research Laboratory (NRL) and the Naval Surface Warfare Center, Carderock Division (NSWCCD).

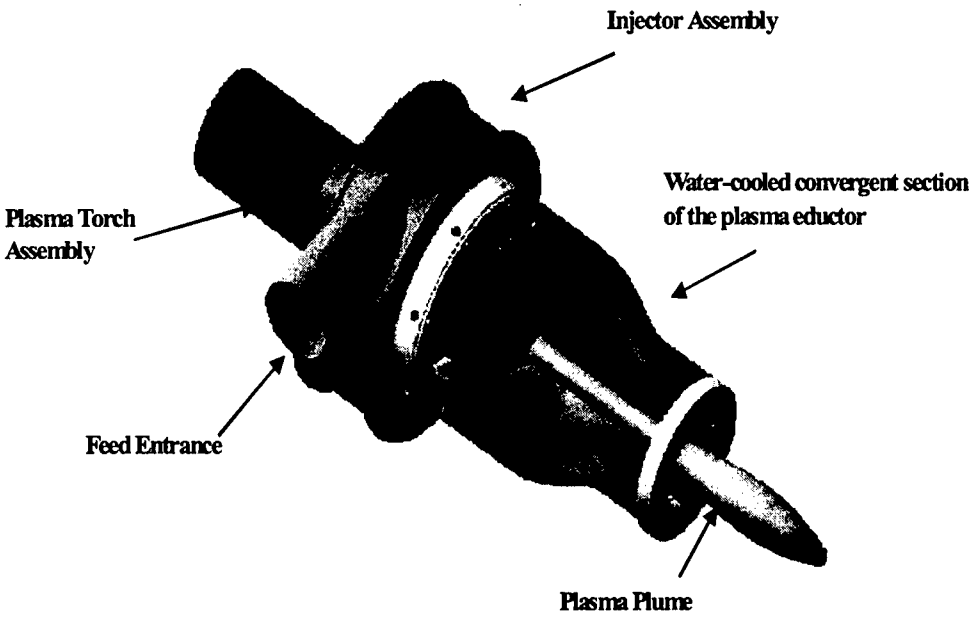


Figure 1 Schematic representation of the pre-prototype plasma fired eductor that is being evaluated for thermal destruction of Navy solid waste

A central element of the PAWDS concept is the Navy-developed Plasma Fired Eductor (PFE) that exposes waste feed particles to the extremely hot, chemically aggressive environment of a plasma arc torch operating on air. The function of the PFE is to cause rapid gasification of combustible materials as they transit its length. The plasma torch forms an electric discharge on the order of 100 kW to heat the torch gas to more that 5000 K. The shape of the PFE, which is shown in Fig. 1, is intended to force a strong interaction between the particles and the plasma plume. The PFE design was developed to address shipboard integration criteria such as size, weight, ship motion, and tolerance to mechanical and thermal shock as well as insensitivity to vibration.

The plasma temperature is a function of the electric discharge power and the air mass flow rate through the torch. Conditions are selected to give a high degree of dissociation of oxygen to enhance thermal destruction rates due to atom-molecule reactions as well as the high temperature kinetics.

The major components of the combustible wastes are paper and cardboard. Two preparation methods have been assessed:

- Disk milling, which makes a fine powder with particles <0.5 mm in largest dimension
- Shredding in a classified paper shredder, set for particles <3/32 in (2.4 mm).

Batches of these materials were prepared for test by moistening to the desired amount (5%, 20%, 40% by weight).

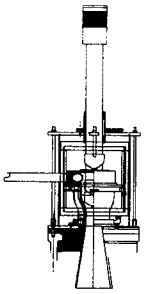


Figure 2 Plasma fired eductor and feed distribution ring mounts atop the NRL Retech plasma reactor. Feed suspended in carrier air enters at the top of the eductor and swirls down around the plasma plume through the eductor throat, assuring rapid heating and good mixing. A diffuser section provides a smooth transition for the gas flow into the secondary combustion chamber below.

The main purpose of the PFE is to rapidly gasify the feed. The high plasma temperature creates fast kinetics by dissociation of oxygen to atoms, giving oxygen atom-molecule reactions, which are typically much faster than similar reactions with oxygen molecules. In addition, the high temperature promotes fast reactions, and the eductor throat forces good mixing. To avoid overheating in the eductor, it is the goal at the design feed rate of 5 pounds per minute to operate at about 50% stoichiometry. Reaction air comes from two sources: torch air at a typical flow rate of 4.9 scfm, and the balance as carrier air that transports feed into the eductor. The exhaust gases from the eductor pass into the chamber of the Retech reactor, where secondary combustion air is added and completes the combustion process.

The pre-prototype eductor has been mounted on the NRL Retech plasma reactor, as shown in Fig. 2, for experiments conducted to address several questions critical to successful design and operation of the prototype PFE that will be used for the ATD program. These include:

- Determination of the quantity of thermal energy deposited in the eductor wall, so that cooling can be designed to maintain safe operating temperatures and to help with selection of materials for the eductor liner.
- Investigation of feed material properties required for satisfactory gasification.
- Measurement of waste moisture content that can the system tolerate, and determination of the tradeoffs between sample preparation methods in terms of size and moisture.

Shakedown experiments were conducted without feed to determine such parameters as thermal loading on the eductor walls. Safety procedures have been integrated into system operation and control, and have been shown to safely shut down the system when necessary. Operating procedures have been developed and implemented for tests in a varied test matrix. Lessons learned from early tests have been incorporated as the test program has progressed.

On-line data collection has been successfully implemented for a large number of data channels. This permits real time system control and enhances system safety. Test results are rapidly disseminated to team members for use in their own analytical methods.
Chemistry tests have been conducted with feed materials from various preparation methods and with various moisture contents.

Observations based on experience with operating the eductor under various conditions and with the various feed materials include:

1. For most test runs, the eductor walls have been unexpectedly cool. This seems to be due to the flow of cool carrier air along the wall, which is injected with a large swirl component. When this flow was shut off for one run, the liner quickly overheated and melted. Thus, this cooling mechanism seems to be very effective. For theoretical reasons, it seems likely that hotter walls would improve destruction rates. For design of the ATD unit, the plan is to increase the eductor wall temperature to produce a larger gasification volume in the PFE

2. Increasing feed rate gives better eductor performance, which is thought to be due to increased heat release from more chemical reactions and from coalescence of the flames from individual particles into a unified fireball. There has not been an opportunity to look for an upper limit to this effect because the current reactor chamber is limited by off-gas handling and by the amount of secondary combustion air that can be used. The ATD unit will be designed to take advantage of the improved operation at higher feed rate.

3. Destruction tests have been run with very fine disc milled material (DM-1) with particles <0.5 mm in their largest dimension, and with shredded paper and cardboard from a classified document shredder that produces particles < 3/32 inch (2.4 mm) (DPC 3/32). Moisture levels of 5%, 20% and 40% have been used, and 8.5% plastic (high density polyethylene) has been added to DPC 3/32 at 20% moisture. Operation was judged subjectively by observing the flame that emerged from the diffuser at the end of the eductor, and samples of ash and off-gases were collected as well as gas and wall temperature measurements.

4. The eductor has demonstrated effective destruction of both DM-1 and DPC 3/32, at moisture levels of 5% and 20%. Jumping the moisture to 40% appeared to result in high unburned carbon content; increasing torch power might permit a water content that high. The limiting factor is likely to be heat transfer. It was previously observed in pre-eductor tests at NRL that wet objects vent steam at about 100 °C until they have dried. Thus until the material has dried, it is not exposed to the high temperature of the plasma gases. Maximizing the surface area of the particles should improve the heat transfer and drying, and may permit higher moisture content. CFD calculations should be invaluable in clarifying the test data.

5. Ash samples that have been analyzed were all collected after the material passed through the eductor and the secondary combustor, and thus do not specifically describe eductor performance. However, with residual C as low as 1.4% (compared to the IMO limit of 10%), the results are very encouraging. Since we are quite sure that the secondary combustor was not well designed for this purpose, the eductor appears to achieve good carbon burnout.

6. The torch position has been varied from fully forward in the eductor throat, and 1 and 2 inches back. Moving the torch back from the PFE throat exposes the feed material to the heat sooner and enhances destruction.

Conditions in the eductor are such that direct observation and sampling are virtually impossible. In order to better understand chemical and transport effects in the eductor, computational flow dynamic (CFD) modeling is being developed. Initial stage CFD modeling has been performed for the plasma eductor and has provided some insight into the eductor performance. CFD modeling is being used to assess trends on eductor performance with respect to particle size, moisture content, and plasma torch energy. One of the main objectives will be to determine if the plasma torch provides adequate heat release for organic waste gasification. Also, the modeling should indicate if temperatures at the eductor exit would promote NOx formation and if temperatures are higher than necessary for adequate gasification of the organic wastes. Studies of lower torch energies will be performed in the CFD studies, which will provide critical information on the finite mixing rates of the torch exit stream with the organic waste stream and the effects on gasification and NOx formation with lower torch energies.

The presentation will describe the experimental setup for these pre-prototype PFE tests and will present results of experiments and calculations. Implications for the ATD prototype PAWDS design and testing will be discussed.

LIGHT-SCATTERING MEASUREMENTS OF MORPHOLOGICALLY EVOLVING FLAME-SYNTHESIZED OXIDE AGGREGATES

Umit O. Koylu[†*], Yangchuan Xing[‡], and Daniel E. Rosner[‡]
[†] Department of Mechanical Engineering, Florida International University, Miami, FL 33174
[‡] Department of Chemical Engineering, Yale University, New Haven, CT 06520

Introduction. Various ultrafine powders, such as carbon black, titania, and silica, are routinely produced as fine particles by vapor-condensation combustion synthesis processes in industry. These powders are of technological importance because of their desirable optical, mechanical, catalytic, and/or electrical properties. To attain the objective of producing inorganic oxides of prescribed size and morphology for a wide variety of technological applications, a comprehensive understanding of the factors governing their formation, growth, coagulation, and sintering processes needs to be gained. It is also necessary to determine how flame conditions can be tailored to obtain a particular product because particle evolution is directly related to flame structure. Achieving these goals requires diagnostic techniques that can provide a real-time assessment of local particle/aggregate properties, e.g., size, distribution, morphology, number density, and specific surface area. Furthermore, the *in situ* laser-based methods become increasingly important for industrial-scale operations in which the quality of the final product depends not only on the combustion conditions but also on the effective on-line monitoring of the particulates.

In a previous work [1], we began our investigation of the sintering of aluminum oxide aerosol in a laminar counterflow flame that allowed observations of aggregate collapse using *ex situ* thermophoretic sampling (TS) and transmission electron microscopy (TEM) techniques. The objective of the present study was to implement a novel light-scattering (LS) technique to obtain a reliable understanding of particle evolution mechanisms in flames and to probe the rate of aggregate sintering (here refers to the size reduction of aggregates at high temperatures) in detail. The following discussion is brief; additional details can be found in Refs. [2, 3].

Experimental Methods. A rectangular laminar counterflow flame reactor was used to synthesize alumina nanoparticles. The burner has two identical rectangular slots vertically positioned with a separation distance of 15 mm. Methane and oxygen were introduced from the lower and upper channels, respectively. For the experiments reported here, gas flow rates yielded a fuel/air momentum flux ratio of 5.4, an equivalence ratio of 0.77, and nominal strain rate of 8.6 s^{-1}. Under these experimental conditions, a flat blue laminar nonpremixed flame with uniform transverse properties was stabilized. With a coordinate system attached to the center of the lower fuel slot, the flame sheet location was at z_{FLP} = 6.7 mm, as indicated by the maximum temperature of about 2200 K.

Liquid trimethylaluminum (TMA) was fed into an evaporator before being injected into the methane fuel stream. Aluminum oxide (Al_2O_3) particles were synthesized by the reaction of water vapor in the flame with the TMA precursor. The particle inception plane (PIP) and particle stagnation plane (PSP), located from the onset and fall-off of the LS signals, respectively, were at z_{PIP} = 1.6 mm and z_{PSP} = 10.2 mm. Alumina particles formed by TMA hydrolysis at the PIP on the fuel side of the burner rapidly coagulated to form aggregates. They then entered a region with the temperature rising at a rate of ca. 33,000 K/s, attaining temperatures sufficient to initiate aggregate sintering. The restructuring process in this heating environment continued with aggregates passing through the flame. Particles were ultimately ejected from the reactor near or at the PSP.

Evolution of aggregates due to the various rate processes within our counterflow burner is characterized here using *in situ* angular laser-scattering measurements. A schematic diagram of the optical set-up is shown in Fig. 2, which allowed scattering measurements at various angles between $\theta = 4°$ and $\theta = 160°$. The optics was calibrated by measuring the scattering signal from nitrogen molecules under identical conditions.

We also implemented, for the first time, an extension of the thermophoretic technique, designated the Thermophoretic Sampling Particle Diagnostic (TSPD), for inferring not only particle/aggregate size and

* Corresponding author, koyluu@eng.fiu.edu

morphology but also local volume fraction of inorganic particles in order to support the LS data. The specific thermophoretic sampling instrumentation was identical to that developed by Koylu et al. [4] utilizing an extension of the experimental and theoretical methods established by Refs. [5, 6]. This involved rapid insertion of a grid attached to the tip of a thin substrate into the hot flame to extract representative particles/aggregates using the thermophoresis phenomenon. After being exposed to our alumina-producing flame, the sampling grids were subsequently examined with a TEM followed by computer image analysis.

Theoretical Methods. Spherical scattering theories (Rayleigh and Mie) are not suitable for most flame-generated particulates that exist in the form of aggregates of many smaller spherules. In such cases, a more elaborate theory is necessary to account for the more complex aggregate geometry, following the Rayleigh-Debye-Gans scattering theory for fractal aggregates (RDG-FA). This simple formulation has been shown to accurately represent the scattering properties of carbonaceous soot aggregates [7, 8]. Although the assumption of touching spherules within an aggregate starts failing at locations close to the flame sheet, we still cautiously continued to employ the RDG-FA analysis because of lack of an alternative *in situ* method for such restructuring aggregates.

Our interpretation of light-scattering data follows exclusively that outlined by Koylu [9]. Briefly, this analysis involves determination of the fractal dimension, D_f, from the slope of scattered signal at large angles vs. $q = (4\pi/\lambda)\sin(\theta/2)$ on a logarithmic scale. The absolute values of such a fit also yield the particle number density, once spherule diameter is independently known from the TSPD measurements. The aggregate size distribution can then be obtained from the measured angular variation of scattered light because the entire angular scattering pattern relative to the forward direction depends only on pdf(N, number of spherules in an aggregate).

Results and Discussion. To track *in situ* the changes in aggregate size/morphology/number density, we measured absolute scattering intensities at as many as 20 angles between 4° and 160°. Typical angular scattering patterns at various vertical positions in our flame reactor are shown in Fig. 2, which also indicates the angular scattering regimes in which K_{vv} was relatively independent of q at small angles (Guinier regime) and appeared to decrease with q at large angles (power-law regime). As can be seen, scattering in the forward direction (small q) was always substantially larger than the backward direction (large q). This alone is clear evidence that the alumina particles in our reactor departed from the Rayleigh scattering behavior that would be expected for small isolated spherical particles. The increase in the scattered light in the forward direction relative to the backward direction from $z = 2.3$ mm to 6.35 mm implies a continuous aggregation process.

Figure 3 shows two optically inferred aggregate radii at various axial positions in our counterflow nonpremixed flame. The mean radius of gyration, R_{gm}, was obtained by re-plotting the results of Fig. 2 in the form of $K_{vv}(0°)/K_{vv}(q)$ vs. q^2. Such a plot yields a linear slope of $R_{gm}/3$ in the Guinier regime, which corresponds to scattering angles of less than 20° during the present experiments. Although the alumina aggregates produced in our flame have mostly nonspherical shapes, the volume-equivalent radius, R_{eq}, is also included in Fig. 3 because it allows a comparison of our results to past studies in the literature that used a similar Mie scattering analysis [10].

As can be seen from Fig. 3, the optically measured R_{gm} increased rapidly after PIP, but leveled off before FLP. In fact, from $z = 3$ mm to 6 mm, R_{gm} increased from about 80 nm to 150 nm, almost a change of 100% corresponding to a growth rate of more than 20 nm/mm. However, from $z = 6$ mm to 7 mm, a sharp decrease (to about 90 nm) in radius of gyration was observed. This corresponds to a net size shrinkage rate of more than 60 nm/mm, probably because of the significant particle sintering near the flame. This overall behavior is also supported by the variation of R_{eq} with z, i.e., a continuous increase and decrease around the maximum temperature. The differences between the values of R_{gm} and R_{eq} at each position in Fig. 3 can be explained by considering that R_{gm} is an N^2-weighted average whereas R_{eq} is related to the first moment of aggregate size distribution.

The fractal dimension, D_f, of the alumina aggregates was determined from the slope of *in situ* LS measurements of Fig. 2, which shows a limited linear variation with q at large angles. In order to ensure a power-law scattering behavior, we inferred D_f from least-square fits at angles between $\theta = 110°$ and 160°. Results of this procedure yielded an increase in D_f from 1.60 to 1.84, which is an indication of aggregates becoming more compact as the temperature of the surrounding gases increased toward the flame. The fractal dimension at other positions (mainly

above z_{FLP}) could not be obtained because of the inaccessibility of the power-law regime at the laser wavelength (λ = 514.5 nm) employed here. Furthermore, our independent TEM observations [1, 3] confirmed this apparent increase in the fractal dimension within the flame.

Local particle volume fractions obtained from the LS data are presented in Fig. 4 together with estimates from the TSPD experiments and theoretical predictions. The measured particle volume fractions were on the order of 0.1 ppm, decreasing after the initial formation region mainly due to the temperature gradient of the host gases. Because our LS interpretation is only suited for fractal aggregates, particle volume fractions after z = 6.6 mm were not quantified for presentation in Fig. 3. But in the domain of self-consistency, the alumina concentrations determined from the *in situ* LS technique generally agreed with the *ex situ* TSPD technique, which was implemented in this study for the first time for oxide nano-particles with significant sintering. Both LS and TSPD experiments were also in satisfactory agreement with the above-mentioned theoretical mass-balance calculations, meriting further application of these two techniques to similar particle-laden environments.

Conclusions.

1. To characterize the alumina nano-particles synthesized in a laminar flame reactor, *in situ* laser-scattering measurements were interpreted by properly accounting for aggregate fractal morphology. Optically determined aggregate parameters (apart from spherule diameter) were generally consistent with our independent thermophoretic sampling/TEM image-analysis experiments in the same flame.

2. The local fractal dimension increased from 1.60 to 1.84 with the pre-flame axial position, confirming our TEM evidence of morphological evolution of alumina aggregates due to the high-temperature sintering process.

3. Local particle volume fractions (ca. 0.1 ppm), inferred from the above-mentioned *in situ* LS technique also agreed with the *ex situ* TSPD technique, which was implemented here for the first time for inorganic particles.

4. Based on the present measurements, the mean aggregate shrinkage rate associated with alumina spherule sintering near the flame zone (ca. 2200 K) was estimated to be about 16 nm/ms, also in agreement with TEM evidence from the same portion of the flame.

This ability to track the evolution of flame-generated particles using both *in situ* and *ex situ* experimental techniques now opens the door to reliably: i) infer the intrinsic kinetic laws governing nano-aggregate restructuring at very high temperatures, and ii) develop/validate two-phase flame structure mathematical modeling techniques [11, 12]. These are necessary steps toward the longer-range 'sol reaction engineering' goal of reliably and economically predicting the behavior of combustors/reactors, which deliberately or inadvertently produce partially aggregated/restructured suspended submicron particulate matter.

Acknowledgments: This research was sponsored by AFOSR Grant No. 97-1-00266 and NSF Grant No. CTS-9711954.

REFERENCES

1. Y. Xing, U. O. Koylu, and D. E. Rosner, *Combust. Flame* **107:** 85-102 (1996).
2. Y. Xing, U. O. Koylu, and D. E. Rosner, *Appl. Opt.* **38:** 2686-2697 (1999).
3. Y. Xing, Ph.D. Dissertation, Yale University, 1997.
4. U. O. Koylu, C. S. McEnally, D. E. Rosner, and L. D. Pfefferle, *Combust. Flame* **110:** 494-507 (1997).
5. R. A. Dobbins and C. M. Megaridis, *Langmuir* **3:** 254-259 (1987).
6. D. E. Rosner, D. W. Mackowski, and P. Garcia-Ybarra, *Combust. Sci. Tech.* **80:** 87-101 (1991).
7. U. O. Koylu and G. M. Faeth, *J. Heat Transf.* **116:** 971-979 (1994).
8. T. L. Farias, U. O. Koylu, and M. G. Carvalho, *Appl. Opt.* **35:** 6560-6567 (1996).
9. U. O. Koylu, *Combust. Flame* **109:** 488-500 (1997).
10. J. L. Katz and C.-H. Hung, *Combust. Sci. Tech.* **82:** 169-183 (1992).
11. P. Tandon and D. E. Rosner, *Chem. Eng. Communic.* **151:** 147-168 (1996).
12. Y. Xing, D. E. Rosner, U. O. Koylu, and P. Tandon, *AIChE J.* **43:** 2641-2649 (1997).

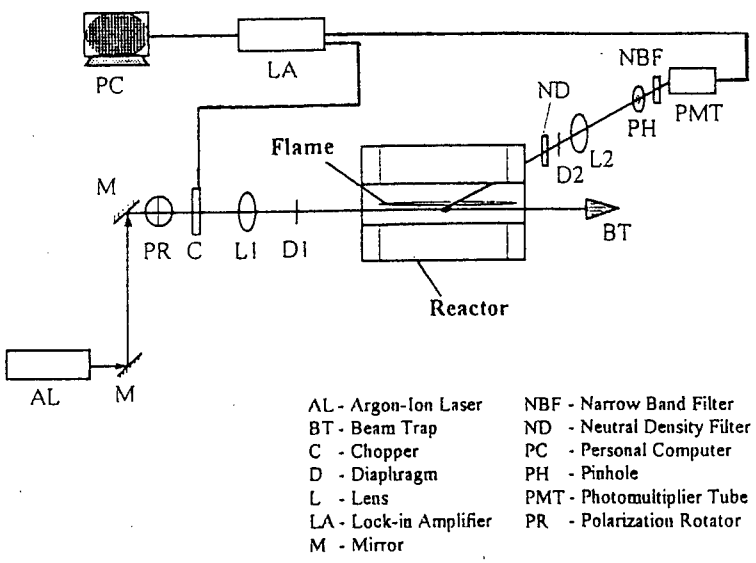


Fig. 1 Schematic of the angular light-scattering apparatus.

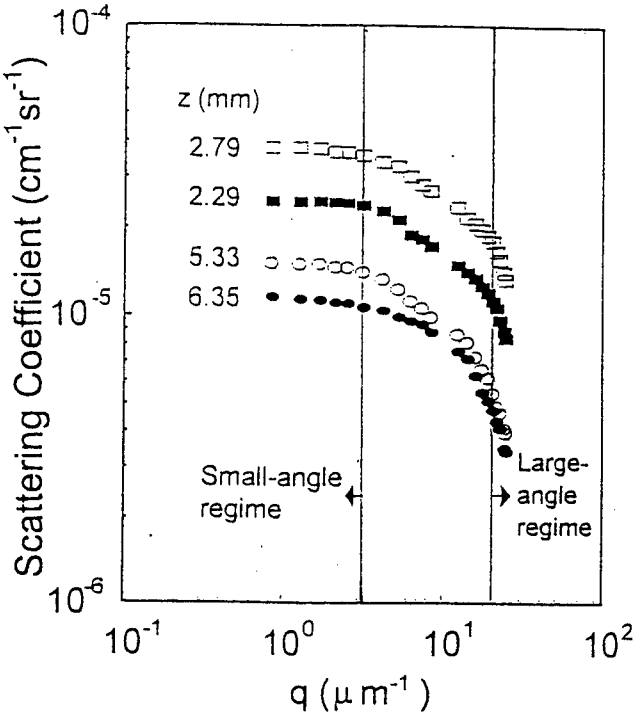


Fig. 2 Measurements of the scattering coefficent as a function of $q=(4\pi/\lambda)\sin(\theta/2)$.

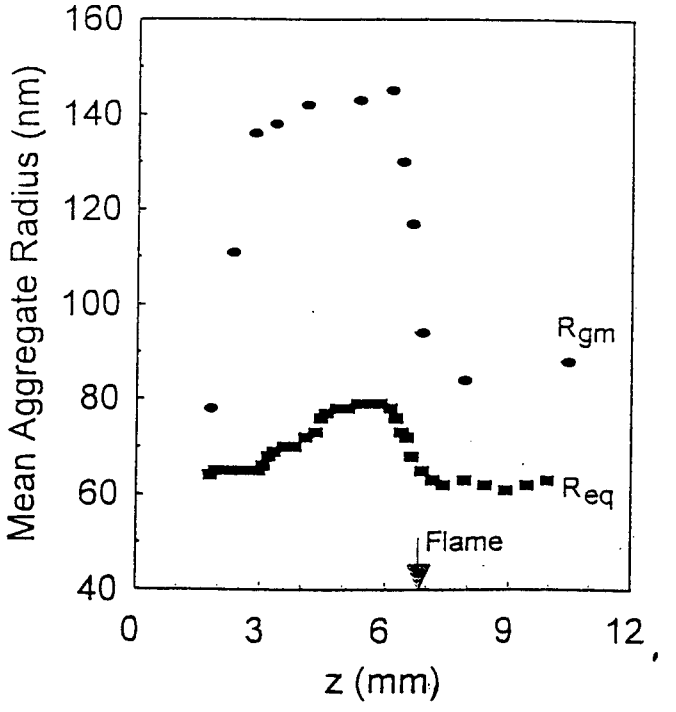


Fig. 3 Inferred mean aggregate radius of gyration, R_{gm}, and volume-equivalent radius, R_{eq}.

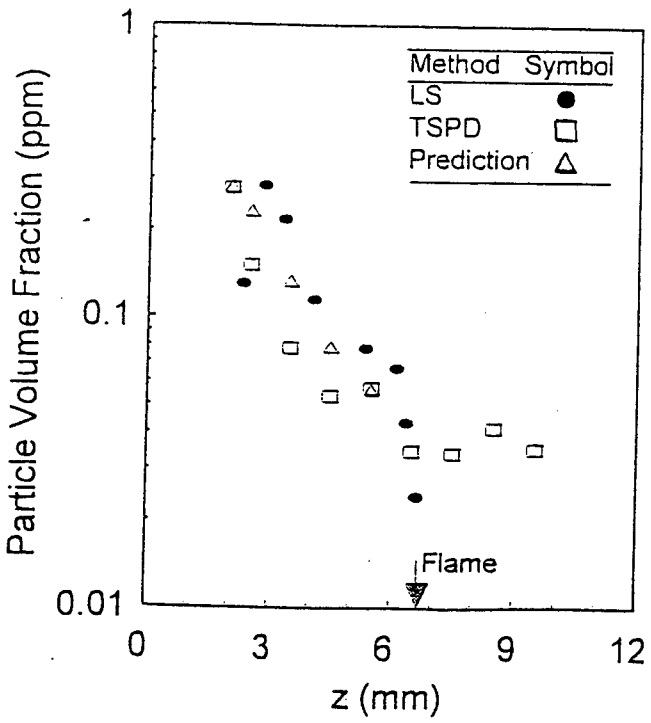


Fig. 4 Particle volume fractions obtained from the in situ laser scattering measurements, the ex situ TSPD, and mass-balance predictions.

Flame Inhibition by Ferrocene, Carbon Dioxide, and Trifluoromethane Blends: Synergistic and Antagonistic Effects

G.T. Linteris and **M.D. Rumminger**
National Institute of Standards and Technology
Gaithersburg, MD 20899-8651; linteris@nist.gov; mrum@asme.org
(current address for MDR: Sandia National Laboratories; MS 9052; Livermore, CA 94551)

The production of CF_3Br has been banned. As a flame inhibitor, iron pentacarbonyl ($Fe(CO)_5$) is about two orders of magnitude more efficient than CF_3Br, but it is flammable and highly toxic, and its addition to premixed flames at mole fractions above a few hundred ppm does not further reduce the burning velocity. If other iron compounds can be identified which show the same strong inhibition but are less toxic and don't lose their effectiveness, they may find use in fire suppressants. Ferrocene ($Fe(C_5H_5)_2$ or Fec) modifies the sooting tendency of flames, is added to materials as a flame retardant and is an antiknock agent. It is far less toxic than $Fe(CO)_5$, and it may produce the same iron-containing intermediates. Here, we present the first measurements of flame inhibition by ferrocene, compare it with $Fe(CO)_5$ and CF_3Br, and present data showing how combining it with other compounds can overcome the loss in effectiveness experienced by both it and $Fe(CO)_5$.

Flame inhibition by bromine, alkali metals, and transition metals have been described in the literature, and their reduced effectiveness at higher mole fractions has been discussed in detail [1-3]. Since the chemicals are believed to act through homogeneous gas-phase catalytic radical recombination cycles, the inhibition mechanism requires a radical superequilibrium to be most effective. Consequently, once radicals are reduced to equilibrium levels via inhibitor addition, further reduction in the overall reaction rate from additional inhibitor is minimal. This loss in effectiveness due to radicals approaching their equilibrium values has been demonstrated for increasing mole fraction of inhibitor in calculations employing both an idealized "perfect" inhibitor [2] and $Fe(CO)_5$ [3], and has been discussed by Rosser et al. [4] and Hastie [5]. Nonetheless, the measured loss in effectiveness of $Fe(CO)_5$ occurs at a lower mole fraction than expected based on these calculations; the actual cause appears to be condensation of iron compounds and the resulting limit to the gas-phase iron-species concentrations [6]. Regardless of the cause of the loss of effectiveness, previous researchers [4,5,7-10] have suggested that combinations of thermally acting and catalytic agents might prove beneficial. The effectiveness of iron pentacarbonyl in premixed flames has been shown to be greatly increased at lower oxygen mole fraction, and the effect has been attributed to the larger superequilibrium ratio (the peak radical mole fraction divided by the equilibrium value) which exists at lower oxygen mole fraction [1]. In contrast, the effectiveness of relatively inert agents such as N_2 and CO_2 is not a strong function of the oxygen mole fraction in the oxidizer stream, $X_{O2,ox}$. (In the present work we find that addition of 10% CO_2 to flames with $X_{O2,ox}$ equal to either 0.21 or 0.244 reduces the normalized burning velocity by about half, whereas $Fe(CO)_5$ is more than twice as effective for $X_{O2,ox} = 0.21$ than for 0.244 [1]). Since adding a thermal agent raises the superequilibrium ratio, the possibility exists for very effective blends of catalytically and thermally acting agents. Consequently, we report here the burning velocity of premixed flames in the presence of combinations of a thermal agent CO_2, (which does not lose its effectiveness at higher mole fraction) and catalytic agents (which are superbly effective at low inhibitor mole fraction).

The premixed laminar flame speed S_L provides a measure of the effect of the inhibitor on the overall reaction rate. The experimental arrangement, described in detail previously [1,10,11], has been modified only to accommodate a new evaporator for ferrocene and heating of the gas lines and burner tube. A Mache-Hebra nozzle burner (1.0 cm ± 0.05 cm diameter) produces a premixed Bunsen-type flame about 1.3 cm tall with a straight sided schlieren image which is captured by a frame-grabber board in a PC. Digital mass flow controllers hold the equivalence ratio ϕ, $X_{O2,ox}$, and the flame height constant while maintaining the inlet mole fraction of the inhibitor X_{in} at the desired value. The inhibitors are N_2, CF_3H, CO_2, Fec, and $Fe(CO)_5$. The average burning velocity is determined from the reactant flows and the schlieren image using the total area method. As in earlier research, the fuel gas is

methane (Matheson[1] UHP, 99.9%), and the oxidizer stream consists of nitrogen (boil-off from liquid N_2) and oxygen (MG Industries, H_2O < 50 ppm, and total hydrocarbons < 5 ppm). The inhibitors used are Fec (Aldrich, 98%), $Fe(CO)_5$ (Aldrich), CF_3Br (Great Lakes), N_2, and CO_2 (Airgas). The $Fe(CO)_5$ is added to N_2 carrier gas using a two-stage saturator in an ice bath. Because the vapor pressure of Fec is much lower than that of iron pentacarbonyl, Fec addition at mole fractions up to 500 ppm requires both higher bath temperature (70 to 80 C, held within 0.01 C) and higher nitrogen carrier gas flow rates (up to 350 cm^3/min) relative to $Fe(CO)_5$. Also, the solid state of Fec requires an evaporator with larger surface areas for heat and mass transfer. Our evaporator design, based upon that of Megaridis [12], has a 30 ± 5 cm^3 packed bed (to provide the bulk of the ferrocene), followed by thirty sublimation stages (to insure that the carrier gas is saturated at the bath temperature); each stage consists of a 5 mm layer of ferrocene, 2.36 cm in diameter, on a 60 mesh stainless screen and a 4 mm gap. Temperature controllers maintain the transfer lines at 353 K ± 3 K and the burner tube at 353 K ± 1 K. For all flames, the equivalence ratio (in the absence of inhibitor) is 1.0, and agent mole fraction is calculated relative to the reactant total without the inhibitor.

The experimental burning velocity reduction caused by the addition of Fec and $Fe(CO)_5$ to the stoichiometric methane flames are presented in Figure 1. Data are plotted as normalized burning velocity, which is the burning velocity of the inhibited flame divided by the value for the same flame in the absence of inhibitor. (For Figs. 1 to 4, the solid lines are fits to the data.) As Figure 1 shows, Fec (closed symbols) reduces the burning velocity as effectively as does $Fe(CO)_5$ (open symbols), and it does not appear to lose its effectiveness until higher mole fraction. As with $Fe(CO)_5$, the magnitude of the inhibition is strongly dependent upon the oxygen mole fraction in the oxidizer, with oxygen-deprived flames inhibited much more strongly.

Figure 2 presents experimental data for addition of pure CO_2 (or pure N_2) and CO_2/Fec blends at four values of the equivalent percentage of Fec in CO_2: 0, 0.053%, 0.2%, and 0.54%. The last data point in a series represents the maximum value of X_{in} at which a flame could be stabilized. The blends of the inert and chemically acting agents are shown to be highly effective. Addition of about 10% of pure CO_2 (or 25% pure N_2) reduces S_L by a factor of two. Addition of the equivalent of 0.1% Fec to CO_2 reduces the required CO_2 by about a factor of two, and 0.6% Fec reduces the required CO_2 by ten, making this blend about as effective as CF_3Br (for which addition of about 1% halves the burning velocity). It is important to note that the flames with CO_2/Fec combinations in Figure 2 do not display the large loss in effectiveness, i.e. the plateau region, occurring in most of the curves in Figure 1. Although one might expect the slightly cooler, slower flames with added CO_2 to have more condensation of iron species, the greater efficiency of the catalytic cycle in the diluted flames predominates.

Other compounds may be convenient for blending with catalytic agents. Hydrofluorocarbons are of interest since they are presently used as halon replacements. These compounds have been found to reduce the burning velocity of premixed methane-air flames by reducing *peak* H-atom mole fractions through reactions forming HF and by lowering the temperature of the flame. Since they have also been shown to reduce the *equilibrium* mole fractions of radicals in flames lower than expected based on temperature reduction alone [13], they might be expected to show enhanced performance relative to CO_2 when combined with catalytic agents. Figure 3 presents the burning velocity reduction caused by pure CF_3H addition to the above flames; a mole fraction of about 5% is required to reduce S_L by two. Data are also presented for addition of the equivalent of 0.35% Fec in CF_3H. Unlike ferrocene addition to CO_2, in which 0.35% Fec in CO_2 reduces the amount of CO_2 required by a factor of about five, this amount of ferrocene in CF_3H reduces the amount of CF_3H required only by about 25%. This poor performance may be due to reactions between iron species and fluorine which reduce the gas-phase mole fraction of the active iron-species intermediates, effectively poisoning the iron catalyst [5,14].

To further illustrate the synergistic behavior of Fec with CO_2 , and the antagonistic behavior of Fec with CF_3H, we examine the performance of the blend relative to individual contributions from each component. We define the normalized flame speed at each inhibitor mole fraction X_{in} as $N_{SL}(X_{in})$, and the reduction in the normalized

[1] Certain commercial equipment, instruments, or materials are identified in this paper to adequately specify the procedure. Such identification does not imply recommendation or endorsement by the National Institute of Standards and Technology, nor does it imply that the materials or equipment are necessarily the best available for the intended use.

flame speed as R_{SL} (X_{in}) = 1 – $N_{SL}(X_{in})$. Assuming that the flame speed reduction of a two-component blend $R_{SL}(X_{in})|_{blend}$ is a linear combination of the contribution from each component, $R_{SL}(X_{in,1}, X_{in,2})|_{blend} = X_{in,1}R_{SL,1} + X_{in,2}R_{SL,2}$, the predicted normalized burning velocity of the blend is $N_{SL}(X_{in,1},X_{in,2})|_{blend} = 1 - R_{SL}|_{blend}$. The ratio of the predicted to the actual normalized flame speed for several blends is shown in Figure 4. A value greater than unity shows that the blend provides a reduction in the normalized burning velocity more than expected based on a linear combination of the contribution from each component, while a value less than one shows the converse. In Figure 4, the curve near unity shows the result for a blend of 2/1 molar ratio of N_2 to CO_2; that is, for thermally acting agents in these flames and in this range of inhibitor mole fraction, the reduction in flame speed from CO_2 and N_2 is additive. As the figure shows, CO_2 with 0.54% Fec is significantly more effective than would be expected based on a linear combination of the performance of Fec and CO_2 alone, while CF_3H and Fec is significantly less effective than the sum of each individually.

We have presented the first data on ferrocene as a flame inhibitor, and shown it to be as efficient as $Fe(CO)_5$ at reducing the burning velocity of premixed methane flames. The results imply that either agent acts as an effective precursor for the active iron-species intermediates. For the data presented here, ferrocene does not appear to lose its effectiveness as drastically as does $Fe(CO)_5$, and its inhibition has just as strong a dependence on $X_{O2,ox}$. As a result, blends of CO_2 and Fec show very strong inhibition, overcoming the loss of effectiveness observed for pure Fec or $Fe(CO)_5$. Further, blends of CO_2 and Fec reduce the burning velocity of premixed methane-air flames more strongly than expected based on the performance of each individually. Blends of CF_3H and Fec, however, have been found to be much less effective than expected based on the performance of each individually, implying that iron species and halogens may enter into undesired reactions which poison the catalytic cycles. Nonetheless, if means can be identified to safely introduce gas-phase iron compounds into fires, combinations of catalytically and relatively inert thermally acting inhibitors may prove to be an efficient approach to solving a problem which threatens the global environment.

We thank Prof. Dino Megarides of UIC for helpful discussions, and for sending us his ferrocene evaporator. We also thank Dr. Wing Tsang for stimulating conversations and suggestions throughout this research. This research was supported in part by NGP MIPR No. W74RDV83528667.

[1]. Reinelt, D. and Linteris, G.T., *Twenty-Sixth Symposium (International) on Combustion*, The Combustion Institute, Pittsburgh, 1996, pp. 1421-1428.
[2]. Babushok, V., Tsang, W., Linteris, G.T., and Reinelt, D., *Combust. Flame* 115:551 (1998).
[3]. Rumminger, M.D., Reinelt, D., Babushok, V., and Linteris, G.T., *Combust. Flame* 116:207 (1999).
[4]. Rosser, W.A., Inami, S.H., and Wise, H., *Combust. Flame* 7:107 (1963).
[5]. Hastie, J. W., *High Temperature Vapors*, Academic Press, New York, 1975.
[6]. Rumminger, M.D. and Linteris, G.T., "An Experimental Study Of The Role Of Particles In Flame Inhibition By Iron Pentacarbonyl", in preparation for submission to *Combustion and Flame*. 1999.
[7]. Rosser, W. A, Inami, S. H., and Wise, H., *Study of the Mechanisms of Fire Extinguishment of Liquid Rocket Propellants,* WADC Technical Report 59-206, 1959.
[8]. Lott, J.L., Christian, S.D., Sliepcevich, C.M., and Tucker, E.E., *Fire Technology* 32:260 (1996).
[9]. Noto, T., Babushok, V., Hamins, A., and Tsang, W., *Combust. Flame* 112:147 (1998).
[10]. Rumminger, M.D. and Linteris, G.T., "Inhibition of Premixed Carbon Monoxide-Hydrogen-Oxygen-Nitrogen Flames by Iron Pentacarbonyl", submitted to *Combustion and Flame*, March 1999.
[11]. Linteris, G.T. and Truett, L., *Combust. Flame* 105:15 (1996).
[12]. Zhang, J. and Megaridis, C.M., *Twenty-Fifth Symposium (International) on Combustion*, The Combustion Institute, Pittsburgh, 1994, pp. 593-600.
[13]. Linteris, G.T., Burgess, D.R., Babushok, V., Zachariah, M., Tsang, W., and Westmoreland, P., *Combust. Flame* 113:164 (1998).
[14]. Tsang, W., "Personal Communication, April 1999.

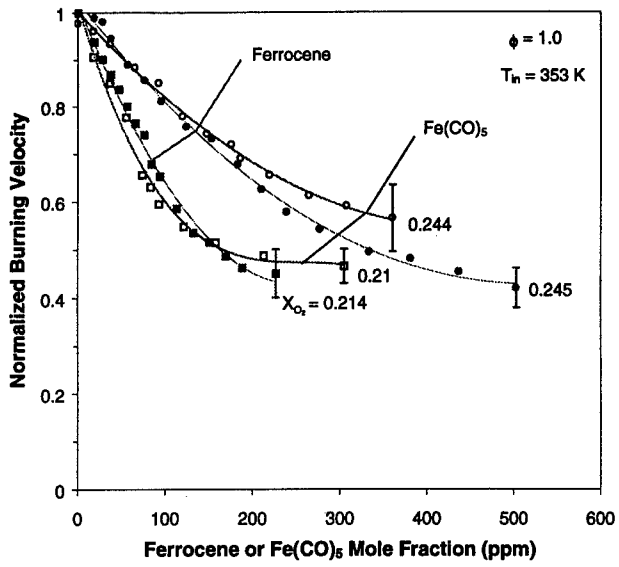


Figure 1 – Normalized burning velocity of premixed $CH_4/O_2/N_2$ inhibited by ferrocene and $Fe(CO)_5$ for several values of the oxygen mole fraction in the oxidizer $X_{O2,ox}$.

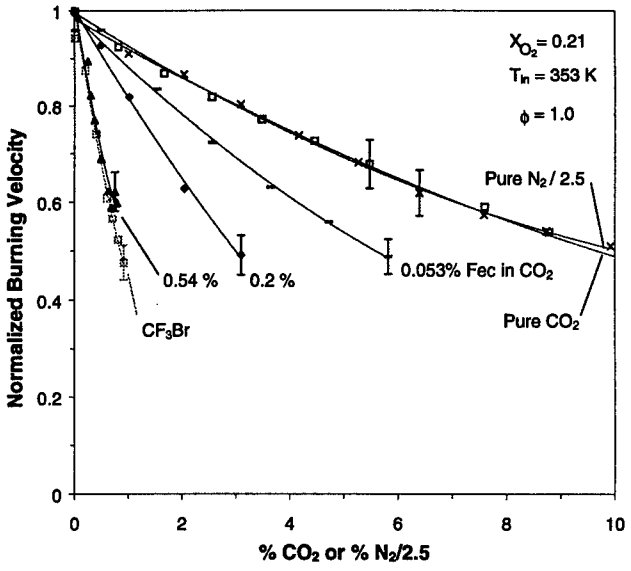


Figure 2 - Normalized burning velocity of $CH_4/O_2/N_2$ flames inhibited by pure CO_2 and pure N_2, and by blends of CO_2 and ferrocene. The equivalent percentage of ferrocene in CO_2 is given, and data for CF_3Br are shown for comparison.

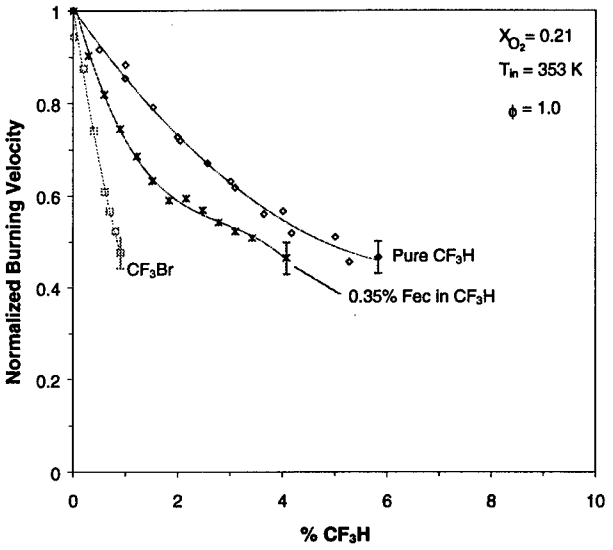


Figure 3 - Normalized burning velocity of premixed $CH_4/O_2/N_2$ flames inhibited by pure CF_3H and by CF_3H with 0.35% ferrocene, together with data for CF_3Br.

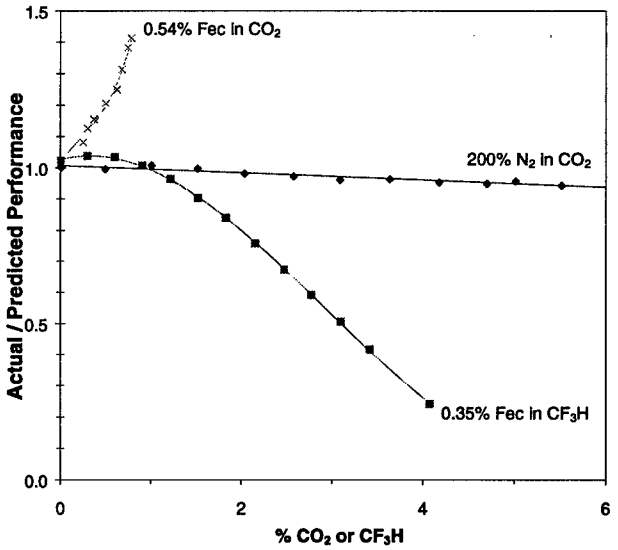


Figure 4 – Index of actual performance of inhibitor blend as compared to the predicted performance based on a linear sum of the burning velocity reduction caused by each component.

EQUIVALENCY OF THE RANKINGS OF INHIBITOR EFFECTIVENESS FOR COMBUSTION OF HYDROCARBON FUELS

Valeri Babushok, Wing Tsang, William Grosshandler
National Institute of Standards and Technology, Gaithersburg, MD 20899
(vbabushok@nist.gov, wing.tsang@nist.gov,william.grosshandler@nist.gov)

Introduction

The search for alternatives to halon 1301 has involved numerous flame studies, with the effectiveness of different agents compared using a range of gaseous and liquid fuels. Methane is the most convenient fuel for investigating the inhibition and extinction of laminar flames through chemical kinetics modeling because its combustion mechanism does not involve as many multi-carbon species. The concern with methane, or any one hydrocarbon, is that a given fuel may produce inhibitor rankings that are not representative of hydrocarbons in general. Trees et al. [1] compared the performance of thirteen agents (fluorocarbons, nitrogen, and CF_3Br) in extinguishing counter-flowing and co-flowing laminar diffusion flames of pure hydrocarbons, jet fuels, and hydraulic fluids. The relative ranking of the agents using all the fuels was practically the same, within the uncertainty of the experiments. In this paper we wish to examine the theoretical basis for generalizing the relative ranking of chemically active agents across different fuels, focusing on C_1 to C_4 alkanes, by carrying out a sensitivity analysis on the detailed kinetics of combustion. The results, although not complete, give a semi-quantitative picture of the transferability of suppressant effectiveness data for various hydrocarbon fuels.

Calculational Procedure and Kinetics Models

Simulations were carried out for methane, ethane, propane, butane and isobutane flames. The Chemkin suite of programs was used. The basic kinetic model was that of C_1-C_2 hydrocarbon combustion, used in our previous studies [2]. To describe the combustion of propane and butane, the block of reactions containing C_3 and C_4 compounds from the model of Marinov et al. [3] was added to the data base. For isobutane chemistry, an additional block of reactions based on the work of Tsang [4] was incorporated. The reactions of the additives CF_3Br and iron pentacarbonyl $Fe(CO)_5$ were taken from earlier publications [2, 5].

Mechanisms of alkane combustion: The basis of the present work is the flame velocity of fuel/air mixtures with and without suppressants. An examination of the sensitivity coefficients for the effect of the individual rate constants on the flame velocity with the various C_1 to C_4 alkanes as fuels show that the same set of reactions is the major contributor in all cases. Indeed, the number of reactions with sensitivity levels more than 10% of that for the main chain branching process is very small. The important reactions determining burning velocity are the following:

$$H + O_2 \rightarrow OH + O$$
$$HCO + M \rightarrow CO + H + M$$
$$CO + OH \rightarrow CO_2 + H$$
$$H + O_2 + M \rightarrow HO_2 + M$$

For methane the burning velocity is also sensitive to the reactions

$$H + CH_4 \rightarrow CH_3 + H_2$$
$$CH_3 + H + M \rightarrow CH_4 + M$$

For ethane combustion the reactions,

$$C_2H_5 + H \rightarrow CH_3 + CH_3$$
$$C_2H_5 + M \rightarrow C_2H_4 + H + M$$

contribute more than 10 % to the sensitivity of burning velocity in comparison to the main chain branching process, $H + O_2 \rightarrow OH + O$. For propane there are no reactions that effect the burning velocity to the extent of the reactions listed above for ethane and methane. Some of the important reactions that contribute to the sensitivity of burning velocity are

$$C_3H_5(allyl) + H \rightarrow C_3H_6$$
$$C_3H_6 + O \rightarrow CH_3CHCO + H + H$$
$$C_3H_6 + H \rightarrow C_3H_5(allyl) + H_2$$
$$iC_3H_7 + H \rightarrow C_2H_5 + CH_3$$

With n-butane combustion, the abstraction reactions,

$$C_4H_{10} + H \rightarrow sC_4H_9 + H_2$$
$$C_4H_{10} + OH \rightarrow sC_4H_9 + H_2O$$

influence the burning velocity at the 3 % to 5 % level in comparison to that of the main chain branching reaction. For the combustion of isobutane, reactions of formation and consumption of i-C_4H_8 and i-C_4H_7 species are most important. However, the sensitivity analysis demonstrate that the sensitivity to the rate constants involving these reactions is less than 10 % of the main chain branching process.

There are of course many reactions with relatively small sensitivity coefficients. The issue is whether the consequences on the flame velocity of all of these reactions with small sensitivity coefficients may in fact be as large as that of the reactions with large sensitivity coefficients. The simultaneous variations of rate constants were performed for groups of reactions involving C_1-C_2 and C_3-C_4 species using a butane/air mixture. The tested reactions have sensitivity coefficients ranging from 2 % to 4 % of the coefficient for the main chain branching process. The cases with positive and negative sensitivity coefficients were modeled separately and also together. The specific variations involve reducing rate constants by a factor of two. The calculations show that these changes are manifested in effects that are smaller than would be warranted by a direct summation of the consequences of the individual reactions. Simultaneous change of rate constants for reactions with different signs of the sensitivity coefficient leads to cancellation of the effects and thus relatively small overall influence of these reactions. Similar results were obtained for propane flame propagation. It can be concluded that the sum of the reactions with small sensitivity coefficients does not lead to effects on flame properties that are larger than that from the main reactions. On this basis we give in Table 1 a summary list of the reactions with the highest sensitivity in terms of effects on the burning velocity. The majority of the reactions shown have sensitivity coefficients that are no less than 10 % of that for $H + O_2 \rightarrow OH + O$. It can thus be seen that the reactions that control the flame velocity involve in all cases the breakdown products. Particularly noteworthy is the absence of processes involving propane or butane. The similarities in the calculated burning velocity, adiabatic flame temperature and maximum mole fractions of the key radicals shown in Table 2 are, therefore, not surprising.

Table 1. Relative sensitivity coefficients of burning velocity to rate constants of different reactions

Reaction	Methane	Ethane	Propane	Butane	Iso-butane
$H + O_2 \rightarrow OH + O$	1 (0.294)**	1(0.217)**	1(0.241)**	1 (0.243)**	1 (0.376)**
$H + O_2 + M \rightarrow HO_2 + M$	-0.255	-0.186	-0.198	-0.188	-0.194
$H + CH_4 \rightarrow CH_3 + H_2$	-0.138				
$CH_3 + H + M \rightarrow CH_4 + M$	-0.101				
$HCO + M \rightarrow H + CO + M$	0.344	0.188	0.216	0.202	0.193
$HCO + H \rightarrow CO + H_2$	-0.102	-0.088	-0.094	-0.089	-0.073
$CO + OH \rightarrow CO_2 + H$	0.321	0.367	0.386	0.4	0.42
$C_2H_5 + H \rightarrow CH_3 + CH_3$	-0.063	-0.273	-0.098	-0.114	-0.057
$H + C_2H_4 + M \rightarrow C_2H_5 + M$	0.078	0.273	0.085	0.1	0.067
$aC_3H_5 + H \rightarrow C_3H_6$		-0.025	-0.066	-0.074	0.11

** Absolute value of sensitivity coefficient for $H+O_2=OH+O$ shown in brackets.

Table 2. Properties of C_1-C_4 hydrocarbon flames

Fuel	Burning velocity,cm/s	T_{ad}, K	H_{max},mole fract.	OH_{max},mole fract.	O_{max},mole fract.
Methane	41.4	2238	7.1×10^{-3}	7.8×10^{-3}	3.4×10^{-3}
Ethane	45.8	2276	8.7×10^{-3}	8.2×10^{-3}	4.4×10^{-3}
Propane	44.1	2289	9×10^{-3}	8.1×10^{-3}	4.5×10^{-3}
Butane	43.2	2289	8.9×10^{-3}	8×10^{-3}	4.5×10^{-3}
Iso-butane	39.8	2289	8.4×10^{-3}	7.9×10^{-3}	4.3×10^{-3}
Heptane	43.1	2298	8.8×10^{-3}	$8.x10^{-3}$	4.6×10^{-3}

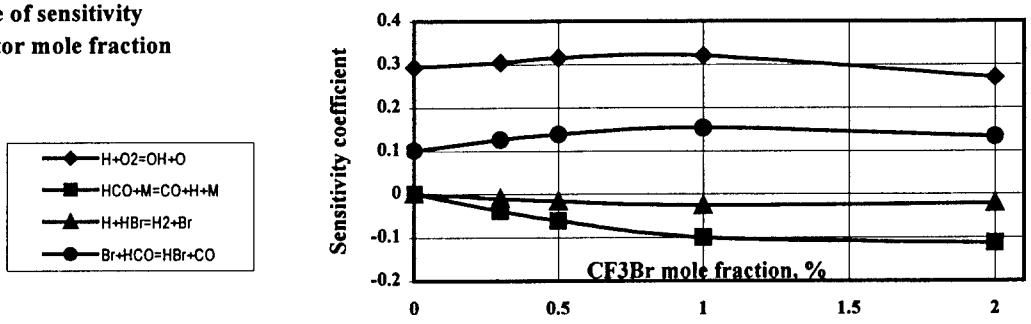
Sensitivity Analysis for Systems Containing CF_3Br: We next consider the situation where CF_3Br is added to a reaction mixture. The uncertain issue is the contributions of the suppressant to reactions involving the parent fuel. If this were important it would lend a degree of specificity to tests with different fuels. The modeling of methane, ethane and propane flames with added CF_3Br demonstrates that the pattern of sensitivity coefficients is

very similar to that for the situation without suppressant. This indicates that the overall mechanism has not changed. Particularly interesting is the nature of the contributions from the species that are traceable to the CF_3Br. The key observation is that the most sensitive reactions of CF_3Br or its breakdown products are with the breakdown products of the fuel. The reactions with the fuel itself or the larger fragments do not apparently make any contributions. Thus the specificity introduced by the different fuel types is also lost from the point of view of inhibition. The following are the reactions, involving brominated species, with the largest sensitivity coefficients:

$$Br + HCO \rightarrow HBr + CO$$
$$H + HBr \rightarrow H_2 + Br$$
$$H + CF_3Br \rightarrow HBr + CF_3$$
$$Br + Br + M \rightarrow Br_2 + M$$

Simulations with different concentrations of the suppressant demonstrate that the pattern for reactions of alkane oxidation remains practically the same with approximately the same sensitivity coefficients for the main reactions. This can be seen in Figure 1. As expected increasing additive molefraction is directly manifested in the increasing sensitivity to the set of inhibitor reactions given above. Thus the sensitivity coefficient with respect to the flame velocity for the reaction $Br + HCO \rightarrow HBr + CO$ increases from 12.5 % at 0.3 % mole fraction of additive to 42 % at 2 % mole fraction, while that of the combination process $Br + Br + M \rightarrow Br_2 + M$ increase from 0.14 % at the lowest CF_3Br level and 17 % at the highest for a stoichiometric methane/air flame. It is important to note that an increase in CF_3Br mole fraction from 0.3 % to 2.0 % leads to a factor of three decrease in flame velocity approximately. However the set of reactions responsible for the flame velocity has not been altered, only their relative contributions to the overall phenomena. The sensitivity coefficients of the fluorinated compounds (CHFO species) are all small. This is in line with the general consensus that fluorinated compounds by themselves are not effective suppressants. An increase in CF_3Br leads to an increase in sensitivity coefficients of reactions with fluorinated species. However, they still remain small in comparison with relative contributions from reactions with bromine-containing inhibitor species. Thus the contributions from reaction with fuel molecules considered here are relatively unimportant for inhibition effects.

Fig. 1. Dependence of sensitivity coefficients on inhibitor mole fraction



Extinction Behavior: Chemical influences on flame propagation are most pronounced at low concentrations. However as the concentration of suppressant is increased, a saturation effect occurs [2,5]. This decrease in chemical effects means that near extinction, contributions from heat capacity and dilution become much more important [2]. The cause of this decrease can be attributed to two sources: the concentrations of the active radicals are driven down to their equilibrium concentrations, and in the case of metals there is the condensation of the active species. The limits for the latter are set by the saturated vapor pressure of the compounds or related compounds responsible for suppression. Thus it is not possible to linearly extrapolate the results from experiments which have been conducted in low concentration range of suppressant loading to determine extinction conditions for highly effective chemical suppressants.

It is interesting to estimate the minimum quantity of highly effective agent required for flame suppression. The gas phase model of iron pentacarbonyl inhibition is used to estimate the maximum possible effect. Calculations were conducted for a stoichiometric premixed methane/air flame, and showed that 0.15 % 0.3 % mole fraction of $Fe(CO)_5$ is required for suppression of a methane flame. For comparison the calculated extinction mole fraction of CF_3Br is 3.5 %. An important consequence is that the differences in suppression effectiveness

are much less at higher concentration than at the lower levels where chemistry is most manifest. This sets a strict limitation on the range of possible improvement of agent suppression effectiveness in the case of high efficiency compounds such as those containing Fe, Pb, Cr, K, Na, and may in fact be no more than an order of magnitude larger in comparison to CF_3Br. It is however interesting that this compression in agent effectiveness when the entire range is considered does not appear to change the ranking of the various agents.

Other Fuels: All of the fuels examined above are alkanes. While Trees et al. [1] found similar rankings for alkanes, jet fuels and hydraulic fluids, there is no reason why rankings for substantially different types of fuels should be the same. For example, recent studies of N_2O + CO combustion in the presence of $Fe(CO)_5$ show a promotion effect instead of inhibition [6]. It may well be worthwhile to draw a distinction between fuel types. Here the observation of Warnatz [7] is extremely important. In flames the hydrocarbon is attacked by the O, H, and OH radicals. The larger alkyl radicals formed in this manner then decompose to smaller alkyl radicals by fast elimination of alkenes. The rapidity of the decomposition of the larger alkyl radicals is such that the structure of higher hydrocarbon flames is centered around the oxidation of the methyl and ethyl radicals. These oxidation steps are the rate controlling processes in the combustion of alkanes and alkenes, which is the reason for the similarity of all alkane and alkene flames [7]. Such similarities are reflected in the narrow range of burning velocities, normalized composition profiles of reactants and main products for the combustion of alkane fuels [8].

A possible remaining issue is the role of fuels containing aromatic groups. This is most uncertain for benzene, since new species are introduced. However for alkylated aromatic compounds one would expect results to follow the general trends with increasing length of the alkyl substitutent. The present analysis gives the rationale for projecting data on relative suppressant effectiveness in one fuel to another and can be useful in rationalizing the large volumes of data that are available.

Summary

We have applied sensitivity analysis to the mechanism of suppressant action on the combustion of C_1 to C_4 hydrocarbons to demonstrates that the main reactions determining burning velocity are the same for alkane flames. These results demonstrate that similar inhibitor rankings for combustion of different fuels are largely due to the reactions of a number of small radicals that are common to all of these systems. These radical concentrations are reduced through the addition of suppressants. The active agents in the case of these suppressants are likely to be formed or recycled by the breakdown products common to all hydrocarbon fuels. The use of effectiveness rankings from one alkane to another is justified, and may be extendable to hydrocarbon fuels in general.

Acknowledgements

We would like to thank N. Marinov for his kinetic model and helpful discussions, D.R. Burgess, Jr., for help with the sensitivity analysis and useful discussions. Financial support through the NGP program sponsored by SERDP, the U.S. Army, and the U.S. Navy is gratefully acknowledged.

References

1. Trees, D., Seshadri, K., and Hamins, A., Halon Replacements: Technology and Science, ACS Symposium Series 611, American Chemical Society, Washington, DC, pp. 190-203, 1995.
2. Noto, T., Babushok V. I., Hamins, A., and Tsang, W., *Combustion and Flame 112,* 147-160 (1998).
3. Marinov, N.M., Castaldi, M.J., Melius, C.F., and Tsang, W., *Combust. Sci. Technol 128*,.295-342 (1997).
4. Tsang, W., *J. Phys. Chem. Ref. Data, 19*, 1-68 (1990).
5. Rumminger, M.D., Reinelt, D., Babushok, V., and Linteris, G.T., *Combustion and Flame, 116*:207-219 (1999).
6. Rumminger, M.D. , and Linteris, G.T., "Role of Particles in Flame Inhibition by Iron Pentacarbonyl," Halon Options Technical Working Conference, Albuquerque, April , 1999.
7. Warnatz, J. *Eighteenth Symposium (Int.) on Combustion*, The Combustion Institute, Pittsburgh, pp. 369-384, 1981.
8. Fristrom, R.M., *Flame Structure and Processes*, Oxford University Press, 1995.

AN INVESTIGATION OF EXTINGUISHMENT BY THERMAL AGENTS USING DETAILED CHEMICAL KINETIC MODELING OF OPPOSED FLOW DIFFUSION FLAMES

William M. Pitts (wpitts@nist.gov) and Linda G. Blevins (lblevins@nist.gov)
National Institute of Standards and Technology, Gaithersburg, MD 20899-8653

1. INTRODUCTION

The manufacture of halons, which are widely used in fire extinguishing systems, was banned in 1984. The search for effective alternatives continues with a large effort known as the Next Generation Fire Suppression Technology Program (NGP). As part of the NGP, NIST is investigating whether highly effective thermal agents, which obtain their effectiveness solely by heat extraction and dilution, are feasible. The paper by Sheinson et al. provides a good introduction [1]. Simple heating (i.e., heat capacity), phase changes, endothermic molecular decomposition (which is classified as a physical process as long as the initial agent and its products do not participate in the combustion chemistry), and simple dilution can modify flame temperatures and therefore contribute to flame extinction

This paper summarizes the results of a detailed chemical kinetic modeling investigation of laminar opposed-flow methane/air diffusion flames designed to provide an improved understanding of the extinguishment of fires by thermal agents. A particular focus was to test the hypothesis that the effectiveness of a thermal agent depends on the location of heat absorption relative to the flame zone. An internal report has been prepared summarizing the kinetic modeling and also includes the results of an extensive data base search of potential thermal agents and modeling results for the effectiveness of thermal agents in cooling solid surfaces [2].

2. DETAILED CHEMICAL KINETIC MODELING

An opposed flow laminar diffusion flame model was selected because for the majority of fires the fuel and air are initially separated and therefore burn as diffusion flames. Two excellent reviews have been provided by Tsuji [3] and Dixon-Lewis [4]. These flames are usually modeled as pseudo one-dimensional flow systems using a similarity transform to reduce the two-dimensional equations. Fuel and oxidizer velocity profiles at the burner exits are assumed to be plug flows having exit strain rates equal to 0 s^{-1}. Absolute strain rates increase as the flow moves toward the stagnation plane. With increasing exit flow velocities the flame is subjected to higher strain rates, and it gradually becomes weaker until it abruptly undergoes extinction. A number of parameters are used to quantify the effect of strain rate on a laminar flame including a global strain rate, a_g, the maximum strain rate outside of the thermal boundary layer on the oxidizer side, a_o, and the stoichiometric scalar dissipation, χ_s.

For this investigation, a series of laminar opposed flow diffusion flames of methane and oxidizer have been calculated as a function of exit flow velocities (assumed to have equal magnitudes) and the concentration of various thermal agents added to the air. For each concentration of added agent, an extinction condition is identified which corresponds to a given velocity magnitude and corresponding measures of strain rate and χ_s. A focus of this work is the identification of the minimum concentration of an agent required to extinguish buoyancy dominated fires. The extinguishing concentration is therefore expected to correspond to a particular extinction condition.

3. CALCULATIONAL APPROACH

The code Oppdif [5] developed by Sandia National Laboratories, now available from Reaction Design* of San Diego, CA, was used. Oppdif solves the psuedo-one-dimensional equations for plug flows. The detailed chemical mechanism used was GRI-Mech 1.2 [6] which consists of 32 chemical species undergoing 177 reactions.

Figure 1 includes a plot of maximum temperature, T_{max}, versus exit flow velocities calculated for a methane/air diffusion flame (0% added N_2). The fuel is 100% methane and air is assumed to be composed of 0.781 N_2, 0.210 O_2, and 0.009 Ar mole fractions. As expected, T_{max} decreases with increasing velocity. Extinction is calculated to occur for a velocity of 320 cm/s with a maximum flame temperature of 1785 K. The value of $|a_o|$ at extinction is 509 s^{-1} which is roughly 25% higher than measured experimentally [7,8,9]. Tanoff et al. have shown

*Certain commercial equipment, instruments, or material are identified in this paper in order to adequately specify the experimental procedure. Such identification does not imply recommendation or endorsement by the National Institute of Standards and Technology, nor does it imply that the materials or equipment are necessarily the best available for the purpose.

that calculated values of a_o are highly dependent on the detailed mechanism [10] and also found that GRI-Mech over predicts the extinction strain rate.

4. METHANE FLAMES BURNING IN AIR DILUTED WITH THERMAL AGENTS

Only two experimental measurements of extinguishing concentration for methane flames burning in air diluted with a thermal agent were identified. Simmons and Wolfhard [11] and Ishizuka and Tsuji [12] reported values of 33.8% and 31.9%, respectively, for nitrogen added to air. Calculations were performed for methane reacting with air containing various percentages of added nitrogen. Figure 1 includes the results. As the percentage of added nitrogen increases, the fuel and oxidizer exit velocity magnitudes sufficient to cause flame extinction decrease. The T_{max} at extinction also decreases with increasing nitrogen concentration. Plots of T_{max} versus velocity magnitude become steeper as the nitrogen concentration increases. The value of T_{max} for the experimental extinguishing concentration is 1545 K. This is close to the experimental value of 1483 K [12]. The velocities of the fuel and air at extinguishment are calculated to be 21.42 cm/s, corresponding to an absolute value of global strain rate of $a_g = 37.5\ s^{-1}$.

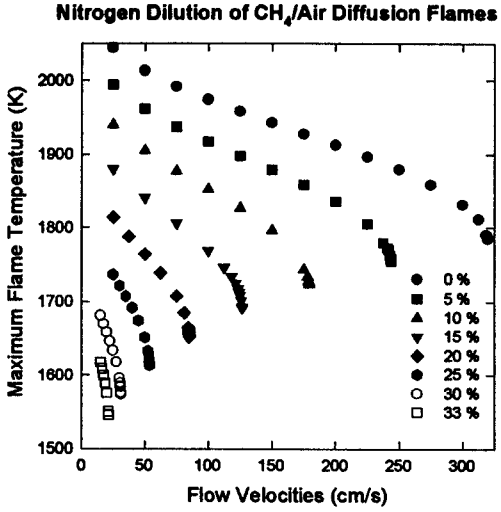


Figure 1. Maximum flame temperature versus flow velocity magnitudes for methane burning in nitrogen-diluted air.

An important question is what strain rate is appropriate to use when determining the minimum value of an added thermal agent required to extinguish diffusion flames at normal gravity? The only discussion of this point of which we are aware was presented by Hamins et al. [13] These authors compared cup burner measurements (heptane fuel) of extinguishing concentrations for a variety of agents with corresponding measurements made in a counterflow flame. When the concentrations of added agents for the opposed flame were comparable to those observed to cause extinguishment in the cup burner test, the global strain rate was on the order of 50 s^{-1}. Due to the use of different boundary conditions and fuels between the current investigation and those for Hamins et al., as well as slightly different definitions for the global strain rates, absolute quantitative comparisons are not appropriate. However, it is clear that the strain rates have comparable magnitudes in each case.

It is interesting to speculate about why lower and lower strain rates can not be sustained for flames at normal gravity. The most likely reason is that buoyancy effects result in a lower limit for the minimum strain rate perpendicular to a flame surface. Buoyancy always accelerates hot combustion gases relative to the cold oxidizer with the result that the flame surface is subject to a nonzero strain rate. The results of Hamins et al. [13] and the current findings suggest this minimum strain rate is on the order of a few tens of inverse seconds.

As already pointed out, we have identified no additional measurements of extinguishing concentrations for thermal agents added to methane/air diffusion flames. However, Ishizuka and Tsuji did make measurements for methane burning in an artificial "air" consisting of 21% oxygen and 79% argon diluted with argon [12]. The extinguishing argon concentration was 54.3%. Extinction for a calculated flame burning in Ar "air" with the extinguishing concentration of added Ar occurred for a T_{max} of 1473 K and exit velocities of 15.9 cm/s. These values are both slightly lower than found for the methane/air flame diluted with nitrogen. However, they are remarkably close when one recalls that the use of argon instead of nitrogen results in a significantly different flame structure. In fact, if one simply assumes that extinguishment occurs for the same maximum flame temperature, i.e., roughly 1550 K, as for the nitrogen-diluted air flame, it is possible to estimate the required argon concentration as 52%. This is only 4% less than the experimental value. Thus, assuming that flame extinguishment occurs for the concentration necessary to reduce the maximum calculated flame temperature at extinction to 1550 K should provide an excellent estimate for the percentage of an arbitrary thermal agent required to extinguish a fire.

Opposed flow diffusion flame calculations have been used to estimate the extinguishing concentrations, i.e., the concentration necessary to lower the maximum flame temperature at extinction to 1550 K, for methane burning in air diluted with Ar, He, CO_2, and H_2O. Each of these gases is expected to act primarily as a thermal agent. The

Table 1. Extinguishing Concentrations (Mole Fraction) of Thermal Agents

Thermal Agent	Current Work	Cup Burner [1]	Cup Burner [14]	Cup Burner [15]	Cup Burner [16]
Nitrogen	0.33	0.30	0.33	0.32	0.30
Argon	0.43	0.41	-	0.41	0.38
Helium	0.34	0.32	-	0.31	-
Carbon Dioxide	0.22	0.21	0.20	0.23	0.20
Water	0.28	-		-	-

results are tabulated in Table 1. As already discussed, the only experimental values for opposed flow methane diffusion flames we have identified are for nitrogen. Cup burner values of extinguishing concentrations using heptane fuel have been reported for some of these agents by Sheinson et al. [1], Babb et al. [14], Hamins et al. [15] and Moore et al. [16] and are included in Table 1. The maximum difference between values calculated for methane and the experimental values for heptane is 12%, with the vast majority being less than 10%. With the exception of carbon dioxide, the cup burner measurements are somewhat lower than for the counterflow flame. These differences could be due to the use of different fuels or to the effects of burner configuration. The close tracking of the calculated results and the experimental findings suggests that detailed chemical kinetic modeling can accurately predict the amount of a thermal agent required to extinguish opposed flow diffusion and cup burner flames.

The differences in the extinguishing concentrations of helium and argon are interesting since these agents are both monatomic gases and have the same heat capacities. The fact that helium is a more efficient extinguishing agent means that at least one other parameter, in addition to heat capacity, is important in determining extinguishing efficiency. A related observation was reported by Coward and Hartwell for the inerting of premixed flames and was attributed to the much higher thermal conductivity of helium which distributes the heat of combustion over a larger region of space and therefore weakens the flame [17]. The same explanation is most likely valid for diffusion flames. Sheinson et al. reached the same conclusion [1].

5. SURROGATE AGENT STUDIES OF EXTINCTION AND EXTINGUISHMENT

A goal of the current work was to test the hypothesis that the effectiveness of a thermal agent depends on the location, relative to the high temperature flame zone, where heat extraction occurs. A surrogate thermal agent, X, was used as a test. The molecular weight, thermodynamic properties, and transport properties of X are identical to those of argon, but it can undergo a simple reaction with ambient gases to generate a new species, Y, i.e.,

$$X + M \rightarrow Y + M \quad . \qquad (1)$$

Y is also very similar to argon, the only difference being that its heat of formation is assigned an arbitrary positive value instead of being zero. When Reaction (1) takes place it extracts heat and cools the local surroundings by an amount equal to the heat of reaction, $\Delta H_{X\text{-}Y}$. Since X and Y do not react with any other species, the reaction is simply a heat sink and therefore meets the definition of a thermal agent. The rate constant for Reaction (1) is expressed as

$$k_{X \rightarrow Y} = A T^{\beta} e^{-E_a/RT} \quad , \qquad (2)$$

where A is the pre-exponential factor, β is the temperature exponent, E_a is the energy of activation, R is the gas constant, and T is temperature. For the calculations which follow, initial values were chosen for A and β, and only the value of E_a was changed in order to vary $k_{X \rightarrow Y}$.

Figure 2 compares calculated flame temperature versus distance from the fuel exit for two flames having fuel and oxidizer exit velocity magnitudes of 25 cm/s and with 5% X added to the air. For each $A = 1 \times 10^{10}$ $cm^3/(mole\ s)$, $\beta = 0$, and $\Delta H_{X\text{-}Y} = 96.1$ kJ/mole. The only difference between the two calculations is the value of E_a which equals 25.1 kJ/mole for one and 50.2 kJ/mole for the other. For the lower E_a, X begins to react immediately upon leaving the oxidizer exit which results in the temperature drop evident on the oxidizer side for positions well removed from the flame zone. When the E_a is increased to 50.2 kJ/mole the conversion of X to Y is very slow at room temperature, and there is no significant drop in temperature in the ambient region of the flow. However, as the temperature increases X begins to convert to Y, and heat is absorbed in higher temperature flame regions. Interestingly, maximum flame temperatures are identical within the uncertainty of the calculations. Since flame

extinguishment depends primarily on the maximum flame temperature at extinction, this suggests the effectiveness of a thermal agent is independent of the spatial location where the heat extraction occurs, indicating that the original hypothesis concerning the effect of heat extraction position was incorrect.

6. SUMMARY

It has been shown that detailed chemical kinetic modeling can be used to make quantitative predictions of the amount of a thermal agent required to extinguish a fire. Results for four well known thermal agents are in good agreement with experimental values. The calculations suggest that strain rates in fires are on the order of a few tens of inverse seconds and that the maximum flame temperature at extinction for the extinguishing condition is approximately 1550 K. The location of the heat absorption relative to the flame front does not affect the ability of a thermal agent to extinguish a flame as long as the agent is convected to the flame zone.

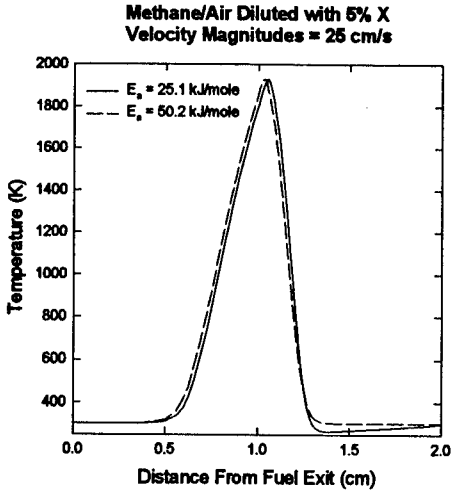


Figure 2. Temperature versus distance from fuel exit for methane/air diluted with 5% X flame.

7. ACKNOWLEDGMENT

This research is part of the Department of Defense's Next Generation Program Fire Suppression Technology Program, funded in part by the DOD Strategic Environmental Research and Development Program under Contract W74RDV73243630

8. REFERENCES

1. R. S. Sheinson, J. E. Penner-Hahn, and D. Indritz, *Fire Safety J.* **15**, 437, 1989.
2. W. M. Pitts, J. Yang, M. Huber, and L. G. Blevins, *Characteristics and Identification of Super-Effective Thermal Fire-Extinguishing Agents—First Annual Report*, NIST Internal Report, Gaithersburg, MD, 1999, to appear.
3. H. Tsuji, *Prog. Energy Comb. Sci.* **8**, 93, 1982.
4. G. Dixon-Lewis, *23rd Symp. (Intl.) Comb.*, The Combustion Institute, Pittsburgh , PA, 305, 1990.
5. A. E. Lutz, R. J. Kee, J. F. Grcar, and F. M. Rupley, *OPPDIF: A Fortran Program for Computing Opposed-Flow Diffusion Flames*, SAND96-8243, Sandia National Laboratories, Livermore, CA, 1996.
6. *GRI-MECH 1.2*, M. Frenklach, H. Wang, C.-L. Yu, M. Goldenberg, C. T. Bowman, R. K. Hanson, D. F. Davidson, E. J. Chang, G. P. Smith, D. M. Golden, W. C. Gardiner, and V. Lissianski, http://www.me.berkeley.edu/gri_mech/
7. H. K. Chelliah, C. K. Law, T. Ueda, M. D. Smooke, and F. A. Williams, *23rd Symp. (Intl.) Comb.*, The Combustion Institute, Pittsburgh, PA, 503, 1990.
8. P. Papas, J. W. Fleming, and R. S. Sheinson, *26th Symp. (Intl.) Comb.*, The Combustion Institute, Pittsburgh, PA, 1405, 1996.
9. J. Du and R. L. Axelbaum, *26th Symp. (Intl.) Comb.*, The Combustion Institute, Pittsburgh, PA, 1137, 1996.
10. M. A. Tanoff, R. R. Dobbins, M. D. Smooke, D. R. Burgess, Jr., M. R. Zachariah, and W. Tsang, *Halon Options Technical Working Conference*, Albuquerque, NM , 116, May 6-8, 1997.
11. R. F. Simmons and H. G. Wolfhard, *Comb. Flame* **1**, 155, 1957.
12. S. Ishizuka and H. Tsuji, *18th Symp. (Intl.) Comb.*, The Combustion Institute, Pittsburgh, PA, 695, 1981.
13. A. Hamins, D., Trees, K. Seshadri, and H. K. Chelliah, *Comb. Flame* **99**, 221, 1994.
14. M. Babb, S. R. Gollahalli, and C. M. Sliepcevich, *J. Propul. Power* **15**, 260, 1999.
15. A. Hamins, G. Gmurczyk, W. Grosshandler, R. G. Rehwoldt, I. Vazquez, T. Cleary, C. Presser, and K. Seshadri, "4. Flame Suppression Effectiveness," in *Evaluation of Alternative In-Flight Fire Suppressants for Full-Scale Testing in Simulated Aircraft Engine Nacelles and Dry Bays* (W. L. Grosshandler, R. G. Gann, and W. M. Pitts, Eds.), NIST SP 861, Gaithersburg, MD, April, 1994.
16. T. A. Moore, C. A. Weitz, and R. E. Tapscott, *Halon Options Technical Working Conference*, Albuquerque, NM, 551, May 7-9, 1996.
17. H. F. Coward and F. J. Hartwell, *J. Chem. Soc.*, 1522, 1926.

EFFECT OF DILUTION ON EXTINCTION LIMITS OF SURFACE INTERACTING DIFFUSION FLAMES WITH DETAILED CHEMISTRY AND TRANSPORT*

M. Gummalla[1], D. G. Vlachos[1**], and M. A. Delichatsios[2]
[1]Department of Chemical Engineering, University of Massachusetts, Amherst, MA 01003
[2]Renewable Resources Associates, Lexington, MA 02173

ABSTRACT

Numerical simulations are carried out to study the effect of dilution on $H_2/O_2/N_2$ flame extinction using numerical bifurcation theory. It is found that dilution affects slightly the ignition and extinction temperatures, defined as saddle node bifurcations, over a wide range of oxidant dilutions. The locus of the extinction limits of self sustained flames at low dilution levels is insensitive to the fuel flow rate, in qualitative agreement with the experiments of [1], and leakage of O_2 occurs implying that simplified reaction mechanisms may be adequate for describing fire suppression under such conditions.

INTRODUCTION

The ban of fluorochlorohydrocarbons as fire suppressants owing to stringent environmental regulations has created a critical need for developing and evaluating systematic and effective replacements. Due to inherent complexity of flow and chemistry, fire suppression of condensed fuels is not a well understood phenomenon. A promising means of determining and analyzing fire suppression is via numerical bifurcation theory which can provide not only the critical conditions for flame extinction but also fundamental understanding of the underlying physics. Understanding extinction of laminar gaseous diffusion flames interacting with surfaces is a first step in developing a more complete picture about fire suppression.

The necessity for detailed chemistry to predict the extinction limits under certain flow conditions has recently been shown [2]. It has been found that at low strain rates the isola of adiabatic points opens up through an infinite bifurcation and only the thermal quenching limit at low fuel flow rates exists, whereas at high strain rates, two extinction modes exist, namely the thermal quenching and the blowoff or stretch limit, originally introduced by Tsuji [3].

In the present study we analyze the effect of dilution on flame extinction of hydrogen-oxidant mixtures. Inert gases, such as nitrogen, argon, and helium are used as diluents introduced from both the fuel side and the oxidizer side (presented here). The limiting fuel concentration and the limiting oxygen concentration required to maintain a diffusion flame are determined and the effect of dilution on the conductive heat flux curves is studied to evaluate the extinction criteria for condensed fuels [4].

MODEL

The stagnation point flow configuration is considered here. The fuel is ejected from the surface of a burner, and the oxidizer (oxygen + inert gas) flows countercurrently. A rigorous similarity transformation converts the two dimensional conservation equations into a one dimensional problem, making computations tractable. We consider compressible flow and constant pressure throughout the domain. The gas-phase governing differential equations are [5].

$$\frac{\partial}{\partial\tau}\left(\frac{\partial f}{\partial\eta}\right)=\frac{\partial}{\partial\eta}\left[\frac{\rho\mu}{\rho_e\mu_e}\frac{\partial^2 f}{\partial\eta^2}\right]+f\frac{\partial^2 f}{\partial\eta^2}+\frac{1}{2^k}\left(\frac{\rho_e}{\rho}-\left(\frac{\partial f}{\partial\eta}\right)^2\right) \tag{1}$$

$$\frac{\partial\Theta}{\partial\tau}=\frac{1}{c_p}\frac{\partial}{\partial\eta}\left[\frac{\rho\lambda}{\rho_e\mu_e}\frac{\partial\Theta}{\partial\eta}\right]+f\frac{\partial\Theta}{\partial\eta}-\frac{\partial\Theta}{\partial\eta}\sum_{j=1}^{N_s+1}\frac{c_{p_j}}{c_p}\frac{\rho X_j V_j}{\sqrt{2^k\rho_e\mu_e a}}-\frac{1}{2^k a\rho c_p T_r}\left(\sum_{i=1}^{N_r}(-\Delta H_i)r_i\right) \tag{2}$$

$$\frac{\partial X_j}{\partial\tau}=\frac{\partial}{\partial\eta}\left[\frac{\rho X_i V_i}{\sqrt{2^k\rho_e\mu_e a}}\right]+\frac{W_j}{2^k a\rho}\sum_{i=1}^{N_r}\nu_{ij}r_i,(j=1,\ldots,N_s) \tag{3}$$

$$\sum_{j=1}^{N_s+1}X_j=1\,. \tag{4}$$

The ideal-gas law is employed as an equation of state. To conserve overall mass, the mass fraction of the inert gas-phase species (e.g., N_2) is determined from Eq. 4. Here ρ, μ, c_p, and λ are the density, viscosity,

* Acknowledgment is made to National Science Foundation under contract number CTS-9710413
** Corresponding author

specific heat, and thermal conductivity of the mixture. $\Theta=T/T_r$ is the non dimensional temperature, where T is the temperature and T_r is a reference temperature. W_j, X_j, and V_j are the molecular weight, mass fraction, and velocity of species j. ΔH_i and r_i are the heat and molar rate of the ith gas-phase reaction. N_S and N_r are the number of species and gas-phase reactions, respectively, and ν_{ij} is the stoichiometric coefficient of the jth species in the ith reaction. Axisymmetric flow is considered here with k=1. $\tau=2at$ is the dimensionless time and a is the strain rate. At steady-state the left hand side of the Eqs. 1-3 is equal to zero.

The boundary conditions for simulating a diffusion flame are listed below:

At $\eta \to \infty$:
$$\frac{\partial f}{\partial \eta} = 1, \tag{5}$$
$$\Theta = \Theta_e, \tag{6}$$
$$X_j(\infty) = X_{j_e}, \quad j = 1,\ldots,N_S+1. \tag{7}$$

At $\eta = 0$:
$$f(0) = f_w, \tag{8}$$
$$\frac{\partial f}{\partial \eta} = 0, \tag{9}$$
$$\Theta(0) = \Theta_w \quad \text{(isothermal case)}, \tag{10}$$
$$\frac{\partial \Theta}{\partial \eta} + \frac{\rho_e}{\rho \lambda T_r}\sqrt{\frac{\mu_e}{2^k \rho_e a}}\left[\hat{P}_w - \varepsilon\sigma T_r{}^4(\Theta_w^4 - \Theta_e^4) - f_w\sqrt{2^k \rho_e \mu_e a}\sum_{j=1}^{N_s+1} X_j^o(h_j - h_j^o)\right] = 0, \tag{11}$$
$$\rho X_j V_j = f_w\sqrt{2^k a \rho_e \mu_e}(X_j - X_j^o), \qquad j = 1,\ldots..N_s. \tag{12}$$

The boundary conditions at the surface ($\eta = 0$) need explanation. Eq. 8 is obtained by equating the normal velocity at the surface to the fuel ejection velocity, whereas Eq. 9 is the no slip condition at the surface. For the energy boundary condition, either the temperature at the surface can be fixed (Eq. 10) or the temperature is allowed to vary obeying the adiabatic condition (i.e., the conductive flux at the surface is equal to the sum of enthalpic flux to preheat the fuel from ambient conditions, the heat input or release ($\hat{P}_w$) to the surface, and the surface heat losses (e.g., by surface radiation), as in Eq. 11. The mass fractions of the species at the surface are obtained by equating the convective flux of a species at the left of the surface (typically fuel and diluent are only ejected) to the convective and diffusive flux of the gaseous species at the right of the surface (Eq. 12). In all the above equations, the stream function, f, is defined as

$$-f = \frac{\rho u}{\sqrt{2^k \rho_e \mu_e a}}, \tag{13}$$

the species velocity is given by $V_j = V_j^D + V_j^T$, (14)

where the ordinary diffusion velocity is $V_j^D = -\frac{D_j W_j}{X_j \overline{W}}\frac{\partial Y_j}{\partial \eta}$, (15)

and the thermal diffusion velocity is $V_j^T = -\frac{D_j W_j k_T}{X_j \overline{W}\, T}\frac{\partial T}{\partial \eta}$. (16)

Here σ and ε are the Boltzmann factor and the emissivity of the surface. u is the axial velocity and Y is the mole fraction. Subscripts w and e correspond to the wall and oxidizer entrance conditions. Superscript o corresponds to the conditions at η=0, and k is the geometry factor. $\overline{W}$ is the average molecular weight.

The equations are discretized using a finite difference scheme [6]. Steady-state equations are solved using a dynamically adaptive multiple weights arc-length continuation algorithm and Newton's method [7]. The continuation algorithms used allow to pass around the turning points, and to predict accurately the critical points (like isothermal ignition and extinction limits). Detailed transport, including Dufour effect and thermal diffusion, used result in varying transport parameters along the domain of the distributed system making these bifurcations simulations computationally intensive.

The primary continuation parameters considered in the present study are the surface temperature, the fuel ejection velocity ($-f_w$), and the mole fraction of oxygen in the oxidant (β). The detailed mechanism used is the Miller-Bowman reaction scheme with 20 reactions involving 9 species [8]. For all simulations, the

pressure is 1 atm, the ambient temperature is taken to be 25 ^{o}C, and the strain rate is 50 s^{-1}. Surface radiation is not considered in the present study (i.e., ε =0).

RESULTS

Fig. 1a shows the mole fraction of H_2 at the surface as the surface temperature increases for β=0.2. When the surface temperature is near 900 K, there is hysteresis with two turning points one at higher temperature termed the ignition (Ig.) which is associated with a sudden drop in the mole fraction of the reactant (H_2), and the other at lower temperature termed the extinction (Ex.). Both turning points follow Semenov definitions. The locus of the surface temperatures at ignition and extinction as a function of the mole fraction of oxygen in the oxidant is shown in Fig. 1b. Over the range of β considered, the surface temperatures at ignition and extinction show a weak dependence on dilution, caused probably by kinetics since the reactivity near the turning points is low as shown in Fig. 1a.

The locus of adiabatic points vs. fuel flow rate (satisfying Eq. 11, not shown) exhibits a left turning point called an extinction limit, below which (keeping the same strain rate and dilution level) the flame cannot sustain itself. The locus of such extinction limits of self-sustained flames is shown in Fig. 2 by plotting the fuel flow rate at the surface (solid line), mole fraction of oxygen at the surface (dashed line), and the mole fraction of water (dotted line) in the reaction zone (at the position of maximum flame temperature) vs. the mole fraction of oxygen in the oxidant. All these curves indicate two distinct modes at low and high β, with the nature of extinction along these branches being different. For low dilution there is leakage of oxygen to the surface, as shown in Fig. 3a (hence complete combustion will take place in the case of hydrocarbons [2]), with maximum mole fraction of water and temperature at or near the surface (as seen in Fig. 3b). This result has important ramifications for modeling fire suppression as details of the hydrocarbon species desorbing from a condensed fuel surface are typically not known. Thermal quenching causes flame extinction along this branch. However, at high dilution, the maximum temperature is off the wall and most of the oxygen is reacted prior to its reaching the surface, as seen in Fig. 3, unlike the case of high β. Flame extinction at low β is due to chemical limitations in the reaction zone. There exists a critical oxygen content (β_c) below which no flame can exist, and this is determined by the asymptote of the almost vertical branch (schematically shown by the dotted line) in Fig. 2.

Fig. 4 shows the wall heat flux (conductive flux) Q vs. the fuel flow rate, for three different β values at a fixed surface temperature. The surface temperature is maintained at 550 K except for the one indicated. It is seen that the maximum heat released decreases as the dilution level increases, for the same surface temperature, and the turning point corresponding to the gaseous flame extinction (indicated by solid circles) approaches the maximum heat flux condition often associated with extinction of condensed fuels. As the fuel flow rate decreases, there is leakage of oxygen from the point of maximum heat flux to the gaseous flame extinction point (not shown), and the flame temperature decreases thus causing extinction. Also shown in the same figure is the flux curve for β=0.11 at a surface temperature of 350 K. Gaseous extinction occurs at a higher fuel flow rate for flames maintained at lower surface temperature (e.g., 350 K), and the flame thickness is higher compared to the flames maintained at higher temperatures (e.g., 550 K).

CONCLUSIONS

Numerical bifurcation theory has been used with detailed chemistry and transport to predict the effect of dilution on the extinction limits for $H_2/O_2/N_2$ system (and the other diluents not discussed here) using the Miller-Bowman reaction mechanism. Two parameter bifurcation diagrams of the extinction limits vs. the mole fraction of oxygen in the oxidant have been presented showing the critical oxygen concentration below which no stabilized flames exist. It is found that at low dilution levels, oxygen leaks through the reaction zone and the extinction limits are insensitive to the fuel flow rate.

REFERENCES

1. S. Ishizuka and H. Tsuji, *in* "Eighteenth Symposium (International) on Combustion, The Combustion Institute, Pittsburgh", p. 695, 1981.
2. M. Gummalla, D. G. Vlachos, and M. A. Delichatsios, *Combust. Flame* **submitted** (1999).
3. H. Tsuji and I. Yamaoka, *in* "Eleventh Symposium (International) on Combustion, The Combustion Institute, Pittsburgh", p. 979, 1967.
4. M. A. Delichatsios and D. G. Vlachos, *in* "Eastern States Section, Chemical and Physical Processes in Combustion, December", p. 285, Hilton Head, SC, 1996.
5. B. Rogg, *Combust. Flame* **73**, 45 (1988).
6. S. V. Pantakar, "Numerical Heat Transfer and Fluid Flow,". McGraw-Hill, New York, 1980.
7. V. Giovangigli and M. D. Smooke, *J. Comp. Phys.* **68**, 327 (1987).
8. J. A. Miller and C. T. Bowman, *Prog. Energy Combust. Sci.* **15**, 287 (1989).

Fig. 1, Effect of dilution on ignition & extinction

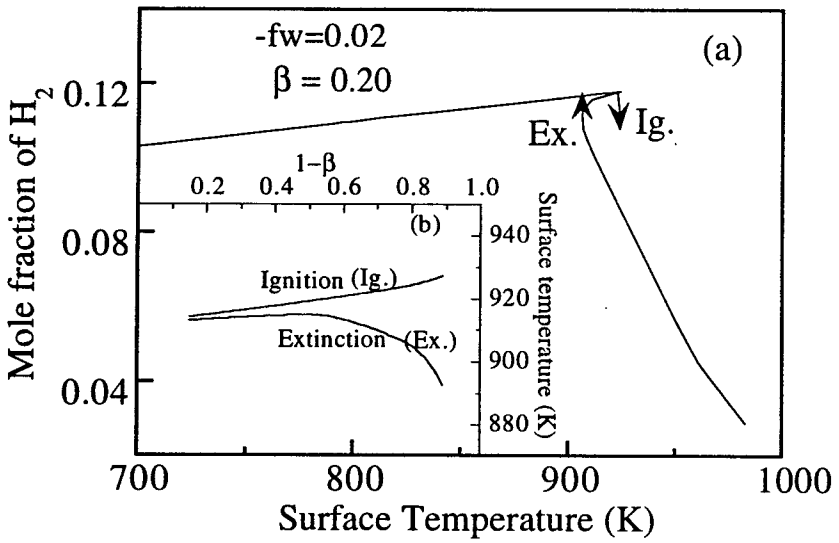


Fig. 2, Adiabatic extinction limit curves

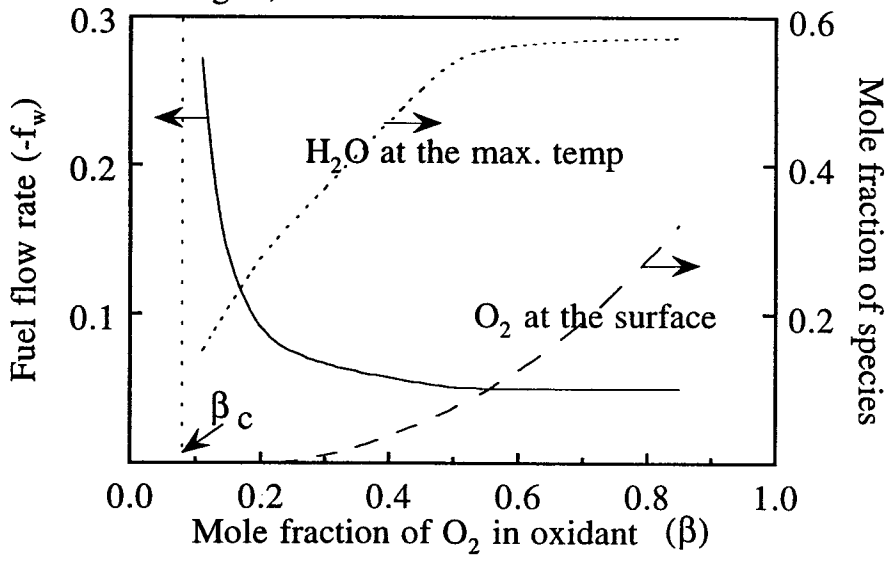


Fig. 3, Profiles at adiabatic extinction limits

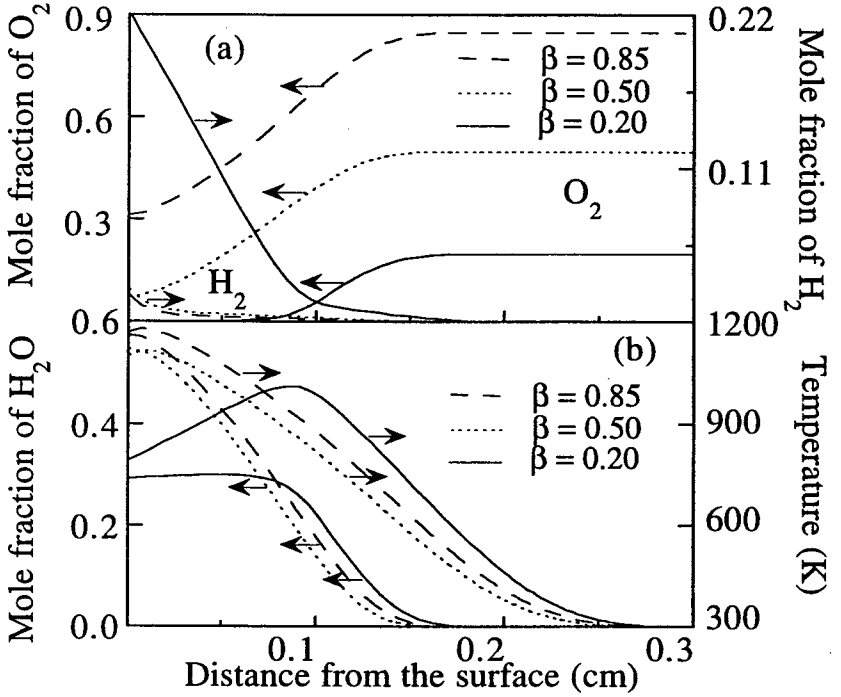
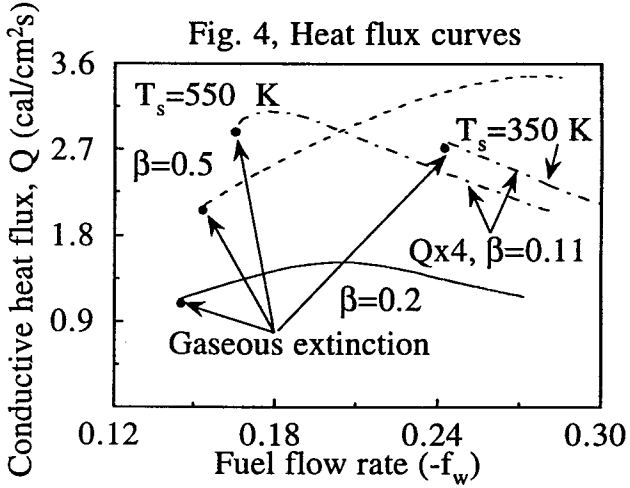


Fig. 4, Heat flux curves



Unsteady Extinction Behavior of Counterflow Diffusion Flames: Experiments and Modeling

Vito S. Santoro, Amable Liñán and Alessandro Gomez

Yale Center for Combustion Studies
Department of Mechanical Engineering
Yale University
New Haven, CT 06520-8286
(alessandro.gomez@yale.edu)

Introduction

The interaction of a laminar vortex with a flame offers a scenario that is intermediate in complexity between laminar flames and turbulent ones. Effects of time-dependence and curvature can be studied in a well-controlled environment and shed light on phenomena that are relevant to turbulent flames. In this study the interaction of a toroidal vortex and a laminar counterflow diffusion flame was examined. Such a system has been the object of experimental and numerical investigations in gaseous diffusion flames [1-3], as well as in spray flames [4]. The present emphasis is on the quantitative characterization of the extinction behavior, particularly in the comparison between quasi-steady extinction and vortex-induced one.

Experimental Methods

Details of the experimental configuration were reported in [4]. Briefly, an axisymmetric counterflow diffusion flame was established in a vertical configuration, with the oxidizer being fed from the top, methanol and inert from the bottom. Liquid methanol was prevaporized and helium was used as inert gas. Both sides of the burner terminated in a contraction with an exit diameter of 12.5 mm and a separation distance of 12 mm. The steady flame was perturbed by periodically-generated laminar toroidal vortices from the oxidizer side. A suitably-synthesized voltage function was applied across the loudspeaker, causing the latter to force air through a 1.5 mm tube impulsively, similarly to [5]. Particular care was required for the design of the voltage function to avoid ringing and overheating of the coil of the loudspeaker. The amplitude of the voltage function was used to control the strength of the vortex generated. Conditions were such that the vortex diameter was much larger than the thickness of the mixing layer, in order to minimize curvature effects.

The vortices were visualized using planar light scattering of submicron TiO_2 particles, produced by hydrolysis of $TiCl_4$. From this images the vortex dimension was derived and repeatability was verified. To monitor the flame dynamics under vortex excitation, formaldehyde planar induced fluorescence was used, pumping it with the third harmonic of a Nd:YAG laser, and detecting the fluorescence signal at 415 nm with a gated single stage image intensifier coupled to a CCD. This technique provide a complementary marker of the flame since the peak of heat release corresponds to the location where the formaldehyde concentration precipitously drops [4]. These diagnostic techniques were complemented by single-point phase-locked LDV measurements to monitor the instantaneous strain rate along the flame centerline.

Results and Discussion

The following phenomenology was observed. Under vortex excitation, localized wrinkling in the vicinity of the centerline was observed, which, for sufficiently strong vortices, yielded *local* extinction, with the development of a "hole" in the middle of the flame. After passage of the vortex, the now annular flame closed in and re-established a flat and uniform diffusion flame. Flame strain rates were measured along the centerline of the burner by following the procedure detailed in [4]. Phase-averaged velocity data at different locations on the centerline enabled us to compute a velocity gradient near the flame, whose evolution in time is shown in Fig.1 (t=0 is defines as the time at which the pulse was applied to the loudspeaker). The peak of the strain rate is here defined as the vortex-induced extinction strain rate.

In Fig. 2 a more complete set of experimental results, as compared to [4], is presented. The vortex-induced extinction strain rates are reported as a function of the fuel mass fraction, for a given oxidizer mass fraction and a given baseline strain rate (55 1/s). Also shown in the same figure are the results of the "quasi-steady" extinction (open symbols), which was obtained by increasing the mass flux from both sides slowly, until extinction was observed. The remarkable difference between the "quasi-steady" extinction strain rate and the vortex-induced one is apparent. Such a difference was already reported in some previous computational work [8] and experimental work [9] on counterflow diffusion flames with oscillating strain rates.

A qualitative explanation of the phenomenon can be obtained from an estimate of the order of magnitude of the characteristic times involved into the process: the mechanical time (τ_m=1/K), the chemical time (τ_{ch}=1/(β^2K)) and the vortex time, based on the rising time of the voltage function. For a strain rate of K=50 1/s, a Zeldovich number β of order10 and a rising time of the voltage function of order 1 ms, the ordering of the time scales is as follows: $\tau_{ch}<\tau_{unsteady}<\tau_{mech}$. Therefore, the vortex introduces unsteadiness in the outer diffusive-convective layer, while the inner reactive-diffusive layer behaves in a "quasi-steady" manner, since the characteristic chemical time is much smaller than the characteristic unsteady time. As a result, even though the instantaneous strain rate is much larger than the "quasi-steady" extinction strain rate, the flame is subject to a strain rate "damped" through the outer layer.

This explanation can be formalized with a simple model. Using a thermal-diffusive model, constant transport properties and a one step Arrhenius kinetics, Linan and Williams [10] derived an equation for the mixture fraction for ignition with time dependent strain rate, as follows:

$$(\delta^2/\alpha_0)Z_t - \eta\{(\delta^2/\alpha_0)(\frac{\delta_t}{\delta} + K_0 + \frac{d\ln\rho_0}{dt})\}Z_\eta = Z_{\eta\eta} \qquad (1)$$

where K represents the instantaneous strain rate, δ the thickness of the mixing layer, α the thermal diffusivity, ρ the density, η the non-dimensional spatial coordinate, η=y/δ(t), t the time, and the subscript 0 stands for conditions at time t=0. A self-similar solution for equation (1) can be found by setting the expression in brackets equal to a constant, that is

$$(\delta^2/\alpha_0)(\delta_t/\delta + K_0 + d(\ln\rho_0)/dt) = 1. \qquad (2)$$

If the change of density in time due to a change in pressure is neglected, this equation governing the thickness of the mixing layer becomes

$$\delta\delta_t + \delta^2 K = \alpha \qquad (3)$$

The solution of this equation, non-dimensionalized with respect to the thickness of the mixing layer at t=0 (δ_0) can be written as

$$\delta^2/\delta_0^2 = (1 + 2\int_0^t \exp(\int_0^{t'} 2K(t'')dt'')dt') \times \exp(-2\int_0^t K(t')dt') \qquad (4)$$

and can be readily integrated for a given temporal profile of strain rate. Finally, the thickness of the mixing layer can be related to the effective strain rate, using the relation $\tau_{mech} = \delta^2/\alpha$, yielding

$$(\delta/\delta_0)^2 = (K_0/K_{eff}). \qquad (5)$$

A number of approximations were introduced in the derivation of eq. (4), including the assumption, implicit in seeking a self-similar solution, that curvature effects in the experiments to be modeled are negligible. Nevertheless, this simplified approach can be used to gain a semi-quantitative insight into the

problem. To use this model, we introduced the experimental K(t') in eq. (4) and recovered an effective strain rate, K_{eff} from eq. (5). In fig. 3 the temporal profiles of the experimental instantaneous strain rate (symbols) and of the effective strain rate (line) at the flame are reported. The inset shows the temporal details of the leading edge of the curve. Two observations are in order: 1) there is a time delay between the change of the effective strain rate and the instantaneous one; and 2) the maximum of the instantaneous strain rate and the effective ones occurs at the same time. The first observation implies that the flame has its own response time, and a time delay is required before any change is felt by the reaction zone. The second observation is supported by the experimental results, since the time at which extinction is observed by the formaldehyde images and the time at which the instantaneous strain rate reaches its maximum was found to be the same. The peak value of the effective strain rate was calculated for all the experimental conditions in fig.2. The results of this analysis are reported in fig. 4, together with the "quasi-steady" extinction strain rates and the instantaneous vortex-induced values. The model correctly captures the fact that the effective strain rate "felt" by the flame approaches the "quasi-steady" values, implying that the instantaneous strain rate is not appropriate to describe this time-dependent problem. The flame has its own characteristic response time and the temporal history of the perturbation must be considered as well [10].

Additional experimental work and modeling will be presented on the necessary overstrain introduced by the vortex to bring about extinction under conditions in which the chemical composition is fixed and the baseline strain rate is varied.

References

[1] Thevenin, D., et al., *26th Symp. (Intern.) on Combustion*, 1079 (1996).
[2] Thevenin, D., et al., *27th Symp. (Intern.) on Combustion*, 719 (1998).
[3] Katta, V. R., et al., *27th Symp. (Intern.) on Combustion*, 587 (1998).
[4] Santoro, V. S., et al., Abstract presented at the Joint Meeting of the US Sections of the Combustion Institute, Washington DC, March 15-17, 1999.
[5] Roberts,W.L. and Driscoll, J.F., *Combustion and Flame,* 87:245-256, (1991)
[6] Gao, L.P., et al., *26th Symp. (Intern.) on Combustion*, 1739 (1996)
[7] Bauerle, B., et al., *26th Symp. (Intern.) on Combustion*, 2619 (1996)
[9] Linan, A., et al., *Combustion and Flame*, 95:31-46, (1993)
[10] Ghoniem, A. F., et al., *24th Symp. (Intern.) on Combustion*, 223 (1992)
[11] Kistler, J. S., et al., *26th Symp. (Intern.) on Combustion*, 113, (1996)

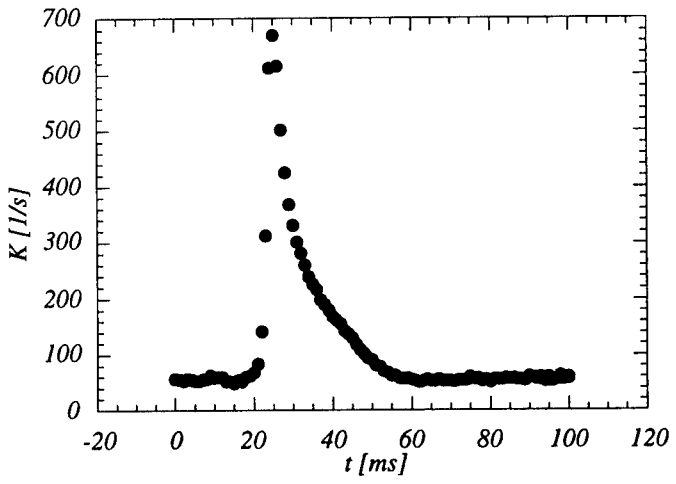


Fig.1: Strain rate as function of time, as measured at the flame.

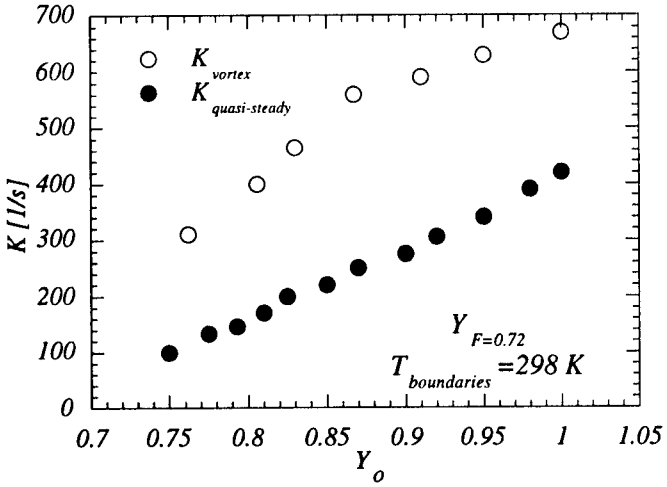


Fig.2: Quasi-steady and vortex-induced extinction strain rates as a function of the oxidizer mass fraction.

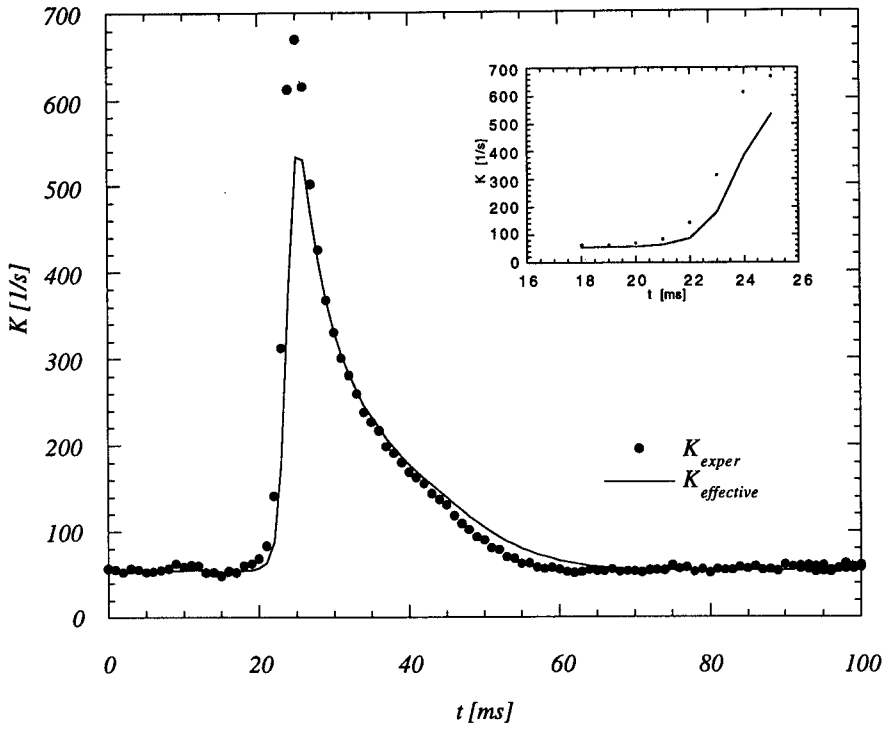


Fig.3: Temporal profile of the experimental instantaneous strain rate (symbols) and of the effective strain rate (line) at the flame.

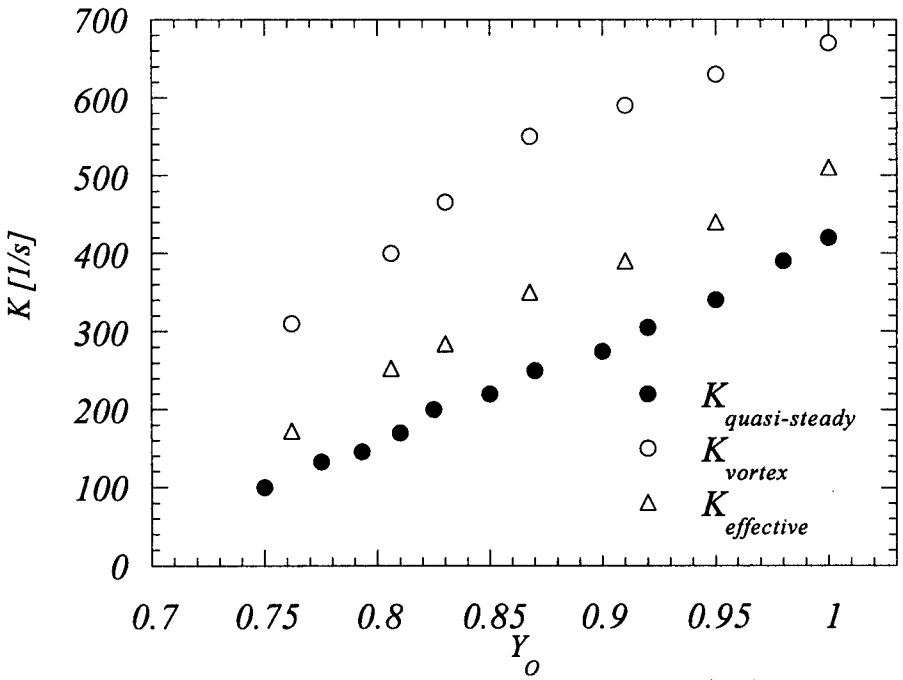


Fig.4: Extinction strain rate as a function of oxidizer mass fraction.

Vortex Injection of Noble Gases in an Opposed-Jet Burner

G. J. Fiechtner,[1,2] J. R. Gord,[1] C.D. Carter,[1,2] K. D. Grinstead, Jr.,[1,2] V. R. Katta,[1,2] P.-H. Renard,[3] and J. C. Rolon[3]

[1]Air Force Research Laboratory, Propulsion Directorate,
Wright-Patterson Air Force Base, OH 45433-7103, USA.
[2]Present Address: Innovative Scientific Solutions, Inc., 2766 Indian Ripple Road, Dayton, OH 45440-3638, USA. G.J.F. Contact E-Mail: gjfiech@ward.appl.wpafb.af.mil, Tel: (937) 255-8373.
[3]Laboratoire d'Énergétique Moléculaire et Macroscopique, Combustion, École Centrale Paris and CNRS, Grande Voie des Vignes, 92295 Châtenay-Malabry Cedex, France.

1. Introduction

Numerical modeling and experimental measurements of reacting flows have led to important advances in the understanding of combustion. Numerous investigations, including those on the interaction of a laminar flame and a vortex, have contributed to these advances. The resulting data are useful in a variety of applications such as the identification of fundamental regimes of vortex-flame interactions.[1] Vortical structures are an important feature in unsteady and turbulent combustion, and experimental data can be used to develop models for use in practical combustion areas such as experimental gas turbine combustors. Using a burner developed at École Centrale Paris and CNRS, we recently performed a series of studies in which numerical predictions[2] were later validated using measurements of flame extinction in a nonpremixed hydrogen/air flame by an air-filled vortex.[3] The recent ban on the manufacture of halon has led to the need for alternative fire suppressants. In this study, we explore the possibility of extending vortex-flame extinction studies to basic research in fire-suppression dynamics. A valve-switching mechanism is demonstrated for filling a vortex with a fluid. Synchronization of the filled-vortex injector with laser diagnostics is then demonstrated. In the preliminary results presented here, local flame extinction is promoted with a helium-filled vortex. We propose that carefully-controlled vortex-flame experiments and modelling can be a useful tool in the search for Halon replacements.

2. Background

The search for replacements for bromine-containing fluorocarbons has resulted in intense research. These studies[4] have addressed the effect of halon replacements on global parameters such as burning velocity, HF and CF_2O production, extinction strain rate, flame temperature, and species concentration profiles (see, for example, Reference 4 and the references therein). During past development of combustion codes for gas turbine combustor modelling, experimental studies of vortex-flame interactions have been of great benefit.[5] Similar benefit may result from vortex-flame studies when applied to the problem of fire suppression. Numerous experimental studies of the interaction dynamics of vortices and flames have been conducted. For premixed flame fronts, most measurements have been made using two types of flames. Hertzberg et al.[6] and Escudie[7] conducted an experiment in which a Karman vortex street was produced using a cylindrical rod in a cross flow of premixed gases. A V-flame was supported behind a wire positioned downstream of the rod that produced the vortex street. Planar tomographic imaging was used to study the interaction of the vortex street and the flame. A similar interaction of a Karman vortex street and a flame was investigated by Lee et al.[8] using PLIF imaging of OH and by Nye et al.[9] using both OH PLIF and PIV. A disadvantage of using the vortex street is the difficulty in isolating a single vortex. Samaniego[10,11] developed a means of injecting an isolated line vortex through a horizontal slot in the wall of a vertical wind tunnel and presented results on the interaction of a line vortex and a V-flame. Schlieren images of the time-dependent vortex-flame interaction along with CH emission data from the entire flame were presented. Paul and coworkers[12-14] studied vortex-flame interactions using the Samaniego burner; PLIF measurements of OH and CH radicals were reported initially, and quantities such as heat release were presented during later studies.

In a second type of study involving premixed combustion, Jarosinski et al.[15] studied a flame that was ignited at one end of a tube of premixed gases. A vortex was injected at the other end of the tube. The interaction dynamics were then photographed using a mercury-xenon arc lamp and a rotating-drum streak camera with a rotating-disc shutter. Recently, Driscoll and co-workers produced an impressive series of papers concerning a similar vortex-flame facility in which PIV, OH PLIF, or a combination of these imaging techniques was applied (see Driscoll et al.,[16] Mueller et al.,[17] Sinibaldi et al.,[18] and the references therein).

Nonpremixed flames have also been the subject of experimental study. Rolon and co-workers (see Renard et al.,[19] Thevenin et al.,[20] and the references therein) recently developed an apparatus in which a vortex was injected into a flame supported between the nozzles of an opposed-jet burner. Takagi and coworkers[21,22] performed planar Rayleigh-scattering measurements of temperature on a similar type of opposed-jet burner in which a small jet of fuel or air was injected using a micro-nozzle with an inner diameter of only 0.25 mm. Either a jet of air was injected from the air side of the diffusion flame or a jet of fuel was injected from the fuel side. Chen and Dahm[23] developed a facility for generating a nonpremixed burning layer that wraps into a vortex ring. The facility permits experiments to be performed under conditions of both normal gravity and microgravity, allowing the study of the influence of buoyancy.

3. Apparatus and Procedure

The opposed-jet burner used in these experiments has been described elsewhere.[3] The flame is supported between upper and lower nozzles that are separated by 40 mm, each with an exit diameter of 25 mm. The fuel consists of hydrogen diluted with nitrogen and flows from the upper nozzle. Air flows from the lower nozzle. Unique to this type of apparatus is a tube with ~2-mm inner diameter that is installed concentrically within the lower nozzle. This tube is attached to a cylinder that contains a piston which, in turn, is attached to an actuator. Feeding an appropriate current to the actuator causes a solenoid to force the piston upward abruptly, resulting in the emergence of a vortex from the tube. The vortex travels upward within the surrounding oxidizer flow. As configured during past experiments, a flow of air is supplied to the vortex tube such that, in the absence of a vortex, the exit velocity matches the velocity of the air from the surrounding nozzle. The air supply has been modified for the present experiments by inserting two three-way valves—one connected to the air supply and the other connected to the helium supply. For filling a vortex with helium, the vortex piston is moved to its farthest position from the flame, at which time the currents supplied to the two three-way valves are reversed. The air valve switches to vent air to the fume hood, and the helium valve switches to provide a flow of helium to the vortex nozzle. When the desired amount of helium has been delivered, the solenoid currents are again reversed such that the air valve admits air to the vortex nozzle and helium is vented to the fume hood. At this instant, upward motion of the vortex piston is initiated, forcing a vortex into the opposed-jet burner. To minimize the impact of room-air disturbances, upper and lower guard flows of nitrogen are supported through outer nozzles, which are concentric with the respective upper and lower inner nozzles that support the flame.

PLIF measurements are accomplished by exciting hydroxyl radicals at 281.3414 nm via the $R_1(8)$ transition of the (1,0) band in the A-X system. Fluorescence from the A-X (1,1) and (0,0) bands is detected at right angles using WG-295 and UG-11 colored-glass filters, a 105-mm-focal-length f/4.5 UV lens, an image intensifier, and CCD pixels that are binned in 2x2 groups, resulting in an imaged area of 25.6 x 38.4 mm^2. The bottom of the image is 0.25-mm above the surface of the lower nozzle. A color table is used, with a maximum value set to 120% of the maximum signal for the flame condition in which a vortex is not injected. The low-signal color is assigned by calculating the background noise and selecting a minimum value that is two standard deviations above this level. Therefore, in cases where "extinction" of the OH layer is observed, "extinction" refers to signal levels that fall below this minimum value and are, therefore, assigned the last color in the table. All images represent the signal collected during a single laser shot, and no smoothing of the resulting images is attempted.

4. Results and Discussion

The PLIF images of OH shown in Figure 1 correspond to an air-filled vortex that interacts with the hydrogen-air flame. An effective temporal delay of 1 ms is used between images. "Extinction" of the OH layer is absent. Initially, the vortex creates a small dent in the flame, and this dent begins to grow. In the later interaction stages, the OH PLIF signal level is observed to increase by more than a factor of five over the levels observed without a vortex.

The images of Figure 2 are taken under experimental conditions identical to those for the images of Figure 1, except that the vortex is filled with helium. Local extinction of the OH layer takes place at a point on the top surface of the vortex. After extinction, the vortex travels upward toward the other nozzle through the hole created in the flame. The flame then burns back behind the vortex and closes the hole.

While acquiring the data in Figures 1 and 2, simultaneous images were captured using Rayleigh scattering. Rayleigh scattering can be used to compute the temperature in the vicinity of the flame; this temperature is needed to place OH images on a quantitative basis.[3] In addition, the helium vortex entrains surrounding air before

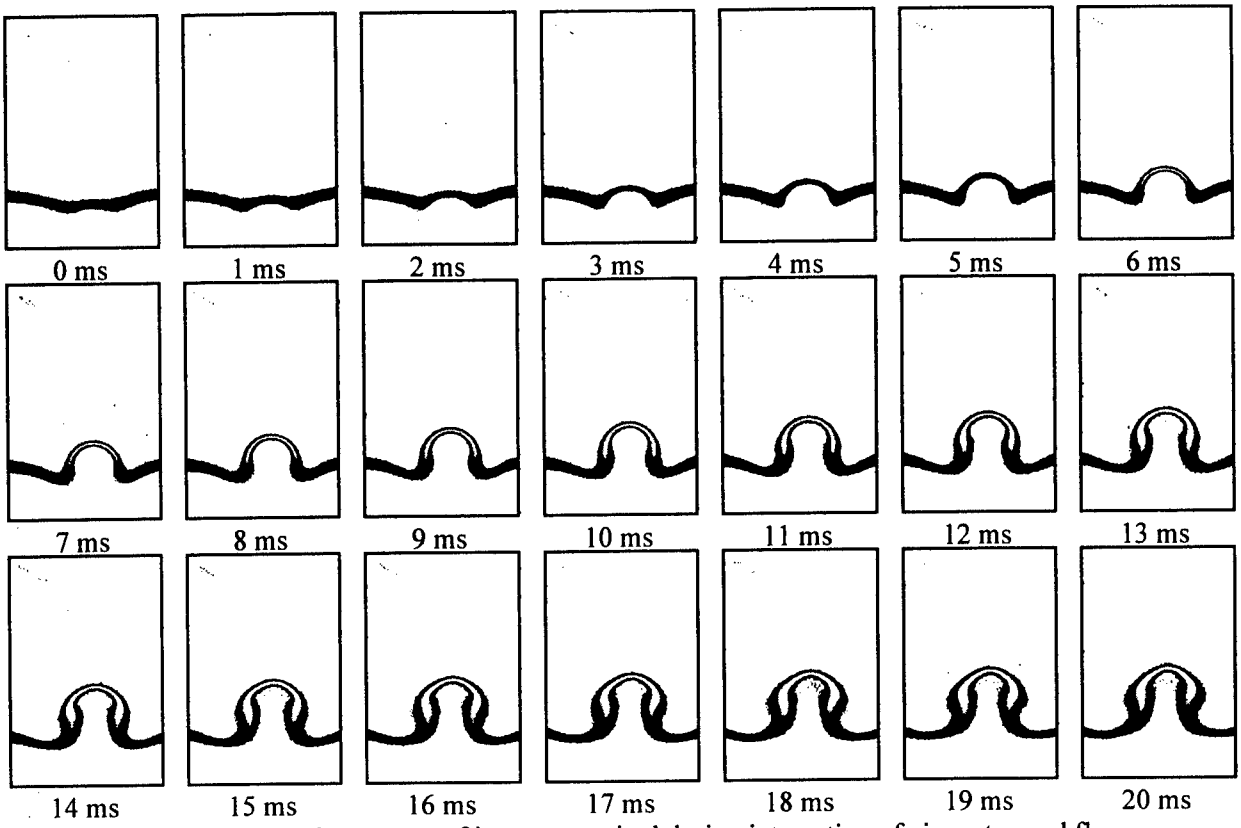


Figure 1. Temporal sequence of images acquired during interaction of air vortex and flame.

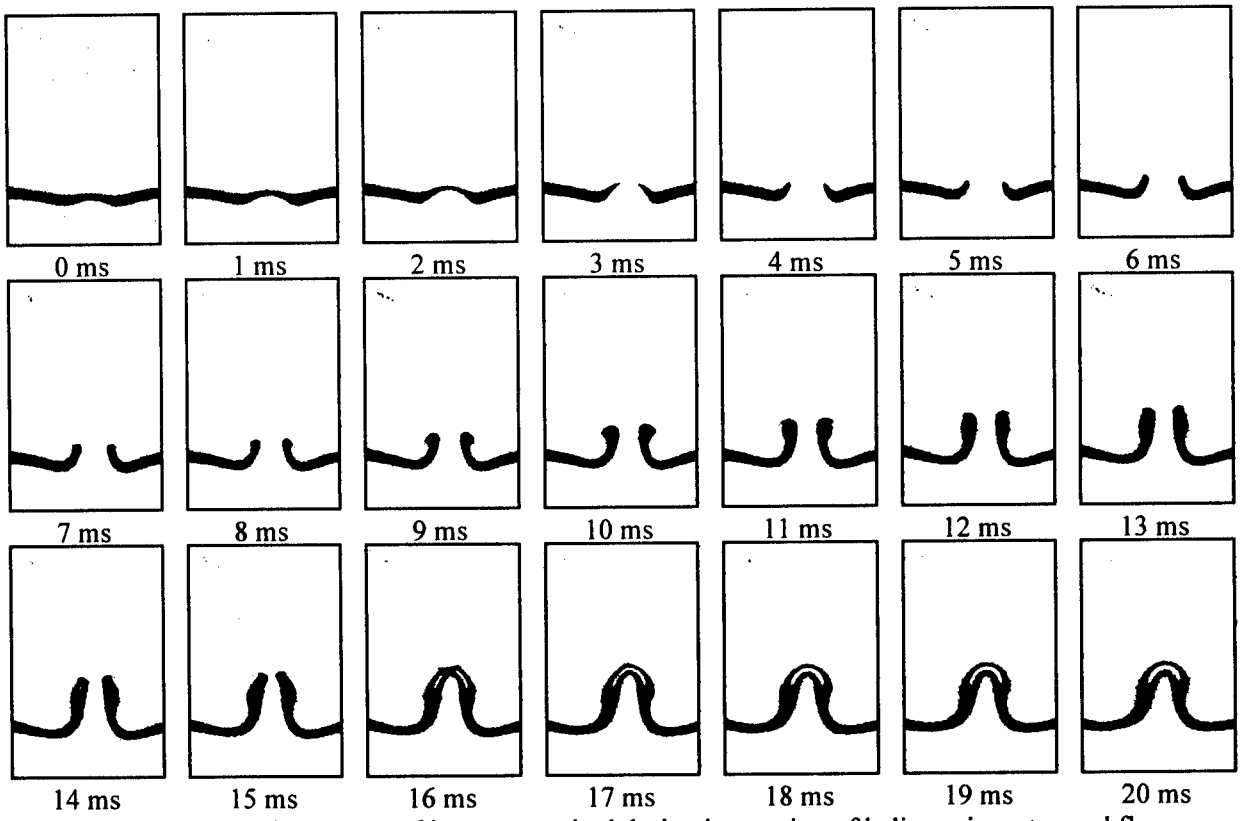


Figure 2. Temporal sequence of images acquired during interaction of helium-air vortex and flame.

reaching the flame, and Rayleigh scattering can be used to estimate the concentration of helium in the vortex. Future studies will utilize hydrocarbon fuels, and more realistic suppressants will be used to fill vortices.

5. Conclusions

The apparatus of Rolon and co-workers[1,20] has been used to study the interaction of a vortex and a flame using PLIF measurements of OH. The process of filling the vortex has been demonstrated to be highly repeatable. A preliminary experiment has been completed in which a helium-air vortex extinguished a hydrogen-air flame locally at a point. An analogous vortex filled exclusively with air does not extinguish of the flame.

Acknowledgements

The authors thank Dr. R. D. Hancock and Capt. I. Vihinen for assistance in assembly and construction of the burner. The authors also acknowledge Drs. R. D. Hancock, W. M. Roquemore, and K.-Y. Hsu for the stimulating discussions of vortex-flame dynamics. Finally, the authors wish to thank Ms. M. M. Whitaker for editorial comments. This work is supported by U. S. Air Force Contracts F33615-95-C-2507 and F33615-97-C-2702.

References

1. P.-H. Renard, J. C. Rolon, D. Thevenin, and S. Candel, *Combust. Flame* **117**, pp. 189-205, 1999.
2. V. R. Katta, C. D. Carter, G. J. Fiechtner, W. M. Roquemore, J. R. Gord, and J. C. Rolon, *Twenty-Seventh Symposium (International) on Combustion*, The Combustion Institute, Pittsburgh, PA, pp. 587-594, 1998.
3. G. J. Fiechtner, C. D. Carter, V. R. Katta, J. R. Gord, J. M. Donbar, and J. C. Rolon, *37th AIAA Aerospace Sciences Meeting and Exhibit*, Reno, NV, AIAA 99-0320, 1999.
4. D. L'Espérance, B. A. Williams, and J. W. Fleming, *Combust. Flame* **117**, pp. 709-731, 1999.
5. W. M. Roquemore and V. R. Katta, *International Conference on Optical Technology and Image Processing in Fluid, Thermal, and Combustion Flow*, Yokohama, Japan, Paper No. KL-310, 1998.
6. J. R. Hertzberg, M. Namazian, and L. Talbot, *Combust. Sci. Technol.* **38**, pp. 205-216, 1984.
7. D. Escudie, *Prog. Astronaut. Aeronaut.* **113**, pp. 215-239, 1988.
8. T.-W. Lee, J. G. Lee, D. A. Nye, and D. A. Santavicca, *Combust. Flame* **94**, pp. 146-160, 1993.
9. D. A. Nye, J. G. Lee, T.-W. Lee, and D. A. Santavicca, *Combust. Flame* **94**, pp. 167-176, 1996.
10. J.-M. Samaniego, *Annual Research Briefs--1992*, Center for Turbulence Research, NASA Ames Research Center/Stanford University, pp. 431-441, 1992.
11. J.-M. Samaniego, *Annual Research Briefs--1993*, Center for Turbulence Research, NASA Ames Research Center/Stanford University, pp. 205-218, 1992.
12. Q.-V. Nguyen and P. H. Paul, *Twenty-Sixth Symposium (International) on Combustion*, The Combustion Institute, Pittsburgh, PA, pp. 357-364, 1996.
13. H. N. Najm, P. H. Paul, C. J. Mueller, and P. S. Wyckoff, *Combust. Flame* **113**, pp. 312-332, 1998.
14. P. H. Paul and H. N. Najm, *Twenty-Seventh Symposium (International) on Combustion*, The Combustion Institute, Pittsburgh, PA, pp. 43-50, 1998.
15. J. Jarosinski, J. H. S. Lee, and R. Knystautas, *Twenty-Second Symposium (International) on Combustion*, The Combustion Institute, Pittsburgh, PA, pp. 505-514, 1988.
16. J. F. Driscoll, D. J. Sutkus, W. L. Roberts, M. E. Post, and L. P. Goss, *Combust. Sci. Technol.* **96**, pp. 213-229, 1994.
17. C. J. Mueller, J. F. Driscoll, D. L. Reuss, and M. C. Drake, *Combust. Flame* **112**, pp. 342-358, 1998.
18. J. O. Sinibaldi, C. J. Mueller, and J. F. Driscoll, *Twenty-Seventh Symposium (International) on Combustion*, The Combustion Institute, Pittsburgh, PA, pp. 827-832, 1998.
19. P.-H. Renard, J. C. Rolon, D. Thevenin, and S. Candel, *Twenty-Seventh Symposium (International) on Combustion*, The Combustion Institute, Pittsburgh, PA, pp. 659-666, 1998.
20. D. Thevenin, P.-H. Renard, J. C. Rolon, and S. Candel, *Twenth-Seventh Symposium (International) on Combustion*, The Combustion Institute, Pittsburgh, PA, pp. 719-726, 1998.
21. T. Takagi, Y. Yoshikawa, K. Yoshida, M. Komiyama, and S. Kinoshita, *Twenty-Sixth Symposium (International) on Combustion*, The Combustion Institute, Pittsburgh, PA, pp. 1103-1110, 1996.
22. K. Yosida and T. Takagi, *Twenty-Seventh Symposium (International) on Combustion*, The Combustion Institute, Pittsburgh, PA, pp. 685-692, 1998.
23. S.-J. Chen and W. J. A. Dahm, *Twenty-Seventh Symposium (International) on Combustion*, The Combustion Institute, Pittsburgh, PA, pp. 2579-2586, 1998.

Flow Field Considerations for Counter Flow Burners

M.P. Davis[1], J.W. Fleming, B.A. Williams, H.D. Ladouceur[2]
Combustion Dynamics Section, Code 6185, Chemistry Division
Naval Research Laboratory, Washington, DC 20375-5342 USA

[1]Graduate Student, WPI
[2]Corresponding author: Code 6112, douglad@ccf.nrl.navy.mil

INTRODUCTION

Many computational combustion tools (e.g. Sandia OPPDIF code [1]) of opposed jet, counter flow diffusion flames apply a simplified potential flow model for the fluid flow portion of the problem. The resulting solution (for no flame) yields a stagnation region between the two burners and an axial velocity component that is independent of radius. Rolon [2] recognized the need for experimental evidence to provide justification for a potential flow assumption. His results indicate that for a range of velocities and for two common burner designs (straight tubes with screens and dual converging nozzles) there are large discrepancies between the assumed flat radial profile and experimental measurements. This paper investigates the flow field that exists between the nozzles of various counter flow burners through the use of a commercially available CFD package. Better understanding of this flow regime will lead to improved burner designs that more closely approximate the one dimensional treatment used in the combustion models.

The potential flow model ignores viscous effects, resulting in a failure to predict boundary layer development along the tube walls. A no-slip boundary condition at the tube walls causes fluid adjacent to the walls to be retarded, thereby increasing the velocity of the fluid along the centerline (in order to satisfy mass continuity). This results in a much higher centerline velocity (for the same flow rate) than that predicted by the potential flow model. A simple potential flow model was examined by neglecting viscous effects and solving the reduced Navier-Stokes equations. The solution is that of Laplace's equation for the velocity potential, which was evaluated for a geometry describing two 1 cm diameter tubes separated by 1 cm using a finite element package (FLEXPDE) [3]. This potential flow model consistently under predicts the observed flow velocity. This is reasonable since the acceleration of the fluid core within the tubes by viscous boundary layer growth is neglected.

In the case of two opposed flows, the situation is more complicated. Flow in both tubes will develop boundary layers resulting in the center core being accelerated. If the separation distance between the two tubes is small, the velocity profile at the tube exits will be greatly affected by the presence of the other tube due to the higher pressure stagnation region formed by the two impinging streams. The shape and length of the burner tubes, the tube separation distance, and the inlet flow velocities all play important roles in determining the shape of the radial velocity profile at the tube exits.

The opposed flow problem was studied using PHOENICS [4], a widely utilized CFD software. The geometry and flow conditions can be easily modified, and parametric studies were run to investigate different burner configurations over the entire desired range of strain rates. PHOENICS is used to better understand the fluid mechanics involved, as well as being a useful design tool to determine optimal burner geometries that produce flow fields more appropriate for the one-dimensional models.

COMPUTATIONAL SETUP

The CFD calculations were performed using PHOENICS version 1.6, running on an SGI workstation. PHOENICS uses a finite volume approach to provide solutions of differential equations having transient, convection, diffusion, and source terms. For this application, the appropriate equations are the incompressible Navier-Stokes equations. The user is able to specify geometry, boundary conditions, fluid properties, as well as many other options that control the solution procedure, output, etc. Taking advantage of the axisymmetric nature of the problem, the solution was specified in a single plane and then rotated to produce the desired 3-D burner. Boundary conditions were specified along each of the four edges of the solution domain as well as along the tube walls. At each of the tube inlets, a uniform velocity was set, and no-slip conditions were

specified for each tube surface. For the far field radial boundary, a pressure boundary condition was utilized to set the pressure to 1 atmosphere.

RESULTS

Calculations were performed for a single, 50 cm long, 1 cm diameter straight tube flowing N_2 in order to assess the predictive capability of the code. For comparison, experimental measurements of the radial profile of the axial velocity were made on a single burner tube having the same dimensions as were used in the PHOENICS calculation. Data were collected at a height of 1 mm above the tube exit plane and a N_2 flow rate of 2.1 SLPM using an LDV system (QSP, Inc.) seeded with 0.3 μm diameter alumina particles entrained into the N_2 flow. Figure 1 plots both the measured and PHOENICS calculated axial velocities as a function of tube radius. Excellent agreement is observed between the measured and calculated velocities.

Calculations were carried out to investigate the effects of tube length on the shape of the radial velocity profiles. Figure 2 shows radial profiles of the axial velocity for N_2 flowing at an inlet velocity of 40 cm/s for tubes of lengths 3, 5 and 10 cm. The profiles show the viscous effects that predominate along the tube walls, lowering the local velocity, giving rise to a boundary layer, and accelerating the core fluid. For longer tube lengths, the boundary layer grows until a parabolic velocity profile results, after which the velocity profile ceases to change with increasing tube length (fully developed flow). The 10 cm tube demonstrates this, as the flat portion of the profile near the centerline has nearly vanished. For the 3 cm long tube, the velocity profile within 2 mm of the tube centerline is flat, closely approximating the one dimensional assumption made in the flame models. Thus, the degree of flatness in the radial profile can be varied by the length of the tube.. The optimal tube length depends on several factors including gas properties, temperature, and most importantly flow rate.

Converging nozzles are also used to generate flat radial profiles. However, the flat radial profile for an unopposed nozzle is affected by the presence of an opposing nozzle. Figure 3 presents the axial velocity across the nozzle exit for flow between two opposed converging nozzles. The contour of the nozzles is that specified by Rolon [2] and is described by an exponential curve. The opposed flows are presented for five strain rates, a, defined as the maximum axial velocity gradient in the streamwise direction. For higher flow velocities, a higher pressure area develops along the centerline at the stagnation plane, causing an axial velocity depression transverse to the flow. This results in the "M" or "W" shaped profiles seen in Figure 3. Such profiles were observed experimentally by Rolon [2] at similar strain values. This same nozzle produces an extremely flat profile in isolation.

The same phenomenon that causes the dip in the profile for the opposed converging nozzles will tend to flatten out the curvature from viscous effects seen in an unopposed straight tube. Thus, in order to achieve a flat profile near the flame zone, the exit radial profile for the isolated burner must lie somewhere between that of a fully developed parabolic flow and that of a nozzle designed to yield a completely flat profile. Computational determination of the optimum nozzle shape is an inverse problem, one that is not easily solved. Calculations with various contours suggest that a cubic or fourth order curve does a better job at producing flatter radial profiles for opposed flow conditions. Calculations are continuing to address this issue as well as to predict the results of Figure 2 for opposed tubes.

The choice of the optimum counter flow burner design depends on several parameters including choice of fuel and oxidizer, strain rate range of interest and whether one will be using powders or liquid aerosols in either flow. Straight tubes with movable flow straighteners are much easier to build than a converging nozzle, although flow straighteners complicate the introduction of aerosols. The structures imposed on the profile due to individual screen openings must also be considered. However, the possibility of producing flatter velocity profiles over a larger range of strain rates by varying the lengths of straight tubes will have clear advantages.

CONCLUSIONS

It has been shown that CFD can provide valuable insight into the flow physics of counter flow diffusion flame burners. Although no combustion is modeled here, many CFD software packages have the ability to tackle both the flow geometry and the chemistry (e.g., PHOENICS 3.1).

These results can serve as a starting point for those interested in designing an opposed flow burner that provides a one dimensional flow field more amenable to one dimensional flame models. For a given burner design, the radial velocity profiles will be very different depending on flow velocity, tube separation, length, and burner shape. It is possible to obtain a relatively flat radial velocity profile although this can only strictly be accomplished at a specific flow velocity and tube separation. Either straight tubes, converging nozzles, or variable length sections of straight tubes have the potential of being able to extend the range of strain that could be studied while maintaining some aspect of one dimensionality.

ACKNOWLEDGEMENTS

This research is sponsored by the Department of Defense's Next Generation Fire Suppression Technology Program funded by the DoD Strategic Environmental Research and Development Program. The authors would like to thank Will Gorton and Mike Kozma for their assistance..

REFERENCES

[1]. OPPDIF: A Fortran Program for Computing Opposed-Flow Diffusion Flames", SANDIA Report SAND96-8243, UC-1409, May 1997.

[2]. "Counter Jet Stagnation Flows", J.C. Rolon, D. Veynante, and J.P. Martin, *Exp. in Fluids*, **11**, 313-324 (1991).

[3]. FLEXPDE: Finite Element Analysis for Partial Differential Equations, SPDE, Inc., Fremont, CA (1995)

[4]. PHOENICS, Version 1.6, Concentration Heat and Momentum, Limited (CHAM), Bakery House, London, (1992).

Figure 1: Axial Velocity vs. Radial Position for a Single 50 cm Tube

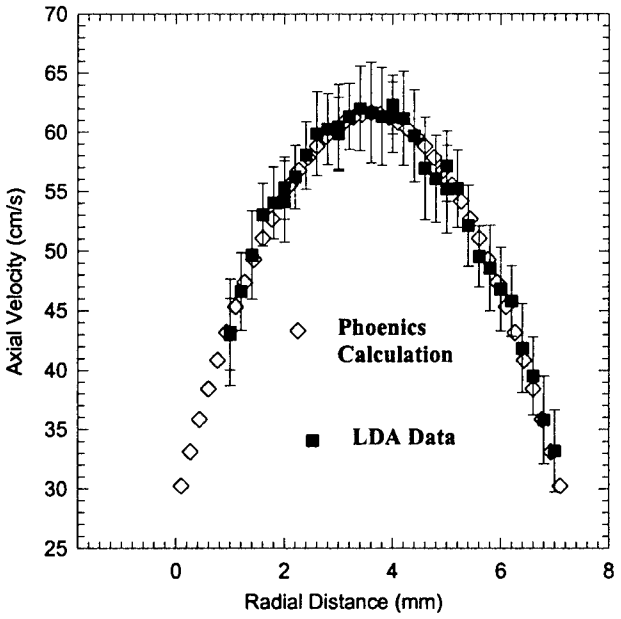


Figure 2: PHOENICS Calculations for a Single Tube of Axial Velocity vs Radius for Varying Tube Lengths

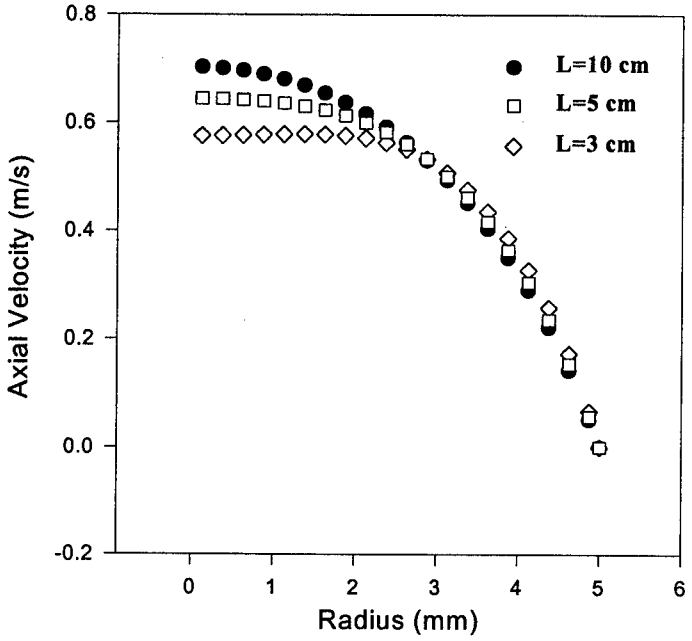
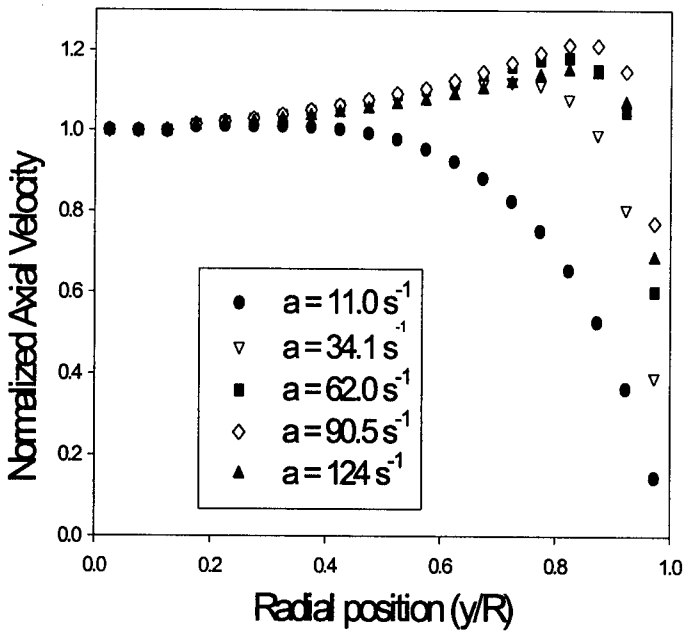


Figure 3: Normalized Axial Velocity at Tube Exit vs Radial Position For Two Opposed Converging Nozzles



TUESDAY SESSIONS
OCTOBER 12TH

Fall Technical Meeting, Eastern States Section, North Carolina State University, October 11-13, 1999.

Experimental Observation of The Formation and Development of a Laser Ignition Kernel

by

Tran X. Phuoc and Fredric White
Federal Energy Technology Center
U.S. Department of Energy
P.O. Box 10940, MS 84-340
Pittsburgh, PA 15236-0940
Phone: (412) 386-6024
Fax: (412) 386-6204
e-mail: tran@fetc.doe.gov

ABSTRACT

The high speed digital video camera is used in the study of single and multi-point laser spark ignition of CH_4-air mixtures in a constant-volume cell. The tests are carried out using two Q-switched Nd-Yag lasers lasing either at 1064 or 532 nm. Firing of the lasers was controlled by a digital delay/pulse generator. Two modes of firing were used: sequential firing, and simultaneously firing. The camera is configured to record the formation and temporal development of the ignition kernel, detonation wave velocities, and flame propagation speeds.

INTRODUCTION

When a high-energy, and short-pulse laser beam is focused into a small volume, a laser spark plasma is generated. A spark produced by this way has time scales much shorter than the kinetic time scale and the chemical induction time. It is apparently a localized point source of highly reactive chemical intermediates. Its temperature (in the order 10^6 K) and pressure (in the order of 10^3 atm) can be reached at the end of the laser pulse. This extreme condition relative to the ambient gas leads to the development of a rapidly expanding shock wave that is of sufficient strength to ignite a gaseous combustible mixture, liquid fuel sprays, or even to extinguish a diffusion flame. In our previous studies [1,2] on laser-induced spark ignition of CH_4-air mixtures having fuel volume fraction from 6.5 to 17% (equivalence ratio, ER, from 0.66 to 1.95), we reported that laser-induced spark ignition works moderately at fuel-lean conditions, but it favors fuel-rich conditions. The minimum ignition energy has its lowest value remaining at about 3 to 4 mJ for a mixture having 10 to 15% methane by volume (ER = 1.058 to 1.68) and it increases sharply toward the far-lean and the far-rich sides of the stoichiometry. Our result is about one order of magnitude higher than the minimum ignition energy reported by Lewis and von Elbe [3] using electric spark ignition (about 0.4 mJ) and the

computational prediction of Sloane [4] and Sloane and Ronney [5] using detailed chemical, hydrodynamic, and transport models (about 0.5 mJ for ER = 0.55, 0.10 mJ to 0.122 mJ for stoichiometric ratio, and 0.7 to 0.8 mJ for ER = 1.33). In comparison with the work reported by Lim et al. [6], our results are similar to theirs for a picosecond laser, but are higher than those measured by a nanosecond laser beam by a factor of about 3.

In the present work, both single and multi-point laser ignition will be studied. Using high-speed video visualization technique, we will focus on the dynamic formation and expansion of a laser-induced spark kernel generated in air, nitrogen, CH_4, H_2, C_3H_8, CH_4-air, H_2-air, and C_3H_8-air mixtures. Data on fundamental issues including spark pressure, temperature, absorption, emission, and expansion velocity, etc. will be measured and investigated.

EXPERIMENTAL APPARATUS

Detailed description of the research apparatus was given in [2]. For the present study, the laser ignition system consisted of two Q-switched Nd-Yag lasers. The laser beams were delivered and focused into the ignition cell using two separate 75 mm-focal length lenses. The lenses were mounted on two separate translational stages so that the focal points inside the chamber could be moved. Firing of the laser was controlled by a digital delay/pulse generator (Stanford Research System, DG535)

Several diagnostic devices were used to study the laser-induced ignition process. A high-speed digital imaging system (SENSICAM) was used to record spark formation and growth. The camera was operated with 'DoubleShort mode' and triggered by a TTL signal fed from the DG535. For space-resolved studies of laser-induced spark emission, the emissions lines were monitored using a Multichannel Instaspec IV CCD detection system (Oriel). It consisted of a front illuminated 1024 x 128 pixel format CCD detector head (Model 78430, Oriel), a MS260i imaging spectrograph (Model 74050, Oriel), a single-track fiber optic cable (Model 77403, Oriel), and a F-NO matcher (Model 77529, Oriel). The MS260i had a micrometer driven entrance slit with its width is variable from 4 μm to 3 mm and its height is from 2 to 12 mm. It was equipped with three gratings covering a spectrum of 250 to 900 nm. The emission light from the spark plasma was collected using the fiber-SMA with the F-NO matcher attached to the entrance slit of the MS260i spectrograph which was set at 25 μm for the present study. The spectral lines spread over through the MS260i exit slit and were detected by the detector which was operated under full-vertical binning mode. Signals from the detector were then analyzed by the InstaSpec software and a Gateway 500 Mhz computer.

RESULTS AND DISCUSSIONS

Typical results on the spark size are shown in Fig. 1, and images of the sparks are presented in Fig. 2. It was observed that the laser-induced spark was created after the laser was fired for about 270 to 350 ns. The spark had a short life (about 5 to 11 μs, depending on the laser energy) and was elongated in the direction of the laser beam. Separation of the spark plasma into several points along the laser beam and behind the focal point was also often observed. For methane lean or rich mixtures,

the spark had an oval shape, and its average long axis varied from about 0.8 to 2 mm while its short axis varied from about 0.4 to 1.2 mm, depending on the methane volume fraction. For stoichiometric and near-stoichiometric methane-air mixtures, the spark became cylindrical in shape; its length and radius were about 0.8 mm and 0.3 mm, respectively. The results are in the same order with the minimum flame kernel radius of 0.3 mm reported by Lewis and von Elbe [3]. In comparison with other laser-induced spark studies, our results are very much in agreement with the results reported by Klimkin et al. [7], Spiglanin et al. [8], and Lim et al. [6].

REFERENCES

1. Phuoc, T.X., and White, F., "Laser-Induced Spark Ignition of CH_4 - Air Mixtures," Joint Technical Meeting of the United States sections at The George Washington University, March 15-17, 1999 .

2. Phuoc, T.X., and White, F., "Laser-Induced Spark Ignition of CH_4 - Air Mixtures," to be published in Combustion and Flame, 1999.

3. Lewis, B., and von Elbe, G. *Combustion, Flames and Explosions of Gases*, 3rd ed. Academic Press, New York, 1987, p. 215.

4. Sloane, T.M., *Combustion Science and Technology*, 73:351 (1990).

5. Sloane, T.M., and Ronney, P.D., *Combustion Science and Technology,* 88:1 (1992).

6. Lim, E.H., McLLroy, A., Ronney, P.D., and Syage, J.A., in *Transport Phenomena in Combustion,* (S.H. Chan, Ed.), Taylor & Francis, 1996, p. 176.

7. Klimkin V.F., Soloukhin, R.I., and Wolansky, P., *Combustion and Flame,* 21:111 (1973).

8. Spiglanin, T.A., Mcilroy, A., Fournier, E.W., and Cohen, R.B., *Combustion and Flame,* 102:310 (1995).

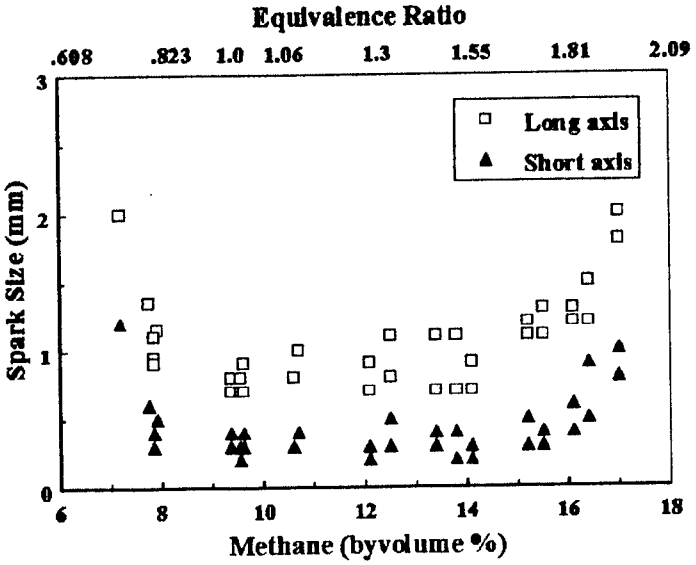


Figure 1. Measured ignition spark sizes of methane/air mixtures at 1 atm versus methane volume fraction.

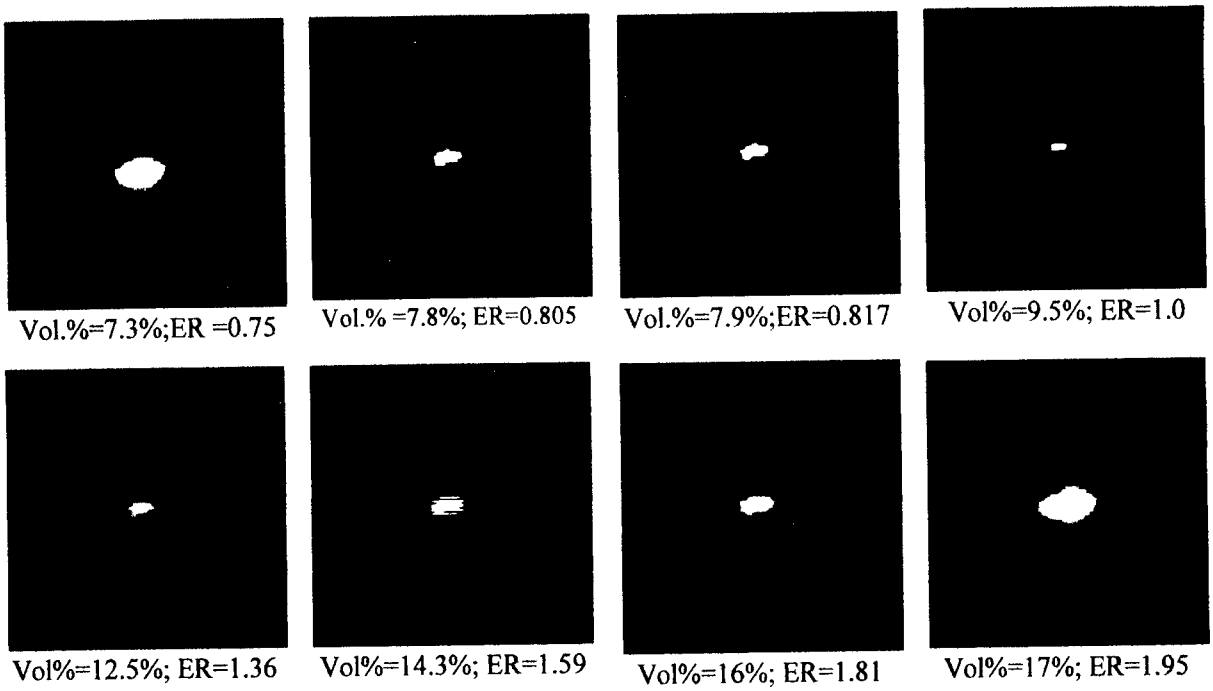


Figure 2. Images of ignition spark size for CH_4-air mixture as a function of methane concentration by volume (or equivalence ratio, ER).

Preliminary Test of Flame Kernel-Vortex Interaction

Yin Xiong, William L. Roberts
Department of Mechanical & Aerospace Engineering
North Carolina State University
P.O. Box 7910, Raleigh, NC, 27695-7910

Introduction:

This abstract describes preliminary results from a research project aimed at providing fundamental information regarding the chemistry-turbulence interaction. According to modern flamelet theory, a turbulent flame can be thought of as an ensemble of stretched laminar flamelets. The stretch, a measure of the hydrodynamic strain and flame curvature, can either increase or decrease the local laminar burning velocity. A turbulent flow field is inherently unsteady. Thus, to fully understand the turbulence- chemistry interaction, it is important to study the effect of a time-varying stretch rate on these flamelets. This is an extremely complex interaction and must be simplified considerably if any insight is to be gained. The objective of this research project is to gain a better understanding of how the local fluid dynamics affects the growth of spark-generated premixed flame kernel. This goal will be achieved by studying the interaction of a single well- defined eddy with known length and velocity scale with a flame kernel at different stages of growth. This abstract will discuss the experimental apparatus and the preliminary test results on flame kernel growth and vortex translational velocity measurements.

Experimental Apparatus:

• *Combustion Chamber*

A large stainless steel combustion chamber (25.4 cm in inside diameter and 30.5 cm in height) with its supporting platform was built for pressurized and non-pressurized combustion tests (Figure 1). Four side-arms (15 cm inside diameter) were welded to the chamber. 13 mm thick quartz windows are mounted on these side arms for flame image acquisition and laser diagnostics. A pair of electrodes are inserted into the chamber from two side arms in opposing directions, and the spark can be generated at the center point of the chamber between the gap of the electrodes. There are three positions to adjust the electrodes vertically, and the distance between the tips of the electrodes is continuously adjustable to investigate the influence on ignition energy. There is one inlet for reactants and four outlet ports for products flowing into and out of the chamber. Solenoid valves (normally open) are used to control the on/off of the four outlet ports.

• *Spark Ignition System*

A digital distributorless ignition system was built with a high energy, transistor-based ignition circuit and traditional ignition coil. This ignition system, with microsecond level response time, can build up to 35,000 V transient voltage difference between the tips of the electrodes, with the appropriate distance. The spark intensity also depends upon the pulse width of the trigger signal to the ignition circuit, which can be digitally controlled. The electrodes are made of stainless steel, and are coated by ceramic insulation tubes. The electrodes neck down to a diameter of 0.4 mm to minimize heat loss and flow disturbance.

• *Vortex Generation Apparatus*

To simulate various turbulent length and velocity scales, a single, well-defined vortex toroid is generated. Four sharp-edge stainless steel orifices with different diameters (2 mm, 5 mm, 10 mm and 20 mm) have been built for vortex generation. The characteristic length scale of the vortex scales directly with the orifice diameter. These orifices were attached to four different cylinders, which will hold these orifices exactly 10 orifice diameters above the ignition point inside the main combustion chamber (Figure 1). The ratio of cylinder diameter (inner) to orifice diameter is held approximately constant at 6.5. A large stepping linear actuator from UltraMotion was selected to drive these pistons with a thrust of 70 lbs. The distance the piston moves determines the amount of fluid expelled from the orifice. The velocity of the piston determines the characteristic velocity of the vortex toroid.

• ***Digital Driving and Control System***

A PC-based digital system has been built to drive, control and coordinate the entire flame-vortex apparatus. The digital system is based on LabView software and uses data acquisition boards from National Instruments (PC-TIO-10 and AT-MIO-16E). This system can be used as the front control panel and interactive interface for the apparatus. It includes triggering the spark ignition system, driving the linear actuator, triggering the camera, synchronizing the laser, timing and energizing the solenoid valves, and measuring the pressure inside the combustion chamber during tests.

Results:

• ***Flame kernel growth***

Flame kernels and their subsequent fully developed flames have been generated in CH_4/air mixtures using the ignition system described above, using a constant intensity spark. Kernel images of CH chemiluminescence at different stages of kernel growth have been acquired using an ICCD camera. From the comparison of these images, it is clear that the spark and flame kernels generated by this ignition system are very repeatable, both spatially and temporally. Figure 2 shows a typical CH* image of a growing flame kernel. The distance between the two electrodes is 3 mm, the spark duration is 2 ms, CH_4/air mixture equivalence ratio is 0.6, and the image is acquired 15 ms after triggering the spark.

Figure 3 shows the growth of a kernel in a gas mixture with an equivalence ratio of 0.8 during its first 20 ms after the spark, both in vertical and horizontal directions. Good linearity of these lines shows that the flame kernel grows at a constant speed within the premixed media. This is not the laminar burning velocity, however, due to expansion of hot products pushing the deflgration wave outward. This sequence is made up from 10 separate runs and shows the repeatability of the apparatus.

• ***Measurement of vortex translational velocity***

The ability to generate repeatable vortices of different sizes and strengths is an important precondition for further investigation of kernel-vortex interactions. The local translational velocity at the ignition point has been measured, both by hot-wire and standard camera-VCR system using Mie scattering of smoke particles. Dozens of repeatable vortices with different characteristic sizes (from 2 mm to 20 mm) and translational velocities (from under 10 cm/s to above 100 cm/s) have been obtained by varying the piston speed, piston travel and size of orifice. These tests show that the microsteps per strike, piston speed and the finesse of cylinder surface are among the most important factors determining vortex repeatability. It has been found that smaller orifices, shorter travel distances and faster piston speeds provide the highest vortex repeatability.

A vortex ring has two components of velocity, translational and rotational, in the laboratory coordinate system. Because of the small size of the investigated vortices, PIV is not likely to be implemented to measure the rotational velocity of vortex rings. The translational velocity of the vortex is assumed to be equal to the maximum rotational velocity. Figure 4 shows some results of vortex translational velocity measured by Mie scattering video system vs. piston speed with three different orifices.

Mie scattering tomography of the generated vortices has been acquired, and Figure 5 shows a typical image. Great inside detail is shown from this picture of 20 mm vortex, around ignition point.

Acknowledgment

This work is currently supported by the National Science Foundation, Grant CTS-9702277, under the technical direction of Dr. F. Fisher.

Reference:

[1] D. A. Eichenberger, W.L.Roberts, " Effect of Unsteady Stretch on Spark-Ignited Flame Kernel Survival", Combustion and Flame, Vol. 118, pp469-478, 1999.

[2] A.Eckbreth, "Laser Diagnostics for Combustion Temperature and Species", Abacus Press, Cambridge, MA (1996).
[3] Roberts, W.L. and Driscoll, J.F., "A Laminar Vortex Interacting with a Premixed Flame: Measured Formation of Pockets of Reactants," Combustion and Flame, vol.87, p245-256, 1991.
[4] Glezer, A., and Coles, D., " An Experimental Study of a Turbulent Vortex Ring", Journal of Fluid Mechanics, vol. 211, pp243-283, 1990.
[5] Roberts, W.L., Driscoll, J.F., Drake, M.C., and Ratcliffe, J., Twenty-Fourth Symposium (International) on Combustion, The Combustion Institute, Pittsburgh, 1992, pp. 169-176.
[6] Muller, C.J., Driscoll, J.D., Roberts, W.L., Drake, M.C., and Smooke, M.D., Combustion and Flame, vol. 100, pp.323-331, 1995.
[7] Nguyen, Q.-v., and Paul, P.H., Twenty-Sixth Symposium (International) on Combustion, The Combustion Institute, Pittsburgh, 1996.

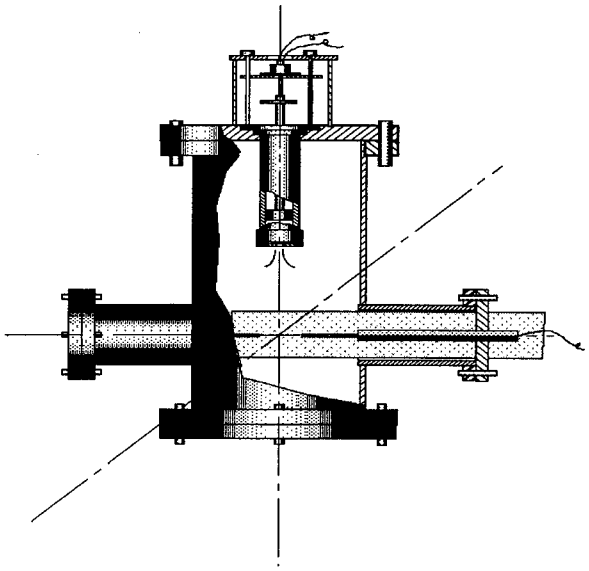


Fig.1 Experimental Setups (main combustion chamber)

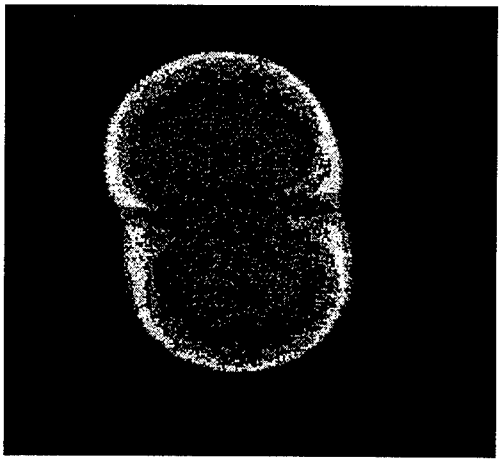


Fig. 2 Flame kernel

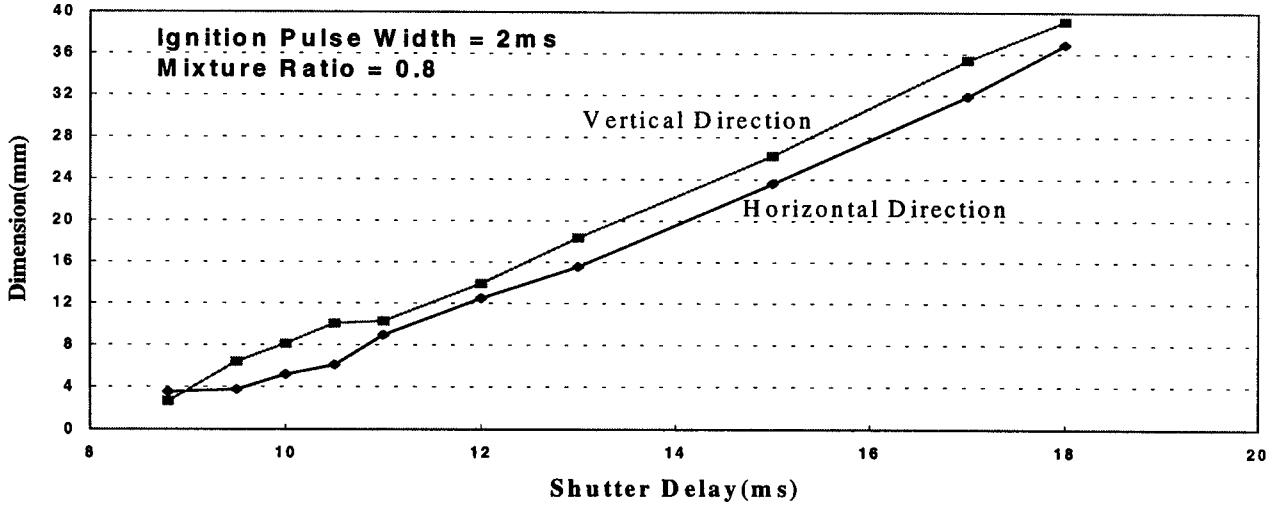


Fig. 3 Growth of flame kerne in diameters of X,Y

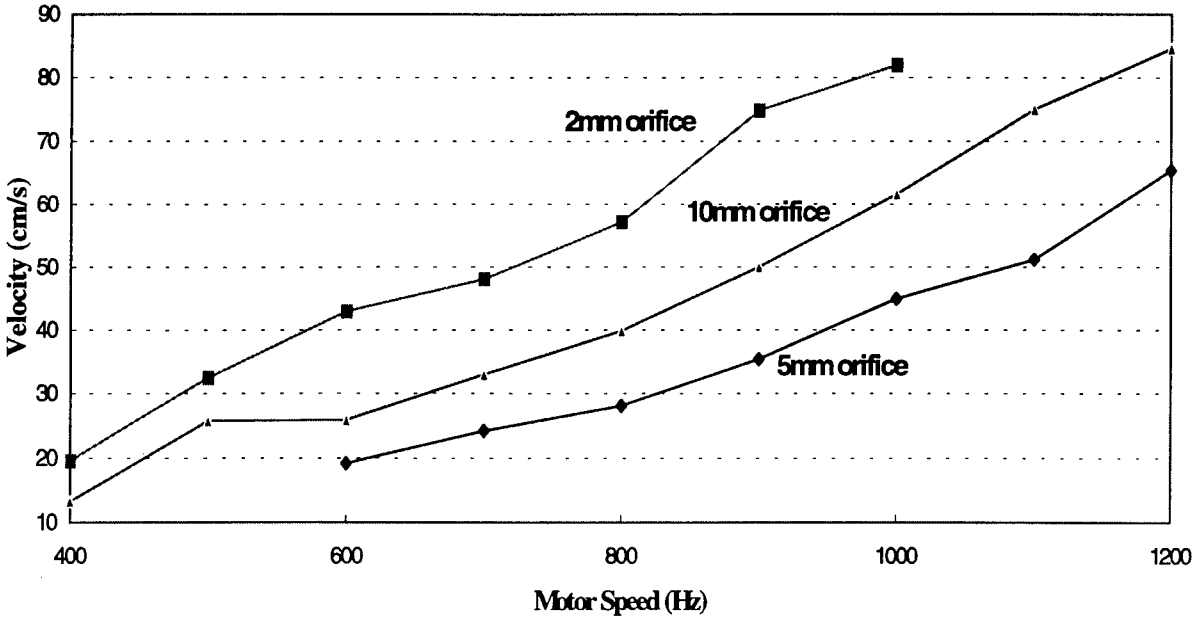


Fig. 4. Instant vortex velocity for 2,5,10mm orifices from video system

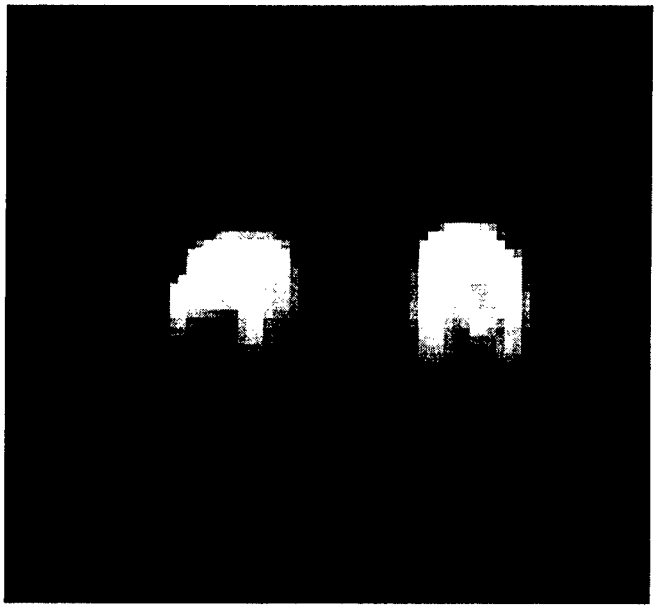


Fig. 5. Mie Scattering Tomography of a Vortex

Non-Premixed Ignition of n-Heptane and iso-Octane in a Laminar Counterflow*

J. D. Blouch and C. K. Law
Department of Mechanical and Aerospace Engineering,
Princeton University, Princeton, NJ 08536

Introduction

The ignition characteristics of n-heptane and iso-octane are of interest for their role as reference fuels for engine knock and their different fuel structures. Understanding the combustion chemistry of these two fuels gives general insight into the combustion of linear and branched alkanes, which are major constituents of practical fuels. Considerable research has been conducted on them, but most of it has focused on homogenous mixtures. These investigations have included studies of autoignition temperatures [1], ignition delay in shock tubes [2] and rapid compression devices [3], studies of pyrolysis and oxidation in flow reactors [4,5], and measurements of flame speeds [6]. Detailed chemical models have been developed to describe their combustion behavior. Smaller empirical models have also been developed to facilitate calculations [5,6].

In many situations, however, ignition occurs in strongly non-homogenous environments with large temperature and concentration gradients. It is therefore of interest to investigate whether results obtained from and validated through homogenous experiments apply under these circumstances. To address this issue, a combination of experimental and numerical techniques have previously been used to investigate non-premixed ignition in a laminar counterflow for hydrogen [7,8], methane [9], ethane, propane, n-butane, and iso-butane [10]. Ignition in this configuration provides an additional test for the comprehensiveness of the chemical models due to the highly non-uniform conditions experienced by the reactants as they are swept through the flow field.

The present study extends the non-premixed work to n-heptane and iso-octane. In addition to experimental observations, empirical models are evaluated for application to this problem. In the following, the experimental procedure will be described, followed by presentation and discussion of the results.

Experimental and Numerical Procedure

The experimental equipment and technique have been described extensively elsewhere and only a brief overview will be given here. The burner [7] is made from quartz tubes (20mm inside diameter) that are aligned axially and separated by one tube diameter. A fuel/inert mixture is sent through the bottom burner, and air issues from the upper burner. Both the upper and lower burner tubes are surrounded by a nitrogen coflow to improve the counterflow stability and to isolate the reactants from the environment. The air is heated by a silicon carbide heater that is controlled by a temperature controller.

Since the ignition apparatus requires fuel in a gaseous form, the liquid n-heptane and iso-octane fuels have to be prevaporized as described in Davis *et al.* [11]. Care is taken to keep the partial pressure of the gaseous fuel below the vapor pressure of the fuel, and a gas analyzer is used to verify the fuel concentration. The low vapor pressures of n-heptane and iso-octane limit the range of fuel concentrations and pressures that can be examined experimentally.

Flow rates of fuel mixture and air are set so that the stagnation surface is midway between the burner tubes. Laser doppler velocimetry is used to measure the axial velocity profile in the flow field, and the strain rate is determined by finding the axial velocity gradient on the oxidizer side of the

* For presentation at the 1999 Technical Meeting of the Eastern States Section of the Combustion Institute, Raleigh, NC, October 11-13.

stagnation surface. The temperature of the air is then increased until a flame is observed. The flame is extinguished, and the temperature at the oxidizer exit is recorded using a K-type thermocouple with a bead diameter of about 180 microns. This temperature is corrected for radiation losses [7] and is defined as the ignition temperature. Earlier hydrogen and ethane experiments were reproduced on the present apparatus to ensure that the current results can be compared to the previous experiments.

Calculations are performed using the flame continuation method of Nishioka *et al.* [12] with the model of Held *et al.* [5] for n-heptane, Davis *et al.* [6] for iso-octane, and detailed transport. Neither of the mechanisms include reactions associated with low temperature chemistry. The calculations find points along the steady-state S-curve, and the ignition temperature is taken to be the oxidizer boundary temperature at the lower turning point of the hydrogen radical concentration. Sensitivity analysis is performed by perturbing the reaction rates and observing the effect on the oxidizer boundary temperature. A *lower* boundary temperature for a given hydrogen concentration indicates *enhanced* reactivity. To avoid any confusion, the negative of the normalized sensitivity coefficients is reported here so that the intuitive relation, where positive sensitivity indicates higher reactivity, is maintained.

Results and Discussion

The effects of strain rate on the ignition temperature of n-heptane and iso-octane are shown in Figs. 1 and 2 respectively. The qualitative trends are similar to the other hydrocarbon fuels studied; an increase in ignition temperature as the strain rate rises. Iso-octane has a significantly steeper slope (0.22 K/s^{-1}) than the other fuels, while n-heptane has a slope (0.14 K/s^{-1}) similar to ethane, which is steeper than the other fuels studied (0.09 K/s^{-1}). This slope gives a rough estimate of the sensitivity of ignition temperature to strain rate. For both fuels, the qualitative agreement between experiment and calculation is good, although the experimental values are approximately 100K lower. The experiments have a relative error of about ±5K. However, there is a significantly larger absolute error due to uncertainties in the radiation model applied to the thermocouple measurements. This error affects all of the experimental data similarly, and representative values of this effect are indicated by the error bars in Figs 1 and 2. The difference between experimental and computational results is similar in magnitude to the disagreement found with ethane [10], and for all three fuels the measured ignition temperatures are consistently higher than the calculated ones.

Figures 3 and 4 display the effect that pressure has on the ignition temperature of n-heptane and iso-octane. The maximum pressure available to experimentation for both fuels is limited by the vapor pressure, which is why a low fuel concentration was chosen for this set of experiments. These results are qualitatively similar to butane over a similar temperature and pressure range. The experimental temperatures are again about 100K lower than the calculated values, and the iso-octane experiments are qualitatively similar to the calculations. However, the n-heptane experiments show a steeper slope at pressures above one atmosphere, meaning that the experimental temperatures are less dependent on pressure under these conditions.

The absence of low temperature chemistry is not expected to account for the difference between calculated and experimental results. Evidence of this includes the shape of the curves in Figs. 3 and 4, which is similar to the first, high temperature regime found for both butane isomers. In this regime, low temperature plays only a small role, and does not assume a major role until the second regime is entered at higher pressures where the curves become flatter (higher pressure sensitivity). This is not observed for either fuel under the conditions examined here. In addition, the normalized sensitivity coefficients for n-heptane and iso-octane, shown together in Fig. 5 at their respective ignition temperatures, show many of the classical high temperature reactions (such as those found in both shock tube [5] and flame speed [6] studies).

Furthermore, calculations for ethane showed that low temperature chemistry did not have a qualitative effect on the shape of the calculated S-curve at one atmosphere. The quantitative effect was to *decrease* ignition temperature slightly since the low temperature reactions compete with the high

temperature chain branching reactions that lead to ignition. The fact that the dominant chain branching mechanisms for both low temperature and high temperature chemistry are not qualitatively different between butane, n-heptane, and iso-octane suggests that the earlier results may provide some insight into the current situation. This is reinforced by the fact that the sensitivity coefficients for the present fuels are similar to the ignition sensitivity results for ethane. This means that the addition of low temperature chemistry may not improve the agreement between the experiments and calculations and would likely make it somewhat worse.

The high sensitivity of strongly exothermic reactions, such as CO_2 formation, indicates that heat release plays an important role in ignition. To show this, the role of heat release in ignition was investigated by removing the heat release terms from the energy equation. The result is shown in Fig. 6 where an S-curve with heat release is compared to one with the heat release "turned off." As with ethane, there is no effect until the ignition temperature is approached; yet without heat release a turning point is never reached and the system reactivity continues to increase monotonically with temperature. Similar results were found with n-heptane.

Figure 7 compares the non-premixed ignition temperatures of fuels studied to date. It is seen that after methane, the ignition temperatures increase with molecule size until n-heptane and iso-octane, which are somewhat lower than n-butane and iso-butane respectively. In contrast, autoignition temperatures in homogenous systems show a decreasing trend with increasing carbon number that becomes nearly constant beyond hexane. The non-monotonic trend suggests that the coupling between kinetics and transport is very complex and has a significant effect on the diffusive ignition characteristics of these fuels. Nevertheless, these results show that the qualitative response of n-heptane and iso-octane is not very different from that of ethane, propane, n- butane, and iso-butane.

Acknowledgement

This work has been supported by the Army Research Office under the technical monitoring of Dr. D. Mann. We thank Dr. S. G. Davis and Professor H. Wang for helpful comments.

References

1. M. Zabetakis, in *Flamability Characteristics of Combustable Gasses and Vapors* Bulletin 627, US Bureau of Mines (1965).
2. D. J. Vermeer, J. W. Meyer and A. K. Oppenheim, *Combust. Flame* 18, 327-336 (1972).
3. R. Minetti, M. Ribaucour, M. Carlier and L. R. Sochet, *Combust. Sci. Technol* 113-114, 179-192 (1996).
4. T. J. Held, A. J. Marchese and F. L. Dryer, *Combust. Sci. Technol.* 123, 107-146 (1997).
5. F. L. Dryer and K. Brezinsky, *Combust. Sci. Technol.* 45, 199-212 (1986).
6. S.G Davis and C. K. Law, *Twenty-Seventh Symposium (International) on Combustion*, The Combustion Institute, Pittsburgh, PA, 1998, pp. .
7. C.G. Fotache, T.G. Kreutz, D.L. Zhu and C.K. Law, *Combust. Sci. Technol.* 109, 373-394 (1995).
8. T.G. Kreutz and C.K. Law, *Combust. Flame* 104, 157-175 (1996).
9. C.G. Fotache, T.G. Kreutz and C.K. Law, *Combust. Flame* 108, 442-470 (1997).
10. C.G. Fotache, H. Wang and C.K. Law, *Combust. Flame*, in press.
11. S.G. Davis, H. Wang, K. Brezinsky and C.K. Law, *Twenty-Sixth Symposium (International) on Combustion*, The Combustion Institute, Pittsburgh, PA, 1996, pp. 1025-1033.
12. M. Nishioka, C.K. Law and T. Takeno, *Combust. Flame* 104, 328-342 (1996).

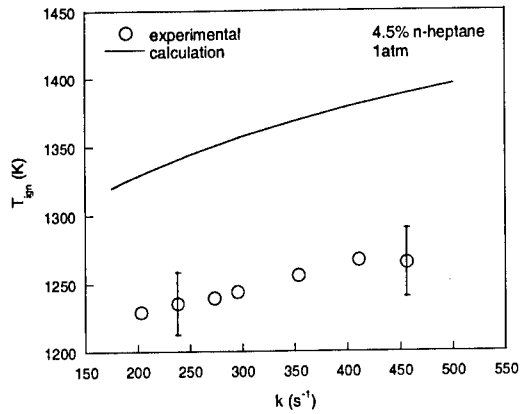


Figure 1: Effect of strain rate on ignition for n-heptane.

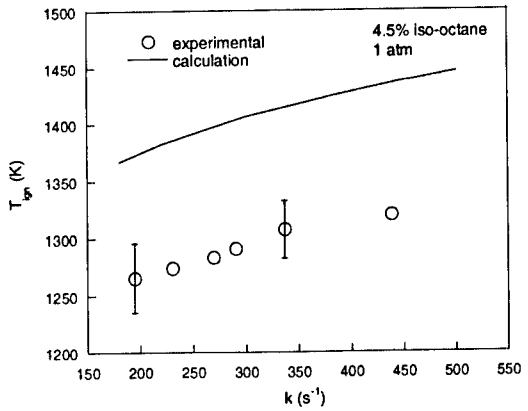


Figure 2: Effect of strain rate on ignition for iso-octane.

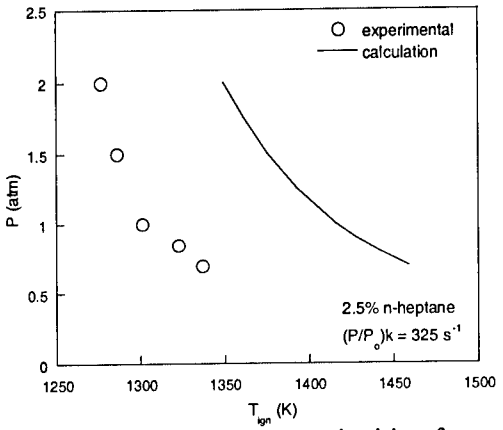


Figure 3: Effect of pressure on ignition for n-heptane. P_o = 1 atm.

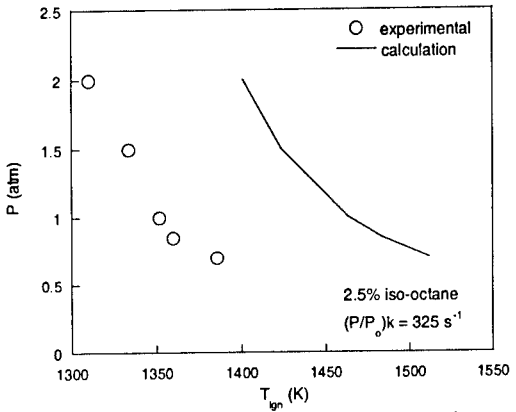


Figure 4: Effect of pressure on ignition for iso-octane. P_o = 1 atm

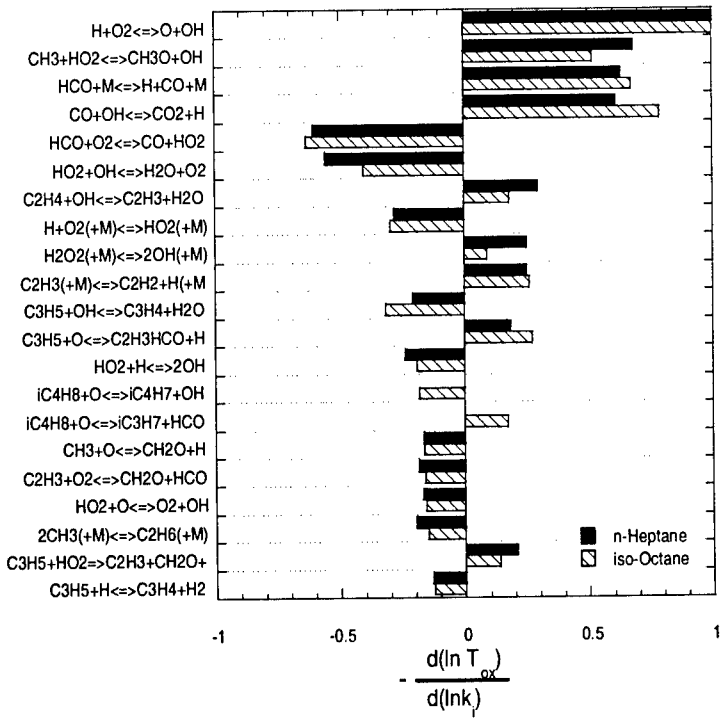


Figure 5: Normalized sensitivity coefficients at 1406K (iso-octane) and 1358 K (n-heptane).

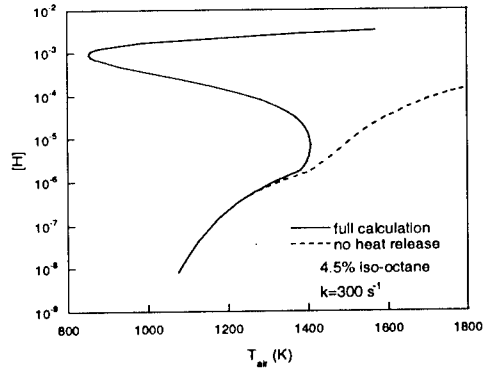


Figure 6: Effect of heat release on ignition.

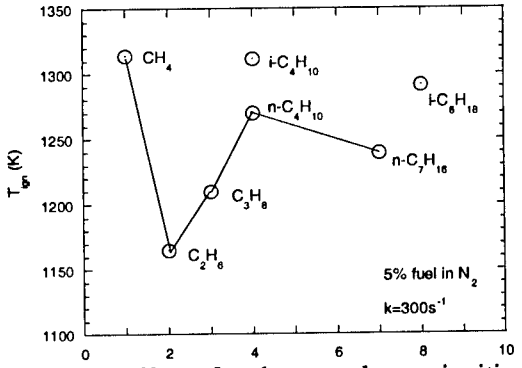


Figure 7: Effect of carbon number on ignition temperature.

DEVELOPMENT OF AN ANALYTICAL CRITERION FOR THE IGNITION OF PREMIXED ALKANE/AIR MIXTURES NEAR PLATINUM SURFACES[#]

P. Aghalayam and D. G. Vlachos*
Department of Chemical Engineering, University of Massachusetts Amherst, Amherst, MA 01003-3110
vlachos@risky.ecs.umass.edu

ABSTRACT

A generalized criterion to predict the ignition temperatures of various alkane/air mixtures over platinum as a function of their inlet composition has been developed. The agreement of the criterion with predictions using detailed chemistry is excellent for methane/air mixtures. By extending this criterion to the ignition of higher alkanes, values of sticking coefficients for the adsorption of hydrocarbons have been calculated. The activation energy of adsorption is found to decrease with increasing carbon number. Reasonable comparison of the predictions with experimental data has been obtained for ethane, propane, and butane.

INTRODUCTION

Catalytic combustion of hydrocarbons is important as it is an efficient and relatively clean process [1]. Ignition of the combustion mixture is an unavoidable step during the start-up. Experimental data on complete bifurcation diagrams for many hydrocarbons has recently been published [2]. An apparent activation energy for ignition of hydrocarbons over a platinum catalyst has been derived using various approximations [2]. An analytic criterion describing the ignition of H_2/air mixtures has first been derived in [3], by developing a reduced kinetic mechanism and a simplied model for the transport. A similar one has also been derived recently for CH_4/air mixtures [4].

In this study, an analytical expression capable of predicting ignition over a large range of CH_4/air compositions is developed, based on the reaction mechanism of [5]. Application of this analytical criterion to derive activation energies and sticking coefficients for the adsorption of higher alkanes including ethane, propane, and butane is also undertaken.

MODEL

A stagnation-point flow configuration is considered here, where a premixed fuel/air mixture impinges onto a flat catalytic surface which is resistively heated. The governing equations and numerical methods are described in [6]. A comprehensive surface reaction mechanism to describe the ignition of methane/oxygen/nitrogen mixtures near platinum surfaces, proposed in [5], is used. The mechanism consists of 7 species among 20 interfacial reactions. The GRI 1.2 reaction mechanism is employed for the gas-phase chemistry.

BRIEF NOTE ON RESULTS OF SIMULATIONS WITH FULL CHEMISTRY

Fig. 1 shows the predictions of ignition for a 10% inlet CH_4/air mixture, using the full surface reaction mechanism of [5] for the conditions indicated. As the heat input to the system is increased, the surface temperature first increases. At a certain heat input, the system jumps to high temperatures, with a correspondingly sharp increase in the reactivity. This turning point is termed as an ignition. Fig. 1 shows that prior to ignition the major species on the catalyst is adsorbed oxygen, O*, with a coverage (fraction of adsorbed sites) of ~1.0. Other species such as C* and H* are present in very low concentrations prior to ignition. Upon ignition, the O* comes off the surface.

Table 1: Simplified Surface Reaction Mechanism for CH_4/Air Ignition

Reaction	k_0 (s^{-1} or sticking coefficient)	E (Kcal/mol)	
$CH_4 + 5* \rightarrow C* + 4H*$	0.1	10.3	R1
$O_2 + 2* \rightarrow 2O*$	$3\ 10^{-4}$	0	R2
$2O* \rightarrow O_2 + 2*$	$5\ 10^{12}$	52.0	R3
$C* + 2O* \rightarrow CO_2 + 3*$	$5\ 10^{13}$	15.0	R4
$2H* + O* \rightarrow H_2O + 3*$	$1\ 10^{15}$	2.5	R5

Acknowledgement is made to the Office of Naval Research with Dr. G. D. Roy through a Young Investigator Award under contract number N00014-96-1-0786.

* Corresponding author.

Analysis indicates that the ignition is driven by the site-competition between methane and oxygen. In particular, the ignition temperature is only strongly dependent on the sticking coefficients of methane and oxygen, and O* desorption [5], i.e., the rate limiting step is adsorption of the fuel and surface reactions are fast. Steady-state balances for surface species can be used to eliminate reactions from the full set (see [3] for a similar analysis of hydrogen/air mixtures). Table 1 above shows the reduced surface reaction mechanism obtained, following the methodology for H_2/air mixtures, consisting of 4 surface species and 5 reactions.

ANALYSIS OF THE SURFACE CHEMISTRY AT IGNITION

The reduced surface chemistry for methane listed in Table 1 may be used to derive the steady-state balances for the surface species (except the vacancies):

$$\frac{d\theta_{C*}}{dt} = 0 = r_1 - r_4, \quad (3) \qquad \frac{d\theta_{H*}}{dt} = 0 = 4r_1 - 2r_5, \quad (4) \qquad \frac{d\theta_{O*}}{dt} = 0 = 2r_2 - 2r_3 - 2r_4 - r_5. \quad (5)$$

Substituting Eqs. 3 and 4 into Eq. 5 yields

$$r_2 - r_3 - 2r_1 = 0. \quad (6)$$

Assuming that the adsorption of methane and oxygen are both second order in vacant catalyst sites, Eq. 6 becomes

$$(k_2 - 2k_1)\theta_*^2 = k_3\theta_{O*}^2. \quad k_1 = \frac{s_1 p_1 \exp(-E_1 / RT_s)}{\sqrt{2\pi M_1 RT_s}}, \qquad k_2 = \frac{s_2 p_2}{\sqrt{2\pi M_2 RT_s}} \quad (7)$$

where s_i are the sticking coefficients, M_i are molecular weights, E_1 is the activation energy for methane adsorption, and p_1 and p_2 are the partial pressures of methane and oxygen, respectively.

Prior to ignition, the major species on the surface is oxygen, as shown in Fig. 1. Thus, we may assume that the fractional coverage of vacant sites is (given that the other species are negligible)

$$\theta_* = 1 - \theta_{O*}. \quad (8)$$

Using Eqs. 7 and 8, we obtain,

$$\theta_* = \frac{-K + \sqrt{K}}{1 - K} \sim \sqrt{K}, \text{ where } \quad K = \frac{k_3}{k_2 - 2k_1}. \quad (9)$$

K is a small number (and thus θ^* can be approximated as above).

Using Eqs. 3-5 and the fact that reactions R2 and R3 are the reverse of each other, the heat generated by the surface reactions may be written as

$$\sum_{i=1}^{N_s} r_i^s \Delta H_i^s = r_1(\Delta H_1 + 2\Delta H_2 + \Delta H_4 + 2\Delta H_5). \quad (10)$$

Furthermore, the heat of complete combustion of methane is

$$\Delta H_{CC} = \Delta H_1 + 2\Delta H_2 + \Delta H_4 + 2\Delta H_5 = -191 Kcal / mol. \quad (11)$$

Thus, the total heat of surface reactions in the boundary condition may be written as

$$\sum_{i=1}^{N_s} r_i^s \Delta H_i^s = k_1 \theta_*^2 \Delta H_{CC}. \quad (12)$$

DEVELOPMENT OF AN ANALYTICAL CRITERION FOR IGNITION

Based on asymptotic analysis, the energy boundary condition at the catalyst wall may be written as [4]

$$0.57 \mathrm{Pr}^{2/5}(T_s - T_e) + \frac{\mathrm{Pr}}{C_p\sqrt{2\alpha\rho_e\mu_e}}(r_1\Delta H_{CC} + \varepsilon\sigma(T_s^4 - T_e^4) + h_l(T_s - T_e) - P_w) = 0, \quad (13)$$

where Pr is the Prandtl number, C_p is the heat capacity of the inlet mixture, α is the strain rate, ρ_e and μ_e are the inlet density and viscosity, respectively, ε is the surface emissivity, P_w is the input heat flux to the surface, h_l is the convective heat loss, and T_s and T_e are the surface and inlet temperatures respectively. Given the rate expression for r_1, and Eq. 9, Eq. 13 provdes the surface temperature for a given P_w. Using singularity theory, at ignition [3],

$$\frac{dP_w}{dT_s} = 0. \quad (14)$$

Differentiating the boundary condition with respect to T_S yields (ignoring the temperature dependence of the heat of combustion, which is small)

$$0.57 \mathrm{Pr}^{2/5} + \frac{\mathrm{Pr}}{C_p\sqrt{2\alpha\rho_e\mu_e}}[\Delta H_{CC}\frac{dr_1}{dT_s} + 4\varepsilon\sigma T_S^3 + h_l] = 0. \quad (15a)$$

$$\frac{dr_1}{dT_s} = k_1\left[\frac{KE_3}{RT_s^2} + \frac{2K^2}{k_3}k_1\left(\frac{E_1}{RT_s^2} - \frac{1}{2T_s}\right)\right] + k_1\theta_*^2\left(\frac{E_1}{RT_s^2} - \frac{1}{2T_s}\right), \quad (15b)$$

where E_1 and E_3 are the activation energies of R1 and R3 respectively, and R is the ideal gas constant.

Since catalytic ignition temperatures are low enough, we can ignore the radiation term as a first approximation. The heat loss h_l has been estimated from experiments in [7]. The Prandtl number and the properties of the gas-mixture can be easily calculated. Thus, Eq. 15 can be used to obtain ignition temperatures as a function of the inlet fuel composition, and compare with the available experimental data. A similar criterion has been developed recently in [4] although in that study, the inlet was preheated in order to ignite the mixture. Moreover, the kinetic parameters used there (obtained from [8]) are such that no ignition is predicted by the criterion beyond ~30% inlet CH_4 in air, whereas the experiments indicate ignition up to 80% CH_4 in air. Finally, the activation energy of desorption of O* had to be adjusted in order to give reasonable comparisons with the experimental data [4].

Fig. 2 shows the ignition temperatures for methane/air mixtures obtained experimentally, along with the predictions using the ignition criterion. It is seen that there is very good agreement between the experimental data and the criterion. Some deviations occur in the very fuel-lean and very fuel-rich regimes. This is expected since the simplifications made in the surface chemistry become less valid near cusp points.

GENERALIZING THE CRITERION TO HIGHER ALKANES

The ignition criterion may be derived for other alkanes, assuming the same mechanism, i.e., an O* covered surface prior to ignition and relatively fast surface reactions. The lumped adsorption step of an alkane may be represented as

$$C_xH_y + (x+y)^* \rightarrow xC^* + yH^*.$$

The other steps in the simplified surface reaction mechanism are the same as listed above for methane. Thus, for any alkane C_XH_Y (with y=2x+2), we get, for second order adsorption in vacancies,

$$(k_2 - xk_1 - \frac{y}{4}k_1)\theta_*^2 = k_3\theta_{O*}^2. \quad (16)$$

Eq. 16 is used to derive an analytic criterion for the higher alkanes using the approach outlined above. The albegra is similar, with only the denominator of K changing to reflect the different stoichiometry

$$K = \frac{k_3}{k_2 - (x + y/4)k_1}. \quad (17)$$

The higher alkanes show a different behavior of ignition temperature vs. composition compared to methane [2]. While over most the composition regime, a promotion of ignition by the fuel is observed, i.e., the ignition temperature drops with increasing inlet fuel composition, at fairly fuel-rich conditions, a minimum in the ignition temperature is seen, with the fuel inhibiting its ignition beyond this composition. Since the criterion has been developed for promoting fuels, the data has only been analyzed up to this minimum. This minimum has been used as an estimate of the pre-exponential of adsorption. The numbers thus obtained are tabulated below. We have also calculated an activation energy using the bond-order conservation (BOC) theory [9] and obtained 8.7 Kcal/mol for the hydrogen abstraction from ethane, on platinum. Experiments on Pt(111) surfaces have indicated that the sticking probabilities increase with increasing carbon number [10]. Using the sticking coefficients and activation energies we have obtained here, at fixed temperatures, we obtain the same trend for the rate constants of adsorption of the different alkanes. Previous calculations have shown a decreasing apparent activation energy for the hydrocarbon ignition process, with increasing carbon number [2], assuming partial equilibrium between molecular adsorption-desorption of the hydrocarbon, and rate limiting step being the surface reaction. However, our calculations for methane indicate that the adsorption is the rate-limiting step and the surface reactions are fast prior to ignition. The ignition temperatures versus the modified equivalence ratio predicted in this study are shown in Fig. 3, along with the experimental data [2].

Table 2: Kinetic Parameters for the Adsorption of the Alkanes

	Methane	**Ethane**	**Propane**	**Butane**
Sticking Coeff.	0.1	0.14±0.06[a]	0.03±0.01[a]	0.01±0.005[a]
E_1 (Kcal/mol):				
This work [b]	10.6	8.4± 1.0[a]	5.0±0.5[a]	3.4±0.5[a]
BOC	12.0	8.7	-	-

[a]The error bars reflect an uncertainty of ~10 K in ignition temperature of the minimum point, and ~0.02 in Θ due to uncertainties the estimation of the minimum point. Propane and butane are insensitive to changes in composition, and the error bars for these reflect temperature uncertainties only.

b These numbers are for the parameters listed in Table 1 (other than the fuel adsorption).

CONCLUSIONS

A simple analytical criterion for the ignition of methane/air mixtures over platinum surfaces has been developed for a resistively heated platinum foil using singularity theory and a reduced surface reaction mechanism. The latter has been obtained based on O* being the dominant species on the surface prior to ignition, and the surface reactions being fast. Good agreement between the criterion predictions, the full calculations, and the experimental data has been found.

The criterion has subsequently been applied to the ignition of higher alkanes (ethane, propane, and butane). The sticking coefficient and activation energy for the adsorption of each alkane has been obtained from a fit of the experimental data, in the regime where the fuel promotes ignition. Predicted activation energies for methane and ethane are in reasonable agreement with independent BOC predictions.

REFERENCES

1. Pfefferle, W. C. and Pfefferle, L. D., *Prog. Energy Combust. Sci.* 12: 25-41 (1986).
2. Veser, G. and Schmidt, L. D., *AIChE J.* 42: 1077-1087 (1996).
3. Bui, P. A., Wilder, E. A., Vlachos, D. G., and Westmoreland, P. R., *Combust. Sci. Technol.* 129: 243-275 (1997).
4. Trevino, C., *AIChE J.* 45: 567-573 (1999).
5. Bui, P.-A., Vlachos, D. G., and Westmoreland, P. R., *Surf. Science* 385: L1029-1034 (1997).
6. Bui, P. A., Vlachos, D. G., and Westmoreland, P. R., *Ind. Eng. Chem. Res.* 36: 2558-2567 (1997).
7. Fernandes, N., Park, Y. K., and Vlachos, D. G., *Combust. Flame* 118: 164-178 (1999).
8. Deutschmann, O., Schmidt, R., Behrendt, F., and Warnatz, J., *Twenty Second Symposium (International) on Combustion, The Combustion Institute, Pittsburgh*, 1996, pp. 1747-1754.
9. Shustorovich, E. and Sellers, H., *Surface Science Reports* 31: 1-119 (1998).
10. McMaster, M. C., Arumainayagam, C. R., and Madix, R. J., *Chemical Physics* 177: 461-472 (1993).

Fig. 1

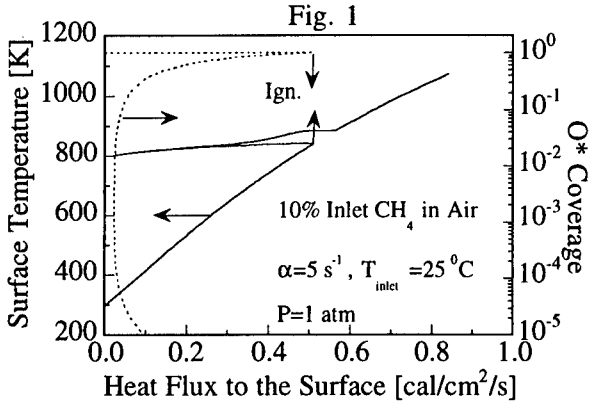


Fig. 2

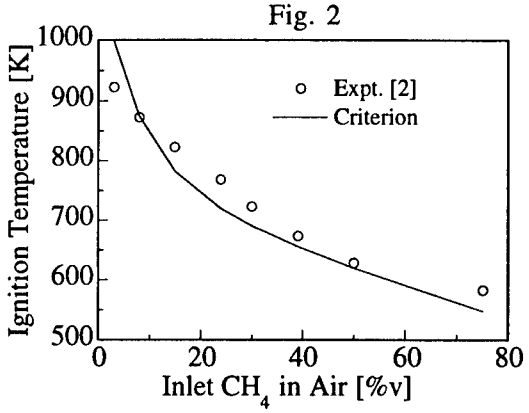
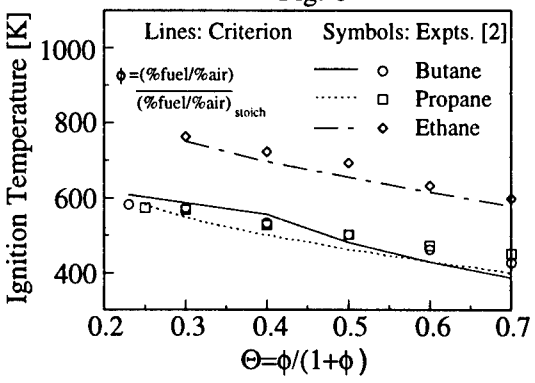


Fig. 3



Investigation of the Effect of Additives on the Composite Ignition Delay of JP-7 and JP-8

D. C. Kirk, J. L. Graham, and S. S. Sidhu*, University of Dayton Research Institute, Dayton, OH 45469-0132
*sidhu@udri.udayton.edu

L. Q. Maurice, Propulsion Directorate, Air Force Research Laboratory, WPAFB, OH 45433

Abstract

Performance studies have established the potential operational gains offered by airbreathing engines such as ramjets, supersonic combustion ramjet (scramjet) and combined cycle systems flying in the hypersonic regime at moderate altitudes.[1] A significant challenge in developing these propulsion systems is the propellant packages that will fuel them. For example, liquid hydrogen offers excellent energetic and vehicle coolant perspectives, however, the logistics, safety, and the high cost limit its use.[2] Hence, there is considerable interest in developing alternative high performance fuels. Consequently, the U.S. Air Force has defined a program to develop technologies required for a fixed geometry scramjet engine capable of operation in the Mach 4-8 flight regime using conventional JP-based hydrocarbon fuels.[3,4]

The practical application of a candidate fuel demands long-term storability, high density, and suitable ignition and combustion characteristics. Furthermore, with the evolution of regeneratively cooled engine and airframe technology, an acceptable fuel will need to have the appropriate cooling capacity. Hydrocarbon fuels are of particular interest because of their general availability and handling characteristics. Unfortunately, present hydrocarbon jet fuels do not meet the strict combustion time restrictions of hypersonic flight.[2, 5]

In an effort to improve the ignition characteristics of JP-fuels emphasis has been placed on combustion enhancement techniques.[5-7] Thermal and highly reactive free radical mechanisms are responsible for ignition enhancement and numerous techniques have been proposed that involves either one or both of these mechanisms. Examples of proposed methods include hot gas piloting, photo irradiation, energy intensive ignition sources (laser, plasma, etc.), heterogeneous catalysts, and homogeneous catalysts. The optimum method for the initiation of combustion in scramjets should be reliable and flexible in operation, and not require excessive ancillary equipment onboard the vehicle. The homogeneous catalyst technique is arguably preferred because additives are carried along as part of the fuel and as such provides the potential of eliminating special hardware and/or additional power sources that are inherent with the other techniques. Moreover, a large commercial market currently exists for combustion initiators in diesel fuels.[8]

The efficacy of several compounds in reducing ignition delay in gaseous n-heptane ignition delay times has been established.[6] However, liquid evaporation and mixing also contributes to the overall ignition delay when droplets are injected in heated gases, and they may even be the most important factors if the chemical timescales are short compared to the physical timescales. Hence, it is also necessary to establish the effectiveness of combustion promoters in liquid jet fuels. Jet fuels are complex mixtures of hydrocarbons that meet general physical property specifications to meet operational requirements.[9] A general summary of the properties of jet fuels has been recently compiled.[10] Jet fuels are noted to comprise paraffins, naphthenes and aromatic compounds. Thus, as with neat hydrocarbons, the addition of additives containing oxygen and nitrogen based groups should shorten ignition delays of JP-fuels. Accordingly, the experimental study described herein is based upon the use of chemical additives as a means of enhancing the combustion characteristics of JP-7 and JP-8.

The ignition delays of neat and modified jet fuels are measured using a single pulse shock tube designed and built at the University of Dayton Research Institute (UDRI).[11] This system, shown in Figure 1, includes provisions for studying light fuels as premixed vapors, or injecting low vapor pressure fuels as liquids. The shock tube itself comprises a 7.6 cm ID by 2.74 meter long driver section, a 5.08 cm ID by 2.75 meters long driven section, and a 5.08 cm ID by 0.9 meter long test section. The system also includes a 30.5 cm ID by 61 cm long dump tank and an evacuation subsystem. The driven and test sections are connected through a pneumatic ball valve controlled through the system's automatic digital firing system. The dump tank is connected to the system through a manually operated ball valve. The entire structure is fabricated from 1.27 cm thick 304 stainless steel.

For the purposes of this study the test section is equipped with high speed pressure transducers, to measure the speed of the incident shock and hence define the exposure conditions, and a high speed fuel injector. The later consists of a diesel fuel injector fitted with a single stroke positive displacement fuel pump. The pump delivers a small volume (50μl) of fuel in a precisely timed manner and in a narrow spray pattern that does not impinge on the walls of the tube. The fuel is introduced 500μs behind the reflected shock which allows for the vibrational relaxation of the bath gas prior to injecting the fuel. This procedure permits considerable latitude in the types of fuels and range of conditions that may be tested. This is particularly significant for the present effort in

which the low vapor pressure of jet fuels severely limit the test environment if a conventional premixed sample system were employed. Furthermore, injecting the fuel directly into the test section allows the measurement of a composite ignition delay that includes both the physical and chemical components of the ignition process. The fuel pump is equipped with a pressure transducer to record the timing and performance of the injection sequence. The test section is fitted with an optical access port to monitor the radiation emitted from the ignition process. The detector used in conjunction with this port includes a narrow bandpass filter and a silicon photodiode. The filter is selected with a peak transmission centered on the 309 nm emission line of hydroxyl (OH) radicals.

Ignition delays are measured for neat JP-7 and JP-8, and these fuels blended with 500 ppmv 2-ethylhexyl nitrate (EHN), 500 ppmv of a proprietary additive (PA-1), and 10,000 ppmv (1%) EHN. Air is used as the driven gas to give a high degree of comparability with the conditions within a scramjet combustor. The reflected shock conditions are calculated using a real gas model described by Gardiner [12] and enthalpy data for oxygen and nitrogen from the JANAF tables.[13] Using helium as the driver gas, initial conditions are selected to give a nominal final pressure behind the reflected shock of 2 bar and temperatures from 1300 to 1800 K. As these are liquid spray combustion experiments the equivalence ratio varies from fuel lean near the end of the fuel spray to fuel rich at the start of the fuel spray which is consistent with liquid injection engines.

Results for neat fuels are summarized in Figure 2. The data show that at 1300 K the ignition delay of both fuels is approximately 1.65 ms. As the temperature is increased to 1800 K the ignition delay of JP-7 decreases slowly to 1.12 ms while that for JP-8 decreases to 0.87 ms.

Ignition delay measurements for neat and modified JP-7 are summarized in Figure 3. These results show the EHN and PA-1 do not have a significant effect on the ignition delay of JP-7 at a concentration of 500 ppmv. However, increasing the concentration of the EHN from 500 to 10,000 ppmv decreases the ignition delay over the temperature range considered. Specifically, at 1300 K the ignition delay decreases from 1.65 to 1.39 ms and from 1.12 to 0.89 ms at 1800 K.

The ignition delay data for neat and modified JP-8 are summarized in Figure 4. These data show that the addition of 500 ppmv EHN also does not have a measurable effect on JP-8 ignition delay. However, increasing the concentration from 500 to 10,000 ppmv increasingly improved the ignition delay at the lower end of the temperature range studied. For example, at 1300 K the ignition delay decreased from 1.65 to 1.33 ms while at 1800 K the delay decreased from 0.87 to 0.83 ms. By contrast, the addition of 500 ppmv PA-1 improved the ignition delay throughout the temperature range considered. Specifically, at 1300 K the delay decreased from 1.65 to 1.61 ms while at 1800 K the delay decreased from 0.87 to 0.65 ms.

Comparing the ignition delays of neat JP-7 and JP-8 (Figure 2), it is evident that JP-8 has a higher apparent activation energy of ignition than JP-7. This may be attributed to the higher aromatic content of JP-8 (~ 10% by volume [10]) than JP-7 (~ 3% by volume [10]). JP-8 features lower ignition delays than JP-7 at higher temperature (1800 K), arguably due to the lower vapor pressure of JP-7. At high temperatures, the liquid-vapor phase change dominates ignition delays of liquid fuel sprays, as the temperature is sufficiently high to initiate ignition chain reactions as soon as the fuel is vaporized.

The effect of the additives on JP-7 and JP-8 is shown in Figures 3 and 4, respectively. As these figure illustrate, the selected additives increased the slope of the ignition curves, indicating an increase in the cetane number and thus a decrease in the ignition delay.[8] However, the slope of the ignition curves is so small over the temperature range considered that it is difficult to visually observe the increase in slope or apparent activation energy of ignition. To emphasize this point, the effect of PA-1 on JP-7 and JP-8 is shown in Figure 5. It becomes clear that the addition of PA-1 increases the slope of the JP-7 ignition curve by 56% and that of JP-8 by 26%. It is easier to see the increase in the case of JP-8 (Figure 3) than in JP-7 (Figure 2), arguably attributable to the larger ignition activation energy of JP-8.

The ignition curves of JP-7 and JP-8 with 10,000 ppmv EHN feature very similar slopes, hence similar overall ignition characteristics (see figure 6). This is in direct contrasts with the behavior of neat fuels as shown in Figure 2 and also of also 500 ppmv EHN mixtures. The 10,000 ppmv EHN- JP fuel results are also in contrasts to 10,000 ppmv EHN-diesel results which show that addition of EHN increases the slope of diesel ignition curves by 14%.[8] The slope of the ignition curves decreases by 28% for JP-8 and remains constant for JP-7. This suggests that in the 10,000 ppmv EHN-JP fuel blend, the ignition process is dominated by the combustion of EHN and not the base fuel.

Present results show that there is a need for ignition delay studies of neat EHN to validate the conclusion that at high concentration, EHN ignition dominates the ignition of JP-7 and JP–8. There is also a need to study intermediate additive concentrations to fully understand the effect of EHN and PA-1 on ignition of JP-7 and JP-8. Most importantly, a broader temperature range must be considered. Developing the latter is arguably predicated on a better understanding of the fundamental mechanisms of combustion enhancement of practical fuels via chemical additives. These tests are ongoing and the results of work-in-progress will be presented.

References

1. Billig, F. and Pirkle, J., Research and Exploratory Development III-19. Scramjet Propulsion Research Z310BHP. John Hopkins University, Applied Physics Lab. Silver Springs, MD, 1968-1969.
2. Maurice, L. Q., Edwards, J. T. and Griffiths, J. F., and, "Liquid Hydrocarbon Fuels for Hypersonic Propulsion," AIAA Progress in Aeronautics and Astronautics, S.N.B. Murthy and E.T. Curran, Editors, in press, 1999.
3. Tishkoff, J. M., Drummond, J. M., Edwards, T. and Nejad, A. S., "Future Directions of Supersonic Combustion Research: Air Force/NASA Workshop on Supersonic Combustion," AIAA 97-1017, January 1997.
4. Mercier, R. A. and Ronald, T. M. F., "Hypersonic Technology (HyTech) Program," ISABE 97-7027, XIII International Symposium on Air Breathing Engines, Chattanooga, TN, September 1997.
5. Colket, M. B. and Spadaccini, L. J., "Scramjet Autoignition Study," XIV International Symposium on Air Breathing Engines, Florence, Italy September 1999.
6. Davidson, D. F., Hitch, B., Horning, D. C. and Hanson, R. K., "Shock Tube Ignition Time Measurements for n-Heptane/Oxygen/Argon Mixtures with and without Additives," 1st Joint Meeting of the U.S. Sections of the Combustion Institute, Washington DC, 1999.
7. Morris R. A., Arnold, S. T., Viggiano, A. A., Maurice, L. Q., Carter, C. and Sutton, E., "Investigation of the Effects of Ionization on Hydrocarbon-Air Combustion Chemistry," Proceedings of the 2nd Weakly Ionized Gas Workshop, 24-25 April, Norfolk, Virginia, 1998.
8. Suppes, G. J. Rui, Y., Rome, A. C., and Chen, Z., "Cetane-Improver Analysis and Impact of Activation Energy on the Relative Performance of 2-Ethylhexyl Nitrate and Tetraethylene Glycol Dinitrate, Ind. Eng. Chem Res., 36, 4397, 1997.
9. Coordinating Research Council, "Handbook of Aviation Fuel Properties," CRC Report No. 530, 1983.
10. Edwards, T. and Maurice, L. Q., "Surrogate mixtures to represent complex aviation and rocket fuels," AIAA 99-2217, 34th Joint Propulsion Conference and Exhibition, Los Angeles CA.
11. Sidhu, S. S., Graham, J. L., Taylor, P. H., and Dellinger, B., "The Origin of Organic Pollutants from the Combustion of Alternative Fuels: Phase V/VI," Final Report for National Renewable Energy Laboratory, Contract XAU-3-12228-02, April 1998.
12. Gardiner, W. C., Jr., Walker, B. F., and Wakefield, C. B., "Mathematical Methods For Modeling Chemical Reactions In Shock Waves," Shock Waves in Chemistry; Marcel Dekker, New York, pp. 319, 1981.
13. Stull, D. R., and Prophet, H., JANAF Thermochemical Tables, 2nd ed., NBS NSRDS 37, 1971; and later supplements.

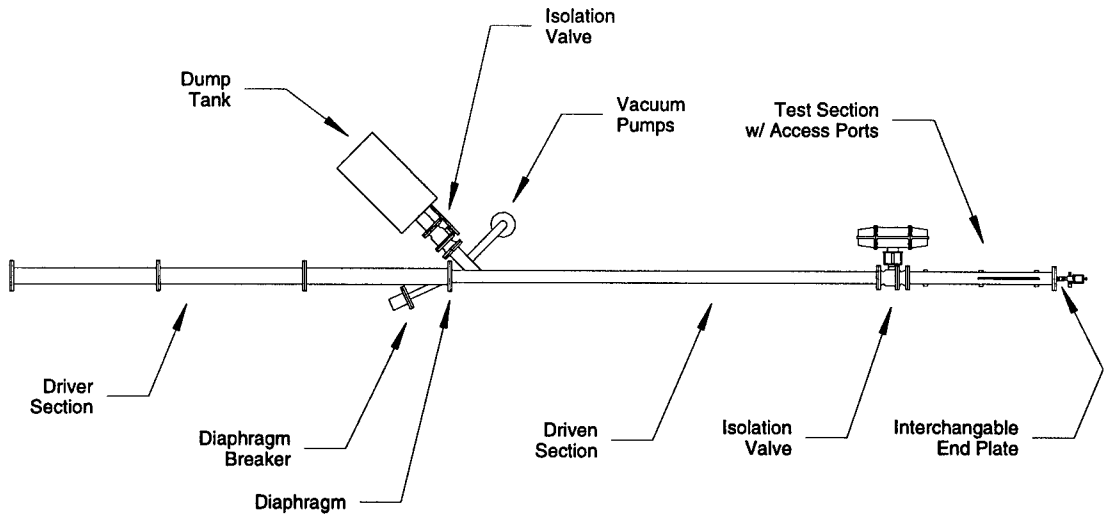


Figure 1. A schematic drawing of the UDRI Shock Tube.

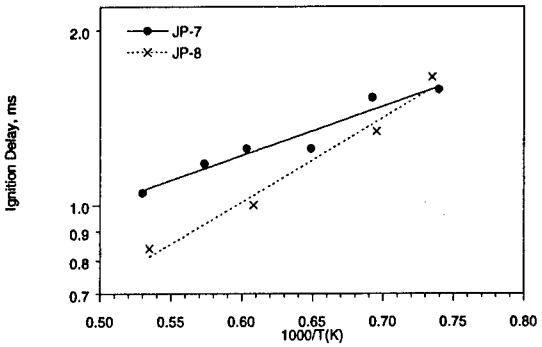


Figure 2. Ignition delays for neat JP-7 and JP-8 fuels at 2 bar in air.

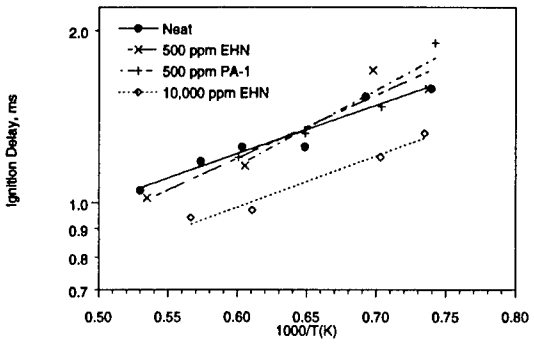


Figure 3. Impact of 2-ethylhexyl nitrate (EHN) and a proprietary additive (PA-1) on ignition of JP-7 at 2 bar in air.

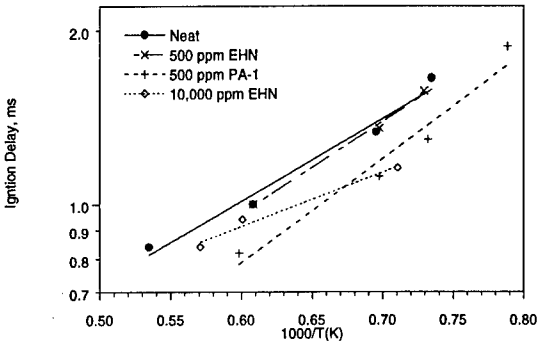


Figure 4. Impact of 2-ethylhexyl nitrate (EHN) and a proprietary additive (PA-1) on ignition of JP-8 at 2 bar in air.

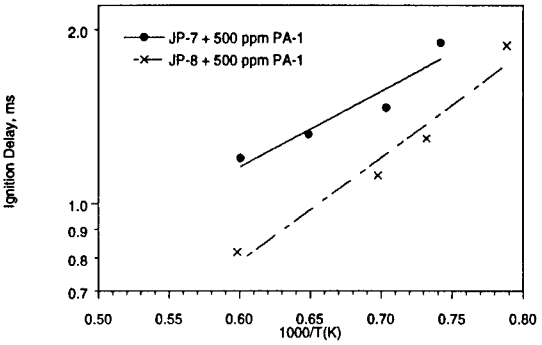


Figure 5. Comparison of effect of 500 ppmv of proprietary additive (PA-1) on ignition delay times of JP-7 and JP-8 in air.

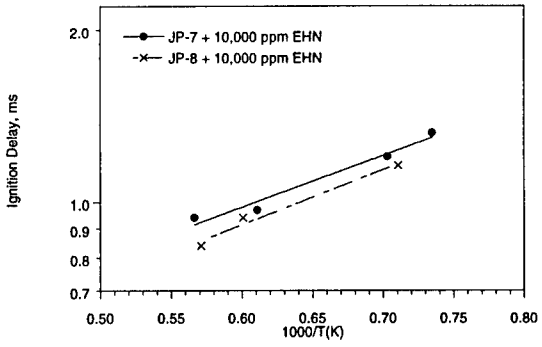


Figure 6. Effect of 500 ppmv of 2-ethylhexyl nitrate (EHN) on ignition delay of JP-7 and JP-8 in air.

Measurement of the Ignition Delay Times of PMMA Spheres in Reduced Gravity

Jordan Conley (conl1534@rowan.edu), Michelle Hillen (hill7961@rowan.edu),
Brian Dericks (deri5128@rowan.edu), Steve Shaw (RCShaw@prodigy.net),
William Abraham (abra5780@rowan.edu), John C. Chen (jchen@rowan.edu)

Departments of Mechanical, Chemical and Electrical Engineering
Rowan University
Glassboro, NJ 08028-1701

Abstract

Polymers have become such a common material in all aspects of our society; anything from automobiles to toothbrushes consists of many types of plastics. One of the most common polymers is polymethylmethacrylate (PMMA). The International Space Station (ISS), which is in the midst of construction, will have many components fabricated from PMMA. We believe that this study of the combustion of PMMA could contribute to the development of guidelines for safety procedures and maintenance routines for fire prevention and fire fighting on the ISS.

Polymer combustion is a complex process that involves the coupling of melting, pyrolysis, heat and mass transfer, and gas-phase combustion. This study focuses on one aspect of polymer combustion, namely ignition. Several ground-based studies have already been conducted on the combustion of spherical polymer beads involving various ignition methods. Few of these experiments, however, measured the ignition delay time, the period between sample injection and ignition, as a function of the experimental conditions. Such measurements are important for determining material flammability and for validating numerical models of combustion. Furthermore, earth-based measurements are strongly influenced by gravity, as we have observed in our experiments, and it is well established that under microgravity, the ignition delay times will be distinctly different.

We have constructed an experiment to measure the ignition-delay times of PMMA spheres at low gravity. The experiment consists of a tube furnace, injector unit, high-speed video camera, and various controllers. The spherically symmetric flame produced under reduced gravity will allow us to analyze the results readily using a relatively simple model of ignition, while such an analysis at normal gravity is extremely complicated and computationally burdensome. The overall objective is to measure the ignition delay of PMMA spheres in air as a function of bead diameter and furnace temperature. Gravity has a strong influence on the ignition process and the delay time, and these measurements will aid in understanding the process on earth and in space. Furthermore, knowledge gained from our study will be of use to researchers studying polymer combustion through experiments and numerical models.

Introduction

The overall goal of this project is to measure ignition delay time, defined to be the period between sample injection and ignition, and observe the combustion of polymethelmethacrylate (PMMA) spheres under reduced gravity conditions. To achieve this goal, we have built a flight apparatus that permits the visualization of the ignition and burning of small PMMA spheres by injection into a hot-gas tube furnace. We are aware of no other studies conducted under reduced gravity to measure the ignition delay time, although several current studies are examining the overall combustion behavior of PMMA [1, 2] or other materials in microgravity [3, 4]. Our results will be particularly pertinent to these researchers in guiding their design of the ignition apparatus.

The overall goal will be achieved by the successful completion of the following objectives:

- Construct a test cell with optical access to observe and record the ignition and combustion of small polymer spheres in reduced gravity and normal gravity (1-g) environments.
- Construct a partial-free-floating test apparatus to eliminate the transmission of undesired motions due to the aircraft.
- Measure the ignition delay of four sizes of PMMA spheres (2, 3, 4, 6 mm diameter) in air (21% oxygen) under a range of furnace temperatures (600 – 800°C).
- Obtain and record visual data for determining flame diameters during the combustion of the PMMA spheres under various conditions.

Prior to the in-flight experiments, we will conduct several ground-based tests. These will determine all the experimental parameters and serve as a comparison to the low-gravity results. These pre-flight experiments will also help eliminate any possible complications and allow us to perform the in-flight tests more efficiently. Certain parameters of our experiment will only be measured during the flight. For instance, since the test is free-floating, three accelerometers will measure the low-level acceleration in the x, y, and z directions only during flight tests.

In Fig. 1 below, an ignition sequence from one of our ground-based experiment is shown. We injected a 4-mm diameter PMMA sphere into the tube furnace set to a temperature of 550oC, and observed the ignition and combustion processes with a high-speed video camera. The camera records the PMMA sphere inside the tube furnace; the long wire on the bottom left of the picture is the thermocouple monitoring the furnace temperature. The sequence shows the asymmetric ignition point near the bottom of the sphere due to polymer melting, as well as the effects of buoyancy as the flame develops. These effects would be absent in reduced gravity, and thus the ignition process, including the delay time, will be strongly influenced.

The in-flight experiments will examine parameters affecting the ignition delay times of Polymethylmethacrylate (PMMA) spheres, including diameter and furnace temperature. The range of values for each parameter is listed in Table 1. We will measure the ignition delay of each sphere using a high-speed camera. We expect to conduct one test on every other parabolic trajectory, using the time in between for video downloading and preparation for the next run. We will repeat each combination of experimental conditions at least twice, in case of gravity fluctuations during the test. With over thirty parabolic maneuvers during each flight, we can achieve our test objectives and collect sufficient data.

Experiment

Table 1 below shows the experimental conditions that we plan to explore. All tests will be conducted using commercially available PMMA spheres in air.

Experimental Condition	**Range of values**
Sphere diameter	3.0, 4.0, 5.0 and 6.0 mm
Furnace temperature	500°C – 800°C

Table 1: Range of experimental conditions to be studied in ground and flight tests.

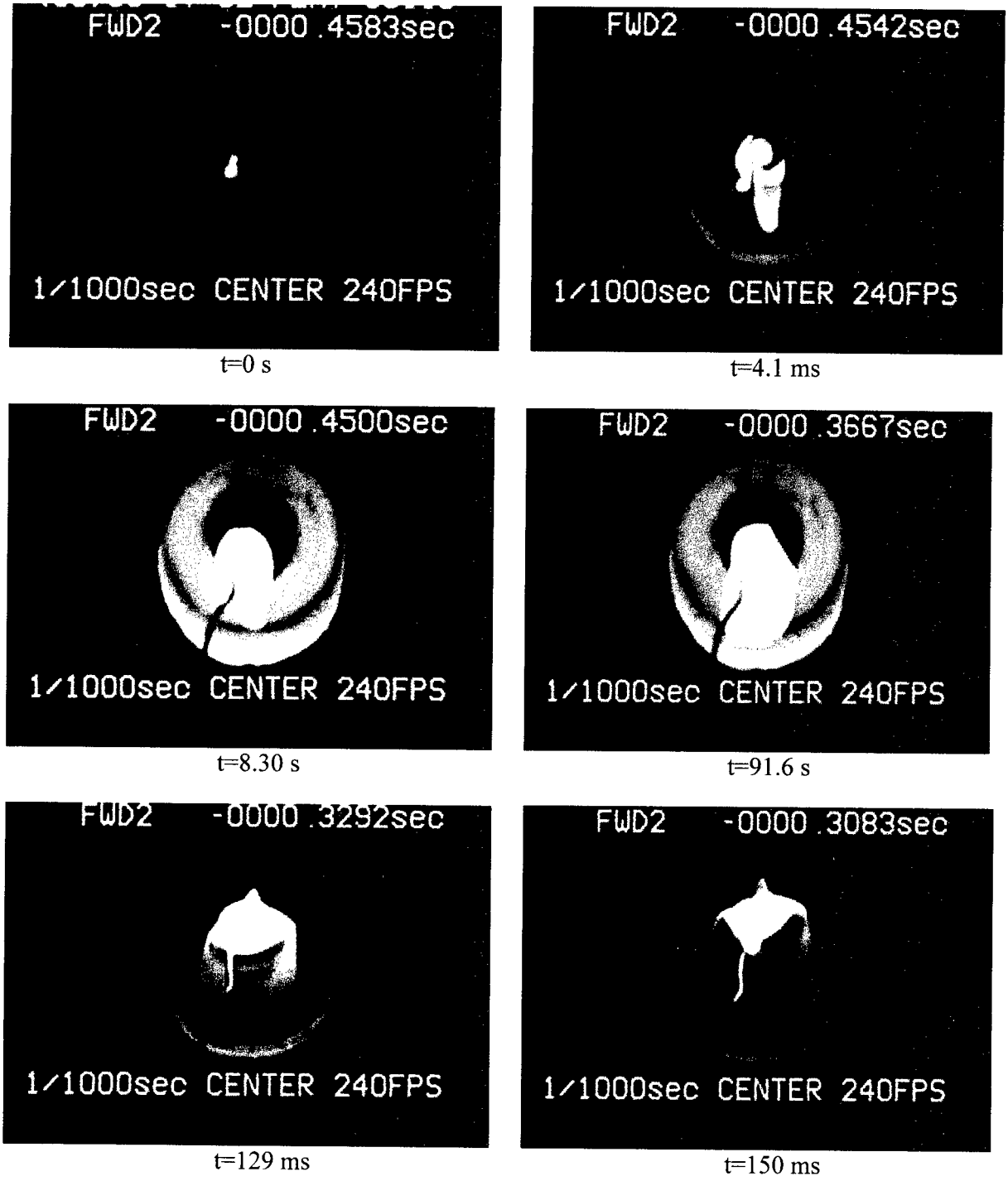


Fig. 1: Ground-based (1-g) ignition sequence of a 4-mm PMM sphere at 550°C.

This experiment consists of a test cell assembly designed to enclose and isolate the experiment area in an aluminum frame, a holding basin to contain the test cell assembly during the non-experimental stages of the flight, and a diagnostic system to collect, process and store the data.

The test cell (Figure 2) is comprised of six essential components: the aluminum plate which acts as a base for the other components; the tube furnace; a temperature controller to maintain the proper temperature of the tube furnace; the injector unit; the video camera which is attached to the diagnostic system; and the aluminum frame that protects the entire assembly. This assembly is designed to be free-floating during the reduced gravity tests. The aluminum plate is a 0.25" thick and 18" by 36" in size. It acts as a breadboard for aligning and holding all the other components of the test cell assembly in place.

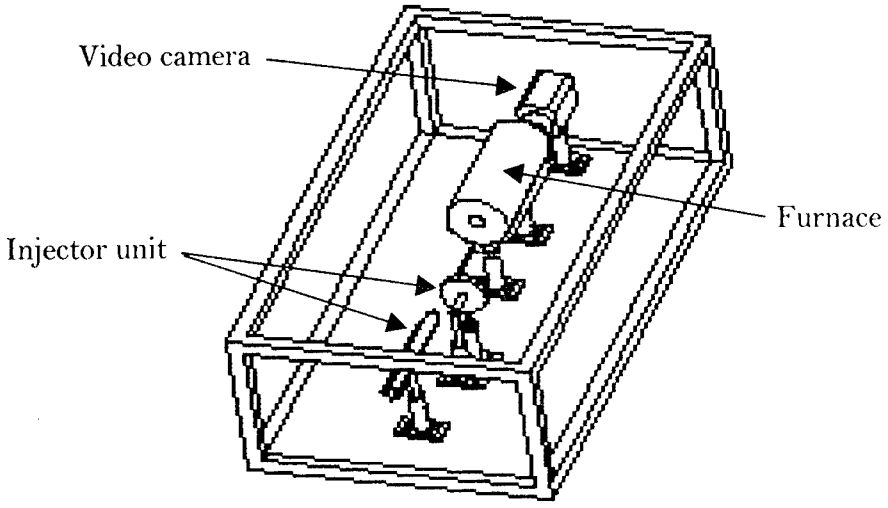


Fig. 2: Schematic of the flight apparatus, including the base/frame, injector unit, furnace, and high-speed video camera.

Results

We are scheduled to conduct our reduced gravity flights in early August, and will complete the data reduction shortly thereafter to compared with our preliminary results from ground-based tests.

References

1. Yang, J.C., Hamins, A., and Donnelly, M.K. "combustion of a Polymer (PMMA) Sphere in Microgravity," NIST Report No. NISTIR 6331, U.S. Department of Commerce (1999).

2. Hanai, H., Maruta, K., Kobayashi, H., and Niioka, T. "Pulsating Flame Propagation of PMMA Particle Cloud in Microgravity," *Twenty-Seventh Symposium (International) on combustion*, The Combustion Institute, pp. 2675-2681 (1998).

3. Fujita, O., Ito, K., and Tagashira, T. "Measurement of Flame Propagation Speed of Coal Dust Using a Microgravity Environment," *Heat Transfer in Microgravity*, ASME Proceedings, 269:59-66 (1993).

4. Pu, Y., Podfilipski, J., and Jarosinski, J. "Constant Volume combustion of Aluminum and Cornstarch Dust in Microgravity," *Combust. Sci. and Tech.*, 135:255-267 (1998).

CONTROLLING THE SELF-IGNITION BEHAVIOR OF SILANE

Wing Tsang and Valeri Babushok
National Institute of Standards and Technology
Gaithersburg MD 20899

ABSTRACT

Computer simulation has been used to determine the effect of the addition of iodine and hydrogen iodide on the self-ignition properties of silane. Very small amounts of iodine (in the 200ppm range) and somewhat large amounts of hydrogen iodide can render silane non-pyrophoric at room temperature. Larger quantities are necessary at higher temperatures. Ignition delay in the presence of additives is strongly dependent on temperature. Differences for cases with and without additives disappear at sufficiently high temperatures. Results are interpreted in terms of the reactions of active radicals with silane and the additive leading to drastic changes in the direction of chemical processes.

INTRODUCTION: It is well known that silane is pyrophoric or flammable upon exposure to air[1]. Due to its wide use in chemical vapor deposition and other materials applications, this represents an important safety issue and considerable efforts must be devoted to the prevention of self-ignition in the presence of air [2]. A method to ameliorate this situation would be useful. Recently we have developed a general mechanism and the corresponding kinetics data base for the combustion of silane[3]. For the first time, both low and high temperature combustion behavior of silane could be simulated on the basis of purely gas phase reactions. A particularly important result is the observation that the chain carriers in the combustion process are essentially the same as those for organic fuels. This suggests that under combustion conditions the usual fire suppressants will have consequences on silane combustion systems similar to those for hydrocarbon fuels. At the low temperatures of the present applications, suppressant molecules are stable, thus there is no possibility of initiating decomposition processes. Their reaction with chain carriers should alter the ignition behavior of fuels such as silane and render it non-pyrophoric. In this paper we report on simulation studies involving the addition of iodine and hydrogen iodide to silane-air mixtures.

PROCEDURES: The modeling results described above were derived from the CHEMKIN suite of programs[4]. The kinetic model of silane combustion used in this work is based on a recently published paper[3] and is in turn derived from suggested mechanisms for silane oxidation and pyrolysis It has been extensively adjusted to take into account recent experimental and ab initio studies for Si-containing species. Some additional reactions have been added to the kinetic scheme to complete the reaction pathways for the consumption of the species and also as much as possible to fit experimental observation dealing with the combustion properties of silane.. The chemical kinetic model consists of 220 elementary reactions with 39 species. The data base has been posted in the NIST web site [5]. The calculations involve studies using the plug flow model and after setting the initial conditions following the temporal behavior of the system and determining whether ignition occurs. If it occurs one can also observe the time to ignition or the ignition delay.

One of the compounds that we have extensively studied as a fire suppressant was CF_3I[6]. As a result, the set of reactions involving the important chain carriers and iodine atoms and molecules are already in place. Some specific reactions of interest are:

$H+I_2 \Rightarrow HI+I$	$H+HI \Rightarrow H_2+I$	$H+I_2 \Rightarrow IOH+I$
$OH+HI \Rightarrow H_2O+I$	$OH+SiH_4 \Rightarrow H_2O+SiH_3$	$H+SiH_4 \Rightarrow H_2+SiH_3$
$I+SiH_4 \Rightarrow HI+SiH_3$	$I+O_2 \Rightarrow IO+O$	$I+I+M \Rightarrow I_2+M$

It is important to note that the reactions involving radical attack on iodine and hydrogen iodide are also used for describing flame suppression. The rate constants for the first six reactions are all very large. This is especially the case for those involving the iodine molecule and is a reflection of the very weak I-I bond. To a lesser extent this is also true for reactions with hydrogen iodide. The weakness in bonds formed with iodine atoms is also reflected in the very small rate constant for iodine attack on silane. This is largely due to the endothermicity of the reaction. It is clear that under these circumstances unreactive iodine-atoms are replacing highly reactive silyl radicals. With such a model it is also possible to consider the situation when HI is used as the suppressant. It should be noted that for ignition only the initial reactions are of importance.

RESULTS: The effect on hydrogen atom yields in silane-air mixtures in the absence and presence of iodine can be seen in Figures 1. It can be seen that for the former, after a very short ignition delay, one obtains a spike where high concentrations of hydrogen atoms are rapidly achieved and then decays as the reaction is completed. This is accompanied by an abrupt increase in the temperature. In contrast, when enough iodine molecules are added, one obtains a miniscule step increase in the hydrogen atoms after an induction time of the order of many seconds and the temperature is unchanged.

The general effect as a function of reaction conditions can be seen in Figure 2. The results are expressed in terms of a self-ignition region on an explosion diagram for oxygen and silane mixtures for particular concentrations of the additive. The drastic effect of iodine addition is readily seen. Also included in Figure 4 are similar data for hydrogen iodide. It is about an order of magnitude less effective than iodine itself. Increasing additive has the consequence of squeezing the region where ignition can occur. The general situation for increases in temperature is summarized in Figures 3-4. With increasing temperature the region for self ignition increases. At 500 K, in the absence of additive almost the entire space is covered and the amount of additive required to suppress ignition is increased both for hydrogen iodide and iodine.

Figures 5 and 6 give results on ignition delays. We have marked in Figure 2 the two regions where calculations have been carried out and they all lead to results that are similar to Figure 6. The sensitivity to the amount of iodine present does not get large until one approaches the ignition limit, where one obtains the precipitant increase in ignition delay that indicates that the mixture is no longer flammable. We are not certain about the rationale for not obtaining ultimately an infinite number. It could well be that there are calculational errors at the very long ignition times. Alternatively, this could be due to depletion of the iodine. Figure 6 shows the temperature dependence of the ignition delay for mixtures with and without iodine. It can be seen that for the mixture with iodine the temperature dependence is much stronger. Thus at a sufficiently high temperature the ignition delay with and without iodine becomes equal.

DISCUSSION: The results described above can be completely understood in terms of the chain branching nature of the ignition process. In the presence of an additive active radicals are converted into less active species, hence chain branching never occurs. At low temperatures, differences in the chemistry from activation energy effects are increased. Thus the process is particularly sensitive to

small amounts of the additive. Once ignition occurs the additional contributions from the high temperatures generate so many radicals so that much more additive is needed to moderate the process. Note that the higher temperatures can also activate more reactions that contribute additional radicals to the reactive pool and indeed radicals from the decomposing additive will make contributions as the temperature increases. Thus although the reactions for the reduction of the ignition region and flame suppression are similar, due to the conditions where they are applied the consequences and sensitivities are quite different. These results lead to interesting questions regarding how the capability for preventing ignition should be assessed in fire suppressants. Certainly there are many phenomena in fire situations such as re-ignition in pool fires or flame-over in room fires that are suggestive of ignition processes. One would expect that suppressants with greater capability for the prevention of ignition could be more effective under such situations. All of the present results are based on simulations. We hope to carry out experiments verifying some of the predictions in the near future.

REFERENCES

1. Moeller, T., "Inorganic Chemistry, An Advanced Textbook", John Wiley and Sons, New York, 1952
2. Tamanini, F., Chaffee, J. L., and Jambor, R. L., "Reactivity and Ignition Characteristics of Silane/Air Mixtures"; Presented at the 32nd Loss Prevention Symposium, American Insitute of Chemical Engineers, New Orleans, LA , 1998, Tamanini, F., Braga, A. C; SSA Journal, 11:21-36, 1997, Britton, L.G. "Combustion Hazards of Silane and its Chlorides", Paper 12b, Loss Prevention Symposium, Houston, TX, 1989.
3. Babushok, V., Tsang, W., Burgess, D. R., and Zachariah, M. R., 27th Int'l Symp. On Combustion, in press
4. Kee, R. J., Miller, J. A., Jefferson, T. H. CHEMKIN; A General Purpose, Problem Independent, Transportable, Chemical Kinetics Code Package SAND80-8003, Sandia National Laboratories, 1989
5. http://fluid.nist.gov/836.03/chmech/mechanisms.html
6. Babushok V; Noto T; Burgess DRF; Hamins A; Tsang W, Comb and Flame 108, 61-70,1997

Figure 1. H-atom concentrations in the absence and presence of iodine. The iodine is in sufficient concentration to prevent self-ignition

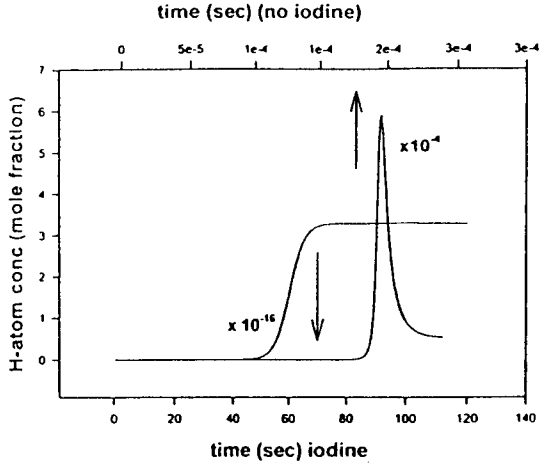


Figure 2. Self ignition regions for various amounts of HI and I_2 at 300 K. Difference between silane+ oxygen+ additive/10 and 100 is. N_2. Numbers are additives in ppm. HI results are in italics and dashed lines. Open circles represent silane-oxygen mixtures used for results in Fig 5.

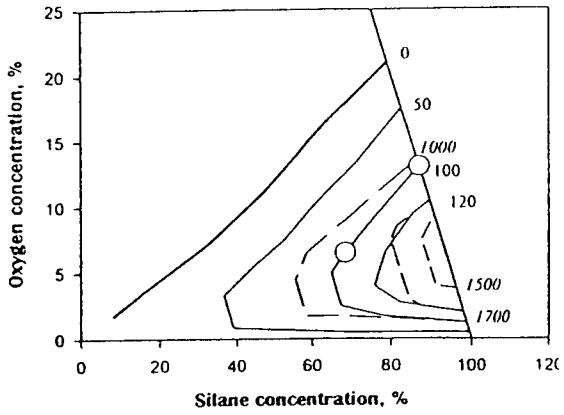


Figure 3: Self ignition regions for quantities of iodine (ppm) in silane-oxygen mixtures at 500 K. Difference between 100 and sum of concentrations of O_2+silane+[additive/10^4] is % N_2

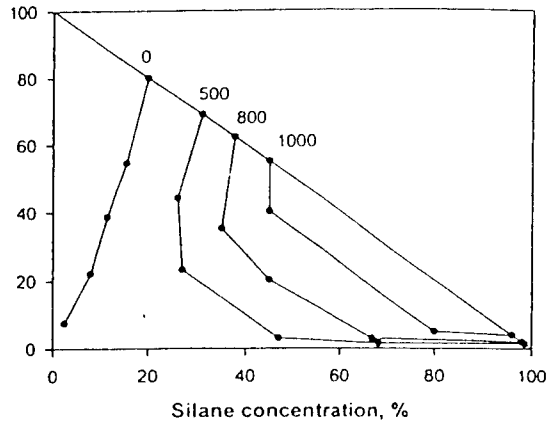


Figure 4: : Self ignition regions for quantities of HI (ppm) in silane-oxygen mixtures at 500 K. Difference between 100 and sum of concentrations of O_2+silane+[additive/10^4] is % N_2

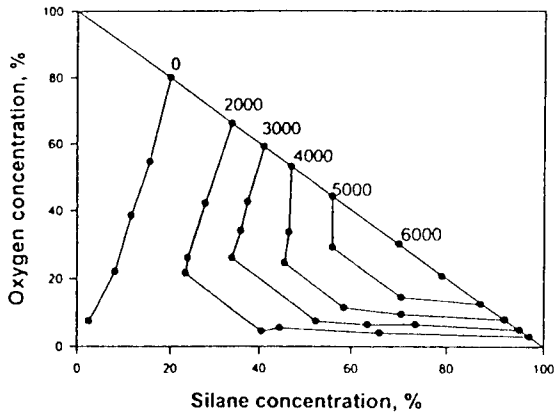


Figure 5: Ignition delay as a function of concentration. Silane-oxygen concentrations as represented by open circles in Figure2

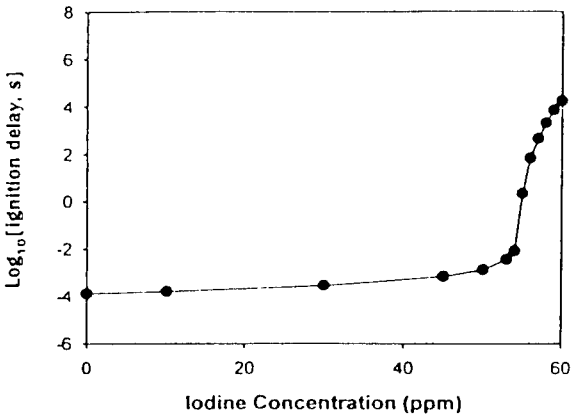
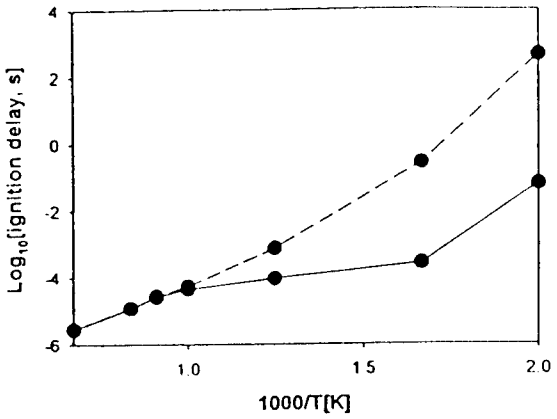


Figure 6: Ignition delay as a function of temperature in the presence and absence of iodine. Mixture conditions: $SiH_4/O_2/N_2/H_2/I_2$ = 2/4/86/8/0[solid line] or .005[dotted line]



NO_2 Emission from Burke-Schumann Flames

Jose E. Navedo and Ruey-Hung Chen*
Department of Mechanical, Materials and Aerospace Engineering
University of Central Florida
Orlando, FL 32816-2450

ABSTRACT

The NO_2/NO_x ratio in Burke-Schumann type flames were experimentally studied. It was found that without the local extinction or flame lift-off, CH_4 and C_3H_8 flames produce lower values of NO_2/NO_x than H_2 flames, in contrast to turbulent jet diffusion flames. This lends further support to the argument that fuel leakage in turbulent diffusion flames due to local extinction renders the neighboring/surrounding air to be doped with fuel; when the fuel used is a hydrocarbon it oxidizes NO into NO_2.

While the flame temperatures of these Burke-Schumann flames were kept nearly equal, it was further found that flames producing lower NO levels also produce higher values of NO_2/NO_x. With helium dilution, H_2 flames can produce lower NO levels and higher NO_2/NO_x ratios than CH_4 and C_3H_8 flames. It was concluded that in the absence of local flame extinction and fuel leakage, high NO_2/NO_x ratios are linked to lower NO levels. It is also found that when the NO levels of these flames are kept fixed, the NO_2/NO_x ratio increases with decreasing flame temperature.

INTRODUCTION

Some recent studies on NO_x emission from nonpremixed flames have concentrated on the ratio of NO_2 to NO_x, the latter being the sum of NO and NO_2. They include simple turbulent jet diffusion flames, turbulent coaxial jet diffusion flames, gas turbine flames, and droplet flames [1-7]. The interests in knowing how much of NO_x is NO_2 is partly due to the fact that NO_2 is more water soluble, enabling a convenient post combustion scrubbing of NO_x [8].

It has been known that hot gas jets (not flames) containing "initial NO" yield higher NO_2/NO_x ratio as the mixing is enhanced, when the jet temperature is lower, and when the NO concentration is lower [9-11]. When the surroundings is doped with hydrocarbons, the ratio increases while the total NO_x level remains constant [12]. The enhancing ability of hydrocarbons in general increases with the size of the molecules and is specifically related to the ability of the fuel in generating HO_2. HO_2 oxidizes NO to NO_2 through the reaction $NO + HO_2 = NO_2 + OH$ [13]. Similar results have been reported for turbulent jet diffusion flames, as the flame jet contains "initial NO" observed by a far-field probe [5]. In turbulent jet diffusion H_2 flames, it was found that addition of a small amount (5 % by volume) of CH_4 to the fuel has appreciable effects on the NO_2/NO_x ratio, increasing the ratio two-fold as the flame approaches its blowout limit [5]. In contrast, the NO_2/NO_x ratio of the H_2 flames does not exhibit an increasing trend toward blowout limits. It was believed that the local extinction and the flame lift-off rendered the surrounding air to be doped with fuel that leaked through the flame. It is not known, however, without the local flame extinction and/or flame lift-off, hydrocarbon flames may still produce a higher percentage of NO_2 than H_2 flames. Furthermore, due to the local and instantaneous strain rate variation, the flame temperature fluctuations may be so significant that a single measured flame temperature may lose its meaning. Also there has been no systematic effort in controlling the "initial NO" for the purpose of isolating effects of flame temperature.

It was decided to examine the NO_2/NO_x ratio in laminar diffusion flames of the Burke-Schumann type. In these flames experimental conditions were chosen to be far from flame blowout limits. These flames also lack the spectrum of turbulent scales and no local extinction exists for fuel leakage to be likely. Diffusional mixing is the only mixing mechanism present. H_2, CH_4, and C_3H_8 were used as fuels. Various degrees of inert dilution were used so that the measured flame temperatures in flames can be kept nearly equal. Under these conditions, only the effect of flame temperature, the "initial" NO, and the fuel type (H_2 vs. hydrocarbons) are the determining factors on the NO_2/NO_x ratio. If the fuel type is the dominant factor, then the NO_2/NO_x ratio should be higher in hydrocarbon flames, as in turbulent CH_4 diffusion flames. If an opposite trend is observed, it would lend further support to local extinction and/or flame liftoff as necessary for hydrocarbon flames to have higher NO_2/NO_x ratios.

EXPERIMENT

The Burke-Schumann flame apparatus is as shown in Figure 1. The inside diameter of the fuel tube (c), made of stainless steel, is 4.6 mm and that of the air tube (b), made of vycor glass, is 60 mm. This gives the ratio $c = a/b = 0.077$. The distance between the burner exit and the downstream end of vycor glass tube is 47 cm. The air and fuel stream velocities were kept equal, whether the fuel is diluted or not, so that there

was no shear instability. Burke-Schumann flame conditions [14] were maintained except the fuel Lewis number and mass flux. The fuel Lewis number varied as a result of various inert dilution, for the purpose of comtrolling flame temperature. The oxidizer is always air. The Reynolds numbers based on the air diameter were typically less than 150. The Peclet number (Pe) based on the fuel tube diameter was typically greater than 20 for velocity (U_F) above 10 cm/sec. The flows therefore were at the high Peclet number limit [15], where diffusion processes occur predominantly in the cross-stream direction. Only results of flames with high Peclet numbers are reported. Experimental conditions and measured flame temperature are listed in Table 1.

The reader is referred to Ref. 16 for all experimental details. The NO_X analyzer was calibrated daily and run to run using calibration gases and had an accuracy of 0.2 ppm in the 0-20 ppm range . The repeatability from run to run or day to day was within about 5 %.

RESULTS AND DISCUSSION

For the following presentation, the NO_x emission level and the flame temperature will be taken as independent variables and their effects on the NO_2/NO_x ratio will be examined.

Effects of Flame Temperature

Some measurements of the NO_2/NO_x ratio was carried out to demonstrate the effects of flame temperature while the initial NO level is fixed. Flames of 80% H_2-20% Ar ($T_f \approx 2{,}160$K) and 40% H_2-60% He flames ($T_f \approx 2{,}243$K) were chosen, so that there is no effect of H_2 vs. hydrocarbon fuels. The results are as shown in Figure 2. These flames have similar NO levels, 1.05 - 1.20 ppm, over the velocity range studied, while their flame temperatures differ by about 80K. The results of the NO_2/NO_x ratios of these two fuel mixtures, if different, will be due to the difference in their flame temperatures as discussed in the Introduction section. It can be seen that the 20% Ar-diluted H_2 flames yield a higher values of the NO_2/NO_x ratio, 27 - 35 % compared to 20 - 26 % of the 60% He-diluted flames.

When the initial NO level and the flame temperature are similar, the NO_2/NO_x ratio is expected to be similar. One example can be found in Figure 3. The 40% Ar- and 40% He-diluted CH_4 flames have similar NO levels, within 10% of each other in the range of 2.1 - 2.4 ppm. Their flame temperatures are within 1 %, about 1,950 ± 20K. No significant difference in their NO_2/NO_x ratios can be seen from Figure 3.

Another example involves 60% CH_4-40% He and 40% C_3H_8-60% Ar flames, shown in Figure 4. The NO levels of these two flames are essentially the same, ≈ 4.3 ppm, and their flame temperatures are also within 1 % of each other (2,073 and, 2,046 K, respectively). Again, no difference in their NO_2/NO_x ratios can be seen. It is noted that in Figure 4 two different fuels, CH_4 and C_3H_8, were compared and the conclusion is similar to those of Figures 2 and 3, each of which compares the same fuel but different diluents.

It can be concluded that a lower flame temperature leads to higher values of the NO_2/NO_x ratio while all other flame parameters are kept the same. These effects of flame temperature are therefore similar to those found in hot gas jets and turbulent jet diffusion flames, as discussed above.

Effects of the "Initial" NO Level

Two groups of flames were studied for the effects of the "initial" NO level. Flames in each group have the flame temperature measured to be within 10K of each other. The flame temperature of these two groups are considered to have a fixed value. Their flame temperatures are listed in Table 1.

The results of NO_x emission and the NO_2/NO_x ratio of 80% H_2-20% Ar, 80% CH_4-20% He, and 60% C_3H_8-40% He flames are shown in Figure 5. It is interesting to note that the NO_x level of H_2 flames ($T_{f,max}$ = 2,160K) are substantially lower than those of CH_4 ($T_{f,max}$ = 2,151K)and C_3H_8 ($T_{f,max}$ = 2,163K) flames. It is also noted that the NO_2/NO_x ratios are substantially higher for H_2 flames (27 - 35%) than for CH_4 and C_3H_8 flames (11 - 16%). The lift-off of the CH_4 and C_3H_8 flames are essentially zero and no leakage of these fuels into the air stream should be of any concern. The effects of the low NO level is consistent with previous findings; that is, the lower the NO level, the higher the NO_2/NO_x ratio. This observation deserves special notice because if there is any fuel effect existing on the NO_2/NO_x ratio, CH_4 and C_3H_8 flames should have higher values of NO_2/NO_x than the H_2 flames. In fact, the oxidizing ability of these fuels is known to be in the order C_3H_8 > CH_4 > H_2 [13] and a small amount of hydrocarbon fuel in the air stream can cause a qualitative reversal of the magnitude of the NO_2/NO_x ratio of these flames [5]. Therefore, it can be concluded that the effect of low NO levels helps to increase the NO_2/NO_x ratio.

A comparison between the 80% CH_4-20% He, and 60% C_3H_8-40% He flames (Figure 5) also reveals that the lower the NO level, the higher the NO_2/NO_x ratio. The 80% CH_4-20% He flames generated a lower NO_x level (5.5 - 6.5 ppm) and a higher value of the NO_2/NO_x ratio (≥ 13%), while 60% C_3H_8-40% He flames generated a NO level > 7.5 ppm and a smaller values of the NO_2/NO_x ratio (≤ 13%). However, it should be noted that the difference in the NO level and the NO_2/NO_x ratio between these two flames are not so substantial as those between these two and the 80% H_2-20% Ar flames. Nonetheless, the effects of the initial

NO level still appears to exist. According to the above-mentioned relative oxidizing power of C_3H_8 and CH_4, the results of the NO_2/NO_x ratio could have been reversed if there is fuel leakage.

The other group of flames consists of 40% C_3H_8-60% He and 60% CH_4-40% He flames (measured flame temperature equal to 2,075K and 2,073K, respectively). Their results are shown in Figure 6. Over the velocity range studied, the NO_x levels is higher for 40% C_3H_8-60% He flames (approximately 6.0 ppm) than for 60% CH_4-60% He flames ($\approx$ 4.5 ppm). The NO_2/NO_x ratios of the 60% CH_4-40% He flames are higher ($\approx$ 14%) than those of 40% C_3H_8-60% He flames ($\approx$11%). Although the differences in both the NO level and the NO_2/NO_x ratio are not so significant as those shown in Figure 5, the effects of the low NO level again exists.

CONCLUSION

The ratio of NO_2/NO_x was investigated using H_2, CH_4, and C_3H_8 flames diluted with He and Ar. The degree of dilution was chosen so that the NOx level and flame temperature can be independently varied for several groups of flames. The NO_2/NO_x ratio was found to increase with decreasing NOx emission levels while the flame temperature was kept fixed. The NO_2/NO_x ratio was also found to increase with decreasing flame temperatures while the NOx level was maintained constant. The fuel Lewis number and inert dilution affect the NO_2/NO_x ratio in that if they resulted in a lower flame temperature and/or a lower NOx level for the same degree of dilution by different inert diluents, they will lead to a higher value of the NO_2/NO_x ratio.

REFERENCES

1. Chen, R.-H. (1995) *Combust. Sci. Tech.* **110-111**, 443-460.
2. Chen, R.-H. (1996) *Combust. Sci. Tech.* **120**, 321-333.
3. Chen, R.-H. and Driscoll, J. F. (1990) *Twenty-Third Symposium (International) on Combustion*, The Combustion Institute, Pittsburgh, PA, 281-288.
4. Driscoll, J. F., Chen, R.-H. and Yoon, Y. (1992) *Combust. Flame* **88**: 37-49.
5. Chen, R.-H. (1998) *Combust. Flame* **112**: 188-198.
6. Hargreaves, K. J. A., Harvey, R., Roper, F. G. and Smith, D. B. (1981) *Eighteenth Symposium (International) on Combustion*, The Combustion Institute, Pittsburgh, PA, 133-142.
7. Noyce, J. R. and Sheppard, C. G. W. (1982) *Combust. Sci. and Tech.* **29**, 37-52.
8. Nelson, P. F. and Haynes, B. S. (1994) *Twenty-Fifth Symposium (International) on Combustion*, The Combustion Institute, Pittsburgh, PA, 1003-1010.
9. Sano, T. (1984) *Combust. Sci. Tech.* **38**, 129-144.
10. Sano, T. (1985) *Combust. Sci. and Tech.* **43**, 259-269.
11. Hori, M. (1988) *Twenty-second Symposium (International) on Combustion*, The Combustion Institute, Pittsburgh, PA, 1175-1181.
12. Jaasma, D. and Borman, G. (1980) *Combust. Sci. Tech.* **23**, 83-88.
13. Hori, M., Matsunaga, N., Malte, P. C. and Marinov, N. M. (1992) *Twenty-Fourth Symposium (International) on Combustion*, The Combustion Institute, Pittsburgh, PA, 909-916.
14. Burke, S. P. and Schumann, T. E. W. (1928). *Indust. Eng. Chem.* **29**, 998.
15. Chung, S. H. and Law, C. K. (1984). *Combust. Sci. Tech.* **37**, 21-46.
16. Chen, R.-H., Navedo, J. N. and Chew, L. (1997) *Combust. Sci. Tech.* **127**, 293-318.

TABLE I
Experimental conditions

Fuel*	Measured flame temperature ($T_{f,max}$, K)
80% H_2-20% He	2,293
40% H_2-60% He	2,243
40% CH_4-60% Ar	1,969
40% CH_4-60% He	1,928
60% CH_4-40% He	2,073
40% C_3H_8-60% He	2,071
40% C_3H_8-60% Ar	2,046
80% H_2-20% Ar	2,160
60% C_3H_8-40% He	2,163
80% CH_4-20% He	2,151

* Degree of dilution by volume.

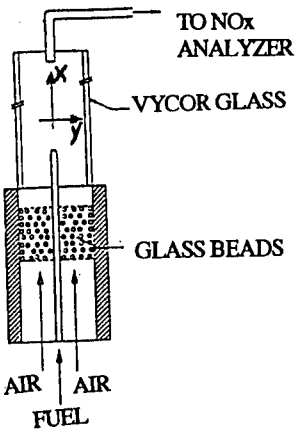


Figure 1. Experimental Apparatus.

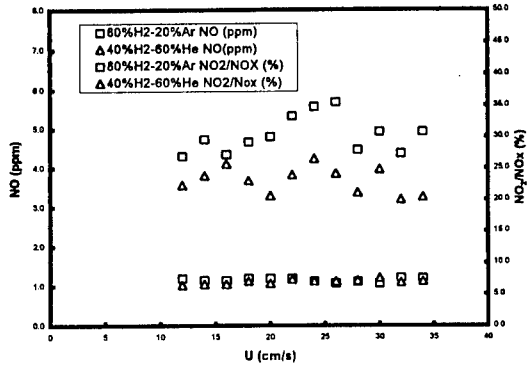


Figure 2. The NO_x levels and the NO_2/NO_x ratio of 80% H_2- 20% Ar flames (flame temperature = 2,160K) and 40% H_2- 60% He flames (T_f = 2,243K), showing that a lower flame temperature leads to a higher NO_2/NO_x ratio given the same NO_x level.

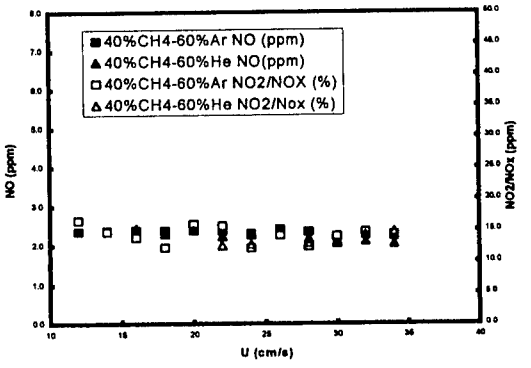


Figure 3. The NO_x levels and the NO_2/NO_x ratio of 40% CH_4- 60% Ar flames (T_f = 1,969K) and 40% CH_4- 60% He flames (T_f = 1,928K), showing that similar flame temperatures and similar level of NO_x leads to similar values of the NO_2/NO_x ratio.

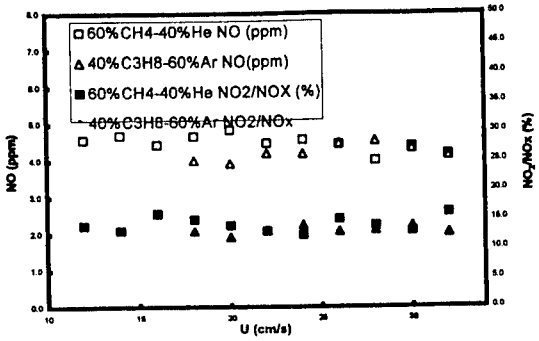


Figure 4. The NO_x levels and the NO_2/NO_x ratio of 60% CH_4- 40% He flames (T_f = 2,073K) and 40% C_3H_8- 60% Ar flames (T_f = 2,046K), showing that similar flame temperatures and similar level of NO_x leads to similar values of the NO_2/NO_x ratio.

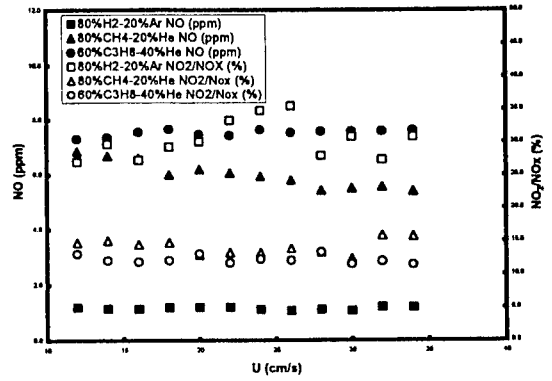


Figure 5. The NO_x levels and the NO_2/NO_x ratio of (1) 80% H_2- 20% Ar flames (T_f = 2,160K), (2) 80% CH_4- 20% He flames (T_f = 2,151K) and (3) 60% C_3H_8- 40% He flames (T_f = 2,163K), showing that for similar flame temperatures, lower levels of NO_x leads to higher values of the NO_2/NO_x ratio.

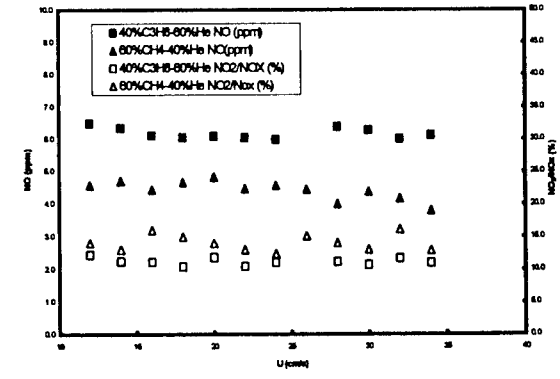


Figure 6. The NO_x levels and the NO_2/NO_x ratio of (1) 60% CH_4- 40% He flames (T_f = 2,073K) and 40% C_3H_8- 60% He flames (T_f = 2,071K), showing that for similar flame temperatures, lower levels of NO_x leads to higher values of the NO_2/NO_x ratio.

Nitric Oxide Emission Indices from Time-Varying and Steady Methane-Air Jet Diffusion Flames

Emily Wilson and J. Houston Miller
Department of Chemistry
The George Washington University
Washington, DC 20052
wilsone@gwu.edu,houston@gwu.edu

Introduction

The focus of considerable research in combustion is the effective control of nitrogen oxide emissions from stationary combustion sources such as industrial process heaters and power generation facilities. Nitrogen oxides have long been known to contribute to acid rain formation and stratospheric ozone depletion. However, new evidence points to a much greater need for NO_x control to mitigate against tropospheric ozone formation as well (Seinfeld, 1991). Most large-scale combustors are turbulent. Unfortunately model development for turbulent combustion typically relies on one of several chemical simplifications (for example, single step chemistry or flamelet libraries). These chemical sub-models may be inadequate to predict NO_X formation, which is affected by a wide range of combustion parameters, including aerodynamic strain, radiative cooling, and superequilibrium concentrations of radicals (Driscoll et al., 1992).

Over the past two decades, a number of experimental studies have been performed whose goal is the parameterization of NOx emissions from turbulent, jet diffusion flames. The emission index for NOx (defined as grams of NOx produced per kilogram of fuel burned.) has been found to depend on flame length (Peters and Donnerhack, 1981), radiant fraction (Turns and Lovett, 1989), oxygen enrichment, and fuel pre-heat (Yap et al., 1998). Of course, many of these parameters are dependent on one another and all may be loosely bundled under the heading of chemistry-flow field interactions.

In the current study, the emission indices for NO from both laminar and steady flickering flames jet flames were measured using tunable diode laser absorption spectroscopy (TDLAS). In recent years several groups have investigated flame flickering phenomena, using both unforced and forced conditions (Pearson and Proctor, 1991; Chen and Roquemore 1986, Shaddix and Smyth, 1996a, 1996b, Smyth et al., 1997). The forced flames can be used to represent a wide variety of low velocity, buoyant diffusion flames which exhibit flickering instabilities (Strawa, and Cantwell, 1985). As such, these flames can provide new insights into the interaction of chemical processes and complex flowfields.

Experimental Procedure

The experimental arrangement used in the present study was derived from several previous studies in our laboratory and will only be briefly described here. Axisymmetric laminar diffusion flames have been established on a coannular burner (Santoro et al., 1987), which consists of a 1.11 cm diameter fuel tube surrounded by a 10.2 cm diameter air annulus. The air chamber is filled with glass beads, followed by several fine mesh screens and a 2.54 cm thick ceramic honeycomb section with 0.15 cm square cells to provide a uniform air flow velocity. No beads or screens have been used for flow conditioning in the fuel tube, which is 13.7 cm long and extends 0.4 cm above the honeycomb. The methane fuel velocity was 8.0 cm/s, and the co-flow air velocity was 10.4 cm/s. To create the time varying flame, a 10 Hz sine wave, produced by a laboratory computer, was amplified with a P.A. amplifier and was applied to a polypropylene woofer speaker (Radio Shack). The speaker was coupled

with a rubber gasket to a plenum through which the fuel flows. Various forcing amplitudes were studied as characterized by the peak-to-peak AC voltage applied to the speaker.

Combustion product mixtures were sampled at roughly 2 cm above the visible flame tip along the burner axis of symmetry using an uncooled quartz microprobe (probe orifice of 120-140 um) similar to that used in previous mass spectral studies of combustion species (Norton et al, 1993). Sampled gas was introduced through Teflon tubing into a into a 36 meter Herriot multipass absorption cell (New Focus). Continuous sampling through the cell was accomplished by pumping with a rotary pump. By throttling the pump flow rate, a pressure of 30 torr was maintained inside the cell as measured by a capacitance manometer attached to the cell.

The tunable diode laser used in these experiments was held in a liquid N_2 dewar (Laser Photonics) and produced light between 1905 cm^{-1} and 1930 cm^{-1}. The beam was collimated and passed through a monochromator to isolate a single lasing mode. The beam was modulated using a tuning fork chopper. For the specific NO transitions studied here, the monochromator was set to allow transmission of light in the wavelength region 1912 to 1913 cm^{-1}. The beam was directed into the absorption cell and finally focused onto a l-N_2 cooled InSb detector. The signal from the detector was then split into two lock-in amplifiers. The first was referenced to a high frequency, sinusoidal modulation applied to the laser current, yielding the "2f" signal for wavelength modulation spectroscopy, WMS (Miller et al., 1993; Skaggs and Miller, 1995). The second lock-in was referenced to the chopper, providing a measure of the laser power. The long pathlength, coupled with WMS, provided the sensitivity necessary for the detection of nitric oxide at sub-ppm levels.

Figure 1 presents a typical spectral scan, here collected in a steady flame. Within the scanned spectral region, four prominent absorption features are evident. In addition to the two NO (R10.5) peaks whose 0.0017 cm^{-1} splitting could not be resolved, two $H_2{}^{18}O$ lines and one CO_2 (P26) line were observed. Spectra were fit using software developed in our lab leading to simultaneous determination of both carbon dioxide and NO concentrations. Turns and Lovett (1989) showed that simultaneous measurement of carbon dioxide and NOx could be used to accurately determine the emission index from:

$$EI_{NO} = \frac{\left[X_{NO}\right] \cdot MW_{NO} \cdot 1000}{\left[X_{CO_2}\right] \cdot MW_{CH_4}}$$

where X_i is the mole fraction and MW_i is the molecular weight.

Results, Discussion, and Future Directions

Figure 2 shows the emission indices measured for a series of flames including the steady case (speaker excitation voltage equals zero). Visual inspection shows that the forced flames span a range which includes the "moderately" and "vigorously" forced cases studied in Smyth's laboratory at NIST. Our data shows an early decrease in emission index as voltage is applied to the speaker. However, the emission index does not continue to decrease as the voltage is increased further. Visually, the flames lengthen with only modest excitation. However, at higher forcing amplitudes, the flames appear shorter and wider.

A recent modeling study has been performed to follow the perturbation of NOx chemistry with oscillation in counterflow flames (Im et al., 1999). This group found a decrease in the observed maximum NO concentration's dependence on stoichiometric scalar dissipation rate as the frequency of the perturbation was increased. However, in contrast to what is typically assumed for turbulent jet flames, the majority of the NO formed in these counterflow flames was produced via the prompt mechanism.

Measurements at NIST as well as the companion modeling work performed at NRL (Kaplan et al., 1996) have shown that soot production is greater in the forced flames as compared to the steady flames due to the fact that the residence time within the active growth region is longer. Their work suggests a decrease in the radiant fraction with flickering. Obviously, for soot these two effects are correlated. How these changes in flow-field upon forcing affect NO production and reburn is not as clear. The flickering jet flames might show both a dependence on temperature (through increased radiant fraction) and on strain rate.

In the coming months we hope to pursue several objectives that may shed light on these preliminary results. We will expand our experiments to include similar measurements for nitrogen dioxide. We also will use a pulsed sampling probe to make time-resolved NOx measurements above and within the flickering flames. Finally, we hope that the parallel efforts in our laboratory in flamelet-modeling of diffusion flame structure (Trouvé et al., 1999), may help to explain the experimental work.

Acknowledgment:

This work was supported through a grant from the National Science Foundation.

References:

Chen, L.-D. and Roquemore, W.M. (1986), Combustion and Flame 66:81.

Chou, Chen-Pang; Chen, Jyh-Yuan; Yam, Clement G.; Marx, Kenneth D. (1998), *Combust. Flame*, 114(3/4), 420-435.

Driscoll, James F.; Chen, Ruey Hung; Yoon, Youngbin (1992), *Combust. Flame*, 88(1), 37-49.

Im, Hong G.; Chen, Jacqueline H.; Chen; Jyh-Yuan (1999), *Combust. Flame*, 118(1/2), 204-212.

Miller, J.H., ELreedy, S., Ahavazi, B., Wlodu, F., and Hassanzadeh, P. (1993), *Appl. Optics* 32:6082-6089 .

Norton, T.S., Smyth, K.C., Miller, J.H., and Smooke, M.D. (1993), *Combust. Sci. and Tech.* 90:1-34.

Pearson, I.G. and Proctor, D. (1991), Experimental Heat Transfer, Fluid Mechanics, and Thermodynamics, p. 316 (1991).

Peters, N.; Donnerhack, S. (1981), *Symp. (Int.) Combust., [Proc.]*, 18th, 33-42.

Santoro, R.J., Yeh, T.T., Horvath, J.J. and Semerjian, H.G. (1987), Combustion Science and Technology 53:89 .

Seinfeld, J., (Chairman), *Rethinking the Ozone Problem in Urban and Regional Air Pollution*, National Research Council Committee on Tropospheric Ozone Formation and Measurement, National Academy Press, Washington, 1991.

Shaddix, C. R. and Smyth, K. C. (1996a), *Combust. Flame*, 106, 392-405.

Shaddix, Christopher R.; Smyth, Kermit C. (1996b), *Combust. Flame*, 107, 418-452.

Skaggs, R.R., and Miller, J.H. (1995), *Combust. Flame 100*, 3:430-439 .

Smyth, Kermit C.; Shaddix, Christopher R.; Everest, David A. (1997), *Combust. Flame*, 111, 185-207.

Strawa, A.W. and Cantwell, B.J. (1985), *Physics of Fluids* 28:2317 .

Trouvé , A, Myre, D.D., Mavriplis, C., and Miller, J.H. . (1999), Chem. Phys. Processes in Combustion.

Turns, S. R.; Lovett, J. A. (1989), *Combust. Sci. Technol.*, 66, 233-249.

Yap, L. T.; Pourkashanian, M.; Howard, L.; Williams, A.; Yetter, R. A. (1998), *Symp. (Int.) Combust., [Proc.]*, 27th(Vol. 1), 1451-1460.

Figures

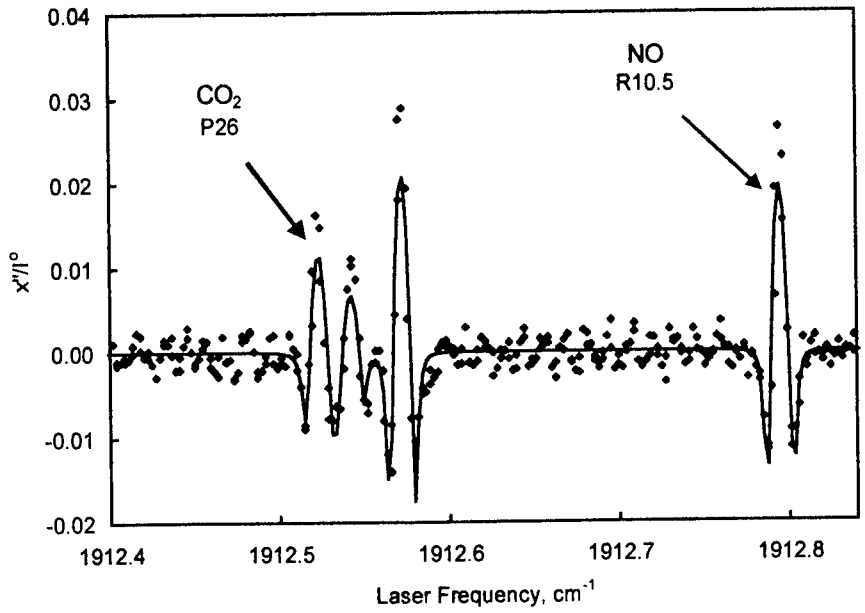


Figure 1: Representative spectrum collected above steady flame illustrating simultaneous carbon dioxide and nitric oxide detection. Solid line is fit of spectral data.

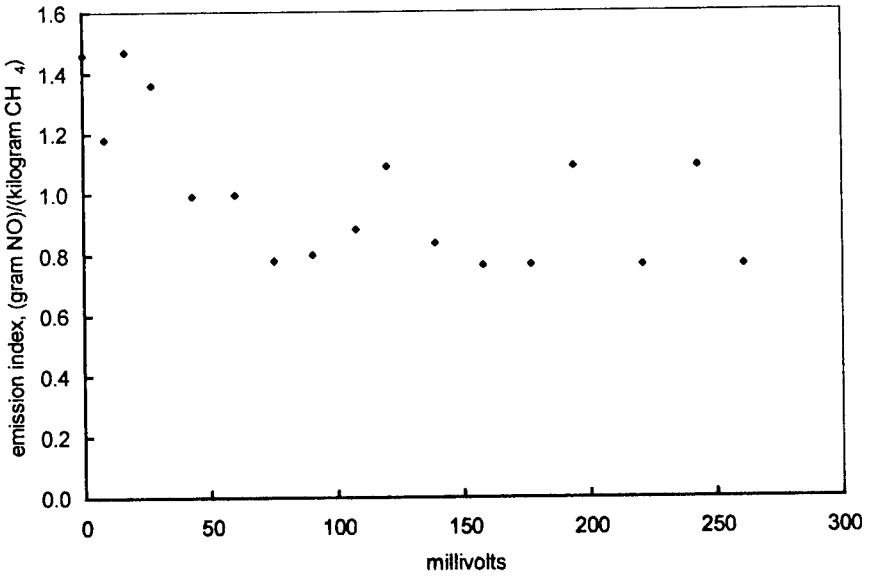


Figure 2: Emission Index for nitric oxide as a function of speaker forcing peak-to-peak voltage.

A FLAMELET-BASED APPROACH FOR DIRECT NUMERICAL SIMULATION OF LAMINAR METHANE-AIR JET DIFFUSION FLAME STRUCTURE

A. Trouvé *, D. D. Myre †, C. Mavriplis *, and J. H. Miller ◇

* Mechanical Engineering Department
The George Washington University
Washington, DC 20052

† Aerospace Engineering Department
US Naval Academy
Annapolis, MD 21402

◇ Department of Chemistry
The George Washington University
Washington, DC 20052

1 Direct numerical simulation of laminar diffusion flames

Computational studies of laminar flames play a central role in our understanding of basic combustion phenomena as well as in the development of physical and chemical sub-models relevant to turbulent combustion applications. Different mathematical formulations may be found in the literature for the numerical simulation of laminar flames. These different formulations correspond to different degrees of complexity in the treatment of chemistry and molecular transport. For instance, while the most advanced simulations use the latest, detailed, high-fidelity descriptions of multi-step chemical kinetics and multi-component molecular transport [1-4], many studies adopt simpler formulations based on global chemical reaction schemes and Fick's diffusion law.

The choice of the adequate level of complexity is a key step in many studies, that is aimed at optimizing, for a given particular problem, the trade-off between performance, accuracy and computational cost. While full formulations with detailed chemistry and molecular transport are of considerable interest [1-4], they remain severely constrained by their high demand of computer power and are therefore not well-suited for parametric studies. Current approaches to obtain more tractable, less demanding formulations include the reduced chemistry approach, where the chemical system is parametrized in terms of a small number of reaction progress variables and its evolution is described using a simplified chemical kinetics model. While the reduced chemistry approach has many attractive features, it remains an expensive method for the computation of laminar flames, where the coupling between chemistry and molecular mixing has to be handled carefully.

We consider in the present paper an alternative approach for the simulation of laminar diffusion flames based on the classical flamelet theory [5-6]. In the flamelet theory, the reaction zone is viewed as an ensemble of strained laminar flame elements, and the local flame structure is obtained from a generic model problem corresponding to an opposed-flow laminar diffusion flame. Solutions of this generic problem are conveniently pre-computed and stored in a look-up table (a flamelet

library). The flamelet library approach thereby achieves good accuracy (the flamelet solutions are computed using a full formulation with detailed chemistry and molecular transport) as well as low computational cost (the flamelet solutions are pre-computed and coupled to the main flow solver via an inexpensive look-up table strategy). In its simplest version, the flamelet library is constructed using only two parameters, the mixture fraction Z and the scalar dissipation rate χ [5-6]. Additional parameters may be needed, however, to account for flame curvature, transient effects, radiative heat losses, and partial premixing [5].

In the present study, we apply the flamelet approach to the computation of a laminar, plane, co-flowing, CH_4-air jet diffusion flame. The flamelet library is constructed using : a standard opposed-flow flame code based on the CHEMKIN-II software package [7] ; multi-step kinetics for $C/H/O/N$ species based on the GRI-Mech 2.11 mechanism (48 species/277 reactions) [8] ; and multi-component molecular transport, as described by Ern and Giovangigli [9,10]. In an initial step, the flamelet library is limited to its simplest version with Z and χ as the only parameters. These parameters are obtained using a multi-dimensional, compressible Navier-Stokes solver. The solver features a high-order finite difference scheme that is sixth-order accurate in space [11] and third-order in time ; boundary conditions are specified with a method proposed by Poinsot and Lele [12]. The simulations describe the overall flame structure, in terms of fuel oxidation, heat release and N_2 chemistry, and are ultimately aimed at bringing relevant information on NO_x formation processes.

2 Experimental/computational evaluation of the flamelet approach

The validity of the flamelet approach for accurate simulations of laminar jet diffusion flames may be evaluated by comparing flamelet predictions with experimental measurements and/or full computational results. An example of such a validation test is presented in Figure 1. Figure 1 presents typical flamelet variations of CH_4, CO_2 and CO mole fractions with mixture fraction, and compares these variations to those observed in laminar, axisymmetric, CH_4-air diffusion flames, both experimentally [13,14] and computationally [1]. The experimental points are tunable diode laser absorption spectroscopy (TDLAS) measurements, combined with an estimate of the local carbon element mass fraction to define mixture fraction, and a contour-smoothing post-processing technique to improve the signal-to-noise ratio [15]. For clarity in Figure 1, the points correspond to a single height of $z = 10$ mm above the burner (where $\chi_{st} \approx 0.5$ s^{-1}, see [16] for further details). The full computational results are based on a formulation with detailed chemistry (26 species/83 reactions) and molecular transport. Again, for the sake of clarity, we only use a sub-set of the full computational solution. This sub-set corresponds to a height of $z = 7.7$ mm above the burner (where $\chi_{st} = 0.63$ s^{-1}, see [17] for further details).

In Figure 1, the observed level of agreement (and slight discrepancies) between experimental data and full computational results is similar to that found in previous studies [17,18]. Figure 1 also shows that the flamelet solutions : correctly describe CH_4 variations ; tend to underpredict the peak CO_2 value ; tend to overpredict the peak CO value ; and tend to overestimate CO_2 and CO levels in the fuel rich region (for mixture fractions larger than 0.2). A separate comparison of flamelet and full computational results for temperature also indicates that the flamelet temperatures are too high on the rich side of the flame. These discrepancies are consistent with similar results obtained by Smooke *et al.* [2]. While the source of the discrepancies remains unclear, it is possibly related

to transient effects associated with the flame stabilisation region. Work is in progress to develop a formulation that incorporates these effects in the flamelet-based simulations.

REFERENCES

[1] Smooke, M. D., Lin, P., Lam, J. K. and Long, M. B., *Twenty-Third Symposium (International) on Combustion,* The Combustion Institute, Pittsburgh, PA, 1990, pp. 575-582.

[2] Smooke, M. D., Xu, Y., Zurn, R. M., Lin, P., Frank, J. H. and Long, M. B., *Twenty-Fourth Symposium (International) on Combustion,* The Combustion Institute, Pittsburgh, PA, 1992, pp. 813-821.

[3] Smooke, M. D., Ern, A., Tanoff, M. A., Valdati, B. A., Mohammed, R. K., Marran, D. F. and Long, M. B., *Twenty-Sixth Symposium (International) on Combustion,* The Combustion Institute, Pittsburgh, PA, 1996, pp. 2161-2170.

[4] Mohammed, R. K., Tanoff, M. A., Smooke, M. D., Schaffer, A. M. and Long, M. B., *Twenty-Seventh Symposium (International) on Combustion,* The Combustion Institute, Pittsburgh, PA, 1998, pp.693-702.

[5] Peters, N., *Prog. Energy Combust. Sci.* 10:319-339 (1984)

[6] Peters, N., *Twenty-First Symposium (International) on Combustion,* The Combustion Institute, Pittsburgh, PA, 1986, pp. 1231-1250.

[7] Kee, R. J., Rupley, F. M. and Miller, J. A., "CHEMKIN-II: a Fortran chemical kinetics package for the analysis of gas-phase chemical kinetics", Sandia National Laboratories report SAND89-8009, 1990.

[8] Bowman, C. T., Hanson, R. K., Davidson, D. F., Gardiner, W. C., Lissianski, V., Smith, G. P., Golden, D. M., Frenklach, M. and Goldenberg, M., *GRI-Mech version 2.11, http://www.me.berkeley.edu/gri_mech/,* 1996.

[9] Ern, A. and Giovangigli, V., *Multicomponent transport algorithms.* Lecture Notes in Physics, New Series "Monographs" m24, Springer-Verlag, 1994.

[10] Ern, A. and Giovangigli, V., *J. Comp. Phys.* 120:105-116 (1995)

[11] Lele, S. K., *J. Comp. Phys.* 103:16-42 (1992)

[12] Poinsot, T., and Lele, S. K., *J. Comp. Phys.* 101:104-129 (1992)

[13] Skaggs, R. R. and Miller, J. H., *Twenty-Sixth Symposium (International) on Combustion,* The Combustion Institute, Pittsburgh, PA, 1996, pp. 1181-1188.

[14] Skaggs, R. R., Ph.D. thesis, Dept. of Chemistry, George Washington Univ., 1997.

[15] Myre, D. D., Skaggs, R. R. and Miller, J. H., *First Joint Meeting of the US Sections of the Combustion Institute,* Washington, DC, 1999.

[16] Myre, D. D., Ph.D. thesis, Mechanical Engineering Dept., George Washington Univ., *in preparation.*

[17] Norton, T. S., Smyth, K. C., Miller, J. H. and Smooke, M. D., *Combust. Sci. and Tech.* 90:1-34 (1993)

[18] Kaplan, C. R., Patnaik, G. and Kailasanath, K., *Combust. Sci. and Tech.* 131:39-65 (1998)

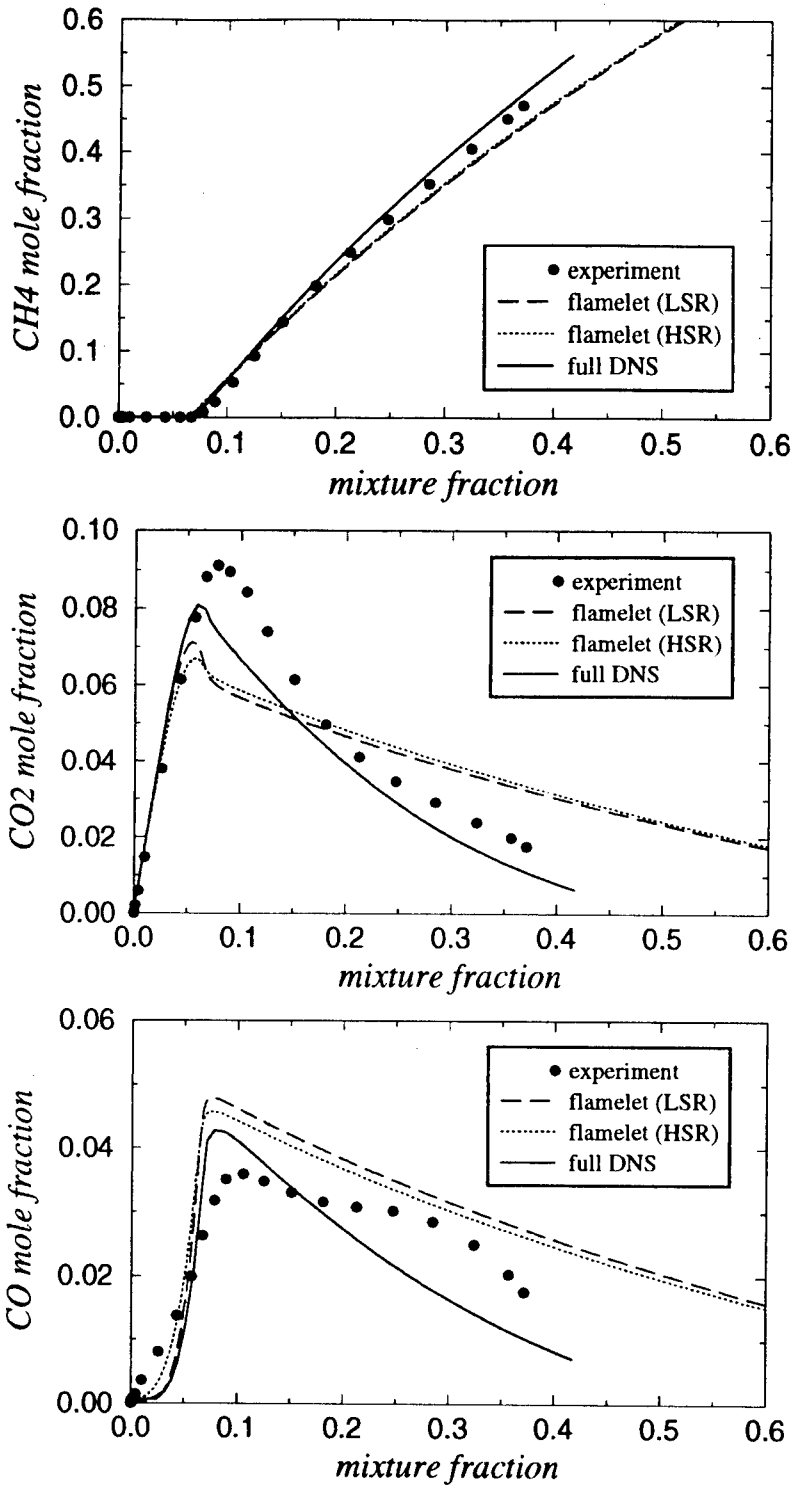


Figure 1: Variations of CH_4, CO_2 and CO mole fractions with mixture fraction. Comparison between flamelet calculations (long-dashed curves), experimental data (points) [13,14], and full computational results (solid line) [1]. The flamelet calculations correspond to opposed-flow, plane, CH_4-air diffusion flames, with LSR (HSR) corresponding to low (high) strain rates conditions, $\chi_{st} = 0.3$ s^{-1} ($\chi_{st} = 3.1$ s^{-1}).

Spectral Element Direct Numerical Simulations of Laminar Diffusion Flames

Andrew Tangborn
JCET, University of Maryland Baltimore County, Baltimore, MD
tangborn@jcet.umbc.edu
Catherine Mavriplis
Department of Mechanical and Aerospace Engineering
the George Washington University
Washington, DC
J. Houston Miller
Department of Chemistry
the George Washington University
Washington, DC
houston@gwis2.circ.gwu.edu

Introduction

The spectral element method (Patera, 1984) is a high order discretization technique for the direct numerical simulation of complex physical phenomena. The high order afforded by spectral discretization within each element makes the method suitable for transitional regime flows such as those of steady and unsteady laminar and transitional diffusion flames. The flexibility of the finite element approach allows for efficient grid resolution of the flame structure. The fluid dynamics solver has been developed to include grid adaptivity (Mavriplis and Hsu, 1997) and parallel algorithms (Feng and Mavriplis, 1999). These features of the solver will enhance the capability for accurate flame simulations. Coupling the chemistry with the fluid solver, however, remains a significant task. This paper addresses this task to build an efficient and effective diffusion flame simulation tool.

The conserved scalar approach of Bilger (Bilger, 1976) has been shown to be effective for modeling diffusion flames (Peters, 1986). In this approach, mixture fraction is the conserved scalar, being governed by a conservation equation with no sources or sinks. This single equation can replace conservation equations for all of the chemical species, thereby significantly reducing the computational effort required. This assumption is at the root of the flamelet theory approach to modeling turbulent non premixed flames.

Within the conserved scalar approach, however, chemical heat release must be accounted for in the energy conservation equation. There has been a considerable body of work aimed at characterizing the heat release region of both premixed and non-premixed flames (Najm et al, 1998). Unfortunately, most of this work is for diluted flames, as opposed to neat flames. In a recent study of flickering methane air flames, Kaplan et al (Kaplan et al, 1996) used a simple model for heat release that is derived from a conserved scalar treatment of fuel consumption following Bilger (Bilger, 1976):

$$\dot{\omega}_{CH_4} = -\rho D(\nabla\xi)^2 Y''_{CH_4}(\xi) \tag{1}$$

where (is the mixture density, Y_{CH_4} is the mass fraction of the methane, D is the mixture diffusion coefficient and (is the mixture fraction. Five chemical species, CH_4, O_2, N_2, CO_2, and H_2O were

tracked in the flow and heat release was calculated by multiplying the above fuel consumption rate by the heat of combustion.

Recent experimental measurements by our group (Tolocka and Miller, 1998) have characterized the fuel consumption rate through formaldehyde concentration measurements using TDLAS (tunable diode laser absorption spectroscopy). This study showed that the rate of methane destruction could be determined by the rate of formaldehyde formation, as Bilger et al (Bilger et al, 1990) had suggested. The analysis also verified that the heat release correlates well with the methane destruction rate. The experimental results, however, over predicted the HCO· concentration, which would mean that the heat release rate is also over predicted. Their experimental correlation produced a slope of -136 (kJ/mol) which is substantially less than the heat of combustion for methane (-89 kJ/mol). The aim of this paper is to test this model for heat release into the spectral element conserved scalar model for accurate simulation of laminar diffusion flames.

Model

The flame is modeled using the direct numerical solution approach where the full incompressible Navier-Stokes equations are solved along with a conservation equation for mixture fraction as follows:

Conservation of mass

$$\vec{\nabla} \cdot \vec{v} = 0 \tag{2}$$

Conservation of momentum

$$\rho \frac{\partial \vec{v}}{\partial t} + \rho(\vec{v} \cdot \vec{\nabla})\vec{v} = (\vec{\nabla} \cdot \mu\vec{\nabla})\vec{v} - \vec{\nabla}p + \rho\vec{g} \tag{3}$$

Conservation of energy

$$c_p \rho \frac{\partial T}{\partial t} + c_p \rho(\vec{v} \cdot \vec{\nabla})T = (\vec{\nabla} \cdot k\vec{\nabla})T + Q(\xi) \tag{4}$$

Conservation of ξ (Mixture Fraction)

$$\rho \frac{\partial \xi}{\partial t} + \rho(\vec{v} \cdot \vec{\nabla})\xi = (\vec{\nabla} \cdot \rho D\vec{\nabla})\xi \tag{5}$$

Where $\vec{v} = (u, v)$ is the axisymmetric velocity field, the density ρ is determined from the ideal gas law in the gravitational term and energy equations. Fluid properties are mixture diffusion coefficient $D = D(T)$, conductivity $k = k(T)$, specific heat $c_p = c_p(T)$ and viscosity μ. Heat release uses the Tolocka and Miller model, equation (1), as a starting point , with a factor α introduced to adjust heating until the correct temperature and flame height are achieved

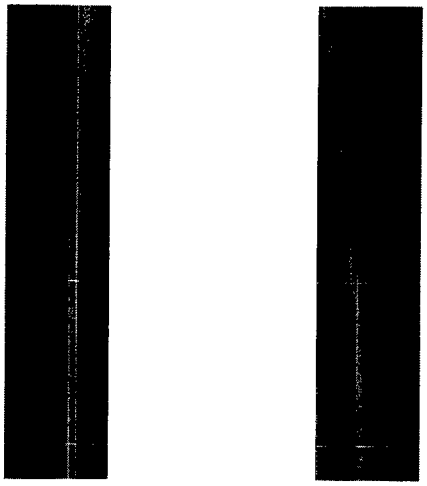
$$Q(\xi) = -\alpha(136 kJ/mol)\rho D(\nabla\xi)^2 Y''_{CH_4}(\xi) \tag{6}$$

Discretization

The computational domain is divided into 69 subdomains. Within each subdomain, Legendre polynomials of order (7×7) are introduced as basis functions and Gauss-Lobatto quadrature is used to obtain the discretized equations. Small elements are concentrated along the flame front in order to resolve the steep gradients in temperature and mixture fraction.

Calculations of Flames

We test the above heat release model on two different flame geometries and compare with experimental results in one case and a full chemistry computational flame in the second. Figures 1 and 2 show computational and experimental temperature and mixture fraction (ξ) fields for a Methane diffusion flame with a fuel inlet diameter of $D_{fuel} = 1.1$ cm and average inlet velocity



(a) Numerical (b) Experimental

Figure 1: Numerical and Experimental temperature fields for the 1.1 cm fuel inlet burner

$u_{inlet} = 10.4$ cm/s. The computations use a heat release factor of $\alpha = 2.5$. In both cases the flame height (where $\xi = 0.055$ along the centerline) is around 7 cm, and the maximum temperature is a little under 2000 K. The second flame ($D_{fuel} = .4$ cm and $u_{inlet} = 35$ cm/s) is compared with the full chemistry simulation of Smooke *et al.* (1990), also using $\alpha = 2.5$. Both computations predict a flame height of 3.8 cm, indicating that the heat release model can successfully be applied to a variety of geometries without repeatedly *tuning* the model. Correlations between individual species and mixture fraction are derived from full chemistry computations and used to calculate species concentrations for CO, CO_2 and CH_4.

Conclusions

We have presented simulations axisymmetric Methane diffusion flames using a spectral element discretization method and a mixture fraction based heat release model. Good agreement is found with experimental and full chemistry flames in two different geometries. Future work is directed towards calculating slow chemistry concentrations from the mixture fraction, velocity and temperature fields.

Acknowledgments

Part of this work was supported by the George Washington University Research Enhancement Fund through the Center for the Study of Combustion and the Environment. Partial support is provided by NSF through grant CTS-9729578. The second author would like to thank Elaine Oran and the Naval Research Laboratory for providing support during her sabbatical year.

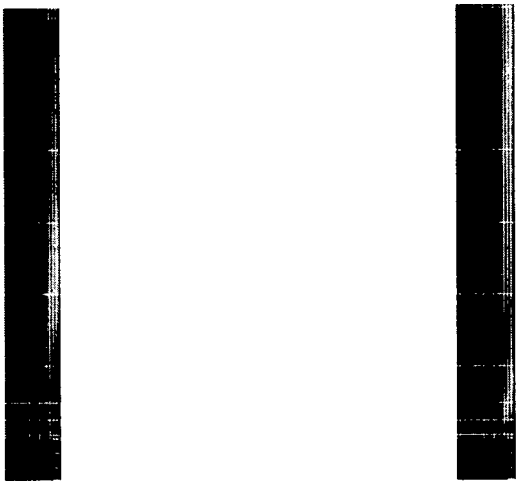
References

R. W. Bilger, Combustion Science Technology, 13:155-170, 1976.

R. W. Bilger, S. H. Starner, and R. J. Kee, Combustion and Flame, 80, pp.135-149, 1990.

H. Feng and C. Mavriplis, Parallel Implementation of the Spectral Element Method with Non conforming Mesh, Eleventh International Conference on Domain Decomposition Methods, C.-H. Lai, P. E. Bjorstad, M. Cross and O. B. Widlund editors, 1999.

C. R. Kaplan, C. R. Shaddix, and K. C. Smyth, Computations of Enhanced Soot production in Time-Varying CH4/Air Diffusion Flames, Combustion and Flame, 106, pp. 392-405, 1996.



(a) Mixture Fraction (b) Temperature

Figure 2: Numerical mixture fraction and temperature for the 0.4 cm fuel inlet burner

C. Mavriplis and L.-C. Hsu, "A Two-Dimensional Adaptive Spectral Element Method", Proceedings of the 13th AIAA Computational Fluid Dynamics Conference, Snowmass, June 1997.

H. N. Najm, P. H. Paul, C. J. Meuller, and P. S. Wyckoff, Combustion and Flame, 113, pp. 312-332, 1998.

A. T. Patera, "A Spectral Element Method for Fluid Dynamics; Laminar Flow in the Channel Expansion", J. Comput. Phys., 54, pp.468, 1984.

N. Peters, Laminar Flamelet Concepts in Turbulent Combustion, Twenty-first Symposium (International) on Combustion, The Combustion Institute, pp. 1231-1250, 1986.

M. Smooke, P. Lin, J. Lam and M. Long, Computational and Experimental Study of a Laminar Axisymmetric Methane-Air Diffusion Flame, Yale University Report ME-101-90, 1990.

M. P. Tolocka and J.H. Miller, Measurements of Formaldehyde Concentrations and Formation Rates in a Methane-air, Non-premixed Flame and Their Implications for Heat-release Rate, Twenty-seventh Symposium (International) on Combustion, The Combustion Institute, pp. 633-640, 1998.

Experimental and Computational Study of Coflow Laminar Diffusion Flames in a Microgravity Environment

Kevin T. Walsh, Joseph Fielding, Marshall B. Long, and Mitchell D. Smooke

Yale University
Department of Mechanical Engineering
New Haven, CT 06520-8284
marshall.long@yale.edu

Introduction

The ability to predict the coupled effects of complex transport phenomena with detailed chemical kinetics in diffusion flames is critical in the modeling of turbulent reacting flows and in understanding soot formation and radiative transfer. In addition, the factors that affect extinction in diffusion flames are of practical importance in areas such as fire suppression and engine efficiency. The goal of our characterizations of coflow laminar diffusion flames is to bring to microgravity the multidimensional diagnostic tools available in normal gravity, and in doing so provide a broader understanding of the successes and limitations of current combustion models. This will lead to a more detailed understanding of the interaction of convection, diffusion and chemistry in both buoyant and nonbuoyant environments.

The flame under investigation is a lifted axisymmetric laminar diffusion flame, which has been characterized previously both experimentally and computationally [1-5]. The fuel is nitrogen-diluted methane surrounded by an air coflow. Experimentally, temperature and major species (CH_4, N_2, O_2, H_2O, CO, CO_2, H_2) concentrations were measured simultaneously with Rayleigh and Raman scattering [4]. Laser-induced fluorescence (LIF) measurements were performed to measure number densities of minor species. Quantitative, linear LIF measurements were made for OH [2], NO [3] , and CH [5]. Modeling work has employed different kinetic schemes, including a 26 species C_2 hydrocarbon mechanism [2] and GRI Mech 2.11 [6]. Both produced excellent agreement for temperature and major species [4]. Computed peak concentrations of OH and CH were within 15% and 20%, respectively, of their measured values.

Two-dimensional laser imaging techniques such as Rayleigh scattering and laser-induced incandescence (LII) are difficult to perform in microgravity facilities due to experimental size, weight, and power requirements. In the last few years, highly compact, pulsed Nd:YAG lasers have become available to alleviate these problems. However, many practical issues remain in making such measurements on the KC-135 reduced-gravity aircraft, among them spurious light scattering in Rayleigh measurements and possible flame fluctuations as a result of g-jitter. With these concerns in mind, this work describes two-dimensional temperature and soot volume fraction measurements performed on the KC-135. Temperature measurements are carefully compared with the predictions of a two-dimensional flame model. In performing this microgravity study, improvements to the computational model have been made and new calculations performed for a range of gravity and flow conditions. Results from the experiments and computations are presented in the following sections.

Burner Configuration

The burner used in this experiment contains a central fuel jet (4 mm diameter) surrounded by coflowing air (50 mm diameter). The standard flow conditions, which have been measured and modeled extensively in normal gravity, consist of fuel composed of 65% CH_4 diluted with 35% N_2 by volume (denoted 65/35 in later discussion). The plug flow exit velocity of both fuel and coflow was 35 cm/s. These conditions produce a blue flame roughly 3 cm in length with a lift-off height of 5.5 mm in normal gravity. Flame structure, lift-off, and soot production can change widely as the CH_4/N_2 fuel composition is varied, which allows for robust comparison of measurement with prediction. The fuel mixture can range from 100% CH_4 (denoted 100/0) to 40% CH_4 (denoted 40/60), with the exit velocity held fixed at 35 cm/s.

Computational Approach

The computational model used to compute the temperature field, velocities, and species concentrations, solves the full set of elliptic two-dimensional governing equations for mass, momentum,

species, and energy conservation on a two-dimensional mesh [3]. The resulting nonlinear equations are then solved on an IBM RS/6000 Model 590 computer by a combination of time integration and Newton's method. The chemical mechanism was a simple 26-species, C_2 hydrocarbon mechanism [2], which shows better agreement with measured lift-off than GRI Mech 2.11.

Flame computations indicated that the predicted lift-off height is highly sensitive to the convergence parameters used in the computation. At each fuel mixture and gravity level, the convergence tolerances are tightened until the computed result is unchanged, indicating a final solution has been reached. Computations were performed for CH_4/N_2 mixtures ranging from 30/70 to 75/25. Calculations were not performed for fuel mixtures less dilute than 75/25 since these flames were observed to produce soot, which was not included in the computational model.

Experimental Configuration

The μg coflow laminar diffusion flame experiment consists of three racks -- an experiment rack, an external control rack, and a laser rack. The experiment rack holds a windowed combustion vessel that contains the burner, stepper motor, and ignition system. The pressure vessel is maintained at standard atmospheric pressure for flame stability and to match the computed conditions. A three path exhaust system involving a computer-controlled servo valve, an orifice plate, and pressure relief valve is used to keep the pressure inside the combustion vessel constant to better than 1%. A cooled CCD camera and a lens-coupled image intensifier are used to measure the laser-produced signal. Also housed in the experiment rack is a color video camera, the methane fuel supply, mass flow controllers and power supply, and relays allowing computer control of various components. The external control rack contains a microcomputer system to regulate and monitor experimental systems, along with a VCR and video monitor to view the flame in real time. The laser rack contains a compact, high-power pulsed Nd:YAG laser, which requires its own mount and associated equipment. This laser produces up to 220 mJ per pulse in the green (at 532 nm) and operates at 10 Hz. The timing electronics used to gate the image intensifier are also housed in this rack. The 532 nm beam is shaped into a 7 mm tall sheet, steered through a window and brought to a focus over the burner centerline. The beam then exits through another window and is stopped in a power meter, which measures the laser energy. Accelerometer measurements quantified the positive and negative unsteady forces (g-jitter) present during a given low-g maneuver. In the first flight, the airplane accelerometer signal was recorded over a 10 s period coincident with data acquisition. In recent work, a three-axis accelerometer was mounted directly to the experiment rack to provide a more accurate measure of local acceleration.

Measurement and Image Processing

Temperature measurements take place with Rayleigh scattering, which is an elastic light scattering mechanism that can be used to measure number density. The Rayleigh signal (S_R) at a given point is directly proportional to number density and Rayleigh cross section (σ_R) of the gas mixture at that point. Since our measurements take place at atmospheric pressure, the ideal gas law can be used to relate number density to temperature (T), which gives us an expression for the measured Rayleigh image as

$$S_R(x,y) = k\frac{\sigma_R(x,y)}{T(x,y)}$$

where k is a constant determined from the Rayleigh signal in the ambient air region of the image, where T=300 K and σ_R is known.

Non-sooting flames were observed to be stable under the influence of "g-jitter," so the temperature field could be reliably measured with a 100 shot integration. To perform Rayleigh thermometry, images from uniform concentrations of helium and air must accompany flame measurements to account for spuriously scattered light and non-uniform detector response. These three images are acquired and combined at each of 10 downstream locations and later tiled together to form a Rayleigh image of the entire flame. A "stripe correction" is then performed to account for non-uniformities in the laser beam profile. This Rayleigh image is then converted into an initial temperature profile by assuming a spatially constant Rayleigh cross section. The computed major species profiles are then used to obtain the Rayleigh cross section as a function of temperature. This double-valued function is then utilized with the initial measured temperature profile to iteratively account for spatial variations in the Rayleigh cross section, $\sigma_R(x,y)$. A self-consistent temperature distribution is reached after 5 or 6 iterations.

Since sooting flames have been observed to fluctuate in the unsteady acceleration of the KC-135, time-averaged Rayleigh scattering and LII measurements may not be appropriate at these flow conditions. However, single-shot measurements were made to provide an instantaneous flame characterization. These time-resolved measurements were indexed with the accelerometer signal to provide information on the effect g-fluctuations have on the soot and temperature distributions.

Results

The temperature distribution was successfully measured in 100 shot integrations at a number of flow conditions, including 50/50, 65/35, and 80/20, where soot interferences begin to be visible in a small section of the flame tip. Measured and computed temperature distributions in the 65/35 flame are directly compared in Fig. 1. Good agreement in flame structure and lift-off height can be seen in the normal gravity flame. In the μg flame, we see the computations successfully predict that when the influence of gravity is removed, the high temperature zone becomes shorter and wider. Stray light reflections prohibited measurements less than 6 mm above the burner surface, so the computed and measured flame anchoring regions cannot be directly compared in μg. However, the centerline temperatures shown in Fig. 2 provide a more quantitative comparison of measurement and prediction. In the normal gravity flame, agreement in lift-off and peak temperature is good, although the flame length is somewhat over-predicted. Agreement in the nonbuoyant flame is excellent - flame lift-off, the lower peak temperature, and shorter flame length are all well predicted.

Single shot temperature measurements were made over a wide range of flow conditions to check the temporal stability of the thermal field under the influence of g-jitter. These measurements were made at the two furthest downstream locations, from 45 mm to 55 mm above the burner surface. This region was chosen because it is the least stable region where soot is not present at any flow condition. Time resolved Rayleigh measurements were made at the 50/50, 65/35, 80/20, and 100/0 fuel mixtures. Individual shots were compared to averages of four single shots to determine the amount of temperature fluctuations. Results indicate that the stability of the 50/50 and 65/35 flames in g-jitter is comparable to their normal gravity counterparts while individual 100/0 snapshots in μg can be displaced 600 μm from their average Rayleigh signal contour. The images examined were sampled during parabolas where the average acceleration was ~0.01 g and the rms fluctuations were 0.02 g.

Single shot LII measurements, which are proportional to relative soot volume fraction, were made at the 100/0 flow condition. This can be seen in Fig. 3. Each image consists of three downstream locations tiled together, measured at different times. After it was observed that the distributions fit together, they were all found to have a similar g-level and g-history. In the image on the left, the acceleration was travelling linearly downward from 20% of Earth's gravity down to g=0, while the image on the right was taken during a constant g=0 interval. The two LII images have a difference in peak soot concentration of 50% as well as differences in spatial distribution, illustrating the sensitivity of soot production to g-jitter.

In the future, further temperature measurements are planned to assess existing combustion models. Additionally, soot calibrations are planned and a 2-D soot model is under development to allow direct comparison of LII measurements with computations.

References

1. Smooke, M.D., Lin, P., Lam, J., and Long, M.B., *Twenty-third Symposium (International) on Combustion*, The Combustion Institute, Pittsburgh, PA, 1991, pp 575-582.
2. Smooke, M.D., Xu, Y., Zurn, R.M., Lin, P., Frank, J.H., and Long, M.B., *Twenty-fourth Symposium (International) on Combustion*, The Combustion Institute, Pittsburgh, PA, 1992, pp 813-822.
3. Smooke, M.D., Ern, A., Tanoff, M.A., Valdati, B.A., Mohammed, R.K., Marran, D.F., and Long, M.B., *Twenty-sixth Symposium (International) on Combustion*, The Combustion Institute, Pittsburgh, PA, 1996, pp 2161-2170.
4. Marran, D.F., *Ph. D. Thesis*, "Quantitative Two-Dimensional Laser Diagnostics in Idealized and Practical Combustion Systems", Yale University, New Haven, CT, 1996.
5. Walsh, K. T., Long, M. B., Tanoff, M. A., and Smooke, M. D., *Twenty-seventh Symposium International) on Combustion*, The Combustion Institute, Pittsburgh, PA, 1998, pp 615-623.
6. Bowman, C.T., Hanson, R.K., Davidson, D.F., Gardiner Jr., W.C., Lissianski, V., Smith, G.P., Golden, D.M., Frenklach, M., Wang, H., and Goldenberg, M., *GRI-Mech version 2.11*, http://www.gri.org, 1995.

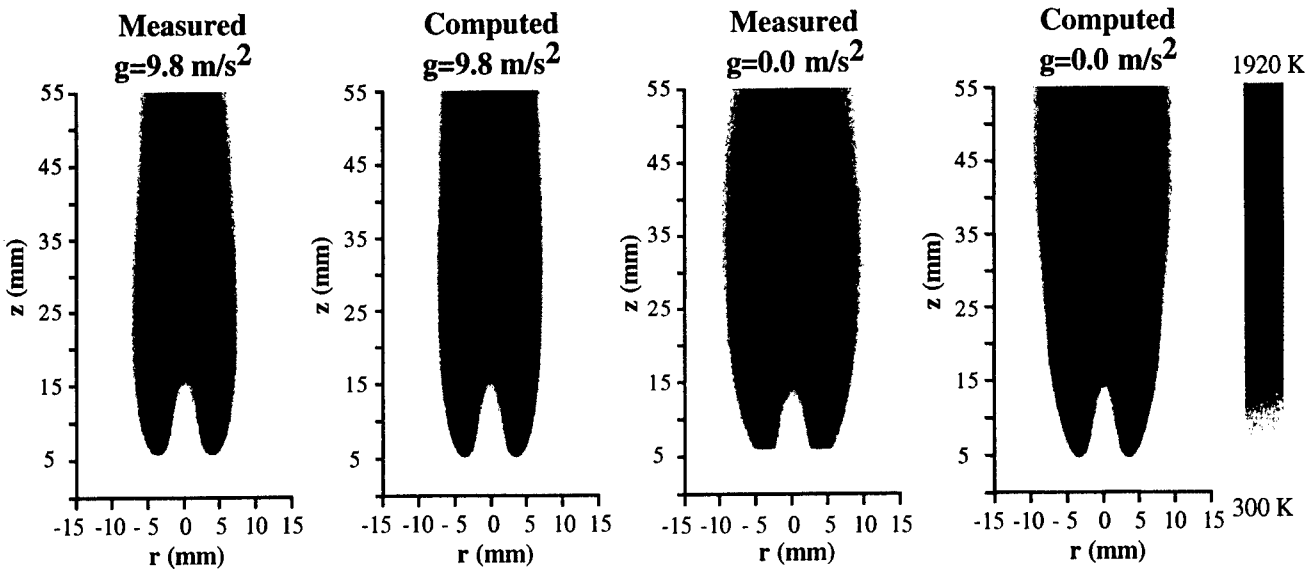


Figure 1. Measured and computed temperatures for the 65% CH_4:35% N_2 fuel mixture.

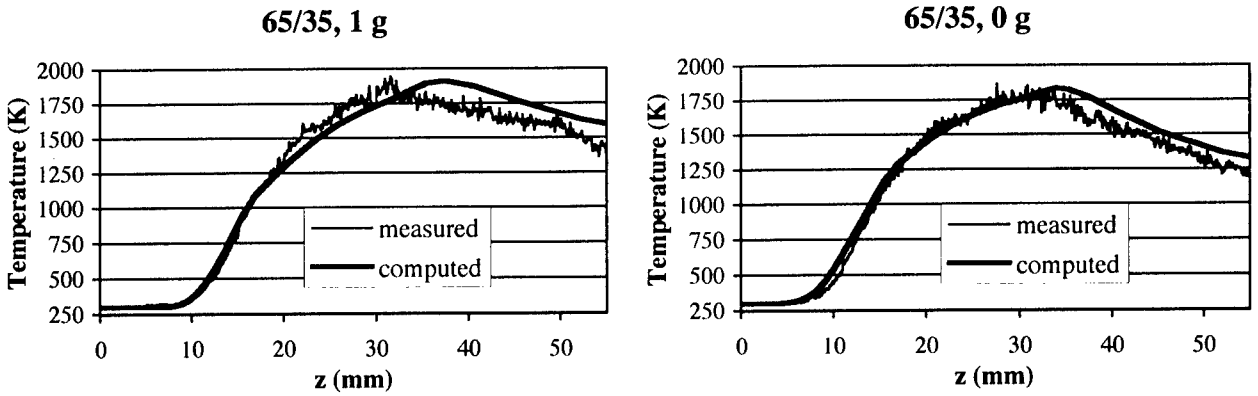


Figure 2. Centerline temperatures taken for the 65/35 fuel mixture in normal and zero g.

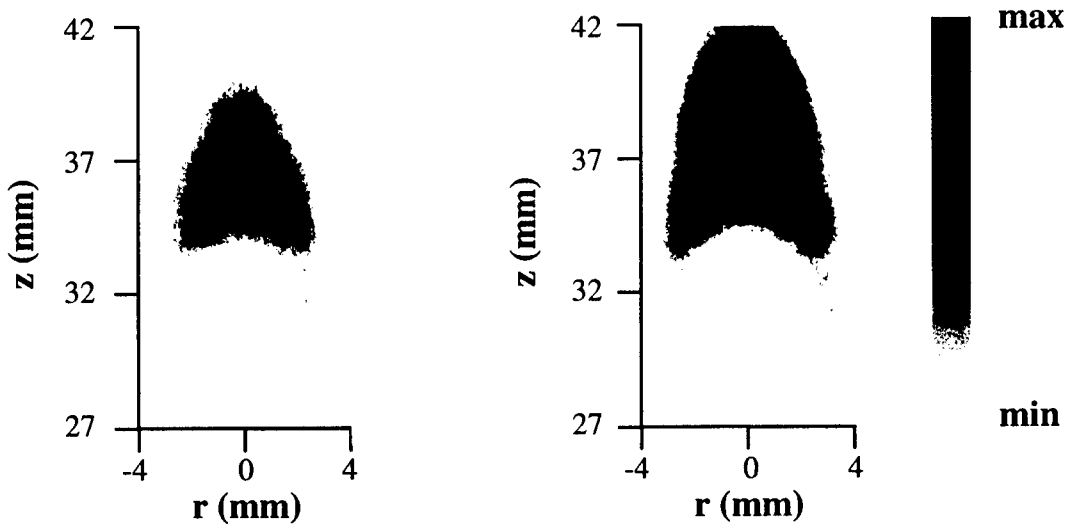


Figure 3. Uncalibrated, single-shot LII images from 100% CH_4 flame, taken during different portions of a low-g parabola. On the left, g is decreasing to zero, while on the right g is steady and equal to zero.

Simultaneous PIV and OH-PLIF Measurements in an Unsteady Counterflow Propane-Air Diffusion Flame

Eric J. Welle and William L. Roberts[1]
North Carolina State University
Department of Mechanical and Aerospace Engineering
Box 7910
Raleigh, NC 27695-7910
Wlrobert@eos.ncsu.edu

Campbell D. Carter
Innovative Scientific Solutions, Inc.
2786 Indian Ripple Rd.
Dayton, OH 45440-3638

Jeffrey M. Donbar
Advanced Propulsion Div. AFRL/PRSS
Wright-Patterson Air Force Base, OH 45433-7103

Introduction

Turbulent diffusion flames are of particular interest because of their presence in most practical combustion devices. Flamelet theory is a method that characterizes turbulent diffusion flames as a collection of strained, laminar, one dimensional flamelets [1], which are dependent upon the mixture fraction and instantaneous scalar dissipation rate. An assumption of traditional flamelet theory is that the flamelet in a turbulent flow field responds quasi-steadily to the unsteady strain rates of the turbulent flow field. A turbulent flow field is composed of eddies with a wide range of length and time scales. If the turbulent Reynolds number is sufficiently large, there exists a range of eddy sizes where the characteristic turnover time of the smallest eddies are comparable to the diffusion time of the laminar flamelet [2]. The large scale eddies establish the magnitude of the mean strain rate and fluctuations around this mean value are caused by the smaller eddies and these conditions can lead to a wide range of characteristic frequencies [3]. For this reason, it is necessary to investigate the frequency response of flamelets in an attempt to extend the applicability of the flamelet theory.

The purpose of this investigation was to quantify the strain rate and OH fluctuations in a propane-air flame when exposed to velocity fluctuations. A counterflow diffusion burner was used because of its ability to properly represent flamelets [1]. PIV measurements were used to quantify the strain rate fluctuations and the OH field was measured using Planar Laser-Induced Fluorescence (PLIF).

Experimental Apparatus

Figure 1 is a schematic of the PIV-OH measurement system. The PIV measurements were made using two Nd:YAG lasers (λ = 532 nm). The sheets were overlapped with a thickness of ~500 μm. X60 3M-Zeelan hollow zeospheres, with a mean diameter of 2.2 μm, were used to seed the flow. The PIV images were recorded using a Kodak Mega Plus Model ES1.0 digital camera fitted with an AF Micro Nikkor, 105 mm lens, using an f# of 8. An interference filter centered around 532 nm with a FWHM of 3 nm was also used to ensure the exclusion of all light sources except the Nd:YAG beams.

[1] Corresponding Author

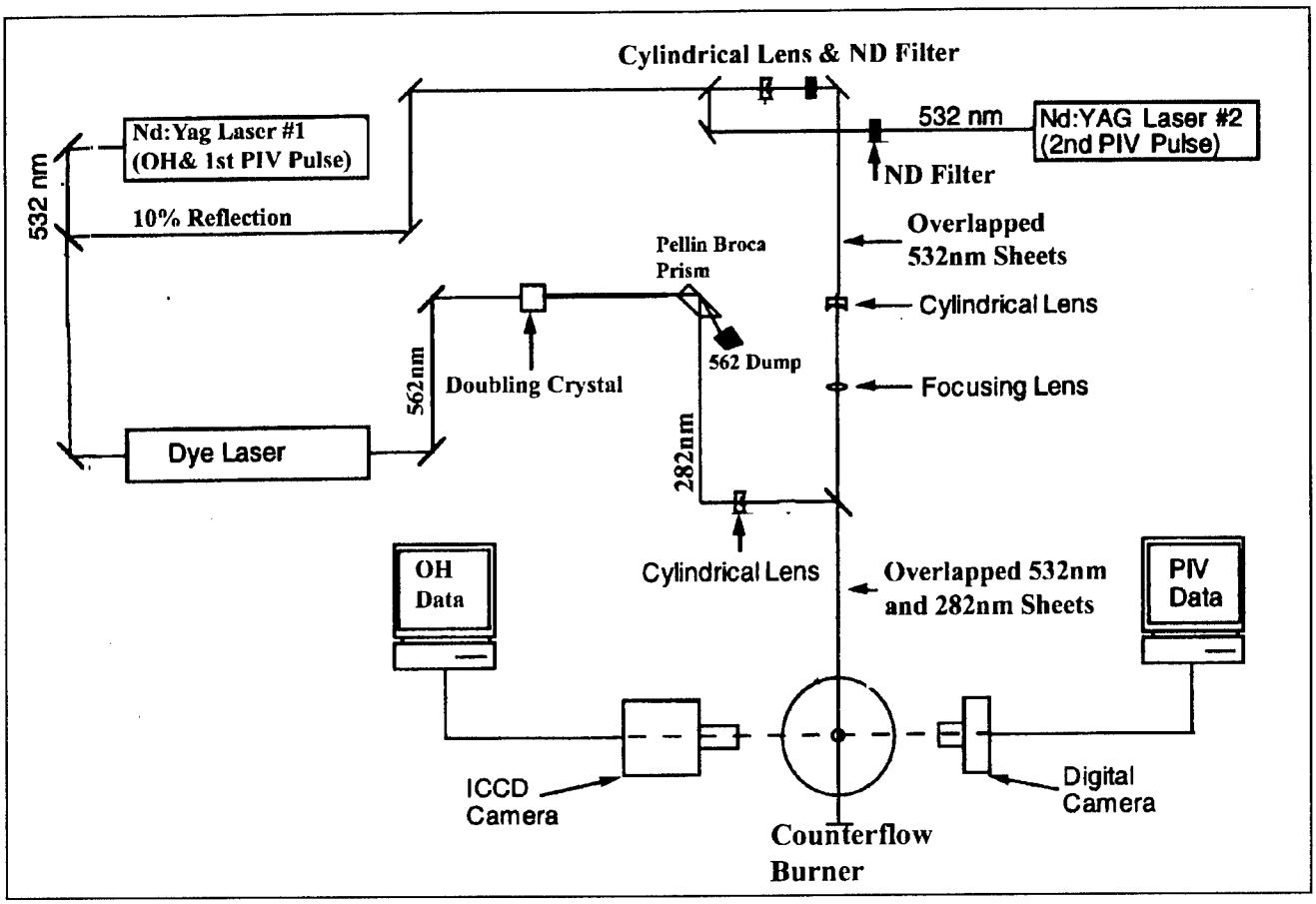


Figure 1: Optical Layout for PIV and OH-PLIF measurements

The OH measurements were made using a Nd:YAG pumped dye laser, which was running Rhodamine 590 dye, and the output was doubled down to ~282 nm. The $R_1(8)$ transition of the $A^2\Sigma+ \leftarrow X^2\Pi$ (1,0) band was excited and detected using a Princeton Instruments intensified camera. The $R_1(8)$ transition was chosen because of its reduced sensitivity to temperature fluctuations relative to other transitions. A 105 mm lens operating at f# 4.5 with UG11 and WG295 filters was used to collect the OH fluorescence. The 10 mJ UV pulse was approximately 10 ns in duration.

A schematic of the counterflow diffusion flame burner is shown in Figure 2. The oxidizer and fuel tubes are 25.4 mm in diameter and have a 12.7 mm separation distance. To flatten the exit velocity profiles, five 25.4 mm, 80 mesh, stainless steel screens were fitted into the reactant tubes. Upstream of the screens, multiple copper rings were press fitted into the reactant tube inlets to act as flow straighteners. The burner was water cooled on the fuel side to prevent preheating and suction was provided to remove combustion products. There is an annulus around the oxidizer side which provides a nitrogen co-flow to prevent oxidizer preheating and air entrainment.

Plenums are located on the fuel and oxidizer sides and are capped with 20 cm loudspeakers, which impose the velocity fluctuations. The speakers are driven by a Stanford Research Systems DS335 signal generator in series with a McIntosh amplifier.

Results & Conclusions

An unsteady flow field was applied to the counterflow diffusion flame by inputting a sinusoidal signal from the function generator that was then amplified before being input to the speakers. Measurements were made at the zero amplitude with positive slope (0+), maximum amplitude (Max),

zero amplitude with negative slope (0-), and minimum amplitude (Min) positions within the sine wave, as it appears on an oscilloscope. The response of the reaction zone was characterized by measuring the full width half maximum (FWHM) value of the OH field. The strain rate (K) was determined by evaluating the gradient of the axial velocity profile at the centerline of the burner on the oxidizer side of the stagnation plane. No corrections for thermophoretic effects have been made, but previous studies have shown that accurate velocity measurements can be performed prior to the preheat zone without accounting for thermophoretic effects [4]. All results reported are for an initial steady global strain rate(GSR) of 90 s^{-1}. The oxidizer side GSR was calculated using $4U_{air}/L$, where U_{air} is the air exit velocity calculated from mass flow rates, and L is the separation distance between the reactant tubes.

Figures 3 and 4 report the results of the variation in measured strain rate and the FWHM of the OH field at the four temporal locations. The steady values of the FWHM and the measured strain rate are also included for reference. The steady strain rate was measured to be 68 s^{-1}. At the thirty and fifty Hertz oscillation cases, the maximum measured strain rates occurred at the 0- temporal location, which indicates a phase lag between the velocity fluctuation and the strain rate. This is consistent with previous measurements in this burner [5]. The maximum measured strain rate at 0- was 45% larger for the 30 Hz case and 27% larger for the 50 Hz case than the steady strain rate. It can also be seen in Figures 3 and 4 that the reactions zones are responding in a quasi-steady manner. The OH field thickness decreases with increasing strain rate and the converse is also true. In a previous study, the temperature field was measured at a GSR 30 s^{-1} and the OH field was found to be thinnest and coolest at the 0- temporal location, which is consistent with findings in this study [6]. At 30 and 50 Hz, when the instantaneous strain rate is larger than the steady strain rate, the OH field is thinner than the steady case.

The results for the imposed oscillation of 100 Hz are shown in Figure 5. A mild increase in strain rate is accompanied by an increase in the thickness of the OH field. The changes in the thickness of the OH field are reported in millimeters so for such small differences no strong conclusions can be made from these results, but this trend was also noted for identical flow conditions with an increased forcing amplitude. It was also found that the measured strain rate for the 100 Hz case did not peak at the 0- temporal location, but instead the maximum value occurred at the Min location. The results for the applied fluctuation of 100 Hz suggest the flame is not responding in a quasi-steady manner at this condition.

References

1. Peters, N. (1984) Laminar Diffusion Flamelet Models in Non-Premixed Turbulent Combustion, Prog. Energy Comb. Sci., 10:319-339.

2. Im, H.G., Law, C.K., Kim, J.S., Williams, F.A. (1995) Response of Counterflow Diffusion Flames to Oscillating Strain Rates, Combustion and Flame, 100:21-30.

3. Egolfopoulos, F.N., Campbell, C.S., (1996) Unsteady counterflowing strained diffusion flames: diffusion-limited frequency response, J. Fluid Mech., 318:1-29.

4. Sung, C.J., Kistler, M., Nishioka, M., Law, C.K. (1996) Further Studies on the Effects of Thermophoresis on Seeding Particles in LDV Measurements of Strained Flames, Combustion and Flame,105:189-201.

5. DeCroix, M.E., Roberts, W.L., (1998) Study of Transient Effects on the Extinction Limits of an Unsteady Counterflow Diffusion Flame, accepted for publication in Comb. Sci. Tech.

6. Santoianni, D.A,(1999) Temperature Imaging in Unsteady Propane-Air Counterflow Diffusion Flames using Planar Laser-Induced Fluorescence of OH, Master Thesis at North Carolina State University.

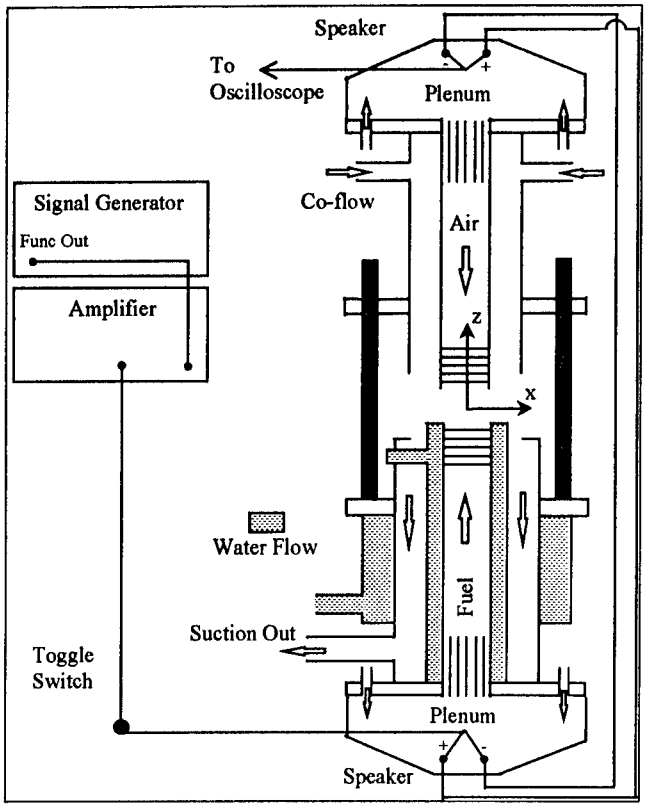


Figure 2: Counterflow Diffusion Flame Burner

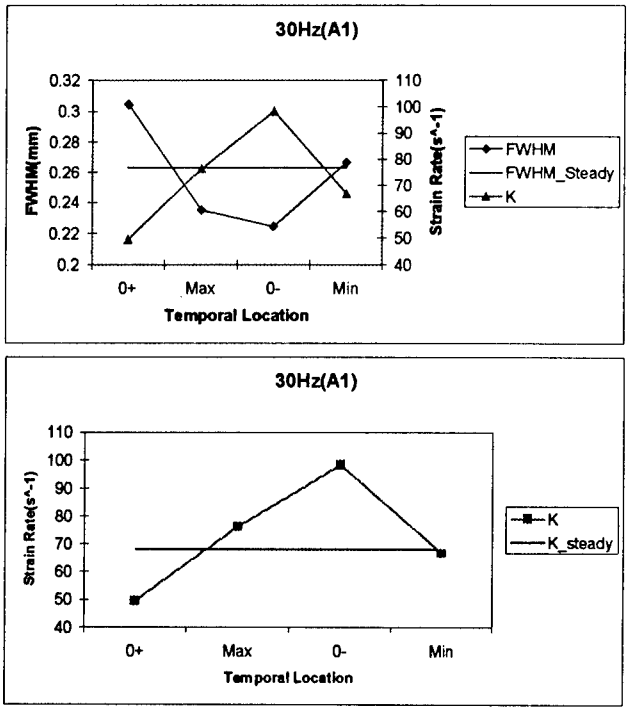


Figure 3: The full width half max of the OH field and the measured strain rate for the four temporal locations at 30Hz and a forcing amplitude A1=0.46Vp-p.

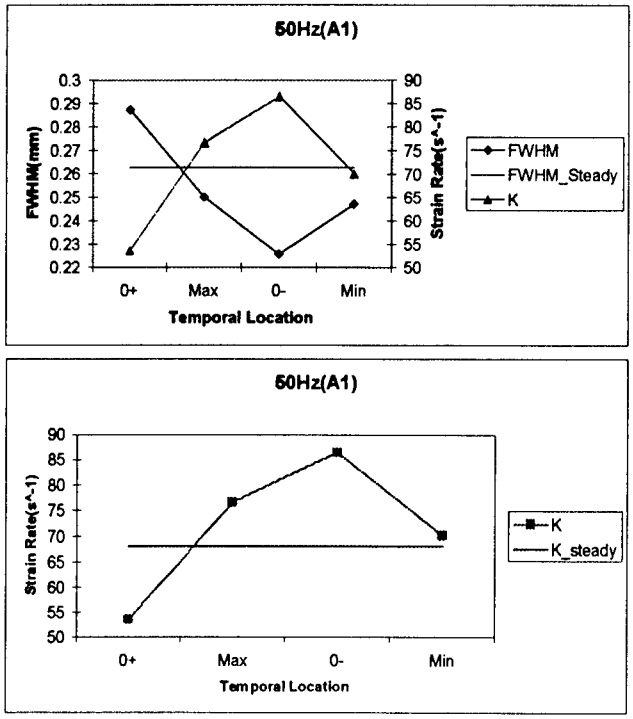


Figure 4: The full width half max of the OH field and the measured strain rate for the four temporal locations at 50Hz and a forcing amplitude A1=0.70Vp-p.

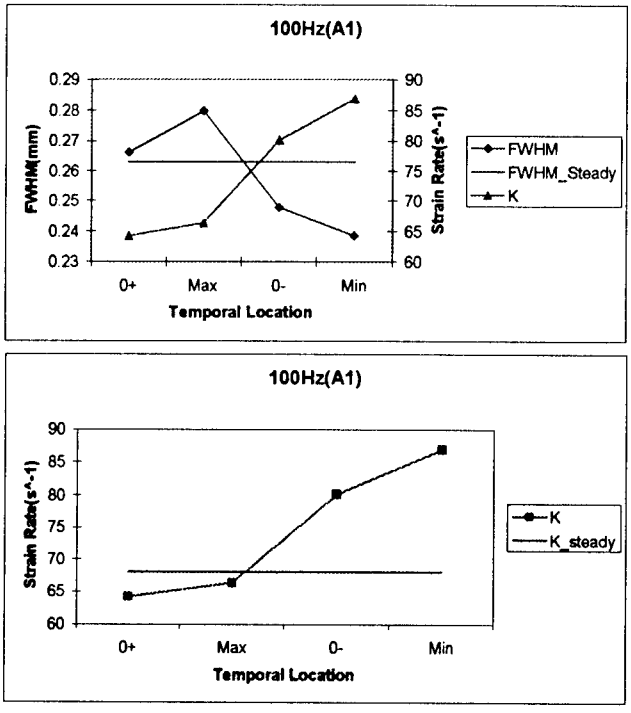


Figure 5: The full width half max of the OH field and the measured strain rate for the four temporal locations at 100Hz and a forcing amplitude A1=1.0Vp-p.

COMPUTATIONAL AND EXPERIMENTAL STUDY OF AMMONIUM PERCHLORATE DIFFUSION FLAMES

M. D. Smooke
Department of Mechanical Engineering
Yale University
New Haven, CT
mitchell.smooke@yale.edu

R. A. Yetter
Department of Mechanical and Aerospace Engineering
Princeton University
Princeton, NJ

T. P. Parr and D. M. Hanson-Parr
Weapons Division
Naval Air Warfare Center
China Lake, CA

Introduction

Many solid rocket propellants are based on a composite mixture of ammonium perchlorate (AP) oxidizer and polymeric binder fuels. In these propellants, complex three-dimensional diffusion flame structures between the AP and binder decomposition products, dependent upon the length scales of the heterogeneous mixture, drive the combustion via heat transfer back to the surface. Changing the AP crystal size changes the burn rate of such propellants. Large AP crystals are governed by the cooler AP self-deflagration flame and burn slowly, while small AP crystals are governed more by the hot diffusion flame with the binder and burn faster. This allows control of composite propellant ballistic properties via particle size variation.

Previous measurements on these diffusion flames in the planar two-dimensional sandwich configuration yielded insight into controlling flame structure, but there are several drawbacks that make comparison with modeling difficult [1,2]. First, the flames are two-dimensional and this makes modeling much more complex computationally than with one-dimensional problems, such as RDX self- and laser-supported deflagration [3]. In addition, little is known about the nature, concentration, and evolution rates of the gaseous chemical species produced by the various binders as they decompose. This makes comparison with models quite difficult. Alternatively, counterflow flames provide an excellent geometric configuration within which AP/binder diffusion flames can be studied both experimentally and computationally.

Experimental Approach

In a typical counterflow diffusion flame experiment, two laminar plug flow jets (one fuel and one oxidizer) are directed towards each other and impinge in the middle of the domain. Properly designed, this configuration leads to a one-dimensional flame along the stagnation point streamline that can be modeled with less computationally intensive one-dimensional codes. In addition, the experimentalist has complete control over many flame parameters including fuel chemistry, fuel thermal properties (via dilution, for example), and flame strain rate. In our case, the oxidizer side is not a jet but a solid pellet of AP. Although AP does not normally self-deflagrate at pressures below 200 to 800 PSIA (depending on purity), it was found that the counterflow diffusion flame configuration is self-sustaining even at 1 atm, and that nearly perfect planar multi-flame structures have been imaged

with methane and ethylene as fuels. Fuel mixtures can be selected in order to simulate the decomposition products of various binders, or a single fuel can be implemented to better understand the kinetics involved.

The flame configuration is illustrated in Figure 1. The fuel exit diameter is 7.75 mm and the AP pellet diameter is 10.1 mm. Both the AP and fuel flows are surrounded by nitrogen shroud flows (26.8 mm diameter for the fuel and 23.0 mm for the AP). The shroud flows were set to match the fuel and AP decomposition gas flows. The fuel flow rate is controlled with a calibrated flow meter but the AP decomposition gas flow rate is controlled by the AP solid regression rate. The AP pellet and the ethylene jet were separated by 5.0 mm with an ethylene average flow speed of 20.5 cm/s, yielding an AP regression rate of 0.113 mm/s and a strain rate of approximately 311 s^{-1}. The AP surface location is maintained with a mechanical stage that offsets the regression rate. The AP was ultra high purity grade (UHP) from Kerr McGee Corporation, pressed to 98.2% TMD. UHP AP was used because the flame structure and even the regression rate are sensitive to impurities in normal research grade AP.

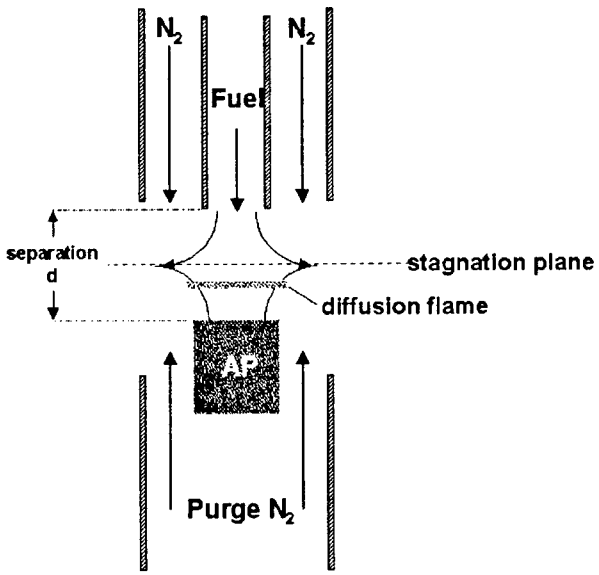


Figure 1 – Schematic of experimental configuration for ethylene vs. AP counterflow flame system.

Diagnostics applied to the counterflow AP diffusion flame include thermocouple and OH rotational measurements for the temperature and planar laser induced fluorescence (PLIF) imaging for the OH. The PLIF laser pumped the R1(3), R1(8), R1(10), R1(12), and R1(14) lines of the (1,0) A-X OH transition. The temperature is then obtained from a Boltzmann population distribution plot. Thermocouples (50μm diameter) were used for fuel side temperature profiles (where the OH rotational temperature measurements are not possible). A two-dimensional optical multichannel analyzer (OMA) was applied for spatially resolved chemiluminescence emission profiles and will be used for absorption measurements to quantify the PLIF species profiles. One axis is the normal spectral dispersion while the other axis is spatially resolved as height off the AP surface. The flames are largely one-dimensional so a single spatial coordinate is sufficient.

Computational Approach

To model the AP diffusion flame system, we consider a laminar counterflow flame stabilized in the vicinity of the stagnation plane between two axisymmetric, counterflowing streams. One stream contains the fuel and the other the AP decomposition products as determined in [4]. The AP surface temperature is maintained at its 1 atm decomposition temperature of 825K. The complete formulation of the mathematical model for solving the finite burner separation problem with plug flow boundary conditions starts with the elliptic form, in cylindrical coordinates, of the two-dimensional equations describing the conservation of total mass, individual chemical species mass, momentum and energy for the reactive flow occurring between the fuel and the AP solid [5,6]. To reduce the complexity of the problem, we seek a similarity solution of the governing equations which reduces the governing equations to a nonlinear, two-point boundary value problem in the axial (z) direction along the stagnation point streamline. These equations are discretized with an adaptive finite difference algorithm and solved using Newton's method. The system is closed with an equation of state (in this case, the ideal gas law) and appropriate boundary conditions.

The soot formation model is based on our prior work developed for one and two–dimensional flames [7,8]. Soot formation is described by coupling dynamical section equations for particle growth with the governing gas phase conservation equations. The aerosol dynamical equations [9] use the discrete size spectrum or sectional method with particle kinetics that include surface growth and oxidation and coalescence. Particle transport by thermophoresis and diffusion is included. Particle inception is based on an expression involving calculated local concentrations of gas phase species and a steady-state expression for PAH production. Surface growth is dependent on local temperatures and concentrations of acetylene using an expression derived from experimental measurements. Oxidation by molecular oxygen and the hydroxyl radical are included. Thermal radiation (particle/gas) is represented by a sink term in the gas dynamic energy equation in the optically thin limit. Scrubbing of gas phase species by particle growth and particle thermochemistry is also included. The result is a strongly coupled gas-particulate system which enables the researcher to demonstrate the complex interaction between gaseous species, soot production, temperature and radiation with extensive parametric variations.

The AP/ethylene combustion mechanism combines GRIMech 2.11 [10] with the AP mechanism reported in [4,11], the nitrogen-chlorine submechanism from [12,13] and the ethylene and ring formation chemistry in [8]. The combined mechanism contains a total of 105 chemical species participating in 660 reversible chemical reactions.

Results

The model predicts an AP decomposition flame above the AP surface, followed by an ethylene/AP-products diffusion flame, in agreement with experimental observations of the OH profile and excited state CH. Both flame structures lie to the AP side of the stagnation plane. We compare experimentally determined temperature, OH (absolute), NO (absolute), CN (relative) and soot volume fraction profiles with the corresponding computed results.

Acknowledgments

This work was supported in part by the Office of Naval Research and in part by the Air Force Office of Scientific Research.

References

1. Parr, T. P. and Hanson-Parr, D. M., "AP Diffusion Flame Structure", 33rd JANNAF Combustion Meeting, Monterey, CA, November 1996.
2. Parr, T. P. and Hanson-Parr, D. M., Twenty-sixth Symposium (International) on Combustion, The Combustion Institute, Pittsburgh, p. 1981, 1997.
3. K. Prasad, R. Yetter and M. D. Smooke, *Comb. Sci. and Tech.*, 124:35, (1997).
4. Ermolin, N.E., Korobeinichev, O.P., Tereshchenko, A.G., and Fomin, V.M., *Comb. Exp. and Shock Waves*, **18**, p. 46, (1982).
5. Smooke, M.D., Crump, J., Seshadri, K., Giovangigli, V., Twenty-third Symposium (International) on Combustion, The Combustion Institute, Pittsburgh, p. 463, 1990.
6. Chelliah, H.K., Law, C.K., Ueda, T., Smooke, M.D., Williams, F.A., Twenty-third Symposium (International) on Combustion, The Combustion Institute, Pittsburgh, p. 503, 1990.
7. Hall, R. J., Smooke, M. D., and Colket, M. B.: in Physical and Chemical Aspects of Combustion: A Tribute to Irvin Glassman, ed. by R. F. Sawyer and F. L. Dryer, Combustion and Science and Technology Book Series, Gordon and Breach, 1997.
8. C. McEnally, A. Shaffer, M. B. Long, L. Pfefferle, M. D. Smooke, M. B. Colket and R. J. Hall, Twenty-Seventh Symposium (International) on Combustion, 1998.
9. Gelbard, F., and Seinfeld, J. H., *J. Coll. Int. Sci.*, 78, p. 485, (1980).
10. Bowman, C. T., Hanson, R. K., Davidson, D. F., Gardiner Jr., W. C., Lissianski, V., Smith, G. P., Golden, D. M., Frenklach, M., Wang, H., and Goldenberg, M.,: GRI-Mech version 2.11, http://www.gri.org, (1995).
11. Ermolin, N.E., Korobeinichev, O.P., Tereshchenko, A.G., and Fomin, V.M., *Comb. Exp. and Shock Waves*, **18**, p. 61, (1982).
12. Roesler, J.F., Yetter, R.A., and Dryer, F.L., *Comb. and Flame*, **100**, p. 495, (1995).
13. Roesler, J.F., Yetter, R.A., and Dryer, F.L., *Comb. Sci. and Tech.*, **101**, p. 199, (1994).

Thermo-Chemical Conversion Of The Intermediates of Biomass Pyrolysis

TRAVIS FISHER, MOHAMMAD HAJALIGOL, BRUCE WAYMACK, AND DIANE KELLOGG
PHILIP MORRIS USA, RESEARCH CENTER, P.O. BOX 26583, RICHMOND, VA 23261

INTRODUCTION

Biomass substrates, upon heating, undergo a series of competitive and consecutive reactions to form the final products. It's well known that cellulosic carbohydrates, such as cellulose, pectin, and glucose, form a wide range of products during thermo-chemical conversion including some intermediates (primary products) where their immediate precursors are the parent starting materials (1-3). In this work, three well-known primary pyrolysis products of cellulosic carbohydrates were studied. The objective of this study is to identify the primary and secondary products of these intermediates when they undergo pyrolysis. These compounds are 1,6-anhydro-β-D-glucopyranose (also known as levoglucosan - LG), 5-hydroxy-methyl-furfural (5-HMF), and hydroxy-acetaldehyde dimer (HAA); all were purchased from Acros (Fischer Scientific).

EXPERIMENTALS AND RESULTS

A Netzsch thermo-gravimetrical analyzer (TGA) coupled with a differential scanning calorimeter (DSC) and a mass spectrometer (MS) was used in this study to monitor the weight loss, heat flow, and mass spectra of the evolved volatiles as a function of time (temperature). A detailed description of the setup is given elsewhere (4). To briefly describe, a small sample of starting material (10-15 mg) is placed on the balance sample holder and heated at a constant heating rate (5-60 °C /min) to a desired temperature (1000 °C) using an inert gas, like helium, with a flow rate of about 150 ml/min. For LG samples, the instrument was "burned-out" at 1200°C for 1-hour using a Helium/21% Oxygen gas mixture in between each trial due to the copious deposition of carbonaceous residue in the analyzer chamber. Conversely, the 5-HMF and HAA trials did not require this 'burning-out' process and were run in succession. Comparison of the TG weight loss for the three intermediates, 5-hydroxy-methyl furfural (5-HMF), hydroxy-acetaldehyde (HAA), and 1,6-Anhydro-β-D-glucopyranose (LG), displayed strikingly diverse characteristics. The weight loss for 5-HMF ranged from 89 to 91 percent for heating rates ranging from 5 to 20 °C/min. On the contrary, the HAA and LG both yielded 100% weight loss; although a comparison is somewhat misleading. HAA showed 100 percent weight loss with no visible carbonaceous char build-up or deposition on the balance stem in the sample chamber of the instrument. However, LG produced significant char build-up, which necessitated the aforementioned "burning-out" process.

TG/DSC/MS results show that 5-HMF first melts around 36 °C, then evaporates and/or pyrolyzes between 160 and 200 °C. HAA melts around 100 °C, and then evaporates and/or pyrolyzes around 125 °C. LG first goes through what is described as solid-phase transition into a plastic crystalline state at around 110 °C (5), then melts around 170 °C and finally evaporates and/or pyrolyzes around 240 °C.

The DTG and DSC peaks, as expected, shift to higher temperatures with increasing heating rate for all three materials tested. Tables 1 through 3 show the relationship that exists between DTG and DSC peak temperatures, as well as the respective heat of product evolution and/or evaporation, for 5-

HMF, HAA and LG, respectively. When the natural log of the heating rates are plotted against the inverse DTG (or DSC) peak temperatures, an apparent activation energy (E_a) can be derived from the slope. The estimated activation energies (E_a) from the respective slopes are equal to 73.1, 99.8 and 124 kJ/mole for 5-HMF, HHA, and LG, respectively. Since the thermo-chemical conversion processes of these compounds are controlled by their evaporation, these estimates of E_a, should be close to their respective latent heats of vaporization. In fact, 124 kJ/mole is in good agreement with the heat of vaporization with literature data(6) for LG. Another look at the data shows that these estimates do not match the heats of reaction measured by the DSC for the evaporation step of the respective compounds; i.e., Peak # 2 for 5-HMF (Table 1), Peak # 2 for HAA (Table 2), and Peak # 3 for LG (Table 3). With HAA, the heat of reaction becomes less endothermic as heating rate increases, suggesting that more exothermic reactions (pyrolytic decomposition of starting materials) are taking place with increasing heating rate. On the other hand, 5-HMF and LG show the opposite trend, such that, the heats of reaction become more endothermic with increasing heating rate. In the case of HAA, the change in the heat of reaction with heating rate is less than for either 5-HMF or LG, and that is why the measured (DSC data) heat of reaction for HAA is closer to the estimated heat of evaporation by the above method (E_a).

A strong correlation also exists between the evolution of masses, (monitored by the mass spectrometer), with the inverse of the DTG peak temperatures. Figures 1 through 3 show the natural log of areas for mass 126 (5-HMF), mass 60 (HAA) and mass 73 (LG) as a function of the inverse of the DTG peak temperature. These data indicate that at lower heating rates, the process is more evaporation, and as the heating rate increases, the extent of starting material decomposition increases (lower areas of parent compound masses at higher heating rates). This is consistent with the results from DTG and DSC data, except for HAA, where the area of mass 60 remains relatively constant over the range of heating rates studied. Therefore, during a thermo-chemical process, the primary products of 5-HMF, HAA and LG are themselves.

Table 1: 5-Hydroxy-Methyl Furfural (5-HMF) DTG/DSC data.

HEATING RATE (^{O}C/MIN)	DTG PEAK #1 (^{O}C)	DTG PEAK #2 (^{O}C)	DSC PEAK #1 (^{O}C)	DSC PEAK #2 (^{O}C)	DSC PEAK #3 (^{O}C)	PEAK #1 HEAT OF REACTION (J/G)	PEAK #2 HEAT OF REACTION (J/G)	PEAK #3 HEAT OF REACTION (J/G)
5	163.8	202.3	35.4	N/A	199.8	-83.78	-113.7	-83.31
10	170.4	226.5	36	172.1	229.0	-97.47	-135.6	-32.84
20	193.2	N/A	36.5	200.9	N/A	-83.35	-232.2	N/A

Table 2: Hydroxy-acetaldehyde (HAA) DTG/DSC data.

HEATING RATE (^{O}C/MIN)	DTG PEAK (^{O}C)	DSC PEAK #1 (^{O}C)	DSC PEAK #2 (^{O}C)	HEAT OF REACTION (J/G)
5	122.9	99.3	124.5	-1013.0
10	132.5	104.8	137.0	-992.0
20	143.7	110.9	156.3	-979.5
60	157.9	126.6	176.6	-835.8

Table 3: 1,6-Anhydro-β-D-glucopyranose (LG) pyrolysis data.

HEATING RATE (^{O}C/MIN)	DTG PEAK (^{O}C)	DSC PEAK #1 (^{O}C)	DSC PEAK #2 (^{O}C)	DSC PEAK #3 (^{O}C)	PEAK #3 HEAT OF REACTION (J/G)
5	236.3	112.4	178.0	239.9	-119.7
10	250.9	113.5	178.2	256.9	-138.1
20	268.6	111.2	176.1	282.1	-164.3

The study of secondary products of decomposition is underway. Using a CDS pyroprobe coupled with a GC/MS, we have independently confirmed that the major products of the thermo-chemical conversion process of the three compounds studied are the starting materials. In the case of 5-HMF, the principle secondary products were methyl furfural and number of other substituted furan compounds.

ACKNOWLEDGMENTS

Authors wish to thank Philip Morris USA management for their support and encouragement of basic research studies.

REFERENCES

1. Antal, M. J., Jr., in Advances in Solar Energy Vol. 1 (Boer, K and Duffie J., Eds.), American Solar Energy Society, Boulder, CO, 1982, PP. 61-111.
2. Antal, M. J., Jr., in Advances in Solar Energy Vol. 2 (Boer K. and Duddie, J., Eds.), American Solar Energy Society, Plenum, New York, 1985, PP. 175-255.
3. Hajaligol, M. R., Howard, J. B., Longwell, J. P., and Peters, W. A., Ind. Eng. Chem. Process Des. Dev., 21:457-465, (1982).
4. Hajaligol, M., Waymack, B., and Kellogg, D., in Fuel Chem. Preprint, Vol. 44, No. 2, Fuel Chem. Div., ACS, Anaheim, CA, 1999.
5. Shafizadeh, F., Philpot, C. W., and Ostojic, N., *Carbohyd. Res.*, 16: 279-287, (1971).
6. Milosavljevic, I., Oja, V., and Suuberg, E. M., Ind. Eng. Chem. Res., 35:653-662 (1996).

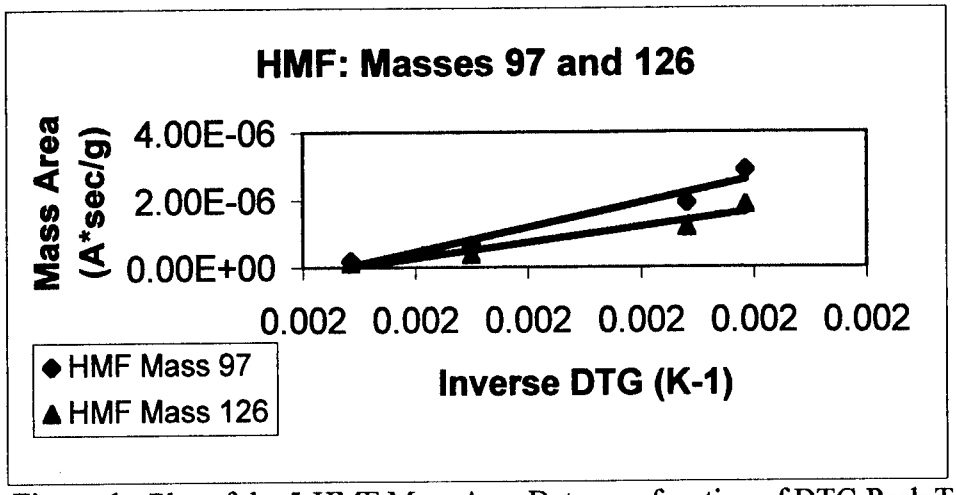


Figure 1: Plot of the 5-HMF Mass Area Data as a function of DTG Peak Temperature.

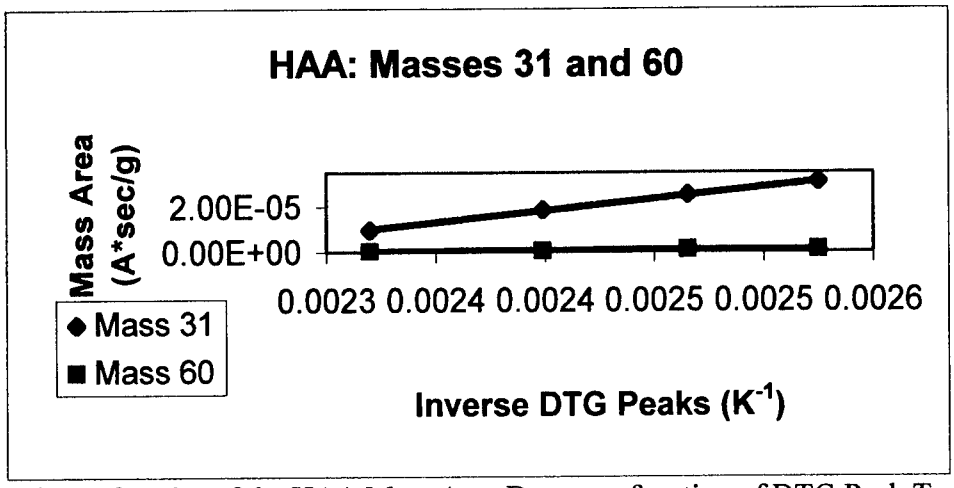


Figure 2: Plot of the HAA Mass Area Data as a function of DTG Peak Temperature.

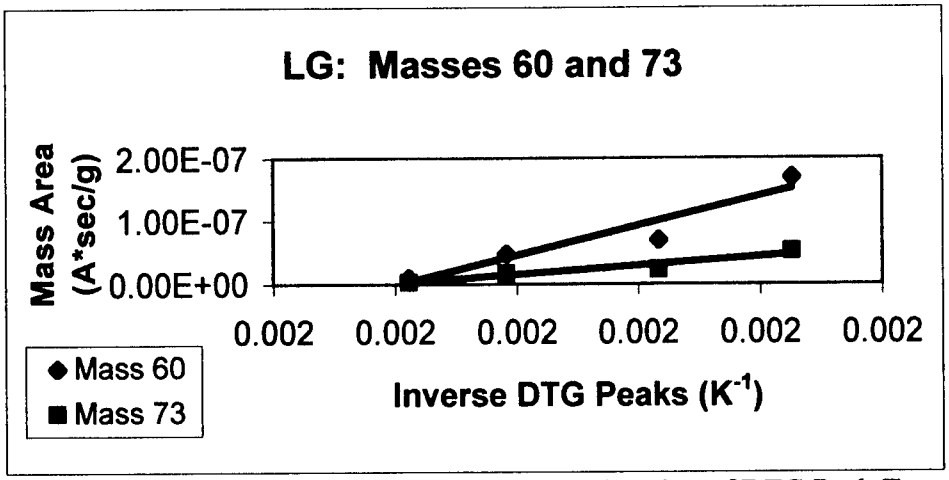


Figure 3: Plot of the LG Mass Area Data as a function of DTG Peak Temperature.

Pyrolysis and Oxidation of Polyethylene in a Steady State Flow Reactor

Byung-Ik Park and Joseph W. Bozzelli
Department of Chemical Engineering, Chemistry, and Environmental Science,
New Jersey Institute of Technology, Newark, NJ 07102
bozzelli@tesla.njit.edu

Introduction

Polyethylene is a major thermoplastic in municipal refuse along with the polymers: polypropylene, polystyrene, and polyvinyl chloride. Polyethylenes differ in physical property and structure depending on processing conditions for their polymerization. Low density polyethylene (LDPE) has a highly branched structure and high density polyethylene (HDPE) has a linear structure with short branches. Polyethylenes soften and melt upon heating, without much change in chemical and physical properties. Polyethylenes are readily molded into household goods, fiber, packaging materials, etc. [1]. Use of polyethylene has increased due to its' applicability and durability; polyethylenes are a key component in the annual volume growth of plastics in solid wastes. Combustion of solid wastes and municipal waste is increasing due to limited landfill capacities and increased value in waste to energy. This increase in plastics combustion has led to increased public concern over toxic air emissions from waste combustion [2].

There is no through study on polyethylene combustion showing the formation and distribution of intermediate products, or on the reactor parameters needed for complete conversion of these intermediates under reaction conditions of known fuel equivalence ratio (ϕ), under continuous flow of both fuel and air - demonstrated steady state operation. In this study a continuous feed of solid polyethylene is fragmented and vaporized in the first zone of the reactor, a volatilization at 400°C. The vaporization products then undergo further oxidation reaction at varied - higher temperatures in the second zone, main reactor. Gas products at each temperature of the main reactor are identified and quantified at a known ϕ. Fuel equivalence ratio is identified as an important parameter that can be utilized to help reduce emission of products of incomplete combustion (PICs) and achieve complete conversion to minerals, CO_2 plus H_2O. Our data shows that polyethylene can be efficiently combusted to CO_2 and H_2O at 2 seconds reaction time, $\phi = \sim 0.28$, and 650°C under steady state reaction conditions.

Experimental

A continuous air and polymer feed, dual stage reactor, operating under steady state conditions was used to study the thermal oxidation of polyethylene, as previously described in the pyrolysis and oxidation of cellulose and polystyrene [3]. The first zone or volatilization oven is maintained at constant temperature of 400°C. The second reactor zone, main reactor is controlled in the range 400 to 650°C within ±10°C at 2.0 seconds residence time and at $\phi = \sim 0.28 \pm 0.04$. The medium density polyethylene used was purchased from Aldrich Chemicals: average M_w 6300, average M_n 2500, specific gravity 0.940 gm/cm^3, and melting point 109 -111°C. The powder was ground and sieved into the particle size range of 0.15 – 0.3 mm. Polyethylene powder was filled uniformly into an open-top or U-channel tube of about 20 cm length made of quartz or stainless steel with half circle cross-section area of 0.1 cm^2. The boat is fed slowly into the volatilization oven by a continuous feed mechanism with volatilization rates around 24 mg/min under steady state conditions. Gas phase polymer fragments are continuously produced in the volatilization oven and flow directly into the main reactor where further oxidation reaction occurs at the increased temperature of the main reactor. A continuous air flow serves as the oxidant to entrain and carry the vaporized polymer fragments through the vaporization and main reactor. Samples of vapor phase combustion products are collected from the effluent of the reactor, through heated (220°C) transfer lines and injected into the three GCs via gas sampling valves. The three on-line gas chromatographs are used with a 5% polyphenyl methyl siloxane capillary column, 30 mm x 0.53 mm x 1.2 μm and two packed (Super-Q and Carbosphere) columns for qualitative and quantitative analysis [3]. Gas products are also collected in an impinger containing 30 ml of methylene chloride at 0°C and concentrated to 1ml for GC/MS analysis. The GC/MS system consisted of Varian Ion Trap Saturn II with Varian GC 3400 and an DB-5 (J & W Scientific), 30 m x 0.25 mm x 0.25 μm.

Results

Major products in the pyrolysis and oxidation of polyethylene are alkanes, alkenes, alcohols, aldehydes, and ketones. Gas products over 1% of carbon mass balance are CO, CO_2, ethene, formaldehyde, propene, propane,

butene, pentanal, and methylfuran under conditions where both the volatilization and main reactor are at 400°C. 90 species between C_1 to C_{22}, among over 250 products, are positively identified. Carbon mass balances from 400 to 500°C are relatively low, 60.44 to 69.40% due to loss of acids and to non-volatile macromolecule formation. Acids are also believed to be major products in the oxidation of polyethylene [4-6], but are not detected in this study. Macromolecules are reported up to C_{55} at around 400°C by Seeger and Gritter [7].

Gas chromatograms from three different columns at 400°C, 550°C, and 625°C two seconds reaction time are illustrated in Figure 1. Major products, C_1 to C_6 of Super-Q column and C_5 to C_{22} of DB-5 capillary column, are seen to decompose into carbonyl compounds, CO and CO_2 as monitored on the Carbosphere column, as main reactor temperature is increased. This change in product distribution is valuable for reaction path identification and for understanding the conversion of gas products as a function of main reactor temperature at a constant time.

Figure 2 illustrates product yields of alkanes from C_1 to C_6. The relative order in concentration is: propane (highest) > hexane > butane > methane > ethane > pentane (lowest) at 400°C for both the volatilization oven and main reactor. Propane and hexane are major alkane products. Alkanes from C_2 to C_6 decrease in concentration with increase of temperature in the main reactor; at 625°C all intermediate products are mineralized into H_2O and CO_2. Methane is a small exception, it shows maximum concentration at 600°C and is at a trace level at 625°C. At high temperature of main reactor alkanes are rapidly decomposed into the oxygenated species via radical reaction with O_2, β-scission reactions, and reactions with the active radical pool: R., RO., ROO., O, OH, and H. Propene is a prominent gas product due to cleavage of C-C bonds in the β position to double bonds in alkenes [8], as shown by propene levels in Figure 3. The order in abundance for alkene is: ethene (highest) > propene > butene > pentene > hexene (lowest). Ethene shows a maxima at the main reactor temperature of 600°C. C_3 to C_6 alkenes decrease significantly above 550°C.

Major aldehyde species observed are: pentanal, formaldehyde, and acetaldehyde, as shown in Figures 4 and 5. Formaldehyde, acetaldehyde, and acrolein remain steady in concentration up to 550°C, and then decrease rapidly to trace levels at 600°C. Aldehydes from C_5 to C_8 show formation similar to lower molecular weight aldehydes below C_5 and are completely converted at 575°C of the main reactor. Ketones are observed with the ketone group at the 2 or 3 substitution position; this observation is in good agreement with the results reported by Bravo and Hotchkiss [9]. Order of ketones in concentration are shown in Figure 6: 2-hexanone > 2-methyl-3-pentanone > 3-methyl-2-hexanone > 3-heptanone > 3-octanone in order of concentration. These ketones are rapidly decomposed at 575°C.

CO levels are a reasonable parameter to analyze the extent of conversion, and as an indicator of complete combustion. Hydrocarbons in the range of C_1 to C_{22} decrease in concentration as temperatures increase to 575°C while CO increases, as observed in Figure 7. CO remains steady at 64.26% and 64.13% at 600 and 625°C while CO_2 increases from 13.96% to 31.13%. Carbon mass balance at 625°C is 96.54%, which results primarily from CO and CO_2; plus low concentrations of methane, ethene, ethane, and acetone. Carbon mass balance is 97.62% at 650°C where only CO_2 plus H_2O are detected as combustion products.

Most products are hydrocarbons and oxygenated hydrocarbons. Oxygenated hydrocarbons increase in concentration to 500°C and then decrease while hydrocarbons increase to 550°C and then remain steady to 600°C probably due to the high concentration of C_1 to C_4. Conversion of hydrocarbons above C_4 to lower molecular weight hydrocarbons below C_4 is observed in this temperature range of 400 to 650°C.

Reference

1. Mark, H.F.; Bikales, N.M.; Overberger, C.G.; Menges, G. Encyclopedia of Polymer Science and Engineering, Second, ed.; John Wiley & Sons: 1985, Vol. 6, 429-490.
2. Paabo, M.; Levin, B.C. *Fire Mater.* **1987**, 11, 55-70.
3. Park, B-I.; Bozzelli, J.W.; Booty, M.; Bernhard, M.J.; Mesuere, K.; Pettigrew, C.A.; Shi, J.; Simonich, S.L. *Environmental Science and Technology* 1999, Vol 33, in press.
4. Costa, L.; Luda, M.P.; Trossarelli, L. *Poly. Deg. and Stab.* **1997**, 55, 329-338.
5. Khabbaz, F.; Albertsson. A-C.; Karlsson, S. *Poly. Deg. and Stab.* **1999**, 63, 127-138.
6. Hoff, A.; Jacobsson, S. *J. Appl. Polym. Sci.* **1981**, 26, 3409-3423.
7. Seeger, M.; Gritter, R.J *J. Appl. Polym. Sci., Polym. Chem. Ed.* **1977**, 15, 1393-1402.
8. Tsuchiya, Y.; Sumi, K. *J. Appl. Polym. Sci. A-1* **1968**, 6, 415-4124.
9. Bravo, A.; Hotchkiss, J.H *J. Appl. Polym. Sci.* **1993**, 47, 1743-1748.

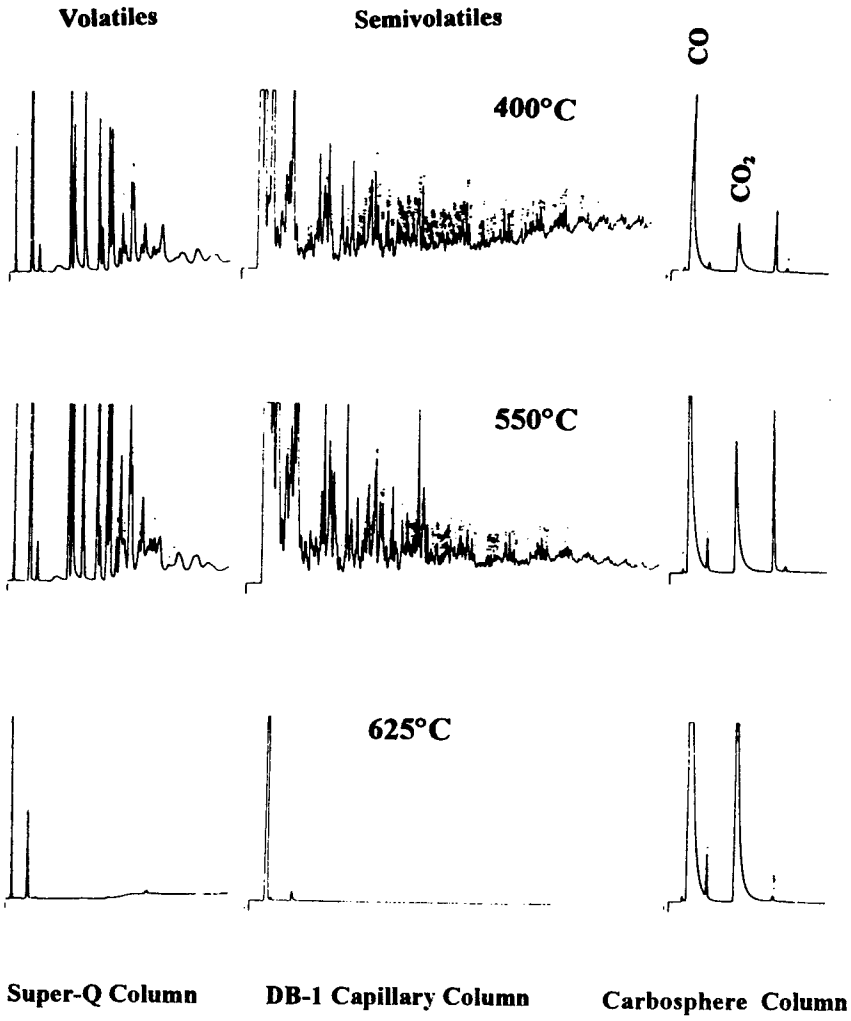


Figure 1. Polyethylene oxidation products from on-line GCs with different columns at the main reactor temperature of 400, 550, and 625°C

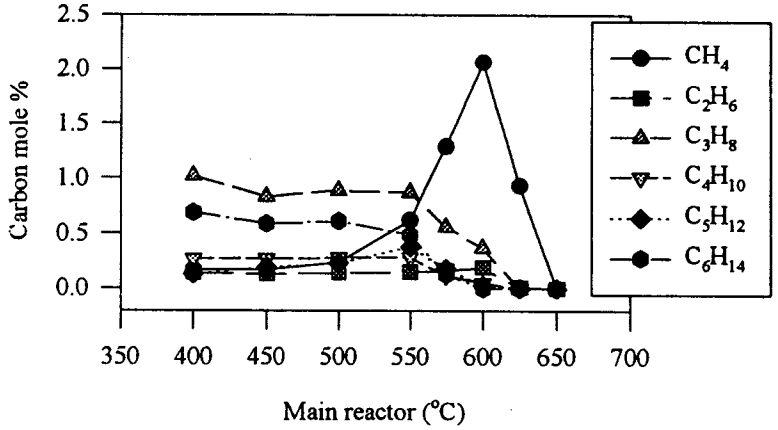


Figure 2. Product yields for alkanes at 2.0 sec. residence time in the oxidation of polyethylene

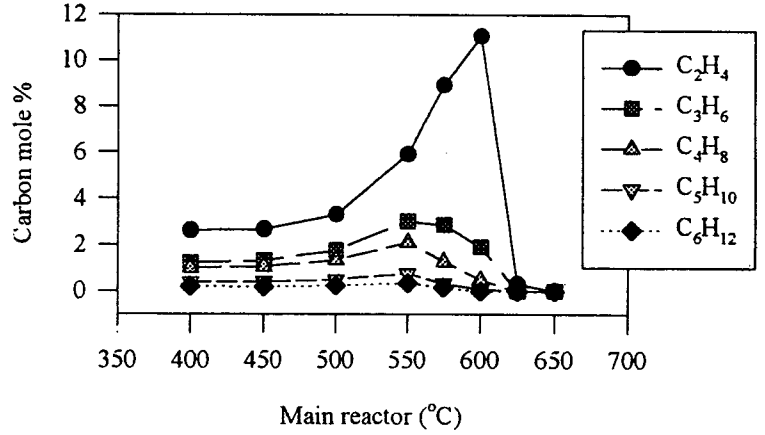


Figure 3. Product yields for alkenes at 2.0 sec. residence time in the oxidation of polyethylene

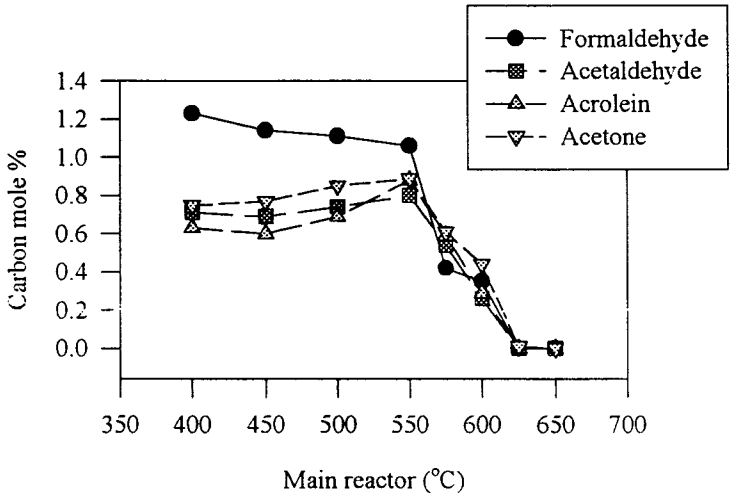


Figure 4. Product yields for $C_1 \sim C_3$ aldehydes at 2.0 sec. residence time in the oxidation of polyethylene

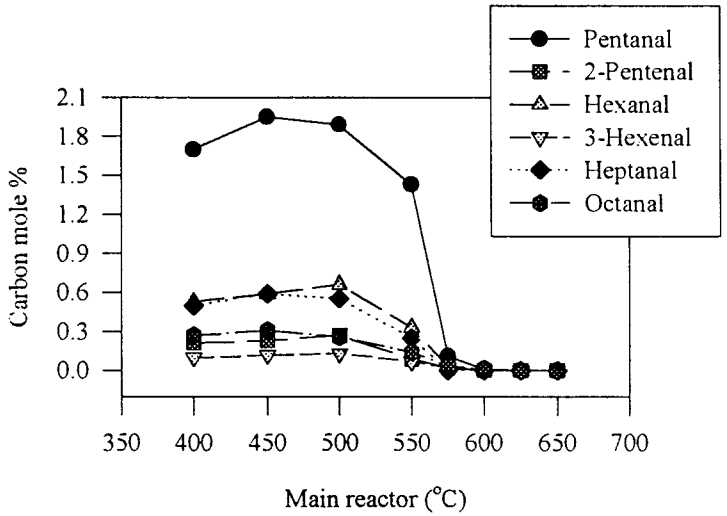


Figure 5. Product yields for C_5 - C_8 aldehydes at 2.0 sec. residence time in the oxidation of polyethylene

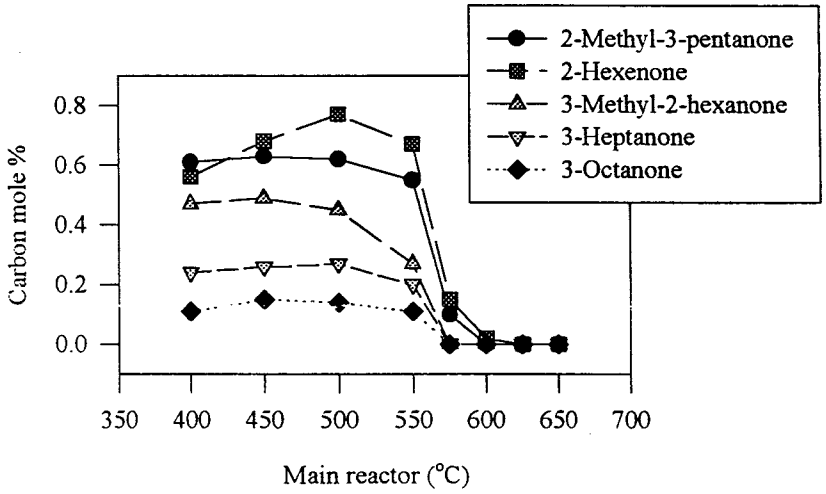


Figure 6 Product yields for ketones at 2.0 sec. residence time in the oxidation of polyethylene

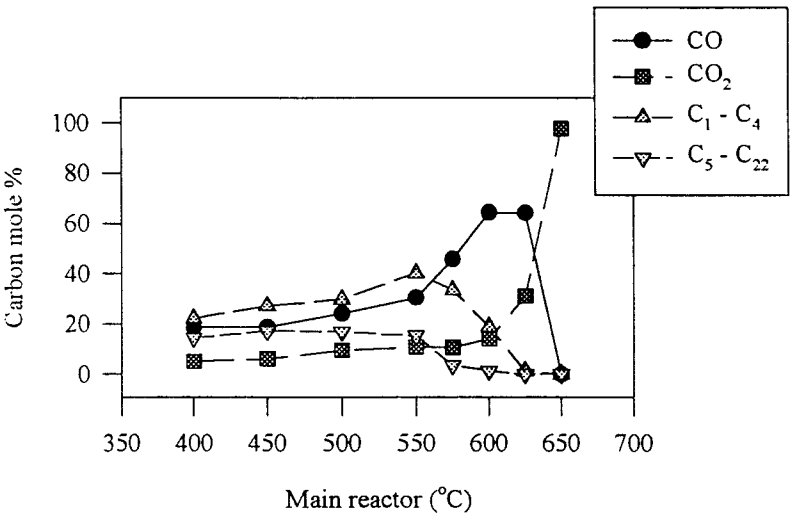


Figure 7. Total product yields at 2.0 sec. residence time in the oxidation of polyethylene

Competitive Chlorination of Benzene and Phenol over Model Fly Ash Surfaces

Phillip Edwards, Richard Striebich, and Sukh Sidhu
Environmental Science and Engineering
University of Dayton Research Institute
Dayton, OH 45469-0132
sidhu@udri.udayton.edu

Polychlorinated dibenzo-p-dioxins and polychlorinated dibenzofurans (PCDD/F or simply "dioxins") are a class of 210 isomeric species which are known to cause a number of serious adverse health effects in humans and animals.[1] Their ability to initiate cancer, severe skin disorders, and reproductive disorders originally caused concern over their exposure as a contaminant in commercial chemicals including PCBs, Agent Orange, and synthetic creosote. However, it was the discovery of their presence in the effluent of municipal waste incinerators in the late 70's and early 80's and the realization that broad segments of the population are exposed to these chemicals that raised the most concern.[2] Subsequent research has shown that combustion or thermal processes that contain a source of chlorine emit measurable quantities of PCDD/F, and it is now generally accepted that combustion is the major source of PCDD/F in the environment.[3] The US-EPA's dioxin reassessment has concluded that the background levels of PCDD/F in the environment and human body burdens are just below the threshold of significant health effects and that increases, or even continued emissions at current levels, will result in observable, adverse human health effects. Consequently, EPA has launched a Combustion Strategy designed to reduce the emissions of dioxins and "dioxin-like" compounds from combustion sources. The initial focus has been on municipal waste combustors and facilities that burn hazardous wastes. However, many other thermal and combustion sources are now the target of potential regulation.[4]

The current approach of the combustion strategy to reduce the environmental burden of dioxins is to either require the addition of costly control devices or to eliminate the source from existence. This is clearly an infeasible approach for the large majority of our nation's combustion and thermal processes. Thus to continue to allow the use of combustion while reducing PCDD/F emissions, we must find methods to prevent their formation. Because there are so many combustion sources of PCDD/F, developing a prevention strategy for one source alone will be unsuccessful. Thus a basic understanding of the mechanism of formation and the development of fundamental combustion modification strategies that are applicable to a wide range of sources must be implemented. Our approach is to examine different elementary steps in the pathways of PCDD/F formation from a prevention perspective, identify the rate controlling reactions and conditions, and develop methods for reducing their rate and ultimately the yield of PCDD/F.

The chlorination experiments are designed to elucidate three different aspects of hydrocarbon chlorination on model surfaces: 1) define the role of various oxidation states of copper, 2) investigate the effect of $AlCl_3$, $FeCl_3$, KCl, and NaCl addition on hydrocarbon chlorination under cool zone conditions, and 3) study competitive chlorination between known PCDD/F precursors. Phenol and benzene, which are documented to undergo chlorination and form PCDD/F on fly ash, were used as reaction probes. This allows us to determine how the different transition and alkali metal complexes contribute to chlorination. With this critical information, we can then proceed to develop methods for prevention by controlling the concentration of HCl in cool zone or, possibly more practically, by varying the metal concentration in fly ash.

All experiments are performed using the System for Thermal Diagnostic Studies (STDS) (Figure 1). The STDS is a high-temperature flow reactor coupled with an in-line gas chromatograph/mass spectrometer (GC/MS) system designed to simulate the reaction conditions in a combustor post-flame zone. The setup is described in detail elsewhere [5]. Briefly, the STDS consists of four integrated units: 1) a control console for precise adjustment of temperature, pressure, residence time and the respective gas flows; 2) a thermal reactor compartment containing a high temperature furnace (Lindberg) housed within a gas chromatograph (HP 5890) to allow precise sample introduction into and out of a quartz reactor; 3) a gas chromatographic oven (HP 5890)

containing a silicosteel trap and a capillary column (DB-5, J & W Scientific) for separation of organic reaction products; 4) a mass spectrometer (HP 5970B MSD) for product identification and quantification.

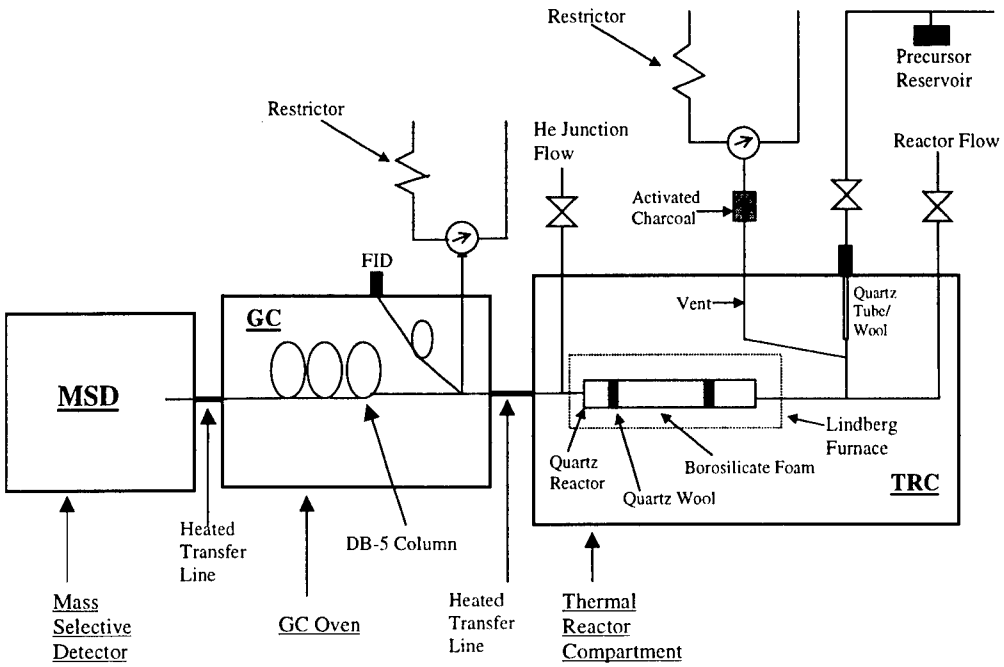


Figure 1: Schematic of the System for Thermal Diagnostic Studies (STDS) as modified for this heterogeneous combustion study.

In order to investigate competitive chlorination, small amounts of both benzene and phenol were injected into a reaction gas mixture consisting of 4% oxygen in helium. This stream was directed into a packed quartz reactor containing the catalyst surface. Flows were controlled to maintain a 15 ms residence time of the reaction gas on the catalyst surface. Recent experiments have addressed a catalyst mixture containing various chlorination sources: calcium chloride (40 mg), potassium chloride (5 mg), iron chloride (5 mg) and aluminum chloride (5 mg). These materials were used without a borosilicate foam plug to provide information on the catalytic effect without the support material. Pulses of benzene and phenol were transported through the quartz reactor, and products were then transported out of the reactor and trapped in a cryogenically cooled GC-MS system for in-line product identification.

Results and Discussion

Initial results indicate that both benzene and phenol are readily chlorinated when they are introduced into the system. A typical chromatogram for phenol (Figure 2) shows a wide variety of reaction products containing many chlorinated and non-chlorinated compounds. This particular analysis shows large yields of chlorophenol and smaller amounts of other phenolic reaction products, some of which are chlorinated. Large yields of non-chlorinated dibenzofuran were observed as well smaller amounts of non-chlorinated dibenzodioxins.

A summary of the results for the competitive chlorination of benzene and phenol on the iron, calcium, aluminum, and potassium chloride catalyst mixture at 400 °C is shown in Figure 3 with yields of chlorinated products for each system shown in Table 1. At these conditions, the formation of chlorinated aliphatic compounds was favored for benzene compared to phenol (by a factor of more than 2). However, phenol was much more likely to undergo catalytic chlorination to form chlorinated aromatic products than was benzene. This difference was largely due to the large yields of chlorophenol from phenol (benzene formed small yields of chlorobenzene by comparison). The phenol also formed phenoxy-phenols or dimers of phenol itself, as well as

chlorobenzenediol. Since chlorophenol is a major product, it seems likely that chlorophenoxy radical recombination is likely to occur as further experiments are conducted at slightly higher temperatures. Further studies will focus on the formation of PCDD/F through this mechanism.

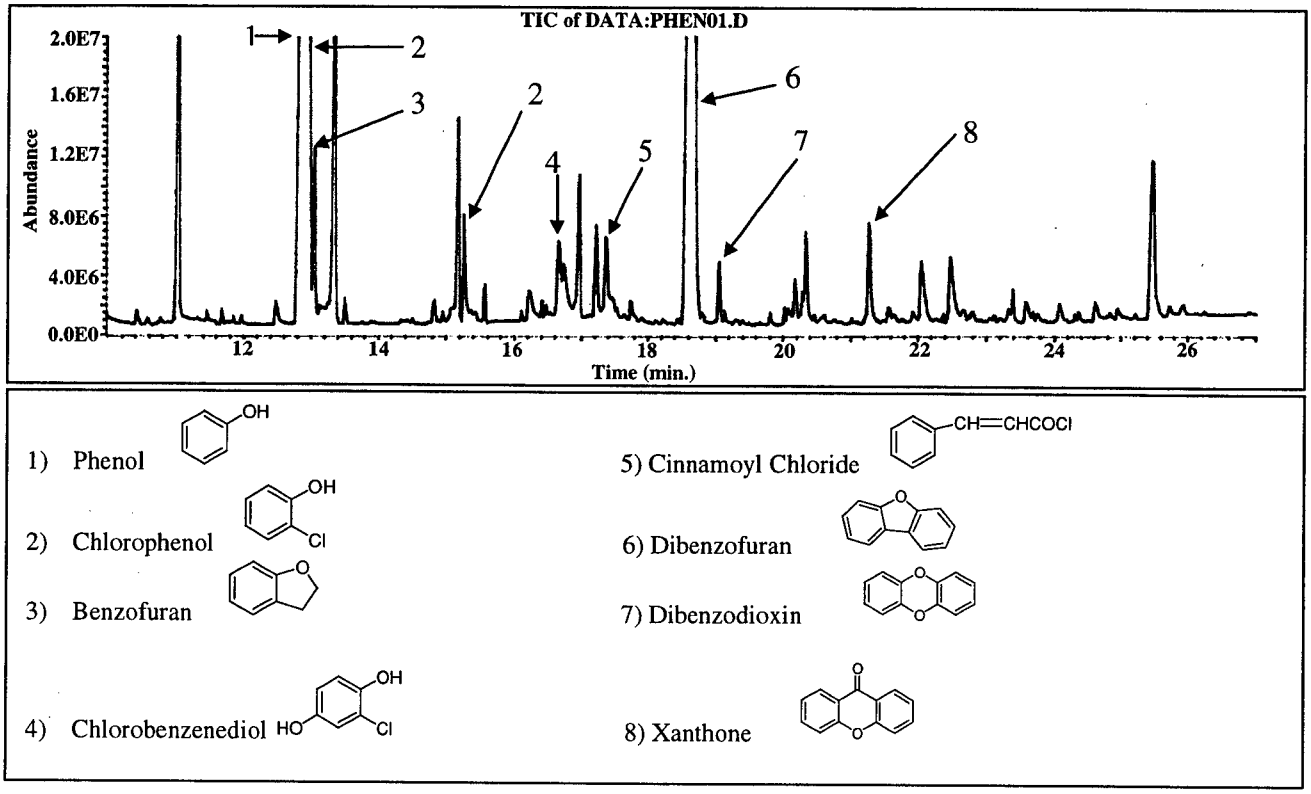


Figure 2: Total Ion Chromatogram for Phenol Chlorination on $CaCl_2$, KCl, $FeCl_3$, $AlCl_3$ at 400 °C.

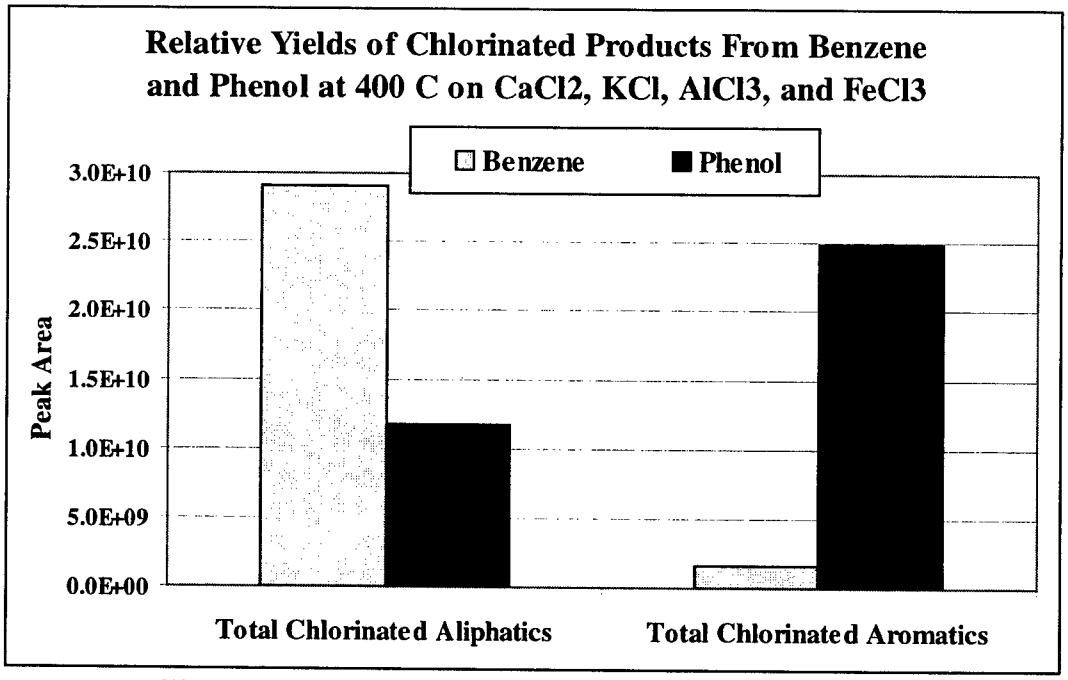


Figure 3: Relative yields of Total Chlorinated Products From Benzene and Phenol on $CaCl_2$, KCl, $FeCl_3$, $AlCl_3$ at 400 °C.

Table 1: Yields of Reagents and Chlorinated Products From Benzene and Phenol on $CaCl_2$, KCl, $FeCl_3$, $AlCl_3$ at 400 °C.

Compound	Peak Area per mmol Benzene Injected	Peak Area per mmol Phenol Injected
Benzene (C6H6)	1.6E+11	2.6E+09
Phenol (C6H5OH)	9.0E+01	1.3E+11
Dichloromethane (CH2Cl2)	1.5E+10	7.4E+09
Trichloromethane (CHCl3)	8.3E+09	2.2E+09
Tetrachloromethane (CCl4)	5.4E+09	2.0E+09
Chloroethene (C2H3Cl)	7.9E+07	1.9E+04
Trichloroethene (C2HCl3)	1.7E+08	7.2E+07
Tetrachloroethene (C2Cl4)	4.4E+08	7.4E+07
Chlorobenzene (C6H5Cl)	8.1E+08	3.8E+07
Dichlorobenzene (C6H4Cl2)	7.5E+07	1.2E+09
Trichlorobenzene (C6H3Cl3)	1.6E+06	2.0E+07
Tetrachlorobenzene (C6H2Cl4)	8.2E+07	1.2E+08
Pentachlorobenzene (C6HCl5)	1.1E+08	1.1E+08
Hexachlorobenzene (C6Cl6)	1.2E+08	9.3E+07
Chlorophenol (C6H4ClOH)	3.6E+08	2.2E+10
Dichlorophenol (C6H3Cl2OH)	ND	8.4E+08
Trichlorophenol (C6H2Cl3OH)	ND	1.2E+08
Tetrachlorophenol (C6HCl4OH)	2.4E+07	4.5E+07
Pentachlorophenol (C6Cl5OH)	ND	1.7E+07

Quantification of products is still being performed. We continue to study the formation of non-chlorinated dibenzofuran from phenol, which did not occur in the benzene reactions. Subsequent chlorination of the dibenzofuran may be possible (just as was the case with chlorination of benzene) resulting in the formation of trace PCDF compounds. Work also continues on the examination of the chlorination reactions of benzene and phenol on different surfaces (borosilicate foam with and without various catalysts). No PCDD/F were observed in this analysis due to the less sensitive scanning mode that was used. Further studies will include selected ion monitoring analysis (SIM) for both the chlorinated and non-chlorinated furans and dioxins.

References

1. Fiedler, H., **Organohalogen Compd.**, **11**, 221, 1993.

2. US-EPA, National Dioxin Study Tier 4 - Combustion Sources. Engineering Analysis Report. RTP, NC: OAQPS. EPA-450/4-84-014h

3. Thomas, Valerie M. and Spiro, Thomas S., **Environ. Sci. Technol.**, **30** (2), 82, 1996.

4. US-EPA, Workshop on Formation and Sources of Dioxin-Like Compounds, Chevy Chase, MD, November 17-20, 1996.

5. Rubey, W. A. and Grant, R. A., **Rev. Sci. Instrum.**, **59**, 265, 1988.

Chlorination of Raw Meal Organics in Cement Kiln Preheat Zone

Nabil Kasti, Sukh Sidhu and Richard Striebich
Environmental Science and Engineering
University of Dayton Research Institute
Dayton, OH 45469-0132
Sidhu@udri.udayton.edu

Portland cement plants have been identified by the US-EPA as major sources of HAPs emissions, including hydrocarbons, hydrochloric acid, and polychlorinated dibenzo-p-dioxins and polychlorinated furans (PCDD/F). As such that they have been targeted for additional, stringent regulation under the auspices of the Clean Air Act Amendment (CAAA) and EPA's Combustion Strategy. Affordable cement is obviously essential for the growth of both domestic and world-wide infrastructure, and thus it is important devise efficient, yet cost effective, methods for the prevention of HAPs.

To devise cost-effective methods for prevention of HAPs, their formation mechanism must be understood; this mechanism is the focus of this contribution. In previous work, cement kiln raw meal was desorbed under cement kiln preheat zone conditions (4% O2, temperature range of 30 –500 C) [1]. The results of these experiments showed that cement kiln raw meal contains a wide range of organics including benzene, toluene, naphthalene, alkanes, C_{14}-C_{18} carboxylic acids, phthalates and their derivatives and natural products like cholesterol. To gain better insight into the speciation of raw meal organics, the total organics thermally desorbed from each sample were divided into different molecular weight ranges and different chemical classes. From these classifications, it was observed that most of the organics are in the 200 to 300 amu molecular weight range and are C_{14}-C_{18} carboxylic acids. The second largest group includes organics that are natural products and that have molecular weights greater than 400 amu. Aromatics and aliphatics (molecular weight less than 200 amu) form a small fraction of the total organics desorbed from raw meal. These results are consistent with the hypothesis that organics are present in raw meal as long chain carboxylic acids or phthalates, cholesterols, and their derivatives. These results are also consistent with the work of Saiz-Jimenez [2], which proposes that unsaturated fatty acids are the major constituents of humic substances. Upon pyrolysis, fatty acids undergo decarboxylation, fragmentation, cyclization and aromatization reactions, yielding a homologous series of alkyl benzenes or alkyl furans (in presence of oxygen). The formation of the homologous series of alkylated benzenes and naphthalenes from aliphatic precursors is not only of interest regarding structural configuration of humic substances but also has immense importance in HAPs formation reactions.

The raw meal sample was obtained from a local preheater cement kiln. Semi-quantitative analyses of raw meal and cement kiln dust were performed using X-ray diffraction and infrared absorption (FTIR) techniques. In X-ray diffraction analyses it was assumed that all elements were present as oxides. Raw meal showed small amounts of chlorine. In addition to the elements indicated in table 1, sample contained a trace of sulfur, however, the peak was below quantification limit (0.2%). The surface area of the sample was measured using B.E.T. method. The total surface area was 2.5 m^2/g.

To investigate HAPs formation reactions from raw meal organics, condensate was collected by desorbing hydrocarbons from raw meal and collecting them in a dry-ice cold trap. The hydrocarbon condensate thus collected had both aqueous and organic phase. These two phases were difficult to separate; leading to an inconsistent inlet concentration of organics, which resulted in inconsistent results. To overcome the problems associated with water, a benzene and myristic acid mix (65%/35% by weight) was used to simulate raw meal hydrocarbons. Myristic acid represents the long chain carboxylic acid and phthalate functionalities that constitute the majority of the raw meal hydrocarbons. Benzene represents the aromatic decomposition products of natural humic substances and

Table 1. Elemental Analysis of Cement Kiln Raw Meal

Elements	Weight %
Mg	1.7
Al	4.6
Si	11.7
K	1.6
Ca	40.6
Fe	3.1
Cl	0.2

also acts as a solvent. We studied the chlorination of the benzene and myristic acid mix over three different surfaces: catalyst mix A (40 mg $CaCl_2$, 5 mg KCl, 5 mg $AlCl_3$, and 5 mg of $FeCl_3$), catalyst mix B (40 mg $CaCl_2$ and 5 mg KCl), and Catalyst mix A+ thermally-desorbed raw meal. These catalyst compositions are based on the raw meal elemental composition and should help elucidate role of transition and alkali earth metals in the chlorination of raw meal organics.

All experiments were conducted on a high temperature flow reactor system referred to as the System for Thermal Diagnostic Studies (STDS). The detailed design of STDS has been published elsewhere [3]. In brief, the STDS consists of four integrated units: (1) a control console for precise adjustment of temperature, pressure, residence time and carrier gas flow; (2) a thermal reactor compartment that is housed within an HP 5890 gas chromatograph (GC) to allow precise temperature control of sample lines into and out of the reactor; (3) a gas chromatographic chamber (HP 5890 GC) for separating products; and (4) a mass spectrometer (HP 5970B MSD) for product identification and quantitation. A 3-mm inner diameter, packed-bed, fused-silica reactor was used for this study. One-centimeter quartz wool plugs were placed on each side of catalyst to hold it in place and to avoid particle entrainment into the GC-MS.

The STDS was operated to simulate the conditions occurring in preheating zone of cement kiln. 1 μl of reactant mix (benzene + myristic acid) was injected into the STDS using a liquid syringe. In addition, a reaction gas was also introduced into the STDS, which contained 4% O_2, which is typical of cement kilns. The vaporized reactant mix and reaction gas were swept into the in-line, catalytic reactor of the STDS where the chlorination reactions were studied. The experimental data was acquired for temperatures of 300 C, 400 C, and 500 C, with a gas-phase, mean-reaction time of 15 ms and nearly constant total pressure of 1.1 atm. Chemical analysis of the gaseous reactor effluent was performed. The reactor effluents were cryogenically trapped and then subjected to programmed temperature gas chromatograph using a DB-5 (J & W Scientific), 30m, 0.25 micron film thickness, 0.25 mm I.D. capillary column held at a trapping temperature of –60 C. The GC was temperature programmed from –60 C to 290 C (10 minute hold) at 10 C/min. Scanning (scanning 15 to 350 amu) mode was used to identify products formed from these catalytic reactions.

Results and Discussion

In these experiments, organic components simulating raw meal organics were exposed to temperatures between 300 and 500 C in 4% oxygen. In the case of benzene and myristic acid over catalyst A (figure 1), benzene was degraded very little, as its concentration was similar over the temperature range investigated. Clearly, the myristic acid, simulating long chain carboxylic acid functionalities being evolved from the raw meal, was degraded selectively compared to the benzene. Products formed included mono- through tetra- chlorinated methanes and ethylenes, which increased greatly in concentration from 300 to 400 C, with maximum yields expected somewhat above 400 C.

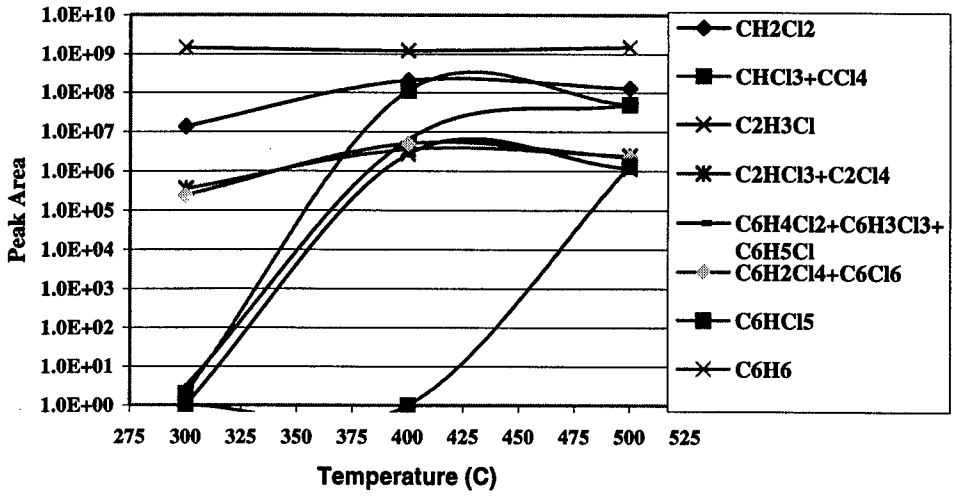


Figure 1. Product profiles for chlorination of myristic acid/ benzene mixture over catalyst A ($CaCl_2$, KCl, $AlCl_3$, $FeCl_3$).

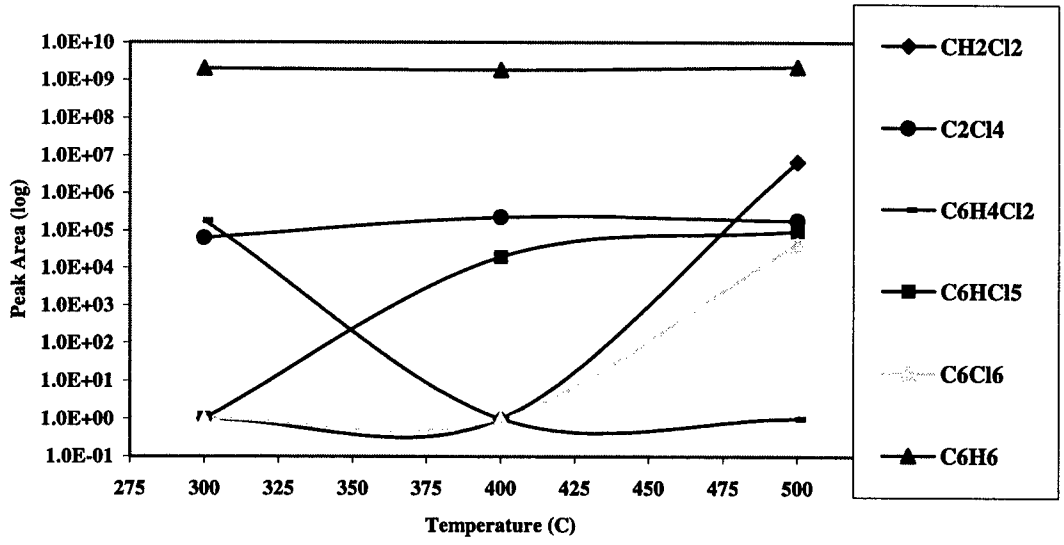


Figure 2. Thermal chlorination profile for myristic acid/benzene mixture in catalyst Mix A with raw meal.

The mono- through tri-chlorinated benzenes also increased in concentration with a maximum formation rate at about 400 C. The concentration of the hexachlorobenzene only increased by one order of magnitude (compared with 8 orders of magnitude for mono- through tri-chlorinated benzenes). Hexachlorobenzene was observed as a product in the 300 C exposure whereas the mono- through tri-chlorinated benzenes did not form until temperatures of greater than 300 C.

These products seem consistent with the fragmentation and decarboxylation of the long chain acids into light hydrocarbons, which are readily chlorinated. These light chlorinated compounds are then free to cyclize and form chlorinated aromatic functionalities. Higher levels of chlorination of aliphatic compounds are therefore likely to contribute to higher levels of chlorination of the benzene rings, as previously postulated [4]. Chlorinated phenols were only observed at one temperature (400 C) over catalyst A.

Desorbed raw meal added to catalyst A gave results (shown in Figure 2) which suggest that chlorinated product yields change greatly with the addition of the meal. No mono-, tri- or tetra-chlorobenzenes were observed with the addition of the desorbed meal. The dichlorobenzene concentration decreased from a maximum at 300 C to a minimum between 400 and 500 C. In contrast with this result, catalyst A without the meal showed no formation of dichlorobenzene until temperatures of 400 C. The hexachlorobenzene did not form at all under these conditions (with desorbed meal) until a temperature of 500 C was reached. In the catalyst A run without the meal, the hexachlorobenzene formed at the lowest temperature 300 C. Clearly the addition of the desorbed raw meal decreased the variety of chlorinated products (both aliphatic and aromatic) at all temperatures. Adsorption and desorption experiments are anticipated to further evaluate the behavior of the observed products in these experiments.

The major compounds observed in this preliminary study were also present as major chlorinated hydrocarbons in cement kiln emissions data [4]. Other studies conducted with catalyst A and another catalyst containing no transition metals (Fe and Al) indicated that transition metals such as these are not necessary for chlorinating of the organic materials, at least for temperatures between 300 and 500 C.

Products for the introduction of benzene only (no myristic acid) into catalyst A showed that chlorinated product yields decreased for temperatures between 300 and 500 C. Mono-, tri- or tetra-chlorobenzenes were observed. The di- and tri-chlorophenol concentration decreased from a maximum at 300 C to a minimum between 400 and 500 C under these conditions, i.e., using benzene as a reactant versus a mixture of benzene and myristic acid.

The data generated from this surface catalyzed chlorination experiments is being used to develop a HAPs formation mechanism. This formation mechanism will not only provide the information to develop process modifications which prevent HARS formation, but will also provide fundamental data on the origin of pollutant formation.

References

1. Sidhu S., and Dellinger, B., *Proceeding of the International Specialty Conference on Waste Combustion in Boilers and Industrial Furnaces*, A&WMA, Kansas City, Missouri, March, 1995, p. 119.
2. Saiz-Jimenez, C., *Environ. Sci. Technol.*, **28**: 1773 (1994).
3. Rubey, W.A., and Grant, R.A., *Rev. Sci. Instrum.* **59**: 265 (1988).
4. Taylor, P.H., Sidhu, S.,Rubey, W.A., Dellinger, B., Wehrmeier, A., Lenoir, D. and Schramm,K., *27th Symposium on Combustion/The Combustion Institute* 1998, pp 1769-1775.

Characterization Of Chars From Poly-Phenolic Compounds

RAMESH SHARMA, MOHAMMAD HAJALIGOL, PAMELA MARTOGLIO, JAN WOOTEN AND VICKI BALIGA

Research Center, Philip Morris U.S.A., P.O. Box 26583, Richmond, VA 23261

Poly-phenolic compounds exist in a variety of forms in the nature. Lignin in wood and chlorogenic acid in the extracts of coffee beans or tobacco leaves are a few examples of poly-phenols in the natural products. During smoking the chlorogenic acid of tobacco undergoes pyrolysis and combustion reactions to form gaseous products and a solid char. The composition and the nature of the gaseous products and char may be governed by the pyrolysis conditions.

In this work, the effect of pyrolysis conditions on yield and characterization of chars from chlorogenic acid was studied. The char was produced at atmospheric pressure under oxidative and inert atmospheres at temperatures ranging from 250° to 750°C. The inert runs were made with helium as the carrier gas; the oxidative runs with 2% oxygen in helium. The uncondensed gaseous product was analyzed by mass spectrometry. The characterization of the product char was done in terms of its elemental analysis and surface area, and by Fourier-transform infrared (FTIR) and solid-state ^{13}C nuclear magnetic-resonance (NMR) spectroscopy. The surface morphology of the char was studied by scanning electron microscopy (SEM) and Environmental SEM. The results of char characterization are discussed in relation to the evolved gases.

Chlorogenic acid, obtained from Fisher Scientific, is a predominantly *trans* compound with 99% purity. When heated to temperatures of 250°C or above, it decomposes to form a gaseous product and a solid char. The yield of char varies from 80% at 250°C to 20% above 600°C. The presence of oxygen enhances the rates of pyrolysis reactions such that the char yield becomes virtually negligible above 550°C. The data analysis indicated a relatively high activation energy (40 kJ/mol) for non-oxidative pyrolysis suggesting that the reactions probably were not transport-limited. The gaseous products consist mainly of phenol, catechol, benzene, and benzoic acid in addition to water, CO and CO_2. Among these, catechol, and benzoic acid were also reported in the cigarette smoke[1]. Sakuma *et al.*[2] and Zane and Wender[3] observed similar compounds in the products from chlorogenic acid pyrolysis. Schlotzhauer and Chortyk[4] observed, in addition, hydroquinone, resorcinol, 5-hydroxymethylfurfural,and neochlorogenic acid. However, it should be realized that the mass spectrometric analysis alone, as used in this study, is not sufficient for a complete identification of the isomeric compounds.

The char is obtained as a volcano-like cone. It was noted that the external surface of the cone is smooth and glassy indicating that chlorogenic acid forms a melt at high temperatures. This is consistent with its melting point (208°C). SEM and the Environmental SEM analyses indicate that the decomposition of chlorogenic acid is accompanied by the formation of bubbles that grow as the reaction proceeds until the bubbles break allowing the gaseous products to escape. The formation, growth, and breaking of the bubbles and, in turn, the evolution of the gaseous products and char, is determined by the experimental conditions. At low temperatures, the char particles have irregular appearance with a few bubbles inside the particles. Some bubbles have long and irregular shapes, suggesting that they may have initiated from fissures. The melt consists of solid regions of smooth texture and bubbles and the underlying surfaces are filled with bubbles. At higher temperatures, the particles become more rounded and the bubbles become larger and in some cases the bubble film is broken probably by the escaping gases which may have been released into another closed bubble or to outside. The surface of the melt becomes increasingly rough due to the growth of globular, rod-like, and platelet structures which degrade further to leave a carbonized frame of bubbles and pores. Fig. 1 shows a typical SEM micrograph of the surface of the char at 750°C. As can be seen clearly, some of the bubbles are still

intact whereas the others are broken. The melt structure is completely carbonized at this temperature. In the presence of oxygen, these carbonized structures degrade and disappear completely above 550°C.

The elemental analysis of char samples (Table I) showed that both the hydrogen and oxygen contents of char decrease as the pyrolysis temperature is increased. The hydrogen content decreases from 5% for chlorogenic acid to 2% for the char prepared at 750°C and the oxygen content from 42% to about 5%. This shows that the char becomes more carbonaceous in nature at high temperatures. Interestingly, the elemental analysis of char was not altered significantly by the use of the oxidative atmosphere.

The surface area of the char samples was measured using a Quantachrome Autosorb using nitrogen as an adsorbate. The chars which were prepared below 550°C have a negligible surface area but the area increases dramatically to 196 m^2/g for char prepared at 650°C, before decreasing slightly at 750°C. Thus, the use of high temperatures seems essential in order to create a char with a high surface area. The presence of oxygen enhances the surface area and lowers the temperature for the maximum surface area to 450°C.

Fig. 2 shows the solid-state ^{13}C CP/MAS NMR spectra of chlorogenic acid and its chars. The spectrum for chlorogenic acid suggests that the chlorogenic acid is mainly crystalline in nature and contains aliphatic, aromatic, phenolic, carbonyl, and carboxyl structures. The NMR spectra of chars differ progressively with temperature from that of chlorogenic acid. At 250°C, the resonance bands tend to be broad indicating an increase in the amorphous nature of the sample. Since the resonance bands do not change appreciably in number or intensity, the changes appear to be mostly due to melting and to the formation of an amorphous state. Above 250°C, there is a steady loss of oxygen functionality indicated by the loss of carbonyl absorptions. For 350°C char, the spectrum indicates that the phenolic, carboxyl and carbonyl groups are still present at this temperature, although the concentration of the latter two groups is considerably small. It is believed that the aliphatic and oxygen groups create links and loops between aromatic clusters of various sizes[5]. The resonance bands corresponding to carbonyl groups mostly disappear. As the temperature is increased further, the char loses its aliphatic character completely and becomes more and more aromatic in nature. The resonances corresponding to phenolic groups also decrease progressively in intensity until they become almost totally absent in the 650°C char. The oxygen bonded carbons are no longer distinguishable and only a very small aliphatic remains, indicating a complete carbonization of the char. The char at 750°C could not be analyzed due to the extreme charging of the sample. Essentially similar results were obtained from the NMR analysis of the oxidative chars indicating that many of the carbons in the char that react with oxygen are lost probably by de-volatilization. These results appear to be at variance from those for chars prepared from cellulose[6] where it was observed that the aliphatic resonance of the char was significantly reduced while the resonance of aromatic carbons bonded to oxygen increased. The difference could be due to the difference in the substrate as well as in the experimental conditions used.

The FTIR results, presented in Fig. 3, also suggest dramatic chemical changes in chlorogenic acid above 250°C. Both the hydroxyl and carbonyl groups are lost increasingly as the pyrolysis temperature is increased although the loss of hydroxyl groups is not as rapid as that of the carbonyl groups. The aliphatic character of the char decreases as the temperature is increased. On the other hand, the aromatic character, the C=C and the aromatic ring activities increase and are highest at 650°C. At 750°C, all the bands due to OH, CH, CH_2, and CH_3 stretches have vanished and there is a weak band for C=O. The char is mainly an aromatic polymer of carbon atoms. Boon et al.[7] observed a similar loss of oxygen functionality and an increase in the aromatic character of the cellulose chars at high temperatures. As with NMR analysis, the FTIR analysis showed essentially no effect of oxygen on the char characteristics.

The results of characterization are consistent with the evolution of the gaseous products. As the pyrolysis temperature is increased, the char looses much of its oxygen and hydrogen to the gaseous products such as water, CO, CO_2, catechol, phenol, and benzoic acid, with the char becoming more carbonaceous in nature and low in crystallinity.

REFERENCES

1. SCHLOTZHAUER W.S., SNOOK, M.E., CHORTYK, O.T., AND WILSON, R.L.: J. Anal. Appl. Pyrol. 22, 231 (1992).
2. SAKUMA, H., MATSUSHIMA, S., MUNAKTA, S., AND SUGAWARA, S.: Agric. Biol. Chem. 46(5), 1311 (1982).
3. ZANE, A., AND WENDER, S.H.: Tob. Sci. 7, 21 (1963).
4. SCHLOTZHAUER, WS AND CHORTYK, O.T.: Tob. Sci. 25, 6 (1981).
5. FLETCHER, T.H., SOLUM, M.S., GRANT, D.M., AND PUGMIR, R.J.: Energy Fuels 6, 643 (1992).
6. SHAFIZADEH, F. AND SEKIGUCHI, Y.: Comb. Flame 55, 171 (1984).
7. BOON, J.P., PASTOROVA, I, BOTTO, R.E., AND ARISZ, P.W.: Biomass Bioenergy 7, 25 (1994).

TABLE I

Elemental analysis of chars from chlorogenic acid

Sample	Temp. [^{o}C]	Carrier gas	C	H	O	C/H
Chlorogenic acid	-	-	53.4	5.1	41.8	0.9
Char	250	He	56.8	5.0	38.1	0.9
Char	350	He	69.9	4.0	21.5	1.4
Char	450	He	74.4	3.6	17.4	1.7
Char	550	He	81.1	3.1	10.9	2.2
Char	650	He	84.8	2.7	6.5	2.6
Char	750	He	86.5	1.9	5.5	3.8
Char	250	2% O_2 in He	56.4	5.1	38.3	0.9
Char	350	2% O_2 in He	68.1	4.1	23.3	1.4
Char	450	2% O_2 in He	61.5	3.0	16.9	1.7
Char	550	2% O_2 in He	79.6	3.2	12.1	2.1

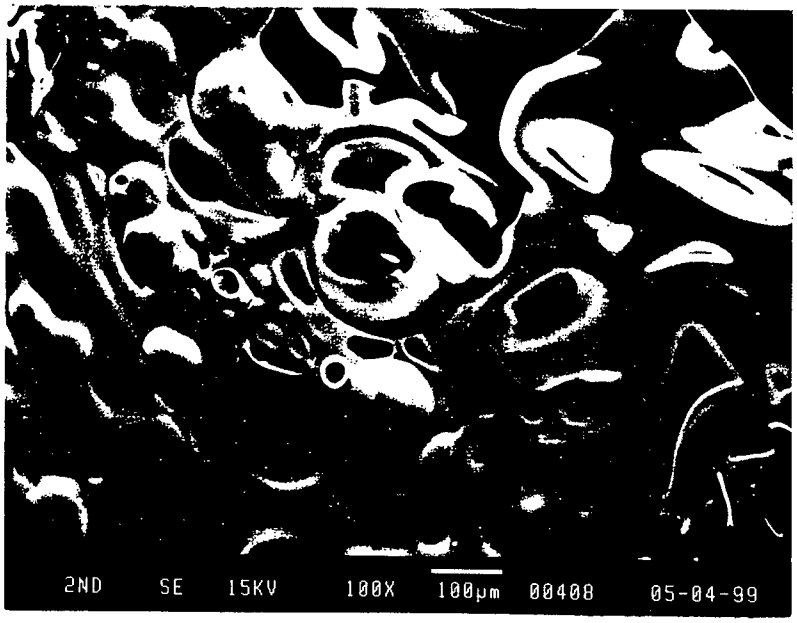


FIG. 1. A typical micrograph of the surface of the char formed at 750°C.

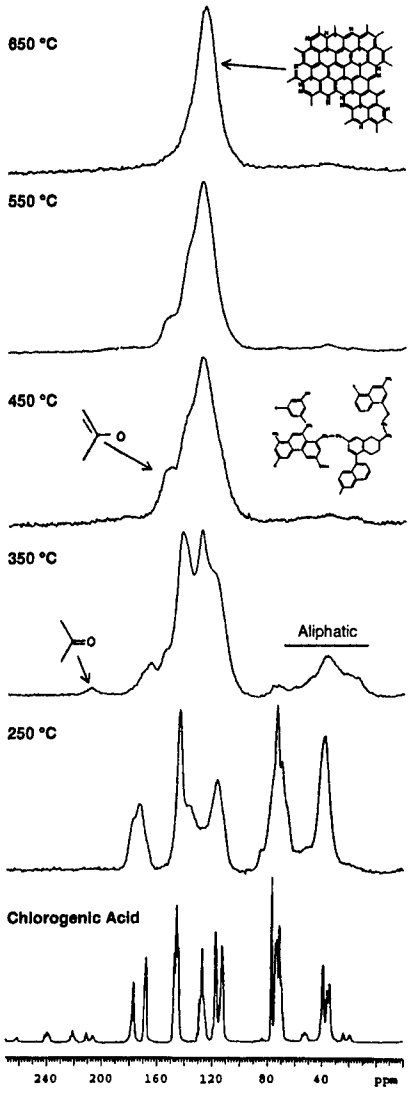


FIG. 2. ^{13}C CP/MAS NMR spectra of chlorogenic acid chars at different charring temperatures.

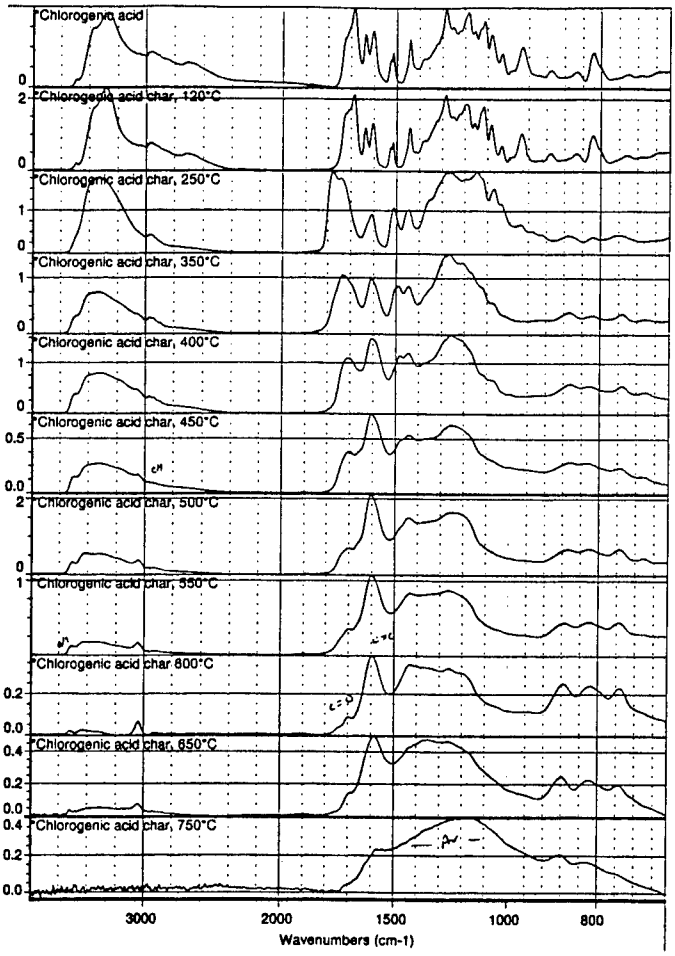


FIG. 3. FTIR spectra of chlorogenic acid chars at different charring temperatures.

Pyrolysis Kinetics Of Cellulosic Materials

BRUCE WAYMACK, MOHAMMAD HAJALIGOL, AND TRAVIS FISHER
Research Center, Philip Morris USA, P.O. Box 26583, Richmond, VA 23261

INTRODUCTION

Many decades of research have generated a wealth of knowledge on the kinetics and thermal degradation of cellulosic materials; and many elegant reviews have appeared in different scientific communities (1-5). It has been well established in the literature that in a moderate temperature range (below 400°C), cellulose rapidly undergoes complete degradation by pyrolysis, forming a variety of permanent gases, a condensable liquid called tar, and a solid residue called char. For pure cellulose, a single step reaction seems to be adequate to describe the whole phenomenon. The solid residue, primary char, that is formed at a moderate temperature can undergo a transformation step to produce a more stable char at higher temperatures. This latter step, which is part of the aromatization of carbonaceous materials, was proven to exist by many researchers (5-7) in a moderate to high temperature range (above 400°C). While this step does not represent a significant loss of material compared to the first step of decomposition, it is very important in the formation of the primary carbon skeleton for the high temperature graphitization processes. In addition, chemical species that are evolved during this step could be very different than those formed during the primary decomposition. In an earlier presentation by the Authors (8), evolution of many aromatic compounds were detected from pre-charred cellulose during heating to higher temperatures.

The objective of this study is to provide experimental evidence for this second step and to estimate the reaction kinetic parameters. Cellulosic materials used in this study are pure samples of Avicel PH-102 and Whatman Filter paper 41 and a natural cotton sample containing about 5000 ppm potassium. Potassium is known to be a char promoter. In order to eliminate the influence of secondary cracking reactions of primary pyrolysis products on the results, pre-charred samples of starting materials were prepared at around 350 °C, and then, were used to confirm the second step.

EXPEIMENTALS AND RESULTS

Experimental work was performed using a thermal gravimetric analyzer equipped with a differential scanning calorimeter (DSC) and a mass spectrometer (MS). A detailed description of the experimental setup is given elsewhere (8). Briefly, a small sample of material (1-20 mg) is placed on the balance sample holder, then heated at a constant heating rate under an inert atmosphere. Weight, heat flow and peak intensity of masses of interest are monitored and recorded as a function of time. To minimize gas phase reactions and mass transfer effects, a relatively slow heating (≤60°C/min) regime and a high gas flow rate (150 ml/min) were employed in this study.

Weight loss data for the Avicel cellulose decomposition are presented in Figure 1. At the heating rate of about 20 °C/Min., as expected, cellulose rapidly decomposes between 300 to 350°C (Curve # 1). Following this sharp weight loss, as can be seen from curve #1, there is a gradual weight loss (about 5% of starting cellulose) up to about 700 °C. This gradual weight loss can be more readily observed and detected as another step (curve # 3) in decomposition if a pre-charred sample of Avicel cellulose is heated separately. As can be seen from curve # 3, most of the weight loss for the pre-charred sample takes place between 350 to 700 °C. The derivative (DTG) of two weight loss (TG) curves are given by curves # 2 and 4 in Figure 1. The DTG data provide two distinct T_{max} , one around 335 °C for the first step decomposition reactions and one around 420 °C for the second step reactions. The latter T_{max}

depends on the conditions under which pre-charred samples are prepared, and could be as high as 500 °C. In some previous work with DSC, this second step was probably detected as a small exotherm right after the endothermic decomposition step (6,7). Depending on the condition at which pre-charred samples are prepared, the second step reaction would become at least thermo-neutral to partially exothermic. This observation is depicted in Figure 2, and indicates that after about 70% weight loss of the starting cellulose the reactions become at least thermo-neutral if not slightly exothermic.

Weight loss data were used to estimate global kinetic parameters of the reactions. We used a kinetics software model which is based on a least square regression routine, and provides an optimal value for the parameters based on the minimum mean of residues. For pure cellulose decomposition a two step reactions was assumed. The first step represents the major decomposition with gases, liquids and primary char as products. The second step is for the reactions of primary char to form a high temperature char. A first order reaction for the formation of the primary char and a second order reaction for the formation of the high temperature char were assumed. At this time, we do not have any theoretical basis for the assumption of the second order reaction except the goodness of fit. This needs to be further explored.

Kinetic information were obtained by fitting the experimental data with the above kinetic scheme, and results are tabulated in Table 1 for all three cellulose samples used in this study. The first step activation energy and frequency factor for Avicel decomposition agrees well with the cellulose decomposition kinetic data in the literature. Kinetic data for the Whatman filter paper is slightly lower than Avicel cellulose, nevertheless, it falls within the bulk of data and it is still in good agreement with the available literature. The small difference could be attributed to the effects of degree of polymerization, crystallinity, source, etc. For the natural cotton, on the other hand, the apparent activation of the primary decomposition reaction is much lower, 115 KJ/mole vs. 210 KJ/mole for avicel cellulose. This is expected, since it is well known that alkali metals affect the decomposition reactions and obviously reduce the activation energy.

Weight loss data of pre-charred samples were fitted to a single step second order reaction model. The kinetic parameters obtained from this model is tabulated in Table 2. The activation energies for the second step, as expected, are low than the first step but consistent for all the materials tested in this study. It is know that char forming steps have much lower activation energies than decomposition step.

ACKNOWLEDGMENTS

Authors wish to thank Philip Morris USA management for their support and encouragement of basic research studies. Technical assistance of our colleagues Dr. Diane Kellogg, Mr. Joshua Edgar, and Dr. Ramesh Sharma are gratefully appreciated.

REFERENCES

1. Antal, M. J., Jr., in Advances in Solar Energy Vol. 1 (Boer, K and Duffie J., Eds.), American Solar Energy Society, Boulder, CO, 1982, PP> 61-111.
2. Antal, M. J., Jr., in Advances in Solar Energy Vol. 2 (Boer K. and Duddie, J., Eds.), American Solar Energy Society, Plenum, New York, 1985, PP. 175-255.
3. Antal, M. J., Jr. And Varhegyi, G., Ind. & Eng. Chem. 34:703-717 (1985).
4. Safizadeh, F., in Fundamentals of Thermochemical Biomass Conversion (Overend, R., Milne, T., and Mudge, L., Eds.), Elsevier. 1985, PP. 183-217.
5. Varhegi, G., Emma, J., and Antal, M. J., Jr., Energy & Fuel, 8:1345-1352 (1994).

6. Briodo, A, Weinstein, M. in Proceedings of the 3rd International Conference on Thermal Analysis (Weidenman, Ed.), Birkhauser Verlag: Basel, 1971, PP. 285-296.
7. Milosavljevic, I., Oja, V., and Suuberg, E. M., Ind. & Eng. Chem. Res., 35:653-662 (1996).
8. Hajaligol, M., Waymack, B., and Kellogg, D., in Fuel Chem. Preprint, Vol. 44, No. 2, Fuel Chem. Div., ACS, Anaheim, CA, 1999.

Table 1. Kinetics Parameters for the Thermal Decomposition of Cellulose Samples.

PARAMETERS	VALUES, FOR AVICEL, PH-102	VALUES, FOR WFP-41	VALUES, FOR NAT. COTTON
E, KJ/mole	211.	200.	115.
log k_0, S^{-1}	16.1	14.51	7.7
React. Order	1.00	1.00	1.00

Table 2. Kinetic Parameters for the aromatization of primary Char Samples.

PARAMETERS	VALUES, FOR AVICEL, PH-102	VALUES, FOR WFP-41	VALUES, FOR NAT. COTTON
E, KJ/mol	56.	59.	66.
log k_0, S^{-1}	1.7	2.3	2.3
React. Order	2.00	2.00	2.00

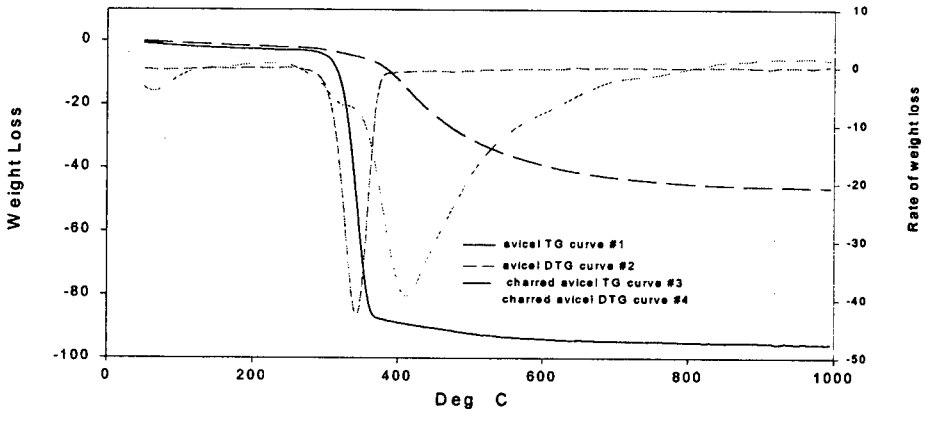


Figure 1. Weight loss (TG) and Derivative of Weight Loss (DTG) for Avicel (1, 3) and Pre-charred Avicel (2, 4) as a Function of Temperature.

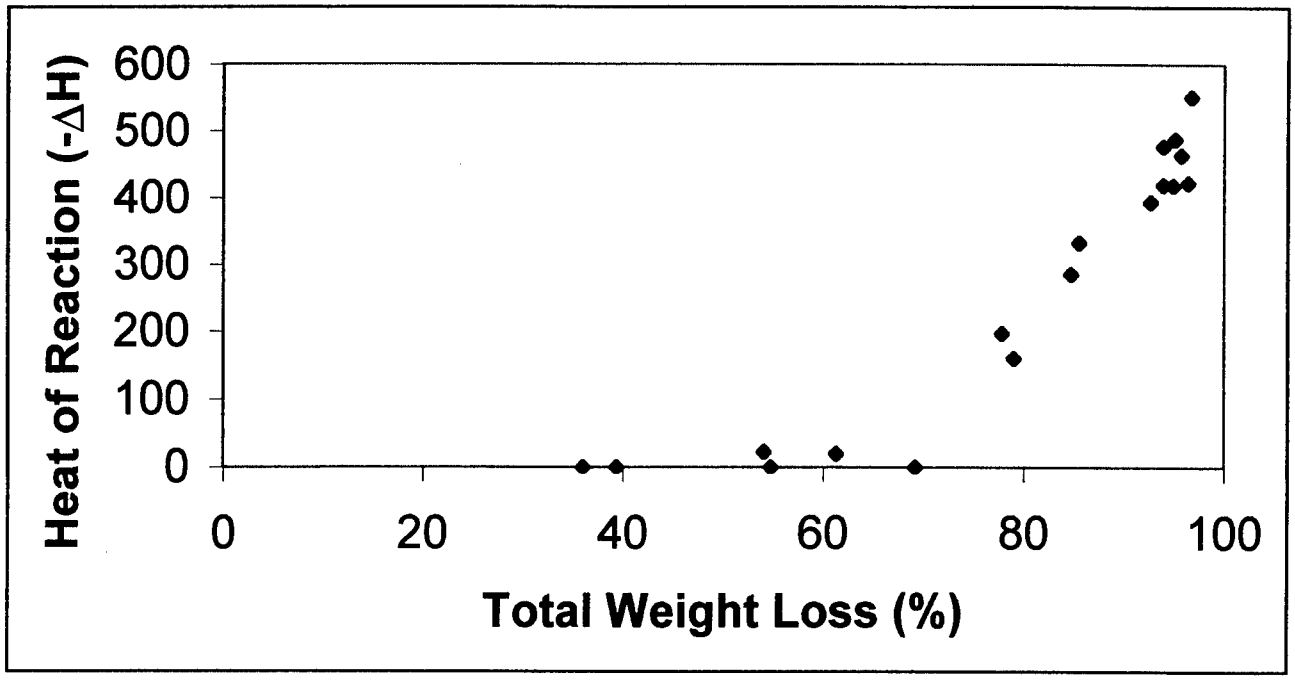


Figure 2. Heat of Reaction of Pre-Charred Avicel Samples as a Function of Pre-Charring Conditions (or Char Weight Loss in the TGA).

Evaluation and comparison of Heat of Combustion Value and Fuel Test Data for a Synthetic Refuse-Derived Fuel

Sukrut S. Thipse and Chad Sheng.
New Jersey Institute of Technology, Newark, NJ 07102, USA
Phone: 973-596-5853. e-mail: sst4131@tesla.njit.edu

Introduction. Heat of combustion and other fuel test data provide useful indicators in assessing the practical value of a fuel. The heat of combustion, also referred to as the calorific value, heat content or higher heating value of a fuel is the total energy that can be made available by complete combustion of the fuel in oxygen. A significant proportion of the municipal solid waste (MSW) stream is burned in large-scale municipal waste combustors (MWCs), and the thermal energy produced can be sufficient for energy recovery steps to be commercially viable. Waste fuels and refuse-derived fuels (RDF) thus have some potential as alternatives or supplements to traditional fossil fuels as a source of energy. Other fuel test data, such as fuel nitrogen, sulfur and chlorine content, give an indication of the type and concentrations of species that can be produced in MWC emissions, some of which may be formed as products of incomplete combustion (PICs).

A popular, standard method for measuring the heat of combustion of a fuel is the bomb calorimeter method, in which a powdered fuel sample is ignited and combusted in a sealed, near-adiabatic pressure vessel containing an atmosphere of oxygen in excess of the amount needed to completely convert the fuel sample. It is an effective and reliable method which usually releases all of the heat energy that can be obtained from the fuel, since conditions are such that it is highly likely that combustion is complete, as the test method assumes. Its effectiveness stems from the ability to test samples quickly and conveniently in a closed system, thus ensuring complete retention and recovery of all combustion products. It has been used extensively, and data on heat of combustion of many common fuels and materials is available in the literature [1-4]. Other fuel tests are included in the proximate and ultimate analysis of a fuel, for which standard ASTM test procedures are established [5].

Synthetic refuse-derived fuel was developed as part of the operation of a pilot-scale combustor at NJIT for research on the combustion of waste fuels. A baseline formula for waste fuel, given below, was decided upon using data from the USEPA [6] so as to be representative of municipal solid waste in the USA after some recycling. Series of tests were performed to characterize the fuel, including measurement of heat of combustion, proximate fuel analysis, and most of the tests from ultimate fuel analysis.

We present results of these tests on our synthetic waste fuel. Heat of combustion is determined by three methods: (1) Synthetic waste fuel sample tested in bomb calorimeter; (2) Components of synthetic waste fuel tested separately in bomb calorimeter, results then weighted by mass fraction and summed; and (3) Literature values for separate components of synthetic waste fuel weighted by mass fraction and summed. Bomb calorimeter tests for each material follow ASTM test method E711-87 (dry basis). Values for synthetic waste fuel heat of combustion determined by each method are compared. These results are compared with literature values given for the heat of combustion of refuse-derived fuels [1-4]. The literature values span a broad range because of the varied composition of waste fuel samples. This is due principally to the heterogeneous nature of real waste, quantities of inert species, which can be altered by the extent of recycling and waste fuel processing, and moisture content.

Data from proximate and ultimate fuel analysis of the synthetic waste fuel is also presented. This is compared with test data for separate fuel components and literature values, when available [2,6].

Composition and manufacture of synthetic waste fuel. From data made available by the USEPA [5], it was decided that a suitable composition for baseline synthetic waste in the USA, after some recycling, would be as shown in Table I. This contains a slightly higher component of plastic than is usual (14% vs. 9%), but the data show the amount of plastics in waste to have increased steadily over the last twenty years. It is also low in inert particulate (9% vs. approximately 25%). Both factors tend to increase the heat of combustion of the mixture.

Table I. Composition of baseline synthetic waste stream by mass.

Component	Mass %
Paper (newsprint)	35
Water	20
Wood (hardwood mulch)	17
Plastic (low density polyethylene)	14
Metal (iron)	8
Waste food (animal feed)	5
Inert (silica and alumina)	1

Components were sourced locally and selected for consistency over time, availability and cost of purchase.

The primary combustion chamber of the pilot-scale unit has volume 0.11 m^3 with a moving grate of dimensions 0.26m by 0.56m onto which solid synthetic waste fuel is fed at an adjustable rate in the range 8 to 13 kg/hr. It is important that the pilot-scale combustor operates in a steady state so as to simulate the operation of large-scale MWCs and generate meaningful emissions data. Similarly, the fuel residence and burnout times in the pilot-scale experiments are to be representative of conditions in real, large-scale units, which are of the order of 20 to 40 minutes and 20 minutes, respectively. Components of the synthetic waste fuel must therefore be size reduced to ensure a relatively homogeneous fuel mixture with near-constant chemical composition of fuel on the grate, and the mixture must be compacted to ensure adequate burnout time.

Components are weighed out separately and then mixed and size reduced in a small hammermill shredder to linear dimension of 1.2 cm or less. The mixture is then compacted into cylindrical pellets of 2.5cm diameter and average 5cm length in a commercial-grade pellet mill. The synthetic fuel pellets formed are similar in density (solid density about 710 kg/m^3) to pelleted refuse-derived fuels, and are generally similar in size and appearance.

Results and Discussion. Bomb calorimeter data for each test material was averaged over five runs. The test method (ASTM E711-87) stipulates that the sample material is powdered and its moisture content is brought into equilibrium with laboratory air before firing in the calorimeter. The heat of combustion found by the method is thus given on a 'dry basis', not an 'as fired' basis

which includes moisture content. Bomb calorimeter data is shown in Table II together with literature values.

Table II. Heat of combustion of synthetic waste fuel and separate components using ASTM test E711-87, together with literature values. All values are given on dry basis. Experimental data for synthetic waste fuel is averaged over samples from a single fuel batch.

Test Material	Heat of Combustion (cal/gm)	Literature Value (cal/gm)	Reference
Synthetic fuel pellets	4,565.02	See text	
Paper	4,487.79	4,714	Newsprint, [1].
Plastic	1,1918.28	1,1073	LD Polyethylene, [1]
Metal	1,841.09	1,580	[2]
Wood	4,630.77	4,700	[1]
Food	4,784.55	4,600	[1]
Inert	1,543.43	Unknown	

Data is given in [1] for heat of combustion of MSW sampled from a U.S. city in the early 1970s as ranging from 1,300 cal/gm to 4,200 cal/gm with average near 2,800 cal/gm.. Data in [6] from the Delaware Reclamation Project, gives heat of combustion of MSW after some recycling in the range 2,000 cal/gm to 4,200 cal/gm with average near 2,700 cal/gm. This data is given on an `as fired' (i.e., wet) basis, and much of the variation seems to be due to variation in moisture content between samples. If the dry basis figure for our synthetic fuel is adjusted for 20% moisture then an `as fired' value of 3,650 cal/gm is found. Literature values quoted in Table II are for materials whose description best fits that of separate components of the synthetic fuel, for example, iron aggregate of mean particle size 1 mm is used in synthetic fuel preparation, whereas the literature value is for iron filings. The animal feed used to simulate waste food in the synthetic fuel consists mostly of mixed cereal grains with some fat, whereas the nearest material for which literature data is available is dried vegetable waste. All of these materials, like newsprint, contain a high proportion of cellulose, so that their heats of combustion are close in value.

An estimated heat of combustion for the synthetic fuel can be calculated by multiplying experimentally determined values for each of the separate components by their mass fractions, then adding. This leads to a calculated value of 4428.43 cal/gm (dry basis). The difference between this and the experimentally determined value given in Table I is 3%, which is less than the estimated error in the calorimeter test method. The size reduction and compaction steps of fuel preparation therefore have negligible influence on heat of combustion.

Data in Table III gives results of other tests performed on the synthetic waste fuel together with available values from the literature. No literature value has been included for moisture content, which is highly variable. For example, the data in [1] as quoted above for heat of combustion gives a moisture content range from 10% to 66% by mass, whereas [6] gives an average of 32%. Much of the variation in the literature values for as fired heat of combustion values is probably due to variation in moisture content rather than effects due to heterogeneity and proportion of inert component in fuel.

Data for sulfur and chlorine content of separate synthetic waste fuel components will also be presented.

Table III. Test data for synthetic waste fuel and literature values. ASTM test number given in parentheses. Experimental data for synthetic waste fuel is averaged over samples taken from three separate fuel batches. Literature data of [6] is averaged.

Test Type	Mass %	Literature Value & Reference
Moisture (E949-88)	19.5	See text
Volatile matter (E897-88)	55.7	39.54, [6].
Ash (E830-87)	21.0	21.60, [6].
Sulfur (E775-87)	0.30	0.01 to 0.40, [1]; 0.23, [6].
Chlorine (E776-87)	0.57	0.13 to 0.95, [1].
Nitrogen (E778-87)	0.42	0.44, [6].

Conclusions:

The experimental values of heat of combustion for the synthetic waste are slightly higher than the range of values for MSW found in literature. Nevertheless it can be concluded that the synthetic fuel is indeed a representative formula for the MSW. There is good agreement between the two experimental values of heat of combustion for the synthetic RDF found out by burning the synthetic fuel directly and by burning its components separately.

References:

1. Thermodynamic Data for Waste Incineration. ASME, 1979. American Society of Mechanical Engineers, 345 East 47th St., New York, N.Y. 10017.
2. Combustion and Incineration Processes, Applications in Environmental Engineering. W.R. Niessen, 1978. Marcel Dekker, New York.
3. Handbook of Hazardous Waste Incineration. C.R. Brunner, 1989. TAB Books, Blue Ridge Summit, PA 17294.
4. Refuse-derived fuels: technology, processing, quality and combustion experiences. A.K. Gupta and E.M. Rohrbach. In, Proceedings of the Fifteenth National Waste Processing Conference, Detroit, 1992, p 49-59. American Society of Mechanical Engineers FACT Vol. 13, 1991.
5. Annual Book of ASTM Standards, 1996. Sections 5 and 11. American Society of Testing and Materials, 100 Barr Harbor Dr., West Conshohocken, PA 19428.
6. USEPA. Characterization of Municipal Solid Waste in the United States: 1986 update. EPA530-R-97-015.

Fast Chemical Reaction effect upon Diffusivity

Wm. T. Ashurst*, Habib N. Najm and Phillp H. Paul
Combustion Research Facility, Sandia National Laboratories
Livermore, CA 94551-0969

Introduction

During flame propagation into premixed fuel and air the flame structure depends upon the chemical reaction rates and the diffusion of the various species created in the breakup of the fuel molecule. Some of the species created in hydrocarbon flames have very fast reaction rates, so fast as to be limited by the gas kinetic collision rate [1]. For these species, what is the appropriate diffusivity to be used in solving the reacting flow equations for the flame structure? To study this issue we use molecular dynamics simulations of a fast passive reaction and determine the displacements of the reactive atoms. By comparison with the non-reacting species we can determine the effect of reaction upon the diffusivity.

Molecular Dynamics Model

The molecular dynamics (MD) simulations assume the Lennard-Jones (LJ) potential, $\phi = 4\epsilon[(\sigma/r)^{12} - (\sigma/r)^6]$, where σ is the atomic diameter, ϵ is the potential energy well depth, and the atomic mass is m. We consider only one species, and all quantities are expressed in terms of m, σ and ϵ; the time unit is $\tau = \sigma\sqrt{m/\epsilon}$. The reduced temperature and number density are $kT/\epsilon = 2.5$ and $n = N\sigma^3/V = 0.01$, where the number of atoms N is 500 and the volume is V; the discrete time step is 0.004τ. Using the LJ values of argon ($\epsilon/k = 120$K, $\sigma = 3.5 \times 10^{-8}$ cm and $m = 39.95$ amu/molecule), these conditions correspond to a temperature of 300K and a pressure of ten atmospheres. The atomic velocities are adjusted with a Gaussian constraint so that at each time step the thermal temperature is the desired value, we have a constant N,V,T system [2].

The model chemical reaction is a passive one and does not affect the atomic dynamics. After achieving equilibrium conditions each atom is marked as allowed to react if it undergoes a sufficiently energetic collision at some future time. We consider the irreversible bimolecular reaction $A + M \rightarrow 2B$, where M is either A or B, and to achieve this reaction we mark *all* the atoms as type A and let them react into type B. This is possible because we allow the reaction to occur without regard to the other atom type in the reacting collision. Thus, we may consider the reacting atom, type A, to be in a dilute condition. The diffusivity is obtained from the mean square displacement of the atoms $< r^2 >$, using the Einstein relation [3], $< r^2 >= 6Dt$, when $t \rightarrow \infty$. Each atomic displacement will be

* E-mail: ashurs@ca.sandia.gov

recorded during this time period, those of type A will determine the diffusivity D_A, that is, the reactive species diffusivity. Since the reaction is passive *all* atoms will contribute to the normal diffusivity, which we label as D_B. The MD code is structured to examine each possible pairwise interaction at each time step (a neighbor list is maintained to reduce the cost of this step). During the determination of the pairwise distance the potential energy of this atom pair is determined, and when this energy exceeds a threshold value, these particular atoms are considered to have reacted during that time step (if they are of type A). The calculations are performed within a periodic system. When an atom crosses a periodic boundary, its spatial origin for that time period is adjusted by adding or subtracting the periodic edge length. Thus, the atom may traverse through the periodic images of the system and its displacement is not restricted by the domain size [4]. When all the atoms have reacted, a few hundred more time steps are done, and then a new time origin is defined and the above process is repeated. A thousand realizations are obtained within a few hours on a workstation.

The threshold potential energy value is 0.01ϵ for the results presented below. The decay of the reactive atoms is well described by $n_A(t) = n_A(0)\exp(-zt)$, with a rate constant of $z = 0.105/\tau$. We compare this rate with the gas kinetic collision rate, the number of collisions per volume per time is $Z = 4n^2\sqrt{\pi kT/\epsilon}$, where n is the reduced number density. With $kT = 2.5\epsilon$, the collision rate is $Z = 11.2n^2$. Thus, $Z/n = 0.112/\tau$, using $n = 0.01$, and the numerical constant compares favorably with the decay rate found above. Therefore, within these simulations the chemical reaction rate is close to the gas kinetic collision rate.

With this threshold value of 0.01ϵ, an atom may undergo a collision with another atom and not react if the separation distance remains beyond σ. Thus, reactive atoms may acquire negative potential energy and be subjected to attractive forces during a collision without reacting. Examination of those atoms which react last in a particular realization indicates a series of collisions with only negative potential energy. These mild collisions will alter the atom trajectory only slightly from its original path, as opposed to the changes caused by collisions with strong repulsive forces. Hence, we expect the long-surviving A-atoms to acquire a large displacement during their lifetime because any collision which reverses their course will also cause them to react. A large mean square displacement of the reactive atoms implies a larger diffusivity – the Einstein relation is $< r^2 >= 6Dt$. The question here is, given the lifetime of the reactive atoms, what is their appropriate diffusivity?

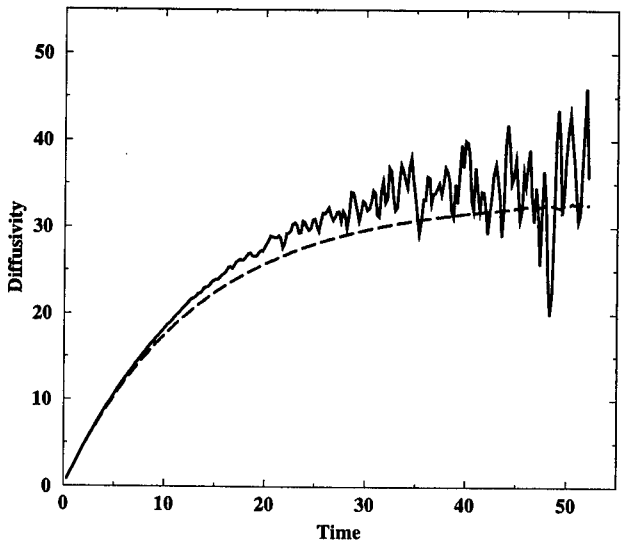


Figure 1. Diffusivity of reacting D_A (bold line) and non-reacting D_B (dashed line) species, defined from the slope of the mean square displacement.

Diffusivity Results

The mean square displacement is determined at intervals of ten time steps, these values are then further averaged into groups of five to yield estimates spaced at $50\delta t(= 0.2\sigma\sqrt{m/\epsilon})$. In the long-time limit, the mean square displacement is $< r^2 >= 6Dt$, and thus a time derivative of $< r^2 > /6$ will approach a constant value of D as time increases. In Figure 1, the diffusivity of the non-reacting species, D_B is just approaching a constant value by the time 99% of the reacting species have reacted. During the time interval of 20 to 50, the reactive diffusivity D_A shows an increasing scatter while it is also approaching a constant value. The increasing scatter is due to the few atoms that contribute to this portion of the time record, the reacted amount changes from 90% to 99% over the time interval of 21 to 44. There are 3,000 realizations at time zero, but only 78 realizations are left at the ending time shown in Figure 1. Figure 2 presents a diffusivity ratio, D_A/D_B versus the amount reacted, the enhancement due to reaction remains small and most of the reaction occurs before the time period when the diffusivity has reached its macroscopic value.

While there is an enhancement of D_A over D_B, it is important to note that, during the reactive lifetime, both diffusivities are smaller than the continuum value. Therefore, the temporal dependence of diffusivity observed in Fig. 1 may be used to formulate an effective diffusivity for reacting species. A highly reactive species can have a lifetime that is

small relative to the time necessary to reach the constant D limit. Under these conditions, its diffusion rate could be related to an effective diffusivity based on MD data and the species lifetime. As such, this effective diffusion coefficient is expected to vary directly with lifetime, as in Fig. 1, or inversely with reaction rate. Thus, use of a continuum diffusivity when reaction rates are very fast, implies that the estimated displacement will be too large.

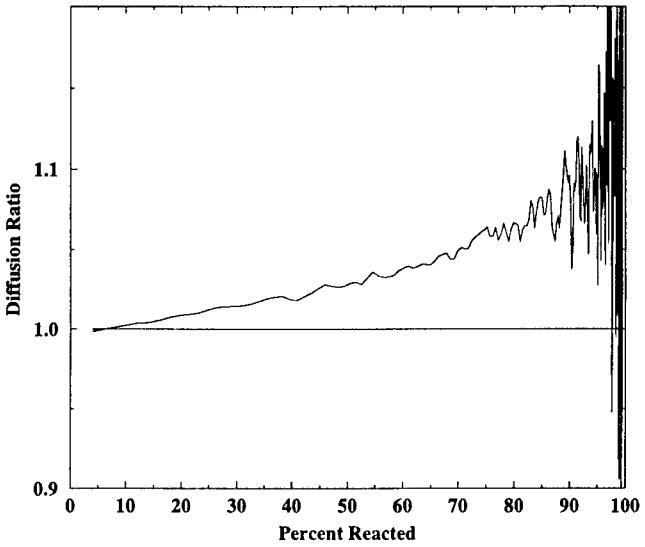


Figure 2. Diffusivity ratio of reacting to the non-reacting species D_A/D_B, from Figure 1, as a function of the amount of reaction.

Acknowledgments

This work was supported by the United States Department of Energy through the Office of Basic Energy Sciences, Division of Chemical Sciences.

References

1. Paul, P. and Warnatz, J., *Twenty-Seventh Symposium (International) on Combustion, The Combustion Institute*, Pittsburgh, PA, 1998, pp. 495-504.
2. Hoover, W. G., *Computational Statistical Mechanics*, Elsevier, Amsterdam, 1991.
3. Hansen, J.-P. and McDonald, I. R., *Theory of Simple Liquids*, Academic Press, London, 2nd edition, 1986.
4. Wang, H., Molecular Dynamics Study of Radical Diffusion Coefficients, *Joint Technical Meeting of the US Sections of the Combustion Institute*, Washington, DC, March 15-17, 1999, pp. 413-416.

Reaction of Unimolecular Dissociation of Formyl Radical, HCO —> H + CO, Studied Over 1 – 100 bar Buffer Gas Pressure Range

Lev N. Krasnoperov, Evgeni N. Chesnokov

Department of Chemical Engineering, Chemistry and Environmental Science
New Jersey Institute of Technology, University Heights, Newark, NJ 07102
krasnoperov@admin.njit.edu

Introduction

Unimolecular dissociation of formyl radical (HCO) is of significant importance in the hydrocarbon combustion mechanisms [1,2]:

$$HCO \longrightarrow H + CO \qquad (1)$$

Formyl radical is produced in reactions of H-atom abstraction from formaldehyde. Formaldehyde is produced in the reaction of methyl radicals with atomic oxygen. Unimolecular decomposition of formyl radical (reaction 1) leads to the chain branching *via* interaction of hydrogen atoms produced in this reaction with molecular oxygen. Competition of unimolecular dissociation of formyl radical (reaction 1) with termination in reactions with O_2, OH and H effects the chain branching rate, and, therefore, a number of important characteristics of combustion (such as the autoignition thresholds, the flame propagation speed, *etc.*) [1,2].

Unimolecular dissociation of formyl radical received significant attention in recent years also due to its "non-classical RRKM" behavior and significant role of tunneling. The radical has relatively weak C-H bond (bond energy is 63.2 kJ mol^{-1} [3]) and large vibrational frequencies. Due to these reasons, formyl radical has isolated resonances at energies above the dissociation threshold. These resonances have been extensively studied both using spectroscopic techniques and theoretically.

Isolated resonances have significant impact on the kinetics of reaction 1, particularly on the pressure fall-off curve [4]. Due to the isolated resonances the high-pressure rate constant for the reverse reaction (H + CO addition) is about 2.5 orders of magnitude lower than one which would be expected for a "regular" RRKM behavior. Due to the long lifetime of the resonances (compared to the lifetime of a collision complex which obeys classical RRKM behavior) the characteristic transition pressure is also lowered from about 3000 bar to *ca.* 10 bar (at ambient temperature) [4]. The theoretically predicted transition region lies within the experimentally accessible pressure range (1 - 100 bar).

Despite of the importance of this reaction in combustion mechanisms, there was only one direct study of reaction 1 under conditions of thermal activation [5]. The buffer gas pressure in this study was less than 10 Torr. At these pressures reaction 1 is well in the low-pressure region at the temperatures used in this study, therefore no information on the transition region and the high-pressure limit rate constant could be directly derived from the experimental data.

In the current work, reaction 1 was directly studied over an extended buffer gas pressure range (1 – 100 bar). The results of the current measurements are in discrepancy of factor *ca.* 2-3 with the previous data. Pressure dependence of the rate constant of reaction 1 was observed.

Experimental

Reaction 1 was studied using excimer laser photolysis coupled to UV transient absorption spectroscopy and a high-pressure flow system. The buffer gas (He) pressure range 1 – 100 bar and the

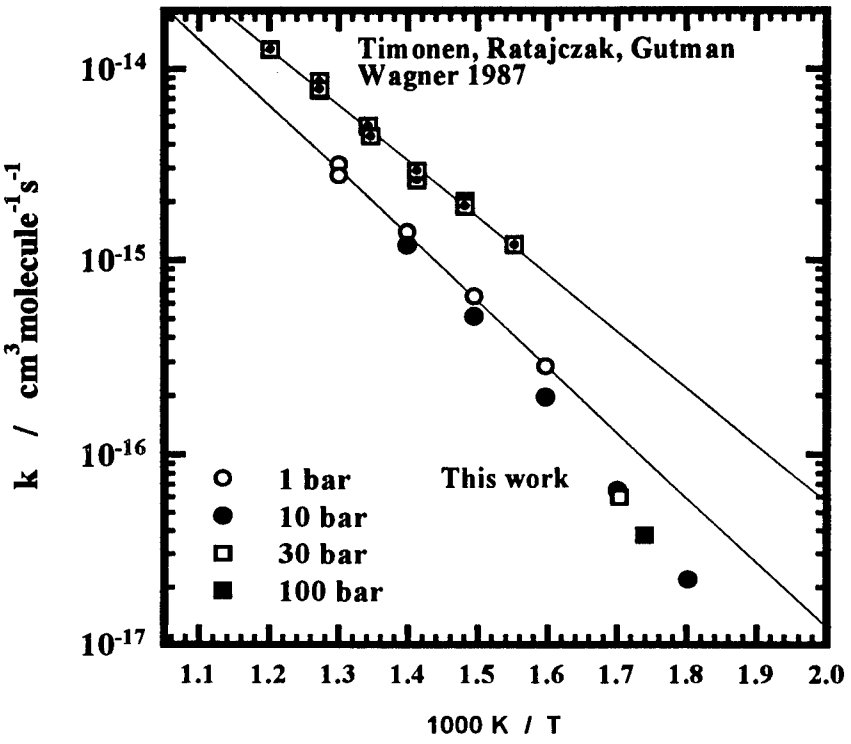


Fig. 1. Second Order Rate Constant of Reaction 1. Squares – Ref. 5.

temperature range 282-442 K were employed. A heatable high-pressure flow reactor of new design is described. Formyl radicals were prepared by pulsed photolysis of acetaldehyde at 308 nm (XeCl excimer laser):

$$CH_3CHO + h\nu(308\ nm) \longrightarrow CH_3 + HCO \qquad (2)$$

Kinetics of formyl radical decay was monitored by absorption in VU (216-230 nm). Several experiments were performed using absorption of HCO in visible region ("red" transition of HCO radical). Low initial absorptions were employed (in the range 0.02% – 0.36%), to minimize interference from secondary reactions. The pressure and temperature ranges correspond to the lifetime range of formyl radical 8 – 900 μsec.

Results

Transient absorption profiles were measured at sixteen combinations of temperature and pressure. At each temperature and pressure, the laser energy was varied to establish the role of radical-radical processes. A number of checks was performed to verify possible interference of radical reactions with the precursor molecule. Several experiments were done using red transition of the radical as well as

a different precursor molecule (C_2H_5CHO). The results are shown in Fig. 1 together with the previous measurements. The solid line is linear regression drawn through the points taken at 1 bar pressure. A preliminary expression for the second order rate constant obtained from the data at 1 bar is:

$$k_1(He) = 7.69x10^{-11}exp(-65040 \text{ Joule mol}^{-1}/RT) \text{ cm}^3\text{molecule}^{-1}\text{sec}^{-1} \quad (3)$$

The dissociation rate constants measured in this work are systematically and consistently lower than those reported in the only previous direct work [5]. The difference is factor of 2.2 at the highest temperature of the experiments and factor of 3.5 at the low end. This is a significant discrepancy of potential importance in the combustion modeling, as well as in the theoretical treatment of reaction 1.

We performed a number of checks and experiments with the purpose to find a flaw/error in our experiments. In particular, experiments with photolysis of acetaldehyde at 193 nm were designed to evaluate the role of the secondary reaction of methyl radicals and hydrogen atoms with the precursor molecule. This is the only possible interference which can lead to lower measured rate constants. The major route of acetaldehyde photodissociation at 193 nm leads to production of methyl radical and hydrogen atom:

$$CH_3CHO + h\nu(193 \text{ nm}) \longrightarrow CH_3 + H + CO \quad (4)$$

Experiments with photodissociation of acetaldehyde at 193 nm with recording of transient absorption profiles of HCO and CH_3 radicals allowed to establish an upper limit on the contribution of the reactions of H-atoms and CH_3 radicals with acetaldehyde and to rule out this source of the discrepancy. All other possible sources of errors can lead only to an increase of the apparent decay rate.

In the experiments, we found the second order rate constant to be pressure dependent, the effect which is more pronounced at low temperatures. This is due to the pressure fall-off, theoretically predicted based on the theory of isolated resonances [4]. As it was mentioned before, no pressure fall-off is expected for reaction 1 over the pressure range of the study based on the classical RRKM theory.

Acknowledgment

This work was supported by the Petroleum Research Fund administered by the American Chemical Society (Grant # 31640-AC6).

References

1. Miller, J.A., Kee, R.J., and Westbrook, C. K. *Ann. Rev. Phys. Chem.* 41: 345-387 (1990).
2. Warnatz, J. *In: Combustion Chemistry.* Springer-Verlag, New York, 1984, p. 197.
3. Becerra, R., Carpenter, I.W., and Walsh, R. *J. Phys. Chem. A*, 101: 4185 - 4190 (1997).
4. Wagner, A.F., and Bowman, J.M. *J. Phys. Chem.* 91: 5314-5324 (1987).
5. Timonen, R.S., Ratajczak, E., Gutman, D., and Wagner, A.F. *J. Phys. Chem.* 91: 5325-5332 (1987).

KINETIC AND MECHANISTIC STUDIES OF THE REACTION OF HYDROXYL RADICALS WITH TRICHLOROETHYLENE

LeAnn B. Tichenor, Abdulaziz El-Sinawi, Takahiro Yamada and Philip H. Taylor*
Environmental Science and Engineering, University of Dayton Research Institute
300 College Park, Dayton, OH 43469-0132 U.S.A., *taylorp@udri.udayton.edu

Jingping Peng, Xiaohua Hu and Paul Marshall
Dept. of Chemistry
University of North Texas
P. O. Box 305070, Denton, TX 76203-5070 U.S.A.

INTRODUCTION

Past and present manufacturing and disposal practices have resulted in the release of trichloroethylene into the atmosphere at significant rates. The amount of this highly volatile compound emitted in the U.S. alone has been estimated to be ~2.5x 10^5 metric tons annually.[1] Knowledge of reactions facilitating the breakdown of this compound is necessary to both predict the natural decomposition that is occurring in the atmosphere and determine appropriate disposal practices.

The dominant atmospheric loss reaction is expected to be the reaction with OH radicals since chloroethenes do not absorb radiation at wavelengths > 300 nm, nor do they react significantly with O_3 or NO_3 in the gas phase.[2] Rate constants at low temperatures (220 K to 430 K) have been reported previously, and the work reported here validates those rate expressions.[3-6] High temperature incineration is considered to be the best available technology for the safe disposal of these toxic compounds. The fastest process contributing to the destruction of halogenated hydrocarbons is the reaction with OH radicals.[7,8] Given the importance of high-temperature reaction of the OH radical with chloroethenes both in natural and planned decomposition, knowledge of the reaction rate constants and reaction mechanisms over an extended temperature range is essential to predict the true nature of the breakdown of these compounds.

EXPERIMENTAL APPROACH AND DATA REDUCTION

The experimental procedures were similar to those used in previous studies of the reaction of OH radicals with halogenated hydrocarbons.[9,10] The method used to generate the precursor for the hydroxyl radical varied from previous experimentation. Initial testing of C_2HCl_3 was performed using 193 nm photolysis of N_2O/H_2O as the OH source, as had been done previously. The resulting room-temperature rate measurements exceeded previously reported values by a factor of two.[3-6] Because of the large absorption cross-section of C_2HCl_3 (~5 x 10^{-18} cm^2/molecule),[11] additional measurements were conducted at low excimer laser fluences (<1 mJ cm^{-2}), with no observed reduction in rate coefficients. These results made operation at 193 nm unacceptable and necessitated the use of a different OH generation method. To minimize substrate photolysis, HONO was used as a hydroxyl radical source, which dissociated to NO and OH when exposed to near-UV radiation of 351 nm. A XeF excimer laser (Lamba Physik Compex Model 102) was used as the photodissociation source. Initial $[OH]_0$ ranged from ~2 – 4 x 10^{11} molecules cm^{-3}, and was determined based on the measured excimer fluence (9-18 mJ cm^{-2}), the published value of the absorption cross-section for HONO, 2.12 x 10^{-19} cm^2/molecule at 351 nm,[12] a quantum yield of 1.0,[13] and measured values of $[NO_2^-]$ taken to represent [HONO] determined using ion chromatography (~5 x 10^{13} molecules cm^{-3}).

Initial C_2HCl_3 concentrations ranged from ~3 x 10^{13} to ~6 x 10^{14} molecules cm^{-3}. All experiments were conducted at a total pressure of 740 ± 10 Torr. Samples of C_2HCl_3 were obtained from Aldrich with 99.9% purity. Gas chromatography-mass spectrometry (GC/MS) analyses indicated that this purity was met or exceeded.

The rate of disappearance of the OH may be presented as:

$$-d[OH]/dt = k[A_o][OH] + k_d[OH]$$

where: k = bimolecular rate constant,

$A_o = C_2HCl_3$ concentration,

k_d = first-order rate for the reaction of OH with impurities; considers diffusion out of the reaction volume.

This relationship holds in the absence of any secondary reactions that may form or deplete OH. Solution of this equation yields $[OH] = [OH]_o \exp(-k't)$, where $k' = k + k_d$. For all experiments, reactive and diffusive OH radical decay profiles exhibited exponential behavior and were fitted by the following nonlinear expression:

$$[OH] = [OH]_o \exp(-k' t) + \gamma$$

where γ is the constant background signal level and t is the time delay between the two lasers. Because the C_2HCl_3 concentration was much greater than the [OH], pseudo first-order exponential OH decays were observed and the individual temperature dependent rate constants were determined by $k' = k [C_2HCl_3] + k_d$, where the bimolecular rate constant, k, is the slope of the least squares fit of k' versus the $[C_2HCl_3]$. OH decays were observed over two to three decay lifetimes over a time interval of 0.1 to 20.0 ms.

RESULTS AND DISCUSSION

Absolute rate coefficients for k_1 are presented in Table 1. Random error limits ($\pm 2\sigma$) were well below 20% in most cases.

Table 1: Absolute Rate Coefficients for k_1[a]

Temp (K)	$10^{12}k_1$ (cm^3 $molecule^{-1}$ s^{-1})	Temp (K)	$10^{12}k_1$ (cm^3 $molecule^{-1}$ s^{-1})
291	1.81±0.26	500	1.37±0.32
292	1.49±0.18	500	1.62±0.50[b]
292	1.61±0.40[b]	502	1.37±0.32
293	1.70±0.28	505	1.23±0.18
294	1.55±0.22	508	1.37±0.32
326	1.56±0.14	562	1.22±0.20
330	1.50±0.18	621	1.40±0.22
356	1.44±0.22	650	1.28±0.34
410	1.40±0.20	699	1.35±0.30[b]
417	1.41±0.22	709	1.67±0.12
422	1.38±0.32	719	1.64±0.26
467	1.40±0.10		

[a] Errors represent $\pm 2\sigma$ and do not include the 5-10% uncertainty estimated for possible systematic errors.
[b] C_2DCl_3.

When identifying possible side reactions, two reactions of concern are hydroxyl and/or a C_2HCl_3 reaction with excess HCl and H_2O. These two compounds were present in the system as carryovers from the HONO reactor. These and other possible side reactions were simulated numerically using reaction rate constants published in the NIST Chemical Kinetics Database.[14] The results of this analysis indicated that side reactions would not impact significantly on the reaction under observation with the input concentrations used. In the absence of reactant impurities, sources of systematic error were then limited to thermally-induced secondary reactions. The possibility of thermally-induced side products was investigated by varying the total gas flow rate. k_1 was found to be independent of the residence time in the mid to high-temperature regions, implying a lack of thermal reaction of the substrates in this zone. Above 720 K, an excess of OH radical generation in the absence of the photolytic laser pulse was observed, and OH decays were not measurable.

All known experimental measurements for k_1 are summarized in Figure 1. This work extends experimental measurement beyond the limit of ~430 K reported previously. A variety of techniques were used in collecting these data. Examination of Figure 1 shows agreement at room temperature, within combined experimental uncertainties, between our work and that reported previously.[3-6] (Data collected

using the relative rate method has not been included in our comparison.) A three-parameter Arrhenius fit yielded $k_1(T) = (8.97\pm0.42) \times 10^{-19} T^{2.0} \exp(901.3\pm19.2)/T$, where k is in units of cm^3 $molecule^{-1}s^{-1}$.

The complex temperature dependence of the data is qualitatively consistent with variational transition state theory (VTST) calculations of the entrance channel for the addition of OH to the H substituted side of the double bond of the substrate, which is based on PMP4/6-311+G(d,p) energies, the dominant site for addition.[6] These calculations exhibit a negative temperature dependence at low temperatures followed by a transition to a positive temperature dependence above ~500 K. The calculated transition state is below the total energy of the reactants and is responsible for the negative temperature dependence at low temperatures. The transition to a positive temperature dependence at higher temperatures is due to the increasing importance of the partition function that characterizes the transition state relative to the reactants. Rate coefficient measurements with C_2DCl_3 at 292, 500, and 699 K did not exhibit a measurable isotope effect, indicating the absence of H atom abstraction reactions.

In addition to empirically predicting the reaction rate expression for the reaction of C_2HCl_3 with the hydroxyl radical, the reaction pathways and kinetics were analyzed using thermodynamic properties. The potential energy diagram for these intermediate states and subsequent products is shown in Figures 2 for OH radical attack at the α (CHCl) site of the substrate. The potential energy surface was evaluated using group additivity (GA) method and semi-empirical molecular orbital (MO) method PM3.[15] The THERM computer code[16] was used to perform GA calculation and MOPAC computer code[17] was used to perform PM3. The energy level of reactants was obtained from literature[18,19] and those of intermediate radicals and products were obtained using THERM. All of activation energies, E_as, except entrance channel were estimated by taking a difference between enthalpies of formation ($H_f°_{298}$) of reactant and its transition state (TS) determined by PM3 calculation.

ACKNOWLEDGEMENTS

The authors acknowledge support from the Environmental Protection Agency (Grant R82-6169).

REFERENCES

1. Thomas, R., Byrne, M., Gilbert, D., Goyer, M. and Moss, K. (1981) An Exposure and Risk Assessment for Trichloroethylene, EPA-440/4-85-019.
2. Atkinson, R., Aschmann, S. M. and Goodman, M. A. (1987) *Int. J. Chem. Kinet.*, **19**, 299.
3. Howard, C. J. (1976) *J. Chem. Phys.*, **65**, 4771.
4. Davis, D., Machado, U., Smith G., Wagner, S. and Watson, R. T., unpublished data (1977) cited in Watson, R. T. *J. Phys. Chem. Ref. Data* **6**, 871 and references 3, 7, and 24.
5. Chang, J. S. and Kaufman, F. (1977) *J. Chem. Phys.*, **66**, 4989.
6. Kirchner, K., Helf, D., Ott, P. and Vogt, S. (1990) *Ber. Bunsenges. Phys. Chem.*, **94**, 77.
7. Fairchild, P. W., Smith, G. P. and Crosley, D. R. (1982) *Nineteenth Symp. (Int.) on Combustion*, The Combustion Institute, p.107.
8. Warnatz, J., Bockhorn, H., Moser, A. and Wenz, H.W. (1982) *Nineteenth Symp. (Int.) on Combustion*, The Combustion Institute, p. 197.
9. Fang, T. D., Taylor, P. H., Dellinger, B., Ehlers, C. J. and Berry, R. J. (1997) *J. Phys. Chem.*, **101**, 5758.
10. Fang, T. D., Taylor, P. H. and Berry, R. J. (1999) *J. Phys. Chem. A*, **103**, 2700.
11. Zabel, F. (1974) *Ber. Bunsenges. Phys. Chem.*, **78**, 232.
12. Demore, W. B., Goldent, D. M., Hampson, R. F., Kurylo, M. J., Howard, C. J., Ravishankara, A. R., Kolb, C. E. and Molina, M. J. (1997). Chemical Kinetics and Photochemical Data for Use in Stratospheric Modeling, #12, National Aeronautics and Space Administration.
13. Cox, R. A. (1974) *Journal of Photochemistry*, **3**, 175.
14. Mallard, W. G. (1998) NIST Chemical Kinetics Database 2Q98, NIST Standard Reference Database 17, U. S. Department of Commerce, Gaithersburg, MD.
15. Stewart, J. J. P. (1989) *J. Comput. Chem.* **10**, 209.
16. Ritter, E. R. and Bozzelli, J. W. (1991) *J. Chem. Info. Comput. Sci.* **31**, 400.
17. Frank J. Seiler Research Lab. (1983) *MOPAC: A General Molecular Orbital Package.*

18. Stull, D. R. and Prohet, H. (1971) *JANAF Thermochemical Tables* 2nd ed., U. S. Department of Commerce, Gaithersburg, MD.
19. Stull, D. R., Westrum, J. E. F. and Sinke, G. (1987) *The Chemical Thermodynamics of Organic Compounds* Stull, D. R., Westrum, J. E. F. and Sinke, G. (1987) John Wiley & Sons, New York.

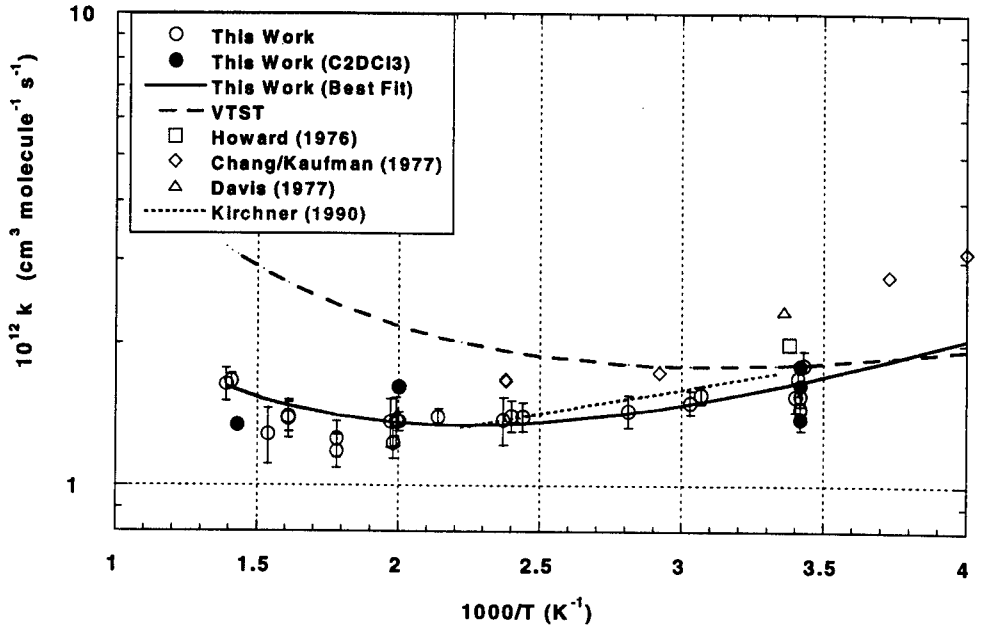


Figure 1. Arrhenius plot of kinetic data for k_1. Also shown are the results of previous studies, a modified Arrhenius three-parameter expression, and the results of variational transition state theory calculations. (P=740±10 Torr)

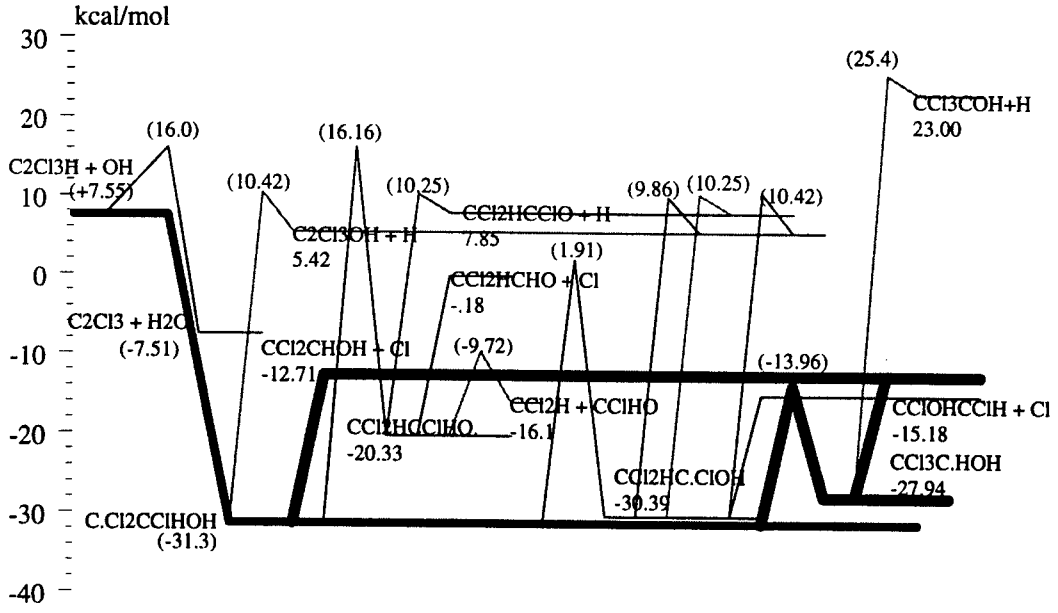


Figure 2. Potential energy diagrams for the OH addition to C_2HCl_3 (α-site). Adduct stabilization, isomerization, H- and Cl-atom elimination channels are shown. Surface was evaluated using GA for the intermediate radicals and products and PM3 for E_a estimation.

Kinetics of Radical-Radical Reactions: $C_2H_5 + C_2H_5$, $C_2H_5 + CH_3$, and $C_3H_5 + CH_3$.

Vadim D. Knyazev,[*,a,b] Eugene Shafir,[a] Irene R. Slagle[*,a]

[a] Department of Chemistry, The Catholic University of America, Washington, DC 20064
[b] National Institute of Standards and Technology, Division of Chemical and Physical Properties, Gaithersburg, MD 20899-8380
e-mail: knyazev@cua.edu

Radical-radical recombination and disproportionation reactions constitute an integral part of the overall mechanism of oxidation and pyrolysis of hydrocarbons. These reactions serve as chain termination processes in the combustion environment and lead to molecular weight growth. Directly obtained rate constant data on these types of reactions are sparse as such systems are difficult to study experimentally due to the high reactivity of the chemical species involved.

In the current work, we report on the direct experimental determination of the rate constants of three alkyl radical-radical reactions:

$$C_2H_5 + C_2H_5 \rightarrow \text{products} \quad (1)$$
$$C_2H_5 + CH_3 \rightarrow \text{products} \quad (2)$$
$$C_3H_5 + CH_3 \rightarrow \text{products} \quad (3)$$

Rate constants for reaction 1 were measured at two densities of He ([He] = 3×10^{16} and 12×10^{16} atoms cm^{-3}) in the temperature range 298 - 400 K. Rate constants for reactions 2 and 3 were measured at [He] = 12×10^{16} atoms cm^{-3} and T = 298 - 700 K.

Experimental method and results.

1. $C_2H_5 + C_2H_5$ reaction.

The method of photolytic production of ethyl radicals was based on the approach used by Krasnoperov et al. for their experimental kinetic study of SiH_3 radical recombination.[1] C_2H_5 radicals were produced by the reaction of Cl atoms with C_2H_6. Chlorine atoms were formed by 193-nm laser photolysis of oxalyl chloride[2] and subsequent thermal decomposition of ClCO radical[3]

$$ClC(O)C(O)Cl \xrightarrow{193\ nm} 2Cl + 2CO \quad (82\%)^{2} \quad (4a)$$
$$\rightarrow Cl + CO + ClCO \quad (18\%)^{2} \quad (4b)$$
$$ClCO \rightarrow Cl + CO \quad (5)$$

Thermal decomposition of ClCO, reaction 5, has a high rate constant ($k_5 \geq 600$ s^{-1}) even at room temperature and [He] = 3×10^{16} atoms cm^{-3}.[3] Thus, photolysis of oxalyl chloride provides a "clean" photolytic source of Cl atoms (in the sense that no other reactive species are formed in the photolysis process in any appreciable amounts).[1] Cl atoms formed in reactions 4 and 5 were immediately converted into C_2H_5 radicals by reaction with C_2H_6:

$$Cl + C_2H_6 \rightarrow C_2H_5 + HCl \qquad (6)$$

Ethane concentrations were in large excess over those of chlorine atoms ([C_2H_6] = (1-100) $\times10^{14}$ molecules cm^{-3}, $[Cl]_0 = (2\text{-}12)\times10^{12}$ atoms cm^{-3}) and sufficient to ensure the complete conversion of Cl atoms to ethyl radicals.

Ethyl radical decay was subsequently monitored in time-resolved experiments using photoionization mass spectrometry. Details of the experimental apparatus[4] used have been described before.

Important processes of C_2H_5 radical decay were those of self-reaction (reaction 1) and heterogeneous wall loss

$$C_2H_5 \rightarrow \text{heterogeneous loss} \qquad (7)$$

Kinetics of C_2H_5 decay (Figure 1) was fitted with an analytical expression derived from kinetic equations 1 and 7 to obtain the values of k_1 and k_7. Since different parts of the [C_2H_5] vs. time dependence have very different sensitivities to the rates of reactions 1 and 7, both k_1 and k_7 could be determined from the fitting.

The results of experiments performed at T = 300 K and 400 K and [He] = 3×10^{16} and 12×10^{16} atoms cm^{-3} yield the value of $k_1 = (2.9 \pm 0.6)\times10^{-11}$ molecule^{-1} s^{-1} cm^3, independent of temperature and bath gas density within the experimental range. C_4H_{10} and C_2H_4 were observed as primary products of reaction 1.

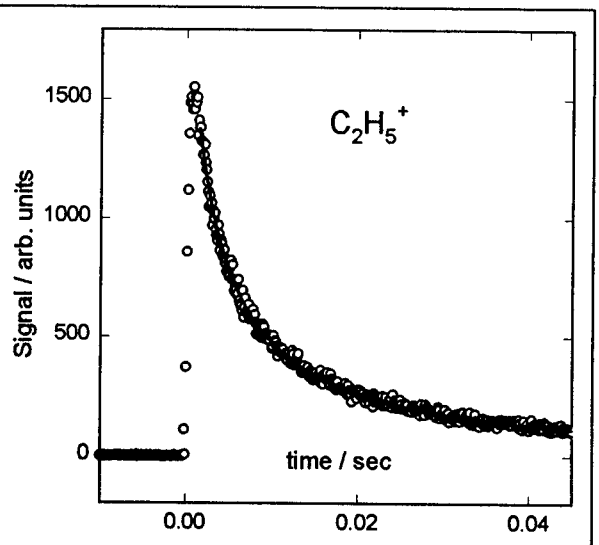


Figure 1. Kinetics of the C_2H_5 signal decay. T = 300 K, [He]= 12×10^{16} atoms cm^{-3}, $[C_2H_5]_0 = [Cl]_0 = 5.53\times10^{12}$ molecules cm^{-3}, [C_2H_6] = 1.1×10^{14} molecules cm^{-3}.

2. $C_2H_5 + CH_3$ and $C_3H_5 + CH_3$ reactions.

The $C_2H_5 + CH_3$ and $C_3H_5 + CH_3$ rate constant measurements were performed using a technique similar to that applied by Niiranen and Gutman to the studies of the $SiH_3 + CH_3$ and $Si(CH_3)_3 + CH_3$ kinetics.[5] 193-nm photolysis of acetone

$$CH_3C(O)CH_3 \xrightarrow{193\ nm} 2\ CH_3 + CO \qquad (8)$$

was used to produce methyl radicals. Under the experimental conditions used in the current work, reaction 8 accounts for more than 95 % of acetone photolysis.[6] Either C_3H_5 (allyl) or C_2H_5 radicals were formed simultaneously with the production of CH_3 radicals by the 193-nm photolysis of allyl bromide or diethyl ketone, respectively. Experimental conditions (in particular, radical precursor concentrations) were selected to create a large excess of initial concentrations of methyl radicals over the total combined concentration of all the remaining radicals formed in the system. The initial concentrations of methyl radicals (determined quantitatively by measuring the photolytic depletion of acetone) were typically 20-80 times higher than those of C_3H_5 or C_2H_5. Under these conditions, the recombination of methyl radicals

$$CH_3 + CH_3 \rightarrow C_2H_6 \qquad (9)$$

was essentially unperturbed by the presence of the other radicals. At the same time the kinetics of C_3H_5 (or C_2H_5) was completely determined by the reaction with CH_3 and practically unaffected by the self-recombination reaction and by reactions with other active species (such as Br atom) formed in the system. Heterogeneous loss was the only additional sink of methyl and allyl (or ethyl) radicals that had to be taken into account. Typical temporal radical signal profiles are presented in Figures 2 and 3.

For this mechanism consisting of reactions 9 and 2 (or 3) and radical wall loss processes and for the initial conditions described above, the system of corresponding differential equations can be solved analytically. This analytical solution was used to fit experimental signal profiles in order to obtain the rate constants of interest, k_2, k_3, and k_9. The essential feature of this method is that the exact knowledge of the initial concentration of allyl (or ethyl) radicals is not required for the determination of the rate constants. In this respect, the approach described is similar to the pseudo-first-order method frequently applied to studies of kinetics of second order reactions.

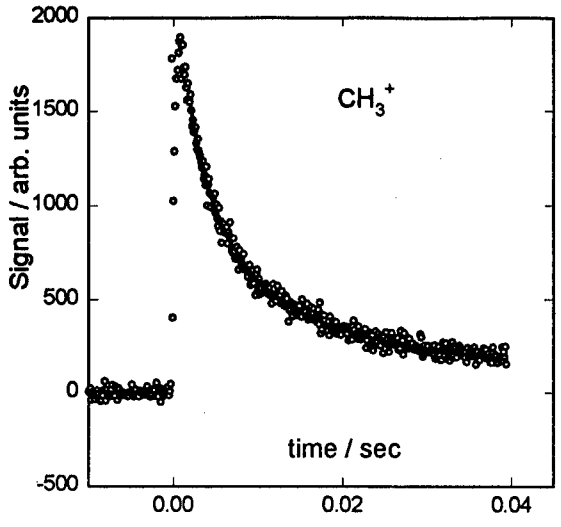


Figure 2. Kinetics of the CH_3 signal decay. T = 300 K, [He]= 12×10^{16} atoms cm^{-3}, $[CH_3]_0 = 3.62\times10^{12}$ molecules cm^{-3}, $[C_2H_5]_0 = 6.4\times10^{10}$ molecules cm^{-3}.

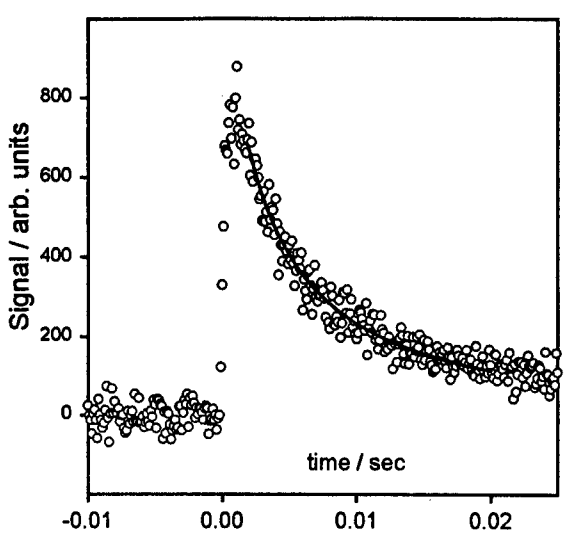


Figure 3. Kinetics of the C_2H_5 signal decay. Experimental conditions are those of Figure 2.

Rate constants of both reactions 2 and 3 exhibited negative temperature dependencies that could be fitted with Arrhenius expressions:

$$k_2 = 4.4\times10^{-11} \exp(243\ K/T)\ molecule^{-1}\ s^{-1}\ cm^3$$

$$k_3 = 4.2\times10^{-11} \exp(225\ K/T)\ molecule^{-1}\ s^{-1}\ cm^3$$

Acknowledgment

This research was supported by the Division of Chemical Sciences, Office of Basic Energy Sciences, Office of Energy Research, U.S. Department of Energy under Grant No. DE-FG02-94ER1446.

References.

1. Baklanov, A. V.; Krasnoperov, L. N. *Manuscript in preparation. Preliminary report has been presented at the 15th International Symposium on Gas Kinetics in Bilbao, Spain, 1998.*
2. Hemmi, N.; Suits, A. G. *J. Phys. Chem. A,* **1997**, *101*, 6633.
3. Nicovich, J. M.; Kreutter, K. D.; Wine, P. H. *J. Chem. Phys.*, **1990**, *92*, 3539.
4. Slagle, I. R.; Gutman, D. *J. Am. Chem. Soc.* **1985**, *107*, 5342.
5. Niiranen J. T.; Gutman, D. *J. Phys. Chem.* **1993**, *97*, 9392.
6. Lightfoot, P. D.; Kirwan, S. P.; Pilling M. J. *J. Phys. Chem.* **1988**, *92*, 4938.

The Reaction of C_6H_5 with CO: Kinetic Measurement and Theoretical Correlation with the Reverse Process

Gi-Jung Nam, Wensheng Xia, J. Park and M. C. Lin
Department of Chemistry, Emory University, Atlanta, GA 30322

I. Introduction

Phenyl radicals play a pivotal role in the combustion of gasoline in which small aromatic hydrocarbons (benzene, toluene and xylenes) are added (up to 30%) as anti-knock agents.[1] The C_6H_5 radical is also believed to be involved in the formation of polycyclic aromatic hydrocarbons (PAH's) which are precursors of soot.[2-4]

Phenyl radicals and carbon monoxide co-exist under sooting conditions; their interaction may affect the concentration of C_6H_5 and thus the chemistry of soot formation. The kinetics of the $C_6H_5 + CO \rightarrow C_6H_5CO$ (1) reaction is unknown, although the rate constant for the reverse process, the decomposition of the benzoyl radical, has been reported by Solly and Benson[5] more than 30 years ago. In their study with the I_2-catalyzed decomposition of benzaldehyde, in a narrow temperature range of 614-667 K, the first-order (high pressure) rate constant,[5] $k_{-1}^{\infty} = 4 \times 10^{14} \exp(-14800/T)\ s^{-1}$, was evaluated by extrapolating the rate coefficients obtained in the fall-off region using assumed transition-state structure and vibrational frequencies by both RRK and RRKM theories.[6] Their result was found to be consistent with the heat of the dissociation reaction at 298 K, $\Delta H_1^{\circ} = 26 \pm 2$ kcal/mol, with a 3 kcal/mol C_6H_5-CO addition barrier.[5] To our knowledge, no other kinetic data exist for the reaction in either direction since this early study.

In the present investigation, we apply the technique of cavity ringdown spectroscopy (CRDS), which has been developed for kinetic applications in our laboratory since 1992,[7-13] to measure the rate constant for the $C_6H_5 + CO$ addition reaction over the temperature range 300-500 K at 10-120 Torr pressure. In order to correlate our kinetic data with those of Solly and Benson mentioned above,[5] we have also carried out quantum chemical calculations to provide the molecular and transition-state parameters for a more reliable prediction of the T, P-effects on the rate constants for both forward and reverse directions by means of the RRKM theory.[6]

The CRDS method measures the decay times of injected probing photons in the absence (t_c^0) and presence (t_c) of absorbing species. Since the measured values of t_c and t_c^0 are much smaller than the chemical decay time of the radical t', depending on the concentration of the molecular reactant, the following kinetic relationship holds[7-13]

$$\ln(1/t_c - 1/t_c^0) = A - k't', \qquad (I)$$

where A is an experimental constant, which contains time-independent experimental parameters such as the length of the cavity, the velocity of light, the refractive index of the medium, etc. The slopes of the $\ln(1/t_c - 1/t_c^0)$ vs. t' give the first-order rate coefficients, k', for the decay of the C_6H_5 radical in the presence of a specified molecular reactant concentration. A standard plot of k' vs. [CO], provides the second-order rate constant, k", according to the relationship,

$$k' = k^0 + k"[CO], \qquad (II)$$

where k^0 is the first-order decay coefficient of the radical in the absence of a molecular reactant; it is a convoluted decay rate, consisting of the losses by diffusion, pumping and recombination reactions.

The results of the second order rate constants for the C_6H_5 + CO reaction are presented in Fig. 1(a). A weighted least squares analysis of this kinetic data gave rise to k" = $10^{11.85\pm0.08}$ exp[(-1447 ± 64)/T] $cm^3\ mol^{-1}\ s^{-1}$ in the temperature range 295-500 K. The large errors in the reaction rate at higher temperatures in comparison with ones at lower temperatures are attributed to the generation of C_6H_5 and CO by the decomposition of C_6H_5 + CO. This was investigated in the decomposition of benzoyl radical to a phenyl radical and carbon monoxide in the 614 – 667K temperature range by Solly and Benson.[5]

The measured kinetic data for the C_6H_5 + CO reaction and those of Solly and Benson[5] for the reverse reaction have been analyzed by RRKM calculations using the molecular and transition state parameters computed by different quantum chemical methods. The geometry of reactants, products and transition states have been optimized using three different methods, HF, MP2 and hybrid density functional B3LYP method. Vibrational frequencies have been used for characterization of stationary points, zero-point energy (ZPE) corrections and transition-state-theory (TST) and Rice-Ramsperger-Kassel-Marcus(RRKM) theory calculations of the rate constants[6]. In RRKM calculation, vibrational frequencies obtained by B3LYP/6-311G(d,p), MP2/6-31G(d,p) and HF/6-311G(d,p) were scaled by 1.0, 0.9434 and 0.8929, respectively. The moments of inertia and vibrational frequencies of all species obtained at three levels will be used in our rate constant calculations. The C-CO bond length of the transition state increases in the order: HF (2.0 Å) < MP2 (2.2 Å) < B3LYP (2.5Å). As shown in Fig. 1(a), the fitting of the measured forward rate constant indicates that the tighter transition state structure predicted by the HF method gives the best agreement with our experiment data at 40 torr. At lower temperatures, P-effect is negligible.

By using iterative fitting, we obtained the self-consistent energetic parameters. The activation barrier of the reaction C_6H_5 + CO → C_6H_5CO is 2.41 kcal/mol, and C_6H_5CO dissociation energy converges to 26.3 ± 0.5 kcal/mol at 0 K. Using $\Delta_fH°_0(C_6H_5)$ = 84.3 kcal/mol[14] and $\Delta_fH°_0(CO)$ = -27.2 kcal/mol[15] we got the heat of formation for C_6H_5CO, 30.8 kcal/mol at 0 K and 27.6 kcal/mol at 298 K, which is consistent with Benson's value (26.1 kcal/mol)[5]. For comparison, Simoes and Griller gave 27.7 ± 2.6 kcal/mol determined by their photoacoustic calorimetry.[16] In a recent study, Zhao et al.[17] reported 30.6 ± 0.7 kcal/mol for $\Delta_fH°_{298}(C_6H_5CO)$, 84.3 ± 0.6 kcal/mol for $\Delta_fH°_{298}(C_6H_5)$ by their isodesmic reactions; but in their paper they also gave 30.3 kcal/mol for $\Delta_fH°_0(C_6H_5CO)$, 27.8 kcal/mol for $\Delta_fH°_{298}(C_6H_5CO)$ obtained by G2(MP2,SVP) calculations. This value agrees with ours very well.

Our RRKM calculations using the predicted TS geometry and the reaction barrier, $E°_{-1}$ = 28.7 kcal/mol give the high-pressure rate constant, $k_{-1}^{\infty} = 1.44\times10^{15}$ exp(-15200/T) s^{-1}. This result correlates very well with our forward rate constant obtained at 40 torr pressure, converted to k_{-1} with the equilibrium constant $K_{eq} = k_{-1}/k_1 = 7.45\times10^2$ exp(-13340/T) mol/cm^3, and those of Benson exptrapolated to the high-pressure limit, as shown in Fig. 1(b).

Acknowledgment. The authors are grateful for the support of this work from the Basic Energy Sciences, Department of Energy, under contract no. DE-FG02-97-ER14784. We are also thankful to Dr. W. H. Kirchhoff for providing us NERSC CPU time for the quantum chemical calculations.

References

(1) Sawyer, R. F. *Twenty-forth Symposium (International) Combustion*; The Combustion Institute: Pittsburgh, 1992; p 1423.
(2) Glassman, I. *Combustion*, 2nd ed., Academic Press, NY, 1986.
(3) Fahr, A.; Mallard, S. G.; Stein, S. E. *Twenty-first Symposium (International) on Combustion*, The Combustion Institute, Pittsburgh, PA, 1986; p 825.
(4) Fahr. A; Stein, S. E. *Twenty-second Symposium (International) on Combustion*, The Combustion Institute, Pittsburgh, PA, 1988; p 1023.
(5) Solly, R. K.; Benson, S. W. *J. Am. Chem. Soc.* **1971**, *93*, 2127
(6) Diau, E. M. G.; Lin M. C. *J. Phys. Chem.* **1995**, *99*, 6589.
(7) Yu, T.; Lin, M. C. *J. Am. Chem. Soc.* **1993**, *115*, 4371.
(8) Lin, M. C.; Yu, T. *Int. J. Chem. Kinet.* **1993**, *25*, 875.
(9) Yu, T.; Lin, M. C. *J. Phys. Chem.*, **1995**, *99*, 8599.
(10) Yu, T.; Lin, M. C. *J. Am. Chem. Soc.* **1994**, *116*, 9571.
(11) Yu, T.; Lin, M. C. *Combust. Flame*, **1995**, *100*, 169.
(12) Park, J. Chakraborty, D.; Lin, M. C. *J. Phys. Chem.* **1999**, *103*, 4003.
(13) Park, J.; Lin, M. C. *Cavity-Ring-Down Spectrometry-A New Technique for Trace Absorption Measurements*, ACS Publication Series 720, 1999, Chapter 13, p 196
(14) G. E. Davico, V. M. Bierbaum, C. H. Depuy, G. B. Ellison, and R. R. Squires, J. Am. Chem. Soc., 117, 2590(1995)
(15) JANAF Table
(16) J. A. Martinho Simoes and D. Griller, Chem. Phys. Lett. 158, 175(1989).
(17) H.-Q. Zhao, Y.-S. Cheung, C.-L. Liao, and C. Y. Ng, Wai-Kee Li, J. Chem. Phys. 107, 7230(1997).

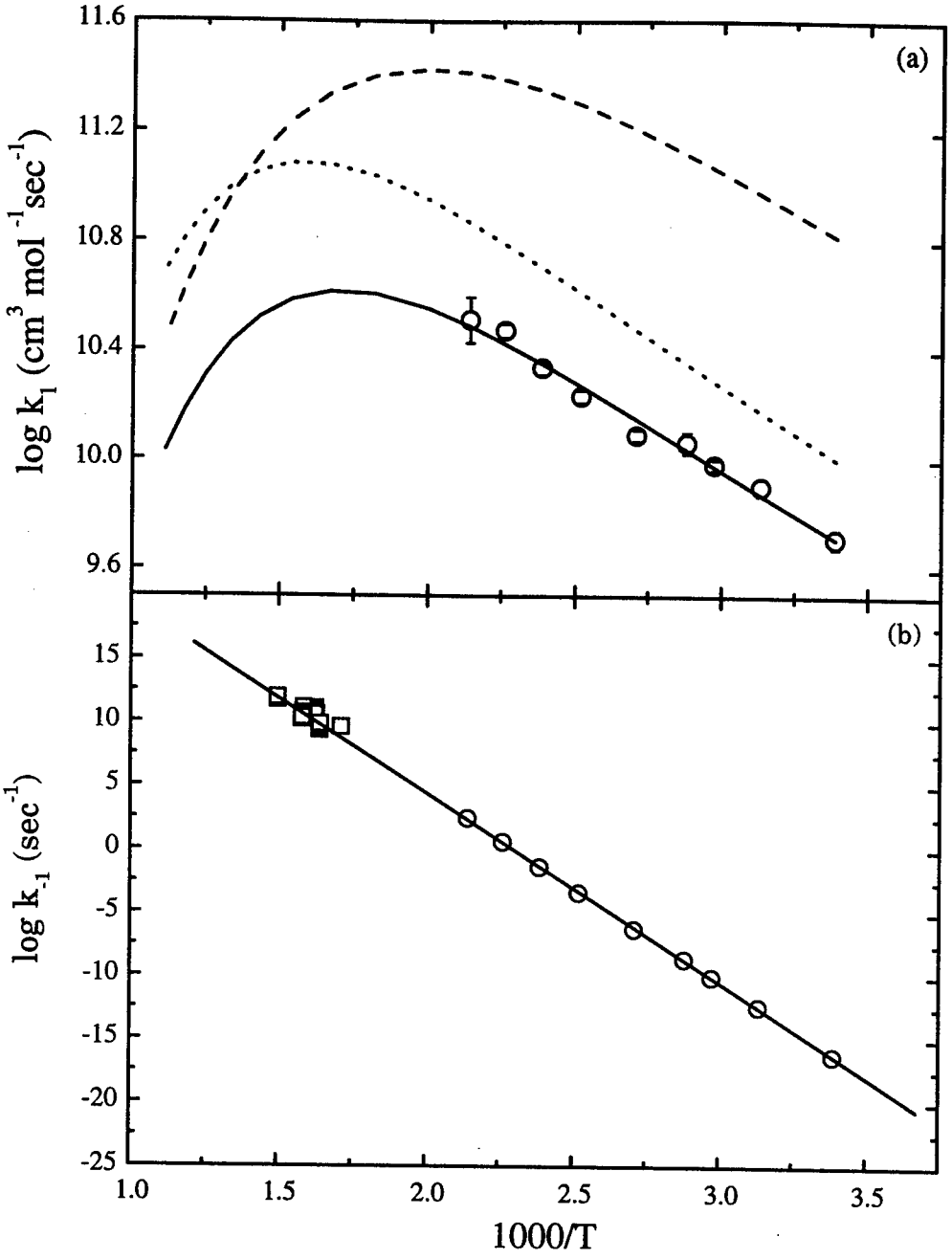


Fig.1. (a) Arrhenius plot for the C_6H_5 reaction with CO at the total pressure 40 Torr. ○, experimental result (this work); solid, dashed, dotted lines are the RRKM results calculated with TS parameters computed at HF/6-311G(d,p), B3LYP/6-311G(d,p), MP2/6-31G(d,p) basis set, respectively, with E_1° = 2.41 kcal/mol. (b) Correlation of Benson's data (□) extrapolated to the high-pressure-limit and our experimental rate constants for the reversed reaction of C_6H_5 + CO → C_6H_5CO converted to k_{-1}^∞ with the equilibrium constant K_1 given in the test.

EXPERIMENTAL AND THEORETICAL STUDIES OF THE $C_6H_5 + C_6H_6$ REACTION

J. Park, S. Burova, A. S. Rodgers and M. C. Lin
Department of Chemistry, Emory University, GA 30322
jpark05@emory.edu, chemmcl@emory.edu

The reaction of phenyl radical with benzene is of great importance to incipient soot formation chemistry and to the combustion of lead-free gasoline in which small aromatic hydrocarbons are key ingredients providing high-octane values. The kinetics of this reaction was first studied by Stein and coworkers[1,2] using a low pressure Knudsen cell-mass spectrometric technique in the temperature range 1000-1330 K by monitoring the formation of biphenyl:

$$C_6H_6 + C_6H_6 \rightarrow C_{12}H_{10} + H. \qquad (1)$$

They reported the expression, $k_1 = 3\times10^{12}$ exp(-4300/T) $cm^3/(mol\ s)$, assuming the rate constant for the recombination reaction of phenyl radicals:

$$C_6H_5 + C_6H_5 \rightarrow C_{12}H_{10} \qquad (2)$$

to be $k_2 = 3\times10^{12}$ $cm^3/(mol\ s)$. Combination of their high-temperature, low-pressure data with that determined at room temperature in solution by Scaiano and Stewart[3] gave rise to the approximate expression, $k_1 = 4\times10^{11}$ exp(-2000/T) $cm^3/(mol\ s)$.

Recently, Manion and Tsang[4] measured the rate constant for the reverse process,

$$H + C_{12}H_{10} \rightarrow C_6H_5 + C_6H_6 \qquad (-1)$$

in a single-pulsed shock tube using H + 1,3,5-$(CH_3)_3C_6H_3$ as a reference reaction with hexamethyl ethane as the H-atom source in the temperature range 1018-1135 K at pressures near 2 atm. This high-pressure high-temperature result, with $k_{-1} = 4.1\times10^{13}$ exp(-4418/T) $cm^3/(mol\ s)$, is reported to be consistent with Fahr and Stein's low-pressure Knudsen cell data mentioned above.

The $C_6H_5 + C_6H_6$ reaction is believed to take place by an addition/elimination mechanism via the $C_{12}H_{11}$ (phenyl cyclohexadienyl radical) intermediate for both forward and reverse processes.[1-5] In view of the expected strong P, T-effects on the stabilization vs. decomposition of the excited intermediate under combustion conditions, because of the low stability of the cyclohexadienyl adduct[6], we have carried out a theoretical study of the reaction using the combination of a hybrid density functional theory and the statistical Rice-Ramsperger-Kassel-Marcus (RRKM) theory calculations to correlate our low-temperature kinetic result, measured by the sensitive cavity ringdown technique[7-11], with the aforementioned high-temperature data.

All experiments for the $C_6H_5 + C_6H_6$ reaction were performed by the cavity ringdown spectroscopy (CRDS) techniqu eunder slow-flow conditions using Ar as the carrier gas and C_6H_5NO as a C_6H_5 precursor to provide a total pressure of 40 Torr. As described in detail elsewhere,[7-11] the CRDS method measures the decay times of the injected probing photons in the absence (t_c^o) and the presence (t_c) of absorbing species. These photon decay times can be related to the concentration of the species at time t' after its generation by the equation[6-11],

$$\ln\left(1/t_c - 1/t_c^o\right) = C - k't' \qquad \text{(I)}$$

where C is a constant which contains experimental parameters such as the initial concentration of the radical species of interest, the cavity length (50 cm), the refractive index of the absorbing medium, etc.

The slopes of the $\ln(1/t_c - 1/t_c^o)$ vs. t' plots for the reaction of C_6H_5 with C_6H_6 yield the pseudo-first-order rate coefficients, k', for the decay of C_6H_5 in the presence of known, excess C_6H_6 concentrations as specified. A standard plot of k' vs. reagent concentration gives the averaged second-order rate constant k'' from its slope according to the relationship

$$k' = k^o + k''[C_6H_6] \qquad \text{(II)}$$

where k^o is the radical decay constant in the absence of the molecular reactant X due to the loss of the radical by diffusion away from the probing beam and recombination reactions (e.g., C_6H_5 + NO and $C_6H_5 + C_6H_5$).

The results are graphically presented in Fig. 1(a) together with Fahr and Stein's low-pressure data.[1,2] These data were reevaluated by using our reported C_6H_5 recombination rate constant $k_2 = 1.39\times10^{13}$ exp(-55/T) $cm^3/(mol\ s)$.[12] A weighted least-squares analysis including these two sets of data gave rise to

$$k_1 = 10^{(11.93\pm0.40)} \exp[-(2006\pm51)/T] \quad cm^3/(mol\ s)$$

In order to confirm the mechanism, we have performed RRKM calculations for the formation and decomposition of the excited phenyl cyclohexadienyl adduct, $C_{12}H_{11}^{\#}$, to correlate the forward and reverse rate constants measured under varying T, P-conditions according to the following scheme:

$$C_6H_5 + C_6H_6 \underset{-a}{\overset{a}{\rightleftharpoons}} C_{12}H_{11}^{\#} \underset{-b}{\overset{b}{\rightleftharpoons}} C_{12}H_{10} + H \qquad (1, -1)$$

$$C_{12}H_{11}^{\#} \xrightarrow{c} C_{12}H_{11}\ (+M),$$

where "#" represents internal excitation and M denotes a third body (i.e., a molecular quencher). All molecular parameters of molecular species, the reactants, the adduct and the bipheny product, and the transition states involved in the reaction were calculated at the B3LYP/6-311G(d,p) level of theory.

On account of the lack of reliability in the predicted reaction energies at the present level of theory, the energy barriers for the forward addition ($C_6H_5 + C_6H_6$), E_a^o, and the reverse addition (H + $C_{12}H_{10}$), E_{-b}^o, were adjusted to fit the experimental values of k_1 and k_{-1}. The value of the entrance barrier, which fits most satisfactorily the C_6H_5 decay rate constants measured by CRDS, is $E_a^o = 2.7$ kcal/mol. Similarly, by fitting both Fahr and Stein's data for biphenyl formation from $C_6H_5 + C_6H_6$ and Manion and Tsang's results for benzene production from H + $C_{12}H_{10}$, we obtained $E_{-b}^o = 4.7$ kcal/mol.

As shown in Fig. 1, the high-temperature experimental data determined directly for the forward[1,2] and reverse[4] reactions can be reasonably correlated with our low-temperature results by the RRKM theory, using the molecular parameters (i.e., moments of inertia and vibrational

frequencies) and the energy of the adduct afforded by quantum calculations. For the reverse H + $C_{12}H_{10}$ reaction, the overall barrier for the production of C_6H_6, is 6.5 + 2.7 = 9.2 kcal/mol; it is close to Manion and Tsang's apparent activation energy, 8.8 kcal/mol, measured near 1000 K at about 2-atm pressure.[4] Under their experimental conditions, the stabilization of the excited $C_{12}H_{11}$ adduct and the production of benzene are competitive. Accordingly, the radical adduct may participate in other reactions, such as the scavenging of H atoms by the process H + $C_{12}H_{11}$ → H_2 + $C_{12}H_{10}$.

The forward and reverse addition barriers, E_a^o = 2.7 and E_{-b}^o = 4.7 kcal/mol, appear to be reasonable. For the C_6H_5 addition process, we have measured by CRDS the activation energies for the reactions with C_2H_2[13] and C_2H_4[14], 3.1 and 4.5 kcal/mol, respectively. They are comparable with the 4.0-kcal/mol value for the C_6H_6 reaction. For the H + $C_{12}H_{10}$ addition process, the value of E_{-b}^o is about half that of H + C_6H_6,[6] 8.9 kcal/mol. This large difference in the addition barriers may be attributed in part to the large activation energy needed to overcome the resonance stabilization in C_6H_6 and in part to the retention of some resonance energy in $C_{12}H_{11}$ across the two π -systems (i.e., the two C_6 rings).

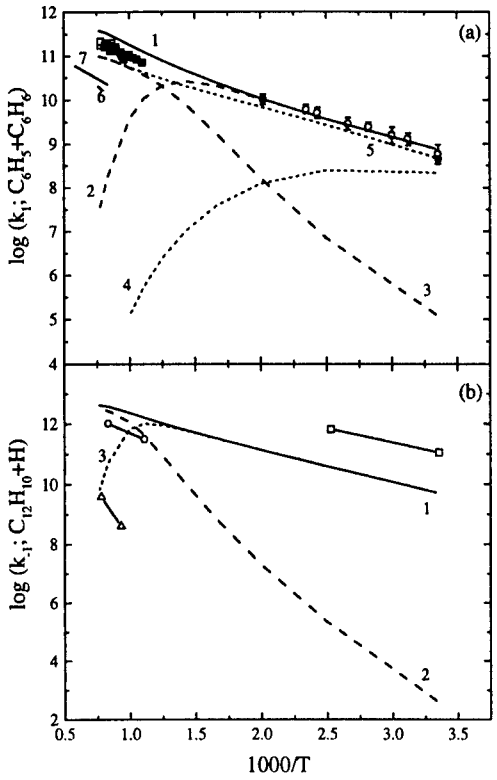


Figure 1. Comparison of the experimental and theoretically predicted results for C_6H_5 + C_6H_6 ⇔ $C_{12}H_{10}$ + H in the forward and reverse directions. (a) 1, k_{tot} (inf); 2, $k_{C_{12}H_{11}}$ (40 Torr); 3, $k_{C_{12}H_{10}+H}$ (40 Torr); 4, $k_{C_{12}H_{11}}$ (10 mTorr); 5, $k_{C_{12}H_{10}+H}$ (10 mTorr); 6, Ref. 15; 7, Ref. 16. ○, this work, □ and ■, Ref. 1 and Ref. 2 (both data were rescaled using our phenyl radical recombination data (Ref. 12); △, Ref. 3. Solid line, least-squares fitting in combination with those rescaled data of Ref. 1 . (b) 1, k_{tot}; 2, $k_{C_6H_5+C_6H_6}$ (2 atm); 3, $k_{C_{12}H_{11}}$ (2 atm); ○, Ref. 4; □, Ref. 17; △, Ref. 18.

For practical kinetic modeling, we have calculated the rate constants for the two branching reactions, (1b) and (1c), at different pressures covering the temperature range 300 - 2500K. They are summarized in Table I. The equilibrium constant for the overall process, C_6H_5 + C_6H_6 = $C_{12}H_{10}$ + H, $K_1 = 1.45\times10^{-13}\ T^{3.23}\ \exp(3998/T)$, may be used to convert these rate constants for the reverse displacement reaction.

Acknowledgment. The authors are grateful for the support of this work from the Basic Energy Sciences, Department of Energy, under contract no.DE-FG02-97-ER14784. We are also thankful to Dr. W. H. Kirchhoff for providing us NERSC CPU time for the quantum chemical calculations.

References

(1) Fahr,A.; Stein,S.E. *Twenty-Second Symposium (International) on Combustion*; The Combustion Institute; Pittsburgh, PA, 1989; p 1023.

(2) Fahr, A.; Mallard, W.G.; Stein, S.E. *Twenty-First Symposium (International) on Combustion*; The Combustion Institute; Pittsburgh, PA, 1988, p 825.

(3) Scaiano, J. C.; Stewart, L. C. J. Am. Chem. Soc. **1983**, *105* 3609.
(4) Manion, J. A.; Tsang, W. Proceedings of Chemical and Physical Processes in Combustion, 1996 Fall Technical Meeting, p. 527.
(5) Louw, R.; Lucas, H. J. *Rec. Trav. Chim.* **1973**, *92*, 55.
(6) Mebel, A. M.; Lin, M. C.; Yu, T.; Morokuma, K. *J. Phys. Chem.* A **1997**, *101*, 3189.
(7) Yu, T.; Lin, M. C. *J. Am. Chem. Soc.* **1993**, *115*, 4371.
(8) Lin, M. C.; Yu, T. *Int . J. Chem. Kinet.* **1993**, *25*, 875.
(9) Yu, T.; Lin, M. C. *J. Am. Chem. Soc.* **1994**, *116*, 9571.
(10) J. Park, D. Chakraborty and M. C. Lin, *J. Phys. Chem.* **1999**, *103*, 4003.
(11) Park, J.; Lin, M. C. *Cavity-Ring-Down Spectrometry-A New Technique for Trace Absorption Measurements*, ACS Publication Series 720, 1999, Chapter 13, p 196.
(12) Park, J.; Lin, M. C. *J .Phys. Chem.* **1997**, *101* 14.
(13) Yu, T.; Lin, M. C.; Melius, C. F. *Int. J. Chem. Kinet.*, **1994**, *26*, 1095.
(14) Yu, Y.; Lin, M. C. *Combust. Flame*, **1995**, *100*, 169.
(15) Weissman, M.; Benson, S. W. *Int. J. Chem. Kinet.* **1984**, *16*, 307.
(16) Sauer, M. C., Jr.; Mani, I. *J. Phys. Chem.* **1970**, *74*, 59.
(17) Asaba, T.; Fujii, N. *Proc. Int. Symp. Shock Tubes Waves* **1971**, *8*, 1.
(18) Ritter,E. R.; Bozzelli, J. W.; Dean, A. M. *J. Phys. Chem.* **1990**, *94*, 2493.

TABLE 1: Effects of Temperature and Pressure on the Rate Constant[a] for the $C_6H_5 + C_6H_6$ Reaction.

T	k_{1b}	k_{1c}	k_{1b}	k_{1c}	k_{1b}	k_{1c}
(K)	10 mtorr		40 torr		2 atm	
300	4.79×10^{8}	2.14×10^{8}	1.27×10^{5}	7.59×10^{8}	3.35×10^{3}	7.59×10^{8}
500	6.93×10^{9}	1.20×10^{8}	1.60×10^{8}	1.05×10^{10}	4.90×10^{6}	1.08×10^{10}
700	2.04×10^{10}	1.01×10^{7}	7.83×10^{9}	2.60×10^{10}	7.29×10^{8}	4.40×10^{10}
1000	5.51×10^{10}	1.23×10^{5}	5.37×10^{10}	3.70×10^{9}	3.81×10^{10}	5.00×10^{10}
1500	8.43×10^{10}	1.27×10^{1}	8.43×10^{10}	5.09×10^{5}	8.43×10^{10}	1.93×10^{7}
2000	8.01×10^{9}	1.37×10^{-4}	8.01×10^{9}	5.46×10^{0}	8.01×10^{9}	2.07×10^{2}
2500	1.62×10^{8}	6.20×10^{-10}	1.62×10^{8}	2.49×10^{-5}	1.62×10^{8}	9.46×10^{-4}

[a]In units of $cm^3/(mol\ sec)$. k_{1b} and k_{1c} represent the formation of $C_{12}H_{10} + H$ and $C_{12}H_{11}$, respectively.

Kinetic Study on Vinyl Radical Addition to Chloroethene

Takahiro Yamada, Michael Steiger, Philip H. Taylor
Environmental Science Group
University of Dayton Research Institute
300 College Park Dayton, OH 45469
yamada@udri.udayton.edu

Joseph W. Bozzelli
Chemical Engineering, Chemistry and Environmental Science
New Jersey Institute of Technology
University Heights Newark, NJ 07102

Introduction

Reaction pathways and kinetics are analyzed on vinyl radical (C_2H_3) addition to chloroethene (C_2H_3Cl) reaction. The composite ab initio methods CBS-Q and G3(MP2) are used to analyze potential energy surface for vinyl radical addition to carbon which has two hydrogens (α-addition) and carbon which has one chlorine and one hydrogen (β-addition), respectively. Entropy ($S°_{298}$ unit in cal/mol-K) and heat capacities ($C_p(T)$s ($300 \le T/K \le 1500$) unit in cal/mol-K) of reactant (C_2H_3), intermediate radicals, and transition states (TSs), and products are calculated based on geometric parameters and frequencies derived from ab initio calculations. Quantum Rice-Ramsperger-Kassel (QRRK) analysis is used to calculate the energy dependent rate constants k(E), and the master equation is used to account for the collisional stabilization of adduct and isomer.

Modeling

1. Potential Energy Surface

CBS-Q[1], a well established, high level composite ab initio calculation, is used to analyze the potential energy surface of the α-addition reaction, the more favored reaction than β-addition reaction. G3(MP2)[2], which was recently proposed and is indicated to be comparable to high level composite ab initio calculations with shorter calculation times, is used for the β-addition reaction to save computational resources. The entrance reaction of the β-addition reaction, $CHCLCH_2 + C_2H_3 \rightarrow C\bullet H_2CHCLCH{=}CH_2$ is also calculated using CBS-Q to compare the overall α- and β-addition reaction rate constants. The energy levels of intermediate radicals, TSs, and products are estimated by relative energy difference from reactants. The energy level of reactants is obtained from literature[3,4]. CBS-Q[1] uses frequencies of HF/6-31G(d') level of theory and geometry of MP2/6-31G(d') level followed by single point calculations of QCISD(T)/6-31+G(d'), MP4(SDQ)/CBSB4 and MP2/CBSB3. G3(MP2)[2] uses frequencies of HF/6-31G(d) and geometry of MP2(full)/6-31G(d) followed by single point calculations of QCISD(T)/6-31G(d) and MP2=(fc)/G3MP2large. Scaled zero point vibrational energy (ZPVE × 0.8929) and thermal corrections to 298 K are also incorporated.

2. $S°_{298}$ and $C_p(T)$ ($300 \le T/K \le 1500$) Estimation

Geometric parameters and frequencies derived by HF/6-31G(d') and HF/6-31G(d) levels of theory are used to calculate $S°_{298}$ and $C_p(T)$s for α- and β-addition reactions respectively. Contribution of hindered internal rotational frequencies for $S°_{298}$ and $C_p(T)$s are calculated separately based on rotational barrier heights and moments of inertia. Pitzer and Gwinn's [5] general treatment of internal rotation is used to calculate hindered internal rotational contribution to $S°_{298}$ and $C_p(T)$s.

3. High-pressure Limit A Factors (A_∞) and Rate Constants (k_∞) Determination with ab initio Calculations for Transition State Compounds

For the reactions where thermodynamic properties of transition states are calculated by ab initio methods, k_∞s are fit by three parameters A_∞, Δn, and $E_{a,\infty}$ over the temperature range of 200 to 2,000K as expressed as

$$k_\infty = A_\infty(T)^{\Delta n}\exp(-E_{a,\infty}/RT).$$

High-pressure limit A factors (A_∞) of unimolecular reactions are calculated using the canonical transition state theory (TST) along with ab initio data on determination of the structure, vibrational and rotational contributions to $S°_{298}$ of TSs. Loss (or gain) of internal rotors and change of optical isomer and symmetry numbers are also incorporated into the calculation of $S°_{298}$ for each TS. $S°_{298}$ of reactants and TSs are then used to determine the pre-exponential factor, A, via canonical TST[6] for a unimolecular reaction, $A=(k_bT/h_p)\exp(\Delta S^{\neq})$, where h_p is Planck's constant, k_b is the Boltzmann constant, and $\Delta S^{\neq}$ is equal to $S°_{298,TS} - S°_{298,reactant}$.

4. Quantum Rice-Ramsperger-Kassel Analysis with Master Equation

Quantum Rice-Ramsperger-Kassel (QRRK) analysis[7,8] is used to calculate energy dependent rate constants, k(E). Master equation analysis is used to account for collisional stabilization in the reaction mechanism of $C_2H_3Cl + C_2H_3$.[8]

Reduced sets of three vibrational frequencies and their degeneracies (totaling 3N-6, where N is number of atoms in the energized adduct) plus energy levels of one external rotor are used to yield the ratio of density of states to partition coefficient, $\rho(E)/(Q)$. Each set of vibrational frequencies and respective degeneracies is computed from fitting heat capacity data, as described by Ritter (CPFIT computer code)[9]. Lennard-Jones parameters, σ_{LJ} (in angstroms) and ϵ/k (in Kelvin) are obtained from tabulations[10].

Results and Discussion

Figures 1 and 2 show potential energy diagrams for chloroethene plus vinyl radical α- and β-addition reactions respectively. The energy levels of the intermediate radicals for both reaction systems show quite similar results. The activation energies for H shift for both reaction systems also shows similar values (c.a. 48 kcal/mol). The comparison of entrance channels, both of which are calculated by CBS-Q[1] theory, shows that the β-addition channel has 1.3 kcal/mol higher activation energy than the α-addition. Figure 2 shows that the chlorine elimination reactions need less energy than hydrogen and methyl radical elimination reactions. The $\Delta H_f°_{298}$s of Cl elimination are 16.4 and 19.6 kcal/mol from the stabilized adduct, $C•H_2CHClCH=CH_2$, and its isomer, $CH_3CHClC•=CH_2$ respectively, whereas H and CH_3 elimination are higher in energy, c.a. 41 and 38 kcal/mol respectively. Chlorine shift reaction also needs less energy than H shift reactions, which are 10.2 and 48.3 kcal/mol, respectively based on G3(MP2) calculation results.

Figure 3 and 4 show QRRK results, k vs. temperature at 1 atm., for α- and β-addition reaction, respectively. The overall rate constant for α-addition reaction shows 1.4 to 1.0 order magnitude larger values than that for β-addition reaction through the temperature range of 298 to 2000K. Adduct stabilization reaction dominates the reactions up to temperature of 770K in the α-addition reaction. H elimination reaction becomes more important than other reactions at temperature above 770K. Predominance of H elimination reaction suppresses the dissociation reaction back to reactants. The chlorine elimination reaction to form buta-1,3-diene dominates the reaction paths through entire temperature range in β-addition adduct formation.

References

(1) Ochterski, J. W.; Petersson, G. A.; Montgomery, J. J. A. J Chem Phys 1996, 104, 2598.
(2) Curtiss, L. A.; Redfern, P. C. J Chem Phys 1999, 110, 4703.
(3) Stull, D. R.; Westrum, E. F.; Sinke, G. C. The Chemical Thermodynamics of Organic Compounds; Robert E. Krieger Publishing Company: Malabar, FL, 1987.
(4) Tsang, W. Blackie Academic and Professional 1996, 22.
(5) Pitzer, K. S.; Gwinn, W. J Chem Phys 1942, 10, 428.
(6) Benson, S. W. Thermochemical Kinetics; A Wiley-Interscience Publication: New York, NY, 1976.
(7) Dean, A. M. J Phys Chem 1987, 89, 4600.
(8) Chang, A. M.; Bozzelli, J. W.; Dean, A. M. in process of submittal.
(9) Ritter, E.; Bozzelli, J. W. Int J Chem Kinet 1991, 23, 767.
(10) Reid, R. C.; Prausinitz, J. M.; Sherwood, T. K. The Properties of Gases and Liquids; McGraw-Hill Co.: New York, 1979.
(11) Bozzelli, J. W.; Chang, A. Y.; Dean, A. M. Int J Chem Kint 1997, 29, 161.
(12) Barat, R. B.; Bozzelli, J. W. J Phys Chem 1992, 96, 2494.

Table 1. Input Parameters[a] and High-Pressure Limit Rate Constants (K_∞)[b] for QRRK Calculations[c] and the Resulting Rate Constants (T = 298K) ($CHClCH_2 + C_2H_3 \Rightarrow C\bullet HClCH_2CH{=}CH_2$)

Input parameters for QRRK Calculations
High - Pressure Limit Rate Constants

	Reaction	$A(S^{-1}$ or $cm^3/(mol\ s)$[d]	k_∞ n	E_a (kcal/mol)[e]
1	$CHClCH_2 + C_2H_3 \Rightarrow C\bullet HClCH_2CH{=}CH_2$	1.16E+3	2.96	2.58
-1	$C\bullet HClCH_2CH{=}CH_2 \Rightarrow CHClCH_2 + C_2H_3$	5.28E+11	0.87	40.31
2	$C\bullet HClCH_2CH{=}CH_2 \Rightarrow CHCl{=}CHCH{=}CH_2 + H$	2.28E+9	1.49	35.03
3	$C\bullet HClCH_2CH{=}CH_2 \Rightarrow CH_2ClCH_2C\bullet{=}CH_2$	6.54E+8	1.04	48.33
-3	$CH_2ClCH_2C\bullet{=}CH_2 \Rightarrow C\bullet HClCH_2CH{=}CH_2$	2.61E+8	1.04	38.32
4	$CH_2ClCH_2C\bullet{=}CH_2 \Rightarrow CH_2ClCH{=}C{=}CH_2 + H$	1.14E+13	0.19	36.03
5	$CH_2ClCH_2C\bullet{=}CH_2 \Rightarrow C.H_2Cl + CH_2{=}C{=}CH_2$	1.46E+11	0.98	26.71

Calculated Reaction Parameters at P=1atm, $k=A(T/K)^n(-E_a/RT)$ (Temp=250-2000K)

	Reaction	A	n	E_a (kcal/mol)	k_{298} (s^{-1} or $cm^3/(mol\ s)$)
1	$CHClCH_2 + C2H3 \Rightarrow C\bullet HClH_2OCH{=}CH_2$	5.22E+38	-8.71	11.72	3.73E+8
2	$CHClCH_2 + C2H3 \Rightarrow CHCl{=}CHCH{=}CH_2 + H$	6.45E+6	2.08	9.69	7.06E+4

[a] Reduced frequency sets (from CPFIT, ref.[11] : 398.1 cm^{-1} (8.439); 1122.2 cm^{-1} (11.905); 2977.0 cm^{-1} (5.656). Lennard-Jones parameters: $\sigma_{ij} = 5.20$Å, $\epsilon/k = 533.08$. [b] The units of A factors and rate constants k are s^{-1} for unimolecular reactions and $cm^3/(mol\ s)$ for bimolecular reactions. [c] ΔE down of 600 cal/mol is used. [d] Arrhenius A factor is calculated using TST and entropy of transition state (TS), $\Delta S^{\neq}_{298}$ from HF/6-31G(d'). [e] E_a is estimated based on QBS-Q energies with scaled ZPVE and thermal correction to 298.15K. The three parameters A, n, and E_a for k's are fit over the temperature range of 300 to2000K.

Table 2. Input Parameters[a] and High-Pressure Limit Rate Constants (K_∞)[b] for QRRK Calculations[c] and the Resulting Rate Constants (T = 298K) ($CHClCH_2 + C_2H_3 \Rightarrow C\bullet H_2CHClCH{=}CH_2$)

Input parameters for QRRK Calculations
High - Pressure Limit Rate Constants

	Reaction	$A(S^{-1}$ or $cm^3/(mol\ s)$[d]	k_∞ n	E_a (kcal/mol)[e]
1	$CHClCH_2 + C_2H_3 \Rightarrow C\bullet H_2CHClCH{=}CH_2$[f]	2.73E+2	2.87	3.77
-1	$C\bullet H_2CHClCH{=}CH_2 \Rightarrow CHClCH_2 + C_2H_3$	6.31E+10	0.98	43.04
2	$C\bullet H_2CHClCH{=}CH_2 \Rightarrow CH_2{=}CClCH{=}CH_2 + H$[g]	3.10E+9	1.57	41.20
3	$C\bullet H_2CHClCH{=}CH_2 \Rightarrow CH_2{=}CHCHCH_2 + Cl$[h]	3.90E+13	0.0	16.4
4	$C\bullet H_2CHClCH{=}CH_2 \Rightarrow CH_2ClC\bullet HCH{=}CH_2$	2.90E+9	0.99	10.17
5	$C\bullet H_2CHClCH{=}CH_2 \Rightarrow CH_3CHClC\bullet{=}CH_2$[i]	1.02E+8	1.29	48.04
6	$CH_2ClC\bullet HCH{=}CH_2 \Rightarrow CH_2{=}CHCHCH_2 + Cl$[h]	3.90E+13	0.0	32.3

Calculated Reaction Parameters at P=1atm, $k=A(T/K)^n(-E_a/RT)$ (Temp=250-2000K)

	Reaction	A	n	E_a (kcal/mol)	k_{298} (s^{-1} or $cm^3/(mol\ s)$)
1	$CHClCH_2 + C2H3 \Rightarrow CH_2{=}CHCHCH_2 + Cl$ (Direct Dissociation)	5.54E+2	2.68	3.80	3.87E+6
2	$CHClCH_2 + C2H3 \Rightarrow CH_2{=}CHCHCH_2 + Cl$ (Through TS)	1.83E+4	2.29	5.55	7.21E+5

[a] Reduced frequency sets (from CPFIT, [11] : 398.1 cm^{-1} (8.439); 1122.2 cm^{-1} (11.905); 2977.0 cm^{-1} (5.656). Lennard-Jones parameters: $\sigma_{ij} = 5.20$Å, $\epsilon/k = 533.08$. [b] The units of A factors and rate constants k are s^{-1} for unimolecular reactions and $cm^3/(mol\ s)$ for bimolecular reactions. [c] ΔE down of 600 cal/mol is used. [d] Arrhenius A factor is calculated using TST and entropy of transition state (TS), $\Delta S^{\neq}_{298}$ from HF/6-31G(d). [e] E_a is estimated based on G3(MP2) energies with scaled ZPVE and thermal correction to 298.15K. The three parameters A, n, and E_a are fit over the temperature range of 300 to 2000K. [f] E_a is estimated based on CBS-Q energy. [g] A, n and E_a for k's are estimated based on reaction $CH_3CHClC\bullet{=}CH_2 \rightarrow CH_3CCl{=}C{=}CH_2 + H$. [h] A is obtained from ref. [12] $C_2H_4Cl \rightarrow C_2H_4 + Cl$. [i] E_a is estimated using B3LYP/6-31G* level of theory.

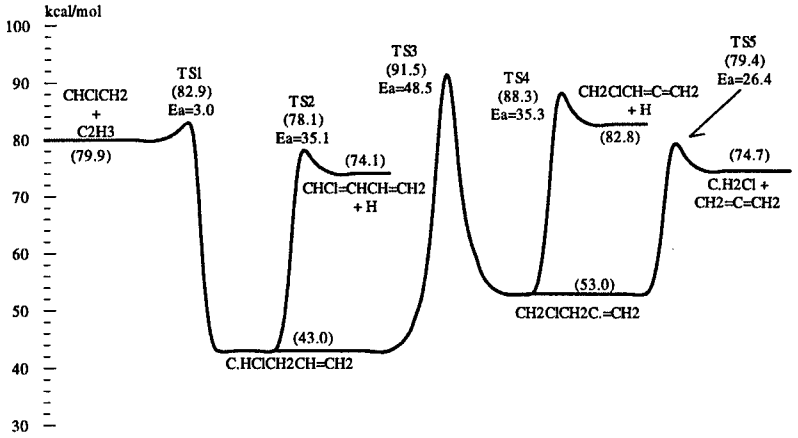


Figure 1. Potential Energy Diagram (α-addition) $CHClCH_2 + C_2H_3$ (CBS-Q)

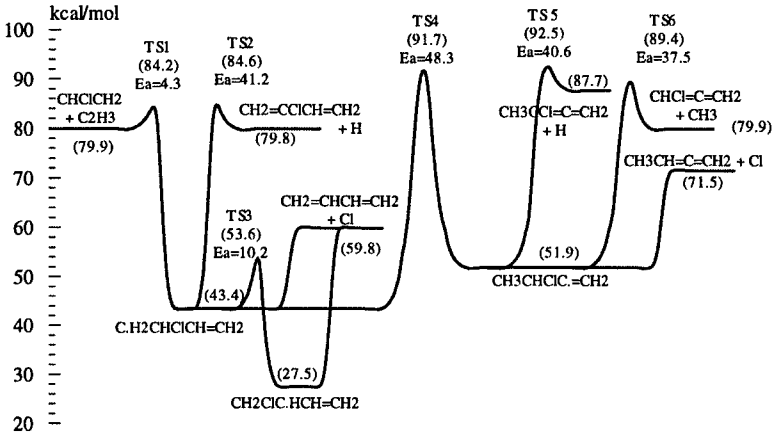


Figure 2. Potential Energy Diagram (β-addition) $CHClCH_2 + C_2H_3$ (G3(MP2))

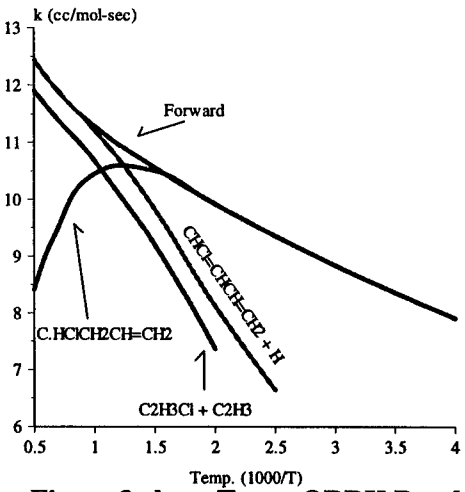


Figure 3. k vs. Temp. QRRK Result (α-addition)

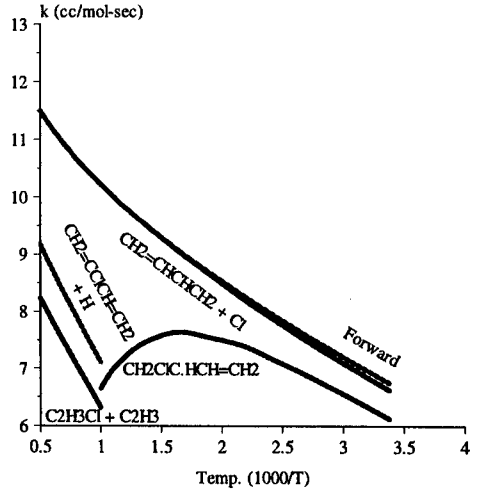


Figure 4. k vs. Temp. QRRK Result (β-addition)

Unimolecular Reactions of *o*-C_6H_4: the Significant Effect of Isomerization on the Decomposition process

L. V. Moskaleva*, L. K. Madden and M. C. Lin**
Department of Chemistry, Emory University, Atlanta, GA 30322
e-mail: *lmoskal@emory.edu, **chemmcl@emory.edu

Introduction

The role of arynes in aromatic nucleophilic substitution has been long recognized;[1] however, their role in the combustion of aromatic hydrocarbons has been largely ignored. In our recent theoretical study of the phenyl radical unimolecular decomposition,[2] we have concluded that the commonly assumed ring-opening process leading to the formation of C_4H_3 and C_2H_2,

$$C_6H_5 \rightarrow l\text{-}C_6H_5 \rightarrow C_4H_3 + C_2H_2, \quad (1)$$

is less important than the fragmentation process producing *ortho*-benzyne and a hydrogen atom,

$$C_6H_5 \rightarrow o\text{-}C_6H_4 + H. \quad (2)$$

Accordingly, one would expect that *o*-C_6H_4 may play a significant role in the combustion of lead-free gasoline which contains as much as 20-30% of small aromatics including benzene, toluene, and xylenes.

In the present study, we have investigated energetics for the decomposition reaction

$$o\text{-}C_6H_4 \rightarrow C_4H_2 + C_2H_2, \quad (3)$$

at high levels of theory, including the G2M method[3]. In addition, we have explored the possibility of isomerization reactions,

$$o\text{-}C_6H_4 \rightarrow m\text{-}C_6H_4, \quad (4)$$

$$m\text{-}C_6H_4 \rightarrow p\text{-}C_6H_4, \quad (5)$$

that may have an effect on the observed rate of reaction (3) because of their possible depopulation of *o*-C_6H_4 at high temperatures. This effect was examined by carrying out multichannel RRKM calculations under varying P, T-conditions.

Computational Methods

The geometries of the C_6H_4 isomers, all the transition states and products, except those involved in *o*-C_6H_4 fragmentation, were fully optimized using Becke's three parameter density functional B3LYP[4,5] with the standard 6-31G(d) basis set. For the *o*-benzyne fragmentation to form $C_2H_2 + C_4H_2$, the MP2/6-31G(d) optimization method was employed. In addition, an MP2/6-31G(d) geometry optimization was performed for the *ortho-meta* isomerization step to ensure consistent treatment of the two rate determining transition states, TS_{dec} and TS_{om}. The vibrational frequencies, computed at the same level of theory as respective optimizations, were used for characterization of stationary points and for statistical-theory calculations (MP2 frequencies were scaled with a factor of 0.9676). Absolute energies for each optimized structure were then calculated at the RCCSD(T)/6-31G(d,p) and the G2M(rcc,MP2)[3] levels.

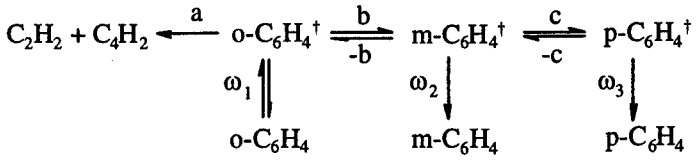
The GAUSSIAN 94[6], MOLPRO 96[7] programs were employed for the MO computations.

Results and Discussion

The potential energy diagram at the G2M level for the entire system studied is presented in Figure 1. The transition state for *ortho-meta* isomerization, TS_{om}, was calculated to be 16.5 kcal/mol lower than that for fragmentation, TS_{dec}, at our best G2M level.

The RRKM calculations were performed for the lowest energy path which included decomposition and isomerization pathways, the latter being terminated at the *meta-para* isomerization. This should be a reasonable approximation since the barrier for the Bergman decyclization process, TS_{berg}, is small and it is exothermic by 10.5 kcal/mol which should minimize the reverse reaction.

The following mechanistic scheme was employed:



where the dagger represents internal excitation and ω_j (j = 1,2,3) stands for the effective quenching frequency for the j-th reaction step.

Figure 2 gives Arrhenius plots of k_{tot} (the observed overall rate constant for the disappearance of o-C_6H_4, which is represented by a sum of k_{dec}, $k_{\omega 2}$, and $k_{\omega 3}$, the individual rate constants for the decomposition to form C_4H_2 and C_2H_2) at different pressures for the temperature range 1000-3000 K. It can be seen that especially at high temperatures pressure dependence is significant. The contributions to k_{tot} from different channels are shown in Figure 3. In the high-pressure limit the expressions for the formation of 1,3-butadiyne, m-C_6H_4 and p- C_6H_4 over the temperature range 1000-3000 K are as follows:

$$k_{dec} = 3.27\times10^{16} e^{-46952/T}\ \mathrm{s}^{-1},$$

$$k_{o,m} = k_{\omega_2} = 2.06\times10^{14} e^{-37067/T}\ \mathrm{s}^{-1},$$

$$k_{o,p} = k_{\omega_3} = 5.60\times10^{-38} T^{11.4} e^{-36834/T}\ \mathrm{s}^{-1}.$$

It is evident that the decomposition and isomerization channels are strongly competing; the decomposition dominates at temperatures above 2000 K, whereas the m-benzyne formation becomes dominant at lower temperatures. The isomerization process accounts for as much as 99% of the o-C_6H_4 depletion at 1000 K because of its lower barrier. The result suggests that the reactions of both m-C_6H_4 and l-C_6H_4 should be included in the kinetic modeling of soot formation processes.

Acknowledgment

The authors gratefully acknowledge the support received from the Department of Energy, Office of Basic Energy Sciences, Division of Chemical Sciences through Contract DE-FGO2-97ER14784. Also, we are thankful to the Cherry L. Emerson Center for Scientific Computation for the use of various programs and computing facilities.

References

1. J. March, *Advanced Organic Chemistry*, 3rd ed.; Wiley & Sons: New York, 1985.

2. L. K. Madden, L. V. Moskaleva, S. Kristyan and M. C. Lin, *J. Phys. Chem.*, 1997, **101**, 6790.
3. A. M. Mebel, K. Morokuma and M. C. Lin, *J. Chem. Phys.*, 1995, **103**, 7414.
4. A. D. Becke, *J. Chem. Phys.*, 1993, **98**, 5648.
5. C. Lee, W. Yang and R. G. Parr, *Phys. Rev. B*, 1988, **37**, 785.
6. M. J. Frisch, G. W. Trucks, H. B. Schlegel, P. M . W. Gill,. B. G. Johnson, M. A. Robb, J. R. Cheeseman, T. Keith, G. A. Petersson, J. A. Montgomery, K. Raghavachari, M. A. Al-Laham, V. G. Zakrzewski, J. V. Ortiz, J. B. Foresman, J. Cioslowski, B. B. Stefanov, A. Nanayakkara, M. Challacombe, C. Y. Peng, P. Y. Ayala, W. Chen, M. W. Wong, J. L. Andres, E. S. Replogle, R. Gomperts, R. L. Martin, D. J. Fox, J. S. Binkley, D. J. Defrees, J. Baker, J. P. Stewart, M. Head-Gordon, C. Gonzalez and J. A. Pople, *GAUSSIAN 94, REVISION A.*1; Gaussian, Inc., Pittsburgh PA, 1995.
7. MOLPRO is a package of *ab initio* programs written by H.-J. Werner and P. J. Knowles, with contributions from J. Almlöf, R. D. Amos, A. Berning, D. L. Cooper, M. J. O. Deegan, A. J. Dobbyn, F. Eckert, S. T. Elbert, C. Hampel, R. Lindh, A. W. Lloyd, W. Meyer, A. Nicklass, K. Peterson, R. Pitzer, A. J. Stone, P. R. Taylor, M. E. Mura, P. Pulay, M. Schütz, H. Stoll and T. Thorsteinsson.

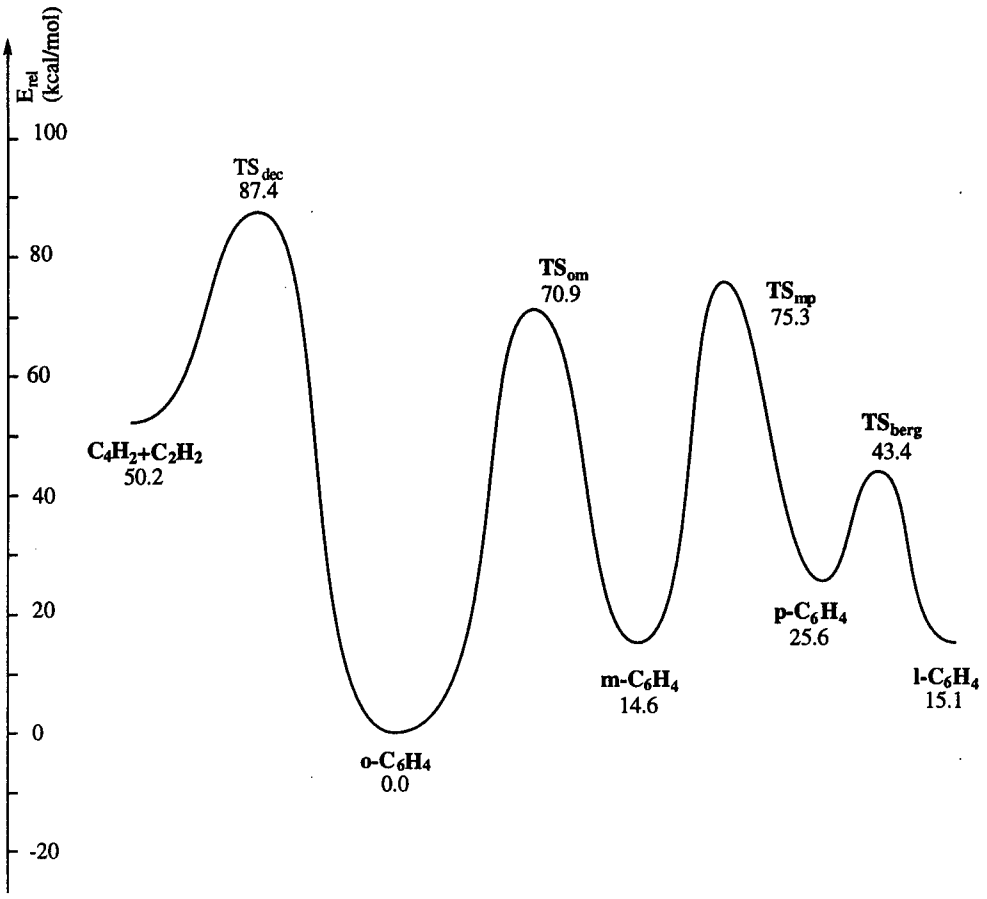


Figure 1. Potential energy diagram for the o-C_6H_4 isomerization/decomposition. ZPE corrected energies are given as calculated at the G2M(rcc,MP2) level.

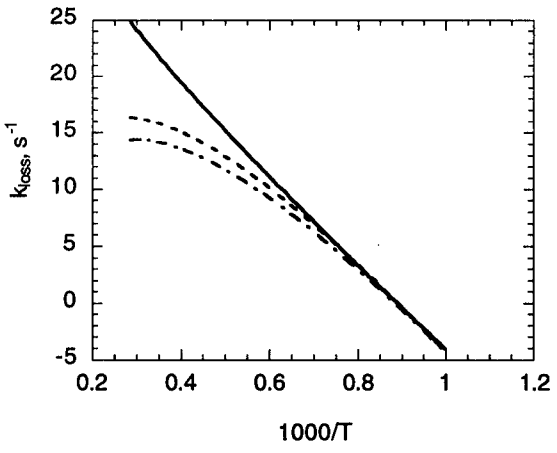


Figure 2. Predicted total rate constants at different pressures and temperatures. Solid curve: the high pressure limit; dashed curve: 1 atm; dash-dotted curve: 100 torr.

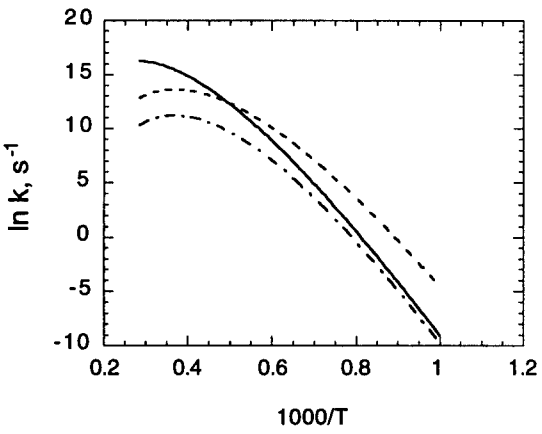


Figure 3. Calculated branching rate constants describing the production of $C_4H_2 + C_2H_2$ (solid curve), *m*-C_6H_4 (dashed curve), and *p*-C_6H_4 (dash-dotted curve) at 1 atm.

APPLICATION OF LASER INDUCED INCANDESCENCE TO THE DETECTION OF SOOT YIELDS IN COMBUSTION TEST FACILITIES

W.T. Rawlins, B.L. Upschulte, P.A. Mulhall, K.R. McManus,
J.H. Frank, E.T. Wetjen, M.G. Allen
Physical Sciences Inc.
20 New England Business Center, Andover, MA 01810
rawlins@psicorp.com

C. Wey
Dynacs, Inc.
Cleveland, OH

M.J. Rabinowitz
NASA Glenn Research Center
Cleveland, OH

1. Introduction

The technique of laser induced incandescence (LII) is well suited for the detection of low soot concentrations relevant to the development of advanced gas turbine engines. Through careful design of a spatially integrating photometric system, it is possible to detect laser induced incandescence signals corresponding to soot concentrations as low as 0.1 mg/m^3 (volume fraction 5×10^{-11}). We have designed and implemented an LII system with a dual-wavelength, fast-response photometric receiver which records the detailed time history of the incandescence signal following the laser pulse. The photometric measurements are analyzed to determine absolute soot concentrations and path-averaged particle temperature histories. The temperature-versus-time profiles are used to infer mean particle sizes through straightforward analysis of the heat transfer physics. We have developed and tested this approach through a series of detailed LII spectral and temporal measurements in laboratory diffusion and flat premixed flames. The PSI LII system is scheduled for a test series in July 1999 on a flame tube test facility at NASA Glenn Research Center. This presentation will describe the overall technical approach, instrumentation design, laboratory flame measurements, and preliminary flame tube test results.

2. Methodology

Laser induced incandescence is observed as a short-lived (~1 μs) pulse of continuum grey-body radiation from soot particles that have been heated to near-vaporization temperatures by a repetitively pulsed laser. We use a pulsed Nd:YAG laser, frequency-doubled to 532 nm, with a 10 ns pulse width and a 10 Hz repetition rate. We use laser intensities of ~10 MW/cm^2 or less to achieve negligible mass loss due to particle vaporization. During the laser pulse, the soot particles are rapidly heated by absorption to temperatures in the vicinity of 4000 K, resulting in intense thermal radiances which are much brighter than the ambient flame. Following cessation of the laser pulse, the particles cool very rapidly (~10^9 K/s), primarily via a combination of vaporization mass loss and conductive cooling by the surrounding gas, resulting in a rapid decay of the thermal emission intensity. These cooling rates are strongly dependent upon particle size. If the mass loss due to vaporization is minimal, then the magnitude and decay rate of the incandescent emission can be used to probe the soot concentration and particle size, respectively.

A detailed treatment of the LII phenomena must consider the disparate effects of simultaneously observed large and small particle sizes on the heating and cooling rates and on the spectral behavior of the emission. However, for LII observations of flame-generated soot at visible and infrared wavelengths, the mean particle sizes are usually small enough, and the size distributions are narrow enough, that these effects are not observable. For example, in our observations of the spectral distributions of LII following cessation of the laser pulse, we observe continuum spectra which conform well to single radiometric temperatures and near-Rayleigh-limit particle sizes, as shown by the curvefits in Figure 1. The radiance from a field of soot particles at a given temperature is

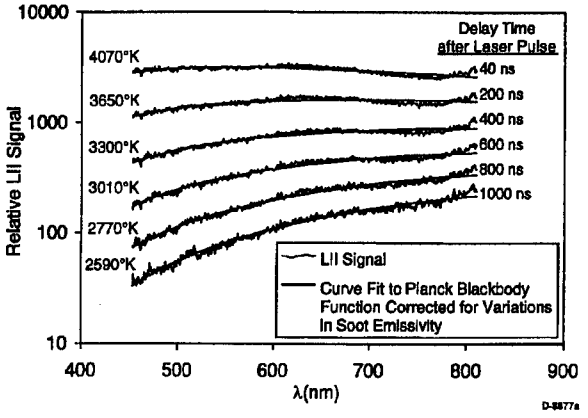


Figure 1. LII spectra at various delay times (ethylene/air diffusion flame)

$$I = (1 - \exp(-\sigma_a[C]z))N_{\lambda,T} \tag{1}$$

where σ_a is the volumetric soot absorption cross section (wavelength dependent), [C] denotes soot concentration, z is the depth of field of the emission measurement, $N_{\lambda,T}$ is the Planck blackbody function, and the emissivity term in parentheses reduces to the linear form at low soot concentrations. For typical flame-generated soot particle size distributions, i.e. mean radii of 20-40 nm and log-normal width parameters of ~0.5 or less, $\sigma_a(\lambda)$ at visible and infrared wavelengths is reasonably well described through Mie calculations using published indices of refraction. That is, the deviation from size-independent volumetric absorption is small, and absorption and emission are insensitive to shape effects in this regime. Thus measurements of the absolute radiance, I, can be used to determine the soot concentration (or volume fraction), provided the temperature is also known.

As illustrated in Figure 1, the radiometric temperature at a given time can be determined from the spectral distribution over a range of wavelengths. Similarly, T can be determined from measurements at just two wavelengths, simply by taking the ratio of I_1/I_2 from Eq. (1):

$$T = \frac{C}{\ell n\left\{\left(I_1\sigma_2/I_2\sigma_1\right)\left(\lambda_1/\lambda_2\right)^5\right\}}\left(1/\lambda_2 - 1/\lambda_1\right) \tag{2}$$

where C = 14388 μm·K. Differentiation of Eq. (2) shows that the radiometric temperature determination is quite insensitive to moderate uncertainties in the ratio of the soot cross sections at the two wavelengths. Thus the dual-wavelength approach provides a measure of the path-averaged temperature-versus-time profile, as well as of the absolute soot concentration, through application of Eqs. (1) and (2).

A schematic of our dual-wavelength laboratory setup is illustrated in Figure 2. We have chosen 469 and 750 nm for the two wavelengths, which are defined by narrow-band interference filters. Through use of fast-response photomultiplier tubes, we can observe the LII rise and decay with 2 ns time resolution. Typical dual-wavelength LII data are shown in Figure 3, and the corresponding particle temperature profile is shown in Figure 4.

3. Particle Sizing

Inversion of the LII profiles to determine detailed particle size distributions is difficult, especially considering our observation that the radiation at any given time can be described by a single, path-averaged temperature. However, the observed cooling rates can be used to infer an "effective" particle size, which is near the mean size of a log-normal distribution. At early times, the particle cooling rates are dominated by vaporization effects, which are difficult to quantify with an accurate thermophysical model. Indeed, our time-resolved data in this regime disagree markedly with a commonly used Clausius-Clapeyron based model of the vaporization heat and mass loss. However, at temperatures below ~3500 K, the dominant cooling mechanism is conductive cooling by the surrounding gas, which can be accurately described by classical fluid dynamics formulations. For atmospheric pressures, the mean free path is much larger than the particle size, and the conductive heat loss is well described by spherical molecular flow heat transfer. This results in an expression for cooling rate, dT/dt, which is inversely proportional to particle diameter. This predicted behavior matches well with our observations, and fitting of the dT/dt versus T data in the conductive cooling regime provides an estimate of the "effective" particle size. For a log-normal distribution, this "effective" size is intermediate between the mean size and D_{30} values determined by light scattering techniques.

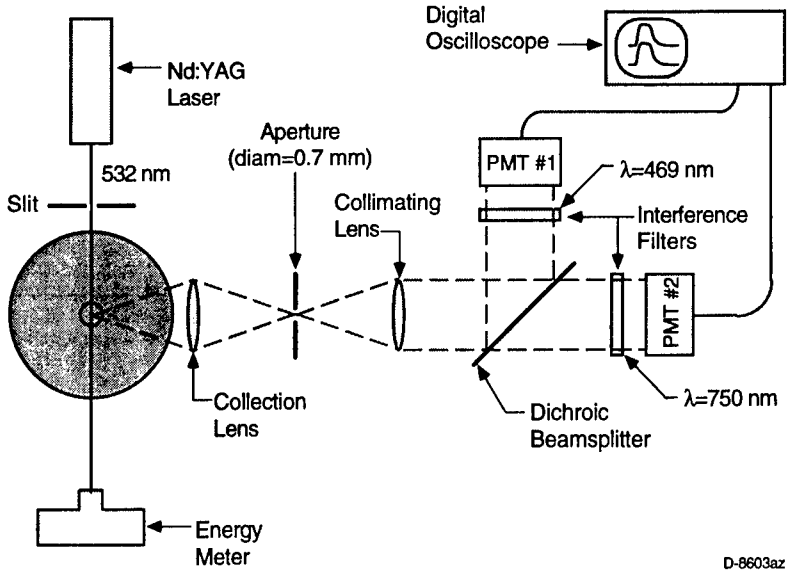


Figure 2. Experimental setup for high-speed dual-wavelength LII detection in a laboratory flame.

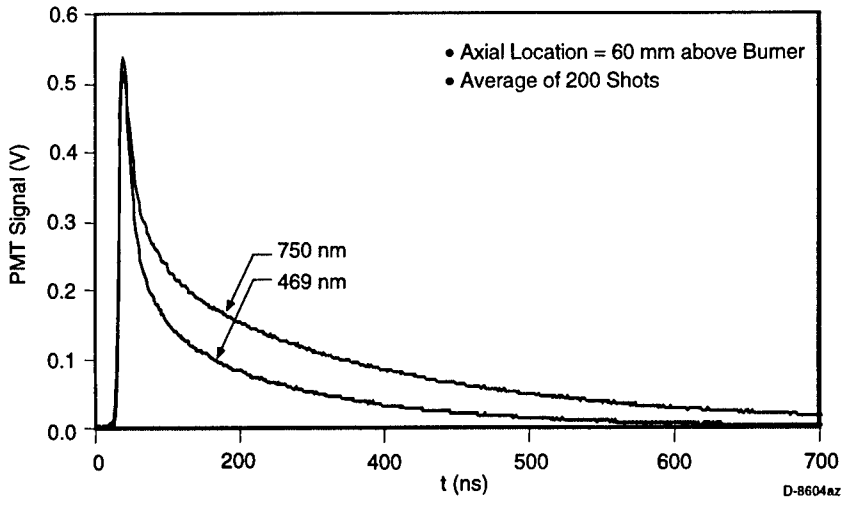


Figure 3. Dual-wavelength LII signal vs time (ethylene/air diffusion flame)

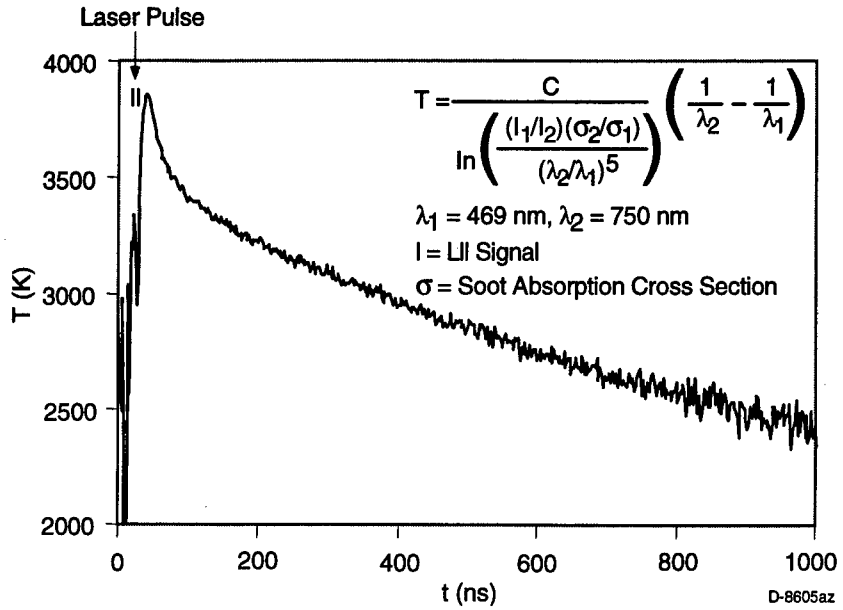


Figure 4. LII particle temperature versus time, from the data in Figure 3.

4. The PSI LII Instrument

We have developed a portable instrumentation package consisting of a Big Sky pulsed Nd:YAG laser, a fiber-coupled dual-wavelength photometer, and a computer controlled data acquisition system. The photometer consists of two bandpass-filtered photomultipliers and a fast-response digital oscilloscope. LII signals acquired by the oscilloscope are read, processed, and displayed in real time by the computer. The detector fields of view are nearly co-aligned with the laser beam to provide maximum viewing volume and sensitivity. The absolute responsivities of the two detectors are calibrated using a blackbody, and have been verified in soot concentration measurements in a laboratory flat flame using a co-aligned HeNe laser extinction diagnostic. In the laboratory flame, we have observed soot concentrations ranging from ~3 to ~1 × 10^{-4} g/m^3 (volume fractions of 1.5 × 10^{-6} to 5 × 10^{-11}). Measurements on the flame tube test rig will address the effects of window transmission and practical facility operations, as well as the effects of elevated pressures on the particle sizing analysis.

Acknowledgement

This work was sponsored by the NASA Glenn Research Center under Contract NAS3-97032.

A SIMPLE TWO-ANGLE LASER-SCATTERING TECHNIQUE FOR CHARACTERIZATION OF SOOT IN FLAMES

Umit O. Koylu
Department of Mechanical Engineering
Florida International University
Miami, FL 33174
E-mail: koyluu@eng.fiu.edu

Introduction

It is of technological interest to understand the factors governing the complex soot processes in combustion systems. This goal can be accomplished if soot can be fully characterized using reliable diagnostic techniques that are capable of yielding all the particle/aggregate parameters. Unfortunately, most studies in the literature mainly report soot volume fraction, f_v, and/or equivalent radius, R_{eq}. Generally, such nonintrusive data are obtained from the analysis of either extinction/scattering measurements based on unsuitable spherical models or the recently developed laser-induced incandescence technique. Although these findings are useful, they give an extremely limited insight into the underlying mechanisms for various soot processes, such as nucleation, growth, aggregation, and oxidation. This can be appreciated by realizing that both f_v and R_{eq} are not fundamental quantities for describing soot phenomena. For example, the soot volume fraction is the product of primary particle (spherule) volume and number density, i.e., $f_v = (4\pi a^3/3)n_p$. Although a and n_p are directly associated with the soot growth and nucleation processes respectively, f_v alone cannot provide a fundamental understanding of each of these processes as it only represents an overall effect. A similar discussion also holds for the volume-equivalent soot radius. Considering that $R_{eq} = N^{1/3}a$ (N is the number of soot spherules per aggregate), it is clear that such an inadequate approach is unable to separate the effects of aggregation and growth processes, as respectively indicated by the parameters N and a.

For a comprehensive treatment of soot-containing flames, the proper analysis of in situ optical experiments has been established by various investigators [1-6] based on the Rayleigh-Debye-Gans scattering theory. By accounting for the aggregate morphology, this analysis method can yield all the soot parameters of interest, i.e., spherule radius, particle number density, fractal dimension, and aggregate size distribution. However, this elaborate inverse technique is generally applicable when multi-angle scattering data are available, e.g., at every 10° between 20° and 160°. Such measurements are both time-consuming and complicated, and may not be feasible in some combustion environments, such as the forced laminar and non-premixed turbulent flames that are currently under investigation in this laboratory. Thus, in order to reduce the experimental efforts significantly, the main objective of the present study is to simplify optical diagnostics by exploring the feasibility of soot characterization from only two-angle (dissymmetry) light-scattering (LS) measurements.

Assumptions

Classical determination of fractal dimension, D, involves the best-fit slope of relative LS measurements at large angles. D defines how the number of spherules in an aggregate, N, varies statistically with aggregate radius of gyration, R_g, i.e., $N = k_g (R_g/a)^D$, where k_g is the fractal prefactor. After extensive in situ LS measurements as well as ex situ thermophoretic sampling/transmission electron microscopy (TS/TEM), D and k_g of soot aggregates have been established as universal properties. In fact, they are found to be remarkably insensitive not only to flame conditions and fuel type but also to particle

chemical composition (see [7] and references cited therein). Therefore, we will use $D = 1.8$ and $k_g = 2.2$, which appear to represent a wide range of combustion-generated aggregates.

The previous in situ analysis [6] inferred aggregate size distribution, pdf(N), by fitting a log-normal distribution to the entire relative angular scattering pattern. First, many aerosols reasonably follow a self-preserving size distribution that gives a geometric width of $\sigma_N = 2.3$. Because this value is also in good agreement with the values found for soot aggregates [3-6], it will be directly used during our interpretation of LS measurements for mean aggregate size. Second, Sorensen et al. [3] pointed out that an exponential scaling distribution represents the cluster-cluster aggregation process in flames better than log-normal distribution, which may fail for moments higher than the second. Consequently, we will improve the scattering analysis by considering a scaling distribution with $\sigma_N = 2.3$.

Optimum Scattering Angles

A scaling aggregate size distribution, together with the above fractal properties, eliminates the need to make multi-angle LS experiments, which are required to determine only D and σ_N. Then, the important question arises: What are the optimum scattering angles?

This important issue can be addressed by using a simple sensitivity analysis of dissymmetry ratio, $R_{vv} = K_{vv}(\theta)/K_{vv}(180-\theta)$, to aggregate size, $x_a = 2\pi R_g/\lambda$, as illustrated in Fig. 1. As can be seen, R_{vv} is somewhat sensitive to x_a for small aggregates ($R_{vv} \rightarrow 1$), implying a need for better measurement accuracy for the classical determination of radius of gyration. On the other limit of large aggregates, the dissymmetry ratio cannot discriminate for x_a as R_{vv} saturates to $[\sin((180-\theta)/2)/\sin(\theta/2)]^D$. Furthermore, the region in which R_{vv} is extremely sensitive to x_a broadens as θ is decreased. These observations clearly suggest that the dissymmetry measurements become more sensitive to aggregate size when the two scattering angles are further separated from each other. Thus, optimum scattering experiments should include the minimum and maximum angles, say typically 20° and 160°. This will generally ensure the reliable inferral of mean aggregate size as the aggregation process continues with residence time in flames.

Two-Angle LS Analysis

The following interpretation method is based on the measurements of scattering coefficients at two angles of $\theta_1 = \theta$ and $\theta_2 = 180-\theta$, $K_{vv}(\theta_1)$ and $K_{vv}(\theta_2)$, and extinction coefficient, K_{ext}. In the general case of $\exp[D(1-r^2)/2] < R_{vv} < r^D$, where $r = \sin(\theta_1/2)/\sin(\theta_2/2)$, soot parameters can be obtained as follows:

(i) Spherule radius, a, from the ratio of scattering coefficient at θ_2 and extinction coefficient,

$$a = \frac{\lambda}{2\pi}\left\{4\pi\frac{E}{F}\frac{K_{vv}(\theta_2)}{K_{ext}}\frac{[2\sin(\theta_2/2)]^D}{k_g}\right\}^{1/(3-D)}$$

(ii) Once $x_p = 2\pi a/\lambda$ is determined from the above equation, particle number density, n_p, from the absolute value of scattering at θ_2,

$$n_p = K_{vv}(\theta_2)\frac{k^2}{x_p^6 F}\frac{[2x_p\sin(\theta_2/2)]^D}{k_g}$$

(iii) Mean aggregate size, $\overline{N}$, can be solved from the following expression related to the dissymmetry ratio,

$$R_{vv}(\theta) = \frac{\overline{N}^2}{\overline{N}}\frac{(q_2 a)^D}{k_g}\left[1-\frac{(q_1 a)^2}{3k_g^{2/D}}\frac{\overline{N}^{2+2/D}}{\overline{N}^2}\right]$$

Because the exponential scaling distribution function gives the ratio of various moments as $\overline{N}^2/\overline{N} = 2\overline{N}$ and $\overline{N}^{2+2/D}/\overline{N}^2 \cong 3.5\overline{N}^{2/D}$ for $D = 1.8$, mean radius of gyration, $\overline{R}_g$, can be alternatively obtained from

$$R_{vv}(\theta) = 2(q_2\overline{R}_g)^D\left[1-\frac{3.5}{3}(q_1\overline{R}_g)^2\right]$$

In the above formulation, λ is the wavelength of light source, $k = 2\pi/\lambda$, $q = 2k\sin(\theta/2)$, and E and F are functions of the soot refractive index.

Sometimes, the general case given above may not be satisfied if one of the angles does not correspond to the Guinier or power-law scattering regime. Such extreme experimental conditions may be encountered when aggregates are either very small (e.g., lightly sooting flames) or very large (e.g., heavily sooting flames). In these two special cases of $1 < R_{vv} < \exp[D(1-r^2)/2]$ and $R_{vv} = r^D$, measurements at a lower or higher wavelength may be necessary. Note that this should not be viewed as a shortcoming of the present two-angle LS analysis as the same issue is also pertinent to the multi-angle method.

Preliminary Implementation

The above-outlined simple particulate diagnostic was applied to the LS data reported in Ref. [5] for a laminar non-premixed ethylene flame. For this particular experiment with an Ar^- laser ($\lambda = 514.5$ nm), the absolute scattering and extinction measurements yielded $K_{vv}(\theta_1 = 20°) = 3.4 \times 10^{-3}$ cm^{-1}sr^{-1}, $K_{vv}(\theta_2 = 160°) = 0.7 \times 10^{-3}$ cm^{-1}sr^{-1}, and $K_{ext} = 0.2$ cm^{-1}. Under such typical flame conditions, $r = \sin(10°)/\sin(80°) = 0.176$ such that $\{\exp[D(1-r^2)/2] = 2.4\} < \{R_{vv}(20°) = K_{vv}(20°)/K_{vv}(160°) = 4.9\} < \{r^D = 22.7\}$ for $D = 1.8$, justifying the use of the general case discussed before.

The results of such a two-angle LS analysis, with an exponential scaling distribution of $\sigma_N = 2.3$ and a soot refractive index of $E = 0.23$ and $F = 0.18$, are summarized in Table 1. The multi-angle LS interpretation of Ref. [6] and independent TS/TEM observations of Ref. [5] are also included in the table for comparison. Verifying its application, this preliminary implementation of the present method yields spherule radius, a, particle number density, n_p, and soot volume fraction, f_v, that are in excellent agreement with the detailed in situ and ex situ measurements. Although the mean aggregate size obtained from the proposed LS analysis is about 18% smaller due to a smaller geometric width, the agreement is still within experimental uncertainties of both in situ and ex situ methods.

Conclusions

1. A simple soot diagnostic method based on two-angle scattering and extinction measurements is proposed to infer spherule size, particle number density, and mean aggregate size.
2. A sensitivity analysis of dissymmetry ratio to aggregate size suggests optimum scattering angles to be minimum and maximum possible, e.g. 20° and 160°.
3. The feasibility of implementation of the present data analysis is demonstrated in a laminar flame in comparison to the detailed multi-angle scattering and independent sampling experiments.

With the significant reduction in experimental efforts, it now appears to be possible to conveniently use the powerful laser-scattering technique in complex combustion systems. Although these preliminary results are promising, further soot studies employing this in situ technique are needed in the near future.

Acknowledgments: This research was sponsored by NSF Grants CTS-9711954 and CTS-9876475.

References

1. R. A. Dobbins, R. J. Santoro, and H. G. Semerjian, *Twenty-Third Symposium (International) on Combustion*, The Combustion Institute, Pittsburgh, 1990, pp. 1525-1532.
2. P. A. Bonczyk and R. J. Hall, *Langmuir* 7: 1274-1280 (1991).
3. C. M. Sorensen, J. Cai, and N. Lu, *Appl. Opt.* 31: 6547-6557 (1992).
4. R. Puri, T. F. Richardson, R. J. Santoro, and R. A. Dobbins, *Combust. Flame* 92: 320-333 (1993).
5. U. O. Koylu and G. M. Faeth, *J. Heat Transf.* 116: 971-979 (1994).
6. U. O. Koylu, *Combust. Flame* 109: 488-500 (1996).
7. U. O. Koylu, Y. Xing, and D. E. Rosner, *Langmuir* 11: 4848-4854 (1995).

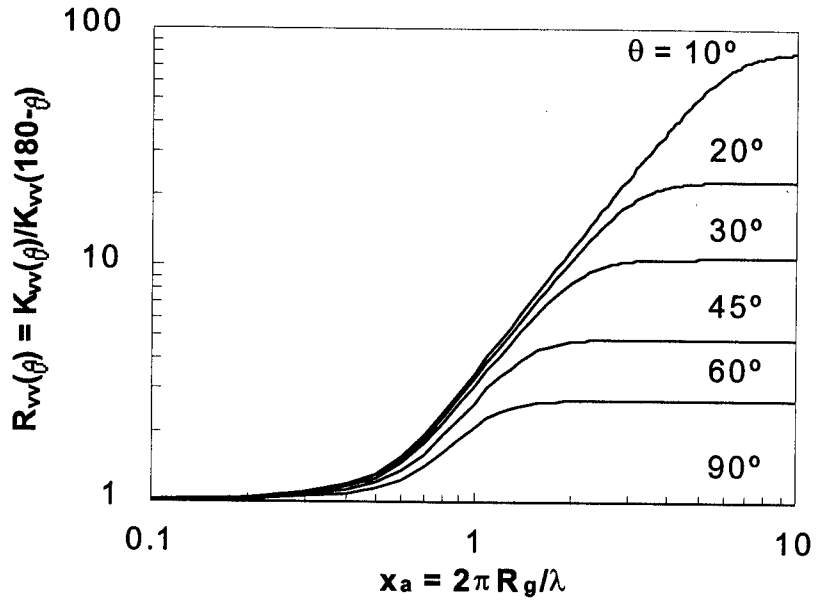


Figure 1. Optimum scattering angles from a sensitivity analysis of dissymmetry ratio vs. aggregate size.

Soot Parameter	Simplified Two-angle Scattering	Detailed Multi-angle Scattering	TS/TEM
a (nm)	10.6	10.4	10.5
n_p (cm^3)	4.7×10^{11}	4.8×10^{11}	—
f_v (ppm)	2.3	2.2	—
$\overline{R}_g$ (nm)	73	86	85
$\overline{N}$	71	86	83
σ_g	2.3	2.4	2.7
D	1.8	1.74	1.73

Table 1. Comparison of methods in a laminar non-premixed flame.

The Shock Tube as a Device for Examining Particulate Emissions from the Combustion of Alternative Diesel Fuels

J. L. Graham*, D. C. Kirk, R. C. Striebich, and S. S. Sidhu
University of Dayton Research Institute, 300 College Park, Dayton, OH 45469-0132, USA,
*grahamjl@udri.udayton.edu

Abstract

Airborne particulate pollution has emerged as a global problem. In time-series analyses the concentration of fine particles in the atmosphere has been proved to correlate with illness and mortality [1]. Motor vehicle emissions are considered a major anthropogenic source of air pollution. Although compression ignited engines produce less total engine emissions than spark ignited engines, they form large quantities of fine particulate matter. Field studies in various urban areas have indicated that diesel powered vehicles are major source of suspended particulate matter [2,3]. These particulate matter emissions are particularly noticeable under high load conditions when the fuel-to-air ratio is increased and local pockets of poor mixing result in a pyrolytic reaction that initiates particulate matter formation [4]. It is estimated that in the United States diesel powered vehicles produce 10^{11} gram soot annually. The main constituents of diesel particles are elemental (EC) and Organic (OC) carbon. Diesel particles contain several carcinogenic substances, such as polycyclic aromatic hydrocarbons, and thus pose health risks for humans and animals [5]. The submicron diesel particles also affect urban visibility by dominating the absorption of solar light because of their high EC to OC emission ratios [6]. These small airborne particles with diameters less than 2.5 μm have a high probability of deposition deep in the respiratory tract and are likely to trigger or exacerbate respiratory diseases [7]. It is also well documented that fine particles that have a mass median diameter of <2.5 μm can initiate lung tumors and result in mortality increases in population [8].

The chemical makeup of the small particles seems to be responsible for tumors, however, the identity of responsible mutagens is not known. Initially, bacterial-based mutagenicity essays of extracts of particulate matter indicated that PAHs and nitro-PAHs were responsible for nearly all the mutagenic activity of the extracts [9]. However, recent findings have emphasized that perhaps it is the semi-polar oxy-PAHs that are responsible for most of the mutagenic activity [10]. In either case, the actual chemicals responsible for most of the health affects that has led EPA to propose tough new standards are not known. These EPA standards have led to use of mono-ester-diesel fuels (bio-diesel) and other alternative diesel fuels as a passive control strategy for reducing particulate matter emissions [11,12]. Even though these alternative fuels have demonstrated decreased total hydrocarbon emissions the level of soluble organic fraction (SOF) associated with total particulate matter has increased [13]. This increase in SOF raises concerns about the overall toxicity of particles formed during combustion of alternate diesel fuels. However, there is only limited and somewhat contradictory information available concerning the health effects of particulate emissions from diesel engines using alternate diesel fuels.

The development of alternative diesel fuels is being driven by the need to reduce the environmental impact of emissions and not engine performance. However, the conventional protocol for evaluating new fuels is to sample the exhaust of a test engine running with the new fuel. Modifications are usually required to the test engines (fuel injection, timing, air/fuel ratio, etc.) for each fuel and may not necessarily represent optimal performance for any particular fuel. This procedure is expensive, time consuming, and the comparison of emissions is complicated by the changes made to the test engine to accommodate each fuel. Consequently, there is a need for a relatively simple test protocol for evaluating the emissions from alternative diesel fuels.

The University of Dayton Research Institute (UDRI) has been investigating the organic emissions (volatile and particulate) from a conventional diesel fuel (D2) and 3 alternative diesel fuels (compressed natural gas, dimethyl ether, bio-diesel) using a versatile single pulse reflected shock tube. The shock tube is ideally suited for this task as it can easily generate the high pressure and temperature environment of a CI engine, typically 750-1,000 C and 20-50 atm.[14] This allows different fuels to be exposed to identical combustion conditions representative of the full range of temperatures and pressures which may be experienced in a diesel engine. The UDRI system, shown in Figure 1, includes provisions for studying light fuels as premixed vapors, or injecting low vapor pressure fuels as liquids. The shock tube itself comprises a 7.6 cm ID by 2.74 meter long driver section, a 5.08 cm ID by 2.75 meters long driven section, and a 5.08 cm ID by 0.9 meter long test section. The system also includes a 30.5 cm ID by 61 cm long dump tank and an evacuation subsystem. The driven and test sections are connected through a pneumatic ball valve controlled through the system's automatic digital firing system. The dump tank is connected to the system through a manually operated ball valve. The entire structure is fabricated from 1.27 cm thick 304 stainless steel.

Light gaseous fuels (CNG and DME) were prepared as premixed gases in air within the shock tube's test section with the pneumatic isolation valve closed. This valve is opened by the automatic fire control system just

prior to rupturing the diaphragm and closes approximately 0.5 s afterwards sealing the combustion products in the test section. Liquid fuels (D2 and bio-diesel) are introduced using a Bosch diesel fuel injector fitted with a single stroke positive displacement fuel pump. The pump delivers a small volume (50μl) of fuel in a precisely timed manner and in a narrow spray pattern that does not impinge on the walls of the tube. The fuel is introduced 500μs behind the reflected shock which allows for the vibrational relaxation of the bath gas prior to injecting the fuel. As with the gaseous fuels, the fire control system closes the test section isolation valve approximately 0.5 s afterwards sealing the combustion products in the test section.

For the collection of combustion products the test section is fitted with two high volume particulate samplers in series and 20 L Tedlar sample bags as shown in Figure 1. Immediately following each test, the isolation valve is closed, the exhaust valve to the sampling system is opened, and the test section is purged with 20 L (10 change-volumes) of dry helium. As the gas is swept from the system the high volume samplers collect the particulate fraction on glass fiber filters (GFF), while the volatile gases are captured in the Tedlar bag. The bag is then removed and evacuated through an sorbent trap packed with 60/80 mesh Tenax TA, thereby collecting the volatile organic fraction of the exhaust. The GFFs were weighed before and after each test to gravimetrically measure the mass of particulate formed. The GFFs and sorbent traps were then spiked with deuterated internal standards and individually analyzed via thermal desorption gas chromatography mass spectrometry (GC/MS). The collected particulates were also examined by scanning electron microscopy and bulk carbon analysis.

As an example consider the results are shown in Figures 2-5 which summarize the detailed analysis of the exhaust emissions from CNG. These are shown as an example of the results from a gaseous fuel. Specifically, CNG was prepared as a premixed gas in dry air with an equivalence ratio of 3. Data was initially obtained at a pressure of 24 atm and temperatures from 700 to 1400 C. From these tests a nominal temperature of 880 C was selected for detailed chemical analysis of the exhaust.

Bulk analysis of the collected particulate includes total mass, examination by scanning electron microscopy (SEM), and carbon analysis. With respect to carbon mass, CNG gave a total carbon yield of 0.30% (mass particulate/mass fuel) which compares with yields within the range of 0.25 to 0.61% obtained from propanol combustion under similar conditions.[15] The SEM photograph given in Figure 2 shows the particulate from CNG consists of a fleece-like material composed of smaller components which are estimated to be less than 0.1μm in mean diameter. This is in general agreement with diesel emission data.[16] The results from the bulk carbon analysis from CNG is given in Figure 3. The first three events centered at approximately 80, 170, and 250°C indicate the regions where organic material is evolving from the filter. The last transition is typical of the burn-off from elemental carbon. This suggests a major fraction (70%) of the collected material is high molecular weight material mainly elemental carbon. This result is consistent with the diesel emission data that shows that non-elemental carbon fraction or solvent extractable organic components of diesel aerosol represents 5-40% of particulate mass depending on the fuel and operating conditions.[16-18]

The detailed chemical analysis of the exhaust from CNG is summarized in Figures 4 and 5. These Figures show the GC/MS analysis of the volatile organic fraction collected in the Tedlar sample bags the nonvolatile fraction thermally desorbed from the GFFs, respectively. These traces illustrate the exhaust samples are a complex mixture of organic species spanning a considerable range of molecular weights and structural complexity. Briefly, these figures show a progression from the single ring compounds (benzene, toluene, styrene, etc.) to the first two and three ring structures (indene and acenaphthalene) in the gas-phase samples to the first four ring structures (pyrene and fluoranthene) observed from the particulate material on through five and six ring structures (benzopyrene and indenopyrene).

In summary, the single pulse reflected shock tube is ideally suited as a screening tool to examine the emission characteristics of alternative diesel fuels. Specifically, this technique can expose gaseous or liquid fuels to conditions comparable to those in a CI engine. Most importantly, however, is it can expose fuels to identical conditions of temperature and pressure allowing for an unambiguous comparison of the yields and speciation of emissions. The authors will present a summary of data from the ongoing work with CNG, DME, D2, and bio-diesel, illustrating the general versatility of the shock tube technique for both gaseous and liquid fuels. Future work will extend the present exposure conditions from the 20-30 atm reported here to 50-60 atm, which is more representative of heavy duty diesel engines. Furthermore, because of the highly complex nature of chromatograms, multidimensional gas chromatographic-mass spectrometric (MDGC-MS) analysis will be employed for future samples. This detailed analysis of particulate matter samples should help provide more information concerning the potential health effects of alternative diesel fuels.

References

1. D. W. Dockery, A. Pope, X. Xu, J. D. Spengler, J. H. Ware, M. E. Fay, B. G. Ferris, and F. E. Speizer, N. Engl. J. Med., 329, 1753-1759, 1993.
2. C. Venkataraman and S. K. Friedlander, Env. Sci. & Technol., 28, 563-572, 1994a.
3. R. M. Harrison, A. R. Deacon, and M. R. Jones, Atmos. Environ., 31, 4103-4117, 1997.
4. K. Kageyama and N. Kinehara, SAE Paper No. 820181.
5. R. McClellan, Am. Ind. Hyg. Assoc., 47, 1-13, 1986.
6. R. S. Hamilton and T. A. Mansfield, Atmos. Environ., 25A, 715-723, 1991.
7. L. Rantanen, S. Mikkonen, L. Nylund, P. Kociba, M. Lappi, and N. -O. Nylund, SAE Paper No. 932686.
8. N. Y. Kado, G. N. Guirguis, C. P. Flessel, R. C. Chan, X. -I. Chang, and J. J. Wesolowski, Environ. Mutagenesis, 8(53), 195, 1986.
9. H. Tokiwa, R. Nakagawa, K. Morita, and Y. Onishi, Mutation Res., 85, 195, 1981.
10. J. L. Durant, A. L. Lafleur, E. F. Plummer, K. Taghizadeh, W. F. Busby, Jr., and W. G. Thilly, Environ. Sci. & Technol., 32(13) 1894-1906, 1998.
11. J. F. McDonald, D. L. Purcell, B. T. McClure, and D. B. Kittelson, SAE Technical Paper No. 950400, Warrendale, PA, 1995.
12. D. L. Purcell, B. T. McClure, J. McDonald and H. N. Bausu, Am. Oil Chem. Soc., 73, 381, 1996.
13. K. Schmidt and J. Van Gerpen, SAE Technical Paper No. 961086, Warrendale, PA, 1996.
14. L.V. Armstrong, J.B. Hartman, *The Diesel Engine, its Theory, Basic Design, and Economics*, the Macmillan Co., New York, New York, 1959.
15. R. Wang and P. Cadman, Combustion and Flame, 112, 359, 1998.
16. L. Morawska, N. D., Bofinger, L. Kocis, and A. Nwankwoala, Env. Sci. Technol., 32, 2033, 1998.
17. W. R. Pierson and W. W. Brachaczek, Aerosol Sci. Technol., 2, 1, 1983.
18. A Laresgoiti, A. C. Loos, and A. S. Springer, Env. Sci. Technol., 11, 973, 1997.

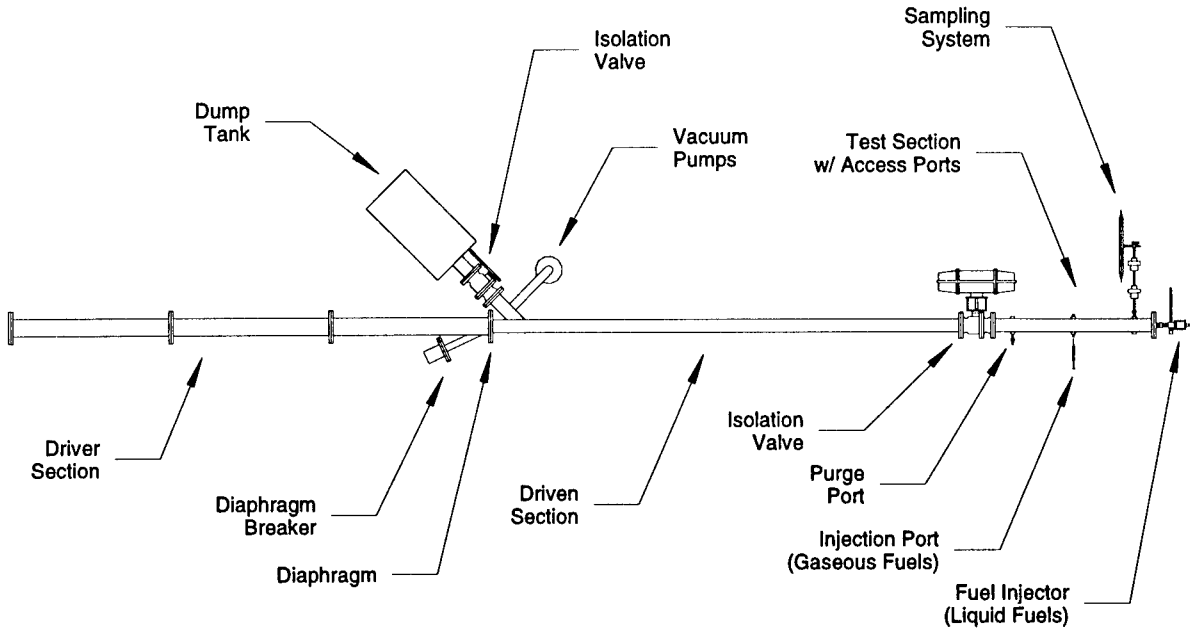


Figure 1. General schematic of the UDRI shock tube configured for particulate and exhaust gas sampling.

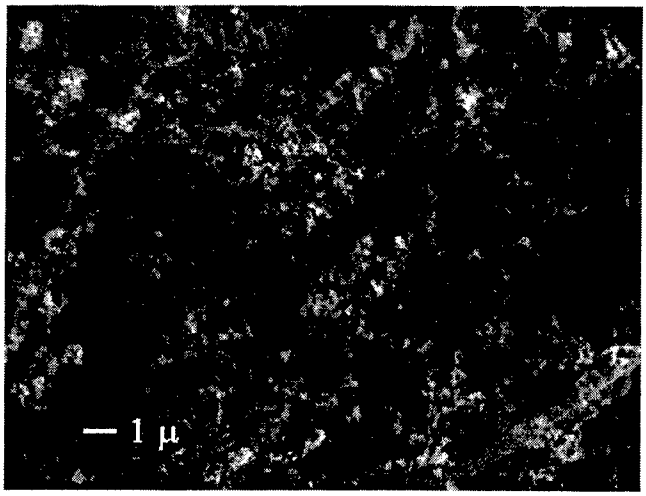


Figure 2. Electron micrograph (10,000x) of particulate collected from CNG exposed to 880C and 24 atm in air.

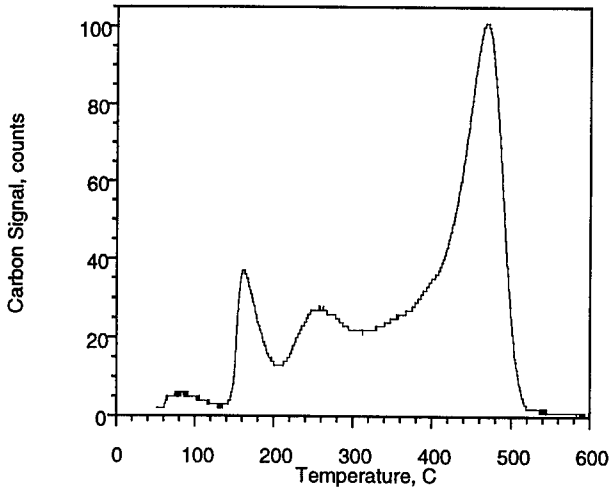


Figure 3. Bulk carbon analysis of particulate collected from CNG exposed to 880C and 24 atm in air.

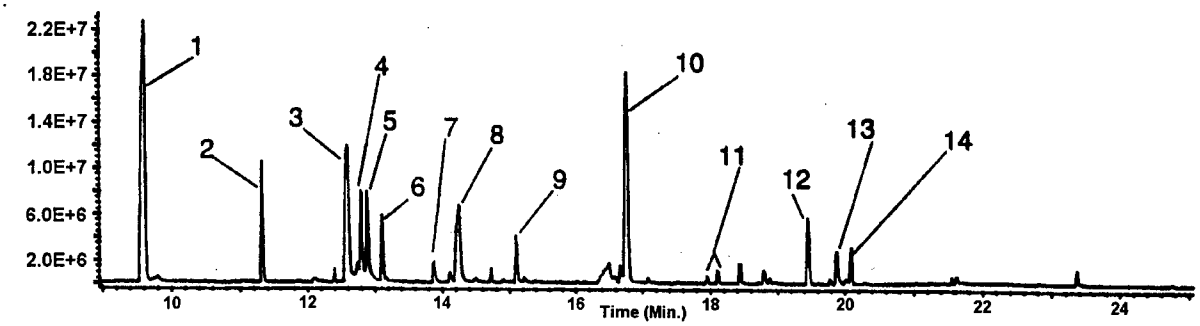


Figure 4. GC/MS data for the organic gaseous emissions from CNG exposed to 880C and 24 atm in air. 1) Benzene, 2) Toluene, 3) Dimethyl Acetamide, 4) d_{10}Xylene (int. std.), 5) Ethyl Benzene, 6) Styrene, 7) Benzaldedyde, 8) Phenol, 9) 2H-Indene, 10) Naphthalene, 11) Methyl Naphthalene, 12) Acenaphthalene, 13) Substituted Ethenyl Benzene, 14) Column Bleed.

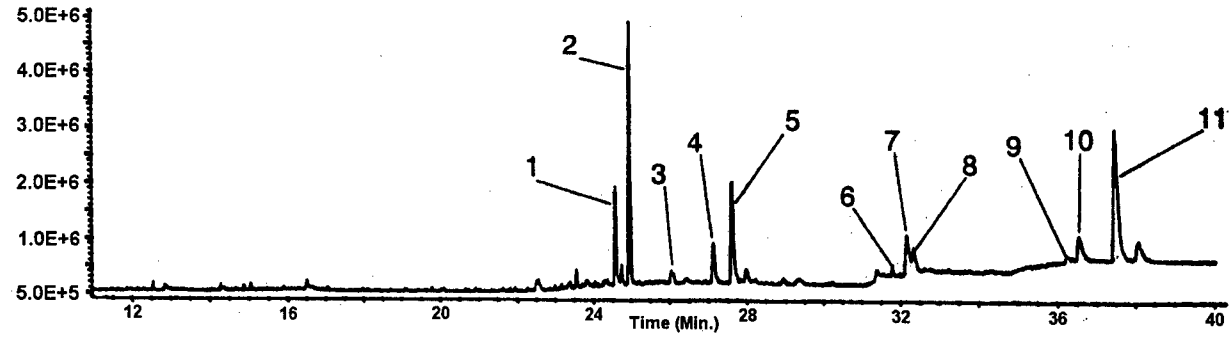


Figure 5. GC/MS data for the organic particulate emissions from CNG exposed to 880C and 24 atm in air. 1&2) Pyrene/Fluoranthene, 3) Methyl Pyrene, 4&5) Benzofluoranthene, 6) Unknown, 7&8) Benzo(e)pyrene, 9-11) Indeno(1,2,3-c,d)pyrene

EXPERIMENTAL STUDY OF NONFUEL HYDROCARBONS AND SOOT IN COFLOWING PARTIALLY PREMIXED ETHYLENE/AIR FLAMES

Charles S. McEnally and Lisa D. Pfefferle
Department of Chemical Engineering and Center for Combustion Studies
Yale University, PO Box 208286, New Haven CT 06520-8286
charles.mcenally@yale.edu; pfefferle@biomed.med.yale.edu

An extensive set of experimental measurements have been made in axisymmetric coflowing nitrogen-diluted ethylene/air partially premixed flames. The ethylene and nitrogen flowrates (220 and 500 cm^3/min) were held constant, while varying amounts of primary air were added to the fuel to produce six flames with primary equivalence ratios (Φ) of ∞, 24, 12, 6, 4, and 3. In each flame centerline profiles were measured of: temperature with thermocouples; major species, acetylene, methane, and formaldehyde with an electron-impact/quadrupole mass spectrometer (EQMS); formaldehyde with laser-induced fluorescence (LIF) excited at 355 nm; C2 to C12 hydrocarbons with a photoionization mass spectrometer (PTMS); PAH fluorescence with LIF excited at 355 nm; soot volume fraction with laser-induced incandescence (LII); soot scattering; and OH radical concentration with LIF.

Selected profiles are shown in Figures 1-9. Several aspects of these results are noteworthy:

1. Partial premixing causes a large increase in oxygenated hydrocarbons such as formaldehyde (Figures 4 and 5) and (not shown) C_2H_2O, C_2H_4O, C_3H_4O, etc. For formaldehyde this increase is observed both in the mass spectrometric measurements, which require extractive sampling, and in the independent in situ LIF measurements.

2. Partial premixing also causes large increases in odd-carbon species such as methane and C_3H_4 (Figures 2 and 3). We attribute this to the increasing importance of reactions such as $C_2H_4 + O \rightarrow CH_3 + HCO$ and $C_2H_2 + O \rightarrow CH + HCO$, and subsequent reactions of the C1 products with C2 species.

3. Large increases are observed in benzene for Φ = 24 and 12 (Figure 6). Acetylene decreases for all Φ (Figure 1), while C4 species are increased only in Φ = 24 at most (not shown); thus the best explanation for the increase in benzene appears to be propargyl recombination.

4. The maximum PAH LIF concentrations scale closely with the maximum soot volume fractions, the peak of the PAH LIF always occurs at the initial appearance of soot, and the disappearance of PAH LIF always coincides with the peak of the soot volume fraction. These observations suggest that the fluorescing material is a direct precursor to soot.

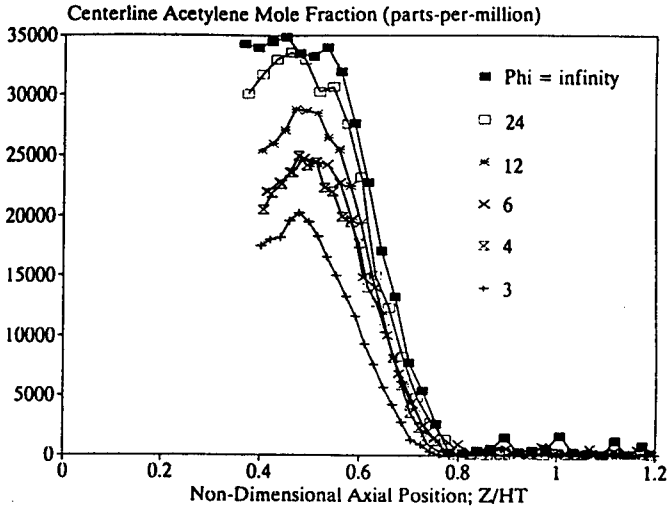


Figure 1. Acetylene mole fractions measured with the EQMS.

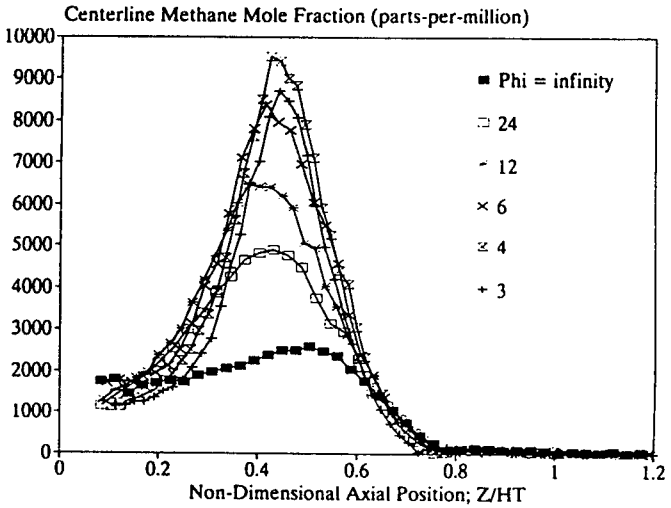


Figure 2. Methane mole fractions measured with the EQMS.

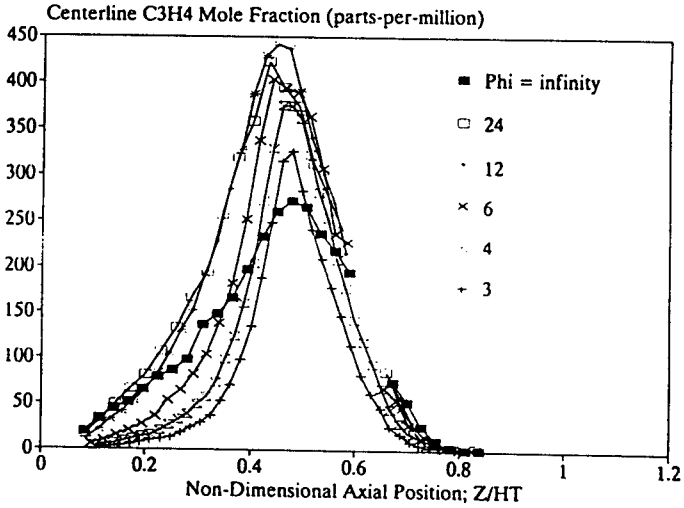


Figure 3. C_3H_4 mole fractions measured with the PTMS.

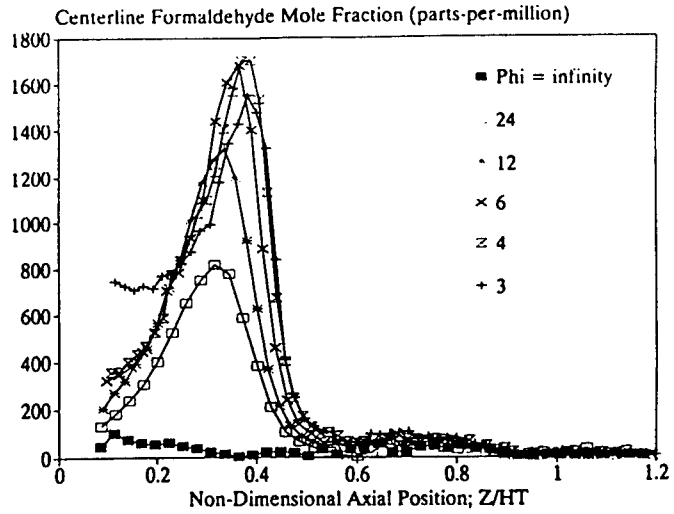


Figure 4. Centerline formaldehyde mole fractions measured with the EQMS.

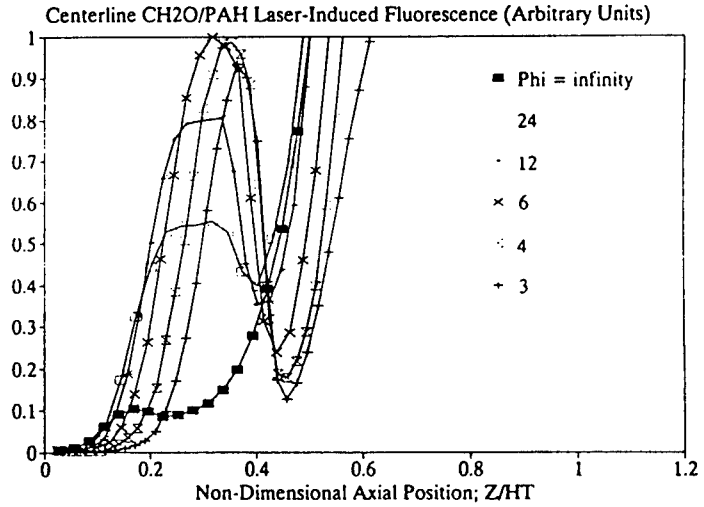


Figure 5. Centerline formaldehyde mole fractions measured with LIF.

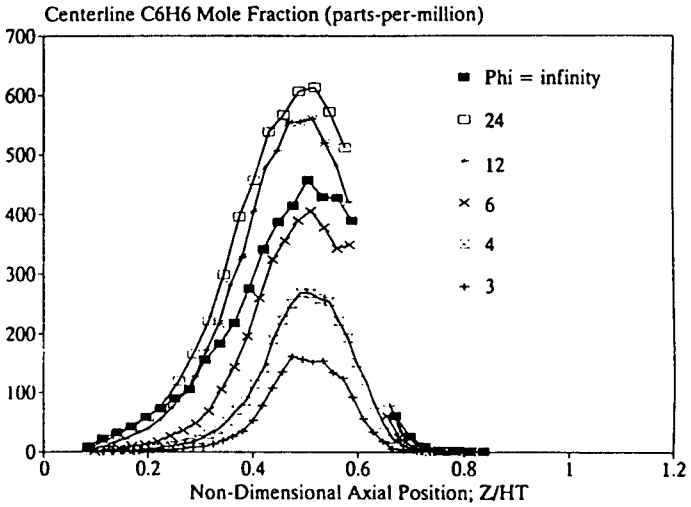


Figure 6. Centerline benzene mole fractions measured with the PTMS.

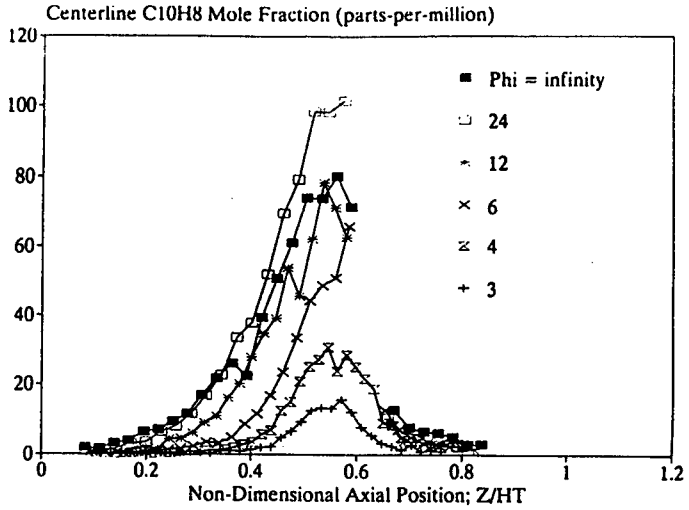


Figure 7. Centerline naphthalene mole fractions measured with the PTMS.

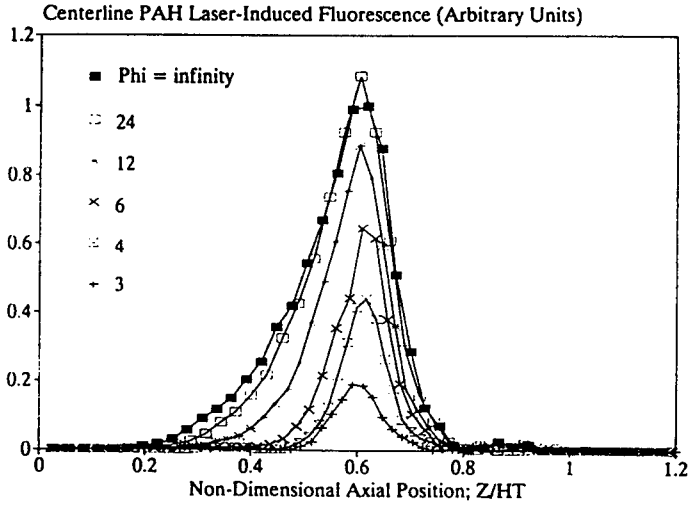


Figure 8. Centerline PAH concentrations measured with LIF.

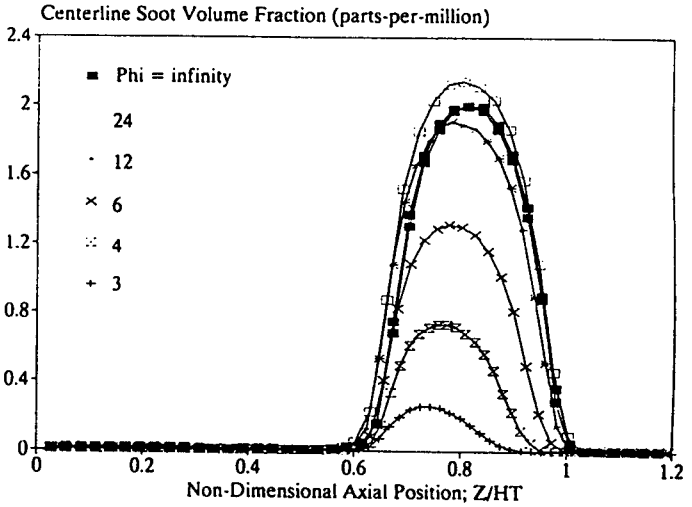


Figure 9. Centerline soot volume fractions measured with LII.

Sooting Characteristics of Normal and Inverse Diffusion Flames

C.R. Kaplan and K. Kailasanath
Laboratory for Computational Physics and Fluid Dynamics
Code 6410, Naval Research Laboratory
Washington, DC 20375
ckaplan@lcp.nrl.navy.mil
kailas@lcp.nrl.navy.mil

Introduction

The ability to control soot formation in nonpremixed combustion is critically important in industrial practice. In recent years, there have been several experimental and numerical investigations on the effects of hydrodynamics and stoichiometry on soot formation in coflowing and opposed jet diffusion flames. Lin et al. [1] experimentally studied the effects of flow properties on soot formation and oxidation in nonpremixed coflowing hydrocarbon-air flames, under conditions of reduced pressure, and showed that soot emissions may be almost entirely suppressed by increasing the air to fuel stream velocity ratio. They suggest the reason for the observed behavior is due to the direction of the soot particle motion with respect to the flame sheet. Other experimental studies have included the work of Wu and Essenhigh [2], who reversed the fuel and air ports of a laminar coflowing methane-air diffusion flame (i.e., the air stream is placed along the centerline axis). These "inverse" diffusion flames were essentially non-luminous with no carbon formation, and in some cases, particularly at higher fuel stream velocities, a luminous region formed as an orange-yellow cap on top of the blue cone-shaped flame. Others [3,4] have modified the direction of the soot particle motion relative to the flame sheet by changing the composition of the reactant streams, rather than by modifying the stream velocities. In this work, we use direct numerical simulations to gain insight into the effects of the flowfield configuration on soot formation in coflowing methane-air diffusion flames. In particular, we discuss the differences in sooting characteristics between a normal and inverse methane-air diffusion flame, and use the details from the simulation to explain those differences.

Results and Discussion

The numerical model solves the time-dependent, axisymmetric, reactive-flow Navier-Stokes equations coupled to submodels for soot formation and radiation transport. It has been described in detail previously [5, and references therein], and will only be briefly described here. The solution to the conservation equations includes both the radial and axial components of the convective and diffusive transport terms. All transport coefficients (viscosity, thermal conduction, and molecular diffusion) are composition- and temperature-dependent. The chemical reaction scheme is the "skeletal" mechanism for methane-air combustion [6], and includes 16 species and 35 reactions. Soot formation is modeled phenomenologically using the integrated soot model of Syed et al [7], and includes terms for nucleation, coagulation, surface growth, oxidation due to O_2 and OH, and thermophoresis. Radiation transport is included based on the assumption that the medium is optically thin.

In all cases, the inner annulus radius is 0.55 cm, the outer annulus radius (for the coflowing stream) is 5 cm, and there is a region of quiescent air from 5 cm to 10 cm radially. One case represents a normal coflowing diffusion flame, in which fuel flows from the inner annulus and air flows from the outer annulus, while the other case represents an inverse diffusion flame, with the air stream in the inner annulus and fuel stream in the outer annulus. In both cases presented here, $V_{fuel} = V_{air} = 10$ cm/s. Figure 1 shows OH mole fraction and soot volume fraction for the two cases, while Table 1 summarizes some of the significant differences in the sooting characteristics of these two cases.

The normal diffusion flame has the typical "wishbone-shaped" structure, in which the soot layer forms on the fuel-rich side of the stoichiometric surface (inside the flame sheet), and the peak soot volume fraction is 6.2e-7. The peak nucleation rates occur in the low- to mid-section of the annular region. Peak surface growth rates also take place in the annular region; but these peak surface growth rates begin at a higher elevation than the peak nucleation rate. The peak surface growth rate is approximately 500 times greater than the peak nucleation rate, which suggests that surface growth is the dominant route for soot formation. Oxidation due to OH is important near the top of the flame, as this is the region where the OH field overlaps with the sooting region (at lower heights in the flame, the OH field is outside of the sooting region). Oxidation due to O_2 occurs in two regions: these rates are low at the lower elevations in the flame,

and then become greater at higher elevations in the flame. Near the top of the flame, the O_2 and OH oxidation rates reach their peak values, however, the peak OH oxidation rate is an order of magnitude greater than the peak O_2 oxidation rate. By looking at the relative locations of the nucleation, surface growth and oxidation regions, the simulations indicate that soot formation takes place in sequential order; that is, nucleation occurs first, followed by surface growth, followed by oxidation, however, there is some overlap between the different creation and destruction processes.

The inverse diffusion flame is a very short, under-ventilated flame located close to the burner surface, and is qualitatively similar to the inverse flames studied by Wu and Essenhigh [2]. The sooting characteristics of inverse flames are vastly different from those of normal diffusion flames. The peak soot volume fraction is 3.6e-9, which is a factor of 200 lower than the normal diffusion flame with the same fuel and air flow rates. Peak number density is a factor of five lower than that for a normal diffusion flame. Soot does not form in an annular region like it does in normal diffusion flames. Rather, the sooting region sits on top of the inverse diffusion flame, which was also observed experimentally by Wu and Essenhigh [2]. This inverse flame emits soot, as shown in Fig. 1. The nucleation region is located immediately above the flame sheet, which is then followed by a region of surface growth. While the peak nucleation rates for inverse diffusion flames are slightly lower than those of normal diffusion flames, the peak surface growth rate in inverse flames is much lower than that for normal diffusion flames. This suggests that surface growth is more severely suppressed than nucleation in the inverse diffusion flame configuration, and this is evidenced by the fact that the soot volume fraction is 200 times lower than that for normal diffusion flames, while the number density is only five times lower.

In inverse flames, oxidation rates due to OH and O_2 are much lower than for normal diffusion flames. For these inverse diffusion flames, the peak O_2 oxidation rate is a factor of 10 greater than the peak OH oxidation rate. This is due to the fact that the OH region in the inverse flame is so small, and there is very little overlap between the OH and sooting regions. There is significant overlap between O_2 concentration and soot at the higher elevations of the flame (along the centerline), however, the temperature in this region is low (less than 1100 K) and therefore O_2 oxidation does not occur at the higher elevations. The peak O_2 oxidation rate occurs in the region right above the flame sheet, where O_2 and soot are present and the temperature is still high. In inverse flames, the surface growth rate continues after oxidation has ceased, which contributes to the soot emitting qualities of inverse flames, even though the quantity of soot is small.

To elucidate the differences in sooting characteristics between normal and inverse flames, we follow the pathline of a soot parcel as it is convected through the flame to obtain information on its temperature and stoichiometry history as a function of residence time in the flame. These parthlines are shown in Figure 2. In this discussion, we have chosen to follow the pathline which passes through the maximum sooting region. This method of analysis follows that developed earlier in Reference 8. In normal diffusion flames, the particle pathlines start in the fuel rich region and travel along a path of decreasing mixture fraction. As the particle travels from a fuel-rich to a stoichiometric region, the temperature rises. After crossing the flame sheet, the temperature and the mixture fraction decrease. The soot creation processes (nucleation and surface growth) begin before the particle crosses the flame sheet. Also, the peak soot volume fraction is reached before the particle crosses the flame sheet, where the particle then gets oxidized, primarily due to OH.

In inverse diffusion flames, the particle being tracked starts in the fuel-lean region near the burner, then quickly (in 4 ms) passes through the stoichiometric region, and then follows a path of increasing mixture fraction and decreasing temperature. The nucleation process, which occurs at around 12 ms, and all subsequent soot formation and destruction processes, begin after the particle has crossed the flame sheet. The peak soot volume fraction is sustained for a long period of time, because the oxidation rates are slow while surface growth continues. In fact, surface growth continues after oxidation ceases, causing these inverse flames to emit soot.

Acknowledgments

This work was sponsored by the Office of Naval Research through the Naval Research Laboratory, 6.1 Computational Physics Task Area. The computations were performed on a SGI Origin 2000 under a grant of High Performance Computing (HPC) time from the DoD HPC Shared Resource Center, Naval Research Laboratory.

	Normal 10/10	Inverse 10/10
Peak Soot Volume Fraction	6.2e-7	3.6e-9
Peak Soot Number Density (cm^{-3})	9.1e9	1.6e9
Total Soot Mass (g)	6.2e-7	9.6e-10
Location of sooting region	Annular region, fuel-rich side of flame sheet	Fuel-rich region on top of flame sheet
Peak Nucleation Rate (g/cm^3-s)	3.5e-8	3.1e-8
Peak Surface Growth Rate (g/cm^3-s)	1.9e-5	1.9e-7
Peak OH Oxidation Rate (g/cm^3-s)	3.5e-5	1.3e-8
Peak O_2 Oxidation Rate (g/cm^3-s)	1.9e-6	1.1e-7
Particle pathlines show that:	All soot formation and destruction processes begin before particle crosses flame sheet. Peak soot volume fraction occurs before particle crosses stoichiometric surface. Creation and destruction processes cease around same time, resulting in no soot emission.	All soot formation and destruction processes begin after particle crosses flame sheet Peak soot volume fraction maintained for long residence time due to very low oxidation rates. Surface growth continues after oxidation ceases, causing flame to emit soot.

Table 1. Differences in sooting characteristics between normal and inverse diffusion flames. In both cases, $V_{fuel} = V_{air} = 10$ cm/s.

References

1. Lin, K.-C. and Faeth, G.M., *J. Propulsion and Power*, **12**:10-17 (1996).

2. Wu, K.-T., and Essenhigh, R. H., *Twentieth Symposium (International) on Combustion*, The Combustion Institute, Pittsburgh, pp. 1925-1932 (1984).

3. Sugiyama, G. *Twenty-Fifth Symposium (International) on Combustion*, The Combustion Institute, Pittsburgh, pp. 601-608, 1994.

4. Du, J. and Axelbaum, R.L., *Combust. Flame*, 100:367-375 (1995).

5. Kaplan, C.R., Patnaik, G., and Kailasanath, K., *Combust. Sci. Technol.*, **131**:39 (1998).

6. Smooke, M.D., ed., *Reduced Kinetic Mechanisms and Asymptotic Approximations for Methane-Air Flames*, No. 384 in Lecture Notes in Physics, Springer-Verlag, Berlin, 1991.

7. Syed, K.J., Stewart, C.D., and Moss, J.B., *Twenty-Third Symposium (International) on Combustion*, The Combustion Institute, Pittsburgh, p. 1533, 1990.

8. Kaplan, C.R., Shaddix, C.R. and Smyth, K.C., *Combust. Flame*, **106**:392-405 (1996)

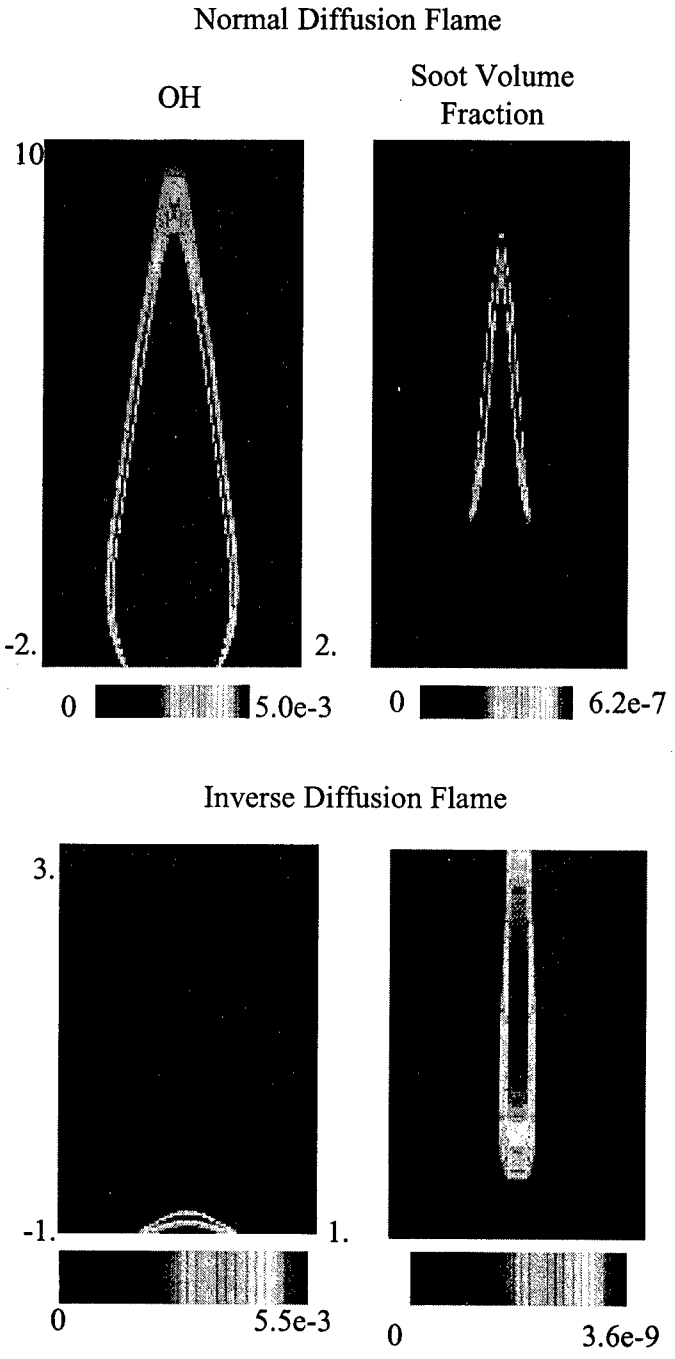


Figure 1. Images of OH mole fraction (showing location of stoichiometric surface) and soot volume fraction for normal and inverse diffusion flames. In both cases, $V_{fuel} = V_{air} = 10$ cm/s.

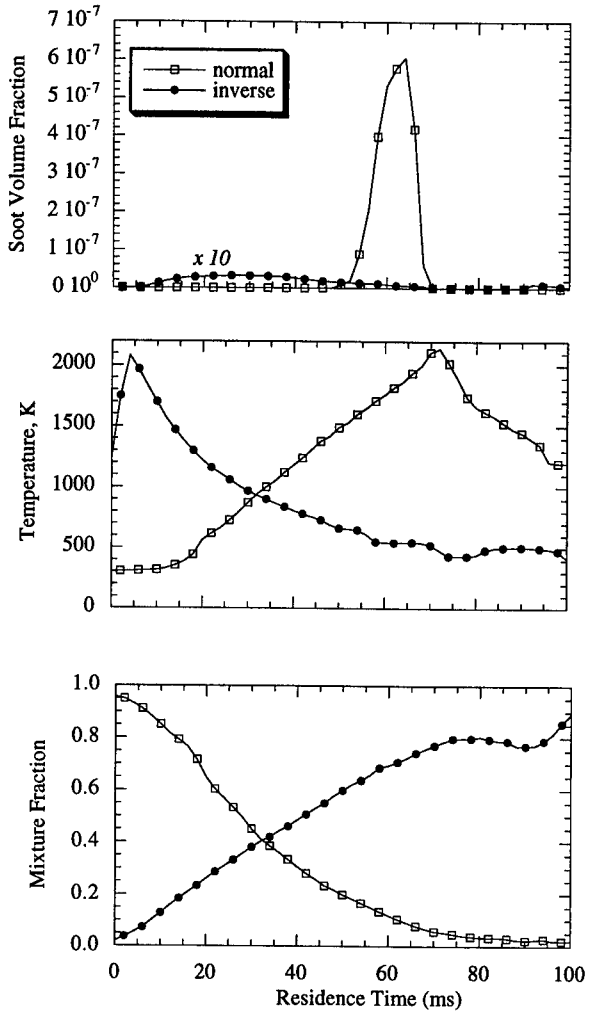


Figure 2. Plots of soot volume fraction, temperature, and mixture fraction as a function of residence time along the pathline going through the maximum sooting region for normal and inverse flames. Soot volume fraction for the inverse flame has been multiplied by a factor of 10 for presentation clarity.

Growth of Soot Particulates in Laminar, Premixed Flames

by
D. Liscinsky, M. Colket, B. True, R. Hall, and A. Bhargava
United Technologies Research Center
E. Hartford, CT 06108

Presentation to the Eastern States Section of the Combustion Institute
North Carolina State University, October 11-13, 1999

Soot production in a premixed flat flame of ethylene, oxygen, and argon surrounded by an argon co-flow is being studied in the UTRC atmospheric laboratory flame facility. The long term objective of this work is to obtain surface growth rates of particles at temperatures above 2000K, a condition likely to be present in soot formation zones of advanced combustors. Sparse data exists at such conditions. Yet growth mechanisms advanced by Colket and Hall [1] and Frenklach and coworkers [2] indicate a rapid drop in growth with increasing temperatures above 1900K, consistent with the limited data sets in this region, but essentially no data is available at temperatures above 2100K; extrapolations are required. This abstract describes recent results on developing the capability for such measurements and comparison of the results to literature values.

Experimental Methods:
The water-cooled porous plug hastalloy burner is 57mm in diameter and operates over a wide range of conditions. Flame stabilization is provided by a 195mm diameter ceramic disk, located 30mm above the burner. Vertical translation of the burner allows spatially accurate measurements to be made that can be converted to residence time with calculated velocities. Results are reported for flames with a variety of C/O ratios.

(1) Temperature Particle Densitometry (TPD)
Soot volume fraction was measured using temperature particle densitometry (TPD) [3,4]; it consists of rapid insertion of a thermocouple into the flame and recording the junction temperature as a function of time. A fit of the temperature history to a thermophoretic mass transfer model allows the calculation of soot volume fraction. The thermocouple assembly also follows [4] in that the bead is stretched (to avoid sagging) between supports 50mm apart (to avoid conduction losses). An uncoated type R thermocouple with bead size of 0.17 mm and a butt-welded bead (0.076 mm) were used. The data acquisition system was triggered optically to begin recording with insertion times being less that 100ms.

The data reduction methodology described by McEnally et al. [4] was used. One of the parameters in the calculation is the soot deposit density. This was obtained by collecting soot on a Pt. wire. The weight and diameter of the wire were determined before and after soot deposition. With known volume and mass of the accumulated soot, the soot deposit density was determined.

(2) Laser Extinction
Soot volume fraction was measured optically by laser extinction. The beam of a chopped cw HeNe laser (632.8 nm) was directed through the flame at various heights and the transmitted intensity recorded by a photodiode after passing through an aperture and a narrow-band (12nm) optical filter. There is a linear relationship between extinction and soot volume fraction if the primary particles are in the Rayleigh range.

(3) Particle Size
Thermophoretic sampling followed by analysis of photomicrographs using transmission electron microscopy (TEM) provided measurement of soot primary particle diameter (d_p). Samples were collected from the flame directly onto standard 3mm diameter carbon coated TEM grids using a computer controlled 2-stage pneumatic sampling system programmed to exposed the grid for 35 milliseconds before withdrawing from the flame. Collection onto the cold surface stopped heterogeneous reactions and preserved particle morphology.

Results:

(1) Temperature and Soot Volume Fractions

Soot volume fraction and temperatures in a $C_2H_4/O_2/Ar$ flame, with C/O=0.8, were extracted from the TPD results. Gas temperatures were obtained from the junction temperature-time history shortly after insertion (less than 2 seconds from the time of insertion), while soot volume fractions were derived from the temperature profile of the thermocouple fully covered by soot (beyond 10 seconds after insertion). Soot volume fraction was also obtained by laser extinction.

The temperature measured in the flame, as a function of height above burner, is shown in Figure 1. Shown in the figure are the profiles obtained with the butt-welded thermocouple and for a thermocouple that had a junction bead size of 0.178 mm. The wire diameter for both thermocouples was 0.05 mm. The temperatures with both thermocouples are within 50 K of each other and follow the same general shape. Also shown in the figure are the temperatures measured by Harris and Weiner [5] in the 'same' C/O=0.8 flame. They used a Kurlbaum technique [6] to measure temperature. As seen in the figure their values are around 100 K lower than our measurement. The discrepancy may be attributed to different experimental techniques, burner design and heat transfer rates. Also shown in the figure are the temperature measured by Xu et al. [7] and Benish et al. [8] for a $C_2H_4/O_2/N_2$ flame (same O2/dilutant level as our flames but with N_2 replacing Ar) with C/O=0.78 and 0.79, respectively. According to equilibrium calculations, the equilibrium temperatures of the two flames differ by 300 K, with the nitrogen flame being cooler. The comparison between the different literature profiles and our measurement indicates some differences, but the agreement in the overall shape and magnitude is encouraging. We are in the process of making these measurements with coated thermocouples to examine the possible effect of radical recombination on the thermocouple wire surface.

For determination of the soot volume fraction f_v from the TPD results, one of the critical parameters is the soot deposit solid fraction, ϕ. Figure 2 shows the measurements of this parameter at several heights above the burner surface. As seen in the figure, except for a couple of points, the effective density of this soot deposit on the wire remained constant at 0.023 ± 0.0012 gm/cm^3, much lower than the known density of single soot particles. The single measurement of ϕ close to the burner surface was higher and could be due to experimental error as collection of soot at distances closer to the burner surface is more erroneous. Alternatively, this high value may be because the soot deposit solid fraction is denser near to the burner surface. Low in the flame the existence of soot as isolated spheroids could result in dense packing of a soot accumulation, while higher in the flame the existence of soot in aggregate form would be expected to result in less dense packing. The soot deposit density was then divided by the known soot particle density of 1.8 gm/cm^3 to obtain ϕ for the f_v calculations. The constant value of 0.023 was used for all heights in this work.

Shown in Figure 3 are the soot volume fractions measured in the flame as a function of height above the burner surface. Measurements were performed with several different thermocouples, but for clarity purposes only the results from the butt-welded thermocouple are shown. The data from all thermocouples agreed well with each other. Soot volume fraction was also measured optically by laser extinction and is shown for comparison purposes. Also shown in the figure are the soot volume fractions measured by Harris and Weiner [5] in a similar flame and by Xu et al.[8] measured in a $C_2H_4/O_2/N_2$ flame at C/O of 0.78. As seen the soot volume fraction agrees generally with literature data. The comparison between the different techniques is also within experimental errors.

Measurements were made as a function of height above the burner for the flame with C/O = 0.8. In addition measurements were made 12.7 mm above the burner as a function of C/O ratio. Those results are shown in Figure 4. A numerical inversion to reduce errors due to nonuniformities in the flame or uncertainty in pathlength has not yet been applied to the data shown in Fig. 4.

(3) Soot Primary Particle Size

All 6 flames were thermophoretically sampled at 6 heights above the burner using 35 ms grid exposures made at the midpoint of the burner. Soot primary particle diameters were then measured by inspection of

photomicrographs made at 36,000x. At least 3 photomicrographs were acquired from each grid and examined in order to generate Table A. Although the edges of the particles are in general not "sharp", particle diameter could be determined within 20%.

Particles were not observed on the grids from flames with C/O less than 0.68. At larger C/O ratios the measurements indicate that diameter increases with increasing height and increasing C/O ratio as shown in Table A. The number of primary particles/agglomerate also increases similarly although these measurements are not reported. The series of photomicrographs shown in Fig. 5 graphically indicates the trend in soot formation with increasing residence time. These results agree well with those reported in [7].

References:

1. Colket, M. B. and Hall, R. J.: in Soot Formation in Combustion, Mechanisms and Models, H. Bockhorn, Ed., Springer Series in Chemical Physics 59, Springer-Verlag, (1994).
2. Kazakov, A. Wang, H, and Frenklach, M., Combustion and Flame, **100**, 111 (1995).
3. Koylu, U. O., McEnally, C. S., Rosner, D. E., and Pfefferle, L. D.,Combustion and Flame, **110**, 494 (1997).
4. McEnally, C. S., Koylu, U. O, Pfefferle, L. D., and Rosner, D. E., Combustion and Flame, **109**, 701(1997).
5. Harris, S. J. and Weiner, A. M, Combust. Sci. Tech., **32**, 267 (1983).
6. Dalzell, W.H. and Sarofim, A.F., A.S.M.E., J. Heat Transfer **91**,100 (1969).
7. Xu, F. Sunderland, P. B., and Faeth. G. M., Combustion and Flame, **108**, 471 (1997).
8. Benish, T. G. Lafeur, A. L., Taghizadeh, K., and Howard, J. B., Twenty-Sixth Symposium (Int'l) on Combustion, The Combustion Institute, Pittsburgh, 2319 (1996).

We are pleased to acknowledge AFOSR for partial support of this work under contract F49620-98-C-0008.

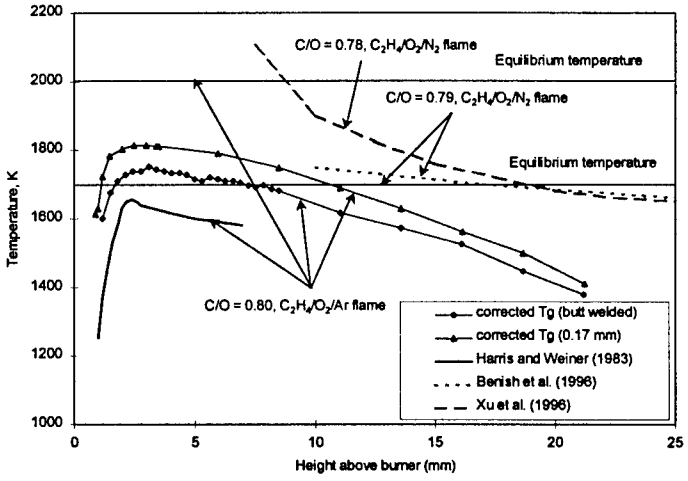


Fig. 1. Profile of flame temperature for a $C_2H_4/O_2/Ar$ flame with C/O=0.8, as a function of height above burner surface.

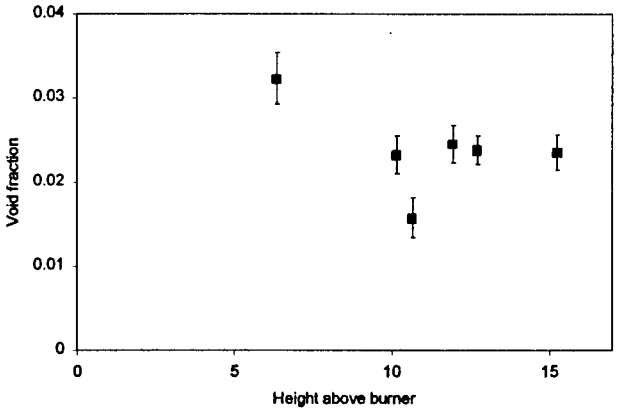


Fig. 2. Measured soot deposit density as a function of height above burner surface for a $C_2H_4/O_2/Ar$ flame with C/O=0.8.

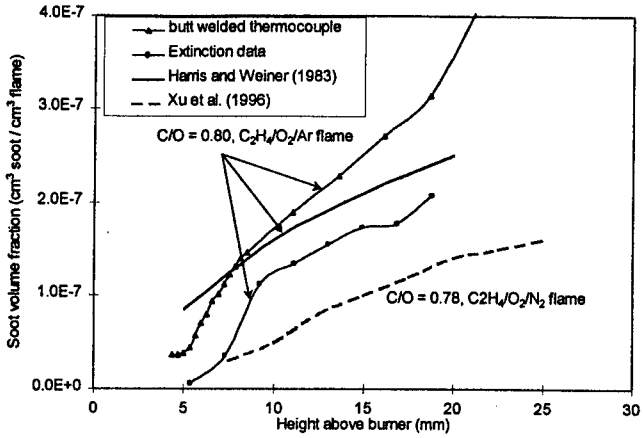


Fig. 3. Soot volume fraction profile measured by different techniques, as a function of height above burner surface for a flame with C/O=0.8.

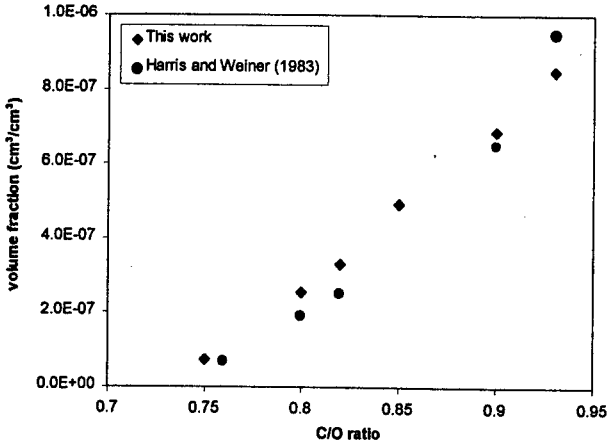


Fig. 4. Soot Volume Fraction measured via Extinction for flames with different C/O at 12.7 mm above the burner surface.

Flame Number	C/O	Range of Avg d_p (nm)
1	0.56	No particles
1a	0.62	No particles
1b	0.68	14 - 17
1c	0.75	14 - 19
2	0.80	14 - 20
3	0.93	19 - 31

Table A: Range of mean primary particle diameter from 5 to 20 mm above each flame

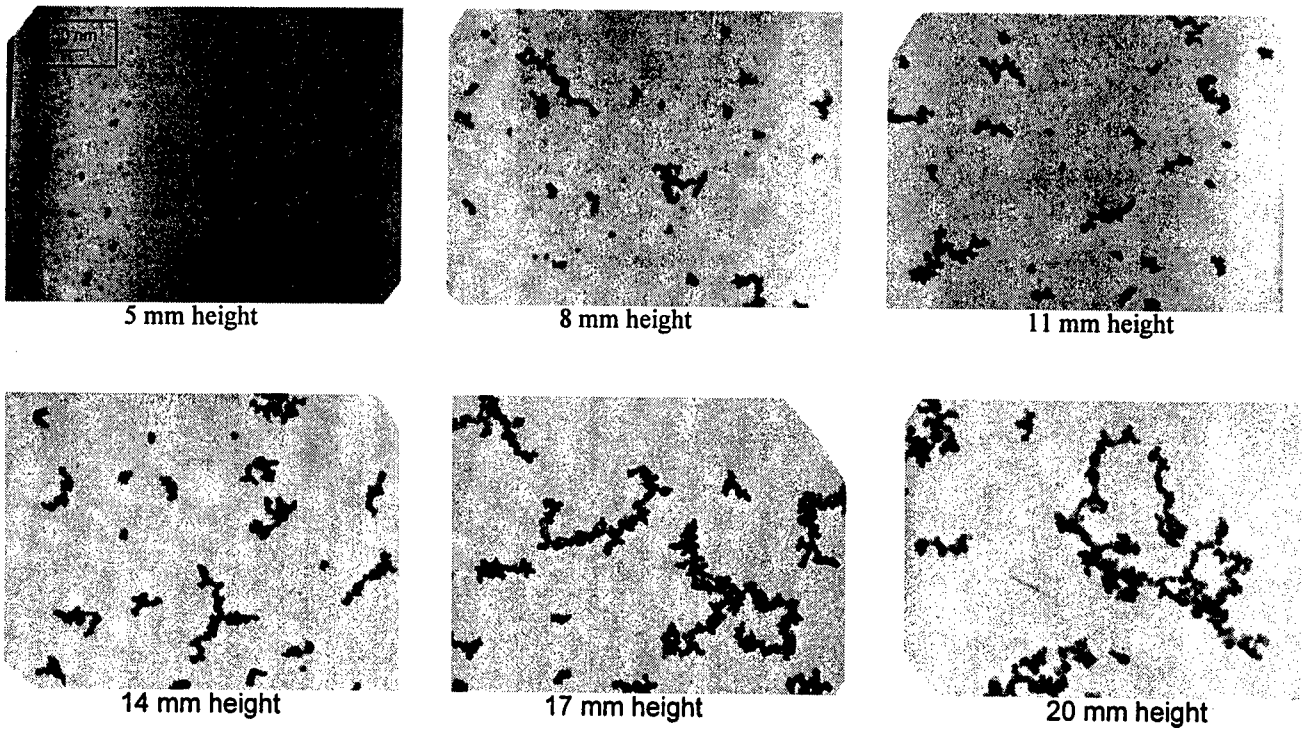


Figure 5: TEM Photomicrographs along the axis of the C/O = 0.93 flame (36,000x)

Towards Quantitative Modeling of Soot Formation in Coflow Diffusion Flames

by
M. D. Smooke (mitchell.smooke@yale.edu),
Departments of Mechanical and Chemical Engineering
Yale University, New Haven, CT 06520
and
M. B. Colket (colketmb@utrc.utc.com) and R. J. Hall (hallrj@utrc.utc.com)
United Technologies Research Center
E. Hartford, CT 06108
Presentation to the Eastern States Section of the Combustion Institute
North Carolina State University, October 11-13, 1999

Recently, a detailed model with fully coupled, elliptic, two-dimensional equations including soot production was developed and compared to experimental data from a methane/air [1] and a diluted ethylene/air [2] axisymmetric, laminar, coflow diffusion flames. The two-dimensional model includes a detailed transport, finite rate (detailed) chemistry gas phase system coupled with aerosol dynamical equations in the sectional representation. The soot model had been developed for laminar flames [3] and used to model soot production in an opposed jet diffusion flame [4]. Detailed submodels for the inception, growth, oxidation, and dynamics of soot particulates, as well as effects of radiation, are included in the model. In both coflow simulations, predictions in the annular layer just inside the flame (wing tips) compared well with experiments; but the predictions along the centerline were noticeably underpredicted (by a factor of two to three). In both flames the experimental soot profiles peaked along (or near to) the centerline but for the model, the soot peaked in the wing tips. Kennedy, et al [5] underpredicted centerline levels (factor of 10) whereas predictions in the annular regions were quantitative. Alternatively, Kaplan, et al [6] presented results that agreed well, at least qualitatively, with the experiments. The objective of this work is to examine possible causes of our under predictions along the centerline.

Possible causes include (1) limited numbers of soot 'sections' our particle dynamics algorithm uses for modeling the range of aerosol sizes; (2) an inappropriate balance between the inception rates and the surface growth rates; (3) lack of treatment of soot agglomeration and/or ageing; and (4) an inadequate PAH formation (or inception) model. The importance of each of these effects was tested through analytical studies. The present work was focused principally on the ethylene flame and the results are described below. (Other possibilities include inaccuracies in fuel-rich, gas-phase kinetics and prediction of bulk flame properties, but since the bulk flame parameters, including benzene and acetylene concentrations, are predicted well at least for the ethylene flame, these issues are not addressed here.)

Number of Soot Sections

Soot dynamics are modeled as coalescing, solid carbon spheroids undergoing surface growth in the free molecule limit. The particle range of interest is divided into sections or bins [7] (linear on a logarithmic scale). In the coflow computations, we previously used 12 sections for the methane flame and 9 sections in the ethylene flame due to memory limitations. In the premixed and counterflow studies, we found some sensitivity to soot predictions for heavily sooting flames. Hence, we recently recomputed the ethylene flame on a larger machine (4Gbyte) using a larger number of particle sections. Computed radial profiles of soot volume fractions are shown in Figure 1 for solutions with 9, 15, 20, and 25 sections at a height of 22 mm. This height was selected as the experimental-model comparisons were good lower in the flame and in the wings. As can be seen in this figure, there is virtually no difference between the solutions as a function of number of sections used in the computations, but still, we fall significantly below the experimental values. There were also insignificant differences at lower heights in the flame between the computed numbers.

Inception vs. Surface Growth

In one of our prior studies [4], we explored the possibility of a higher inception rate in the model. We had dropped this procedure since it is somewhat arbitrary/artificial and requires a counterbalance of a reduction in

the (literature) surface growth rates. The possibility that a low inception rate (in the model) contributed to the present problem was considered since benzene (presumably a tracer for PAH species) attained its peak value high in the center of the flame. Using 20 sections, we explored a variety of multiplication factors on both the inception rate and the surface growth rates. A predicted curve using a factor of eight increase on the inception rate and a factor of xx decrease in the surface growth rate is shown in Figure 1 in comparison to the data. The comparisons are a little better, but the perturbations to the model to achieve these results are significant and arguably close to being excessive, despite some uncertainties in inception and growth rates.

Primary Particle Aging

The existing sectional soot growth model is based on the assumption of spherical, liquid-like particles that coalesce with one another, undergo surface growth, and are not constrained by any maximum size. Experimental evidence in many flames, however, is that while the spherical model is accurate for young soot, older soot particles tend to consist of chainlike aggregates of relatively small primary particles which have fused together rather than coalescing. Further, the primary particles do not grow indefinitely, but tend to reach a limited maximum diameter that is not strongly sensitive to flame or fuel, suggestive of a surface reactivity decay or "aging" process. A model for including aggregation and aging effects is described elsewhere at this meeting [8], but has not been undertaken in the present work; instead a heuristic approach to primary particle size limitation has been incorporated. For all particle sections corresponding to diameters beyond a limiting size (20 nm is a value suggested by experiments), the sectional surface growth coefficients are set equal to zero. This assumption effectively truncates the growth of soot volume fraction, since the coalescence or agglomeration events that the particles could then undergo do not change volume fraction. There is no size limitation imposed for oxidation processes; larger particles, which have formed through agglomeration, can be oxidized. Soot formed in the coflow flame wings tends to be older and reaches the maximum size before centerline soot. This primary particle size limitation provides better qualitative agreement with experiment, although there still is quantitative disagreement (factors of 2-3).

Inception Model

In the original model used in [1,2], inception rates are computed using steady-state expressions for the formation of naphthalenyl radical and phenanthrene; the expressions are based on presently understood reaction mechanisms and local concentrations of gas-phase species, (i.e. H, H_2, C_2H_2, phenyl, etc.). To gain some insight on the computed values, a scatter plot of inception rates as a function of temperature is shown in Figure 2 for the diluted ethylene flame. The preponderance of points depicts a bell shaped curve peaking around 1600K. A second bell is apparent that peaks slightly higher in temperature, 1650K, at larger levels. An analysis of the points indicated that the higher temperature curve with fewer points characterize soot inception along the centerline while the other curve depicts processes occurring in the annular region, just inside the flame front (denoted as wing). These results suggest that the two environments for inception along the centerline and the wings of the flame may be slightly different; different reaction mechanisms may dominate for the two regions. This conclusion appears to be compatible with the observations in the work by Dobbins and coworkers [9] on particle evolution along the centerline of a coflow (pure) ethylene flame.

To test the possibility that another mechanism was contributing along the centerline of the flame, we considered four alternative PAH growth mechanisms that have been recently promoted in the literature. The reversible mechanisms include (A) naphthalene formation via combination of benzyl and propargyl [10,11], (B) naphthalene formation via combination of cyclopentadienyl, (C) a reaction sequence involving vinylidene addition to the benzene ring, and (D) naphthalene formation via sequential addition of acetylene to phenyl but incorporating an H-atom shift in the intermediate adduct [12]. For each of these sequences, steady-state expressions were computed and net rates calculated at several different heights along the burner using the computed gas temperatures and local concentrations. A comparison of the net rates of these four reactions is shown in Figures 3a and 3b relative to the dominant process of naphthalenyl formation used in the original coflow calculations (BASE). Several other reaction sequences were investigated, including reactions initiated with phenyl-toluene combination. In general, these rates were very low at least for the ethylene system. The

relative rates of this latter sequence and that of sequence (A) listed above increase substantially in the methane flame in which there is ready access to methyl radicals.

Figures 3a and 3b demonstrate that virtually throughout the flame, no other reaction sequence approaches the rates of production achieved by the original mechanism, except reaction sequence (D) is faster low (at 10 mm) in the center of the flame. Despite the relatively faster rates at this location, the absolute production rates at this location are very low so it is questionable whether sequence (D) can explain the observed phenomena. However, the higher relative inception rates along the centerline with lower relative rates along the wings were consistent with the phenomena we were trying to reproduce. Hence, we added an inception rate term, following sequence (D), into the coflow code. The effect of adding this inception term is shown in Figure 1, where it is apparent that it does not resolve the major discrepancies between experiment and theory.

Conclusions

We have examined a number of factors in an attempt to explain disagreements between modelling and experiment in sooting, axisymmetric, coflow diffusion flames, where a tendency of soot to peak near the flame centerline was observed experimentally, but not confirmed by modelling, where peak soot levels were in the wings [1,2]. Previous calculations were limited in the numbers of soot size sections that could be employed, but sensitivity studies employing much larger numbers of sections show little dependence of calculated soot parameters on number of sections. A heuristic approach to modelling primary particle size limitation was pursued, in which surface growth was truncated for particles beyond a specified size; this did improve the qualitative agreement between experiment and theory by limiting growth more in the wings than in the centerline. Perturbations of the existing naphthalenyl formation-based inception rate, surface growth, and oxidation were examined, and will be discussed. Four new inception models based on alternative PAH formation mechanisms were tested; one of these was found to produce higher relative inception rates along the centerline with lower relative rates along the wings, consistent with the phenomena we were trying to reproduce.

References

1. Smooke, M. D., McEnally, C. S., Pfefferle, L. D., Hall, R. J., and Colket, M. B., Combustion and Flame 117:117-139 (1999).
2. McEnally, C. S., Schaffer, A. M., Long, M. B., Pfefferle, L. D., Smooke, M. D., Colket, M. B., and Hall, R. J., Twenty-Seventh Symposium (International) on Combustion, The Combustion Institute, pp. 1497-1505 (1998).
3. Colket, M. B. and Hall, R. J.: in Soot Formation in Combustion, Mechanisms and Models, H. Bockhorn, Ed., Springer Series in Chemical Physics 59, Springer-Verlag, (1994).
4. Hall, R. J., Smooke, M. D., and Colket, M. B.: in Physical and Chemical Aspects of Combustion: A Tribute to Irvin Glassman, ed. by R. F. Sawyer and F. L. Dryer, Combustion and Science and Technology Book Series, Gordon and Breach, p. 189, 1997.
5. Kennedy, I. M., Rapp, D. R., Santoro, R. J., and Yam, C., Combustion and Flame, **107**, p. 386, (1996).
6. Kaplan, C. R., Shaddix, C. R., and Smyth, K. C., Combustion and Flame, **106**, p. 392, (1996).
7. Gelbard, F. and Seinfeld, J.H., J. Coll. Int. Sci., **78**, p. 485, (1980).
8. Hall, R.J. and Colket, M.B., presentation at the Eastern States Section of the Combustion Institute, North Carolina State University, October 11-13, 1999.
9. Dobbins, R. A., Govatzidakis, W. Lu, Schwartzman, A. F., and Fletcher, R. A., Combust. Sci. Tech. **121**, p. 103 (1996).
10. Colket, M. B. and Seery, D. J., Twenty-Fifth Symposium (International) on Combustion, The Combustion Institute, p. 883 (1994).
11. Marinov, N., Pitz, W., Westbrook, C., Lutz, A., Vincitore, A., and Senkan, S., Twenty-Seventh Symposium (International) on Combustion, The Combustion Institute, p. 605 (1998).
12. Moriarty, N. J., Brown, N. J., and Frenklach, M., "Hydrogen Migration in the Ethenyl-Benzene Radical", presented at the First JMUSSCI, Washington, D.C., March 14-17, 1999.

We are pleased to thank AFOSR for partial support of this work under contract F49620-98-C-0008.

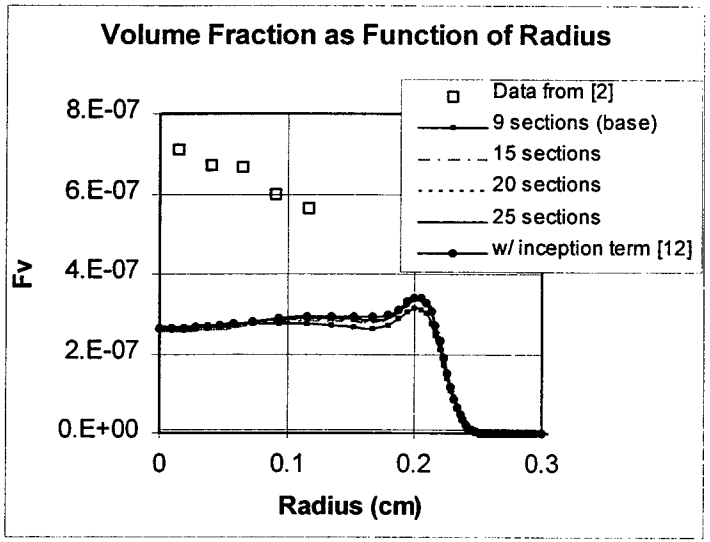


Figure 1. Sensitivity of Soot Model Predictions to Number of Soot Size Classes in Ethylene Flame Simulation

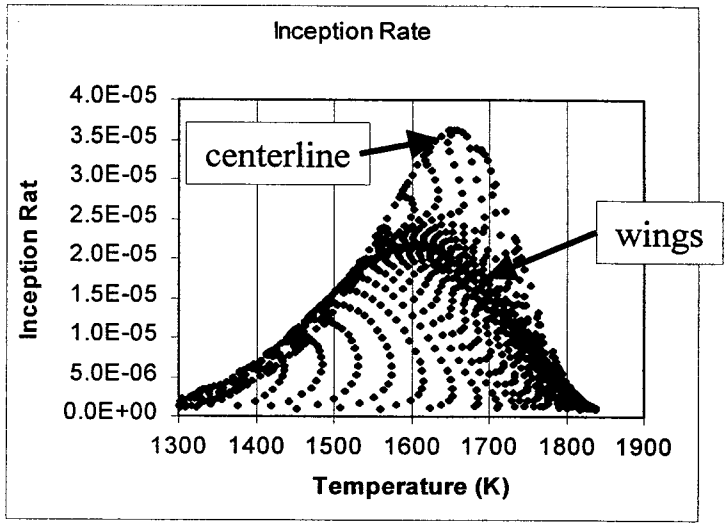
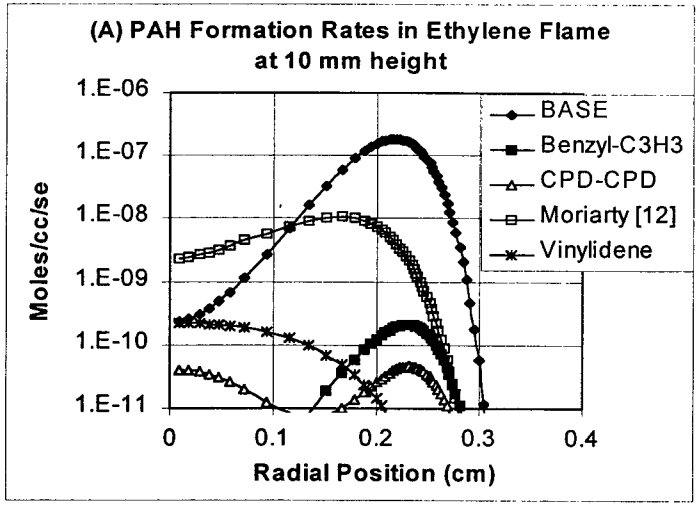


Figure 2. Inception Rate vs. Temperature at All Grid Points in the Ethylene Flame Simulation



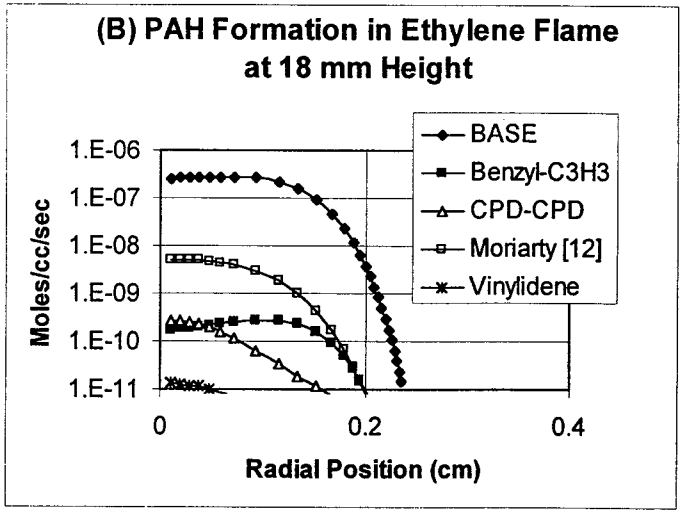


Figure 3. Comparison of Steady-State PAH Formation Rates in Ethylene Flame Simulations

Calculations of Soot Aggregate Growth and Oxidation Using a Sectional Size Representation

Robert J. Hall (hallrj@utrc.utc.com) and
Meredith B. Colket (colketmb@utrc.utc.com)
United Technologies Research Center
East Hartford, CT 06108

In modeling the growth of soot particles, it has been conventional to assume that the particles consist of isolated spheroids, which undergo surface growth and oxidation and coalesce with one another on impact. The experimental evidence, however, is that while the coalescing spheroid picture is accurate for very small, young, particles, older soot particles tend to consist of chainlike, aggregates of primary spheroids which fuse together on impact without coalescing. The aggregation process is important in soot formation because it affects the particle surface area available for growth and oxidation. Further, the primary particles within aggregates do not grow indefinitely, but tend to reach a limited maximum size not strongly dependent of flame and fuel. In order to have a more realistic description of soot growth, the sectional aerosol dynamics representation (Ref. 1) that has been used to model the growth of spheroidal aerosols is being extended to model soot aggregates, as well. The new computer model is based on an extension of the DISGLOM program (Refs. 2,3).

The algorithm being employed has provision for a "discrete" size range of precursor or nascent particles whose masses are multiples of some inception growth species. The discrete size range is joined to an isolated spheroid size range whose boundaries vary linearly on a logarithmic scale as in the conventional sectional model; these "liquid" particles are assumed to coalesce on collision. Beyond an arbitrarily determined size, particles are assumed to fuse with one another, leading to formation of chainlike aggregates of smaller primary particles. The conventional spheroid sectional analysis tracks the total mass density within set sectional boundaries; the extended sectional analysis tracks not only the mass density, but also the number of primary particles within an aggregate section. The transition from liquid to solid particles occurs at a particle diameter that is an input item, and the mass fractal dimension of the aggregates is also assumed. Aggregate-aggregate collisions leading to larger aggregates are prescribed at rates based on the assumed fractal dimension. Coefficients for surface growth and oxidation arising from gas phase acetylene, hydroxyl radical, and oxygen have been added. These surface processes are treated formally as coalescence events, with account taken of continuum effects; thus, the program should be applicable to high-pressure problems as well. Within an aggregate section particles of differing primary particle populations are allowed, but all primary particles within a bin are assumed to be the same size, consistent with DISGLOM. There is typically a mild variation of average primary particle size with aggregate section. These primary particles can grow not only by the conventional acetylene-driven surface growth processes, but also by coalescence with any smaller "liquid" particles. It is possible to specify a maximum primary spheroid size beyond which all growth processes affecting the primary spheroids are shut off, or to impose a surface reactivity decay rate. These features represent a heuristic start to modeling surface aging effects and the tendency of primary spheroids to reach maximum sizes that are largely independent of the type of flame and fuel. An approximation made for oxidation is that the smallest aggregate size class does not oxidize down into a smaller aggregate size class, but rather into the largest "liquid" size class. The model does not, therefore, precisely describe the final stages of aggregate particle burnout.

Application of the new sectional soot formation model to describe the formation of soot aggregates in premixed flames is presented here. The model features are illustrated with a simulation of the premixed ethylene flames of Harris and Weiner (Ref. 4). In previous studies of these flames (Ref. 5) profiles of temperature, velocity, and growth/oxidation species concentrations were generated using CHEMKIN. These profiles have now been used to generate new soot growth predictions for these flames on a post-processing basis, assuming that soot growth scrubbing of gas phase species and temperature depression by radiative loss are small. The previous studies were based on the assumption that benzene formation determined the rate-limiting step in nucleation; these calculations are based on a newer nucleation model in which a two ring aromatic species of mass 127 a.m.u. ($C_{10}H_7$) is the nucleation species (Ref. 6). One discrete bin of this mass was included. Five liquid bins terminating at D_0 = 20 nm diameter, where solidification was assumed to begin, were included, followed by seven aggregate bins terminating at a sphere-equivalent diameter of about 1000 nm. Two flames were modeled, with C/O ratios of 0.80, and 0.94, as shown in Figure 1. A surface growth rate first order in acetylene concentration was employed that is consistent with that reported in Ref. 4 (about 25% larger than the value used in Refs. 5,6). Oxidation rates by O_2 and OH are taken from Refs. 7,8.

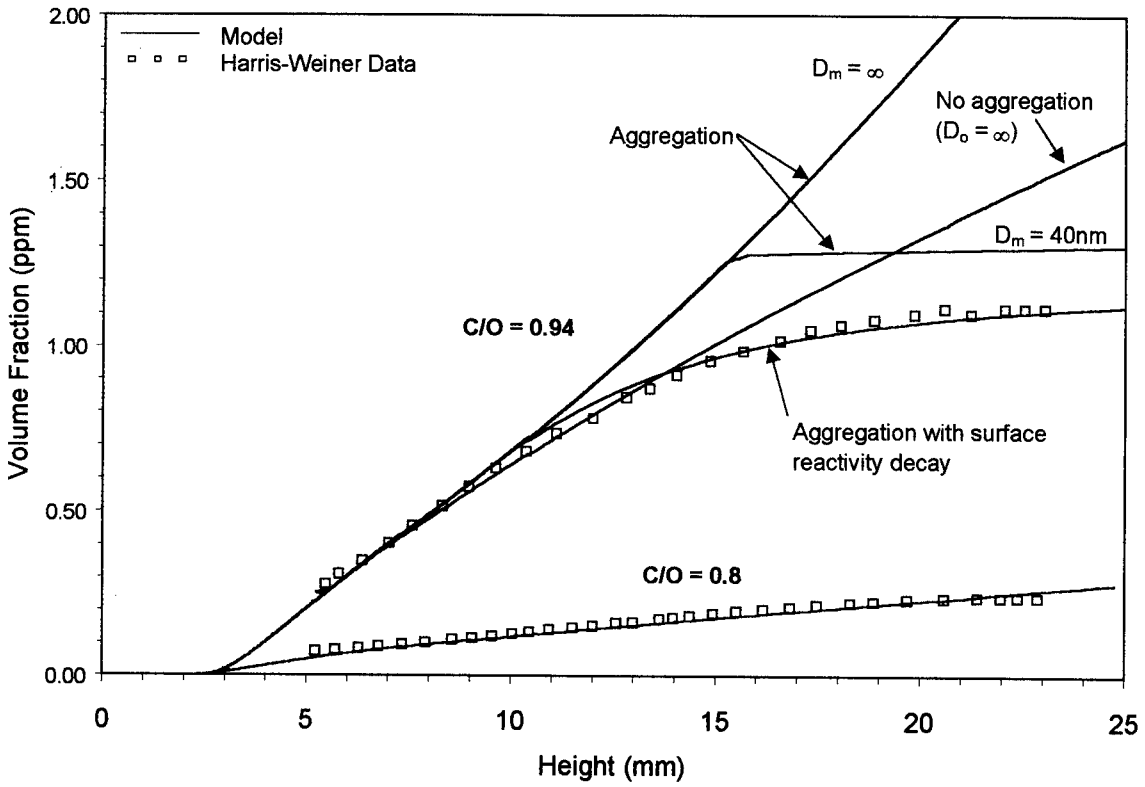


Figure 1. Comparison of Aggregate Model Predictions with Experimental Premixed Flame Measurements of Harris and Weiner (Ref. 4)

For the richer flame, the spheroid only model ($D_0 = \infty$) results in an overprediction of soot at the top of the flame, as shown in Figure 1. From a height of 3 mm, where the temperature peaks, a fall-off of about 130 K occurs to the top of the flame. The decay of surface growth rate with this decrease in temperature (31.8-kcal activation energy assumed) is insufficient to explain the fall-off in growth, however. The aggregate simulations were then carried out on the richer flame assuming no restriction

on the final size D_m of the primary spheroids. Significant divergence is observed between the aggregate and spheroid only models beginning at the point where aggregates start to occur (formation of 20 nm spheroids), with the aggregate model in poorer agreement with experiment at the top of the flame. This arises because with solid aggregates no surface area destruction occurs as a result of coagulation, unlike the case for liquid-like particles. For the solid aggregates, surface area increases due to acetylenic surface growth, and the volume fraction grows more rapidly than is observed. When a more realistic limit on the size of the primary spheroids is imposed (D_m = 40 nm), growth is observed to terminate in a way more consistent with experiments. The unphysical discontinuity in the growth curve arises from the assumption that surface growth truncates sharply at D_m = 40 nm; in reality there would be a smoother variation with primary particle diameter. When an aging rate is used to describe the decay of surface site reactivity (Ref. 9), with the onset of aging determined by the point at which the aggregate and spheres only models begin to diverge, better agreement with experiment results, as shown. A slightly slower aging rate than that reported in Ref. 9 (50% of the Ref. 9 value) was found to give the best fit to experiment. For the C/O=0.80 flame the aggregation effects are less pronounced because the particles remain predominately in the liquid sections to the top of the flame, and all models give sensibly the same result.

Accounting for the formation of chainlike aggregates represents an advance in soot modeling capability. However, application to premixed flames has shown that the initial effect of including aggregate effects is to worsen the agreement between experiment and theory because of the different ways aggregation and coalescence affect particle surface area. Agreement with experiment is restored only with inclusion of a surface reactivity decay at a rate that is roughly consistent with the value reported in the literature.

Acknowledgement

This work has been supported in part by the Air Force Office of Scientific Research under contract F49620-94-C-0059. The encouragement of Julian Tishkoff and discussions with Steven Rogak (University of British Columbia) are gratefully acknowledged.

References

1. F. Gelbard and J. H. Seinfeld, J. Coll. Int. Sci., **78**, 485 (1980).
2. J.J. Wu, Doctoral dissertation, Cal. Tech, Pasadena (1986).
3. S.N. Rogak, Doctoral dissertation, Cal. Tech, Pasadena (1991); S.N. Rogak, Aerosol Sci. and Tech., **26**, p. 127 (1997).
4. S.J. Harris and A.M.Weiner, Comb. Science and Tech., **32**, p. 267 (1983).
5. M.B.Colket and R.J.Hall, *Proceedings of the International Workshop on Mechanisms and Models of Soot Formation* (H.Bockhorn, Ed.), Springer-Verlag, Heidelberg, (1994).
6. R.J.Hall, M.D.Smooke, and M.B.Colket, in *Physical and Chemical Aspects of Combustion, A Tribute to Irvin Glassman* (F.L.Dryer and R.F.Sawyer, Eds.), Gordon and Breach, Amsterdam, (1998).
7. J. Nagle and R.F. Strickland-Constable, in *Proceedings of the Fifth Conference on Carbon*, Pergamon, London, 1962, p. 154.
8. K.G. Neoh, J.B. Howard, and A.F. Sarofim, in *Particulate Carbon: Formation During Combustion*, (D.C. Seigla and G.W. Smith, Eds.), Plenum, New York, 1981, p. 261.
9. R.A. Dobbins, Comb. Science and Tech., **121**, 103 (1996).

Preferential-Diffusion Effects on Premixed Hydrogen-Fueled Flames: Measurements and Predictions

O.C. Kwon and G.M. Faeth
Department of Aerospace Engineering
The University of Michigan
Ann Arbor, Michigan 48109-2140

Introduction. Recent experimental and computational studies of effects of flame stretch on laminar premixed flames in this laboratory [1-5] were extended to consider hydrogen/oxygen flames at normal temperature and pressures of 0.3-3.0 atm with various diluents. This work was undertaken in order to consider how this flame system is affected by varying diluents chosen to modify the preferential-diffusion properties of the various species and heat. Outwardly-propagating spherical flames were used to find the sensitivities of laminar burning velocities to flame stretch (represented by Markstein numbers) and the fundamental laminar burning velocities for unstretched (plane) flames. Present measurements, supplemented by earlier findings [1, 6-10], were also used to evaluate corresponding numerical simulations of the experimentally-observed flames, based on detailed H_2/O_2 reaction mechanisms of Mueller et al. [11], Frenklach et al. [12], and Marinov [13].

Experimental Methods. Experiments were carried out in a 360 mm diameter spherical windowed combustion chamber used for recent studies of laminar-premixed-flame/stretch interactions [1-5] with the test mixture ignited at the center of the chamber. The flames were observed using high speed motion picture shadowgraphy, limiting observations to flame diameters greater than 10 mm to avoid ignition disturbance and less than 60 mm to obtain flames at nearly constant pressure. Measurements were limited to $\delta_D/r_f \leq 2\%$, similar to Refs. 1-5, so that effects of curvature and transient phenomena associated with large flame thicknesses were small. Finally, radiative heat losses were less than 5% of the rate of chemical energy release within flames and were ignored. For these conditions, the laminar burning velocity and flame stretch are given by the following expressions [1-5]:

$$S_L = (\rho_b/\rho_u)dr_f/dt, \qquad K = (2/r_f)dr_f/dt \tag{1}$$

where the density ratio was computed based on the algorithms of McBride et al. [14] and Reynolds [15] with both yielding the same results, ignoring preferential diffusion effects by convention. Effects of stretch on laminar burning velocities were correlated similar to Refs. 1-5, as follows:

$$S_{L\infty}/S_L = 1 + MaKa \tag{2}$$

where Ma and Ka are based on local length and time scales for a stretched flame.

Computational Methods. Numerical simulations of outwardly-propagating spherical laminar premixed flames were carried out using the RUN-1DL code of Rogg [16]; calculations for unstretched (plane) flames were carried out using the PREMIX code of Kee et al. [17]. Transport approximations and thermochemical and transport data were similar to past work [1-5].

Results and Discussion. Predicted and measured laminar burning velocities are plotted as a function of Karlovitz number, as suggested by Eq. 2, in Fig 1 for argon-diluted hydrogen/oxygen flames. For the present test range ($Ka < 0.12$), both measurements and predictions yield linear variations of

$S_{L\infty}/S_L$ as a function of Ka, which implies constant Ma for each reactant mixture. This behavior was typical of results for the present test range and is similar to past observations correlated according to Eq. 2 [1-5], which provides a very concise representation of flame/stretch interactions. Values of $S_{L\infty}/S_L$ vary in the range 0.8-1.4 even though maximum Ka < 0.12 which is well away from quenching conditions. In addition, predictions are in good qualitative agreement with the measurements.

Both measured and predicted results for outwardly-propagating flames were extrapolated to Ka→0 to find $S_{L\infty}$. The various measurements and predictions of $S_{L\infty}$ for hydrogen/air and argon-diluted hydrogen/oxygen flames are plotted in Fig. 2 and in Fig. 3, respectively. Another prediction of $S_{L\infty}$ found directly from the unstretched (plane) flame computations is not shown on these plots, but it always showed 4-7% higher values than predicted outwardly-propagating flames, with their differences attributed to different property data bases and mechanisms. Effects of changing the diluent from N_2 to Ar are consistent with increasing radical concentrations, due to increasing temperatures, increasing laminar burning velocities. The measurements of $S_{L\infty}$ for hydrogen/air flames are in good agreement each other except for those by Aung et al. [1] which are smaller than others for fuel-rich conditions. Finally, the comparison between measurements and predictions shows that prediction by H_2/O_2 reaction mechanism of Mueller et al. [11] is in best agreement with the measurements although Marinov [13]'s mechanism yields better agreement for very fuel-rich conditions.

Measured and predicted Ma for hydrogen/air and argon-diluted hydrogen/oxygen flames are plotted in Fig. 4 and in Fig. 5, respectively. Present hydrogen flames with N_2 or Ar dilution exhibit negative Markstein numbers at fuel-lean conditions, which is consistent with classical preferential-diffusion ideas. Effects of changing the diluent from N_2 to Ar on Ma are not significant since the mass diffusivity of hydrogen for Ar increases somewhat relative to for N_2 but it is compensated with increasing thermal-diffusion effects. The agreement among the measurements is fair, especially excellent between values from Taylor [8] and the present results except at very fuel-lean conditions. Present measurements and predictions also exhibit encouraging agreement; nevertheless, discrepancies between predictions and measurements at very fuel-lean and very fuel-rich conditions merit additional consideration.

Fig. 6 is an illustration of the variation of Ma with pressure for fuel-lean (ϕ = 0.6) and fuel-rich (ϕ = 4.5) conditions of argon-diluted hydrogen flames. Increasing pressure tends to enhance preferential-diffusion instability; it should be noted that even though the magnitudes of Ma at low and high pressures are comparable for ϕ = 4.5, the actual effects of preferential-diffusion/stretch interactions are much weaker at high pressures because the mass diffusivity D_u used to normalize Markstein lengths into Ma is inversely proportional to pressure. This enhanced preferential-diffusion instability is due to increased flame sensitivity to radical concentrations as these concentrations become small due to enhanced three-body recombination reaction rates at elevated pressures.

Nomenclature. D = mass diffusivity; K = flame stretch; Ka = Karlovitz number, KD_u/S_L^2; L = Markstein length; Ma = Markstein number, L/δ_D; P = pressure; r_f = flame radius; S_L = laminar burning velocity; t = time; T = reactant temperature; δ_D = characteristic flame thickness, D_u/S_L; ϕ = fuel-equivalence ratio; ρ = density; the subscripts b, u and ∞ refer to burned and unburned properties and the unstretched flame condition, respectively.

Acknowledgments. This research was supported by the Rackham Fellowship Program of the University of Michigan.

References.

1. Aung, K.T., Hassan, M.I., and Faeth, G.M., Combust. Flame, 109:1-24 (1997).
2. Aung, K.T., Hassan, M.I., and Faeth, G.M., Combust. Flame, 112:1-15 (1998).
3. Hassan, M.I., Aung, K.T., and Faeth, G.M., Combust. Flame, 115:539-550 (1998).
4. Hassan, M.I., Aung, K.T., Kwon, O.C., and Faeth, G.M., J. Prop. Power, 14:479-488 (1998).
5. Kwon, O.C., Hassan, M.I., and Faeth, G.M., J. Prop. Power, in press.
6. Karpov, V.P., Lipatnikov, A.N., and Wolanski, P., Combust. Flame, 109:436-448 (1997).
7. Vagelopoulos, C.M., Egolfopoulos, F.N., and Law, C.K., Twenty-Fifth Symposium (International) on Combustion, The Combustion Institute, Pittsburgh, 1994, p. 1341-1347.
8. Taylor, S.C., Ph.D. Thesis, University of Leeds, 1991.
9. Egolfopoulos, F.N., and Law, C.K., Twenty-Third Symposium (International) on Combustion, The Combustion Institute, Pittsburgh, 1990, p. 333-340.
10. Sun, C.J., Sung, C.J., He, L., and Law, C.K., Combust. Flame, 118:108-128 (1999).
11. Mueller, M.A., Kim, T.J., Yetter, R.A., and Dryer, F.L., Int. J. Chem. Kinet., 31:113-125 (1999).
12. Frenklach, M., Wang, H., Bowman, C.T., Hanson, R.K., Smith, G.P., Goldin, D.M., Gardiner, W.C., and Lissianski V., World Wide Web location http://www.gri.org/Basic Research/GRI-Mech, 1995.
13. Marinov, N.M., Personal Communications, 1998.
14. McBride, B.J., Reno, M.A., and Gordon, S., NASA TM-4557, 1994.
15. Reynolds, W.C., Department of Mechanical Engineering Report, Stanford University, Stanford, CA, 1986.
16. Rogg, B., CUED/A-THERMO/TR39, University of Cambridge, 1991.
17. Kee, R.J., Grcar, J.F., Smooke, M.D., and Miller, J.A., SAND85-8240, Sandia National Laboratories, Albuquerque, NM, 1993.

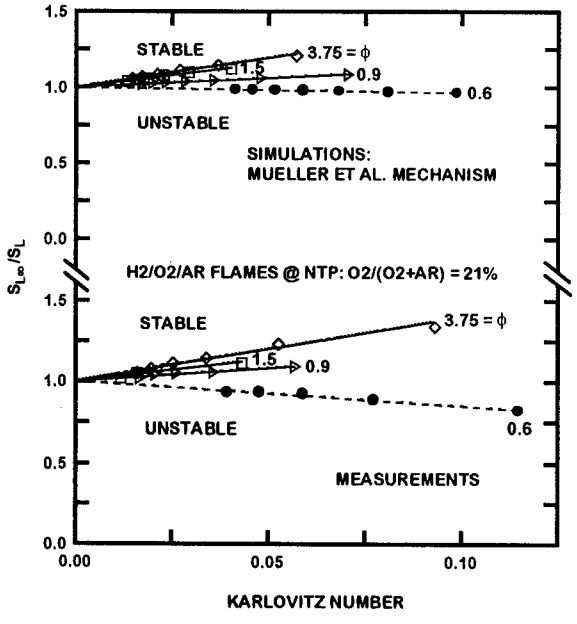


Fig. 1. Measured and predicted laminar burning velocities as a function of Karlovitz number and fuel-equivalence ratio for $H_2/O_2/Ar$ flames at NTP.

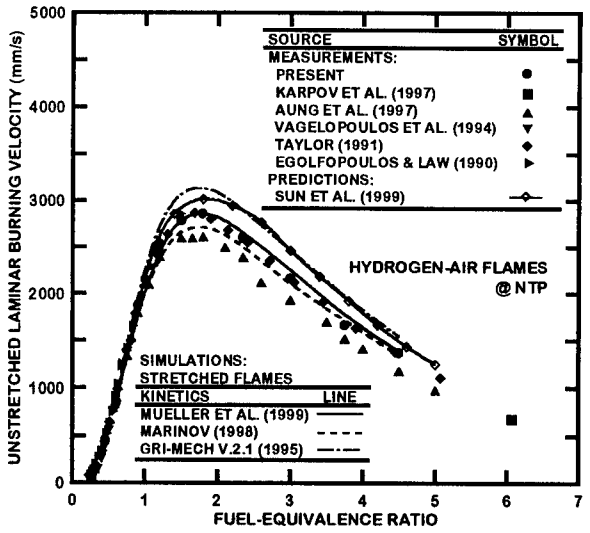


Fig. 2. Measured and predicted laminar burning velocities as a function of fuel-equivalence ratio for hydrogen/air flames at NTP.

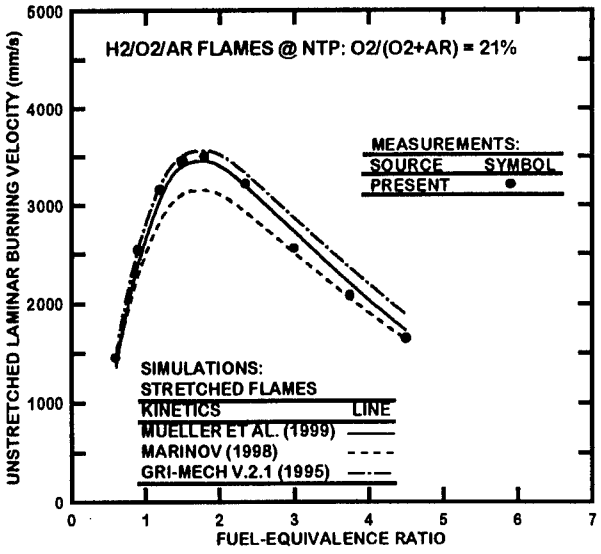


Fig. 3. Measured and predicted laminar burning velocities as a function of fuel-equivalence ratio for $H_2/O_2/Ar$ flames at NTP.

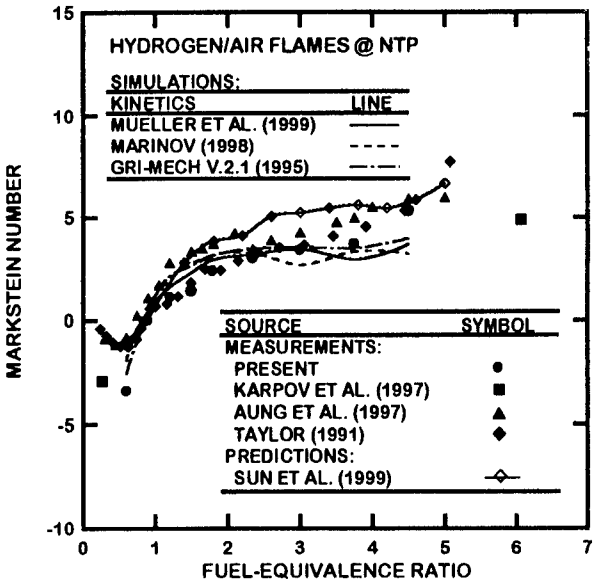


Fig. 4. Measured and predicted Markstein numbers as a function of fuel-equivalence ratio for hydrogen/air flames at NTP.

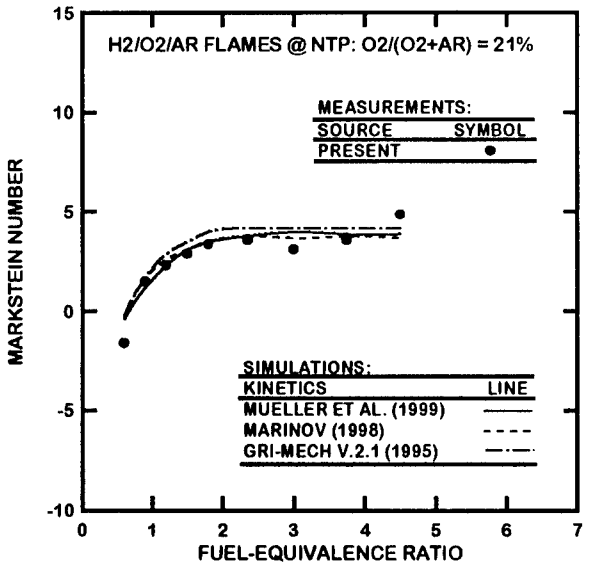


Fig. 5. Measured and predicted Markstein numbers as a function of fuel-equivalence ratio for $H_2/O_2/Ar$ flames at NTP.

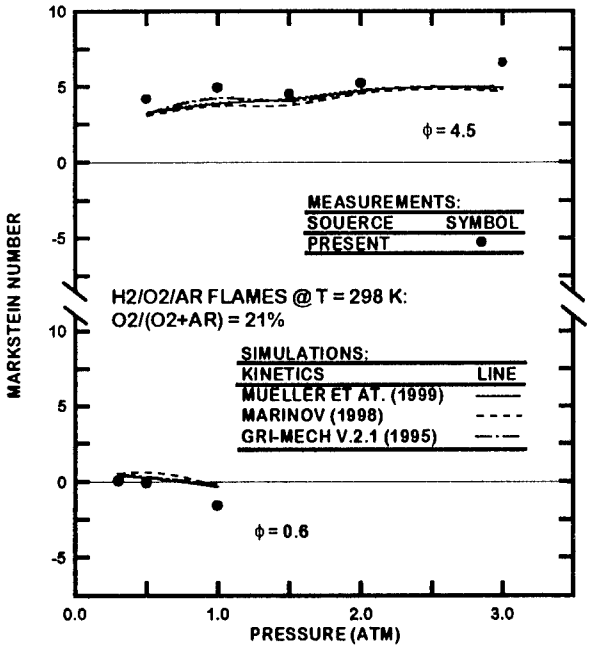


Fig. 6. Effects of pressure on measured and predicted Markstein numbers of $H_2/O_2/Ar$ flames at fuel-equivalence ratios of 0.6 and 4.5 and temperature of 298K.

Temperatures of Positively and Negatively Stretched Flames

Kazuhiro YAMAMOTO[1] and Satoru ISHIZUKA[2]

[1]Department of Mechanical Engineering, Faculty of Engineering, Toyohashi University of Technology
1-1 Hibarigaoka, Tempaku, Toyohashi-shi, Aichi 441-8580, JAPAN

[2]Department of Mechanical Engineering, Faculty of Engineering, Hiroshima University
1-4-1, Kagamiyama, Higashi-hiroshima-shi, Hiroshima 739-0046, JAPAN

Introduction

For modeling turbulent combustion, we usually focus on vortex flow [1-4]. This is because, in turbulent flow, eddies move randomly back and force across the adjacent fluid layers, and the flow no longer remains smooth and orderly. The diffusivity of turbulence causes rapid mixing and increased rates of momentum, heat, and mass transfer, which is important feature of turbulent combustion. Turbulence is swirling, and is characterized by high levels of fluctuating vorticity. The vortex plays an important role in the turbulent combustion. Thus, the studies on flames in the vortex flow are very important to understand the turbulent combustion phenomena.

So far, to investigate the behavior of premixed flames in a vortex flow, we have focused on tubular flames. Since a tubular flame was found to be formed in a stretched, rotating flow field, its extinction limit and flame structure have been studied [5-7]. From these studies, it has been found that its characteristic depends on the Lewis number, Le. For example, the extinction limits depend on Lewis number [5, 6]; for a lean mixture whose Lewis number is less than unity, its flammable range becomes wider, whereas for a mixture whose Lewis number is larger than unity, its flammable range becomes narrower.

However, the flame temperature, which is a direct measure of the burning intensity and closely related to the extinction limit, has not yet been measured except for a methane/air mixture [7]. It is necessary to obtain tubular flame temperatures for various mixtures and discuss the flame characteristics in a stretched flow in terms of stretch effect and Lewis number, so that we can predict the flame behavior of stretched flames and obtain a useful information for modeling the turbulent combustion.

In this study, we have attempted to measure flame temperatures for hydrogen, methane, and propane/air mixtures to investigate the flame temperature in stretched flow with various Lewis numbers. For comparison, we have measured the temperatures of Bunsen flames to examine the curved flame in a uniform flow. By comparing the results of tubular flames, it is possible to clarify the stretch effect on the flame characteristics based of the Lewis number.

Experimental

Figure 1 shows the swirl-type burner used in this experiment. Combustible mixtures are introduced tangentially from the center slit of 3 mm width into a glass tube of 18 mm inner diameter, and the burned gas exits from both ends of the burner; a rotating, stretched flow field can be obtained inside the burner [5]. The glass tube is 120 mm long, and the center slit is 80 mm long.

For comparison, a Bunsen-type burner was used. This burner has a nozzle by which gives a uniform velocity distribution at the exit. A diffusion flame of propane was formed around the burner exit as a pilot flame to stabilize flames. The fuels used are methane, hydrogen, and propane. Temperatures have been measured with a silica coated Pt/Pt-13%Rh thermocouple (wire diameter; 50 μm and 100 μm) unless stated otherwise. In our temperature measurements, we used thermocouple and there is a difference between measured and actual temperatures. A radiation correction of measured temperature was made by the Kaskan's relation [8].

Results and Discussion

Tubular Flame Temperature

In previous studies, both the radial and axial temperature distribution show that the temperature in the inner region is constant and this value was constant. Hence, this temperature is considered to be representative of the tubular flame temperature and we examine this temperature. Figure 2 shows the variations of the tubular flame temperature of various mixtures as functions of the fuel concentration.

To estimate the flame temperature with no stretch, we obtain the adiabatic flame temperature, T_{ad} for hydrogen, methane, and propane/air mixtures by a chemical-equilibrium calculation program developed by the NASA Lewis Center [9]. In this figure, we show adiabatic flame as the solid line.

For methane/air mixtures, the flame temperature decreases monotonically with an decrease of fuel concentration. The flame extinction occurs when the fuel concentration is 4.84. Comparing the flame temperature and adiabatic flame temperature, it is found that the flame temperatures are almost the same as the adiabatic flame temperatures. However, for hydrogen/air mixtures, the flame temperatures are much higher than T_{ad}. There is about 400 ℃ difference. On the contrary, for propane/air mixtures, the flame temperatures are lower than T_{ad} by 50-100 K.

Bunsen Flame Temperature

In order to clarify the tubular flame temperatures formed in stretched flow, a Bunsen flame was also formed for each mixture and we examined its temperature. The Bunsen flame temperature was measured by the present thermocouple, which was located just above the flame tip, about 5 mm downstream from the tip. Figure 3 shows the obtained Bunsen flame temperature, which is the corrected values for radiative heat loss. The adiabatic temperatures are also shown. In methane/air mixtures, the flame temperature is lower than the adiabatic temperature. In hydrogen/air mixtures, as is very different from the behavior of the tubular flame, the flame temperature is lower than the adiabatic flame temperature by 100 ℃. On the contrary, in propane/air mixtures, the corrected flame temperature is slightly higher than the adiabatic flame temperatures. These results are in accordance with the previous experiments [10, 11]. These flame behaviors are quite different from that of the tubular flame.

In hydrogen/air mixtures, a polyhedral flame was formed for Ω = 10.6 ~ 17.5 %, which sometimes rotated on the burner. In this case, we traversed the thermocouple at half height of the Bunsen flame, and measured the temperatures in the luminous region and in the dark regions. These temperatures and the temperature around the Bunsen flame tip are shown in Fig. 4. As seen in this figure, it is found that the temperatures in the luminous region are higher than the temperatures around the tip, while those in the dark region are lower than the tip temperatures. It is interesting to note that the temperature of the luminous region slightly exceeds the adiabatic temperatures.

Discussion

Using a swirl-type burner, the temperature of the tubular flame established in a stretched, vortex flow was determined for lean methane, hydrogen and propane mixtures. The flame temperature on the Bunsen burner was also measured. These temperatures were compared with the adiabatic flame temperature.

From results, it is found that the temperature of the tubular flame is almost the same as the adiabatic flame temperature in lean methane/air mixtures, considerably higher in lean hydrogen/air, and lower in lean propane/air mixtures. It is also found that this response is opposite to that of the temperature around the Bunsen flame tip; the temperature around the flame tip becomes lower than the adiabatic flame temperature by 50 ℃ in lean methane/air mixtures, lower by 100 ℃ in lean hydrogen/air mixtures, and slightly higher in lean propane/air mixtures.

These different characteristics of flame temperatures between the tubular flame and the Bunsen

flame may be attributed to the difference in the flow field where each flame is formed. As shown in Fig. 5(a), the flow in the Bunsen flame is uniform while its flame front is curved, and hence, the Bunsen flame receives a negative stretch. On the other hand, the flow in the tubular flame is divergent while its flame front is flat and hence the tubular flame receives a positive stretch (Fig. 5(b). Therefore, the different dependency of flame temperature on the mixtures could be explained with the Lewis number considerations. That is, in the case of the tubular flame, as it is formed in stretched flow field, the stream tube across the flame zone is divergent, so that a part of the heat generated in the reaction zone and a part of each component of the mixture pass through the boundary of the stream tube by conduction and diffusion, respectively. Therefore, the Lewis number for each fuel/air mixture is also an important parameter. Since the stretch is positive in divergent flow and negative along the Bunsen flame, the response of a tubular flame temperature should exhibit qualitatively opposite behavior.

In the polyhedral flame of lean hydrogen/air mixtures, the temperature in the luminous region measured is higher than adiabatic flame temperature. This result is also due to preferential diffusion of hydrogen; hydrogen diffuses preferentially into the luminous region and the temperature increases, which is shown in Fig. 5(c). Note that the luminous region is convex towards the unburned mixture stream and hence stretch is positive as in the tubular flame, while the dark region is concave towards the unburned mixture stream, resulting in negative stretched flame. Therefore, it is reasonable to consider that the tubular flame temperature corresponds to the temperature in the luminous region, and both the temperatures of hydrogen/air mixture become higher than the adiabatic flame temperature due to preferential diffusion of hydrogen.

Conclusions

Both tubular flame temperatures and Bunsen flame temperatures have been measured for lean methane, hydrogen and propane mixtures. These temperatures have been compared with the adiabatic flame temperature. In the case of the tubular flame, since it is formed in stretched flow and its stream tube across the flame zone is divergent, the flame is affected by a positively stretch. On the other hand, the flow in the Bunsen flame is uniform and its flame front is concave for the flow, and hence, the flame receives a negative stretch. Therefore, the different dependency of flame temperature on the mixtures could be explained with the Lewis number considerations, and the response of these two flames exhibit qualitatively opposite behavior.

References

1. Robert, W. L., and Driscoll, J. F., *Combust. Flame 87*, (1991), pp. 245-256.
2. Poinsot, T., Veynante, D., and Candel, S., *23rd Symposium (International) on Combustion*, (1990), pp. 613-619.
3. Ashurst, W. T., and McMurtry, P. A., *Combustion Science and Technology 66*, (1989), pp. 17-37.
4. Peters, N., and Williams, F. A., *22nd Symposium (International) on Combustion*, (1988), pp. 495-503.
5. Ishizuka, S.: *Twentieth Symposium (International) on Combustion*, (1984), pp. 287-294.
6. Ishizuka, S.: Combustion and Flame 75, 367 (1989).
7. Yamamoto, K., Ishizuka, S. and Hirano, T., *25th Symposium (International) on Combustion*, (1994), pp. 1399-1406.
8. Kaskan, W. E.: *Sixth Symposium (International) on Combustion*, Reinhold Publishing Co., New York, (1957), pp. 134-143.
9. S. Gordon and B. J. McBride, Computer Program for Calculation of Complex Chemical Equilibrium Compositions, Rocket Performance, Incident and *Reflected Shocks, and Chapman-Jouget Detonations*, NASA SP-273 Interim Revision N78-17724, 1976.
10. Mizomoto, M., Asaka, Y., Ikai, S. and Law, C. K.: Twentieth Symposium (International) on Combustion, (1984), pp. 1933-1939.
11. Law, C. K., Cho, P., Mizomoto, M. and Yoshida, H.:Twenty-first Symposium (International) on Combustion, (1986), pp. 1803-1809.

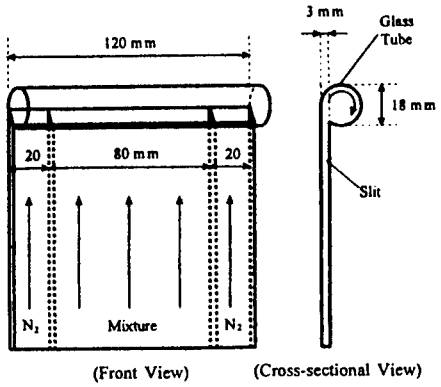


Fig. 1. Swirl-type burner.

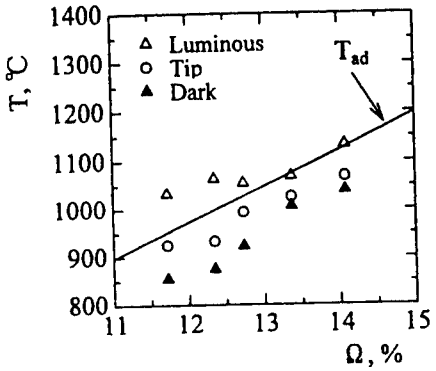


Fig. 4. Comparison between temperature of polyhedral burner flame (luminous, dark and tip regions) and adiabatic flame temperature for hydrogen/air mixtures.

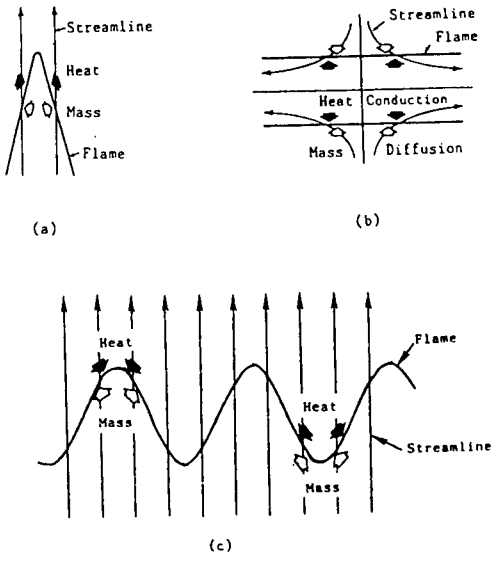


Fig. 5. Schematics illustrating the directions of heat conduction and mass diffusion of limiting reactant in various flames: (a) Bunsen flame, (b) tubular flame, and (c) cellular flame.

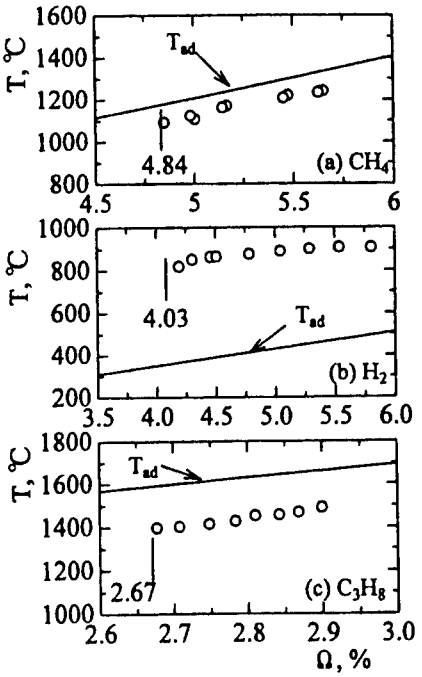


Fig. 2. Comparison between tubular flame temperature and adiabatic flame temperature for (a) lean hydrogen/air mixtures, (b) lean methane/air mixtures, (c) lean propane/air mixtures.

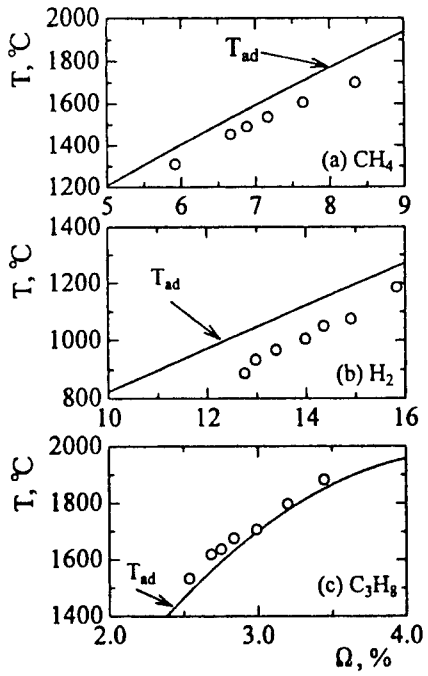


Fig. 3. Comparison between temperature around Bunsen flame tip and adiabatic flame temperature for (a) methane/air mixtures, (b) hydrogen/air mixtures, (c) propane/air mixtures.

BURNING VELOCITY MEASUREMENTS IN MICRO-GRAVITY CONDITIONS

Matthew Ulinski, Zhouyun Li, Mimmo Elia, Cedric Fletcher, and Mohamad Metghalchi
Department of Mechanical, Industrial, and Manufacturing Engineering
NORTHEASTERN UNIVERSITY
360 Huntington Avenue
Boston, MA
Phone: 617.373.2966 Fax: 617.373.2921 Email: metghal@coe.neu.edu

INTRODUCTION

Laminar burning velocity is a fundamental property of combustion. The laminar burning velocity of a fuel is unique for different fuels, fuel mixtures, temperatures and pressures. The determination of the burning velocity is important for use in the modeling turbulent combustion [1]and in the study of reaction rates in chemical processes [2]. In turbulent combustion modeling, there is a need for simple, workable laminar burning velocity correlations as functions of variable mixtures, unburned gas temperatures and pressures. Current development has put emphasis on the burning velocity of fuels under lean conditions, high unburned gas temperature and pressure and with the addition of diluents. It is this emphasis which has lead to this study of the use of the constant volume combustion method in a microgravity environment to determine laminar burning velocity. In this study the laminar burning velocity of methane-air fuel mixtures with ϕ = 0.8 to 1.2, at initial pressure of 1 atm and temperature of 298K in a microgravity environment, have been compared to those collected in a normal gravity environment.

EXPERIMENTAL FACILITY

Over the past fifty years much research has been done to develop correlations for the determining of the burning velocity of different fuels [3-6]. Experimental techniques to develop these correlations include steady state and propagation methods. The constant volume combustion vessel is a propagation technique in which a fuel mixture is ignited at the center of a spherical steel vessel. As the fuel mixture burns, the temperature and pressure of the unburned gas rise By using the constant volume combustion method, laminar burning velocity correlations for a wide range of unburned gas temperatures and pressure can be calculated from data collected in one experiment.

One of the assumptions used in this analysis is that the flame is spherical. Verification of this is done by the use of ionization probes at the walls of the vessel (Figure 1). These probes produce a current when the ionized gas

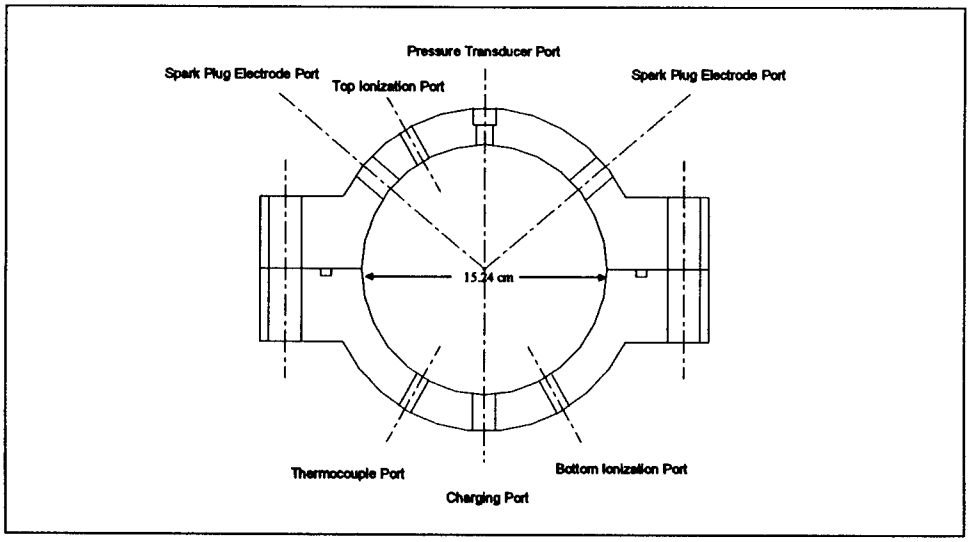


Figure 1: Schematic of the Spherical Combustion Vessel

come in contact with them. Experimental work using the constant volume vessel has shown that the top ionization probe consistently detects the flame front before the lower probe. This is due to the buoyancy of the

burned gases rising in the vessel as the fuel burns. This time lag is significant in mixtures burned at high initial pressures, lean mixtures and high diluent concentrations [7]. To minimize this effect, the authors have built a drop mechanism in which fuel mixture is burned while the constant volume vessel is released into free fall. This allows the mixture to burn in essentially a microgravity environment and reduces the effect of the rising hot gases.

The experimental facility to conduct the microgravity testing consists of the combustion vessel, data acquisition system and dropping mechanism and housing. The combustion vessel (Figure 1) is made of two steel housings which bolt together to form a 15.4 cm diameter spherical chamber. The vessel is fitted with special spark plugs designed to ignite the mixture in the center of the vessel. It is also fitted with ionization probes, a thermocouple and pressure transducer. The pressure transducer is piezoelectric with a frequency response of 100kHz. It is connected to a computer data acquisition system through a charge amplifier. The dropping mechanism (Figure 2) consist of a housing which provides shock absorption for the combustion vessel and a release mechanism to initiate free fall. When released the housing falls two meters (650 milliseconds) into a bed of polyethylene beads. Data acquisition and spark ignition are controlled by a microswitch located on the release mechanism.

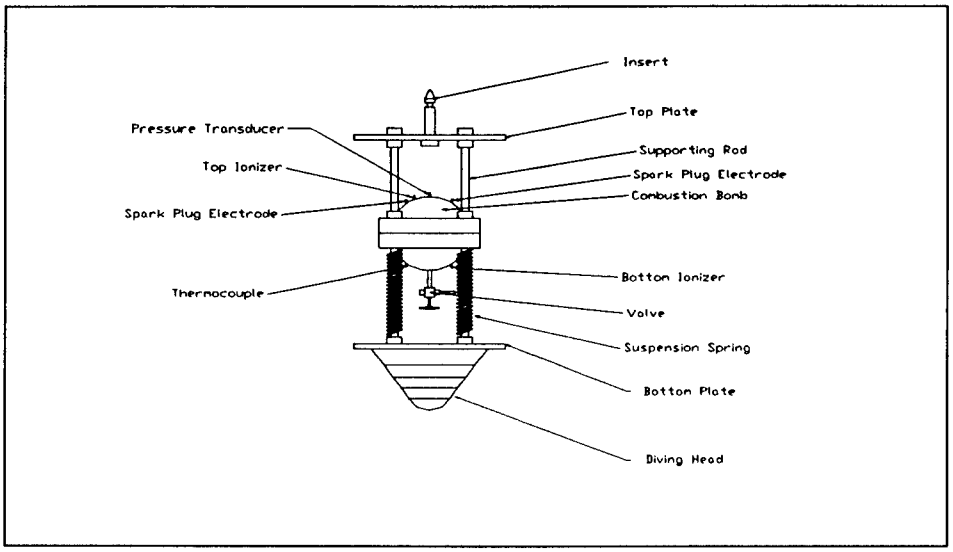


Figure 2: Schematic of Combustion Vessle Dropping Mechanism

MODEL

In this study, laminar burning velocity is calculated using a modification of the method developed by Metghalchi and Keck [8]. In Metghalchi and Keck's method, laminar burning velocity is calculated from the rate of mass fraction of the fuel burned. The mass fraction burned is determined from the pressure data collected during the combustion process in the constant volume combustion vessel. After ignition, the gas consists of two parts: the burned gas at the center of the vessel and the unburned gas. The burned gas expands into the unburned gas. The modifications to Metghalchi and Keck's model allow for thermal gradients in the burned gas, exact calculation of the burned gas properties using an equilibrium code, and consideration of stretch effects (using Bradley's method [9]).

Two conservation equations: the conservation of mass and the conservation of energy equation are solved to yield the mass fraction of the burned gas and the temperature of the burned gas:

$$\frac{V}{m} + \frac{A\delta}{m} = \int_0^x v_b \, dx' + \int_x^1 v_u \, dx' \qquad (1)$$

$$\frac{E}{m} - \frac{Q}{m} = \int_0^x e_b \, dx' + \int_x^1 e_u \, dx' \qquad (2)$$

where:

A = combustion vessel wall area
e = specific internal energy
E = total initial energy of gas in the vessel
m = mass of gas in the vessel
Q = total energy transfer from the boundary layer displacement thickness to the vessel wall
x = mass fraction burned
x' = integration variable
v = specific volume
V = combustion vessel volume
δ = boundary layer displacement thickness

and the subscripts b and u refer the to burned and unburned gas respectively. The boundary layer displacement thickness is defined as:

$$\delta = (1/\rho_\infty)\int_0^\infty (\rho-\rho_\infty)\,dr \qquad (3)$$

where:

ρ = density of unburned gas within the boundary layer displacement thickness
ρ_∞ = density of that portion of unburned gas that compresses isentropically

The boundary layer displacement thickness, $\delta(t)$, was calculated using the method outlined by Metghalchi and Keck. Energy transfer at the boundary to the vessel wall causes the displacement thickness temperature to be lower than the rest of the unburned gas. Therefore, the displacement thickness gas density is higher. Assuming this displacement thickness has the same properties as the core gas, the volume of the vessel must be increased by $A\delta/m$ to account for this density difference. Total energy transfer to the bomb wall is then calculated as :

$$Q = A\int_0^\delta p\,d\delta' \quad \text{where, } \delta' \text{ is the integration variable.} \qquad (4)$$

The two conservation equations (1,2) are solved numerically for the mass fraction burned. Once the mass fraction burned is known as a function of time it can be differentiated numerically to obtain $\dot{x}$. Laminar burning velocity is then calculated as:.

$$S_u = mv_u\dot{x}/A_f \qquad (5)$$

where:

$\dot{x}$ = rate of mass fraction burned
A_f = the area of the flame = $4\pi R_f^2$ (6)

and, R_f, is the radius of the flame front, $R_f=(3V_b/4\pi)^{1/3}$, which is calculated from the volume of the burned gas:

$$V_b = xv_b m \qquad (7)$$

RESULTS AND CONCLUSION

Preliminary results show good agreement between the burning velocity calculated in gravity and microgravity conditions (Figure 3). The results shown compare data collected using the free fall dropping mechanism and data previously collected using the same combustion vessel under normal conditions [9]. The ionization probe signals from the microgravity runs also confirmed that the buoyancy effect had been minimized. The top and bottom ionization probe signals recorded the flame front arrival within a tenth of a millisecond apart, while the ionization signals from the normal gravity tests showed almost 1-2 millisecond difference at initial pressure and temperature of 1 atm and 298K .

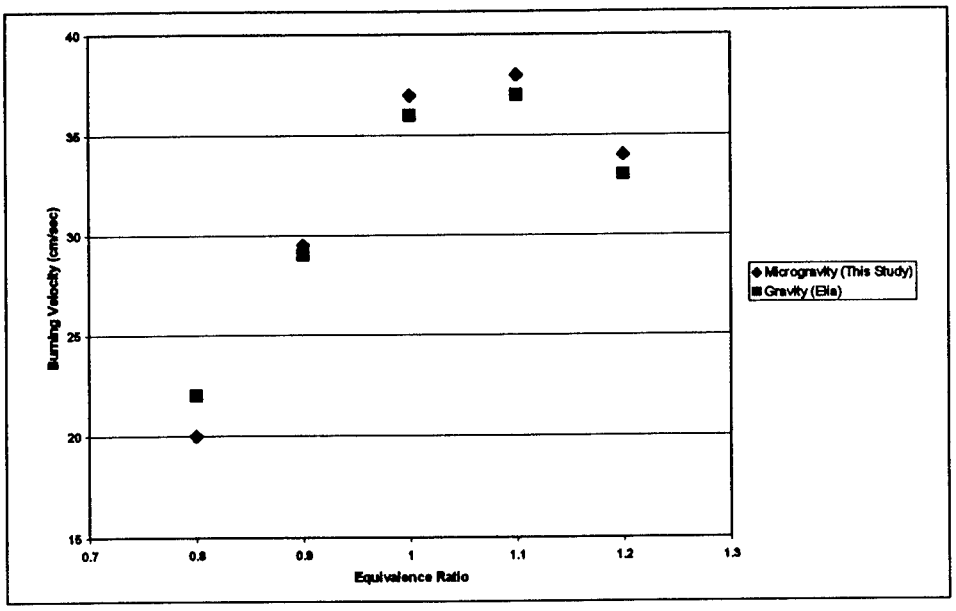


Figure 3: Comparison of Burning Velocity of Methane-Air At P_i = 1 atm and T_I = 298K under Normal Gravity and Microgravity Conditions

REFERENCES

[1] Keck, J. C., "Turbulent Flame Structure and Speed in Spark-Ignition Engines", Nineteenth International Symposium on Combustion, p. 1451-1466. 1982.

[2] Brown, Martin J., Smith, David B., and Taylor, Simon C., "Influence of Uncertainties in Rate Constants on Computed Burning Velocities", *Combustion and Flame*, 117:652-656. 1999.

[3] Clingman, William H., Brokaw, Richard S., Pease, Robert, "Burning Velocities of Methane with Nitrogen-Oxygen, Argon-Oxygen and Helium-Oxygen Mixtures", Fourth Symposium (International) on Combustion. 310-313. 1953

[4] Ryan, T.W., and Lestz, S.S., "The Laminar Burning Velocity of Isooctane, N-Heptane, Methanol, Methane, and Propane at Elevated Temperature and Pressures in the Presence of a Diluent", *SAE Technical Paper Series*, 800103. 1980.

[5] Agrawal, D.D., "Experimental Determination of Burning Velocity of Methane-Air Mixtures in a Constant Volume Vessel", *Combustion and Flame*, 42:243-252. 1981.

[6] Zhu, D.L., Egolfopoulos, F.N., and Law, C.K., "Experimental and Numerical Determination of Laminar Flame Speeds of Methane/(A_r, N_2, CO_2)-Air Mixtures as Function of Stoichiometry, Pressure, and Flame Temperature", Twenty-Second Symposium (International) on Combustion, 1537-1545. 1988

[7] Clarke A, Stone R. and Beckwith P., "The Measurement of Laminar Burning Velocity of Methane/Air/Diluent Mixtures in a constant Volume Combustion Bomb in a micro-gravity Environment", Journal of the Institute of Energy, Vol. 68, p. 130-136. 1995.

[8] Metghalchi, M., and Keck, J., "Burning Velocities of Mixtures of Air with Methanol, Isooctane, and Indolene at High Pressure and Temperature", *Combustion and Flame*, 48:191-210. 1982.

[9] Bradley, Derek, Gaskell, P.H., and Gu, X.J., "Burning Velocities, Markstein Lengths, and Flame Quenching for Spherical Methane-Air Flames: A Computational Study", *Combustion and Flame*, 104:176-198. 1996.

[10] Elia, Mimmo, Laminar Burning Velocity of Methane-Air-Diluent and Methane-Oxygen-Argon Mixtures, Masters Thesis, Northeastern University. 1999.

On the Establishment of Stationary Flame Balls*

L. He, S. D. Tse, and C. K. Law
Department of Mechanical and Aerospace Engineering,
Princeton University, Princeton, NJ 08536

Introduction

Studies on outwardly-propagating flames [1, 2, 3] have frequently assumed that the flame radius is much larger than the flame thickness such that both the structure and flame velocity are only slightly different from those of the planar flame. The structure of the stationary flame ball (SFB) [4], however, is very different in that convective transport is absent while the product and heat release are diffusively transported outward to the ambient. As such, the flame structure assumes a diffusive character and is not localized. Stability analyses by Zeldovich et al. [5] and Deshaies and Joulin [6] through the thermal-diffusion model showed that the adiabatic SFB is unconditionally unstable at its equilibrium radius, tending to either collapse inward for a negative initial perturbation of the flame position, or propagate outwardly for a positive initial perturbation. Based on such an unstable nature of the SFB, Zeldovich et al. [5] indicated that the critical condition for flame ignition should be controlled by the radius of the SFB, and that heat loss could play a stabilizing role because the extent of heat loss increases with increasing flame size. This concept was further developed by Buckmaster et al. [7, 8], via asymptotic analysis, showing that, in the presence of heat loss in the near field, the solution with the smaller equilibrium radius is unstable to one-dimensional perturbations while that with the larger equilibrium radius is stable. It was thus suggested that the SFB observed in experiments carried out in microgravity [9, 10] was stabilized by heat loss, and that SFBs can be observed only when the Lewis number is smaller than unity [11].

In these previous studies the SFB was considered as a particular phenomenon isolated from the propagating flame. However, in practical situations, a propagating flame is first established when an energy source is deposited in a reactive mixture. It is thus of interest to investigate how a propagating flame develops into a motionless SFB. This evolution issue is important because it determines the critical condition for the existence of the SFB. In the present computational work, we first study the transition from an expanding spherical flame to a flame ball, using constant properties and one-step kinetics. Results show that with increasing heat loss from the adiabatic limit, the expanding flame sequentially: (i) evolves into a planar propagating flame, (ii) fails to sustain continuous propagation due to heat loss, and (iii) evolves into the SFB. These results are further substantiated through the simulation of flame propagation in hydrogen/air mixtures.

Results with Simplified Chemistry and Transport

The physical situation simulated is the evolvement of the aerothermochemical flow field subsequent to the deposition of a heat source in a homogeneous medium. We present in this section results obtained by assuming constant transport properties and one-step overall reaction, with a Zeldovich number of $\beta = 20$ and a Lewis number of $Le = 0.3$. The flame radius, defined as the location of the maximum temperature, is plotted in Fig. 1 as a function of time for different values of a heat loss parameter, $H = 0$, 0.5, 10 and 100. It is seen that there are three regimes of the flame response which are respectively separated by some critical values of heat loss, H_{c1}, H_{c2} and H_{c3}. Specifically, when heat loss is very small ($H = 0$ in the limiting case), the flame ignited at the center decelerates asymptotically to the planar flame. When $H_{c1} < H < H_{c2}$ (e.g. $H = 0.5$, 10), the "flame" radius first expands outwardly and then

* For presentation at the 1999 Technical Meeting of the Eastern States Section of the Combustion Institute, Raleigh, NC, October 11-13.

shrinks to the center at $t = 8$ and 0.1 respectively. In these two cases, an SFB cannot be established directly from the point ignition source. When $H_{c2} < H < H_{c3}$ (e.g. $H = 100$), a spherical flame first expands, then shrinks, and finally stabilizes as a stationary spherical flame. Thus an SFB can be reached directly from an expanding flame ignited by a point source. When the heat loss is very large, $H > H_{c3}$, the flame is very difficult to be ignited.

The corresponding maximum flame temperature is shown in Fig. 2. For $H = 0$, the flame temperature decreases steadily to that of the planar flame. As the heat loss is increased to values larger than H_{c1}, say $H = 0.5$ and 10, the flame temperature first decreases slowly and then drops very rapidly around $t = 8$ and 0.1 respectively, indicating clearly the occurrence of extinction of the flame front. Thus the shrinking of the "flame" radius, observed in Fig. 1 for this regime, is simply the consequence of diffusive mixing of the non-reactive hot gas sphere with the cold ambience subsequent to flame extinction. Finally, as H is increased to 100, a different scenario emerges in that the temperature first decreases and then increases to that of the SFB.

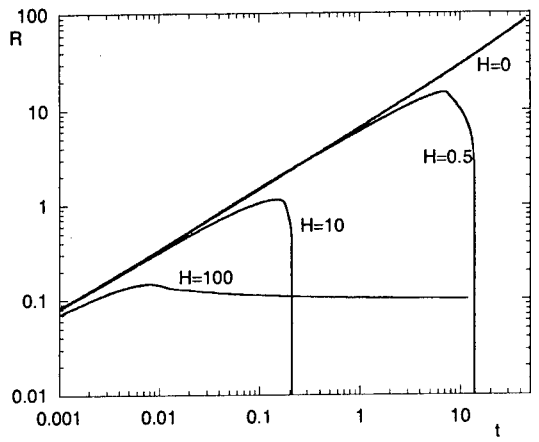


Figure 1. Flame front trajectory for different values of heat loss using simplified chemistry and transport.

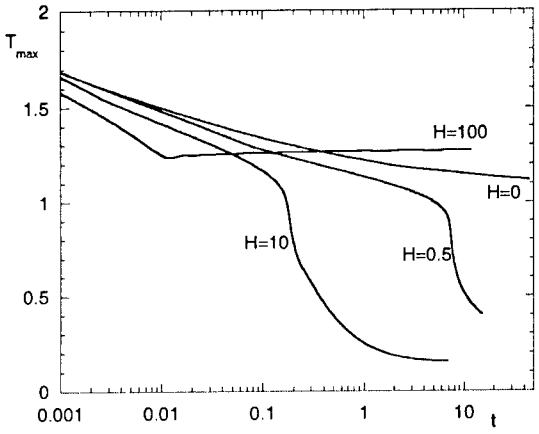


Figure 2. Maximum temperature for different values of heat loss using simplified chemistry and transport.

Flame Dynamics in Hydrogen/Air Mixtures

To investigate the manifestation of the above phenomena in actual fuel/oxidizer systems, simulations were conducted for hydrogen/air mixtures in concentration ranges examined in the space experiments of STS-83 and STS-94 [12]. A one-dimensional, time-dependent flame code using detailed chemical and transport sub-models, developed by Rogg [13], and incorporating optically thin radiation with Planck mean absorption coefficients taken from Hubbard and Tien [14], was employed. Ignition was achieved by minimal energy deposition centered at zero radius. The flame radius, defined as the location of peak heat release, is plotted in Fig. 3 as a function of time for different concentrations of hydrogen in air. The corresponding maximum flame temperature is plotted in Fig. 4. It is seen that, with 3% H_2 in air, the ratio of radiative loss to chemical heat release is too large such that a self-propagating flame can not be established. Movement of the heat release front is entirely due to the externally deposited ignition energy. In the approximate range of 3.5% to 6.5% H_2 in air, a spherical flame propagates outwardly, but then recedes inwardly as it slowly evolves into an SFB. Within this range, the ratio of radiative loss to chemical heat release is optimal for the stabilization and sustenance of the SFB, both computationally and experimentally [12]. In accordance with the understanding discussed above, the maximum in the flame radius history corresponds to the degeneration of the propagating flame structure into that of the diffusion-driven SFB. However, at 7% H_2 in air, Fig. 3 shows that there is not enough radiative loss to

compensate for the increased chemical heat release to dynamically transform the propagating flame into an SFB. Instead, the flame propagates until it self-extinguishes due to radiative loss from its large volumetric size. As the hydrogen concentration is increased, the flame propagates to a larger radius before radiative self-extinction, eg. 11% H_2 in air. However, beyond a critical equivalence ratio, the flame is able to survive permanently, existing asymptotically as a planar flame, eg. 15% H_2 in air. Preliminary calculations incorporating optically thick radiation utilizing a detailed emission/absorption statistical narrow band model reveal that the size of the resulting flame ball is enlarged for the same equivalence ratio. However, the qualitative dynamics of the flames as a function of the ratio of radiative heat loss to chemical heat release is not affected.

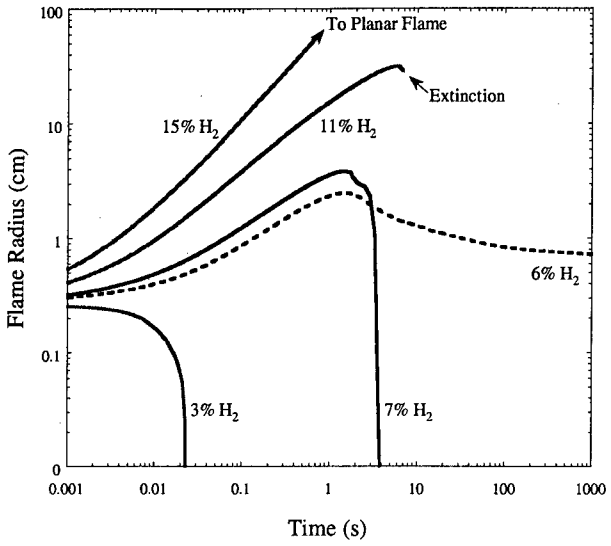


Figure 3. Trajectory of the flame front for different hydrogen/air mixtures assuming optically thin radiation.

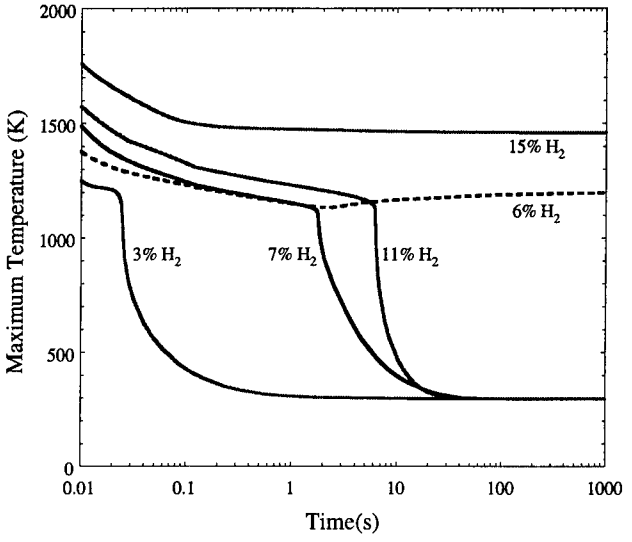


Figure 4. Maximum temperature for different hydrogen/air mixtures assuming optically thin radiation.

Mechanistic Interpretation of Phenomenon

To provide a physical, mechanistic interpretation of the results obtained in the present study, we employ the quasi-steady solution of the simulation, shown in Fig. 5. We start with the flame at the Zeldovich SFB state, and give it a positive displacement such that it is now situated at a location of smaller diffusion velocity. The inherent instability of the Zeldovich flame ball will then cause the flame to continuously propagate outward with increasing velocity. This accelerative expansion of the flame is insensitive to the mixture Lewis number and heat loss rate, and is quickly arrested for sub-unity Lewis number mixtures because of the rapid reduction in the flame temperature as the flame curvature decreases. The propagation velocity is subsequently reduced. Radiative heat loss effect is still not significant at this stage. However, as the flame becomes larger, radiation effect could eventually become important. If the loss is small, then flame expansion continues such that the flame would gradually evolve into one resembling the planar flame. When there is no heat loss, we retrieve the adiabatic planar flame in the limit. When there is only a small amount of heat loss, the response resembles that of the nonadiabatic planar flame, characterized by the existence of the extinction turning point. However, if the loss is quite substantial, then continuous expansion to the near-planar state is not possible. In order to sustain burning in the presence of such strong radiative heat loss, the flame would maintain its spherical geometry so as to retain its elevated flame temperature due to the curvature. The expansion is eventually arrested, resulting in the formation of the SFB.

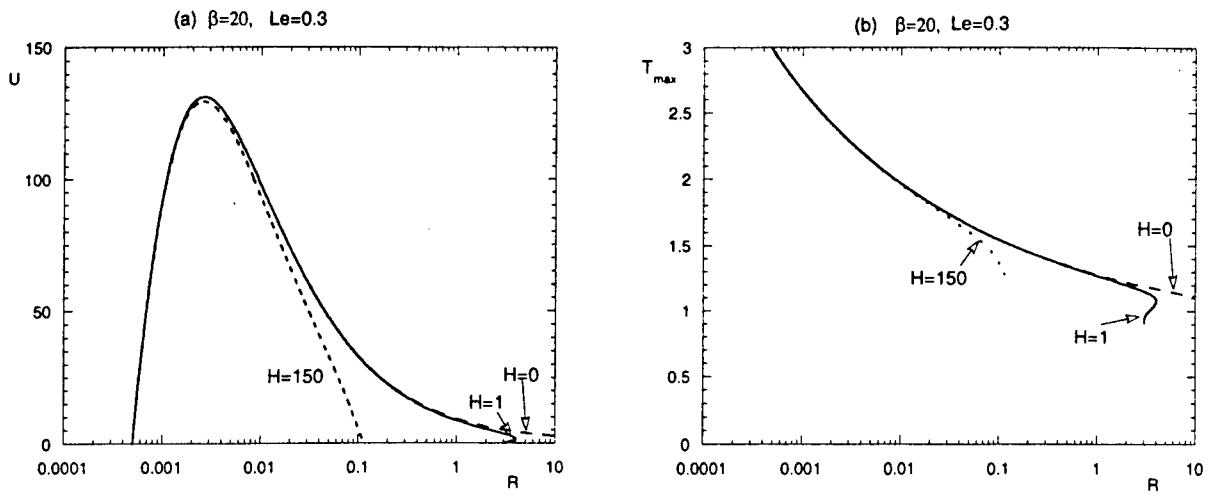


Figure 5. Quasi-steady variation of the flame velocity and temperature at the reaction sheet as a function of the flame radius.

Concluding Remarks

This work has conclusively identified the mechanism and factors responsible for the formation of an SFB from a centrally-ignited premixture. Moreover, the analyses and simulations evince that SFBs can be established from a propagating premixed flame for only a narrow range of mixtures, consistent with that observed in experiments. Although SFBs may be unstable to three-dimensional perturbations perhaps affecting the sizes in which they exist [15], the one-dimensional mechanism described in this work may impact the flame dynamics before such three-dimensional effects can be manifested. As a result, further investigation is needed to determine the true path of SFB formation from ignition.

Acknowledgement

This work was supported by NASA under its Microgravity Combustion Program. We thank Professors Paul Ronney and John Buckmaster for stimulating discussions.

References

[1] Frankel, M. L. and Sivashinsky, G. I. *Combust. Sci. Technol.* 31: 131-138 (1983).
[2] Pelce, P. and Clavin, P. *J. Fluid Mech.* 124, 219-237 (1982).
[3] Sun, C. J., Sung, C. J., He, L. and Law, C. K. *Combust. Flame* 118:108-128 (1999).
[4] Zeldovich, Ya. B., (1944) *Theory of Combustion and Detonation of Gases.* Izd-vo. Akad. Nauk SSSR, Moscow. In Selected works of Yakov Borisovich Zeldovich (J. P. Ostriker, G. I. Barenblatt and R. A. Sunyaev), p. 162-232, 1992.
[5] Zeldovich, Ya. B., Barenblatt, G. I., Librovich, V. B., and Makhviladze, G. M., The Mathematical Theory of Combustion and Explosions, Consultants Bureau, New York 1985.
[6] Deshaies, B., and Joulin, G. *Combust. Sci. Technol.* 37: 99(1984).
[7] Buckmaster, J., Joulin, G. and Ronney, P., *Combust. Flame* 79: 381-392 (1990).
[8] Buckmaster, J., Joulin, G. and Ronney, P., *Combust. Flame* 79: 411-422 (1991).
[9] Ronney, P. D. *Combust. Flame* 82, 1-14 (1990).
[10] Ronney, P. D., Whaling, K. N., Abbud-Madrid, A., Gatto, J. L. and Pisowicz, V. L. *AIAA Journal* 32 (3), 569-577 (1994).
[11] Lozinski, D., Buckmaster and Ronney, P., *Combust. Flame* 97: 301-316 (1994).
[12] Wu, M.S., Liu, J.B., and Ronney, P.D., *Twenty-Seventh Symposium (International) on Combustion*, The Combustion Institute, Pittsburgh, 1998, pp.2543-2550.
[13] Rogg, B., RUN-1DL: *The Cambridge Universal Flamelet Computer Code, User Manual*, University of Cambridge, Cambridge, England (1993).
[14] Hubbard, G.L., and Tien, C.L., *J. Heat Trans.* 100:235-239 (1978).
[15] Wu, M. S., Ronney, P., Colantonio, R. O., and Vanzandt, D. M. *Combust. Flame* 116: 387-397 (1993).

On the Branched-Chain Mechanism of Hydrogen-Chlorine Reactions: Laminar Flame Speed Experiments and Kinetic Modeling of $H_2/Cl_2/N_2$ Mixtures*

J.C. Leylegian† and C.K. Law
Department of Mechanical and Aerospace Engineering
Princeton University
Princeton, NJ 08544-5263 USA
E-mail: jcl@Princeton.EDU

H. Wang
Department of Mechanical Engineering
University of Delaware
Newark, DE 19716-3140 USA

Introduction

Interaction between hydrogen and chlorine occurs in systems involving chemical processing [1] and toxic waste incineration [2]. It is this interaction that is responsible for reduced burning intensity in halogenated flames and increased soot formation in non-premixed combustion [3]. Despite its importance, there is a dearth of data for the direct interaction of these substances at combustion temperatures.

The reactions of the hydrogen-chlorine system have been classically described by a straight-chain mechanism:

$$Cl_2 + M \rightleftarrows 2\,Cl + M \quad (1)$$

$$H_2 + Cl \rightleftarrows HCl + H \quad (2)$$

$$H + Cl_2 \rightleftarrows HCl + Cl \quad (3)$$

$$H + Cl\ (+M) \rightleftarrows HCl\ (+M). \quad (4)$$

However, early studies on H_2/Cl_2 flames [4–6] used a mechanism of energy branching first proposed by Kitagawa [7] in order to predict the experimental data:

$$H + Cl_2 \rightleftarrows HCl^* + Cl \quad (3')$$

$$HCl^* + Cl_2 \rightleftarrows HCl + Cl_2^* \quad (5)$$

$$Cl_2^* \rightarrow 2\,Cl \quad (6)$$

$$HCl^* + M \rightarrow HCl + M\,. \quad (7)$$

The * indicates a vibrationally excited molecule. Here a part of the exothermicity of reaction (3) is stored in the form of vibrational energy in HCl, resulting in a vibrationally excited species HCl^*. Normally this excess energy is rapidly removed by collision (reaction 7), but since hydrogen chloride has a greater bond energy than molecular chlorine, the transfer of excess vibrational energy from HCl to Cl_2 can result in the cleavage of the chlorine molecule. As a result, reactions (5) and (6) are sometimes combined [8]:

$$HCl^* + Cl_2 \rightarrow HCl + 2\,Cl\,. \quad (5')$$

A subsequent study by Corbeels and Scheller [8] measured flame speeds of H_2/Cl_2 mixtures diluted with N_2, also using a Bunsen flame. Their theoretical analyses showed that there was no evidence to support the energy branching mechanism in these flames, despite the fact that reaction (3′) had been experimentally observed [9].

The early studies [6,8] on H_2/Cl_2 flame speeds were conducted using the Bunsen flame technique. It is known that this technique suffers from stretch effects which cannot be easily quantified and removed, especially in the case for mixtures with $Le \neq 1$ [10]. Consequently, the validity of the conclusions reached concerning the participation of the vibrationally excited HCl^* in the reaction process may be questionable as it is highly influenced by the uncertainty in the experimental flame speed data. An additional consideration is that the theoretical analysis of Corbeels and Scheller [8] relied on a semi-empirical analysis of the flame data, without considering the coupled effects of detailed reaction kinetics and species transport. As a result of these uncertainties, the involvement of the vibrationally excited HCl in the reaction kinetics of H_2/Cl_2 flames remains unsettled.

The objective of the present work is to resolve this long-standing, unresolved issue. In doing so, we also hope to gain further insight in the gas-phase reaction kinetics of halogenated species. The laminar flame

---

* For Presentation at the 1999 Fall Technical Meeting of the Eastern States Section of the Combustion Institute, Raleigh, NC, October 11–13, 1999.

† Corresponding Author.

speeds of $H_2/Cl_2/N_2$ mixtures were acquired using the counterflow flame technique [11], which allows the systematic subtraction of flame stretch effects, as encountered but not accounted for in previous studies [6,8]. Concurrently, a numerical study was performed by modeling these flames using detailed chemistry and transport. In addition, data on these flames can also be used as a source of validation for new studies on hydrogen atom diffusivity [12,13].

Experimental and Numerical Methodologies

The laminar flame speed was measured using the counterflow twin-flame technique [11]. The burner and flow system are discussed in detail elsewhere [14]. However, some modifications have been made to the experimental procedure and apparatus, to allow for the safe use of chlorine in this experiment. All tubing used in the flow system was opaque to prevent premature initiation of the reaction via Cl_2 photodissociation. In addition, the calibration of critical orifices for Cl_2 could not be performed directly using a wet test meter due to its solubility in water. Instead, the calibrations were performed using N_2, and the volumetric flow rates were converted to those for Cl_2 by assuming perfect gas behavior, isentropic flow, and sonic conditions at the orifice exit. This method was tested by comparing similar calibrations of the flow meters using gases which are insoluble in water, and agreement between calculation and direct measurement was within 1%.

The laminar flame speeds were obtained by extrapolation of the local minimum velocity ahead of the thermal mixing layer as a function of stretch rate to zero stretch. Both linear [11] and nonlinear [15] extrapolation techniques were employed in the data analyses. Extrapolated results using the two techniques generated qualitatively similar results, with the nonlinear extrapolation yielding flame speeds approximately 3 cm/s lower than the linear extrapolations. Uncertainties in the flame speed measurement are primarily due to the laser Doppler velocimetry (LDV) method, and are generally 1-2 cm/s.

The laminar flame speeds were computed using the Sandia premixed flame code [16–18]. The calculations were performed over a domain of 200 cm, at a pressure of 1 atm and initial temperature 298.2 K, including multicomponent diffusion coefficients and Soret effect. The solution meshes specified maximum relative gradient and curvature values of 0.01. The flame code and transport subroutine libraries were also modified in order to calculate normalized first-order sensitivity coefficients of the solutions to the species diffusivities.

Experimental Results and Predictions based on Straight-Chain Mechanism

Figure 1 shows the measured laminar flame speeds for $H_2/Cl_2/N_2$ mixtures as a function of equivalence ratio at different N_2 mole fractions. Plotted along with these data are the data of Corbeels and Scheller [8] at an N_2 mole fraction of 0.5. The data coincide at $\phi = 1$, but diverge at higher equivalence ratios, with the present data consistently smaller than those of the previous study. This divergence can be attributed primarily to the effect of increasing Lewis number on the negatively-stretched Bunsen flame employed in Ref. 8. This discrepancy was also observed experimentally in lean benzene/air and iso-octane/air flames [19], and is a consequence of flame stretch in nonequidiffusive mixtures [10].

Figure 1 also shows the calculated laminar flame speeds, employing a straight-chain mechanism. The detailed kinetic model consists of 6 reactions and 6 species. The reaction rate constants for the straight-chain portion of the model were taken from Refs. 20–23. The experimental data are found to be in good agreement with the straight-chain model at stoichiometric conditions, but at higher equivalence ratios the experimental flame speeds are higher than those predicted by the straight-chain model. The difference is almost 20 cm/s for 0.5 mole fraction N_2 and $\phi = 2.00$. This would indicate that a straight-chain mechanism cannot satisfactorily predict the laminar flame speeds, especially at lower N_2 dilutions.

Development of a Branched-Chain Model

Because of the inability of the straight-chain mechanism to predict all of the data, a model was developed using the chain-branching mechanism outlined earlier. Preexponential factors for the rate constants of reactions (3′), (5′), and (7) were estimated, using the collision frequency of the hard-sphere model as an upper limit. The heat of formation for HCl* was determined by calculating the lowest quantum vibrational level possessing energy greater than that in the Cl–Cl bond (57.8 kcal/mol). The vibrational frequency and anharmonicity constants used in determining the energies are from Ref. 24. This yields a minimum vibrational energy of 63.6 kcal/mol. Because of the high vibrational frequency of the HCl molecule ($\Theta_v = hc\omega/k_B = 4300$ K), most of the population is in the lowest energy level, even at combustion temperatures. At 1000 K, 98.6% of the population will be in the ground state, and at 2000 K, 88.4% will be in the ground state. As a result, we used a ΔH_f° of 41.6 kcal/mol at 298 K for HCl*, and a minimum activation energy of 18.4 kcal/mol for reaction (3′).

With these constraints on the rate constants, we then optimized the HCl* portion of the model to fit the experimental data. These results can be seen in Fig. 1. As expected, the inclusion of the HCl* chemistry increases the calculated laminar flame speed, due to the increased burning intensity brought about by chain branching. This can only be attributed to chemical effects, since the flame temperature is the same whether or not HCl* is included.

Figure 2 shows the sensitivity analyses performed on the 0.5 mole fraction N_2 flame speed solutions, at equivalence ratios of 1 and 2. For both conditions, the flame speed is more sensitive to reaction (2), which is the major chain propagating step, than any other reaction. Reaction (3) has less effect on the flame speed, and retards flame propagation. This can be attributed to the competition of (3) with reaction (3′),which is the first step in the branching process, as well as the fact that (3) consumes an H atom and releases a less diffusive Cl atom. This effect is more important at higher equivalence ratios, where the sensitivities of flame speed to H and Cl increase and decrease respectively. We also note the relative insensitivity of the flame speed to reactions (5′) and (7). This would indicate that reaction (3′) is the rate-limiting step in the chain-branching process, most likely due to its high activation energy (~20 kcal/mol for (3′) versus ~3 kcal/mol for reactions (5′) and (7)).

It can also be seen that the sensitivity of the laminar flame speed to the mass diffusivity of certain species is comparable to those of the reaction rate constants. At the lower equivalence ratios, the flame speed is more sensitive to N_2 mass diffusivity than any reaction rate constant, but this sensitivity does not vary much with equivalence ratio or N_2 mole fraction over the range of conditions investigated. The sensitivities of flame speed to H, H_2, Cl, and Cl_2 diffusivity are strong functions of equivalence ratio, and it is seen that at lower equivalence ratios the Cl and Cl_2 diffusivities can exert a strong influence on the calculated flame speed, while at higher equivalence ratios H and H_2 become more important. Noting that the sensitivity coefficients are positive for $D_{H,i}$ and in light of a lower H-atom diffusion coefficient as proposed by Paul and Warnatz [25] than the value currently in use [18], the discrepancy between the experimental data and the straight-chain mechanism cannot be resolved by changing the H-atom diffusion coefficient. Even if $D_{H,i}$ can be increased from the current value, it would require its value to be increased by a factor of 2, which is likely to be larger than the uncertainty of the H-atom diffusion coefficient [13].

Concluding Remarks

In this study, laminar flame speeds were measured for $H_2/Cl_2/N_2$ mixtures at different equivalence ratios and nitrogen mole fractions. It is demonstrated that the classical straight-chain mechanism of H_2/Cl_2 reactions cannot adequately predict the laminar flame speeds of these mixtures, especially at high equivalence ratios and low N_2 dilution. A chain-branching mechanism involving vibrationally-excited HCl was then developed and is shown to account for the experimentally determined flame speeds.

This work was sponsored by the Combustion and Thermal Plasmas Program of the National Science Foundation under the technical monitoring of Dr. Farley Fisher.

References

1. Karra, S. B. and Senkan, S. M., Combust. Sci. Technol. 36:123 (1984).
2. Oppelt, E. T., *JAPCA* 37:558 (1987).
3. Glassman, I., *Combustion*, 3 ed., Academic, New York, 1996.
4. Rozlovskiy, A. I., *Z. Fiz. Khim.* 30:2489 (1956).
5. Rozlovskiy, A. I., *Z. Fiz. Khim.* 30:2713 (1956).
6. Slootmaekers, P. J. and Van Tiggelen, A., *Bull. Soc. Chim. Belg.* 67:135 (1958).
7. Kitagawa, T., *Rev. Phys Chem. Japan* 8:71 (1934).
8. Corbeels, R. and Scheller, K., *Tenth Symposium (International) on Combustion*, The Combustion Institute, Pittsburgh, 1965, pp. 65–75.
9. Cashion, J. K. and Polanyi, J. C., *J. Chem. Phys.* 29:455 (1958).
10. Law, C. K., *Twenty-Second Symposium (International) on Combustion*, The Combustion Institute, Pittsburgh, 1989, pp. 1381–1402.
11. Wu, C. K. and Law, C. K., *Twentieth Symposium (International) on Combustion*, The Combustion Institute, Pittsburgh, 1984, pp. 1941–1949.

12. Wang, H. and Law, C. K., Paper presented at the 1996 Fall Technical Meeting of the Eastern States Section of the Combustion Institute, Hilton Head, SC, 1996, pp. 329–332.
13. Wang, H., Paper presented at the 1999 Joint Technical Meeting of the United States Sections of the Combustion Institute, Washington, DC, 1999, pp. 413–416.
14. Leylegian, J. C., Zhu, D. L., Law, C. K., and Wang, H., *Combust. Flame* 114:285 (1998).
15. Tien, J. H. and Matalon, M., *Combust. Flame* 84:238 (1991).
16. Kee, R. J., Rupley, F. M., and Miller, J. A., Sandia Report No. SAND 89-8009, Sandia National Laboratories, Albuquerque, NM, 1989.
17. Kee, R. J., Grcar, J. F., Smooke, M. D., and Miller, J. A., Sandia Report No. SAND 85-8240, Sandia National Laboratories, Albuquerque, NM, 1985.
18. Kee, R. J., Dixon-Lewis, G., Warnatz, J., Coltrin, M. E., and Miller, J. A., Sandia Report No. SAND 86-8246, Sandia National Laboratories, Albuquerque, NM, 1986.
19. Davis, S. G., and Law, C. K., *Combust. Sci. Technol.*, submitted.
20. Frenklach, M., Wang, H., Goldenberg, M., Smith, G. P., Golden, D. M., Bowman, C. T., Hanson, R. K., Gardiner, W. C., and Lissianski, V., GRI Technical Report No. GRI-95/0058, Gas Research Institute, 1994.
21. Wang, H., Hahn, T. O., Sung, C. J., and Law, C. K., *Combust. Flame* 105:291 (1996).
22. Kerr, J. A. and Moss, S. J., *Handbook of Bimolecular and Termolecular Gas Reactions, Volumes I and II*, CRC Press, Boca Raton, FL, 1981.
23. Adusei, G. Y. and Fontijn, A., *J. Phys. Chem.* 98:3734 (1994).
24. Herzberg, G., *Molecular Spectra and Molecular Structure: I. Spectra of Diatomic Molecules*, 2ed., Van Nostrand Reinhold, New York, 1950.
25. Paul, P. and Warnatz, J. *Twenty-Seventh Symposium (International) on Combustion*, The Combustion Institute, Pittsburgh, 1999, p. 495.

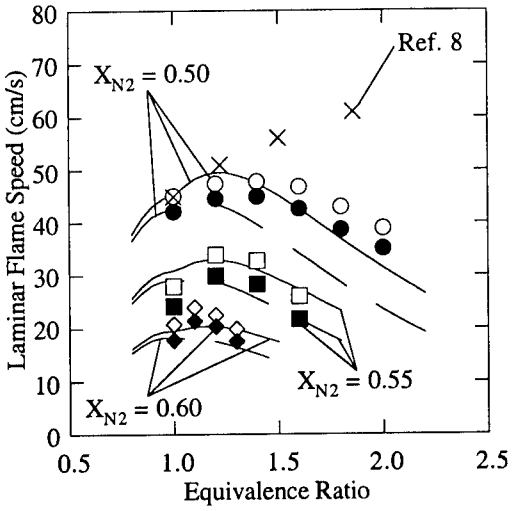


Figure 1: Laminar flame speeds of $H_2/Cl_2/N_2$ mixtures at 1 atm and 298 K. Circles, squares and diamonds are measurements at N_2 mole fractions of 0.5, 0.55 and 0.6. Open and closed symbols are linear and nonlinear extrapolated flame speeds. Also included are the data of Ref. 8 at N_2 mole fraction of 0.5. Solid and broken lines indicate flame speeds calculated with chain-branching and straight-chain mechanisms.

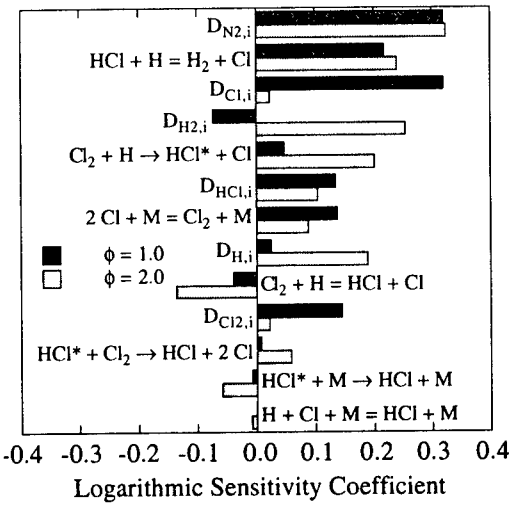


Figure 2: Logarithmic sensitivities of laminar flame speed to reaction rate constants and mass diffusivities for $H_2/Cl_2/N_2$ flame at N_2 mole fraction of 0.5.

Impact of Hydrogen-Doping on Lean-Premixed Methane Flame Stability

Y. Cong and G.S. Jackson
Department of Mechanical Engineering
University of Maryland
College Park, MD 20742
e-mail correspondence: gsjackso@eng.umd.edu

Introduction

The continual push to reduce NO_x emissions from power generation devices such as gas turbines and boilers has led to the wide-scale development and implementation of lean-premixed combustion systems. The challenges of implementing robust, lean-premixed combustion systems include 1) achieving uniform mixing without pre-ignition or flashback, 2) avoiding large acoustic oscillations in the combustion chamber, 3) achieving low CO emissions with low NO_x over the entire operating range of the combustor, and 4) minimizing the possibility of flame-extinction during operation. Various approaches, such as staged (or piloted) fuel injection [1,2], catalytic combustion [3-5], and active control of combustion [6-8], have been investigated to address some of these challenges associated with lean-premixed combustion. Each of these approaches can improve combustor operability but can also present problems either with respect to emissions performance or to overall combustion system reliability. An alternative approach, which involves the use of hydrogen doping in the fuel stream to improve the performance of the lean-premixed combustion system, has recently received some attention [9-11]. While H_2-doping presents its own set of challenges, primarily related to pre-ignition, the suspected benefit of H_2 addition on lean-premixed flame stability motivated the current study on the impact of H_2 addition on extinction in strained premixed methane flames.

The addition of H_2 to a combustor fuel stream might often be accompanied by some amount of CO and H_2O, particularly if an in-line fuel reformer provided the source of H_2. Although the CO and/or H_2O may affect combustor performance, this initial study provides the basis for both a fundamental and practical understanding as to how small amounts of pure H_2 impact flame stability/extinction of lean CH_4 flames. While one recent study illustrated the effects of injecting unmixed H_2 into a lean-premixed methane flame, the actual benefits of H_2-doping in a purely premixed combustion system, for minimal NO_x emissions, remained uncertain. The current study chose a fundamental flame configuration -- the double-jet, counterflow-premixed flame -- to investigate how H_2 addition could improve lean-premixed CH_4 flame stability under highly-strained flow conditions, characteristic of localized conditions in gas turbine premixed combustor flames. Experimental results were compared to 1-D counterflow flame model calculations to examine in more detail the effects of H_2 on the premixed flame structure and to ascertain what the H_2 impact on the CH_4 flames suggests for development of reduced chemical mechanisms for lean-premixed flames.

Experimental Set-Up and Method

The experimental portion of the study used a counterflow flame configuration created by opposing jets of fully premixed fuel and air. Although the double flame created in such a flow configuration can have an influence on the lean flame stability limit [12], the opposed jet configuration was chosen as a means to provide fundamental data on the extinction characteristics of CH_4/H_2 flames. The jet diameters were fixed at 0.8 cm and the nozzle exits were spaced 0.7 cm apart. In light of the goals and motivation of the study, elevated temperatures between 300 and 400°C, characteristic of gas turbine combustor inlet conditions, were chosen for the nozzle exit flow. Unlike in gas turbine combustion chambers, the flames were burning at ambient pressures, and it is expected that higher pressures would tend to extend the lean extinction strain rates observed in this study. The elevated nozzle exit temperatures minimized the impact of undesired buoyancy both by reducing the Grashof number (by a factor of between 20 to 50) from room temperature values and by increasing the nozzle exit velocities due to higher flame speeds. Nozzle exit temperatures were controlled with air heaters upstream of the fuel injection ports. The fuel and air were well mixed in a series of screens and a bed of packed alumina beads upstream of the exit nozzle. Nozzle exit temperatures were controlled by measuring the temperature at the exit of the packed bed. Elevated temperatures permitted a broader exploration of flame stability at lower equivalence ratios (below 0.6) that are more characteristic of overall fuel-air ratios in lean-premixed gas turbine combustors.

The experimental set-up was used to measure lean extinction points for a range of flows/strain rates (characterized by different velocities at the nozzle exit). In order to eliminate the possibility of transient effects on the observed extinction points, the fuel and air flows were controlled with mass flow control valves (Brooks 5850 series) via software calculated flow rates. This allowed for air flows and fuel flows to be simultaneously adjusted to hold flow parameters (most notably nozzle exit velocities) fixed while the equivalence ratio was reduced. The extinction point for a given nozzle exit velocity, temperature, and % H_2 in the fuel was determined by gradually reducing the equivalence ratio (ϕ) at intervals of 0.01. Near the extinction point the flame was kept steady for several minutes before ϕ was further reduced at intervals of 0.005. The extinction point was defined as the value of ϕ at which the flame could not be sustained for periods of more than 20 s. Due to the concerns of intrusive measurement techniques impacting the flame behavior near extinction, no thermocouples or sampling probes were used to investigate the flame. The measured extinction conditions thus served as the primary tool for comparison of experimental results with model predictions discussed in the following section. To ensure that the results used the appropriate centerline velocities to compare with the modeling results, a 2-dimensional CFD model of the nozzle including the packed bed of beads and the external stagnation flow was set up in Fluent. Results from the Fluent model over the range of test conditions gave the increase in the centerline velocity over the average nozzle exit velocity. Calculated increases centerline velocities over average velocities ranged from 5% (at high flow conditions) to 15% (at low flow test conditions). Measured extinction velocities shown in Figures 1a and 1b include the augmentation along the centerline. Errors in the reported velocities are approximately ±4%.

Computational Model

In order to gain a fuller understanding of the impact of H_2 addition on lean CH_4 flames, a computational model was set-up based largely on previous models of counterflow flames [12,13]. The model solves a discretized version of the one-dimensional differential equations that govern the counterflow flame behavior along the central axis of the flow. As in earlier counterflow premixed CH_4 flame models [13,14], volumetric radiative heat loss due to gas phase absorption was included in the energy equation and calculated by assuming optically thin flames and using Planck mean absorption coefficients for CO_2, H_2O, CH_4, and CO [15]. Radiative heat losses are calculated with the assumption that the flame is radiating to an ambient of 25°C (as in the case of the experiments). The model used GRI-Mechanism V2.11 [16] for all simulations presented in this study, but the results for the H_2-enhanced flames are currently being investigated as a tool for developing and evaluating reduced chemistry mechanisms for CH_4 combustion.

Because a primary focus of this study was to investigate the effects of H_2 addition on lean-premixed CH_4 flames, the model was run using a continuation method similar to previous studies [14] with successively increasing strain rates until the so-called extinction turning point was reached. The continuation method was slightly modified from the previous study by implementing an algorithm for selecting the fixed temperature within the flame zone that was decreased to push the flame solution along the path through the maximum strain condition where lean extinction occurs. A curve of solutions of flame temperature vs. strain rate for fuel compositions of pure CH_4 and CH_4 with 2.5%, 5%, and 10% H_2 (by O_2 consumption). The percentage of H_2 is defined based on the amount of O_2 consumed, and thus 5% H_2 refers to a fuel mole fraction of 0.174 and 10% H_2 implies a fuel mole fraction of 0.296. Temperature and species profiles of flames with 0%, 5%, and 10% H_2 for a phi of 0.5 and 0.75 are shown in Figure 2. Unlike previous studies that investigated low strain-rate extinction (caused by radiative losses) in pure CH_4 flames [14,17], modeling in the current study was only used to explore extinction due to stretch at high strain rates because of their greater significance with respect to combustor flames and because of their ability to be demonstrated experimentally at normal gravity. Thus, only the portion of the solution curve which depicts the high strain rate extinction is shown in Figure 2.

Results and Discussion

Both the experiments and the model results showed that a small addition of H_2 can have a substantial impact on the extinction behavior of lean CH_4 flames. The impact has significance both from a practical standpoint and in considering fundamental kinetics and flame structure. The experimental results of extinction flame velocities in Figures 1 for nozzle exit temperatures at 300 and 400°C indicate that replacing only 2.5% of the CH_4 with H_2 can increase the extinction strain by as much as 20%. Furthermore, the addition of 2.5% H_2 allows for stable flames at substantially lower equivalence ratios for a given strain rate (which is roughly proportional to the nozzle exit velocities plotted in Figure 1). Increasing the amount of H_2 to 10% as shown in the 300°C plots in Figure 1a extends flammability limits for a given strain from 0.75 down to 0.55. Although efforts are underway to explore

the leaner conditions (below 0.5), the low velocities were not well suited for the heaters being used in the study and modifications to the rig are being undertaken also to reduce the flame heat losses to the nozzle at the low strain, very lean conditions. The experimental data at 400°C in Figure 1b shows the same trends as the 300°C data but without 10% H_2 conditions which exhibited auto-ignition due to a small recirculation zone inside the mixing chamber. As with the 300°C conditions, heater limitations did not permit exploration of the very lean conditions, and modifications are being implemented to remove the auto-ignition problem and to increase operability at lower velocities (and thus lower equivalence ratios).

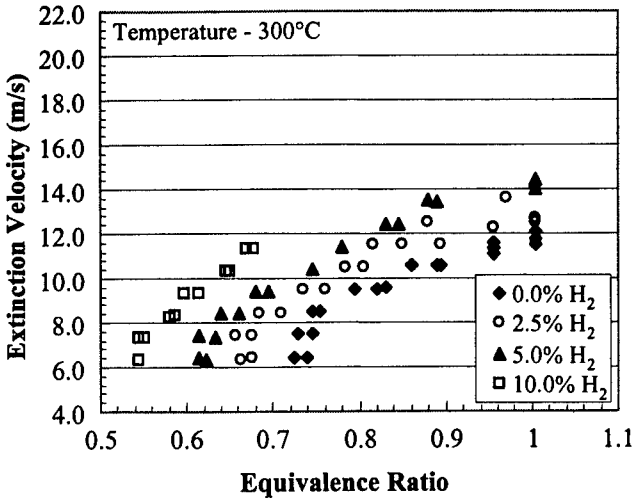
The computational model was also used to study the enhancement of lean flame stability by evaluating the extinction turning point for a range of equivalence ratios at 0, 5, and 10% H_2 addition. Figure 2 shows calculated flame temperatures for two equivalence ratios (0.5 and 0.75). The curves in Figure 2 indicate the turning point where the maximum strain is reached for maintaining flame stability and also how the addition of H_2 greatly extends the extinction strain rate. 10% H_2 extends extinction strain rates for 0.50 equivalence ratio by a factor of 3. Figure 3 shows how the extinction strain rates increase with equivalence ratio and reach a peak between 0.90 and 0.95. The benefit of H_2 addition is seen not only in the higher strain rates but also in the ability of H_2 addition to provide stable flames at equivalence ratios well below that of pure CH_4.

Figure 1b shows how the experimental data compares with predictions from the computational model using GRI-Mech V2.11. Agreement between the experimental and predicted extinction velocities for the pure CH_4 flames are quite good but for the 5% H_2 flames, the model significantly over-predicts the enhancement of the extinction velocity by the H_2 addition. One possible explanation for this discrepancy may lie in the increased importance of in particular HO_2 radicals early in the flame zone and the inability for the mechanism to properly calculate the rates of critical reactions such as $H + O_2 + M \Leftrightarrow HO_2 + M$. Sensitivity analysis of the flame showed that flame speed and temperature was most sensitive to the reactions involving HO_2 formation and splitting. Figure 4, a plot of calculated species profiles for three flames with and without shows how the addition of H_2 impacts the rate of formation of HO_2 and OH radicals upstream of the primary heat release zone. These results and the comparison with experiments suggest that development of reduced mechanisms for CH_4 must focus on properly capturing the HO_2 reactions.

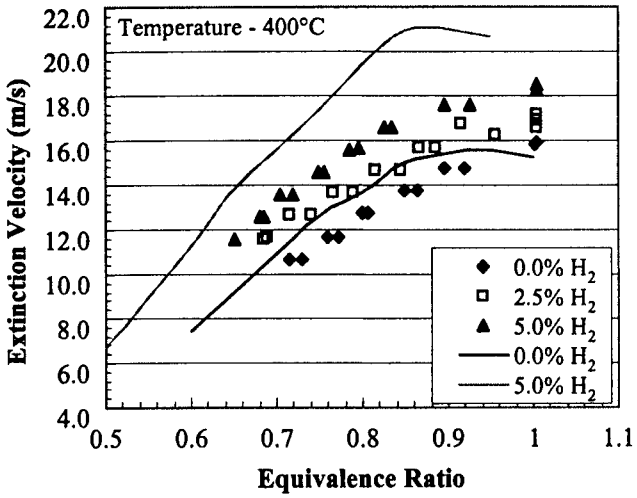
A final note of interest involves the relation of flame temperatures at extinction vs. equivalence ratio (as plotted in Figure 5). In spite of the wide variation in calculated extinction strain rates for the different fuel compositions, extinction flame temperatures are primarily only a function of equivalence ratio (which is proportional to heat release). This suggests the strong influence of thermal effects on extinction, but this remains to be further investigated. Nonetheless, this study has indicated the value of H2 doping not only for extending lean flame stability limits but also for exploring fundamental flame behavior as well.

References

1. Etheridge, C.J., ASME Paper No. 94-GT-255.
2. Willis, J.D., Toon, I.J., Shweiger, T., and Owen, D.A., ASME Paper No. 93-GT-396.
3. Etemad, S., Karim, H., Smith, L.L., and Pfefferle, W.C., *Catalysis Today*, 47:305-313 (1999).
4. Dutta, P., Yee, D.K., and Dalla Betta, R.A., ASME Paper No. 97-GT-497.
5. Puri, R., Stansel, D.M., Smith, D.A. and Razdan, M.K. *J. Eng. Gas Turbines Power*, 119:93-101 (1997).
6. Richards, G.A., et al., *J. Eng. Gas Turb. Power*, 119:340-343 (1997).
7. Lieuwen, T. and Zinn, B.T., *Twenty-Seventh Symp (Intl.) on Comb.*, The Combustion Institute, 1998, pp. 1809-1816.
8. Paschereit, C.O., Gutmark, E., and Weisenstein, W., in *Twenty-Seventh Symp (Intl.) on Comb*, The Combustion Institute, 1998, pp. 1817-1824.
9. Morris, J.D., Symonds, R.A., Ballard, F.L., and Banti, A., ASME Paper No. 98-GT-359.
10. Phillips, J.N. and Roby, R.J., ASME Paper No. 99-GT-115.
11. Nguyen, O.M. and Samuelsen, G.S., ASME Paper No. 99-GT-359.
12. Kee, R.J., et al., *Twenty-Second Symp.(Intl.) on Comb*, The Combustion Institute, 1988, pp. 1479-1494.
13. Law, C.K. and Egolfopoulos, F.N., *Twenty-Fourth Symp.(Intl.) on Comb* The Combustion Institute, 1994, pp. 137-144.
14. Sung, C.J. and Law, C.K., *Twenty-Sixth Symp.(Intl.) on Comb*, The Combustion Institute, 1996, pp. 865-873.
15. Tien, C.L., "Thermal Radiation Properties of Gases", *Advances in Heat Transfer*, Vol. 5, 1968, p.253.
16. Bowman, C.T., et al.., http://www.me.berkeley.edu/gri_mech/.
17. Ju, Y., Guo, H., Maruta, K., and Niioka, T., *Comb. Flame*, 113:603-614 (1998).



(1a)



(1b)

Figure 1 - Experimental results showing exit nozzle velocities at extinction for a range of equivalence ratios for methane with 0, 2.5, 5, and 10% H_2 addition - (a) at 300°C, (b) at 400°C with comparison of model results.

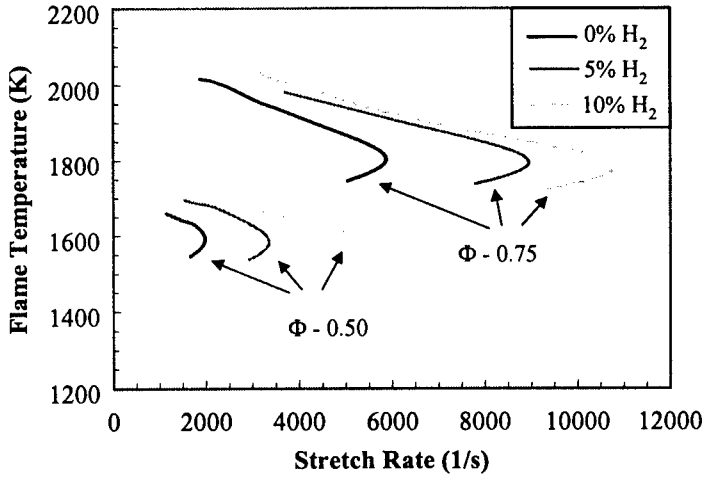


Figure 2 - Calculated stagnation point temperature vs. stretch rate for 0, 5, and 10% H_2 for two equivalence ratios.

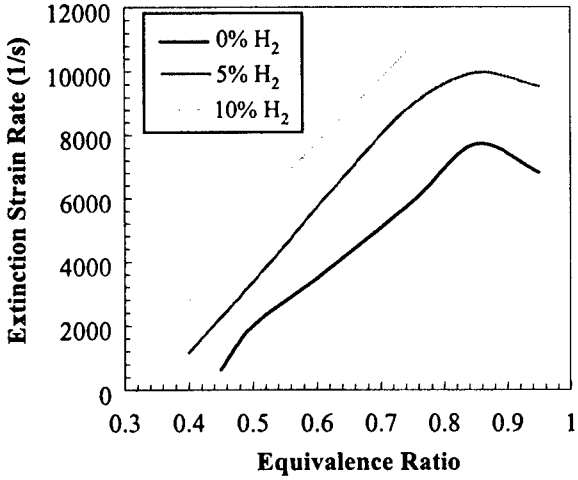


Figure 3 - Calculated stretch rate at extinction vs. equivalence ratio for 0, 5, and 10% H_2.

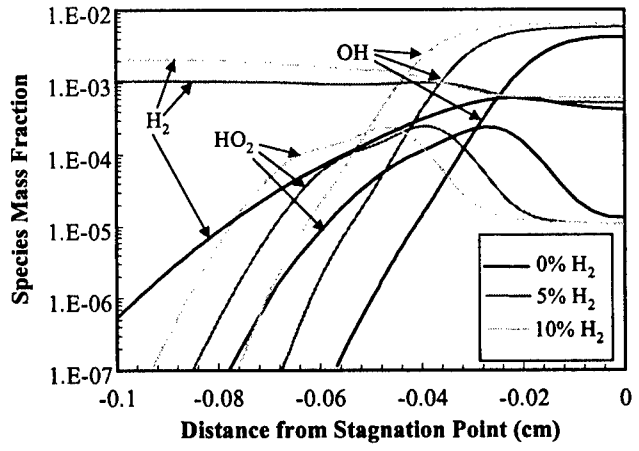


Figure 4 - Calculated H_2, OH, and HO_2 profiles for similarly stretched flames at $\Phi = 0.75$.

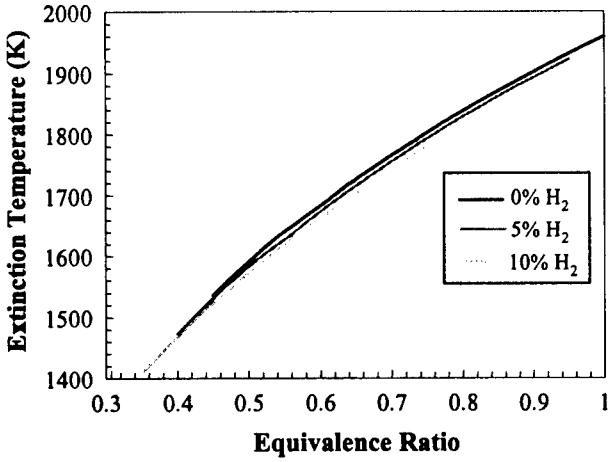


Figure 5 - Calculated extinction flame temperatures vs. equivalence ratio for o, 5, and 10% H_2.

MODIFIED FORM OF THE EQUATION OF MOTION AND ITS SOLUTION FOR LAMINAR FLOW OVER FLAT PLATE AND THROUGH CIRCULAR PIPES AND THE MODIFIED HELMHOLTZ VORTICITY EQUATION

SIAVASH H. SOHRAB
Robert R. McCormick School of Engineering and Applied Science
Department of Mechanical Engineering
Northwestern University, Evanston, IL 60208
Tel: (847)-491-3572 ; Fax: (847) 491-3915 ; Email: s-sohrab@nwu.edu

1. INTRODUCTION

The equivalence between the modified form of the equation of motion in the absence of reactions and the classical *Navier-Stokes* equation of motion is established. The exact solutions of the modified equation of motion for the classical problems of laminar flow over a flat plate and through a circular pipe are presented. A modified form of *Helmholtz* vorticity equation for reactive fields is derived.

2. MODIFIED FORMS OF CONSERVATION AND HELMHOLTZ VORTICITY EQUATIONS

Following the classical methods [1-7], the modified forms of the conservation equations for mass, energy, and momentum in reactive fields were presented as [8]

$$\frac{\partial \rho_m}{\partial t} + \mathbf{w}_m . \nabla \rho_m - D_m \nabla^2 \rho_m = \Omega_m \tag{2.1}$$

$$\frac{\partial T}{\partial t} + \mathbf{w}_m . \nabla T - \alpha_m \nabla^2 T = - \frac{h_m \Omega_m}{\rho_m c_{pm}} \tag{2.2}$$

$$\frac{\partial \mathbf{v}_m}{\partial t} + \mathbf{w}_m . \nabla \mathbf{v}_m - \nu_m \nabla^2 \mathbf{v}_m = - \mathbf{v}_m \Omega_m / \rho_m + \mathbf{F}_m \tag{2.3}$$

where $\mathbf{w}_m$, $\mathbf{v}_m$, Ω_m, and $\mathbf{F}_m$ are the convective and the local fluid velocity, the reaction rate and the body force. Equation (2.3) is the modified form of the equation of motion for reactive fields.

The conservation of vorticity $\omega_m = \nabla \times \mathbf{v}_m$ is presented as

$$\frac{\partial \rho_m \omega_m}{\partial t} + \nabla . (\rho_m \omega_m \mathbf{v}_m) = 0 \tag{2.4}$$

The transport of angular momentum is expressed as the sum of the convective and diffusive parts

$$\mathbf{v}_m = \mathbf{w}_m + \mathbf{V}_{rhgmij} \tag{2.5}$$

with the combined *hydro-diffusive vorticity diffusion velocity* $\mathbf{V}_{rhgmij}$ defined as

$$\mathbf{V}_{rhgmij} = - \nu_m \nabla \ln(\rho_m \omega_m) = - \nu_m \partial \ln(\rho_m \omega_{mj}) / \partial x_i \tag{2.6}$$

when the *Schmidt* number is assumed to be unity $Sc_m = \nu_m / D_m = 1$. Substitutions from (2.5), (2.6), and (2.1) into (2.4) results in the *modified Helmholtz vorticity equation for reactive fields* [9]

$$\frac{\partial \omega_m}{\partial t} + \mathbf{w}_m . \nabla \omega_m - \nu_m \nabla^2 \omega_m = - \omega_m . \nabla \mathbf{w}_m - \omega_m \Omega_m / \rho_m \tag{2.7}$$

The terms on the right-hand-side of (2.7) correspond to the source of vorticity due to vortex-stretching and chemical reactions, respectively. An example of the solution of (2.7) describing spherical flows that are embedded within the boundary layer of viscous counterflows was recently discussed [9].

3. EQUIVALENCE BETWEEN THE MODIFIED EQUATION OF MOTION AND THE NAVIER-STOKES EQUATION

The *original form of the Navier-Stokes* equation with constant transport coefficients and zero coefficient of bulk viscosity $\eta_v = 0$ is given as [2, 3]

$$\rho \frac{\partial \mathbf{v}}{\partial t} + \rho \mathbf{v} . \nabla \mathbf{v} = - \nabla P + \mu \nabla^2 \mathbf{v} + \frac{1}{3} \mu \nabla (\nabla . \mathbf{v}) \tag{3.1}$$

Because the thermodynamic translational pressure P_t is an isotropic scalar, the pressure that appears in the Navier-Stokes equation (3.1) is not P_t. The total stress tensor T_{ij} is expressed as [10]

$$T_{ij} = - P_t \delta_{ij} + \tau_{ij} \tag{3.2}$$

and is used to define the *mechanical pressure* [10]

$$P_m = - (1/3) T_{ii} = P_t - (1/3) \tau_{ii} \tag{3.3}$$

where the normal viscous stress is given by

$$- (1/3) \tau_{ii} = (1/3) \mu \nabla . \mathbf{v} \tag{3.4}$$

When the pressure in (3.1) is identified as the mechanical pressure $P = P_m$, the pressure gradient term on the right-hand side of Eq.(3.1) may be expressed as

$$- \nabla P_m = - \nabla P_t + (1/3) \nabla \tau_{ii} \tag{3.5}$$

However, $\nabla P_t = 0$ because of the isotropic nature of P_t such that (3.5), in view of (3.4) becomes

$$- \nabla P_m = (1/3) \nabla \tau_{ii} = - \nabla [\tfrac{1}{3} \mu (\nabla . \mathbf{v})] = - \tfrac{1}{3} \mu \nabla (\nabla . \mathbf{v}) \tag{3.6}$$

By substitution from (3.6) into (3.1), the original Navier--Stokes equation assumes the form

$$\frac{\partial \mathbf{v}}{\partial t} + \mathbf{v} . \nabla \mathbf{v} - \nu \nabla^2 \mathbf{v} = 0 \tag{3.7}$$

that is almost identical to (2.3) with $\Omega_m = \mathbf{F}_m = 0$ except for the important difference that in (2.3) the convective velocity **w** is different from the local velocity **v**. Because (3.7) involves a diffusion term, and **w** and **v** are related to the diffusion velocity by $\mathbf{v} = \mathbf{w} + \mathbf{V}$, it is clear that (3.7) should in fact be written as (2.3). Having thus established the equivalence between the modified equation of motion (2.3) and the classical Navier-Stokes equation (3.1), some examples of the exact solutions of the former are discussed next.

4. LAMINAR BOUNDARY LAYER FLOW OVER A FLAT PLATE

For laminar boundary layer flow over a flat plate studied by *Blasius* [11, 12], the modified equation of motion (2.3) in the absence of body forces $\mathbf{F} = 0$ and reactions $\Omega_m = 0$, simplifies to

$$w'_x \frac{\partial v'_x}{\partial x'} = \nu \frac{\partial^2 v'_x}{\partial y'^2} \tag{4.1}$$

The convective velocity normal to the plate is absent $w'_y = 0$ and that parallel to the plate is constant $w'_x = w'_o$ outside of the boundary layer. The local fluid velocity $v'_x(x', y')$ inside the boundary layer must vanish at the plate and match w'_o at the edge of the boundary layer $y' = \delta$ as schematically shown in *Figure 1a.* Because the local velocity $v'_x(x', y')$ at any x' changes from $v'_x(x', 0) = 0$ at the wall to $v'_x(x', \delta) = w'_o$ at δ, the convective velocity i.e. the average of local velocity $\langle v'_x \rangle = w'_x$, within the boundary layer becomes a constant given as $w'_x = w'_o/2$ at all axial positions and (4.1) becomes

$$\frac{\partial v_x}{\partial x} = \frac{\partial^2 v_x}{\partial y^2} \tag{4.2}$$

when use has been made of the dimensionless quantities

$$v_x = v'_x/w'_o \quad , \quad x = 2x'/(\nu/w'_o) \quad , \quad y = y'/(\nu/w'_o) \tag{4.3}$$

The introduction of the similarity variable $\eta = y/(2\sqrt{x})$ in (4.2) gives

$$2\eta \frac{dv_x}{d\eta} + \frac{d^2 v_x}{d\eta^2} = 0 \tag{4.3}$$

$$\eta = 0 \qquad v_x(0) = 0$$
$$\eta = \infty \qquad v_x(\infty) = 1 \tag{4.4}$$

with the solution

$$v_x = \text{erf } \eta \tag{4.5}$$

A schematic representation of the velocity profiles within the boundary layer at various axial locations is shown in *Figure 1a.* Also, direct comparisons between the predicted profile (4.5), the experimental observations of *Nikuradse* [13], and the classical solution of *Blasius* [11, 12] are shown in *Figure 1b.* The similarity variable η and the classical $\overline{\eta} = y'\sqrt{w'_o/\nu x'}$ are related by $\eta = \overline{\eta}/(2\sqrt{2})$. As shown in *Figure 1b*, the predicted velocity profile (4.5) is in close agreement with the experimental observations.

The edge of the boundary layer defined as the position where $v'_x = 0.99\, w'_o$ is given by $v_x = \text{erf } \eta^* = 0.99$ resulting in $\eta^* \approx 1.9$ that along with the definition of η gives

$$\frac{\delta}{x'} = \frac{5.374}{\sqrt{Re_{x'}}} \tag{4.6}$$

to be compared with the classical result of *Blasius* [11, 12]

$$\frac{\delta}{x'} = \frac{5}{\sqrt{Re_{x'}}} \tag{4.7}$$

where *Reynolds* number is $Re_{x'} \equiv (w'_o x')/\nu$. Also, the friction coefficient c_f based on (4.5) becomes $c_f = 0.798/\sqrt{Re_{x'}}$ to be compared with the classical result $c_f = 0.664/\sqrt{Re_{x'}}$ [11, 12] The local transverse component of the velocity v'_y can be calculated from the integration of the continuity equation for incompressible flow

$$\frac{\partial v'_x}{\partial x'} + \frac{\partial v'_y}{\partial y'} = 0 \tag{4.8}$$

after substitution from (4.5) leading to

$$v_y = \frac{2}{\sqrt{\pi X}} [\, 1 - \exp\left(-\frac{y^2}{4x}\right)] \tag{4.9}$$

From the above solution in the limit $y \to \infty$ at the outer edge of the boundary layer one obtains

$$v_y = 0.798 \,/\, \sqrt{Re_{x'}} \tag{4.10}$$

to be compared with $v_y = 0.861 \,/\, \sqrt{Re_{x'}}$ based on the classical solution [11, 12]. The predictions of the modified theory are therefore quite close to those of the classical one.

5. LAMINAR FLOW THROUGH A CIRCULAR PIPE

A second classical problem is that of laminar incompressible flow through a circular pipe first studied by *Hagen* [14] and *Poiseuille* [15]. For a pipe with constant cross sectional area A, conservation of mass requires that $\dot{m} = \rho w'_z A = \text{constant}$ and hence $w'_z = w'_o = \text{constant}$. Defining the dimensionless quantities

$$v_z = v'_z/(\nu/r'_o) \quad , \quad t = t'/(\nu/r'^2_o) \quad , \quad r = r'/r'_o \quad , \quad z = z'/r'_o \tag{5.1}$$

where r'_o is the pipe radius, Eq.(2.3) in cylindrical coordinates (r', θ', z') simplifies to

$$\frac{\partial v_z}{\partial t} = \frac{1}{r}\frac{\partial}{\partial r}\left(r \frac{\partial v_z}{\partial r} \right) \tag{5.2}$$

subject to the boundary and initial conditions

$$\begin{aligned} r &= 1 \qquad v_z = 0 \\ r &= 0 \qquad \partial v_z/\partial r = 0 \\ t &= 0 \qquad v_z = v_o(r) \end{aligned} \tag{5.3}$$

where $v_o(r)$ is the initial velocity profile. Since the convective velocity $w_z = w_o$ will be the average of the local velocity v(r, z) over the cross sectional area of the pipe, one arrives at

$$w_o = 2 \int_0^1 v_z \, r \, dr \tag{5.4}$$

By viewing the problem as that of a traveling wave associated with the velocity-front, one introduces a moving coordinate $Z = z - w_o t$ into (5.2) to obtain

$$- w_o \frac{\partial v_z}{\partial Z} = \frac{1}{r}\frac{\partial}{\partial r}\left(r \frac{\partial v_z}{\partial r} \right) \tag{5.5}$$

with a solution

$$v_z(r, z) = B\, [J_0(\beta r) - J_0(\beta)] \exp\left(\frac{\beta^2 Z}{w_o}\right) \tag{5.6}$$

where β^2 is the separation constant and B is an arbitrary constant to be determined. Since $dz/dt = w_z$ and hence $z = w_z t$ with the choice of origins $z = 0$ at $t = 0$, one can express (5.6) as

$$v_z(r, z) = B\, [\, J_0(\beta r) - J_0(\beta)] \exp\left\{\beta^2 \left(\frac{w_z}{w_o} - 1\right) t\right\} \tag{5.7}$$

According to (5.7), if the local velocity profile $v_z(r)$ is such that when used in Eq.(5.4) it leads to the mean velocity $w_z = w_o$, the time dependence of (5.7) vanishes. The constant B is determined by substitution from (5.7) into (5.4), leading to a steady traveling velocity profile

$$v_z(r) = v_o(r) = w_o \frac{J_0(\beta r) - J_0(\beta)}{2\left(\frac{J_1(\beta)}{\beta} - \frac{J_0(\beta)}{2}\right)} \tag{5.8}$$

schematically shown in *Figure 2*. As shown in this figure, the shape of the velocity profile calculated from (5.8) involving *Bessel* function is quite similar to the parabolic profile of the classical solution [12, 14, 15]. It is known that for the *Reynolds* number $Re = w_o = w'_o r'_o/\nu > Re_c = w_{oc} = w'_{oc} r'_o/\nu \approx 2300$, the flow becomes unstable and turbulent. Clearly, the solution (5.7) becomes unstable when $w_z \neq w_o$, since an initial profile such as (5.8) will decay to zero when $w_z < w_o$ and becomes unbounded when $w_z > w_o$ as $t \to \infty$. Therefore, the latter unstable condition corresponds to the onset of turbulence. In practical applications, an external force is always applied to the fluid that opposes the decay of velocity profile by viscous dissipation under the former unstable condition $w_z < w_o$.

ACKNOWLEDGMENTS

This research is supported by NASA micro-gravity research program under grant NAG3-1863.

REFERENCES

[1] Williams, F. A., *Combustion Theory*, Benjamin Cummings, New York, 1985.
[2] de Groot, R. S., and Mazur, P., *Nonequilibrium Thermodynamics*, North-Holland, 1962.
[3] Chandrasekhar, S., *Hydrodynamic and Hydromagnetic Stability*, Dover Publications, New York, 1961.
[4] Bird, R. B., Stewart, E. W., and Lightfoot, N. E., *Transport Phenomena*, Wiley, New York, 1960.
[5] Landau, L. D., and Lifshitz, E. M., *Fluid Dynamics*, Pergamon Press, New York, 1959.
[6] Hirschfelder, J. O., Curtiss, C. F., and Bird, R. B., *Molecular Theory of Gases and Liquids*, Wiley, New York, 1954.
[7] Chapman, S., and Cowling, T. G., *The Mathematical Theory of Non-uniform Gases*, Cambridge University Press, Cambridge, 1953.
[8] Sohrab, S. H., Transport phenomena and conservation equations for multicomponent chemically-reactive ideal gas mixtures. *Proceeding of the 31st ASME National Heat Transfer Conference*, HTD-Vol. **328**, 37-60 (1996).
[9] Sohrab, S. H., Hydrodynamic of spherical flows and geometry of premixed flames near the stagnation point of axisymmetric viscous counterflows. *Fifth International Microgravity Combustion Workshop*, May 18-20, Cleveland, Ohio, 1999.
[10] Panton, R. L., *Incompressible Flow*, Wiley, New York, 1996.
[11] Blasius, H., *Z. Math. u. Phys.* **56**, 1 (1908). Engl. Transl. in NACA TM 1256.
[12] Schlichting, H., *Boundary-Layer Theory*, McGraw Hill, New York, 1968.
[13] Nikuradse, J., Laminare Reibungsschichten an der längsangetrömten Platte. Monograph, Zentrale f. wiss. Berichtswesen, Berlin, 1942.
[14] Hagen, R. L., *Pogg. Ann. Phys. Chem.* **46**, 423 (1839).
[15] Poiseuille, J., *Compt. Rend.* **11**, 961 and 1041 (1840); **12**, 112 (1841).

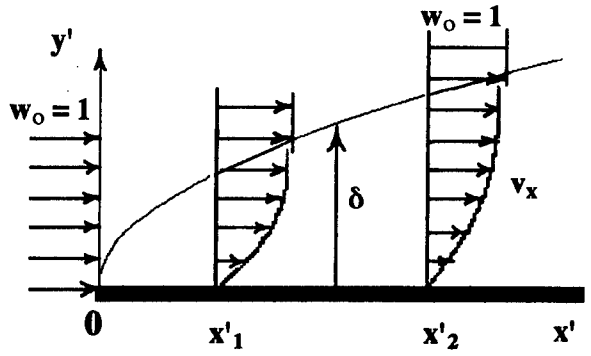


Fig.1a Laminar boundary layer flow over a flat plate with velocity distribution given by Eq.(4.5).

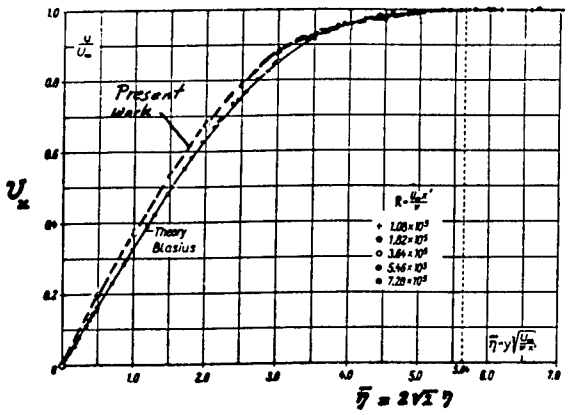


Fig.1b Comparisons between the predicted velocity distribution (4.5) and the measurements of *Nikuradse* [13] and the theory of *Blasius* [11, 12].

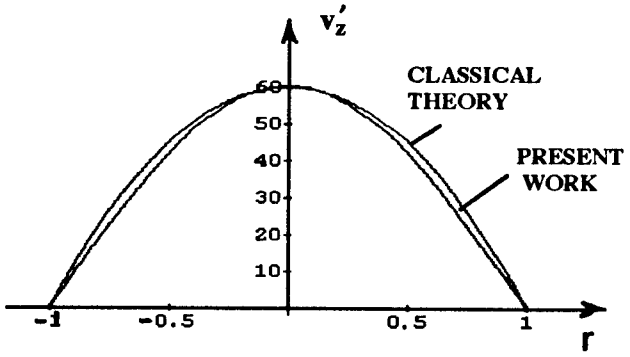


Fig.2 Comparison between the predicted velocity distribution in Eq.(5.8) for laminar flow through a circular pipe and the parabolic distribution according to the classical theory of *Hagen* [14] and *Poiseuille* [15].

NUMERICAL SIMULATION OF ACOUSTIC-FLAME INTERACTIONS IN A ONE-DIMENSIONAL TUBE

A.A. Thaker, and H.K. Chelliah
Department of Mechanical and Aerospace Engineering
University of Virginia, Charlottesville, VA 22903

Introduction

Under certain operating conditions, many reacting flow devices (eg. liquid and solid propellant rocket motors, gas turbine engines, etc.) demonstrate unsteady pressure and velocity fluctuations [1]. Possible causes for such behavior are imperfect fuel elements in solid rockets, or feeder tube oscillations in liquid propulsion systems, and may vary from system to system. In all such cases, however, the unsteady components of pressure modes and velocities are thought to be a small fraction of the steady state modes, and the energy component of the oscillating profiles is very small compared to the time averaged mean value. These unsteady oscillations are related to the acoustics of the combustor which can interact with the finite-rate chemistry or convective-diffusive processes of the combustor. Such coupling can give rise to oscillating heat release, which then is thought to reinforce pressure and velocity oscillations. Such growing oscillations are referred to as combustion instabilities and they continue to grow until losses at the system boundaries limit the growth of these oscillations. Physically, these instabilities are observed in the form of vibrations or a loud buzz or roar emanating from the apparatus. In some cases, the unsteady heat release can be severe enough to damage the apparatus.

Recent environmental regulations have required many combustion devices to operate in very fuel-lean modes, so as to reduce the NO_X levels in the emissions. At the same time, many operators of these devices have identified that the fuel-lean operating condition makes these devices more susceptible to combustion instabilities, especially for minor changes in the system boundary or inflow conditions. In order to further our understanding of this phenomenon, a study of the various mechanisms present in this flow, along with their interactions is required.

Considerable insight about the source of combustion instabilities already exist based on linearized models [1]. However, one major weakness of such an approach is the need to accurately model the nonlinear unsteady source terms. The goal of this effort is to develop and validate these models based on full nonlinear numerical simulations. With this aim, a simple one-dimensional configuration is chosen for the present numerical study. This configuration permits us to evaluate how the acoustic disturbances interact with the chemical and thermal-diffusive time scales and the source terms that lead to the amplification of these disturbances.

Flow Configuration

A simple long tube, closed at one end, and open at the other is considered here, with the flame located midway in the tube (see Fig. 1). Such a configuration should lead to highest growth rates of the combustion-acoustic instability, as predicted by the Rayleigh Criterion [2]. In order to simplify the description of flow field, the numerical model treats this configuration as a strictly 1-D flow, with specified inlet velocity, temperature and composition at the *closed* end (i.e. closed end for acoustic waves), and a prescribed ambient pressure at the exit (*open*

end). The equations governing the flow are described below.

Governing Equations

The conservative form of the one dimensional Navier-Stokes equations used in this analysis can be written as:

$$\frac{\partial \mathbf{Q}}{\partial t} + \frac{\partial \mathbf{F}}{\partial x} = \frac{\partial \mathbf{R}}{\partial x} + \mathbf{S}$$

where

$$\begin{aligned} \mathbf{Q} &= [\rho, \rho u, \rho e, \rho Y_k]^T, \\ \mathbf{F} &= [\rho u, \rho u^2 + p, \rho u e + p u, \rho Y_k u]^T, \\ \mathbf{R} &= [0, \tau_{xx}, -q_x + u\tau_{xx}, -\rho Y_k V_k]^T, \\ \mathbf{S} &= [0, 0, q_{loss}, \dot{w}_k]^T. \end{aligned}$$

Here, $\rho e = \sum_{k=1}^{N} \rho Y_k h_k + \rho u^2/2$, $\tau_{xx} = \mu \frac{\partial u}{\partial x}$, $q_x = -\lambda \frac{\partial T}{\partial x} + \sum_{k=1}^{N} \rho Y_k h_k V_k$. In the initial analysis presented here, a one-step, irreversible reaction is used to model the finite-rate chemistry. Assuming a global Arrhenius type reaction, the pre-exponent and the activation energy are carefully chosen such that the chemical time scale is close to the acoustic timescale for the geometry, i.e. the length of the tube combustor selected.

Numerical Approach

MacCormack method is used to integrate the governing equations in time. For a uniform grid considered here, this scheme approaches second order spatial accuracy. A MacCormack scheme is based on the *predictor-corrector* approach, where the conserved vector $\mathbf{Q}$ is updated in the intermediate predictor step by upwind-differencing the convective flux vector $\mathbf{F}$, and the downwinding in the the subsequent corrector step. In order to eliminate any directional bias, the next iteration reverses the order of upwinding in the predictor and corrector steps. In all iterations, the diffusive flux vector $\mathbf{R}$ is discretized in a direction opposite to the convective flux discretization. A combination of these two steps leads to a more accurate difference scheme than the plain MacCormack approach. The timescale for upwinding in this explicit formulation is taken to be the smallest of the convective, acoustic and the chemical time scales. This approach has been used in the past to model unsteady reacting flows by Prasad [3] and Quinn and Paxson [4]. The chemical source terms and the transport terms are computed using the CHEMKIN and TRANSPORT packages from Sandia.

Initial and Boundary Conditions

To accelerated the solution process, the initial conditions required for the unsteady flow code developed are obtained by the Sandia premix flame code [5]. The output of the premixed code provides steady state spatial profile of the thermodynamic state variables, velocity, and species composition. For the boundary conditions, the values of velocity, temperature and composition are specified at the inlet. A zero pressure gradient at the inlet along with a prescribed pressure and a zero velocity gradient at the exit is used to treat this model as a *closed-open* tube. At

the exit, the species profiles, and the temperature are assumed to have a zero normal gradient.

Results and Discussion

The largest grid resolution allowed in the current analysis was determined by the initial conditions. The output from the premix code was interpolated from a stretched grid to a uniform grid using cubic splines. The grid resolution was determined by computing the heat release rate from the premix solution, and ensuring that this was sufficiently resolved in the interpolated initial condition for the unsteady calculation. As a result, 3001 points were chosen to model the selected domain of 6cm. The equations were integrated in time, with a convective time step of the order 10^{-9}s.

In order to study the interaction of acoustics with the flame, a perturbation in the form of an oscillating heat loss was introduced in the flame. For a given amplitude and mode shape of this perturbation, results for two different frequencies are shown in Figs. 2 and 3. In these figures, the velocity and pressure mode shapes have been plotted every 20000 iterations. Experiments have shown that due to the acoustic nature of this instability (the energy associated with the unsteady component is a small fraction of the mean energy of the flow), the frequency of the instability is very nearly identical to the harmonic frequency of the tube [6]. These figures show the effect of frequency on the peak amplitudes of the pressure and velocity fluctuations. It is seen that the growth of amplitude is higher for the cold frequency perturbation of 6140 Hz (based on the speed of sound in the unburnt mixture at 300 K and a three quarter mode shape) than that for the hot frequency of 7013 Hz (based on a burnt mixture at 1550 K and a three-quarter mode shape). Figure 4 shows the time rate of growth of pressure at x=1.5 cm in the domain, for the two frequencies. It is evident that the instability frequency is close to the cold frequency, based on the peak amplitude. One way to interpret these results is that in keeping the chemical timescale close to the acoustic timescale in the cold-flow case, interactions of the acoustic and chemical phenomena are enhanced, whereas in the higher frequency case, the interactions are smaller due to the difference in the time scales. This interaction is responsible for amplification of the acoustic disturbances in the former case.

For 1D tubes of different lengths or other combustor geometries, the flame-acoustic interactions need not be through finite-rate chemistry, but through acoustic and convective-diffusive interactions. Such investigations are currently underway.

Acknowledgment: This work is supported by NASA Glenn Research Center through a subcontract from VPI, with Dr. Joseph Saus as the technical monitor.

[1] Culick, F.E.C., "Combustion Instabilities in Propulsion Systems," in *Unsteady Combustion*, (F. Culick, M.V. Heitor, and J.H. Whitelaw, eds.), Kluwer Publishers, Dordrecht, Netherlands.
[2] Rayleigh, Lord J., *The Theory of Sound*, Dover, 1945.
[3] Prasad,K., *Combust. and Flame*, **97**:173-200 (1994).
[4] Quinn,D.D. and Paxson, D.E., "A Simplified Model for the Investigation of Acoustically Driven Combustion Instabilities," AIAA 98-3764, Cleveland, OH, July, 1998.
[5] Kee, R.J, Grcar, J.F., Smooke, M.D., and Miller, J.A., "A Fortran Program for Modeling Steady Laminar One-Dimensional Premixed Flames," Sandia Rept. SAND85-8240, July 1987.
[6] McManus, K.R., Poinsot, T., and Candel, S.M., *Prog. Energy Combust. Sci.* **19**:1-29 (1993).

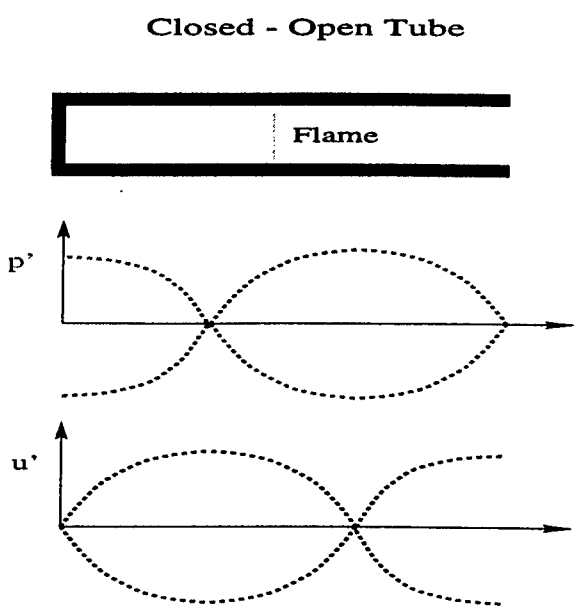


Figure 2: Flow Configuration

Figure 1: Schematic of the flow configuration, with pressure and velocity modes for 1D closed-open tube.

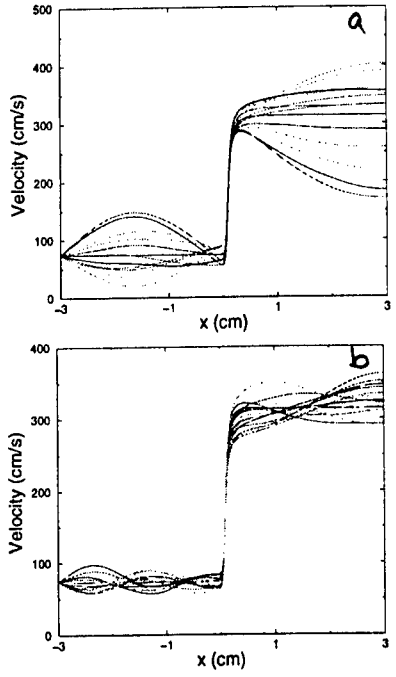


Figure 3: Predicted mode shapes of velocity, for (a) cold frequency of 6140 Hz and (b) hot frequency of 7013 Hz.

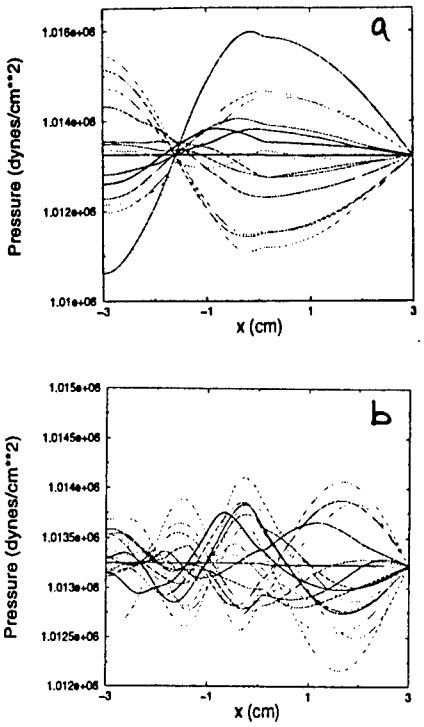


Figure 2: Predicted mode shapes of pressure, for (a) cold frequency of 6140 Hz and (b) hot frequency of 7013 Hz.

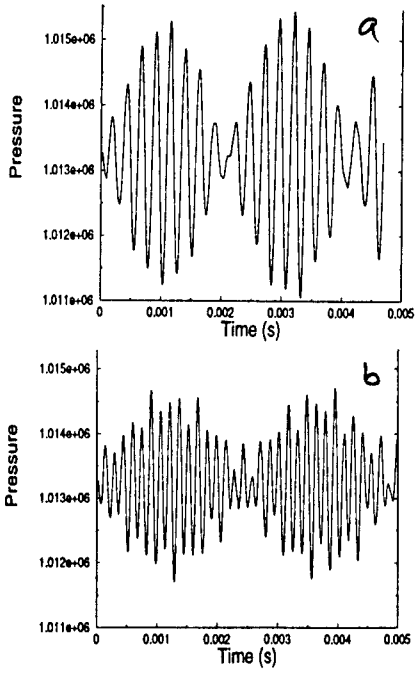


Figure 4: Predicted variation of pressure vs. time at x=1.5 cm, for (a) cold frequency of 6140 Hz and (b) hot frequency of 7013 Hz.

WEDNESDAY SESSIONS
OCTOBER 13TH

COMPUTATIONAL AND EXPERIMENTAL STUDY OF COFLOWING PARTIALLY PREMIXED METHANE/AIR FLAMES

Beth Anne V. Bennett†, Mitchell D. Smooke, Charles S. McEnally, and Lisa D. Pfefferle
Center for Combustion Studies, Yale University
P.O. Box 208284, New Haven, Connecticut 06520-8284

INTRODUCTION

When a burner's fuel stream mixes with a substoichiometric amount of (primary) air before encountering a separate oxidizer (secondary air), the resulting flame is referred to as being *partially premixed*. Many common combustion devices contain partially premixed flames, mainly because of the extremely stable nature of such flames. While today's computers are still not powerful enough to solve exact numerical models of three-dimensional, unsteady, turbulent combustion in realistic devices, the investigation of chemically complex, multi-dimensional laminar flames (such as partially premixed flames) is an important and challenging problem which can be solved via sophisticated adaptive numerical methods.

The current study focuses on six flames, all in an axisymmetric coflow configuration, which are modelled computationally and measured experimentally, using techniques briefly discussed below. The overall equivalence ratios of these flames range from $\Phi \rightarrow \infty$ to $\Phi = 2.464$, which are obtained by holding the CH_4 flow rate constant in the inner jet and incrementing the air flow rate, starting from zero. Thus, the first flame is nonpremixed and the remaining five flames are partially premixed. In this work, computational results are examined throughout each flame; validation of the numerical model and method occurs through comparison with experimental results obtained along each flame's centerline.

NUMERICAL MODEL AND SOLUTION TECHNIQUES

The burner, which is identical for each flame, consists of an inner jet through which fuel (and premixed air) flows, surrounded by a coflow of air. The velocity profile across the inner jet exit is flat for all flames, and that across the outer jet exit is also plug flow; velocity across the thickness of the inner jet wall is zero. Because of physical axisymmetry, the computational domain is two-dimensional, extending radially and axially; the same domain is used for each flame. The radial extent of the domain is large compared with the inner jet's radius, while the domain's axial length is three to six times the flame height.

The model incorporates several standard simplifying assumptions. The gas is taken to be Newtonian, and species diffusion velocities are calculated using Fick's law written in terms of mass fractions. The low Mach number assumption is invoked, and the Soret and Dufour effects are assumed to be negligible. However, viscous dissipation is *not* neglected. Mixture density ρ is calculated from the ideal gas law, using a pressure of 1 atm. All flames are computed using the GRI-Mech 2.11 chemical mechanism [1] without NO_x chemistry. The present model includes an optically-thin radiation submodel [2–4] to calculate the divergence of the net radiative flux.

The governing equations are formulated via a vorticity-velocity approach [5–7]. The N_2 species conservation equation is replaced by the mass fraction unity-summation constraint, and the N_2 diffusion velocity can be determined from the fact that the mass-fraction-weighted sum of all diffusion velocities must vanish. The $N_{species} + 4$ governing equations (and boundary conditions for problems similar to the current one) are stated in [8–10]; the only differences lie in

†Corresponding author: bennett@hexane.eng.yale.edu

the velocities and chemical compositions at the burner surface, as well as the burner dimensions.

Use of an adaptive gridding technique is dictated by the fact that flame front thicknesses, particularly in partially premixed flames, can be as small as one-hundredth of the overall flame height. The local rectangular refinement (LRR) solution-adaptive gridding method, used in the present work, is described in detail in [8–10]. In brief, after a coarse-grid solution is found on the starting (tensor product) grid via a damped modified Newton's method [11], individual boxes of the grid are flagged for refinement via subequidistribution of smoothed positive weight functions through a 2-d generalization of the 1-d theory [12]. Several constraints, which are applied to increase the robustness of the grid, may result in additional boxes being flagged for refinement. All flagged boxes are then refined via subdivision into four smaller boxes of equal size.

Once the solution from the previous grid has been interpolated to the new grid, the governing equations are discretized using the LRR method's *multiple-scale* finite differences, which employ nine-point stencils involving the nearest point in each of the eight compass directions. Multiple-scale discretizations permit the actual solution of the governing equations at the grid-level interfaces, instead of dictating the use of interpolants, as do traditional methods. Conservative discretizations are formed wherever possible, and convective derivatives are upwinded.

The system of strongly coupled, nonlinear partial differential equations is solved using a damped modified Newton's method with a nested BiCG-STAB linear algebra solver (all were extensively modified to handle the unstructured nature of the grids). The spatially-elliptic governing equations are made parabolic in time by appending transient terms to the residual form of the equations [13]. This time-relaxation procedure is employed for a specified number of adaptively-chosen time steps and is then followed by the solution of the steady-state equations. The overall grid adaption process terminates when the weight functions are subequidistributed to within 5%.

EXPERIMENTAL TECHNIQUES

The measurement techniques are described in detail elsewhere [14–16]. To summarize, temperature measurements were made using uncoated thermocouples [15], and species concentrations were determined by extracting gas samples with a narrow-tipped quartz sample probe and analyzing them via on-line mass spectrometry [14]. An electron-impact/quadrupole mass spectrometer was used to measure CH_4, C_2H_2, O_2, and CO_2 mole fractions; mole fractions of C_2H_2O and other higher hydrocarbons were measured using a photoionization/time-of-flight mass spectrometer [14]. OH concentrations were measured using laser-induced fluorescence. Multiple trials were run, and the results were repeatable to within experimental error.

RESULTS AND DISCUSSION

Computational results are presented throughout the domain, and comparison between computational and experimental results occurs along the centerline of each flame. Because the six flames are different heights, trends in the data are more evident when the comparisons of interest are presented as functions of a nondimensional axial distance z/H_T (z is axial distance from the burner surface and H_T is the z at which the maximum temperature occurs) [16].

As the amount of primary oxygen is increased from zero in the nonpremixed flame, a weak inner premixed flame front forms and then grows in strength. Figure 1 shows isopleths of heat release in the $\Phi = 2.464$ flame. Both the conical inner premixed flame and the outer diffusion flame halo are apparent, with more heat release occurring in the former. As in all of the flames studied here, the majority of the heat release occurs very near the burner rim. Figure 2 compares the computational and experimental temperature profiles in each of the six flames. As partial premixing occurs, three effects are apparent in both sets of profiles: the maximum flame temperature increases; a "shoulder" forms due to the increasing heat release from the inner flame;

and the temperature rise above the burner surface is delayed until further downstream because of a decrease in heat transfer radially inward. Although the peak temperatures predicted by the model are all roughly 100K lower than in the experiments, the agreement between the computed and experimentally measured profiles is otherwise excellent. Figure 3 displays the computed and experimental CH_4 mole fractions. For both sets of data, the shapes of the profiles change as partial premixing occurs; the initial concentrations persist further downstream, and the ensuing dropoffs become sharper. Agreement is again extremely good. Similar levels of agreement along the flame centerlines have been observed between computed and experimental data for several other species, including O_2, H_2O, CO_2, OH, C_2H_2, and C_2H_2O. Additional quantities of interest have been examined throughout the computational domain.

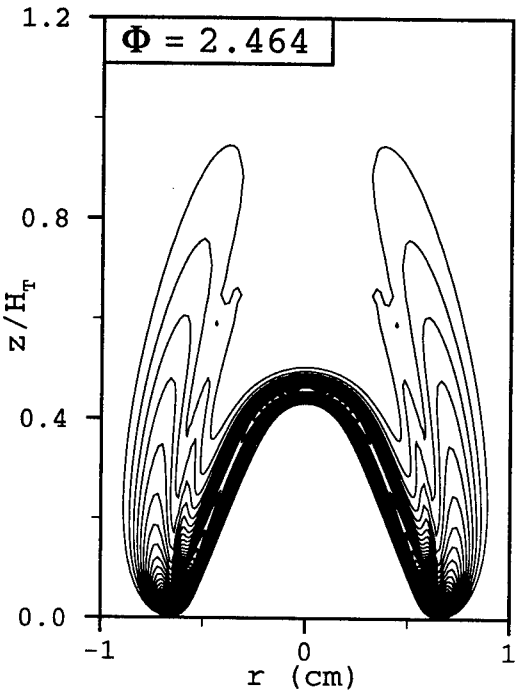
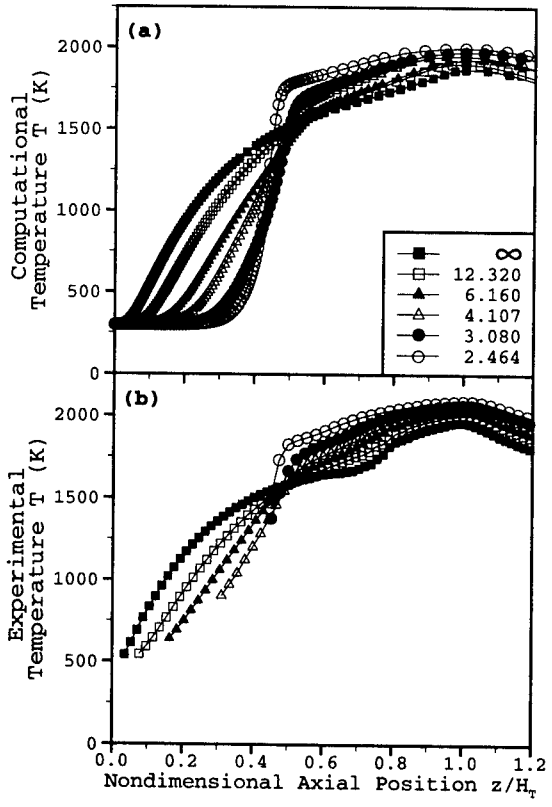
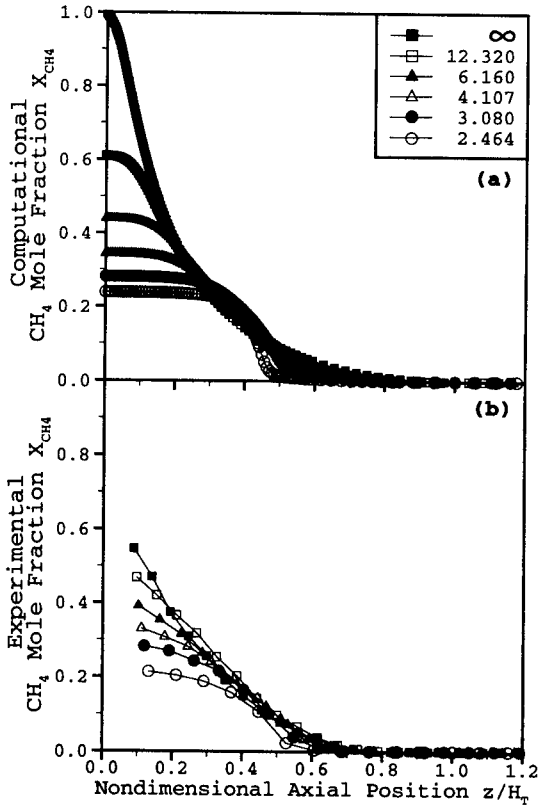


Fig. 1 (right). Computed isopleths of heat release are displayed as functions of radial position (r) and nondimensional axial position (z/H_T) in a portion of the computational domain for the $\Phi = 2.464$ flame.

Fig. 2 (below left). Centerline profiles of temperature, as functions of z/H_T, are displayed. Both (a) computational and (b) experimental results are shown.

Fig. 3 (below right). Centerline profiles of CH_4 mole fraction, as functions of z/H_T, are displayed. Both (a) computational and (b) experimental results are shown.





ACKNOWLEDGMENTS

The first two authors would like to acknowledge support from the Office of Naval Research (Grant N00014-95-1-0412) and the Department of Energy Office of Basic Energy Sciences (Grant DE-FG02-88ER13836). The last two authors appreciate the assistance of Elanor Williams in conducting the experiments, and they would like to acknowledge partial financial support from the United States Air Force (Grant F49620-94-1-0085), the United States Environmental Protection Agency (Grant R821206-01-0), and the National Science Foundation (Grant CST-9714222).

REFERENCES

[1] C.T. Bowman, R.K. Hanson, D.F. Davidson, W.C. Gardiner, Jr., V. Lissianski, G.P. Smith, D.M. Golden, M. Frenklach, H. Wang, and M. Goldenberg, *GRI-Mech version 2.11*, http://-www.gri.org (1995).

[2] D.K. Edwards, "Molecular gas band radiation," *Adv. Heat Transfer* **12**:115–193 (1976).

[3] R.J. Hall, "The radiative source term for plane-parallel layers of reacting combustion gases," *J. Quant. Spectrosc. Radiat. Transfer* **49**:517–523 (1993).

[4] R.J. Hall, "Radiative dissipation in planar gas-soot mixtures," *J. Quant. Spectrosc. Radiat. Transfer* **51**:635–644 (1994).

[5] A. Ern, "Vorticity-velocity modeling of chemically reacting flows," *Ph.D. Thesis*, Yale University, New Haven, CT, 1994.

[6] A. Ern, C.C. Douglas, and M.D. Smooke, "Detailed chemistry modeling of laminar diffusion flames on parallel computers," *Int. J. Supercomput. Appl.* **9**:167–186 (1995).

[7] M.D. Smooke, A. Ern, M.A. Tanoff, B.A. Valdati, R.K. Mohammed, D.F. Marran, and M.B. Long, "Computational and experimental study of nitric oxide in an axisymmetric laminar diffusion flame," *26th Symp. (Int.) on Combustion*, The Combustion Institute, Pittsburgh, PA, 1996, pp. 2161–2170.

[8] B.A. Valdati, "Solution-adaptive gridding methods with application to combustion problems," *Ph.D. Thesis*, Yale University, New Haven, CT, 1997.

[9] B.A.V. Bennett and M.D. Smooke, "Local rectangular refinement with application to axisymmetric laminar flames," *Combust. Theory and Modelling* **2**:221–258 (1998).

[10] B.A.V. Bennett and M.D. Smooke, "Local rectangular refinement with application to nonreacting and reacting fluid flow problems," *J. Comput. Phys.* **151**:684–727 (1999).

[11] P. Deuflhard, "A modified Newton method for the solution of ill-conditioned systems of nonlinear equations with application to multiple shooting," *Numer. Math.* **22**:289–315 (1974).

[12] J. Kautsky and K. Nichols, "Equidistributing meshes with constraints," *SIAM J. Sci. Stat. Comput.* **1**:499–511 (1980).

[13] M.D. Smooke, R.E. Mitchell, and R.J. Kee, "Solution of premixed and counterflow diffusion flame problems by adaptive boundary value methods," in *Numerical Boundary Value ODEs*, U.M. Ascher and R.D. Russell, eds., Birkhäuser, Boston, 1985, pp. 303–317.

[14] C.S. McEnally and L.D. Pfefferle, "Aromatic and linear hydrocarbon concentration measurements in a non-premixed flame," *Combust. Sci. Technol.* **116-117**:183–209 (1996).

[15] C.S. McEnally, Ü.Ö. Köylü, L.D. Pfefferle, and D.E. Rosner, "Soot volume fraction and temperature measurements in laminar nonpremixed flames using thermocouples," *Combust. Flame* **109**:701–720 (1997).

[16] C.S. McEnally and L.D. Pfefferle, "Experimental study of non-fuel hydrocarbon concentrations in coflowing partially premixed methane/air flames," *Combust. Flame* in press (1999).

Effects of Reaction Kinetics and Heat Transfer on Combustion Oscillation of Methane in Perfectly Stirred Reactor*

Matthew T. McGarry and Hai Wang
Department of Mechanical Engineering, University of Delaware, Newark, DE 19716
hwang@me.udel.edu

The goal of this work is to identify the cause of sustained oscillatory combustion behavior in a perfectly stirred reactor (PSR) and to provide a theoretical guidance for locating the parameter space within which combustion oscillations occur. The major motivation derives from the possible application of oscillatory combustion as a mechanism to produce hydrogen from fossil fuels onboard vehicles powered by a hydrogen fuel cell. Taking advantage of the fact that reaction time scales are longer in a PSR when compared to a laminar premixed flame or a plug-flow type reactor, the time delay of soot production could be extended to a larger and a practically controllable value.[1] By introducing combustion oscillation and if the frequency of such oscillations can be manipulated such that the time period of each combustion cycle is shorter than the characteristic time scale of soot formation, one can minimize soot emission. We note that a well-stirred reactor has also been used in many areas of combustion. For example, it has been used to explain turbulent flame phenomena,[2] and to determine oxidation mechanisms of hydrocarbons (e.g., refs 3–8), and to examine cool flame phenomena (e.g., refs. 9-12).

Oscillatory behavior in combustion has been studied because of its relevance to cool flames.[10-14] The work on cool flames established that in a static reactor the existence of oscillatory behavior is due to a coupling between local heat release and heat dissipation rates. Previous work on oscillatory combustion in a PSR has focused on chemical kinetic effects of radical chain branching and termination in a combustion process.[15-19] Baulch et al.[15] experimentally found oscillation on the boundary between the non-reacting and vigorously reacting region of the hydrogen pressure-wall temperature explosion curve. Several conclusions by Baulch et al. were made about the cause of oscillation. Because a combustion process is largely governed by the competition between the radical chain branching reaction $H + O_2 \rightarrow O + OH$ and the radical chain-terminating reaction $H + O_2 + M \rightarrow HO_2 + M$, it was concluded[15] that oscillation is caused by the high third body efficiency of water, the major product of hydrogen combustion, which aids in chain termination. The combustion oscillation is introduced by the following kinetically driven cycle: as water is produced from the combustion reaction, the rate of chain terminating reaction increases, and a decrease in the combustion intensity follows. A decrease in combustion intensity reduces the production of water and thereby reduces the rate of radical chain termination. This is then followed by an increase in the combustion intensity.

The work of Baulch et al. provided the kinetic criterion of combustion oscillation in a PSR. Although kinetics is no doubt an important part of oscillatory combustion, this kinetic criterion is incomplete at best. First, the explanation of combustion oscillation is specific to hydrogen combustion and it remains unclear whether this explanation is generally applicable to combustion of other combustible mixtures. Second, the kinetic criterion requires the knowledge of reactor temperature—a dependent variable of the PSR system. The reactor temperature, in turn, is determined by the coupled heat release and heat dissipation rates. It follows that detailed reaction kinetics alone cannot entirely explain combustion oscillation.

The objective of this work is to re-examine the criterion of combustion oscillation in a PSR. It is hoped that a general criterion can be developed, which is independent of the combustible mixture and consequently detailed reaction kinetics. In doing so, we also hope to provide a theoretical guidance in locating the parameter space within which oscillation should occur regardless what fuel is used.

The work has been conducted in two phases. The first phase of study involves a numerical study of combustion in PSR with the objective of characterizing the combustion responses as a function of various relevant parameters. Methane was used as a fuel to illustrate combustion oscillations in PSR. In the second phase of study the analytical work is accomplished by using a global reaction that is coupled with heat release. An eigenvalue analysis is applied to understand the stability of the solution. Specific causes of combustion oscillation and a general criterion of combustion oscillation are identified in this phase of work.

Methodologies

The numerical codes are originally taken from the standard combustion code library of Sandia National Laboratories. The PSR code[20] was initially written for steady-state PSR problems, and is modified in this work to allow computations for a transient problem. A detailed kinetic model, consisting of 59 species and

* For presentation at the 1999 Eastern States Section of the Combustion Institute Meeting, Raleigh, NC, October 1999.

331 elementary reactions, was employed to describe methane oxidation in PSR. The methane chemistry is taken from GRI-Mech 1.2.[20] The base reaction mechanism of methane was modified and extended to include the combustion chemistry of acetylene and ethylene.[21,22] The modified mechanism also includes the reactions leading to the formation of soot precursors.[21]

To simplify the analysis, we adapted a global and irreversible reaction given by **Reactant → Product(s)** + heat. The governing equations are given by

$$\frac{dC_R}{dt} = -\left[\frac{C_R - C}{\tau} + A\exp\left(-\frac{E}{RT}\right)C_R\right] \tag{1}$$

$$c_p\frac{dT}{dt} = \frac{c_p^* T^* - c_p T}{\tau} - \frac{\chi(T - T_w)}{\rho V} - \Delta h^\circ \exp\left(-\frac{E}{RT}\right) \tag{2}$$

where C_R is the molar concentration of the reactant, $C = C_R + C_P$ the total molar concentration, C_P the molar concentration of the product, and τ the residence time in the reactor, c_p is the specific heat of the mixture in the reactor, Δh° the enthalpy released during the reaction, χ the heat transfer coefficient, T_w the wall temperature of the reactor, ρ the density of the mixture in the reactor, and V the volume of the reactor. The asterisk refers to reactor inlet conditions. Here we have a non-linear system of two equations in the form of $\mathbf{x} = \mathbf{f}(\mathbf{x})$, which can be linearized. We start from a steady-state point ($\mathbf{x}^*$) and perform a Taylor series expansion about ($\mathbf{x}^*$). Neglecting the higher-order terms, we obtain the first-order differential equation, which takes the following form

$$\mathbf{y} = \mathbf{J}\mathbf{y} \tag{3}$$

where $\mathbf{y} = \mathbf{x} - \mathbf{x}^*$, and $\mathbf{J}$ is the Jacobian matrix. The solution is assumed to take the form given by

$$\mathbf{y}(t) = e^{\lambda t}\mathbf{v} \tag{4}$$

where λ is the growth rate and $\mathbf{v}$ is a non-zero fixed vector to be determined. Plugging (4) into (3) yields the classic eigenvalue problem, $\mathbf{J}\mathbf{v} = \lambda\mathbf{v}$, where $\mathbf{v}$ is now an eigenvector of $\mathbf{J}$ with corresponding eigenvalue λ. Solving the typical characteristic equation that accompanies an eigenvalue problem yields the quadratic equation for the eigenvalues

$$\lambda^2 - Tr\lambda + \Delta = 0 \tag{5}$$

where Tr and Δ are respectively the trace and determinant of the Jacobian $\mathbf{J}$.[23] Solving eq. (5) one obtains the expressions for the eigenvalues as $\lambda_1 = \alpha + i\omega$ and $\lambda_2 = \alpha - i\omega$, with $\alpha = Tr/2$ and $\omega = [\Delta - (Tr/2)]^{1/2}$. Once the eigenvalues are known the general solution for $\mathbf{y}(t)$ is given by

$$\mathbf{y}(t) = \beta_1 e^{\lambda_1 t}\mathbf{v}_1 + \beta_2 e^{\lambda_2 t}\mathbf{v}_2 \tag{6}$$

where β's are coefficients.

Examining eq. (6) yields several important conclusions regarding the stability of the solution. One notices that $\mathbf{y}(t)$ is a linear combination of $e^{(\alpha \pm i\omega)t}$, which by Euler's formula, is a linear combination of $e^{\alpha t}\cos(\omega t)$ and $e^{\alpha t}\sin(\omega t)$. Depending on the values of α (and therefore Tr) and ω (assuming it is real), unstable ($Tr > 0$), oscillatory ($Tr = 0$), and stable ($Tr < 0$) solutions can be obtained. Particularly, when $Tr = 0$, the solution becomes imaginary therefore persistently oscillatory. Observing that when ω is imaginary the solution involves only the exponential dependence of real numbers. These solutions are called nodes and can be either stable or unstable depending on whether α is positive or negative.[23]

Results and Discussion

Figure 1 presents the numerically determined boundary defined by the heat transfer coefficient and residence time, which separate the reacting solution from nonreacting condition. A burning solution is obtained beneath the bell-shaped curve, whereas above the bell curve, only frozen, non-reacting solution can be obtained. It is seen that below the critical residence time, no appreciable reaction can take place, because of finite-rate kinetics. At the large residence time, heat dissipation through the reactor becomes severe, where combustion again cannot be sustained. For mixtures with an identical adiabatic flame temperature (achieved by substituting nitrogen by argon), the variation of equivalence ratio does not affect the qualitative feature of the χ-τ boundary. Quantitatively, however, the lower critical residence time increases markedly with an increase in equivalence ratio. This is because the lower τ boundary is determined by the characteristics of detailed reaction processes.

Exhaustive search for oscillation within the combusting domain was carried out. For all equivalence ratios, combustion oscillation was observed only on or near the upper τ boundary, where heat dissipation through the reactor wall and heat release rate are highly coupled. Figure 2 illustrate that inside of the combusting domain (point 1), a decay oscillatory solution can be obtained. At the critical residence time

boundary, we obtained sustained oscillation, whereas outside of the combusting domain, the amplitude of oscillatory increases as time increases, until the system relaxes to the frozen state.

To understand the cause of combustion oscillation in PSR, analytical solution with a global reaction is obtained. Figure 3 shows that such a solution, where θ is the non-dimensionalized temperature, defined as $\theta = E(T - T_w)/RT_w^2$, and t_2 is the non-dimensionalized time, $t_2 = \tau/t_N$, where t_N is the Newton cooling time, $t_N = \rho c_p V/\chi$. It is seen that the temperature solution can be divided into three branches. Branch I corresponds to steady burning without a notable influence from the residence time or heat dissipation through the reactor wall. In Branch II, temperature decreases as t_2 increases because of a gradual increase in the heat dissipation rate. Both branch I and II solutions are stable, whereas the solution in branch III is unstable, as seen by the positive trace values shown in Figure 3. The oscillatory solution is obtained where the trace value is equal to zero. Two such points exist, as shown by the solid symbols in Figure 3. The oscillatory solution at the small t_2 value is not practically important. The oscillatory point at the large t_2 value, however, is practically observable, as seen in our numerical simulation.

Further analytical tests show that the oscillatory solution observed in the numerical computation is entirely a consequence of coupled heat release, which is governed by exponential reaction kinetics characteristic of combustion processes, and heat dissipation through the reactor wall, which is determined by convective heat transfer. Thus, the criterion just described should be applicable to all fuels. Unlike the conclusion reached in ref. 15, we found no evidence of detailed reaction characteristics being the cause of oscillation, although this does not precluded the possibility of oscillation purely driven by kinetic effects.

Acknowledgment *The work is sponsored by the National Science Foundation CAREER Development program (CTS 9874768) under the technical monitoring of Dr. Farley Fisher. The computation was performed at the facility for computational chemistry at the University of Delaware, which is funded by the National Science Foundation (CTS-9724404).*

References

1. Denbigh, K. G and Turner, J. C. R. *Chemical Reactor Theory*, Cambridge University Press, New York, 1984, pp. 64-80.
2. Abdel-Gayed, R. G., Bradley. D. and Lung, F. K. *Combust. Flame* **76**, 213 (1989).
3. Wright, F. J. *Combust. Flame* **15**, 217 (1970).
4. Lam, F. W., Howard, J. B., Longwell, J. P. *Twenty-Second Symposium (International) on Combustion*, The Combustion Institute, Pittsburgh, 1988, p. 323.
5. Chakir, A., Cathonnet, M., Boettner, J. C. and Gaillard, F. *Combust. Sci. Technol.* **65**, 207 (1989).
6. Vaughn, C. B., Howard, J. B. and Longwell, J. P. *Combust. Flame* **87**, 278 (1991).
7. Dagaut, P., Boettner, J.-C., and Cathonnet, M. *Int. J. Chem. Kinet.* **22**, 641 (1990).
8. Chai, Y. and Pfefferle, L. D. *Fuel* **77**, 313 (1998).
9. Felton, P. G., Gray, B. F. and Shank, N. *Combust. Flame* **27**, 363 (1976).
10. Caprio, V., Insola, A. and Lignola, P. G. *Combust. Flame* **43**, 23 (1981).
11. Gray, B. F. and Jones, J. C. *Combust. Flame* **57**, 3 (1984).
12. Griffiths, J. F. and Inomata, T. *J. Chem. Soc.* **88**, 3153 (1992).
13. Wang, X. *Combust. Flame* **75**, 107 (1989).
14. Gray, P. and Griffiths, J. *Combust. Flame* **78**, 87 (1989).
15. Baulch, D. L., Griffiths, J. F., Pappin, A. J. and Sykes, A. F. *Combust. Flame* **73**, 163 (1988).
16. Baulch, D. L., Griffiths, J. F. and Richter, R. *Chem. Eng. Sci.* **46**, 2315 (1991).
17. Coppersthwaite, D. P., Griffiths, J. F. and Gray, B. F. *J. Phys. Chem.* **95**, 6961 (1991).
18. Chinnick, K., Gibson, C. and Griffiths, J. F. *Proc. R. Soc. Lond. A* **405**, 129 (1986).
19. Glarborg, P., Kee, R. J., Grcar, J. F. and Miller J. A. *PSR: A Fortran Program for Modeling Well-Stirred Reactors*, Sandia Report, Sandia National Laboratories, Albuquerque, New Mexico, 1992.
20. Frenklach, M., Wang, H., Goldenberg, M., Smith, G. P., Golden, D. M., Bowman, C. T., Hanson, R. K., Gardiner, W. C. and Lissianski, V. *GRI-Mech–An Optimized Detailed Chemical Reaction Mechanism for Methane Combustion*, GRI Technical Report No. GRI-95/0058, 1995.
21. Wang, H. and Frenklach, M. *Combust. Flame*, **110**, 173 (1997)
22. Sun, C. J., Sung, C. J., Wang, H. and Law, C. K. *Combust. Flame* **107**, 321 (1996).
23. Strogatz, S. H. *Nonlinear Dynamics and Chaos,* Addision-Wesley, Reading, MA, 1994, pp. 129-140.

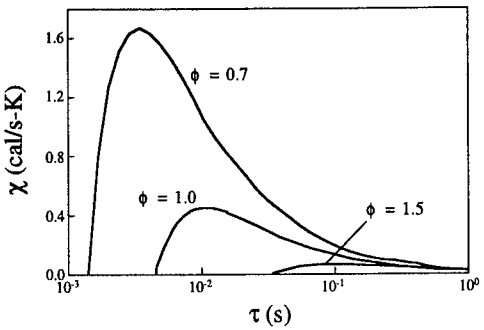


Figure 1. Numerical characterization of the type of solution that exists in the heat transfer coefficient versus residence time parameter space for methane-11%O_2-89%(N_2+Ar) mixtures. The area beneath the bell-shaped curve represents the condition where combustion in PSR is possible. Argon waw used to substitute N_2 for ϕ = 0.7 and 1.5 to achieve identical adiabatic flame temperature for the three equivalence ratios. Other conditions employed in the computation include V = 100 cm^3, p = 1 atm, and $T^* = T_w$ = 300 K.

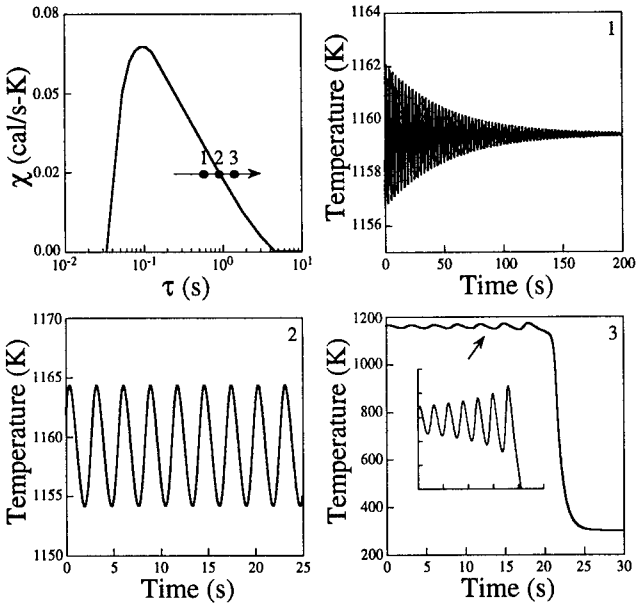


Figure 2. Oscillatory solutions obtained from numerical simulation for the ϕ = 1.5 mixture shown in Figure 1.

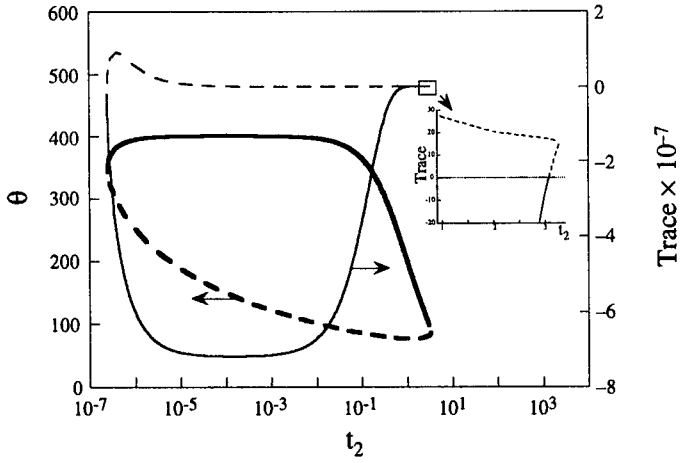


Figure 3. Analytical solutions of temperature (think line) and trace (thin line) as a function of residence time, illustrating the stable (solid line, Tr < 0), unstable (dashed line, Tr > 0), and oscillatory (Tr = 0) solutions.

Thermal Decomposition of Dichlorofluoromethane: An Experimental and Modeling Study

Michael A. Smith
Edward R. Ritter (eritter@email.vill.edu)*
Department of Chemical Engineering
Villanova University
Villanova PA 19085

Abstract

Pyrolytic decomposition of partially halogenated alkanes often proceed through an α, β orα, α HX loss (X = F,Cl). In the case of substituted methanes, α, α HX elimination results in the singlet carbene as a primary decomposition product. In this current study, we pyrolyze dichlorofluoromethane (Refrigerant-21) in a flow-tube reactor at 823 to 948 K. Experimental results show the primary product to be 1,2 dichlorodifluoroethylene. This is consistent with initial HCl elimination to result in ^{1}:CClF, followed by carbene combination to 1,2 dichlorodifluoroethylene. Additional products include C3 and C4 species, their formation is believed to occur via Cl (primarily) or F migration across the ethylene double bond and subsequent combination with the ^{1}:CClF carbene. Trichlorofluoromethane and tetrachlorodifluoroethane are also observed in significant amounts; these two products are believed to result from C-Cl bond breaking with subsequent radical-species chemistry.

Experimental Apparatus

Dichlorofluoromethane was pyrolyzed in a 2.0 cm ID fused silica quartz flow-tube housed within a 6-zone electrically heated furnace which produced an isothermal region of 38 cm. The reactant was 2 % mole fraction in either helium or nitrogen, and pyrolysis was accomplished between 823 K to 948 K. From the discharge end of the reactor, a water-cooled sampling probe was inserted into the flow-tube through a septum. Both the flow tube and probe were mounted on an optical rail assembly that allowed precise positioning of the probe along the centerline of the flow-tube. Samples taken in this manner at known positions corresponded to a given reaction time, times between 0 and 3.125 seconds were studied. Samples were analyzed using both a GC/FID for quantitative analysis and GC/MS for product identification. A schematic of this apparatus is presented elsewhere (1).

Results

For all temperatures studied, the primary products were isomers of 1,2 dichlorodifluoroethylene. These accounted for approximately 50% of observed product. At temperatures below 873K, isomers of trichlorotrifluoropropylene are the next most abundant product. At higher temperatures concentration of these propylene species decrease and tetrachlorodifluoroethane becomes significant, here also other major products include 1,1 dichlorodifluoroethylene and trichlorofluoromethane. Figure 1 shows the conversion and major product across the studied temperature range. Figure 2 the reactant and products vs time at a constant temperature. Minor products include several other ethylene species, trichloromethane, and various perhalogenated C4 species believed to be butynes or butadienes.

---

* Corresponding Author

Figure 1: Reactant and major product yields as carbon as function of temperature at 3.125 sec. reaction time.

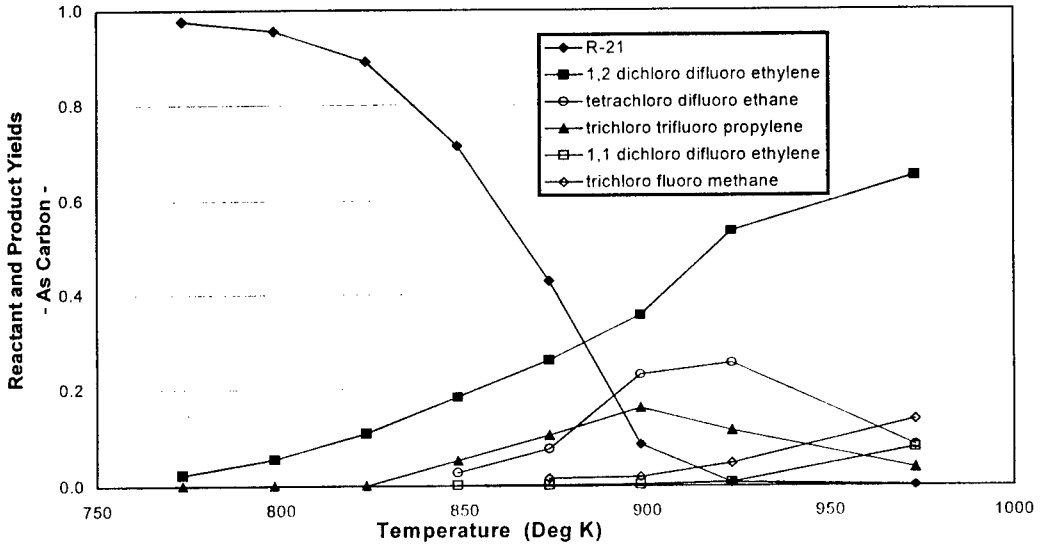
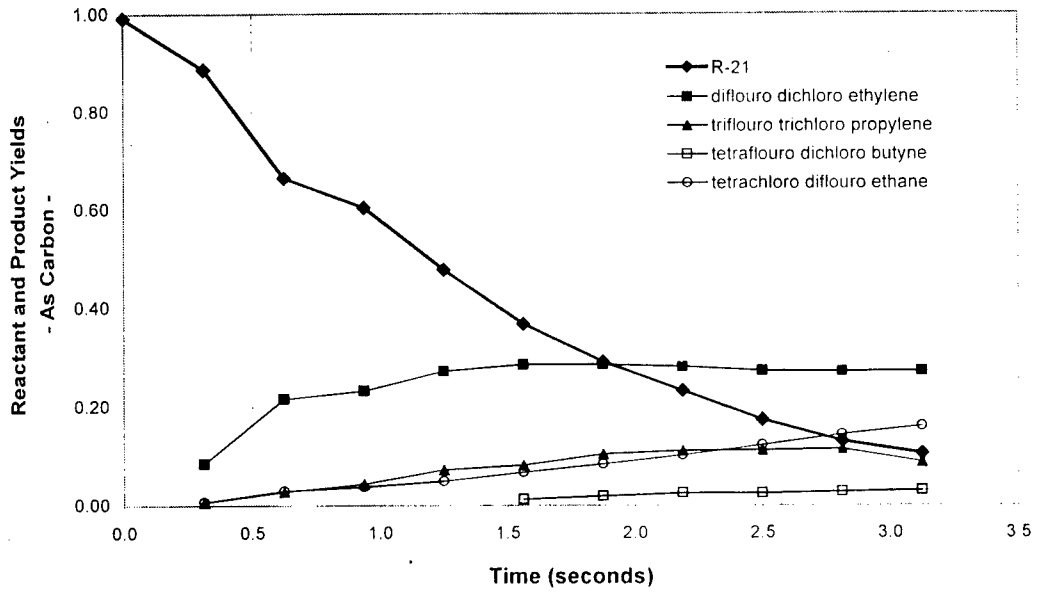


Figure 2: Reactants and products yields as carbon as function of reaction time at 898 K



The initial decomposition step is believed to proceed through one of three pathways:

$$CHCl_2F \leftrightarrow {}^1{:}CClF + HCl$$
$$CHCl_2F \leftrightarrow {\cdot}CHClF + {\cdot}Cl$$
$$CHCl_2F \leftrightarrow {}^1{:}CCl_2 + HF$$

Figure 3 is an energy level diagram for these dissociation pathways. Clearly the most energetically favorable pathway will be HCl elimination. A QRRK calculation on the decomposition of $CHCl_2F$ suggests HCl elimination is more favorable by 2 orders of magnitude than either HF elimination of C-Cl

bond rupture. Our measure of the apparent first order rate constant also closely matches the measured value $k(s^{-1}) = 1.58\ 10^{13} \exp[-52.30\ ^{kcal}/_{mol}/RT]$ given by Kushina et al(4).

The principle product is easily explained by the subsequent combination of the ^{1}:CCIF carbene

$$^1\text{:CCIF} + {}^1\text{:CCIF} \leftrightarrow \text{ClFC=CClF}$$

Formation of propylene species is believed to proceed via an isomerization involving a 1,2 chlorine shift to form a the dichlorofluoromethyl fluoro carbene species (^{1}:$CFCCl_2F$) which then reacts with the abundant ^{1}:CCIF species:

$$\text{FClC=CClF} \leftrightarrow {}^1\text{:}CFCCl_2F$$

$$^1\text{:}CFCCl_2F + {}^1\text{:CCLF} \leftrightarrow \text{ClFC=}CFCCl_2F$$

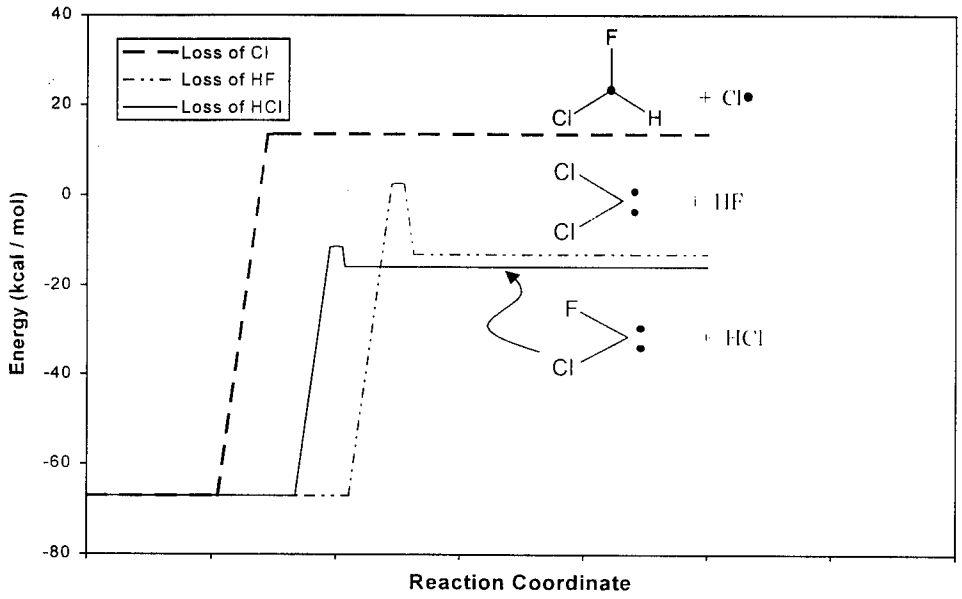


Figure 3: Energy Level Diagram for Dissociation Pathways of Dichlorofluoromethane

Ab-initio calculations on dichlorodifluoroethylene structures show the Cl migration has much lower activation energy than F migration; however, the two resulting carbenes both have similar overall heats of formation so neither is thermodynamically preferred. This suggests the reason why 1,1 dichlorodifluoroethylene is seen only at higher temperatures. At lower temperatures, Cl migrates and the energetically favored species is dichlorofluoromethyl fluoro carbene, which may exist in a state quasi-equilibrium state with 1,2 dichlorodifluoroethylene. Only at higher temperatures is there sufficient energy for fluorine to migrate across the barrier either followed or preceded by chlorine migration to form the 1,1 isomer.

In contrast to the carbene-dominated decomposition of chlorodifluoromethane described by Ritter and DiFelice (1, 2), pyrolysis of dichlorofluoromethane produces significant tetrachlorodifluoroethane, chlorodifluoroethylene and trichlorofluoromethane. This result suggests a significantly greater

importance of radical-based chemistry in this system. One possible set of pathways involves radical/radical combinations:

$CHFCl_2$	→	$\cdot CHFCl + \cdot Cl$	(initial dissociation)
$CHFCl_2 + \cdot Cl$	→	$\cdot CFCl_2 + HCl$	(abstraction)
$\cdot CFCl_2 + \cdot CFCl_2$	→	$FCl_2C\text{-}CCl_2F$	(major product)
$\cdot CHFCl + \cdot CFCl_2$	→	$ClFHC\text{-}CCl_2F$	
	→	$HCl + ClFC{=}CFCl$	(major product)
$\cdot Cl + \cdot CFCl_2$	→	CCl_3F	(major product)
$\cdot CHFCl + \cdot CHFCl$	→	$FClHC\text{-}CHClF$	
	→	$HCl + HFC{=}CFCl$	(minor product)

Alternatively, these same products may also be explained by the insertion of carbenes into Cl_2 or HCl:

$\cdot Cl + \cdot Cl$	→	Cl_2	
$^1{:}CClF + Cl_2$	→	CCl_3F	(major product)
$^1{:}CFCCl_2F + Cl_2$	→	$FCl_2C\text{-}CCl_2F$	(major product)
$^1{:}CFCCl_2F + HCl$	→	$FClHC\text{-}CCl_2F$	(major product)

The barrier to insertion of the carbene $^1{:}CF_2$ into Cl_2 is known to be about 2.1 kcal/mol (5), thus these are expected to be very energetically favorable pathways.

Conclusions

Pyrolysis of dichlorofluoromethane proceeds primarily via HCl elimination to form the $^1{:}CClF$ carbenes. Subsequent combination and isomerization reactions form the majority of observed products. This is completely analogous to the well-described system of chlorodifluoromethane; however, greater significance of C-Cl bond breaking in the current system is likely the route to formation of tetrachlorodifluoroethane as a major product.

References

1 DiFelice, J J and Ritter E R *Paper 17 Thermal Reactions of CHF2Cl under Inert and Reducing Conditions* Presented at Fall Technical Meeting of Eastern States Section of The Combustion Institute, October 25-27, 1993, Princeton NJ

2 DiFelice J.J.; *Thermal Decomposition of CHFCl-CF3 and CHCF2Cl An Experimental and Modeling Study, Masters Thesis Villanova University* 1995

3 NIST Chemical Kinetics Database. V 3.0 NIST Standard Reference Database 17, 1991

4 Kushina I.D., Belferman A.L., and Shevchuk V.U., *Kinet. Catal.* 1972 13, 758-764

5 Mel'nikovich S.V. and Moin F. B., *Kinet. Catal.* 1986 27, 17

THE OXIDATION OF ISO-OCTANE IN THE INTERMEDIATE TEMPERATURE REGIME UNDER BOTH LEAN AND DILUTED STOICHIOMETRIC CONDITIONS

J.-S. Chen and T. A. Litzinger
Department of Mechanical and Nuclear Engineering
The Pennsylvania State University
University Park, PA 16802
jxc156@psu.edu and tal2@psu.edu

H. J. Curran
Lawrence Livermore National Laboratory
Livermore, CA 94551
curran6@llnl.gov

INTRODUCTION

Iso-octane is a primary reference fuel, and as such its oxidation chemistry has been a significant topic in many studies related to autoignition. Several studies have focused on the oxidation of iso-octane in the low temperature regime at elevated pressures under stoichiometric conditions [1-3]. However, autoignition does not occur until the reaction temperatures have entered the intermediate temperature regime, and therefore the low temperature studies do not include all of the chemical phenomena related to autoignition.

Previously, both jet-stirred and plug flow reactors have been used to investigate the oxidation of iso-octane in the intermediate temperature regime at elevated pressures [4, 5]. However, due to significant heat release from the oxidation of iso-octane under these conditions, adding excess nitrogen has become a common practice to ensure the safe operation of flow reactors. Under such a diluted stoichiometric condition, all of the concentrations of fuel, oxygen, and nitrogen are significantly different from those under an actual stoichiometric condition. In contrast, under lean conditions, only the fuel concentration deviates significantly. Therefore, the main objective of this work is to more fully understand the reaction pathways of iso-octane oxidation in the intermediate temperature regime at different stoichiometries and dilution. Both lean and diluted stoichiometric conditions are investigated in this study to identify the differences between them as well as to uncover reaction pathways that are diminished in importance due to the low oxygen concentration of the diluted case.

EXPERIMENTS AND MODELING

Major species of iso-octane oxidation were identified and quantified as functions of time in a high-pressure, plug flow reactor facility. The pressure was set at 9 atm, and the average reaction temperature was approximately 927 K for both lean and diluted stoichiometric oxidation of iso-octane. For the lean oxidation of iso-octane in air, an equivalence ratio of 0.05 was used (the mole fraction of fuel was approximately 8.0e-4). For the diluted stoichiometric oxidation, excess nitrogen was added while the equivalence ratio was held at one. For comparison purposes, it would be ideal to simply replace the extra oxygen in the lean oxidation with nitrogen. Unfortunately, decreasing the concentration of oxygen to match the already very low iso-octane concentration in the lean oxidation, causes reaction rates to reduce significantly leading to few intermediate species with measurable mole fractions. To overcome this shortcoming, the concentration of iso-octane has to be increased from what was used in the lean oxidation. In other words, the mole fractions of iso-octane, oxygen, and nitrogen have to be adjusted at the same time. Due to the limit of the maximum flow rate on the oxygen flow meter, the iso-octane mole fraction can only be increased to 0.002 in diluted stoichiometric oxidation experiments. Because the concentrations of iso-octane and oxygen change simultaneously, it is inappropriate to quantitatively compare the results from the lean oxidation with those from the diluted stoichiometric oxidation. However, discussions of the difference between the lean oxidation and the diluted stoichiometric oxidation are qualitatively viable.

To fully explore the detailed chemical pathways under the range of conditions studied, the experimental measurements are compared with the predictions from a detailed chemical kinetic model being developed at the Lawrence Livermore National Laboratory. The flow reactor is simulated as an isobaric plug flow reactor with negligible axial diffusion of species and energy.

RESULTS AND DISCUSSIONS

Twenty-five species were identified and quantified as functions of time. However, due to the limited space of this abstract, only selected species are presented. Figures 1 and 2 depict the measured and predicted mole fractions of iso-octane under the lean and diluted stoichiometric conditions. The points are the experimental measurements and the lines are the model predictions, with solid lines corresponding to solid symbols and dashed lines to open symbols. This same arrangement remains for all the figures of major intermediate species. Although the iso-octane concentration in the diluted stoichiometric oxidation is approximately 2.5 times the concentration in the lean oxidation, Figures 1 and 2 show that the conversion rate of iso-octane under the diluted stoichiometric condition is slower than that under the lean condition. This is due to the significantly lower concentration of oxygen under the diluted stoichiometric condition.

In the intermediate temperature regime, iso-octyl radicals tend to undergo β-scission to yield smaller alkyl radicals and olefins. These smaller alkyl radicals can react with molecular oxygen to form conjugate olefins and hydroperoxyl radicals:

$$\dot{i}C_8H_{17} \longrightarrow \dot{R}' + \text{olefin}$$
$$\dot{R}' + O_2 \longrightarrow \text{olefin}' + \dot{H}O_2$$

The hydroperoxyl radicals can react with fuel molecules to form hydrogen peroxide which will result in the formation of two hydroxyl radicals. This is an important branching reaction in the intermediate temperature regime.

$$\dot{H}O_2 + RH \longrightarrow H_2O_2 + \dot{R}$$
$$H_2O_2 + M \longrightarrow \dot{O}H + \dot{O}H + M.$$

Owing to the low concentration of molecular oxygen, the reactions which lead to the formation of hydroperoxyl radicals are reduced in significance under the diluted stoichiometric condition. As a result, the overall reaction rate is slower compared with that under the lean condition. The model effectively reproduces the profile of iso-octane under the lean condition but overpredicts the consumption of iso-octane under the diluted stoichiometric condition. Furthermore, CO was not measured in the diluted stoichiometric oxidation although the model predicts an appreciable production of CO.

Among the measured species, iso-butene, propene, and C_7 olefins compose a large fraction of the major species quantified experimentally in this study. These olefins are produced from β-scission of iso-octyl radicals with iso-butene being formed in the highest concentration followed by propene as shown in Figures 1 and 2. Experimental results show that the formation of iso-butene accounts for approximately 50% the consumption of iso-octane which undergoes β-scission under the conditions of the intermediate temperature regime. In contrast, propene formation accounts for approximately only 25% iso-octane consumption via β-scission. Interestingly, the profiles of propene and iso-butene are shown to be closer in the diluted stoichiometric oxidation than they are in the lean oxidation. This phenomenon can be attributed to relatively less iso-butene being produced under the diluted stoichiometric condition. In addition to β-scission of iso-octyl radicals, iso-butene can be produced from the reactions of molecular oxygen with iso-butyl radicals. Because the concentration of oxygen is significantly lower under the diluted stoichiometric condition, iso-butyl radicals preferentially undergo β-scission to produce propene and methyl radicals, rather than add to molecular oxygen:

$$\dot{i}C_4H_9 + O_2 \longrightarrow iC_4H_8 + \dot{H}O_2$$
$$\dot{i}C_4H_9 \longrightarrow C_3H_6 + \dot{C}H_3$$

Consequently, the profiles of propene and iso-butene are relatively closer in the diluted stoichiometric oxidation than they are in the lean oxidation. Similar to the predictions of iso-octane, the model reproduces the profiles of iso-butene and propene effectively under the lean condition but overpredicts their formation under the diluted stoichiometric condition. Moreover, Figures 3 and 4 depict the profiles of C_7 olefins. It must be noted that the measured 4,4-dimethyl-2-pentene represents trans-4,4-dimethyl-2-pentene only. The model reproduces the profiles of both 2,4-dimethyl-2-pentene and 4,4-dimethyl-2-pentene under the lean condition up to 70 msec but overpredicts thereafter. However, the early decline of 2,4-dimethyl-2-pentene is reproduced by the model. Significant discrepancies exist in the predictions of 2,4-dimethyl-2-pentene and 4,4-dimethyl-2-pentene under the diluted stoichiometric condition.

Other selected hydrocarbon species are depicted in Figures 5 and 6, including propadiene, ethane, ethene, and 2-methyl-1-butene. Propadiene is formed in appreciable concentrations in the lean oxidation and is predicted to be produced from the reaction of methallyl radical with molecular oxygen via the following reaction:

$$\dot{i}C_4H_7 + O_2 \longrightarrow C_3H_4\text{-a} + CH_2O + \dot{O}H$$

Under the diluted stoichiometric condition, the reactions which require molecular oxygen become less important as compared with those under the lean condition. Thus, the mole fractions of propadiene become significantly less under the diluted stoichiometric condition than under the lean condition. This phenomenon is also observed in the formation of ethene as illustrated by the following reactions:

$$\dot{C}H_3 + \dot{C}H_3 + M \longrightarrow C_2H_6$$
$$C_2H_6 + \dot{O}H \longrightarrow \dot{C}_2H_5 + H_2O$$
$$\dot{C}_2H_5 + O_2 \longrightarrow C_2H_4 + \dot{H}O_2$$

After ethane is formed via the recombination reaction of two methyl radicals, it can react with hydroxyl radicals to form ethyl radicals. Ethene is then produced from the reaction of ethyl radicals and molecular oxygen. The last reaction is not important under the diluted stoichiometric condition. As a result, the mole fractions of ethane are higher than those of ethene under the diluted stoichiometric condition but the trend is opposite under the lean condition. The model overpredicts the formation of ethane under both lean and diluted stoichiometric conditions. On the other hand, 2-methyl-1-butene, which is predicted to be formed via the recombination of a methallyl

radical with a methyl radical, is always significantly underpredicted by the model. Thus, the rate constants of these recombination reactions in the intermediate temperature regime need to be further verified.

Figures 7 and 8 depicts the profiles of selected oxygenated species including acetone, methacrolein, 2,2,4,4-tetramethyltetrahydro-furan, and iso-butene oxide. Acetone is predicted to be formed through the Waddington mechanism [6-8] mainly from iso-butene with a small quantity from 2,4-dimethyl-2-pentene at high fuel conversion. Due to low concentrations of molecular oxygen, the Waddington mechanism is not expected to be significant under the diluted stoichiometric condition. As a result, the mole fractions of acetone are relatively low in the diluted stoichiometric oxidation. Regarding methacrolein, its mole fractions are less than acetone in the lean oxidation. However, while it is an oxygenated species, its mole fractions become higher than acetone in the diluted stoichiometric conditions. The formation pathway has been discussed previously as shown below [9]:

$$iC_4H_7 + HO_2 \longrightarrow iC_4H_7O + OH$$
$$iC_4H_7O + M \longrightarrow iC_3H_5CHO + H + M$$
$$iC_4H_7O + O_2 \longrightarrow iC_3H_5CHO + HO_2$$

Seemingly, the formation of methacrolein occurs primarily via the second reaction above because the formation of methacrolein is significant under both the lean and diluted stoichiometric conditions. Interestingly, the formation of both methacrolein and acetone are significantly overpredicted by the model under the diluted stoichiometric conditions shown in Figure 8.

In addition to β-scission, iso-octyl radicals, with an addition of molecular oxygen followed by an internal H-atom abstraction, can form hydroperoxyl-iso-octyl radicals which can subsequently produce C_8 cyclic ethers. In addition to 2,2,4,4-tetramethyltetrahydro-furan, 2-tertbutyl-3-methyl-oxetane and 2-isopropyl-3,3-dimethyl-oxetane are measured under the lean condition; however, only 2,2,4,4-tetramethyltetrahydro-furan is measured under the diluted stoichiometric condition because of the low oxygen concentrations. Similarly, the formation of iso-butene oxide is reduced in the diluted stoichiometric oxidation. The mole fractions of iso-butene oxide and 2,2,4,4-tetramethyltetrahydro-furan under the lean condition are reproduced by the model.

SUMMARY

From the observed differences, it can be concluded that the study of the lean oxidation of iso-octane is significant in complementing studies of diluted stoichiometric oxidation. The comparison of these studies is especially important in highlighting the reaction pathways which involve molecular oxygen. Furthermore, the overall performance of the model predictions is acceptable especially in the predictions of lean oxidation. However, significant discrepancies exist in the predictions of the formation of acetone and methacrolein, which are products of iso-butene oxidation, under the diluted stoichiometric condition. Such discrepancies remain as a challenge in further developing a detailed model which is capable of predicting the oxidation of iso-octane under wide ranges of conditions.

REFERENCES

1. Leppard, W. R., "The autoignition chemistries of primary reference fuels, olefin/paraffin binary mixtures, and non-linear octane blending", SAE 922325 (1992).
2. Minetti, R., Carlier, M., Ribaucour, M., Therssen, E. and Sochet, L. R., "Comparison of oxidation and autoignition of the two primary reference fuels by rapid compression", 26th Symp. (Int.) on Combust., 747-753 (1996).
3. Ciajolo, A. and Andrea, D. A., "Controlling steps in the low-temperature oxidation of n-heptane and iso-octane", Combust. Flame, 112:617 (1998).
4. Dryer, F. L. and Brezinsky, K., "A flow reactor study of the oxidation of n-octane and iso-octane", Combust. Sci. Technol., 45:199-212 (1986).
5. Dagaut, P., Reuillon, M. and Cathonnet, M., "High pressure oxidation of liquid fuels from low to high temperature. 1. n-heptane and iso-octane.", Combust. Sci. Technol., 95:233-260 (1994).
6. Ray, D. J. M., Diaz, R. R. and Waddington, D. J., "Gas phase oxidation of butene-2: the role of acetaldehyde in the reaction", 14th Symp. (Int.) on Combust., 259-266 (1972).
7. Ray, D. J. M. and Waddington, D. J., "Gas phase oxidation of alkenes - part II. The oxidation of 2-methylbutene-2 and 2,3-dimethylbutene-2", Combust. Flame, 20:327-334 (1973).
8. Pitz, W. J., Westbrook, C. K. and Leppard, W. R., "Autoignition chemistry of C_4 olefins under motored engine conditions: A comparison of experimental and modeling results", SAE 912315 (1991).
9. Chen, J.-S. and Litzinger, T. A., "The lean oxidation of iso-octane at elevated pressures", the Fall Technical Meeting of Eastern States Section of the Combustion Institute (1996).

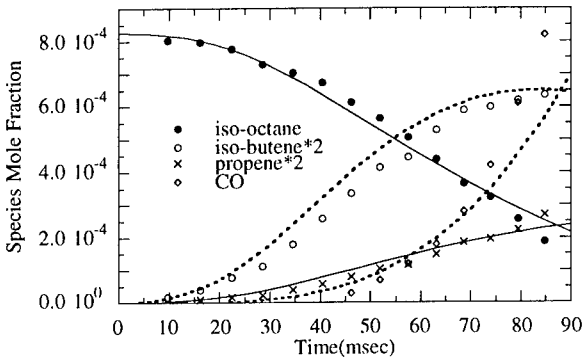


Figure 1. Lean oxidation.

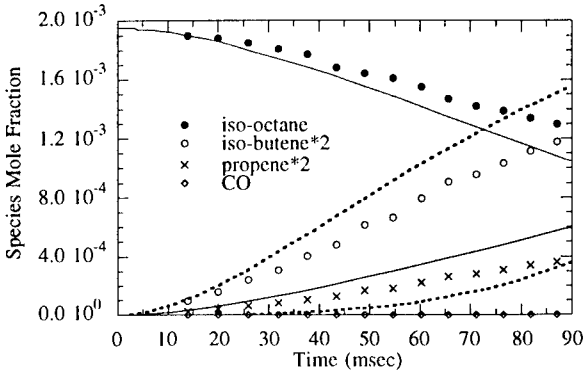


Figure 2. Diluted stoichiometric oxidation.

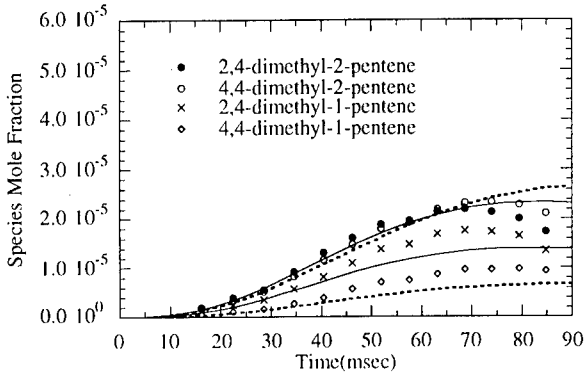


Figure 3. Lean oxidation.

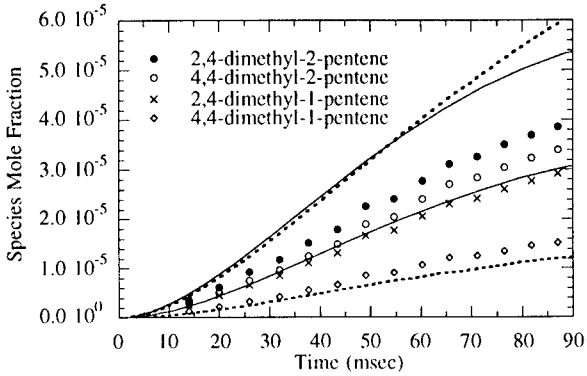


Figure 4. Diluted stoichiometric oxidation.

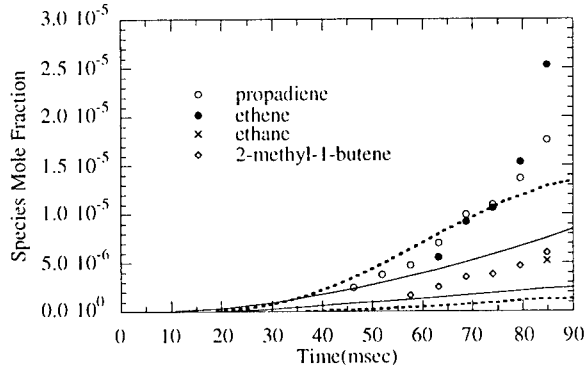


Figure 5. Lean oxidation.

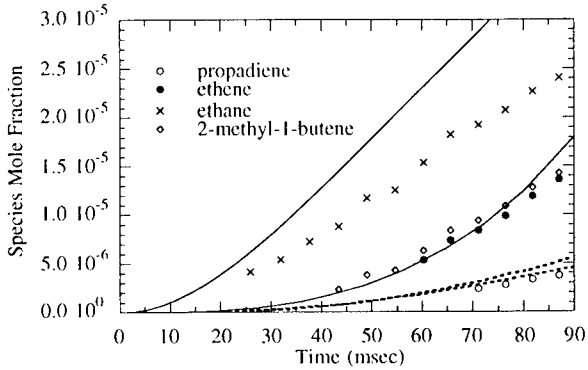


Figure 6. Diluted stoichiometric oxidation.

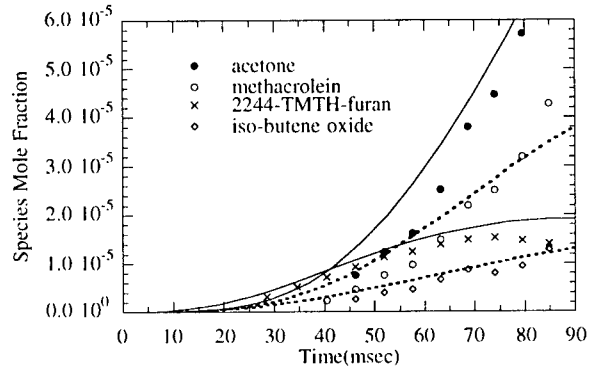


Figure 7. Lean oxidation.

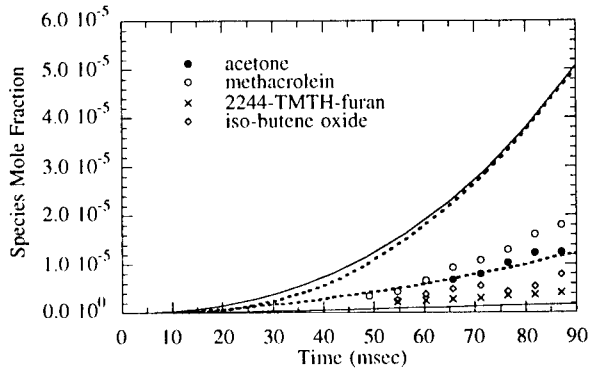


Figure 8. Diluted stoichiometric oxidation.

Figures 1-8: Mole fraction profiles of selected species. Dashed lines correspond to open symbols.

De Novo Synthesis Mechanism of Polychlorinated Dibenzofurans from Polycyclic Aromatic Hydrocarbons and Characteristic Isomers of Polychlorinated Naphthalenes

F. Iino[1)*], T. Imagawa[2)], M. Takeuchi[2)], M. Sadakata[1)] R. Weber[3)]

[1)]Department of Chemical System Engineering, University of Tokyo, 7-3-1 Hongo, Bunkyo-ku, Tokyo, Japan 113-8656

[2)]National Institute for Resources and Environment, 16-3 Onogawa,Tsukuba, Ibaraki, Japan 305-8569

[3)]Ishikawajima-Harima Heavy Industries Co., Ltd., 1, Shin-nakahara-cho, Isogo, Yokohama, Japan 235-8501

*Currently working at U.S. Environmental Protection Agency, National Risk Management Research Laboratory, Air Pollution Prevention and Control Division, Air Pollution Technology Branch, MD-65, 86 TW Alexander Drive, Research Triangle Park,NC, 27711 USA

e-mail:iino.fukuya@epa.gov

Introduction

The emission of polychlorinated dibenzo-*p*-dioxins (PCDDs) and polychlorinated dibenzofurans (PCDFs) from municipal waste incinerators (MWIs) was reported by K. Olie et al. (*1*) in 1977. This report was widely paid attention, because some isomers of PCDD/Fs had been known to be very toxic. L. Stieglitz et al. (*2*) and H. Hagenmaier et al. (*3*) showed that PCDD/Fs are formed not only from precursors such as chlorophenols but also from particulate organic carbon present in fly ash and inorganic chloride. This formation path is so-called "de novo" synthesis. Since then some studies (*4-9*) have been carried out to elucidate the formation mechanism of PCDD/Fs from a carbon matrix.

By means of the identification of the products formed from ^{12}C- and ^{13}C-carbon as starting materials with inorganic copper and chlorine, it was suggested by K. Hell et al. (*10*) that 99% of PCDFs and 75-90% of PCDDs are probably directly released from preformed structures in the amorphous carbon matrix, e.g. biphenyls. There have been, however, very few reports mentioning the relation between the structures of starting materials and the resulting isomers of PCDD/Fs. Therefore, the details on the de novo synthesis formation such as chlorination and incorporation of oxygen still remain unclear.

On the other hand, polychlorinated naphthalenes (PCNs) were found to be contained in fly ash collected from municipal waste incinerators (MWIs) by G. A. Eiceman et al. (*11*) in 1979. K. Ballschmiter et al. (*12*) reported in 1983 that chloroethylenes work as precursors to form PCNs among PCDD/Fs, polychlorinated biphenyls (PCBs) and other chlorinated compounds under a pyrolytic condition. In 1984, the concentrations of PCNs in biological tissue were determined, and the results were ranging from 3 to 62 ng/g-lipid of PCNs (*13*). The 2,3,7,8-tetrachlorodibenzo-*p*-dioxin toxic equivalent factors (TEF) of some PCNs isomers were firstly proposed by A. Hanberg et al. (*14*) in 1990. One of the highest value was determined to be 0.003 for 1,2,3,4,5,6,7-heptachloronaphthalene (HpCN).

However, all 75 isomers of PCNs had not been available at that time. A lack of information on the analysis of the PCNs isomers has prevented not only to know the precise concentration of PCNs but also to discuss the formation mechanism in view of homologues and isomers. Williams et. al. (*15*) reported the relative retention time data of important hexa- and heptachloronaphthelene isomers.

Imagawa et. al. (*15-20*) identified all di- through hexachloronaphthalenes using synthesized and commercial standards. Now the isomer specific analysis is possible for di- through heptachloronaphthalenes.

In this study, the isomer patterns of PCDFs and PCNs from polycyclic aromatic hydrocarbons (PAHs) which are possible carbon sources present in soot were investigated. The more specific structure of the PAHs than the other carbon materials could clearly show the de novo formation mechanisms such as chlorination and incorporation of oxygen to PCDFs. We supposed in this study that PAHs could be one of the possible major carbon sources for PCDFs in MWIs, although they have not been paid much attention. PCDDs were not characteristically formed from the PAHs. The formation paths of PCNs in the MWIs should be also clarified, because not only some of the isomers are toxic, but also PCNs might be a good indicator to show where the de novo formation occurs in the MWIs.

The PAHs for this experiment were selected in terms of their structural differences, so that some of them are structurally related each other and this selection is not necessarily in accordance with the contents of the PAHs in fly ash (*21*).

Formation rates of PCDD/Fs from PAHs are also compared with activated carbon and phenol.

Experiment

Formation Mechanism(*22*)

The PAHs used in this experiment are perylene ($C_{20}H_{12}$), benzo[ghi]perylene ($C_{22}H_{12}$), coronene ($C_{24}H_{12}$), 1,2;8,9-dibenzopentacene ($C_{30}H_{18}$) and ovalene ($C_{32}H_{14}$) as shown in Fig.1. Some of these PAHs are known to be practically emitted from the MWIs (*21*). Graphite particles were sieved to a particle size < 125μm and mechanically mixed with 0.1wt% of the PAHs and 5wt% copper chloride (I). The mixture of 1g was placed in a quartz tube reactor heated at 400°C for 2 hours. The products were collected in an ice-cooled water trap and a florisil trap. The inlet oxygen into the reactor was controlled at 10% by N_2 and air. The total flow rate was 200ml/min.

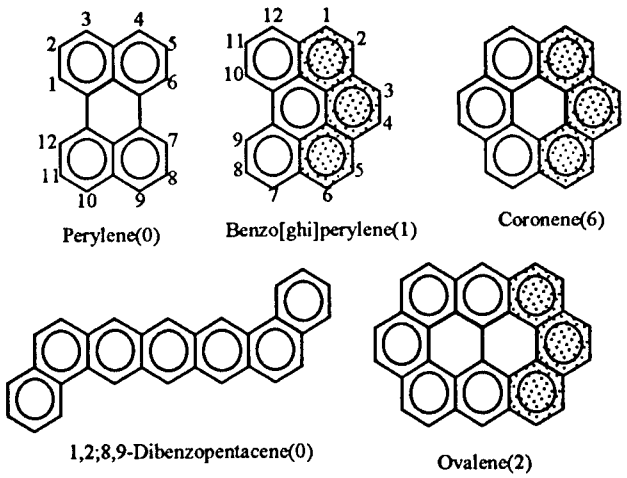


FIGURE 1. Polycyclic aromatic hydrocarbons examined in this study.The numbers in the parentheses are those of pre-structures possibly to give 1,2,8,9-tetrachlorinated dibenzofurans. The shadowed combination is one of those preformed structures.

The products in the traps and residues in the reactor were extracted with ethyl acetate. The extracted samples were separately concentrated with a rotary evaporator to a few ml and were cleaned up with chromatographic columns filled with acidified, alkaline and neutral silicagel. After the sample volumes being finally reduced to 200-300μl, the samples were injected into GC-MS Hitachi M-80B

Formation rate(*23*)

The PAHs used in order to examine formation rates of PCDD/Fs were anthracene, phenanthrene, pyrene, perylene, coronene, 1,2;8,9-dibenzopentacene, ovalene. The samples were prepared by mixing, in a dry condition, silica gel, $CuCl_2 \bullet 2H_2O$, and the single PAH.For comparison of the formation rates, 0.1wt % of activated carbon and phenol, respectively, were also investigated. The reaction for formation rates was controlled at 300°C for 30 min under 10%O_2/N_2 (200ml/min) with air and N_2.

PCDD/Fs

A SP-2331 column (60m, 0.25mm i.d., 0.20μm film thickness) was used for analysis of PCDFs isomers. The column oven temperature was programmed from 200°C to 275°C at a rate of 4°C/min. The identification of PCDFs isomers was carried out according to the retention times investigated by J. J. Ryan et al (*24*). The PCDFs formed were identified from T4CDFs to O8CDF. However, 1,2,4,7-, 1,3,6,7-, 1,3,4,6-, and 1,2,4,8-T4CDF in T4CDFs and 1,2,4,7,8-, 1,2,3,7,9-, and 1,2,3,6,7-P5CDF in P5CDFs could not be identified even by a SP-2331 column owing to the interfering peaks at the same retention times.

PCNs

Columns of DB-5 or DB-1701 (30m, 0.25mm i.d., 0.25μm film thickness) were used for analysis of PCNs isomers. The column oven temperature was programmed from 160°C to 300°C (280°C in the case of DB-1701) at a rate of 4 °C /min. PCN homologues were determined by selective ion monitoring at m/z 196 and 198, 230 and 232, 264 and 266, 300 and 302, and 334 and 336 for di- (DiCNs), tri- (TriCNs), tetra- (TeCNs), penta- (PeCNs) and hexachloronaphthalenes (HxCNs), respectively. The PCNs isomers were identified comparing the retention time with synthesized standards (*18, 20*). The other details on the analysis of PCNs are described with the elution order and retention indices in the previous paper (*25*).

Results and Discussion

Formation Mechanism

There are two characteristic isomers observed, which are 1,2,8,9-T4CDF (64%) from coronene and 2,4,6,7-T4CDF (44%) from perylene. These isomers were reproducibly formed. Even 0.1wt% of the PAHs in graphite provided these higher yields. These characteristic isomers were not formed from the control case of graphite and 5% copper chloride (I)(*26*).

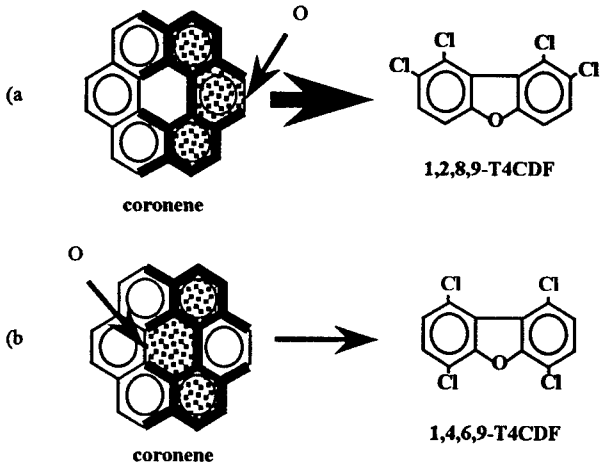


Fig.2 The examples of the formation mechanisms of T4CDF directly formed from coronene. (a) The incorporation of oxygen occurs from the outside of coronene to result in 1,2,8,9-T4CDF and (b) from the inside to form 1,4,6,9-T4CDF.

1,2,8,9-T4CDF was also formed from benzo[ghi]perylene (14%) and ovalene (14%), while 1,2;8,9-dibenzopentacene and perylene gave only 0.3% and 1%, respectively. This difference of the 1,2,8,9-T4CDF yields is considered to be attributed to the structures of the starting materials shown in Fig.1. The shadowed parts in benzo[ghi]perylene, coronene and ovalene (Fig.1) could provide the 1,2,8,9-T4CDF on the assumption that chlorination occurs after the cleavage of a C-C bond. In addition, oxygen needs to be incorporated from the outside of the molecule in order to form 1,2,8,9-T4CDF (Fig.2). The incorporation of oxygen from the inside of the molecule results in 1,4,6,9-T4CDF. The precise relative intensity of 1,4,6,9-T4CDF cannot be determined because the peak of 1,4,6,9-T4CDF overlapped with 2,3,6,8- and 1,2,4,9-T4CDF using whichever column of DB-5 or SP-2331. However, the relative intensity of these three isomers is only 16% so that 1,2,8,9-T4CDF formation is more facilitated than 1,4,6,9-T4CDF. It means that oxygen is relatively easily incorporated from the outside of the molecule. The difference of the yields which are equivalent to the relative intensities of the isomers possibly depends on the symmetry of the molecules. The numbers in the parentheses in Fig.1 indicate how many preformed structures each PAH has. The preformed structure containing a biphenyl can provide the 1,2,8,9-T4CDF. There are no preformed structures in perylene and 1,2;8,9-

dibenzopentacene, whereas benzo[ghi]perylene and ovalene have one and two, respectively. Coronene which gave the highest yield of 1,2,8,9-T4CDF has six combinations of the preformed structure in itself. Consequently, it can be concluded that the structural features of the symmetrical preformed structures of a coronene molecule enabled to amplify one of the de novo formation paths of the PCDFs isomers formed from the PAHs. This path could be also applied in the case of not only graphite but also fly ash which contains some PAHs, although this is one of the numerous de novo formation paths that could occur.

Formation Rates

The PCDFs formation was dominant in every homologue with a ratio of ΣPCDFs/ΣPCDDs being about 10. Perylene has an outstanding potential for the formation from P5CDF to O8CDF than activated carbon. The ratio of the formation rates of perylene and activated carbon ranges from 2.3 (perylene/fine ground activated carbon) to 13 (perylene/activated carbon). The point that should be carefully considered is the difference of volatility of the carbon sources at 300°C. The melting point of perylene is between 277-279°C. At 300°C perylene can be more easily vaporized, which means that the formation rate from perylene to PCDFs can be much higher than that of activate carbon.

The lower chlorinated PCDDs were hardly formed from the PAHs, while phenol was the good precursor for the PCDD formation as generally accepted.

Reference

(1) Olie K.; Vermeulen P.L.; Hutzinger O. Chemosphere **1977**, *6*, 455-459.
(2) Stieglitz L.; Vogg H. Chemosphere **1987**, *16*, 1917-1922.
(3) Hagenmaier H.; Kraft M.; Brunner H.; Haag R. Environ. Sci. Technol., **1987**, *21*, 1080-1084.
(4) Stieglitz L.; Zwick G.; Beck J.; Roth W.; Vogg H. Chemosphere **1989**, *18*, 1219-1226.
(5) Stieglitz L.; Zwick G.; Beck J.; Bautz H.; Roth W. Chemosphere **1990**, *20*, 1953-1958.
(6) Jay K.; Stieglitz L. Chemosphere **1991**, *22*, 987-996.
(7) Addink R.; Olie K., Environ. Sci. Technol. **1995**, *29*, 1425-1435.
(8) Gullett B. K.; Bruce K. R.; Beach L. O. Chemosphere **1990**, *20*, 1945-1952.
(9) Gullett B. K.; Bruce K. R.; Beach L. O.; Drago A. M. Chemosphere **1992**, *25*, 1387-1392.
(10) Hell K.; Stieglitz L.; Zwick G.; Will R. Organohalogen Compd. **1997**, *31*, 492-497.
(11) Eiceman G. A.; Clement R. E.; Karasek F. W. Anal. Chem. **1979**, *51*, 2343-2350.
(12) Ballschmiter K.; Zoller W.; Scholz Ch.; Nottrodt A. Chemosphere **1983**, *12*, 585-594.
(13) Jansson B.; Asplund L. Chemosphere **1984**, *13*, 33-41.
(14) Hanberg A.; Waern F.; Asplund L.; Haglund E.; Safe S. Chemosphere **1990**, *20*, 1161-1164.
(15) Williams D. T.; Kennedy B. ;LeBel G. L. Chemosphere, **1993**, *27* (5), 795-806.
(16) Imagawa T.; Tanaka T. Pollution Control **1988**, *23*, 277-284 (in Japanese).
(17) Imagawa T.; Tanaka T.; Miyazaki A. Pollution Control **1989**, *24*, 159-168 (in Japanese).
(18) Imagawa T.; Yamashita N.; Miyazaki A. J. Environ. Chem. **1993**, *3*, 221-230 (in Japanese).
(19) Imagawa T.; Yamashita N. Chemosphere **1997**, *35*, 1195-1198.
(20) Imagawa T.; Takeuchi M. Organohalogen Compd. **1995**, *23*, 487-490.
(21) Eiceman G. A.; Clement R. E.; Karasek F. W. Anal. Chem. **1979**, *51*, 2343-2350.
(22) Iino F.; Imagawa T.; Takeuchi M.; Sadakata M. Environ. Sci. Technol. **1999**, 33(7), 1038-1043.
(23) Iino F.; Imagawa T.; Takeuchi M.; Sadakata M.; Weber R. Chemosphere in press.
(24) Ryan J. J.; Conacher H. B. S.; Panopio L. G.; Lau B. P. -Y.; Hardy J. A.; Masuda Y. J. Chromatogr. **1991**, *541*, 131-183.
(25) Kannan K. ; Imagawa T.; Blankenship A. L.; Giesy J. P. Environ. Sci. Technol. **1998**, *32*, 2507-2514.
(26) Iino F.; Imagawa T.; Takeuchi M.; Sadakata M. Organohalogen Compd. **1998**, *36*, 89-92.

Further Studies of NOx-Sensitised Oxidations at Low Temperature

Melita Jazbec and Brian S. Haynes

Department of Chemical Engineering, University of Sydney
NSW 2006, Australia
melita@chem.eng.usyd.edu.au
haynes@chem.eng.usyd.edu.au

Natural gas is an important source of energy and, due to its low greenhouse gas emissions, is becoming increasingly popular. However, trace amounts of hydrogen sulfide, which are usually present in natural gas, can be emitted to atmosphere as H_2S or in the oxidised form as SO_x, causing serious pollution problems.

Small amounts of nitrogen oxides have been shown to promote the oxidation of low concentration fuels (of order of hundreds of parts per million) at low temperatures (500-1000 K) [1, 2]. In this study we examine the effect of nitrogen oxides (0-100 ppm) on the oxidation of hydrogen sulphide (100 ppm in N_2 with 5% O_2) at low temperatures (480-600 K) in an atmospheric plug flow reactor.

Glarborg et al. [3] constructed a comprehensive sulphur mechanism based on a study of the effect of SO_2 on moist CO oxidation, with and without NO present. The proposed kinetic model, which also includes interactions between nitrogen and sulphur species, showed a good agreement with their experimental results. University of Leeds [4] proposed a sulphur mechanism similar to the mechanism derived by Glarborg et al. with additional channels forming species S_2, SN, CS and COS.

In this paper, we describe the modelling and experimental results of the reactivity of H_2S with oxygen as a function of NO concentration and temperature. A set of chemical reactions describing sulphur chemistry [3, 4] was added to the previously developed methane oxidation mechanism [1]. Chemical-kinetic modelling was performed with the Sandia Chemkin II/Senkin chemical kinetic packages [5, 6] using a plug flow reactor model and assuming isothermal conditions and atmospheric pressure. The modelling results showed that H_2S oxidation (100 ppm in N_2 with 5% O_2), starts at temperatures above 580 K at 2 seconds residence time. At temperatures below 580 K, the addition of trace amounts of NO promotes the oxidation of H_2S (Figure 1). However, increasing the concentration of added NO results in an inhibition of the H_2S oxidation. At temperatures above 580 K, oxidation of H_2S occurs in the absence of NO, but is progressively more inhibited by the addition of increasing amounts of NO. Not only is the ignition delay prolonged by the addition of NO, but also the final extent of H_2S oxidation is affected (Figure 2) in ways which depend on the NO concentration and temperature.

Based on the modelling, a very simple mechanism is determined for these low-temperature conditions:

$$H_2S + O = SH + OH \quad \text{(R1)}$$
$$H_2S + OH = SH + H_2O \quad \text{(R2)}$$
$$SH + O_2 = SO + OH \quad \text{(R3)}$$
$$SH + O = S + OH \quad \text{(R4)}$$
$$S + O_2 = SO + O \quad \text{(R5)}$$
$$SO + O_2 = SO_2 + O \quad \text{(R6)}$$

H_2S consumption is undertaken via two channels, with O (R1) and OH radical (R2), forming SH. Formed SH radical can be converted into SO through two alternative routes. Either, directly in the reaction with O_2 (R3), or it gets reduced first to S, in the presence of O radical (R4), and then S reacts with O_2 to form SO (R5). The oxidation mechanism is concluded with the formation of SO_2 (R6). The model suggests that oxygen atoms play a key role in the chain-branching and propagation steps. In the excess O_2 employed, it follows that significant formation of ozone, O_3, is formed in the chain-terminating step (R7):

$$O + O_2 + M = O_3 + M \qquad (R7)$$

The O_3 decomposes once the supply of O is exhausted but in the presence of NO, there is expected to be substantial formation of NO_2 (R8)

$$O_3 + NO = O_2 + NO_2 \qquad (R8)$$

This route of formation is different from that usually seen in hydrocarbon, CO, or H_2 systems, where the conversion of NO to NO_2 occurs through peroxy species (R9-R10):

$$H + O_2 + M = HO_2 + M \qquad (R9)$$

$$HO_2 + NO = OH + NO_2 \qquad (R10)$$

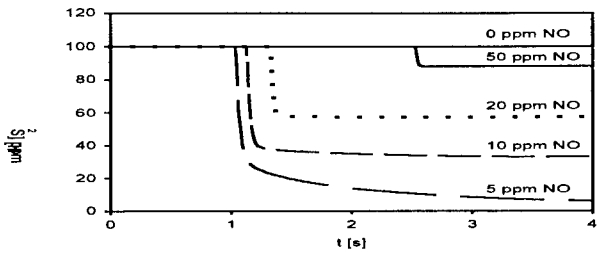


Figure 1: Computed concentration profiles of H_2S, as a function of inlet NO concentration, for the reaction of 100 ppm H_2S in N_2 with 5% O_2 at 500 K.

The low-temperature oxidation of H_2S was studied experimentally in an atmospheric isothermal plug flow reactor. The silica reactor is housed in a temperature-controlled, fan-stirred oven. It has two 4.5-mm i.d. preheat coils (1.5 m and 3.5 m long), a short mixing section, and an 8-mm i.d. reaction section (4.5 m long). The total flow through the reactor (at STP) was held constant. Flow rates of the reacting gases were metered with mass flow controllers to give the desired inlet concentration (100 ppm H_2S, 5 % O_2, 0-100 ppm NO in N_2). Residence times were typically in the range of 1.5 to 3.5 s. Reactor products were quenched and analysed. NO and NO_2 concentrations were determined using a chemiluminescent NO_x analyser (Model 200, API). A sample of the products was diluted with N_2 to achieve less than 1 ppm concentration before it entered the NOx analyser. An FTIR spectrometer (FTS40, Bio-Rad) was used to determine the concentrations of SO_2 and H_2O. The outlet streams from

analysers and reactor were scrubbed through a 1 M $Zn(C_2H_3O_2)_2$ solution to remove any unoxidised H_2S before they were vented to atmosphere.

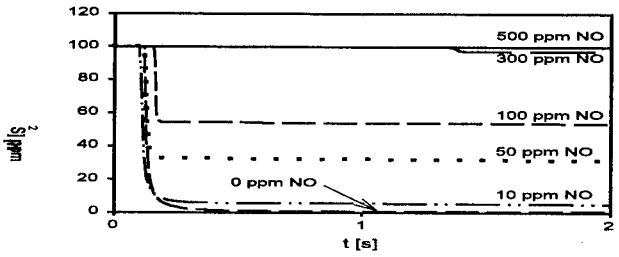


Figure 2: Computed concentration profiles of H_2S, as a function of inlet NO concentration, for the reaction of 100 ppm H_2S in N_2 with 5% O_2 at 600 K.

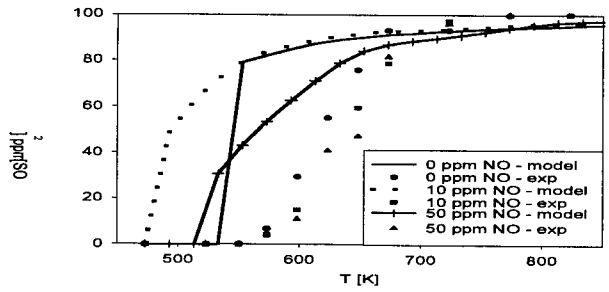


Figure 3: SO_2 concentrations, as a function of temperature, at different inlet NO concentrations, for the reaction of 100 ppm H_2S in N_2 with 5% O_2 at the residence times 1.8-3.2 s.

The experimental results were compared with the modelling results. On Figure 3, SO_2 concentration profiles are plotted as a function of temperature at different NO concentrations. The model predicts a 100 K lower ignition temperature in the presence of 10 ppm of NO than without NO, which was not

observed in the experiments. In fact, the experimental data show that NO did not have any effect at all. Moreover, the model shows a much higher reactivity overall compared to the experimental findings. NO gets converted to NO_2 in the oxidation process. Modelling data predicts a decrease of NO concentration (Figure 4) whereas it remained constant in the experiments.

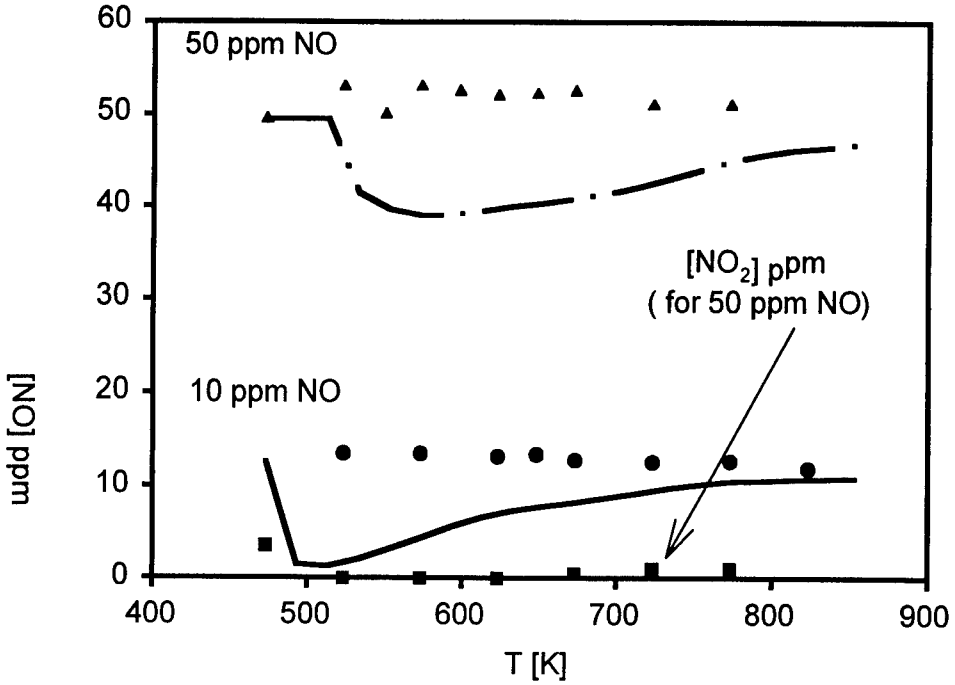


Figure 4: NOx concentration profile as a function of temperature, for the cases of addition of 10 and 50 ppm of NO, for the reaction of 100 ppm H_2S in N_2 with 5% O_2 at the residence times 1.8-3.2 s.

There was no NO_2 observed in the experiments (Figure 4), which indicates that the pathways R8 and R10 are not operating in practice. This suggests that the O atoms are not as prevalent as implied by the model. Consistent with the conclusion is the fact that there was no O_3 observed in the sampled products even though the detection limit for O_3 in the FTIR is 1 ppm.

REFERENCES:

[1] Bromly, J. H., Barnes, F. J., Muris, S., You, X. and Haynes, B. S., "Kinetic and Thermodynamic Sensitivity Analysis of the NO-Sensitised Oxidation of Methane," Combust. Sci. Tech., Vol. 115, pp. 259-296 (1996).

[2] Hori, M., Matsunaga, N., Malte, P. C. and Marinov, N. M., "The effect of Low-Concentration Fuels on the Conversion of Nitric Oxide to Nitrogen Dioxide," 24th Symp. (Int.) on Combustion, The Combustion Institute, pp. 909-916 (1992).

[3] Glarborg, P., Kubel, D., Dam-Johansen, K., Chiang, H.M. and Bozzelli, J.W., Impact of SO_2 and NO on CO Oxidation under Post-Flame Conditions, Int. J. Chem. Kinet., Vol. 28, (1996), p. 773.

[4] http://www.chem.leeds.ac.uk/Combustion/Combustion.html

[5] Kee, R.J., Rupley, F.M. and Miller, J.A., "CHEMKIN II: A Fortran Chemical Kinetics Package for the Analysis of Gas-Phase Chemical Kinetics," Report SAND 89-8009, Sandia National Laboratories, Livermore, CA, 1989.

[6] Lutz, A.E., Kee, R.J. and Miller, J.A., SENKIN: A Fortran Program for Predicting Homogeneous Gas Phase Chemical Kinetics with Sensitivity Analysis, Report SAND 87-8248, Sandia National Laboratories, Livermore, CA, 1988.

LIF-LII Images of a Turbulent Gas-Jet Diffusion Flame

Randall L. Vander Wal
NCMR @ NASA-Lewis Research Center
M. S. 110-3
21 000 Brookpark Rd.
Cleveland, OH 44135
email: randy@rvander.grc.nasa.gov

Introduction

Fuel-rich regions within turbulent diffusion flames can undergo significant pyrolysis [1]. Polycyclic aromatic hydrocarbons (PAHs) and ultimately soot are produced as a result. Both species are significantly more difficult to oxidize than the parent fuel precursor. This resistance towards oxidation creates the potential for emission of these pyrolysis products from flames [2]. Within practical devices such as incinerators, such emissions are known to occur as transient puffs as fuel-rich pockets escape full oxidation [3]. Concurrent with oxidation resistance, increased soot results in lowered flame temperature due to radiative heat loss, further decelerating oxidation [4]. Understanding the formation of fuel pyrolysis products and their transformation into soot is important to possible future control of their formation and presently enhancing their removal through oxidation. Spatial location of the fuel-rich regions in relation to the soot containing regions would also aid modelling studies coupling soot formation with radiation in turbulent diffusion flames [5].

With these opportunities as motivation, initial studies used one- and two-dimensional laser light scattering studies to reveal the soot distribution within turbulent hydrocarbon diffusion flames [6-8]. In each of these laser-light scattering studies from soot, large soot-free pockets were observed throughout a range of axial heights, often bordered by soot pockets and streaks. Qualitatively similar results have been observed in laser-induced incandescence (LII) measurements of soot within turbulent flames [9,10]. An immediate question is whether such soot free regions were fuel-rich pyrolysis regions or fuel-lean oxidative regions.

Different approaches have been applied to distinguish such regions. Laser-induced fluorescence (LIF) of molecular seeds introduced into the fuel stream can suffer early pyrolytic degradation relative to the main hydrocarbon fuel [11]. Particles seeded into the fuel stream will not follow the flow beyond moderate Reynolds' numbers [12]. In this article, LIF of PAHs, naturally produced as a result of fuel pyrolysis processes is used to visualize fuel pyrolysis regions. To obtain sufficient LIF intensity, laser fluences sufficient to excite incandescence were used. Thus the intensity in these images arises from both LIF and LII. These simultaneous LIF-LII images (locating both fuel pyrolysis and soot containing regions) are compared to separate but temporally equivalent LII images (locating only soot containing regions) to spatially distinguish fuel rich pyrolysis regions from soot containing regions. Histogram analyses of the LIF-LII and LII images quantify the spatial distributions of the PAH and soot levels in the inception, growth and oxidation regions within the turbulent diffusion flame.

Experimental

The experimental configuration is similar to previous measurements [13,14]. Light at either 1064 nm or 266 nm was used for LII and combined LIF-LII measurements respectively. Separate Nd:YAG lasers generated each wavelength. An 8x Galilean telescope of spherical UV fused silica lenses followed by a pair of positive spherical cylindrical lenses and aperture formed the 266 nm light into a laser sheet of 20 mm height. An 8x Galilean telescope followed by a 1500 mm spherical cylindrical lens formed the 1064 nm light into a laser sheet. Each laser sheet passed through the jet centerline. Based on pulsewidths of 10 ns and 5 ns for the 1064 and 266 nm light, estimated laser sheet intensities were 7×10^7 W/cm^2 and 8×10^6 W/cm^2 respectively. Spectral characterization of the LIF and LII signals using 266 and 1064 nm light has been discussed elsewhere [13,14]. Due to varying soot loading in the annular region, the calculated laser intensities must be considered an upper bound for the laser intensity across the flame width.

Opposing gated intensified cameras fitted with ultraviolet f4.5/105 mm (adjustable) focal length camera lenses and 40 mm extension tubes captured the LII (using 1064 nm excitation) and simultaneous LIF-LII images (using 266 nm excitation). The object magnification yielded a pixel resolution of 27 pixels per millimeter. The actual spatial resolution, determined by using an a replica of the 1951 Air Force

imaging standard was found to be approximately 70 microns. Bandpass interference filters transmitting 400 - 450 nm preceded each gated intensified array camera. Frame-grabbers digitized the images for transfer to the host computer. Delay generators controlled the relative timing of the camera video signals, the firing of the two lasers and camera detection gates. The delay between the 266 and 1064 nm excitation pulses was 1100 ns thereby yielding essentially simultaneous LIF-LII and separate LII images. The ethylene flow rate through the 2 mm inner diameter vertically oriented stainless tube was 3.0 slm resulting in a lifted flame and cold flow Reynolds number of 2500 based on the burner nozzle inner diameter. The approximate visible flame length was 30 cm.

Simultaneous Paired LIF-LII Images

Image Discussion

The thin soot streaks of low incandescence and fluorescence intensity in Fig. 2, indicative of low soot and PAH concentrations, are consistent with soot formation processes being in the earliest stages at low axial heights within the flame. Since the PAH and soot formation reactions require a finite temperature-time product [15], their appearance indicates that a minimum threshold in temperature-time has been achieved. At this lowest axial height, little time at elevated temperature has elapsed for fuel pyrolysis and soot formation/growth reactions to occur.

With increasing integrated temperature-time, soot formation/growth continues resulting in increased soot concentration at higher axial height as seen in Fig. 3. Similarly, PAH formation/growth also continues with increasing integrated temperature-time resulting in higher PAH concentrations in the fuel-rich regions. That the dark regions near the jet axis seen in Fig. 2 correspond to fuel-rich regions of unpyrolyzed fuel is suggested by the absence of such regions at higher axial heights as in Fig. 3. If turbulence had caused air-entrainment resulting in these dark regions being fuel-lean, then persistence of these regions and additional air-entrainment would be expected to be observed at the higher axial height shown in Fig. 3 as well. Thus the non-fluorescing and non-incandescing regions near the jet axis seen in Fig. 2 likely have not yet reached the minimum threshold in temperature-time for PAH and soot production.

At the highest axial height illustrated by Fig. 4, depletion of PAHs through both soot growth and oxidation processes likely account for the absence of PAHs. Turbulent mixing acts to both break up fuel-rich regions and entrain oxidizer into the fuel-rich regions. Since molecular oxidation proceeds at far faster rates than soot oxidation, it is not surprising to find large regions of unoxidized soot yet no PAHs as seen by the high similarity between the LIF-LII and LII images. Because PAHs represent the end of molecular fuel pyrolysis products and oxidize last among molecular fuel pyrolysis products due to their high thermal stability, the absence of fluorescence in the LIF-LII images at these heights indicates their absence (given their presence at lower axial heights). Thus any region not contributing intensity to the LIF-LII images will not contain fuel (or other fuel pyrolysis products) at high axial heights as demonstrated by the high similarity between the LIF-LII and LII images.

Image Statistical Analysis

In a laser-induced image, two quantities are readily defined. The white count (WC) is calculated here as the summed intensity of all pixels composing the image. A count of all pixels containing a nonzero value may be defined as the number (N). From a series of such images, a histogram of each quantity can be compiled. As each histogram represents a distribution of the quantity of interest, both the average and width of the distribution are of interest.

While the N histograms provide a measure of the spatial extent of the quantity, the WC histograms provide a measure of the intensity. In the LII images, the WC histograms are proportional to the soot concentration for a given imaged region. Comparison between the N histograms of the LIF-LII and separate LII images reveals the spatial extent of the PAH containing regions relative to those containing soot. While comparison between histograms computed from temporally equivalent LIF-LII and LII images would be most instructive, equipment and data storage limitations dictated that the histograms be obtained from temporally uncorrelated LIF-LII and LII images obtained separately.

Figures 5a-5c shows the WC histograms computed from a series of 210 individual LII images obtained at each axial height. For ease of presentation, each histogram has been equally scaled along the abscissa. The average value of the distribution provides a relative value of the mean soot concentration over each spatial location while the width provides a measure of the fluctuation. These values are indicated in each figure. As is suggested by the LII images of Figs. 2-4, the soot concentration increases with increasing axial height, consistent with soot formation/growth times increasing with axial height. This is

imaging standard was found to be approximately 70 microns. Bandpass interference filters transmitting 400 - 450 nm preceded each gated intensified array camera. Frame-grabbers digitized the images for transfer to the host computer. Delay generators controlled the relative timing of the camera video signals, the firing of the two lasers and camera detection gates. The delay between the 266 and 1064 nm excitation pulses was 1100 ns thereby yielding essentially simultaneous LIF-LII and separate LII images. The ethylene flow rate through the 2 mm inner diameter vertically oriented stainless tube was 3.0 slm resulting in a lifted flame and cold flow Reynolds number of 2500 based on the burner nozzle inner diameter. The approximate visible flame length was 30 cm.

Simultaneous Paired LIF-LII Images

Image Discussion

The thin soot streaks of low incandescence and fluorescence intensity in Fig. 2, indicative of low soot and PAH concentrations, are consistent with soot formation processes being in the earliest stages at low axial heights within the flame. Since the PAH and soot formation reactions require a finite temperature-time product [15], their appearance indicates that a minimum threshold in temperature-time has been achieved. At this lowest axial height, little time at elevated temperature has elapsed for fuel pyrolysis and soot formation/growth reactions to occur.

With increasing integrated temperature-time, soot formation/growth continues resulting in increased soot concentration at higher axial height as seen in Fig. 3. Similarly, PAH formation/growth also continues with increasing integrated temperature-time resulting in higher PAH concentrations in the fuel-rich regions. That the dark regions near the jet axis seen in Fig. 2 correspond to fuel-rich regions of unpyrolyzed fuel is suggested by the absence of such regions at higher axial heights as in Fig. 3. If turbulence had caused air-entrainment resulting in these dark regions being fuel-lean, then persistence of these regions and additional air-entrainment would be expected to be observed at the higher axial height shown in Fig. 3 as well. Thus the non-fluorescing and non-incandescing regions near the jet axis seen in Fig. 2 likely have not yet reached the minimum threshold in temperature-time for PAH and soot production.

At the highest axial height illustrated by Fig. 4, depletion of PAHs through both soot growth and oxidation processes likely account for the absence of PAHs. Turbulent mixing acts to both break up fuel-rich regions and entrain oxidizer into the fuel-rich regions. Since molecular oxidation proceeds at far faster rates than soot oxidation, it is not surprising to find large regions of unoxidized soot yet no PAHs as seen by the high similarity between the LIF-LII and LII images. Because PAHs represent the end of molecular fuel pyrolysis products and oxidize last among molecular fuel pyrolysis products due to their high thermal stability, the absence of fluorescence in the LIF-LII images at these heights indicates their absence (given their presence at lower axial heights). Thus any region not contributing intensity to the LIF-LII images will not contain fuel (or other fuel pyrolysis products) at high axial heights as demonstrated by the high similarity between the LIF-LII and LII images.

Image Statistical Analysis

In a laser-induced image, two quantities are readily defined. The white count (WC) is calculated here as the summed intensity of all pixels composing the image. A count of all pixels containing a nonzero value may be defined as the number (N). From a series of such images, a histogram of each quantity can be compiled. As each histogram represents a distribution of the quantity of interest, both the average and width of the distribution are of interest.

While the N histograms provide a measure of the spatial extent of the quantity, the WC histograms provide a measure of the intensity. In the LII images, the WC histograms are proportional to the soot concentration for a given imaged region. Comparison between the N histograms of the LIF-LII and separate LII images reveals the spatial extent of the PAH containing regions relative to those containing soot. While comparison between histograms computed from temporally equivalent LIF-LII and LII images would be most instructive, equipment and data storage limitations dictated that the histograms be obtained from temporally uncorrelated LIF-LII and LII images obtained separately.

Figures 5a-5c shows the WC histograms computed from a series of 210 individual LII images obtained at each axial height. For ease of presentation, each histogram has been equally scaled along the abscissa. The average value of the distribution provides a relative value of the mean soot concentration over each spatial location while the width provides a measure of the fluctuation. These values are indicated in each figure. As is suggested by the LII images of Figs. 2-4, the soot concentration increases with increasing axial height, consistent with soot formation/growth times increasing with axial height. This is

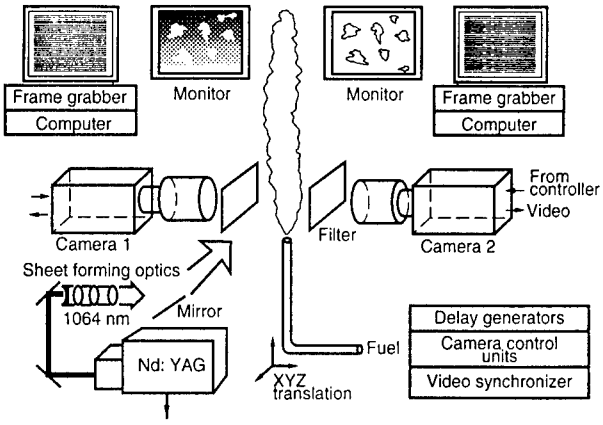


Figure 1.—Experimental diagram.

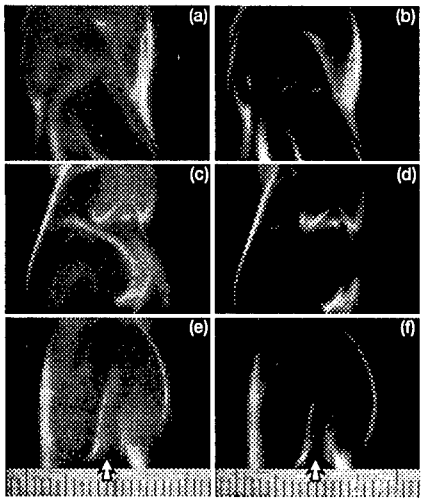


Figure 2.—Simultaneous LIF-LII images (a, c, e) obtained using 266 nm excitation and separate LII images (b, d, f) obtained using 1064 nm excitation. The extent of each image is from 7.6 to 9.5 cm above the burner. The spatial scale is in millimeters. The white arrow locates the jet centerline axis for each column of images.

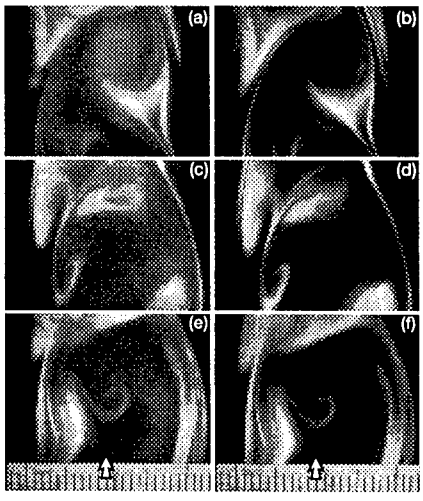


Figure 3.—Simultaneous LIF-LII images (a, c, e) obtained using 266 nm excitation and separate LII images (b, d, f) obtained using 1064 nm excitation. The extent of each image is from 13.1 to 15.0 cm above the burner. The spatial scale is in millimeters. The white arrow locates the jet centerline axis for each column of images.

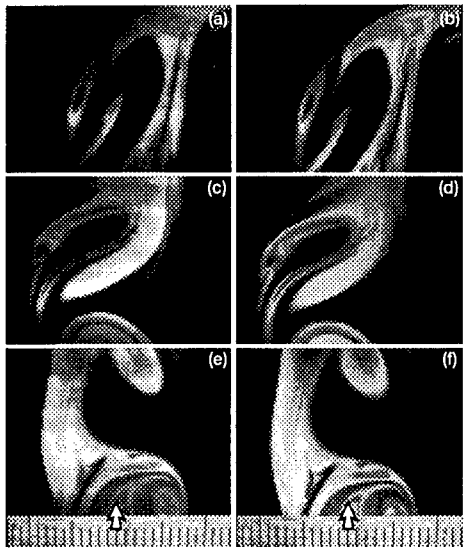


Figure 4.—Simultaneous LIF-LII images (a, c, e) obtained using 266 nm excitation and separate LII images (b, d, f) obtained using 1064 nm excitation. The extent of each image is from 18.6 to 20.5 cm above the burner. The white arrow locates the jet centerline axis for each column of images.

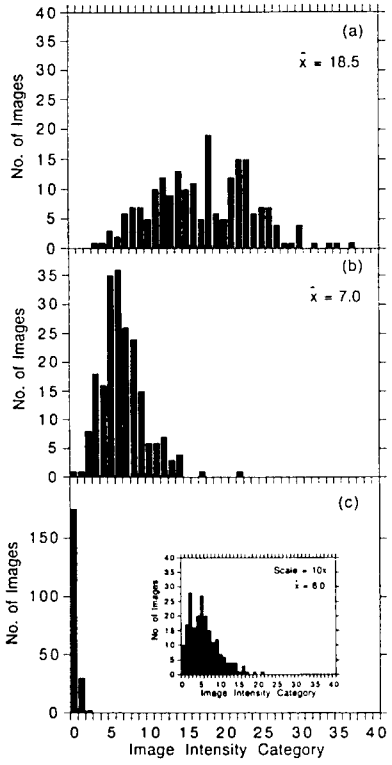


Figure 5.—Histograms of the white count (WC) of pixel intensity from 210 temporally uncorrelated LII images at the axial positions corresponding to Figs. 2-4. The top panel corresponds to image data 18.6-20.5 cm above the burner (illustrated by Fig. 4). The middle panel corresponds to image data 13.1-15.0 cm above the burner (illustrated by Fig. 3). The lower panel corresponds to image data 7.6-9.5 cm above the burner (illustrated by Fig. 2).

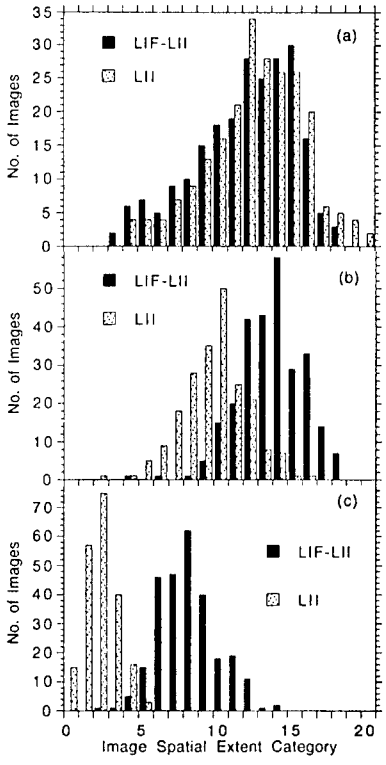


Figure 6.—Histograms of the number (N) of pixels containing nonzero values from 210 temporally uncorrelated LIF-LII and separate LII images at the axial positions corresponding to Figs. 2-4. The top panel corresponds to image data 18.6-20.5 cm above the burner (illustrated by Fig. 4). The middle panel corresponds to image data 13.1-15.0 cm above the burner (illustrated by Fig. 3). The lower panel corresponds to image data 7.6-9.5 cm above the burner (illustrated by Fig. 2).

Flamelet Orientations and the Burning Rate Integral of SI Engine Flames

D. A. Knaus and F. C. Gouldin, Cornell University, Ithaca, NY, contact: fcg2@cornell.edu.
P. C. Hinze and P. C. Miles, Sandia National Laboratory, Livermore, CA.

Introduction

The motivation for measuring flamelet orientations in premixed turbulent flames is due to the relationship between the distribution of flamelet surface orientations and the degree of wrinkling of a flamelet. Flamelet orientations are described by the flamelet surface normal vector, $\underline{N}$, a unit vector oriented in the direction of flamelet propagation. The degree of wrinkling of the flamelet is related to the burning rate through the widely accepted equation [1]:

$$\langle w \rangle = \rho_r S_L I_o \Sigma. \qquad (1)$$

ρ_r is the reactant density. S_L is the unstretched laminar burning velocity. I_o is the mean stretch factor. Σ is the mean flamelet surface to volume ratio. Gouldin [2] has derived an equation relating Σ and $\underline{N}$ statistics:

$$\Sigma = n_{c,\eta} \left\langle \frac{1}{|\sigma_\eta|} \right\rangle_c . \qquad (2)$$

$n_{c,\eta}$ is the flamelet crossing density along a curve η. σ_η is the direction cosine of $\underline{N}$ with respect to η. The bracket indicates an ensemble average. The subscript c indicates that the ensemble average is crossing weighted: the probability associated with a certain $\underline{N}$ is weighted by the probability that a flamelet of orientation $\underline{N}$ crosses η. Another useful quantity is the burning rate integral, B_T, which is analogous to the turbulent burning velocity [3]:

$$B_T = \int_{-\infty}^{\infty} < w > d\eta . \qquad (3)$$

η is a curve defined perpendicular to <c> constant surfaces. Given the distribution of $\underline{N}$ along η and $n_{c,\eta}$, <w> and in turn B_T can be calculated with Eqs. 1, 2 and 3.

Crossed-Plane imaging is a recently developed technique for measuring $\underline{N}$ statistics and $n_{c,\eta}$ [4-6]. Crossed-plane acetone PLIF involves two simultaneous, orthogonal acetone PLIF measurements. Acetone in the reactants is excited and fluoresces, marking the reactant regions as light regions of the images. The acetone is consumed within the flamelet, marking dark regions of the images as product regions. The flamelet is located at the boundary of light and dark regions. The two laser sheets intersect along a line, the measurement line. Tangent vectors to the flamelet curve are measured in each image at points where the flamelet crosses the measurement line. These tangent vectors represent projections of $\underline{N}$ within the plane of the laser sheets. $\underline{N}$ is the normalized cross-product of the tangent vectors. $n_{c,\eta}$ may also be measured from crossed-plane PLIF images by defining discrete segments along a path η, identifying crossings along η, and taking an ensemble average.

In previous work [7,8], $\underline{N}$ orientations were measured in an SI engine within the engine cylinder at three different engine speeds. The current work is an extension of this previous work, including data from a different optical arrangement than previously described which allows measurements to be made within the cylinder head. A single parameter fit based on the PDF of $\underline{N}$ is applied to the data to describe the distribution of $\underline{N}$ orientations. $n_{c,\eta}$ is also measured, and estimates of B_T are made. The B_T data for in-cylinder measurements are further used to estimate the overall engine burning rate, $\dot{m}_b$, and a comparison is made with the prediction of a thermodynamic model for $\dot{m}_b$ based on the cylinder pressure trace.

Experiment

Optical Engine

Measurements are made in a 4-valve, pent-roof optical engine based on a General Motors production engine. The engine is characterized by a bore of 9.2 cm, a stroke of 8.5 cm, and a compression ratio of 9.5:1. The engine is fueled with premixed propane-air, which has been seeded with acetone to permit the acquisition of PLIF images. The propane and acetone are metered such that the overall charge equivalence ratio is 1.0. Acetone makes up approximately 20% of the total fuel load. In-cylinder measurements are made at 30° ATDC at engine speeds of 600, 1200 and 1800 RPM. The spark timing for in-cylinder measurements is 9, 11, and 13° ATDC respectively, chosen so that the flame kernel consistently intersects the measurement line. In-head measurements are made at 600 RPM, 90° ATDC. The spark timing for in-head measurements is 57, 62, and 67° ATDC. The spark timing is severely retarded so that the piston does not block the camera's field of view.

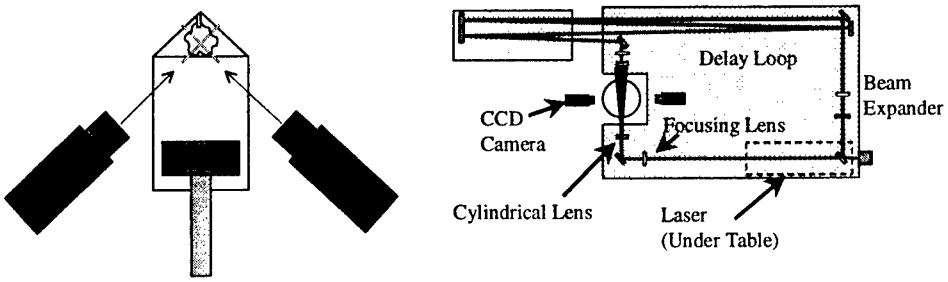


Figure 1. Optical arrangement for in-head measurements.

Optical access is obtained through flat windows in the gables of the head, a full quartz cylinder liner, and through a Bowditch piston arrangement. The optical arrangement for the in-head arrangement is presented in Fig. 1. The optical arrangement for the in-cylinder measurements is described in [7]. The laser sheets are oriented 45° from vertical with the camera optical axes normal to the laser sheets.

PLIF Images

For each measurement condition, 1000 PLIF image pairs are acquired. PLIF images are obtained by exciting the acetone with 266 nm laser radiation generated by quadrupling the output of a pulsed Nd:YAG laser, and broadband collection of the resulting fluorescence using intensified CCD cameras. The maximum sheet thickness within the cylinder is estimated to be less than 0.5 mm. To eliminate interference in the images due to fluorescence induced by the edge-on laser sheet, the arrival times of the laser sheets are separated by approximately 50 ns via an optical delay loop, and the intensifiers on the CCD cameras are gated correspondingly. The image resolution is better than 0.2 mm.

A description of the image processing procedure for in-cylinder measurements can be found in [6,7]. Changes in the image processing procedure for in-head measurements are described here. Due to the proximity of the cylinder head, which results in background reflections, more care is taken to select an appropriate threshold for each image pair. A histogram of pixel intensities along the measurement line is generated and an algorithm selects the threshold level based on the histogram. In some images, reflections create background features bright enough to be interpreted as reactant regions. There is a well-defined linear relationship between a point in space on the measurement line in one image and the same point's location on the measurement line in the other image. Flamelet crossings are identified in the two images, and are only paired if they correspond to the same point along the measurement line in both images within a tolerance. In this way, a background feature that registers a crossing in one image does not match a corresponding crossing in the other image and is discarded. The flamelet curve is fit for each registered crossing, from which tangent vectors are taken, and used to measured $\underline{N}$. Data presented in [7] were subject to a systematic error because the rectangular pixels of the CCD cameras were assumed to be square, that problem has been corrected in the present work. Sample images before and after image processing may be found in [7,8].

$n_{c,\eta}$ is only measured for the in-cylinder images. For the in-cylinder measurements, one laser sheet is oriented vertically and the other horizontally. An approximate η path is defined within the vertical plane, and crossings are identified along η in the vertical images only. An ensemble average of crossing from all images yields $n_{c,\eta}$.

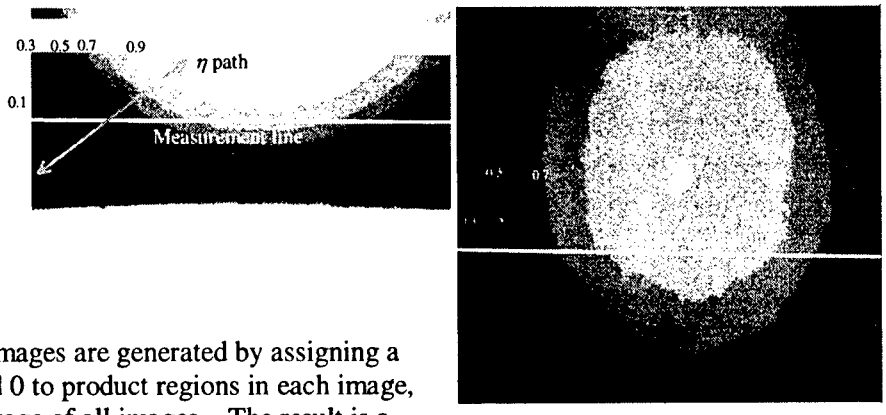


Figure 2. <c> constant contour images for in-cylinder measurements. The left image is generated from a vertically oriented PLIF laser sheet, the right image, horizontally.

<c> Images

For each engine condition, <c> images are generated by assigning a value of 1 to reactant regions and 0 to product regions in each image, and then taking an ensemble average of all images. The result is a <c> "image", where each pixel has a <c> value between 0 and 1. By thresholding at a particular <c> value, the

normal vector to <c> constant surfaces, $\underline{N}_{<c>}$, can be measured the same way $\underline{N}$ is measured. $\underline{N}_{<c>}$ is used to define the polar axis for the spherical coordinate system that $\underline{N}$ orientations are presented in. The <c> images can also be used to give an indication of the width and shape of the turbulent flame brush, Fig. 2. Also shown in Fig. 2 is the location of the measurement line, and an approximate B_T path (η). The measurement line is not along an η path. To estimate B_T, local symmetry is assumed, PDF's of $\underline{N}$(<c>) along η are assumed locally to be equivalent to PDF's of $\underline{N}$(<c>) along the measurement line.

In-Cylinder Results

$\underline{N}$ orientations are presented in spherical coordinates in terms of a polar, ϕ, and an azimuthal angle, θ. The polar axis is aligned with $\underline{N}_{<c>}$. Data are presented in the form of crossing-weighted marginal PDF's in ϕ and θ, Fig. 3. Also shown is a fit based on the joint PDF applied previously to turbulent V-flames. The fit of the crossing-weighted, joint PDF is of the form $P_c(\phi,\theta)\sin\phi d\phi d\theta = A\,|\underline{N}\bullet\underline{n}_y|\exp(-\phi^2/\zeta^2)\sin\phi d\phi d\theta$. A is a normalization constant. ζ is a fit parameter. $\underline{n}_y$ is a unit vector aligned with the measurement line. The fit and data are in good agreement. Values of the fit parameter are presented in Table 1. It is found that ζ varies weakly with <c>, so that an average value is presented.

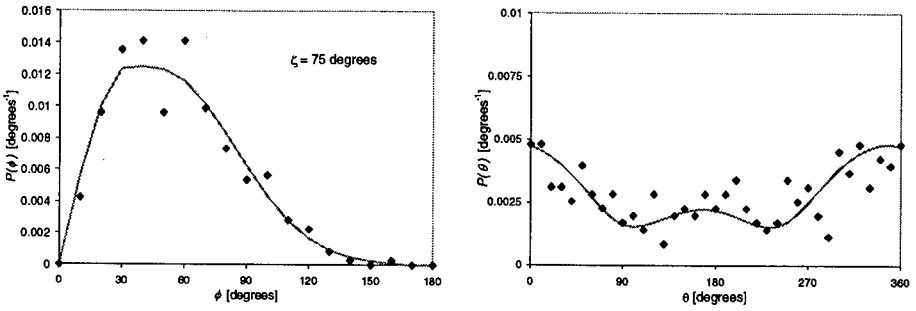
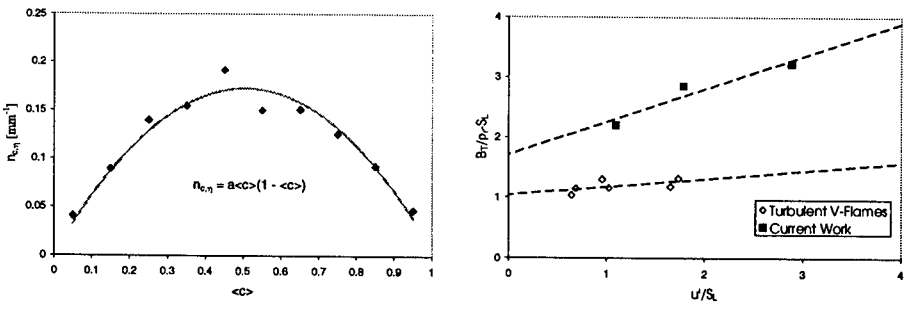


Figure 3. Marginal PDFs in ϕ and θ, 600 RPM,<c> = 0.4-0.6, in-cylinder data. The polar axis is aligned with the normal to the <c> = 0.5 surface. Also shown is a fit based on the joint PDF.

If I_o is taken to be unity, Eq. 3 is written

$$B_T = \rho_r S_L \left\langle \frac{1}{|\sigma_\eta|} \right\rangle_c N_{c,\eta}, \qquad N_{c,\eta} = \int_{-\infty}^{\infty} n_{c,\eta} d\eta. \qquad (4,5)$$

$N_{c,\eta}$ is the average number of flamelet crossings of η. The mean inverse direction cosine term is found by integrating the fit of the joint PDF. $n_{c,\eta}$ is shown as a function of <c> in Fig. 4, and is fit to a function commonly found in the literature [9]. Knowledge of <c> as a function of η allows B_T to be estimated via Eq. 4. Values of the normalized burning rate integral are presented in Table 1, and are plotted in Fig. 5 as a function of turbulence intensity. Turbulence intensity was not measured but estimated based on the mean piston speed. Also shown are data for turbulent V-flames.



Figures 4 and 5. Flamelet crossing density as a function of <c> and normalized B_T data for in-cylinder measurements.

The overall burning rate, $\dot{m}_b$, is related to B_T by integrating B_T over all possible η paths. If B_T is assumed to be independent of η paths, then $\dot{m}_b = B_T A_f$, where A_f is the flame area. Models describing the combustion process in engines almost universally assume a spherical flame geometry centered at the spark plug to specify A_f. We define a flame radius as the vertical distance from the spark to the <c> = 0.5 contour. Values of A_f assuming a hemispherical flame are given in Table 1, along with the resulting values of $\dot{m}_b$. $\dot{m}_b$ is also estimated with a thermodynamic model based on the cylinder pressure trace [10]. Model estimates are systematically higher than estimates based on B_T. This could be attributed to the spherical flame approximation under-estimating A_f [11].

Engine Speed (RPM)	ζ (°)	$\langle 1/\lvert\sigma_\eta\rvert\rangle_c$ (-)	N_c (-)	ρ_r kg/m^3	S_L cm/s	$B_T/\rho_r - S_L$ (-)	A_f (mm^3)	$\dot{m}_b$ (g/s)	$\dot{m}_{b-model}$ (g/s)
600	76	1.77	1.24	2.22	168.4	2.20	3620	30	88
1200	78	1.79	1.59	1.85	206.5	2.85	3320	36	93
1800	96	1.92	1.68	1.97	191.3	3.22	3320	40	94

Table 1. Summary of in-cylinder results.

In-Head Results

Marginal PDFs in ϕ and θ with the same fit applied above are presented in Fig. 7. The polar axis is again aligned with $\underline{N}_{<c>}$. The fit and data are in good agreement for $P_c(\phi)$, however the fit and data are in poorer agreement for $P_c(\theta)$, which is generally true. This may be a result of systematic error introduced by background interference. Another possible explanation is that the close proximity of the cylinder head disrupts the symmetry in θ assumed by the fit. For burn durations of 23, 28 and 33 CAD, measured fit parameters were 35, 46 and 45° respectively. $N_{c,\eta} \approx 1$ for in-head measurements. Normalized burning rate integrals are 1.2, 1.35 and 1.33 respectively.

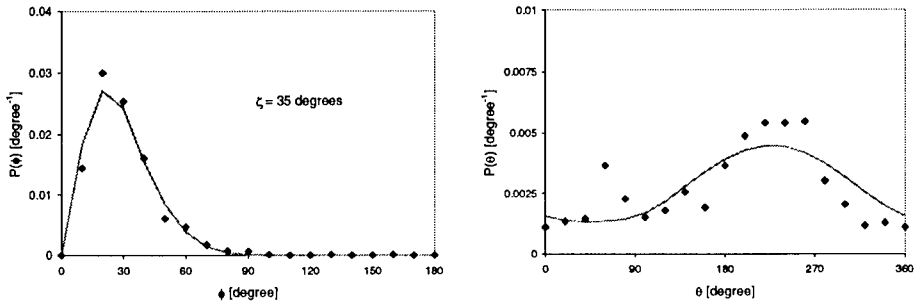


Fig 5. Marginal PDFs in ϕ and θ, 600 RPM,<c> = 0.0-1.0, in-head data. The polar axis is aligned with the normal to the <c> = 0.5 surface. Also shown is a fit based on the joint PDF.

Conclusions

Flamelet orientations are successfully measured in an SI engine. Measurements made in the head were subject to background reflections, complicating image processing. $\underline{N}$ distributions for in-cylinder data agreed well with the same fit applied previously to turbulent V-flames. The same fit was in fair agreement for in-head data, which suggests that the presence of the cylinder head may disrupt the symmetry found in other data. A fit with more than one parameter may be necessary to more accurately characterize $\underline{N}$ distributions for these types of flames. Overall engine burning rates estimated from B_T data are significantly smaller than values predicted by a thermodynamic model, which may be the result of the spherical flame approximation under-predicting A_f.

References

1. Bray, K. N. C., Libby, P. A., Moss, J. B.: *Comb. Sci. Tech.* **41**, 143 (1984).
2. Gouldin, F. C. in *Physical and Chemical Aspects of Combustion: A Tribute to Irvin Glassman*, p. 433, Gordon and Breach, 1997.
3. Gouldin, F. C. (1996). *Twenty-sixth Symposium (International) on Combustion*, The Combustion Institute, pp. 381-388.
4. Bingham, D. C. (1998). Crossed-Plane Laser Tomography: Direct Measurement of Flamelet Orientation and Mean Flamelet Surface Density. M.S. thesis, Cornell University.
5. Bingham, D. C., Gouldin, F. C., Knaus, D. A. (1998). *Twenty-seventh Symposium (International) on Combustion*, The Combustion Institute, pp. 77-84.
6. Knaus, D. A., Gouldin, F. C., Bingham D. C., submitted to Combustion Science and Technology.
7. Knaus, D. A., Gouldin, F. C., Hinze, P. C., Miles, P. C. (1999). *First Joint Meeting of the U. S. Sections of the Combustion Institute*, pp. 204-207.
8. Knaus, D. A., Gouldin, F. C., Hinze, P. C., Miles, P. C., "Measurement of Flamelet Orientation Statistics in an Optical SI Engine and the Burning Rate Integral", to appear in *1999 SAE International Fall Fuels & Lubricants Meeting and Exposition.*
9. Gouldin, F. C., Miles, P. C.: *Combustion and Flame* **100**: 202-210 (1995).
10. Cheung, H. M., Heywood, J. B.: *SAE Paper 932749* (1993).
11. Barr, P. K., Witze, P. O.: *SAE Paper 880129* (1988).

Large-Eddy Simulation of a Turbulent Piloted Methane/Air Diffusion Flame (Sandia Flame D)

Heinz Pitsch[1], Helfried Steiner[2]

[1]Center for Integrated Turbulence Simulations
e-mail: H.Pitsch@stanford.edu
[2]Center for Turbulence Research
e-mail: steiner@ctr-sgi1.stanford.edu

Department of Mechanical Engineering
Stanford University
Stanford, CA 94305-3030

While numerical simulations of turbulent flows applying Reynolds averaging techniques solve equations for ensemble averages, Large-Eddy Simulations (LES) offer the opportunity to resolve the large scales of the turbulent motion. In the present study LES simulations for a turbulent, piloted methane/air diffusion flame are presented and the results are compared to experimental data by Barlow and Frank [1, 2].

The set of equations, which have to be solved in the frame of the current modeling study, can be derived by applying a spatial, density-weighted filter to the continuity equation, the momentum equations, and the mixture fraction transport equation. The unclosed terms in the resulting equations are expressed by using an eddy viscosity type model, such that the subgrid-scale fluxes in the momentum equations and the mixture fraction transport equation are given by

$$\overline{\rho}\left(\widetilde{v_k v_l} - \widetilde{v}_k \widetilde{v}_l\right) = -2\overline{\rho}\widetilde{\nu}_t \widetilde{S}_{kl}\,, \quad \widetilde{S}_{kl} = \frac{1}{2}\left(\frac{\partial \widetilde{v}_k}{\partial x_l} + \frac{\partial \widetilde{v}_l}{\partial x_k}\right) \tag{1}$$

and

$$\overline{\rho}\left(\widetilde{v_l Z} - \widetilde{v}_l \widetilde{Z}\right) = -\overline{\rho}\widetilde{D}_t \frac{\partial \widetilde{Z}}{\partial x_l} \tag{2}$$

where ρ is the density, x_k and v_k are the coordinate and the velocity vector, respectively, Z is the mixture fraction, ν_t is the eddy viscosity, and D_t the eddy diffusivity. Here, the overline denotes a spatially filtered and the tilde a spatially Favre filtered quantity.

The Smagorinsky model is used to obtain the eddy viscosity ν_t, where the Smagorinsky constant is determined by the Dynamic Model as a function of time and space [3]. This procedure needs no model constants and assures that the turbulent fluxes vanish in the limit of a laminar flow. The subgrid-scale diffusivity D_t is computed assuming a constant turbulent Schmidt number $\mathrm{Sc}_t = 0.7$ as $D_t = \nu_t/\mathrm{Sc}_t$.

In the present study a conserved scalar approach is used to describe turbulence-chemistry interactions. The resolved mass fractions of chemical species $\widetilde{Y}_i$ are given by

$$\widetilde{Y}_i(\boldsymbol{x}, t) = \int_{Z=0}^{1} Y_i(Z, x)\widetilde{P}(Z, \boldsymbol{x}, t) dZ\,, \tag{3}$$

where t is the time, x denotes the coordinate in axial direction, and $\widetilde{P}(Z, \boldsymbol{x}, t)$ is the Favre pdf of the mixture fraction. Here, $Y_i(Z, x)$ is obtained using the unsteady flamelet model [4, 5] that provides $Y_i(Z, t_f)$, where the flamelet life time τ can be expressed as function of the axial nozzle distance x [4]. This approach offers the opportunity to use arbitrarily complex chemistry. $\widetilde{P}(Z, \boldsymbol{x}, t)$ is presumed to follow a β-function, whose shape is determined by the mean and the subgrid-scale variance of the mixture fraction. Since no transport equation for the mixture fraction variance is solved, this value has to be modeled. Following Pierce and Moin [6] the mixture fraction variance can be expressed as

$$\overline{\rho}\widetilde{Z''^2} = C_Z \Delta^2 \overline{\rho} |\nabla \widetilde{Z}|^2\,, \tag{4}$$

where the model coefficient C_Z is determined using the Dynamic Procedure.

The unsteady flamelet equations are here exemplarily given by the equation for the species mass fractions Y_i

$$\rho \frac{\partial Y_i}{\partial \tau} - \rho \frac{\chi}{2} \frac{\partial^2 Y_i}{\partial Z^2} - \dot{m}_i = 0\,, \tag{5}$$

where χ is the scalar dissipation rate and $\dot{m}_i$ the chemical production rate of species i per unit volume.

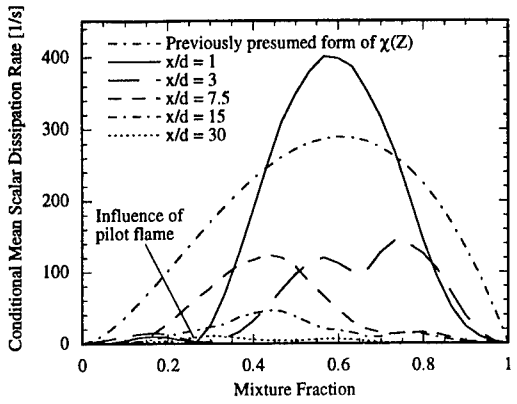


Figure 1: Conditional mean scalar dissipation rate

In Eq. (5), the temporal development of the scalar dissipation rate is unknown and has to be specified from the solution of the turbulent flow field. If the mixture fraction dependence of the scalar dissipation rate is presumed as $< \chi|Z >=< \chi_{st} > f(Z)$, it is sufficient to determine the value at stoichiometric mixture, which can be achieved by [4]

$$\widetilde{\chi} = \int_{Z=0}^{1} < \chi|Z > \widetilde{P}(Z)dZ\,. \tag{6}$$

However, since in the present study a piloted flame is considered, the mixture fraction dependence cannot be prescribed.

This is illustrated in Fig. 1 showing the scalar dissipation rate at different downstream locations, indicating that the scalar dissipation rate is not a simple function of the mixture fraction.Within the pilot stream, which is at $Z = 0.27$, the scalar gradient, and hence the scalar dissipation rate, is zero. Even at far downstream locations the shape of the scalar dissipation rate is still influenced by the pilot flame.

In the present model, the conditional average of the scalar dissipation rate as a function of the axial distance from the nozzle $< \chi|Z > (x)$ is computed by the inversion of the integral in Eq. (6) similar to the approach used by Bushe and Steiner [8]. Applying Eq. (6) to all computational cells of a complete radial cell layer gives

$$\widetilde{\chi}_i = \int_{Z=0}^{1} \langle\chi|Z\rangle\,(x)\,\widetilde{P}_i(Z,\boldsymbol{x},t)dZ\,, \quad i = 1,\ldots,N_c(x)\,, \tag{7}$$

where $N_c(x)$ is the number of cells with equal nozzle distance x. If the continuous function $< \chi|Z > (x)$ in Eq. (7) is approximated on a discrete mixture fraction grid Z_j, $j = 1,\ldots,N_Z$, where N_Z denotes the number of gridpoints of the mixture fraction grid, the integral in Eq. (7) can be approximated by a sum using for example the trapezoidal integration rule as

$$\widetilde{\chi}_i \approx \sum_{j=1}^{N_Z} A_{ij}\,\langle\chi|Z\rangle_j\,, \quad j = 1,\ldots,N_Z\,, \tag{8}$$

where the coefficient matrix A_{ij} contains the pdf and the coefficients of the numerical integration scheme.

Equation (8) represents a system of $N_c(x)$ equations for N_Z unknowns. For $N_c(x) < N_Z$ this can be solved by minimizing the resulting error of the overdetermined system by applying a least squares approach.

The spatially filtered scalar dissipation rate, appearing in Eq. (6), is expressed in terms of the eddy diffusivity and the gradient of the resolved mixture fraction following Girimaji and Zhou [7] as

$$\widetilde{\chi} = 2(D_Z + D_t)\nabla\widetilde{Z}\nabla\widetilde{Z}\,, \tag{9}$$

where D_Z is the molecular diffusivity of the mixture fraction.

In the following the application of the model to a piloted, turbulent methane/air jet diffusion flame is presented. The investigated configuration corresponds to Sandia Flame D, which has experimentally investigated by Frank and Barlow [1, 2]. The fuel consists of 25 % methane and 75 % air by volume, the pilot used to stabilize the flame is slightly lean. The fuel stream Reynolds number is 22400. For the solution of the flamelet equations the GRI 2.11 mechanism [9] has been applied. The calculations have been performed using a spherical coordinate system. The numerical mesh consists with 192 cells in downstream, 84 cells in cross-stream, and 48 cells in tangential direction of approximately 775000 computational cells.

In order to solve the unsteady flamelet equations, the scalar dissipation rate $\chi(x)$, appearing in Eq. (5) has to be expressed in terms of the conditional mean scalar dissipation rate $\langle\chi|Z\rangle$ given by Eq. (8). The closure assumption here is that $\chi(x)$ is given by the conditional mean scalar dissipation rate, which in turn implies that also the results obtained by solving the flamelet equations are conditional mean values. However, in order to study the effect of turbulent fluctuations two different approaches are applied in the following:

1. The scalar dissipation rate is given by the ensemble average of the conditional mean scalar dissipation rate

$$\chi(Z,x) = \overline{\overline{\langle\chi|Z\rangle}}(x) \tag{10}$$

2. The scalar dissipation rate is given by instantaneous realizations of the conditional mean scalar dissipation rate

$$\chi(Z,x) = \langle\chi|Z\rangle(x) \tag{11}$$

For both approaches the resolved mixture fraction $\widetilde{Z}$ and the modeled mixture fraction subgrid-scale variance, which are used to determine the shape of the pdf of the mixture fraction appearing in Eq. (3), are given in accordance with the scalar dissipation rate by either the ensemble averages or instantaneous values.

In the following the results using ensemble averaged data, indicated by the solid lines, is compared to two different realizations using instantaneous data, indicated by the long-dashed and the short-dashed lines, and ensemble averaged experimental data, given by the symbols.

Figure 2 shows that the mean mixture fraction is in good agreement with the experimental data. The RMS of the fluctuations around the mean mixture fraction presented in Fig. 2 are shown in Fig. 3 as a dotted line and compared to the Reynolds averaged experimental data. In addition, Fig. 3 shows the subgrid-scale RMS of the instantaneous realizations and its ensemble average. These values are much smaller than the Reynolds averaged data, indicating that the major part of the turbulent mixture fraction fluctuations is resolved by the Large-Eddy Simulation.

The calculated mean temperature and the mean mass fractions of CO, CO_2, OH, and NO are compared to experimental data in Fig. 2 and Figs. 4-6. In general, the experiments are predicted quite well. However, OH and NO mass fractions seem to be overpredicted in the stoichiometric part of the flame.

The comparison of the results using ensemble averaged and instantaneous data seems to indicate that the ensemble average of the instantaneous solutions, which would correspond to the experiments, can be estimated by the results using ensemble averaged data as far as temperature and major species are concerned. Because of the large turbulent fluctuations in the OH and NO mass fractions both methods might reveal differences. However, this has to be further analyzed with a larger number of single realizations.

Finally, the question should be addressed, whether the turbulent fluctuations, which can be observed in the calculations using the instantaneous data, are caused by the fluctuations of the mixture fraction or by fluctuations in the scalar dissipation rate, which would influence the flamelet solution. Figure 7 shows the mean temperature and the mean NO mass fraction as function of the mean mixture fraction along the centerline. In this representation the temperature obviously reveals no fluctuations, which indicates that the turbulent fluctuations, which can be obtained in Fig. 2 are obviously caused by the fluctuations of the mixture fraction. Fluctuations of the scalar dissipation rate have only a weak influence on the heat release. However, fluctuations can still be observed for the NO mass fraction close to stoichiometric mixture. But these could still be caused by the mixture fraction variance, which could be analyzed by conditioning the data in Fig. 7 on the mixture fraction variance. This would also require more computational data.

Figure 7 also reveals a slight temperature increase around a mixture fraction of $Z = 0.6$, which is not observed from the experimental data. This partially premixed flame, caused by the high oxygen content in the fuel could be the reason for an overprediction of the temperature at stoichiometric conditions, and by that for the overprediction of the NO mass fraction.

References

[1] Barlow, R. S., Frank, J. H., "Experimental Results on Differential Diffusion in Piloted Methane-Air Jet Flames", 3rd International Workshop on Measurement and Computation of Turbulent Nonpremixed Flames, 1998.

[2] www.ca.sandia.gov/tdf/Workshop.html.

[3] Moin, P., Squires, K., Cabot, W., Lee, S., Phys. Fluids A 3, pp. 2746-2757, 1991.

[4] Pitsch, H., Chen, M., Peters, N., Twenty-Seventh Symposium (International) on Combustion, accepted for presentation, 1998.

[5] Pitsch, H., "Unsteady Flamelet Modeling of Differential Diffusion in Turbulent Jet Diffusion Flames", Comb. Flame, submitted, 1999.

[6] Pierce, C. D., Moin, P., Phys. Fluids A 10, pp. 3041-3044, 1998.

[7] Girimaji, S. S., Zhou, Y., Phys. Fluids A 8, pp. 1224-1236, 1996.

[8] Bushe, W. K., Steiner, H., "Conditional moment closure for large eddy simulation of non-premixed turbulent reacting flows", Phys. Fluids A, accepted for publication, 1999.

[9] Bowman, C. T., Hanson, R. K., Davidson, D. F., Gardiner, Jr., W. C., Lissianski, V., Smith, G. P., Golden, D. M., Frenklach, M., Goldenberg, M., http://www.me.berkeley.edu/gri_mech/

Figures

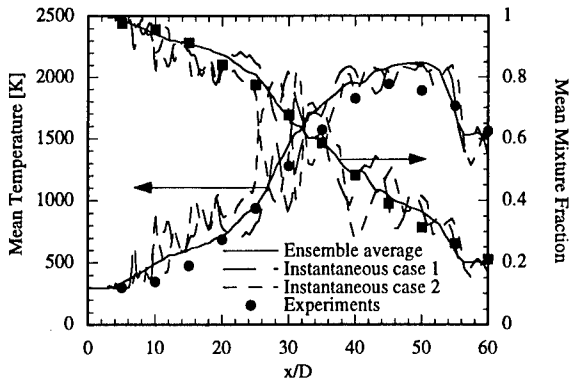


Figure 2: Mean mixture fraction and temperature

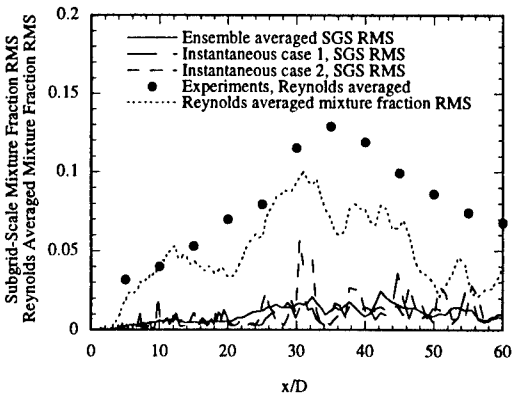


Figure 3: Mixture fraction RMS

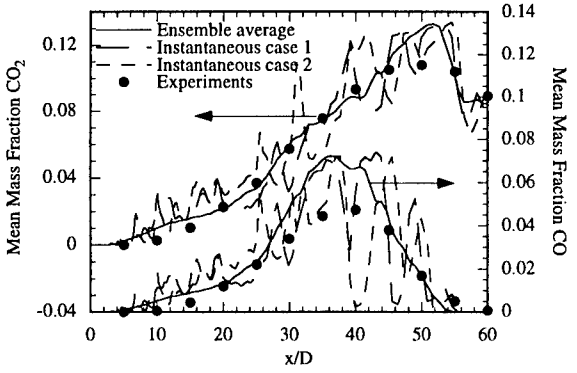


Figure 4: Mean CO and CO_2 mass fractions

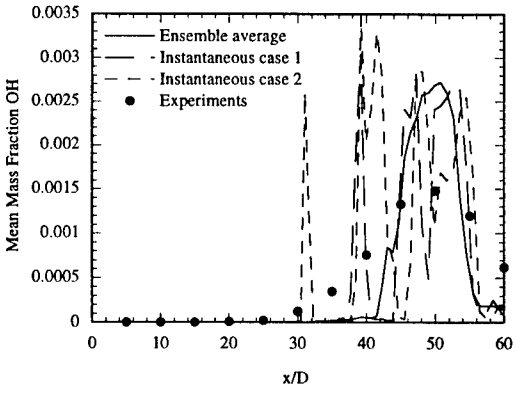


Figure 5: Mean OH mass fraction

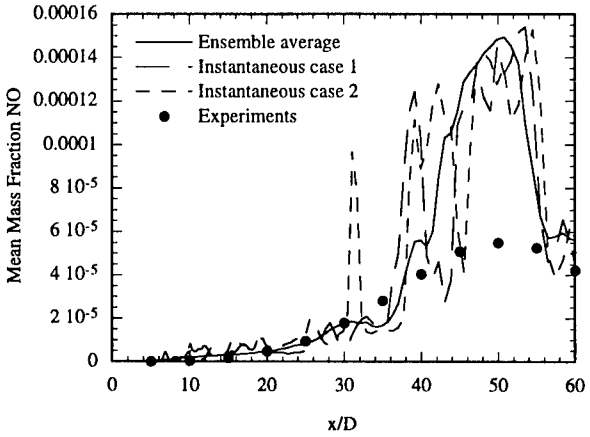


Figure 6: Mean NO mass fraction

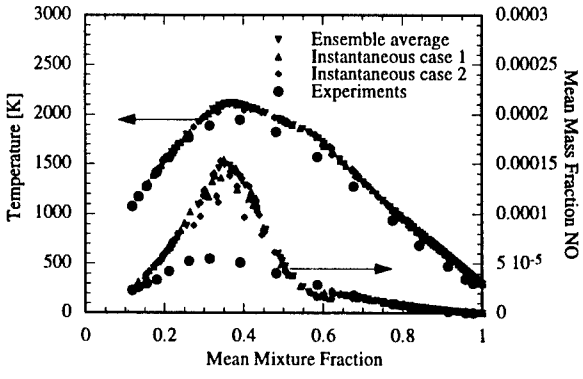


Figure 7: Temperature and NO along centerline

Acknowledgement

This work was supported in part by the US Department of Energy in the frame of the ASCI program.

A MODIFIED COHERENT FLAME MODEL TO DESCRIBE TURBULENT FLAME PROPAGATION IN MIXTURES WITH VARIABLE COMPOSITION

J. Hélie* and A. Trouvé†

* Centre de Recherche en Combustion Turbulente
Institut Français du Pétrole
1 et 4, avenue de Bois Préau,
92852 Rueil-Malmaison Cedex, France

† Department of Mechanical Engineering
The George Washington University
801 22nd Street, NW
Washington DC 20052, USA

1 Introduction

Direct-injection spark-ignition (DI-SI) engines represent one of the most promising technology to achieve further reductions in fuel consumption in automotive transport. Under partial load conditions, these engines use fuel stratification to provide additional control on combustion performance and establish overall fuel lean operating conditions. In stratified DI-SI engines, the fuel-oxidizer mixture features both large- and small-scale spatial variations in unburnt mixture composition. These variations correspond to inhomogeneities in mixture strength into which the spark-ignited turbulent flame propagates.

In turbulent combustion models for SI engines, while the effects of large-scale (grid-resolved) fuel stratification on turbulent flame propagation are sometimes included [1,2], the effects of small-scale (sub-grid scale) variations in mixture composition are usually neglected. The general objective of the present work is to bring basic information on the effects of partial premixing, both at large- and small-scales, and propose relevant modifications of current turbulent combustion models to account for these effects. Similar recent modeling efforts can be found in [3] and [4].

2 Direct numerical simulations

Direct numerical simulations (DNS) are used in the present study to bring basic information onto the effects of partial premixing on the turbulent flame topology and the overall mean reaction rate.

The DNS data base corresponds to three-dimensional partially premixed flames propagating into isotropic turbulent flow [5,6]. The simulations use a single-step overall chemistry model proposed by Westbrook & Dryer to describe propane-air combustion [7]. They also feature different levels of unmixedness and correspond to flame-flow conditions where the flow to flame velocity scale ratio is large, $(u'/s_L) > 1$, and the variations in mixture strength remain small, $(Z'/\widetilde{Z}) \ll 1$. The latter restriction is used as an intermediate step in the present work plan. In this intermediate step, the study is limited to a sub-class of simple flame-flow configurations corresponding to inflammable mixtures, *i.e.* to mixture compositions within the propane-air flammability limits and without the additional complication of premixed flame extinction.

The DNS results show that : (1) under lean-rich conditions, the reaction zone can be described as a staged combustion system with a first stage corresponding to a propagating premixed flame front, that produces partially burnt products, followed by a second stage corresponding to multiple post-diffusion flames, that leads to fully burnt products ; (2) the first premixed stage can be conveniently described using classical laminar flamelet concepts. These results are consistent with recent findings by Haworth *et al.* [8] based on DNS of a similar configuration and including a more detailed propane-air chemistry model. With mixture compositions within the flammability limits, most of the burning occurs in the premixed first stage. Focusing on the primary premixed flame, it is found that : (3) for variations in mixture strength around mean stoichiometric conditions $(\widetilde{Z} \approx Z_{st})$, partial premixing tends to have a net negative impact on the overall mean reaction rate (or equivalently on the turbulent flame speed) ; (4) this effect is related to changes in the mean flamelet structure, *i.e.* to a decrease of the mean flamelet mass burning rate per unit flame surface area with increasing levels of unmixedness ; (5) under the present moderate to large turbulent intensity conditions $(u'/s_L > 1)$, the effect of partial premixing on turbulent flame stretch and flame surface production remains negligible.

3 Modeling

Based on the DNS results, modifications of the Coherent Flame Model (CFM) [9-11] are proposed to account for the effects of variable mixture composition on the primary premixed flame, as well as for the formation of a secondary non-premixed reaction zone downstream of the premixed flame. In the modified CFM model, the two separate combustion stages are described using a conditional two-fluid approach. The conditional formulation allows to distinguish between the fresh fuel in the unburnt gas, that is consumed by the primary premixed flame, and the fuel fragments in the partially burnt gas, that are consumed by the secondary post-flames. The mean reaction rate associated with the primary premixed flame is described using simple extensions of the flamelet-based CFM closure models, whereas the mean reaction rate associated with the secondary post-flames is described using a mixing controlled model proposed by Magnussen & Hjertager [12].

Furthermore, sub-grid scale fluctuations in mixture composition are described using a standard presumed β-Pdf for mixture fraction. In the CFM balance equation for flame surface density, a modified model for the turbulent flame stretch is also proposed to account for this β-shaped Z-distribution. The model guarantees that the total premixed flame surface area remains independent of the level of unmixedness, and that, consistent with the DNS results, the turbulent flame

speed decreases with increasing levels of unmixedness when the mixture compositions are close to stoichiometry (see the lower curves, $\widetilde{Z} = Z_{st}$ and $\widetilde{Z} = 1.25\ Z_{st}$, in Figure 1). In contrast, as seen in Figure 1, the turbulent flame speed is predicted to increase with increasing levels of unmixedness when the mixture compositions are close to the flammability limits (see the upper curves, $\widetilde{Z} = 0.75\ Z_{st}$ and $\widetilde{Z} = 1.75\ Z_{st}$, in Figure 1).

REFERENCES

[1] Baritaud, T. A., Duclos, J. M. and Fusco, A., *Twenty-Sixth Symposium (International) on Combustion,* The Combustion Institute, Pittsburgh, PA, 1996, pp. 2627-2635.

[2] Duclos, J. M. and Zolver, M., *Fourth International Symposium,* COMODIA, 1998, pp. 335-340.

[3] Müller, C., Breitbach, H. and Peters, N., *Twenty-Fifth Symposium (International) on Combustion,* The Combustion Institute, Pittsburgh, PA, 1994, pp. 1099-1106.

[4] Lahjaily, H., Champion, M., Karmed, D. and Bruel, P., *Combust. Sci. and Tech.* 135:153-173 (1998)

[5] Poinsot, T., Veynante, D., Trouvé, A. and Ruetsch, G. R., "Turbulent flame propagation in partially premixed flames", Proceedings of the Summer Program, Center for Turbulence Research, NASA Ames/Stanford University, 1996.

[6] Hélie, J. and Trouvé, A., *Twenty-Seventh Symposium (International) on Combustion,* The Combustion Institute, Pittsburgh, PA, 1998, pp 891-898.

[7] Westbrook, C., and Dryer, F., *Combust. Sci. and Tech.* 27:31-43 (1981)

[8] Haworth, D., Cuenot, B., Poinsot, T. and Blint, R. "Numerical simulation of turbulent propane-air combustion with non-homogeneous reactants : initial results", Proceedings of the Summer Program, Center for Turbulence Research, NASA Ames/Stanford University, 1998.

[9] Marble, F. E. and Broadwell, J. E., "The coherent flame model for turbulent chemical reactions", Project Squid Technical Report No. TRW-9-PU, 1977

[10] Darabiha, N., Giovangigli, V., Trouvé, A., Candel, S. M. and Esposito, E., *France-USA Joint Workshop on Turbulent Combustion,* Springer Verlag, 1987

[11] Duclos, J. M., Veynante, D. and Poinsot, T., *Combust. Flame* 95:101-117 (1993)

[12] Magnussen, B. F. and Hjertager, B. H., *Sixteenth Symposium (International) on Combustion,* The Combustion Institute, Pittsburgh, PA, 1976.

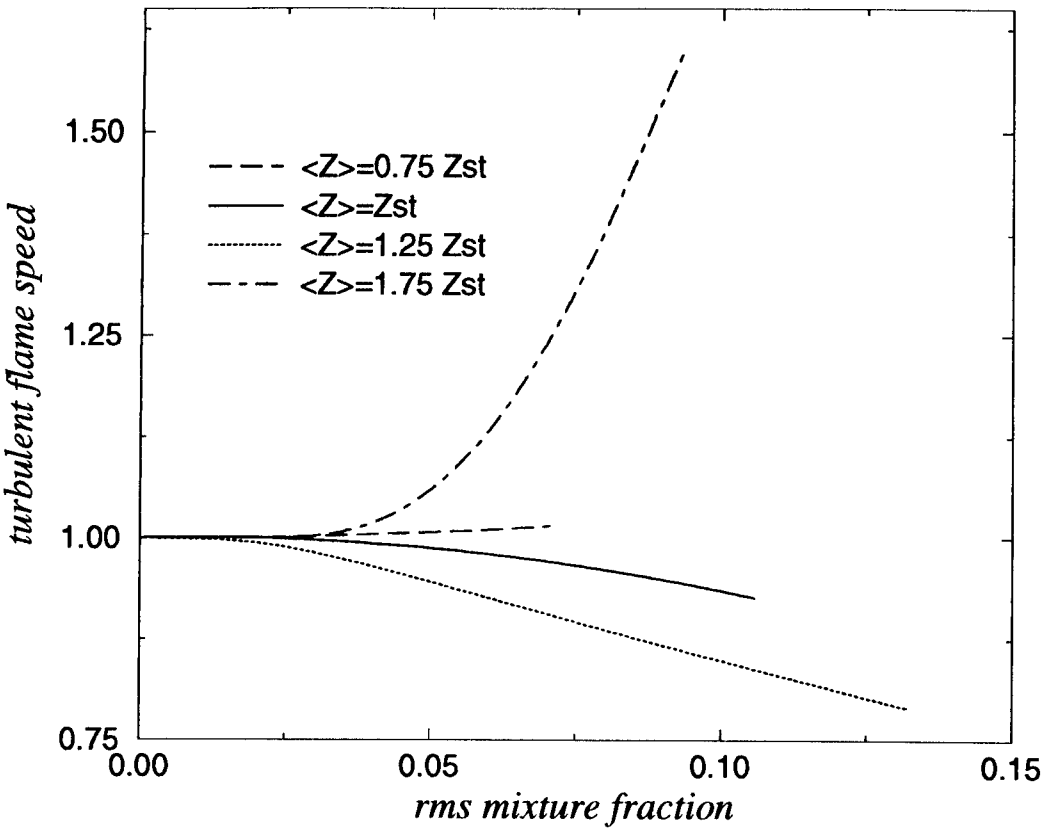


Figure 1: Predicted variations of the turbulent flame speed, s_T, with the degree of unmixedness, $(Z'/\tilde{Z})$. s_T is made non-dimensional with its value obtained under perfectly premixed conditions $(Z' = 0)$.

Direct Numerical Simulation of Forced Compressible Turbulence at Supercritical Pressure: Nitrogen-Hydrocarbon Mixtures

Richard S. Miller
Department of Mechanical Engineering
Clemson University
Clemson, SC, *29634-0921*
richard.miller@ces.clemson.edu

Introduction

A variety of modern air-fuel mixing and combustion devices operate under supercritical conditions, including; gas turbines, diesel engines, and rocket engines. For example, hydrocarbon critical pressures are typically $\sim 15 \rightarrow 30atm$, whereas diesel chambers reach pressures $\sim 50 \rightarrow 60atm$ after fuel ignition and gas turbine combustor chambers operate at nearly steady pressures $\sim 30 \rightarrow 40atm$. Above the critical point "real" gas effects are prevalent and the distinction between gaseous and liquid phases vanishes; therefore, the phase of a supercritical substance is commonly referred to simply as "fluid."[1] Furthermore, non-equilibrium thermodynamic effects from which species concentrations diffuse due to temperature gradients (Soret effect) and thermal energy diffuses due to concentration gradients (Dufour effect) are also known to be significant in supercritical fluids;[2] particularly when large ratios of the molecular weights of the pure compounds are present.[3]

The extent of literature addressing high pressure turbulent flows is very limited. Experimental results show that the behavior of supercritical jets is substantially altered from that of traditional low pressure liquid jets. As the critical point is exceeded the breakup of the jet core into ligaments and droplets ceases abruptly, and further increases in pressure yield behaviors characteristic of low pressure gas-gas jets due to the absence of surface tension and latent heat.[4] Oefelein and Yang[5] performed two-dimensional LES of supercritical mixing layers with a Smagorinsky subgrid model, but did not consider Soret and Dufour diffusion. More recently, Miller *et.al.*[2] included these effects in their direct numerical simulations (DNS) of a temporally developing mixing layer composed of nitrogen and heptane streams.

The objective of the present study is to investigate high pressure mixing phenomena by conducting DNS of "forced" compressible isotropic turbulence of real fluid mixtures. Ultimately, air-hydrocarbon combustion will be studied; however, this paper addresses the relatively simpler systems composed of initially premixed and non-premixed binary mixtures without combustion (*i.e.* mixing only). As will be shown below, Soret effects generate concentration fluctuations due to both temperature and pressure gradients. In forced turbulence, the scalar fields achieve a statistically stationary state resulting from a balance between concentration variance production and dissipation even for perfectly premixed systems. Non-premixed flows initialized with spherical hydrocarbon "droplets" are also considered.

Formulation

The compressible form of the governing equations are derived for a binary mixture of general Newtonian fluids:[2]

$$\frac{\partial}{\partial t}(\rho) + \frac{\partial}{\partial x_j}[\rho u_j] = 0, \tag{1}$$

$$\frac{\partial}{\partial t}(\rho u_i) + \frac{\partial}{\partial x_j}[\rho u_i u_j + p\delta_{ij} - \tau_{ij}] = \rho f_i, \tag{2}$$

$$\frac{\partial}{\partial t}(\rho e_t) + \frac{\partial}{\partial x_j}[(\rho e_t + p)\, u_j - u_i \tau_{ij} + Q_j] = \rho u_i f_i, \tag{3}$$

$$\frac{\partial}{\partial t}(\rho Y_B) + \frac{\partial}{\partial x_j}[\rho Y_B\, u_j + J_j] = 0, \tag{4}$$

where ρ is the density, u_i is the velocity, $e_t = e_i + u_i u_i/2$ is the total energy [internal energy (e_i) plus kinetic], p is the thermodynamic pressure (the temperature is T) and Y_B is the species B mass fraction (the species A mass fraction is $Y_A = 1 - Y_B$). Furthermore, Q_j is the heat flux vector, J_j is the species B mass diffusion flux vector, τ_{ij} is the Newtonian viscous stress tensor (μ is the mixture viscosity), and δ_{ij} is the Kronecker delta function. Large scale stirring is provided by the statistically stationary and solenoidal force f_i based on non-dimensional input forcing amplitude F^*.[6] Finally, the thermodynamic state of the system is described by the cubic Peng Robinson

state equation.[1]

The form of the diffusion fluxes adopted here is presented in a somewhat non-traditional form: $Q_j = Q_j^T + Q_j^Y + Q_j^p$, and $J_j = J_j^T + J_j^Y + J_j^p$, where the superscripts indicate the thermodynamic gradient involved. With this notation, fluctuation theory and non-equilibrium thermodynamics shows that the heat and mass flux vectors for a binary mixture are defined by:[2]

$$Q_j^T = -\left\{\kappa + \rho\mathcal{D}X_A X_B\, \alpha_T \alpha_T''\, \mathfrak{R}/M_m\right\} \frac{\partial T}{\partial x_j}, \tag{5}$$

$$Q_j^Y = -\left\{\rho\mathcal{D}\alpha_d \alpha_T \mathfrak{R}T \left(\frac{M_m}{M_A M_B}\right)\right\} \frac{\partial Y_B}{\partial x_j}, \tag{6}$$

$$Q_j^p = -\left\{\rho\mathcal{D}\alpha_T Y_A Y_B \left(\frac{V_{,B}}{M_B} - \frac{V_{,A}}{M_A}\right)\right\} \frac{\partial p}{\partial x_j}, \tag{7}$$

$$J_j^T = -\left\{\rho\mathcal{D}\alpha_T'' \frac{Y_A Y_B}{T}\right\} \frac{\partial T}{\partial x_j}, \tag{8}$$

$$J_j^Y = -\left\{\rho\mathcal{D}\alpha_d\right\} \frac{\partial Y_B}{\partial x_j}, \tag{9}$$

$$J_j^p = -\left\{\rho\mathcal{D} \frac{Y_A Y_B}{\mathfrak{R}T} \left(\frac{M_A M_B}{M_m}\right) \left(\frac{V_{,B}}{M_B} - \frac{V_{,A}}{M_A}\right)\right\} \frac{\partial p}{\partial x_j}, \tag{10}$$

where $\mathfrak{R}$ is the universal gas constant, the thermal conductivity is κ, the species diffusivity is $\mathcal{D}$, the partial molar volume is $V_{,\alpha}$, the partial molar enthalpy is $H_{,\alpha}$, M_α is the molecular weight of pure species α, the mixture molecular weight is $M_m = X_A M_A + X_B M_B$ (X_α is the mole fraction), and the mass diffusion factor is α_d (related to the fugacity coefficients). Finally, the thermal diffusion factors are related thermodynamically by:

$$\alpha_T'' = \alpha_T - \frac{1}{\mathfrak{R}T} \left(\frac{M_A M_B}{M_m}\right) \left(\frac{H_{,B}}{M_B} - \frac{H_{,A}}{M_A}\right). \tag{11}$$

All thermodynamic variables are derived analytically from the Peng Robinson state equation.

Results

The above equations are solved in a triply periodic "box" configuration with volume L^3 based on a third order Runge-Kutta time integration combined with eighth order accurate central finite differencing for all spatial derivatives. The code is parallelized using the Message Passing Interface (MPI) communication routines (all reported simulations are conducted on 64 processors in a $4 \times 4 \times 4$ spatial decomposition). In order to simplify the investigation, the viscosity is assumed constant and is calculated based on a chosen value for the flow Reynolds number, $\mathrm{Re}_0 = \rho_0 a_0 l_0/\mu$ (the reference velocity and length scales are the sound speed a_0 and $l_0 = L/2\pi$), and the Prandtl and Schmidt numbers are both set equal to 0.7. The thermal diffusion factor α_T is calculated from the molecular weights of the species pairs using the correlation suggested by Curtis and Farrell;[3] $\alpha_T = 2.38 \times 10^{-2} + 0.248 \log_{10}(M_B/M_A)$.

The simulation parameters considered in this study are provided in Table 1 which includes the mixture composition, the grid resolution, the flow Reynolds number and forcing amplitude, the ratio of molecular weights, and the initial density and sound speeds. The species considered are: nitrogen ($p^C = 33.46atm$, $T^C = 126.6K$; superscript C denotes critical properties), heptane ($p^C = 27.04atm$, $T^C = 540.3K$), 3-methylhexane ($p^C = 27.73atm$, $T^C = 535.3K$), and dodecane ($p^C = 17.96atm$, $T^C = 658.2K$). All simulations are initialized as perfectly premixed (50/50 by mass) systems with zero velocity, and initial temperature and pressure $T_0 = 700K$ and $p_0 = 45atm$. The governing equations are then integrated forward in time until a statistically stationary state is achieved. At this point, the simulations are continued until accurate time averaged statistics are obtained. Several simulations are also re-initialized from the fully developed flows with a (non-premixed) spherical hydrocarbon "blob" centered in the domain with a temperature which is depressed $100K$ from the mean temperature in order to characterize effects present in the mixing regions of typical turbulent sprays.

As noted above, the temperature and pressure dependent Soret terms in the mass flux vector "force" the generation of concentration fluctuations within the initially premixed (or long time non-premixed) flows. Figure 1 illustrates instantaneous contours of the heptane mass fraction fluctuations from Run 3, as well as the corresponding normalized energy spectra for the kinetic energy, heptane mass fraction, pressure, and temperature. The time

averaged root mean square (RMS) amplitudes, skewness factors (μ_3), and flatness factors (μ_4) of the species B mass fractions are listed in Table 2 together with other statistics (Mach number, Taylor Reynolds number, Kolmogorov length scale, and compressibility factor) for all simulations. These results show that the concentration fluctuations are highly intermittent with amplitudes which increase both with increasing molecular weight ratio (Runs 4,2,5) and Mach number (Runs 2,3), as well as with decreasing Reynolds number (i.e. increasing diffusivities; Runs 1,2).

The mechanism for mass fraction fluctuation generation is elucidated in Fig.2(a) which shows the temporal variation of the terms in the Favre averaged species B scalar variance transport equation (for homogeneous flow):

$$\frac{d}{dt}\left(<\rho>\widetilde{Y_B''Y_B''}\right) = 2<J_j\frac{\partial Y_B}{\partial x_j}> = 2\left\{<J_j^T\frac{\partial Y_B'}{\partial x_j}> + <J_j^Y\frac{\partial Y_B'}{\partial x_j}> + <J_j^p\frac{\partial Y_B'}{\partial x_j}>\right\}. \quad (12)$$

Clearly, the term containing J_j^Y is the traditional (low pressure) dissipation term. On the other hand, Fig.2(a) shows that the term due to pressure gradients acts as a relatively strong production mechanism and is the primary source of the fluctuations. This explains the influence of the Mach number on the scalar variance since higher Mach numbers are accompanied by larger RMS pressure fluctuations in the flow (e.g. $p_{RMS} \sim 10atm$ for Run3). In contrast, the situation is altered for the non-premixed mixing of hydrocarbon "blobs" as illustrated in Fig.2(b). In this case, relatively large concentration and temperature gradients are present in the initial flow, and the effects of the pressure gradient on the scalar variance are minimal (prior to the completion of mixing).

Forthcoming studies will address real gas and generalized diffusion flux effects on turbulent high pressure mixing/combustion physics and modeling.

Computational resources were provided primarily by the JPL/Caltech Supercomputing Project funded by the NASA Offices of Earth Science, Aeronautics, and Space Science, and partially by the National Computational Science Alliance under grant CTS990040N utilizing the NCSA SGI/CRAY Origin2000.

1. R.C. Reid, J.M. Prausnitz, and B.E. Poling. *The Properties of Gases and Liquids*. McGraw-Hill, New York, New York, 1987.

2. R.S. Miller, K.G. Harstad, and J. Bellan. Direct numerical simulation of supercritical fluid mixing layers applied to heptane-nitrogen. 1999. Submitted.

3. E.W. Curtis and P.V. Farrell. A numerical study of high-pressure droplet vaporization. *Comb. Flame*, 90:85–102, 1992.

4. B. Chehroudi, D. Talley, and E. Coy. Initial growth rate and visual characteristics of a round jet into a sub- to supercritical environment of relevance to rocket, gas turbine, and diesel engines. *AIAA Paper 99-0206*, 1999.

5. J.C. Oefelein and V. Yang. Analysis of hydrogen-oxygen mixing and combustion processes at high-pressures. *AIAA Paper 97-0798*, 1997.

6. S. Kida and S.A. Orszag. Energy and spectral dynamics in forced compressible turbulence. *J. Sci. Compt.*, 5(2):85–125, 1990.

Run	Species A	Species B	N^3	Re_0	F^*	M_B/M_A	$\rho_0[kg/m^3]$	$a_0[m/s]$
1	Nitrogen	Heptane	64^3	75	0.05	3.58	33.9	389.4
2	Nitrogen	Heptane	128^3	450	0.05	3.58	33.9	389.4
3	Nitrogen	Heptane	128^3	150	0.35	3.58	33.9	389.4
4	Heptane	3-Methylhexane	128^3	450	0.05	1.0	94.4	214.5
5	Nitrogen	Dodecane	128^3	450	0.05	6.08	37.1	371.7

Table 1: Simulation and initial thermodynamic parameters.

Run	$< M_C >$	$< \mathrm{Re}_\lambda >$	$< \eta/\Delta x >$	$< pV/\Re T >$	$Y_{B,RMS}$	$\mu_3(Y_B)$	$\mu_4(Y_B)$
1	0.21	16.1	2.10	1.02	3.50×10^{-3}	−0.39	3.56
2	0.20	51.1	1.32	1.02	1.87×10^{-3}	−1.57	7.52
3	0.56	54.8	1.34	1.02	9.75×10^{-3}	−1.06	5.56
4	0.21	52.2	1.31	0.84	6.00×10^{-6}	1.60	7.27
5	0.20	51.0	1.34	1.02	3.20×10^{-3}	−1.75	9.04

Table 2: Premixed flow time averaged statistics.

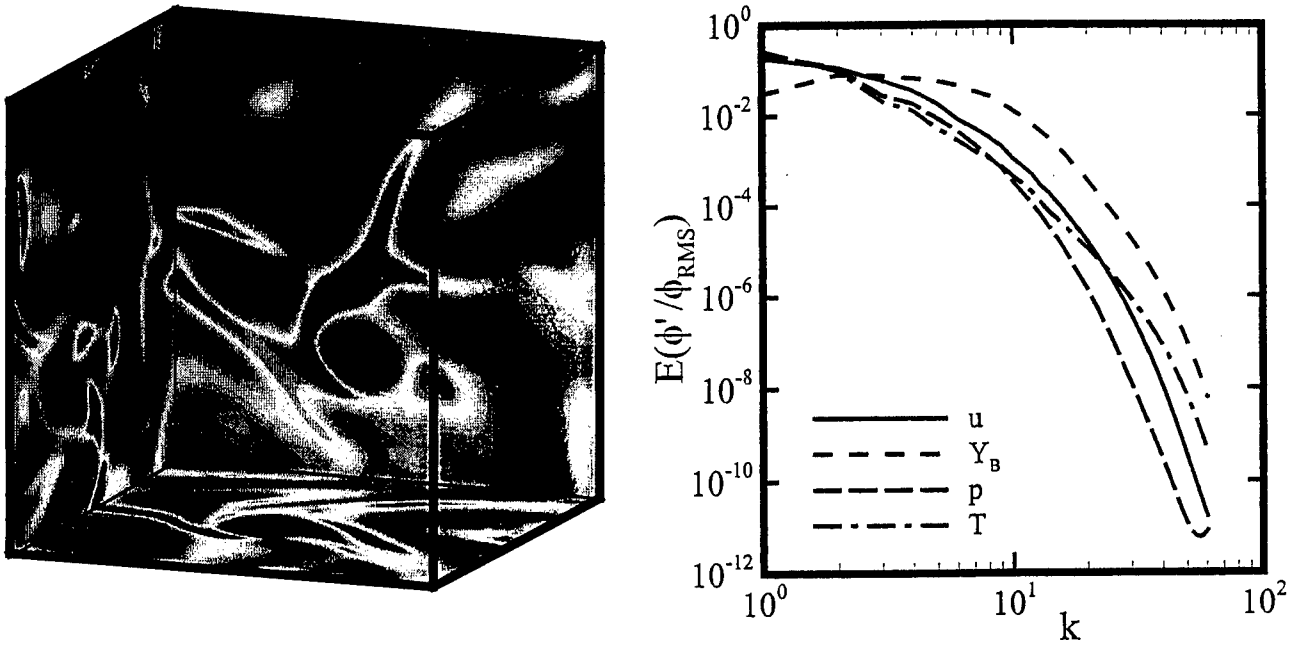


Figure 1: Instantaneous results from Run 3 at $t^* = 125$; (a) contours of heptane mass fraction fluctuations, and (b) normalized energy spectra for kinetic energy, heptane mass fraction, pressure and temperature.

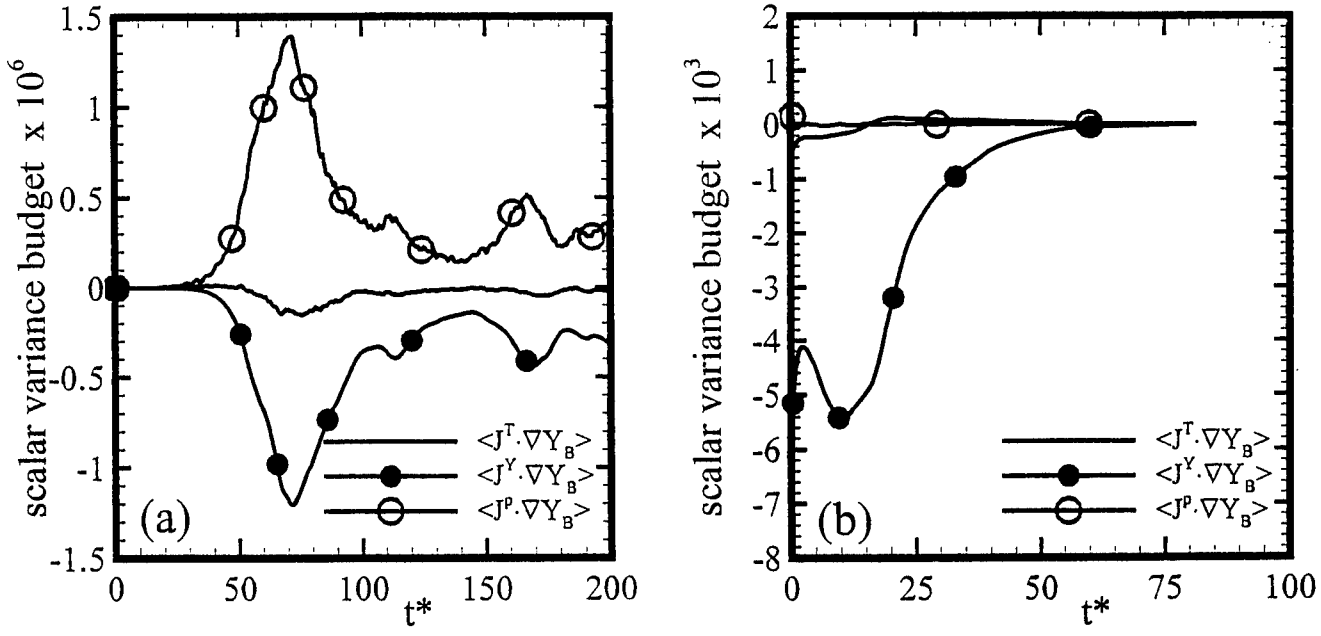


Figure 2: Temporal evolutions of Favre averaged heptane mass fraction variance equation budget for (a) a premixed flow (Run 2), and (b) a non-premixed flow (Run1).

The New Regimes of "Intensely Wrinkled" and "Shredded" Nonpremixed Flames - Images of the Reaction Zones

A. Ratner[1], J. F. Driscoll[1], J.M Donbar[2],
C. D. Carter[3], J. A. Mullin[1], and W.J.A. Dahm[1]

[1]Dept. of Aerospace Engineering, Univ. of Michigan, Ann Arbor 48109
[2]Advanced Propulsion Division, Wright-Patterson AFB OH 45440
[3]Innovative Scientific Solutions, Inc., Dayton OH 45440

Email address: aratner@umich.edu

Two new regimes of turbulent nonpremixed combustion were identified by subjecting flames to significantly larger turbulence levels than can be achieved in conventional jet flames. Reaction zones were imaged using simultaneous CH-OH and PIV-OH diagnostics. In the regime of "Intensely Wrinkled Flames" (IWF), flame wrinkling is significantly larger than has been observed before, and in the regime of "Shredded Flames" (SF) the reactions occur in short, discontinuous segments, which also has not been seen previously. A new parameter is identified (the wrinkling parameter), which is the product of (a) the stretch rate and (b) the residence time during which a flame segment remains in the largest vortices. To create a shredded flame, it is necessary to increase u'/U by using high-speed coflow air with swirl to create internal recirculation, low mean velocities, and sufficient residence time for flame roll-up in eddies.

The fuel decomposition reaction zones/CH layers remain thin (less than 0.5 mm thick) even at high Reynolds numbers, and are thinner than CH layers in a laminar jet flame. It is concluded that CH reaction zones are not broadened by turbulence, but become shredded and extinguished before any broadening can occur. Even at large turbulence intensities there was no evidence of "Distributed Reaction Zones", which lends support to the flamelet modeling approach. There also is no evidence of small scale wrinkling of the reaction zones

Introduction. An important question is whether or not chemical reaction zones undergo fundamental changes as the turbulence intensity is increased indefinitely, as discussed by Bilger [1] and Peters [2]. One prediction is that "laminar flamelets" will become thickened "distributed reaction zones" when the Kolmogorov scale is thinner than the reaction zone. However, the rotational velocity of small eddies may be so small that the turbulent diffusivity associated with small eddies may be insignificant compared to molecular diffusivities, as discussed by Mueller, et al. [3] who showed that small eddies are severely attenuated by gas expansion. Donbar, et al. [4] and Carter, et al. [5] showed that reaction zones in turbulent jet flames are not thicker than in laminar jet flames. A different prediction is that flamelets become thinner as the strain rate increases. A third possibility is that flamelets remain thin but they become shredded and extinguish before they can be broadened. Unfortunately, jet flames do not provide sufficiently large values of u'/U to test this hypothesis. However, a typical gas turbine combustor can do so, since coflow air, swirl and internal recirculation create large values of u'/U, residence times, and integral scales.

Apparatus. Figure 1 shows the Intensely Wrinkled Flame (IWF) burner used in the University of Michigan/GRI/IFRF Scaling 400 studies of nitric oxide formation [6]. A central methane-nitrogen fuel jet is surrounded by a high speed coaxial air with swirl number of 1. The Reynolds number based on the effective jet diameter is 26,200. Figure 2 shows that in the boxed region near the flame tip, the mean velocity is small (typically less than 1.5 m/s) while the turbulence level

(u'/U) is extremely large, exceeding a value of five. The conditions in the box in Fig. 1 approximate "turbulence in a box" having negligible mean velocity and large turbulence level, which has been computed using Direct Numerical Simulations [7].

The Regime of Intensely Wrinkled Flames (IWF). Figures 2-4 show the CH and OH reaction zones in the IWF regime. It is found that the CH layers become thinner (less than 0.5 mm thick) and the OH layers also become thin (1-2 mm thick). Thus increased turbulence does not broaden the CH or OH layers. These observations lend support to the flamelet modeling approach. For large turbulence intensities, the flames in Fig. 4 enter the Shredded Flame regime; the CH and OH layers are fragmented due to local flame extinction. Previously there has been no experimental evidence that flamelets become thinner and become shredded for intense turbulence levels. The velocity field and the OH reactions zones are shown in Fig. 3 in the IWF flames. At some locations the flame wrinkles appear to be correlated with a nearby large eddy, indicating that the wrinkle is formed by the eddy. Eddies in Fig. 3 also cause OH layers to merge, while other eddies roll up the OH layer. At some locations there are flame wrinkles but there are no nearby eddies, which indicates that the wrinkle was formed previously and has been convected with the flow. There is no evidence of small scale wrinkling, indicating that the small scales play no part in the wrinkling process. The images presented in Figs. 2-4 make it possible to define different regimes that are based on actual experimental evidence. The parameter that governs flame wrinkling and extinction is the product of the flame stretch rate (K) and the flame-vortex residence time (t_{res}). Consider a vortex which exert a constant stretch rate K during a time period t_{res}. Integrating the definition of stretch rate ($K = (1/A)\, dA/dt$) yields:

$$K \cdot t_{res} = \ln (A_T/A_L)$$

A_T is the wrinkled surface area; A_L is the area before wrinkling. Thus the product $K \cdot t_{res}$ is a good indicator of the degree of flame wrinkling A_T/A_L. Flame extinction also depends on $K \cdot t_{res}$, as was shown by Mueller et al. [19]. Stretch rates are proportional to $(u'/\ell_I)\,\eta$; the efficiency factor η equals $(\ell_I/\delta_L)^2$ since large vortices are more efficient in the wrinkling process [3]. Residence time depends on (ℓ_I/U), thus:

$$K \cdot t_{res} = c_1 (u'\, \ell_I / \nu)\ (\ell_I / \delta_L)\ (U\, \delta_L / \nu)^{-1}$$

which indicates that Intensely Wrinkled Flames (having large (A_T/A_L) can be achieved by operating at large values of Re, integral scale, and u'/U.

Acknowledgments Diagnostics were provided by Wright-Patterson AFB and NSF Grant CTS 9123834; Fellowship support for A. Ratner was provided by the Association Francois-Xavier Bagnoud. The burner was provided by the Gas Research Institute.

References

1. Bilger, R.W., Twenty-Second Symp. on Combustion, The Combustion Inst., 1988, p 475.
2. Peters, N., Twenty-First Symp. on Combustion, The Combustion Institute, 1986, p. 1231.
3. Mueller, C., Driscoll, J.F., Reuss, D., Drake, M,Comb. Flame , 112, 1998, p. 342.
4. Seitzman, J.M., Ungut, A., Paul, P.H., and Hanson, R.K., Twenty-Third Symp. (International) on Combustion, The Combustion Institute, Pittsburgh, 1990, pp. 637-644.
4. Donbar, J.M., Driscoll, J.F., and Carter, C.D., "Structure of Reaction Zones Within Turbulent Nonpremixed Jet Flames: From CH-OH PLIF Images", submitted to Comb. Flame.
5. Carter, C.D., Donbar, J. M., Driscoll, J.F, Applied Physics B, 66, p. 129, 1998.
6. Hsieh, A., Dahm, W.J.A., and Driscoll, J.F., Combust. Flame, 114, p. 54, 1998
7. Mahalingham, S., Chen, J.H., and Vervisch, L., Combust. Flame 102: 285, 1995.
8. Tryggvason, G., and Dahm, W.J.A., Combust. Flame 83: 207-220, 1991.

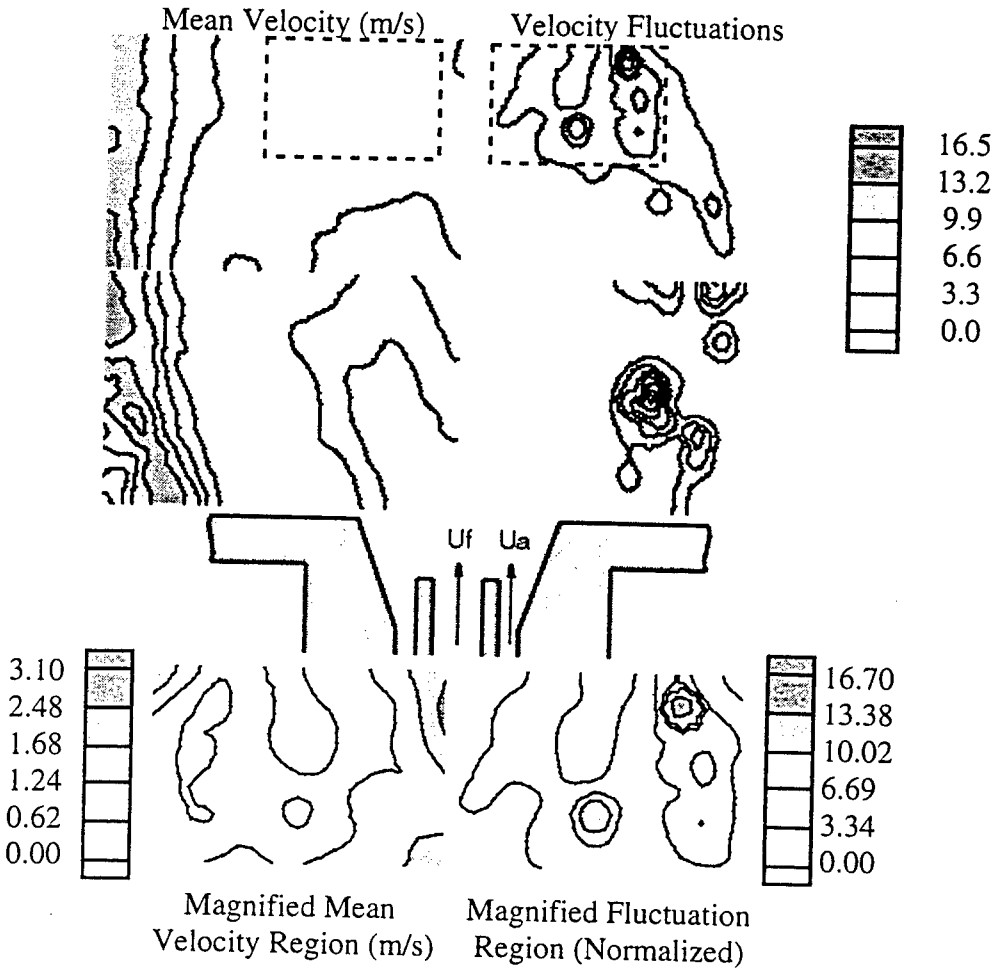


Figure 1. Mean Velocity and Normalized Velocity Fluctuations in a Magnified Region of an "Intensely Turbulent Flame" where Mean Velocity is 1.16 m/s and the Normalized Velocity Fluctuations Average is 5.12.

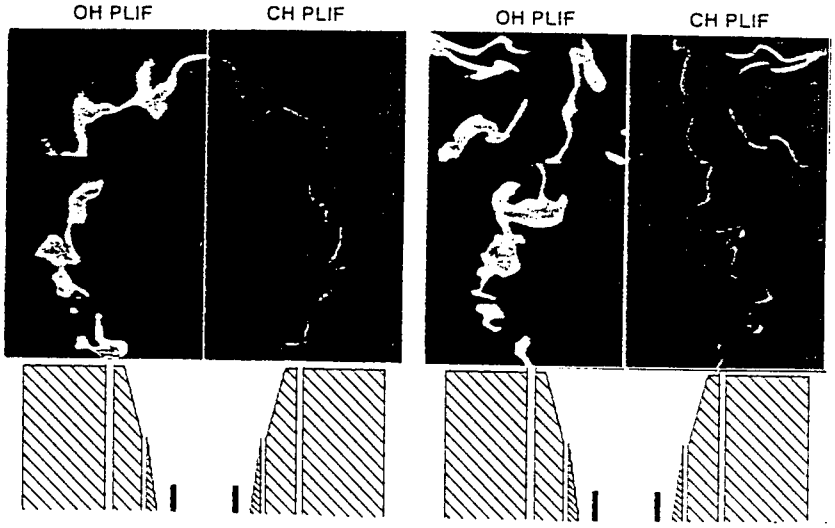


Figure 2. Instantaneous CH and OH PLIF Images.

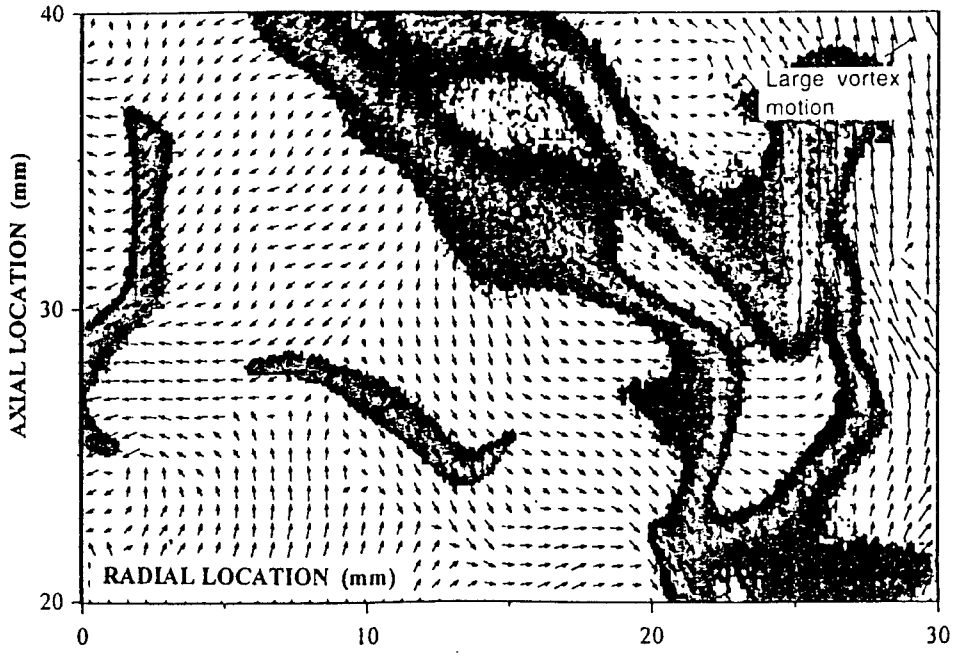


Figure 3. Velocity Field and OH Reaction Layers in the Intensely Wrinkled Flame.

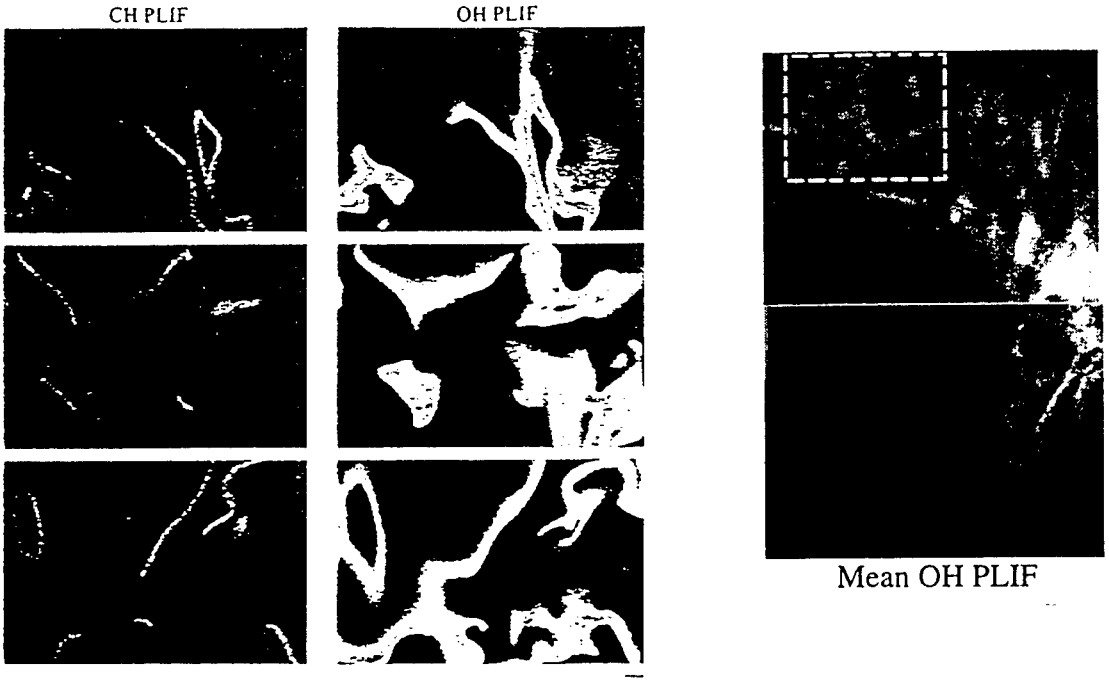


Figure 4. (a) Simultaneous Images of CH and OH Layers in the IWF; (b) Mean OH Concentration Field, from Superimposing 20 Instantaneous OH Images

The IRST model for turbulent premixed non-adiabatic methane flames. Verification of temperature prediction.

Jim B.W. Kok, Jurgen J.J. Louis.
University of Twente, P.O. Box 217, 7500 AE Enschede, The Netherlands.
e-mail: j.b.w.kok@wb.utwente.nl

1. Introduction.

A model is presented to predict turbulent non-adiabatic premixed combustion of methane under gas turbine and atmospheric test rig conditions. The model is used to calculate a 32 kW premixed methane flame in an air cooled combustion chamber. The results are verified by comparison with measurements of profiles of velocity, turbulent kinetic energy, main species, CO and NO concentrations and of temperature. Of specific interest is the effect of radiant heat transfer on the NO and on the CO concentration. Focus in this paper will be verification of temperature prediction.

2. Progress of Chemical Reaction and of enthalpy.

The IRST model presented in this paper uses four mean dimensionless scalar variables for the transport of enthalpy and the reaction progress of hydrogen, carbon monoxide and methane related chemical reactions. These variables are denoted with i,r,s,t respectively. The combustion process is described by a detailed chemical reaction mechanism with 18 elementary reactions and 13 species (Kok et al. 1999). The detailed mechanism is reduced and the progress of the chemical reactions is mapped on three independent variables. For the methane and hydrogen variable a composed concentration is chosen, such that the highly non-linear source terms of present in some two-body reaction kinetics cancel each other. This means that only the source terms of reactions without activation energy remain in the net source term of the combined mass fraction (Kok & Louis (1998), Janicka and Kollmann (1982)). The combined concentration variables become:

$$C_t = 1.00 C_{CH_4} + 1.00 C_{CH_3} \tag{1}$$

$$C_{H_2}^{*} = C_{H_2} - \frac{1}{2} C_{HO_2} + \frac{3}{2} C_H + C_O + \frac{1}{2} C_{OH} \tag{2}$$

The species in the carbon monoxide related chemical reactions are determined by the CO concentration:

$$C_s = 1.00 C_{CO} \tag{3}$$

The concentrations of the 13 species, composed of the elements C, H and O, are mapped on and determined by the 3 composed concentrations. The chemical reaction source terms of the composed species have low activation energies and are not very sensitive to turbulent fluctuations. This allows an approach with an assumed shape Probability Density Function weighting.

The local enthalpy h of the mixture is calculated from the sum of formation enthalpies and thermal enthalpy. The minimum value of the enthalpy is obtained when the mixture is cooled instantly to the temperature of the surroundings. The local enthalpy is normalized using the adiabatic and the minimum enthalpy:

$$i = \frac{h - h_{\min}}{h_{ad} - h_{\min}} = \frac{h - h_{\min}}{U}. \tag{4}$$

The denominator U is determined by the composition and temperature of the fuel /air mixture at the inlet.

3. Mean turbulent transport equations.

The composed concentrations are independent variables, but in a turbulent flow they are statistically correlated with the enthalpy variable i and with each other. To reduce the statistical correlation of the scalar i and the composed concentrations, all composed concentrations are made dimensionless with the completely burnt and the unburned situation. The composed mass fractions of the methane, hydrogen and carbon monoxide variables become then:

$$t = \frac{C_{CH4} - C_{CH4^{unburnt}}}{C_{CH4^{burnt}} - C_{CH4^{unburnt}}} = \frac{C_{CH4} - C_{CH4^{unburnt}}}{Z(i)} \tag{5}$$

$$r = \frac{Y_{H_2^*} - Y_{H_2^*}^u}{Y_{H_2^*}^b - Y_{H_2^*}^u} = \frac{Y_{H_2^*} - Y_{H_2^*}^u}{W(i,t)}, \tag{6}$$

$$s = \frac{Y_{CO} - Y_{CO}^{pb}}{Y_{CO}^u - Y_{CO}^{pb}} = \frac{Y_{CO} - Y_{CO}^{pb}}{V(i,t,r)}. \tag{7}$$

Mean transport equations are formulated by substituting the definitions above of the dimensionless variables in convection-diffusion transport equations, using first order moment closure. Favre decomposition and averaging yields for the *mean* i, t, r and s transport equations:

$$\nabla(\bar{\rho}\,\tilde{\underline{u}}\,\tilde{i}) - \nabla(D\nabla\tilde{i}) = -\bar{S}_i \tag{8}$$

$$\nabla(\bar{\rho}\tilde{\underline{u}}\tilde{t}) - \nabla(D\nabla\tilde{t}) = \bar{S}_t \tag{9}$$

$$\nabla(\bar{\rho}\tilde{\underline{u}}\tilde{r}) - \nabla(D\nabla\tilde{r}) = \bar{S}_r - \overline{(Y_{H_2}^{*u})_t S_t} - \tilde{r}\overline{W_t S_t} + C_{t_2}\overline{W_{tt}}\tilde{r}\bar{\rho}\frac{\tilde{\varepsilon}}{\tilde{k}}\overline{t''^2} + C_{t_2}\overline{(Y_{H_2}^{*u})_{tt}}\bar{\rho}\frac{\tilde{\varepsilon}}{\tilde{k}}\overline{t''^2} \tag{10}$$

$$\nabla(\bar{\rho}\tilde{\underline{u}}\tilde{s}) - \nabla(D\nabla s) = \bar{S}_s \tag{11}$$

The diffusion coefficient D is the sum of conduction and eddy diffusion. The source term S_i describes the radiant heat loss due to volume emission, and is calculated in the model on basis of the temperature and mass fractions of CO_2 and H_2O. It can be assumed that the direct effect of heat loss on t,r,s via source terms related to i will be small. Hence the influence of heat loss on the reaction progress variables is taken into account via the database only. The behavior of the progress variables can be summarized as follows. Initially the fuel/air mixture has t=0, r=0, s=1 and i=1: no methane is converted, there is no hydrogen and no carbon monoxide and no enthalpy has been lost. Due to ignition the methane is converted fast, t increases from 0 to 1 and hydrogen and carbon monoxide are produced. Due to the chemical non-equilibrium the chemical reaction source terms of r and s are large (positive and negative respectively) and r and s are driven to their equilibrium values of 1 and 0 respectively. Small corrections to the chemical source term in the mean r equation are given by the other rhs (positive) terms related to t.

4. Mean chemical reaction source terms.

The chemical source term at the rhs of the t-equation (11) has a maximum at approximately t=0.7 and r=0.5. It becomes small at small t and t=1 (Kok et al. 1999). The value of the source term at small t is important for ignition processes and is at the moment the subject of research. The chemical source term of r behaviour is clearly different from that observed for t. The source term becomes very large for small r and vanishes at r=1 at equilibrium.

In the mapping on the progress variables use is made of elemental balances, steady state of intermediary species CH3, CH_2O, HCO, HO_2 and partial equilibrium assumptions. The reduction leads to a system of nonlinear algebraic equations that is solved on a mesh of i,r,s,t. To speed up flame calculations, the density, temperature, concentrations and source terms are stored in advance on the i,r,s,t mesh in a thermochemical database. In order to take turbulent fluctuations into account, the instantaneous source terms of the now statistically independent variables are Favre weighted over a factorized Probability Density Function P:

$$\tilde{\phi} = \frac{1}{\bar{\rho}} \int_0^1 \rho\phi\; P_i(i)\; P_r(r)\; P_s(s)\; P_t(t)\; di\; dr\; ds\; dt. \tag{12}$$

Single delta functions can be chosen for P_r, P_s and P_t as in this *premixed* flame the influence of higher order moments (fluctuations) of r and t has become negligible. The flame rates that are calculated are turbulent, as the effect of turbulence is taken into account by the specific kind of mapping of all independent chemical species variables on the three progress variables and subsequent PDF averaging. The model is successful, when the mapping is allowed. As discussed in Kok and Louis (1998) this is the case in flames where ignition and heating to temperatures above 1000 K is fast. It can be observed that the ignition area, where the model is less accurate, in the premixed flame investigated here is less than 5 mm (fig. 1). The transport equations and database are coupled through user scalars to a commercial CFD code (CFX

version 4.2), that solves the convective/diffusive equations together with the flow field and turbulence equations. Here a conventional k-ε model was used for the latter. The formation of thermal NO is computed with the Zel'dovich mechanism in a post processing step. For simplicity in this paper just thermal NO is considered, and accordingly experiments are chosen with sufficiently high flame temperature.

5. Set-up of experiments and numerical simulations.

In the experimental set-up at the Lab. of Thermal Eng. of the University of Twente methane and air are premixed and supplied subsequently to a circular perforated plate with diameter 50 mm. (the premixed burner). The burner is mounted to a cylindrical combustion chamber with a diameter of 100 mm and a length of 1.0 m. The outside wall of the combustor is cooled by a forced air flow. In the experiments axial and radial profiles of CO, CO_2, O_2 and NO concentrations were measured at axial distances of 0.032, 0.065, 0.15, 0.30, 0.40 and 0.60 m from the burner exit. Use was made of a sample probe technique (Kok et al. 1999). Radial profiles of axial velocity were measured with 2D back scatter LDA in the laboratory of the Thermal and Fluids Sciences Section of the Department of Applied Physics at the Delft University of Technology. Also at the Delft laboratory measurements were performed of axial and radial profiles of temperature with the use of CARS. For the LDA and the CARS experiments two quartz glass windows were mounted in the combustor. Although not presented here for brevity, of all measurements axial and several radial profiles are available.

The combustion model was implemented in the commercial CFD package CFX . In the simulations the combustor volume is meshed with a 2 dimensional axial symmetric grid with 80x100 cells in a non-uniform distribution. The combustion chamber is modeled up to a length of 0.65 m. The perforated burner disk is modeled as a set of concentric solid rings. The inlet velocity was 4.0 m/s with temperature 300 K (air mass flow rate 32 kg/hr) and air factor 1.1. This results in a thermal power of 32 kW (based on natural gas Higher Heating Value). For the calculation of the radiation source term, the wall temperature was set uniformly to 600 K, but the results are not sensitive to this value. Direct influence of the cooled wall on the mixture adjacent to this wall by conductive and advective heat transport was neglected. The inlet values for k and ε were taken as 0.2% turbulent kinetic energy and 0.5% turbulent rate of dissipation. All modeling constants were set to CFX defaults.

6. Results.

The results of the simulation and the experiment data will be discussed now. The behavior of the mean of the reaction progress variables i,r,s as a function of axial distance at the combustor center is shown in figure 1. The enthalpy variable is unity upstream and decreases at a low rate to 0.85 at 300 mm axial distance. The r variable increases fast from 0 to 1 due to the conversion of methane to hydrogen and the subsequent hydrogen reactions. At 50 mm axial distance the hydrogen system is already in equilibrium. The CO reactions are much slower. At 20 mm axial distance the s variable has decreased from 1.0 to 0.4. But then it takes another 200 mm to decrease s to 0.05 which comes close to equilibrium. The t variable is not depicted, but this is very fast at equilibrium.

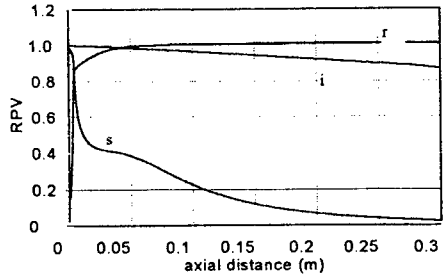


Fig. 1 Predicted center line values i,r,s.

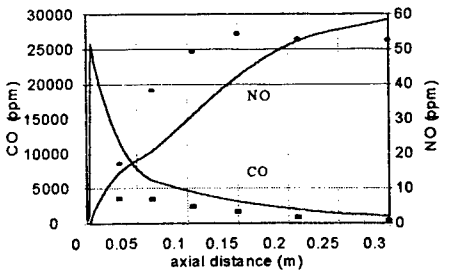


Fig. 2 Center line NO, CO concentration.

The measured and predicted axial profiles of NO and CO are shown in fig. 2. The CO concentration is predicted to increase to 25,000 ppm at 15 mm and to decrease slowly to 1000 ppm at 300 mm. In the range 0-80 mm is measured 3000 ppm, considerably lower than predicted. This is caused by the maximum value of 3000 ppm that can be measured by the analysis apparatus. The first accurately measured CO concentration is 2500 ppm at 100 mm, where 5000 ppm is predicted. At further downstream locations the CO concentration over prediction of 100% is continued. Qualitatively the comparison is good, but quantitatively this can be improved. A possible model deficiency is the over prediction of temperature. The NO concentration increases from 0 to 50 ppm at 200 mm. Downstream of that point the NO production is arrested (due to heat loss) and the NO concentration settles at about 50-60 ppm. This is confirmed by the

measurements.

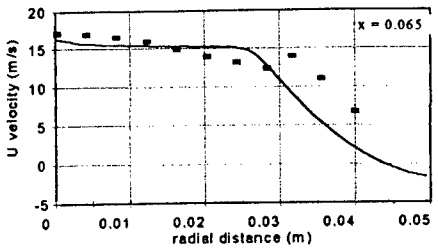


Fig. 3. Radial profile of axial velocity.

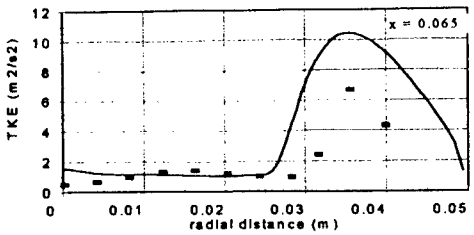


Fig. 4. Radial profile of turbulent kinetic energy.

Radial profiles of axial mean velocity and turbulent kinetic energy are given in figs. 3 and 4 at axial distance 65 mm. Both figures show a core of flue gas flow at about the burner radius of 30 mm. There is a good comparison of predicted and measured mean axial velocity. In the transition area between core and tube wall the largest turbulent fluctuations occur. In this shear layer the turbulent kinetic energy is under predicted, probably due to inaccuracy of the LDA measurements.

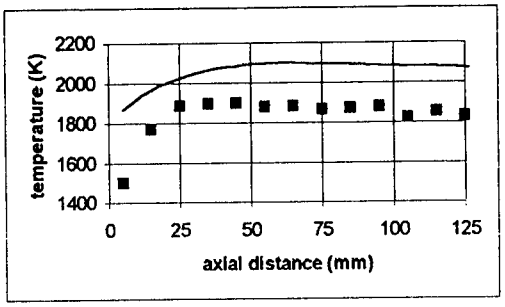


Fig. 5. Centerline mean temperature profile.

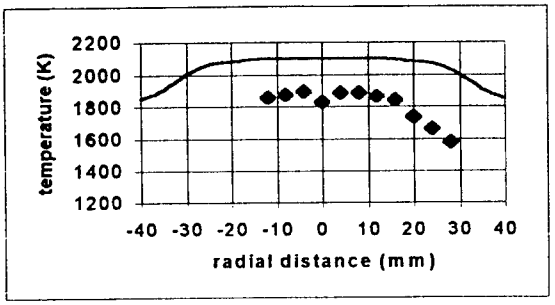


Fig. 6. Radial profile of mean temperature.

The measured and predicted axial profile of mean temperature at the combustor centerline is shown in fig. 5. It can be observed that the model predicts the temperature increase and subsequent decrease downstream 50 mm, but the level of temperature is over predicted by 200 K. This is much more than the measurement inaccuracy of about 50 K. Similar observations apply to the measured radial profile of temperature at axial distance 65 mm. The behavior is correct qualitatively: there is a hot core surrounded by cooler gas. But in the model the core has a radius of 30 mm and temperature 2100 K, and measured is a core of radius 18 mm and temperature 1900 K. The model over predicts the reaction progress and predicts a too fast return to equilibrium. Presently it is investigated if this is due to shortcomings of the mapping of chemical source terms or to incorrect chemistry-turbulence interaction.

7. Conclusion.

A reaction progress variable model, using 4 scalars, to describe a turbulent non-adiabatic premixed methane flame is presented. The model is verified in an experiment with a flat flame in a cylindrical combustor. The predicted mean axial and radial profiles of velocity and turbulent kinetic energy compare with the LDA measurements. The mean species concentrations CO_2 and O_2 are well predicted. The NO and CO centerline profile predictions compare qualitatively. Quantitatively the NO concentration is 20% and the CO concentration is 100% over predicted. This over prediction can be related to the observed temperature. Using CARS accurate temperature measurements are performed on axial and radial profiles. The predicted profiles compare qualitatively with the measured profiles. The predicted temperature is however systematically 200 K too high. The model gives good prediction of velocity and major species concentration. Non-equilibrium minor species are predicted, but accuracy needs to be improved. It seems that the inaccuracy is due to over prediction of the rate of reaction progress. This is the focus of further research.

References.

Janicka, J., Kollmann, W, The calculation of mean radical concentrations in turbulent diffusion flames, *Combust. Flame* 44:319-336 (1982).

Kok, J.B.W., Louis, J.J.J., Modeling turbulent combustion in a CO/H_2 diffusion flame using reaction progress variables, *Combust. Sci.. and Tech.* 131: 225-249 (1998).

Kok, J.B.W., Louis, J.J.J., Yu, J.H., The IRST model for premixed methane flames, accept. for publ. in *Combust. Sci.. and Tech.* 1999.

Initial Observations on the Burning of an Ethanol Droplet in Microgravity

Andrei Kazakov, Bradley Urban, Jordan Conley and Frederick L. Dryer
Department of Mechanical and Aerospace Engineering,
Princeton University, Princeton, NJ 08544

INTRODUCTION

Combustion of liquid ethanol represents an important system both from fundamental and practical points of view. Ethanol is currently being used as an additive to gasoline in order to reduce carbon monoxide and particulate emissions as well as to improve the fuel octane rating. A detailed physical understanding of liquid ethanol combustion is therefore necessary to achieve an optimal performance of such fuel blends in practical conditions. Ethanol is also a relatively simple model compound suitable for investigation of important combustion characteristics typical of more complex fuels. In particular, ethanol has been proposed for studies of sooting behavior during droplet burning [1]. The sooting nature of ethanol has pressure sensitivities similar to that of n-heptane, but shifted to a higher range of pressures (1-3 atm). Additionally, liquid ethanol is miscible with water produced during its combustion forming mixtures with azeotropic behavior, a phenomenon important for understanding multi-component, liquid fuel combustion [2]. In this work, we present initial results obtained in the series of recent space-based experiments [3] and development a detailed model describing the burning of ethanol droplet in microgravity.

EXPERIMENTAL

The microgravity ethanol droplet combustion experiments were performed aboard the STS-94/MSL-1 Shuttle mission within the Fiber-Supported Droplet Combustion-2 (FSDC-2) program [3]. All experiments were carried out in the Glovebox (MGBX) facility using the FSDC-2 experimental apparatus. Ethanol and ethanol/water mixtures were contained in modified, airtight commercial syringe cartridges. To operate the experiment, the fuel cartridge was screwed into the base of the experiment module. The crew turned a plunger screw, forcing fuel through two, opposed, hypodermic needles to the deployment site on a silicon fiber located between the needles and perpendicular to them. After the fuel coalesced into a droplet of the desired size, the needles were slowly retracted to minimize contact of the liquid with the needle surfaces. The stretched droplet was then deployed by rapidly retracting the needles into the bottom of the chamber. Motions of the deployed droplet were allowed to dampen before the ignition button was depressed. This automatically lifted a replaceable igniter wire into place on one side of the droplet (parallel to the fiber), approximately 3.5 mm from the fiber, and simultaneously provided DC electric current to the igniter. When the crew operator detected ignition visually, the igniter button was released, automatically retracting the igniter to the bottom of the test chamber. The manual nature of the experiment can affect the reproducibility and fidelity of the data, in comparison to that obtained in the full-facility Droplet Combustion Experiment (DCE) apparatus. However, FSDC experiments provide substantial scientific insights as well as first-order data on which to base more refined DCE studies.

Imaging data are provided by two video views, one a backlit view of the droplet and the other a perpendicular view of the flame. The video camera for the droplet view was attached to the Glovebox microscope. The second video camera, with a view essentially orthogonal to the microscope, recorded the droplet, the fiber, and the flame. All of the data were recorded using three 8 mm VCR's. The taped camera images were analyzed using microcomputer-based imaging analysis systems. Each droplet combustion test occurred at pressures (0.996–1.107 bar), oxygen mole fractions (0.204–0.222), and relative humidity (39–46%) of the Spacelab environment.

The average droplet gasification rate, $K = d(d_s^2)/dt$, where d_s is an instanteneous droplet diameter, and t the burning time, for pure ethanol and ethanol/water mixtures, as a function of initial droplet size, are presented in Figure 1. The results show that average gasification rate is related to the initial droplet size in a manner similar to n-alkanes and methanol [4-6] and consistent with ethanol data taken recently in the NASA-Lewis 2.2 s droptower [7]. The FSDC-2 ethanol experiments were particularly interesting in that large initial droplets that burned unsteadily and underwent extinction could be re-ignited. The gasification rate of the re-ignited droplet was typically higher in comparison to the prior burn. Larger initial droplet sizes could be re-ignited several times. Eventually, the re-ignited droplets would burn in a sustained fashion to near completion (an extinction diameter that was not measurable). Further data reduction and analyses, complemented by computer simulations are currently in progress.

MODELING

A transient, moving finite-element chemically reacting flow model developed by Cho et al. [8,9] and applied previously to sphero-symmetric combustion of methanol [4], methanol/water [4,5], n-alkane, and n-alkane binary mixture [6] droplets was adopted for the problem of ethanol droplet combustion. The model includes detailed description of gas-phase reaction chemistry and transport, a simplified description of liquid phase transport, and non-luminous radiation [10].

Gas-phase chemistry was described with the detailed reaction mechanism of Norton and Dryer [11], which consists of 142 reversible elementary reactions of 33 species. Another recently published reaction mechanism of high-temperature ethanol oxidation [12] is also under consideration. However, our preliminary comparison of two reaction models using a representative opposite-flow diffusion flame problem [13] indicates that the basic flame structures predicted by these models are very similar. Large differences appear in profiles of primary pyrolysis products, particularly ethylene and acetaldehyde. The mechanism of Marinov [12] strongly emphasized thermal decomposition of ethanol, in comparison to abstraction channels. Other kinetic studies to experimentally characterize ethanol pyrolysis at near 1000 K are underway in this laboratory. The equilibrium vapor pressures for binary ethanol/water mixtures needed to define the boundary conditions on gas-liquid interface were evaluated using recently reported empirical correlations of Kurihara and co-workers [14]. The mixture liquid densities were computed using the excess-volume data of Bai et al. [15] and the correlations for pure compounds complied by Daubert and Danner [16].

The model predictions for 1 mm ethanol droplet burning in air at 1 atm are presented in Figs 2 and 3. As can be seen, the droplet size history fairly closely follows the classical d^2-law [16] with an average gasification rate constant of about 0.58 $mm^2\ s^{-1}$ which compares favorably with the experimental data presented in Fig. 1. This observation also differs from the experimental and numerical results obtained for methanol droplets that have shown significant deviations from the d^2-law predictions due to substantial water accumulation in the liquid phase [6]. As shown in Fig. 3, the model predicts relatively small mass fraction of water present in the ethanol droplet during most of the droplet lifetime, hence, the effect of water condensation on gasification rate is reduced as compared to the methanol cases. Furthermore, the water fractional gasification rate changes its sign relatively early during the process, indicating that condensation of water ceases, and the subsequent increase in water mass fraction in the droplet is caused exclusively by preferential gasification of ethanol. Similar conclusions can be drawn from the analysis of the experimental data for ethanol reported by Lee and Law [18]. Lee and Law have suggested that the observed difference in water condensation between methanol and ethanol droplets is primarily caused by a higher latent heat value of ethanol (9.7 kcal/mol) as opposed to the one of methanol (8.4 kcal/mol). Numerical tests performed in the present study indicated that reducing the latent heat of ethanol to the value of methanol without changing the vapor pressure relationships does not result in significant changes in calculated droplet water content during most of the process. A more detailed

analysis of model predictions reveals that water condensation stops approximately when the droplet composition reaches azeotropic point corresponding to about 4 % of water by mass. By definition, this composition occurs at the maximum of total vapor pressure (Fig. 4). Further increase of water content in the liquid phase leads to the decrease in total vapor pressure, and the subsequent condensation of water vapor becomes unfavorable.

A significant increase in water content in the droplet occurs late in the computed burning history. This observation has not been reported previously and is due to the non-ideal nature of the binary mixture vapor pressure/mass fraction relationship [14] (see Fig. 4).

SUMMARY

New experimental data for the ethanol droplet combustion in microgravity are presented. The reported values of average gasification rate are consistent with available literature trends and preliminary modeling results. The model analysis also indicates that water condensation in the case of ethanol has a smaller effect on droplet gasification rate as compared with previously studied methanol cases. Further analysis of experimental data and model development and validation are currently in progress.

ACKNOWLEDGMENTS

This work was supported by NASA under COOP No. NCC3-487. We gratefully acknowledge the contributions of and collaborations with fellow FSDC-2 team members, Forman Williams (PI), Ron Colantonio, Dan Dietrich, John Haggard, Sue Motil, Vedha Nayagam, and Ben Shaw.

REFERENCES

1. Manzello, S. L., Hua, M., Choi, M. Y., and Dryer, F. L. "Experiments and Model Development for Investigation of Sooting and Radiation Effects in Microgravity Droplet Combustion", Proceedings of the Fifth International Microgravity Combustion Workshop, Cleveland, Ohio, May 18-20, 1999, p. 241.
2. Kim, J. S., Lee, A., and Law, C. K., *Twenty-Third Symposium (International) on Combustion*, The Combustion Institute, Pittsburgh, PA, 1990, p. 1423.
3. Colantonio, R., Dietrich, D., Haggard, J. B., Jr., Naygan, V., Dryer, F. L., Shaw, B. D., and Willams, F. A., "Fiber Supported Droplet Combustion-2", Proceedings of the Microgravity Science Laboratory One Year Science Review Meeting, Huntsville, Alabama, August 25-26, 1998, p. 141.
4. Marchese, A. J., Dryer, F. L., Colantonio, R., and Naygan, V. *Twenty-Sixth Symposium (International) on Combustion*, The Combustion Institute, Pittsburgh, PA, 1996, p. 1209.
5. Marchese, A. J., and Dryer, F. L. *Combust. Flame*, 105:104-122 (1996).
6. Marchese, A. J., Dryer, F. L., and Naygam, V. *Combust. Flame*, 116:432-459 (1999).
7. Colantonio, R., and Naygan, V., "Radiative Heat Loss Measurements during Microgravity Droplet Combustion", Proceedings of the 1997 Central States Section of the Combustion Institute.
8. Cho, S. Y., Yetter, R. A., and Dryer, F. L., *Mathl Comput. Modeling*, 14:790-794 (1990).
9. Cho, S. Y., Yetter, R. A., and Dryer, F. L., *J. Comp. Phys.*, 102:160-179 (1992).
10. Marchese, A. J., and Dryer, F. L. *Combust. Sci. Technol.*, 124:371-401, 1997.
11. Norton, T. S., and Dryer, F. L., *Int. J. Chem. Kinetics*, 24:319-344 (1992).
12. Marinov, N. M., *Int. J. Chem. Kinetics*, 31:183-220 (1999).
13. Lutz, A. E., Kee, R. J., Grcar, J. F., and Rupley, F. M. *OPPDIF: A Fortran Program for Computing Opposed-Flow Diffusion Flames*, Sandia National Lab Report No. SAND96-8243, 1997.
14. Kurihara, K., Minoura, T., Takeda, K., and Kojima, K., *J. Chem. Eng. Data*, 40:679-684 (1995).
15. Bai, T.-C., Yao, J., and Han, S.-J., *J. Chem. Thermodynamics*, 30:1347-1361 (1998).
16. Daubert, T. E., and Danner, R. P. *Physical and Thermodynamic Properties of Pure Chemicals: Data Compilation*, Hemisphere, New York, 1989.
17. Godsave, G. A. E. *Fourth Symposium (International) on Combustion*, The Combustion Institute, Pittsburgh, PA, 1953, p. 818; Spalding D. B. *Fourth Symposium (International) on Combustion*, The Combustion Institute, Pittsburgh, PA, 1953, p. 847.
18. Lee, A., and Law, C. K. *Combust. Sci. Technol.*, 86:253-265 (1992).

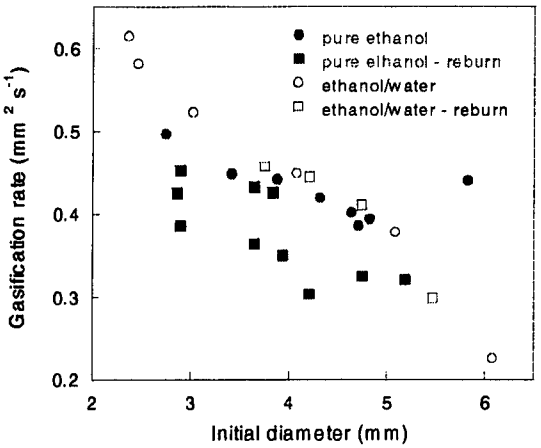


Figure 1. Average gasification rate constant as a function of initial droplet diameter for ethanol droplet burning in air [3].

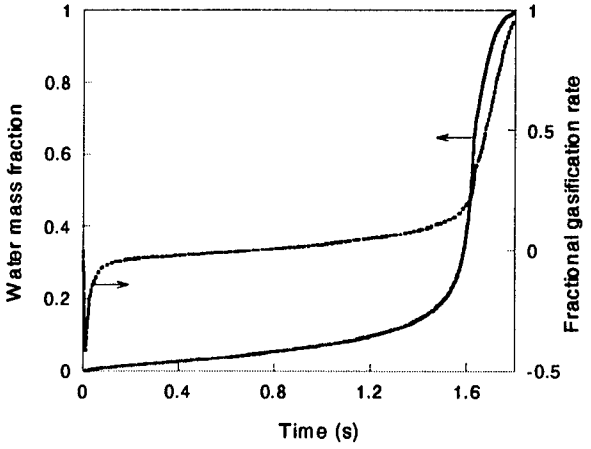


Figure 3. Water mass fraction (solid line) and fractional gasification rate, $\dot{m}_{H_2O}/(\dot{m}_{H_2O}+\dot{m}_{C_2H_5OH})$, where $\dot{m}_{H_2O}$ and $\dot{m}_{C_2H_5OH}$ are mass flow rates of water and ethanol, respectively, on the droplet surface (dotted line).

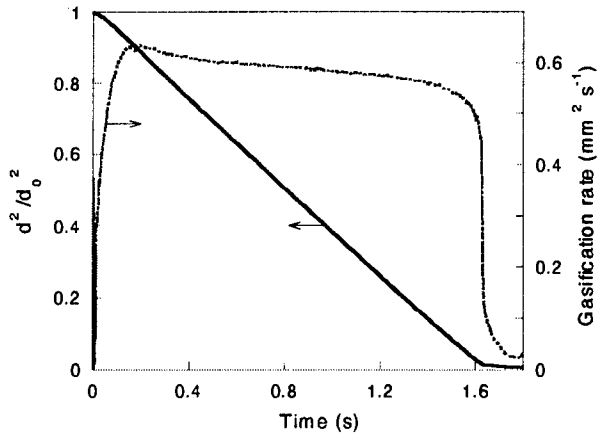


Figure 2. Computed diameter-squared normalized by initial diameter-squared (solid line) and instantaneous gasification rate (dotted line) for 1 mm ethanol droplet burning in air at 1 atm.

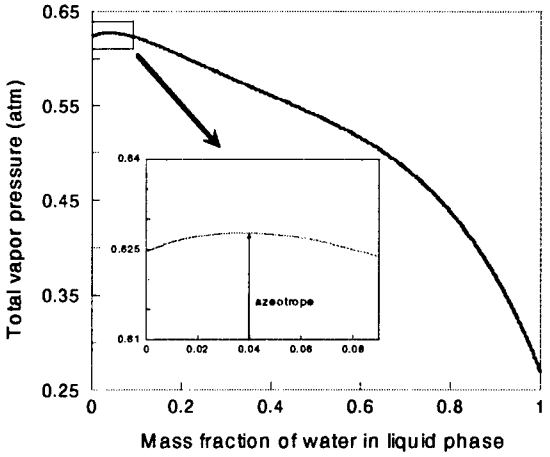


Figure 4. Total equilibrium vapor pressure above the liquid ethanol/water mixture as a function of water mass fraction in liquid phase at 340 K, a representative interface surface temperature predicted by the model.

Benchmark Database for Input and Validation of Multiphase Combustion Models

John F. Widmann, S. Rao Charagundla, and Cary Presser
widmann@nist.gov, scharagundla@nist.gov, cpresser@nist.gov
National Institute of Standards and Technology
100 Bureau Drive, Stop 8360
Gaithersburg, MD 20899-8360

Introduction

Control of process efficiency and the formation of species byproducts from industrial thermal oxidation systems (e.g., power generation and treatment of liquid chemical wastes), is generally based on *a priori* knowledge of the input stream physical and chemical properties, desired stoichiometric conditions, and monitoring of a few major chemical species in the exhaust. Optimization of the performance of these systems is relying increasingly on computational models and simulations that help provide relevant process information in a cost-effective manner.

Although computational fluid dynamics (CFD) offers a cost-effective alternative to experiments, the accuracy of the CFD model must first be assured. This should be accomplished in two ways: verification and validation. Verification involves ensuring that the algebraic and differential equations within the model have been accurately solved. In addition to verifying that the numerical code arrives at the correct solution, it is also necessary to determine if the chosen model accurately represents the physical process of interest. This is the validation step. The objective of this paper is to provide benchmark experimental data for CFD model and submodel validation.

This paper presents data obtained from a baseline spray flame within the reference spray combustion facility at NIST. The spray data presented were collected non-intrusively using phase Doppler interferometry (PDI). The size and velocity distributions of the fuel droplets, droplet number density, and volume flux of fuel droplets within the spray have been obtained. The enclosed combustion chamber provides well-characterized boundary conditions, and wall and ceiling temperature profiles have been measured. Gas temperature and species measurements obtained at the reactor exit can be used for boundary conditions or validation of computational results. The inlet combustion air has been characterized using a 3-D CFD simulation to determine the velocity and turbulence intensity profiles, and the simulation has been validated with experimental data. Gas-phase velocity, temperature, and heat flux measurements are planned for completing this baseline case.

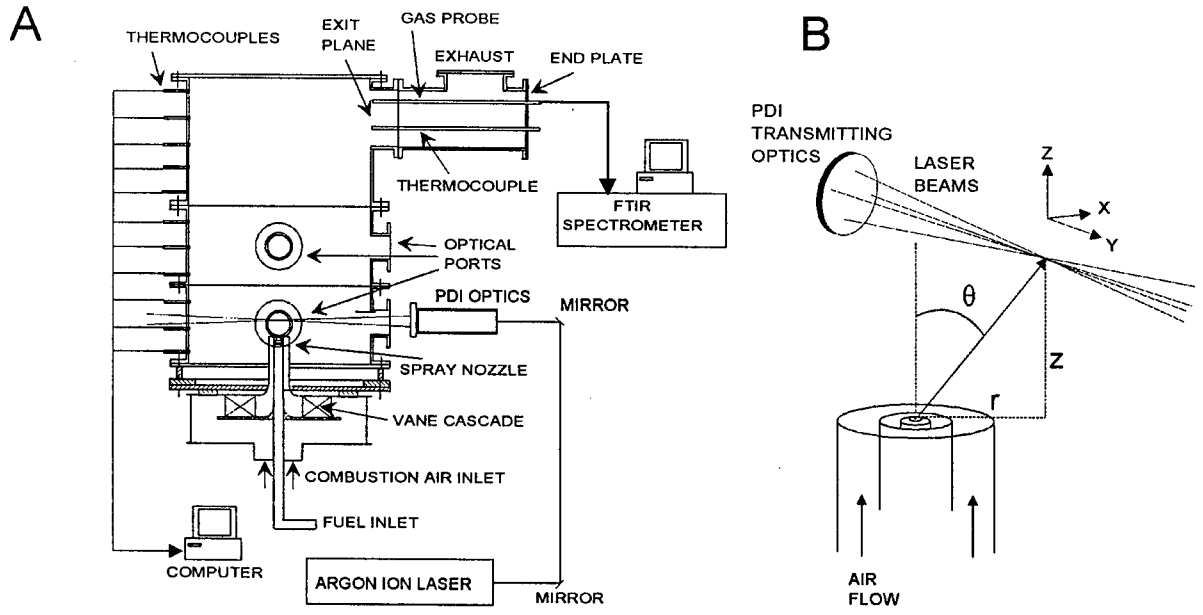


Figure 1. Schematic of (A) the reference spray combustion facility and (B) the nozzle used to generate the spray.

Baseline Case

Spray Combustion Reactor

Experiments were conducted in an enclosed spray combustion facility, shown in Fig. 1A. The experimental facility includes a swirl burner with a movable 12-vane swirl cascade. The cascade is adjusted to impart the desired degree of swirl intensity to the combustion air stream that passes through a 0.10 m diameter passage and coflows around the fuel nozzle. The swirl intensity is a measure of the angular momentum of the combustion air. It is characterized by the swirl number, S, defined as the ratio of the axial flux of angular momentum to the axial flux of linear momentum (Gupta *et al.*, 1984). The vane angle and combustion air flow rate were $50° \pm 2°$ and 56.7 ± 1.7 m^3 h^{-1}, respectively. Recent CFD modeling of the burner results in a swirl number of S = 0.53.

Figure 1B presents a close-up view of the burner and nozzle. The liquid fuel flows through a pressure-jet nozzle and forms a hollow-cone spray with a nominal 60° full cone angle. Methanol was used for these experiments, and the flow rate was maintained at 3.0 ± 0.02 kg h^{-1}. Methanol was chosen as the fuel because the thermodynamic and kinetic data necessary to model the gas phase combustion are readily available (Afeefy *et al.*, 1998; also available on the World Wide Web at *http://webbook.nist.gov/*). The fuel and combustion air were introduced into the reactor at room temperature. The fuel flow rate, combustion air flow rate, wall temperatures, and exiting gas temperatures were monitored and stored using a computer controlled data acquisition system.

The burner is enclosed within a stainless steel chamber to provide improved reproducibility and control of the spray flame. The chamber height is 1.2 m and the inner diameter is 0.8 m. Several windows provide optical access, and a stepper-motor-driven traversing system translates the entire burner/chamber assembly permitting measurements of spray properties at selected locations downstream of the nozzle. Additional details on the design of the burner are available in the literature (Presser *et al.*, 1994). The relevant dimensions necessary for modeling the facility have been summarized in a NIST internal report (Widmann *et al.*, 1999a). Note that the reactor exit is off-axis, which makes the problem non-axisymmetric.

The spray measurements were made using a two-component phase Doppler interferometer to measure the droplet size and velocity distributions and the spray intensity. The receiving optics were aligned at a 30° scattering angle measured from the direction of propagation of the laser beams, and the transmitting and receiving optics were aligned at the same elevation. Additional details of the optical arrangement are available elsewhere (Presser *et al.*, 1994; Widmann *et al.*, 1999a).

Gas-phase species concentrations were measured using Fourier transform infrared (FTIR) spectroscopy. An FTIR spectrometer equipped with a deuterated triglycene sulfate (DTGS) detector was used for extractive sampling of chemical species in the combustor exhaust. A gas sampling system, consisting of an air-cooled sampling probe, a heated gas line, and a vacuum pump, facilitated the transport of the sample gas extracted from the combustion facility into the single-pass gas cell (10 cm path length) in a continuous manner. The sampling probe was designed to aerodynamically quench chemical reactions occurring within the gasses being sampled. The sampling gas line was also provided with a means for purging.

Operating and Boundary Conditions

The fuel flow rate into the reactor was measured with a turbine meter and maintained at 3.0 ± 0.02 kg h^{-1}. The rotation frequency of the turbine meter was calibrated as a function of methanol flow rate, and the analog voltage signal from the turbine meter was read into the data acquisition sytem and calibrated as a function of the turbine frequency. Combining the calibration uncertainties with the standard deviation obtained from repeated observations yields a combined standard uncertainty of 0.0157 kg h^{-1} for the fuel flow rate.

Thermocouples (K-type) were used to measure the wall temperatures and gas temperatures at the exit of the reactor (Widmann *et al.*, 1999a). The gas temperature at the exit plane of the reactor was measured at the same locations as that of the species concentration data. The combined standard uncertainties for the measurements are 3 °C and 5.5 °C for the wall and gas temperatures, respectively.

The combustion air was delivered through the swirl burner at a rate of 56.7 ± 1.7 m^3 h^{-1}. The flow rate was measured using a 6.35 mm i.d. sonic nozzle for which the manufacturer reports a 3 % uncertainty. This uncertainty is significantly larger than those associated with the calibration of the pressure transducer, the uncertainty of the pressure gauge, or the random errors determined from repeated observations. The operating conditions for the baseline case are summarized in Table 1.

Fuel Type	Methanol
Fuel Flow Rate	3.0 kg h^{-1}
Fuel Temperature	Ambient
Equivalence Ratio	0.3
Air Flow Rate	56.7 m^3 h^{-1}
Air Temperature	Ambient
Vane Angle	50°
Swirl Number	0.49
Flame Standoff Distance	~ 5 mm
Chamber Pressure	Ambient

Table 1. Operating conditions for the baseline case.

Fuel Spray Measurements

Experimental data were collected at seven elevations downstream of the nozzle. Some of these data are presented in Figs. 2 - 4 and are available from the authors in electronic format. The mean axial velocity components of the droplets are presented in Fig. 2, and droplet Sauter mean diameters, D_{32}, are presented in Fig. 3.

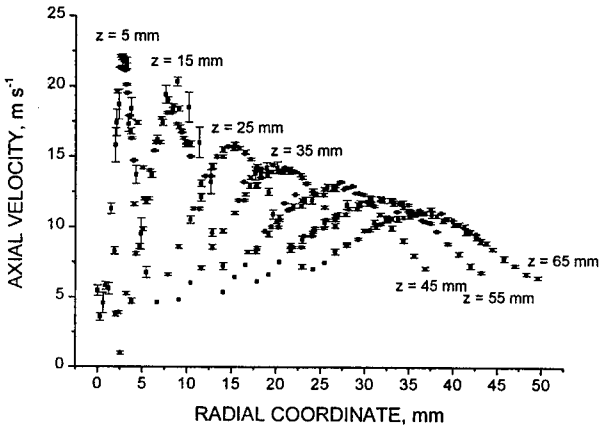


Figure 2. Droplet axial velocity, v_z, at seven axial locations downstream of the nozzle.

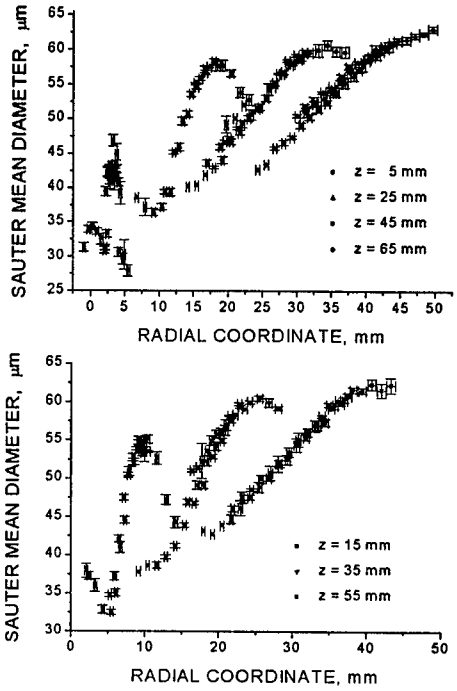


Figure 3. Droplet Sauter mean diameter, D_{32}, at seven axial locations downstream of the nozzle.

Figure 4 presents droplet number densities measured with the PDI at the downstream locations corresponding to data shown in Figs. 2 and 3. The number densities and volume fluxes are corrected for the instrument response time and rejected signals, which is discussed in detail elsewhere (Widmann *et al.*, 1999b). The horizontal error bars express the uncertainty in the radial coordinate, and the vertical error bars correspond to twice the standard error of the mean ($2sn^{-1/2}$). Note that systematic errors associated with the instrument are not included in the figures at this time but should be considered when comparing the data to numerical results. Systematic errors associated with the PDI are discussed elsewhere (Widmann *et al.*, 1999a)

Exhaust Chemical Species Measurements

The absorption spectra obtained with the FTIR spectrometer indicate that combustion was incomplete. Major species identified by the FTIR data include CO_2, CO and CH_3OH. No minor components or reaction intermediates were identified, which is attributed to the short instrument path length. Figure 5 shows the mole fraction of CO_2, CO, and CH_3OH at the exit plane of the reactor. The species concentrations are fairly uniform across the reactor exit plane, suggesting that there is good mixing in this region. Also, the concentration of CO_2 is approximately 50 times greater than that of CO, which indicates that the rate of methanol conversion to CO_2

and H_2O within the reactor is occurring at a rate approximately 50 times faster than the conversion to CO and H_2O.

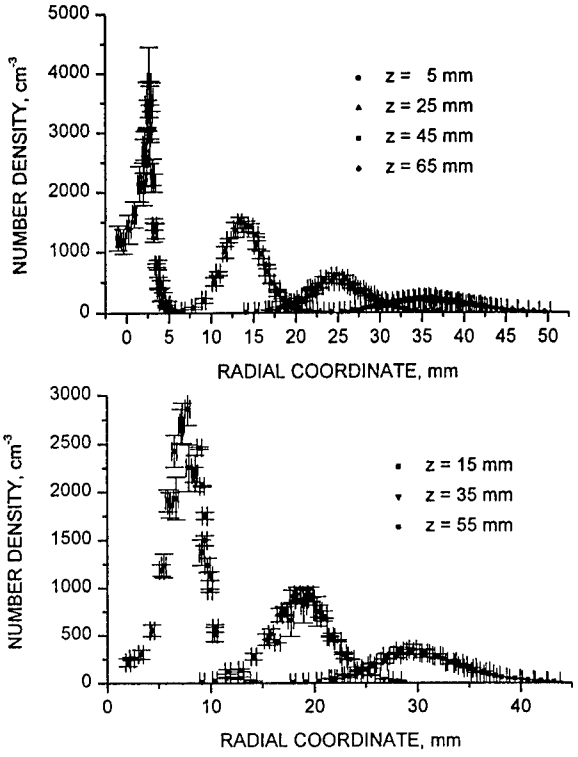


Figure 4. Droplet number density at seven axial locations downstream of the nozzle.

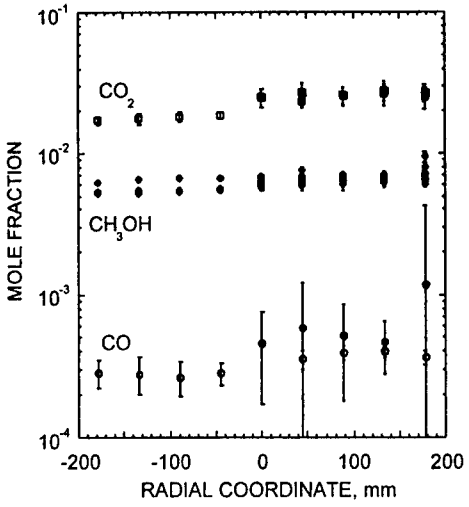


Figure 5. The exit concentrations of various species in the reactor.

Summary

Experimental data were obtained from a reacting methanol spray under well-characterized conditions for the purpose of validating multiphase combustion models and submodels. Droplet size and velocity distributions, number densities, and volume fluxes were measured, and uncertainties in the measurements were estimated. Gas-phase species measurements were made using FTIR spectroscopy, and provide exhaust concentrations of CO, CO_2, and CH_3OH. Wall temperature data are provided, as well as the temperature of the exhaust gas.

References

Afeefy H. Y., Liebman J. F., and Stein S. E., "Neutral Thermochemical Data" in NIST Chemistry WebBook, NIST Standard Reference Database Number 69, Eds. W.G. Mallard and P.J. Linstrom, March 1998, National Institute of Standards and Technology, Gaithersburg MD, 20899.

Gupta, A. K., Lilley, D. G., and Syred, N. (1984). *Swirl Flows*, Abacus Press, Kent, England UK.

Presser, C., Gupta, A. K., Avedisian, C. T., and Semerjian, H. G. (1994). Effect of Dodecanol Content on the Combustion of Methanol Spray Flames. *Atomization and Sprays*. **4**:207-222.

Widmann, J. F., Charagundla, S. R., Presser, C. (1999a). "Benchmark Experimental Database for Multiphase Combustion Model Input and Validation: Baseline Case." National Institute of Standards and Technology Internal Report #6286.

Widmann, J. F., Charagundla, S. R., Presser, C., Yang, G., and Leigh, S. D. (1999b). Analysis of the Sampling Behavior of a Phase Doppler Interferometer, *AIAA 37th Aerospace Sciences Meeting*, January 11-14, 1999. Reno, NV.

EFFECT OF VORTICITY GENERATION ON THE DROPLET DISPERSION OF A HIGH-PRESSURE OUTWARD OPENING INJECTOR

C. Cairoli, A.A. Thaker, and H.K. Chelliah
Department of Mechanical and Aerospace Engineering
University of Virginia, Charlottesville, VA 22903
W. Ren
Induction, Fuel and Emission Component Division
Siemens Automotive, Newport News, VA 23602

Introduction

The traditional spark ignition (SI) engines are very efficient at full loads, with specific fuel consumption marginally higher than indirect-injected compression ignition engines. At part load, however, the SI engine efficiency decreases markedly. One method of improving SI engine at part load efficiency is through the use of a Gasoline Direct Injection (GDI) design. The GDI concept is also expected to reduce the unburnt hydrocarbon and NO_x emission compared to the traditional multi port injection engines. The success of the GDI concept depends largely on the injector performance. There are several types of injectors being developed, including high-pressure swirl injectors and outward opening injectors. The design of these injectors can be facilitated by current computational methods, and the present study is focused on validating such approaches and better understanding the physical phenomena associated with these fuel injector flow fields.

The most important physical phenomenon that needs to be described accurately is the dispersion of fuel droplets generated by the injector. The droplets are typically formed at the edge of the spray cone, and there is an intact core length, which can be characterized by aerodynamic theories [1]. Since the far-field droplet dynamics are found to be insensitive to the near-field liquid core break up process, the near-field droplet dynamics determined independently and provided by Siemens is used in the present investigation on droplet dispersion of an outward opening injector. The droplet dispersion simulations described in the present study are performed using the KIVA-3V code. A brief description of this code and some interesting results on vorticity generation by the droplets and their dispersion phenomena are described below.

Flow Configuration

The in-cylinder dynamics of IC engines are inherently unsteady and turbulent, and involve nonlinear coupling between physical and chemical processes. Consequently, the spatially and temporally evolving fuel spray and fluid flow structures in these engines are extremely complex and sensitive to grid resolution, initial, and boundary conditions. Because of the current computational limitations, the initial computational results reported here are limited to an idealized nonreacting, constant volume chamber at different injector and chamber pressure conditions. The basic premise here is that once the most sensitive physical parameters are identified and accurately modeled, such information can be easily included in a fully reacting engine simulation, subject to the availability of computational resources.

Another important reason for the selection of this simplified geometry is the availability of

experimental data. Siemens Automotive has taken a leading role in compiling experimental data on fuel droplet dispersion as a function of fuel type, injector conditions (eg. pressure, swirl, velocity, cone angle, etc.), chamber pressure, and chamber temperature and is used here to support the present simulations.

Numerical Method

The KIVA family of codes [2-4], with provision for including the two-phase effects, is extensively used in engine flow simulations, including the spray dispersion phenomena. This code solves for either laminar or Reynolds averaged Navier-Stokes equations (RANS), with several options for turbulence submodels. Although the turbulence has an important effect on fluid flow field, and somewhat indirect effect on droplet evaporation, the main focus of this work is on mapping the droplet dispersion phenomena for various injector and chamber pressure conditions assuming a standard two-equation turbulence model. Thus, the predictions reported here may be affected by the accuracy/legitimacy of the turbulence model employed, but the important trends predicted are seen to agree reasonably well with the experiments.

The gas-phase solution procedure of KIVA is based on the finite volume algorithm called the arbitrary Lagrangian-Eulerian (ALE) method [2]. Spatial differences are formed on a finite-difference mesh that subdivides the computational region into a number of small hexahedron cells. The vertices of the cells may be arbitrarily specified functions of time, thereby allowing a Lagrangian, Eulerian or mixed description. The temporal difference scheme used in KIVA is largely implicit. Each time step is divided into two phases - a Lagrangian phase and a rezone phase. In the Lagrangian phase the vertices move with the fluid velocity, and there is no convection across the boundaries. In the rezone phase, the flow field is frozen, the vertices are moved to new user specified positions, and the flow field is remapped or rezoned onto the new computational mesh. This remapping is accomplished by convecting material across the boundaries of the computational cells which are regarded as moving relative to the flow field. The spray model used in KIVA integrates a set of Lagrangian equations for mass, momentum, and energy for a polydisperse system of particles. Unlike the Eulerian description which requires large cell sizes to satisfy the continuum approximation, the Lagrangian equations for droplets do not impose restrictions on the cell size, and thereby can be less diffusive.

Results and Discussion

Experiments performed at Siemens with outward opening injectors have indicated a very interesting dependence of the chamber pressure, the injector cone angle and the injector ring diameter on the droplet dispersion. Furthermore, initial simulations have failed to capture experimentally observed variations of droplet dispersion patterns. This inconsistency between simulations and experiments is found to be directly related to the grid resolution adopted. By accurately resolving the vorticity field, it is shown here that the generation and transport of vorticity affect the droplet dispersion phenomena directly. Recent work by Abraham and others [5] have addressed similar issues related to the adequacy of the grid resolution in predicting Diesel sprays and the subsequent combustion phenomena.

Figure 1 shows the fuel droplet dispersion after 1 msec for a outward opening injector with a ring diameter of 4.4 mm and a cone angle of 90^o. The droplet diameter is assumed to be monodisperse with a diameter of 20 μm. The chamber pressure is at 8.5 bar and a temperature

of 550 K. Under these conditions, the droplets are seen to propagate radially preserving the original spray cone shape. When the ring diameter is reduced to 0.9 mm, with other conditions held the same, the resulting droplet dispersion pattern after 1 msec is shown in Fig. 2. This indicates a significant reduction in the radial penetration of the spray, which is commonly referred to as a collapsed spray. The collapsing of the spray is known to depend on the injector ring diameter, injector cone angle, and chamber pressure.

The underlying cause for the collapse of the spray is related to the fluid flow motion generated by the spray itself. For example, for injector cone angles less than 90^o, a reduction in air entrainment to the core of the spray results in a weaker or stagnant vortical flow structure at the center when compared to that formed outside of the spray. As part of this investigation, it is found that the above described vorticity transport phenomenon is more sensitive to the injector ring diameter than the injector cone angle or chamber pressure. For the two cases shown in Figs. 1 and 2, the corresponding velocity vectors near the injector are shown in Figs. 3 and 4, respectively. It is seen from Fig. 4 that for the 0.9 mm ring diameter condition, the center vortex ring has hardly moved in comparison to the outer vortex ring. All cases where collapsed sprays are observed can be related to such vorticity transport effects.

In order to characterize the possibility of spray collapsing, it is proposed here to utilize the position of the inner and outer vortex ring locations with respect to the injector. Based on the present numerical simulations, the location of two vortex rings as a function of the injector cone angle and the injector ring diameter are shown in Figs. 5 and 6, respectively. For large cone angles and ring diameters, it is seen that the vortex ring locations approach the same distance with respect to the injector origin. Under such conditions, the vorticity on either side of the droplet stream is well balanced with no indication of spray collapsing. In experiments, obtaining such detailed flow field information is possible only through PIV like techniques, but application of these techniques to dense fuel sprays is questionable.

Acknowledgment: This work is supported by Siemens Automotive, Newport News, VA and the Virginia Center for Innovative Technology.

[1] Chehroudi, B., Chen, S.H., Bracco, F.V., and Onuma, Y., "On the Intact Core of Full-Cone Sprays," SAE International Congress and Exposition, Detroit, MI, SAE Paper No. 850125, 1985.

[2] Amsden, A.A., Ramshaw, J.D., O'Rourke, P.J., and Dukowicz, J.K., "KIVA: A Computer Program for Two- and Three-Dimensional Fluid Flows with Chemical Reactions and Fuel Spray, " Report No. LA-10245-MS, Los Alamos National Laboratory, Los Alamos, N.M., 1985.

[3] Amsden, A.A., O'Rourke, P.J., and Butler, T.D., "KIVA-2: A Computer Program for Chemical Reactive Flows with Sprays, " Report No. LA-11560-MS, Los Alamos National Laboratory, Los Alamos, N.M., 1989.

[4] Amsden, A.A. "KIVA-3: A KIVA Program with Block-Structured Mesh for Complex Geometries," Report No. LA-12503-MS, Los Alamos National Laboratory, Los Alamos, N.M., 1993.

[5] Aneja, R. and Abraham, J. *Combust. Sci. Tech.* **138**:233-255 (1998).

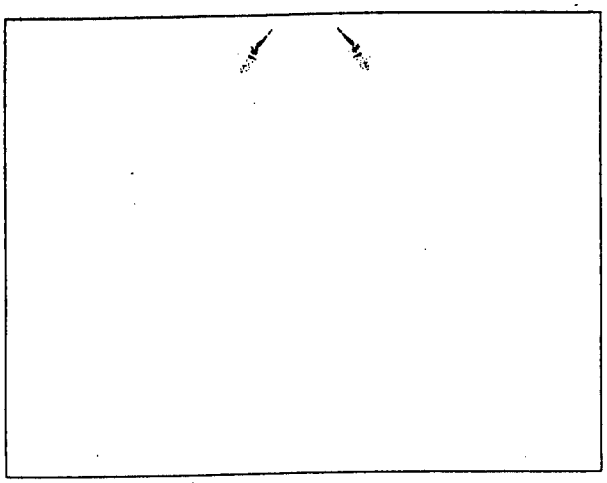


Figure 1: Fuel droplet dispersion for a 4 mm injector ring diameter.

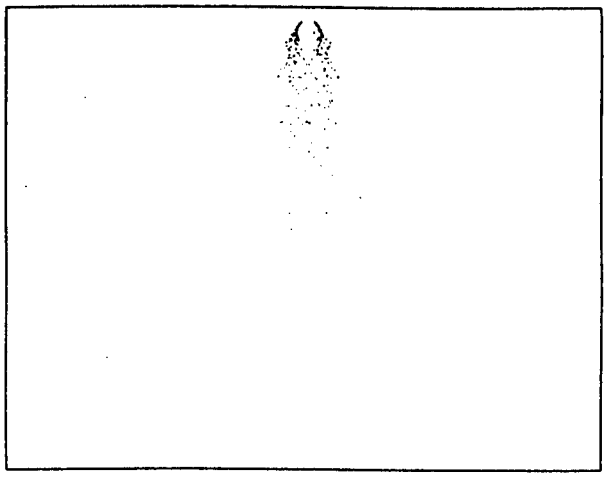


Figure 2: Fuel droplet dispersion for a 0.9 mm injector ring diameter.

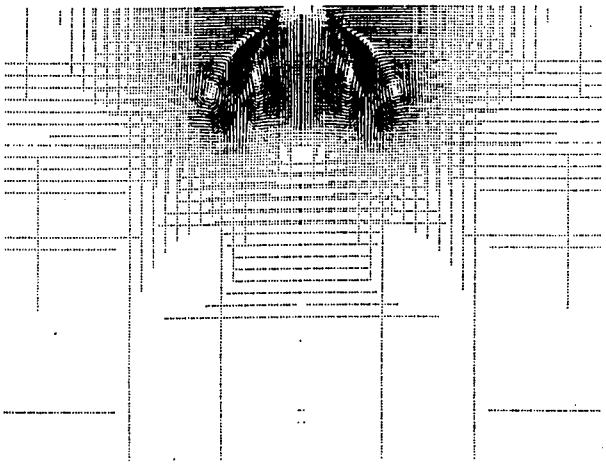


Figure 3: Velocity vector plot for conditions in Fig. 1.

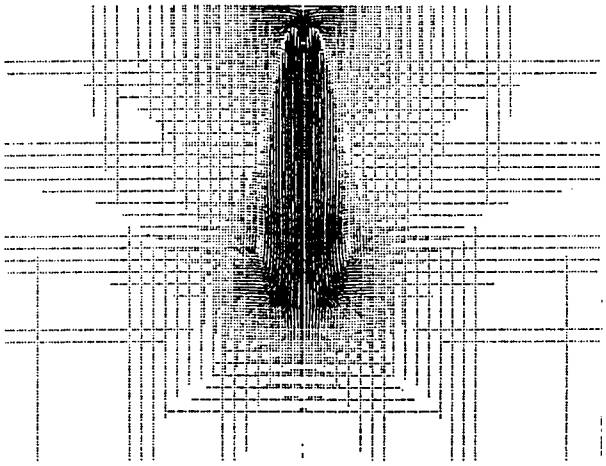


Figure 4: Velocity vector plot for conditions in Fig. 2.

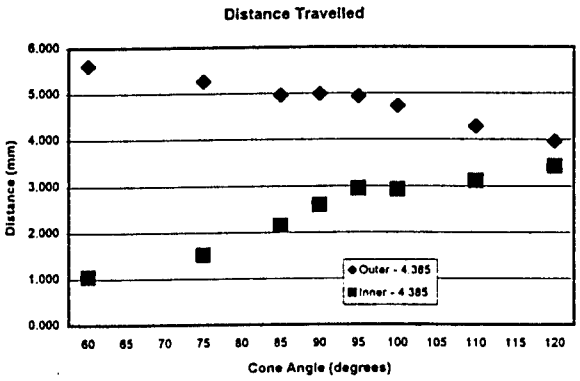


Figure 5: The variation of vortex ring locations vs. injector cone angle.

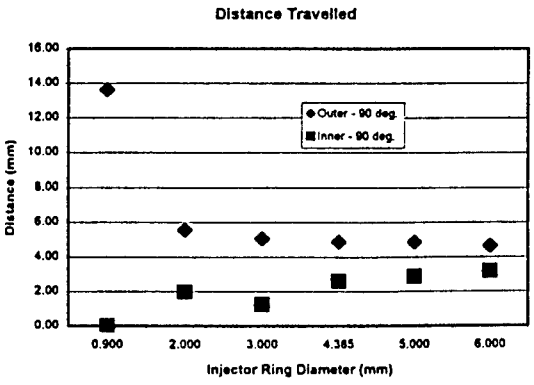


Figure 6: The variation of vortex ring locations vs. injector ring diameter.

Laser Induced Fluorescence Imaging of the Hafnium Monoxide Radical in the Reaction Zone Surrounding Burning Hafnium Metal Droplets

L.F. Ernst, R.A. Yetter, F.L. Dryer
Department of Mechanical and Aerospace Engineering
Princeton University
Princeton NJ 08544

Introduction

Metal powders have long been used to enhance the performance of solid propellants and explosives by increasing flame temperatures. From an energy density standpoint, heavier metals are prohibitive. However, higher molecular weight metals are often acceptable or advantageous in explosives or flares. One particularly energetic metal, Hafnium, exhibits a particularly high adiabatic flame temperature in air (4120K)[1]. The final product of combustion in oxygen, HfO_2, has the highest heat of formation of any oxide (considered on a per oxygen atom basis) at ~1740 kJ/gram-O atom.[2] The objective of the present work is to generate experimental data on the combustion of single Hafnium droplets in oxidizing environments. These data will provide valuable insights into the structure of the reaction zone surrounding burning droplets.

Hafnium has been shown previously to burn with a detached "zone of oxide condensation and/or heterogeneous reaction" [3] when burned in pure O_2 ($P \leq 1$ atm.) As the boiling point of the final product oxide is possibly over 5700K [4], this zone is most likely where gaseous suboxide HfO is fully oxidized to form HfO_2. HfO_2 is also present at the surface of burning droplets (as has been seen observed here) in the form of a thick oxide coat on particles quenched during combustion in air and O_2. Thus, the HfO reacting in the detached zone has diffused through the surface oxide coat, and likely the flux diminishes as the coat thickens. The detached region is not visible over the entire lifetime of a burning particle, but is present for differing amounts of time after ignition depending on the composition and pressure of the oxidative environment. This zone has a very well defined edge, as illustrated in the flashlamp backlit image of Figure 1, a hafnium droplet, initially 210 μm diameter, burning in air at 1 atmosphere, 49 msec after ignition.

The present work, described herein, uses laser induced fluorescence (LIF) to image the gas phase HfO radical between the outer surface of the surface oxide coat and the detached reaction zone. (The gaseous intermediate radical AlO, present in the combustion of aluminum in oxidative environments has been imaged by LIF previously.[6]) The literature on the electronic spectra of HfO is not at all as developed as that of AlO. However, sufficient information was available to identify a strong system conducive to LIF. The $D^1\Pi$-$X^1\Sigma+$ system with (0,0) Q branch bandhead at 425.475 nm was excited, and (0,1) fluorescence around 443 nm was observed. This system was chosen due to the fact that the longer wavelength A-X and B-X systems have been determined to be only weakly allowed singlet-triplet transitions (formerly misidentified in the Vatican Atlas[8] as singlet-singlet transitions, hence the unfortunate capital letter designation remains), and the C-X system lies in the infrared[7].

A brief description of the experimental apparatus, spectroscopic background, and initial observations on the imaging of the HfO for hafnium burning in O_2 is given below.

Experimental Approach

By using an adaptation of the experimental metal droplet generation technique of Bucher, et al.[5] droplets of burning hafnium have been produced. This method was previously conducive to the creation of droplets of soft metals from small diameter wires of the pure elements, but was redesigned to accommodate feedstock of harder metals (i.e. Hf and W.) This revised method produces burning spheres of the desired metal by shearing wire of 0.005" diameter into small cylinders with tungsten carbide blades, and subsequently feeding the cylinders into the path of a CW CO_2 heating laser (10.6 μm.) The heating laser melts single cylinders, and the metal then contracts into a sphere by surface tension, and is subsequently ignited by additional residence in the laser beam. Ignited particles then fall downward through a square cross-section windowed duct, in a co-flowing stream of oxidizer. Flow Reynolds numbers are on the order of 0.1. The duct apparatus is shown in Figure 2.

The windowed duct provides optical access for cameras, photodiodes, and PMTs to observe the combustion process. Typically for a particle being studied with LIF imaging, LIF signal images are recorded by an intensified, fast shuttered (≤20 nsec.) CCD camera (Princeton Instruments ICCD 576-G/RB) through appropriate spectral filters, and by an open shuttered standard CCD camera (TI TC-241 based) through neutral density filters and an optical chopper. Both cameras are computer controlled and use Nikkor F optics. Natural luminous intensity is recorded over the length of the combustion period by a PMT (Thorn EMI 9635B) through neutral density filters. A computer based data acquisition system logs PMT output and optical chopper slot location. LIF excitation is provided by the output beam of a Nd:YAG 355nm pumped dye laser system (Continuum PL8000/ND6000, 1 cm^{-1} linewidth, S-420 dye). Precision delay generators (SRS 545) control experiment timing.

The dye laser system was calibrated so that the wavelength generated matched the desired transition to be pumped. This calibration was done by generating HfO, pumping, and observing the LIF signal from the HfO as the wavelength of the laser was tuned. The general location of a transition can be located within a window of an angstrom of where it would be expected from the published constants[10] (for the D-X (0,0) Q bandhead, the laser was short by 0.7 angstroms.) The HfO used to calibrate the laser in this experiment was obtained by a technique not previously seen in the literature. A solid slab of sintered HfO_2 99.95% pure (Cerac Inc., Milwaukee WI) was laser ablated perpendicular to the surface by a tightly focused (0.2 mm diameter) 70 mJ pulse (532 nm, 10 nsec FWHM) from another doubled Nd:YAG laser (also Continuum PL8000) in a glass jar of air at 10 Torr. The resultant ablation locally heated the HfO_2 to the point of vaporization, and subsequently, dissociation to HfO + O. With the lasers available, this method is far easier than the method of Kalendin, et. al. where HfO_2 powder was resistively heated to 2300-2600K under argon at 5 Torr to produce HfO. In the current method, once created, the HfO diffuses outward from the point of initial creation, and given ~800 nsec forms a strong plume. This plume was then pumped by the unexpanded beam of the dye laser, and HfO fluorescence of the D-X (0,1) system viewed by ICCD through a narrow band interference filter (Melles Griot 03FLR007, centered at 441.6 nm, 4 nm FWHM). A wavelength-selected fluorescence excitation spectra (WSFES) was taken of the (0,0) system (Figure 3.) The dye laser was not narrow enough to reveal clear rotational structure, but the spectra was clear enough for identification of the Q branch bandhead with the assistance of a Fortrat plot (Figure 4) from published constants.[10]

For the experiments on burning droplets, the pumping laser was tuned to the wavelength of the bandhead found by the WSFES, and the pump laser beam (~3/16" diameter) was directed to cross the path of the falling burning particle. The delay generators were set such that the pumping laser would fire as the

particle was totally within the cross section of the pump beam. Proper particle location within the pumping beam was later confirmed on a particle by particle basis by inspection of the image taken with the chopped CCD camera. As scattering of the pump laser was found to be strong off of the condensed phase products, additional blocking was provided for the ICCD by a piece of long-pass filter glass (Shott GG 435) with the cutoff strategically placed between the 425.475nm pump and the passband of the interference filter around 441 nm. Particles initially ~190μm diameter were burned in 100% O_2, 745 Torr, flowing at 50 SCCM. LIF images were taken 38.5 msec after the start of the initial heating laser.

Results and Discussion

Figures 5 a, b, c, and d are typical of burning particles, and respectively show the PMT luminosity trace, chopped CCD image, HfO LIF image, and an enlarged zoom of the nearest (in time) particle shown in the chopped CCD image to the LIF image. Each is for the same particle burning as described above. The chopper exposes the CCD every 1/600 of a second, hence the series of images as the particle travels downward in the field of view of the CCD. The spike in the PMT trace at 38.5 msec is the flash of the LIF pumping laser. The large spike at 54 msec marks the conclusion of the burning of the hafnium particle where it explodes to form a bubble of HfO_2, as zirconium has been seen to do in a 100% O_2 combustion environment.[11] This explosion was observed to be preceded by a radial inward collapse of the outer reaction zone.

The LIF image is quite strong, and the envelope of the LIF image matches the envelope of the bright ring seen in the chopped CCD image. This appears to corroborate the idea that the void between the surface coating of oxide and the visible ring indeed contains the gaseous lower oxide, which will fully oxidize in the outer region.

This LIF imaging technique is particularly well suited to droplet combustion, due to the spherical symmetry of the system. Able inversion techniques have been successfully applied to deconvolve radial distributions of AlO in aluminum/oxidizer systems.[6] This technique can also be applied with HfO for the analysis of the LIF images taken in the current work. This will provide useful data for development of future practical models of hafnium combustion in oxidative environments.

Acknowledgements

This work was supported by the Office of Naval Research under contract N00014-96-1-1152. The authors gratefully acknowledge the support of Dr. Judah Goldwasser at ONR.

References

1. Hertzberg, M., Zlochower, I.A., and Cashdollar, K.L., Twenty-Fourth Symposium (International) on Combustion, The Combustion Institute, Pittsburgh PA, pp.1827-1835
2. Chernogorenko, V.B. and Lynchak, K.A., Combustion, Explosion, and Shock Waves, Vol. 34, 1998, pp. 298-304
3. Marshall, R.L. and Cross, C.W., Western States Section of the Combustion Institute, Paper WSS/CI 70-14, 1970
4. Lide, D.R. ed., CRC Handbook of Chemistry and Physics, 74th edition, 1993
5. Bucher, P., Yetter, R.A., and Dryer, F.L., Proceedings of the Technical Meeting, The Eastern States Section of the Combustion Institute, Clearwater Beach FL, December 1994

6. Bucher, P., Yetter, R.A., and Dryer, F.L., Proceedings of the 34th JANNAF Combustion Subcommittee Meeting, October 27-31, 1997
7. Wentink, T. and Spindler, R.J., J. Quant. Spectrosc. Radiat. Transfer, Vol. 12, 1972, pp.1569-1590
8. Gatterer, A. et. al., Molecular Spectra of Metallic Oxides, Specola Vaticana, Vatican City, 1957
9. Kalendin, L.A., McCord, J.E., and Heaven, M.C., J. Mol. Spec., Vol 173, 1995, pp.37-43
10. Huber, K.P. and Herzberg, G., Constants of Diatomic Molecules, Van Nostrand, New York, 1979
11. Brzustowski, T.A. and Glassman, I., Princeton University Aeronautical Engineering Lab Report No. 586, October 1961

Figures

Figure 1. Backlit image of Hf droplet burinng in air. (Scale is 100 μm per division)



Figure 2. Droplet generator / combustion duct.

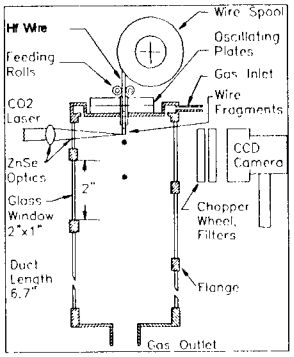


Figure 5b. Chopped CCD image.

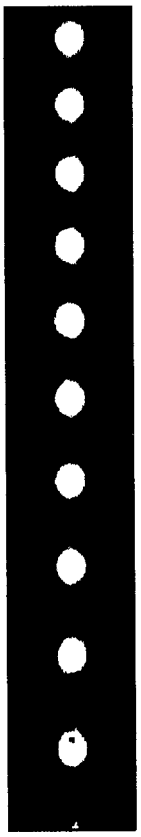


Figure 3. WSFES of D-X (0,0), wavelength as indicated by dye laser readout.

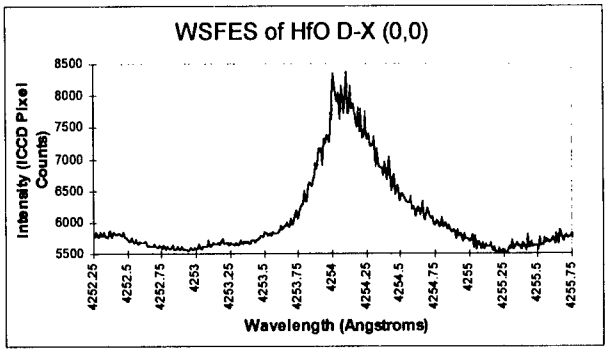


Figure 4. D-X (0,0) Fortrat plot, from constants in Ref. 10.

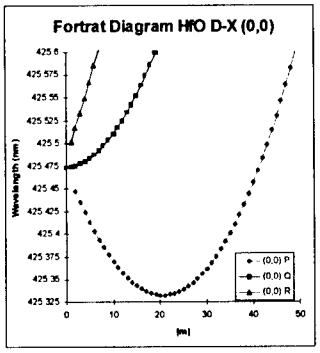


Figure 5a. PMT Trace of burning Hf droplet.

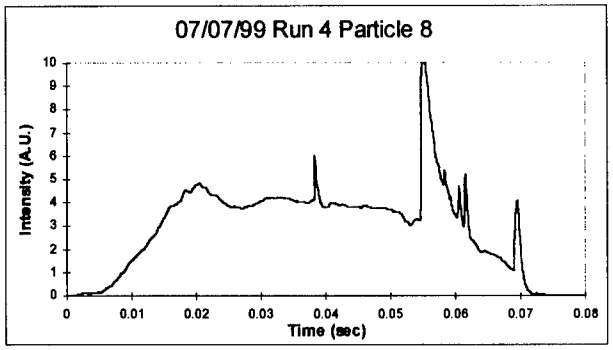


Figure 5c. LIF image of burning droplet.

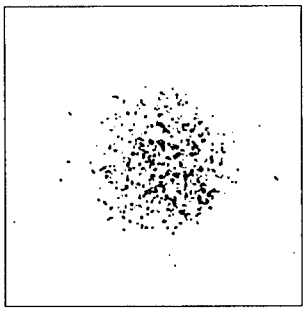
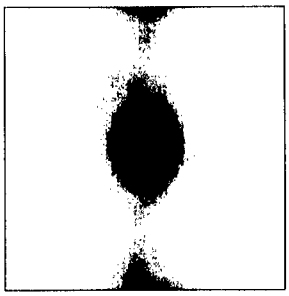


Figure 5d. Zoomed CCD, inverted for clarity.



COMBUSTION OF BORON BY $O_2/NF_3/N_2$ OXIDIZERS

D. G. Keil, E. L. Dreizin, and V. K. Hoffman
AeroChem Research Laboratory, Titan Corporation
Princeton, NJ

H.F. Calcote
ChemIon, Inc.
Princeton, NJ

ABSTRACT

Boron has attracted interest as a fuel for propellant and explosive applications because of its high specific enthalpy of combustion, but its poor combustion properties (ignition times, burning rates, realized energy release) have limited its acceptance and use in practice. Much of the poor performance has been attributed to the condensed phase product, B_2O_3 [1]. Nearly forty years ago it was proposed that boron combustion could be enhanced using fluorinated oxidizers so as to produce predominantly gas phase products. Subsequent experiments demonstrated that volatile BF species were the initial products of the combustion of boron rods in fluorine [2]. It has been predicted that addition of a fluorine-based oxidizer to oxygen-based oxidizers could have a combustion enhancing synergistic effect through energetic formation of the mixed OBF gas phase product [3]. We report here experiments which have demonstrated a synergistic effect on the combustion of boron aerosol clouds in oxidizers consisting of oxygen and nitrogen trifluoride mixtures [4].

EXPERIMENTAL: The constant volume combustion of boron aerosols in different oxidizing atmospheres was characterized by recorded pressure-time curves. Weighed charges of amorphous boron powder with an elemental purity greater than 96% and particle size of about 1 μm (SB Boron Corp., Franklin Park, IL) were swept into a 20 L modified Hartmann apparatus by a pulse of oxidizer from a high pressure resevoir, and, after a short delay, the resultant aerosol ignited with a wire filament heated with a 100 J current pulse. The Hartmann apparatus and the procedure are similar to those used at the US Bureau of Mines (USBM) to characterize explosibility of different materials. [5,6] In this work various $O_2/NF_3/(79\ \%)N_2$ oxidizing mixtures ranging from pure air to 21 % NF_3 in N_2 were used. Boron concentrations were varied from 0.05 to 2.0 g/L, ranging from fuel lean to fuel rich conditions in the aerosol.

The explosions were characterized by the maximum explosion pressure, the maximum rate of pressure increase and the times after ignition at which these are obtained. The ratio of the maximum pressure, P_{max}, to the initial pressure, P_0, when compared to thermodynamic equilibrium values is a measure of the efficiency of the combustion, i.e., the approach to thermodynamic equilibrium products. The maximum rate of pressure increase, $(dP/dt)_{max}$ is a direct measure of the rate of burning.

STOICHIOMETRY:

To compute an effective equivalence ratio for the mixed oxidizer experiments, the following two stoichiometric reactions are considered:

$$B + 0.75\,O_2 \rightarrow 0.5\,B_2O_3 \quad \text{(R1)}$$
$$B + NF_3 \rightarrow BF_3 + 0.5\,N_2 \quad \text{(R2)}$$

The equivalence ratio, ϕ, of the mixture is defined as the ratio of the number of moles of boron present in the experiment (N_{boron}) to the number of moles of boron that would theoretically be oxidized according to the stoichiometries of R1 and R2 ($N_{NF3} + 1.333\,N_{O2}$):

$$\varphi = \frac{N_{boron}}{N_{NF_3} + 1.333 N_{O_2}} \quad \textbf{(1)}$$

reflecting the differing moles of NF_3 and O_2 required for Reactions 1 and 2.

In all mixtures, 79 (mol) % of the gas mixture is N_2. All the oxidizer combinations are defined by the relative percentages of O_2 and NF_3. To do this, a function was chosen which is symmetrical around zero:

$$\chi \equiv [P_{NF_3} - P_{O_2}]/[P_{NF_3} + P_{O_2}] \quad (2)$$

where P is the (partial) pressure of the component gas. The values of χ range from -1 for pure air to +1 for pure NF_3/N_2 oxidizer.

THERMODYNAMIC EQUILIBRIUM PREDICTIONS:

Adiabatic constant volume equilibrium products, pressures and temperatures were calculated using the STANJAN code, an interactive program for chemical equilibrium analysis by the method of element potentials developed by Prof. W. C. Reynolds, Dept. of Mechanical Engineering, Stanford University. For the present calculations, Vers 3.51 dated 7/18/86 was used. which only handles 20 major species. The species considered were selected based on constant pressure equilibrium calculations using the ISP Thermodynamic Equilibrium Code, developed by C. Selph and R. Hall, Air Force Astronautics Laboratory, Edwards AFB, CA. equilibrium code with over 50 B/O/F/N gas phase and condensed phase species. The oxidizer dependence of the calculated equilibrium product distributions and the adiabatic flame temperature for a fixed boron powder concentration close to $\phi = 1$ is illustrated in Fig. 1. This illustrates the effects of oxidizer composition on the equilibrium properties.

BORON CLOUD EXPLOSION RESULTS: At the lowest boron concentration (0.05 g/L) ignition was observed only in mixed oxidizers with $|\chi| \geq 0.7$. At higher boron concentrations ignition was observed in all oxidizers with a minimum fraction of NF_3, $\chi \geq -0.7$. Experimental maximum pressure ratios (P_{max}/P_0)during the combustion of near stoichiometric boron clouds (0.1 g/L) in various oxidizers are compared in Fig. 2 with calculated constant volume adiabatic equilibrium values of the same ratio. With air as the oxidizer ($\chi = -1$), ignition was not observed with the current 100 J igniter energy. Hertzberg et. al.at USBM found that similar concentration clouds did not ignite except at much higher 5000 J ignition energies [6]. Fig. 2 shows that replacing a small fraction of the O_2 with NF_3 ($\chi > -0.7$) leads to ignition at 100 J. At all higher fractions of NF_3, combustion was observed, but the maximum pressures were lower than the

predicted equilibrium values. The ratio of experimental pressure ratios maximize at positive χ values and drop to less than 0.5 in NF3 oxidizer ($\chi = 1$). The highest values were observed in mixed oxidizers. For $\phi > 1$ (boron concentrations of 0.15 to 0.2 g/L), the experimental pressure ratios in the fluorinated oxidizers including NF_3 ($\chi = 1$) approach closer to the calculated equilibrium values.

Fig. 3 illustrates the oxidizer effect on the maximum rate of pressure rise in $\phi \approx 1$ (0.1 g/L boron) aerosols. For combustion in air ($\chi = 1$), the highest maximum rate of pressure rise from USBM experiments (inferred from reported Staub numbers, [6]) using 2500 J ignition energies and occurring in aerosols with much higher boron concentrations is indicated for reference. It represents the fastest (rich) boron/air aerosol combustion. The rates of pressure rise increase dramatically with increasing NF_3 in the oxidizer. Similar to the maximum pressures, Fig. 2, the values for NF_3 oxidizer are lower than for the NF_3-rich mixed oxidizers. The maximum pressure rise rates in boron-rich (> 0.1 g/L) aerosols monotonically increase with increasing oxidizer NF_3 content (χ), paralleling the pressure ratio trends in the same aerosols.

DISCUSSION: Both the maximum pressure ratios and rates of pressure rise in the near stoichiometric aerosols (Figs. 2 and 3) show decreased values in NF_3 ($\chi = -1$) compared with mixed oxidizers. In addition, no ignition is observed in the O_2-dominated oxidizer mixtures. The equilibrium calculations provide insight into the synergy between the two oxidizer components. Calculated adiabatic flame temperatures, Fig. 1, decrease with increasing oxygen content in the oxidizer, minimizing for the case of air. This trend is consistent with the failure of the aerosols in air to ignite. This argument is not convincing for the NF_3-rich oxidizers, and may not fully explain the O_2-rich obserbations. The rates and pressures are highest for the mixed oxidizers, even though the adiabatic flame temperature is nearly independent of χ in the region near NF3 ($\chi = 1$). The chemistry provides an explanation of the mixed oxidizer effect. Over much of the mixed oxidizer compositions, the major equilibrium product is gas phase OBF species. For the oxygen-free NF_3 oxidizer, the fluorinated species F, BF_2, and BF_3 dominate. In air, condensed phase B_2O_3, a species which is believed to inhibit the combustion processes, is the major product. With a little fluorine ($\chi \approx -0.7$), OBF is predicted, yet even in this case a significant mole fraction is B_2O_3 is predicted. Experimental results for other boron concentrations when compared with equilbrium calculations are consistent with the identified synergistic effects in the mixed oxidizers.

ACKNOWLEDGEMENTS: The authors thank Carl Gotzmer and Dr. Richard Miller for their helpful discussions and contributions to this effort. This work was performed under Contract No. N00024-96-C-4149 with PEO-TAD, Naval Sea Systems Command, Arlington, VA.

REFERENCES:

1. King, M..K., in *Combustion of Boron-Based Solid Propellants and Solid Fuels* (K.K. Kuo, and R. Pein, Eds.), CRC Press, Boca Raton (1993), p. 1.
2. Talley, C.P., "Combustion of Elemental Boron," *Texaco Experiment Incorporated TM-1326, TM-1384*, (1962)
3. Brown, R.C., Kolb, C.E., Yetter, R.A., Dryer, F.L., and Rabitz, H., *Combust. Flame* 101, 221 (1995)
4. Keil, D.G., Dreizin, E. L., Hoffman, V. K., and Calcote, H. F., *CPIA Publication 662, Vol. IV*, pp. 237-245, 34th JANNAF Combustion Subcommittee Meeting (1997).
5. Cashdollar, K.L. and Hertzberg, M., *Rev. Sci. Instr.* 56, 596 (1985)
6. Hertzberg, K.L., Zlochower, I.A., and Cashdollar, K.L., *Twenty-Fourth Symposium (Int'l) on Combustion*, The Combustion Institute, Pittsburgh (1992), p. 1827

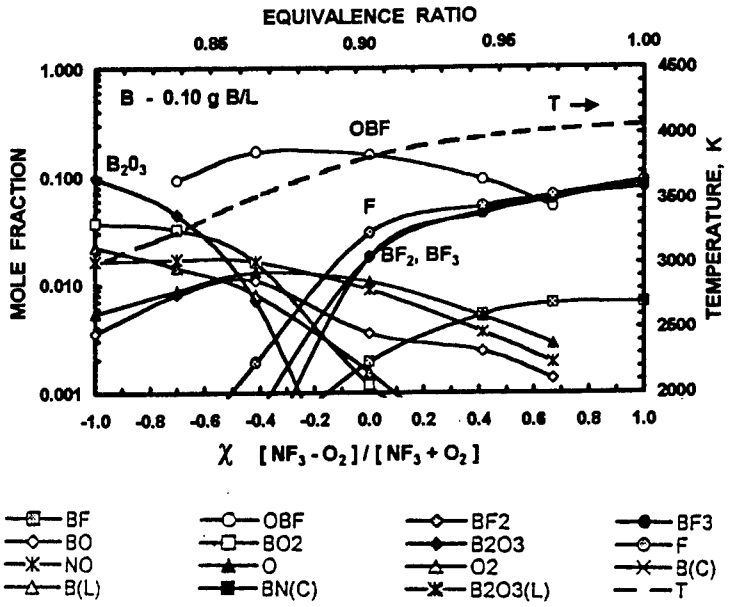


Fig 1. CALCULATED TEMPERATURES AND PRODUCT SPECIES FOR CONDITIONS IN FIGS. 2,3

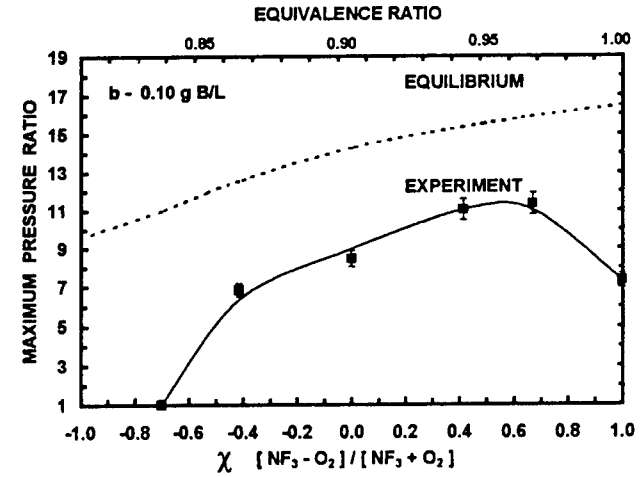


Fig. 2 OXIDIZER EFFECT ON MAXIMUM PRESSURE RATIO IN NEAR STOICHIOMETRIC BORON CLOUD EXPLOSIONS 0.1 g/L boron concentration. Dashed line: calculated for adiabatic thermodynamic equilibrium. Symbols: experiment

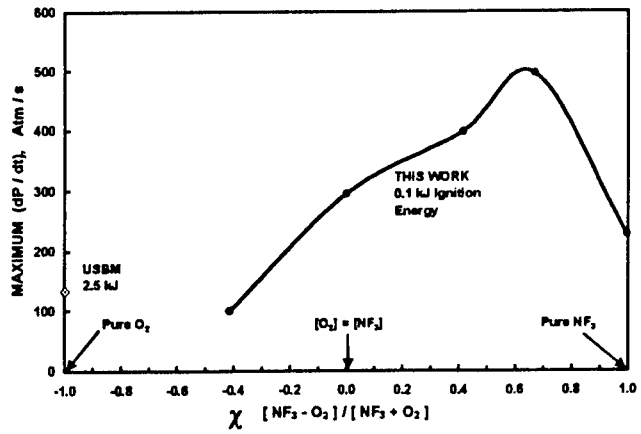


Fig. 3 OXIDIZER EFFECT ON MAXIMUM PRESSURE RATE OF INCREASE IN NEAR STOICHIOMETRIC BORON CLOUD EXPLOSIONS 0.1 g/L boron concentration. USBM:

NUMERICAL STUDY OF THE IMPACT OF COLLISIONS ON PARTICLE DISPERSION IN A SHEAR LAYER.

Marios C. Soteriou and John H. Mosley
Department of Mechanical Engineering
University of Connecticut, U-139, Storrs, CT 06269-3139
email: marios@engr.uconn.edu

The numerical simulation of disperse, particle laden shear flows via the solution of the un-averaged equations of motion, and the absence of phenomenological models, has been the subject of a number of studies in the recent past [1,2]. In these studies, the evolution of the dispersed phase is computed in a Lagrangian fashion by determining the trajectories of individual (or groups of) particles. For the evolution of the continuous fluid phase, on the other hand, Eulerian as well as Lagrangian numerical models have been used.

Early studies considered the two phase flow in the dilute mixture limit in which 'one-way coupling' between the two phases is assumed to exist. In this, the impact of the dispersed phase on the continuous phase is neglected. So are the interactions between particles. More recently, studies have appeared in which the particle phase is allowed to influence the continuous phase [e.g. 3,4]. Typically it is found that the mass-fraction of the particles must be ~0.5 for any effects on the fluid phase to be discernible[1]. Assuming that the particle density is of the order of 10^3Kg/m^3 this implies volume fractions of the order of 10^{-3}-10^{-4}.

In these two-way coupling studies, however, particle-particle interactions are still neglected. There has been only qualitative justification for this [2]. In this work, this assumption is questioned by performing simulations in which collisions between particles are accounted for. It is hoped that this research will: (i) shed light on the impact of collisions in this flow, and (ii) will help in the development of more sophisticated models for these flows.

Methodology

The motion in a two-dimensional, partially confined high Reynolds number shear layer is considered. The continuous phase is of uniform density The particle loading is assumed to be low, i.e. the two phase mixture is in the dilute regime, so that the presence of the particles does not influence the fluid motion. Particle interactions, however, are accounted for. The approach is one in which simulations at very low but incrementally increasing particle volume fraction are performed. The validity of the dilute assumption is assessed per simulation. Under these assumptions, the evolution of the fluid phase is described by the uniform density continuity and Navier-Stokes equations. In this work these equations are transformed in non-primitive form by introducing the Helmholtz decomposition to spit the velocity field, $\mathbf{u}$, into rotational, $\mathbf{u_{rot}}$, and potential, $\mathbf{u_{pot}}$, parts and using the vorticity $\omega = \omega\hat{\mathbf{k}} = \nabla \mathbf{x} \mathbf{u}$ to capture the evolution of rotational field, i.e.

$$\mathbf{u} = \mathbf{u_{pot}} + \mathbf{u}_{\omega} \tag{1}$$

$$\mathbf{u_{pot}} = \nabla\phi \qquad \nabla^2\phi = 0 \tag{2a,b}$$

$$\mathbf{u_{rot}} = \nabla \mathbf{x} (\psi\hat{\mathbf{k}}) \qquad \nabla^2\psi = -\omega \tag{3a,b}$$

$$\frac{D\omega}{Dt} = \frac{1}{Re}\nabla^2\omega \tag{4}$$

where ∇ is the gradient operator, D/Dt is the material derivative, $\hat{\mathbf{k}}$ is the unit vector normal to the plane of motion, t is the time, ϕ is the velocity potential, ψ the streamfunction, and Re is the Reynolds number. An errorfunction inlet profile is assumed for the velocity in order to approximate the experimentally observed flow downstream of the splitter plate. The confining walls are assumed to be slip, impermeable planes.

The evolution of the particle field is accomplished by determining the Lagrangian motion of individual spherical particles. This involves establishing particle paths, χ_p, by integrating

$$\frac{d\chi_p}{dt} = \mathbf{v_p} \tag{5}$$

where $\mathbf{v_p}$ is the particle velocity. This velocity is obtained from an equation of motion which implies that the particle motion is controlled by a balance between the inertia and drag forces:

$$\frac{d\mathbf{v_p}}{dt} = F\,(\mathbf{u_p} - \mathbf{v_p}) \tag{6}$$

where $\mathbf{u_p}$ is the fluid velocity at the particle location which, as noted, is not affected by the presence of the particles even when these particles experience collisions, and $F = \tau_f/\tau_p$, with τ_f being the flow time-scale and τ_p the particle 'aerodynamic' response time. When the particle local Reynolds number is very low, Stokes flow persists in the vicinity of the particle. Consequently, $\tau_p=\rho_p d^2/18\mu$ where ρ_p and d are the particle density and diameter, respectively, and μ the fluid viscosity, and F=1/St where St is the Stokes number. Particles are introduced throughout the inlet of the channel, i.e. both fluid streams are filled with particles at a homogenous volume fraction.

Two main collision scenaria are considered. In the first, (scenario I) the collision has no impact on the particles. In this scenario a log of collisions is simply kept in order to provide a measure of the frequency of the phenomenon as well as to provide a reference value for other scenaria to be considered. In the second scenario (scenario II) particles are assumed to coagulate upon impact to form a larger spherical particle. Future research is to include a third scenario in which particles are to experience elastic collisions. It is recognized that these scenaria are not all inclusive and that phenomena such as fragmentation and inelastic bounce are not captured. The objective of this research, however, is not to provide a comprehensive description of the collision dynamics in this flow. Rather, it is expected to provide a measure of the importance of these collisions to the accurate determination of the evolution of the dispersed phase.

The numerical solution of the non-primitive variable flow equations is accomplished by the Vortex Element Method. In this, the vorticity is discretised over a field of Lagrangian elements each of which is associated with a finite strength, an area, and a local distribution function. The velocity field is obtained via a desingularized Biot-Savart convolution over the field of elements. The evolution of the flow field in time is accomplished by integrating the vorticity equation, locally for each element. This integration is accomplished in two fractional steps. In the first step, the convective step, elements are advected with the local velocity vector while their vorticity is kept constant. In the second integration step, the diffusion step, diffusion effects are simulated using a core expansion scheme which mimics the diffusion process by expanding the element core size. The severe distortion of the flowmap often witnessed in shear flows, which results in increased distance between neighboring elements, may lead to a deterioration of the solution accuracy. To overcome this problem, a scheme of local mesh refinement is adopted, based on local conservation principles, whereby elements are continuously introduced and deleted to ensure core overlap.

The particle motion equation is solved in parallel to the flow equations using an Euler predictor-corrector scheme and by employing sub-stepping. The particle timestep is determined as a function of the flow and particle time scales, that is, as a function of the Stokes number.

Results

Results from collision scenario I indicate that for a given set of fluid conditions and a given particle volume fraction, collisions are maximized at intermediate Stokes numbers. This is an important finding particularly in light of the fact that particle dispersion is also maximized under these conditions [1]. It appears that the number of collisions becomes significant at volume fractions of the order of 10^{-3}-10^{-4}. This suggests that the assumption of negligible collisions made in current two-way models may be questionable. Most of the collisions occur at the outskirts of the vortical structures as indicated in Fig.1a. Increasing the particle volume fraction increases the number of collisions according to a power law with an exponent of ~4/3.

Coagulation of particles (scenario II) appears to have a substantial impact on the evolution of the dispersed phase for the cases where significant number of collisions are experienced under scenario I. In these cases, coagulation results in a substantial reduction of the number of collisions as shown in Fig.1b. Furthermore the locus of the collisions shifts drastically to different spatial locations. A consequence of coalescence is that the dispersed phase shifts from being monodisperse to being polydisperse. This results in enhanced dispersion as coalesced particles, which have larger inertia (higher St), tend to be centrifuged further into the free streams than the smaller initial particles. The impact of particle coalescence on dispersion is quantified in Fig.2.

The preliminary results described above are currently being investigated in more detail. In addition, the case of elastic collisions is being developed to help provide a more general assessment of the impact of particle collisions on the evolution and dispersion of the particle phase.

References

1. Crowe, C.T., Troutt, T.R. and Chung, J.N., "Numerical Models for Two-Phase Turbulent Flows," *Annu. Rev. Fluid. Mech.*, **28**, pp.11-43, 1996.
2. Elghobashi, S., "On Predicting Particle-Laden Turbulent Flows," *Applied Scientific Research*, **52**, pp.309-329, 1994.
3. Elghobashi, S. and Truesdell, G.C., "On the two-way interaction between homogeneous turbulence and dispersed solid particles: I turbulence modification," *Physics of Fluids*, 5(7), pp.1790-1801, 1993
4. Glen, H. and Marshall, J.S., "A Lagrangian Vorticity Method for Two-Phase Particulate Flows with Two-Way Phase Coupling," Journal of Computational Physics, 148, pp.169-198, 1999.

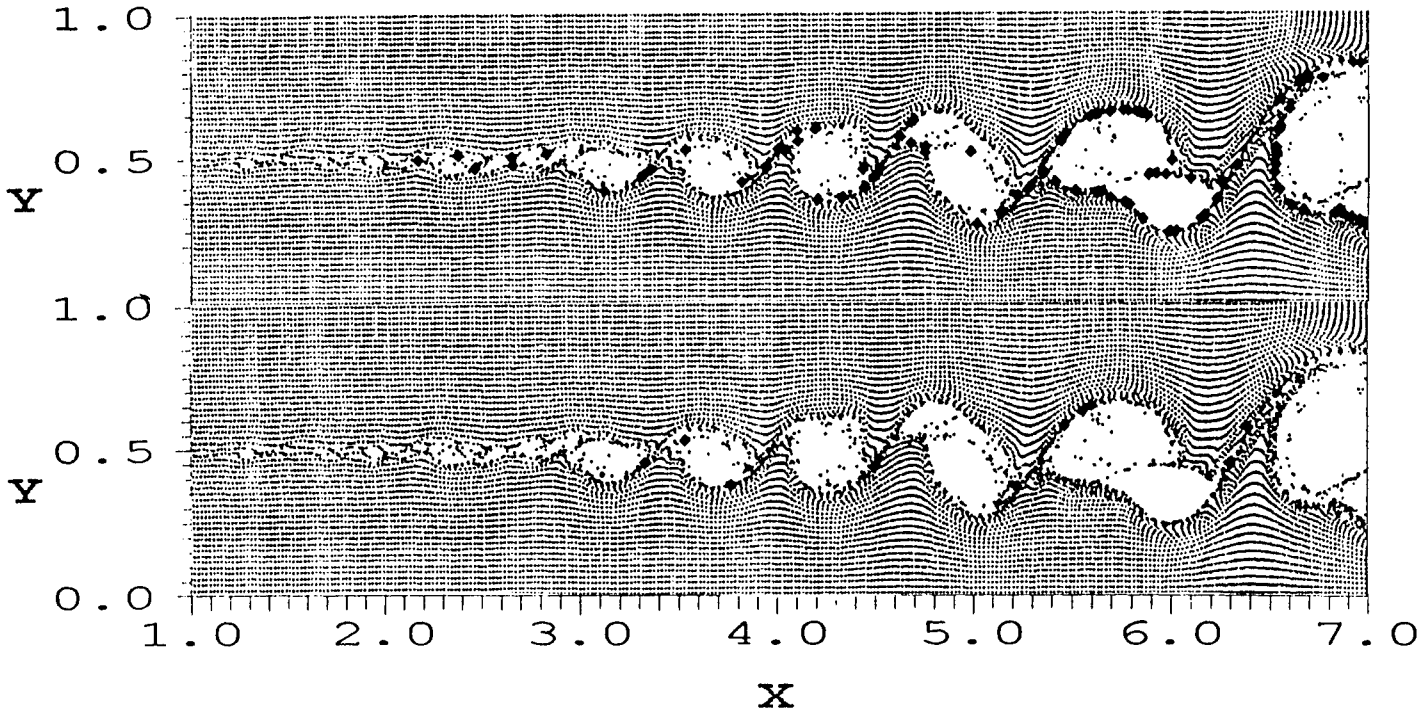


Figure 1. Instantaneous particle field and collision locations in the absence (top) and presence (bottom) of coalescence. Small empty symbols indicate the particle locations, where large full symbols the locations where collisions are experienced. The volume fraction is $\Phi_p=5x10^{-4}$ and the Stokes number is St=1.13.

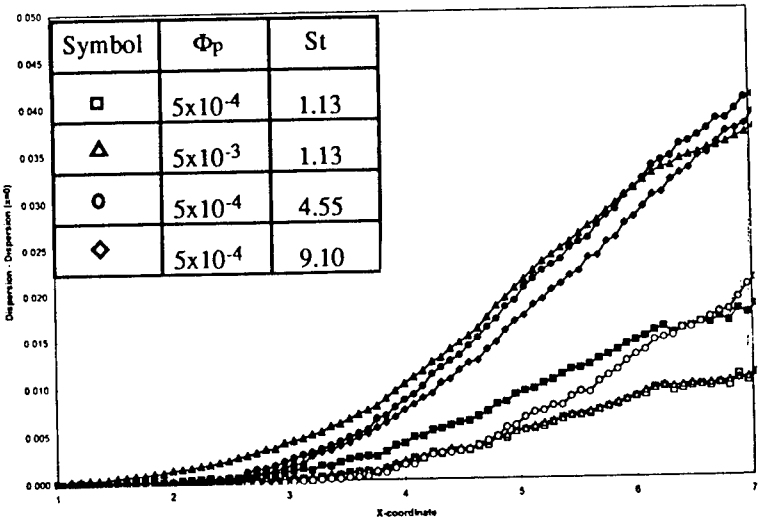


Figure 2. Impact of coalescence on particle dispersion. Empty/full symbols indicate cases without/with coalescence. The volume fractions and Stokes numbers are indicated.

EFFECTS OF PRESSURE, MOLECULAR WEIGHT AND OXYGEN POTENTIAL ON HYDROCARBON DROPLET GASIFICATION AND COMBUSTION CHARACTERISTICS UNDER SUPERCRITICAL PRESSURE ENVIRONMENTS

Yaw D. Yeboah, Jason X. Nie and Kofi B. Bota
Department of Engineering
Clark Atlanta University
Atlanta, GA 30314
e-mail: yyeboah@cau.edu

A novel and versatile droplet experimental setup has been developed at Clark Atlanta University, which consists of a liquid pressurizing and transfer system, a high pressure/temperature chamber, a droplet formation, release and ignition system, and a high speed imaging system. The setup provides quiescent or convective environments under supercritical pressure and temperature conditions. The tests of quiescent environment droplet gasification and convective environment droplet combustion of several different alkane hydrocarbon fuels from hexane (C6) to decane (C10) were conducted under sub- and supercritical pressures with the setup. Specifically, the gasification rates of 1.5-mm-diameter suspended droplets were measured under different conditions. The characteristics of a free-drop non-combusting droplet (~1.5 mm diameter) and a free-drop combusting droplet were studied using a high-speed image system. The results show that both the system pressure and the molecular weight of hydrocarbon fuels have significant effects on the characteristics of droplet gasification and combustion. The gasification rate of a suspended hydrocarbon droplet decreased with the increase of the hydrocarbon molecular weight under a fixed temperature and pressure condition, but it reached its maximum value at the supercritical pressure of each compound. The oscillatory deformation of a free-drop droplet, the buoyancy effects and flame propagation of a combusting free-drop droplet were directly influenced by the system pressure. At the supercritical pressure of decane, the falling rate of its free-drop droplet reached its maximum. On the other hand, the gasification rate of a droplet proportionally decreased with the molecular weight of the hydrocarbon that formed the droplet under both sub- and supercritical pressure conditions. As the molecular weight of hydrocarbons and the system pressure increased, the ignition of the free-drop droplets became more difficult, the combustion rates of the droplets decreased, and the flames of the combusting free-drop droplets became less stable. Increasing the system's oxygen partial pressure led to enhanced ignition, combustion rate and flame stability of the free droplets.

INTRODUCTION

Droplet and spray combustion dynamics play critical roles in the operation of liquid rockets, advanced gas turbines, and diesel engines. Because of their direct relation to practical spray combustion devices, the behaviors of liquid droplets in environments at supercritical pressure and temperatures under normal and microgravity conditions have long been of important research interest. About three decades have passed since the first experimental investigation of free droplet combustion under microgravity was presented by Kumagai and his co-workers [1]. Since then, extensive research has been conducted. However, due to the difficulties involved in conducting droplet combustion experiments, many questions still remain unanswered. One of the experimental difficulties is the ignition of a free droplet without disturbing its shape and movement. Kumagai et al [2] used an electrical spark to ignite a suspended droplet at ambient pressure; even so the electric spark still had some effect on the droplet's shape. The most recent and detailed work was conducted by Litchford and his co-workers [3]. Litchford *et al* used a pre-heated gas jet that came from the bottom of the combustor to ignite the suspended droplet through convective heating. During the ignition process, the droplet was deformed by the aerodynamic force of the hot flow.

The droplet formation and release under high pressure and/or high temperature are also a difficult problem for droplet study. Litchford *et al* [3] and Kumagai *et al* [4] used a tiny tube to transfer the liquid fuel to a metal/quartz wire frame which was used for the droplet suspension. Because of the surface tension between the

tube and the liquid, the droplet was difficult to transfer to the suspension wire, and the transferred droplet size was difficult to control. Further, after the droplet was transferred to the suspension wire, it was more difficult to release to a free droplet [2].

EXPERIMENTAL

Materials: Analytical grades of hexane, heptane, decane and tetradecane were used for this study. Some physical data of the hydrocarbons are listed in Table 1.

Table 1 Some physical properties of selected hydrocarbons

Compound	Molecular Weight	Critical Temp [5]	Critical Pressure [5]	
		(°C)	MPa	Psi
Hexane (C6H14)	86	507.7	3.010	436.6
Heptane (C7H16)	100	540.3	2.756	399.7
Decane (C10H22)	142	617.7	2.104	305.2
Tetradecane (C14H30)	198	693.0	1.62	235.0

Experimental Set-up: The experimental set-up consisted of a liquid-fuel supply system, a gas pressure-control system, a droplet formation system, a high-pressure chamber, an electrical igniter, and an intensified high-speed CCD video system. The detail information was published in Bai et al (1988).

Liquid Fuel Supply System: The liquid fuel supply system consisted of a liquid-fuel reservoir, and a high pressure liquid pump (Eldex Laboratories, Inc., Model B-100-s). The liquid pump operated up to 1500 psi at flow rates from 0 to 150 mL/min. The liquid was transferred by stainless steel tubing. The flow rate was adjusted by the liquid pump and an inlet needle valve between the system and the reaction chamber.

Droplet Formation and Release System: The droplet system developed at CAU consisted of a 200 × 1-mm-o.d. ceramic tube, which had four 0.2-mm-i.d. holes in its axial direction, and a thermocouple [6]. At the position of 30 mm from one end, the wall of the ceramic tube was cut to expose two of the four holes. The thermocouple's two wires were inserted into the two holes of the ceramic tube, and introduced out from the two cuts on the tube wall, where the tip of the thermocouple was left about 10 mm from the end of the ceramic tube. The ceramic tube was then inserted into a 1/8" stainless steel tube that also had two cuts on its wall for the thermocouple wire to go through. The cuts were sealed by high temperature cement. The stainless steel tube was vertically mounted on the top of the combustor, while the ceramic tube was connected to 1/16 stainless steel tubing of the liquid feeding system by a stainless steel union. The pressurized liquid fuel was introduced to the other two unused holes of the ceramic tube. The fuel exited out of the other end and formed a 1.5-mm-dia droplet at the tip of the thermocouple. The rate of a droplet formation was controlled by the liquid flow rate.

High Pressure Chamber: The chamber was cylindrical, which had a test section of a 450 (high) × 95 (dia.) mm, with four quartz windows of 90 (high) × 38 (wide). The chamber was pressurized by a cylinder gas.

Electrical Ignitor: The ignitor consisted of a filament and power supply. The filament was made from a coiled 0.8 mm dia. platinum wire, and was wound into a 4-mm-i.d. ring, which was mounted 20 mm below the tip of the thermocouple. The ignitor ring was carefully aligned so that the free droplet from the thermocouple would pass through without touching the ring [6]. The ignitor was heated by alternative currency. The temperature of the ignition filament could be controlled from ambient to 1400 °C by adjusting the supplying voltage. By supplying 7 V of the a.c. power, the ignitor temperature was found to be about 800 °C.

Optical Measurement System: The optical measuring system consisted of a micro lens (Micro-Nikkor, 200 mm, 1:4, Nikkor) and a high-speed image system (Kodak). The imaging system included an EktaPro Intensified

Imager and an EktaPro Hi-Spec Processor. All of the images were continuously taken at the speed of 1000 frame pictures per second (fps) with the exposure time of ~30 μs.

Experimental Procedure: The experiments were conducted as follows: (1) The combustion chamber with gas (air/N_2) was pressurized to a desired value. (2) The liquid pump was started, and the liquid fuel was pressurized. (3) For the gasification rate measurements, a suspended droplet was used, and the procedure was as follows: the inlet needle valve on the liquid feeding line was opened, and the flow rate was carefully adjusted until a droplet hung on the tip of the thermocouple; the needle valve was quickly closed; the droplet image was recorded by the video system and the temperature change was measured through the thermocouple on which the droplet was suspended. (4) For the combustion test, a free-drop droplet was used. When a droplet had formed at the tip of the thermocouple, the liquid flow rate was carefully increased to have the droplet drop. The video system and the ignitor were then turned on. While a free-drop droplet was falling through the ignitor's filament ring, it was ignited. The burning droplet continued the downward fall or floated backward (i.e. upward) according to the system pressure. The whole process was recorded by the high-speed video system and analyzed.

Experiments were carried out at system pressures from 14.7 to 1200 psi, which covered sub and supercritical pressure of all of the hydrocarbons tested.

RESULTS AND DISCUSSIONS

The tests of quiescent environment droplet gasification and convective environment droplet combustion of several different alkane hydrocarbon fuels from hexane (C6) to tetradecane (C14) were conducted under sub- and supercritical pressures. Specifically, the gasification rates of 1.5-mm-diameter suspended droplets were measured under different conditions. The experimental results indicated that the gasification rate of a suspended droplet under a fixed temperature and pressure condition decreased as the molecular weight (i.e. the number of carbons) of the hydrocarbons increased from hexane to heptane to decane. However, the gasification rate of the suspended droplet for hexane, heptane and decane reached their maximum value at their own supercritical pressure of each compound.

The characteristics of a free-drop non-combusting droplet (~1.5 mm diameter) and a free-drop combusting droplet were studied using a high-speed image system. The results show that both the system pressure and the molecular weight of hydrocarbon fuels had significant effects on the characteristics of droplet gasification and combustion. The oscillatory deformation of a free-drop droplet, the buoyancy effects and flame propagation of a combusting free-drop droplet were directly influenced by the system pressure. At the supercritical pressure (300 psi), the non-combusting free-drop droplet of decane reached its maximum falling rate of 4.23 m/s. When the pressure moved from the supercritical pressure to either lower or higher pressure, the falling rate of the droplet proportionally decreased. As the system pressure decreased to 200 psi and 14.7 psi (ambient), the falling rate of the droplet decreased to 3.97 and 2.15 m/s, respectively. As the system pressure increased to 400 and 600 psi, the falling rate decreased to 4.09 and 3.28 m/s, respectively.

On the other hand, the gasification rate of a droplet proportionally decreased with the molecular weight of the hydrocarbon that formed the droplet under both sub- and supercritical pressure conditions. As the molecular weight of hydrocarbons and the system pressure increased, the ignitions of their free-drop droplets became more difficult, the combustion rates of the droplets decreased, and the flames of the combusting free-drop droplets became less stable. As shown in Table 2, all of the free-drop droplets of hexane were ignited under the system pressure from ambient (14.7 psi) to 1200 psi. The power needed for the ignition proportionally increased from 7.0 to 9.0 V as the system pressure increased from ambient to 1200 psi. The increase of the power required for the ignition may be caused by two factors. One factor is the decrease of the ignitor temperature. As the system pressure increased, the thermal conductivity of the pressured gas increased, so the ignitor's temperature decreased. This temperature decrease was observed from the color change of the heated ignitor during the experiments. The other factor is the decrease of the droplet vapor pressure with the increase of the system pressure. For liquid hydrocarbons, since only their vapor gases can be ignited and form a stable flame in the air or compressed air, the decreased vapor pressure makes the ignition and combustion more difficult.

Table 2 shows that all of the free-drop droplet of heptane were ignited under the system pressure from ambient to 1000 psi, but it needed a higher power than hexane under the same system pressure. Also, it was observed that during the experiment the free-drop droplets of hexane were ignited earlier (relative to the position

of the ignitor) than those of heptane. This should also be caused by the vapor pressure difference of hexane and heptane. As the droplet fell, a concentrated vapor sphere surrounded and moved with it. When the droplet was heated this vapor could be clearly observed from the high speed video images. Hexane's higher vapor pressure led to a larger surrounding vapor sphere that reached the ignitor earlier and was ignited earlier. The size of concentrated vapor sphere of a droplet was found to be proportionally decreased as the system pressure increased, but no have large change was observed when the system pressure passed through the hydrocarbon's supercritical pressure.

As the number of carbon atoms of a droplet hydrocarbon increased to C14 (tetradecane), its free-drop droplets were ignited in all of the system pressure range from ambient to 1000 psi but accompanied with quite different behaviors. At the ambient pressure, the free-drop droplet of tetradecane was ignited by the ignitor at the power of 7.0 V and combusted in the similar way to the droplets of hexane and heptane. As the system pressure increased to near and above the supercritical pressure of tetradecane (≥200 psi), the ignitor power needed for the ignition of the droplet quickly increased to 10 V and the combustion rate of the droplet decreased. As the system pressure was twice as high as the supercritical pressure or higher (≥600 psi), the free-drop droplet was ignited at the ignitor power of 11 V but the flame of the free-drop droplet existed only near the ignitor. As soon as the droplet passed through the ignitor, the flame went off. The free-drop droplets of decane (C10) could not be ignited under the experimental conditions, from ambient to 1000 psi of the system pressure and up to 14 V (~1400 °C) of the ignitor power. With the ignitor on, when the free-drop droplets of decane passed through the ignitor, some smoke formed at the droplet. As the system pressure increased, the formed smoke became stronger.

Table 2 The ignitor power (voltage) needed for the ignition of the free-drop droplets of several hydrocarbons under the different compressed-air system pressures

System Pressure (psi)	**Power Needed** (voltage)			
	Hexane	Heptane	Decane	Tetradecane
Ambient (14.7)	7.0	7.0	Not ignited*	7.0
200	7.0	9.0	Not ignited	10.0
240	-	-	-	10.2
300	7.5	-	Not ignited	10.2
400	8.0	10.0	Not ignited	10.4
600	9.0	10.0	Not ignited	11.0 **
800	9.0	10.3	Not ignited	11.0 **
1000	9.0	10.6	Not ignited	11.0 **
1200	9.0	-	-	-
* The free-drop droplet could be ignited at the ignitor power up to 14 V.				
**The free-drop droplet was ignited at the ignitor, but the flame went off after the droplet passed the ignitor.				

It was found that increasing the system's oxygen partial pressure led to enhanced ignition, combustion rate and flame stability of the free droplets.

REFERENCE

1. Kumagai, S.; Sakai, T. and Okajima, S.; 13th Syposium (International) on Combustion, the Combustion Institute, 1971, p.779.
2. Kumagai, S.; Sakai, T. and Okajima, S.; "Combustion of Free Fuel Droplet in A Freely Falling Chamber," p.779-785.
3. Litchford, R.; Parigger, C. and Jeng, S.; "Supercritical Droplet Gasification Experiments with Forced Convection," AIAA/SAE/ASME/ASEE 28th Joint Propulsion Conference, Nashville, TN, July 6-8, 1992, AIAA 92-3118.
4. Hara, H. and Kumagai, S.; "Experimental Investigation of Free Droplet Combustion under Microgravity," 23rd Symposium (International) on Combustion, the Combustion Institute, 1990, p.1605-1610.
5. Lide, D.R.; CRC Handbook of Chemistry and Physics, 73rd ed., CRC Press Inc., Boca Raton, FL, 1993.
6. T. Bai, J.X. Nie, Y.D. Yeboah, Z. Wang, and A. Chow, "Preliminary Study of the Liquid Droplet Combustion in Different Conditions," *Proceedings of 1998 Spring Combustion Fundamental and Applications Technical Meeting*, Central States Section of the Combustion Institute, Lexington, Kentucky, May 31- June 2, 1998.